Preprints

SECOND CONFERENCE ON SATELLITE METEOROLOGY/ REMOTE SENSING AND APPLICATIONS

May 13–16, 1986

Williamsburg, Va.

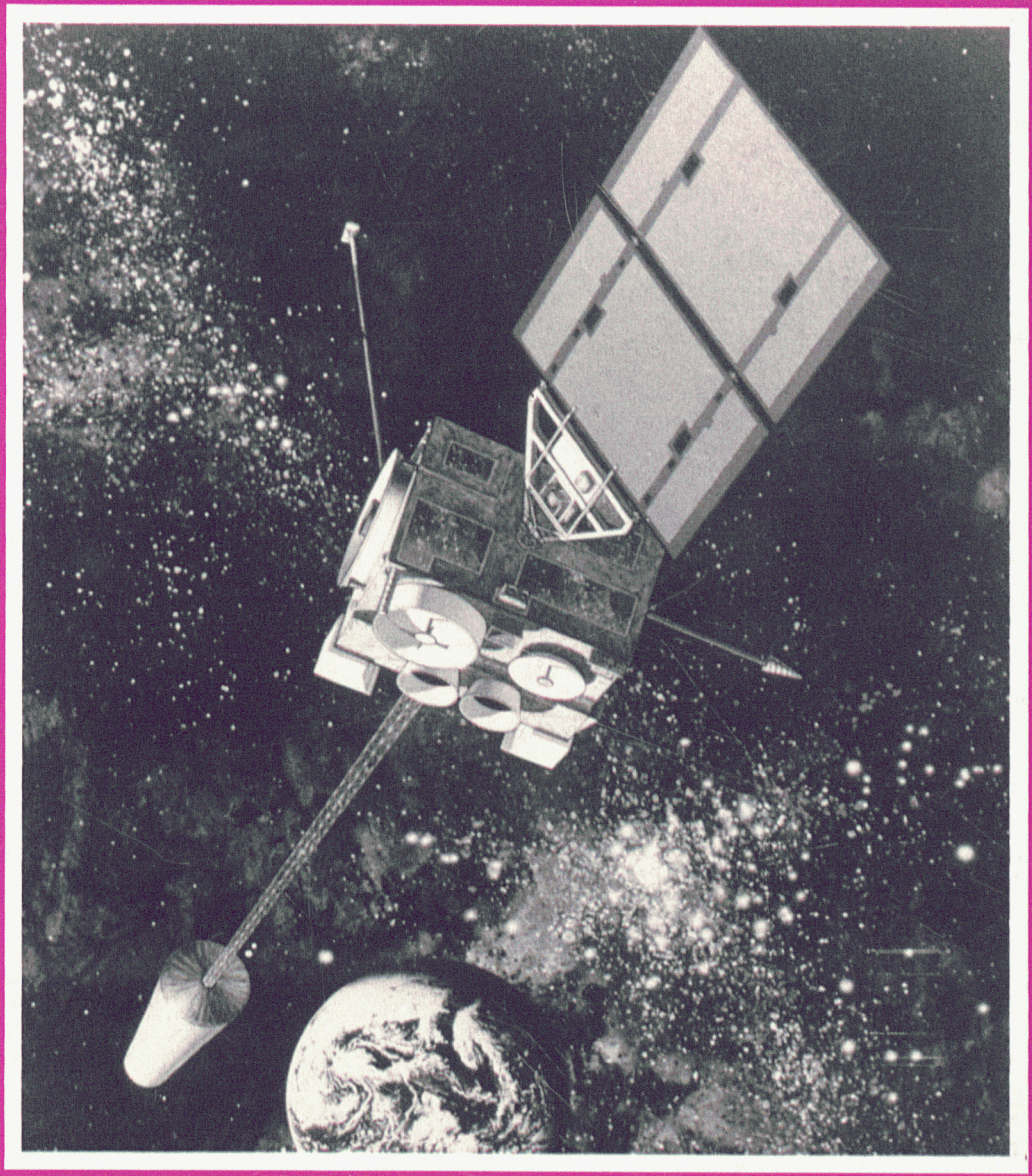

AMERICAN METEOROLOGICAL SOCIETY

AMERICAN METEOROLOGICAL SOCIETY

45 BEACON STREET, BOSTON, MASSACHUSETTS 02108

PERIODICALS—1986

	Nonmember Prices
JOURNAL OF THE ATMOSPHERIC SCIENCES (ISSN 0022-4928)	$200.00*
Volume 43, 1986. Semi-monthly	$30.00†

Original research papers and critical surveys related to the atmospheres of the earth and other planets with emphasis on the quantitative and deductive aspects of the physics and dynamics of atmospheric processes and phenomena.

JOURNAL OF CLIMATE AND APPLIED METEOROLOGY (ISSN 0733-3021)	$120.00*
Volume 25, 1986. Monthly	$15.00†

Original papers and critical surveys concerned with all aspects of climate and the socioeconomic impacts of a changing climate; and with the applications of the atmospheric sciences to operational and practical goals. Its editorial scope encompasses interdisciplinary climate studies and the full range of applications of meteorology to safety, health, industry, the economy, and general well-being of the human community.

JOURNAL OF PHYSICAL OCEANOGRAPHY (ISSN 0022-3670)	$120.00*
Volume 16, 1986. Monthly	$15.00†

Original research and survey papers devoted to the communication of knowledge concerning the physics and chemistry of the oceans and of the processes coupling the sea to the atmosphere. Papers will deal with the theoretical and observational aspects of topics such as: ocean circulation, surface waves, internal waves, inertial oscillations, oceanic turbulence, interpretive regional studies, and oceanic tides and other long-wave phenomena.

MONTHLY WEATHER REVIEW (ISSN 0027-0644)	$120.00*
Volume 114, 1986. Monthly	$15.00†

Original papers, survey papers, and synoptic and climatological summaries and features pertaining to weather observation, analysis, and forecasting.

JOURNAL OF ATMOSPHERIC AND OCEANIC TECHNOLOGY (ISSN 0739-0572)	$80.00*
Volume 3, 1986. Quarterly	$15.00†

Original research and survey papers related to instrument-system descriptions, exploratory measurement techniques, calibration methods, and performance analyses for the mainstream of atmospheric and oceanic technology, including the development of data-acquisition hardware, real-time and post-analysis software, and signal-processing techniques.

WEATHER AND FORECASTING (ISSN 0882-8156)	$80.00*
Volume 1, 1986. Quarterly	$15.00†

Original research and survey papers immediately related to operational forecasting or weather events significant to operational forecast problems including such topics as operational-forecasting techniques, applications of new analysis methods, forecasting verification studies, and case studies with direct application to forecasting.

BULLETIN OF THE AMERICAN METEOROLOGICAL SOCIETY (ISSN 0003-0007)	$60.00*
Volume 67, 1986. Monthly	$15.00†

The official organ of the Society, devoted to editorials, topical reports to members, articles, professional and membership news, conference announcements, programs, and summaries, book reviews, and Society activities.

METEOROLOGICAL & GEOASTROPHYSICAL ABSTRACTS (ISSN 0026-1130)	$450.00*
Volume 37, 1986. Monthly	$15.00†

Abstracts of current world literature in meteorology, climatology, aeronomy, planetary atmospheres, solar-terrestrial relations, hydrology, oceanography, glaciology, cosmic rays, and radioastronomy. The abstracts of books, articles, and reprints are arranged by subject categories with extensive cross-referencing. Monthly author, subject, and geographical indexes. Information on the computerized MGA data base, 1970–1985, may be obtained by writing to the Society.

Back issues of periodicals

The availability and the prices of back issues of AMS periodicals will be furnished on request.

*Subscriptions are accepted on calendar year basis only. †Surface postage and handling for foreign subscriptions.

For additional information, write to the American Meteorological Society.

TL
798
.M4
C62
2nd
1986

SECOND CONFERENCE ON SATELLITE METEOROLOGY/ REMOTE SENSING AND APPLICATIONS

May 13-16, 1986 Williamsburg, Va.

LIBRARY
APR 19 1996
N.O.A.A.
U.S. DEPT. OF COMMERCE

Sponsored by

AMERICAN METEOROLOGICAL SOCIETY

Cover Caption: Cover photo shows an artist's conception of the GOES-NEXT satellite. NOAA and NASA have selected this new three-axis stabilized satellite to serve as the Geostationary Operational Environmental Satellite in the early 1990s.

(Photo courtesy of Ford Aerospace and Communications Corporation.)

Copyright© 1986, American Meteorological Society. This copyright notice applies to only the overall collection of papers; authors retain their individual rights and should be contacted directly for permission to use their material separately. Contact AMS for permission pertaining to the overall collection.

The manuscripts reproduced in this collection of preprints are unrefereed papers presented at the Second Conference on Satellite Meteorology/Remote Sensing and Applications; their appearance in this collection does not constitute formal publication.

AMERICAN METEOROLOGICAL SOCIETY
45 Beacon Street, Boston, Massachusetts 02108-3693 U.S.A.

National Oceanic and Atmospheric Administration
TIROS Satellites and Satellite Meteorology

ERRATA NOTICE

One or more conditions of the original document may affect the quality of the image, such as:

Discolored pages
Faded or light ink
Binding intrudes into the text

This has been a co-operative project between the NOAA Central Library and the Climate Database Modernization Program, National Climate Data Center (NCDC). To view the original document contact the NOAA Central Library in Silver Spring, MD at (301) 713-2607 x124 or Library.Reference@noaa.gov.

HOV Services
Imaging Contractor
12200 Kiln Court
Beltsville, MD 20704-1387
January 26, 2009

FOREWORD

The launch of the first meteorological satellite 26 years ago generated much excitement: we had a new way to probe the atmosphere. Progress in analyzing and interpreting data from the many satellites launched since then has been rapid, and today the field of satellite meteorology is no less exciting.

It has been just two years since the first Conference on Satellite Meteorology/Remote Sensing and Applications, yet over 270 authors in over 150 papers present new results at this the Second Conference. Many of the papers report results from recently-launched satellites carrying the Earth Radiation Budget Experiment (ERBE) and the Stratospheric Aerosol and Gas Experiment II (SAGE II), which will shed light on the atmospheric composition, and their effects on the Earth's weather and climate. However, a glance at the table of contents reveals that no aspect of satellite meteorology has been neglected. Clearly the field is very active, and it promises to be no less active in the future.

The cover photograph illustrates the GOES-NEXT satellite, which will supply new data in the next decade. Hopefully this Conference will point the way toward the application of these and other satellite data to achieve a more complete understanding of the atmosphere and improved ability to predict it.

Stanley Q. Kidder
Program Committee Chairman

TABLE OF CONTENTS

		Page
FOREWORD		iii
AUTHOR INDEX		xiv
SESSION 1: TEMPERATURE, MOISTURE AND OZONE RETRIEVALS		
Chairperson: Christopher M. Hayden, National Environmental Satellite, Data, and Information Services (NESDIS)/NOAA, Madison, Wis.		
1.1	RESULTS OF TUNING THE DMSP MICROWAVE SOUNDER ESTIMATION COEFFICIENTS AT THE AIR FORCE GLOBAL WEATHER CENTER (AFGWC). L. L. Anderson, Jr., F. E. Lomax and O. B. Savaryn, AFGWC/SD, Offutt AFB, Neb.	*
1.2	THE USE OF CLASSIFICATION PROCEDURES TO IMPROVE THE ACCURACY OF SATELLITE SOUNDINGS OF TEMPERATURE AND MOISTURE. Larry M. McMillin, NESDIS/NOAA, Washington, D.C.	1
1.3	THE IMPACT OF TROPOPAUSE HEIGHT ESTIMATE ON TEMPERATURE RETRIEVALS FROM SATELLITE HEIGHT RADIANCES. Marie-Jeanne Munteanu, Goddard Space Flight Center (GSFC)/NASA, Greenbelt, Md.	*
1.4	AUTOMATIC AIR MASSES CLASSIFICATION FOR SATELLITE TEMPERATURE RETRIEVALS. P. Moine, A. Chedin, N. A. Scott, Ecole Polytechnique, Palaiseau; and G. Rochard, Centre de Météorologie Spatiale/EERM, Lannion, France	5
1.5	HIGH RESOLUTION RETRIEVALS FROM THE SATELLITES OF THE TIROS-N SERIES. A. Chedin, C. Levy, N. A. Scott and N. Husson, Ecole Polytechnique, Palaiseau, France	11
1.6	HIGHER RESOLUTION OPERATIONAL SATELLITE RETRIEVALS. A. L. Reale, D. G. Gray, M. W. Chalfant, NESDIS/NOAA, Washington, D.C.; A. Swaroop and A. Nappi, SASC Technologies, Inc., Lanham, Md.	16
1.7	MINIMUM VARIANCE SIMULTANEOUS RETRIEVAL OF TEMPERATURE AND WATER VAPOR FROM SATELLITE RADIANCE MEASUREMENTS. Henry E. Fleming, NESDIS/NOAA; David S. Crosby, The American Univ., Washington, D.C.; and Mitchell D. Goldberg, SASC Technologies, Inc., Lanham, Md.	20
1.8	AN ANALYSIS OF TEMPERATURE AND WATER VAPOR RETRIEVALS USING A MINIMUM VARIANCE SIMULTANEOUS METHOD. Mitchell D. Goldberg, and A. Swaroop, SASC Technologies, Inc., Hyattsville, Md.; Henry E. Fleming and Anthony Reale, NESDIS/NOAA, Washington, D.C.	24
1.9	DETERMINATION OF WATER VAPOR PROFILES AND TOTAL OZONE BURDEN FROM HIRS2/MSU SOUNDING DATA. D. Reuter and J. Susskind, GSFC/NASA, Greenbelt, Md.	30
1.10	AN EVALUATION OF SCAN ANGLE DEPENDENCE IN TIROS-N MICROWAVE MEASUREMENTS. Thomas L. Koehler, Univ. of Kansas, Lawrence, Kans.	*
1.11	Paper Withdrawn.	
1.12	OPTIMUM RETRIEVAL OF PRECIPITABLE WATER FIELDS FROM VAS AND SURFACE DATA. Dennis Chesters, and Louis W. Uccellini, GSFC/NASA, Greenbelt; Wayne D. Robinson, General Software Corp., Landover, Md.	36
1.13	AN EXTENSION OF THE SPLIT WINDOW TECHNIQUE FOR THE RETRIEVAL OF PRECIPITABLE WATER. Thomas J. Kleespies, Air Force Geophysics Laboratory (AFGL), Hanscom AFB, Mass.; and Larry M. McMillin, NESDIS/NOAA, Washington, D.C.	42
1.14	THE REMOTE SENSING OF OZONE FROM TOVS: A PHYSICAL INTERPRETATION OF THE REGRESSION TECHNIQUE. David S. Crosby, NESDIS/NOAA and The American Univ., Washington, D.C.	46

*Manuscript not available; if received in time, it will appear at back of book.

Page

1.15 BALLOON-BASED SOLAR OCCULTATION MEASUREMENTS OF STRATOSPHERIC CONSTITUENT PROFILES. M. P. Weinreb, L. D. Johnson, D. A. Bridges, M. L. Hill, NESDIS/NOAA; and I-Lok Chang, The American Univ., Washington, D.C.; S. Oltmans, Environmental Research Lab. (ERL)/NOAA, Boulder, Colo; A. Sanyal and W. A. Morgan, SM Systems & Research Corp., Lanham, Md. 50

SESSION 2: INTERPRETATION OF RETRIEVALS

Chairperson: Henry E. Fleming, NESDIS/NOAA, Washington, D.C.

2.1 OPERATIONAL REMOTE SOUNDER (TOVS) RETRIEVED TEMPERATURE COMPARABILITY WITH CONVENTIONAL IN SITU INSTRUMENTS. Francis J. Schmidlin, GSFC/NASA, Wallops Island, Va.; and John J. Olivero, The Pennsylvania State Univ., University Park, Pa. 54

2.2 MICROWAVE DERIVED OPERATIONAL SOUNDINGS FROM THE NOAA-6 POLAR ORBITING SATELLITE. A. Swaroop, Andrew J. Nappi, Mitchell D. Goldberg, SASC Technologies, Inc., Hyattsville, Md.; Michael Chalfant and Anthony L. Reale, NESDIS/NOAA, Washington, D.C. 57

2.3 ADJUSTMENT OF A SATELLITE-DERIVED CLIMATOLOGY OF STRATOSPHERIC TEMPERATURE FOR CHANGES IN SATELLITE OBSERVING SYSTEMS. K. W. Johnson, M. E. Gelman, A. J. Miller, F. G. Finger and R. M. Nagatani, Climate Analysis Center, National Meteorology Center (NMC)/National Weather Service (NWS)/NOAA, Camp Springs, Md. 62

2.4 SATELLITE DERIVED MOISTURE PROFILES. Andrew Timchalk, NESDIS/NOAA, Washington, D.C. 64

2.5 RELATIONSHIPS BETWEEN 6.7 MICROMETER IMAGERY AND RADIOSONDE-DERIVED PARAMETERS. Michael R. Stewart, St. Louis Univ., St. Louis, Mo.; and Henry E. Fuelberg, Florida State Univ., Tallahassee, Fla. 67

2.6 DIFFERENTIAL INVERSION AND THE LIMITS OF OBJECTIVE TEMPERATURE INFERENCING. Jean I. F. King, AFGL, Hanscomb AFB, Mass. 73

SESSION 3: DATA ASSIMILATION AND MODEL SENSITIVITY

Chairperson: Gary L. Achtemeier, Illinois State Water Survey, Champaign, Ill.

3.1 EVALUATION OF A MULTIVARIATE VARIATIONAL ASSIMILATION OF CONVENTIONAL AND SATELLITE DATA FOR THE DIAGNOSIS OF CYCLONE SYSTEMS. Gary L. Achtemeier, Harry T. Ochs, III, Stanley Q. Kidder, and Robert W. Scott, Illinois State Water Survey, Champaign, Ill. 76

3.2 APPLICATIONS OF A RECURSIVE FILTER, OBJECTIVE ANALYSIS IN THE PROCESSING AND PRESENTATION OF VAS DATA. Christopher M. Hayden, NESDIS/NOAA; and James Purser, Cooperative Institute for Meteorological Satellite Studies (CIMSS), Madison, Wis. 82

3.3 USE OF SATELLITE THERMAL WINDS IN NUMERICAL WEATHER PREDICTION. E. Kalnay and J. Pfaendtner, GSFC/NASA, Greenbelt, Md. *

3.4 ASSIMILATION OF SATELLITE MOISTURE SOUNDINGS. J. Pfaendtner, Sigma Data Services Corp.; W. E. Baker, E. Kalnay and J. Susskind, GSFC/NASA, Greenbelt, Md. *

3.5 ON THE OPTIMUM USE OF SATELLITE SOUNDINGS WITH THE NUMERICAL MODELS OF THE ISRAEL METEOROLOGICAL SERVICE. Albert Thomasell, Jr., Arnold Gruber, and Harold Brodrick, NESDIS/NOAA, Washington, D.C. *

3.6 INITIALIZATION OF A MESOSCALE MODEL WITH SATELLITE DERIVED TEMPERATURE PROFILES. Michael W. Kalb, Universities Space Research Association (USRA), Marshall Space Flight Center (MSFC)/NASA, Huntsville, Ala. 88

3.7 COUPLING OF VAS DATA ANALYSIS WITH MODELING AT THE MESOSCALE. Alan E. Lipton and T. H. Vonder Haar, Colorado State Univ., Ft. Collins, Colo. 94

*Manuscript not available; if received in time, it will appear at back of book.

Page

SESSION P4: SATELLITE METEOROLOGY AND APPLICATIONS (Poster Session)

Chairperson: Stanley Q. Kidder, Illinois State Water Survey, Champaign, Ill.

P4.1 THE NIMBUS-7 LIMS MAP ARCHIVAL TAPE. Kenneth V. Haggard, Ellis E. Remsberg and James M. Russell, III, Langley Research Center/NASA, Hampton, Va. 97

P4.2 THE USE OF STRUCTURE FUNCTION ANALYSIS TO ESTIMATE NOISE LEVELS AND THE POTENTIAL RESOLUTION OF SATELLITE MEASUREMENTS. Donald W. Hillger, James F. W. Purdom, and T. H. Vonder Haar, Cooperative Institute for Research in the Atmosphere (CIRA), Colorado State Univ., Ft. Collins, Colo. 102

P4.3 VERIFICATION OF SMALL-SCALE WATER VAPOR FEATURES IN VAS IMAGERY USING HIGH RESOLUTION MAMS IMAGERY. W. Paul Menzel, NESDIS/NOAA; Gary J. Jedlovec, CIMSS, Madison, Wis.; and Gregory Wilson, MSFC/NASA, Huntsville, Ala. 108

P4.4 PRECIPITATION EFFECTS ON MICROWAVE SOUNDING UNIT DATA. A. Nappi, A. Swaroop, SASC Technologies, Inc., Hyattsville; N. C. Grody, NESDIS/NOAA, Suitland, Md.; and J. Weinman, Univ. of Wisconsin, Madison, Wis. 114

P4.5 TROPICAL SYNOPTIC INTERPRETATION OF INTER-CHANNEL CORRELATIONS FROM TIROS-N. J. P. McGuirk, L. L. Anderson, Jr., and A. H. Thompson, Texas A&M Univ., College Station, Tex. 118

P4.6 A GLOBAL COMPARISON OF TOTAL OZONE AND TROPOPAUSE PRESSURE FIELDS. Siegfried D. Schubert and Marie-Jean Munteanu, Univ. Of Maryland, College Park, Md. 123

P4.7 COMPARISONS BETWEEN PHYSICALLY RETRIEVED TEMPERATURES FROM NOAA-7 AND NOAA-8 AND CONVENTIONAL ANALYSES OR RADIOSONDE DATA. N. A. Scott, N. Husson, A. Chedin, and J. F. Flobert, Ecole Polytechnique, Palaiseau; G. Rochard and J. Quere, Centre de Météorologie Spatiale/EERM, Lannion, France 126

P4.8 CONSTRUCTING A COHERENT LONG-TERM GLOBAL TOTAL OZONE CLIMATOLOGY FROM THE BUV, MFR, AND SBUV/TOMS DATA SETS. J. S. Ellis and F. M. Luther, Lawrence Livermore National Laboratory, Livermore, Calif. 131

P4.9 TEMPERATURE AND MINOR CONSTITUENT ABUNDANCES IN THE STRATOSPHERE AS MEASURED BY THE NIMBUS 7 STRATOSPHERIC AND MESOSPHERIC SOUNDER. F. W. Taylor, J. J. Barnett, and C. D. Rodgers, Oxford Univ., United Kingdom *

P4.10 IMPACT OF THE INITIAL SPECIFICATION OF MOISTURE AND VERTICAL MOTION ON PRECIPITATION FORECASTS WITH A MESOSCALE MODEL--IMPLICATIONS FOR A SATELLITE MESOSCALE DATA BASE. Pamela E. Mlynczak, David D. Houghton, Univ. of Wisconsin; and George R. Diak, CIMSS, Madison, Wis. 136

P4.11 ANALYSIS AND FORECAST EXPERIMENTS INCORPORATING SATELLITE SOUNDINGS AND CLOUD AND WATER VAPOR DRIFT WIND INFORMATION. Brian M. Goodman, George R. Diak, CIMSS, Madison, Wis.; and Graham A. Mills, Bureau of Meteorology, Melbourne, Australia 142

P4.12 THE EFFECT OF SYNOPTIC SITUATION ON THE IMPACT OF SATELLITE TEMPERATURE SOUNDINGS ON A FORECAST MODEL. Harold J. Brodrick, NESDIS/NOAA, Washington, D.C. *

P4.13 GLOBAL SURFACE WIND AND FLUX FIELD FROM MODEL ASSIMILATION OF SEASAT DATA. R. Atlas, A. S. Busalacchi, E. Kalnay and S. Bloom, GSFC/NASA, Greenbelt, Md.; and M. Ghil, Univ. of California, Los Angeles, Calif. 146

P4.14 APPLICATION OF SATELLITE DATA TO THE VARIATIONAL ANALYSIS OF THE THREE DIMENSIONAL WIND FIELD. Barbara A. Chance and Gary L. Achtemeier, Illinois State Water Survey, Champaign, Ill. 155

P4.15 PREPARATION OF SATELLITE SOUNDINGS FOR INSERTION IN A VARIATIONAL OBJECTIVE ANALYSIS MODEL. Stanley Q. Kidder and Gary L. Achtemeier, Illinois State Water Survey, Champaign, Ill. 159

P4.16 EASTERN PACIFIC MODEL IMPACT STUDY (EPAC) AT THE NATIONAL METEOROLOGICAL CENTER. Anthony J. Mostek and David A. Olson, NMC/NOAA, Camp Springs, Md. 164

*Manuscript not available; if received in time, it will appear at back of book.

Page

P4.17 FOREST FIRE MONITORING USING THE NOAA SATELLITE SERIES. Mike Flannigan, Canadian Forestry Service, Chalk River, Ont., Canada; and T. H. Vonder Haar, Colorado State Univ., Ft. Collins, Colo. 168

P4.18 REMOTELY SENSED ALBEDO OF SNOW-COVERED LANDS. David A. Robinson, Lamont-Doherty Geological Observatory, Columbia Univ., Palisades, N.Y. 173

P4.19 THE EFFECT OF HURRICANE GLORIA ON SEA SURFACE TEMPERATURE PATTERNS. William G. Pichel, Robert A. Warner, and Barbara A. Banks, NESDIS/NOAA; and Craig S. Nelson, NWS/NOAA, Washington, D.C. 178

P4.20 ESTIMATION OF MAXIMUM/MINIMUM TEMPERATURES FROM OPERATIONAL SATELLITE SOUNDER DATA. Paul A. Hubanks, Robbie E. Hood, and Paul A. Davis, Research and Data Systems Corp., Lanham, Md. *

P4.21 A GOES SATELLITE BASED FROST MONITORING SYSTEM-DISCUSSIONS AND RESULTS. Fausto Carlos de Almeida and Jose Aparecido Torsani, Instituto de Pesquisas Espaciais-INPE, Sao Paulo, Brazil *

P4.22 GLOBAL RADIATION ESTIMATION: A COMPARISON BETWEEN SATELLITE AND CONVENTIONAL METHODS. Elisabete Caria Moraes and Fausto Carlos de Almeida, Instituto de Pesquisas Espaciais-INPE, Sao Paulo, Brazil 183

P4.23 HAIL SIZE DIAGNOSIS FROM HRPT DATA. J. M. Bullas, Atmospheric Environment Service, Edmonton, Alta., Canada 187

P4.24 OPERATIONAL ESTIMATIONS OF HAIL DIAMETER FROM VAS-DERIVED VERTICAL SOUNDING DATA. Preston W. Leftwich, Jr., National Severe Storms Forecast Center (NSSFC), NWS/NOAA, Kansas City, Mo. 193

P4.25 DEEPENING RATE OF EXTRATROPICAL CYCLONES ESTIMATED FROM DIVERGENCE OF UPPER LEVEL CLOUD DRIFT WINDS. Gary Ellrod, NESDIS/NOAA, Washington, D.C. 197

P4.26 CLASSIFICATION OF SATELLITE IMAGES OF EXTRA-TROPICAL CYCLONES OVER THE OCEAN BY MEANS OF COMPUTERIZED PATTERN ANALYSIS. Craig R. Burfeind and James A. Weinman, Univ. of Wisconsin, Madison, Wis. 202

P4.27 ON RAINFALL RATE DELINEATION IN THE MIDLATITUDES FROM THE GOES IMAGES. A. A. Tsonis, Univ. of Wisconsin, Milwaukee, Wis. 208

P4.28 EFFECTS OF CONVECTIVE TYPE CLOUDS ON HEAVY SNOW AS VIEWED BY GOES SATELLITE IMAGERY. Samuel K. Beckman, NSSFC/NWS/NOAA, Kansas City, Mo. 212

P4.29 A CUMULUS CLOUD FIELD OBSERVED BY LANDSAT THEMATIC MAPPER. Ross N. Hoffman and Ronald G. Isaacs, Atmospheric and Environmental Research, Inc., (AER, Inc.), Cambridge, Mass. 218

P4.30 Paper Withdrawn.

P4.31 SATELLITE RAINFALL RETRIEVAL BY LOGISTIC REGRESSION. Long S. Chiu, Applied Research Corp., Landover; and Benjamin Kedem, Univ. of Maryland, College Park, Md. 224

P4.32 CLOUD TYPE CLASSIFICATION FROM SATELLITE MULTI-SPECTRAL INFRARED SOUNDER DATA. Lanning M. Penn and Paul A. Davis, Research and Data Systems Corp., Lanham, Md. *

P4.33 THE CHARACTERIZATION OF CUMULIFORM CLOUD FIELDS USING SPACE SHUTTLE PHOTOGRAPHY. J. W. Snow, D. D. Grantham, AFGL, Hanscom AFB; J. H. Willand, SASC Technologies, Inc., Lexington, Mass.; and E. M. Tomlinson, Air Weather Service, Los Angeles AFS, Calif. 228

P4.34 AN INTERMITTENT WAVE PACKET MODEL OF RAIN AND CLOUDS. J. Wilson, S. Lovejoy, and D. Schertzer, McGill Univ., Montreal, Que., Canada 233

P4.35 PRECIPITATION ESTIMATION USING PASSIVE MICROWAVE RADIOMETRY AT 92 AND 183 GHZ: AIRCRAFT RESULTS. Ida M. Hakkarinen, General Software Corp., Landover; and Robert F. Adler, GSFC/NASA, Greenbelt, Md. 237

P4.36 ON THE ESTIMATION OF ANTECEDENT PRECIPITATION INDEX FROM REMOTE SENSING MEASUREMENTS. Alberto J. Flores, Universidad de Buenos Aires, Buenos Aires, Argentina 519

*Manuscript not available; if received in time, it will appear at back of book.

Page

P4.37 REMOTE SENSING OF HYDROLOGICAL VARIABLES FROM THE DMSP MICROWAVE MISSION SENSORS. R. G. Isaacs, Y. Q. Jin, G. Deblonde, R. D. Worsham, and L. D. Kaplan, AER, Inc., Cambridge, Mass. 243

P4.38 ASSESSMENT OF MEASUREMENT ERROR DUE TO SAMPLING PERSPECTIVE IN THE SPACE-BASED DOPPLER LIDAR WIND PROFILER. S. H. Houston and G. D. Emmitt, Simpson Weather Associates, Inc., Charlottesville, Va. 523

P4.39 CONSTRAINTS ON RESOLVING MESO-ALPHA AND MESO-BETA PHENOMENA USING A SPACE-BASED DOPPLER LIDAR WIND PROFILER. G. D. Emmitt and S. H. Houston, Simpson Weather Associates, Inc., Charlottesville, Va. 526

P4.40 STRATOSPHERIC LIMB RADIANCE SIMULATIONS FOR THE HCL CHANNEL OF CLAES. J. L. Mergenthaler and J. B. Kumer, Lockheed Palo Alto Research Laboratory, Palo Alto, Calif. 250

P4.41 QUALITY INDICATORS FOR TRACE GAS CONCENTRATIONS DETERMINED FROM EARTHLIMB EMISSION SPECTRA. W. G. Uplinger and J. B. Kumer, Lockheed Palo Alto Research Laboratory, Palo Alto, Calif. 256

P4.42 SENSITIVITY OF PROPOSED NEW AVHRR CHANNEL FILTERS TO AEROSOLS, WATER VAPOR AND VIEWING ANGLE FACTORS. C. G. Justus and M. V. Paris, Georgia Institute of Technology, Atlanta, Ga. 259

P4.43 CLAES BLOCKER FILTER REJECTION REQUIREMENTS. T. C. James, J. B. Kumer, A. E. Roche, L. W. Sterritt, and W. G. Uplinger, Lockheed Palo Alto Research Laboratory, Palo Alto, Calif. 263

P4.44 RESULTS FROM 1984 AIRBORNE DOPPLER LIDAR WIND MEASUREMENTS. Jeffery Rothermel, USRA, MSFC/NASA, Huntsville, Ala. 269

P4.45 OPTICAL OBSERVATIONS OF CLOUD TOP LIGHTNING. R. J. Blakeslee and H. J. Christian, MSFC/NASA, Huntsville, Ala. *

P4.46 ANALYSIS OF STIERWALT OUT-OF-BAND TRANSMISSION SCATTERING EFFECT FOR DUAL INFRARED FILTERS SERIALLY POSITIONED AT A FOCUS. J. B. Kumer and L. W. Sterrit, Lockheed Palo Alto Research Laboratory, Palo Alto; D. L. Eisenhauer, Optical Coating Laboratory, Inc., Santa Rosa, Calif. 273

P4.47 VICARIOUS CALIBRATION OF GOES VISSR WITH SURFACE OBSERVATIONS OF CLOUD TRANSMITTANCE. M. V. Paris and C. G. Justus, Georgia Institute of Technology, Atlanta, Ga. 278

P4.48 REGIONAL TSUNAMI WARNINGS USING ENVIRONMENTAL SATELLITES. E. N. Bernard and R. R. Behn, Pacific Marine Environmental Laboratory, NOAA, Seattle, Wash. *

P4.49 Paper Withdrawn.

P4.50 COMPARISON OF DIURNAL CHARACTERISTICS OF STRATOCUMULUS CLOUDS OVER CALIFORNIA AND SOUTH AMERICA COASTS USING GOES SATELLITE DATA. Chi-Fan Shih and T. H. Vonder Haar, Colorado State Univ., Ft. Collins, Colo. 282

SESSION J1: EARTH RADIATION BUDGET EXPERIMENT (ERBE) (Joint Session)

Co-Chairpersons: F. B. House, Drexel Univ., Philadelphia, Pa.; J. A. Coakley, Jr., NCAR, Boulder; and T. H. Vonder Haar, Colorado State Univ., Ft. Collins, Colo.

J1.1 THE IMPACT OF CLOUDS UPON THE EARTH'S RADIATION BUDGET. R. D. Cess, SUNY, Stony Brook, N.Y. (Invited Papr) *

J1.2 ERBE DATA AND ITS VALIDATION. B. R. Barkstrom, Langley Research Center/NASA, Hampton, Va. (Invited Paper) J1

J1.3 INITIAL FLIGHT PERFORMANCE OF ERBE INSTRUMENT. J. E. Cooper, M. R. Luther, L. P. Kopia, B. R. Barkstrom, Langley Research Center/NASA; N. Halyo, D. A. Chrisman, Information and Control Systems, Hampton, Va.; and R. D. Cess, SUNY, Stony Brook, N.Y. J4

J1.4 SOLAR IRRADIANCE MEASUREMENTS USING THE EARTH RADIATION BUDGET EXPERIEMT SOLAR MONITORS. R. B. Lee, III, B. R. Barkstrom, M. R. Luther, Langley Research Center/NASA, Hampton, Va.; and R. D. Cess, SUNY, Stony Brook, N.Y. J5

*Manuscript not available; if received in time, it will appear at back of book.

Page

J1.5 ERBE DATA INVERSION. G. L. Smith, R. N. Green, B. A. Wielicki, J. T. Suttles and L. M. Avis, Langley Research Center/NASA, Hampton, Va. J9

J1.6 FIRST DIURNAL RESULTS FROM THE EARTH RADIATION BUDGET EXPERIMENT. E. F. Harrison, P. Minnis, D. R. Brooks, Langley Research Center/NASA, Hampton, Va. J14

J1.7 REVISED REFLECTANCE AND EMISSION MODELS FROM NIMBUS-7 ERB DATA. V. R. Taylor and L. L. Stowe, NESDIS/NOAA, Washington, D.C. J19

J1.8 ERBE BIDIRECTIONAL MODEL CONSISTENCY CHECK. D. G. Baldwin and J. A. Coakley, Jr., NCAR, Boulder, Colo. J23

J1.9 LIMB-DARKENING FUNCTIONS FOR THE EARTH-ATMOSPHERE SYSTEM OVER DESERT SCENES. D. R. Brooks, Langley Research Center/NASA, Hampton, Va. J24

J1.10 IMPLICATIONS OF BROKEN CLOUD EFFECTS ON INTERPRETATION OF ERBE SHORTWAVE SCANNER MEASUREMENTS. R. Davies, Purdue Univ., West Lafayette, Ind. *

J1.11 AN APPROACH FOR VERIFYING CLEAR-SKY RADIATION MODELS WITH ERBS SCANNER MEASUREMENTS. V. Ramanathan and P. Downey, NCAR, Boulder, Colo. J28

J1.12 COMPARISON OF ERBE INFERRED AND MODEL COMPUTED CLEAR-SKY ALBEDOS. B. P. Briegleb and V. Ramanathan, NCAR, Boulder, Colo. J32

J1.13 STUDIES OF THE EARTH'S RADIATION BUDGET USING ERBE AND METEOSAT. G. E. Hunt, C. F. England, and Y. J. Zhu, Imperial College of Science and Technology, London, United Kingdom *

J1.14 DIURNAL VARIABILITY OF EARTH RADIATION BUDGET COMPONENTS AS ESTIMATED FROM ERBS AND METEOSAT DATA FOR NOVEMBER 1984. R. S. Kandel and J. P. Duvel, Laboratoire de Météorologie Dynamique du CNRS, Palaiseau, France *

J1.15 INTERCOMPARISON OF PRELIMINARY EARTH RADIATION BUDGET SATELLITE (ERBS) FLUX ESTIMATES AND GEOSTATIONARY SATELLITE MULTI-SPECTRAL "VAS" RADIANCE MEASUREMENTS. L. D. Herman, NOAA/Systems Design and Applications Branch; W. L. Smith, CIMSS, Univ. of Wisconsin, Madison, Wisc. J34

J1.16 A COMPARISON OF OUTGOING LONGWAVE RADIATION OBTAINED FROM NOAA OPERATIONAL SATELLITE WITH THAT OBTAINED FROM ERBS. A. Gruber, R. Ellingson, S. K. Yang, Univ. of Maryland, College Park, Md.; and F. House, Drexel Univ., Philadelphia, Pa. *

J1.17 COMPARISON OF NIMBUS 7 AND ERBE RADIATION BUDGET EXPERIMENTS. G. G. Campbell and T. H. Vonder Haar, et. al., Colorado State Univ., Ft. Collins, Colo. J38

SESSION J2: STRATOSPHERIC AEROSOL AND GAS EXPERIMENT II (SAGE II) (Joint Session)

Chairperson: P. B. Russell, Ames Research Center/NASA, Moffett Field, Calif.

J2.1 SATELLITE AND AIRCRAFT MEASUREMENTS OF STRATOSPHERIC AEROSOL PARTICLES. M. P. McCormick, Langley Research Center/NASA, Hampton, Va. (Invited Paper) J42

J2.2 STRATOSPHERIC AEROSOL AND GAS EXPERIMENT (SAGE II). L. R. McMaster, Langley Research Center/NASA, Hampton, Va. J46

J2.3 INVERSION OF SAGE II MEASUREMENTS. W. P. Chu, Langley Research Center/NASA, Hampton, Va. J49

J2.4 GLOBAL DISTRIBUTIONS OF SAGE II DATA PRODUCTS. D. Rind, G. Russell and J. Lerner, Institute for Space Studies, GSFC/NASA, New York, N.Y. J52

J2.5 DISPERSION CHARACTERISTICS OF VOLCANICALLY INJECTED AEROSOL AS SEEN BY SAGE I, SAM II AND SAGE II. G. S. Kent, Science and Technology Corp., Hampton, Va. J54

*Manuscript not available; if received in time, it will appear at back of book.

Page

J2.6 MEASUREMENTS OF LOWER STRATOSPHERIC/UPPER TROPOSPHERIC WATER VAPOR BY THE SAGE II INSTRUMENT. J. C. Larson, SASC Technologies; L. R. McMaster, M. P. McCormick, and W. P. Chu, Langley Research Center/ NASA, Hampton, Va. J56

J2.7 VARIATION IN THE POLAR STRATOSPHERIC AEROSOL DURING THE SOUTHERN WINTER OF 1984. C. R. Trepte, SASC Technologies, Hampton, Va. J60

J2.8 A STUDY OF THE STRATOSPHERIC AEROSOL SIZE DISTRIBUTION UTILIZING PRELIMINARY DATA FROM SAGE II AND CORRELATIVE MEASUREMENTS. P. H. Wang, Science and Technology Corp.; T. J. Swissler, SASC Technologies; M. P. McCormick and G. K. Yue, Langley Research Center/ NASA, Hampton, Va. J64

J2.9 RETRIEVAL OF AEROSOL SIZE DISTRIBUTION MOMENTS FROM MULTIWAVELENGTH PARTICULATE EXTINCTION DATA. J. M. Livingston, SRI International, Menlo Park; and P. B. Russell, Ames Research Center/NASA, Moffett Field, Calif. J68

SESSION 5: SURFACE PARAMETER AND AEROSOL DETECTION

Chairperson: Philip A. Durkee, Naval Postgraduate School, Monterey, Calif.

5.1 A METHOD TO DETERMINE SURFACE ALBEDO FROM METEOSAT OBSERVATIONS OVER AFRICA. E. Ruprecht and G. Nacke, Universität Kiel, Kiel, Federal Republic of Germany 284

5.2 Paper Withdrawn.

5.3 MONITORING THE SPRING-SUMMER SURFACE ENERGY BUDGET TRANSITION IN THE GOBI DESERT USING AVHRR GAC DATA. Eric A. Smith, Florida State Univ., Tallahassee, Fla.; and Elmar R. Reiter, Colorado State Univ., Ft. Collins, Colo. 286

5.4 ESTIMATING DUST OPTICAL DEPTH FROM THE RADIATIVE TEMPERATURE DIFFERENCE OF 11 MICROMETER AND 3.7 MICROMETER CHANNELS. S. A. Ackerman and S. K. Cox, Colorado State Univ., Ft. Collins, Colo. 291

5.5 SATELLITE MEASUREMENTS OF PHYSICAL PROPERTIES OF SAHARAN DUST. Tae Young Lee, Applied Research Corp., Landover; Yoram J. Kaufman, Univ. of Maryland and GSFC/NASA; and Robert S. Fraser, GSFC/NASA, Greenbelt, Md. 294

5.6 AEROSOL CHARACTERIZATION WITH DUAL-WAVELENGTH RADIANCE MEASURMENTS. P. A. Durkee, Naval Postgraduate School, Monterey, Calif. 298

5.7 A GLOBAL-SCALE MODEL OF AEROSOL BACKSCATTER AT CO2 WAVELENGTHS FOR SATELLITE-BASED LIDAR SENSORS. David A. Bowdle, USRA, MSFC/NASA, Huntsville, Ala. 303

5.8 THE EFFECT OF LOCAL ADVECTION ON THE INFERENCE OF SOIL MOISTURE FROM THERMAL INFRARED RADIANCES. Peter J. Wetzel, GSFC/NASA, Greenbelt; and Robert H. Woodward, General Software Corp., Landover, Md. 307

5.9 SOIL MOISTURE ESTIMATES FROM SATELLITE INFRARED TEMPERATURES AND THEIR RELATION TO SURFACE MEASUREMENTS. Toby N. Carlson, The Pennsylvania State Univ., University Park, Pa. 313

5.10 CORRELATIONS BETWEEN REMOTELY MEASURED SOIL WATER CONTENT AND SURFACE TEMPERATURES FOR THE BEAUCE REGION, FRANCE. Eileen M. Perry, The Pennsylvania State Univ., University Park, Pa. 317

5.11 NIMBUS-7 SMMR MULTISPECTRAL PASSIVE MICROWAVE CORRELATIONS WITH AN ANTECEDENT PRECIPITATION INDEX. Gregory D. Wilke, AFGWC, Offutt AFB, Nebr.; and Marshall J. McFarland, Texas A&M Univ., College Station, Tex. 322

5.12 THE PROBLEM OF GEOPHYSICAL PARAMETER RETRIEVAL OVER COASTAL OCEANS USING SPACEBORNE PASSIVE MICROWAVE SENSING: SAMIR OBSERVATIONS OF A TROPICAL CYCLONE OVER THE COASTAL REGION. S. M. Bhandari, Indian Space Research Organization, Ahmedabad, India *

*Manuscript not available; if received in time, it will appear at back of book.

Page

5.13 MONTH-TO-MONTH VARIABILITY OF OCEAN-ATMOSPHERE LATENT HEAT FLUX AS OBSERVED FROM THE NIMBUS MICROWAVE RADIOMETER. W. Timothy Liu, Jet Propulsion Laboratory (JPL), Pasadena, Calif. 328

5.14 OBSERVATION OF EL NINO BY THE NIMBUS-7 SMMR. P. H. Hwang, P. Gloersen, GSFC/NASA, Greenbelt; C. C. Fu, D. MacMillan, D. Han and S. T. Kim, SASC Technologies, Inc., Hyattsville, Md. 333

SESSION 6: FORECASTING

Chairperson: Kenneth R. Hardy, AFGL, Hanscom AFB, Mass.

6.1 PATTERN RECOGNITION ANALYSIS OF SATELLITE DATA FOR TROPICAL CYCLONE MOTION AND INTENSITY FORECASTS. Herbert Hunter, Edwin Nunez, Llyle Barker, Nichols Research Corp., Huntsville, Ala.; and Ed Rodgers, GSFC/NASA, Greenbelt, Md. 338

6.2 FORECASTING THE MAXIMUM RAINFALL IN TROPICAL CYCLONES. James B. Lushine, National Hurricane Center, NWS/NOAA, Miami, Fla. 344

6.3 ANALYSIS OF MESOSCALE AIR MASSES WITH VAS RETRIEVALS. Raymond M. Zehr, NESDIS/NOAA, Colorado State Univ., Ft. Collins, Colo. 347

6.4 AN OBJECTIVE COMPARISON OF SEVERE LOCAL STORM PREDICTORS DERIVED FROM VAS TEMPERATURE AND DEW POINT PROFILES. David H. Kitzmiller, NWS/NOAA, Silver Spring, Md. 353

6.5 RESULTS OF THE PROFS REAL-TIME VAS PRODUCT ASSESSMENT. Daniel L. Birkenheuer and John S. Snook, Program for Regional Observing and Forecasting Services (PROFS)/ERL/NOAA, Boulder, Colo. 359

6.6 DETECTION OF MOUNTAIN-INDUCED MESOSCALE WAVE STRUCTURES WITH HIGH RESOLUTION MOISTURE IMAGERY. Gary J. Jedlovec, Univ. of Wisconsin; W. Paul Menzel, Advanced Satellite Products Projects/NOAA, Madison, Wisc.; Gregory S. Wilson, MSFC/NASA, ; and Robert J. Atkinson, General Electric Co., Huntsville, Ala. 365

6.7 Paper Withdrawn.

6.8 APPLICATIONS OF SATELLITE METEOROLOGY IN SUPPORT OF SPACE SHUTTLE OPERATIONS. B. F. Boyd, T. M. Meyers, and C. S. Funk, Eastern Space and Missile Center, Patrick AFB, Fla. 370

6.9 METEOROLOGICAL SATELLITE DATA SERVICES TO DEPENDENT WEATHER OFFICES. K. Spring, L. Neil, L. Funk, and J. Spagnol, Atmospheric Environment Service, Vancouver, B.C., Canada *

6.10 DEVELOPMENT OF MESOSCALE FORECAST PRODUCTS FROM SATELLITE MICROWAVE SOUNDING DATA. James F. W. Purdom, Donald W. Hillger, T. H. Vonder Haar, Debra A. Lubich, Patrick Laybe, CIRA, Colorado State Univ., Ft. Collins; and Carl A. Johnson, PROFS/ERL/NOAA, Boulder, Colo. 376

6.11 UPPER-TROPOSPHERIC AND LOWER-STRATOSPHERIC DYNAMICS ASSOCIATED WITH TROPICAL CYCLONES AS INFERRED FROM TOTAL OZONE MEASUREMENTS. Edward Rodgers, GSFC/NASA, Greenbelt; John Stout and Joseph Steranka, General Software Corp., Landover, Md. 382

6.12 OZONE, JET STREAKS, AND SEVERE WEATHER. Frank S. Sechrist, Millersville Univ., Millersville, Pa.; Ralph A. Petersen, Arlin J. Krueger and Louis W. Uccellini, GSFC/NASA, Greenbelt; Keith F. Brill, General Software Corp., Landover, Md. 388

6.13 TROPICAL STORM FLOSSIE AND THE ARK ROYAL STORM. S. Peteherych, AES; A. F. Davies, Consultant, Downsview, Ont.; G. Muttitt, Consultant, White Rock, B. C., Canada; and G. F. Cunningham, JPL, Pasadena, Calif. 393

SESSION 7: CLOUD OBSERVATIONS AND APPLICATIONS

Chairperson: Phillip A. Arkin, Climate Analysis Center, NMC/NOAA, Washington, D.C.

7.1 EFFECTS OF DATA RESOLUTION ON SATELLITE CLOUDINESS ESTIMATION. Chi-Fan Shih, G. Garrett Campbell and T.H. Vonder Haar, Colorado State Univ., Ft. Collins, Colo. 398

*Manuscript not available; if received in time, it will appear at back of book.

Page

7.2 NEIGHBOR-TO-NEIGHBOR OBJECTIVE SATELLITE ANALYSIS FOR THE DETERMINATION OF SURFACE AND CLOUD MEAN RADIATIVE PROPERTIES. S. K. Cox, S. A. Ackerman, and T. H. Vonder Haar, Colorado State Univ., Ft. Collins, Colo. 402

7.3 VALIDATION OF NIMBUS-7 CLOUD AND SMMR DATA. P. H. Hwang, GSFC/NASA, Greenbelt; H. Y. Yeh, D. S. MacMillan and C. S. Long, SASC Technologies, Inc., Hyattsville, Md. 405

7.4 SATELLITE AND SURFACE BASED REMOTE SENSING OF SIERRA NEVADA WINTER STORMS: APPLICATIONS TO WEATHER MODIFICATION. David W. Reynolds, U.S. Bureau of Reclamation, Auburn, Calif. 409

7.5 OBSERVATIONS OF ARC CLOUD LINES USING RESEARCH AIRCRAFT DATA, RAPID SCAN SATELLITE DATA AND DOPPLER RADAR DATA. Peter C. Sinclair, Colorado State Univ., and James F. W. Purdom, CIRA, Ft. Collins, Colo. 416

7.6 ON THE ACCURACY OF CLOUD TRACK WINDS DERIVED FROM METEOSAT-2 IR IMAGES. Johannes Schmetz and Olli Turpeinen, European Space Operations Centre, Darmstadt, Federal Republic of Germany 422

7.7 AUTOMATED MESOSCALE WINDS DERIVED FROM GOES MULTISPECTRAL IMAGERY. Robert J. Atkinson, General Electric Company; and Gregory S. Wilson, MSFC/NASA, Huntsville, Ala. *

SESSION 8: RAINFALL--MICROWAVE OBSERVATIONS

Chairperson: William E. Shenk, GSFC/NASA, Greenbelt, Md.

8.1 SCALE AND DIMENSION DEPENDENCE IN THE DETECTION AND CALIBRATION OF REMOTELY SENSED ATMOSPHERIC PHENOMENA. S. Lovejoy and S. Schertzer, McGill Univ., Montreal, Que., Canada 426

8.2 OCEANIC RAIN RETRIEVALS FROM SATELLITE PASSIVE 37 GHZ SCATTERING MEASUREMENTS. Roy W. Spencer, USRA, MSFC/NASA, Huntsville, Ala. 432

8.3 MODEL-BASED RETRIEVAL OF TROPICAL CYCLONE RAINFALL RATES USING THE NIMBUS-7 SMMR. William S. Olson, Univ. of Wisconsin, Madison, Wis. 438

8.4 A CLOUD MODEL-RADIATIVE MODEL COMBINATION FOR DETERMINING MICROWAVE TB-RAIN RATE RELATIONS. Gerard Szejwach, Robert F. Adler, GSFC/NASA, Greenbelt; Robert A. Mack, General Software Corp., Landover, Md.; Isabelle Jobard, CNRS, Palaiseau, France 444

8.5 FIELD-OF-VIEW EFFECTS IN ESTIMATING PRECIPITATION FROM SATELLITE MICROWAVE RADIANCES. Robert F. Adler, GSFC/NASA, Greenbelt; and Robert A. Mack, General Software Corp., Landover, Md. 450

8.6 INFLUENCE OF SURFACE ROUGHNESS ON MICROWAVE PASSIVE MEASUREMENTS OF RAIN OVER OCEAN. Masaharu Fujita, Radio Research Laboratory, Tokyo, Japan 456

SESSION 9: RAINFALL--VISIBLE AND INFRARED OBSERVATIONS

Chairperson: Robert F. Adler, GSFC/NASA, Greenbelt, Md.

9.1 VISIBLE AND INFRARED STRUCTURE OF FLORIDA CONVECTION AND ITS IMPLICATIONS FOR ESTIMATING RAINFALL. Andrew J. Negri and Robert F. Adler, GSFC/NASA, Greenbelt, Md. 462

9.2 PRECIPITATION DISCRIMINATION FROM SATELLITE INFRARED TEMPERATURES OVER EASTERN MONTANA. Mitchell Weiss, Research and Data Systems Corp., Lanham, Md.; and Eric A. Smith, Florida State Univ., Tallahassee, Fla. 468

9.3 STATISTICAL PROBLEMS IN RAINFALL ESTIMATES FROM RAINGAUGE, RADAR AND SATELLITE DATA. A. Bellon, and G.L. Austin, McGill Univ., Montreal, Que., Canada 473

9.4 TRANSFERABILITY OF AN IR PRECIPITATION ESTIMATION ALGORITHM. Franklin R. Robertson, MSFC/NASA, Huntsville, Ala. *

*Manuscript not available; if received in time, it will appear at back of book.

Page

9.5 ANNUAL AND INTERANNUAL VARIABILITY IN LARGE-SCALE CONVECTION OVER THE EASTERN PACIFIC AND TROPICAL SOUTH AMERICA. Phillip A. Arkin, Climate Analysis Center, NMC/NOAA, Washington, D.C. 479

9.6 VALIDATION OF THE ESOC PRECIPITATION INDEX. Olli Turpeinen and Johannes Schmetz, European Space Operations Centre, Darmstadt, Federal Republic of Germany 485

SESSION 10: NEW/FUTURE SATELLITE INSTRUMENTS

Chairperson: William W. Vaughan, MSFC/NASA, Huntsville, Ala.

10.1 LIGHTNING MAPPER: THE SENSOR AND ITS APPLICATION. H. J. Christian, MSFC/NASA, Huntsville, Ala. *

10.2 GLOBAL WIND MEASUREMENT FROM SPACE: DOPPLER LIDAR. D. E. Fitzjarrald, MSFC/NASA, Huntsville, Ala. 488

10.3 APPLICATIONS OF SPECIAL SENSOR MICROWAVE IMAGER (SSM/I) DATA. Leslie A. Brenton, Clifford R. Matsumoto, AWS/DNXA, Scott AFB, Ill. 497

10.4 SPACE OPPORTUNITIES FOR TROPOSPHERIC CHEMISTRY RESEARCH. Joel S. Levine, James M. Hoell, Langley Research Center/NASA, Hampton, Va.; and Robert J. McNeal, NASA Headquarters, Washington, D.C. 500

10.5 HIS - REMOTE SENSING FROM THE NASA U-2 AIRCRAFT. W. L. Smith, H. Revercomb, CIMSS; H. B. Howell, H. M. Woolf, NESDIS/NOAA, Madison, Wis.; D. LaPorte, Santa Barbara Research Corp., Santa Barbara, Calif.; H. Buijs, J. N. Berube, BOMEM, Inc., Ville de Vanier, Que., Canada; F. Murcray and D. Murcray, Univ. of Denver, Denver, Colo. *

10.6 INFRARED IMAGING AND SOUNDING FROM A GEOSTATIONARY BODY STABILIZED SPACE CRAFT. William E. Shenk, GSFC/NASA, Verner E. Suomi Univ. of Wisconsin, Fritz von Bun, (NASA Hq.); Forrest Hall, Wayne Esais and Marvin Maxwell (GSFC/NASA). 503

10.7 IDEAS FOR A FUTURE EARTH OBSERVING SYSTEM FROM GEOSYNCHRONOUS ORBIT. William E. Shenk, GSFC/NASA; Fritz Von Bun, NASA HQ., Washington, D.C.; Verner E. Suomi, Univ. of Wisconsin, Madison, Wisc.; Forrest Hall, Wayne Esais, and Marvin Maxwell, GSFC/NASA, Greenbelt, Md. 508

10.8 PASSIVE MICROWAVE RADIOMETER EXPERIMENT FOR GOES-NEXT. Thomas H. Vonder Haar, Colorado State Univ., Ft. Collins, Colo.; William E. Shenk, GSFC/NASA, Greenbelt, Md.; and Donald W. Graul, Ford Aerospace and Communications Corp., Palo Alto, Calif. 514

Please Note: In an attempt to save space in the Table of Contents and the conference program, multiple authors have been grouped according to affiliation. For correct order, please refer to the paper.

*Manuscript not available; if received in time, it will appear at back of book.

AUTHOR INDEX

		Paper	Page
A	Achtemeier, Gary L.	3.1	76
		P4.14	155
		P4.15	159
	Ackerman, S. A.	5.4	291
		7.2	402
	Adler, Robert F.	P4.35	237
		8.4	444
		8.5	450
		9.1	462
	Anderson, L. L.	P4.5	118
		1.1	*
	Arkin, Phillip A.	9.5	479
	Atkinson, Robert J.	6.6	365
		7.7	*
	Atlas, R.	P4.13	146
	Austin, G. L.	9.3	473
	Avis, L. M.	J1.5	J9
B	Baker, W. E.	3.4	*
	Baldwin, D. G.	J1.8	J23
	Banks, Barbara A.	P4.19	178
	Barker, Llyle	6.1	338
	Barkstrom, B. R.	J1.2	J1
		J1.3	J4
		J1.4	J5
	Barnett, J. J.	P4.9	*
	Beckman, Samuel K.	P4.28	212
	Behn, R. R.	P4.48	*
	Bellon, A.	9.3	473
	Bernard, E. N.	P4.48	*
	Berube, J. N.	10.5	*
	Bhandari, S. M.	5.12	*
	Birkenheuer, Daniel L.	6.5	359
	Blakeslee, R. J.	P4.45	*
	Bloom, S.	P4.13	146
	Bowdle, David A.	5.7	303
	Boyd, B. F.	6.8	370
	Brenton, Leslie A.	10.3	497
	Bridges, P. A.	1.15	50
	Briegleb, B. P.	J1.12	J32
	Brill, Keith F.	6.12	388
	Brodrick, Harold	3.5	*
		P4.12	*
	Brooks, D. R.	J1.6	J14
		J1.9	J24
	Buijs, H.	10.5	*
	Bullas, J. M.	P4.23	187
	Burfeind, Craig R.	P4.26	202
	Busalacchi, A. S.	P4.13	146
C	Campbell, G. G.	J1.17	J38
		7.1	398
	Carlson, Toby N.	5.9	313
	Cess, R. D.	J1.1	*
		J1.3	J4
		J1.4	J5
	Chalfant, M. W.	1.6	16
		2.2	57
	Chance, Barbara A.	P4.14	155
	Chang, I-Lok	1.15	50
	Chedin, A.	1.4	5
		1.5	11
		P4.7	126
	Chesters, Dennis	1.12	36
	Chiu, Long S.	P4.31	224
	Chrisman, D. A.	J1.3	J4
	Christian, H. J.	P4.45	*
		10.1	*
	Chu, W. P.	J2.3	J49
C	Chu, W. P.	J2.6	J56
	Coakley, J. A., Jr.	J1.8	J23
	Cooper, J. E.	J1.3	J4
	Cox, S. K.	5.4	291
		7.2	402
	Crosby, David S.	1.7	20
		1.14	46
	Cunningham, G. F.	6.13	393
D	Davies, Alfred	6.13	393
	Davies, R.	J1.10	*
	Davis, Paul A.	P4.20	*
		P4.32	*
	de Almeida, Fausto Carlos	P4.21	*
		P4.22	183
	Deblonde, G.	P4.37	243
	Diak, George R.	P4.10	136
		P4.11	142
	Downey, P.	J1.11	J28
	Durkee, P. A.	5.6	298
	Duvel, J. P.	J1.14	*
E	Eisenhauer, D. L.	P4.46	273
	Ellingson, R.	J1.16	*
	Ellis, J. S.	P4.8	131
	Ellrod, Gary	P4.25	197
	Emmitt, G. D.	P4.38	523
		P4.39	526
	England, C. F.	J1.13	*
F	Finger, F. G.	2.3	62
	Fitzjarrald, D. E.	10.2	488
	Flannigan, Mike	P4.17	168
	Fleming, Henry E.	1.7	20
		1.8	24
	Flobert, J. F.	P4.7	126
	Flores, Alberto J.	P4.36	519
	Fraser, Robert S.	5.5	294
	Fu, C. C.	5.14	333
	Fuelberg, Henry E.	2.5	67
	Fujita, Masaharu	8.6	456
	Funk, C. S.	6.8	370
	Funk, L.	6.9	*
G	Gelman, M. E.	2.3	62
	Ghil, M.	P4.13	146
	Gloersen, P.	5.14	333
	Goldberg, Mitchell D	1.8	24
		2.2	57
		1.7	20
	Goodman, Brian M.	P4.11	142
	Grantham, D. D.	P4.33	228
	Graul, Donald	10.8	514
	Gray, D. G.	1.6	16
	Green, R. N.	J1.5	J9
	Grody, N. C.	P4.4	114
	Gruber, A.	J1.16	*
		3.5	*
H	Haggard, Kenneth V.	P4.1	97
	Hakkarinen, Ida M.	P4.35	237
	Halyo, N.	J1.3	J4
	Han, D.	5.14	333
	Harrison, E. F.	J1.6	J14
	Hayden, Christopher M.	3.2	82
	Herman, L. D.	J1.15	J34
	Hill, M. L.	1.15	50
	Hillger, Donald W.	P4.2	102
		6.10	376
	Hoell, James M.	10.4	500
	Hoffman, Ross N.	P4.29	218

* Paper not available; if received in time, it will appear in back of book.

AUTHOR INDEX

		Paper	Page
H	Hood, Robbie E.	P4.20	*
	Houghton, David D.	P4.10	136
	House, F.	J1.16	*
	Houston, S. H.	P4.38	523
		P4.39	526
	Howell, H. B.	10.5	*
	Hubanks, Paul A.	P4.20	*
	Hunt, G. E.	J1.13	*
	Hunter, Herbert	6.1	338
	Husson, N.	1.5	11
		P4.7	126
	Hwang, P. H.	5.14	333
		7.3	405
I	Isaacs, R. G.	P4.37	243
		P4.29	218
J	James, T. C.	P4.43	263
	Jedlovec, Gary J.	P4.3	108
		6.6	365
	Jin, Y. Q.	P4.37	243
	Jobard, Isabelle	8.4	444
	Johnson, Carl A.	6.10	376
	Johnson, K. W.	2.3	62
	Johnson, L. D.	1.15	50
	Juarez, Dominick J.	10.6	503
	Justus, C. G.	P4.42	259
		P4.47	278
K	Kalb, Michael W.	3.6	88
	Kalnay, E.	3.3	*
		3.4	*
		P4.13	146
	Kandel, R. S.	J1.14	*
	Kaplan, L. D.	P4.37	243
	Kaufman, Yoram J.	5.5	294
	Kedem, Benjamin	P4.31	224
	Kent, G. S.	J2.5	J54
	Kidder, Stanley Q.	3.1	76
		P4.15	159
	Kim, S. T.	5.14	333
	King, Jean I. F.	2.6	73
	Kitzmiller, David H.	6.4	353
	Kleespies, Thomas J.	1.13	42
	Koehler, Thomas L.	1.10	*
	Koenig, Edward W.	10.6	503
	Kopia, L. P.	J1.3	J4
	Krueger, Arlin J.	6.12	388
	Kumer, J. B.	P4.40	250
		P4.41	256
		P4.43	263
		P4.46	273
L	LaPorte, D.	10.5	*
	Larson, J. C.	J2.6	J56
	Laybe, Patrick	6.10	376
	Lee, R. B., III	J1.4	J5
	Lee, Tae Young	5.5	294
	Leftwich, Preston W., Jr.	P4.24	193
	Lerner, J.	J2.4	J52
	Levine, Joel S.	10.4	500
	Levy, C.	1.5	11
	Lipton, Alan E.	3.7	94
	Liu, W. Timothy	5.13	328
	Livingston, J. M.	J2.9	J68
	Lomax, F. E.	1.1	*
	Long, C. S.	7.3	405
	Lovejoy, S.	P4.34	233
		8.1	426
L	Lubich, Debra A.	6.10	376
	Lushine, James B.	6.2	344
	Luther, F. M.	P4.8	131
	Luther, M. R.	J1.3	J4
		J1.4	J5
M	MacMillan, D.	5.14	333
		7.3	405
	Mack, Robert A.	8.4	444
		8.5	450
	Matsumoto, Clifford R.	10.3	497
	Maxwell, Marvin	10.7	508
	McCormick, M. P.	J2.1	J42
		J2.6	J56
		J2.8	J64
	McFarland, Marshall J	5.11	322
	McGuirk, J. P.	P4.5	118
	McMaster, L. R.	J2.2	J46
		J2.6	J56
	McMillin, Larry M.	1.2	1
		1.13	42
	McNeal, Robert J.	10.4	500
	Menzel, W. Paul	P4.3	108
		6.6	365
	MergenthalerJ. L.,	P4.40	250
	Meyers, T. M.	6.8	370
	Miller, A. J.	2.3	62
	Mills, Graham A.	P4.11	142
	Minnis, P.	J1.6	J14
	Mlynczak, Pamela E.	P4.10	136
	Moine, P.	1.4	5
	Moraes, Elisabete Caria	P4.22	183
	Morgan, W. A.	1.15	50
	Mostek, Anthony J.	P4.16	164
	Munteanu, Marie-Jean	1.3	*
		P4.6	123
	Murcray, D.	10.5	*
	Murcray, F.	10.5	*
	Muttitt, Gordon	6.13	393
N	Nacke, G.	5.1	284
	Nagatani, R. M.	2.3	62
	Nappi, A.	1.6	16
		P4.4	114
	Nappi, Andrew J.	2.2	57
	Negri, Andrew J.	9.1	462
	Neil, L.	6.9	*
	Nelson, Craig S.	P4.19	178
	Nunez, Edwin	6.1	338
O	Ochs, Harry T., III	3.1	76
	Olivero, John J.	2.1	54
	Olson, David A.	P4.16	164
		8.3	438
	Oltmans, S.	1.15	50
P	Paris, M. V.	P4.42	259
		P4.47	278
	Penn, Lanning M.	P4.32	*
	Perry, Eileen M.	5.10	317
	Peteherych, Steven	6.13	393
	Petersen, Ralph A.	6.12	388
	Pfaendtner, J.	3.3	*
		3.4	*
	Pichel, William G.	P4.19	178
	Purdom, James F. W	6.10	376
		7.5	416
		P4.2	102
	Purser, James	3.2	82

* Paper not available; if received in time, it will appear in back of book.

AUTHOR INDEX

		Paper	Page
Q	Quere, J.	P4.7	126
R	Ramanathan, V.	J1.11	J28
		J1.12	J32
	Reale, A. L.	1.6	16
		1.8	24
		2.2	57
	Reiter, Elmar R.	5.3	286
	Remsberg, Ellis E.	P4.1	97
	Reuter, D.	1.9	30
	Revercomb, H.	10.5	*
	Reynolds, David W.	7.4	409
	Rind, D.	J2.4	J52
	Robertson, Franklin R.	9.4	*
	Robinson, David A.	P4.18	173
	Robinson, Wayne D.	1.12	36
	Rochard, G.	1.4	5
		P4.7	126
	Roche, A. E.	P4.43	263
	Rodgers, C. D.	P4.9	*
	Rodgers, Ed	6.1	338
		6.11	382
	Rothermel, Jeffery	P4.44	269
	Ruprecht, E.	5.1	284
	Russell, G.	J2.4	J52
	Russell, James M., III	P4.1	97
	Russell, P. B.	J2.9	J68
S	Sanyal, A	1.15	50
	Savaryn, O. B.	1.1	*
	Schertzer, D.	P4.34	233
		8.1	426
	Schmetz, Johannes	7.6	422
		9.6	485
	Schmidlin, Francis J.	2.1	54
	Schubert, Siegfried D.	P4.6	123
	Scott, N. A.	1.4	5
		1.5	11
		P4.7	126
	Scott, Robert W.	3.1	76
	Sechrist, Frank S.	6.12	388
	Shenk, William E.	10.7	508
		10.8	514
	Shih, Chi-Fan	P4.50	282
		7.1	398
	Sinclair, Peter C.	7.5	416
	Smith, Eric A.	5.3	286
		9.2	468
	Smith, G. L.	J1.5	J9
	Smith, W. L.	J1.15	J34
		10.5	*
	Snook, John S.	6.5	359
	Snow, J. W.	P4.33	228
	Spagnol, J.	6.9	*
	Spencer, Roy W.	8.2	432
	Spring, K.	6.9	*
	Steranka, Joseph	6.11	382
	Sterrit, L. W.	P4.46	273
		P4.43	263
	Stewart, Michael R.	2.5	67
	Stout, John	6.11	382
	Stowe, L. L.	J1.7	J19
	Suomi, Verner E.	10.7	508
S	Susskind, J.	1.9	30
		3.4	*
	Suttles, J. T.	J1.5	J9
	Swaroop, A.	1.6	16
		1.8	24
		2.2	57
		P4.4	114
	Swissler, T. J.	J2.8	J64
	Szejwach, Gerard	8.4	444
T	Taylor, F. W.	P4.9	*
	Taylor, V. R.	J1.7	J19
	Thomasell, Albert, Jr.	3.4	*
	Thompson, A. H.	P4.5	118
	Timchalk, Andrew	2.4	64
	Tomlinson, E. M.	P4.33	228
	Torsani, Jose Aparecido	P4.21	*
	Trepte, C. R.	J2.7	J60
	Tsonis, A. A.	P4.27	208
	Turpeinen, Olli	7.6	422
		9.6	485
U	Uccellini, Louis W.	1.12	36
		6.12	388
	Uplinger, W. G.	P4.41	256
		P4.43	263
V	Von Bun, Fritz	10.7	508
	Vonder Haar, T. H.	J1.17	J38
		6.10	376
		7.1	398
		7.2	402
		3.7	94
		P4.2	102
		P4.17	168
		P4.50	282
		10.8	514
W	Wang, P. H.	J2.8	J64
	Warner, Robert A.	P4.19	178
	Weinman, J.	P4.4	114
		P4.26	202
	Weinreb, M. P.	1.15	50
	Weiss, Mitchell	9.2	468
	Wetzel, Peter J.	5.8	307
	Wielicki, B. A.	J1.5	J9
	Wilke, Gregory D.	5.11	322
	Willand, J. H.	P4.33	228
	Wilson, Gregory	P4.3	108
		6.6	365
		7.7	*
	Wilson, J.	P4.34	233
	Woodward, Robert H.	5.8	307
	Woolf, H. M.	10.5	*
	Worsham, R. D.	P4.37	243
Y	Yang, S. K.	J1.16	*
	Yeh, H. Y.	7.3	405
	Yue, G. K.	J2.8	J64
Z	Zehr, Raymond M.	6.3	347
	Zhu, Y. J.	J1.13	*

* Paper not available; if received in time, it will appear in back of book.

THE USE OF CLASSIFICATION PROCEDURES TO IMPROVE THE ACCURACY OF SATELLITE SOUNDINGS OF TEMPERATURE AND MOISTURE

May 12-16
Williamsburg, Virginia

Larry M. McMillin

National Oceanic and Atmospheric Administration
National Evironmental Satellite, Data, and Information Service
Washington, D.C. 20233

1. INTRODUCTION

Most approaches currently being used to convert satellite measurements of radiance to atmospheric parameters are based on vertically smooth relationships between temperature and radiances. These relationships typically take the form

$$T(i)-\overline{T(i)} = \sum_{j=1}^{n} C(i,j)*(r(j)-\overline{r(j)}) \qquad (1)$$

where T(i) denotes the temperature for level i, the bar denotes an average, C(i,j) denotes the retrieval coefficient for level and channel j, and r(j) denotes the measured radiance for channel j. Values of r(j) are given by the radiative transfer equation as

$$r(j) = \int_{\tau(v,s)}^{1} b(v,T)d\tau(v) \qquad (2)$$

where b(v,T) denotes the radiance at wavenumber v emitted by a blackbody at temperature T, $\tau(v)$ denotes the atmospheric transmittance between the top of the atmosphere and a given level, and $\tau(v,s)$ denotes the value at the surface. Values of C(j) change slowly with height and because values of $\tau(v)$ also change slowly with height it follows that the right hand side of Eq. (1) also changes slowly with height. As a result, solutions based on Eq. (1) reflect the broad scale features of $\overline{r(j)}-r(j)$ and the fine scale features of $\overline{T(i)}$. If the fine scale features of $\overline{T(i)}$ are in error, then the error will be carried over into T(i).

Typical solutions are based on information carried in the radiances and in the mathematical constraints imposed on the derivation of Eq.(1). These constraints limit the solution to a rather broad subset of possibilities. If meteorological constraints limit the solution to a smaller subset, knowledge of these additional constraints is not carried in the solution. Although a rigorous solution would combine the features of satellite retrievals with the features of a numerical model, a simpler approach is to use classification techniques to empirically limit the solutions to those that are observed. This approach has recently been discussed by McMillin (1985), Thompson et al. (1985), and Uddstrom and Wark (1985). These approaches use information in the observed radiances, r(j), to select values of $\overline{T(i)}$ and associated values of $\overline{r(j)}$. The improvement in $\overline{T(i)}$ is carried over into T(i).

2. TEST PROCEDURE

The evaluation is based on a collection of measured radiances matched with radiosondes. Because the evaluation is based on real data, the usual concerns about the applicability of the results is avoided. The data were collected over all latitudes and all seasons. Roughly 1/5 of the soundings come from each of 5 latitude zones (60-90 N, 30-60N, 30S-30N, 30-60S, and 60-90S) and roughly 1/4 of the soundings come from each of the four seasons. The sample started with 6000 soundings, but because they had not been screened for missing and obviously bad data, slightly over 5000 were useful. Of these, 1/5 were selected for an independent test set and 4/5 were used for a dependent training set. Samples of this size assure that coefficients derived from the training set are stable and that the results are valid. Because the sample covers all seasons and latitudes, concerns about the generality of the results should be removed. The data set could be used as a baseline to compare different retrieval methods using real, as opposed to simulated, data in addition to the use made for this paper.

Although removal of about 1/6 of the data could raise concerns about the validity of the results if the rejection were done selectively, the rejection procedures were objective. For example one of the more frequent errors concerned the tropopause pressures and temperatures reported by the radiosondes. To check for bad cases, the reported pressure was used to determine the two levels above the reported and the two below. The two above were used to define a line of temperature versus pressure and the temperature of intersection of the line with the reported pressure was noted. Two more temperatures were defined, one using the two temperatures below and one using the temperatures immediately above and below. The maximum and minimum of

these three temperatures were obtained. If the reported tropopause temperature did not lie either within the range or within ±2.5K of the extremes, the sounding was rejected. For most soundings the reported temperature was either within ±1.0K of the nearest point or differed by a large amount.

In the evaluation, the dependent set was used to define classes. Averages of these classes were used as initial profiles and retrieval coefficients were generated using the departures from these averages. The resulting coefficients were then used to retrieve temperatures using the independent set. When the data were collected, one of the things that was kept was the result of the operational retrieval procedure. This result was compared to the result using the new method.

3. HISTORY

The paper by Uddstrom and Wark (1985) served as the starting point for the effort at the National Environmental Satellite, Data, and Information Service (NESDIS). In that paper, soundings were classified by temperature, mean radiance profiles and associated covariances were generated from the resulting classes, and a Baysian classification procedure was used to select the appropriate profile. In their approach, it was necessary to integrate the radiative transfer equation to obtain the radiance profiles associated with the various temperature profiles. Calculated radiances have differed from measured values in systematic as well as random ways and methods to remove systematic effects are not always successful. This is a particular concern for a classification method because the classes are sensitive to small systematic differences in radiances. One way to avoid the problems associated with calculations is to use measured radiances that are matched with radiosondes. Results using this later approach were reported by McMillin (1986) in a meeting held in 1984.

At the same meeting, Wark (1986) reported on a method that used eigenvectors to classify soundings. In his approach, a mean temperature was determined for each profile and departures from the profile mean were obtained as was also done in Uddstrom and Wark (1985). Eigenvectors were generated from these departures and each sounding was expressed as the coefficients of the eigenvectors rather than the radiances themselves. Soundings were placed in classes that were determined by the values of the eigenvectors associated with the largest eigenvalues. An appealing feature of this approach is that the mean profiles progressed in an orderly fashion from tropical to polar as the value associated with the largest eigenvector changed. In addition, this approach did not rely on clustering. Because of this, profiles that happen to be relatively rare can be assigned to classes that match the shape better than would be the case if the classification were to be based on clustering. For these reasons, the eigenvector approach was selected over the earlier clustering method. However, the definition of the classes was still based on radiances rather than temperatures.

A suggestion that tropopause information be used to classify soundings prompted still another approach that was reported by McMillin (1985). In this approach, tropopause pressures as determined by the radiosondes were used to determine the classes. Since the range of the tropopause pressures spanned about 350 mb., and because earlier experience with the other approaches had indicated that the number of useful classes was about 35, classes of 10 mb. intervals were set up. A Bayesian classifier was generated and used to place the profiles into appropiate classes. New means were generated from these classes and used in the evaluation.

Table 1. compares the results obtained by the operational method with the results produced by the original classification which requires the observed tropopause pressure and with the results based on the reclassification using the radiance patterns. As can be seen, knowledge of the tropopause pressure is extremely useful in improving the accuracy of satellite soundings over that produced by the operation, but a large portion of the resulting improvement can be obtained by using the radiances to classify before doing the retrieval.

Table 1. Accuracies of the operational retrieval compared to results from a tropopause classification. A negative value indicates improvement.

Pressure	rms. Temperature Difference	
	Abs. Op.	Relative Tropopause
(mb.)	(K)	(K)
100	1.86	-0.10
115	1.89	-0.17
135	1.94	-0.17
150	2.01	-0.20
200	2.34	-0.44
250	2.31	-0.45
300	2.14	-0.37
350	1.95	-0.34
400	1.97	-0.38
430	1.86	-0.36
475	1.78	-0.28
500	1.79	-0.23
570	1.64	-0.12
620	1.63	-0.08
670	1.68	-0.03
700	1.78	-0.03
780	1.95	-0.09
850	2.33	-0.10

4. PROCEDURE

In the past, several combinations of methods and channel mixtures have been produced. Although the individual effects have not been evaluated some general trends have been observed. One is that the greatest increase in accuracy occurs where the channels are concentrated. Addition of other channels can decrease the accuracy. The second is that the tropopause classification is not the most accurate method for all regions of the atmosphere. Some form of the eigenvector method will have to be used.

In the eigenvector approach, radiances are converted to brightness temperatures, bT(v), and selected channels are used to calculate and average value for the profile. Values of the average, bT′, are obtained from the relation

$$bT' = (1/n) \sum_{j=1}^{n} bT(j). \qquad (3)$$

Departures from the average are determined as

$$x(j) = bT(j) - bT' \qquad (4)$$

and the eigenvectors of x are generated. The vectors of x are expanded in terms of the eigenvectors and then the coefficients of the eigenvectors associated with the four largest eigenvalues are determined. The maximum and minimum values are found and the coefficients are divided into bins of 7 for the first coefficient, 3 for the second, and 2 each for the third and fourth. Sample sizes of the various classes are shown in Table 2. Only 30 classes are populated and some of the populations are small. Table 3 shows the profiles of mean temperature for the five largest classes. The mean of the largest class is typical of tropical soundings, as should be expected. The other four are typical of higher latitudes with lower tropopause heights.

Classes with small populations cause problems in the retrieval step because the inverse of the covariance matrix is unstable. To avoid this problem in the initial evaluation, a new quantity was determined as

$$z(j) = x(j) - \overline{xc(j)} \qquad (5)$$

where $\overline{xc(j)}$ is the mean value for the class. A covariance matrix was generated as

$$cov(j,k) = \sum_{m=1}^{n} z(j) * z(k) \qquad (6)$$

where m is summed over all classes. Although a single covariance was used to simplify the initial evaluation, it will be seen that the resulting retrievals are surprisingly accurate.

The covariances generated in Eq. (6) were used to calculate regression coefficients for the relationship

$$T(i) = \overline{T(i)} + \sum_{j=1}^{n} c(i,j)(bT(j) - \overline{bT(j)}) \qquad (7)$$

where (i) denotes the level and T(i) and $\overline{bT(j)}$ are derived from the small samples. Retrieved temperatures are derived from Eq. (7).

Table 2. Sample sizes of groups as sorted by the values of the first four eigenvectors. Groups are given by classes with the first eigenvector divided into seven classes, the second into three classes, and third and fourth into two classes each.

Eigenvector 2 3 4 Class	Class for 1st Eigenvector 1	2	3	4	5	6	7
1 1 1	0	0	5	31	1	0	0
1 1 2	0	0	0	11	1	0	0
1 2 1	38	269	555	50	0	0	0
1 2 2	0	0	0	0	0	0	0
2 1 1	1	0	108	528	183	1	0
2 1 2	0	0	19	376	1226	239	2
2 1 2	2	103	578	422	5	0	0
2 2 2	0	0	14	22	0	0	0
3 1 1	0	0	0	0	0	0	0
3 1 2	0	0	0	3	176	197	14
3 2 1	0	0	0	0	0	0	0
3 2 2	0	0	0	0	0	0	0

Table 3. Profiles of mean temperature for five classes.

Pressure (mb.)	Class 3121	3221	4211	4221	5212
	Temperature (K)				
100	225.2	216.6	217.6	220.3	206.3
115	224.7	217.3	218.0	220.8	207.4
135	224.3	218.2	218.7	221.4	209.8
150	224.2	218.8	219.2	221.8	211.6
200	222.8	219.6	218.8	221.2	217.6
250	219.8	218.7	219.3	220.8	225.5
300	220.1	220.4	223.9	225.7	234.1
350	226.1	225.5	230.5	232.6	242.2
400	232.2	231.1	237.1	239.2	249.2
430	235.7	234.5	240.9	242.9	253.0
475	240.4	239.1	246.0	248.0	258.2
500	242.8	241.5	248.7	250.6	260.8
570	248.5	247.5	255.2	256.9	267.3
620	252.1	251.2	259.2	260.8	271.3
670	255.3	254.5	262.8	264.1	274.8
700	257.0	256.2	264.8	266.0	276.7
780	261.4	260.1	269.3	270.3	281.1
850	264.6	262.8	272.7	273.4	284.2
920	267.2	264.7	275.9	276.3	287.3
950	268.3	265.1	277.2	277.5	288.5
1000	270.0	265.7	279.0	278.9	290.5

5. RESULTS AND CONCLUSIONS

Some of the various combinations of levels and classifications are in process of being run. Table 4 shows differences from radiosondes for a classification based on eigenvectors and a classification derived from tropopause heights. There are other differences in the procedures so little significance should be attached to the difference between the two. However both are more accurate than the current operational method and it is clear that even with the approximations contained in this preliminary version, there is a significant gain in accuracy over the current operation. The accuracy of the result is more surprising when it is realized that they have been obtained with a set of coefficients that is constant over all seasons and latitudes. Apparently it is important to use the correct mean, but the covariance has relatively little effect on the solution.

Table 4. Accuracies of the operational retrieval compared to classification results. The eigenvector method is denoted by "eigen" and the tropopause method is denoted by "trop".

Pressure	rms. Temperature Difference		
	Abs.	Relative	
	Op.	Trop	Eigen
(mb.)	(K)	(K)	(K)
100	1.86	-0.10	0.06
115	1.89	-0.08	0.00
135	1.94	-0.10	-0.05
150	2.01	-0.15	-0.12
200	2.34	-0.21	-0.11
250	2.31	-0.09	-0.03
300	2.14	-0.17	-0.12
350	1.95	-0.14	-0.12
400	1.97	-0.15	-0.12
430	1.86	-0.14	-0.12
475	1.78	-0.10	-0.08
500	1.79	-0.11	-0.09
570	1.64	-0.09	0.03
620	1.63	-0.07	-0.05
670	1.68	-0.09	-0.06
700	1.78	-0.11	-0.06
780	1.95	-0.16	-0.15
850	2.33	-0.17	-0.16

It is also clear that the method has the potential to significantly improve the accuracy of satellite retrievals. Increases of up to 0.2K in accuracy over the current operation are observed. When this change is compared to either the current accuracy level that is slightly less than 2.0K, or to past changes in sounding accuracy (see McMillin et al. 198), the increase in accuracy is significant. When it is realised that an rms. difference from radiosondes contain errors due to radiosondes and to location and time differences in the matches; and that these differences supress the magnitude of any improvement, the increases in accuracy become very significant. In the middle troposphere accuracies of the new method approach 1.5K and and approach 2.0K in the tropopause region where soundings typically have problems.

6. REFERENCES

McMIllin, L.M., D.G.Gray, H.F.Drahos M.W.Chalfont, and C.S.Novak, 1983: Improvements in the accuracy of operational satellite soundings. J. Climate & Appl. Meteor., 22, 1948-1955.

McMillin, L.M., 1985: The use of a Bayesian classifier to retrieve tropopause heights from satellite measurements. Preprint Volume: Ninth Conf. on Probability and Statistics in Atmospheric Sciences, Va. Beach,358-359.

McMillin, L.M., 1985: Use of typical shape functions of radiance vectors in satellite retrievals. Advances in Remote Sensing Retrieval Methods (eds. A.Deepak, H.Fleming,&M.Chahine),A. Deepak Publishing, Hampton, Va.

Thompson, O.E., M.D. Goldberg, and D.A. Dazlich,1985: pattern recognition in the satellite temperature problem. J. Climate & Appl. Meteor.,24, 30-48.

Uddstrom, M.J., and D.Q. Wark, 1985: A classification scheme for satellite temperature retrievals. J. Climate & Appl. Meteor.,24,16-29.

Wark, D.Q., 1986: Temperature profiles derived from a restricted range of solutions using satellite measurements. Advances in Remote Sensing Retrieval Methods (eds. A.Deepak, H.Fleming,&M.Chahine),A. Deepak Publishing, Hampton, Va.

AUTOMATIC AIR MASSES CLASSIFICATION FOR SATELLITE TEMPERATURE RETRIEVALS

P. Moine[1], A. Chedin[1], N.A. Scott[1], and G. Rochard[2]

[1] Laboratoire de Météorologie Dynamique du CNRS
Ecole Polytechnique, Palaiseau, France

[2] Centre de Météorologie Spatiale / EERM
Lannion, France

1. INTRODUCTION

The major role of a priori information for the satellite retrieval problem is explained by the nature of observed radiances which integrate the atmospheric thermal structure over relatively thick layers. The principal use of that kind of information is here to specify the initial guess in the "3I" (Improved Initialization Inversion) procedure as accurately as possible through a pattern recognition approach.

The "3I" procedure is a physico-statistical algorithm for retrieving meteorological parameters from the satellite data of the Tiros-N series at a spatial resolution of 100 x 100 km². Accounting for the physics of the phenomena involved, this procedure explicitely takes into consideration local properties of each terrain observed, like surface elevation, surface emissivity, percentage of water, viewing angle.

Considerable effort is paid to the optimization of the initial guess solution which is retrieved owing to a large precomputed data set, the "TIGR" (TOVS Initial Guess Retrieval) data set. Created once and for all, this data set comprises for all possible observing conditions (viewing angle, surface pressure, surface emissivity) a total of 1207 atmospheric situations, covering the whole globe and resulting from a sophisticated statistical screening of about 10,000 situations, described by their respective temperature (and water vapor) profiles. Each situation in the TIGR data set is associated with corresponding synthetic TOVS (Tiros-N Operational Vertical Sounder) radiances, thus allowing for a clustering analysis through a dynamic cluster algorithm. The TOVS observations are those not contaminated by the clouds, i.e. stratospheric channels and microwave channels.

Knowledge of the air mass type observed is essential to most of the retrieval methods, physical as well as statistical, the average profile of temperature being very different in each case (tropical, mid or polar type air).

Results of this analysis have been applied to NOAA-7 observations over Europe of several relatively complex meteorological situations for which the forecast was particularly poor.

2. GENERALITIES ON THE CLUSTERING METHOD

The purpose of a clustering process is to separate the objects of a set E in disjoint classes or clusters, the element of which have some given properties in common.

There are two kinds of classification methods :

- the "hierarchical methods" : they give series of partitions in clusters which become larger and larger and propose a choice of partitions, corresponding to the different levels of the "spanning tree" ;

- the "non-hierarchical" methods : among these the "Dynamic Clusters Method" is used here. It is based upon the notion of "strong patterns" and the number (Ne) of ending clusters has to be fixed at the beginning.

3. PRINCIPLE OF THE DYNAMIC CLUSTER ALGORITHM

3.1 Constitution of "strong patterns"

The first step of the algorithm consists in the building up of starting kernels, which are made up with random drawn objects . Instead of defining a class by a single point, its gravity center, which is not necessarily an element of the set, it is defined by several objects constituting a kernel : this kernel will be more representative for the class than a gravity center.

Starting from a set L of kernels L_k ($k \leq N_e$), each object of the set E is assigned to the nearest kernel giving rise to the first partition of E.

From this partition, a new set L is given by the measure based upon a concept of a distance. The new L is a better description of the partition. Again a new partition is obtained and so on, up to a stable situation.

Let K_i be an object of E, indexed by i : $x_{i1},\ldots,x_{in}$. The distance between the object X_i and the kernel K_k is defined as follows :

$$d\ (X_i, P_k) = \sum_{X_j \in P_k} d\ (X_i, X_j)$$

where $d(X_i, X_j)$ is the distance between the two objects X_i and X_j.

The fundamental purpose of defining a distance is to induce an order on the set of couples (X_p, X_q) for any p and q. Several definitions of a distance may be used : Euclid metric, chebychev metric, Minkowsky metric, "chi-square" metric .. In the Dynamic Cluster algorithm, the distance currently used is the Euclid metric, on account of its simplicity :

$$d(X_i, X_j) = \left(\sum_{i=1}^{n} (x_{pi} - x_{qi})^2 \right)^{1/2}$$

The algorithm minimizes a criterion W(L,P) :

$$W(L,P) = \sum_{i=1}^{k} \text{Card Pi} \ [\ \text{Var Pi} + \text{Var Li} + d\ (\ \theta(\text{Pi}), \theta(\text{Li})\ )\ ]$$

where : Pi = class associated to the kernel Li,
θ(Li) = gravity center of the kernel Li
θ(Pi) = gravity center of the class Pi,
Var Li = variance of Li,
Var Pi = variance of Pi.

The final partition depends on initial choice of kernels. This is why several random drawings of initial kernels are realized : the objects, which have always been classed together constitute the "strong patterns". As a result of all the random drawings, these strong patterns are in fact the really homogeneous parts of the objects'set.

A minimum number of experiences is necessary in order that the strong patterns have a real signification. Even if the experience number is large, these strong patterns should not be numerous, relatively to the initial number of data.

3.2 Gathering of strong patterns

The second step of the algorithm consists in gathering the strong patterns according to the "loss of inertia criterion" (see below), in order to obtain the number of classes (Ne) required. A resulting partition is declared acceptable if the inertia of each class is weak and if the inertia between the classes is strong.

If we transform a partition of k (k>Ne) classes into a partition of k-1 classes, by gathering two classes, the inertia between the classes decreases.

The best way of gathering consists in putting together the two classes for which the loss of inertia is the smallest.

The loss of inertia is :

$$L_I = N_A\ d^2\ (g_A, g) + N_B\ d^2\ (g_B, g)$$

(inertia before gathering)

$$- (N_A + N_B)\ d^2\ (g_{AB}/g)$$

(inertia after gathering)

So let it be :

$$L_I = \frac{N_A\ N_B}{N_A + N_B}\ d^2\ (g_A, g_B)$$

where N_A is the number of elements of class A and N_B the number of elements of class B. g_A and g_B are the gravity centers of class A and class B, respectively. g_{AB} is the gravity center of the class obtained after gathering.

At every iteration, this "loss of inertia criterion" decreases and two classes are gathered, till we obtain the desired number of classes.

4. CLASSIFICATION OF THE SITUATIONS ARCHIVED IN THE TIGR DATA SET

The classification has been realized with all the situations of the TIGR data set. The purpose is now to find a clustering in several classes, which are featured not only by the latitude, but also by the season.

Several clusterings have been realized using the algorithm described above, according to different levels of observing conditions : ground pressure and viewing angle. Ten viewing angles are considered from nadir to a maximum value of approximately 60° which correctly sample the range of viewing angles associated with the scanning instruments on board the TIROS-N series : HIRS-2 and MSU. Eleven surface pressure are considered from 1013 mb to 725 mb.

In this set of situations, we distinguish five groups by using 2 criterions :

- latitude ℓ :
  tropical : ℓ<30° ; mid : 30°<ℓ<60° ;
  polar : ℓ>60°
- season : summer, winter.

For each of these 5 groups and each channel j, we normalize the associated brightness temperature according to :

$T(k,j) / S_i(j)$ where $T(k,j)$ is the brightness temperature of channel j for the kth situation and $S_i(j)$ is the variance of channel number j, computed with the set of brightness temperatures of class i, to which $T(k,j)$ belongs (i=1,5). Here we use six channels : HIRS-2 channels nb. 1, 2 and 3 and MSU channels nb. 2, 3 and 4, since they are not contaminated by most of the clouds. The number of ending clusters we impose at the start is five, according to the criterion of latitude and season.

For all the classification conditions (angle and surface pressure), the same results have been obtained and they are noteworthy : only 3 clusters survived, corresponding exactly to the 3 initial groups of latitude, although the number of ending clusters we impose at the beginning of the procedure is five. These 3 classes have been isolated from the very first steps of the algorithm, without any modification by the second steps. This analysis confirms the initial statistical classification of the TIGR dat set. It also provides the way of classifying any observed situation.

5. APPLICATION TO REAL OBSERVATIONS FROM NOAA-7 OVER EUROPE

Within the frame of the "3I" (Improved Initialization Inversion, Chedin et al., 1985) procedure, the preceding clustering algorithm has been applied to nine passes of NOAA-7 over Europe, ranging from September, 1983 to December, 1983.

The spatial resolution of the 3I algorithm is a compromise between the spatial resolution of the two major sounders on board the NOAA's : HIRS-2 and MSU. Retrievals are made for boxes of 2 to 4 (according to the viewing angle) HIRS-2 spots along the scan line by 3 HIRS-2 spots along the sub-orbital track. Such boxes approximately represent a surface of 100x100 km². However, in order to increase the density and check the coherence of the results, an oversampling is introduced along the sub-orbital track and one retrieval is produced every 100x30 km², two consecutive boxes sharing two scan lines (see Figure 1).

For each observation, we compute the distances between this situation and the classification clusters obtained above, the smallest distance indicating the class to which the observations belong. However, the differences in distance between the classes mid and tropical may sometimes become very small loosing their real signification. In the areas of small significance, we may either rely upon the real smallest distance criterion (whatever the number of decimals is) or require an additional criterion to be satisfied prior to assigning a given situation to such or such cluster. Taking into consideration first the large differences in variance $[S_i(j)]$ for the three final classes (typically 3K for the tropical cluster ; 5K for the mid cluster and more than 7K for the polar cluster) and second the influence of these variances on the distance definition, on the final result (for the normalization within could have been performed either larger or more restricted groups of situations in the TIGR data set), we have adopted the following scheme, which consists in slightly moderating the polar situation assignments and slightly promoting the tropical ones.

Consequently, a situation will be declared a polar one only if its distance to the polar cluster is at least 15% smaller than its distance to the mid cluster. On the contrary, a situation declared mid will be changed to tropical if its distance to the tropical cluster is less than 10% smaller than its distance to the mid cluster.

Figures 2 to 5 display the results of this scheme for two examples among the nine considered. Observations correspond to NOAA-7 passes over Europe : orbits nb. 11664, September 27, 1983 and nb. 12681, December 12, 1983.

Figures 2, 3 and 6 illustrates these results for orbit nb. 11664 : on the AVHRR picture (Fig. 2), we can easily see through the spiral-shaped zone of clouds centered on Gabes Gulf over the Mediterranean Sea, a stormy perturbation. It corresponds on the map issued from the classification (Fig. 3) to the tropical area. This area is also apparent on the map of winds (Fig. 6).

Figures 4, 5 and 7 display similar results for orbit nb. 11681 : on the AVHRR picture (Fig. 4), we can notice in the northern part of the orbit a cold front, the cold air mass coming from the arctic latitudes. It corresponds to the polar area on the classification map (Fig. 5) and can also be seen on the map of the winds (Fig. 7). In the middle of the orbit, a warm air mass is apparent on the AVHRR picture through the cloudy zone composed with a lot of cirrus. It is represented on the classification map by a mid zone. In the south of this area, within an anti cyclonic area (Azores, Spania), the sky is clear on the AVHRR picture, corresponding to tropical situations on the classification map.

6. CONCLUSION

The dynamic clusters algorithm is a statistical method, based upon the notion of "strong patterns" and the optimization of a criterion of variance. The introduction of an a priori knowledge of the clusters we try to obtain (latitude-season) allows the physical apsect of the problem to be taken into account. Applied to the TIGR data set, this coupling of physics and statistics leads to the definition of three clusters, each one having its own features.

This clustering method simply allows satellite observations from the TIROS-N series to be classified within one of the three clusters that have been identified. Now entering the 3I Inversion algorithm, this classification scheme is used to improve the initial guess retrieval procedure : instead of searching for the element within the whole TIGR set the closest to the input pattern, it will be searched within the cluster to which the input pattern belongs.

REFERENCES

Chedin, A., N.A. Scott, C. Wahiche, P. Moulinier, N. Husson and I. Cohen (1984) : The Improved Initialization Inversion ("3I") Method : a high resolution physical method for temperature retrievals from the satellites of the Tiros-N series. Conf. on Satellite Meteorology / Remote Sensing Applications. Clearwater Beach, Florida, Publ. AMS, 39-44.

Chedin, A., and N.A. Scott (1984) : Initialization of the radiative transfer equation. Inversion problem from a pattern recognition type approach. Application to the satellites of the Tiros-N series.

Fu, S.K. (Ed.) (1976) : Digital Pattern Recognition, Springer-Verlag, New-York, 206 p.

Diday (1973) : The Dynamic Clusters Method and Sequentialization in Non-Hierarchical Clustering. IRIA Lab., 14 p.

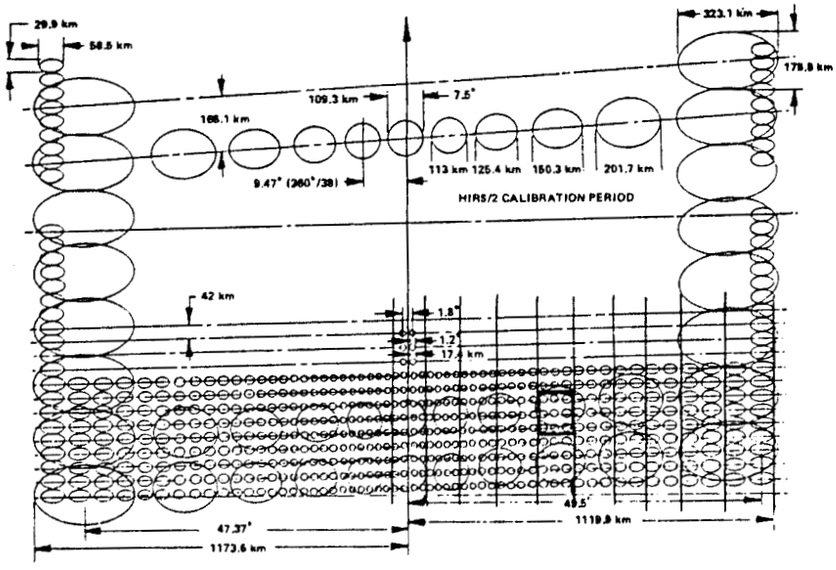

Figure 1

HIRS-2 and MSU scan patterns projected on the Earth's surface. Retrievals consisting of three scan lines and four (small viewing angles) to two (large viewing angles) HIRS spots are made for each box. There is an oversampling along the y-axis (suborbital track) : two consecutive boxes share two scan lines.

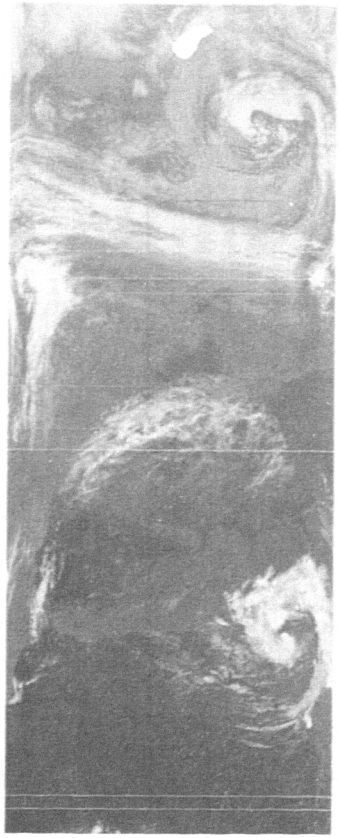

Figure 2

AVHRR picture for
NOAA-7 orbit nb. 11664,
27 September 1983

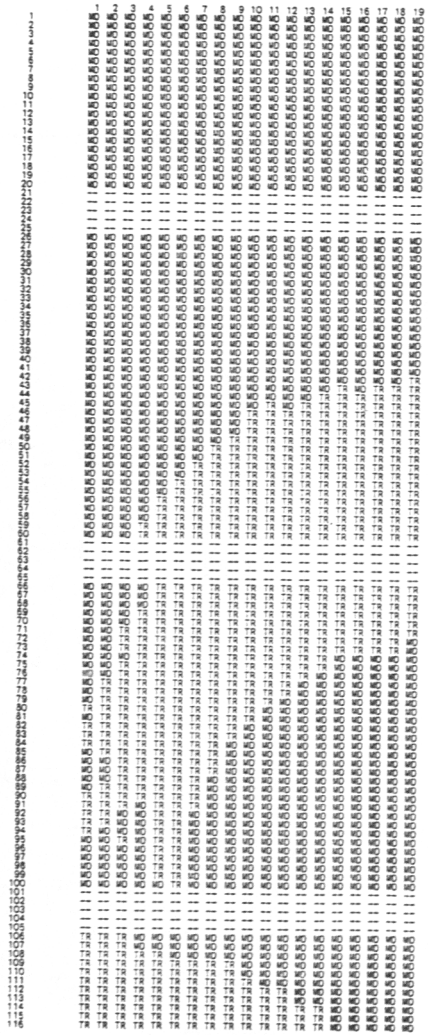

Figure 3

Results of the classification for NOAA-7 orbit nb. 11664
Vertical numbering : scan lines. Horizontal numbering :
boxes. TR : tropical latitudes. MD : mid latitude.
PO : polar latitudes.

Figure 4

The same as Figure 2
but for orbit nb. 12681

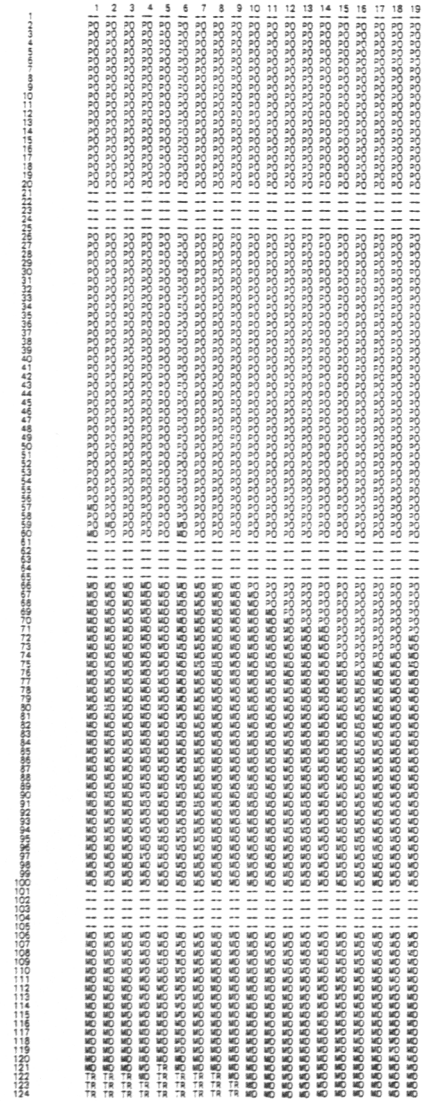

Figure 5

The same as Figure 3,
but for orbit nb. 12681

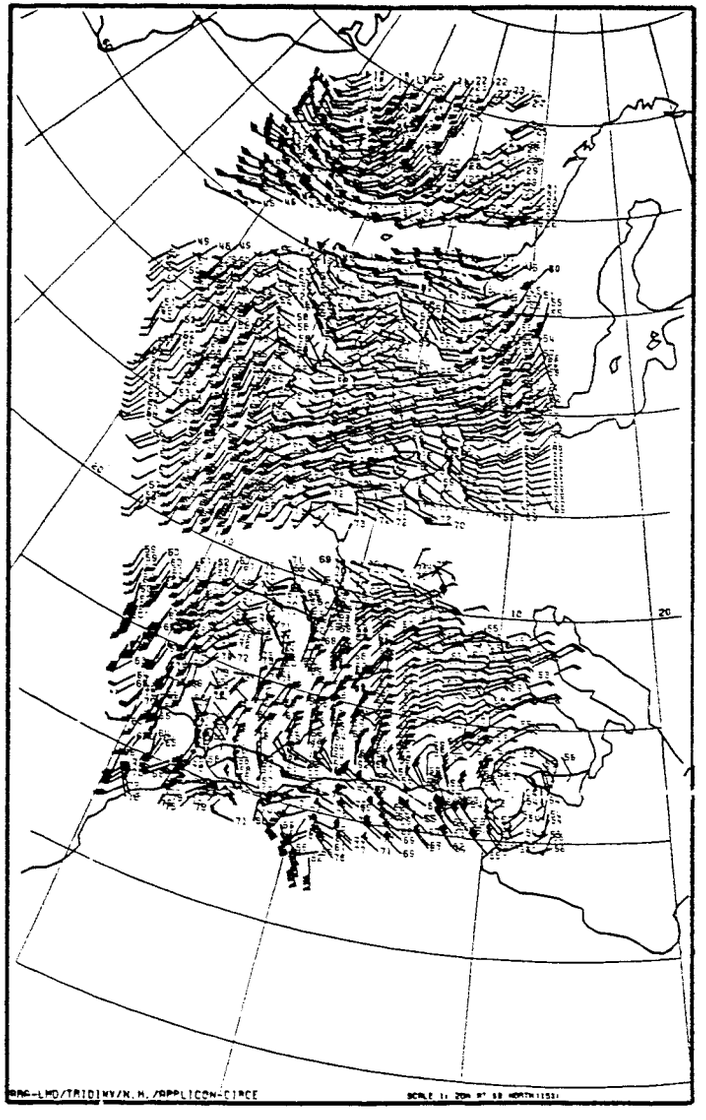

Figure 6

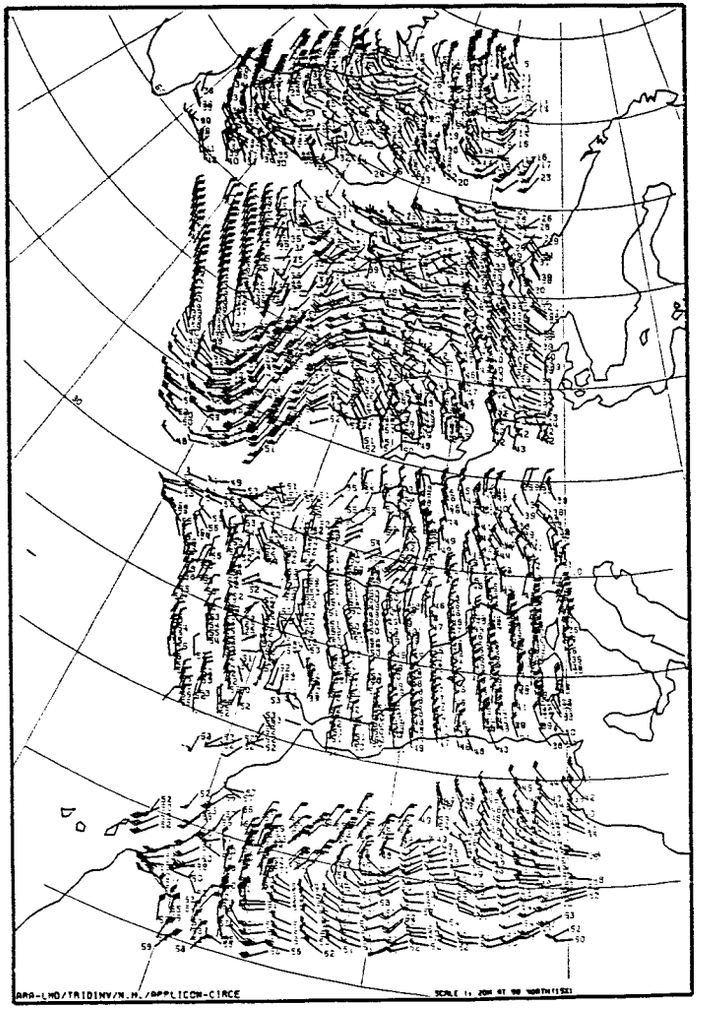

Figure 7

100-500 mb thicknesses (DAM) and thermal winds.

HIGH RESOLUTION RETRIEVALS FROM THE SATELLITES OF THE TIROS-N SERIES

A. Chedin, C. Levy, N.A. Scott and N. Husson

Laboratoire de Météorologie Dynamique du CNRS
Ecole Polytechnique, Palaiseau, France

1. INTRODUCTION

The "3I" (Improved Initialization Inversion) method for retrieving geophysical parameters from the satellites of the Tiros-N series (A. Chedin and N.A. Scott, 1983 ; A. Chedin et al., 1985) has been modified with the purpose of increasing its spatial resolution from one retrieval every box of 100 x 100 km² to one retrieval every HIRS/2 spot, roughly 30 x 30 km². This resolution is strictly achieved within clear areas and is only simulated within cloudy areas through the coupling with the MSU (microwaves) instrument which resolution is coarser. As expected from the method used to "de-cloud" the observations, the so-called "ψ-method" which consists in predicting, for each HIRS/2 spot individually, cleared HIRS/2 radiances from the microwave observations and from an "educated" data set created once and for all, the TIGR (TOVS Initial Guess Retrieval) data set, the real resolution appears to be closer to the HIRS/2 one than to that of the MSU sounder. An application to NOAA-7 observations (Alpex IOP of March 4-5, 1982) is presented and discussed in connection with the coming AMSU (Advanced Microwave Sounding Unit) experiment.

2. METHODOLOGY

The present study has been carried out using the "3I" (Improved Initialization Inversion) algorithm.

2.1 Generalities on the 3I algorithm

The 3I method has been designed for retrieving meteorological parameters from satellite vertical sounders and has already been described in some details in several publications : Chedin and Scott, 1984 ; Chedin et al., 1985). A brief survey of this method is necessary to a better understanding of the results presented here.

The 3I procedure is a physico-statistical method which relies upon an a priori knowledge of the observations (the brightness temperatures in each channel of the vertical sounder) as well as of the parameters (the atmospheric structure). This a priori knowledge is contained in a large data set, the TIGR (TOVS Initial Guess Retrieval) data set, created once and for all, and comprising for all possible observing conditions (viewing angle, surface pressure, surface emissivity) and for about 1200 atmospheric situations covering the whole globe : the transmittance profiles and associated brightness temperatures for each of the TOVS channels, the partial derivatives of these brightness temperatures with respect to such or such atmospheric parameter (Jacobian). Provided the observed brightness temperatures correspond to clear areas or have been properly "cleared" (that is to say : properly de-contaminated from the influence of the clouds), see Section 2.2, the 3I procedure follows two principal steps :

a) Retrieval of the initial guess solution through a pattern-recognition type approach. The observed cleared radiances are first used to retrieve the "best" initial guess solution in a statistical sense. The procedure makes use of the "TIGR" data set. The selected set of observed brightness temperatures is "compared" to each of the computed sets of brightness temperatures and the "closest" is retained.

b) The basis for the retrieval of the "exact" solution is a maximum estimation procedure aimed at minimizing the differences between the brightness temperatures associated with the initial guess and the observed ones. Use is made of the Jacobian associated with the retrieved initial guess, in the "TIGR" data set.

The 3I algorithm has been recently revised and improved in some minor aspects.

2.2 The ψ-method : a de-clouding algorithm

The ψ-method, designed at LMD as a part of the 3I algorithm, is based upon the availability of a good first guess solution for the vertical temperature profile.

The way the observations are decontaminated from the influence of the clouds is an essential aspect of the coupling between

infrared and microwave observations performed by the 3I method. While the procedure for retrieving the initial guess solution in the TIGR data set is direct in case of clear areas, two steps are required for not clear areas. In the first step, comparisons are made between the observations and the archived brightness temperatures in TIGR on the basis of a restricted set of channels, in principle insensitive to clouds, made of infrared stratospheric and microwave channels. From this preliminary initial guess, the cloud clearing algorithm is started based upon the ψ-method. Following this method, a clear infrared brightness temperature is obtained by adding to the initial guess value of the infrared channel considered, the difference between the observed and the initial guess values of a microwave channel , almost insensitive to clouds and peaking approximately at the same level as the infrared one. Since both respond to the same atmospheric layers, the difference in brightness temperature is small and, more importantly, almost constant for small changes in atmospheric parameters. The ψ-method is applied to HIRS/2 channels 3 to 6 and 15. Cleared brightness temperatures for channel 14 are obtained through a regression using, in particular, the previously cleared channels. The coefficients of this regression are obrained from the TIGR data set. Remaining channels are cleared after having retrieved the temperature structure and reliable cloud parameters (amount, height).

This method raises four comments :

a) Contrary to other methods which use several spots or even the entire field to eliminate the effect of clouds, the ψ-method only uses one spot and consequently avoids the assumption about horizontal homogeneity of any parameter.

b) Using the potential of the microwave observations to get information through the clouds and relying upon the "educated" data set TIGR, the ψ-method may be applied within the partially cloudy areas as well as within overcast areas, provided the microwave channels have not been significantly contaminated.

c) Combining infrared and microwaves channels, the ψ-method is better suited to instruments having similar spatial resolution. This is not the case of HIRS/2 and MSU and explains why the 3I algorithm has been adapted to boxes of several HIRS/2 spots. This will be the case of the coming TIROS-NEXT mission (HIRS/2 and AMSU) and possibly of MIMS (Meteosat Infrared and Microwave Sounder) for the 2nd generation Meteosat satellites.

d) The strong correlation between the initialization of the inversion process and the cloud clearing technique must also be pointed out : the quality of the initialization and that of the cleared brightness temperatures are directly connected.

2.3 The high resolution algorithm

To simulate, as far as possible, a sounder with a relatively high spatial resolution, both in the infrared and in the microwave, the 3I algorithm has been modified in order to increase the spatial resolution currently achieved.

Instead of performing one retrieval every 100 x 30 km², a number resulting from a compromise between the resolutions (see Fig. 1) of HIRS/2 and MSU (roughly 100 x 100 km², with an oversampling along the sub-satellite track (see Chedin et al., 1985), the present approach has consisted in making one retrieval every HIRS/2 spot, corresponding to a mean spatial resolution of 30 x 30 km². The coupling between the two sounders has been obtained by interpolating the MSU observations within each HIRS/2 spot. Accordingly, the cloud detection procedure as described in Wahiche et al. (1985) for the "standard" 3I resolution has been modified and adapted to the processing of each HIRS/2 spot. The major modifications are listed below :

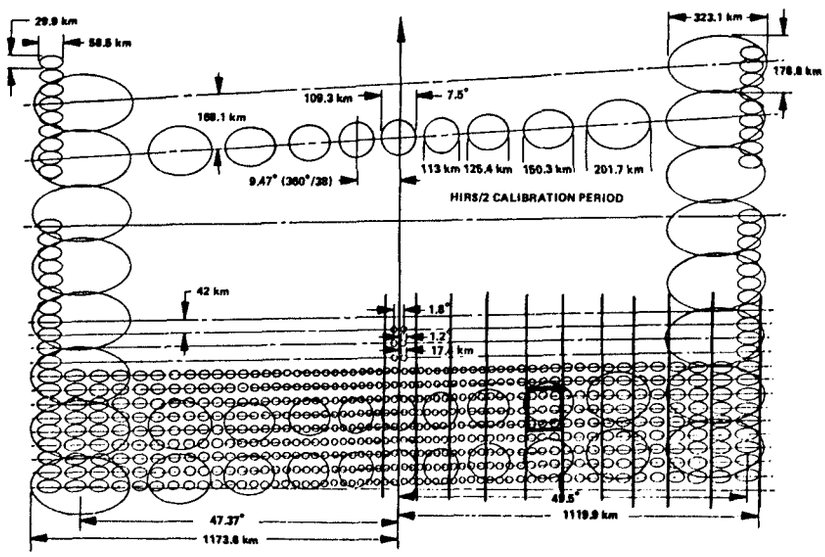

Figure 1

HIRS-2 and MSU scan patterns projected on the Earth's surface.

- the regressions used in the cloud detection algorithm are now specific of each of the three classes into which the TIGR data set is divided. Each HIRS/2 spot is assigned to one of these classes through a classification scheme (P. Moine et al., in the present extended abstracts book) ;

- the concept of "adjacent spots", which plays an important role in the cloud detection algorithm, now takes into consideration the nature of the surface : two geometrically adjacent spots, one over land and one over sea, are not finally declared "adjacent" ;

- variance tests performed over the spot within a box (the 100 x 100 km² areas) have been suppressed.

Figure 2 illustrates the results of the new algorithm for one satellite pass of the ALPEX IOP considered : orbit no. 3587, March 4, 1982 (12.05Z).

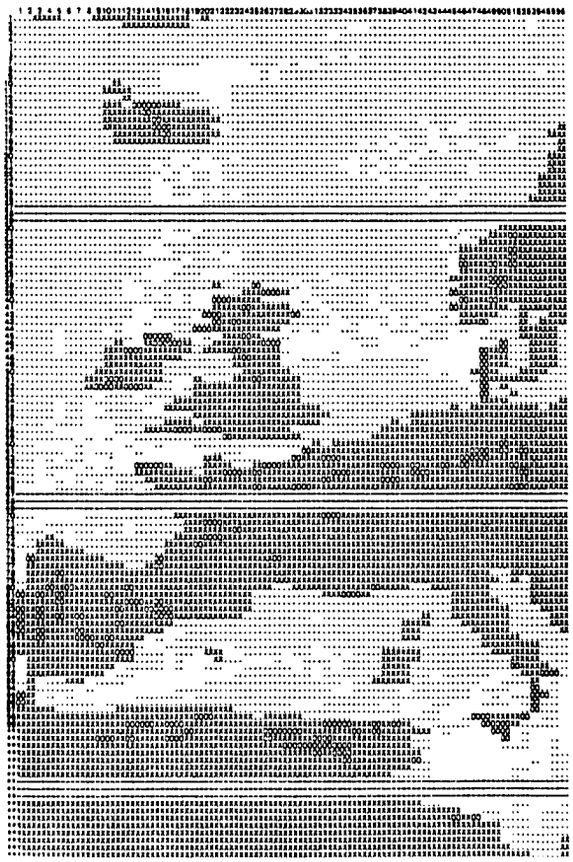

Figure 2

Results of cloud tests. Vertical numbering : scan lines. Horizontal numbering : spots. Blanks and dots respectively indicate clear and not-clear spots over sea. Zero's and X's respectively indicate clear and not-clear spots over land. Dashes : calibration lines.

Following that way, the real horizontal resolution is strictly equal to the simulated resolution within the clear areas (since only HIRS/2 channels are used) and is in between this resolution and the current 3I resolution within cloudy or partially cloudy areas, as expected from the method used to "de-cloud" the observations, the ψ-method which consists in predicting, for each HIRS/2 spot individually, cleared radiances from the microwave observations and from the "educated" data set TIGR. This is illustrated, through an application of this high resolution algorithm to the IOP mentioned above, on Figures 3 to 6.

Figures 3 and 4 display the thermal winds derived from the 3-D thermal structure retrieved from the satellite observations and corresponding to two atmospheric layers : 1000-500 mb and 1000-850 mb for the March 4 observations. Figures 5 and 6 display similar products for the March 5 observations. On these figures, numerous high resolution spatially coherent features may be observed, either over sea or over land. Moreover, the horizontal coverage is almost complete (except the calibration periods) in spite of the presence of large and heavily cloudy areas. The interpretation of these features would require high spatial resolution analysis fields still not available. However, they represent the first evaluation of the benefit one can expect from a high resolution coupled infrared and microwave sounder.

The coming AMSU (Advanced Microwave Sounding Unit) on board the next generation Tiros-N platforms is the instrument appropriate to this approach since the resolution in the infrared and in the microwaves are approximately the same, which is not the case, by far, here.

However, the present results appear encouraging when considering the completeness of the spatial coverage and the relatively satisfactory spatial coherence of the thermal wind fields even for layers 1,5 km thick as the 1000-850 mb and 850-700 mb ones.

The next step, recently started, will consist in merging as far as possible the AVHRR data, currently processed by the CMS Lannion, in the TOVS data, resulting, for clear and partly cloudy areas, in an important improvement in the spatial resolution. This is the principal aim of the "4I" method : Improved Initialization Inversion with Imagery, which should result in a significant improvement in the study of meteorological mesoscale features from satellites.

3. REFERENCES

Chedin, A., and N.A. Scott, 1983 : The Improved Initialization Inversion method. Internal Note LMD n° 117.

Chedin, A., N.A. Scott, C. Wahiche and P. Moulinier, 1985 : The Improved Initialization Inversion method for temperature retrievals from satellites of the Tiros-N series. J. Clim. Appl. Meteor., 24, 128-143.

Wahiche, C., N.A. Scott and A. Chedin, 1985 : Cloud detection and cloud parameters retrieval from the satellites of the Tiros-N series. Accepted by Annales Geophysicae.

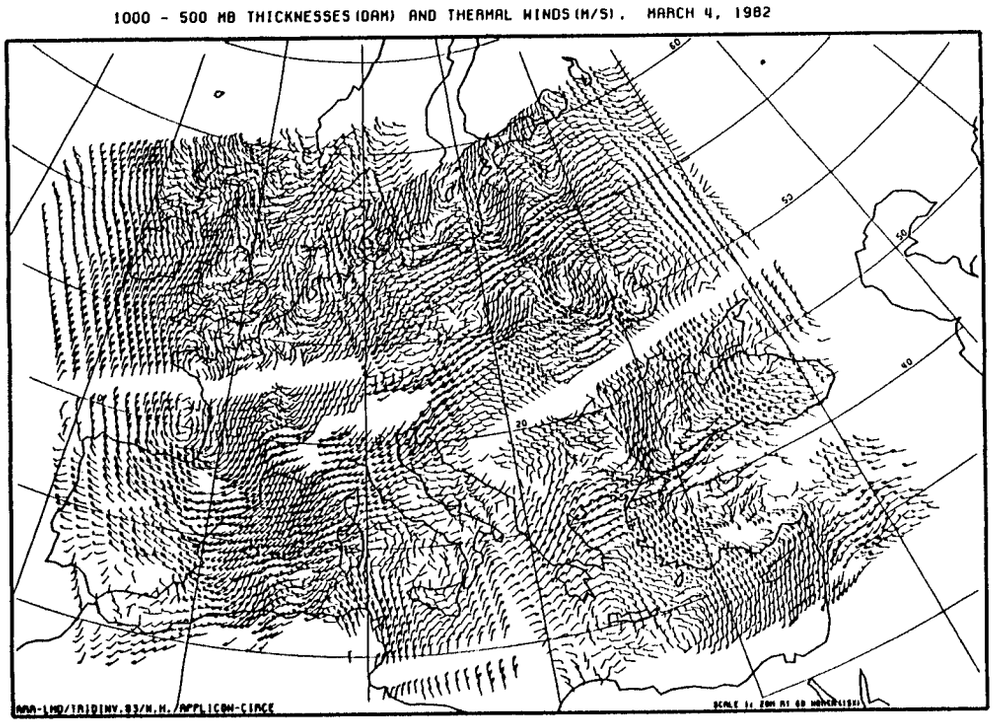

Figure 3

Thermal winds for the layer 1000-500 mb derived from the 3D thermal structure retrieved from NOAA-7 observations, March 4,1982. Two consecucutive orbits are analysed at 12:05Z and 13:45Z. This difference in time explains most of the slight inconsistencies within the overlapping areas.

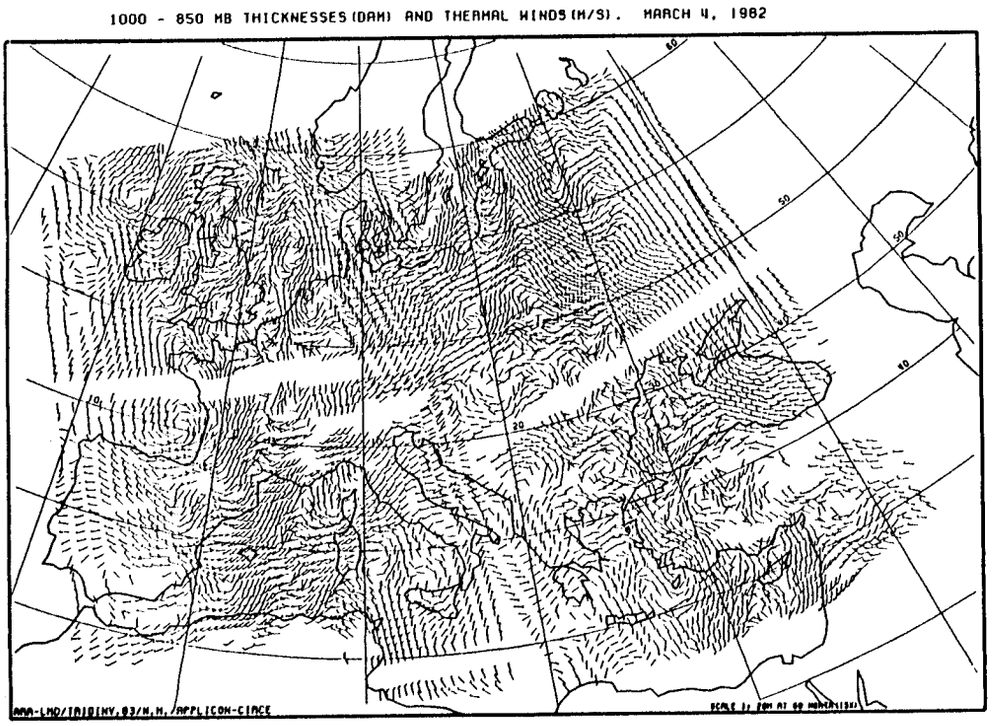

Figure 4

Same legend as Figure 3. Layer 1000-850 mb. March 4, 1982.

1000 - 500 MB THICKNESSES(DAM) AND THERMAL WINDS(M/S). MARCH 5, 1982

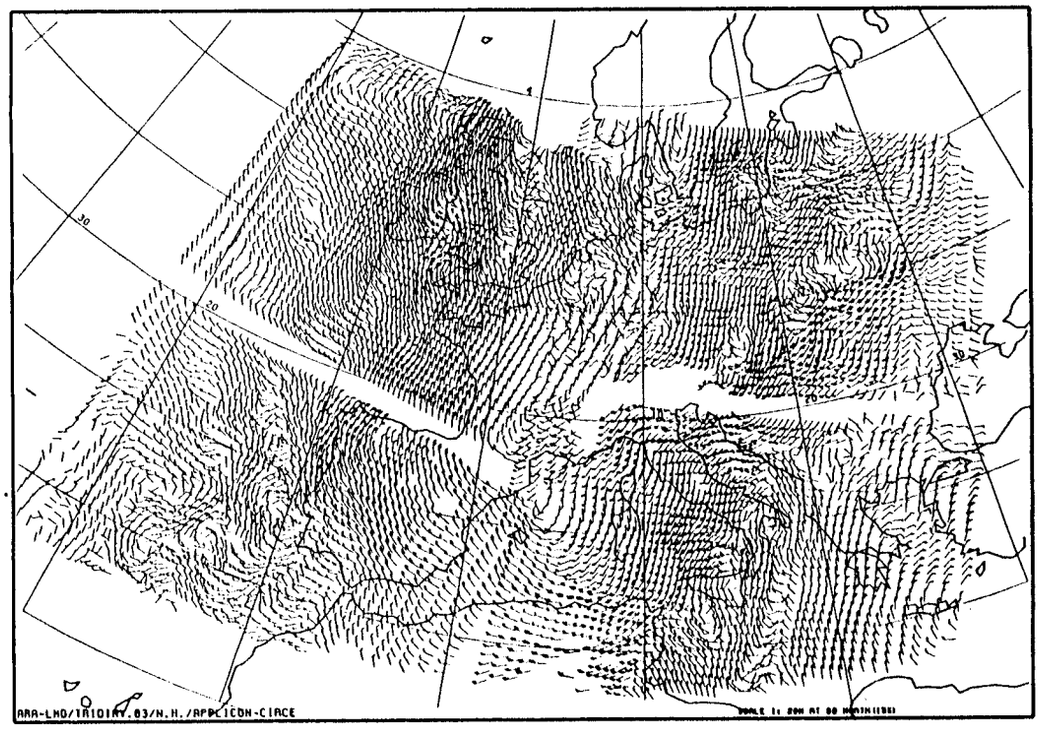

Figure 5

Same legend as Figure 3. Layer 1000-500 mb. March 5, 1982.

850 - 700 MB THICKNESSES(DAM) AND THERMAL WINDS(M/S). MARCH 5, 1982

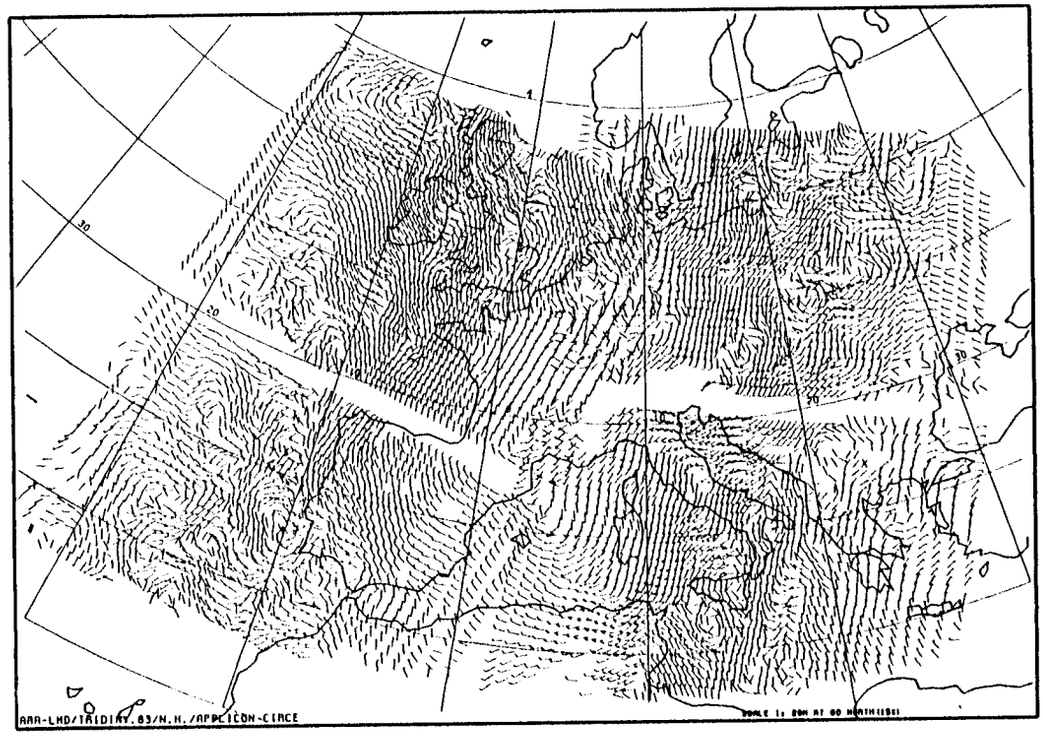

Figure 6

Same legend as Figure 3. Layer 850-700 mb. March 5, 1982.

HIGHER RESOLUTION OPERATIONAL SATELLITE RETRIEVALS

Anthony L. Reale
Donald G. Gray
Michael W. Chalfant

NOAA/NESDIS
Washington, D.C.

Anand Swaroop
Andrew Nappi

SASC Technologies, Inc.
Lanham, MD

1. INTRODUCTION

NOAA/NESDIS currently produces operational temperature and water vapor soundings from the TIROS Operational Vertical Sounder (TOVS) on board the NOAA TIROS-N series satellites. The TOVS consists of three instruments, the second version of the High resolution Infrared Radiation Sounder (HIRS-2), the Microwave Sounder Unit (MSU) and the Stratospheric Sounding Unit (SSU). The HIRS-2 instrument contains 20 channels in the 15 micron and 4.3 micron wavelength range and resolves a field of view (fov) that is approximately 20 Km across at the subsatellite point. The MSU contains 4 channels ranging in frequency from 50.3 to 57.9 gHZ and resolves a fov that is approximately 100 km across at nadir. The HIRS-2 supplemented by the MSU are primarily used to observe the troposphere. The SSU instrument, provided by the British Meteorological Office, contains 3 channels to observe thermal emissions from the stratosphere.

Data from the TOVS sounder is routinely ingested and processed at the NOAA computer facility in Suitland, Md. Vertical profiles of atmospheric temperature at 40 levels and water vapor at 15 levels are produced. Layer mean virtual temperatures for standard layers and layer precipitable water for three layers are computed for each profile and output to "users" along with the corresponding TOVS channel brightness temperatures and various identification parameters. NESDIS' primary objective is to produce quality sounding products in a timely manner for assimilation into NMC forecast models as well as regional and global analyses, particulary over ocean areas.

The following paper discusses the TOVS processing system and associated changes to produce higher resolution soundings. The high resolution system, which has been under development in NESDIS for the past 3 years, was accepted for operational implementation in November of 1985 and is scheduled for implementation early this year. An original sounding resolution of about 250 km across (at nadir) is enhanced to 20 km (at nadir) in the high resolution system. The high resolution system also contains a new filtering procedure which selects a best subset of soundings based on data noise, meteorological content and sounding spatial distribution requirements. The primary objective of the high resolution system is to provide increased information content in meteorologically active regions (ie, storms, fronts, jet streams, etc.).

2. LOW RESOLUTION TOVS SOUNDINGS

A system diagram of the 4 major software modules executed in the TOVS low resolution sounding system is shown in Figure 1a.

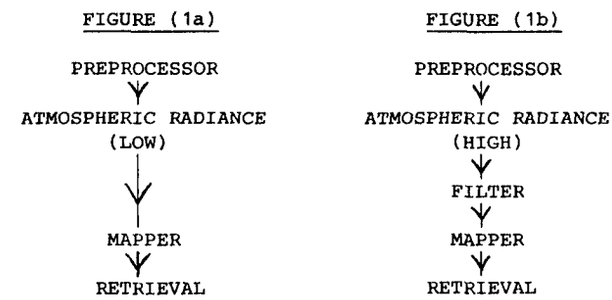

FIGURES 1a and 1b: System diagrams for the TOVS low resolution and high resolution sounding systems respectively.

The atmospheric radiance (AR) module is the heart of the TOVS retrieval process. Prior to the AR module, procedures to ingest, calibrate, screen, correct (ie, for scan angle) and format the measurements from the 27 spectral channels of the TOVS are performed by the Preprocessor module. Preprocessing also includes the interpolation of the MSU measurements to the HIRS-2 fovs. The Preprocessor outputs radiance measurements for the 24 spectral channels (20 HIRS, 4 MSU) located at each HIRS-2 fov over the entire orbit. Radiance measurements for the three SSU spectral channels are output for mapping and eventual use in generating retrievals. Measurements are all corrected to the nadir satellite scan angle.

In the AR module, processing begins by dividing the orbit into equal area blocks called superswaths (see Figure 2). A superswath covers approximately 2200 km x 1500 km. Each superswath is processed independently and is subdivided into a 6 by 5 array of sounding "boxes". A box extends approximately 250 km across at the nadir satellite scan angle. Each box contains a 9 by 7 array of HIRS-2 fovs. As stated, a radiance profile in the 24 spectral

channels of the HIRS and MSU is defined for each HIRS-2 fov.

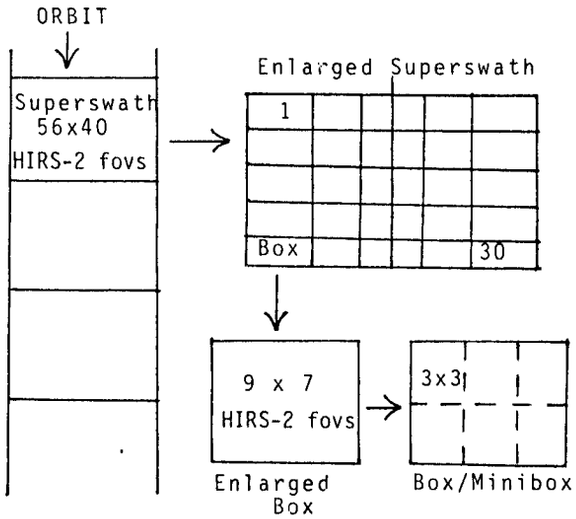

Figure 2: Representation of TOVS data blocking. Shown are the orbital superswath, the low resolution sounding box, and the high resolution sounding minibox.

The AR module processes each sounding box separately and attempts to compute a representative clear column radiance profile for the box. To begin, numerous clear tests are performed on each of the 63 fovs in the box to determine cloud contaminated radiances. Fovs passing all the clear tests are defined as clear. If less than 4 of the 63 fovs in the box are clear, an attempt to de-cloud the contaminated fovs is made using the NStar (N*) method (McMillin, 1978). Cloud corrected radiance profiles for non-clear fovs are then re-tested to determine if the N* calculation was successful; if so the fov is defined as partly cloudy. Unsuccessful fovs are defined as cloudy.

The sounding box is defined as clear if at least 4 of the 63 fovs are clear. A box is defined as partly cloudy if at least 4 of the 63 fovs are clear or partly cloudy. For clear boxes, the clear column radiance profile is the average of the clear fovs. For partly cloudy boxes, the clear column radiance profile is the average for the clear and partly cloudy fovs. Radiance profiles for clear and partly cloudy sounding boxes contain all 24 spectral channels. For cloudy boxes, the radiance profile for the box is the average of all 63 fovs, but contains only 7 spectral channels (3 Stratospheric HIRS, 4 MSU). In all cases, the profile location in the sounding box is defined as the centroid of the averaged fovs.

At the conclusion of the AR module, a clear column radiance profile containing either 24 or 7 spectral intervals is defined for each box in the orbit. Orbital processing is then transferred to the Mapper module where the measurements from the SSU are analyzed and mapped onto a global grid. Separate fields are maintained for each SSU channel. Processing then transfers to the Retrieval module. In this module, the SSU channel radiances are appended to the radiance profiles determined for each box. Statistical regression coefficients are then applied to the clear column radiances to retrieve the TOVS temperature and water vapor soundings for each sounding box. Regression coefficients are based on global samples of TOVS retrieval and radiosonde matchups. These are selected daily and stored offline. Operational coefficient data bases for selected instrument and channel combinations and 5 global latitude zones are updated weekly using the latest matchups.

3. HIGH RESOLUTION TOVS SOUNDINGS

A system diagram of the main software modules executed in the TOVS high resolution sounding system is shown in Fig. 1b. Except for the AR module, the software to produce high resolution TOVS soundings is quite similar to the software to produce low resolution soundings. Changes in the AR module to produce the high resolution soundings are described below. The high resolution system also includes a Filter module which executes immediately after the AR module.

Processing in the AR module is identical to the low resolution system until after the 63 fovs in the box have undergone the clear tests. If cloud contaminated fovs are found, an N* correction of those fovs is attempted regardless of the number of clear fovs found. As in the low resolution case, an unsuccessful N* correction results in a cloudy fov.

At this point, the box is further subdivided into six sounding miniboxes, (see Fig. 2) each containing a 3 by 3 array of fovs. A minibox extends approximately 50 Km across at nadir. For each minibox the 9 fovs are then examined. If one or more of the fovs are clear, the minibox is defined as clear. If only one clear fov was found, it is selected by default. Otherwise a test is done on each clear fov to determine the "clearest". The test applies interchannel regression coefficients (updated each week) to selected HIRS-2 channel radiances to predict MSU channel radiances. The radiance profile for the fov with the smallest difference between the predicted and observed MSU measurement is selected for the clear sounding minibox.

If only partly cloudy fovs are contained in the minibox, the minibox is defined as partly cloudy. Tests are then done to determine the "best" partly cloudy fov to represent the minibox. These tests include the interchannel regression tests described for clear miniboxes and also tests to select the fov with the most successful N* correction. The radiance profile for the best partly cloudy fov is selected for the partly cloudy sounding minibox.

If none of the fovs are clear or partly cloudy, the minibox is defined as cloudy. In this case the fov with the warmest HIRS-2 15 micron window channel measurement is selected. This is done to avoid high clouds which can affect the lowest HIRS-2 stratospheric channel. However, the representative radiance profile for a cloudy sounding minibox is the average of 9 adjacent fovs with the "warmest" fov at the center. Note that averaging only occurs for cloudy miniboxes.

At the conclusion of the AR module for high resolution soundings, a clear column radiance profile is defined for each minibox in the orbit. This represents a six-fold increase

in the number of sounding radiance profiles generated in the low resolution system.

The filter module operates on the minibox radiance profiles generated in the AR module. Its two major functions are 1) to identify radiance profiles that may still be cloud contaminated and 2) to select the best subset of non-contaminated miniboxes for each superswath based on meteorological content and spatial distribution requirements. User inability to handle the high density of soundings produced by the high resolution system warrants the creation of such a subset.

The Filter module processes each superswath independently. The ensemble of minibox radiance profiles for the superswath serve as input. Filtering of the clear and partly cloudy miniboxes is performed separately and prior to the filtering of the cloudy miniboxes. At the conclusion of filtering, each minibox is assigned a "filter flag" which is either Good, Redundant, Questionable or Bad (see table 1).

TABLE 1: Filter flag definitions for clear or partly cloudy miniboxes and cloudy miniboxes.

Filter Flag Definition	Clear or Partly Cloudy Minibox	Cloudy Minibox
Good	1) Not Contaminated 2) Not Redundant	1) Extensive Cloudiness 2) Not Redundant
Redundant	1) Not Contaminated 2) Redundant	1) Extensive Cloudiness 2) Redundant
Questionable	1) Marginal Contaminated or 2) Insufficient Testing	1) Marginal Cloudiness or 2) Insufficient Testing
Bad	1) Significant Contamination	1) Primarily Clear or Partly Cloudy

The filtering of clear and partly cloudy miniboxes consists of 2 major steps: the noise filter to identify cloud contaminated HIRS-2 radiances followed by the redundancy filter to select the "best" subset of clear and partly cloudy miniboxes.

In the noise filter, each minibox is tested by comparing observed test data for the minibox against analyzed test data at the minibox location based on neighboring miniboxes. The test data are difference values between MSU radiances predicted from HIRS-2 radiances using interchannel regression coefficients (updated each week) and observed MSU radiances. Miniboxes for which the observed test data differ significantly from the analyzed test values are flagged "bad". Miniboxes with marginal differences or for which there were too few neighbors to perform the analysis are flagged "questionable". Miniboxes for which the observed and analyzed test values agree are flagged "good".

The good miniboxes then undergo the second step in the filtering process which is the redundancy filter. In this step, each good minibox is systematically compared to neighboring good miniboxes to determine if the radiances for selected HIRS-2 channels are significantly different. If differences are observed, then a meteorologically active region is assumed and the minibox filter flag remains good. If no difference is observed, then the filter flag for the good minibox being tested is reset to "redundant". The spatial distribution of the good miniboxes is also considered in redundancy filtering such that the final set of good miniboxes for the superswath are neither too close nor too far apart.

The Filter module concludes with the filtering of cloudy miniboxes. Since clear and partly cloudy soundings are more desirable than cloudy soundings, the first step in filtering for each cloudy minibox is to determine if there are neighboring clear or partly cloudy miniboxes. If so, the cloudy minibox is flagged questionable or bad in proportion to the number of clear and partly cloudy neighbors in its vicinity. If no clear or partly cloudy miniboxes are found then an extended and consistent cloudy area is assumed and the cloudy minibox is flagged good.

The remaining good cloudy miniboxes then undergo redundancy filtering. This is similar to the procedures for clear and partly cloudy miniboxes except that differences in the MSU radiances are tested.

At the conclusion of the Filter module, the filter flag for each minibox is defined. Processing then transfers to the Mapper and Retrieval modules which operate basically the same as in the low resolution system. It should be noted that the regression coefficients used to produce high resolution soundings are based on closer radiosonde matchups due to the higher density of soundings available. Only good and redundant soundings are considered for matchups.

One final note, the Filter module is controlled by a number of parameters that are external to the operational software. Such parameters as the spacing requirement for the subset of good soundings, redundancy test channels to use, test thresholds, etc. are all input requirements and flexible. At this time, these parameters are set such that the number of good soundings per orbit is approximately equal to the total number of soundings produced in the low resolution system. Overall, about 20% of the high resolution soundings are flagged good, 55% are flagged redundant and 25% are flagged questionable or bad.

4. REMARKS

Satellite soundings provide valuable information for numerical weather forecasts and associated first guess analysis fields particularly over ocean areas where radiosonde observations are not available. The primary motivation for developing the high resolution system was to better utilize the resolving power of the TOVS instrument and ultimately to enhance the potential for sounding impact on numerical

forecast models. A primary requirement of the high resolution TOVS system was that the data noise inherent in the satellite measurements was not enhanced, resulting in increased sounding errors.

The problem of evaluating the high resolution system posed a number of questions on what the best criteria would be. A standard procedure, and in this case the primary criteria, was the comparison of separate samples of co-located satellite soundings and radiosonde measurements for the high and low resolution systems. The co-location time and space windows were within 3 hours and 3° latitude in equatorial distance. The National Meteorological Center (NMC), a primary user of TOVS data, conducted the evaluations. The matchup statistics derived for each system were found to be compatible and the high resolution system was accepted for implementation. Such results imply that at best, the high resolution system maintains previously reported sounding accuracies (McMillin, Gray, et al, 1983). This underplays the potential importance of the high resolution system.

There are a number of problems associated with only using retrieval and radiosonde matchup statistics as the sole evaluation criteria for a sounding system. For example, differences in the matchup samples for each can cause misleading results. Also, errors due to the time and space windows associated with such statistics can systematically affect either system. In this case, the high resolution system is less forgiving of time and space differences between radiosondes and soundings than the low resolution system which contains more averaging procedures.

NESDIS is currently upgrading its matchup collection and evaluation system to remove (as much as possible) inconsistencies due to sampling differences. However, other methods should be incorporated into the evaluation process. Ultimately, it would be best to perform sounding impact studies (Koehler et al, 1982) on numerical models; however, such analysis are not routinely available at this time. Another method is the study of satellite based temperature and moisture fields to determine if more "information" is being generated by either system.

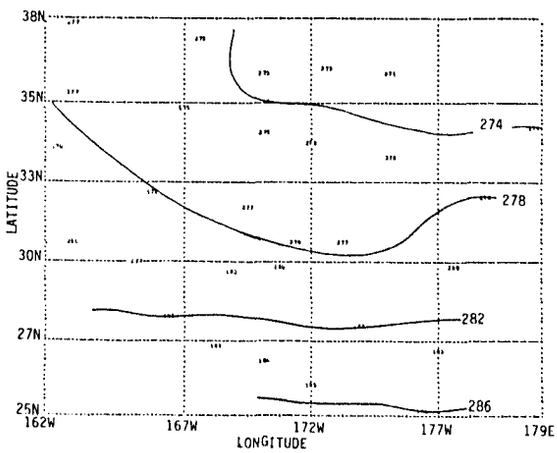

Figure 3a: TOVS low resolution temperature field for 850 mb at 21Z on November 17, 1985.

An example of such analyses are shown in Figures 3a and 3b, which display coincident low resolution and high resolution ("good" soundings only) TOVS retrieval temperatures and analyses at 850 mb. A number of such comparisons done by NESDIS suggest that improved gradient definition and spatial coverage are inherent in the high resolution system.

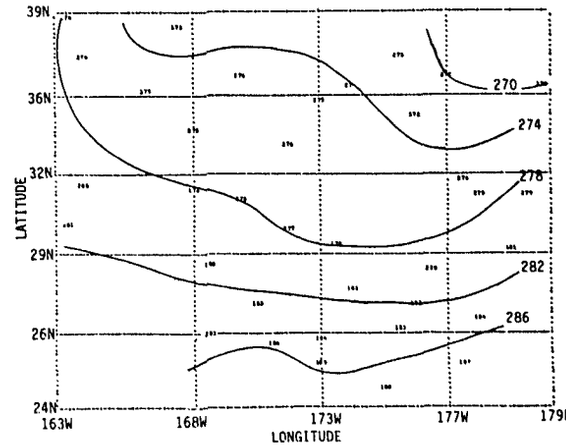

Figure 3b: TOVS high resolution temperature field for 850mb at 21Z on November 17, 1985; good soundings only.

Features such as those shown in the above figures are not addressed in matchup statistics alone, yet they are most important for numerical forecast impacts. NESDIS plans to incorporate such factors to facilitate the evaluation and implementation of future TOVS improvements.

5. REFERENCES

Koehler, T.L., J.C. Derber, B.D. Schmidt and L.H. Horn, 1982: An evaluation of Soundings, Analyses and Model Forecasts Derived from TIROS-N and NOAA-6 Satellite Data. Mon. Wea. Rev., March 1983, 562-571

McMillin, L.M., 1978: An Improved Technique for Obtaining Clear Radiances from Cloud Contaminated Radiances. Mon. Wea. Rev., 106, No. 11, 1590-1597.

McMillin, L.M., D.G. Gray, H.F. Drahos, M.W. Chalfant, and C.S. Novak, 1983: Improvements in the Accuracy of Operational Satellite Soundings. Journal of Climate & Applied Meteorology, Vol. 22, No. 11, 1948-1955.

Smith, W., H. Woolf, C. Hayden, D. Wark, & L. McMillin, 1979: The TIROS-N Operational Vertical Sounder. Bull. Amer. Meteor. Soc. 60, 10, Oct. 1979, 1177-1187.

Swaroop, A., A. Nappi, Z. Ahmad, M. Chalfant, L. McMillin & A. Reale, 1985: Enhanced Soundings over Oceans from NOAA-9 Polar Orbiting Satellite. PREPRINTS, MTS/IEEE Conference and Exposition, 12-14 Nov. 1985, San Diego, CA.

Werbowetzki, A., US Dept. of Commerce, 1981: Atmospheric Sounding Users's Guide. NOAA Tech. Re. NESS 83, April 1981.

1.7

MINIMUM VARIANCE SIMULTANEOUS RETRIEVAL OF TEMPERATURE AND WATER VAPOR FROM SATELLITE RADIANCE MEASUREMENTS

Henry E. Fleming
National Oceanic and Atmospheric Administration
National Environmental Satellite, Data, and Information Service
Washington, D.C. 20233

Mitchell D. Goldberg
SASC Technologies
Lanham, Maryland 20706

David S Crosby
The American University
Washington, D.C. 20016

1. INTRODUCTION

At the First Conference on Satellite Meteorology/Remote Sensing and Applications, Smith and Woolf (1984) presented an algorithm for the simultaneous retrieval of temperature and water vapor profiles, which they called the "one-step" method. The purpose of this paper is to extend and modify this work in three principal directions. First, the major departure of the Smith and Woolf (1984) one-step method from previous methods is to write the radiative transfer equation so as to have separate temperature and moisture components. The temperature component has the usual unknown Planck source function, while the moisture component contains a transmittance difference which is approximated by a one-dimensional Taylor expansion about the unknown moisture profile. Because transmittance is also a function of temperature and pressure, we use a more accurate multidimensional Taylor expansion of transmittance about temperature and pressure, as well as about moisture.

The second modification concerns the form of the solution. Smith and Woolf (1984) expand their solution in terms of a set of basis functions and solve for the coefficients of the expansion. In contrast to this approach, we solve the problem as a minimum variance solution in which the solution covariance matrix replaces the basis functions and the solution vector contains the temperature and moisture profiles explicitly. Our third modification involves the fact that the atmospheric transmittance functions, particularly for water vapor, are not known to the accuracy needed. To compensate for this lack of accuracy, we incorporate our previously-developed technique for removing most of the solution bias error that arises from inaccurate transmittance functions. Details of these three extensions and modifications are presented below.

2. THE RADIATIVE TRANSFER EQUATION

Before discussing the details of our modifications and extensions of the one-step retrieval method, we briefly review the work of Smith and Woolf (1984). When the radiative transfer equation defined for some mean state is subtracted from the general form of the equation, one has the result

$$R - \bar{R} = B_s\tau_s - \bar{B}_s\bar{\tau}_s + \int\left(B\frac{d\tau}{dp} - \bar{B}\frac{d\bar{\tau}}{dp}\right)dp \quad (1)$$

where R is the radiance, B is the Planck function, τ is the atmospheric transmittance function, the subscripts s denote surface conditions, and the bars represent the mean values of the quantities in question. To simplify notation and deal only with the essentials, we have refrained from showing the dependence of all the quantities on wavenumbers and the dependence of B and τ on pressure. Also, all integrations are understood to be from the surface pressure to zero pressure.

Now add and subtract the term $\bar{B}_s\tau_s$ outside the integral in (1) and add and subtract the term $\bar{B}d\tau/dp$ inside the integral in (1). This yields the equation

$$\Delta R = (\Delta B_s)\tau_s + \bar{B}_s(\Delta\tau_s) + \int\left[(\Delta B)\frac{d\tau}{dp} + \bar{B}\frac{(\Delta d\tau)}{dp}\right]dp \quad (2)$$

where the delta quantities represent the deviation of variable in question from its mean state. When the right-most term in (2) is integrated by parts, one has the required result:

$$\Delta R = (\Delta B_s)\tau_s + \int\left[(\Delta B)\frac{d\tau}{dp} - (\Delta\tau)\frac{d\bar{B}}{dp}\right]dp \quad (3)$$

Except for the second term in the integral, equation (3) has the usual form of the radiative transfer equation on which the minimum variance solution is based. For details see Rodgers (1976). It is the second term of the integral that is new and is the one used by Smith and Woolf (1984) to extract the moisture information by expanding the transmittance deviation $\Delta\tau$ in a Taylor approximation. Note that the factor $d\bar{B}/dp$ is based on a mean profile which is known.

3. THE TAYLOR EXPANSION

The Taylor expansion of $\Delta\tau$ in (3) used by Smith and Woolf (1984) is one-term expansion about precipitable water vapor. However, our studies show that this approximation can be in error by as much as one hundred percent of the true $\Delta\tau$ at the maximum value of true $\Delta\tau$ for the channels most sensitive to water vapor. One of the difficulties in using the one-dimensional Taylor expansion is that it ignores the pressure and temperature dependence of the atmospheric transmittance. The obvious remedy for this difficulty is to use a linear, multidimensional Taylor expansion of $\Delta\tau$ about temperature and pressure, as well as about precipitable water vapor. When this is done, we find that the pressure term is an important contributor to the total transmittance, but that the temperature term generally is much less important. Unfortunately, even though the multidimensional expansion improves the approximation of $\Delta\tau$ substantially, some of the errors are still as large as fifty percent of the true $\Delta\tau$.

Further improvement in the Taylor expansion is clearly needed. There are two obvious options for potential imporovement. One option is to use higher order terms in the expansion, but this creates a nonlinear retrieval problem whose solution is much less tractable than that of the linear problem. We prefer not to go in this direction. The second option is to keep the expansion linear, but to evaluate the partial derivatives at values other than the initial mean values, as is normally done.

Note that $\Delta\tau = \tau - \bar{\tau}$ where τ is the true, but unknown, value of the transmittance and $\bar{\tau}$ is the known mean value. It is known from the theory of the Taylor formula with remainder that there exist values of pressure, temperature and moisture that lie between their true and mean values for which the linear multivariate Taylor formula is exact. Even though one can never know what these intermediate values are, we can use this idea in another way.

Consider the Taylor expansion

$$\tau - \bar{\tau} = \Delta\tau = \varepsilon \left(\overline{\frac{\partial\tau}{\partial U}} \Delta U + \overline{\frac{\partial\tau}{\partial p}} \Delta p + \overline{\frac{\partial\tau}{\partial T}} \Delta T \right) \quad (4)$$

where U is precipitable water vapor, p is pressure, T is temperature, ε is a pressure dependent factor to be determined and the delta quantities again represent the deviation of the variable in question from its mean state. The partial derivatives in (4) are evaluated at the known mean value of the variable in question and are so denoted by placing bars over the partial derivatives. Now instead of trying to find the intermediate values of the independent variables which will make (4) exact, we try to find τ. One finds true τ by finding the true T and U profiles from which τ is calculated. But this is just as impossible as finding the intermediate values of T and U that make (4) exact. Nevertheless, this strategy is different because all that we really need to do is find profiles T_o and U_o that approximate the true profiles T and U in such a way that transmittance function τ_o, calculated from the approximate profiles, is closer to the true τ than is $\bar{\tau}$.

Finding approximate profiles T_o and U_o that are appropriate is easy. For example, the T_o profile can be obtained from a minimum variance or multivariate linear regression algorithm designed to retrieve only temperature. The profile U_o can be obtained in like manner using an algorithm designed specifically to retrieve water vapor. If these algorithms use $\bar{T}$ and $\bar{U}$ as their initial (first guess) approximations, the retrieved T_o and U_o profiles should yield a τ_o that is closer to τ than is $\bar{\tau}$, which is based on $\bar{T}$ and $\bar{U}$.

The stage is now set to evaluate (4). One uses the pairs $(U_o,\bar{U})$, $(p_o,\bar{p})$, and $(T_o,\bar{T})$ to evaluate the delta quantities in (4), and the partial derivatives are evaluated for $\bar{T}$, $\bar{U}$, and $\bar{p}$. (The determination of p_o and $\bar{p}$ is described below.) On the left-hand side (4) one replaces τ by τ_o and $\Delta\tau$ by $\Delta\tau_o$. Now everything is known except ε, which can be determined uniquely for each pressure level by dividing $\Delta\tau_o$ by the known parenthetical quantity on the left-hand side. With ε in hand, one has an exact expression for $\Delta\tau_o$. It turns out in practice that $\Delta\tau_o$ is a sufficiently good approximation to $\Delta\tau$, that the just-derived left-hand side of (4) can be used to approximate $\Delta\tau$ in (3).

When (4) is applied to (3), one has

$$\Delta R_o = (\Delta B_s)\tau_s + \int \left[(\Delta B)\frac{d\tau}{dp} - \varepsilon(\Delta U)\overline{\frac{\partial\tau}{\partial U}}\frac{d\bar{B}}{dp} \right] dp \quad (5)$$

where

$$\Delta R_o = \Delta R + \int \varepsilon \left[\overline{\frac{\partial\tau}{\partial p}}(\Delta p_o) + \overline{\frac{\partial\tau}{\partial T}}(\Delta T_o) \right] dp \quad (6)$$

with

$$\Delta p_o = p_o - \bar{p} \quad (7)$$

It is important to note that even though (4) is made exact for $\Delta\tau_o$ and not for $\Delta\tau$, this approach is not as unreasonable as it may appear. The reason is that τ_o and the associated independent variables were used in (4) only to determine ε, and so when (4) is applied to (3), the most important quantity, ΔU, is again treated as an unknown. Furthermore, $\Delta\tau_o$ usually is a good approximation to $\Delta\tau$. In any case, we find in practice that this is indeed a very satisfactory approach, particularly when the solution to (5) is iterated and the iterates are used each time to update ε, p_o, T_o, U_o and τ in (5) and (6).

3.1 Pressure term deviation

We digress briefly to explain the derivation of the pressure term in the Taylor expansion (4). Since $\tau = \tau(p,T(p),U(p))$, the ordinary (i.e., total) derivative of τ with respect to p is the slope of the tangent to the curve on the surface τ which is determined by the parametric equations $T = \bar{T}(p)$ and $U = \bar{U}(p)$. This derivative is known. On the other hand, the partial derivative of τ with respect to pressure is the slope of the tangent to the curve in which the surface represented by τ is intersected by a plane perpendicular to the p, T, U-plane and parallel to the p-axis. Consequently, the partial derivative is not equal to the ordinary derivative and must be calculated from the "chain rule" for multivariate functions as follows:

$$\overline{\frac{\partial\tau}{\partial p}} = \frac{d\bar{\tau}}{dp} - \overline{\frac{\partial\tau}{\partial T}}\frac{d\bar{T}}{dp} - \overline{\frac{\partial\tau}{\partial U}}\frac{d\bar{U}}{dp} \qquad (8)$$

where all the terms on the right-hand side are known.

The factor Δp in (4), as defined by (7), also requires clarification. If p_o is the particular value of the independent variable p at which we wish to evaluate τ_o, then $\bar{p}$ must be the pressure value at which $\bar{\tau}$ has the same value as $\tau_o(p_o)$, that is, $\bar{p}$ is chosen such that

$$\bar{\tau}(\bar{p}) = \tau_o(p_o) \qquad (9)$$

In other words, one must solve (9) for $\bar{p}$, which is then used in (7), and (7) in turn is used in (6) along with (8).

4. MINIMUM VARIANCE SIMULTANEOUS SOLUTION

In Smith and Woolf (1984), (5) is solved by linearizing the Planck function B and expanding the resulting ΔT and ΔU profiles as linear combinations of basis functions. Consequently, the solution-vector elements are the unknown expansion coefficients. Also, because only the first term inside the parentheses in (4) is used by Smith and Woolf, ΔR, and not ΔR_o, of (6) is used as the measurement vector. While this is a valid way of solving (5), we would like to suggest an alternative procedure in which one solves for ΔT and ΔU directly.

In our procedure for solving (5), we replace the coefficient solution vector by a solution vector containing the profiles ΔT and ΔU, and the basis functions are replaced by a temperature-water vapor covariance matrix. The specific details are as follows.

First, ΔR_o, ΔB_s, and ΔB are linearized with respect to temperature as in Smith and Woolf (1984), which leaves ΔT_s, ΔT, and ΔU as the unknown quantities and ΔT^* as the known measurement vector in which T^* is the brightness temperature. Then a numerical quadrature rule is applied to (5) which enables one to write the linearized form of (5) in the matrix form

$$\Delta V = SA^T(ASA^T + N)^{-1}\Delta T^* \qquad (10)$$

where the superscript "T" denotes matrix transposition, "-1" denotes matrix inversion, ΔV is the m-dimensional vector of retrieved temperature and moisture deviations, S is the covariance matrix of the solution vector whose dimension is m x m, A is the matrix of weighting functions of dimension n x m, N is the system noise covariance matrix of dimension n x n, and ΔT^* is the n-dimensional vector of measured brightness temperature deviations. The two vectors represent deviations from mean vectors which are explained in greater detail in the next section.

The individual components in (10) require additional explanation. For example, the solution vector ΔV is explicitly of the form

$$\Delta V = [\Delta T_1, \ldots, \Delta T_t, \Delta T_s, \Delta U_1, \ldots, \Delta U_u]^T \qquad (11)$$

where the elements of the vector were defined previously, t is the number of pressure levels in the retrieved temperature profile, and u is the number of pressure levels in the retrieved precipitable water vapor profile. It follows from (11) and the description of m in the previous paragraph that

$$m = t + u + 1 \qquad (12)$$

and that the matrix S has the block form:

$$S = \left[\begin{array}{c|c|c} S_1 & S_2 & S_3 \\ \hline S^T_2 & S_4 & S^T_5 \\ \hline S^T_3 & S_5 & S_6 \end{array}\right] \qquad (13)$$

In (13) S_1 is the t x t temperature covariance matrix, S_6 is the u x u precipitable water vapor covariance matrix, S_4 is a scalar representing the variance of the surface temperature, S_3 is the t x u covariance matrix which carries the correlations between temperature and moisture, the t-dimensional vector S_2 carries the correlations between the surface and air temperatures, and the u-dimensional vector S_5 carries the correlation between the surface temperture and the moisture.

The matrix A in (10) also can be written in block form, that is,

$$A = [A_1 | A_2 | A_3] \qquad (14)$$

In (14) the components A_1, A_2, and A_3 are of dimension n x t, n x 1, and m x u, respectively. Furthermore, the individual elements of the components are products of three factors, two of which are linearization factor and a quadrature weight; the third factor is $d\tau/dp$ for A_1, τ_s for A_2, and for A_3 it is $\varepsilon\,\overline{\partial\tau}/\partial U)(d\bar{B}/dp)$. The quantities N and ΔT^* need no further clarification.

We indicated in Section 3 that the solution to (5) had to be iterated to update the quantities ε, τ, and those with zero subscripts. Since (10) is the numerical solution to (5), it too must be iterated, and in addition, one must be careful to iteratively update the linearization factors that are part of the matrix A. The iterative process can be made explicit by using the iteration index k to write (10) in the form:

$$\Delta V_{k+1} = SA^T_k(A_kSA^T_k + N)^{-1}\ \Delta T^*. \qquad (15)$$

The iterations are continued until the radiances calculated from the radiative transfer equation, based on the most recent solution profiles, agree with the measure radiances to within the system noise level for each channel. The reason for not iterating ΔT^* is explained in Section 5. Thus one sees that for each iteration of (15), we have a minimum variance solution which is "simultaneous" in that the single solution vector (11) determines the temperature and moisture

profiles and the surface temperature all in one step.

We digress briefly to point out that one could solve for the water vapor mixing ratio profile Q(p) directly in (10) and (11) instead of for the precipitable water vapor profile U(p). This is accomplished by making the substitution

$$\Delta U(p) = \frac{1}{g}\int_0^p \Delta Q(p')\, dp' \qquad (16)$$

(where g is acceleration due to gravity) for ΔU in (5), applying an appropriate numerical quadrature rule to the integral, and algebraically regrouping terms into groups which contain only terms with the common factor q(p) for each fixed p. This changes the form of the elements in only the component A_3 of (14) and it replaces the elements ΔU in (11) with the elements ΔQ; otherwise, the form of the equations and the number of elements stays the same.

5. TRANSMITTANCE ERRORS

The atmospheric transmittance functions used in the matrix A of (14) generally are not known to the accuracy needed because of errors in the models and spectroscopic parameters used to calculate the functions. This affects the procedures used in the retrieval algorithm in the following way. Fleming, et al (1986) found that transmittance errors propagate into the minimum variance solution mainly as bias errors and that these bias errors by and large can be removed by using mean profiles of temperature, moisture, and radiance in the algorithm which are calculated from coincidently-measured ensembles of these quantities—not from the radiative transfer equation.

In our case this means that in the deviations

$$\begin{aligned} \Delta T^* &= T^* - \overline{T^*}, \\ \Delta T &= T - \overline{T}, \\ \Delta U &= U - \overline{U} \end{aligned} \qquad (17)$$

of (10) and (11), one uses the ensemble mean profiles for the bared quantities. When the profiles $\overline{T^*}$, $\overline{T}$, and $\overline{U}$ are calculated from an ensemble of triplets (T^*, T, U) that are measured coincidently in time and space, the proper relationship between the satellite radiances and the in situ profiles is established through the mean profiles. This largely compensates for the distortion of this relationship among the unbarred quantities in (17) caused by using incorrect transmittance functions in the radiative transfer equation.

The significance of the bias-error remedy in the iterative procedure (15) is that the vector ΔV_{k+1} is of dimension m = t + 1 + u and has the explicit form

$$\Delta V_{k+1} = \begin{bmatrix} T_{k+1} - \overline{T} \\ \hline (T_s)_{k+1} - \overline{T_s} \\ \hline U_{k+1} - \overline{U} \end{bmatrix} \qquad (18)$$

while the n-dimensional vector ΔT^* has the form given in (17). In a typical iteration scheme the barred quantities in (18) and in ΔT^* would be replaced by quantities that carry the iteration index k instead of the bar. If this were done, the relationship between T^*_k and the in situ profiles T_k and U_k would become increasingly distorted as the iteration process progressed. Clearly, we cannot use the typical iteration scheme. Instead, to avoid the solution bias errors resulting from incomplete knowledge of the transmittance functions, we must hold the barred quantities fixed, as in (17) and (18), and for these quantities we must specifically use mean profiles calculated from coincident measurements.

6. CONCLUSIONS

Because the companion paper by Goldberg, et al (1986), is devoted almost entirely to analyzing results from the minimum variance simultaneous (MVS) retrieval method, no results will be given in this paper. Briefly, one can conclude from those results that in meteorologically active areas the temperatures from the MVS solution are slightly more accurate than those obtained from the NESDIS operational regression retrievals, when radiosonde temperatures are used as ground truth. In less active regions such as the tropics, the opposite conclusion can be drawn.

For water vapor, the MVS solution is consistently more accurate than the NESDIS operational regression retrievals in the important water vapor-ladened layer from 700 to 1000 mb. No comparisons of either temperature or moisture with the Smith and Woolf (1984) method are available.

We can conclude that the minimum variance simultaneous retrieval method is competitive with the operational method in temperature accuracy and superior to it in moisture accuracy in the 700 to 1000 mb layer. Furthermore, solutions from the MVS method consistently satisfy the radiative transfer equation to within the system noise levels, which is not always the case for solutions from other retrieval methods, see Goldberg, et al (1986).

7. REFERENCES

Fleming, H. E., D. S. Crosby, A. C. Neuendorffer, 1986: Correction of satellite temperature retrieval errors due to errors in atmospheric transmittances. To be published in J. Climate Appl. Meteor., 25.

Goldberg, M. D., A. Swaroop, H. E. Fleming, A. Reale, 1986: An analysis of temperature and water vapor retrievals using a minimum variance simultaneous method. In this Preprint Volume.

Rodgers, C. D., 1976: Retrieval of atmospheric temperature and composition from remote measurements of thermal radiation. Rev. Geophys. Space Phys., 14, 609-624.

Smith, W. L., and H. M. Woolf, 1984: Improved vertical soundings from amalgamation of polar and geostationary radiance observations. Preprint Volume: Conference on Satellite Meteorology/Remote Sensing and Applications, June 25-29, 1984, Clearwater, Florida.

1.8

AN ANALYSIS OF TEMPERATURE AND WATER VAPOR RETRIEVALS USING A MINIMUM VARIANCE SIMULTANEOUS METHOD

Mitchell D. Goldberg and Anand Swaroop
SASC Technologies Inc.
5809 Annapolis Rd.
Hyattsville, MD. 20784

Henry E. Fleming and Anthony Reale
NOAA/NESDIS
Washington, D.C. 20233

1. INTRODUCTION

The retrieval of atmospheric temperature and water vapor profiles from the TIROS-N satellite radiometric measurements became a NOAA/NESDIS operational product in 1979. The retrievals supplement conventional radiosonde observations and provide the only available information on the thermal and moisture structure of the atmosphere over remote regions (e.g., oceans). The primary user of satellite-derived profiles is the National Meteorological Center (NMC). NMC uses the information as input into their numerical weather prediction models. Since 1979, the method for retrieving temperature and water vapor has been based on multivariate linear regression. Regression coefficients are required to be updated on a weekly basis from the most recent matchups of radiosonde and satellite data in order to maintain the representativeness of the apriori information. Therefore, operational retrievals are dependent to a large extent on radiosonde availability.

In an attempt to reduce the radiosonde dependency, NOAA/NESDIS is considering a physical retrieval algorithm as an alternative to regression. The term physical reflects the fact that the algorithm is derived from the radiative transfer equation. Two candidates are being considered for the physical retrieval system. Both require only a small sample set of matched data from which only apriori means are generated. The first candidate is the well known and cited Minimum Variance algorithm (Rodgers, (1976)). The minimum variance algorithm produces only atmospheric profiles of temperature. However, profiles of water vapor mixing ratio are also required as a product. Water vapor retrievals are being provided by a regression technique that uses fixed coefficients, so that there is only a small dependency on radisondes to update the mean profile. This method will be referred to as fixed coefficient (FC) regression. The second candidate algorithm solves for temperature and water vapor simultaneously, and is actually a form of minimum variance. Appropriately, this algorithm is called the Minimum Variance Simultaneous (MVS) solution. The MVS algorithm is an extension of work done by Smith and Woolf (1984). Since physical retrievals are based on the radiative transfer equation (RTE), one would expect the retrievals to satisfy the measured radiances. However, it will be shown that this statement is true for only the second of the two physical retrieval algorithms. The ability to satisfy the measured radiances depend on the manner in which the RTE is used, and its applicability to the real time measurements.

This paper will discuss the forms of the radiative transfer equation applicable to the derivation of both type of physical retrieval algorithms. Ensemble rms statistics compare the accuracy of both physical retrievals with retrievals from the present operational regression method. Additionally, statistics assessing the ability of the various retrieval methods to satisfy the measured radiances are presented.

2. RADIATIVE TRANSFER EQUATION

The classical minimum variance algorithm is based on the following form of the radiative transfer equation:

$$R_\upsilon - \overline{R}_\upsilon = (B_\upsilon^S - \overline{B}_\upsilon^S)\tau_\upsilon^S + \int (B_\upsilon - \overline{B}_\upsilon)\frac{d\tau_\upsilon}{dp}dp \qquad (1)$$

where R represents radiance received by the satellite at frequency υ, B is Planck function of the atmospheric temperature profile, the superscript S denotes the surface condition, τ is atmospheric transmittance, and p is pressure. The barred quantities define a mean

condition. The limits of integration are understood to be from the pressure at the surface to the pressure at the top of the atmosphere. Note that in the above equation $\bar{R}$ is defined as:

$$\bar{R}_\upsilon = \bar{B}_\upsilon^s \tau_\upsilon^s + \int \bar{B}_\upsilon \frac{d\tau_\upsilon}{dp} dp \qquad (2)$$

However, whenever $\bar{R}$ is calculated directly from an ensemble of measured radiances, it must be written in the form:

$$\bar{R}_\upsilon = \overline{B_\upsilon^s \tau_\upsilon^s} + \overline{\int B_\upsilon \frac{d\tau_\upsilon}{dp} dp} \qquad (3)$$

In our studies, it was found that because of the very weak correlation between profiles of temperature and the derivative of transmittance, eq.(3) can be approximated by:

$$\bar{R}_\upsilon = \bar{B}_\upsilon^s \bar{\tau}_\upsilon^s + \int \bar{B}_\upsilon \frac{d\bar{\tau}_\upsilon}{dp} dp \qquad (4)$$

There is a problem in that while $\bar{R}$ based on eq.(4) can easily be calculated, $\bar{R}$ based on eq.(2) cannot be because the unknown ambient temperature profile is needed to calculate the transmittance functions and their derivatives. However, it is eq.(2) that is needed because it is that form of $\bar{R}$ that arises in the derivation of the classical minimum variance solution. (Note that the root of the problem is that the minimum variance solution is for a linear problem, whereas we really have a nonlinear problem because of the temperature dependence of the transmittance functions.) The only way to obtain a good approximation to eq.(2) is to iterate it, that is, apply the most recent temperature retrieval to the calculation of τ^s and $d\tau$ in eq.(2). The minimum variance algorithm is iterated until the RTE, defined by eq.(1), converges to the measured radiances to within their noise levels.

Fleming et al. (1986) found that $\bar{R}$ calculated via radiative transfer physics produced bias errors in the solution, because of errors due to uncertainties in the parameters and model for computing atmospheric transmittances. The remedy they suggested and which is applied in this study is to compute $\bar{R}$ from an ensemble of measured radiances. Note that in the absence of transmittance errors, the measured $\bar{R}$ is equivalent to eq.(3), and therefore a good approximation to eq.(4).

Even though the application of a measured $\bar{R}$ removes bias errors from the retrieval, the RTE as defined by eq.(1) will not be satisfied because this $\bar{R}$ is not defined by eq.(2). Therefore in practice the minimum variance solution will not satisfy the RTE because the transmittance cannot be known exactly. These difficulties disappear when the minimum variance simultaneous (MVS) algorithm is used.

The MVS algorithm avoids the previous problems, because the radiative transfer equation is now written as follows:

$$R_\upsilon - \bar{R}_\upsilon = \left[B_\upsilon^s \tau_\upsilon^s + \int B_\upsilon \frac{d\tau_\upsilon}{dp} dp \right] - \left[\bar{B}_\upsilon^s \bar{\tau}_\upsilon^s + \int \bar{B}_\upsilon \frac{d\bar{\tau}_\upsilon}{dp} dp \right] \qquad (5)$$

which can be rewritten as,

$$R_\upsilon - \bar{R}_\upsilon = B_\upsilon^s \tau_\upsilon^s + \int \Delta B_\upsilon \frac{d\tau_\upsilon}{dp} dp - \int \Delta\tau_\upsilon \frac{d\bar{B}_\upsilon}{dp} dp \qquad (6)$$

where $\Delta\tau = \tau - \bar{\tau}$ and $\Delta B = B - \bar{B}$. The MVS algorithm solves for temperature and water vapor profiles via the first and second integral terms, respectively. The derivation of eq.(6) from eq.(5), and the equation defining the MVS solution are in Fleming et al. (1986), which is in these proceedings.

3. DATA

Results in this paper are derived from a January 1985 data set containing real-time radiance measurements from the High Resolution Infrared Radiation Sounder (HIRS/2), Microwave Sounding Unit (MSU), and the Stratospheric Sounding Unit (SSU) instruments on the NOAA 7 polar orbiting satellite. A complete description of these instruments can be found in Smith et al. (1978). The radiance measurements are clear column and limb corrected to nadir, and are colocated with radiosonde profiles of temperature and water vapor mixing ratio. The radiosonde profiles are used as truth in the computation of rms retrieval errors. The data were sorted into these latitide zones:

a. Tropical 30S-30N (112 cases)

b. Midlatitudinal 30N-60N (54 cases)

c. Polar 60N-90N (88 cases)

Channel selections for the operational temperature and water vapor retrievals, minimum variance, FC water vapor regression, and MVS are given in Table 1. Transmittance functions were generated using the model developed by Weinreb et al. (1981).

Table 1. Channel selection as a function of retrieval method.

HIRS/2	Wave-Number (cm^{-1})	Operation Temperature	Operation Water	Minimum Variance	FC Water Vapor Regression	MVS
1	668	x	x			
2	679	x	x	x		x
3	691	x	x	x	x	x
4	704	x	x	x	x	x
5	716	x	x	x	x	x
6	732	x	x	x	x	x
7	748	x	x	x	x	x
8	898	x	x	x	x	x
9	1028	x	x			
10	1217	x	x		x	x
11	1364	x	x		x	x
12	1484	x	x		x	x
13	2190	x	x	x	x	x
14	2213	x	x	x	x	x
15	2240	x	x	x	x	x
16	2276	x	x	x	x	x
SSU						
1	665	x	x	x	x	x
3	665	x	x	x	x	x
MSU	Frequency (GH_z)					
2	53.76	x	x	x	x	x
3	54.96	x	x	x	x	x
4	57.95	x		x	x	x

4. RESULTS

4.1 Radiances calculated from the MVS RTE

If atmospheric transmittances were not a function of temperature and water vapor, then τ would be equal to $\bar{\tau}$, the $\Delta\tau$ integral term would vanish, and eqs.(6) and (1) would be identical. However, because transmittance is a nonlinear function of these parameters eqs.(6) and (1) have distinct forms. In order to assess the contribution from the factor $\Delta\tau$ in the integrand of eq.(6), we conducted a simulation study. Two arbitrary sets of mean profiles of temperature and water vapor were computed for each of the 3 latitude zones. Unbarred quantities in eq.(6) were computed from one set of mean profiles, while the other set was used to compute the barred quantities. Results from this study are shown in Table 2. The radiances in the column labeled A represent the sum of the surface term and the ΔB integral term in eq.(6), whereas those represented by the $\Delta\tau$ integral term, including the minus sign, are given by column B. The fractional contribution of B relative to A and B is given by column C, and is computed by dividing the absolute value of B by the sum of the absolute values of A and B. Comparing results from the tropical, middle latitudes and polar zones, it becomes apparent that the contribution from the $\Delta\tau$ integral term generally decreases from lower to higher latitudes. This is primarily due to the poleward decrease of water vapor. Therefore in practice, the ability of the minimum variance solution to satisfy the RTE decreases from higher to lower latitudes. It should be noted that the $\Delta\tau$ integral term is not only dependent on water vapor; other parameters such as temperature, ozone, and pressure play a role. However, water vapor appears to be the dominant parameter.

4.2 Retrieval Results

Temperature and water vapor solution rms errors of the three retrieval methods are shown in figures 1a-b through 3a-b. Radiosonde values are used as ground truth. In the tropical zone, Fig. 1a, the operational temperature retrievals have the smallest retrieval errors between 780 and 1000 mb. Above 780 mb, all three methods are comparable. In Fig. 1b, the MVS water vapor retrievals near the surface are associated with the smallest errors, whereas the largest errors were from FC regression. In addition to fixed coefficients, FC regression differs from the operational regression in that its predictand is dewpoint temperature, as opposed to

Table 2. Calculated Components of the MVS Radiative Transfer Equation.

	Tropics			Middle Latitudes			Polar		
HIRS	A	B	C	A	B	C	A	B	C
2	0.234	0.007	0.030	-2.414	0.029	0.019	0.088	-0.019	0.178
3	0.046	0.197	0.810	-2.645	0.200	0.070	-0.473	0.004	0.008
4	1.898	-0.054	0.027	0.928	-0.179	0.162	-3.256	0.431	0.271
5	3.667	-0.805	0.180	3.891	-0.720	0.156	-7.637	0.585	0.071
6	5.000	-1.601	0.242	6.089	-1.074	0.150	-12.198	0.512	0.040
7	6.370	-3.169	0.332	9.219	-1.458	0.137	-20.361	0.280	0.014
10	4.465	-2.178	0.323	7.462	-0.541	0.068	-14.948	-0.063	0.004
11	2.236	-1.416	0.388	2.787	-1.455	0.343	-4.220	0.417	0.090
12	1.071	-0.515	0.325	1.596	-1.044	0.395	-1.282	0.374	0.226
13	0.304	-0.075	0.198	0.377	-0.017	0.043	-0.567	0.001	0.002
14	0.181	-0.022	0.108	0.173	-0.002	0.011	-0.251	-0.000	0.000
15	0.069	-0.006	0.080	0.052	-0.003	0.055	-0.066	0.001	0.000
16	0.015	-0.000	0.000	0.005	0.000	0.000	-0.010	0.000	0.000
MSU									
2	3.252	-0.070	0.021	4.570	0.119	0.023	-8.474	0.106	0.012
3	0.603	0.195	0.244	-0.355	0.146	0.291	-2.921	0.052	0.017
4	2.219	0.242	0.098	-6.996	-0.192	0.027	-0.097	0.001	0.010
SSU									
1	1.444	0.008	0.045	1.697	0.110	0.062	0.647	0.029	0.043
3	1.368	0.035	0.069	4.540	0.164	0.035	-6.292	0.006	0.001

* units are in (mw/m^2-sr cm^{-1}) except (K) for MSU channels.

$$A = B_U^S \tau_U^S + \int \Delta B_U \frac{d\tau_U}{dp} dp \qquad C = \frac{|B|}{|A|+|B|}$$

$$B = -\int \Delta\tau_U \frac{d\overline{B}_U}{dp} dp$$

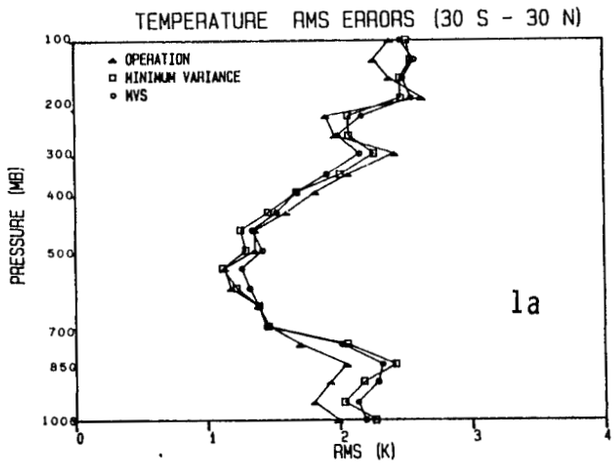

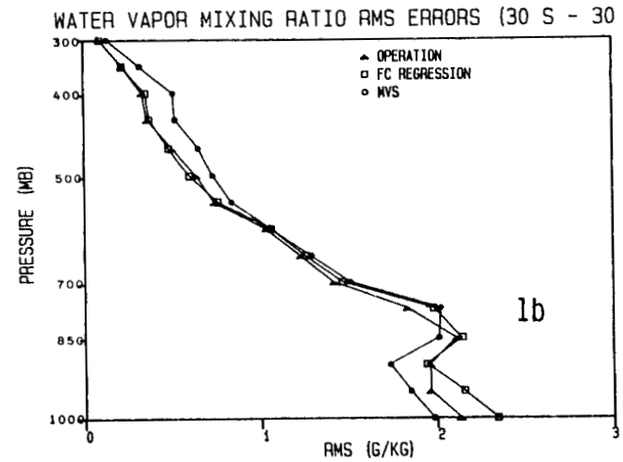

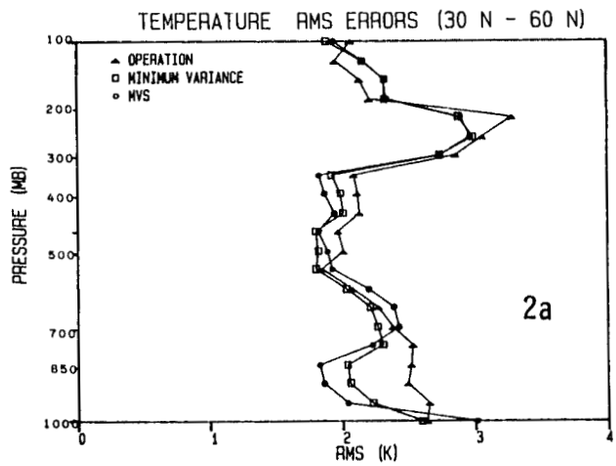

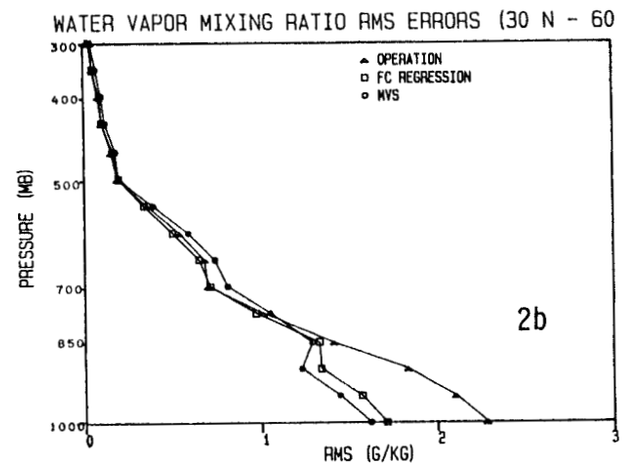

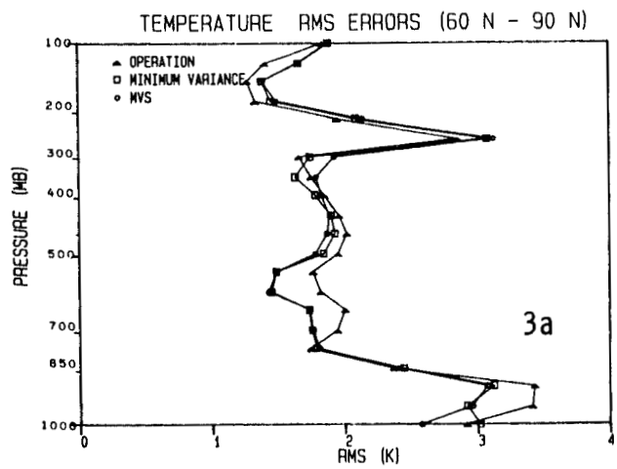

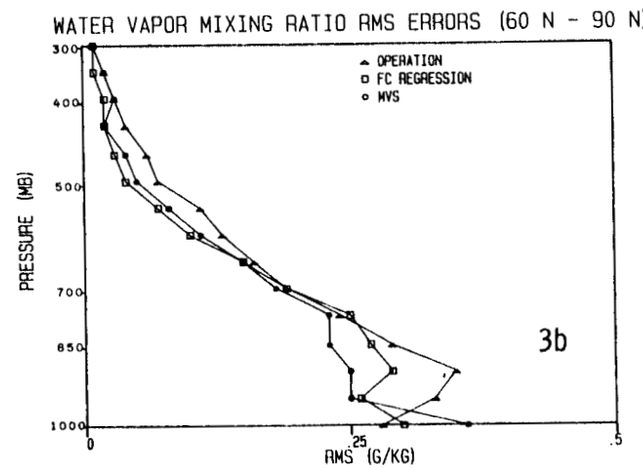

Figures 1a-3a. Temperature retrieval error profiles for operational regression, minimum variance and MVS; for tropics, midlatitudinal and polar zones, respectively.

Figures 1b-3b. Water vapor mixing ratio retrieval error profiles for operational regression, FC regression and MVS; for tropics, midlatitudinal and polar zones, respectively.

mixing ratio. When comparing temperature retrieval errors for the middle latitudes, Fig. 2a, it appears that both of the physical retrieval methods are more accurate than the operational regression method. With the exception of the 1000 mb level, MVS retrieval errors below 780 mb are smaller. (We currently are investigating the boundary problem associated with MVS, it appears to occur only within this latitude zone.) Near the surface the smallest water vapor errors are again associated with MVS, whereas rms errors from the operational retrievals are relatively large, as seen in Fig 2b. Temperature rms errors for the polar region, Fig 3a, show that with respect to the operational retrievals, both physical retrieval methods generally have lower retrieval errors below 300 mb. Notice that errors associated with both of the physical methods are very similiar. This probably indicates that the $\Delta\tau$ integral term in eq.(6) has little contribution, since the amount of water vapor is very small. For the sake of completeness, water vapor errors are shown in Fig 3b. Note that the abscissa scale was enlarged.

4.3 Brightness Temperature Statistics

The question of the ability of retrieved solutions to satisfy measured radiances within the instrumental noise is often overlooked. Physical retrievals are expected to satisfy the RTE since they are based on radiative transfer physics; therefore we decided to test the agreement of the forward calculation of radiances, using the retrieved solution, with the measured radiances. In order to compare radiances of different wavenumbers, both measured and retrieval calculated radiances were converted, using the inverse Planck equation, to brightness temperatures. The standard deviation of differences between calculated and measured brightness temperatures were computed for the 3 latitude zones, and are shown in Table 3. RMS errors were not calculated since they might include bias errors due to incorrect transmittances, whereas the standard deviation, by definition, excludes systematic errors.

In examining Table 3, the dominant feature in all 3 zones is the ability of the MVS solution radiances to agree better with the measurements than the solution radiances from the other two methods. This is not a surprising observation, since the RTE applicable to the MVS method is the correct physical model for the real-time measurements; second, since both temperature and water vapor are solved simultaneously, the RTE is simultaneously satisfied for all channels; and third, the correlations that exist between temperature and moisture are realistic.

The worst discrepancy between measured and calculated radiances is for the operational results, which is not surprising. Radiances in the infrared spectrum have a nonlinear dependency on temperature and water vapor, and therefore linear regression cannot be expected to satisfy these measurements. On the other hand, since the Planck function is linear with respect to temperature in the microwave region, brightness temperatures calculated from the operational retrievals agrees well with measurements from the MSU instrument.

Table 3. Standard Deviation of Calculated and Measured Brightness Temperatures Differences

	TROPICS			MIDDLE LATITUDE			POLAR		
HIRS	Operation	Minimum Variance	MVS	Operation	Minimum Variance	MVS	Operation	Minimum Variance	MVS
2	0.49	0.25	0.27	0.49	0.33	0.35	0.50	0.40	0.41
3	0.51	0.27	0.29	0.51	0.37	0.39	0.50	0.40	0.41
4	0.34	0.28	0.23	0.43	0.38	0.29	0.26	0.24	0.14
5	0.46	0.42	0.22	0.44	0.47	0.24	0.29	0.26	0.16
6	0.59	0.59	0.27	0.40	0.56	0.26	0.36	0.29	0.17
7	0.93	0.75	0.38	0.47	0.69	0.36	0.36	0.41	0.27
10	1.10	0.76	0.39	0.65	0.79	0.33	0.35	0.58	0.28
11	3.36	2.69	1.55	1.64	1.57	0.67	1.14	0.74	0.54
12	4.89	4.00	2.36	2.79	2.69	1.63	3.33	1.10	0.66
13	0.89	0.63	0.34	0.52	0.52	0.27	0.38	0.28	0.16
14	0.59	0.42	0.18	0.47	0.34	0.16	0.37	0.23	0.17
15	0.29	0.34	0.18	0.55	0.33	0.25	0.40	0.41	0.28
16	1.18	1.08	1.18	1.26	0.98	1.04	0.67	0.77	0.68
MSU									
2	0.36	0.57	0.41	0.42	0.64	0.42	0.47	0.48	0.52
3	0.32	0.38	0.42	0.29	0.47	0.39	0.20	0.37	0.37
4	0.38	0.28	0.28	0.47	0.43	0.44	0.57	0.30	0.29
SSU									
1	0.87	0.73	0.77	0.77	0.92	0.91	1.06	0.90	0.90
3	0.75	0.11	0.14	1.13	0.37	0.37	0.44	0.74	0.74

The channels having the worst agreement, between calculated and measured brightness temperatures, were HIRS 11 and 12. Transmittances generated for these channels are extremely sensitive to water vapor content, and also have the greatest model uncertainty.

5. SUMMARY AND CONCLUSIONS

It has been shown that in the relatively moist layer of the lower atmosphere, water vapor retrieval errors from the MVS algorithm are consistently smaller than the errors associated with the two regression methods. With respect to temperature, the operational retrieval appear to have an advantage in the tropics, whereas in the more meteorological active zones both physical retrieval methods perform quite well. The results and theory indicate that the MVS algorithm has an advantage over classical minimum variance. First of all, MVS solves the RTE simultaneously for temperature and water vapor, and second the integrated solutions are in best agreement with the measured radiances.

Also important is the reduced dependency of the physical retrieval on radiosonde data. Parallel testing in real time with the operational retrievals is planned to begin later this year. Afterwards a decision will be made to decide whether or not to replace the current operational algorithm with a physical retrieval method.

6. ACKNOWLEDGEMENTS

The authors would like to thank the following persons affiliated with SASC Technologies; David Niver, for providing the FC regression coefficients, and Dr. Zia Ahmad for his useful suggestions. They would also like to thank Charles Novak and Michael Chalfant of NOAA/NESDIS for providing the resources to conduct this study.

7. REFERENCES

Fleming, H.E., D.S. Crosby, and A.C. Neuendorffer, 1986: Correction of satellite temperature retrieval errors due to errors in atmospheric transmittances. To be published in J. Climate Appl. Meteor.,25.

Fleming, H.E., M.D. Goldberg, and D.S. Crosby, 1986: Minimum variance simultaneous retrieval of temperature and water vapor from satellite radiance measurements. Preprint Volume of this Conference.

Rodgers, C.D., 1976: Retrieval of atmospheric temperature and composition from remote measurements of thermal radiation. Rev. Geophys. Space Phys., 14, 609-624.

Smith, W.L., H.M. Woolf, C.M. Hayden, D.Q. Wark, and L.M. McMillin, 1979: The TIROS-N operational vertical sounder. Bull. Amer. Meteor. Soc., 60, 1177-1187.

Smith, W.L., and H.M. Woolf, 1984: Improved vertical soundings from an amalgamation of polar and geostationary radiance observations. Preprint Volume: Conference on Satellite Meteorology/Remote Sensing and Applications, June 25-29, 1984, Clearwater Beach Florida. Published by Amer. Meteorol. Soc., Boston, MA.

Weinreb, M.P., H.E. Fleming, L.M. McMillin, and A.C. Neuendorffer, 1981: Transmittance for the TIROS operational vertical sounder. NOAA Tech. Report NESS 85, National Earth Satellite Service, Washington D.C., 60 pp.

1.9

DETERMINATON OF WATER VAPOR PROFILES AND TOTAL OZONE BURDEN FROM HIRS2/MSU SOUNDING DATA

D. Reuter and J. Susskind
NASA/Goddard Space Flight Center
Laboratory for Atmospheres
Greenbelt, MD 20771

1. INTRODUCTION

The Goddard Laboratory for Atmospheres has developed a physically based retrieval scheme for analysis of HIRS and MSU radiances which determines atmospheric and surface conditions such that, when substituted in the radiative transfer equations representative of the observations, match those observations to within a specified noise level. The method is fundamentally different from the statistical one used operationally at NOAA NESDIS, which was employed to produce the soundings in the official FGGE data base. The products obtained from the GLA system are atmospheric temperature-humidity profiles, total ozone burden, sea and land surface temperature, sea ice and snow cover, and cloud heights and amounts. The details of the radiative transfer calculations and the basic algorithm are described in Susskind et al. (1983) and Susskind et al. (1984).

A number of improvements have been made to the processing system described in Susskind et al. (1984). Susskind and Reuter (1985) show that the accuracy of sea-surface temperatures retrieved from the HIRS2/MSU data is at least as good as that obtained operationally from AVHRR. In Susskind et al. (1986) the improved method of cloud parameter retrievals is discussed. This paper, dealing with fields of total ozone burden and humidity, will briefly describe the elements of the new algorithms to retrieve these quantities, which were not original products of the system.

The total ozone content of the atmosphere is an important variable for at least two reasons, indicative of both stratospheric and tropospheric processes. The ozone content of the stratosphere is determined by photochemical processes dependent on the amount of sunlight and various trace constituents. Long term trends of total ozone, as well as the annual cycle, are measures of natural phenomena as well as the effects of the accumulation of man-made trace constituents upon the ozone layer in the stratosphere. The total ozone content is also indicative of the depth of the ozone rich stratosphere, or equivalently, the height of the tropopause. This is related to the tropospheric air mass and is a useful quantity in monitoring air mass and in improving the sounding accuracy of remote sensors. Water vapor profiles are important both for initializing general circulation models to help improve forecasts, as is currently done with the retrieved temperature profiles, and also as an indicator of atmospheric circulation.

2. METHOD

The method used for retrieving atmospheric constituent profiles is similar to that used for the temperature retrievals, in that heavy reliance is placed on the ability to accurately model the response of a given channel to changes in a given atmospheric constituent, as opposed to using statistical relationships between brightness temperature and constituent amount. Since the retrieval process is identical in form for both water vapor and ozone, the following flow description will be given in terms of humidity soundings. Differences between the two constituent retrieval processes will be detailed following the description of the method. For reasons to be given later, the water vapor and ozone retrievals are carried out after the ground and atmospheric temperature retrieval has been performed. The water vapor retrieval utilizes HIRS2 channels 8 and 10 in the 11 and 8 μm window regions and channels 11 and 12 in the 6.7 μm water vapor band. The ozone retrievals utilize channel 9 in the 9.6 μm ozone band. The observations used are cloud corrected (reconstructed clear column) radiances, which are the estimates of radiances which would have been observed if no clouds were present. The reconstructed radiances are obtained as part of the temperature retrieval process by a method detailed in Susskind et al., 1984.

The iterative relaxation method for determination of atmospheric water vapor proceeds in the following steps:

1 Given the retrieved atmospheric and surface temperatures and a first guess water vapor distribution, $q^{\circ}(P)$, the brightness temperature, Θ_i^c which would be expected to be observed in a given channel may be calculated from the radiative transfer equation. The first guess will be modified according to the difference between Θ_i^c, and $\tilde{\Theta}_i$ the reconstructed (observed) brightness temperature, and the sensitivity of Θ_i^c to changes in humidity.

2 In order to estimate the sensitivity of brightness temperatures to humidity changes, the entire guess water vapor profile is alternately increased and decreased by a fixed fraction δ and the brightness temperature is calculated for both cases, for each channel to be used in the retrieval. Using this scaling approximation, the change in brightness temperature in channel i for a fractional change in water vapor of $\pm\ \delta$ is then estimated as

$$\Delta\Theta^c_{i\pm} = \Theta^c_i [q^N(P)] - \Theta^c_i [q^N(P)\cdot(1\pm\delta)] \qquad (1)$$

3 Each channel i then provides an estimate of the fractional change to be made in humidity, f_i, computed according to

$$f_i = \left(\frac{\tilde{\Theta}_i - \Theta^c_i}{\Delta\Theta^c_{i\pm}}\right)(\pm\delta) \qquad (2)$$

Where $\Delta\Theta^c_{i+}$ or $\Delta\Theta^c_{i-}$ is used in the denominator depending on which has the same sign as the numerator.

4 Since each channel senses a different region of the atmosphere and there are also sources of noise, the 4 estimates of f_i will not be the same in general. A fractional change, $\varepsilon(P_j)$ must be found at each of the n discrete pressure levels used in modeling the radiative transfer equation. This is done by weighting the values of f_i according to

$$\varepsilon(P_j) = \sum_i W_i(P_j) f_i / \sum_i W_i(P_j) \qquad (3)$$

where $W_i(P_j)$ represents the relative sensitivity of channel i to humidity changes at P_j. In these calculations, $W_i(P_j)$ was approximated by the analog of the temperature sounding weighting function

$$W_i(P_j) = \left(\frac{d\tau_i}{d\ln P}\right)_{P_j} \qquad (4)$$

which is faster to compute than the actual sensitivity function relating changes in brightness temperatures to changes in humidity at specific levels, and provides essentially identical soundings. Equation (3) is evaluated at mid-mandatory levels and the values of $\varepsilon(P_j)$ are linearly interpolated in P at intermediate values P_n.

5 Using the values of $\varepsilon(P)$ determined in step 4, the $N+1^{th}$ estimate of the water vapor profile at the n discrete pressure levels is found as

$$q^{N+1}(P_n) = q^N(P_n)(1 + \varepsilon(P_n)) \quad . \qquad (5)$$

If, for any level, $q^{N+1}(P)$ is found to correspond to a relative humidity of greater than 100%, then for that level $q^{N+1}(P)$ is set to the value of the specific humidity which corresponds to 100% relative humidity. Furthermore, because of the limited sensitivity of the infrared brightness temperatures to changes in water vapor near the surface, the values of $\varepsilon(P)$ beneath the mandatory level pressure closest to the surface are set to the value of $\varepsilon(P)$at that mandatory level. This profile is used to obtain new values for the atmospheric transmittances for the 4 channels which are then used to calculate new estimates of the brightness temperatures $\Theta^c_i[q^{N+1}(P)]$. If the residuals between $\Theta^c_i[q^{N+1}(P)]$ and $\tilde{\Theta}_i$ are sufficiently small, or if there is little change in the residuals, the process is considered to have converged and $q^{N+1}(P)$ is taken to be the retrieved water vapor profile. If this is not the case, steps 2 through 5 are repeated. Currently the process is limited to at most five iterations.

There are some exceptions to this procedure in actual practice. For example, if a temperature retrieval is not performed for any reason, or, if the temperature retrieval is flagged as nonconvergent, then no water vapor retrieval is performed. Furthermore if the sensitivity of a given channel to changes in water vapor content, as defined in step 2 above, is too small, then that channel is not used in the retrieval process. This is accomplished be setting $W_i(P) = 0$ for the channel. This situation arises occasionally for channels 8 and 10 which sense near the surface where there is sometimes little thermal contrast. Indeed, for an isothermal atmosphere and a surface with unit emissivity, a passive sounding has no information about water vapor content. Channel 8 also has very little sensitivity to water vapor under very dry conditions, in which case it becomes nearly transparent.

After a full iterative cycle has been performed, the residual differences between the observed and calculated brightness temperatures may be used to reject a retrieved profile. At the present time only a very gross check is done and a water vapor retrieval is rejected if the rms of the residuals of channels 11 and 12 is more than 2° or if the absolute value of the residual of either channel 8 or 10 is more than 5°. A looser criterion is used for these channels because they are affected by uncertainties in ground temperature and surface emissivity.

As stated before the ozone retrieval uses the same process, however, only 1 channel is used. Therefore $\varepsilon(P_j)$ in equation (3) is always equal to f_i from equation (2) and the shape of the first guess ozone profile, which is based on climatology, is not modified, only the absolute amount is changed. The sensitivity of the total ozone retrieval to the assumed shape of the distribution is expected to be less than for the water vapor retrieval. The effect of a change in the profile of an atmospheric constituent is to alter the region of the atmosphere which is probed by a channel and, for channels sensing in the lower troposphere, to affect the contribution of the surface term. Because of this, accurate water vapor distributions may only be obtained if the atmospheric and surface temperatures are well determined, and the sensitivity of the retrievals to changes in humidity near the surface is low. Therefore, retrievals are highly guess dependent near the surface and the distribution and the accuracy of a retrieved profile is dependent upon the first guess shape of the water vapor distribution. Since most of the ozone is in the cold and relatively isothermal (compared to the surface) stratosphere, a change in the shape of the first guess ozone distribution, which primarily affects only the location of the peak of the sensitivity function in the stratosphere, has little effect on the computed brightness temperature. A change in the total ozone column density, however, modifies the effect of the surface term. Since there is generally a large thermal contrast between the surface and the stratosphere, the brightness temperature is thus quite sensitive to total ozone amount and relatively insensitive to shape.

As currently implemented, the water vapor retrieval is carried out before the ozone retrieval because water vapor has some effect on brightness temperatures in channel 9, while ozone has little effect on the radiances in the water vapor channels. The temperature retrievals are not repeated using the retrieved constituent profiles.

3. RESULTS

Table 1 gives the accuracy of the humidity retrievals for a few coarse layers in terms of the rms differences from radiosondes, the percent error, and the percent improvement with respect to the 6 hr forecast first guess. These statistics are for June 1-7, 1979 and are representative of global colocations ± 3 Hrs, ± 110 km excluding coastal stations (where humidity gradients may be large). As may be seen from this table, even near radiosondes, where the six hour forecast is expected to be quite good, the retrievals have the ability to significantly improve upon the guess in the upper levels.

The 6 hr forecast humidity is not improved in the lowest level, where sensitivity to water vapor is least. Significant improvement in humidity over the first guess does occur in this level when a poorer first guess is used. The forecast first guess may not be as good away from radiosondes and the potential for improvement over the forecast in the lowest level therefore exists.

Figures 1a and b show fields of the ratio of the water vapor in the layer above 700 mb to the total water vapor column density for the months of June and January 1979. High values of this ratio generally indicate divergence, which brings water out of the boundary layer, and low values indicate subsidence. High values also occur over cold surfaces, which have the effect of drying out the air in the boundary layer.

The circulation indicated by this ratio, which should be relatively large in the presence of convection and relatively small in regions of subsidence, is very consistent with that indicated by the cloud heights and cloud amounts generated in the HIRS retrieval process (Susskind and Reuter, 1986). If one looks at just the total precipitable water field, these circulation features are not evident at all, as most of the precipitable water is in the boundary layer which, especially over oceans, is affected more by the surface temperature than the atmospheric circulation.

Ozone has been monitored almost exclusively, whether from the ground or space, using measurements at ultra-violet frequencies. For example the TOMS and SBUV instruments monitor total radiation backscattered by the atmosphere in frequencies sensitive to ozone absorption. Consequently, these measurements can be taken only during the day, and, in polar regions, only during the summer half of the year. There is no constraint about the location of the sun in the HIRS2 analysis and hence soundings can be done day and night as well as all year in polar regions. This gives the potential of twice daily monitoring of the tropopause height as well as the ability to study for the first time the entire winter portion of the ozone annual cycle in the polar regimes.

The retrieved field of total ozone for June 11, 1979 OZ ± 12 hours is shown in figure 2a. This is a composite of 3 AM and 3 PM local time soundings. Features of atmospheric circulation are clearly depicted in the O_3 fields. Note for example the ridge (low ozone burden) through most of the United States with a sharp trough off the west coast and over the great lakes. Figure 2b shows the field retrieved from TOMS (total ozone mapping spectrometer) on NIMBUS-7 taken at local noon. It is apparent that the synoptic features indicated in TOMS are reproduced very well by HIRS2/ MSU. Figure 3 shows the zonal mean total ozone amounts determined for June 2-12, 1979 from both TOMS and HIRS2. The zonal means agree very well throughout the southern hemisphere up to 60°S where the TOMS data stops. This indicates that meaningful measurements of O_3 in the polar winter can be achieved. Small differences exist in the northern hemisphere at mid-latitudes. We are examining possible reasons for this.

Figure 4 shows a monthly mean field for the difference between total ozone retrieved during the day and night for June 1979. As the total ozone is expected to stay fairly constant over the course of a day, it is gratifying to see only small differences (< 10 Dobson units) over most of the globe. This also indicates that the error in the day-night difference in retrieved ground temperature over land must not be large because the retrieved ground temperature influences the retrieved total ozone burden. We have found that an error of 1° in surface temperature corresponds to about 10 Dobson units, so the day-night ground temperature differences must be good to about 2°C.

REFERENCES

Susskind, J., J. Rosenfield, and D. Reuter, 1983: An accurate radiative transfer model for use in the direct inversion of HIRS2 and MSU temperature sounding data, J. Geophys. Res., 88C, 8550-8568.

Susskind, J., J. Rosenfield, D. Reuter, and M. T. Chahine; 1984: Remote sensing of weather and climate parameters from HIRS2/MSU on TIROS-N, J. Geophys. Res., 89D, 4677-4697.

Susskind, J. and D. Reuter, 1985: Retrieval of sea surface temperatures from HIRS2/MSU. J. Geophys. Res., 90C, 11602-11608.

Susskind, J., and D. Reuter, 1986: Cloud fields retrieved from analysis of HIRS2/MSU sounding data. Sixth Conference on Atmospheric Radiation, Williamsburg VA, May 12-16, 1986.

Table 1: Accuracy of Retrieved Precipitable water (.1 g/cm^2)

	June 1-7, 1979		± 3 Hrs ± 110 km	
Layer	RMS Value Radiosonde	RMS Error Retrieval	% Retrieval Error	% Guess Improvement
1000 mb - 1 mb	23.09	6.27	27%	2%
1000 mb - 700 mb	20.19	5.80	29%	-3%
700 mb - 500 mb	4.36	1.78	41%	9%
500 mb - 300 mb	1.37	0.68	49%	22%

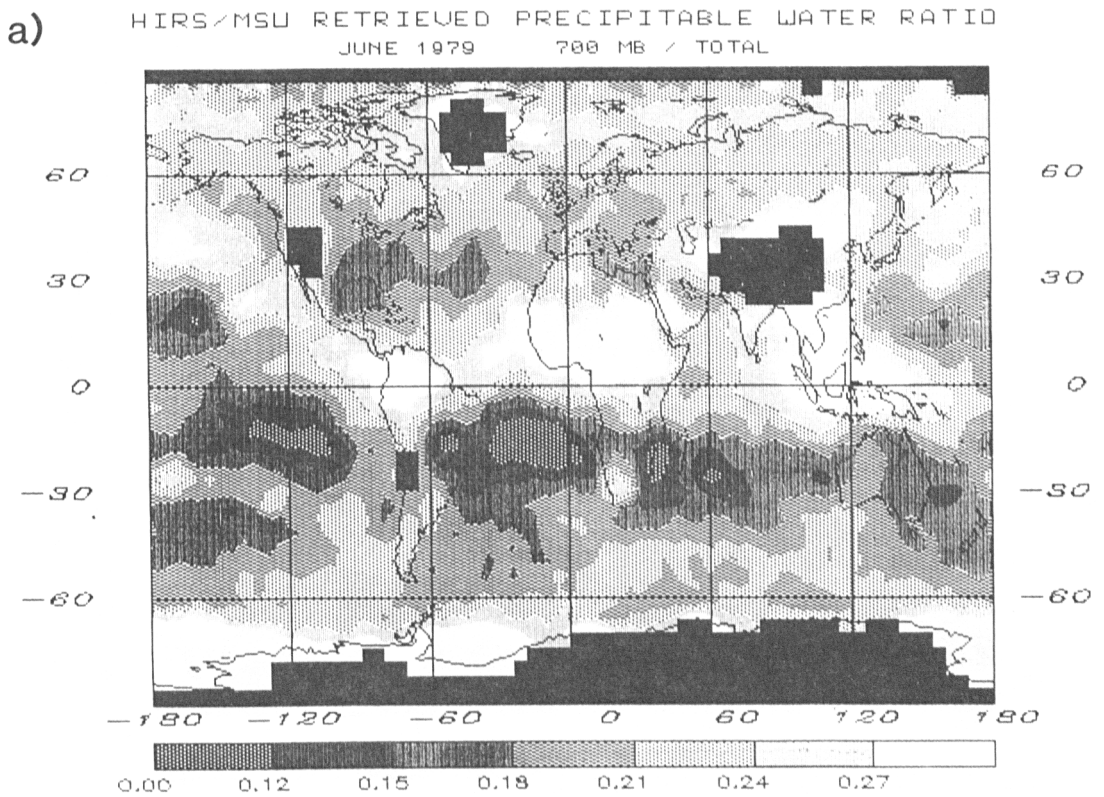

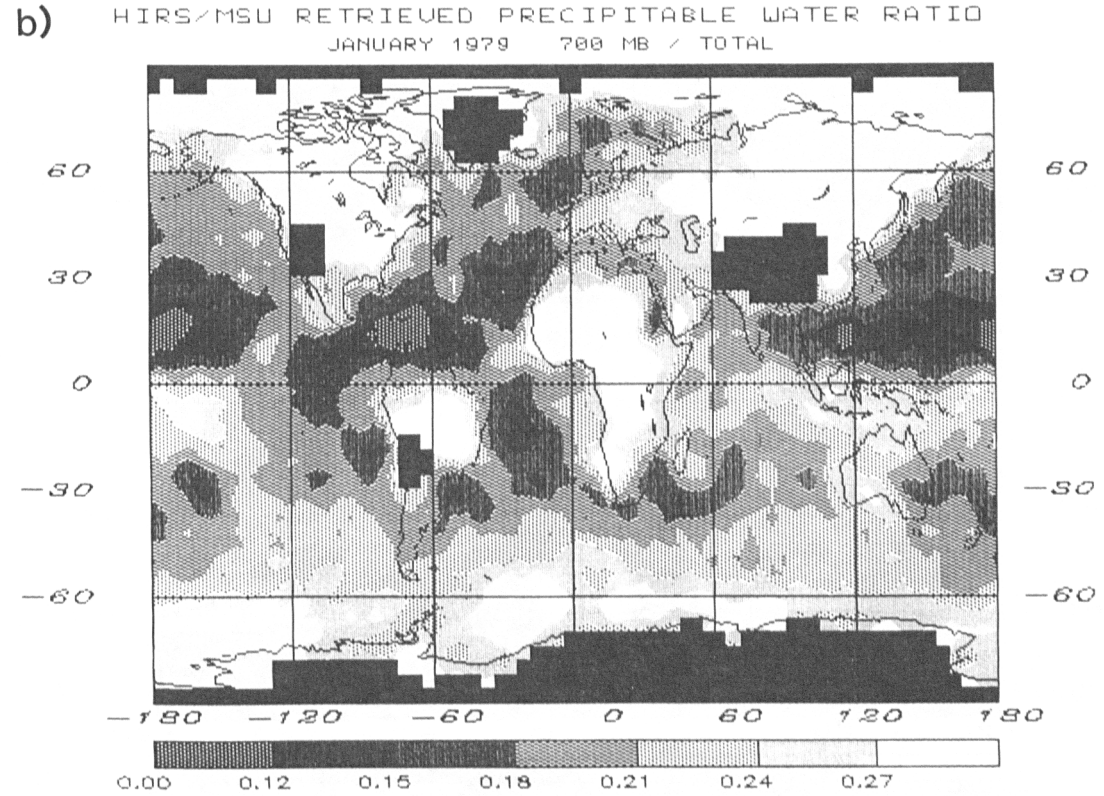

Fig. 1 Ratio of precipitable water above 700 mb to total precipitable water on a 4° x 5° grid. Areas where the surface pressure is less than 850 mb or where no retrievals were produced are given in black. a) June 1979, b) January 1979.

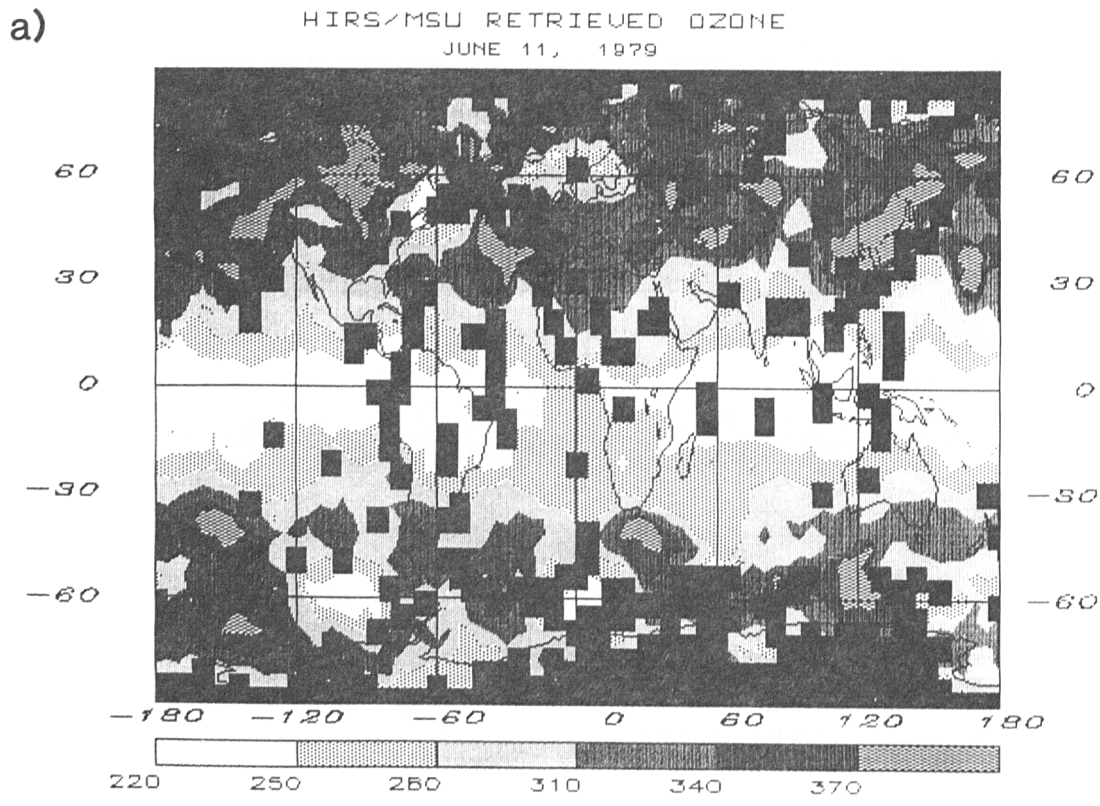

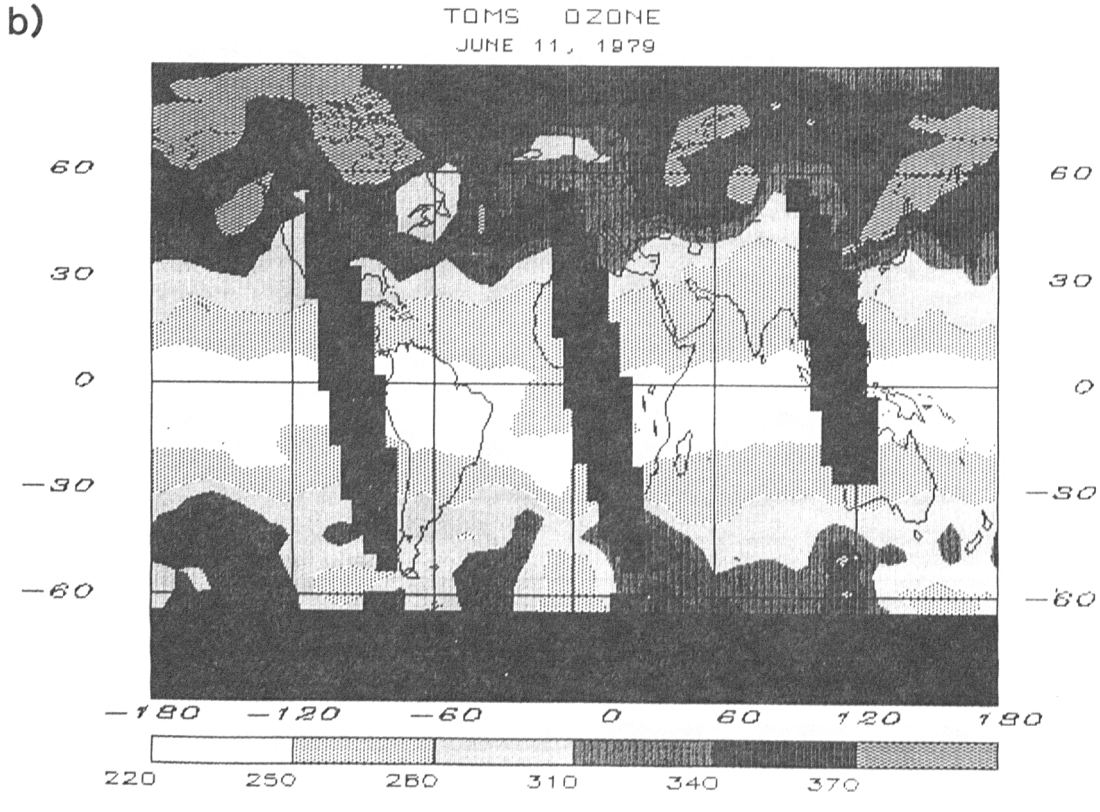

Fig. 2 Retrieved total ozone in Dobson units for June 11, 1979. Areas with no data are given in black. a) HIRS2/MSU data on a 4° x 5° grid, b) TOMS data on a 5° x 5° grid.

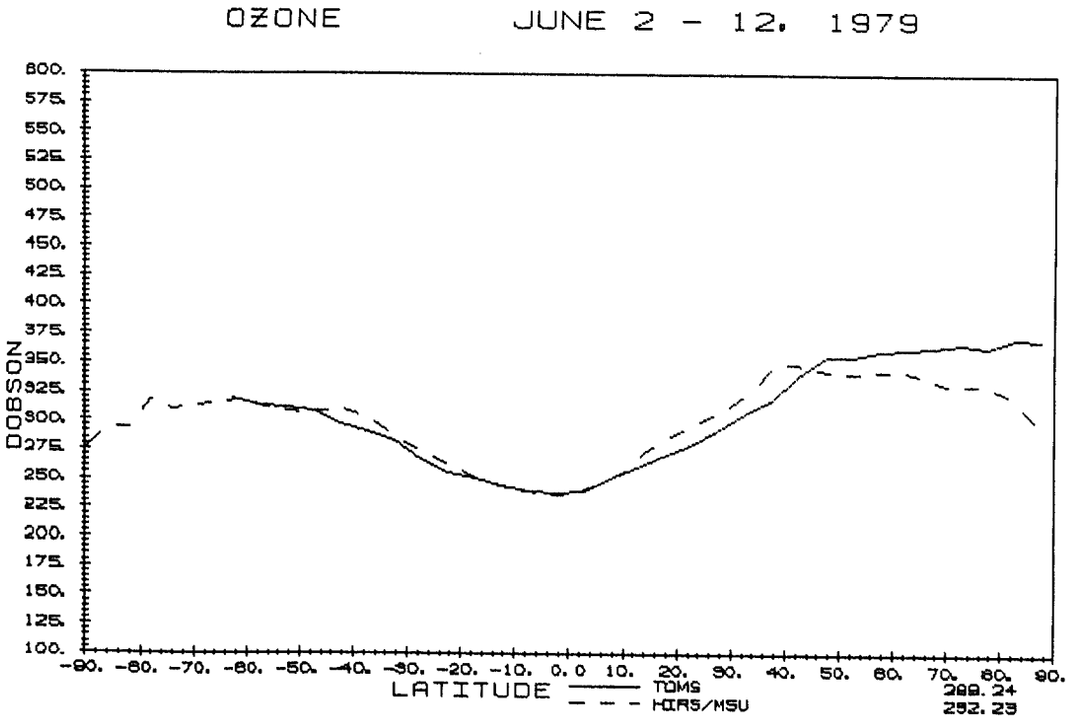

Fig. 3 Zonal mean total ozone from HIRS2/MSU and TOMS for period of June 2-12, 1979.

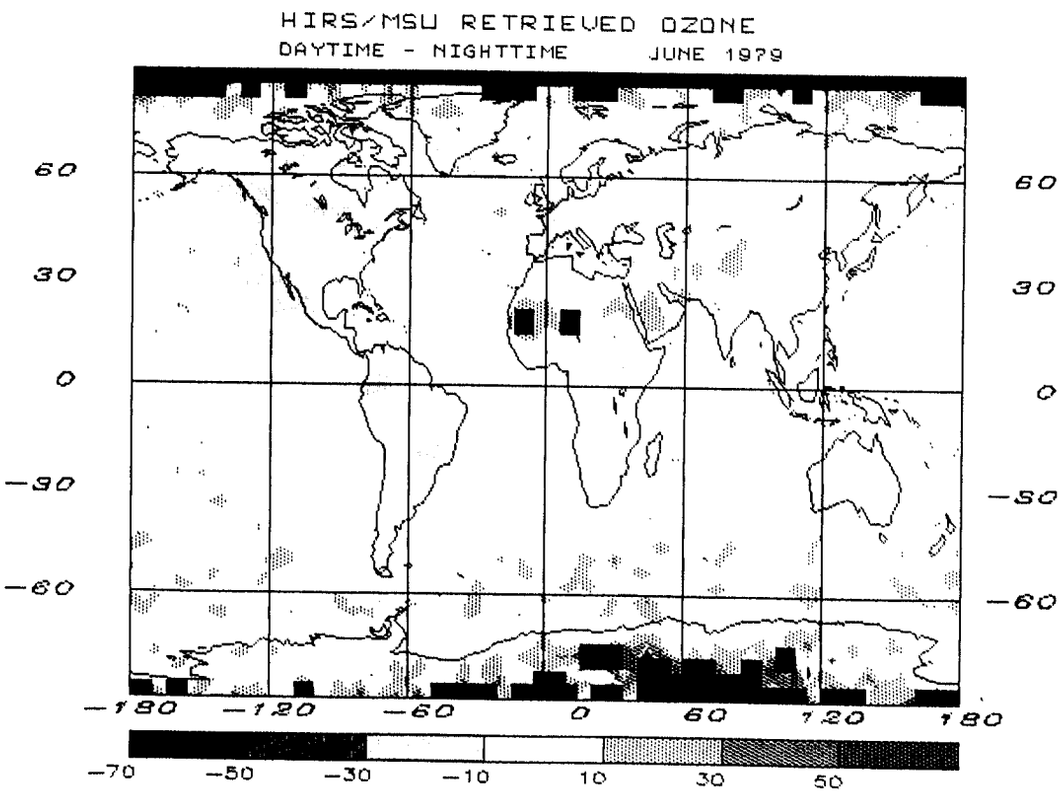

Fig. 4 Daytime (3 PM) - Nighttime (3 AM) total ozone in Dobson units from HIRS2/MSU data for the month of June 1979.

OPTIMUM RETRIEVAL OF PRECIPITABLE WATER FIELDS FROM VAS AND SURFACE DATA

DENNIS CHESTERS — *Laboratory for Atmospheres, Greenbelt, MD 20771*

WAYNE D. ROBINSON — *General Software Corp., Landover, MD 20785*

LOUIS W. UCCELLINI — *Laboratory for Atmospheres, Greenbelt, MD 20771*

1. INTRODUCTION

Convective storms draw much of their energy from latent heat stored in low-level water vapor. Most of the variance in low-level moisture occurs on horizontal scales less than 300 km and time scales less than a day (Browning, 1980). Geosynchronous satellite observations with water vapor sensitive channels are required to resolve these important sub-synoptic features.

Low-level precipitable water (PW) fields have been retrieved experimentally over the central United States at mesoscale resolution using the infrared channels from the VISSR Atmospheric Sounder (VAS) on GOES. Chesters *et al.* (1983) retrieved PW at 15 km resolution by utilizing the differential water vapor absorption between the two VAS "split window" channels. Lee *et al.* (1983) retrieved PW manually at 50 km resolution, utilizing all twelve of the VAS channels together with conventional surface temperature and dewpoint measurements in a regression algorithm. Recently, Chesters *et al.* (1985 and 1986) automated Lee *et al.*'s (1983) regression algorithm to retrieve atmospheric data at <u>every</u> VAS sounding-field-of-view (SFOV) so that retrievals can be prepared as high resolution sounding images like those from the "split window" algorithm.

This study compares VAS retrievals of PW with various channel selections in the regression algorithm and with the "split window" algorithm. The aim is to provide guidelines for algorithm and channel selection in order to encourage operational retrieval of low-level mesoscale moisture fields from VAS data and routine dissemination of satellite-format sounding images for use in mesoscale forecasts.

2. ALGORITHMS

The "split window" algorithm is a linearized radiation transfer model with a single thick layer radiating at an average temperature T_{air} above the emitting surface T_{sfc}. VAS brightness temperature T^*_υ in bandpass υ is controlled by transmittance $\tau_\upsilon(PW)$ determined with a dry absorption coefficient k_υ and with p- and e-type water vapor absorption coefficients a_υ and b_υ:

$$T^*_\upsilon = T_{sfc}\,\tau_\upsilon(PW) + T_{air}\,(1 - \tau_\upsilon(PW)), \qquad (1)$$
$$\tau_\upsilon(PW) = \exp[\,-(k_\upsilon + a_\upsilon PW + b_\upsilon PW^2)\,].$$

The VAS "split window" channels (7 and 8) provide 2 measurements of T^*_υ for 3 unknowns (PW, T_{sfc} and T_{air}). Equation (1) is reduced to 2 unknowns by using an average value of T_{air} determined empirically from radiances observed at radiosonde sites within an air mass where PW and hence $\tau_\upsilon(PW)$ is known. Clouds are detected when T^*_υ is colder than T_{air}. A cloudy SFOV is assigned an off-scale PW value represented with a black or white pixel in a "split window" image.

In the linear regression algorithm, all VAS channels and/or conventional surface data are used as predictors (R_υ) of PW. A signal/noise (S/N) conditioning factor is used to stabilize the retrieval matrix (C_υ). Regression also provides a statistical measure of the relative contribution (F_υ) of each predictor to PW by multiplying each element of the retrieval matrix C_υ by the standard deviation (σ_υ) from the mean value $\langle R_\upsilon \rangle$ in the corresponding predictor from the radiosonde training set for the air mass. The first few predictors with the largest contributions usually retrieve most of the information in a set of observations.

$$\Delta PW = PW - \langle PW \rangle, \quad \Delta R_\upsilon = R_\upsilon - \langle R_\upsilon \rangle, \qquad (2)$$
$$C_\upsilon = \langle \Delta PW\, \Delta R_\mu \rangle \bullet [\langle \Delta R_\mu\, \Delta R_\upsilon \rangle + \delta_{\mu\upsilon}(S/N)^{-2}]^{-1}, \quad \text{for RAOB training.}$$
$$F_\upsilon = \sigma_\upsilon C_\upsilon,$$
$$PW = \langle PW \rangle + C_\upsilon \bullet [R_\upsilon - \langle R_\upsilon \rangle], \quad \text{retrieved at every SFOV.}$$

The signal/noise (S/N) conditioning factor in equation (2) is normally set to a realistic value (10/1), but may also be set to a low value (1/10) to suppress unwanted predictors. Cloudy areas are retrieved as off-scale values of PW, displayed as black or white pixels in a VAS sounding image.

All retrievals in this study are carried out with the same VAS and conventional datasets gathered over the central United States on 13 July 1981, a relatively cloud-free day with a wide range of low-level moisture conditions within a pre-convective midsummer environment (Mostek *et al.*, 1986). The morning and evening synoptic radiosondes provide 51 cloud-free sites for empirical determination of T_{air} in the "split window" algorithm (Eq. 1) and of C_υ and F_υ in the regression algorithm (Eq. 2). These radiosonde sites are re-used to calculate dependent estimates of the PW accuracy for each algorithm. The conventional surface temperature (T_{sfc}) and dewpoint (D_{sfc}) reports are objectively analysed and bilinearly interpolated into satellite coordinates with the same resolution and format as the VAS radiance channels. In fact, T_{sfc} and D_{sfc} often replace the noisy VAS upper air channels 1 and 2 in the predictor dataset for low-level moisture.

The inclusion of conventional surface data as a statistical predictor of PW is motivated by Smith's (1966) and Lee *et al.*'s (1983) successes. The use of three or fewer VAS channels to retrieve PW is motivated by the fact that the VAS instrument is routinely operated in a multi-spectral imaging (MSI) mode, restricted to transmitting VISSR data (visible and 11 μm infrared) and only one or two additional infrared channels. The additional channels in this study are selected by examining theoretical weighting functions $d\tau_\upsilon/d\ln P$ (Fig. 1) and the empirical contribution functions for the VAS plus SFC predictors (Fig. 2). These considerations point to VAS channels 5, 6, 7, 8 and D_{sfc} as the principal predictors of PW. The apparent contribution (Fig. 2) from VAS channel 2 is regarded as a coincidental correlation between upper air condtions and low-level moisture for this case.

3. SFOV RESOLUTION

Random noise in the soundings is reduced by horizontally averaging the VAS radiances. The VAS instantaneous field-of-view is approximately 15 km at nadir, but the detector is over-sampled so that individual samples occur at approximately 4 km intervals along each scanline as GOES spin-scans its infrared footprint across the Earth. Radiance data at 15 km resolution is less noisy when 4 samples are averaged together instead of being single-sampled (SS) at every 4th observation.

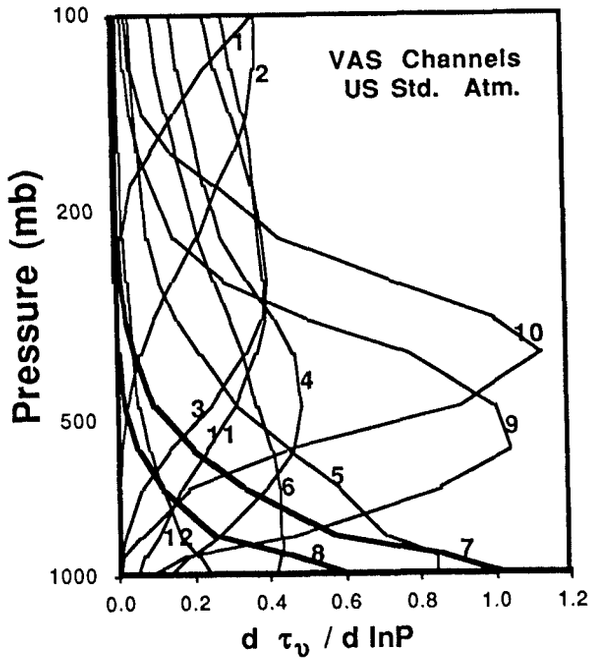

Fig. 1. Weighting functions for the 12 VAS channels. Channels 7 and 8 (highlighted as the "split window") estimate low-level moisture by differential water vapor absorption between 11.1 and 12.7 μm. Channels 5 and 6 are long- and short-wave differentiators of low-level water vapor and temperature.

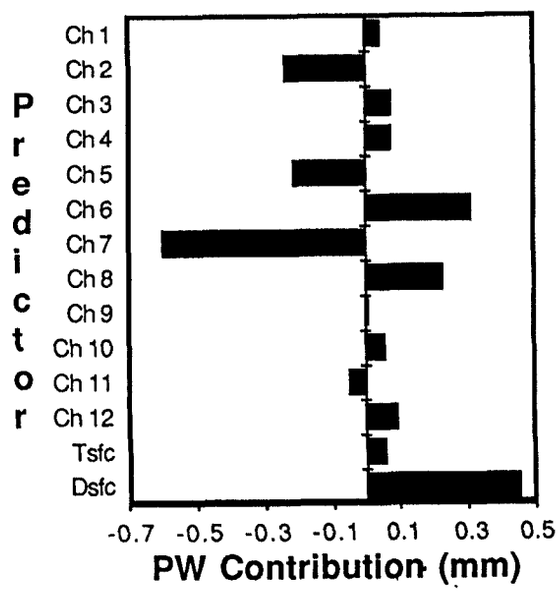

Fig. 2. Contribution functions to regression retrievals of PW on 13 July 1981 by all 12 VAS channels plus conventional surface temperature and dewpoint. The dominant statistical contributions from VAS channels 5, 6, 7, 8, and D_{sfc} are consistent with physical expectations.

Fig. 3 compares statistical accuracy and image quality at SS, 15, 30, 60 and 120 km resolution. Cloud contamination introduces more systematic error for larger SFOV, eventually overwhelming the gains from averaging the random error. Objective error estimates are listed as RMS differ - ences between VAS and radiosonde PW values for each SFOV size in Fig. 3. Optimum numerical and image results for the "split window" algorithm are provided at 15 to 60 km resolution. Similar regression results (not shown) indicate that 30 to 60 km SFOV resolution is optimal for that method.

Smith *et al.* (1985) experimented with rarely used half-size infrared detectors on VAS to create "split window" PW images at 8 km resolution. Some small PW features were seen at this remarkably high resolution, but objective error values at radiosonde sites (such as in Fig. 3) were not presented, and it is unclear whether or not the small features were due to unresolved clouds. Smith *et al.*'s (1985) key suggestion was to replace the unretrievable image pixels in overcast areas with the corresponding GOES visible data. Fig. 3f presents the results of this kind of substitution using the GOES visible data in Fig. 4b. The shadows in the cloudtops do indeed enhance one's understanding of the overcast areas, and are preferrable to the gaping holes in the VAS "split window" PW coverage.

4. CHANNEL SELECTION

Optimum channel selection is determined by comparing the statistical accuracy and image quality of several PW retrieval experiments at 2300 GMT on 13 July 1981 (Fig. 4):

• Fig. 4a presents a conventional analysis of PW from the afternoon **RAOB** reports, indicating a large area of extremely moist air over the central Midwest with a strong PW gradient to the High Plains and a drier area over southern Illinois and eastern Tennessee. A histogram of PW values is displayed, maximized at 41 mm with a standard deviation (σ) of ± 6.4 mm. This radiosonde analysis is "ground truth" for PW, even though it lacks mesoscale information.

• Fig. 4b presents the corresponding **GOES visible** image, indicating broken convective clouds in many areas. The clouds over northern Illinois and eastern Iowa developed stong convective storms, while southern Illinois remained non-convective.

•Fig. 4c presents **SFC-only** regression retrievals using conventional surface temperature and dewpoint alone. As noted by Smith (1966), the surface reports are a useful indicator of the overlying PW, with an RMS error (ε) of ± 6.9 mm in this case. Surprisingly, no additional mesoscale

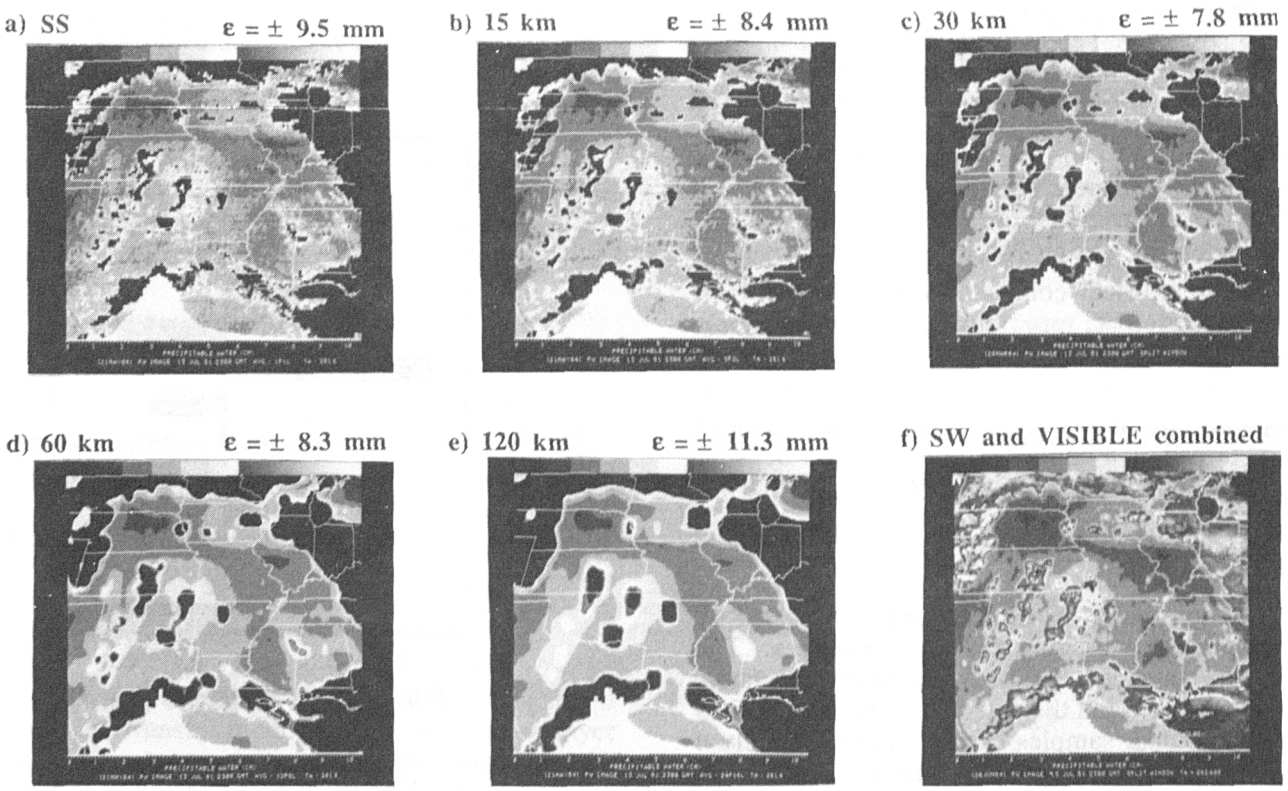

Fig. 3. Sounding images and RMS accruacy of PW retrievals from the VAS "split window" as a function of SFOV size for: a) single-samples (SS), b) 15 km, c) 30 km, d) 60 km, and e) 120 km horizontal resolution. Panel (f) presents a PW image with the overcast areas replaced by corresponding GOES visible images of the cloud tops, as suggested by Smith *et al.* (1985).

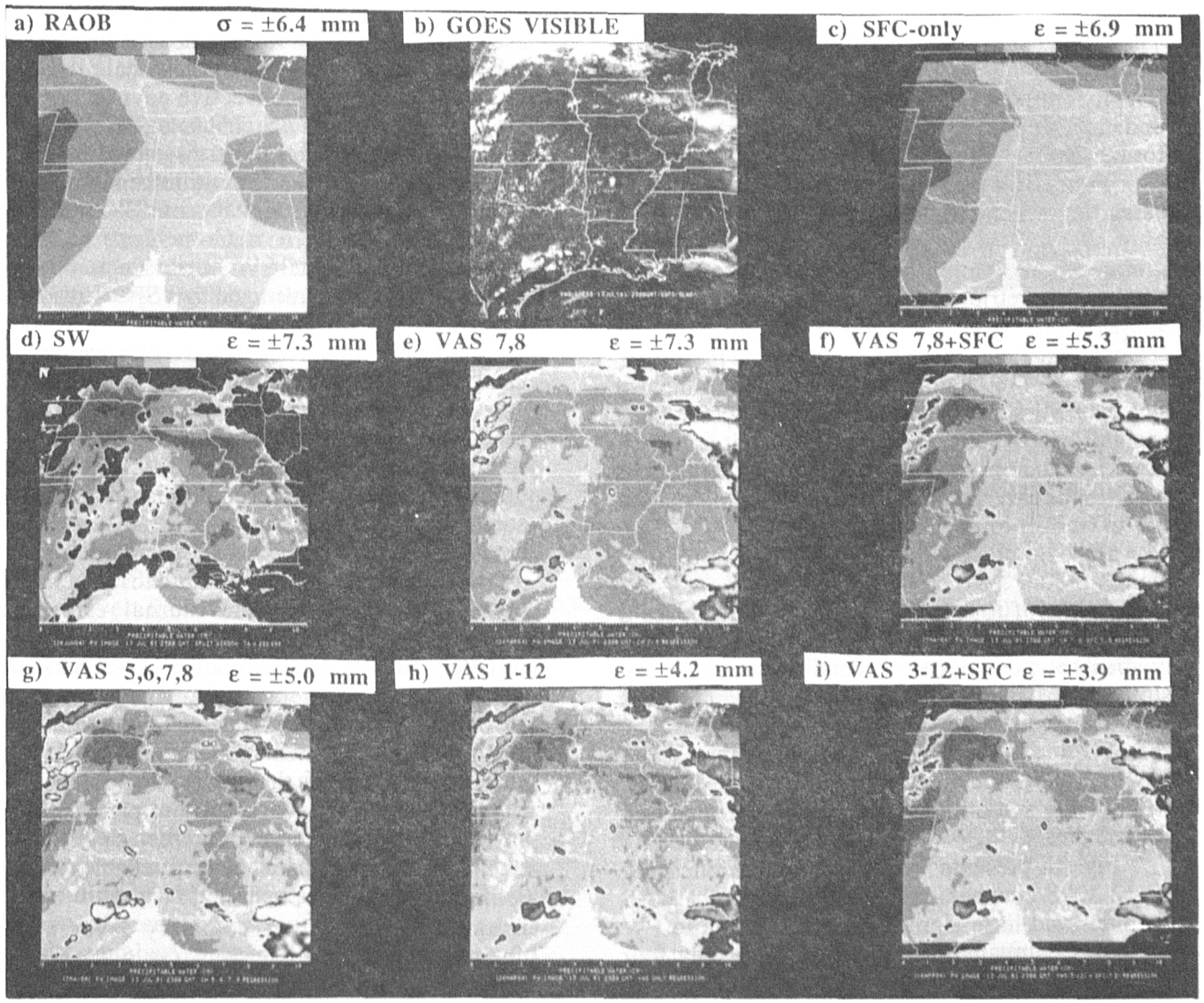

Fig. 4. PW statistics and images at 2300 GMT on 13 July 1981: a) RAOB analysis, b) GOES visible, c) SFC-only regression retrievals, d) "split window" physics, e) VAS 7,8 regression, f) VAS 7,8+SFC regression, g) VAS 5,6,7,8 regression, h) VAS-all regression, and i) VAS 3-12+SFC regression. PW values are imaged with a 5-level grey scale with steps at 10 mm intervals from 0 to 60 mm. For example, the humid air over the central Midwest contains PW values from 40 to 50 mm. Retrieved values from 60 to 106 mm indicate off-scale soundings over overcast areas, displayed as entirely black in Fig. 4d or as continuous shades of grey in Figs. 4e to 4h. Histograms of PW values are provided at the bottom of each PW image, also on a scale from 0 to 106 mm. The four-predictor PW retrievals (VAS 7,8+SFC in Fig. 4f and VAS 5,6,7,8 in Fig. 4g) provide good results with modest effort. The "split window" is the best two-predictor algorithm. More than four or five key predictors deliver little more useful information about low-level PW.

detail is supplied by the surface data (compare to Fig. 4a), and the dry region over southern Illinois and eastern Tennessee is missed due a moist but shallow boundary layer in that region that is unrepresentative of the overlying air.

• Fig. 4d presents SW, the "split window" PW retrievals. Dramatically detailed mesoscale features are discovered in the cloud-free areas, such as a dry slot across northern Missouri, southern Illinois and western Tennessee. Despite the mesoscale detail, these "split window" PW values show excessive spread on the histogram, too much contrast in the image, and poor absolute accuracy at the radiosonde sites (±7.3 mm).

• Fig. 4e presents **VAS 7,8** regression using the two VAS split window channels 7 and 8 alone. The two-predictor PW field also indicates a dry slot from Nebraska to southern Illinois. However, PW magnitudes and gradients are significantly underestimated, and absolute accuracy is as poor as for the "split window" retrievals.

• Fig. 4f presents **VAS 7,8+SFC** regression using the two VAS split window channels 7 and 8 plus surface temperature and dewpoint. This minimal combination of key VAS channels and surface data retrieves a good representation of the sub-synoptic gradients and magnitudes in the regional PW field and also supplies some mesoscale details from the satellite radiances, such as the dry slot over Missouri. Absolute accuracy (±5.3 mm) is significantly better than with the "split window" or two-predictor regression. However, the thin but moist boundary layer in southern Illinois causes PW to be over estimated in that region.

• Fig. 4g presents **VAS 5,6,7,8** regression using the four VAS low-level channels 5, 6, 7 and 8. This set of four key channels also retrieves a good representation of both the subsynoptic gradients and the mesoscale details, such as the dry slot over Missouri connecting the minima over Nebraska and southern Illinois. However, the retrieved images are noisier than the VAS 7,8+SFC four-predictor retrievals in Fig. 4f, without the smoothing provided by the analysed surface data.

• Fig. 4h presents **VAS 1-12** regression using all 12 VAS channels. The additional eight VAS channels add little significant contribution to PW retrievals compared to the results from only four key channels used in Fig. 4g. If anything, the PW images suffer more random noise.

• Fig. 4i presents **VAS 3-12+SFC** regression using VAS channels 3 to 12, plus surface temperature and dewpoint. As found by Lee *et al.* (1983), the addition of conventional surface data somewhat smooths and improves the accuracy of the PW retrievals. However, the results are only slightly better than the VAS+SFC four-predictor PW fields in Figs. 4f. The apparent improvement in absolute accuracy is mostly due to the reduction in dependent residual variance when one introduces additional predictors for the same training dataset.

6. SUMMARY

VAS radiances and conventional surface temperature and dewpoint data are used in several combinations within a regression algorithm to determine the optimum resolution and accuracy of low-level precipitable water fields retrieved from geosynchronous satellite observations. Point retrievals at radiosonde sites are used to determine the numerical accuracy of each retrieval technique, and sounding images of the retrieved PW fields are used to determine the relative accuracy and spatial coherence of PW features at mesoscale resolution in a midsummer pre-convective environment over the United States. VAS channels 5, 6, 7 and 8 (at 13.3, 4.5, 12.7 and 11.2 μm) and the surface dewpoint contribute the most information to the regression-based retrievals of PW. The best compromise between random noise and cloud contamination in the PW retrievals is obtained when radiances are averaged to a SFOV resolution between 15 and 60 km.

The best PW regression retrievals are obtained using ten VAS channels plus conventional surface data, but the improvement is marginal over a four-predictor regression scheme using the two VAS split window channels (7 and 8) with either two other low-level VAS channels (5 and 6) or conventional surface temperature and dewpoint as predictors. The regression retrievals require both morning and evening synoptic radiosonde data for training, and suffer some diurnal errors (not shown) due to the lack of midday training. Ancillary surface data introduces useful horizontal smoothing to the sounding images, but it also introduces the hazard of erroneous prediction of the overlying PW when the boundary layer is unrepresentative of the lower troposphere. A physical "split window" algorithm provides better PW estimates than regression when only the 11.1 and 12.7 μm VAS channels are available (as when the GOES satellite is operated in a multi-spectral imaging mode), when boundary layer surface dewpoint data is misleading (as occurs during inversions), or when radiosonde training is limited to only one time period (as might occur operationally).

Robinson *et al.* (1986) are publishing a more comprehensive analysis of this data using independent datasets, more training and testing variations, full color illustrations, and a time-series of sounding images which demonstrate the reliability of each algorithm during the diurnal cycle.

Acknowledgements: Funds were provided by NASA's Mesoscale Atmospheric Processes Research Program. All sounding images were created on the Atmospheric and Oceanographic Image Processing System (AOIPS) at NASA/GSFC. Mr. A. Mostek (currently at NOAA/NMC) prepared some of the sounding image datasets. Mr. D. Larko and Mr. J.M. Villardo (Research and Data Systems) developed the software to interpolate surface data to satellite resolution.

APPENDIX: A FAST CONTOURING ALGORITHM FOR VAS SOUNDING IMAGES

A wide range of PW values had to be presented on a limited range grey scale in Figs. 3 and 4. For reproduction in a limited black-and-white medium, a fast contouring method is planned for future VAS sounding images. Contours from conventional objective analysis of satellite soundings are often unsatisfactory because they are distorted by missing or off-scale values in cloudy areas and because objective analysis requires considerable computer time.

The following data processing method manipulates the grey scale image directly and introduces off-scale values (black or white contours) at regular intervals in the sounding image. A step-by-step numerical example illustrates the method for contouring PW at intervals of 10 mm:

1. Convert the PW at each SFOV to an integer (e.g. 25.7 mm to the number 26). Save a copy of this pixel array – it is the uncontoured grey level image normally displayed on an image terminal.

2. Truncate the values in the array to the nearest factor of 10 (e.g. the number 26 becomes 20). The image becomes a series of "plateaus" at the desired contour intervals.

3. Make a running average over the array, replacing each pixel with an average of the surrounding pixels. Pixels at the boundaries between different areas acquire intermediate values (e.g. the number 25 between areas numbered 20 and 30). Interiors remain the same (e.g. areas full of 20's remain 20's). This "rounds" the edges of the "plateaus".

4. Convert the pixels that were unchanged by the running average to the number 1 (e.g. number 20 or 30 becomes 1) and convert the changed pixels to the number 0 (e.g. number 25 becomes 0). This contour array has 0's at the rounded edges of the "plateaus", and 1's at the interiors of the "plateaus".

5. Multiply each pixel in the contour array times the corresponding pixel in the grey level array from the first step (e.g. 0 times 30 creates a zero level contour representing 30.1 mm of PW, but 1 times 26 leaves a number 26 representing 25.7 mm of PW).

Fig. 5 presents the results of contouring the sounding image in Fig. 4d, which is PW retrievals from the "split window". More mesoscale detail can be discerned with 5 mm intervals in the contoured image of Fig. 5 than with 10 mm intervals in the greybar image of Fig. 4d. Such contouring can even be helpful on a color-coded image for those viewers who happen to be colorblind.

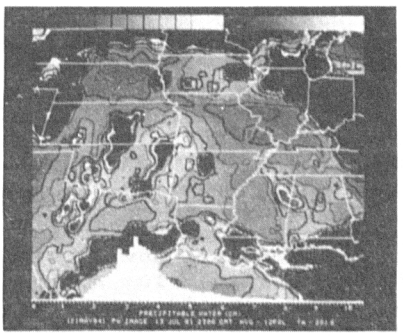

Fig. 5. Contours of the PW sounding image in Fig. 4d. Two-pixel wide contours were created at 10 mm intervals from 10 to 50 mm, and one-pixel wide contours were added at 10 mm intervals from 0.5 to 5.5 mm.

On the AOIPS at NASA/GSFC, a VAS-retrieved 512 by 512 pixel field can be contoured in less than 2 minutes, while objective analysis and contour drawing require approximately 20 minutes. Hardware in the image terminal on AOIPS expedites the computation by accessing both the rows and the columns of pixels in an image with equally high speed for rapid two dimensional averaging.

REFERENCES

Browning, K.A., 1980: Review of local weather forecasting. *Proc. Royal Soc. London,* **A371,** 197-211.

Chesters, D., L.W. Uccellini and W.D. Robinson, 1983: Low-level water vapor fields from the VISSR Atmospheric Sounder (VAS) "split window" channels. *J. Clim. Appl. Meteor.,* **22,** 725-743.

Chesters, D. and A. Mostek, 1985: High resolution images of atmospheric conditions computed directly from VAS satellite radiances. *Preprint, Int'l Conf. on Interactive Info. Proc. Sys. for Meteorology, Oceanography and Hydrology,* Los Angeles, Amer. Meteor. Soc., 261-268.

Chesters, D., A. Mostek and D.A. Keyser, 1986: VAS sounding images of atmospheric stability parameters. Conditionally accepted by *Weather and Forecasting.*

Lee, T.H., D. Chesters and A. Mostek, 1983: The impact of conventional surface data upon VAS regression retrievals in the lower troposphere. J. Clim. Appl. Meteor., 22, 1853-1874.

Mostek, A., L.W. Uccellini, R.A. Petersen and D. Chesters, 1986: Assessment of VAS soundings in the analysis of a pre-convective environment. Accepted by *Mon. Wea. Rev.*, to appear in the January 1986 issue.

Robinson, W.D., D. Chesters and L.W. Uccellini, 1986: Optimized retrievals of precipitable water fields from combinations of VAS satellite and conventional surface observations. Accepted by *J. Geophys. Res.*.

Smith, W.L., 1966: Note on the relationship between total precipitable water and surface dewpoint. *J. Appl. Meteor.,* **5,** 726-727.

Smith, W.L., G.S. Wade and H.M. Woolf, 1985: Combined atmospheric sounding/cloud imagery -- a new forecasting tool. *Bull. Amer. Meteor. Soc.,* **66,** 138-141.

AN EXTENSION OF THE SPLIT WINDOW TECHNIQUE FOR THE RETRIEVAL OF PRECIPITABLE WATER

Thomas J. Kleespies
Air Force Geophysics Laboratory
Hanscom AFB, Bedford MA

Larry M. McMillin
NOAA/NESDIS
Washington D.C.

1. INTRODUCTION

The split window takes its name from the fact that not one but two measurements are made in the atmospheric window region near 11 micrometers. The two channels are situated such that they "see" the same absorbers, but in differing amounts. The intent of split window observations is to correct for the effects of atmospheric attenuation, and arrive at a better estimate of surface temperature than can be achieved from a single channel observation. McMillin and Crosby (1984) present a detailed discussion of the split window technique and a review of the literature.

In this paper we extend the concept of the split window to deduce the atmospheric attenuation, and since the primary absorber near 11 micrometers is water vapor, we can estimate precipitable water.

2. MATHEMATICAL DERIVATION

The upwelling longwave infrared radiance from a plane parallel, non scattering atmosphere in local thermodynamic equilibrium can be written as

$$I = B_s\tau_s + \int_{\tau_s}^{1} B d\tau \qquad 1)$$

where I is the radiance measured by the satellite, B is the Planck radiance, τ is transmittance from a given level to the top of the atmosphere, the subscript s refers to the surface of the earth, and the integral is the radiance originating from the atmosphere alone. Equation 1 may also be written as

$$I = B_s\tau_s + \bar{B}_a(1-\tau_s) \qquad 2)$$

where $\bar{B}_a$ is a weighted average given by

$$\bar{B}_a = \frac{\int_{\tau_s}^{1} B d\tau}{\int_{\tau_s}^{1} d\tau} \qquad 3)$$

Consider observations of the earth under conditions where the surface contribution to the outgoing infrared radiance varies markedly, but where the atmospheric contribution changes very little. We can now write a set of four equations, one for each of the two channels, and one for each of the different surface observing conditions:

$$I^1_{11} = B^1_{s_{11}}\tau_{s_{11}} + \bar{B}_{a_{11}}(1 - \tau_{s_{11}}) \qquad 4a)$$

$$I^1_{12} = B^1_{s_{12}}\tau_{s_{12}} + \bar{B}_{a_{12}}(1 - \tau_{s_{12}}) \qquad 4b)$$

$$I^2_{11} = B^2_{s_{11}}\tau_{s_{11}} + \bar{B}_{a_{11}}(1 - \tau_{s_{11}}) \qquad 4c)$$

$$I^2_{12} = B^2_{s_{12}}\tau_{s_{12}} + \bar{B}_{a_{12}}(1 - \tau_{s_{12}}) \qquad 4d)$$

where the superscripts 1 and 2 refer to the viewing conditions and the subscripts 11 and 12 refer to the nominal 11 and 12 micrometer channels in the split window. We can eliminate the atmospheric term $\bar{B}a$ by differencing to yield two equations

$$\Delta I_{11} = \Delta B_{s_{11}}\tau_{11} \qquad 5a)$$

$$\Delta I_{12} = \Delta B_{s_{12}}\tau_{12} \qquad 5b)$$

where

$$\Delta I_{11} = I^1_{11} - I^2_{12} \qquad 6a)$$

$$\Delta B_{11} = B^1_{11} - B^2_{12} \qquad 6b)$$

and similarily for ΔI_{12} and ΔB_{12}.

The ratio of transmittances in the two channels may be formed by dividing equations 5) to yield

$$\frac{\tau_{11}}{\tau_{12}} = \frac{\Delta I_{11}\ \Delta B_{s_{12}}}{\Delta I_{12}\ \Delta B_{s_{11}}} \qquad 7)$$

Following the approach of McMillin (1971), equation 7) can be linearized by converting from radiances to temperatures, the ΔB_s become ΔT_s and cancel, and we are left with

$$\frac{\tau_{11}}{\tau_{12}} = \frac{\Delta T_{11}}{\Delta T_{12}} \qquad 8)$$

To review, we have derived an expression for the ratio of transmissivities in the split window near 11 micrometers. Inherent in the derivation are multiple observations of the earth through the split window under conditions where the surface contribution to the upwelling radiance changes markedly, but the atmospheric contribution is essentially invariant. The resulting ratio of transmittances is then shown to be merely the ratio of the differences in brightness temperatures observed under the two conditions. This ratio can be shown to be related to precipitable water (see Chesters et al., 1983).

3. SIMULATION OF TECHNIQUE

In order to test this technique, radiances were computed simulating data from the Advanced Very High Resolution Radiometer (AVHRR) using techniques described by Weinreb and Hill (1980). Temperature and moisture profiles were taken from 304 radiosondes in North America for three consecutive synoptic times beginning at 12Z, 8 June 1982. Since all reporting radiosondes were used, a wide diversity of airmasses were available, from tropical to arctic, and from a range of surface elevations. Local zenith angles were randomly assigned to the radiosondes in order to simulate the distribution of local zenith angles encountered during satellite overpasses of the radiosonde network. The brightness temperatures were perturbed with normally distributed random noise with a mean of zero and standard deviation of .12 degrees Kelvin, in order to emulate the instrumental error. The surface skin temperature was taken to be the surface air temperature, then incremented 10 degrees for the T's in equation 8. The comparison between the estimated and actual transmissivity ratios are given in Figure 1. The relative lack of scatter is indicative that the assumptions used in the derivation of equation 8) are valid, at least in a theoretical sense.

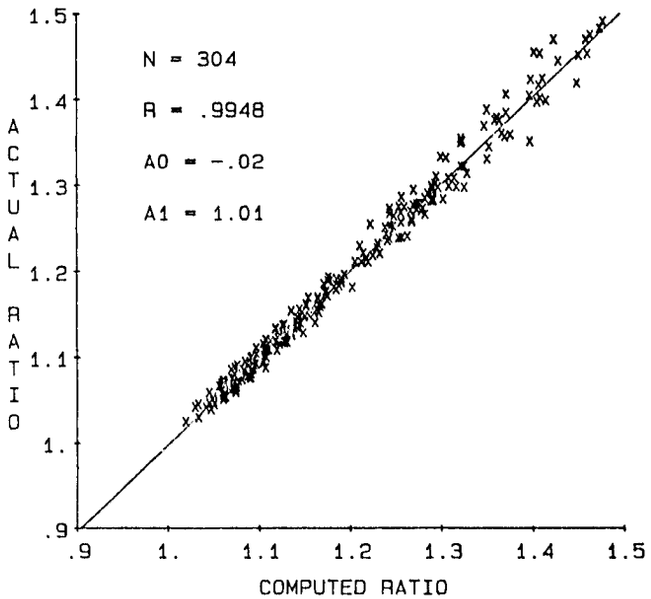

Figure 1. Comparison between actual transmittance ratio and transmittance ratio computed from equation 8.

Next it is desirable to be able to relate this transmissivity ratio to an atmospheric parameter. Since the transmissivities are from the surface to the top of the atmosphere, and the primary absorber is water vapor, it follows that we should try to relate the transmissivity ratio to total water in the column. Simple linear regression between the transmissivity ratio and precipitable water was performed as a first attempt. The choice of a linear relationship is justified by the scatter diagram of actual transmission ratio versus precipitable water in Figure 2. The radiosonde precipitable water was adjusted by the secant of the zenith angle to make it correspond with the slant path of the transmissivities. The regression coefficients were derived from the radiosondes mentioned above, and tested on an independent set of 308 radiosondes in North America for three consecutive synoptic times beginning on 12Z, 10 June 1982. Transmissivity ratios were computed from the independent set of radiosondes using a 10 degree Kelvin surface temperature difference and a NEDT of .12 degrees Kelvin. Again random zenith angles were assigned to the

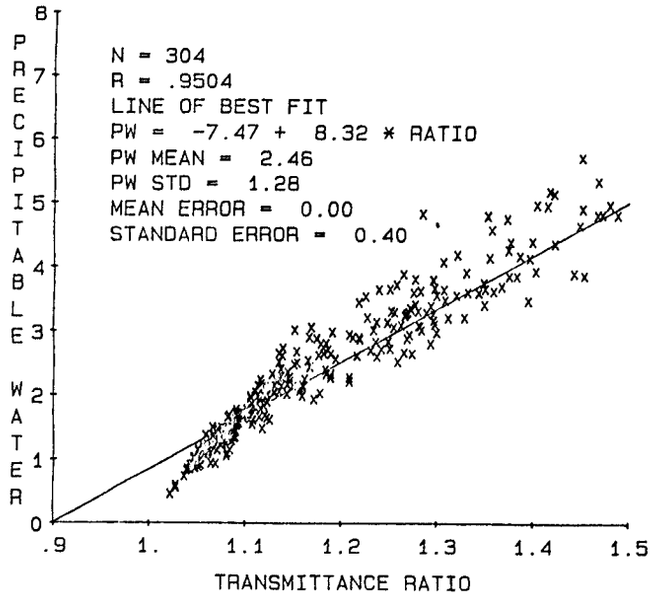

Figure 2. Actual transmittance ratio versus precipitable water.

radiosondes. The precipitable water was computed from this transmissivity ratio with the regression coefficients determined from the dependent set. The comparison with the estimated and observed precipitable water is shown in Figure 3. As can be seen the results are quite good, with an explained variance of .903 .

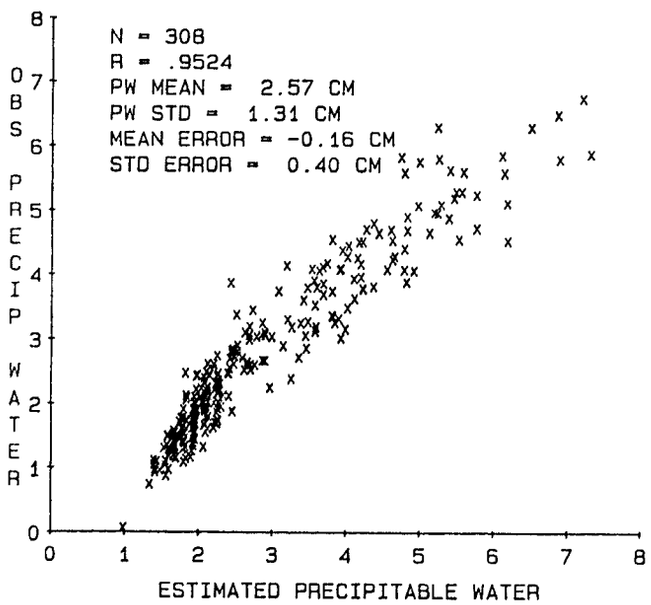

Figure 3. Precipitable water estimated by linear regression from transmittance ratio, versus observed precipitable water for independent radiosondes.

4. DISCUSSION

Thusfar the observational conditions have not been specified under which the surface contribution to the upwelling radiance changes, while the atmospheric contribution does not. Two situations immediately come to mind. The first has to do with the diurnal cycle of land surface heating. Figure 4 is a plot of 11 micrometer brightness temperature as observed by GOES W over an 11 hour period on 17 September 1983. The rate of change of brightness temperature during the local morning is in excess of 5 degrees per hour. Over a two hour period the ten degree brightness temperature change which discussed above can be seen. It is unlikely that the local absorber state would change dramatically over a two hour period, and if it did the surface would probably be obscured by clouds. Observation of diurnal temperature change is practical only from geosynchronous satellites.

The second situation is observing the earth cotemporally at adjacent contrasting surfaces. For example, measuring the brightness temperatures of a lake and the surrounding land. It might even be possible to use the heat island effect of a city with the contrasting cooler temperatures of the surrounding countryside. It is important however that the contrasting surface temperatures be geographically close, so that the assumption of invariant atmospheric temperature is met. This situation is viable for both geosynchronous and polar orbiting satellites.

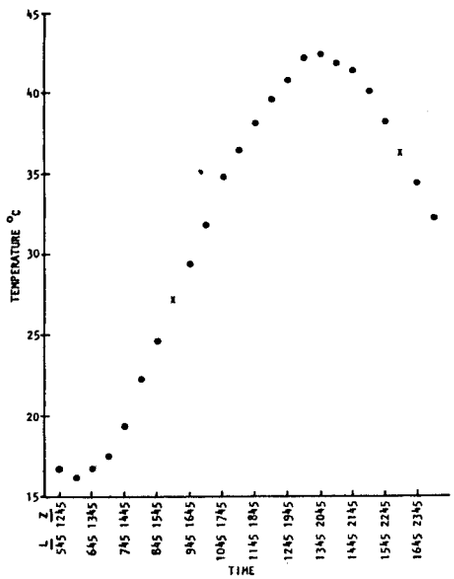

Figure 4. Eleven micrometer brightness temperature as a function of time as observed by GOES W on 17 September 1983. Average of 3x3 array of 7 km resolution elements, upper left corner at 36N, 120W, about 110 km NW of Bakersfield CA.

A technique has been presented which extends the split window technique to multiple observations in space or time. This extension allows for a simple derivation of transmittances of the split window, which can be related to precipitable water. Simulations of computed radiances with realistic instrument noise indicate that the technique yields an excellent estimate of the ratio of transmittances of the split window channels. Simple linear regression between the ratio and precipitable water also gives very good results. Testing of the technique with real AVHRR and VAS data is the logical next step in this research effort.

5. ACKNOWLEDGEMENTS:

The authors wish to express their appreciation to Mr. Mike Hill of NOAA/NESDIS for providing the radiative transfer code used in this study.

6. REFERENCES

Chesters, Dennis, Louis W. Uccellini and Wayne D. Robertson, 1983: Low Level Water Vapor Fields from the VISSR Atmospheric Sounder (VAS) "Split Window" channels. J. Clim. Appl. Met., Vol 22, No.5. pp 725-743.

McMillin, L.M., 1971: A method of determining surface temperatures of spectral radiance at two wavelengths, Ph.D. dissertation, Iowa State Univ., Ames.

McMillin, L.M., and D.S. Crosby, 1984: Theory and Validation of the Multiple Window Sea Surface Temperature Technique, J. Geoph. Rsch. Vol 89, No. C3, pp 3655-3661.

Weinreb, Michael P., and Michael L. Hill, 1980: Calculation of Atmospheric Radiance and Brightness Temperatures in Infrared Window Channels of Satellite Radiometers, NOAA Technical Report NESS 80, 40pp.

1.14

THE REMOTE SENSING OF OZONE FROM TOVS: A PHYSICAL INTERPRETATION OF THE REGRESSION TECHNIQUE

David S. Crosby

National Oceanic and Atmospheric Administration
National Environmental Satellite, Data, and Information Service
Washington, D.C. 20233

and

The American University
Washington, D.C. 20016

1. INTRODUCTION

The TIROS operational vertical sounder TOVS on the TIROS-N series of NOAA environmental satellites sense the upwelling radiation in several spectral intervals. These radiances are used to determine the vertical temperature and moisture distributions of the atmosphere. The 9.6 μm channel of these instruments is in an absorption band of ozone, and the measured radiances in this channel are affected by changes in the amount and distribution of atmospheric ozone. The radiances from the 9.6 μm channel are used with radiances from the other channels to infere the global distribution of ozone.

The ozone retrieval is carried out using a multiple linear regression procedure (Planet et al, 1984). Total ozone is regressed against estimated clear column brightness temperatures (BT). This technique has been used since 1979.

Many remote sensing techniques are subject to the criticism that they are not directly measuring the parameter of interest. That is, the remote sensing procedure may be measuring some other physical parameter which is correlated with the desired quantity. For example it is possible to predict total ozone using the temperature of the lower stratosphere. However, in this paper strong evidence is presented that changes in ozone are being measured by the satellite and the regression technique in using this measurement. This evidence is provided by a careful analysis of the regression results and their relationship to the radiative transfer equation.

2. RADIATIVE TRANSFER EQUATION

In order to explain the reasoning used in the analysis, it is necessary to review the properties of the radiative transfer equation. In the form we will use the radiative transfer equation may be written as

$$I(\nu) = B[\nu, T(p_s)]\,\tau(\nu,p_s) - \int_0^{p_s} B[\nu, T(p)]\, d\tau/dp(\nu,p)dp \qquad (1)$$

In equation (1), $I(\nu)$ is the upwelling radiance in a channel having a small range of wavenumbers centered at ν. $B[\nu, T(p)]$ is the Planck function at wavenumber ν and temperature $T(p)$, p is the pressure, p_s the surface pressure, and $\tau(\nu,p)$ is the atmospheric transmittance from any given level to the top of the atmosphere averaged over the spectral interval of the channel.

For our purposes it is not necessary to give the physical details of equation (1). We can write an approximation to this equation in the form

$$I(\nu) = \Sigma B[\nu, T(p_i)]*A(\nu,p_i) \qquad (2)$$

For the remainder of the discussion we will consider everything in the form of equation (2). The p_i are the quadrature points used for integration over atmospheric pressure (Weinreb and Hill, 1980). Fig. 1 gives a typical shape for $B(\nu, T(p_i))$ for ν around 1028. The shapes of the $A(\nu,p_i)$ are weakly affected by temperature. However, some of the $A(\nu,p_i)$ are significantly affected by changes in the amount of the variable gases, especially water vapor and ozone.

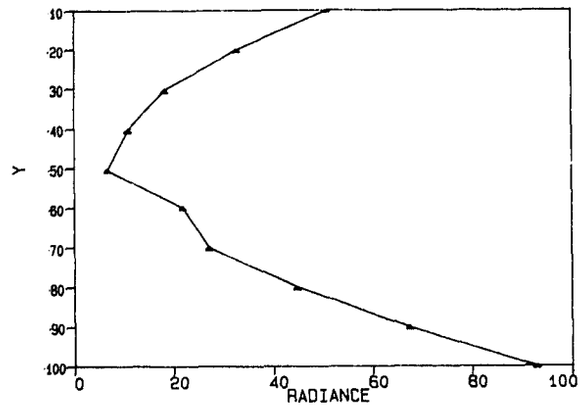

Fig. 1. Plot of typical radiance profile vs y for r = 1028. The variable y is proportional to pressure to the 2/7 power.

We are especially concerned with the ozone sensing channel whose wavenumber is 1028 cm^{-1}. Using the numbering system of TOVS this will be referred to as channel 9. Fig. 2 gives the shape of $A(1028, p_i)$ for two different ozone profiles. The $A(\nu, p_i)$ are usually referred to as weighting functions. One of the profiles is typical of a situation where there is an average amount of ozone (Ω = 330 DU), the second is typical where there is a relatively small amount of ozone (Ω = 290 DU).

Note that the second peak of the functions $A(1028, p_i)$ occurs above the troposphere in a cold part of the atmosphere. This is seen in the plots of Fig. 1 and Fig. 2. Also note that the $A(1028, p_i)$ with the smaller amount of ozone has a larger peak at the surface where $B(1028, p_i)$ is a maximum. Since the radiance is approximately the dot product of the vectors $A(1028, p_i)$, and $B(1028, p_i)$, it should be expected that an increase in the amount of ozone should decrease the measured radiance at this wavenumber.

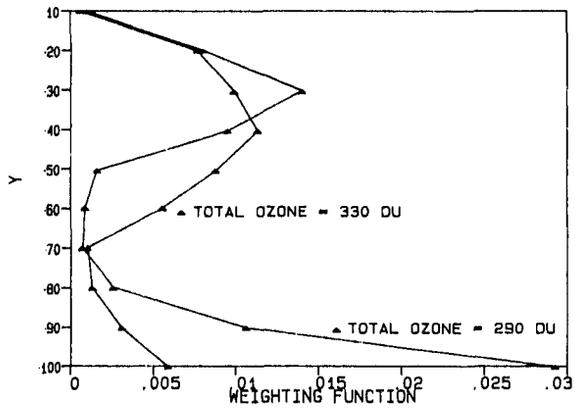

Fig. 2. Plot of channel 9 weighting functions vs y. The variable y is proportional to pressure to the 2/7 power.

If the radiance was only a function of the shape of $A(1028, p_i)$ then the problem of estimating total ozone would be straight forward. It would only be necessary to have simultaneous measurements of the total ozone and the radiances at this wavenumber to derive a prediction equation. However, this is not the case. The radiance is also a function of the Planck function profile $B(\nu, p_i)$ and the surface radiance $B(\nu, p_s)$. Fig. 3 is a plot of real measurements of I(1028) against I(898). The radiances for I(898) are from a window region and hence almost entirely a function of the surface radiance. The strong dependence of I(1028) on the surface radiance is seen from this plot. Also I(1028) is a function of $B(1028, p_i)$ and changes in the ozone amount are correlated with $B(1028, p_i)$. It is far from obvious that the measurements in the ozone channel, I(1028), can be used to estimate ozone.

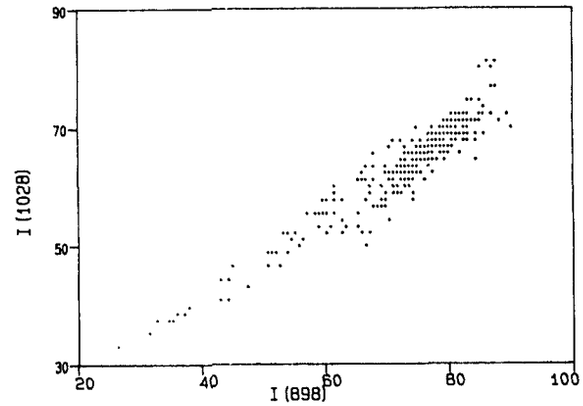

Fig. 3. Ozone channel radiance vs window channel radiance.

3. ANALYSIS OF REGRESSION RESULTS

In the analysis which follows the radiances have been converted to brightness temperatures. The conversion is not linear but it is monotonic so that the essentials of the arguments are unchanged. The technique is used to predict total ozone is a multivariate regression procedure. The predictors were brightness temperatures. For details of the operationally produced total ozone see Planet et al. (1984). The operational technique uses a standard regression procedure with the brightness temperatures from channels 3, 8, and 9 (these channels have been described or they are described below). Hence, we will examine the model

$$\hat{\Omega} = \overline{\Omega} + C_3 (BT_3 - \overline{BT}_3) + C_8 (BT_8 - \overline{BT}_8) + C_9 (BT_9 - \overline{BT}_9) \qquad (3)$$

In this model the bar represents the mean, $\hat{\Omega}$ is the predicted total ozone, BT_i is the brightness temperature for channel i and C_i is the regression coefficient for channel i. Channel 3, for which ν = 691 cm^{-1}, has a weighting function which peaks in the upper troposphere. Channel 8 is a window channel and is described above. Table 1 gives the C_i's for these three channels for one year of data by month. All data sets used in this paper were from a set collected from November 1, 1979 to October 31, 1980. The TOVS measurements were from the NOAA-6 satellite system. The total ozone measurements used as the dependent variable or ground truth for all the data sets in this paper were from the TOMS (Total-Ozone Mapping Spectrometer) instrument on the NIMBUS-7 Satellite (Fleig et al., 1982). The data set for Table 1 is for latitudes from 30° N to 60° N.

Table 1

	Jan	Feb	March	April	May	June
C_3	7.83	7.06	8.37	9.01	3.90	.91
C_8	3.97	3.54	3.95	3.28	3.12	3.51
C_9	-8.37	-8.25	-8.84	-7.41	-7.31	-7.43

Table 1 (Contd.)

	July	Aug	Sept	Oct	Nov	Dec
C_3	.92	2.77	5.58	7.99	7.54	6.13
C_8	2.95	2.31	2.39	3.13	3.80	5.14
C_9	-6.25	-4.02	-3.31	-4.72	-6.24	-8.45

REGRESSION COEFFICIENTS FOR TOTAL OZONE USING CHANNELS 3, 8, AND 9

The first thing to note about the coefficients in Table 1 is the stability they exhibit, especially the coefficents of channels 8 and 9. An explanation of their relationship is as follows: Channel 9 senses radiation from the surface, which is warm, and from that portion of the atmosphere where the ozone is at a maximum, which is cold (see Fig. 1 and Fig. 2). Hence, an increase in ozone amount will cause the measured temperature in channel 9 to decrease. That is total ozone and BT_9 are inversely related. This is the reason for the negative sign of the coefficient of channel 9. However, most of the changes in channel 9 will be caused by the variability of the surface temperature. The positive coefficient of channel 8, which is directly related to the surface temperature, compensates for that part of the variability in channel 9 which is due to changes in the surface temperature. Thus the sign of the channel 8 coefficient must be opposite to that of the channel 9 coefficient.

In order to minimize the possibility of irrelevant correlations, two changes were made to the operational regression procedure: (1) latitude was used as a predictor; (2) each of the predictor variables (brightness temperature) and the response variable (total ozone) were fitted with a cubic spline. The spline was constructed to fit monthly means. These modifications should reduce the spatial and seasonal correlations. As a result, we produce an average total ozone $\Omega(t)$ and brightness temperature $BT(\nu_i,t)$ for each day of the year, t. The dependent variable and the independent variables are now deviations from these predicted daily averages:

$$\Delta\Omega = \Omega - \Omega(t) \quad (4)$$

$$\Delta BT(\nu_i) = BT(\nu_i,t) \quad (5)$$

New regression equations were producted using these deviations. A multiple linear regression procedure was used which gives an equation of the form

$$\hat{\Omega} = \overline{\Delta\Omega} + \Sigma\, C_i(\Delta BT(\nu_i) - \overline{\Delta BT(\nu_i)}) + C^*L \quad (6)$$

In this equation L represents latitude.

We can now use this new regression procedure to demonstrate that the brightness temperatures of channel 9 are a function of total ozone. This new procedure was applied to 3881 sets of measurements from the region 0° to 30° N for the entire year. The deviations in total ozone $\Delta\Omega$ and $\Delta BT(1028)$ were regressed against the variables $\Delta BT(679)$, $\Delta BT(704)$, $\Delta BT(716)$, $\Delta BT(898)$, $\Delta BT(1217)$, $\Delta BT(2213)$, $\Delta BT(2240)$, and latitude. This gives the equations

$$\hat{\Omega} = \overline{\Delta\Omega} + \Sigma\, C_i(\Delta BT(\nu_i) - \overline{\Delta BT(\nu_i)}) + C^*L \quad (7)$$

and

$$\widehat{BT(1038)} = \overline{\Delta BT(1028)} + \Sigma\, A_i(\Delta BT(\nu_i)) + A^*L \quad (8)$$

Using equations 7 and 8 the residuals R are computed. We have

$$R\Omega = \Omega - \hat{\Omega} \quad (9)$$

and

$$RBT(1028) = BT(1028) - \widehat{BT(1028)}. \quad (10)$$

$R\Omega$ was regressed against RBT(1028) which gave an equation of the form

$$R\Omega = -5.53(RBT(1028)). \quad (11)$$

Equation 11 says that a one unit decrease in RBT(1028) gives an increase of 5.53 Dobson units in the predicted total ozone. This is exactly what could be expected from the physical considerations discussed earlier in this paper. Fig. 4 gives a plot of $R\Omega$ against RBT(1028) for this data set. Note the clear association of an increase in RBT(1028) to a decrease in $R\Omega$. Such plots are now a standard tool in multivariate regression and are called partial regression plots. This plot was produced by the SAS REG package (1982).

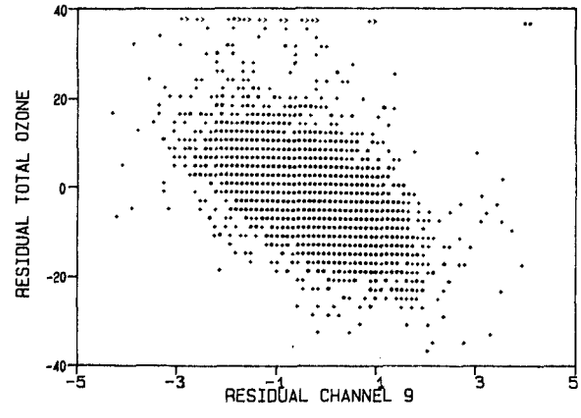

Fig. 4. Partial Regression Residual Plot. Residual total ozone vs residual channel 9 brightness temperature.

Using this same data set, it was found that the root mean squared error of the difference between the measured total ozone (measured by TOMS) and the predicted total ozone changed from 10.06 to 8.39 Dobson units when channel 9 was included in the regression. For a data set thsi large, this is a significant reduction.

4. CONCLUSIONS

Any regression technique is subject to the criticism that it is only measuring irrelevant correlations with the parameter of interest. By analyzing the data from the TOVS regression procedures, strong evidence has been provided that the TOVS is measuring total ozone directly. These measurements of the changes in total ozone are at least partially independent of changes in temperature.

5. REFERENCES

Fleig, A. J., K. L. Klenk, P. K. Bhartia, and D. Gordon, 1982: User's Guide for the Total-Ozone Mapping Spectrometer (TOMS) Instrument First-Year Ozone-T Data Set, NASA Ref. Pub. 1096, 43pp.

Planet, W. G., D. S. Crosby, J. H. Lienesch, and M. L. Hill, 1984: Determination of total ozone amount from TIROS radiance measurements. J. Clim. Appl. Met., 23, 308-316.

SAS, 1982: SAS User's Guide: Statistics. SAS Institute, Gary, North Carolina, 584 pp.

Weinreb, M. P. and M. L. Hill, 1980: Calculation of atmospheric radiances and brightness temperatures in infrared window channels of satellite radiometer. NOAA Tech. Report NESS 80, 40 pp.

BALLOON-BASED SOLAR OCCULTATION MEASUREMENTS OF STRATOSPHERIC CONSTITUENT PROFILES

M. P. Weinreb, L. D. Johnson, P. A. Bridges, and M. L. Hill
National Oceanic and Atmospheric Administration
National Environmental Satellite, Data, and Information Service
Washington, D.C. 20233

I-Lok Chang
The American University
Washington, D.C. 20016

S. Oltmans
National Oceanic and Atmospheric Administration
Environmental Research Laboratories
Boulder, Colorado 80303

A. Sanyal and W. A. Morgan
SM Systems and Research Corporation
Lanham, Maryland 20801

1. INTRODUCTION

We have been conducting a series of balloon-based solar occultation experiments to prove that the concept of solar occultation, implemented with a multidetector infrared spectrometer, is practical for satellite-based long term monitoring of trace gases in the stratosphere. The third of these experiments took place on July 5, 1985, at Palestine, Texas. From an altitude of 39 km, the instrument measured the intensity of infrared solar radiation for several hours before and during sunset. The measurements were made in the absorption bands of ozone, water vapor, nitric acid, and Freon-12. This paper describes the experiment and presents the retrieved ozone and water vapor profiles. The results for nitric acid and Freon-12 will be presented elsewhere.

In situ measurements of the ozone and water vapor profiles, the former with ECC-sondes and the latter with frost-point hygrometers, were also made at Palestine at the time of the occultation soundings. A comparison between the in situ soundings and the occultation soundings is also presented in this paper.

2. DESCRIPTION OF EXPERIMENT

The occultation geometry is illustrated in Figure 1. The basic measurements are of the solar intensity as a function of solar zenith angle between 90° and roughly 95°. After being converted to measurements of limb transmittances vs tangent height, they are processed in a retrieval algorithm that yields profiles of mixing ratio vs altitude.

The instrument, described in Weinreb et al. (1984), was designed for simplicity and reliability. Briefly, it is a multi-detector spectrometer that detects radiation continuously in a number of discrete infrared spectral intervals (channels), four of which are described in Table 1. The detectors need not be cooled, since the spectral resolution is not high and the bright sun is the source of radiation. A Cassegrain telescope focuses the solar radiation onto the spectrometer. The instrument's angular field of of view is 8 arc minutes.

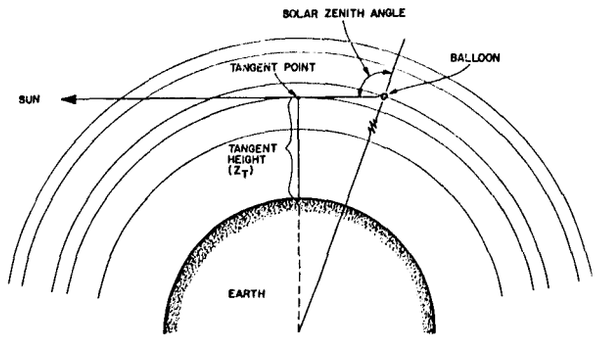

Fig. 1. Solar occultation geometry.

Table 1. Spectral intervals of spectrometer

Channel number	Central waveno. (cm^{-1})	Half-power bandwidth (cm^{-1})	Species
3	980	6	Ozone (low altitude)
4	998	6	Ozone (high altitude)
5	1507.0	3	Water vapor (high altitude)
6	1528.5	4.5	Water vapor (low altitude)

In this flight we used a new sun seeker, built by the University of Denver, to reflect the solar radiation into our instrument. This seeker consists of a pair of flat mirrors, one movable and

one stationary, and operates like the seeker described in Murcray et al. (1967). It enabled us to sound the atmosphere down to an altitude of 12 km.

Overall, the instrument operated reliably and provided clean data. There were, however, two exceptions. First, there was a failure in the signal electronics for channel 3 (980 cm^{-1}). As a result, data in only the 998 cm^{-1} channel were available for the ozone retrieval. Second, because of an interruption in the telemetry from the gondola to the ground, we received no data for the tangent heights between 38 and 36 km.

3. DATA REDUCTION

The flight data were received as a stream of volts vs time. However, the retrieval algorithms require the data to be expressed as transmittances vs tangent height. Times of observation were converted to solar zenith angles by calculations based on the ephemeris of the sun. Then the solar zenith angles were transformed to tangent heights with an atmospheric ray trace, which included effects of refraction. The calculations also accounted for motion of the instrument's field of view over the face of the sun, as monitored by two pairs of detectors inside the telescope.

We transformed the voltages measured during the occultation period to transmittances by dividing them by the 100% signals, i.e., the signals that would be measured in the absence of any atmosphere. Direct measurement of the 100% signal is impossible in most channels because there is a small but significant amount of absorbing gas in the atmosphere above the balloon. Instead, we inferred the 100% signals by extrapolating to zero absorber amount from the signals measured before the solar zenith angle reached 90°.

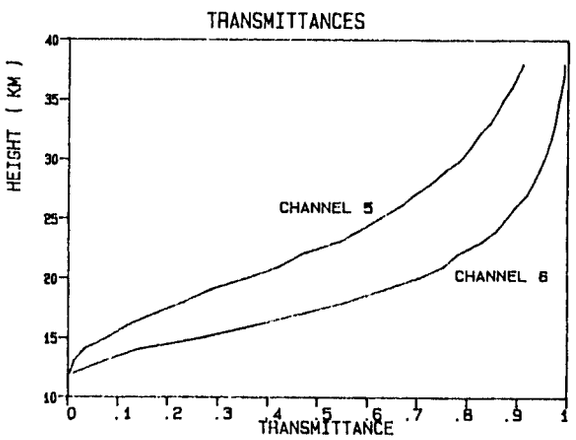

Fig. 2. Measured transmittances vs tangent height for water vapor channels.

As was mentioned previously, the data for the tangent heights between 38 and 36 km were lost. We inferred "measured" voltages for these tangent heights by interpolating with cubic Hermite polynomials between the measurements on either side of the gap. The transmittances derived from those "measurements" might have errors comparable in magnitude to the signal (i.e., the measured absorption), since atmospheric absorption is small at these levels. Therefore, we do not present retrievals for altitudes above 35 km. However, those errors have smaller effects on the retrievals at lower altitudes, and below 30 km their influence disappears.

The data in the two water vapor channels, expressed as transmittances vs tangent height, are displayed in Fig. 2.

The process of retrieving constituent concentrations from the data requires computations of transmittances. For ozone and water vapor we used an efficient approximation (Weinreb and Neuendorffer, 1973) fitted to line-by-line calculations performed by FASCODE (Smith et al., 1978) with molecular line data from the 1982 AFGL tape (Rothman et al., 1983). Because the spectral intervals of the spectrometer are relatively narrow, they could be chosen to minimize effects of interfering spectra of other gases. For example, in channel 4, absorption by gases other than ozone is negligible. However, in channels 5 and 6 (water vapor) the transmittance calculations must include the effect of collision-induced absorption by oxygen (Shapiro and Gush, 1966), which is very important for tangent heights less than 25 km. Our calculations used coefficients from Shapiro and Gush (1966). We verified the results of the oxygen calculations by comparing them with atmospheric measurements (Rinsland et al., 1982).

Knowledge of the atmospheric profiles of temperature and height vs pressure is needed in the data reduction, first for determining the altitude of the balloon from the on-board pressure measurements, and also in the transmittance calculations. Those profiles were acquired from the upper-air analysis prepared by NOAA's Climate Analysis Center.

The mixing ratios were retrieved from the measured transmittances by iterative application of a Levenberg-Marquardt algorithm, a matrix inverse method (Chang and Weinreb, 1985).

4. ERROR ANALYSIS

Errors in the retrieved profiles can be caused by errors both in the measured transmittances and in the retrieval algorithm. We found that the largest error sources in the measurements are likely to be the procedures for specifying the altitude of the balloon and the zenith angle of the line of sight, and the procedure for converting the measured volts into transmittances. Errors in the transmittances derived from the interpolated data between 38 and 36 km are important in the retrievals only at levels above 30 km. Random noise in the measurements is not expected to be as important as the systematic errors just discussed.

The most significant errors in the retrieval algorithm are those in the calculated transmittances. Those errors are due to imprecision in our knowledge of the spectral response functions of the spectrometer, limitations in our knowledge of spectroscopic parameters, and errors in the approximation to the line-by-line calculations. In addition, the collision-induced absorption by molecular oxygen is likely to be in error by several percent, since it is modelled relatively crudely.

To estimate the uncertainties in the retrieved profiles, we performed retrievals both

before and after perturbing the measurements and the calculated transmittances by the errors estimated from each source mentioned above. We interpretated the difference between the two retrieved profiles as the estimate of the uncertainties in the retrievals.

5. RESULTS

Figure 3 shows the ozone retrieval, along with two profiles measured with ECC's at Palestine within a few hours of the experiment. One ECC was launched one hour after the experiment was completed, the other several hours later. The estimated errors in the retrieval are listed in Table 2. The errors associated with the ECC's are estimated to be roughly 5% in the region of the atmosphere below 30 km. Above 30 km, the ECC data may be biased between 5 and 15% low. However, at almost all levels the retrieval and the ECC sounding agree within the uncertainties of each.

The estimated errors in the retrieval are listed in Table 2. The large errors at 18 km and below are associated primarily with the rapid increase in the measured transmittances with tangent height (Fig. 2). As a result, pointing errors and uncertainties in the balloon altitude translate into large uncertainties in the measured transmittances. The uncertainties associated with the hygrometer data are roughly 0.5 ppmv at levels below 25 km and 1 ppmv above 25 km. Up to 28 km the retrieval is consistent with the hygrometer data within the expected errors of each. However, we cannot explain why the two profiles diverge with increasing altitude. Near the tropopause (15 km) the hygrometer data show high-frequency variations in the vertical on a scale of one kilometer or less, and the measurements from the two hygrometers differ considerably. We believe that these are real temporal and spatial variations in the atmosphere. The retrieval can no more than hint at such fine structure in the vertical, since the weighting functions are wider than one kilometer at this altitude.

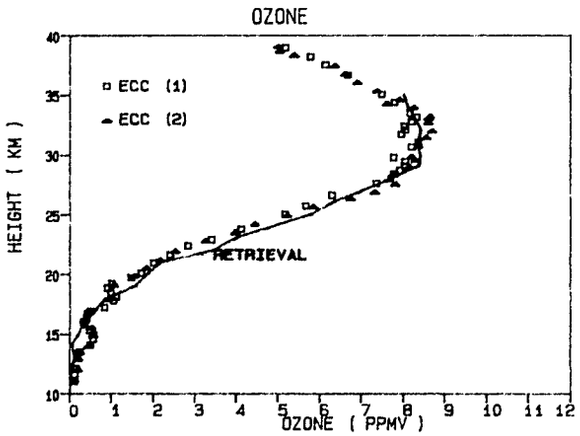

Fig. 3. Ozone retrieval (solid line) and ECC profiles.

Table 2. Estimated retrieval errors.

Altitude (km)	Errors (ppmv) Ozone	Water vapor
12	0.02	-
14	0.03	4.6
16	0.06	2.1
18	0.14	1.4
20	0.1	0.7
22	0.2	0.6
24	0.3	1.1
26	0.5	0.7
28	0.7	0.6
30	0.8	0.9
32	0.8	1.2
34	0.8	1.8

Figure 4 shows the water vapor retrieval, along with two profiles measured with frost-point hygrometers at Palestine within a few hours of the experiment. The first hygrometer was launched six hours before the remote measurement was completed; the second three hours after the first.

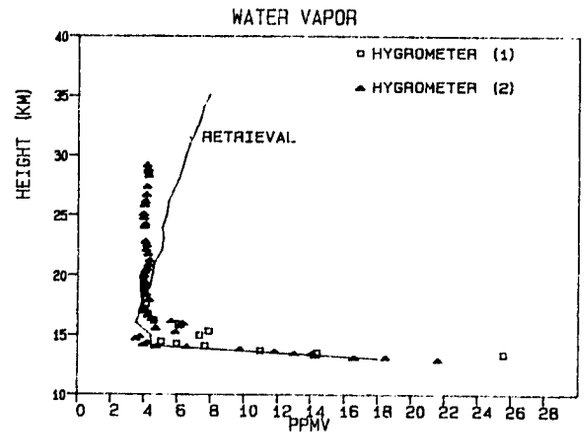

Fig. 4. Water vapor retrieval (solid line) and frost-point hygrometer profiles.

6. CONCLUSION

Applying the concept of infrared solar occultation with a balloon-borne multidetector spectrometer, we have retrieved ozone and water vapor profiles that are in reasonable accord with conventional soundings. In common with other limb sounding techiques, this technique is sensitive to errors in assigning the measurements to the proper tangent heights (e.g., errors in pointing and in determining the altitude of the observing instrument) and to errors in calculating limb transmittances.

The results presented here are evidence that this technique, implemented on a satellite, could provide accurate soundings of ozone, water vapor and other stratospheric constituents. For monitoring the stratosphere from operational satellites, the technique is particularly attractive, because it involves unsophisticated instrumentation with a history of reliability. In addition, since neither spectral scanning nor

interferometry are used, data rates are low, and the retrieval procedure is relatively uncomplicated.

7. ACKNOWLEDGMENTS

Dr. David Murcray and his group at the University of Denver provided the gondola and sun-seeker and made the flight arrangements. We thank Mr. John Kosters, who built the sun-seeker and integrated the instrumentation with the gondola, for his help at Palestine. The balloon and helium were supplied by NASA through the auspices of Dr. Robert T. Watson. The telemetry and the data recording system were provided by Mr. Walter R. Nagel and his group at NASA/Goddard Space Flight Center. We thank the National Scientific Balloon Facility at Palestine for their cooperation and for a well-coordinated launch and recovery operation. We are grateful to Mr. Melvyn E. Gelman of NOAA's Climate Analysis Center for providing temperature and height profiles from the upper-air analysis.

8. REFERENCES

Chang, I-Lok and M. P. Weinreb, 1985: Retrieval calculations applied to solar occultation measurements. In Advances in Remote Sensing Retrieval Methods (A. Deepak Publishing, Hampton, Virginia.)

Murcray, D. G. , F. H. Murcray, and W. J. Williams, 1967: A balloon-borne grating spectrometer. Appl. Opt., 6, 191-196.

Rinsland, C. P., M. A. H. Smith, R. K. Seals, Jr., A. Goldman, F. J. Murcray, D. G. Murcray, J. C. Larsen, and P. L. Rarig, 1982: Stratospheric measurements of collision-induced absorption by molecular oxygen. J. Geophys. Res. 87, 3119-3122.

Rothman, L. S., R. R. Gamache, A. Barbe, A. Goldman, J. R. Gillis, L. R. Brown, R. A. Toth, J. -M. Flaud, and C. Camy-Peyret, 1983: AFGL atmospheric absorption line parameters compilation: 1982 edition. Appl. Opt. 22, 2247-2256.

Shapiro, M. M. and H. P. Gush, 1966: The collision-induced fundamental and first overtone bands of oxygen and nitrogen. Can. J. Phys. 44, 949-963.

Smith, H. J. P., D. J. Dube, M. E. Gardner, S. A. Clough, F. X. Kneizys, and L. S. Rothman, 1978: FASCODE - fast atmospheric signature code (spectral transmittance and radiance). U.S. Air Force Scientific Report No. 2, AFGL-TR-78-0081, 149 pp.

Weinreb, M. P., W. A. Morgan, I-Lok Chang, L. D. Johnson, P. A. Bridges, and A. C. Neuendorffer, 1984: High-altitude balloon test of satellite solar occultation instrument for monitoring stratospheric O_3, H_2O, and HNO_3. J. Atmos. and Oceanic Tech. 1, 87-100.

Weinreb, M. P. and A. C. Neuendorffer, 1973: Method to apply homogeneous-path transmittance models to inhomogeneous atmospheres. J. Atmos. Sci., 30, 662-666.

2.1

OPERATIONAL REMOTE SOUNDER (TOVS) RETRIEVED TEMPERATURE COMPARABILITY WITH CONVENTIONAL IN SITU INSTRUMENTS

Francis J. Schmidlin
NASA Goddard Space Flight Center
Wallops Flight Facility
Wallops Island, VA 23337

and

John J. Olivero
Department of Meteorology
The Pennsylvania State University
University Park, PA 16802

1. INTRODUCTION

Operational meteorological satellite products, beginning with the launch of TIROS N in 1978, have begun to have an impact on synoptic analysis and forecasting (Smith et al., 1979, Ohring, 1979, Tracton et al., 1980). In principle, the use of these products were expected to aid in many other types of atmospheric studies. The method of retrieving temperature profiles from radiances has been studied and attempts at improving these (i.e., reducing rms differences between retrievals and in situ measurements) have been conducted for a number of years and are well founded (Phillips et al., 1979; Uddstrom and Wark, 1985; and Thompson et al., 1985). In the current study we are investigating the comparability of satellite and in situ products over long time scales (30 days to several years), that is, seasonal and interseasonal variability, a use satellite retrieved data must ultimately support.

Table 1

List of Colocated Radiosonde and TOVS Comparison Data

San Andres	12.6N	81.7W
Grand Canyon	19.3N	81.4W
Merida, Mexico	21.0N	89.6W
Key West	24.6N	81.7W
Charleston	32.9N	80.0W
Cape Hatteras	35.3N	75.6W
Wallops Island	37.8N	75.5W
Chatham	41.7N	70.0W

2. DATA SOURCE AND ANALYSIS PROCEDURE

Our data consists of retrieved temperature derived from NOAA-6 and NOAA-7 as obtained from the TIROS Operational Vertical Sounder (TOVS) archives, and U.S. (NWS) radiosondes along a quasi-meridional chain from the tropics to mid-latitudes. Although three of the radiosonde sites were not U.S. territory, the sites are part of the cooperative station program and use U.S. radiosondes. All synoptic radiosonde flights from the stations chosen were included in the compilation. Satellite retrievals used in the analysis were those colocated within a 2° are radius from each radiosonde. All data, satellite and radiosonde, were averaged for each month for each station. The colocated sites are listed in Table 1.

During this initial investigation of seasonal time scales we chose the annual cycles at each pressure layer, for each station, as characterized by the monthly mean temperature differences between January and July for each year of the study. In the troposphere the amplitude of this cycle tends to increase markedly with latitude while this trend reverses in the lower stratosphere. Since TOVS temperatures are reported for pressure layers and radiosonde temperatures are reported for standard (constant) pressure surfaces the two data sets were made compatable by calculating the layer "thickness" temperature of the radiosonde temperatures for similar layers reported by TOVS.

3. RESULTS

Let us consider the 100-70 hPa layer as representative of the lower stratosphere. In Figure 1, we see the amplitude of the annual cycle in layer mean temperature for each of the instruments plotted as a function of latitude for calendar year 1982, the only year for which both NOAA-6 and NOAA-7 retrieved temperatures can be simultaneously compared with radiosonde temperatures. Both satellites appear to underestimate the annual cycle by as much as 3-4° K, except for Merida, Mexico (21N) and Chatham, MA (41.7N). NOAA-6 data fall noticably closer to the radiosonde measurements than do NOAA-7. Figures 2a

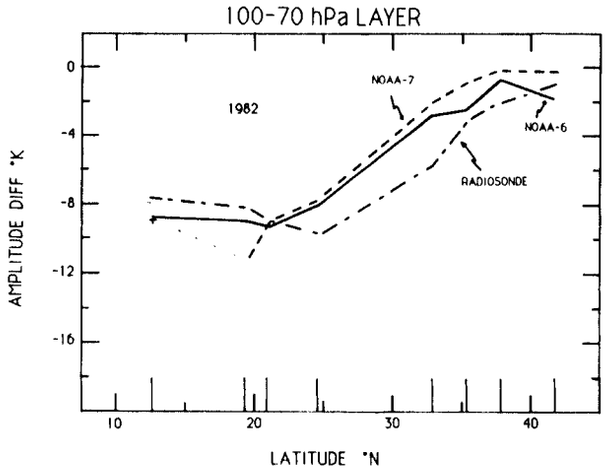

Fig. 1. Amplitude difference of January/July monthly mean temperatures for 1982 for 100-70 hPa pressure layer. The colocated data were compared at the latitudes indicated by the vertical line. For the name of the sites refer to Table 1.

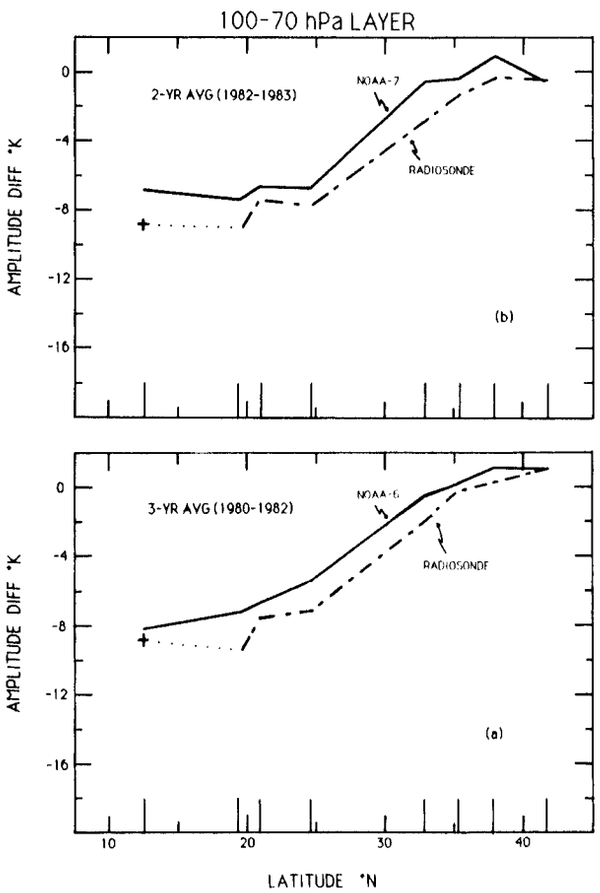

Fig. 2a and 2b. Annual cycle differences similar to data shown in Fig. 1 except (a) averaged over a 3-year period for NOAA-6 and radiosondes, and (b) averaged over 2 years for NOAA-7 and radiosondes.

and 2b show direct comparisons of NOAA-6 and NOAA-7 data with radiosonde data for the years of their overlap, 1980-1982 and 1982-1983, respectively. The curves shown in Figures 2a and 2b represent the average amplitude difference for the years indicated on the figures. The differences calculated between NOAA-6 and radiosondes, and NOAA-7 and radiosondes are slightly less than those shown for the single year of 1982 in Figure 1. San Andres (12.6°N) had reported radiosonde data only for 1981 shown on the figures as a relative indication of the difference.

We have chosen the 700-500 hPa layer as representative of the lower to mid troposphere. In Figure 3 is shown the satellite and radiosonde observations in the same format as used for Figure 1. At these levels the satellites agree fairly well with the radiosondes except at the extremes of the latitudes considered ($\phi<20°$, $\phi>35°$N). The tendency is for NOAA-7 TOVS retrieved temperatures to slightly underestimate the annual amplitude with respect to the radiosondes. As in Figures 2a and 2b the direct comparisons of NOAA-6 and NOAA-7 with radiosondes for the years of overlap are shown in Figures 4a and 4b, respectively. NOAA-6 is within ±1°K of the radiosonde measurements with a tendency to underestimate the poleward increase in annual cycle amplitudes at this level. NOAA-7 routinely shows the amplitude lying within 0.5-1°K over the latitude range shown. NOAA-6, on the other hand, crosses the radiosonde somewhere in the vicinity of 30°N latitude with the satellite underestimating the annual cycle in mid-latitudes and overestimating it in lower latitudes.

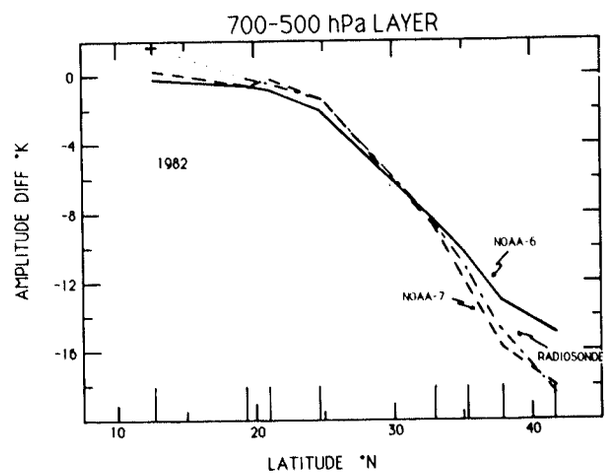

Fig. 3. Similar to Fig. 1 except for 700-500 hPa layer.

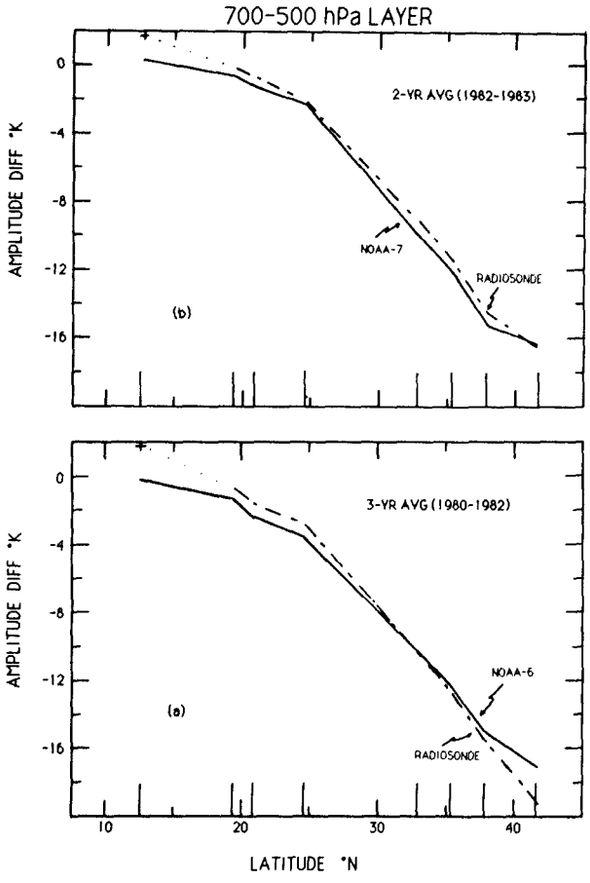

Fig. 4a and 4b. Similar to Fig. 2a and 2b except for 700-500 hPa layer.

4. SUMMARY

Monthly layer-mean TOVS retrieved temperatures for NOAA-6, NOAA-7, and monthly layer-mean radiosonde temperatures were compared from the tropics to mid latitudes over the years 1980 through 1983. The difference in the January/July mean temperatures were defined as characterizing the amplitude of the annual cycle. Representative pressure layers of 700-500 hPa and 100-70 hPa provide insight into differences in the amplitude of the annual cycle observed from the three instruments. This study is a preliminary investigation into the application of satellite products for climatological studies; considerably more work is necessary and planned.

5. REFERENCES

Smith, W.L., H.M. Woolf, C.M. Hayden, D.Q. Wark, and L.M. McMillin, 1979: The TIROS N Operational Vertical Sounder. Bull. Am. Meteorol. Soc., 60, 1177-1187.

Ohring, G., 1979: Impact of Satellite Temperature Sounding Data on Weather Forecasts. Bull. Am. Meteorol. Soc., 60, 1142-1147.

Tracton, M.S., A.J. Desmarais, R.J. van Haaren, and R.D. McPherson, 1980: The Impact of Satellite Soundings on the National Meteorological Center's Analysis and Forecast System. Mon. Wea. Rev., 108, 543-586.

Phillips, N., L. McMillin, A. Gruber, and D. Wark, 1979: An Evaluation of Early Operational Temperature Soundings from TIROS-N. Bull. Am. Meteorol. Soc., 60, 1188-1197.

Uddstrom, M.J., and D.Q. Wark, 1985: A Classification Scheme for Satellite Temperature Retrievals. J. Climate Appl. Meteor., 24, 16-29.

Thompson, O.E., M.D. Goldberg, and D.A. Dazlich, 1985: Pattern Recognition in the Satellite Temperature Retrieval Problem. J. Climate Appl. Meteor., 24, 30-48.

2.2

MICROWAVE DERIVED OPERATIONAL SOUNDINGS FROM THE NOAA-6 POLAR ORBITING SATELLITE

Anand Swaroop, Andrew J. Nappi
and Mitchell D. Goldberg

SASC Technologies, Inc.
5809 Annapolis Road
Hyattsville, MD 20784

Michael Chalfant and Anthony L. Reale

NOAA/NESDIS
Washington, DC 20233

1.0 INTRODUCTION

Global temperature and humidity soundings are operationally produced at NOAA/NESDIS in a near real time environment utilizing radiance measurements from two polar orbiting satellites. The two polar satellite operational system is essential for the continuous monitoring of global atmospheric changes. The NOAA-7 and NOAA-8 satellites were operational in early 1984. The equator crossing times for NOAA-8 were approximately 7:30 and 19:30 local time and were approximately 03:30 and 15:30 local time for NOAA-7. Thus, NOAA-7 and NOAA-8 provided the coverage for all parts of globe every 4-8 hours. After the complete failure of the instruments on board the NOAA-8 satellite in June 1984, NOAA/NESDIS, had limited satellite data coverage. A decision was made by NOAA/NESDIS to reactivate the NOAA-6 satellite and produce temperature soundings based on the radiance measurements from the Microwave Sounding Unit (MSU) and Stratospheric Sounding Unit (SSU) since High resolution Infrared Radiation Sounder (HIRS) was not functioning that time. This paper deals with the changes made to the TIROS-N Operational Vertical Sounder (TOVS) processing system to retrieve temperatures utilizing data from MSU and SSU only. As several studies have been conducted in the past to evaluate the accuracies of satellite soundings, Phillips et al. (1979), Brodrick et al. (1981) and McMillin et al. (1983), the NOAA-6 temperature soundings based on MSU data at pressures 1000-115 mb. are evaluated statistically in this paper against the conventional radiosonde measurements as well as NOAA-7 temperature retrievals based on HIRS, MSU and SSU data. Comparisons are also made with the NMC analyses to further examine the accuracy of microwave based retrievals.

2.0 INSTRUMENT CHARACTERISTICS

The operational instruments on board NOAA-6 are MSU and SSU. The MSU is a 4 channel Dicke radiometer making passive measurements of the radiation emitted by molecular oxygen in the 50 GHz band. The SSU instrument is a pressure modulated radiometer with three channels at a wavenumber of 667 cm^{-1}. The SSU senses the radiation emitted by carbon dioxide in the stratosphere. The Table 1 provides the characteristics of various channels of MSU and SSU and Figure 1 shows the corresponding weighting functions. The field of view (FOV) of MSU and SSU resolve a circular area of 110 km and 148 km in diameter, respectively, at nadir. The SSU instrument has 8 FOVs per scan line and covers a linear distance of approximately 1500 km on the earth's surface. The MSU covers a linear distance of approximately 2250 km and has 11 FOVs per scan. A more detailed description of these instruments has been given by Schwalb (1979), and Smith et al. (1979).

3.0 RETRIEVAL PROCESS

In the normal mode when all HIRS, MSU and SSU instruments are functioning, the transformation of satellite measured radiances to temperature and humidity profiles requires many adjustments which are routinely done in the TOVS processing system. These adjustments include limb correction to HIRS, MSU and SSU channel radiances, asymmetric scan bias correction to MSU, water vapor attenuation correction to HIRS channels

Table 1

The Characteristic of MSU and SSU channels.

MSU	Frequency (GHz)	Level of peak energy contribution
1	50.31	surface
2	53.73	700 mb
3	54.96	300 mb
4	57.95	90 mb

SSU	Wavelength (μm)	Level of peak energy contribution
1	15.0	15.10 mb
2	15.0	4.0 mb
3	15.0	1.5 mb

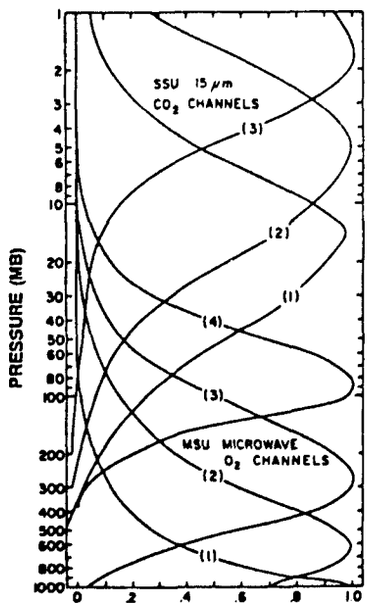

Fig. 1 The Normalized Weighting functions for MSU and SSU channels.

sensitive to water vapor and correction to HIRS radiances for removal of cloud effects. Since the SSU instrument does not scan as far as HIRS or MSU does, the SSU measured radiance data is analyzed to a (2.5^{o} x 2.0^{o}) grid in order to fill the inter-orbit data gaps. The temperature profiles are retrieved at 250 km resolution using the TOVS clear column radiances as input to statistical regression method. The required regression coefficients are updated weekly using the coincident radiosonde and satellite retrievals for the latest two weeks, in order to incorporate seasonal variations. The three types of temperature profiles normally produced are clear, partly cloudy (or N*) and totally cloudy. However, the totally cloudy retrievals are based on radiances measured by three stratospheric HIRS channels, three MSU channels (2-4) and three SSU channels and are therefore less accurate compared to clear and partly cloudy retrievals. A complete description of the TOVS processing system is given by Werbowetzki (1981).

The failure of HIRS instrument necessitated the utilization of data from the MSU and SSU to retrieve temperature profiles for NOAA-6. The TOVS processing system was reconfigured to produce soundings from NOAA-6 without functioning HIRS instrument. All the adjustments required for HIRS channel radiances have been removed for the NOAA-6 data processing. Since MSU and SSU radiances are generally not affected by clouds, the correction for cloud effects is no longer required for NOAA-6. The MSU radiances are corrected for limb effects, asymmetric scan bias and are colocated to HIRS field of view (FOV) for further processing. These are also examined for possible rain contamination. The set of all MSU channel radiances averaged over 63 HIRS FOVs (7 scan x 9 FOVs) is computed to be used in conjunction with regression coefficients to retrieve temperature profiles at 250 km resolution. However, the NOAA-6 temperature soundings, are not classified as clear, N* or totally cloudy, but may be considered to have an accuracy equivalent to totally cloudy retrievals. The retrieved temperatures at pressure levels between 1000 and 115 mb are based on only MSU channels 2,3 and 4 over land. However, an additional predictor, skin-temperature, is used for temperature retrievals over ocean. The temperatures retrieved at pressure levels between 100 and 0.1 mb utilize the data provided by SSU channels 1-3 in addition to MSU channels 3 and 4.

4.0 Results

The temperature sounding data from NOAA-6 have been statistically evaluated using radiosonde observations as ground truth. The coincident radiosonde data and NOAA-6 retrievals based on microwave data were collected for the month of November 1984. All the matchups were within 3 hours and within a 1 degree spatial window for the mid latitudes (30°N-60°N) and within a 3 degree spatial window for the tropics (30°N-30°S) both over land and ocean.

The mean biases and RMS errors for NOAA-6 retrieved temperatures minus radiosonde for 1000 and 115 mb pressures are shown in Figures 2 and 3 for the mid

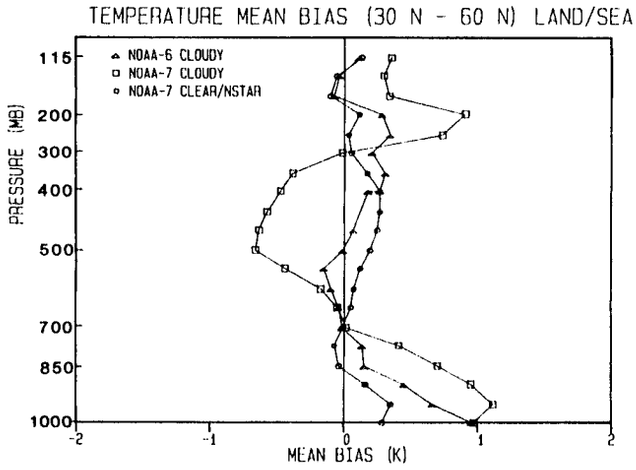

Fig. 2 Retrieval - Radiosonde Temperature Mean Biases (^{o}K) versus pressure (mb) for November 1984 in mid latitudes (30°N-60°N) over land and sea.

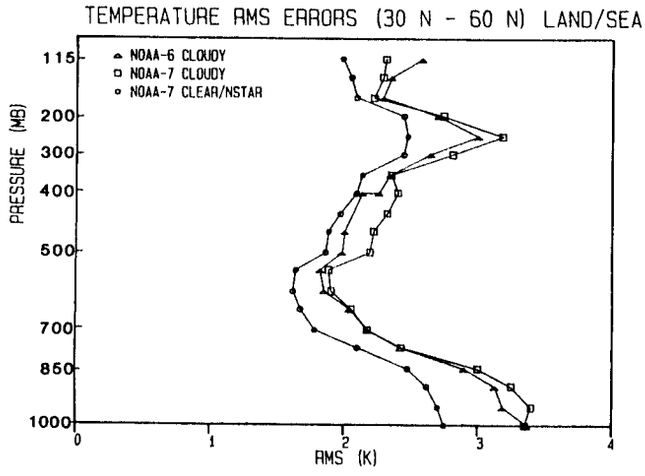

Fig. 3 Retrieval - Radiosonde Temperature RMS errors (^{o}K) versus pressure (mb) for November 1984 in mid latitudes (30°N-60°N) over land and ocean.

latitudes (30°N-60°N) and in Figures 4 and 5 for the tropics (30°N-30°S). Also the NOAA-7 mean biases and RMS errors for clear/N* as well as cloudy retrievals minus radiosonde for the month of November 1984 are also shown in Figures 2-5 for comparison purposes. The sample sizes used in computation of statistics for various types of soundings from NOAA-6 and NOAA-7 for the month of November 1984 are given in Table 2.

It is apparent from these figures that the totally cloudy retrievals from both NOAA-6 and NOAA-7 have consistently higher mean bias and RMS errors compared with clear/N* retrievals from NOAA-7. This may be due to the limited number of the channels employed in retrieving the cloudy temperature profiles. The comparison of mean biases and RMS errors for the cloudy retrievals for NOAA-6 and NOAA-7 reveal quite interesting features. The NOAA-6 microwave-based temperature retrievals have a small warm bias (less than 0.5^{o}K) in both latitude bands, 30°N-60°N and 30°N-30°S, except at the surface where it is about 1°K and are lower than NOAA-7 cloudy mean biases. The NOAA-7 totally cloudy mean biases fluctuate about zero and are larger for the mid-latitudes than for the tropics. The comparison of RMS errors reveals that RMS errors for NOAA-6 cloudy retrievals are between the RMS errors for NOAA-7 clear/N* and the totally cloudy retrievals for both the mid-latitudes and the tropics. This indicates that the NOAA-6 temperature retrievals based on microwave data are statistically reasonable. Furthermore, it is also

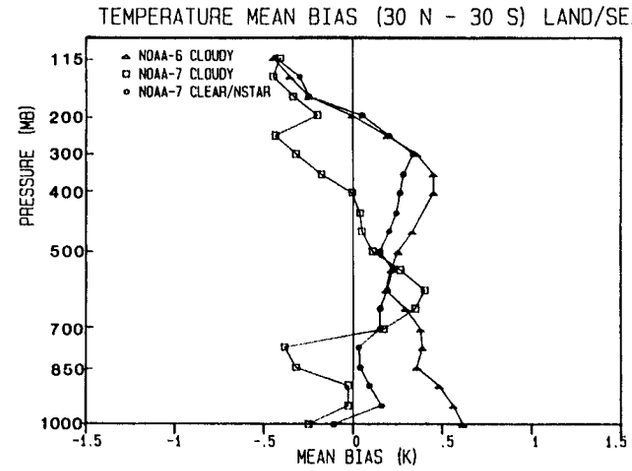

Fig. 4 Retrieved - Radiosonde Temperature Mean Biases (^{o}K) versus pressure (mb) November 1984 in tropics (30°N-30°S) over land and ocean.

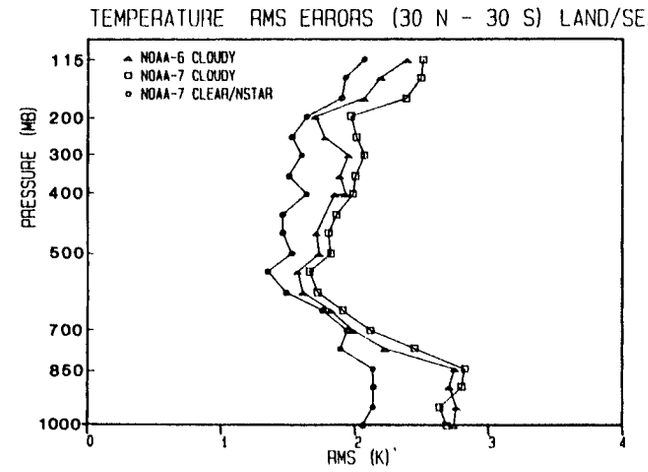

Fig. 5 Retrieved - Radiosonde Temperature RMS errors (^{o}K) versus pressure (mb) for November 1984 in tropics (30°N-30°S) over land and ocean.

Table 2
The Sample Size of Matchups Used in Statistical Evaluation

Satellite	Latitude Zone	Sounding Type	Number of Matchups
NOAA-6	60°N-30°N	cloudy**	977
	30°N-30°S	cloudy**	980
NOAA-7	60°N-30°N	cloudy	495
	30°N-30°S	cloudy	615
NOAA-7	60°N-30°N	clear/N*	972
	30°N-30°S	clear/N*	977

** based on only MSU data.

evident from these results that the RMS errors for NOAA-6 totally cloudy retrievals are generally lower in the tropics than the mid latitudes. This may be attributed to more active weather in the mid latitudes, in general, than in the tropics. The RMS errors are also larger at pressure levels near the surface and may be due to the dominant surface effects as well as to the clouds in the lower atmosphere.

To further examine the accuracy of microwave based soundings, data from a NOAA-6 orbit on 30 January 1986 at 2324 GMT was compared to the NMC global analysis data for 0000 GMT January 31, 1986. The timeliness of the satellite data with respect to the NMC analysis provided a good opportunity for a case study comparison.

Figures 6, 7 and 8 show the contours of analyzed NMC temperatures in degrees Kelvin and the microwave-based retrieved temperatures for NOAA-6 satellite for an area extending from 25° to 50° North latitude and from 60° to 95° West longitude at 3 levels - 700, 500 and 300 mb. This area encompasses the eastern U.S. and western Atlantic ocean.

At 300 mb, the NOAA-6 data are generally within about 1°K to 2°K of the NMC analysis except near the right edge of the orbital path where the effects of residual asymmetric scan bias for channel 3 are possibly causing larger errors. At the 500 mb level the retrievals differ from the analysis by 2°K to as much as 4°K even at low scan angles. The retrievals at 700 mb, where the weighting function for MSU channel 2 peaks, are generally quite good, being within 2°K of the NMC analyzed temperatures. Once again, the data at high scan angles appears to be of lower quality than the remainder of the data. This may be due to the errors inherent in the limb correction.

5.0 CONCLUSIONS

The NOAA-6 soundings based on microwave data at pressures between 1000 and 115 mb are consistent with NMC analyses as well as with NOAA-7 cloudy soundings. The RMS errors are generally slightly lower for NOAA-6 soundings compared to NOAA-7 totally cloudy data for both the tropics and the mid latitudes.

Overall, the microwave-based retrievals tend to be in good agreement with NMC analyzed temperature data at the pressure levels where the MSU channel 2 and 3 weighting functions peak, and have larger errors at levels in between.

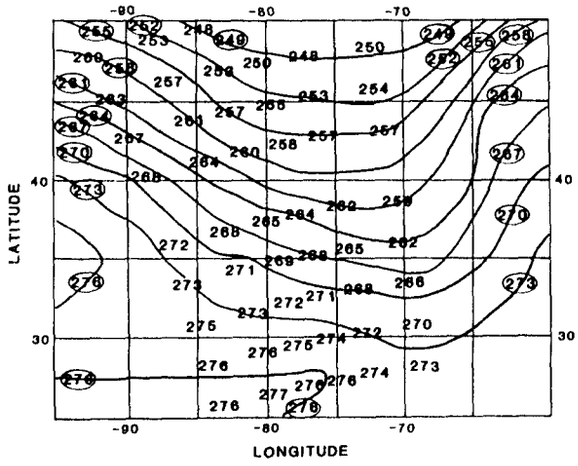

Fig. 6 NOAA-6 retrieved temperatures at 700 mb for January 30, 1986 at 2423 GMT are annotated in bold numbers. The contours of 700 mb temperatures analyses from NMC at 00:00 GMT January 31, 1986 are shown at 3 degree intervals.

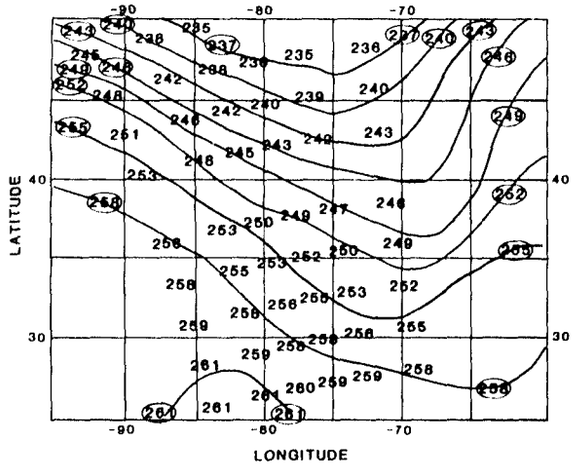

Fig. 7 NOAA-6 retrieved temperatures at 500 mb for January 30,1986 at 23:24 GMT are annotated in bold numbers. The contours of 500 mb temperature analyses from NMC at 00:00 GMT January 31, 1986 are shown at 3 degree intervals.

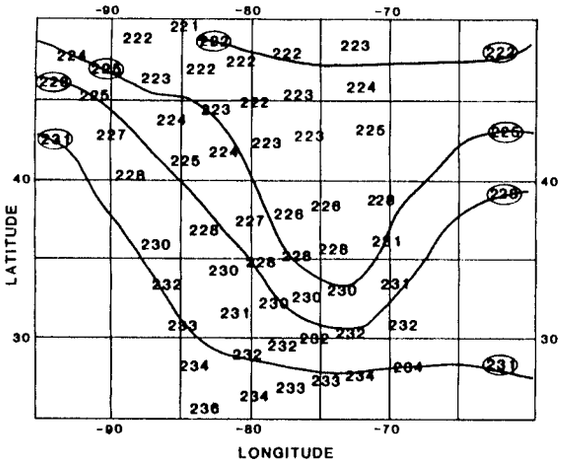

Fig. 8 NOAA-6 retrieved temperatures at 300 mb for January 30, 1986 at 23:24 GMT are annotated in bold numbers. The contours of 300 mb temperature analyses from NMC at 00:00 GMT January 31, 1986 are shown at 3 degree intervals.

6.0 ACKNOWLEDGEMENTS

The authors wish to acknowledge; Mr. Charles Novak of NOAA/NESDIS and Dr. Z. Ahmad, Mr. Charles Brown and Mr. Mike Liu of SASC Technologies, Inc. for their helpful suggestions and comments. The authors are also thankful to Ms. Lorna Crawford for neatly typing the manuscript.

7.0 REFERENCES

Broderick, H.J., C. Watkins, and A. Gruber, 1981: Statistical and Synoptic Evaluations of TIROS-N and NOAA-6 Retrievals, NOAA Tech. Report NESS 86, 48 pp.

McMillin, L.M., D.G. Gray, H.F. Drahos, M.W. Chalfant, and C.S.. Novak, 1983: Improvements in the Accuracy of Operational Satellite Soundings, J. Climate Appl. Meteor., 22, pp. 1948-1955.

Phillips, N., L.M. McMillin, A. Gruber, and D.Q. Wark, 1979: An Evaluation of Early Operational Temperature Soundings from TIROS-N, Bull. Amer. Meteor, Soc. 60, pp. 1188-1197.

Schwalb, A. 1978, The TIROS-N/NOAA A-G Satellite Series, NOAA Tech. Memorandum, NESS 95, 75 pp.

Smith, W.L., H.M. Wolf, C.M. Hayden, D.Q. Wark and L.M. McMillin, 1979: The TIROS-N Operational Verticial Sounder, Bull. Amer. Meteor. Soc. 60, pp. 1177-1187.

Werbowetzki, A., 1981: Atmospheric Sounding User's Guide, NOAA Tech. Report, NESS 83, 82 pp.

ADJUSTMENT OF A SATELLITE-DERIVED CLIMATOLOGY OF STRATOSPHERIC TEMPERATURE FOR CHANGES IN SATELLITE OBSERVING SYSTEMS

K. W. Johnson, M. E. Gelman, A. J. Miller, F. G. Finger, and R. M. Nagatani
Analysis & Information Branch, Climate Analysis Center, NMC, NWS, NOAA,
Camp Springs, MD, 20233

The Analysis and Information Branch (AIB) of the Climate Analysis Center(CAC) is developing a dynamic climatology of the stratosphere and lower mesosphere, based upon the NMC daily northern and southern hemisphere analyses of temperatures and heights carried out at the standard levels of 70, 50, 30, 10, 5, 2, 1, and 0.4 mb (roughly 18-56 km). Our current climatology is based on analyses carried out during the period of October 1978 through mid-June 1984. Since one primary purpose of this climatology is to search for long-term trends in atmospheric temperature, it is necessary to recognize variations in the bias between the true atmospheric temperature and the analyzed fields. This problem is of special concern at levels above 10 mb, because at these levels the NMC analysis is completely dependent upon temperature profiles derived from operational satellite radiance observations.

The temperature retrieval technique for pressures lower than 10 mb depends upon a historical sample of rocketsonde-radiosonde profiles for deriving regression coefficients used to transform the radiance observations into temperature profiles. Since the regression coefficients for deriving temperatures between 5 and 0.4 mb are not updated (as they are for coefficients for levels between 1000 and 10 mb) it is necessary to examine retrieved information for bias against coincident in situ (i.e., rocketsonde) observations. However rocketsonde information is not available until a considerable time after the satellite observations have been used in the operational meteorological analyses; therefore bias calculations must currently be carried out well after the fact. Biases between rocketsonde and co-located satellite temperature analyses were discussed by Gelman and Miller at the Fifth Conference on the Meteorology of the Stratosphere and Mesosphere at Boulder in 1985. Generally the analysis from satellite data is up to 6°K warmer than the rocketsonde observations at the 5-mb level, 1 to 5°K degrees colder at the 2-mb level, 3 to 8°K colder at the 1-mb level and up to 6°K warmer at the 0.4 mb-level.

The effect of the change in satellite instrumental systems may be clearly seen by comparing 2-mb daily zonal mean temperatures at 60 degrees N from daily analyses for the period 28-31 August 1983 (NOAA 7) with those for the period 2-5 September 1983 (NOAA 8). This data is summarized in Table 1

TABLE 1

DATE	ANALYZED ZONAL MEAN TEMPERATURE AT 2-MB, 60°N (°K)
Aug. 28	262.5
29	262.4
30	262.2
31	261.7
Sept. 2	257.1
3	257.1
4	256.5
5	256.2

During this autumn period slow radiational cooling with only occasional small-amplitude disturbances should result in a slow, steady temperature decrease. The average temperature for 28-31 August is 262.2°K, while the average temperature for 2-5 September is 256.7°K. The analyzed temperature change is -4.63°K from 31 Aug. to 2 Sept. Similar decreases in zonal mean temperature may be found at 30°N and 80°N (-3.65 and -3.64°K respectively). The 2-mb temperature bias against rocketsonde for the NOAA 7 satellite is -1.1°K, and for the NOAA 8 satellite is -4.9°K. So the value of the rapid decrease in analyzed temperature between August 31 and September 2 is close to the difference between the biases between the temperatures derived from the respective satellite instruments and rocketsondes.

Similar sudden jumps in analyzed mean zonal temperatures are found for each change of satellite or method of data processing during the period of reference (October 1978 - June 1984). These changes need to be considered in developing a consistent dynamic climatology of the stratosphere. Our present strategy at the AIB is to adjust each monthly mean temperature field using rocketsonde minus satellite analysis bias figures. Height fields are then recalculated hydrostatically upwards for levels at which temperature fields have been adjusted. (Daily values are not adjusted, and original, unadjusted temperature and height fields are also preserved in our archive.) A grand mean for each calendar month is then calculated at each grid point (5 degrees latitude-longitude grid.

The resulting monthly temperatures and height fields are stored as a climatological product available at the standard levels cited above. In addition previously calculated standard deviations of daily values from monthly means are combined using standard statistical

techniques to give an over-all estimate of the standard deviation of daily values from the climatological mean at each grid point. The reported standard deviation thus includes trends within the month as well as instrumental variability not accounted for and variations between years.

A summary of temperature results for January in the Northern Hemisphere is found in Table 2.

TABLE 2

LEVEL(mb)	MINIMUM TEMPERATURE (deg. K)	MAXIMUM STANDARD DEVIATION OF TEMPERATURE (deg. K)
2	235	13
1	245	11
0.4	251	9

Current results are stored as digitized fields on magnetic tape and analyzed fields of temperature and height for each month and each level are displayed on northern and southern hemisphere polar stereographic maps.

Since this adjustment technique has proven to be useful in developing a consistent climatological base for the northern hemisphere, we intend to extend it to the southern hemisphere and to begin to study deviations of each month's values from the climatological values for that month. As more information becomes available, we plan to extend the data base entered into the climatological means and standard deviations. We also hope to carry back a part of this climatology to 1964, when the, then, Upper Air Branch began analyses in the upper stratosphere over a part of the Northern Hemisphere. With all of these modifications we hope to move closer to a determination of long-term climatological temperature trends in the stratosphere and lower mesosphere.

2.4

SATELLITE DERIVED MOISTURE PROFILES

Andrew Timchalk

Satellite Applications Laboratory, NOAA/NESDIS
Washington, DC

1. INTRODUCTION

The derivation of an accurate spatial and temporal atmospheric water vapor distribution remains a problem over sparse data areas. Rawinsonde measurements of moisture are by far the most reliable, however, relatively few rawinsonde measurements are made over the vast oceanic areas of the Earth.

Beginning as early as 1968, the National Environmental Satellite Service (NESS now NESDIS) routinely supplied bogus moisture information to the National Meteorological Center (NMC) based on subjective evaluation of satellite cloud pictures. This method (bogus), after going through some evolutionary development, currently is given third priority after raobs and surface ship observations in specifying the moisture fields that are assimilated into the NMC forecast models. Neither the TIROS Operational Sounder (TOVS) nor the VISSR Atmospheric Sounder (VAS) remotely sounded moisture values are used directly by the forecast models.

Office Notes by Chu (1977) and Parrish (1978) describe the humidity analysis procedures used in NMC's operational prediction models. Studies performed by Hirano and Polger (1977-1978) and Hirano (1978) showed mixed results when the satellite cloud bogus humidity profiles were incorporated into the operational models. They found in evaluating forecasts for periods up to 48 hours, that moisture bogusing tended to alleviate a 12 HR dry bias, but in doing so, bogusing induced excessive rainfall in the plains to the north of the Gulf of Mexico. Precipitation threat scores were similar or better at 12 HR with bogusing, but much variability was found in the later forecast periods.

The main objective of this study was to determine whether the TOVS moisture profiles are more (less) accurate than the bogus profiles derived from Geostationary Meteorological Satellite (GOES) cloud pictures. The results should serve as a quantitative measure of the present state-of-the-art in determining moisture profiles from weather satellites. In addition, the results also reveal the strengths and weaknesses of each of the satellite moisture retrieval methods.

2. METHODS

2.1 Bogus Method

The bogus method is based on 13 typical relative humidity profiles which are assigned by examining GOES East and GOES West cloud pictures. Relative humidity percentages for any given profile are specified at six mandatory pressure levels from 1000 to 300 mb. These profiles are used by NMC over ocean areas and parts of Mexico only if no raob or surface ship observations are present. At the present time, bogus humidity profiles are provided twice daily to NMC for a 2.5 lat x 2.5 long grid area bounded by: 20N - 57.5N 65W - 180W (ocean areas only). The profiles were developed over a period of time by correlating RH profiles with synoptic situations as identified by satellite imagery.

Moisture is assimilated into the Global Model at six mandatory levels from 1000 to 300 mb and into the LFM Model for three layers between 1000 and 500 mb.

The cloud analysis procedure is such that obvious cloud category areas are first delineated within the analysis boundaries. The remaining areas (default Category 8) represent regions where no weather systems are present, i.e., clear skies, or in the extratropics, regions of scattered to broken low clouds in the form of strato-cumulus or stratus. Thus, in the analysis scheme, Category 8 is the most commonly observed category. For a complete description of the moisture bogus program, refer to Smigielski et al. (1982).

Of the 460 grid point within the analysis boundaries, Category 8 is normally assigned to more than one-half of the points. It is in these large areas, where inactive weather systems are present, that Category 8 is assigned. Further, it is in these large areas (clear and partly cloudy) that one would expect the TOVS method to out perform

the cloud bogus method.

2.2 TOVS Method

The TOVS moisture values are determined by using a statistical eigenvector regression method developed by Smith et al. (1979). TOVS mixing ratio values are calculated by applying Equation (1) at 15 different pressure levels from 1000 to 300 mb and by using 15 of the 27 TOVS sounding channels.

$$MRi = MRAi + Cij(TBOj - TBAj) \qquad (1)$$

In Equation (1), MRi is the retrieved mixing ratio at the ith level. MRAi is the average mixing ratio at the ith level, TBAj is the average brightness temperature for the jth channel, and the Cij's are the coefficients for each of the 15 channels (j) and 15 pressure levels (i). All of the terms on the right hand side of Equation (1), except for TBOj, are obtained a priori and are updated on a weekly basis. TBOj is the TOVS observed brightness temperature for each channel at the location for which the moisture retrieval is made.

3. PROCEDURE

For this study, RAOB, bogus, and TOVS data were collected during 1984, primarily during the months May through September. Bogus classifications were obtained from the daily operational file. TOVS retrievals were extracted from the operational NESDIS Data Staging Disk (DSD3) five-day rotating file. Bogus and TOVS data were both required to be located within a 90 n mi radius of the RAOB location. Bogus times are chosen to be nominally one hour before the 00 and 12 GMT synoptic times. The TOVS retrievals were required to fall within a three hour window centered on those synoptic times.

Extensive statistical analyses of these data have been made and results will be published in a NESDIS Technical Report.

4. RESULTS

The single best measure of accuracy for most operational purposes is the RMSE. Table A shows a comparison of the bogus and TOVS MR RMSE values separated by a slash for each category at the six mandatory pressure levels.

In Table A at 1000 mb, we see that the RMSE for the bogus MR values for Categories 2-7 were smaller (better) than those of the TOVS values. But in Categories 8-13, the TOVS RMSE values were better. At 850 and 700 mb, the TOVS RMSE values were smaller than the bogus values for all categories. At 500, 400, and 300 mb the results were mixed, but generally the bogus MR RMSE values were only slightly better than the TOVS.

The bottom row in Table A shows the RMSE for all categories combined. For the 1103 matchups, the RMSE values were larger for the bogus method than for the TOVS method at all levels, except 400 and 300 mb. TOVS RMSE values were markedly lower than the bogus ones at the 850 and 700 mb levels.

Table A
MIXING RATIO
RMSE(g/kg) Bogus/TOVS

		Pressure Level (mb)					
Cat	No	1000	850	700	500	400	300
1	-	-	-	-	-	-	-
2	6	1.32/2.45	3.37/2.39	2.71/1.67	1.60/0.96	0.49/0.51	0.12/0.14
3	107	2.54/3.75	2.45/2.21	1.65/1.49	1.09/0.89	0.61/0.48	0.16/0.13
4	60	3.28/4.01	4.14/2.38	2.16/1.75	1.15/0.92	0.48/0.55	0.15/0.17
5	-	-	-	-	-	-	-
6	11	2.53/4.34	3.19/2.12	2.98/2.40	0.84/0.72	0.53/0.37	0.13/0.13
7	57	2.25/3.12	3.18/2.06	1.56/1.48	0.82/0.95	0.34/0.51	0.10/0.51
8	678	3.54/3.28	3.88/2.52	2.40/1.69	0.84/0.89	0.38/0.51	0.11/0.14
9	68	3.42/3.24	3.05/2.49	2.61/2.17	0.92/0.91	0.90/0.50	0.26/0.14
10	63	4.11/2.52	3.03/2.81	2.52/1.57	0.65/0.76	0.24/0.40	0.06/0.12
11	7	6.82/1.95	7.05/1.57	3.74/1.71	1.16/1.07	0.55/0.34	0.14/0.07
12	13	5.06/2.67	6.51/2.77	2.51/1.66	0.76/0.84	0.86/0.49	0.21/0.14
13	33	3.25/2.55	2.95/2.58	3.31/1.61	1.49/0.96	0.57/0.43	0.28/0.16
	1103	3.43/3.31	3.69/2.47	2.36/1.70	0.91/0.89	0.47/0.50	0.14/0.14

5. SUMMARY

TOVS moisture values, when available, were on a par with or better than the cloud bogus moisture values. Except for matchups near dense broken/overcast cloud areas and at levels above 500 mb, the TOVS method showed less RMSE than did the bogus values.

An advantage of the TOVS method is that it is fully automated and can be applied globally; however, some accompanying disadvantages are that the retrievals are asynoptic and that they are made only in clear and partly cloudy areas.

The major advantage of the bogus method is that profiles are available at synoptic time and over areas where no TOVS moisture values are retrieved. The disadvantage of the bogus method is that the moisture values are less accurate than the TOVS in clear and partly cloudy areas. Further, the bogus method is only partially automated and requires subjective interpretation of cloud imagery.

6. REFERENCES

Chu, R., 1977: "Humidity analyses for operational prediction models at the National Meteorological Center." NMC Office Note, Part I.

Hirano, R. and P. Polger, 1977-78: "Satellite moisture bogusing Part I - Impact study." NMC Office Note, June 1977. "Part II - Evaluation of techniques." NMC Office Note, Jan. 1978.

Hirano, R., 1978: "Satellite relative humidity bogus using a fixed LAT-LON network: the first two weeks." NMC Office Note, March 1978.

Parrish, D., 1977: "Humidity analyses for operational prediction models at the National Meteorological Center." NMC Office Note 140, Part II.

Smigielski, F., T. Burtt, S. Hirsch, 1982: "Moisture bogus program." NOAA/NESS/SAB Office Operations Note (Chapter 225), Effective date Feb. 1982, pp. 22.

Smith, W. L., H. M. Woolf, C. M. Hayden, D. Q. Wark, and L. M. McMillin, 1979: "The TIROS-N operational vertical sounder." Bull. Amer. Meteo. Soc., 60, 1177-1187.

RELATIONSHIPS BETWEEN 6.7 MICROMETER IMAGERY AND RADIOSONDE-DERIVED PARAMETERS

Michael R. Stewart

Department of Earth
and Atmospheric Sciences
Saint Louis University
St. Louis, MO 63103

Henry E. Fuelberg

Department of Meteorology
Florida State University
Tallahassee, FL 32306

1. INTRODUCTION

Satellite radiometers have been designed to detect infrared (IR) energy emitted by atmospheric water vapor, and some of the wavelengths, e.g., the 6.3 and 6.7 μm channels, are affected primarily by vapor in the middle troposphere. Water vapor imagery first was obtained from polar orbiting platforms; however, it now is available from geostationary satellites such as METEOSAT and GOES. The sensor onboard GOES is called the Visible Infrared Spin-Scan Radiometer (VISSR) Atmospheric Sounder (VAS).

Applications of water vapor imagery include the preparation of high resolution humidity fields, wind determination from tracking image features, and locating areas of convective instability. In addition, the imagery has been related to locations of the subtropical (Martin and Salomonson, 1970) and polar (Ramond et al., 1981) jet streams. With the latter, warm (dry) regions delineated tropopause breaks often associated with polar frontal activity. However with the subtropical jet, maximum radiance coincided with areas of subsidence. Finally, with the assumption that vapor is conserved within an atmospheric volume, water vapor imagery has been used as a tracer to infer tropospheric dynamics (Rodgers et al., 1976).

Interpretation of 6.7 μm imagery is not straight forward. Black body temperature (TB) is affected by vapor content, the temperature at which the vapor occurs, and viewing angle. Weldon and Holmes (1984) concluded that greatly differing vertical vapor distributions can produce similar radiances. On the other hand, Petersen et al. (1984) emphasized that image interpretation is unambiguous in areas of low humidity because warm low-level temperatures observed through the dry air aloft will contrast with cooler temperatures produced by the surrounding midlevel moisture. The 6.7 μm radiation is not significantly affected by the earth's surface, except for areas of high elevation in a dry atmosphere. Similarly, low clouds usually have little effect on the imagery. On the other hand, cirrus and cumulonimbus clouds are readily evident in both the 6.7 μm and standard window channels.

This study uses special mesoscale radiosonde data to investigate a pronounced warm (dry) "streak" in 6.7 μm imagery. The goals are to describe relationships between the images and various thermodynamic and kinematic patterns diagnosed from ground-based data, and to explain causes for image variability by using water vapor budget analyses.

2. METHODOLOGY

The period of study is the 6-7 March day of the 1982 Atmospheric Variability Experiment (AVE)/VAS Ground Truth Field Experiment. Twenty four National Weather Service (NWS) radiosonde sites over the south-central United States collected special data at 3 h intervals, and nested within this domain were thirteen special sites over central Texas having an average spacing of 125 km. VAS images were available at times corresponding to the ground-based data.

Only the NWS profiles were used in several aspects of the investigation. Sounding data were objectively analyzed onto a 158 km grid mesh at the surface and at 50 mb intervals between 900 and 100 mb. However, the last level with humidity information usually was 350 mb. Vertical motions were computed using the kinematic method with a lower boundary condition of zero. The profile was adjusted to zero at 100 mb using standard techniques.

Water vapor budgets were calculated from sonde data using

$$P - E = -\frac{1}{g}\int_{p_t}^{p_b}\left(\frac{\partial w}{\partial t} + \vec{V}\cdot w\vec{V} + \frac{\partial(\omega w)}{\partial p}\right)dp \quad (1)$$

where P-E represents the combined effects of precipitation and evaporation, w is mixing ratio, and ω is vertical motion in isobaric coordinates. Since the LHS is computed as a residual, it also includes transfers of vapor between resolvable and unresolvable scales as well as effects of computational errors. Centered finite differencing was used to calculate all spatial derivatives and most temporal derivatives.

3. WEATHER CONDITIONS

Synoptic maps at 1200 GMT 6 March 1982 (Fig. 1) show conditions at the beginning of the special data collection period. At the surface, weak high pressure covered much of the southcentral United States. A stationary front stretched along the Gulf Coast, and a cold front was rapidly advancing southward through the Northern Plains. In the upper levels, the dominant feature was a major trough. At 500 mb (not shown), warming over Kansas and the Texas Panhandle suggested that the cold dome associated with the trough now was collapsing. At 200 mb (Fig. 1), a jet streak was located over northern Mexico, just south of Arizona, and a second streak was centered over the Atlantic Coast.

Figure 2 is a schematic of cirrus cloud cover and 6.7 μm image patterns. At the first time (1100 GMT 6 March), clouds blanketed the eastern half of the study area; however, a well defined line of clearing progressed eastward during the day, and by 0230 GMT 7 March, only the eastern edge of the domain still was affected. Clouds in the northwestern corner were associated with the advancing front. The initial 6.7 μm image (Fig. 2) indicates a large dry (warm) area over Arizona and southwestern New Mexico, and further east, there are two narrow warm streaks having a northeast-southwest orientation. Parallel mesoscale features also are evident over central Texas at 2030 GMT. The southernmost components lie near the edge of the cirrus clouds, but nearby low clouds (not shown) should have little effect on the patterns. During the course of the period, the dry area over the Southwest expands and moves eastward, covering most of Texas by 0230 GMT. The dual character of the image streak diminishes, and by 2330 GMT there is only one distinct feature which merges with the broader area advancing eastward. Animated loops of actual images indicate that enlargement of the warm (dry) region within the study area arises both from advection and local development. This hypothesis is supported by water vapor budgets to be presented later.

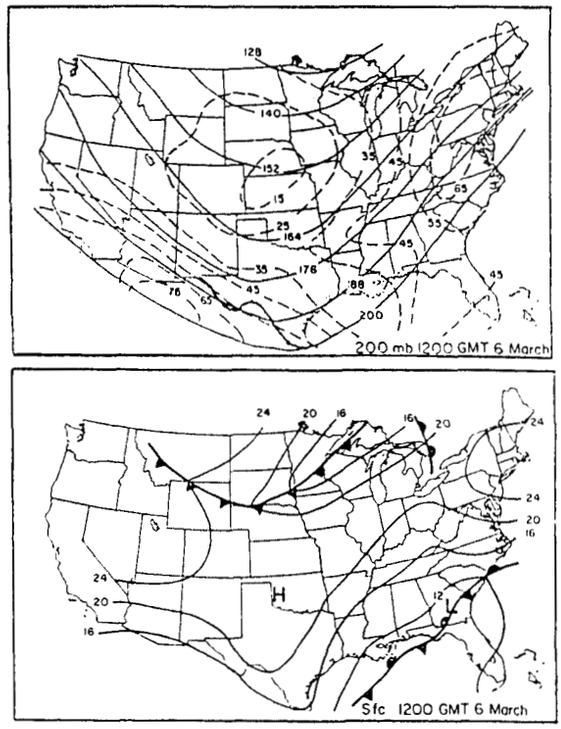

Fig. 1. National Meteorological Center analyses. At 200 mb, isotachs (dashed) are in m s^{-1}.

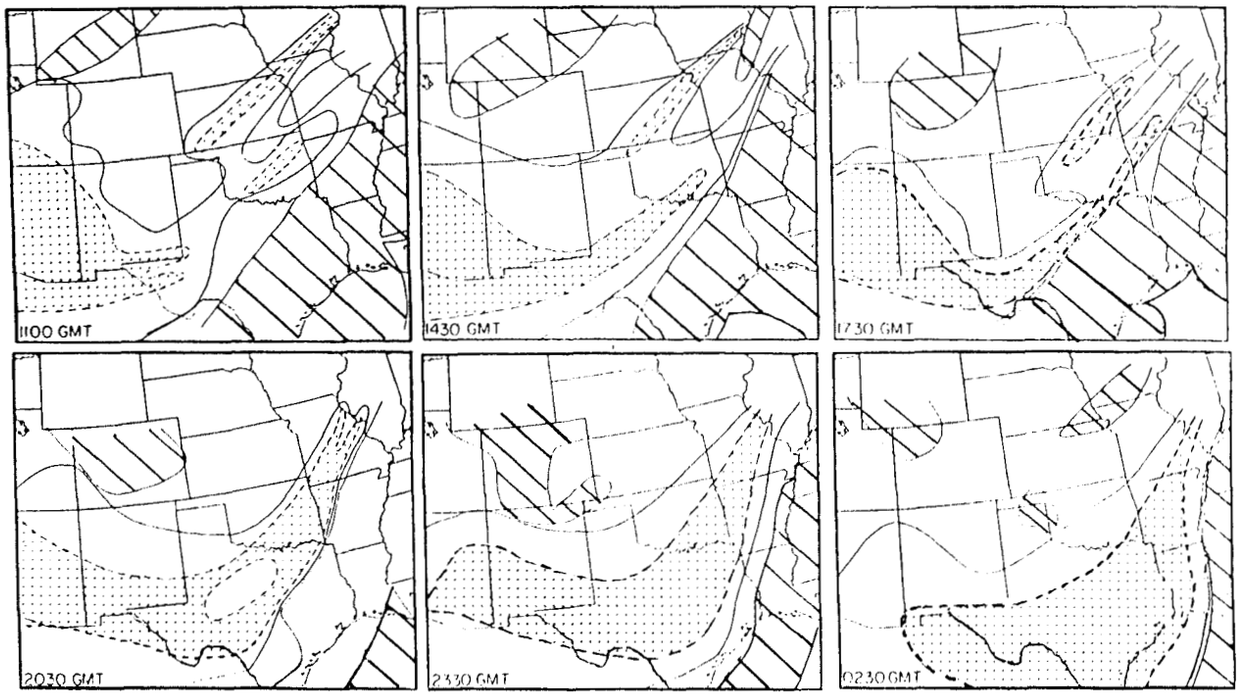

Fig. 2. Subjectively determined cirrus cloud locations (hatched) and schematics of 6.7 μm TB. The thin line denotes 240 ≤ TB ≤ 244 K while shading represents TB > 244 K.

4. IMAGE RELATIONSHIPS

Being mesoscale phenomena, the parallel warm (dry) streaks in Fig. 2 lie between the NWS radiosonde stations. They are best positioned within the network of special sites in central Texas at 2030 GMT. At that time TBs for the dry segments are 245 and 248 K, and in the region between them, the temperature is approximately 243 K. Thus, streak duality is not pronounced. Mixing ratios from the special network and nearby NWS stations were hand analyzed with the goal of verifying the double streak. That is, no radiosonde data were violated, but the images were used as guides whenever several analysis interpretations were possible. Patterns at 700 mb (Fig. 3) show the cloudy, humid area over the southeastern Texas containing mixing ratios exceeding 5 g kg^{-1}. Over clear regions, however, values range from 1.4 g kg^{-1} at Albuquerque to 0.5 g kg^{-1} only a few hundred kilometers southeastward at Abilene, TX. In agreement with the images (Fig. 2), the mixing ratios show two dry regions with northeast-southwest orientations. Values for the moist area in between are only about 0.3 g kg^{-1} greater. Mixing ratios at 700 mb show better image agreement than those at other levels, but patterns of precipitable water (not shown) exhibit less correlation.

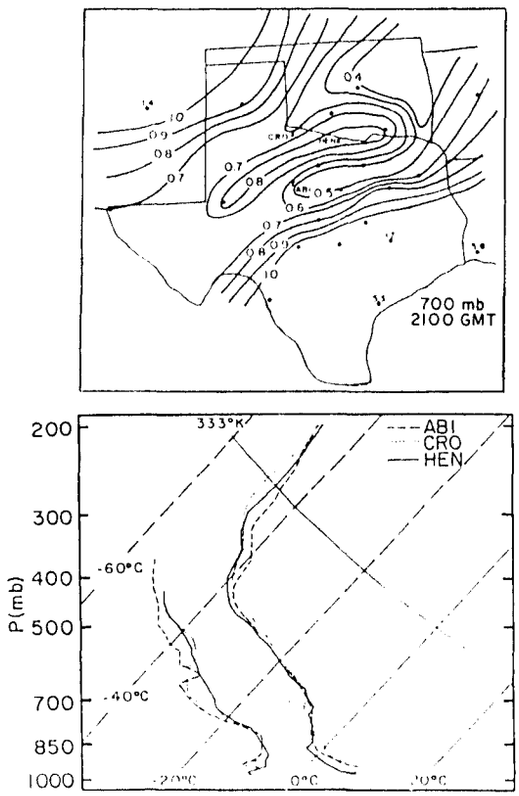

Fig. 3. Top: Mixing ratios (g kg^{-1}) at 700 mb on 2100 GMT 6 March 1982. The analysis was terminated at 1 g kg^{-1}. Bottom: Skew T-log p diagram for Abilene, Crowell, and Henrietta, TX at 2100 GMT. Locations are shown on the top panel.

Soundings for Henrietta (HEN), Abilene (ABI), and Crowell (CRO), TX corresponding to the moist and two dry areas, respectively, also are shown in Fig. 3. Although tropospheric temperature profiles are similar, 700 mb dewpoints for ABI and CRO are 2-3°C colder (drier) than at HEN. When these soundings were input to a radiative transfer model, the drier profiles yielded 6.7 μm weighting functions (not shown) with lower altitude peaks and greater simulated radiances, thereby agreeing with observed imagery. Thus, in summary, there is ground-based verification for the dual character of the image steak, even though it is a subtle feature that is not obvious even in the special mesoscale radiosonde data.

Although it would be desirable to study mesoscale characteristics of the image streak in greater detail, poor placement with respect to the special radiosonde sites makes this virtually impossible. Therefore, in the remainder of this paper, only its synoptic scale aspects will be considered. Precipitable water (PW), calculated from the NWS sites, is given for the 800-350 mb layer in Fig. 4. The

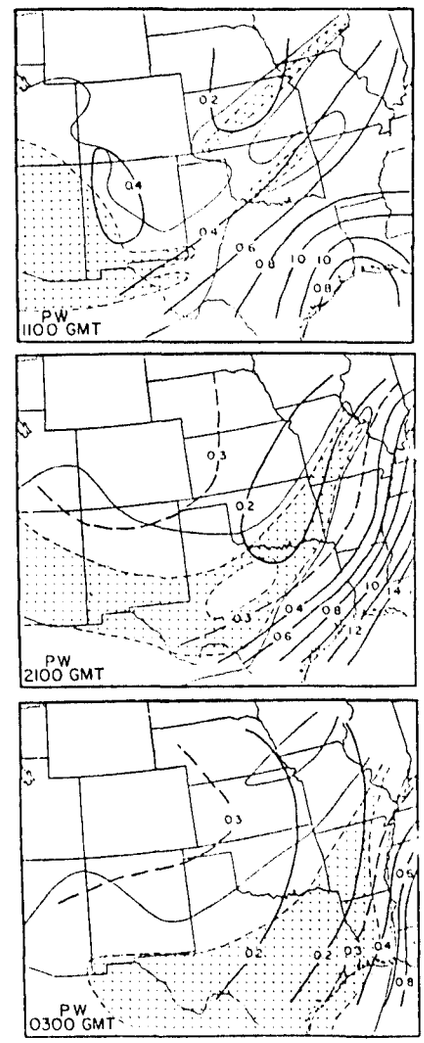

Fig. 4. Precipitable water (cm) for the 800-350 mb layer. Image schematics are as in Fig. 2.

surface-800 mb region is not included because its high moisture content dominates PW although radiative transfer calculations indicate less than a 10% contribution to total 6.7 μm radiation. In general, there is ground-based verification for most of the large scale image features; however, it is interesting that warm TB over the southwest corner does not correspond to minimum PW.

The review section noted relations between water vapor imagery and jet streams. For the current case, this is explored through vertical cross sections (Fig. 5) from Denver, CO (DEN) to Boothville, LA (BVE). At 2100 GMT, the polar front is associated with strong gradients of temperature and mixing ratio. The jet stream (top panel), located near the front, contains winds in excess of 50 m s^{-1}. Ramond et al. (1981) observed that the maximum 6.7 μm radiance band near polar jets accurately delineated the tropopause break, i.e., the farthest poleward point reached by the overhanging warm, moist subtropical air. On 6-7 March, TBs plotted along the top of the cross sections (Fig. 5) show that greatest radiance (the streak) corresponds to the tropopause break, thereby agreeing with the Ramond et al. concept. It should be noted, however, that cross sections through this region at earlier times (not shown) indicated tropopause breaks even though the image steak was not yet well defined. Thus, the mere presence of a break does not seem to guarantee a warm (dry) image feature, suggesting that other factors contribute as well.

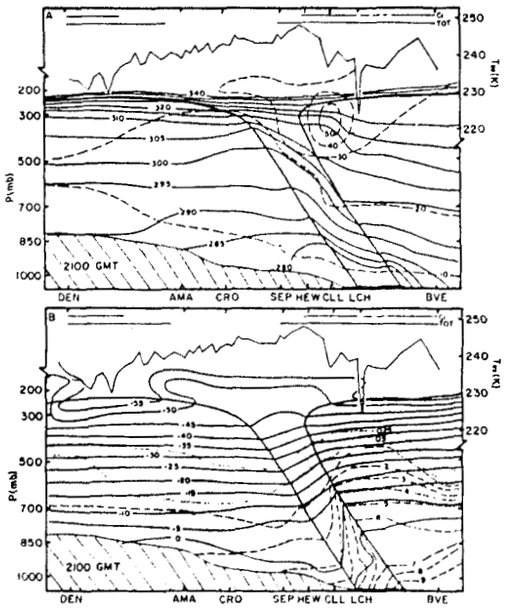

Fig. 5. Cross sections from DEN to BVE at 2100 GMT 6 March. At the top, potential temperature (solid) is in °K, and wind speed (solid) is in m s^{-1}. At the bottom, temperature (°C) is solid, and mixing ratio (g kg^{-1}) is dashed. TB and cloud locations are along the top of each panel.

Subsidence associated with the jet stream and trough/ridge pattern is a likely cause for the dry region constituting the image streak. Middle tropospheric vertical motions at 1100 GMT (Fig. 6) show ascent over the southeastern half of the domain that agrees with the precipitation and cloudiness. Northwest of the jet axis, however, there is widespread subsidence in the area of the developing image pattern. Over the southwest corner, descent also corresponds with dry conditions. Patterns at 2100 GMT are similar to those 10 h earlier. Specifically, there is ascent from Missouri to southern Texas where there is cloud cover, but there is subsidence elsewhere. Thus, the area of strong subsidence again corresponds to the warmest (driest) region on the 6.7 μm image. It should be noted that satellite-derived ozone concentrations (not shown) are greatest in the region of the developing streak, thereby suggesting the downward intrusion of dry stratospheric air, possibly associated with tropopause folding (Chesters and Uccellini, 1985, personal communication). Finally, vertical motions at 0300 GMT (Fig. 6) continue the evolution noted earlier.

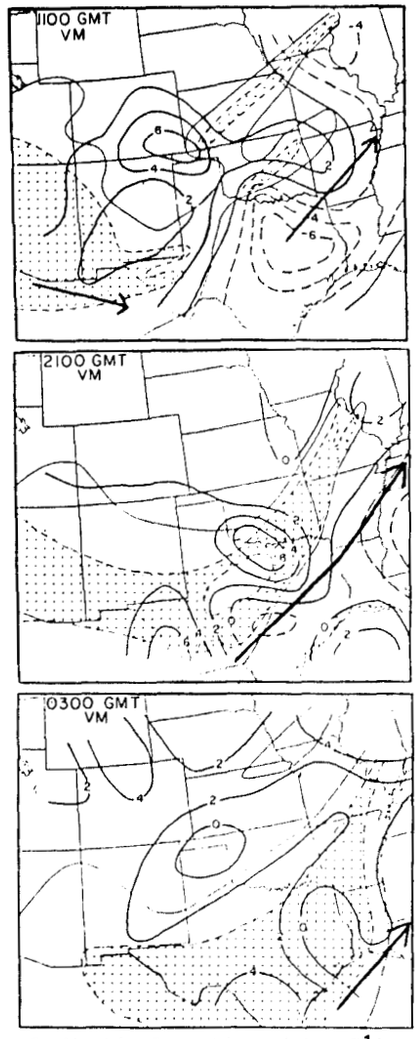

Fig. 6. Vertical motion (μb s^{-1}) at 500 mb. Schematics of 6.7 μm imagery are as in Fig. 2. The axis of the jet stream also is indicated.

According to Reiter's (1963) advective jet model for straight line flow, ascending (descending) motions are expected in the left front and right rear (right front and left rear) quadrants of jet streaks. With cyclonically curved flow as on 6-7 March, motions on the left side should be enhanced whereas those on the anticyclonic side should be undefined. The validity of this simplified approach is somewhat suspect since Shapiro and Kennedy (1981) noted that straight line dynamics are not applicable to cases when upper level jets are embedded within synoptic wave regimes.

In the current case, vertical motions do not always agree with the simplified model. For example, if it is assumed that the AVE-VAS region is influenced by the jet streak over the Atlantic Coast (Fig. 1), there is the predicted descent in the left rear quadrant and ascent in right rear sector. On the other hand, at the first time, one might expect at least the western half of the domain to be dominated by the streak over northern Mexico, and at 2100 and 0230 GMT, most of the region should be similarly affected. In that case, the simplified models predict ascent, not the observed descent, in the left front quadrant. We currently are exploring the structure of the jet stream in much greater detail in an attempt to better understand its relation to water vapor imagery on 6-7 March. At this point, however, subsidence, whatever its origin, appears to be an important factor in forming the dry image streak.

5. WATER VAPOR BUDGETS

Water vapor budget analyses now are used to explore variations in TB. The underlying assumption is that fluctuations in 6.7 μm radiation are attributable mostly to changes in humidity. Equation (1) first was evaluated at the individual grid points; then, these results were averaged over three subareas enclosing particular image features: the developing dry streak from Texas to Missouri, the consistently dry area over the southwest corner of the network, and a region of increasing vapor over the Midwest. Locations of the averaging areas moved with the feature enclosed; an example is given in Fig. 7. Finally, results for each area were composited into space-time averages. Only integration over the 800-350 mb layer is presented in Table 1 because radiative transfer calculations indicated that the surface - 800 mb layer had little effect on TB. Furthermore, trial water vapor budgets including the lower layer exhibited few differences from those being shown. Area averaged TB (not shown) also was calculated for the three regions in Fig. 6. These values were based on pixels that were not cloud contaminated.

Near the developing dry streak over Texas (Fig. 7), the local derivative (Table 1) indicates decreasing water vapor content (-43.85×10^{-6} g cm^{-2} s^{-1}) corresponding to a steady increase in TB from 238.3 to 246.0 K. Horizontal flux divergence is the dominant vapor sink (32.98×10^{-6} g cm^{-2} s^{-1}) while vertical flux divergence is a secondary sink. Average vertical motion over the area at 500 mb is 1.25 μb s^{-1} (subsidence). The residual term (P-E) indicates a relatively weak vapor source (-5.04×10^{-6} g cm^{-2} s^{-1}). Since the dry streak and averaging area were on the edge of cloud cover to the southeast, positive P-E could represent evaporation of the nearby clouds. Also, there is strong vertical wind shear which could cause upward eddy transport

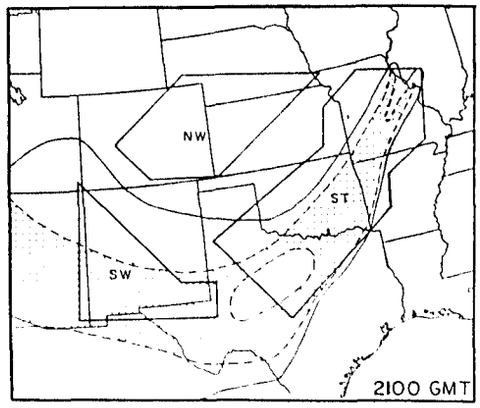

Fig. 7. Locations of averaging regions at 2100 GMT. Image schematics are as in Fig. 2.

Table 1: Area-time averaged water vapor budgets for limited regions enclosing image features. Values are integrated for the 800-350 mb layer and are 10^{-6} g cm^{-2} s^{-1}, except for 500 mb ω which is μb s^{-1}.

Feature	Times	$\partial w/\partial t$	$\vec{\nabla} \cdot w \vec{V}$	$\partial(\omega w)/\partial p$	P-E	ω_{500}
Dry Streak	1100-0230 GMT	-43.85	32.98	15.91	-5.04	1.25
Southwest Dry Area	1100-2030 GMT	-39.91	28.79	18.04	-6.92	3.58
Midwest Humid Area	1100-0230 GMT	13.70	-1.64	11.32	-23.38	1.70

of moisture from the more humid air near the surface. Finally, data and computational uncertainty must be acknowledged as well.

Current results agree with those of Rodgers et al. (1976) who also noted that warm (dry) image streak formation was produced by both horizontal and vertical transports. On the other hand, Ramond et al. (1981) emphasized the role of vertical motions in producing such streaks. During 6-7 March, however, horizontal transport clearly was the dominant mechanism.

For the warm (dry) region over the Southwest (Fig. 7), only the first four times were averaged because the area later merged with the dry streak farther east (already described). In fact, the vapor budget for this feature (Table 1) is very similar to that of the streak itself. Specifically, decreasing humidity (-39.91 g cm^{-2} s^{-1}) associated with TB increasing from 243 to 250 K again is attributable to vapor sinks by both horizontal and vertical flux divergence. P-E continues to indicate a relatively weak source.

The final image feature is a relatively cool (moist) area that initially was over Colorado but steadily advanced southeastward (Fig. 7). The vertical sum of $\partial w/\partial t$ (Table 1) is 13.70 x 10^{-6} g cm^{-2} s^{-1}, indicating moderately increasing vapor content. Although horizontal flux convergence is a weak vapor source to this area, vertical flux divergence associated with the subsidence more than counteracts. Thus, the residual term is the greatest source for increasing vapor content. Animated loops of 6.7 µm and standard IR images indicate that middle and upper level cloud cover is dissipating as it moves southeastward, and Petersen et al. (1984) suggested that evaporating cirrus may produce cool (moist) areas on 6.7 µm imagery. That appears to be a likely factor in the current case as well.

6. CONCLUSIONS

This paper has described our initial efforts toward understanding 6.7 µm imagery on 6-7 March 1982. Based on special mesoscale radiosonde data, there was ground-based verification for some small scale and subtle image features. In a larger sense, the developing warm (dry) image streak was attributable both to subsidence and horizontal flux divergence of vapor. The streak was located near the tropopause break associated with the polar front.

Our current research on this case considers tropopause folding and additional relationships between jet streaks and image features. Trajectory calculations also are being planned. Water vapor imagery is an exciting new tool for a better diagnosis and understanding of the atmosphere; however, it is clear that much remains to be done.

ACKNOWLEDGEMENTS

Sharon Wittig did an excellent job of typing the manuscript. The research has benefited from discussions with Roger Weldon and Susan Holmes of NOAA/NESDIS who provided the radiative transfer program. Dennis Chesters, Dennis Keyser, and Lou Uccellini of NASA/Goddard also gave helpful insights. Gary Jedlovec and Greg Wilson of NASA/Marshall supplied some of the data and were very helpful when HEF was on sabbatical leave at Marshall.

Finally, the authors gratefully acknowledge the support of NASA through Contract NAS8-35330 to Saint Louis University and Grant NAG8-033 to Florida State University. Both awards are under the auspices of the Atmospheric Sciences Division, Marshall Space Flight Center, Huntsville, AL.

REFERENCES

Martin, F.L., and V.V. Salomonson, 1970: Statistical characteristics of subtropical jet stream features in terms of MRIR observations from Nimbus 2. J. Appl. Meteor., 9, 508-520.

Petersen, R.A., L.W. Uccellini, A. Mostek, and D.A. Keyser, 1984: Delineating mid and low-level water vapor patterns in preconvective environments using VAS moisture channels. Mon. Wea. Rev., 112, 2178-2198.

Ramond, D., M. Corbin, M. Desbois, G. Szejwach, and P. Waldteufel, 1981: The dynamics of polar jet streams as depicted by the METEOSAT water vapor channel radiance field. Mon. Wea. Rev., 109, 2164-2175.

Reiter, E.R., 1963: Jet Stream Meteorology. Univ. of Chicago Press, 515 pp.

Rodgers, E.B., V.V. Salomonson, and H.R. Kyle, 1976: Upper tropospheric dynamics as reflected in NIMBUS-4 THIR 6.7 µm data. J. Geophys. Res., 81, 5749-5758.

Shapiro, M.A., and P.J. Kennedy, 1981: Research aircraft measurements of jet stream geostrophic and ageostrophic winds. J. Atmos. Sci., 38, 2642-2652.

Weldon, R., and S. Holmes, 1984: Characteristics of water vapor imagery. Manuscript available from NOAA/NESDIS, Washington, D.C. 20233.

2.6

DIFFERENTIAL INVERSION AND THE LIMITS OF OBJECTIVE TEMPERATURE INFERENCING

Jean I.F. King

Air Force Geophysics Laboratory
Hanscom AFB, MA 01731

1. DIFFERENTIAL INVERSION THEORY

Transfer theory relates the upwelling thermal radiance of the atmosphere to the integral transform over pressure of the Planck intensity $\mathcal{B}(p)$ and a kernel weight function $\mathcal{H}(p/\bar{p})$ which depends on the line character of the sampled frequency interval. Thus,

$$\mathcal{R}(\bar{p}) = \int_0^\infty \mathcal{B}(p)\, \mathcal{H}(p/\bar{p})\, dp/p, \qquad (1)$$

where $\mathcal{R}(\bar{p})$ is the radiance of the sensing channel whose weight function peaks at $p = \bar{p}$.

A change of independent variables $\mathcal{B}(p) = B(-\ln p)$, $\mathcal{R}(\bar{p}) = R(-\ln \bar{p})$, and $\mathcal{H}(p) = W(\ln p)$ converts the radiance expression into the convolution integral

$$R(\zeta) = \int_{-\infty}^{\infty} B(z)\, W(\zeta - z)\, dz \equiv B * W, \qquad (2)$$

where $z = -\ln p$ and $\zeta = -\ln \bar{p}$ are height-like variables.

Application of the bilateral Laplace transform using the Faltung theorem results in

$$r(s) = b(s)\, w(-s). \qquad (3)$$

The bilateral weight transform

$$w(-s) = \int_{-\infty}^{\infty} e^{-sz} W(z)\, dz = \int_0^\infty p^{-s} \mathcal{H}(p)\, dp/p \equiv \Omega(1-s) \qquad (4)$$

may be viewed as a generalized Γ- function.

We proceed by expanding the reciprocal Ω -function in a Maclaurin's series

$$\frac{1}{\Omega(1-s)} = \sum_{k=0}^{\infty} \lambda_k s^k, \qquad (5)$$

with the coefficients

$$\lambda_k = \frac{[w^{-1}(0)]^{(k)}}{k!}. \qquad (6)$$

The parenthetical superscript denotes a k -fold differentiation with respect to the transform variable s.

The Planck transform with this substitution for the Ω -function can now be expressed as

$$b(s) = \sum_{k=0}^{\infty} \lambda_k s^k\, r(s), \qquad (7)$$

whose inverse transform yields the <u>differential inversion formula</u> (King 1983)

$$B(z) = \sum_{k=0}^{\infty} \lambda_k D^{(k)} R(z) = R(z) + \lambda_1 R'(z) + \lambda_2 R''(z) + \ldots \qquad (8)$$

This formula has been derived earlier in a formal context for Laplace transform inversion by Widder (1971).

2. INVERSION COEFFICIENTS AND THE GENERALIZED WEIGHT FUNCTION

The inferred Planck intensity depends on the inversion coefficients, whose values in turn derive from the particulars of the weight function. We now develop closed-form expressions and numerical values for the <u>generalized exponential weight function</u>.

$$\mathcal{H}_m(p) = \frac{m^m}{\Gamma(m+1)}\, p \exp(-m p^{1/m}), \qquad (9)$$

which satisfies the normalization requirements

$$\int_0^\infty \mathcal{H}_m(p)\, dp/p = \int_{-\infty}^{\infty} W_m(z)\, dz = 1. \qquad (10)$$

The convenience and flexibility of this choice is seen by noting that m = 1 and m = 1/2 are weight functions associated with the Goody-statistical and Elsasser band models.

The bilateral Laplace transform of the weight function follows as

$$\int_{-\infty}^{\infty} e^{-sz} W_m(z)\, dz = \int_0^\infty p^{-s} \mathcal{H}_m(p)\, dp/p = \Gamma_m(1-s) \qquad (11)$$

where we have defined the mth order Γ -function as

$$\Gamma_m(s+1) = \frac{\Gamma[m(s+1)]}{m^{ms}\,\Gamma(m)} . \qquad (12)$$

The evaluation of the coefficients λ_k, as we see from Eqs. (4), (6), and (12), requires the derivatives of the Γ- function. The first derivative is related to the digamma or ψ -function

$$\psi(s) = \Gamma'(s)/\Gamma(s), \qquad (13)$$

while the higher derivatives are related to the polygamma functions through the formula

$$\psi^{(k)}(s) = \frac{d^{k+1}}{ds^{k+1}} \ln \Gamma(s). \qquad (14)$$

The closed form expressions for the λ_k inversion coefficients λ_k (k = 0, 1, ..., 6) as a function of the weight parameter m are given in King (1985). For integer and half-integer argument, the polygamma functions are expressible in terms of the Riemann zeta-functions. Tables for these digamma and polygamma functions are found in Abramowitz and Stegum (1964).

The evaluation of these functions which are displayed in Tables 1 and 2 is straightforward but tedious. We note that as the weight function becomes increasingly concentrated corresponding to smaller m, that all λ_k's vanish for k>1, while $\lambda_1(m \to 0) \to -1$. This implies that even for a delta-type weight function there is a residual shift between the Planck intensity and the radiance profile minima, which is to say that

$$p_{min} \neq \bar{p}_{min} ,$$

where

$$\mathcal{B}_{min} = \mathcal{B}(p_{min}), \; \mathcal{R}_{min} = \mathcal{R}(\bar{p}_{min}).$$

Furthermore the extent to which the odd coefficients differ from zero is a measure of the asymmetry of the weight function. Thus

$$\lambda_i \neq 0 \; (i = 1,3,\ldots) \rightarrow W(-z) \neq W(z).$$

3. TRANSFORMATION THEORY FOR ARBITRARY WEIGHT FUNCTIONS

We recall from Eqs. (3) and (8) that the Planck intensity for a weight function of order m is given by the differential inversion formula

$$B(z) = L^{-1}\left[\frac{r(s)}{W_m(-s)}\right] = D_m[R(z)], \qquad (15)$$

where the differential operation is defined as

$$D_m \equiv \sum_{k=0}^{\infty} \lambda_k(m) \frac{d^k}{dz^k} . \qquad (16)$$

The variation of weight function shape with height in the atmosphere requires the use at each level of the appropriate m-value differential coefficients $\lambda_k(m)$. One can account for this m-variation in another way which avoids the clumsy substitution of new differential coefficients with each level temperature inference. Instead of varying the coefficients, the radiance R and weight function peak $\bar{z}$ can be m-scaled so that only the differential coefficients for m = 1 will appear in the inversion formula.

To do this we note that Eq. (15) can be written as

$$B(z) = L^{-1}\left[\frac{r'(s)}{W_1(-s)}\right], \qquad (17)$$

where the radiance transform is scaled as

$$r'(s) = \frac{W_1(-s)}{W_m(-s)} r(s). \qquad (18)$$

Upon substitution for the weight function transforms from Eq. (12) and performing the scaled inversion implied by Eq. (17), we obtain

$$B'(z'+\delta) = \Gamma(m)\, D_1[R'(z'+\delta)], \qquad (19)$$

$z' = mz$ (space contraction)

$R' = e^{-z(m-1)} R$ (radiance stretching)

$\delta = m \ln m$ (refractive space shift).

TABLE 1. Inversion Coefficient for Exponential Weight Function ($m = 1$)

λ_0	1.
λ_1	-.57721 56649
λ_2	-.65587 80715
λ_3	.04200 26350
λ_4	.16653 86114
λ_5	.04219 77346
λ_6	-.00962 19715
λ_7	-.00721 89432
λ_8	-.00116 51676
λ_9	.00021 52417
λ_{10}	.00012 80503
λ_{11}	.00002 01349
λ_{12}	-.00000 12505

TABLE 2. Differential Inversion Coefficients for Representative Weight Functions

	Delta Function	Strongly Peaked	Elsasser	Statistical	Strong Clustering
	$m = 0$	$m = .1$	$m = .5$	$m = 1$	$m = 4$
λ_0	1.	1.	1.	1.	1.
λ_1	-1.	-.8121169848	-.6351814227	-.5772156649	-.5207067709
λ_2	0	-.1773994973	-.4151225552	-.6558780715	-2.1350158750
λ_3	0	-.0110348444	-.0014993282	.0420026350	.3050207816
λ_4	0	.0004253445	.0416237314	.1665386114	2.2390138114
λ_5	0	.0001167500	.0104035581	.0421977346	.4628141296

REFERENCES

Abramowitz, M. and I.E. Stegun, 1964. Handbook of Mathematical Functions, U.S. Government Printing Office, Washington, DC.

Chandrasekhar, S., 1950, Radiative Transfer, Oxford University Press, London.

King, J.I.F., 1983, Differential Inversion. In Preprint Volume, Ninth Conference on Aerospace and Aeronautical Meteorology, Omaha, NE. (Available from Am. Meteorol. Soc., 45 Beacon St., Boston, MA 02108.

King, J.I.F., 1985, Theory and Application of Differential Inversion to Remote Temperature Sensing, Proceedings of the Workshop on Advances in Remote Sensing Retrieval Methods, Oct 30-Nov 2, 1984, Williamsburg, VA, Deepak Publ. Co.

Widder, D.V., 1971, An Introduction to Transform Theory, Academic Press, New York.

3.1

Evaluation of a Multivariate Variational Assimilation of Conventional and Satellite Data for the Diagnosis of Cyclone Systems.

Gary L. Achtemeier, H. T. Ochs, III, S. Q. Kidder, and R. W. Scott
Climate and Meteorology Section
Illinois State Water Survey
Champaign, Illinois 61820

1. INTRODUCTON

The proliferation of new methods to measure the state of the atmosphere through remote sensing and advanced immersion techniques has led to the need to merge data collected from these new measurement systems with data collected routinely by traditional methods. These data include a number of different variables that are diverse in measurement accuracy and in observation location. Therefore, it is desirable to merge the data so that the hybrid product will contain the best approximation to the significant meteorological variables. This paper reports on the development of a diagnostic method to merge data of different source, type, quality and location in a dynamically consistent manner. We further develop and improve upon a diagnostic variational objective analysis technique developed by Achtemeier (1975) for the study of cyclone scale weather systems.

In most cases, the creation of a dynamically consistent hybrid set of data is accomplished through some form of data assimilation coupled with an initialization for a numerical model. Observational data is blended with model forecast fields through an interpolation technique (Cressman, 1959; Gandin, 1963; Schlatter; 1975) in which the forecast fields, used as a first guess, are updated with the observations. These methods are multivariate; wind observations are used in the interpolative analysis of the height and temperature fields and vice versa. Then some initialization procedure such as dynamic initialization (e.g., Miyakoda and Moyer, 1968; Nitta and Hovermale, 1969) or normal mode initialization (e.g., Baer and Tribbia, 1977; Machenhaur, 1977) brings the hybrid data set into consistency with a numerical model. Highly sophisticated dynamically consistent data assimilation schemes such as those described by McPherson, et al., (1979), Bengtsson, et al., (1982), Ghil. et al. (1979), Temperton (1984), and many others produce accurate representations of the state of the synoptic scale atmosphere. These hybrid data sets, though admittedly modified to be consistent with the scales of motion permitted by the models, may be useful for diagnostic studies as well as for initial states for forecast models.

The approach taken here is to develop a purely diagnostic method for the dynamic merger of diverse data. This is not to say that the variational method is superior to the data assimilation methods used with prognostic models, only that it is, by design, independent of numerical models and is therefore different from the other methods. It serves a different purpose, namely the diagnosis of the morphology and energetics of cyclone systems, whereas many studies of numerical forecasts with mixed data sets are focused upon improved forecast skill. However, the variational model may eventually be of value in comparisons with existing data assimilations and may provide insights that could lead to improvements in both methods.

The goal of our research is a variational data assimilation method that incorporates as dynamical constraints, the primitive equations for a moist, convectively unstable atmosphere and the radiative transfer equation. Variables to be adjusted include the three-dimensional vector wind, height, temperature, and moisture from rawinsonde data, and cloud-wind vectors, moisture, and radiance from satellite data. This presents a formidable mathematical problem. In order to facilitate thorough analysis of each of the model components, we defined four variational models that divide the problem naturally according to increasing complexity. The first variational model (MODEL I) contains the two nonlinear horizontal momentum equations, the integrated continuity equation, and the hydrostatic equation. Model development problems associated with an internally consistent finite difference method, a nonlinear hybrid terrain-following vertical coordinate, formulations for the pressure gradient terms, formulations for the velocity tendency terms and the development of a convergent solution sequence will be addressed elsewhere. The subject of this paper is to briefly describe the assimilation model and present some sample results.

2. A VARIATIONAL APPROACH TO DIAGNOSTIC DATA ASSIMILATION

This diagnostic objective analysis is an adaptation of Sasaki's (1958) method of variational analysis. The dynamic constraints, M_i, for MODEL I are the two nonlinear horizontal momentum equations, the hydrostatic equation, and an integrated continuity equation. These constraints have been transformed into the Lambert conformal map image projection and into a hybrid nonlinear sigma vertical coordinate. The equations have been nondimensionalized and presented in powers of the Rossby number. An additional transformation removes most of the impacts of unlevel terrain. Furthermore, thermodynamic variables are partitioned into mean and perturbation variables. The variational adjustments are carried out only on the scale of the meteorological perturbations.

The variational analysis melds satellite data with conventional data at the second stage of a two-stage objective analysis. All data are

gridded independently in the first stage and are combined in the second stage. The gridded observations to be modified are meshed with the dynamic constraints through Sasaki's (1970) variational formulation. The finite difference analog of the adjustment functional is

$$\tilde{F} = \Delta x \Delta y \sum_i \sum_j a_i b_j I_{ij} \qquad (1)$$

The integrand $I_{i,j}$ is

$$I = \pi_1 (u-u^o)^2 + \pi_1 (v-v^o)^2 + \pi_2 (\dot{\sigma}-\dot{\sigma}^o)^2 + \pi_3 (\phi-\phi^o)^2$$
$$+ \pi_4 (\bar{T}-\bar{T}^o)^2 + \pi_5 (\phi_x - \phi_x{}^o)^2 + \pi_5 (\phi_y - \phi_y{}^o)^2 + \pi_6 (\phi_\sigma - \phi_\sigma{}^o)^2$$
$$+ \pi_7 (\xi_u - \xi_u{}^o)^2 + \pi_7 (\xi_v - \xi_v{}^o)^2 + 2\lambda_1 M_1 + 2 \lambda_2 M_2 + 2 \lambda_3 M_3$$
$$+ 2 \lambda_4 M_4 \qquad (2)$$

The weights π_i, i=1,7 are Gauss' precision moduli (Whittaker and Robinson, 1926). The gridded observations (u^o, v^o, $\dot{\sigma}^o$, ϕ^o, T^o, ξ_u^o, ξ_v^o) to be adjusted enter in a least squares formulation and receive precision modulus weights according to their relative observation accuracies. The strong constraints to be satisfied exactly are introduced through the Lagrangian multipliers λ_i, i=1,4.

Objectively modified meteorological variables are determined by requiring the first variation on F to vanish. A necessary condition for the existence of a stationary set is that the functions are determined from the domain of admissible functions as solutions of the Euler-Lagrange equations. The variation is to be carried out at every point (r,s) within the grid. Thus, setting the weights $a_i=b_j=1$ and differentiating the integrand (2) with respect to the arbitrary variable (α_{ij}), the Euler-Lagrange operator in finite differences is

$$\frac{\partial I_{i,j}}{\partial \alpha_{r,s}} = I_{\alpha_{i,j}} \frac{\partial \alpha_{i,j}}{\partial \alpha_{r,s}} = I_{\alpha_{i,j}} \delta_r^i \delta_s^j = 0 \qquad (3)$$

The Kronecker delta functions δ_r^i, δ_s^j, equal 1 where r=i or s=j and are zero elsewhere.

Carrying out the operations specified by (3) leaves 11 Euler-Lagrange equations some of which are complicated nonlinear partial differential equations. An iterative method is proposed for the solution so that at the first cycle level, the higher order terms are expressed with observed variables and are expressed by previously adjusted variables at subsequent cycles. At any particular solution cycle, these terms and the terms that are determined by observed variables are specified and can be treated as forcing functions.

Following this approach, the Euler-Lagrange equations transform into a set of eleven simple algebraic or linear partial differential equations. Through reduction of variables, the number of equations is reduced to two diagnostic equations in geopotential and a velocity adjustment potential. These elliptic second order partial differential equations are easily solved by standard methods.

3. SOME RESULTS OF THE ASSIMILATION

Because this assimilation is not an initialization for a numerical prediction model, the often used procedure of determining the best initial analysis by finding the best forecast does not apply. We instead use three diagnostic criteria which, although they may be somewhat more subjective than measures of forecast skill, have found use in the verification of diagnostic analyses (Krishnamurti, 1968; Achtemeier, 1975; Otto-Bliesner et al, 1977). These criteria are measures of a) the extent to which the assimilated fields satisfy the dynamical constraints, b) the extent to which the assimilated fields depart from the observations, and c) the extent to which the assimilated fields are realistic as determined by pattern recognition. The last criterion requires that the signs, magnitudes, and patterns of the hypersensitive vertical velocity and local tendencies of the horizontal velocity components be physically consistent with respect to the larger scale weather systems.

The case study used for the verification of MODEL I was a short wave over the Central Plains on 1200 GMT 10 April 1979. Shown in an objective analysis of the 500 mb heights (Fig. 1), this disturbance was one of a progression of short waves that were embedded within southerly flow between a synoptic scale trough over the Great Basin and a high pressure ridge over the eastern United States. It was not accompanied by severe mesoscale convective systems as were the short waves that followed it through the Central Plains. Light precipitation (shaded patches) at 1235 GMT was mostly from relatively shallow convective elements embedded within middle tropospheric clouds (6 km). This case was selected because TIROS-N temperature soundings coexist with NASA-AVE 3-hr rawinsonde data over a large area of the central United States. The 3-hr rawinsonde data are required to provide verification for the diagnosed 3-hr local tendencies of the horizontal velocity components. Furthermore, this SESAME case data has been the subject of several synoptic and mesoscale diagnostic analyses. These studies provide additional verification fields for MODEL I.

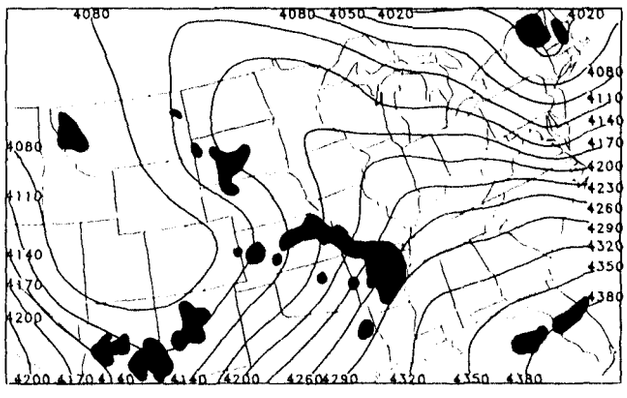

Fig. 1. The 500 mb height field at 1200 GMT, 10 April 1979 showing a weak short wave disturbance over the Central Plains.

The model domain extends from a smoothed surface to 100 mb and over most of the U.S. and parts of southern Canada. Variables are located on a 100 km by 100 km horizontal staggered grid.

The precision moduli for variables that are directly observed are calculated from the RMS values for that variable. Gradients of some observed variables are also included in the assimilation and the RMS errors for the gradient must be calculated from the observed RMS values. Finally, the RMS errors for some variables that are not directly observed must be estimated from the equations that related them to the RMS errors of other observed variables.

Our calculations revealled that the geopotential height is the most accurately observed variable and then the winds and the temperatures. The developmental components of the local velocity tendencies are estimated to be the least accurately determined variables. These values are of course estimates of the actual weights because they are developed from mean observational errors and do not necessarily represent the actual observational error for this case study. Further, the estimated errors for non-observed quantities obtained through approximations do not necessarily strictly obey the assumptions made in their derivations. Therefore, we adjusted the precision moduli so that the heights, winds, and temperatures were approximately equally weighted.

Adjusted variables at two successive cycles were averaged and reintroduced into the dynamic constraints. Residuals were computed as remainders of algebraic sums of individual terms of each constraint. The RMS error (Glahn and Lowry, 1972) for each level was then found. Residuals vanish (constraint satisfaction) when variables at two successive cycles are unchanged. A measure of the convergence of the variational method to constraint satisfaction is the difference between the initial RMS error of the residuals of the unadjusted variables substituted directly into the dynamic equations and the RMS values at each cycle. These differences are divided by the initial RMS errors, converted to percent and expressed in Tables 1 and 2 as percent reduction of the initial RMS error.

Table 1 shows how the reductions of the initial RMS error for the two horizontal momentum equations varies for each pass through the cyclical solution sequence for the eight adjustable levels of the Model. The error is approximately cut in half with each cycle through the fifth cycle. The solution stabilizes near 90-95 percent error reduction and there is no further significant improvement in the assimilation after the fifth cycle. In fact the assimilated fields do not satisfy the constraints quite as well out to the eighth cycle. The percent RMS error reductions behave similarly for the two equations except that the final error reductions for the v-component equation are one to four percent less than for the u-component equation.

The percent RMS error reductions for the integrated continuity and hydrostatic equations are shown in Table 2. The errors for the integrated continuity equation are reduced approximately by 70 percent by the fourth cycle and remain relatively unchanged through the eighth cycle at levels 2 and 3. The solution for the six upper levels improves to approximately 90 percent by the eighth cycle. These improvements are, of course, dependent upon the magnitudes of the initial RMS errors. We first calculated the vertical velocity by the O'Brien (1970) method and then determined the RMS errors for the integrated continuity equation. Had we assumed that the initial vertical velocity was zero, the initial RMS errors would have been much larger than the values used in Table 2 and the error reductions would have been 100 percent by the fourth cycle.

The RMS errors for the hydrostatic equation are halved at each cycle and the percent error reduction increases monotonically to near 100 percent by the eighth cycle.

Table 1

Percent NOSAT RMS error reduction with respect to initial RMS residuals for the u- and v-horizontal momentum equations.

CYCLE	LEVEL 2	3	4	5	6	7	8	9
				u-component				
0	0	0	0	0	0	0	0	0
1	52	52	52	50	50	49	50	49
2	78	77	76	73	73	73	75	75
3	90	88	87	84	85	84	86	86
4	95	93	91	90	90	90	91	90
5	96	95	93	92	93	93	92	91
6	95	95	93	93	94	94	93	91
7	94	94	93	93	94	94	92	91
8	92	94	92	92	93	93	92	90
				v-component				
0	0	0	0	0	0	0	0	0
1	52	52	51	52	50	50	50	49
2	75	78	76	78	76	75	75	73
3	84	87	86	89	87	86	86	83
4	88	90	89	91	90	90	90	86
5	92	92	90	91	90	91	90	87
6	94	93	90	91	90	91	90	87
7	94	93	90	90	90	90	90	87
8	90	93	90	90	90	90	89	86

Table 2

Percent NOSAT RMS error reduction with respect to initial RMS residuals for the integrated continuity and hydrostatic equations.

CYCLE	LEVEL 2	3	4	5	6	7	8	9
				Integrated Continuity				
0	0	0	0	0	0	0	0	0
1	50	50	50	50	50	50	50	50
2	65	60	39	51	57	57	63	72
3	70	65	43	56	62	60	67	78
4	70	68	55	65	71	69	75	82
5	70	69	66	74	79	78	82	84
6	71	70	75	81	85	85	86	87
7	70	69	82	87	90	90	90	89
8	70	68	87	90	92	93	92	91
				Hydrostatic				
0	0	0	0	0	0	0	0	0
1	50	50	50	50	50	50	50	50
2	75	75	75	75	75	75	75	75
3	87	88	88	87	87	87	87	87
4	93	94	94	94	94	94	94	94
5	96	96	97	97	97	97	97	97
6	98	98	98	98	98	98	98	98
7	98	98	99	99	99	99	99	99
8	98	98	100	100	100	100	100	100

The variational assimilation produced significant adjustments in height, temperature, and wind velocity in order that the values of these variables are solutions of the dynamic constraints. However, these modifications can cause large and physically unrealistic changes in other important variables such as vorticity, divergence, and vertical velocity and other quantities that involve derivatives of the basic variables. In addition, the local tendencies of the horizontal velocity components are sensitive to small errors in the basic variables when they are determined from the arithmetic sum of the other terms of the horizontal momentum equations. The patterns of these hypersensitive variables must be physically realistic when compared with other data sets such as cloud fields, precipitation, and independent measurements of the variable itself. Thus, the hypersensitive variables provide a critical test of the accuracy of the MODEL I dynamic assimilation.

Figure 2 shows the vertical velocities in cm sec^{-1} at level 6 (500 mb) for 1200 GMT 10 April 1979 as developed from the kinematic method of O'Brien (1970) applied to the objective analyses of the initial observations and from the more general kinematic method that is part of MODEL I. The O'Brien kinematic method, which uses gridded wind data only, produced a general area of rising motion over the Rocky Mountain States and the plains west of the Mississippi River within the area of southwesterly flow in advance of the upper tropospheric trough and behind the preceding upper level ridge (Fig. 2a). General subsidence is over the Eastern States in advance of the ridge. Upon closer inspection, it is seen that the field of rising motion breaks down into several large vertical velocity centers (magnitudes greater than 10 cm/sec) which are located between rawinsonde sites. These strong ascent centers are separated by areas of weak vertical motion of either sign. This type of pattern (vertical velocity centers located between data collection sites) is typical of the kinematic technique when applied to univariate objective analyses of the components of the horizontal wind field. Our wind data was gridded with a successive corrections method that is an adaptation of the method developed by Barnes (1964).

The relationship between this vertical velocity field and the precipitation areas as observed by radar (shaded areas) within the region of interest for this study, namely, the weak short wave trough over Kansas and Missouri, is not quite fortuitous. Precipitation is not located within the 10 cm sec^{-1} vertical velocity center located over southeastern Colorado nor within the 4 cm sec^{-1} center over northern Missouri. However, precipitation is located along the axis of upward motion that connects these two centers. The precipitation area in Missouri turns southward into Arkansas, a region of weak vertical velocity of both signs. It is also typical with the kinematic method to find areas of precipitation overlapping into regions with downward vertical motion. Several isolated showers are found within an area identified by the GOES visible imagery as containing fields of swelling cumulus, the area located over Oklahoma and northeast Texas. The kinematic analysis positions a center of downward motion over this area.

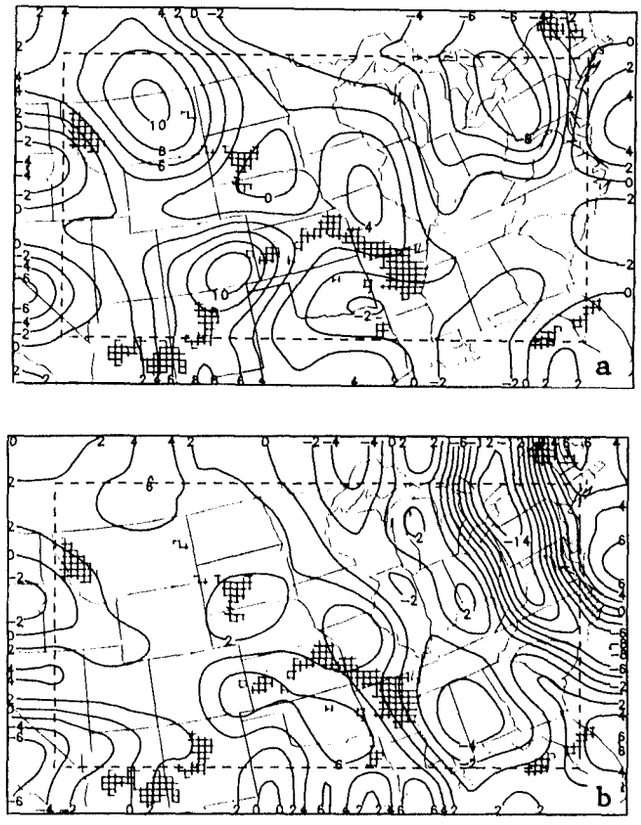

Fig. 2. Vertical velocities (cm s^{-1}) on level 6 (500 mb) at 1200 GMT, 10 April 1979 from a) the kinematic method (O'Brien, 1970) applied to the objective analyses of the initial wind field and b) from the MODEL I adjusted wind field. Hatching delineates areas of precipitation.

The vertical motion field developed by the SAT variational analysis (Fig. 2b) is representative of both SAT and NOSAT analyses. This pattern is similar to the kinematic analysis on the large scale in that the ascent areas are positioned from the Mississippi River westward into the Rocky Mountain States. However the smaller scale patterns are different. Gone are the large centers of upward vertical motion. The 10 cm sec^{-1} positive motion center over Montana in the kinematic analysis is not found in the variational analysis. This reduction was brought about by the decrease of convergence in the lower troposphere as the horizontal wind field was made to more closely balance the height field. The 10 cm sec^{-1} ascent center over southeastern Colorado has been reduced and shifted into western Kansas in alignment with precipitation observed there. The variational analysis also places a 6 cm sec^{-1} center of upward motion over Oklahoma and northeastern Texas as part of a zone of positive vertical velocity that extends from western Kansas through eastern Oklahoma and into Louisiana. This pattern compares favorably with the convective showers over Oklahoma and Texas but is located behind the position of the short wave trough (Fig. 1). It is oriented along the main precipitation band but is generally located to far to the southwest of it. We note that the

observations were taken approximately one hour before the precipitation patterns and that, given the rapid northeastward movement of the short wave trough, could account for about 50 km of the displacement between the two patterns.

The solution sequence of the variational assimilation requires that the developmental components of the local tendencies of u and v be found from the arithmetic sum of the other terms of the horizontal momentum equations. The developmental components are recombined with the advective components, redimensionalized, and expressed as 3-hr changes. These tendencies are compared with the observed 3-hr tendencies of u and v calculated from the high frequency rawinsonde data collected over the central part of the U. S. as part of the NASA-AVE SESAME project and with the 3-hr tendencies calculated with values from the initial gridded fields substituted in place of the adjusted fields in the horizontal momentum equations. In making these comparisons, we assume that the observed 3-hr tendencies represent "ground truth" subject to the following qualifications. First, in keeping with the synoptic scale of the analysis, we have gridded only 3-hr tendencies taken from data collected at standard NWS observing sites. Second, the ground truth tendencies are calculated over the 3-hr interval from 1200-1500 GMT and are therefore centered at 1330 GMT. The tendencies found from MODEL I are centered at 1200 GMT. Therefore, some phase shift should be observed between the patterns. Third, to the extent that the tendencies calculated from the SESAME data suffer from mesoscale "noise", the patterns will not accurately represent the true pattern of synoptic scale tendencies.

Strongest jet stream winds were located at level 8 (300 mb). Large magnitudes and gradients of the velocity can combine to create large tendencies if the terms of the horizontal momentum equations do not compensate. The 3-h tendency field obtained from the initial data (Fig. 3a) is a pattern of large magnitude centers of alternating sign spaced at approximately the average observation separation. These centers imply unrealistically large changes in v over three hours. With allowances for horizontal displacement of the pattern over 1.5 h, the only correspondence with the observed 3-h tendency field is the sign of the pattern along the eastern part of the domain. The SAT analysis (Fig. 3c) reproduces most of the features of the observed 3-h tendencies. The positive tendency center near the lower boundary of the grid (Texas-New Mexico border) in the SAT analysis appears over the Texas panhandle at 1330 GMT in the observed tendencies (Fig. 3b). Furthermore, the relative minimum over Oklahoma is moved into southeastern Kansas. These displacements are in accord with the rapid northeastward movement of the weather systems through the area. Relative horizontal displacements were smaller within the weaker flow near the long wave ridge over the eastern part of the domain. Here the SAT analysis preserved the area of larger positive v-tendencies but located the maximum over Illinois rather than over Mississippi as found in the observed tendencies.

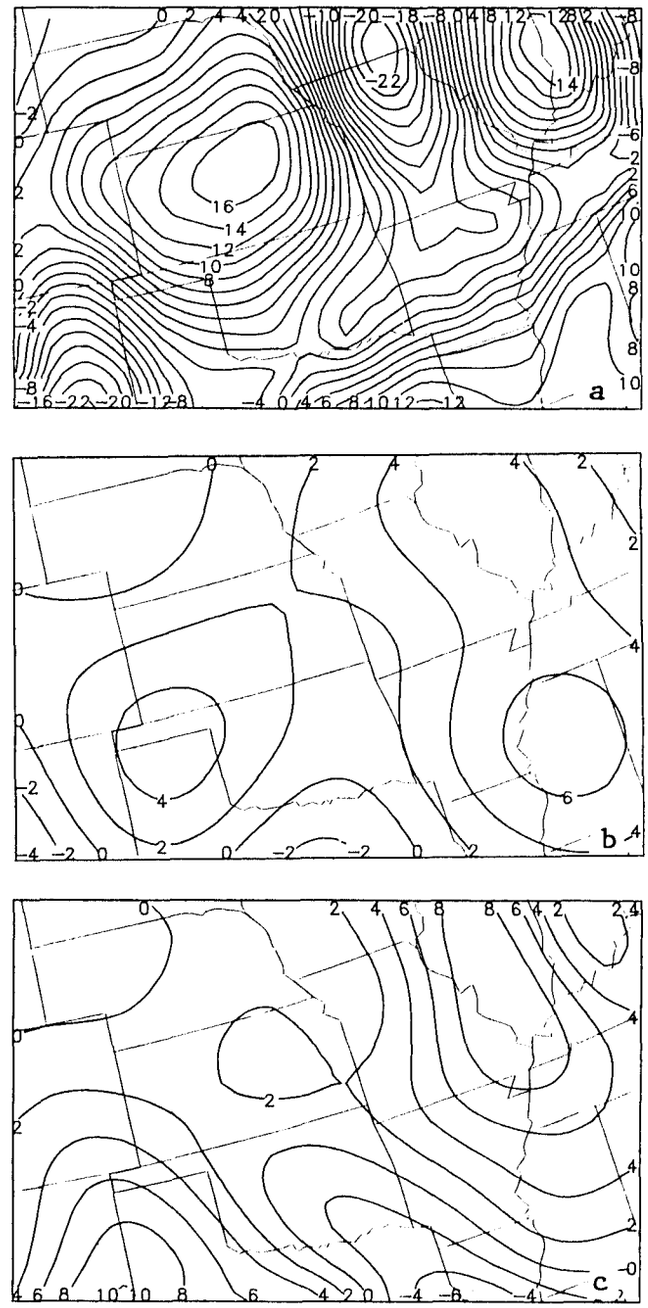

Fig. 3. Fields of a) initial, b) observed, and c) SAT v-tendencies for level 8 (300 mb) for the central region of the U. S. roughly covered by the SESAME-AVE rawinsonde network. Units are in m s^{-1} $3h^{-1}$.

4. DISCUSSION

Now, does this variational assimilation method produce better hybrid data fields than other methods? Since no intercomparison studies have been performed, we cannot offer definitive answers to the question. However, we believe that the variational model should provide quality analyses if the following two criteria are satisfied. First, the variational assimilation method we have developed is a physical model.

Four of the basic primitive equations that govern flow in free atmosphere subject to the assumptions that apply to hydrostatic and synoptic conditions have been used in the model derivation. Since the real atmosphere obeys these equations, it is expected that the three dimensional fields of meteorological variables should be reasonable approximations to the true atmosphere if they are solutions of the dynamic equations. Furthermore, advanced versions of this model that include the energy equation as a fifth constraint should provide analyses that are superior to the results presented here.

Second, the dynamical equations permit many solutions. Therefore, the error characteristics of the observations and the horizontal distributions of the G-function that make up the precision moduli should be known with accuracy. The sensitivity of the variational model to the values given to these weights is currently not fully known and is the subject of investigation in the ongoing model development.

Finally, we note from the results of the pattern recognition that the variational analysis produced physically reasonable fields of the hypersensitive variables. Model I produced the first relatively accurate diagnostic fields of local tendencies of the velocity components apart from initialization schemes for numerical prediction models. Our continued model developments should improve upon these results.

ACKNOWLEDGEMENTS

This research was supported by the National Aeronautics and Space Administration (NASA) under contract NAS8-34902.

REFERENCES

Achtemeier, G. L., 1975: On the Initialization problem: A variational adjustment method. Mon. Wea. Rev., 103, 1090-1103.

Baer, F., and J. Tribbia, 1977: On complete filtering of gravity modes through nonlinear initialization. Mon. Wea. Rev., 105, 1536-1539.

Barnes, S. L., 1964: A technique for maximizing details in numerical weather map analysis. J. Appl. Meteor. 3, 396-409.

Bengtsson, L., M. Kanamitsu, P. Kallberg and S. Uppala, 1982: FGGE 4-dimensional data assimilation at ECMWF. Bull. Amer. Meteor. Soc., 63, 29-43.

Cressman, G. P., 1959: An operational objective analysis system. Mon. Wea. Rev., 87, 367-374.

Gandin, L. S., 1963: Objective analysis of meteorological fields. Isdat., Leningrad. [Israel Program for Scientific Translations, Jerusalem, 1965, 242 pp.]

Ghil, M., M. Halem and R. Atlas, 1979: Time-continuous assimilation of remote-sounding data and its effect on weather forecasting. Mon. Wea. Rev., 107, 140-171.

Glahn, H. R., and D. A. Lowry, 1972: The use of model output statistics (MOS) in objective weather forecasting. J. Appl. Meteor., 11., 1203-1211.

Krishnamurti, T. N., 1968: A diagnostic balance model for studies of weather systems of low and high latitudes. Rossby number less than one. Mon. Wea. Rev., 96, 197-207.

Machenhaur, B., 1977: On the dynamics of gravity oscillations in a shallow water model, with applications to normal mode initialization. Beitr. Phys. Atmos., 50, 253-271.

McPherson, R. D., K. H. Bergman, R. E. Kistler, G. E. Rasch, and D. S. Gorden, 1979: The NMC operational global data assimilation system. Mon. Wea. Rev., 107, 1445-1461.

Miyakoda, K., and R. M. Moyer, 1968: A method of inialization for dynamical weather forecasting. Tellus, 20, 115-130.

Nitta, T., and J. B. Hovermale, 1969: A technique of objective analysis and initialization for the primitive forecast equations. Mon. Wea. Rev., 97, 652-658.

O'Brien, J.J., 1970: Alternative solutions to the classical vertical velocity problem. J. Appl. Meteor., 9, 197-203.

Otto-Bliesner, B., D. P. Baumhefner, T. W. Schlatter, and R. Bleck, 1977: A comparison of several data analysis schemes over a data-rich region. Mon. Wea. Rev., 105, 1083-1091.

Sasaki, Y., 1958: An objective analysis based upon the variational method. J. Meteor. Soc. Japan, 36, 77-88.

_____, 1970: Some basic formalisms in numerical variational analysis. Mon. Wea. Rev., 98, 875-883.

Schlatter, T. W., 1975: Some experiments with a multivariate statistical objective analysis scheme. Mon. Wea. Rev., 103, 246-257.

Temperton, C., 1984: Variational normal mode initialization for a multilevel model. Mon. Wea. Rev., 112, 2303-2316.

Whittaker, E., and G. Robinson, 1926: The Calculus of Observations (2nd Edition). London, Blackie and Son, LTD., p176.

APPLICATIONS OF A RECURSIVE FILTER, OBJECTIVE ANALYSIS IN THE PROCESSING AND PRESENTATION OF VAS DATA

Christopher M. Hayden

NOAA/NESDIS Systems Design and Applications Branch
Madison, Wisconsin

James C. Purser

Cooperative Institute for Meteorological Satellite Studies
Madison, Wisconsin

1. INTRODUCTION

An objective analysis system for interpolating randomly spaced observations to a regular grid is a key ingredient in the processing of temperature and moisture retrievals from satellite measured radiances. For example, surface data (temperature and moisture) have been shown (Lee et al., 1983) to be crucial to the accuracy of lower atmospheric profiles obtained from satellites. To include these data in the retrieval processing it is convenient to represent them as a regular gridded array. Similarly, for amalgamating the measurements of different instruments (e.g. the infrared and microwave instruments of the NOAA polar orbiting satellites) it is convenient to represent one set as a gridded array. In another phase of the processing, objective analysis becomes important for objective quality control which ultimately involves the comparison of individual datum with an estimate derived from a field of values. Finally, objective analysis is required for the presentation of contoured fields of meteorological parameters. In the utilization of VAS data, grids are prepared for image overlays to aid the forecaster using an image graphics device. In this application, cosmetics are at least as important as "fit" to the input observations, and this changes the requirements placed on the objective analysis system.

The object of this paper is to present the properties of a recursive filter (RF) analysis system which has been developed on the University of Wisconsin McIDAS system for processing and display of VAS data. The system has two features which make it particularly appropriate for these tasks. First, it is practical because it is simple and fast. Second, it is highly tunable. The latter might seem on first blush to be a disadvantage, and all would agree that it is desirable to have a fixed system which works well under any situation. However, experience suggests that such a paragon exists only in the city of Oz. Given a finite number of tasks, presumably on a repeating basis (e.g. the daily editing of a certain parameter over a certain area), it is not too burdensome to have an equivalent number of sets of tuning parameters for the analysis system. It is the business of the researcher to define these.

In the next section, the RF technique is described. This is followed by a section where synthetic fields of known amplitude and period are sampled and recomposed by the RF using several variations of the tuning factors and varied data configurations. Although by no means exhaustive, this section reveals some of the personality of the system. A fourth section deals briefly with applications of the RF in VAS retrieval processing, giving examples of surface fields and the editing capability achieved with the RF.

2. THE RECURSIVE FILTER ANALYSIS SYSTEM

The RF analysis system is adapted from a version developed at the British Meteorological Office (Purser and McQuigg, 1982). We shall first discuss the basic properties of the recursive filter and then describe how it is incorporated into a complete analysis model.

The fundamental algorithm is disarmingly simple (and therefore very fast on the computer). For any row or column of the grid, a new estimate B at gridpoint n is obtained from a previous estimate A and the new estimate at the preceding gridpoint according to the relationship:

$$B_n = \alpha B_{n-1} + (1-\alpha) A_n \qquad n>1 \tag{1}$$

The smoothing parameter α controls the spatial scale of the filter. The recursion of (1) can be expanded to give

$$B_n = (1=\alpha)(A_n + \alpha A_{n-1} + \ldots + \alpha^m A_{n-m}) \tag{2}$$

which may be symbolically represented as

$$B = E*A \qquad E = (1-\alpha)\ \alpha^n \tag{3}$$

E is the convolution kernel which acts on the field of prior estimates A. A continuous analogue to (3) gives

$$E(x) = \frac{1}{x} e^{-x/\lambda} \qquad \lambda^2 \cong \alpha/(1-\alpha)^2 \tag{4}$$

where λ is a characteristic scale related to the smoothing parameter. Thus, the filter is

exponential with a shape dependent on the smoothing parameter α.

In practice, (1) is applied repeatedly across a row or column in alternating directions to ensure symmetry. This affects the smoothing properties inasmuch as the aggregate attains equivalence to convolving the field with a Gaussian filter whose standard deviation is given by

$$\sigma = \sqrt{2L}\,\lambda \tag{5}$$

where L is the number of iterations of the symmetric pair and the units are grid intervals. For details, see Purser and McQuigg (1982). It is interesting to note that in this sense the RF is revealed to be closely analogous to the Barnes (1963) system which employs a Gaussian filter directly.

It is advantageous to introduce the analysis gridlength δ explicitly by expressing λ in terms of a characteristic wavelength R. Let

$$\sigma^2 = (R/\delta)^2 = 2L\lambda^2 \tag{6}$$

and from (4)

$$\lambda^2 = (R/\delta)^2/2L = \alpha/(1-\alpha)^2 \tag{7}$$

Thus, the smoothing parameter is defined by the gridlength and a characteristic wavelength and the number of iterations which are the option of the analyst.

The formalism developed so far implicitly assumes convolutions extending over an unlimited number of point on each line. In reality, boundaries intervene. However, by selecting suitable starting conditions for each application of the elementary filter (1), it is possible to simulate the effect of an infinite continuation of the grid, thereby reducing spurious boundary effects in the analysis. The starting conditions for filter E depend on the number of preceding applications of the opposing filter, which we call W. If there has been no previous application, then the starting condition is simply:

$$(E*A)_1 = B_1 = (1-\alpha)\,A_1 \tag{8}$$

When W has been applied once, the starting condition should acknowledge the presence of an exponential "tail" for the continuation of both A and B beyond the boundary. Or:

$$B_{n-1} = \alpha B_n \qquad i \leq 1 \tag{9}$$

From (9) and (1) at n=1:

$$\begin{aligned} B_o &= \alpha B_1 \\ B_1 &= \alpha B_o + (1-\alpha)A_1 \end{aligned} \tag{10}$$

and eliminating B_o gives the appropriate starting condition:

$$B_1 = \frac{(1-\alpha)}{(1-\alpha^2)}\,A_1 \tag{11}$$

Corresponding starting conditions can be obtained in the case of N1 previous applications of the opposing filter W to yield formulas for B_1 involving $A_1,\ldots A_n$.

The preceding describes how we may specify a filtering procedure to control the scales represented in the gridded analysis. But before we may proceed to this stage, it is necessary to assign values to the gridpoints from random observations, in order to form the field A. In the RF, two fields are defined. The first is the "observation residual" representing the difference between the observations and a previous estimate. For each observation, the residual is calculated at the location of the observation. This value, weighted by a quality estimate for that observation, is spread to the four surrounding gridpoints using bilinear weighting. The second grid is the "weights", or observation quality, distributed in the same manner. The recursive filter, described by (1) is used to smooth both grids. It is passed repeatedly over both rows and columns for NI iterations. The updated analysis is formed by adding the smoothed "observational residuals", divided by the smoothed weights, to the previous estimate.

As mentioned at the beginning of this section, the complete RF is a successive approximation method. This is accomplished by making several (NA) of the passes described in the previous paragraph, successively introducing finer scale by successively decreasing the characteristic wavelength R. A large wavelength (RO) is defined on the initial pass and reduced exponentially to RL for the final pass. An additional "filter factor" (RF) is included to arbitrarily modify the width of the Gaussian filter on all passes as a control over the closeness of fit to the observations. Note that the characteristic wavelength, according to (7), defines a smoothing α for the entire grid. In the RF analysis, however, after the initial pass, the α is modified to vary spatially according to the "weight" grid of the previous pass. This has the desirable feature that finer scale is introduced only where observation density and quality are appropriate.

It is conventional in meteorological analysis systems to use an initial guess derived from a previous analysis or forecast. In the RF framework, this could be done by using the guess as the initial estimate for determining "observation residuals" on the first pass. However, to increase the flexibility of the system, we have chosen a different option. Values selected from the first guess are treated as pseudo observations. These are selected at a uniform, but optional density (GINC). Yet another analysis parameter (WGS) assigns a quality to these pseudo observations which is processed exactly as the quality indicator for observations (currently fixed at 1.), except for the final pass when it is set to zero.

3. APPLICATIONS TO SYNTHETIC FIELDS

A synthetic field of 500 mb temperature was constructed over the eastern U.S. and Atlantic. It represents the sum of three fields derived using the equation:

$$T(i,j) = \bar{T} + S(j) - A\,\mathrm{SIN}\,(2\pi Ni/L_x + Dy) \tag{12}$$

where i and j are the east-west, north-south grid directions, $\overline{T}$ is a mean temperature (250K), D is a north-south tilt factor ($\pi/2Ly$) and L_x, L_y are the number of gridpoints in the i and j directions, respectively. The other parameters and their values for the three fields are

S: north-south slope (4,2,1)
A: amplitude (8,2,1)
N: wave number (1,3,5)

The procedure reported in this section was to sample this grid; reconstruct the field using RF; and fourier analyze the result. This permits us to empirically examine the filter properties.

A first set of experiments considers data density. For these, pseudo data were taken with a uniform distribution, though variable density, over the complete grid of 51*101 gridpoints covering the area shown in Fig. 1. These data were analyzed with the RF using no first guess and a fixed set of filter parameters (RF=1., R0=500, RL=10). Table 1 presents the amplitudes of the first six wave numbers across the middle and top rows of the grid for the original field and analyses using seven different data densities. The table shows that the analysis performs as expected. Consider first the middle row which is least plagued by boundary problems. The largest scale (wave number 1) is retained reasonably faithfully down to a density of 162 observations. Below this it begins to degrade rapidly. Wave number 2 is held only to a density of 280 observations and wave number 5 to 650 observations. As the signal is smoothed, it is increasingly aliased into the adjacent wave numbers, but only until the immediately larger wavenumber is "lost" (i.e. at a density of 42 for wave number 2 and 72 for wave number 4). The latter fact attests that the RF does not introduce scale below that available from the observations.

The numbers shown for the top row demonstrate that the boundaries behave somewhat differently from the interior. Wave number 1 is not smoothed. Wave numbers 3 and 5 are more slowly smoothed. The aliasing to other wave numbers is similar, but more rapid and to a higher level.

Results obtained by varying the smoothing parameters RF or RL on the synthetic data sets are shown in Table 2. Only the interior row is shown; relative differences at the boundary of the grid are comparable to those shown in Table 1. For these experiments, a data density of 162 observations was selected. It is apparent from the table that the two parameters effect much the same changes. With either, the smoothing increases as the parameter is increased, and the aliasing is well controlled. Note that nearly identical results are obtained for (RF=1.0, RL=40) and (RF=1.5, RL=20). However, they are not redundant in that the aliasing into low wave numbers is controlled when RL is varied. Also, two degrees of freedom are very useful. For example, it appears (as will be shown later) that the boundaries are somewhat better behaved with a low value of RF. But the low value may introduce spurious detail in the interior, particularly with noisy data. A compensating value of RL can be used to avoid the detail.

Table 1

Fourier analysis of middle and top rows of grids analyzed with varying uniform density N. WN1 through WN6 are ampitudes of wave numbers 1-6. Input signal at WN1, WN3, and WN5 as show by ORIG.

N	WN1	WN2	WN3	WN4	WN5	WN6
ORIG	8.00	.00	1.99	.00	.99	.00
650	8.00	.00	1.99	.01	.98	.01
280	7.99	.01	1.98	.01	.92	.01
162	7.93	.08	1.89	.07	.74	.02
110	7.86	.19	1.70	.14	.50	.03
72	7.61	.44	1.39	.21	.31	.02
56	7.38	.56	1.11	.16	.21	.07
42	6.93	.70	.77	.11	.13	.05
33	6.61	.68	.57	.13	.14	.11
ORIG	8.00	.00	1.99	.00	.99	.00
650	8.05	.09	2.02	.09	.99	.09
280	8.09	.19	2.03	.18	.96	.22
162	8.14	.33	2.03	.31	.88	.35
110	8.21	.47	1.98	.45	.75	.44
72	8.26	.44	1.82	.63	.78	.55
56	8.34	.37	1.67	.62	.69	.51
42	8.19	.70	1.49	.80	.71	.57
33	8.32	.99	1.37	.86	.69	.58

Table 2

Fourier analysis of middle row analyzed with variable tuning factors. Default values are RL = 10, RF = 1.0, N = 162.

RF	WN1	WN2	WN3	WN4	WN5	WN6
0.3	7.96	.04	1.94	.04	.89	.04
0.5	7.96	.04	1.95	.04	.89	.04
1.0	7.93	.08	1.89	.07	.74	.02
1.5	7.73	.33	1.48	.14	.35	.03
2.0	7.12	.55	.88	.04	.16	.05
RL						
5	7.93	.07	1.89	.07	.75	.02
10	7.93	.08	1.89	.07	.74	.02
20	7.93	.08	1.86	.06	.69	.02
30	7.93	.09	1.73	.01	.50	.06
40	7.82	.09	1.39	.10	.32	.10

A final experiment with the synthetic data is presented to demonstrate that the RF is (within reason) insensitive to the grid mesh. Figure 1 shows the 162 observation analysis at 101x51 and its difference from an anlaysis at a resolution of 51x26. The only difference is in a very high frequency harmonic of nearly zero amplitude over the ridge line.

The preceeding discussion has dealt with uniform data distributions. These are generally not the case in meteorology, owing to the expense of ocean-launched radiosondes and cloud interference with remote satellite soundings. It has also not treated the question of using an initial guess, nor the difficulty of

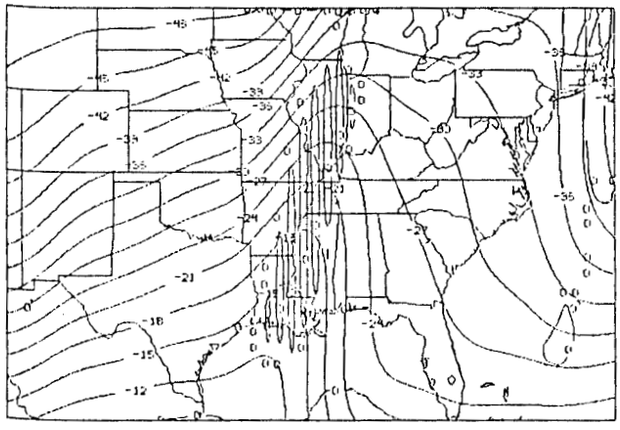

Fig. 1. Analysis performed over 101x51 grid and its difference from one at 51x26.

accounting for variable observation errors. All of these can be investigated as easily as the question of data density. However, space limitations for this article and the reader's patience permit our offering here only an hors d'oeuvre.

From the analytical field, observations were extracted at the locations of the standard radiosondes. The analysis obtained from these with RF=0.5 (which we now expect to be better than default for this case) and no initial guess is shown as Fig. 2a. The error associated with this analysis is given as Fig. 2b. Part of the error is due to the radiosonde density (approximately equivalent to the 52 observation synthetic experiment discussed previously), but the much larger part is due to data voids in areas of high gradient. It is here that judicious application of a first guess field should provide relief. As one example, let us assume that analysis produced by the uniform distribution of 52 observations is available to serve as a first guess. The error associated with that field is given in Fig. 3a and the error of the analysis using that guess is shown in Fig. 3b. The final analysis now has the attributes of the first guess in the data void areas, and, although it is barely discernible in the figures, is slightly improved over the guess where there are radiosondes. In short, the RF appears to incorporate the guess an appropriate manner.

To this point we have considered only the "perfect" observation. We can now look at the effect of introducing realistic error. For this purpose, we have derived a pseudo satellite retrieval distribution, leaving gaps in the coverage where we would expect them for an atmosphere with the characteristics of the simulated field. Data values were picked from the perfect field, adding random error generated from a Gaussian distribution with a standard deviation of 1.8K (the approximate error of satellite retrievals at 500 mb). In addition, bias errors of +1 or -1 were added over broad areas, positive ahead of the ridge and negative behind. From these data, analyses were made (without a first guess) varying the filtering parameters RF and RL. Figure 4 presents the analysis error for RL=10 and RF=1.5 (top) and 1.0 (bottom). Two conclusions can be drawn from the figure.

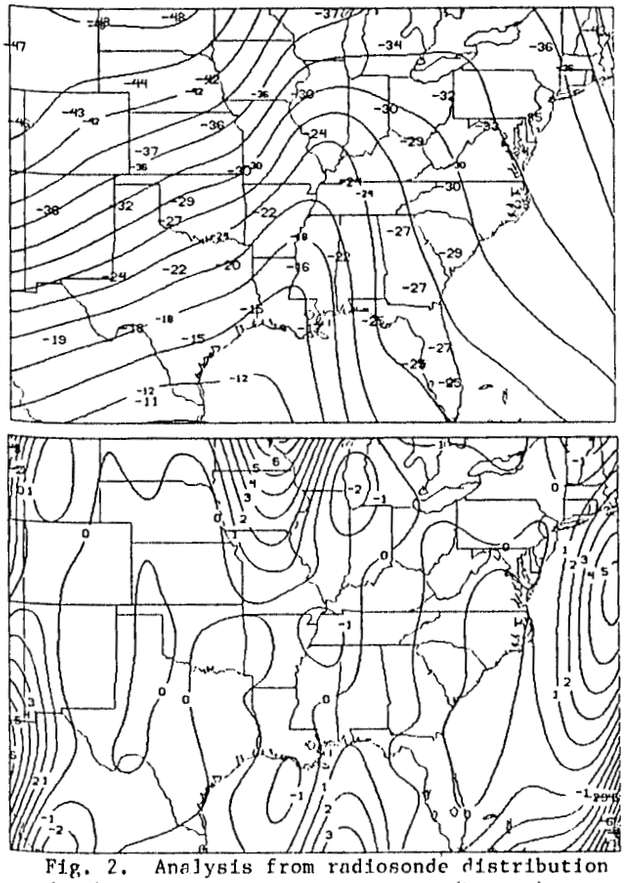

Fig. 2. Analysis from radiosonde distribution (top); no guess. Analysis error (bottom).

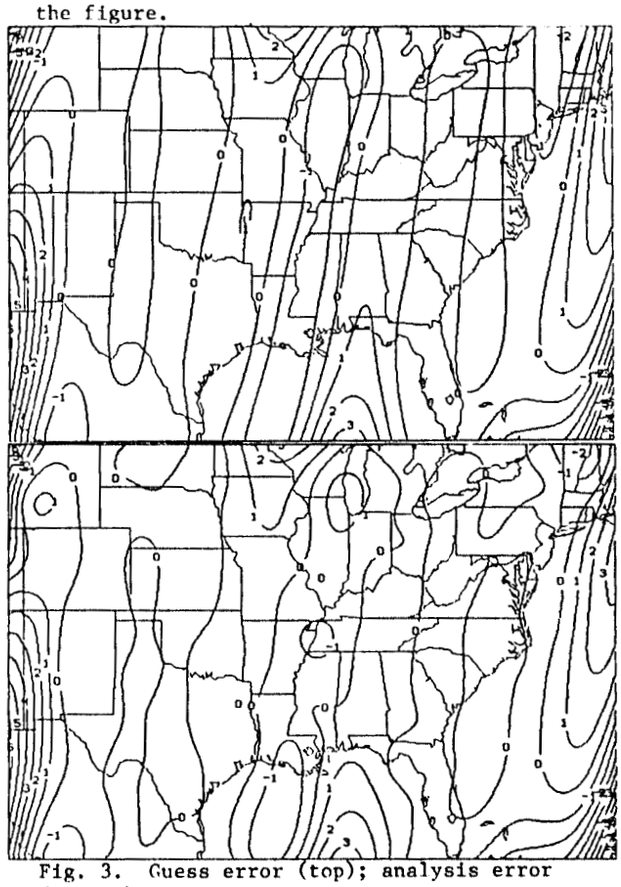

Fig. 3. Guess error (top); analysis error (bottom).

First, RF=1.0 draws too closely to the data. RF=1.5 appears to be approximately correct since, apart from the boundaries, only the large scale bias error remains. In fact, the data fit for this analysis was 1.7K, very close to the input error, whereas the data fit for the RF=1.0 analysis was 1.2K. This shows empirically what is intuitively obvious, that the filtering parameters should be selected to fit no closer than the observation error. The second conclusion to be drawn from Fig. 4 is that the boundaries are better behaved when RF is small. We are not sure why this is the case, but we can take advantage of it by tightening the RF and controlling the scale with RL. An example of this is shown in Fig. 5 which shows the analysis and data fit obtained with RF=0.5 and RL=30. This is a very good analysis, indeed, with an error deviation of 0.8K (less than half the observation error) when compared to the perfect field (excluding the boundaries). One should be advised, however, that as usual, simulation is painting too rosy a picture since a Gaussian error analyzed with what is essentially a Gaussian filter is somewhat of a scam.

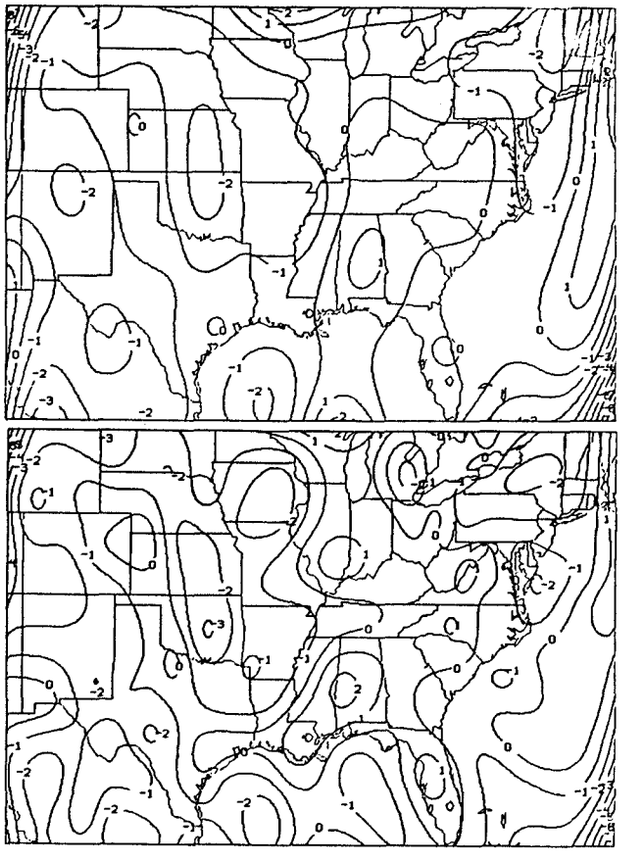

Fig. 4. Analysis error from satellite distribution (with random error). Top: RF=1.5. Bottom: RF=1.0.

4. APPLICATIONS TO REAL FIELDS

The recursive filter analysis is used in three ways in processing VAS data. It is used to provide estimates of surface temperature and dewpoint which are used to modify the lower levels of the guess temperature and moisture profiles. It is used to objectively edit VAS retrievals which are processed over the Eastern Pacific for the National Meteorological Center (NMC). It is used to provide gridded fields of geopotential for the estimate of gradient winds to accompany the temperature moisture retrievals. Here we shall give examples of the first two, but leave the last for a more complete treatment elsewhere.

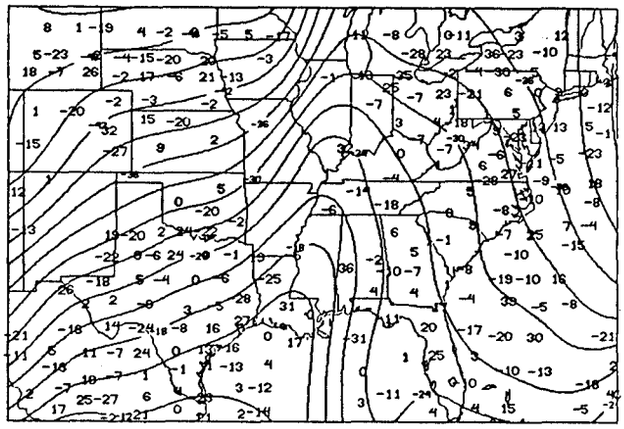

Fig. 5. Same as Fig. 4, but RF=0.5, RL=30. Data fit is also shown.

Figure 6 is an example of what can happen when the quality of the surface grids is not carefully controlled. The figure shows temperature moisture profiles over the Atlantic at the same location, processed three hours apart in support of the Genesis of Atlantic Lows Experiment (GALE). Each Skew-T shows first guess and final profiles, and in both cases the radiance data has had little impact on the guess. More importantly, the soundings indicate a stabilization of the atmosphere over the three hour period with the Lifted Index increasing from -12 to -2. This nonsense was perpetrated by the surface analyses at the earlier time period which were erroneously warm and moist due to poor extrapolation by the RF into a data void area. No guess field for the RF was being used at the time. The moral is that the RF should not have been used so carelessly. It is well to remember that stability indices are one of the prime requirements given by NMC for the operational geostationary sounders on GOES-NEXT.

Figure 7 shows the VAS retrieval locations for a typical GALE case. Solid blocks in the figure indicate that the retrieval was edited. The top of the figure is from a manual editing using an experienced operator; the bottom is from an automatic editor using the RF. In the automatic editor, a parameter is analyzed using data and first guess. The data are screened against the analysis, and rejected if they deviate by a pre-determined amount. The most noteworthy difference resulting from the editing procedures is that the operator has excised large blocks of retrievals (note especially the Maryland, Pennsylvania, New York, Ohio corridor, and the area south of Labrador). In doing this, he must suspect systematic error (i.e., cloud contamination) which cannot be detected by the RF procedure. Figure 8 portrays the difference between 500 mb geopotential analyses derived from the unedited and manually edited retrievals. The large

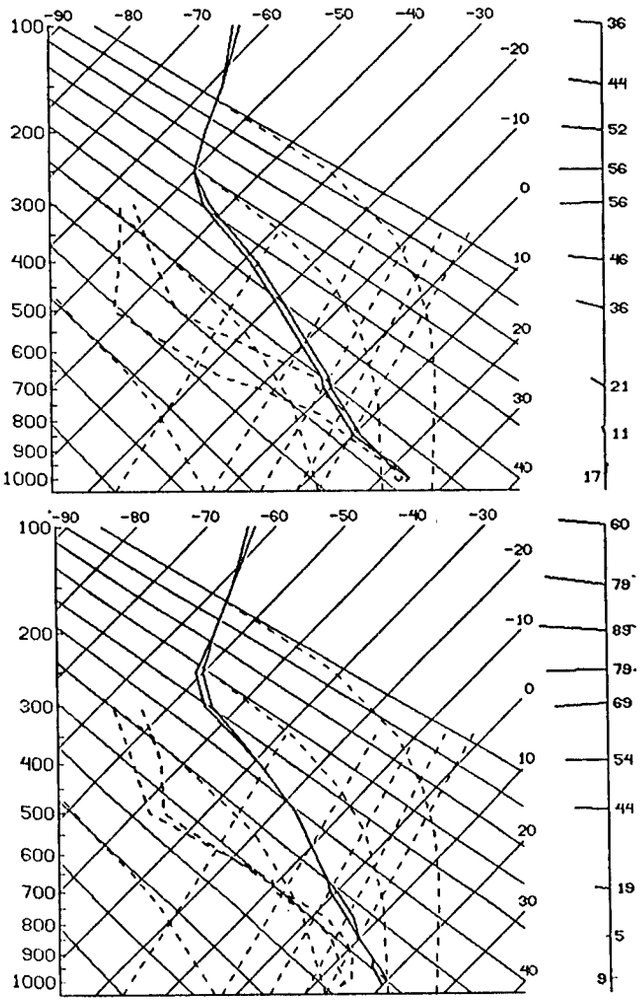

Fig. 6. VAS retrievals over GALE; three hours apart.

centers previously referred to are not present in the comparable comparison with the automatic editor. This case is typical, and we must therefore conclude that the RF cannot provide the auto-editing capability which operations so much desires; at least not until the retrieval algorithm can detect and avoid causes of systematic error.

5. SUMMARY

We have described an analysis system which we have found to be extremely useful in a man-computer interactive environment. It contains most of the features which are generically desirable, is computationally efficient, and is very flexible with tuning parameters whose effects are easily understood. Several examples with synthetic data have been included to elucidate these features. In applications with real VAS data we have given, perversely, two examples where the RF system fails, or is at best wanting. These, of course, are the interesting and informative cases. In the vast majority of applications the RF works very well.

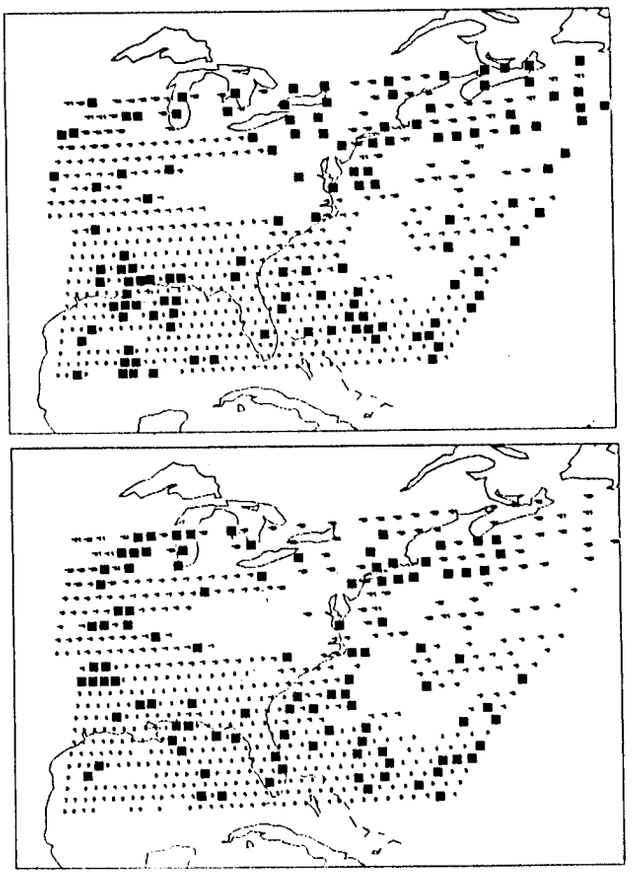

Fig. 7. Manually (top) and objectively (bottom) edited VAS.

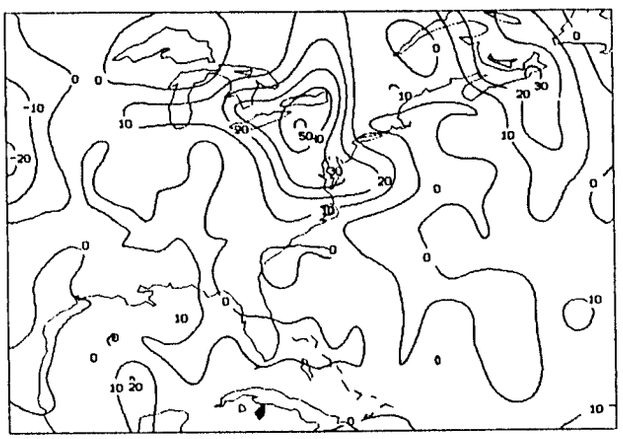

Fig. 8. Difference of 500 mb geopotential analyses: edited vs. unedited.

6. REFERENCES

Barnes, S. L., 1964: A technique for maximizing details in numerical weather map analysis. J. Appl. Meteor., 3, 396-409.

Lee, T-H., D. Chesters, and A. Mostek, 1983: The Impact of Conventional Surface Data upon VAS Regression Retrievals in the Lower Troposphere. J. Clim. and Appl. Met., 22, 1853-1874.

Purser, R. J. and R. McQuigg, 1982: A successive correction analysis scheme using recursive numerical filters. Met. O 11 Tech. Note, No. 154, British Meteor. Service, Bracknell, England.

INITIALIZATION OF A MESOSCALE MODEL WITH SATELLITE DERIVED TEMPERATURE PROFILES

Michael W. Kalb

Universities Space Research Association
Marshall Space Flight Center
Huntsville, AL 35812

Introduction

A mesoscale model simulation by Kalb (1985) which used mandatory level SESAME-AVE I rawinsonde data to describe the initial state, suggested that the low vertical resolution of satellite data may not be a serious problem if it is consistent with the vertical resolution afforded by a particular numerical prediction model. That simulation showed that horizontal mesoscale mass field structure discerned by SESAME-AVE radiosonde data was important to the model "forecast" and was supported initially by mass balanced winds. Those findings motivated the present study which examines the relative performances of that radiosonde data and TIROS-N satellite derived temperature profile data in mesoscale model simulations for the same case of 10 April, 1979.

The purpose of this paper is to explore the potential capability that satellite based temperature profiling systems might have on mesoscale numerical weather prediction, either independently or in conjunction with ground based information. The primary focus is on the impact of satellite temperature profile data on model mesoscale precipitation accumulation field fields.

2. Experiment Design

This study is based on four mesoscale model simulations initialized at 2100 GMT 10 April and ending at 0600 GMT 11 April, 1979 (9 hours). These employ various combinations of satellite versus rawinsonde temperature, observed versus balanced low level winds, and static versus dynamic initialization of low level winds (see Fig. 1). These simulations examine the performance of satellite temperature profile data in a mesoscale model and the degree to which low level wind information derived from the U.S. hourly surface network might complement a-synoptic satellite temperature data in prescribing mass fields and mass-balanced winds for a model initial state.

Simulations A and B are the primary experiments which provide the most direct comparison between satellite and rawinsonde temperature data. Both initial states have the same surface pressure, moisture distribution and use the same static initialization for all prognostic model variables. Both have low level winds specified from observed surface wind analyses. Differences between simulations A and B can be linked to differences in the initial radiosonde and satellite temperature fields.

Simulation C differs from B in that it uses balanced winds for the low levels rather than incorporating observed surface winds. This simulation assumes that only temperature and moisture data are available (e.g., over oceans), thus requiring that winds be computed from the satellite mass field at all levels. This simulation was conceived by recognizing that the hourly surface network is perhaps the only source of information which is always available to complement a-synoptic mass and mass balanced wind fields prescribed from satellite temperature data alone.

The inclusion of a realistic low level divergent wind field is thought to be important since the formation of moist convection at a location is often preceded by intense local moisture convergence. Such a correlation was found by Homan and Vincent (1982) and Moore (1982) for convective precipitation which occurred on 10 April, 1979 within the domain considered in the present study. Cumulus convection may be initiated in the model through the release of potential instability which can be enhanced via low level moistening. Therefore, local low level accumulation of moisture in the model by advection and divergent properties of the low level wind field could be important in the model, as in nature, for determining when and where convection may begin. Since verification in this study focuses on precipitation, experiments which examine the role of the low level wind field assume greater signifi-

EXPERIMENT	PRIMARY DATA SOURCE	LOW LEVEL WINDS	INITIALIZATION OF LOW LEVEL WINDS
A	SESAME RADIOSONDES	OBSERVED	STATIC
B	TIROS-N SATELLITE	OBSERVED	STATIC
C	TIROS-N SATELLITE	BALANCED	STATIC
D	TIROS-N SATELLITE	OBSERVED	DYNAMIC

Fig. 1 Experiment design.

cance. The observed surface divergence and streamlines are shown in Fig. 2. The area of maximum convergence near the Texas Panhandle is also a maximum of moisture convergence.

In simulation D, a simple dynamic initialization was used to force the same initial observed low level wind field into the model, while upper level winds adjust. This period of continuous insertion was chosen to be approximately equal to the 1-1/2 h initialization / adjustment period which characterized the four LAMPS simulations. Experiment D was performed to preclude elimination (due to adsjustment processes) of any valuable information contained in the initial low level wind observations.

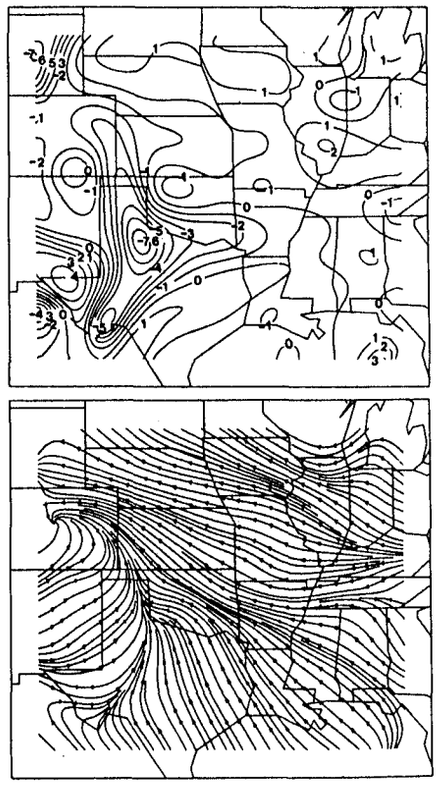

Fig. 2 2100 GMT surface winds used in the model initial state. a) divergence, 10 s. b) streamlines.

3. Data Acquisition and Analysis

To take advantage of both rawinsonde data from the SESAME-AVE regional scale observing network and simultaneously observed satellite temperature profiles, the time period 2100 tO 0600 GMT 10-11 April, 1979 was selected for this study. This period coincides with the most severe weather period associated with the Wichita Falls tornado outbreak.

The availability of TIROS-N temperature soundings over the same domain at nearly the same time as the SESAME rawinsonde data presented a unique opportunity to explore their relative impacts on a mesoscale numerical simulation. Differences in the representation of the model initial

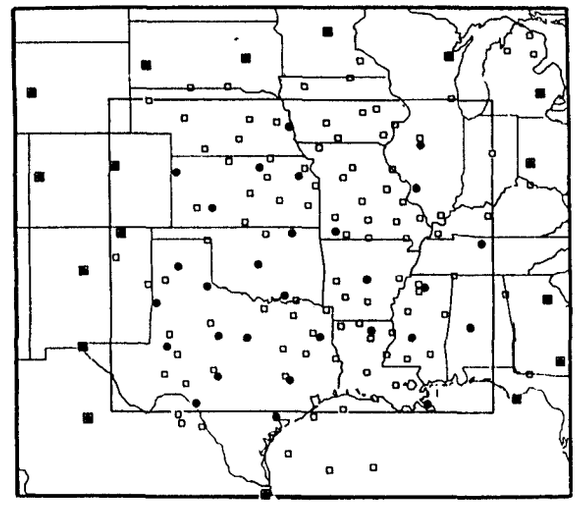

Fig. 3 Mesoscale model domain (inner rectangle) and distribution of rawinsonde (●) and satellite data (□) at about 2100 GMT.

temperature structure provide the basis for comparing satellite versus rawinsonde/based simulations. Experimental control was achieved by ensuring both initial states had the same moisture distribution as well as winds diagnosed from the mass field.

The satellite data set consisted of 89 vertical temperature profiles at 2040 GMT with values at mandatory pressure levels. These were derived from TIROS-N satellite radiance measurements methods described by Smith (1979) and processed at the University of Wisconsin using interactive computer techniques in which an operator selects cloud-free fields of view for making temperature retrievals.

The areal coverage of satellite and radiosonde data for the initial states at 2100 GMT are shown in Fig. 3. The satellite data had several data voids. A large cloud shield over Oklahoma associated with heavy rainfall prevented satellite soundings from being made there (see Fig. 4). A satellite data void in southwest Texas demarcates the western edge of the TIROS-N orbital swath. To help with the objective analysis along the western edge of the model domain in the data void region in Colorado, two SESAME rawinsonde soundings were included as indicated in Fig. 3. Except for these two observations, in all satellite model simulations, data in the domain interior was provided only by the satellite and without benefit of a first guess field. Outside the model domain conventional 12 hourly synoptic rawinsonde observations were time interpolated to 2100 GMT and included in both the rawinsonde and satellite data sets. The objective analysis and interpolation procedures for transferring station data to the model grid mesh is described in Kalb (1983).

In experiments A, B, and D, observed surface winds were used to construct a low level divergent wind field affecting the lowest five levels of the model (0. to 1.25 km). In these cases winds at model levels 2 through 5 were computed by linear interpol-

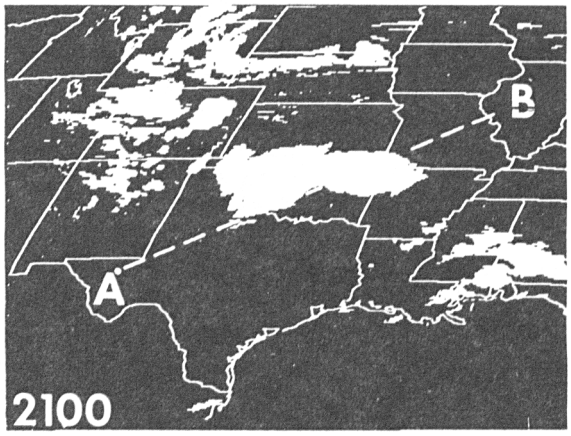

Fig. 4 Satellite infrared cloud image at 2100 GMT, 10 April, 1979. Image has been enhanced to show dominant structures.

ation of u and v components between the observed surface values and balanced values at level 6 giving an Ekman type turning of the low level winds with height.

Only mandatory pressure levels were used from the SESAME-AVE rawinsondes. This was done so that vertical sampling (resolution) would be less of a factor in the comparison of satellite and rawinsonde temperature profiles, and thus, emphasize differences due to horizontal sampling and the volumetric nature of the satellite measurements.

The initial wind fields were computed from both the satellite and rawinsonde geopotential height analyses using the non-linear balance equation to ensure that the initial wind fields depended only on temperature structure. In regions where the balance equation was non-elliptic, winds were constrained to have zero absolute vorticity in order that geopotential height (and temperature) fields not be altered according to common practice. Details may be found in in Kalb (1983).

To further facilitate the comparison of satellite and rawinsonde model simulations on the basis of temperature, it was necessary to provide both initial states with equivalent moisture information, the goal being to obtain a satellite moisture analysis representing the same physical distribution of moisture perceived by the rawinsonde network, but sampled at independent satellite locations. Satellite derived moistures were not used. Instead, "bogus" specific humidity values were derived at satellite data locations which when objectively analyzed gave essentially the same moisture distribution as the SESAME rawinsonde data. These moisture values were obtained by the following procedure:

1. ANALYZE RAOB q.
2. INTERPOLATE RAOB ANALYSIS TO SAT LOCATIONS TO CREATE SATELLITE OBSERVATIONS q.
3. ANALYZE SAT OBSERVATIONS q.
4. SUBTRACT SAT ANALYSIS FROM RAOB ANALYSIS TO CREATE A DIFFERENCE FIELD.
5. DIFFERENCES SMALL ? ——YES——→ STOP
   NO ↓
6. INTERPOLATE DIFFERENCES TO SAT LOCATIONS AND ADD THEM TO THE OLD SAT OBSERVATIONS TO GENERATE NEW SAT OBSERVATIONS.
7. ANALYZE NEW SAT q OBSERVATIONS.
8. GO TO STEP 4.

Satellite and rawinsonde specific humidity fields were very close as seen in Fig. 5, but could never be the same by this procedure due to differences in data sampling locations and densities.

Since initial satellite and rawinsonde specific humidity analyses were essentially the same, their relative humidities would be different and could affect the outcome of the model precipitation simulations. However, if the satellite data were to be truly independent of rawinsonde information, then an absolute measure of moisture had to be used. Available SESAME relative humidities implicitly contain information about rawinsonde temperature.

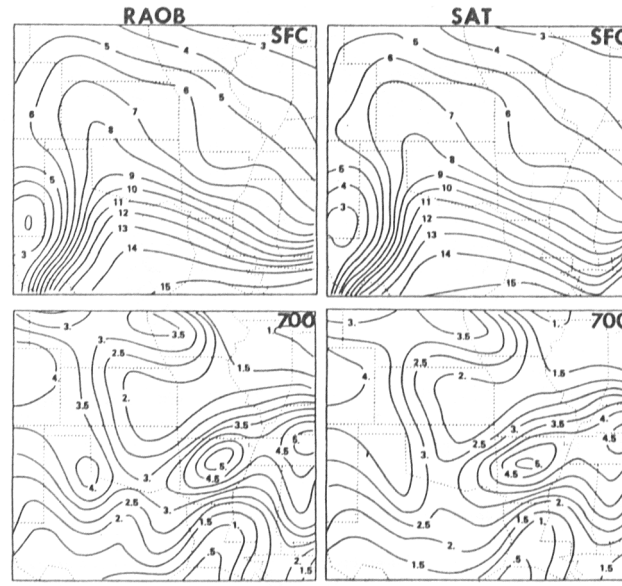

Fig. 5 Initial rawinsonde and satellite specific humidity analyses at 700 mb and at the surface (2100 GMT).

4. Model Description

The model employed for this study was the Drexel University LAMPS (Limited Area Mesoscale Prediction System) mesoscale model. The reader should consult Perkey (1976) for details as only a cursory description of the model is provided here. LAMPS is a 15 level, fully moist primitive

equation model with terrain following height coordinates. The top of the model is at 16 km. Prognostic model variables include horizontal wind components, virtual potential temperature, rain water, cloud water, specific humidity. A modified Exner function is predicted at the model top and diagnosed hydrostatically at all lower levels. Vertical velocity (dz/dt) is also diagnosed.

Boundary conditions are time varying based on observed rawinsonde data as described in Kalb (1985). The planetary boundary layer is modeled with K-theory. Fluxes of heat, moisture and momentum through the surface layer are handled with Monin-Obukhov similarity. Precipitation is partitioned into grid-resolved and parameterized (convective) modes both of which incorporate Kessler type microphysical conversions between the various states of atmospheric water.

The model simulations in this study were performed on a 35 km resolution 44 by 50 grid as shown in Fig. 3.

5. Initial Fields

850 mb height and temperature fields at 2100 GMT in Fig. 6 show that the satellite temperature data were able to depict much of the basic structure in the SESAME rawinsonde sonde data. Regional temperature biases in excess of 3 K are found and biases in the height fields exceed 25 m in northeast Colorado (a satellite data sparse area). The satellite data depicted observed short wave features through Oklahoma, Texas and Nebraska, although their amplitudes were smaller than for the same waves in the rawinsonde data.

At 200 mb (Fig. 7) regional biases in the temperature fields are larger. Height differences are greatest over Oklahoma (-64 m) and the difference patterns correspond well with the the data void there caused by cloud cover (see Fig. 4). Isotachs in the cross section of Fig. 8 illustrate significant differences between rawinsonde and satellite balanced momentum fields. Satellite winds show faster jet winds located lower in the troposphere relative to the rawinsonde. Isentropes in Fig. 8 also indicate differences in static stability over the central part of the cross-section, a factor which could be important to the initiation of precipitation in the model. Thus, while the satellite was able to reproduce basic patterns, significant differences existed between the satellite and rawinsonde depictions of the initial state due to spatial sampling and to the nature of the measurements themselves. These differences are reflected in the results of the model simulations.

6. Model Results

The model precipitation response may be linked to satellite or rawinsonde temperature through a) changes in static stability, b) relative humidity (since the absolute moisture fields were held nearly constant while satellite temperatures were

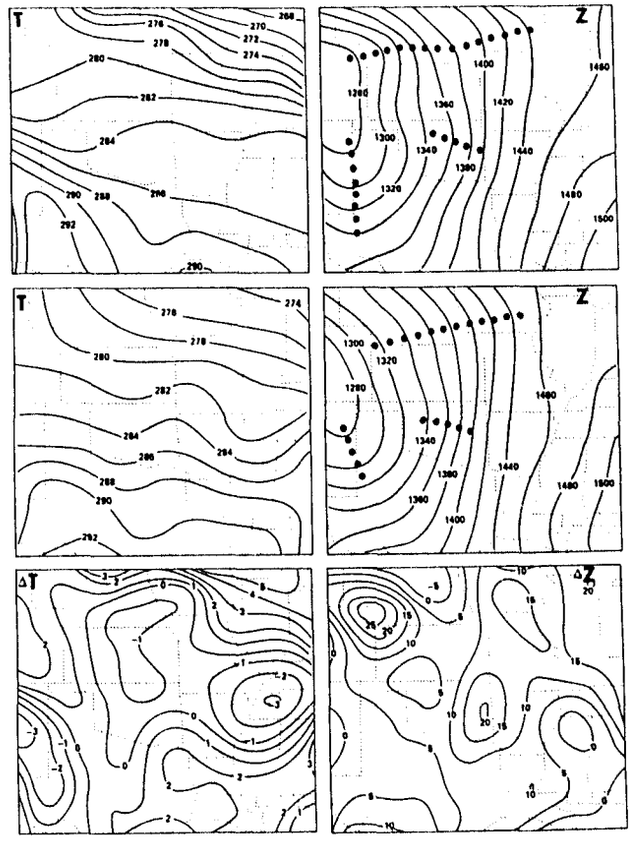

Fig. 6 Satellite and rawinsonde 850 mb temperature (K) and height fields (m) at the initial time. Top panels: rawinsonde. Middle panels: satellite. Bottom panels: difference fields: (satellite-rawinsonde).

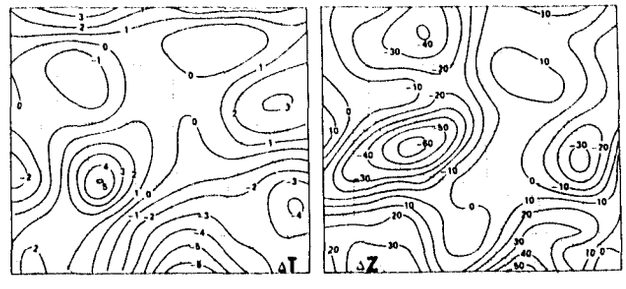

Fig. 7 200 mb temperature and height difference fields (satellite-rawinsonde).

different), or c) through differences in the wind field. In addition model precipitation may be initiated in a parameterized convective mode or by grid scale moist processes. These complexities render nearly impossible the isolation of cause and effect relationships between model precipitation response and each of the above induced alterations to the initial states. However, the intent of this paper is not to explore these details, but merely to examine the performance of a mesoscale model if initialized with information derived only from satellite temperature soundings. The importance of this study is that it sets performance

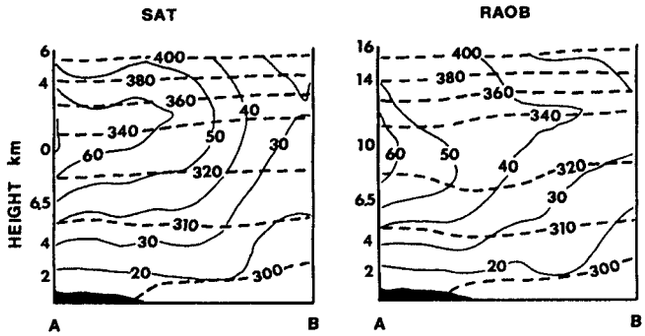

Fig. 8 Vertical cross-sections at 2100 GMT for wind speed (m/s) and potential temperature (K). Cross-section corresponds to line AB in Fig. 4.

limits on the ability of satellite temperature profile data to substitute for a large mesoscale a-synoptic mass field unobtainable from conventional operational observation networks.

Total 9-h precipitation accumulations for the four model simulations in Fig. 9 are to be compared to the observed 9-h accumulations in Fig. 10 based on hourly surface reports. Satellite based simulations depicted mesoscale precipitation patterns better than did the rawinsonde simulation A by producing two distinct verifiable precipitation areas: 1) a "main" area extending northeastward from central Texas to central Missouri, 2) a "secondary" area extending from the eastern tip of the Texas Panhandle northeastward into Kansas. The rawinsonde simulation accumulation did not exhibit these verifiable features, but gave a precipitation maximum in the area of Wichita Falls, similar to that observed. The broad area of precipitation extending from Colorado to Missouri in simulation A was associated with a northward propagating low level short wave as discussed in Kalb (1985). A similar short wave in the satellite simulations was not as distinctly associated with model precipitation as in the rawinsonde simulation. For the model domain as a whole, almost all of the precipitation in the satellite simulations was in the convective mode, while precipitation was about equally partitioned between convective and resolved modes in the rawinsonde simulation. This may result from the response of the model convective parameterization to different representations of the static stability distribution.

Continuous insertion of observed low level winds produced similar accumulation patterns as simulation B, except that the orientation of the main precipitation area was more obviously and distinctly aligned along a southwest to northeast axis as in the observed accumulation field. The physical mechanism behind this positive impact is not understood, but linkage between the initial wind field and total precipitation accumulation many hours later must be very complex since the continuous insertion also had impacts on the evolution of the mass and wind fields (See Kalb,

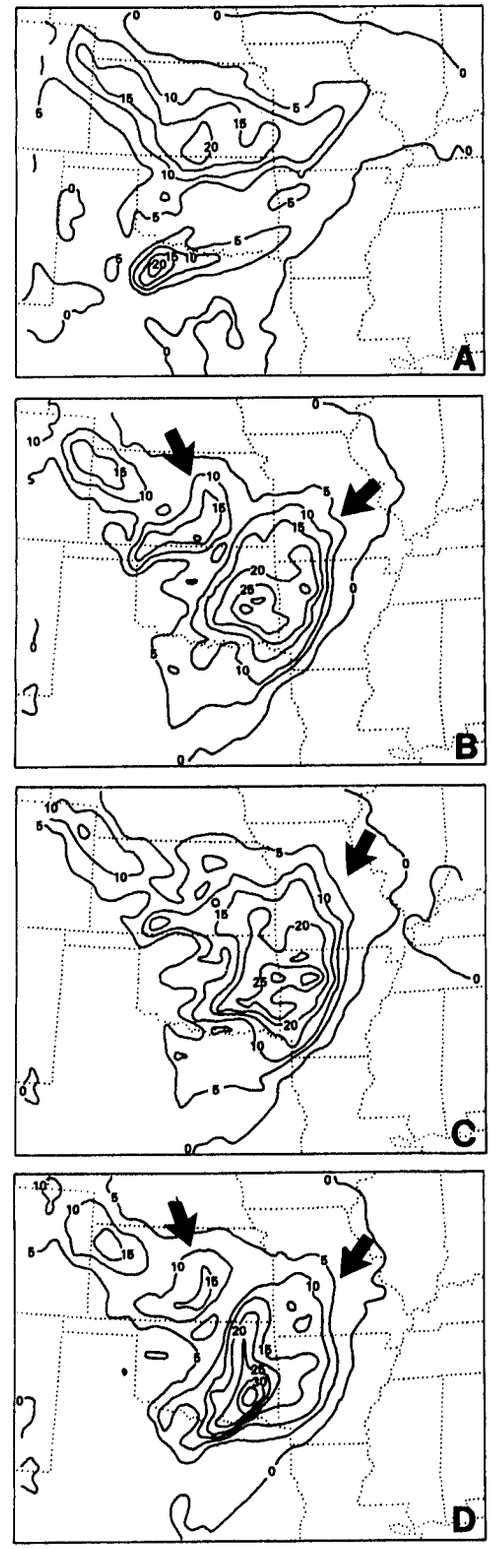

Fig. 9 Model simulated 9-h precipitation accumulations (mm). Letters in lower right corner of panels identify the simulation.

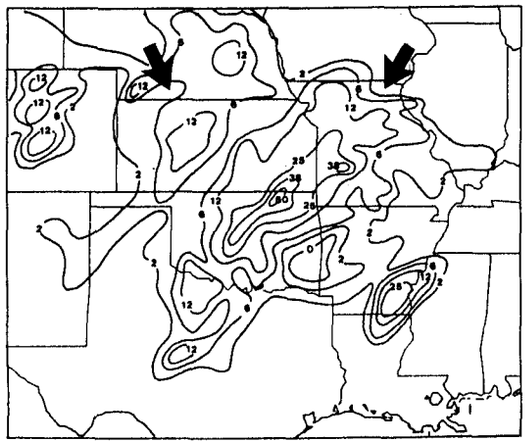

Fig. 10 Observed 9-h precipitation accumulations (mm) for same period as simulated.

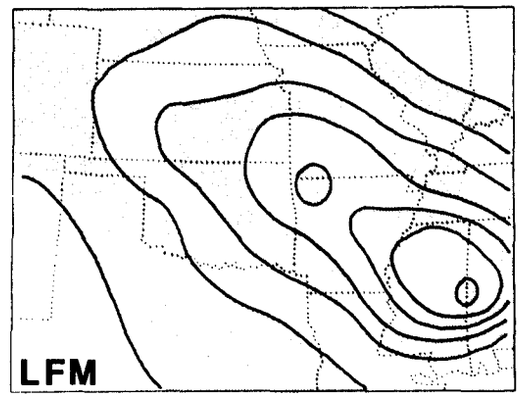

Fig. 11 LFM 12-h forecast precipitation accumulations for 0000 GMT to 1200 GMT 11 April. Contour interval is 0.5 inches.

1983) which could actually have been responsible for these changes in the precipitation simulation.

Neglect of realistic low level winds (simulation C) resulted in more significant changes to the precipitation accumulations. In particular, the accumulation maximum in central Kansas was eliminated. It can be concluded that the inclusion of more realistic low level wind information may had a beneficial impact on a model precipitation simulation. However, the hypothesized relationship between low level moisture convergence via the initial wind field and precipitation was not evident in the results of this study, since the area where imposed moisture convergence was greatest in simulations B and D (near the Oklahoma/Texas border) did not correspond to the most significant changes in precipitation accumulations caused by the exclusion of observed low level winds.

In the satellite simulations,the main precipitation area was located about 100 miles too far to the east relative to observed precipitation. Certain other aspects of the observed accumulations such as a maximum in southeast Arkansas do not appear in any of the model simulations. Despite such shortcomings, when these simulations are compared to the operational LFM forecast accumulations for about the same period (6-h overlap, Fig. 11) it is seen that the LAMPS model, even initialized with satellite temperature data and mass winds, provided a much superior depiction of observed precipitation accumulation.

7. Conclusion

The apparent success of the satellite precipitation simulations may have been due as much to the SESAME moisture analysis and LAMPS model moist physics and resolution as to the representation of the temperature field. Yet, the fact that a reasonable precipitation simulation resulted, still speaks for the quality of the satellite temperature data set obtained for this case study. It is clear that, at least for this case, the use of satellite temperature profiles produced a better mesoscale precipitation accumulation forecast than either the LFM or the LAMPS mesoscale model initialized with SESAME rawinsonde temperature data. These experiments illustrate that a carefully processed satellite temperature profile data with fairly uniform domain coverage can give a reasonable depiction of the large meso-alpha distribution of mass may permit construction of a-synoptic meteorological data sets of sufficient quality for use in meso-alpha scale numerical weather prediction.

Acknowledgements. The author expresses his appreciation to Dr. David D. Houghton of The University of Wisconsin for his guidance during this research. This research was supported under NSF grant ATM-8005369 and NASA contract NAS8-34767.

References

Homan, J. H. and D. G. Vincent, 1982: Mesoanalysis of the severe storm outbreak of 10-11 April 1979. Preprints 12th conf. on severe local storms. AMS, pp. 359-362.

Kalb, M. W., 1983: Initialization of a mesoscale model for April 10, 1979 using alternative data sources. PhD Thesis, University of Wisconsin-Madison, 230 pages.

Kalb, M. W., 1985: Results of a limited area mesoscale model simulation for 10 April 1979. Mon. Wea. Rev., 113, 1644-1661.

Moore, J. T., 1982: The forcing and evolution of three dimensional moisture convergence during the 10-11 April 1979 severe weather outbreak. Preprints 12th conf. on severe local storms. AMS pp. 209-212.

Smith, W. L., H. M. Woolf, C. M. Hayden, D. Q. Wark and L. M. McMillin, 1979: The TIROS-N operational vertical sounder. Bull. Amer. Met. Soc., 60, 1177-1187.

3.7

COUPLING OF VAS DATA ANALYSIS WITH MODELING AT THE MESOSCALE

Alan E. Lipton
Thomas H. Vonder Haar

Department of Atmospheric Science
Colorado State University
Fort Collins, CO 80523

1.0 INTRODUCTION

Satellite-based remote sounders and mesoscale numerical models have both been used extensively for analyzing the atmosphere. A coupling of these two tools has potential for producing better analyses of water vapor concentration and other mesoscale variables than either could produce alone. By coupling we mean that information from the model atmosphere aids interpretation of satellite data, and satellite-based retrievals influence the characteristics of the model atmosphere. Kreitzberg (1976) proposed a merger of technologies such as this. The feasibility of coupled water vapor analysis is the subject of this paper.

Hillger and Vonder Haar (1981) and Chesters, et al. (1982) have demonstrated that satellite-based sounders are useful tools for measuring the potential for development of deep convection. The greatest strengths of satellite sounders are their ability to detect gradients of temperature and water vapor in the horizontal at the mesoscale, and their high temporal resolution. Two major weaknesses of present-day satellite sounders are the mediocre absolute accuracy and the poor vertical resolution of retrieved parameters. These problems are particularly accute in retrieval of water vapor concentration, and can be substantially alleviated only by using information from non-satellite sources to guide the retrieval process.

The use of ancillary data in retrieval of water vapor parameters has generally been limited to incorporation of surface observations (e.g., Hayden, et al., 1981), nearby radiosonde observations (e.g., Hillger and Vonder Haar, 1981), or statistics from historical radiosonde data (e.g., Lipton, et al., 1986). Mesoscale models can contribute ancillary data at a much greater detail than is available from standard observations.

A mesoscale model can be used as an elaborate and powerful interpolater/extrapolater in space and time. However, a model's depiction of water vapor is limited by the accuracy and completeness of the data used for the initialization. Standard synoptic observations are not adequate to detect mesoscale variations. Soundings retrieved from VISSR Atmospheric Sounder (VAS) data are available at the mesoscale and have been used in model initialization by Cram and Kaplan (1985). They found that the water vapor profiles were counterproductive because they were inconsistent with other features of the model atmosphere. The inconsistencies seem to have stemmed from the fact that their profiles were retrieved independent of model feedback.

Coupling the interpretation of satellite sounder data with implementation of a mesoscale model is a means to avoid some of the hindrances encountered when the two technologies are dealt with as separate entities. Accuracy of retrievals can be improved since coupling allows satellite data from several consecutive measurement times to be analyzed together. The time intervals between satellite views (typicaly one to three hours) can be bridged by a model that accounts for the transport of water vapor during the intervals.

Coupled analysis of water vapor has particular potential for success at the mesoscale, since concentrations can vary greatly over short scales of space and time. Some of the variations result from circulations induced by local terrain variations, such as land/water contrasts, soil characteristics, and surface elevation irregularities. Mesoscale models are capable of simulating these effects (Mahrer and Pielke, 1977). Modeling of flow near the Front Range of northeastern Colorado has shown that locally-induced circulations can have a significant impact on water vapor distributions during one diurnal cycle (D. J. Abbs, personal communication). It is yet to be seen how the potential for deep convection may be influenced by the interaction of local circulations with previously existing synoptic and mesoscale gradients in water vapor concentration.

2.0 FEASIBILITY STUDY

2.1 Idealized Simulation

We chose to test the feasibility of coupled analysis by means of idealized studies, in which the model is assumed to perfectly simulate atmospheric flow. The employed model is a version of the Colorado State University Regional

Atmospheric Mesoscale Modeling System (RAMMS) (Mahrer and Pielke, 1977; Mahrer and Pielke, 1978; McNider and Pielke, 1981). Figure 1 shows the simple topography used for two-dimensional simulations, which is a rough approximation of an east-west cross section through northeastern Colorado. The horizontal grid covered 705 km at a spacing of 15 km, and there were 26 levels in the vertical from 10 to 13,500 m above ground level. Simulations were initiated at sunrise (05 LST) with a mid-summer temperature sounding from Denver, Colorado and a uniform geostrophic wind of 3 m/s from the east.

Figures 1, 2 and 3 depict some features of the influence of a local circulation on water vapor concentrations. The initial water vapor distribution (Fig. 1) included anomalously high values in the lower eastern portion of the domain. After eight hours of integration, diabatic effects had superimposd an east-west circulation on the background flow (Fig. 2). The water vapor distribution after eight hours (Fig. 3) reflects the mesoscale and synoptic flows, along with the development of a well-mixed layer. The challenge to coupled analysis is to reproduce the water vapor fields using only indirect information: radiances that would be observed if a satellite viewed the idealized atmosphere, and the advection and fluxes implied by the model simulation.

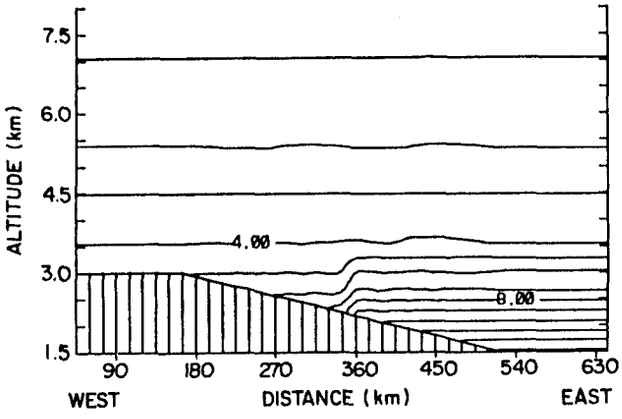

Fig. 1. A vertical cross section of modeled specific humidity (g/kg) at sunrise (05 LST). Contours are at intervals of 1 g/kg. Vertical hatching denotes the terrain. Horizontal distance is relative to the western boundary of the model domain.

2.2 Coupling Strategy

Coupled analysis requires a mechanism for communication between the water vapor retrieval algorithm and the model atmosphere. The model-to-satellite guidance can consist of using model-generated profiles of temperature and water vapor as initial guesses in an iterative retrieval procedure (e.g., Smith, 1970). The impact of the initial guess on the shape of the final retrieved profile can be exploited to improve the vertical resolution of satellite-based soundings. If, for example, the model depicts subsidence over a region, then the effect of the flow on the water vapor distribution can be communicated to the interpretation of satellite radiances.

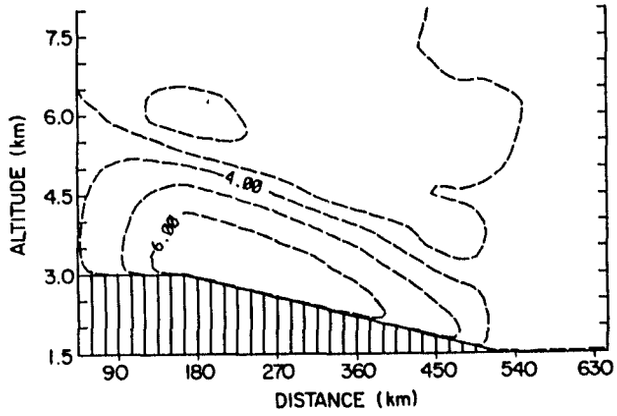

Fig. 2. A vertical cross section of modeled westerly wind component (m/s) at eight hours after sunrise (13 LST). Dashed contours indicate easterly (negative) velocities, and are drawn at intervals of 1 m/s.

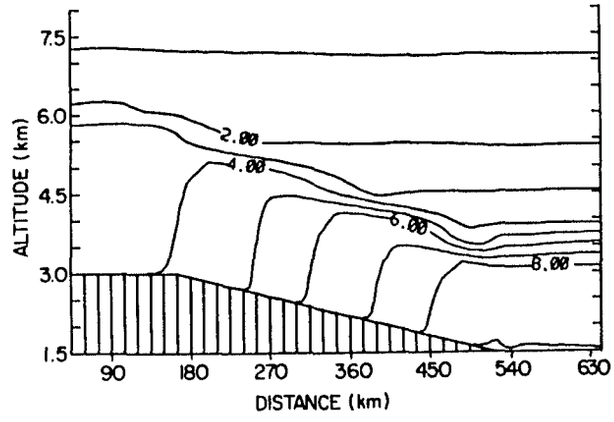

Fig. 3. As in Fig. 1, but for eight hours after sunrise (13 LST).

It is straightforward, from a technical standpoint, to introduce water vapor data into a model domain. Direct insertion is possible since water vapor has only a minor effect on atmospheric flow. Insertion can be done at initilization and again at subsequent times as fresh satellite data become available. The inserted profiles are retrieved from satellite data using model parameters from the previous time step as initial guess data. Thus, the analysis is both coupled and time-continuous.

3.0 CONCLUSION

Mesoscale numerical model simulations have been used to demonstrate that a locally-induced circulation can give rise to diurnal changes in the distribution of water vapor on the mesoscale. The ability of a model to depict these changes enables the water-mass continuity law to play a role in retrieving water vapor concentrations from a series of satellite measurements. Demonstrations of coupled satellite/model water vapor analyses will be presented at the conference.

4.0 ACKNOWLEDGEMENTS

We thank Don Hillger for reviewing the manuscript, Moti Segal for his help in using the mesoscale model, and Loretta Wilson for typing the manuscript. The research reported here was supported by NOAA contract NA84AA-H-00020. Computer support was provided by the National Center for Atmospheric Research, which is funded by the National Science Foundation.

5.0 REFERENCES

Chesters, D., L. W. Uccellini, and A. Mostek, 1982: VISSR Atmospheric Sounder (VAS) simulation experiment for a severe storm environment. Mon. Wea. Rev., 110, 198-216.

Cram, J. M., and M. L. Kaplan, 1985: Variational assimilation of VAS data into a mesoscale model; assimilation method and sensitivity experiments. Mon. Wea. Rev., 113, 467-484.

Hayden, C. M., W. L. Smith, and H. M. Woolf, 1981: Determination of moisture from NOAA polar orbiting satellite sounding radiances. J. Appl. Meteor., 20, 450-466.

Hillger, D. W., and T. H. Vonder Haar, 1981: Retrieval and use of high-resolution moisture and stability fields from Nimbus-6 HIRS radiances in pre-convective situations. Mon. Wea. Rev., 109, 1788-1806.

Kreitzberg, C. W., 1976: Interactive applications of satellite observations and mesoscale numerical models. Bull. Amer. Meteor. Soc., 57, 679-685.

Lipton, A. E., D. W. Hillger, and T. H. Vonder Haar, 1986: Water vapor vertical profile structures retrieved from satellite data via classification and discrimination. Mon. Wea. Rev. (in press).

Mahrer, Y., and R. A. Pielke, 1977: A numerical study of the airflow over irregular terrain. Beitr. Phys. Atmos., 50, 98-113.

Mahrer, Y., and R. A. Pielke, 1978: A test of an upstream spline interpolation technique for the advective terms in a numerical mesoscale model. Mon. Wea. Rev., 106, 818-830.

McNider, R. T., and R. A. Pielke, 1981: Diurnal boundary layer development over sloping terrain. J. Atmos. Sci., 38, 2198-2212.

Smith, W. L., 1970: Iterative solution of the radiative transfer equation for the temperature and absorbing gas profile of an atmosphere. Appl. Opt., 9, 1993-1999.

THE NIMBUS 7 LIMS MAP ARCHIVAL TAPE

K. V. Haggard, E. E. Remsberg, J. M. Russell III
Atmospheric Sciences Division
NASA Langley Research Center
Hampton, Virginia

1. INTRODUCTION

The Limb Infrared Monitor of the Stratosphere (LIMS) experiment used a thermal infrared limb scanning radiometer to measure radiances in selected regions from 6.2 μm to 15 μm see Russell and Gille, 1978; Gille et al. 1980, and Gille and Russell, 1984. The measurements obtained were later processed to infer middle atmospheric temperature and trace species profiles for ozone (O_3), water vapor (H_2O), nitrogen dioxide (NO_2), and nitric acid (HNO_3). These profiles were calculated at approximately 4° latitude increments from 64° south to 83.5° north, for the period from October 24, 1978, through May 28, 1979. This data set has been archived on magnetic tape at the National Space Sciences Data Center (NSSDC) under the name Langley Inverted Profile Archival Tape (LAIPAT).

To study the propagation characteristics of planetary waves and the transport of trace gas species, it is necessary to represent accurately not only the time mean state, but also the transient wave motions of temperature, geopotential height, and trace gas concentrations. The observed wave motions in the stratosphere are mainly planetary waves of wave number 3 and less, with temporal scales of the order of a few days to about 4 weeks. Thus, these waves are easily detectable with the LIMS sampling pattern, which makes as many as 28 measurements per day at each latitude. Attempts to observe these waves are best handled by calculating synoptic fields from the data. The Kalman filter technique is an appropriate procedure for estimating these fields. An approach very similar to that described in Rodgers (1976, 1977) and Kohri (1981) was used to calculate the noon GMT synoptic fields for the LAIPAT data. In addition, the resulting synoptic temperature fields were used with the NMC 50 mb heights to calculate height fields that are in hydrostatic balance with the LAMAT temperatures. These synoptic fields have been archived at NSSDC under the name Langley Map Archival Tape (LAMAT). The details of the calculations for the LAMAT are described in the papers by Haggard et al. (1986 a,b) and Remsberg et al. (1986).

This paper briefly outlines some of the steps used to produce the LAMAT data, and shows examples and discusses some particular features of the data.

2. NIMBUS 7 ORBIT CHARACTERISTICS

The orbit characteristics of the Nimbus 7 spacecraft play an important role in the analysis and interpretation of the LAMAT data. The spacecraft is in a Sun-synchronous orbit and the LIMS tangent point (central point of the measurement) is a closed loop on a latitude--local solar time grid (figure 1). The tangent point track has been divided into two segments, or nodes. The ascending node, node 1, is that portion of the track where the tangent point moves from south to north. The descending node, node 2, is that portion where the tangent point moves from north to south. The entire track, i.e. node 1 plus node 2, is referred to as the combined node or node 3. The second curve on figure 1 shows the terminator on December 21 at 30 km. Note that while the node 1 and 2 measurements are generally made in sunlight and darkness, respectively, the region near the poles may be

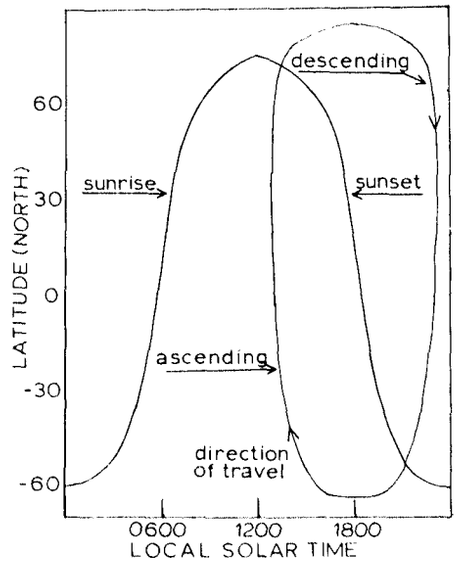

Figure 1.- LIMS tangent point track and teriminator for Dec. 21 and 30 KM vs. local solar time.

in sunlight (or darkness) for both nodes. The common feature of node 1 (or node 2) is that at each latitude, all measurements were taken

at the same local solar time. The LAMAT maps have been calculated for each constituent and each node, with the exception of NO_2, which was calculated for only nodes 1 and 2, and height, which was done for only node 3. The pressure levels, in mb, for which the LAMAT maps were calculated are 100, 70, 50, 30, 16, 10, 7, 5, 3, 2, 1.5, 1, 0.7, 0.5, 0.4, 0.2, 0.1, 0.05. The pressure and approximate height range of maps by constituent is shown in table 1.

Parameter	Pressure Range (MB)	Height (KM)	Nodes
Temperature	100. - 0.05	16-70	1,2,3
H_2O	100. - 0.05	16-70	1,2,3
NO_2	100. - 1.0	16-48	1,2,
HNO_3	100. - 2.0	16-43	1,2,3
Height	100. - 0.05	16-70	3

Table 1.- Pressure range and nodes of LAMAT constitutents.

3. THE FIELD MODEL

At each pressure and latitude the synoptic field has been modeled as a Fourier series in longitude with time dependent coefficients. Thus, the field is given by:

$$T_{t,\theta}(\lambda) = \sum_m A_{m,\theta,t} \cos(m\lambda) + B_{m,\theta,t} \sin(m\lambda) \qquad (1)$$

where

A and B are the time dependent coefficients.
λ = longitude
θ = latitude
t = time
p = pressure
m = wave number
($\leq$ 6 for node 3
$\leq$ 4 for nodes 1 and 2)

When there were not enough data points per day to support the calculation of the desired number of Fourier components, the number of terms (or wave numbers) in the series were reduced. This selection of the order of the series was done on a monthly basis. Thus, for a given month (not a calendar month) the order of the series was calculated as (number of points/day - 1)/2. As a result, the coefficients of the series have some discontinuities in their history.

4. EXAMPLES OF LAMAT MAPS AND DATA FITS

The maps in figure 2 show the 10 mb, node 3 LAMAT temperature fields for February 1, and 9, 1979. These maps bracket a period of rapid increase in the polar temperature during a sudden stratospheric warming and illustrate the sharp longitudinal and meridional gradients present in the data that can be resolved by the Kalman filter. On February 1, there is a large meridional temperature gradient. While it cannot be seen from these two figures alone, the complete data set shows that as the temperature maximum at 50° east moves eastward and toward the pole, this region of strong gradients is rotated and swept over the pole, producing the rapid increase in the polar temperature.

One method of evaluating the accuracy of the LAMAT fields is to calculate the standard deviation of the differences between the calculated synoptic field and the asynoptic LAIPAT data. This calculation has been made and included on the LAMAT. However, this deviation must be used with some caution. It was calculated by a direct comparison between the field and the measurements for each day without any consideration of the time variation

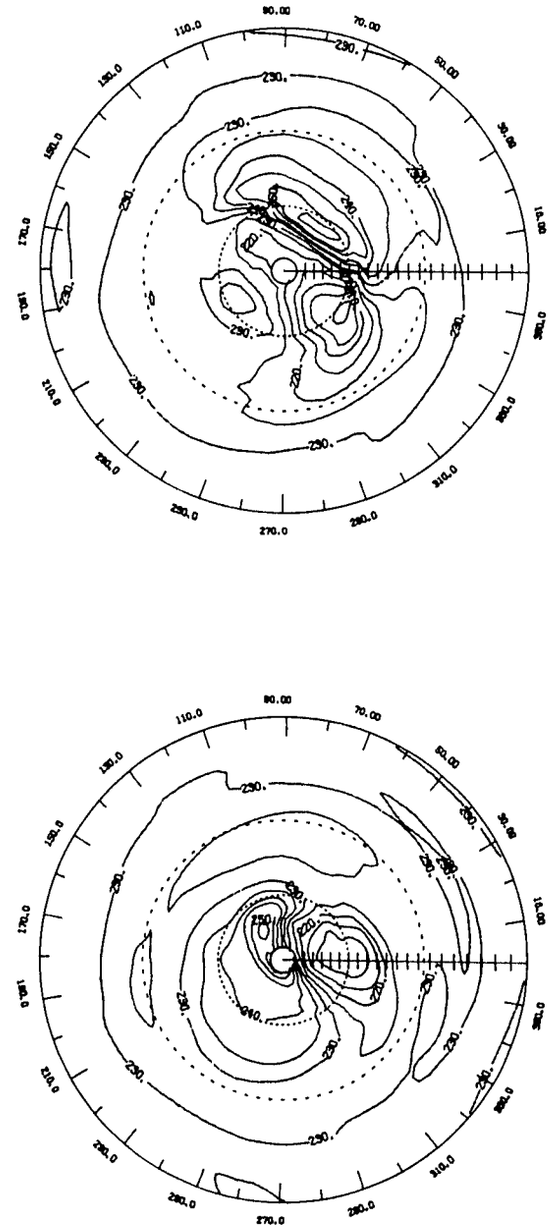

Figure 2.- Northern Hemisphere temperature maps.
(a) Feb. 1, 1979
(b) Feb. 9, 1979

within the day. Thus, the calculation for the maps in figure 2 was made by neglecting the rapid temperature changes within the day. The effects of calculating the standard deviation in this way can be seen in figure 3. The

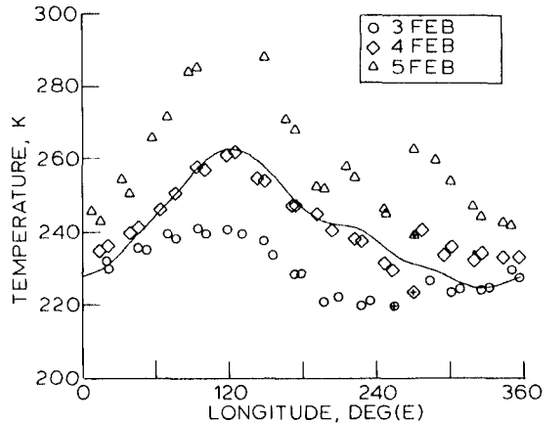

Figure 3.- LAMAT temperature for Feb. 4, 1979, 5 mb, 83.5°N and LAIPAT data for Feb. 3-5.

measured data are 5 mb, node 3 temperatures at 83.5° north for February 3, 4, and 5, 1979. The first data for each day are marked with a + sign, and the time order of the data for each day is left to right (east to west). The solid line is the LAMAT field for noon GMT on February 4. The noontime measurements were taken at about 80° east where the fit between the synoptic field and the data is excellent. As the time difference between the map and the data increases, the fit becomes less accurate. But this is as it should be. The fit is estimating the value that the measurement would have been for that longitude as though the measurement had been made at noon GMT on February 4. However, in calculating the standard deviation for this day, the time variation in the data was neglected. Thus, this deviation represents the quality of the LAMAT data only when there was little temporal variation in the data. This deviation should only be taken as an indication of the quality of the maps. If it is close to the precision of the LIMS data, the map provides a good fit to the measurements. If it is much larger than the data precision, it only indicates there may be a problem, possibly with the estimate, and the data should be examined to determine the cause.

An overall picture of the fit between the LAIPAT data and the LAMAT maps can be obtained by comparing averaged zonal mean fields and the standard deviations discussed above. An example of this comparison is shown in figures 4 and 5. The January mean of the zonal mean ozone is shown in figure 4, and the mean percent standard deviation of the fit between the LAMAT and LAIPAT is given in figure 5. Between about 2 and 10 mb and south of 30° south, the percent standard deviation is less than 2.5. In the Northern Hemisphere, where there are more active waves, the standard deviation is larger, due in part to the effect of the temporal variations. Of course, the percent deviation increases in regions of low mixing ratio. In general, it has been found that high absolute standard deviations are well correlated with regions of high wave variation.

It is important to remember that this measure of the present agreement between the synoptic data and the calculated synoptic maps has been provided as an aid to examining the fields, not as an absolute measure of the quality of the map.

5. DIURNAL VARIATIONS

Since the LIMS sampling pattern does not allow for a detailed mapping of the diurnal

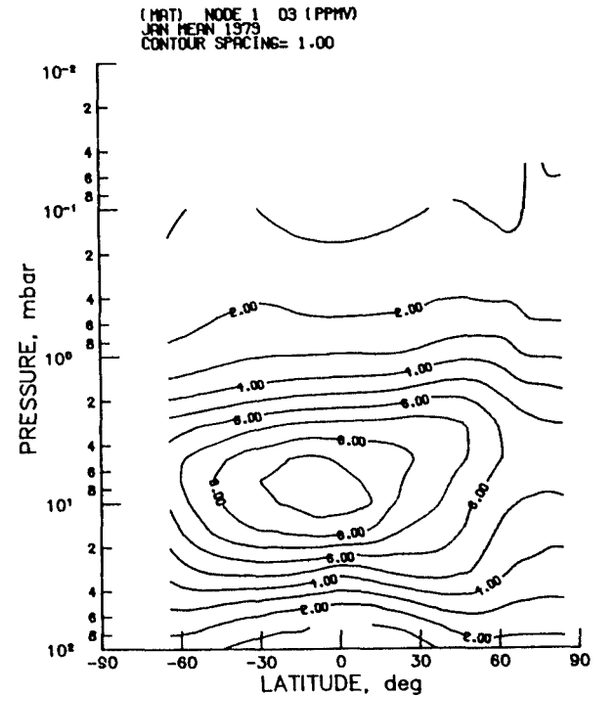

Figure 4.- January zonal mean ozone for ascending node.

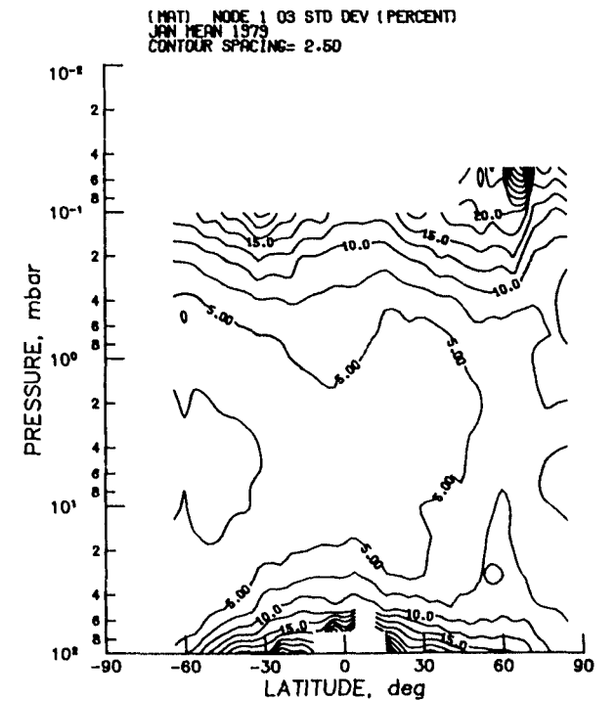

Figure 5.- Percent standard deviation of January zonal mean ozone for ascending node.

variation, no attempt was made to include such an estimate in the model. However, all of the LAIPAT constituents have some diurnal variations in at least some pressure-latitude regions, and the mapping for nodes 1 and 2 was calculated, in part, to help one determine the effects of diurnal variations. The presence of a strong diurnal component can have an adverse effect on the calculation of the combined node (node 3) maps. For example, if there is a strong diurnal variation in a field and if a series of measurements of one node (node 2) is missing, the zonal mean estimate will become biased toward the other node (node 1). Such an effect shows up not only in the zonal mean, but also in the wave components of the Fourier series. If there is any doubt about the presence of a diurnal wave, the node 1 and 2 results should be examined separately.

The most dramatic instance of a diurnal variation in the LIMS data is, of course, for NO_2, where no attempt was made to fit a combined node field. However, the node 1 and 2 fields used up four wave numbers to fit the data. The "maps" produced in this way cannot be considered synoptic maps. Nevertheless, the use of the wave components is essential to obtaining a good estimate for the "zonal" mean value for each node. Of course, it is not correct to refer to the first term (the m = 0 term) in equation (1) as a zonal mean for either NO_2 node. This first term is just the mean value of the measurement for the local solar time for which data were taken. Thus, instead of being a zonal mean, smoothed over the response time of the filter, it is the mean for a particular time in the dirunal cycle, smoothed over the response time of the filter. The use of the non-zero components (m greater than zero) in equation (1) allows one to estimate the effects of the dynamic field and, thus, keep those effects from being erroneously interpreted as changes in the "mean" value. When "maps" of the NO_2 field are examined, the effects of the dynamic field can be seen, demonstrating that the use of the components is justified.

6. AVERAGING AND DATA SMOOTHING

The Kalman filter produces a certain degree of smoothing of the data, but every effort was made to keep this smoothing to a minimum. It was felt one could always do additional smoothing if necessary, but once the field is smoothed it is impossible to go backward. There are features of the fields that need to be considered when averaging or smoothing. Some coefficients for the Fourier series have not been calculated, but have been set to zero. If all of the coefficients past a certain order are zero, they were not calculated. Recall that these zeros were set for the extended period of each Kalman filter run, i.e., about 1 month. Just because these values were set to zero does not mean they were also zero in the data. Rather, it indicates that there were not enough data to calculate those coefficients. For example, there is a large amount of data from the LAIPAT in the 100 and 70 mb equatorial regions that was deleted because of cloud contamination. In some cases there were not enough data to make any calculations; in others, only a zonal mean or perhaps a mean and one wave was calculated. Conversely, a lack of higher order coefficients does not mean that no equatorial waves were absent in the stratosphere, only that there was insufficient information to make a determination.

The same care described in the preceding paragraph for time smoothing also applies to spatial smoothing. It is recommended that spatial smoothing be done by smoothing the Fourier coefficients locally, i.e., over narrow latitude ranges. The use of a global smoothing technique, such as spherical harmonics, can produce waves where no waves were calculated, and such techniques should be considered with caution. Furthermore, the LAMAT fields provide analytic expansions in longitude. This characteristic can be used to advantage in smoothing because one only needs to reduce the appropriate higher order Fourier coefficients in order to obtain further longitudinal smoothing.

7. SUMMARY

The LAMAT contains calculations of synoptic maps for the LIMS temperature, constituents, and geopotential height fields for the duration of the LIMS experiment. These fields have already proven useful in the study of wave propagation and trace species transport in the middle atmosphere. The data have also been used to calculate derived quantities such as wind fields, potential vorticity, and eddy transport of trace gases.

8. REFERENCES

Gille, J. C.; Bailey, P. L.; and Russell, J. M. III. 1980: Temperature and composition measurements from the LRIR and LIMS experiments on Nimbus 6 and 7. Phil. Trans. Roy. Soc., London A., 293, 205-218.

Gille, J. C., and J. M. Russell, 1984: The limb infrared monitor of the Stratosphere (LIMS): experiment description, performance and results. Journal of Geophysical Research, 89, No. D4, pp. 5125-5140, June 30.

Haggard, K. V., E. E. Remsberg W. L. Grose, J. M. Russell III, and B. T. Marshall, 1986 (a), Description of the Nimbus 7 LIMS map archive tape temperature and geopotential height. NASA Technical Paper TP-2553.

Haggard, K. V., B. T. Marshall, R. J. Kurzeja, E. E. Remsberg and J. M. Russell III, 1986 (b), Description of the Nimbus 7 LIMS map archive tape water vapor and nitrogen dioxide. NASA Technical Paper (in preparation).

Kohri, W. J., 1981: LRIR observations of the structure and propagation of stationary planetary waves in the northern hemisphere during December 1975. NCAR Cooperative Ph. D. Thesis, Drexel University, Philadelphia, PA.

Remsberg, E. E., R. J. Kurzeja, K. V. Haggard, and J. M. Russell 1986: Description of the Nimbus 7 LIMS Map Archive Tape - Ozone and nitric acid. NASA Technical Paper (in preparation).

Rodgers, C. D., 1976 Retrieval of atmospheric temperature and composition from remote measurements of thermal radiation. Rev. Geophys. Sp. Phys., 14, 609-624.

Rodgers, C. D., 1977 Statistical principles of inversion theory. Inversion methods in Atmospheric Remote Sounding, Edited by Adarsh Deepak, Academic Press, pp 117-138.

Russell, J. M. III, and J. C. Gille, 1978 The Limb Infrared Monitor of the Stratosphere (LIMS) experiment. The Nimbus 7 Users Guide, edited by C. Madrid, Goddard Space Flight Center, Greenbelt, Md., pp. 71-103,

THE USE OF STRUCTURE FUNCTION ANALYSIS TO ESTIMATE NOISE LEVELS AND THE POTENTIAL RESOLUTION OF SATELLITE MEASUREMENTS

Donald W. Hillger
James F.W. Purdom
Thomas H. Vonder Haar

Cooperative Institute for Research in the Atmosphere (CIRA)
Colorado State University
Fort Collins, CO 80523

1.0 INTRODUCTION

Structure function analysis is a means of interpreting both the noise level and gradient information in a set of measurements. Structure values, or mean-squared differences, are calculated for pairs of earth-located satellite-based measurements as a function of their relative locations, and by considering all possible combinations of satellite fields-of-view (Hillger and Vonder Haar, 1979). In the simplest case homogeneity and isotropy are assumed and the structure is calculated as a function of pair-separation distance only. One result of the structure analysis is an estimation of the magnitude of noise in the analyzed data. This is accomplished by extrapolation of the structure to zero separation distance. Comparison with a separate set of independent measurements is not required. Another result of structure analysis is the mean gradient of the analyzed data. The potential horizontal resolution of satellite measurements depends on both of these results of structure analysis: the noise level in the measurements and the available gradient information in the analyzed field (as measured by the standard deviation of the measurements). For example, in cases where the natural variability of the measurements is low (the mean gradient is a measure of this), the noise level of the measurements must be low enough to avoid masking horizontal variations at scales comparable to the resolution provided by the satellite instrument. This can be interpreted by means of a signal-to-noise ratio obtained by structure analysis of the analyzed fields.

In this study structure analysis is performed on brightness temperatures derived from the VISSR Atmospheric Sounder (VAS). Both real and simulated data are analyzed in order to aid in interpretation of the results. Initial indications show that the noise levels as estimated by structure analysis are greater (worse) than the required accuarcy of the VAS data. VAS data used in this study, however, were not averaged spatially, so higher noise levels can be expected than for temporally and spatially averaged measurements. The goal was to determine the extent to which the VAS measurements must be spatially averaged in order to obtain the desired pre-launch noise specifications. The amount of averaging is dependent on the VAS channel being considered and results were interpreted in terms of the potential (useful) resolution that can be obtained from each channel. This has an impact on how each channel is used experimentally or operationally in the retrieval of atmospheric temperatures and water vapor.

2.0 STRUCTURE ANALYSIS

The structure function is defined as the mean-squared difference between measurements as a function of the vector separation between the measurement earth-locations. The structure function of temperature measurements at points r_1 and r_2 separated by vector $r = r_1 - r_2$ is

$$STR(r) = \langle T(r_1) - T(r_2) \rangle \qquad (1)$$

where < and > represent the (time) mean (Gandin, 1963).

The vector separation contains both distance and direction information. The complexity of the analysis is reduced by the assumptions of homogeneity and isotropy. The homogeneous assumption is satisfied if the structure function is independent of translation of the vector r. This means that the structure is a function of the vector orientation only. The isotropic assumption is satisfied if the structure function is independent of the vector orientation. The allows the structure to be reduced to a function of separation distance only. Both assumptions taken together result in a structure analysis as a simple function of distance, STR(d), where $d=/r/$.

In order to apply the structure analysis to a set of satellite measurements, the structure function is computed as a spatial mean, rather than as a time mean. This is accomplished by considering all possible combinations of pairs of satellite measurements within a single analysis region. For example, the measurement at the first field-of-view (FOV) is compared to the measurements at all other FOVs. Then the measurement at the second FOV is compared to the measurements at all but the first FOV. (The first FOV is avoided in order to avoid duplication of combinations.) The process is continued until all possible combinations of FOVs are considered. The

number of combinations resulting from given numbers of FOVs is illustrated in Table 1. For a 20 by 20 array of satellite data the number of combinations of paired FOVs is 79 800. Even with relatively few FOVs the statistical base of combinations is quite large.

This statistical base is divided into 'bins' depending on the separation distance between the FOVs. The size of the bins is best determined by the inherent spacing of the individual FOVs in the satellite data. For the VAS data used in this study the mean separation between adjacent FOVs is about 14 km between elements (along the scan line) and 24 km between scan lines. Figures 1 (a and b) show the number of pairs of measurements as a function of distance in the line and element directions, respectively, for a 19-line by 20-element array of VAS data. The figures show the regular spacing of paired measurements in each direction. The first peak in each figure represents all pairs of measurements from adjacent FOVs. The second peak represents paired measurements separated by 2 FOVs, etc.

Figure 1c shows a similar frequency distribution of pairs of measurements in all directions. Because of the multitude of distance and angle combinations this figure does not show the regular pattern of Figures 1a and 1b. It would be hard to choose a suitable bin size for structure computation based on this figure. Therefore, a bin size of approximately 14 km, equal to that in the element direction, was used for isotropic computations.

2.1 Noise Estimation By Structure Analysis

One feature of structure analysis is the ability to estimate the noise level in a set of measurements. If a single temperature measurement has a random error component δ, then the measurement T can be divided into its real and noise components.

$$T = t + \delta \qquad (2)$$

It can be shown that the structure function of noisy measurements

$$STR = str + 2\,\sigma^2 \qquad (3)$$

is equal to the structure of the real measurements plus twice the mean-squared random error $\sigma^2 = \overline{\delta^2}$.

Table 1

Number of Combinations of FOVs Taken 2 at a Time (Paired).

Number of FOVs	Number of Unique Pairs
2	1
4 (2x2)	6
9 (3x3)	36
16 (4x4)	120
25 (5x5)	300
100 (10x10)	4 950
400 (20x20)	79 800
900 (30x30)	404 550

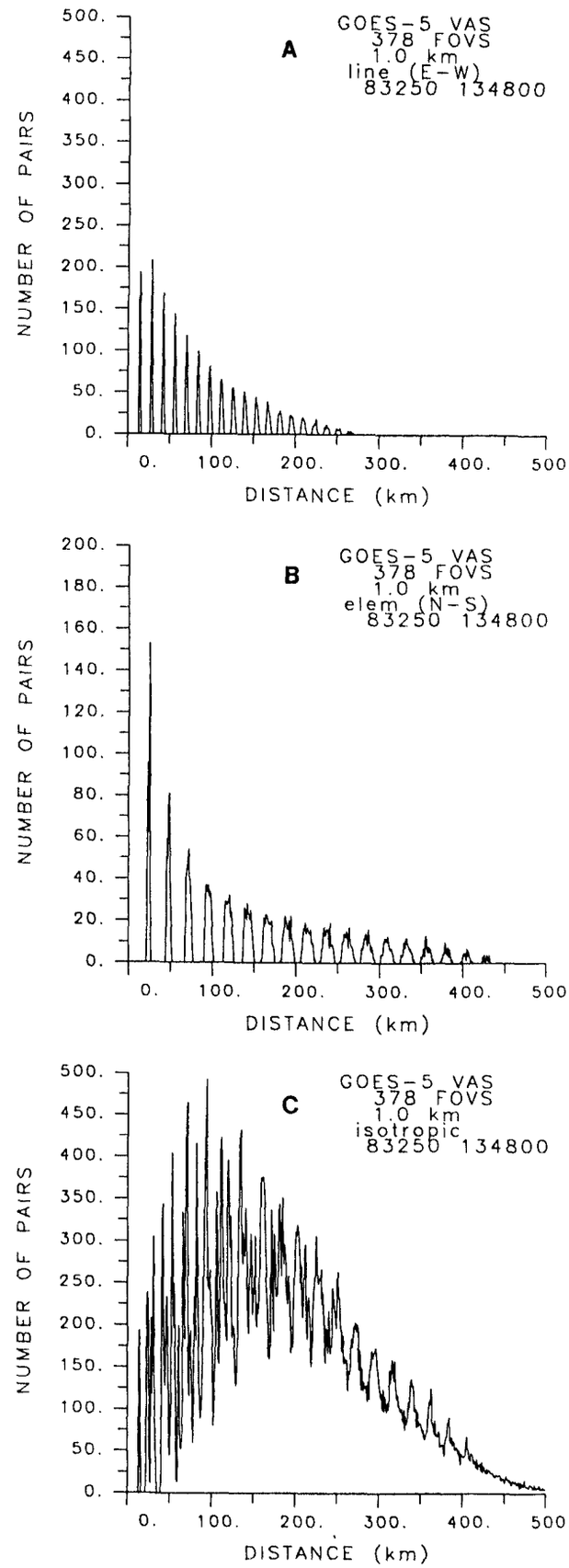

Figure 1. Number of pairs of VAS FOVs as a function of separation distance for a) along-line analysis, b) along-element analysis, and c) isotropic analysis.

Random noise therefore increases the structure by a fixed value independent of separation distance. This allows the error to be determined by extrapolating the structure to zero separation distance where normally str(d=0) = 0., since by definition $t(r_1) - t(r_1) = 0$.

Noise estimation is best illustrated by simulating ideal measurements, with and without added noise. In this case, measurements were simulated at the spacing of VAS FOVs. Simple linear gradients were generated along each scan line and the structure was computed in the same orientation. Figure 2a shows the structure of the simulated measurements without noise. The $y=x^2$ appearance is due to the mean-squared nature of the structure function of a linear gradient. Notice that the structure (or mean-squared difference) at closely-spaced or adjacent FOVs is nearly zero. Figures 2 (b and c) are the structure functions of the same simulated linear gradient with normally-distributed random noise of $\sigma = 0.3$ and 0.5, respectively. The structure for adjacent FOVs is now 0.18 and 0.5, respectively, twice the mean-squared random error. Increased noise is also evident by the small-scale variations in the structure as a function of distance.

In analyzing our data we based noise estimates on the structure at the minimum separation of the data rather than extrapolating the structure to zero separation distance. This was done because of the multitude of results which can be obtained by various extrapolations. The effect of using the structure at minimum separation was an overestimation of the random error component, but in most cases the overestimation was minimal.

2.2 Spatial Scales in Structure Analysis

The gradient information in a set of satellite measurements is also best illustrated by simulated measurements. Whereas Figure 2a is the structure function of a simulated linear gradient, Figure 3a is the structure of a simulated sine wave of wavelength approximately 350 km. By combining the sine wave and the linear gradient the resultant

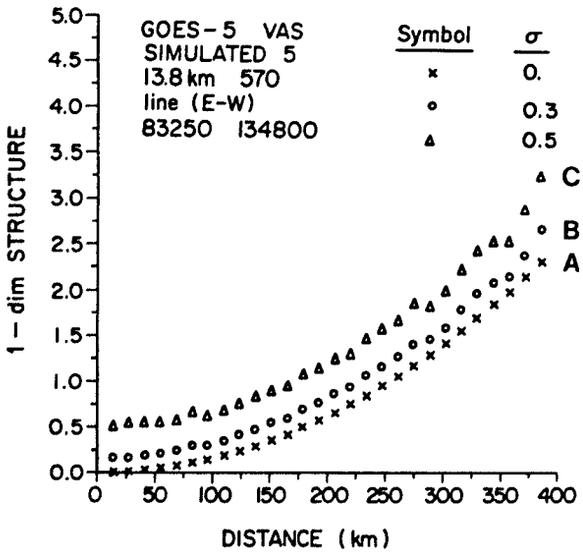

Figure 2. Structure analysis of a simulated linear gradient with a) no added noise, b) noise with a standard deviation of 0.3, and c) noise with a standard deviation of 0.5.

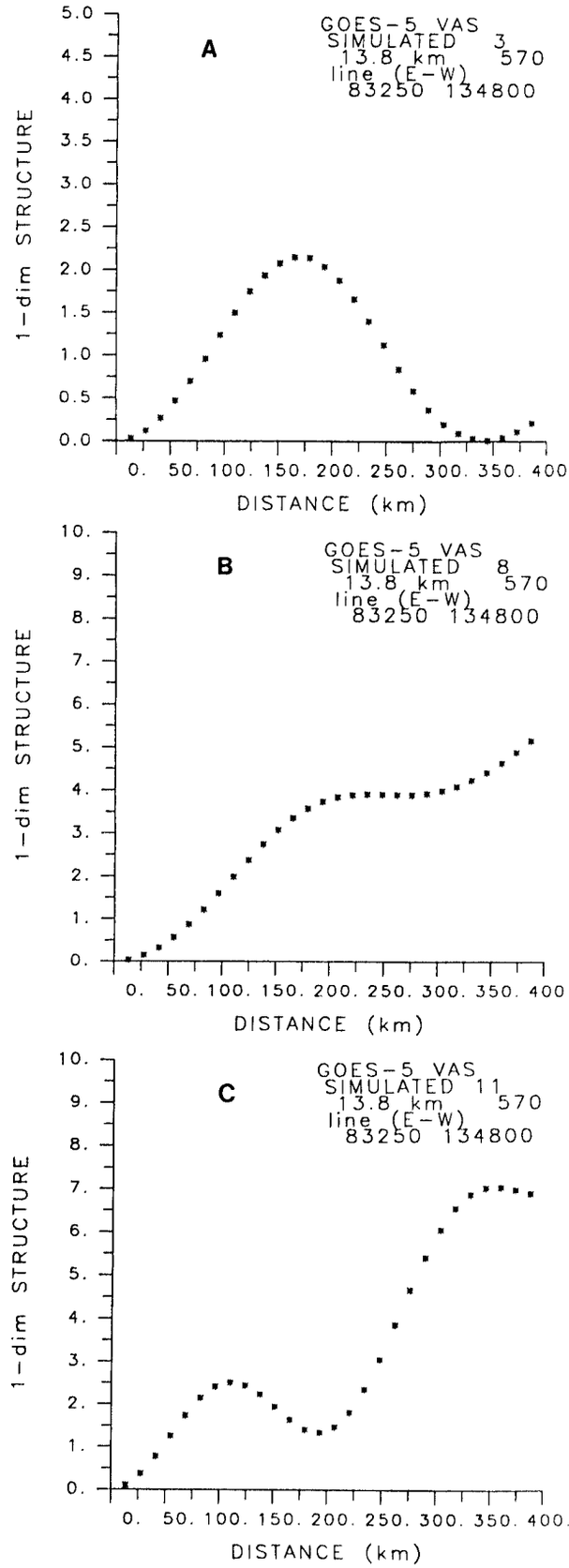

Figure 3. Structure analysis of spatial scales of a) a sine wave of 350 km wavelength, b) a sine wave of 350 km wavelength plus a linear gradient, and c) a sine wave of 200 km wavelength plus a linear gradient.

structure is shown in Figure 3b. Figure 3c shows a similar sine wave and linear gradient combination, this time the sine wave has a wavelength of approximately 200 km.

These figures illustrate how various spatial scales are manifest in the structure function. Since real data contains many such spatial scales of various amplitudes, the results may not be as clearly defined, but some of the predominant spatial scales may be evident.

3.0 STRUCTURE RESULTS FROM VAS

Structure analysis was performed on a sample of VAS measurements for 7 September 1983 at approximately 1348 UTC and Figures 4 (a, b, and c) show the structure of channels 4, 8, and 9, respectively. The analysis was performed in a cloud-free region as determined by the visible channel and infrared window channel.

Figure 4a shows the rather flat structure and high noise level for VAS channel 4 which measures temperatures peaking at approximately 50 kPa. The noise level is estimated to be 0.74 K for this channel. Not much variation or gradient is shown over small distances, but larger structure values beyond 300 km show that a larger-scale gradient exists.

Figure 4b shows the structure for VAS channel 8, which is an infrared window channel. The estimated noise level of 0.43 K is about half that of VAS channel 4. A much larger gradient also exists beyond 300 km, and the small hump from 50 to 100 km shows evidence of spatial structure of approximately 150 km wavelength. This was also evident in channel 4 (Figure 4a).

Figure 4c is the structure functions for VAS channel 9, an H_2O channel with a weighting function peak at about 60 kPa. The estimated noise level is 0.83 K, which is larger than VAS channel 4, but there is more gradient information in this channel. The structure is almost linear to 400 km, which shows evidence of more structure at shorter rather than longer wavelengths (by comparison to the structure of a linear gradient in Figure 2b).

Table 2 summarizes the results of the noise estimation for 11 of the 12 VAS channels. (Channel 11 was missing from the data that were used). Two adjacent areas were analyzed, and are designated Areas 1 and 2. The structure-estimated noise levels should be compared to the observed single sample noise (SSN) values which were obtained by temporal averaging of each channel during calibration sequences (this is the right-hand column under the SSN heading). Results are similar for the two noise estimates, from structure and observed calibration sequences. The channels with the highest noise levels (1, 2, and 9) were similarly identified by both methods.

One way to interpret the estimated noise level in a given channel is to compare it to the variability of the measurements in that channel. This is done by a signal-to-noise (STN) ratio. The STN is the ratio of the variability of the data sample, as quantified by the standard deviation of the measurements, to the estimated noise. Therefore, the STN is a measure of the ability of a channel to detect gradient information above the noise in that channel. Some of the channels with low STN ratios are channels 1 through 4. This is not only because these channels are noisy, but because there is less natural variability higher in the atmosphere

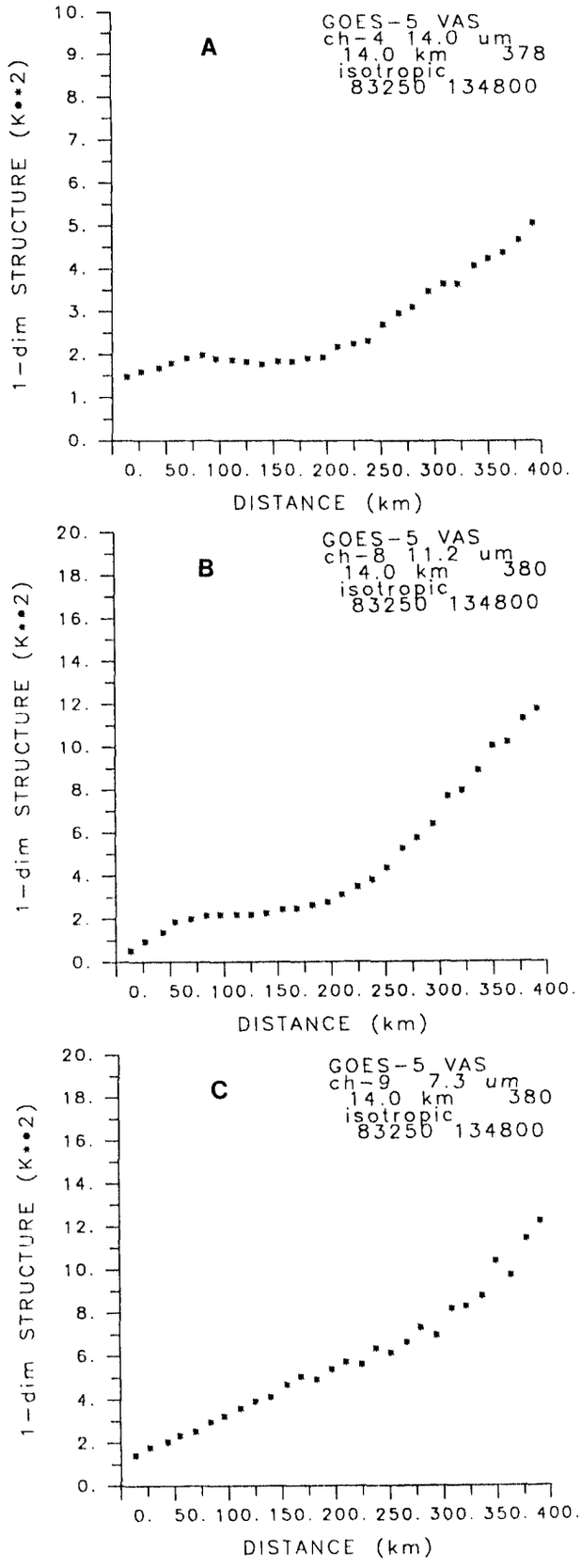

Figure 4. Structure analysis of VAS infrared data for 7 September 1983 at approximately 1348 UTC for channels a) 4 (CO_2), b) 8, (window), and c) 9 (H_2O). The channels show different noise levels and different spatial scales.

Table 2

Structure function analysis of noise levels for VAS brightness temperatures. (Noise is given in Kelvins, signal-to-noise is a ratio.)

VAS channel	Wavelength (μm)	Noise level (Signal-to-Noise) Area 1 (568 FOVs)	Area 2 (567 FOVs)	SSN* Pre	SSN* Obs	SFOV	Required Number of FOVs
1	14.7	2.91 (1.1)	2.71 (1.1)	5.3	3.0	0.3	82 (9x9)
2	14.5	0.84 (1.4)	0.80 (1.3)	2.2	1.7	0.3	7 (3x3)
3	14.3	0.56 (1.2)	0.53 (1.2)	1.8	1.1	0.3	3 (2x2)
4	14.0	0.74 (1.4)	0.49 (1.6)	1.2	0.8	0.2	6 (3x3)
5	13.3	0.57 (2.4)	0.41 (3.1)	1.0	0.6	0.2	4 (2x2)
6	4.5	0.34 (3.2)	0.33 (3.7)	1.6	0.6	0.1	11 (3x3)
7	12.7	0.53 (2.9)	0.38 (4.2)	1.0	0.6	0.2	4 (2x2)
8	11.2	0.43 (3.2)	0.38 (4.4)	0.1	0.13	0.2	4 (2x2)
9	7.3	0.83 (2.0)	0.80 (2.5)	3.4	1.6	0.4	4 (2x2)
10	6.8	0.68 (3.0)	0.66 (3.1)	1.6	1.0	0.5	2 (2x2)
11	4.4	NA	NA	6.7	2.7	0.3	NA
12	3.9	0.36 (3.4)	0.53 (3.5)	0.8	0.3	0.1	13 (3x3)

* Single-Sample Noise (Chesters and Robinson, 1983)

Pre = Pre-launch before temporal or spatial averaging,
Obs - Observed (GOES-5) with temporal averaging during calibration

+ Required Sounding FOV accuracy with temporal and spatial averaging

(mainly the stratosphere) where these channels have their peak emission. Channels with low STN ratios need to be averaged spatially in order to improve the STN in those channels. The STN, therefore, is an inverse measure of the necessary averaging.

The sounding field-of-view (SFOV) accuracy, second from the last column in Table 2, is an indication of the accuracy necessary for each channel to be used in the retrieval process. By employing some spatial averaging, random noise is reduced by the square root of the number of samples in the average. For example, by averaging 4 FOVs the noise should be reduced by a factor of 2, or by averaging 9 FOVs the noise should be reduced by a factor of 3. The last column in Table 2 is a measure of the minimum averaging necessary to achieve the SFOV accuracy when starting with the structure-estimated noise. It was obtained as the square of the ratio of the SFOV accuracy to the structure-estimated noise. A conclusion is that most channels must be spatially averaged in groups of at least 4 FOVs. From this measure, as well as the STN ratios, it is also evident that the upper-tropospheric and stratospheric channels require more spatial averaging than the lower tropospheric channels.

3.1 Spatial-Scale Analysis With Orientation

Variations in the structure functions with orientation for real VAS data are shown in Figures 5 (a, b, and c). Figure 5a is the isotropic structure analysis of VAS Channel 7, which is a water vapor channel with peak emission from near the surface. The structure function shows a relative maximum near 100 km, which is an indication of a spatial feature of about 200 km wavelength.

By breaking down the isotropic analysis into the along-line and along-element components, the structure functions in Figures 5b and c were obtained. Figure 5b shows that the along-line (approximately east-west) analysis contains the

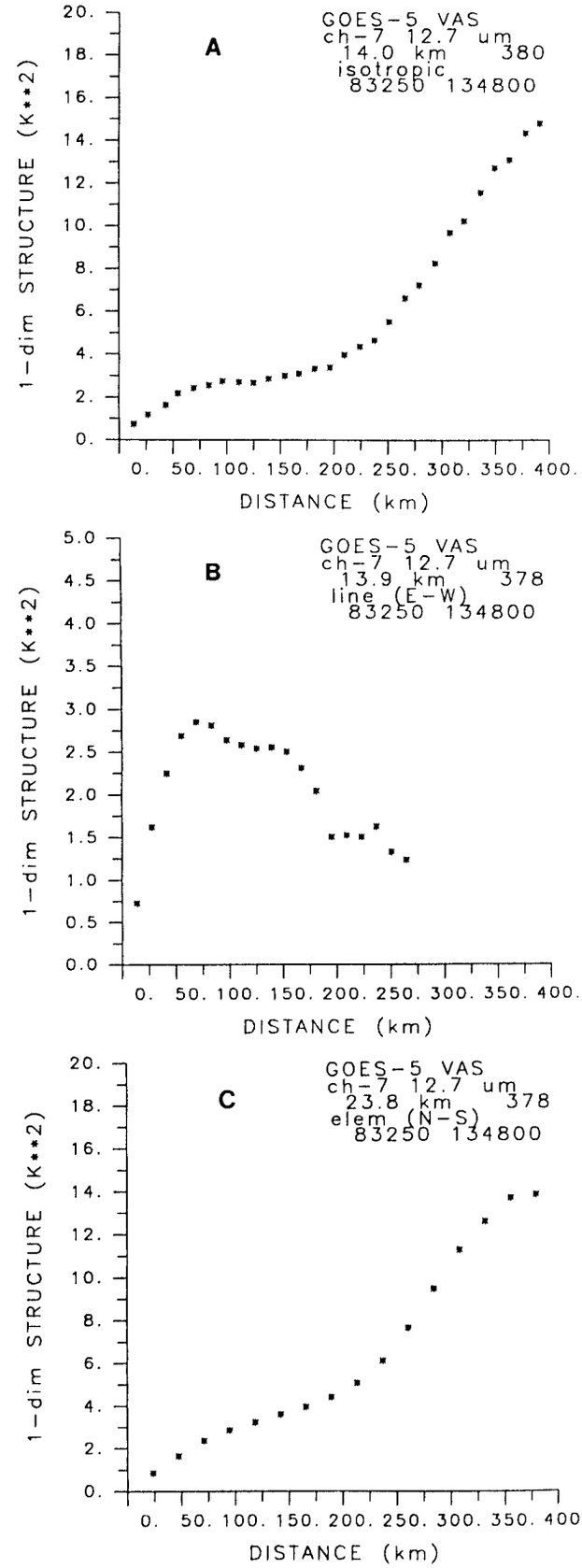

Figure 5. Structure analysis of VAS channel 7 (near window) for 7 September 1983 at approximately 1348 UTC in the a) isotropic, b) along-line (east-west), and c) along-element (north-south) directions.

wave feature of approximately 200 to 250 km wavelength. On the other hand, the along-element analysis (approximately north-south) has little indication of this east-west wave. Rather, a more gradual slope is evident at small structure distances.

4.0 SUMMARY AND CONCLUSIONS

Structure function analysis is an effective means of interpreting satellite data, to determine both the noise levels and the spatial scales or gradient information in a set of measurements. The structure analysis can be performed in an isotropic mode as well as either along or perpendicular to the scan lines. This allows the interpretation of spatial scales as a function of the orientation of the data. Simulated data at the spatial resolution of VAS data was used to aid in the spatial scale analysis. Results of the noise analysis indicate that the VAS channels have noise levels similar to those estimated during VAS calibration sequences. However, to reduce noise levels to the required sounding FOV accuracy, spatial averaging of VAS data must be employed. The amount of averaging necessary was determined by comparing the structure-estimated noise levels to the sounding FOV accuracy required for using VAS data in a temperatures and water vapor retrieval process . We conclude that most channels must be spatially averaged in groups of at least 4 FOVs, with upper-tropospheric and stratospheric channels requiring more spatial averaging than lower tropospheric channels.

ACKNOWLEDGEMENTS

This work was performed under NOAA Grant NA85RAH05045. We thank Mr. Alan Lipton for a review of the manuscript. The VAS data used in this study were obtained from the NESDIS branch at the University of Wisconsin.

REFERENCES

Chesters, D. and W.D. Robinson, 1983: Performance Appraisal of VAS Radiometry for GOES-4, -5, and -6. NASA Technical Memorandum 85125, 55 pp.

Gandin, L.S., 1963: Objective Analysis of Meteorological Fields. Translated from Russian, Israel Program for Scientific Translations, Jerusalem, 242 pp. [NTIS Ref: TT-65-50007].

Hillger, D.W., and T.H. Vonder Haar, 1979: An analysis of satellite infrared soundings at the mesoscale using statistical structure and correlation functions. J. Atmos. Sci., 36, 287-305.

P4.3

VERIFICATION OF SMALL-SCALE WATER VAPOR FEATURES IN VAS IMAGERY USING HIGH RESOLUTION MAMS IMAGERY

W. Paul Menzel

NOAA/NESDIS Advanced Satellite Products Project
Madison, Wisconsin

Gary Jedlovec

Cooperative Institute for Meteorological Satellite Studies
Madison, Wisconsin

Gregory Wilson

Marshall Space Flight Center
Huntsville, Alabama

1. INTRODUCTION

The Multispectral Atmospheric Mapping Sensor (MAMS) is a new instrument designed to produce high resolution imagery in eight visible and three infrared spectral bands from an aircraft platform. Thermal emission from the earth's surface, clouds, and atmospheric water vapor is measured at 12.3, 11.2, and 6.5 microns at up to 50 meter horizontal resolution. Similar infrared spectral bands are part of the VISSR Atmospheric Sounder (VAS) which is capable of 6.9 km horizontal resolution from its geostationary orbit. Sequences of 6.7 micron VAS images have been used to track water vapor structures and to infer atmospheric motion vectors (Stewart et al., 1985). They have also been used to investigate small scale atmospheric moisture variability (Jedlovec, 1984). The high resolution MAMS data give credence to the small scale variations in the VAS water vapor imagery.

The purpose of this paper is two-fold. We shall (1) describe the MAMS instrument and the radiance characteristics, and (2) intercompare some VAS and MAMS radiances and images.

2. MAMS INSTRUMENT CHARACTERISTICS

The MAMS is a modification of NASA's Airborne Thematic Mapper (Daedalus, 1982). The MAMS has two major components, the scan head and the spectrometer (Fig. 1). The scan head consists of the primary collecting telescope, a rotating scan mirror, a motor encoder assembly, and two controlled thermal sources. The field of view is defined by the aperture which is available in two different sizes, 2.5 mrad and 5.0 mrad. The spectrometer consists of optical elements which spectrally separate the polychromatic input energy, lenses which focus the separated energy onto sensors, detectors which convert optical energy to an electrical signal, and pre-amplifiers which condition the signal. The energy collected by the spectrometer is separated into four distinct optical paths using dichroic filters; three paths for the infrared data (one for each spectral band) and one for the visible and near infrared data. The spectrometer detectors are silicon for the visible radiation and mercury cadmium telluride for the thermal infrared radiation. The visible detector is an eight element array which converts optical energy to electrical energy. The spectral response of each band is determined by the dispersion characteristics of the prism placed in the optical path and the location of the array in the dispersed beam. The thermal infrared detectors are each housed in a vacuum dewar which contains a cooled long wave filter which defines the particular spectral band. Each infrared detector has an associated pre-amplifier to process the electrical signal. The spectral bands are summarized in Table 1. The spectral response functions for the three infrared channels of the MAMS (Fig. 2) were specified to be similar to the 6.7, 11.2, and 12.7 micron channels on VAS (also shown in Fig. 2).

The MAMS produces high resolution imagery in these visible and infrared spectral bands from a high altitude aircraft at 20 km as shown in Fig. 3. The horizontal ground resolution, GR, of each individual field of view is 100

Table 1

Rangle of MAMS Spectral Bands

8 visible (microns)	3 infrared (microns)
.42- .45	6.20- 6.85 (upper level water vapor)
.45- .52	10.32-12.02 (window)
.52- .60	12.20-12.56 (lower level water vapor)
.60- .62	
.63- .69	
.69- .75	
.76- .90	
.90-1.05	

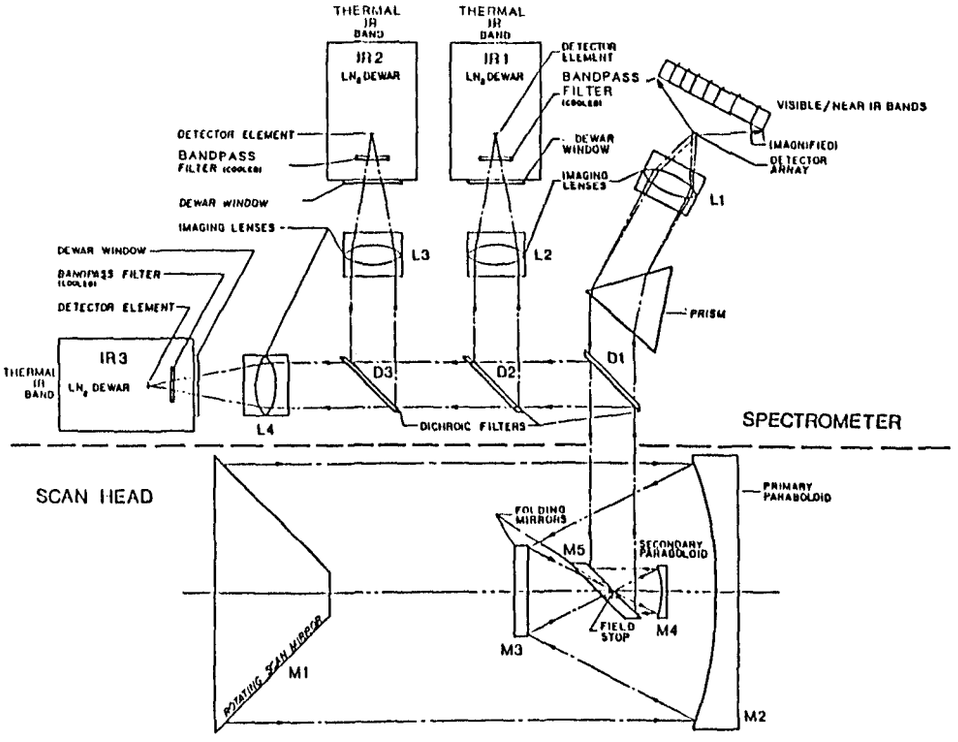

Fig. 1. Schematic of MAMS spectrometer and scan head.

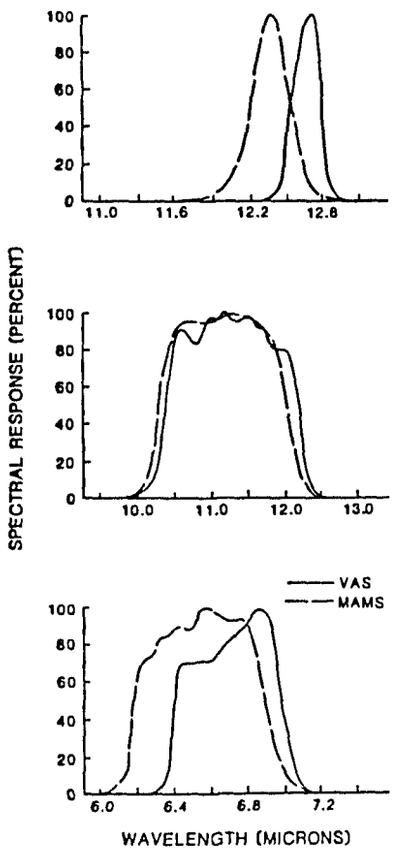

Fig. 2. Spectral response curves indicating the sensitivity of the MAMS and VAS instruments in the 12 micron, 11 micron, and 6 micron regions.

meters (50 meters if the smaller 2.5 mrad optics are used). The total field of view for one scan is 86° which covers the width, w, of the entire cross path of roughly 40 km. The scan rate is 6.25 revolutions per second (12.50 when the 2.5 mrad optics are used) and produces 67% overlap, 1-P, of each scan line with the previous one for nominal aircraft speed (740 km/hr). On each scan line 716 samples are taken so that there is 52% overlap of neighboring pixels along a scan line (4% when the 2.5 mrad optics are used). These overlaps can be used to good advantage to reduce the noise in the scene by spatial averaging.

Radiometric calibration of the infrared data is accomplished by viewing two blackbody sources and by assuming the detector response is linear with respect to radiance (a fractional nonlinearity of less than 5×10^{-4} is observed). Calibration occurs every scan line by viewing a warm and then a cold blackbody of known temperature. For a given spectral band, the radiance is determined from the temperature through the convolution of the normalized spectral response and the Planck function. The calibrated radiances are transformed back into temperatures using the inverse Planck relation with the nominal spectral band center wavelength.

Prior to flight, the gain and offset for each spectral band are adjusted electronically in order to minimize the likelihood of saturation over hot scenes and to maximize the effective operating range. The 6.5 micron band is adjusted to cover 210 to 280°K, while the 11.2 and 12.3 micron bands operate from 220 to 340°K. An eight bit digitizer is used so that for the 6.5 micron band the gain is approximately .3°K per count, and for the remaining surface viewing bands it is approximately .5°K per count.

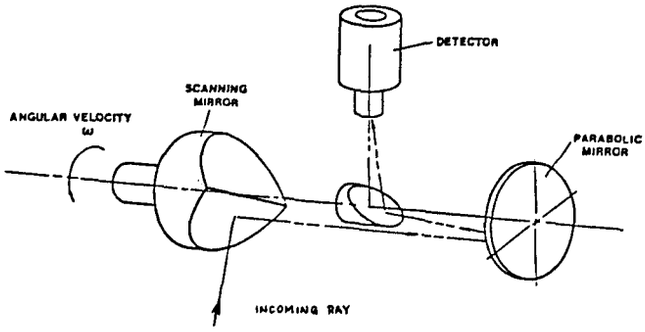

Fig. 3a. A simplified schematic of the inflight configuration of the optical elements of the MAMS.

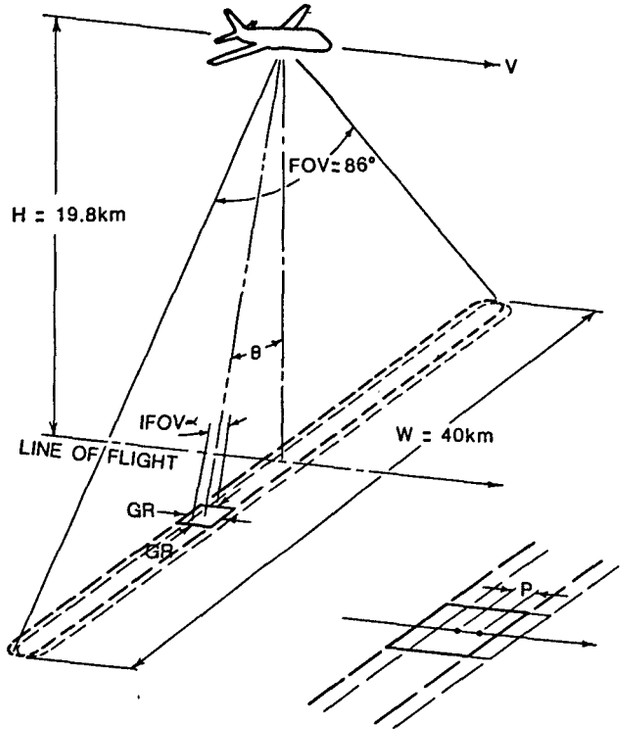

Fig. 3b. Scanning geometry for the MAMS instrument onboard a NASA U2/ER2 aircraft. Lower insert shows position of the center of the nadir ifov for two adjacent scans.

Truncation errors are assumed to be roughly half these values.

The infrared detectors on MAMS exhibit some low frequency noise so that samples taken at 52 microsecond intervals for the spin rate of 6.25 revolutions per second (26 microsecond sampling occurs at 12.5 rps) experience noise contributions with significant correlation. An analysis of covariance (Menzel, 1980) of the noise with the 5 mrad aperture reveals that after averaging ten consecutive samples noise is reduced by a factor of .54, .52, and .37, respectively, in the three infrared spectral bands in order of increasing wavelength (uncorrelated noise would have a factor of $1/\sqrt{10}$ or .32).

Inflight single sample noise values were determined from multiple samples over a uniform portion of the ocean. For a sample size of 100, the single sample noise values with the 5 mrad aperture were found to be .2, .1, and .4°K, respectively, for the spectral bands in order of increasing wavelength (for the 2.5 mrad aperture the values were .5, .2, and .9°K).

3. DATA INTERCOMPARISONS

Radiances for the MAMS and VAS spectral responses were simulated for each band and sensor in a radiative transfer calculation. A representative atmospheric transmittance was computed using a band model and radiosonde temperature and moisture profiles. Table 2 shows that the MAMS detects radiances within one to two mW/ster/m^2/cm^{-1} of the VAS detected radiances. The MAMS spectral responses are shifted to shorter wavelengths (as shown in Fig. 2), hence less radiance is detected. This translates into brightness temperature differences of less than a degree Kelvin.

Table 2

Intercomparison of Simulated Data

	6 micron	11 micron	12 micron
R(MAMS)	7.86	96.5	109.5
T(MAMS)	254.8	287.3	286.0
R(VAS)	8.73	97.5	111.6
T(VAS)	253.9	287.3	285.4
$\Delta T_{MAMS-VAS}$	0.9°K	0.0	0.6

radiances in mW/ster/m^2/cm^{-1}, temperatures in °K

Radiances from the MAMS and VAS were collected simultaneously over a relatively isothermal area of ocean off the California coast on 18 May 1985. Table 3 presents the comparison. After compensating for the inherent spectral differences of the two instruments, the MAMS data is within .5, 2.5, and 1.5°K of the VAS data, respectively, for the spectral bands in order of increasing wavelength. The observed split window channel differences (11 micron less 12 micron) are comparable, 2.5°K for MAMS and 2.1°K for VAS and thus showing similar low level moisture concentrations. The observed water vapor channel data (6 micron) show MAMS detecting upper level moisture concentrations very much like VAS, with MAMS showing somewhat less attenuation than VAS. These comparisons

Table 3

Intercomparison of Observed Data

	6 micron	11 micron	12 micron
R(MAMS)	6.01	99.9	111.1
T(MAMS)	247.1	289.5	287.0
R(VAS)	6.80	97.0	111.1
T(VAS)	246.5	287.1	285.0
$\Delta T_{MAMS-VAS}$	.6°K	2.4	2.0

radiances in mW/ster/m^2/cm^{-1}, temperatures in °K

are quite reasonable, since the spatial resolution of each sensor is very different (VAS at 7 km and MAMS at .05 km at nadir), the navigation of the MAMS data is from visual siting of landmarks only, and non-nadir viewing of the MAMS has not yet been taken into account.

Imagery from the MAMS and VAS were compared from flights over Oklahoma and Kansas on 12 May 1985. The goal of the intercomparison is to verify small scale features observed in the VAS water vapor images with the higher resolution MAMS data. These water vapor inhomogeneities in the VAS data have been used to obtain motion vectors when several images are considered in sequence. While the imagery is often too amorphous to track winds reliably with a correlation technique, it has produced good wind fields by single pixel tracking (Stewart et al., 1985). The MAMS data tends to verify that small scale gradients (down to several single pixels) in the VAS data are real. Fig. 4a shows the VAS 6.7 micron images with the MAMS flight track superimposed while Fig. 4b shows the 6.3 micron MAMS data (at 400m resolution for display) gathered in flight from C to H. These images were enhanced to delineate the moisture features. Brighter (colder) regions represent clouds or relatively high water vapor content and darker (warmer) areas represent drier air in the middle layer of the atmosphere. The MAMS images are not limb corrected and, therefore, images appear brighter (colder) toward the edges. The moisture features compare very nicely; starting at G, MAMS shows a dry tongue giving way to a moist ridge which becomes less moist at H. Fig. 5a shows single pixel resolution of the VAS image covering the MAMS track from E to F of Fig. 4a; Fig. 5b displays the MAMS data covering the boxed region of Fig. 5a. The temperatures from brightest to darkest pixels within the boxed-in area differ by 5°K indicating that these fluctuations are not instrument noise, but real atmospheric features. Six of the VAS features are corroborated nicely by the MAMS image. This lends credence to the assertion that the VAS distinguishes moisture features which are small enough to represent a wind vector, yet large enough to exist in several successive images. The features we are examining were discernible for at least two hours in the VAS images.

4. CONCLUSION

The MAMS measures thermal emission from the earth atmosphere system in eight visible and three infrared spectral bands (12.3, 11.2, and 6.5 microns) at up to 50m horizontal resolution. These infrared bands are very similar to three of the VAS infrared spectral bands. The instrument was flown aboard a NASA U-2 in May-June 1985 and corresponding VAS data was collected. MAMS radiometric performance is comparable to that of VAS. The MAMS exhibits somewhat less attenuation from water vapor than VAS because its spectral bands are shifted to shorter wavelengths away from the absorption band center. Intercomparisons of these images give credence to small scale variations in the VAS water vapor imagery. Attempts are underway to identify the scales of which these features must be tracked to depict the preconvective environment.

The MAMS has been developed to combine high resolution visible and infrared measurements to study small scale atmospheric moisture variability, to monitor and classify clouds, and to investigate the role of surface characteristics in the production of clouds, precipitation, and severe storms. As part of the Cooperative Huntsville Meteorological Experiment (COHMEX), the MAMS will be flying this summer to gather data for these studies.

5. ACKNOWLEDGEMENTS

This work was performed on the University of Wisconsin Man-computer Interactive Data Access System (McIDAS) under NASA support. Mr. John Arvesen and Mr. Jeff Myers at NASA/Ames contributed to the MAMS data collection and processing. Mr. Bob Atkinson at NASA/MSFC assisted in the calibration of the flight data.

6. REFERENCES

Daedalus, 1982: Operator's Manual: AADS1268 digital multi-spectral scanner system. Daedalus Enterprises, Ann Arbor, MI.

Jedlovec, G. J., 1984: Mesoscale analysis of 6.7 micron image data from the VISSR Atmospheric Sounder (VAS) for several case studies. Conf. on Satellite/Remote Sensing and Appl. AMS, Boston, 185-190.

Menzel, W. P., 1980: Prelaunch study report of VAS-D performance. Repot on NASA contract NAS5-21965, Space Science and Engineering Center, University of Wisconsin, Madison, WI.

Stewart, T. R., C. M. Hayden, and W. L. Smith, 1985: A note on water-vapor wind tracking using VAS data on McIDAS. BAMS, 66, 9, 1111-1115.

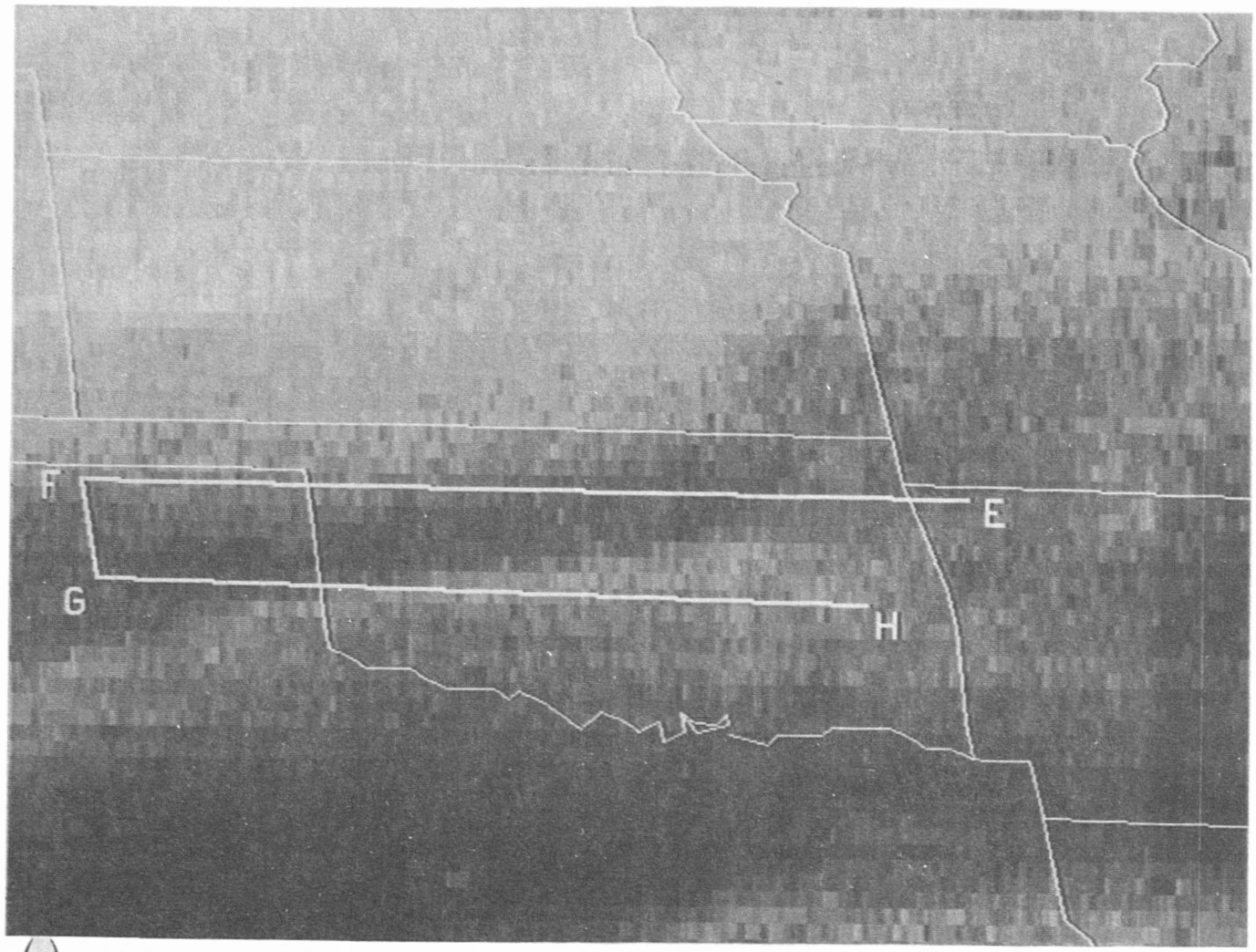

(A)

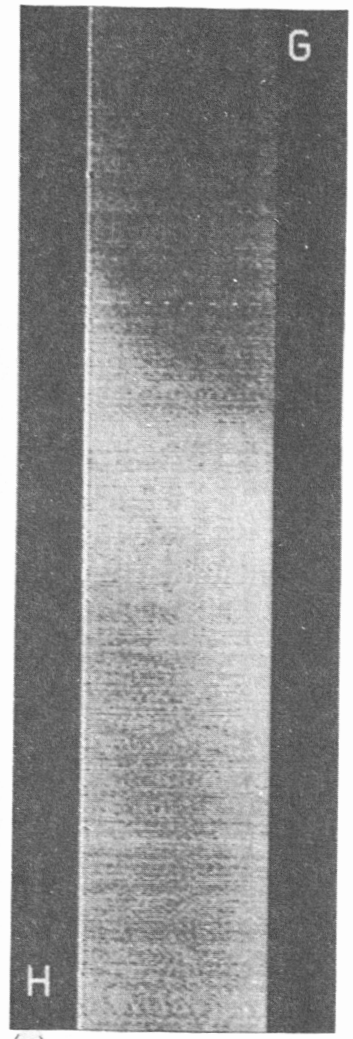

(B)

Fig. 4a. Enhanced VAS water vapor image with the MAMS flight track superimposed for 18 May 1985 at 1701 GMT.
Fig. 4b. Corresponding MAMS 6.3 micron enhanced image gathered in flight from G to H on 18 May 1985 at 1707 GMT.

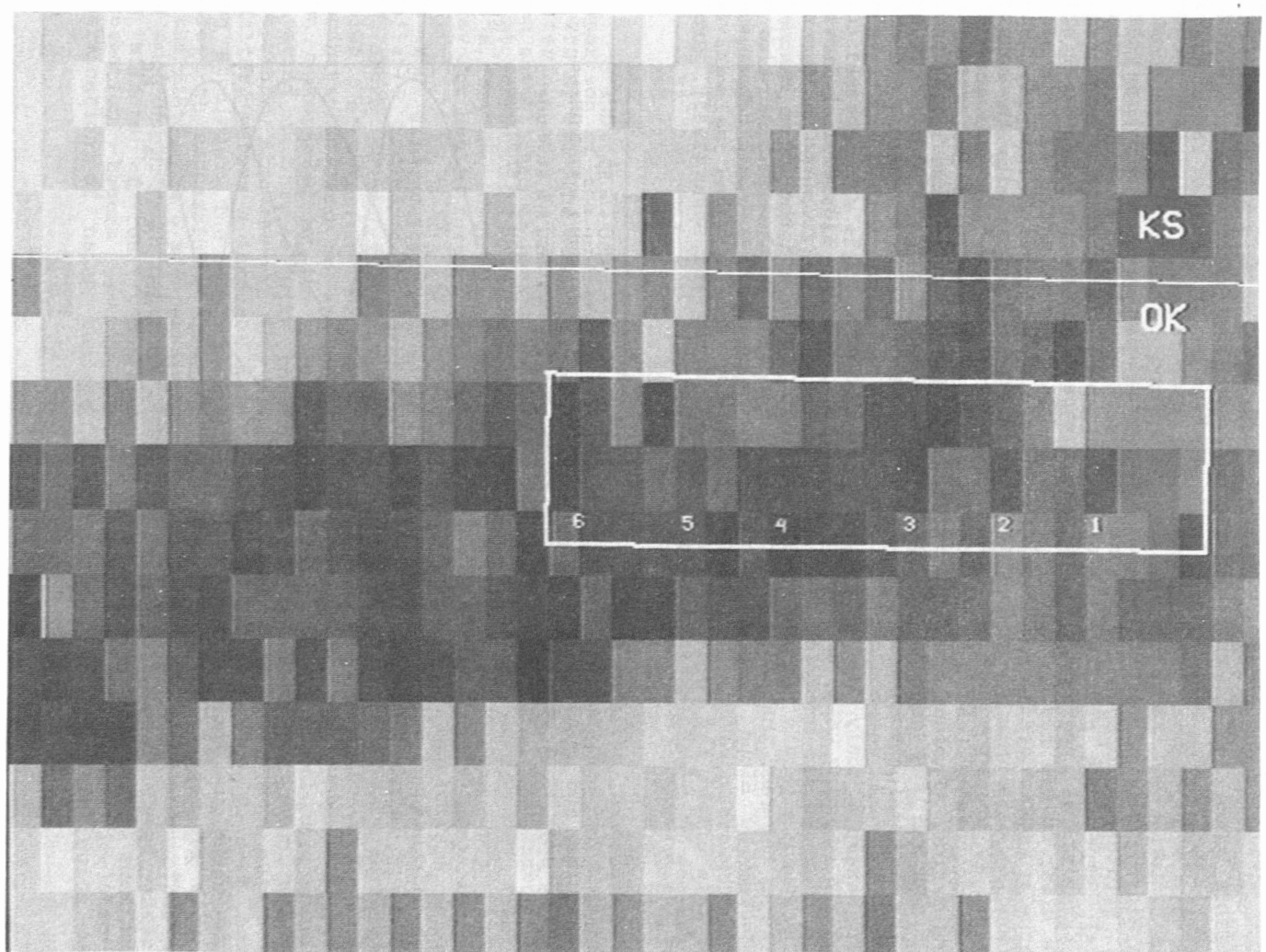

(A)

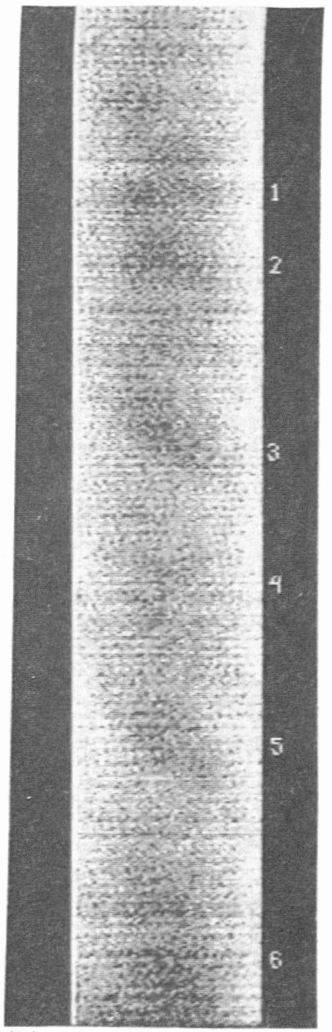

(B)

Fig. 5a. Magnification of 4a showing single pixel variation along flight track E to F.
Fig. 5b. Corresponding MAMS data covering the boxed area of 5a. Six comparable water vapor gradient features are labeled.

P4.4

Precipitation Effects on Microwave Sounding Unit Data

A. Nappi, A. Swaroop
Systems and Applied Sciences Corporation Technologies
Hyattsville, MD 20704

N.C. Grody
NOAA/NESDIS
Suitland, MD 20233

J. Weinman
University of Wisconsin
Madison, Wisconsin 53706

1.0 Introduction

Satellite derived global temperature and moisture soundings have been produced operationally from the TIROS-N series satellites at NOAA/NESDIS since 1979. The NOAA Polar orbiting satellites provide radiance measurements from a 20 channel High Resolution Infrared Radiation Sounder (HIRS/2), a 4 channel Microwave Sounding Unit (MSU) and a 3 channel Stratospheric Sounding Unit (SSU). Vertical temperature profiles are produced by a statistical regression scheme which utilizes clear column radiances for the infrared channels and a coefficient data base. These sounding data consist of retrieval temperature at 40 pressure levels from 1000 mb to 0.1 mb, geopotential heights and water vapor mixing ratios. Various combinations of HIRS/2, MSU and SSU sounding channels are used in the regression scheme to produce soundings for different meteorological conditions. For example, only the 4 microwave, 3 stratospheric sounding unit, and 3 stratospheric HIRS/2 channels are used for cloudy retrievals. The heavy emphasis placed on microwave data reflects the fact that they are relatively unaffected by cloud liquid water. The lowest two channels however, are the most affected and this effect may become significant in the presence of precipitating cloud.

Various methods have been devised to minimize the effect of rain con tamination on the brightness temperatures and ultimately the quality of the final retrieved profile. The current TIROS Operational Vertical Sounder (TOVS) approach determines which microwave scan spots are precipitation contaminated and removes them from consideration for making a retrieval. This approach utilizes both infrared and microwave data, however, for cases of infrared instrument failure, as occurred on NOAA-6, a method dependent only upon microwave data is necessary. This has been developed and employs a median comparison filter which compares the limb-corrected brightness temperatures for a microwave scan spot with a median value computed from a surrounding field of data. This techniques has been tested on various types of meteorological cases and will become an operational algorithm.

2.0 The TOVS Microwave Sounding Unit

Measurements from the 4-channel microwave sounding instrument on board the NOAA Polar orbiting satellites are used in the operational retrieval algorithm. The sounder has radiometers which measure radiation in the oxygen band at 4 frequencies; 50.30, 53.74, 54.96 and 57.95 GH_z. There are 11 scan spots or fields of view (FOV) per scan line. The size of the spots is approximately 110 km. at nadir. The TOVS processing software further divides the data into fields of 10 lines by 11 spots, making the technique fairly simple. Figure 1 displays the weighting functions associated with each of the 4 microwave channels and indicates the contribution of temperature, at different pressure levels, to the brightness temperature. As previously stated, only the lowest 2 frequencies are adversely affected by cloud liquid water and that effect is most significant for the 53.74 GH_z channel for precipitating clouds. Figure 1 indicates that the contribution from this channel peaks at about 700 mb and the other channels either peak too high in the atmosphere to be significantly affected by precipitation, or are affected by the surface, as well as precipitation, Grody and Shen (1982), Grody (1983).

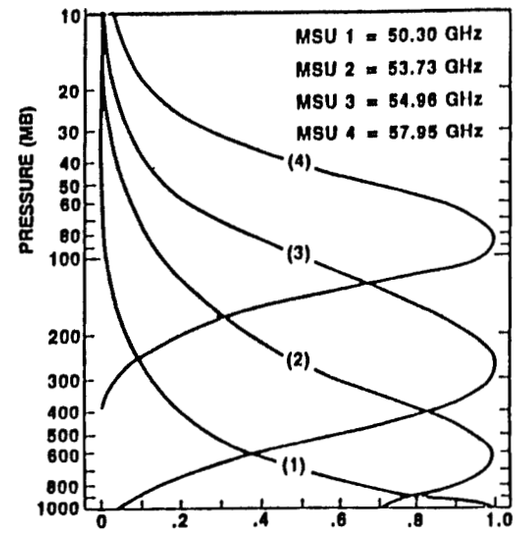

Over oceans, the current TOVS techni- que to identify precipitation contamination uses an algorithm which depends upon both the 53.74 and 50.30 GH_z window channel to obtain the amount of liquid water attenuation. However, due to the variable emissivity over land, which renders the window channel unreliable, this approach is modified to use the 11 micron window channel of the HIRS/2 instrument instead for land areas. When no infrared data are available, as is the case for satellite NOAA-6, this approach falters and no determination of rainfall attenuation is possible over land. Since the 50.30 GH_z channel is not usable, but the 53.74 GH_z channel is essentially opaque to the surface, a technique was developed to use solely the 53.74 GH_z channel with the median filter approach.

3.0 The Median Filter Approach

The use of median filters in identifying discontinuities in data fields has been referred to by WU, et al. (1985) and Shultz (1985) and is well suited to the task of correcting for noise in the elements of an array. For a field of values, such as the 10 by 11 array of MSU brightness temperatures, noise spikes can be easily isolated and the noise eliminated. One method of achieving this is to replace the noisy element with the median value for the array. Obviously, determination of what constitutes noise for a given set of numbers is crucial to the proper application of a median filter for those values. A critical value must be determined, to which the array elements are compared. If the critical value is exceeded, the noisy element is removed or replaced with the median value. This type of median filter is known as a comparison filter. An example of this technique for a 3 x 3 filter for an array of brightness temperatures, degree Kelvin, might be as follows:

252	252	253
253	250	254
253	254	255

Comparison of the unfiltered central point, at 250°K, with the median of 253°K produces a difference of 3°K. If the critical value has been established to be 3°K or less, this data point is removed and the value of the median, 253°K, may be inserted in its place in the array for use in further processing.

The MSU grid pattern provides a readily available 2 dimensional array for applying the above median filter technique. The scales of motion involved in heavy precipitation tend to approximate the size area encompassed by the 3 spot by 3 line filtering techniques with the 110 km MSU footprint. Also the validity of using a 3 x 3 filter, versus a larger 5 x 5 filter, has been studied. The results indicated that while both successfully identify the median of the field, the 5 x 5 technique encompasses too much north-south distance (~550 km) and the effects of real temperature gradient information become smoothed while the determination of noise becomes imprecise. The meridional temperature contrast overrides, in some cases, the local, precipitation driven anomaly and cause an unrepresentative median to be computed. Comparison with this value may cause unwarranted removal of valid data, or unintended inclusion of noisy measurements. Experiments using the 3 line by 3 spot median comparison filter, as well as previous work by Grody (1983) have indicated that attenuation due to rainfall affects the 53.74 GH_z microwave channel most severely and it appears that a decrease of greater than about 1°K in the limb corrected brightness temperature for that channel is a signature of significant rain contamination. This corresponds well with radar echoes of intensity 2 or higher (greater than 0.2 inches/hour) and seems to be valid for squall line convective type precipitation over land or ocean. For these reasons, the comparison median filter technique which identifies contaminated data uses only 53.74 GH_z channel, with a 3 x 3 filtering array and a critical threshold value of 1°K. Case studies using this approach are presented for both land and sea cases in the next section.

4.0 Case Study Results

Two case studies are presented to illustrate the effect of rain contamination on microwave sounding unit data and the use of a median filter approach to attempt to lessen that effect. One case involves rainfall from a squall line over the United States, the other involves rainfall from a hurricane over both sea and land.

The first case shown involves data from 12 September, 1984 during Hurricane Diana. This storm was bringing heavy rains to the North Carolina coast and the adjacent ocean area. A TOVS orbit passed over this area at about 1245 GMT 12 September. Figure 2 presents NMC radar data contoured at intensity levels 1 and 3, at 1135 GMT and the contours of the 53.74 GH_z channel limb-corrected brightness temperatures drawn every 0.5°K. The effect of the precipitation is shown by the decrease of the brightness temperature over the area of strong radar echoes. A cold anomaly exists in the otherwise uniform field which might be expected with this type of tropical system. To further examine this effect, the brightness temperatures at individual scan spots around this system are given in Figure 3. The hundreds digit is dropped for clarity. Once again, it is obvious that a cold anomaly exists in a fairly uniform field which even hints of a warm intrusion as evidenced by the southwest-northeast orientation of the 258.5 and 258.0 isotherms. The amount of decrease in temperature due to precipitation appears to be in excess of 1.5°K. Figure 4 gives the median filtered field minus the measured one. The area of greater than 1°K temperature decrease is shown and corresponds well with the heavy rain area. These values are typical of many of the cases examined. The filtering technique has isolated the region of rain contamination quite well. Figure 5

represents the effect on the temperature field of adding the decrease detected by the filter to the original values. This resulting median corrected brightness temperature field indicates that the cold anomaly has been removed (compare figures 3 and 5). The dashed line indicates the position of the filtered out cold anomaly. Notice that the overall structure of the field remains mostly unchanged, preserving the integrity of the synoptic-scale temperature gradient information.

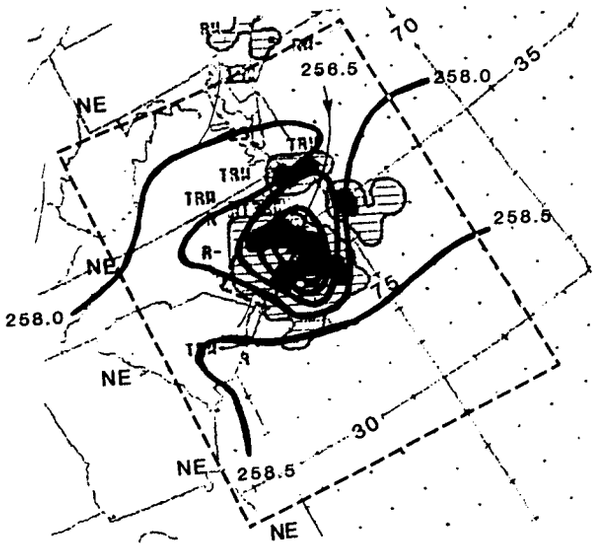

Figure 2. NMC radar summary and 53.74 GH_z channel brightness temperature for 1135 GMT 12 September, 1984. Temperature contour interval is 0.5°K. Radar echoes are contoured by intensity. Contour interval is 2. Shading indicates greater than level 3 echo.

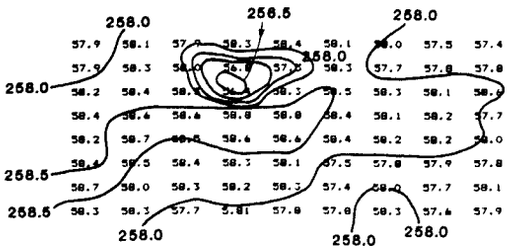

Figure 3. Limb corrected unfiltered 53.74 GH_z channel brightness temperature for 1246 GMT 12 September, 1984. Hundreds digit is dropped for clarity. Contour interval is 0.5°K.

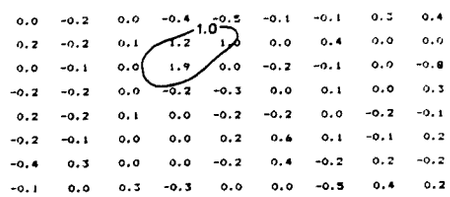

Figure 4. Median minus measured brightness temperature in °K for 1246 GMT 12 September, 1984. Hundreds digit is dropped for clarity. Contour interval is 1.0 °K.

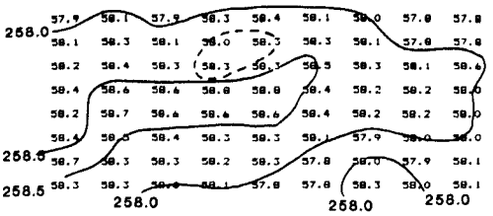

Figure 5. Median corrected brightness temperature in °K for 1246 GMT 12 September, 1984. Hundreds digit is dropped for clarity. Contour interval is 0.5°K.

The second case is presented in similar fashion as the first and involves a squall line studied by Grody (1983). Figure 6 shows the radar echoes and 53.74 GH_z limb-corrected brightness temperature contours every 2°K. The radar data is for 1935 GMT 11 April 1979 and the satellite data is for approximately 2040 GMT. A much more dramatic example of the effect of rainfall can be seen, as a large decrease due to precipitation occurs in an area of a temperature ridge. A synoptic scale surface temperature gradient exists across the squall line but the heavy convective rainfall, often exceeding level 4 intensity (greater than 2.2 inches/hour) appears to cause severe attenuation in the 53.74 GH_z channel. A more detailed view is provided by figure 7 which shows a minimum spot value of 242.2°K surrounded by measurements in the 250-255°K

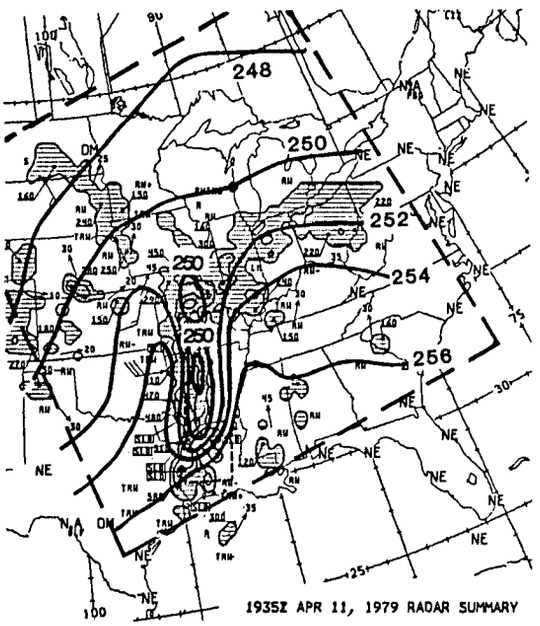

Figure 6. NMC radar summary and 53.74 GH_z channel brightness temperature for 1935 GMT 11 April, 1979. Temperature contour interval is 2°K. Radar echoes are contoured by intensity. Contour interval is 2. Shading indicates greater than level 3 echo.

range. The field is severely contorted by the large decreases in temperature along the length of the squall line. Figure 8 depicts the median field minus the measured one. The values approaching 9°K are by far the largest of any case studied. This case represents a worst case scenario for rain contamination. Notice that the attenuation is quite significant over large linear extent of about 6 array elements. Figure 9 presents the median corrected brightness temperature. Though a rain induced temperature trough still exists, the severity of the effect is dramatically lessened (compare figures 7 and 9). Brightness temperatures have increased by up to 8°K in the affected area. The dashed line indicates the extent of the affected area. Temperature retrievals made with this data should show much less effect due to precipitation.

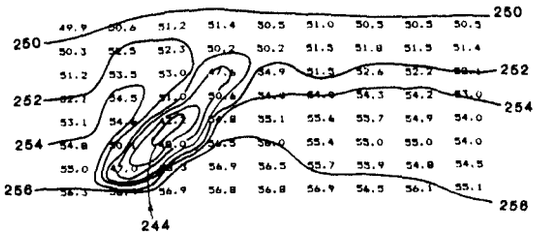

Figure 7. Limb corrected unfiltered 53.74 GH_z channel temperatures for 2040 GMT 11 April, 1979. Hundreds digit is dropped for clarity. Contour interval is 2°K.

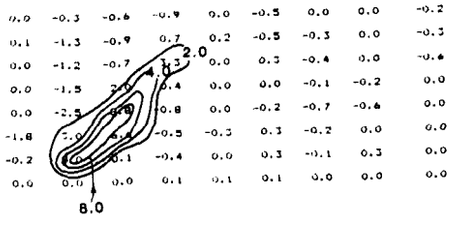

Figure 8. Median minus measured brightness temperature in °K for 2040 GMT 11 April, 1979. Values greater than 2.0°K are contoured. Contour interval is 2.0°K.

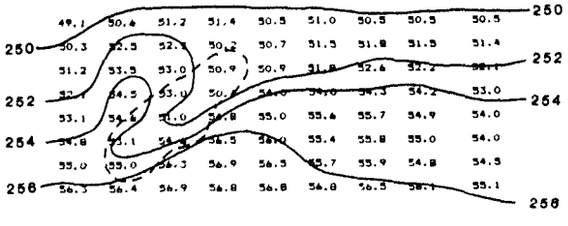

Figure 9. Median corrected brightness temperature in °K for 2040 GMT 11 April, 1979. Hundreds digit is dropped for clarity. Contour interval is 2°K.

5.0 Conclusion

It has been shown that liquid water in the form of rainfall produces attenuation in the 53.74 GH_z channel, limiting its usefulness in a retrieval scheme. This effect reduces the measurements by more than 1°K for moderate to heavy rain. Two cases have been presented which graphically illustrate this rain effect and a new technique has been presented which attempts to remove the degradation. A comparison median filter approach has been developed for use by the TOVS system and a 3 x 3 filter is applied to the data to isolate rain induced noise which may lead to erroneous retrievals. Use of this filter for these cases reveals quite encouraging results. The effects of attenuation were removed in a typical case and greatly reduced in a worst case scenario. Currently the affected data as removed from consideration for making retrievals, although it should be possible to obtain retrievals using the median corrected brightness temperature field. Production of successful, accurate retrievals in rain areas will greatly enhance the contribution of the microwave instrument to making high quality global soundings.

Acknowledgements

The authors wish to acknowledge the following people for their help and useful suggestions: Charles Novak and Michael Chalfant of NESDIS and Dr. Zia Ahmad, and Michael Liu of SASC Technologies. The authors are also thankful to Ms. Lorna Crawford for typing the manuscript.

References

Grody, N.C., 1983: Severe Storm observations using the Microwave Sounding Unit. Journal of Climate and Applied Meteorology, Vol. 22, No. 4, 609-625.

Grody, N.C. and W. C. Shen, 1982: Observations of Hurricane David using the Microwave Sounding Unit. NOAA Tech. Rep. NESS 88, 52 pp.

Schultz, H. 1985: A Median filter approach for correcting errors in a vector field. Digest, Volume 1, 1985 International Geosciences and Remote Sensing Symposium (IGARSS '85), Amherst, Mass.

Smith, W., Wolf, H. Hayden, C., Wark, D. McMillin L., 1979: The TIROS-N Operational vertical sounder. Bulletin Amer. Meteor. Soc. 60, pp 1177-1187

Swaroop, A., Nappi, A., Ahmad, Z., Chalfant, M., McMillin, L. Reale, A., 1985: Enhanced Soundings over oceans from NOAA-9 Polar orbiting satellite. Preprints, MTS/IEEE Conference and Exposition, San Diego, CA.

WU, R., Weinman, J., Chin, R., 1985: Determination of rainfall rates from GOES Satellite images by a pattern recognition technique. Journal of Atmospheric and Ocean Technology, Volume 2, 314-330.

P4.5

TROPICAL SYNOPTIC INTERPRETATION OF INTER-CHANNEL CORRELATIONS FROM TIROS N

J. P. McGuirk, L. L. Anderson, Jr., and A. H. Thompson

Department of Meteorology, Texas A&M University
College Station, TX 77843-3146

1. INTRODUCTION

In the tropical northeast Pacific, a synoptic event, called a "moisture burst," occurs commonly (Smith et al., 1986; McGuirk and Thompson, 1984). The data-sparse nature of the region precludes accurate diagnoses of the structure of these events. The most appropriate data set for the study of these systems is quantitative satellite data, particularly individual channel brightness temperatures. This data format is preferable to the reconstructed temperature and moisture profiles because the reconstructions have a tendency to smooth in both the horizontal and the vertical.

This paper describes synoptic variability contained in a set of TIROS N brightness temperatures for a nine-day period during January 1979, between the dateline and 90°W and between 30°N and 20°S. The spatial coherence of each channel is described as functions of interchannel differences and geographic and synoptic variations. Second, horizontal and vertical patterns of individual channels are examined through empirical orthogonal functional (EOF) decomposition. Finally, response surface regression models are developed to predict missing TIROS N channels from available TIROS N and NOAA-5 data.

All three analyses present considerable organized synoptic variability in tropical systems for which the synoptic thermodynamic signal is normally weak.

2. SPATIAL COHERENCE

To examine the spatial coherence of the brightness temperatures in a given channel, the correlation coefficient was calculated for each observation with respect to all other observations during the same synoptic time and throughout the domain. The correlations were stratified by horizontal separation distance between pairs of observations. Separation distances ranged between zero and 2500 km, in 250 km increments. For nearly all channels and nearly all separation distances, at least 150 pairs of observations contributed to the correlation coefficient for a given time period, yielding a 95% confidence estimate of ±0.1 for the amplitude of the correlation coefficient at any specific separation distance.

2.1 Inter-Channel Differences

A single time period, 24 January 1979 at 12 GMT, was selected to examine the differences in horizontal coherence between the different TIROS N channels. The channels were divided into six groups, based on the absorbing characteristics at the specific wavelength of the channel, as well as the shape of the channel weighting function. The channels of a given group possessed similar coherence properties. See Table 1 for these groups and Smith et al. (1979) for a detailed description of channel characteristics.

Table 1

Channel groupings for spatial correlations.

Emission source	Channel numbers
Tropospheric (thermal)	13, 14, 15, 16
Tropospheric (thermal, H_2O sensitive)	4, 5, 6, 7
Water vapor	10, 11, 12
Stratospheric	1, 2, 3
Surface (window, boundary layer)	8, 13, 14, 18, 19
Microwave (MSU 1, 2, 3, 4) noted as 21, 22, 23, 24	

By way of example, Fig. 1a shows the correlation coefficient as a function of separation for the two tropospheric thermal groups. For zero separation, the correlation is 1.0; observations correlate perfectly with themselves. As the separation distance increases, the channel observations become less correlated, as expected. For distances greater than 750 km, the correlation in channels more sensitive to water vapor falls off much more rapidly. These correlation profiles are compared most easily through the integral length scale (the area under the correlation curve to the left of the first zero crossing). This scale provides a single number estimating the mean correlation distance; it should be related to the length scale of atmospheric variation. The maximum difference in integral length scales in Fig. 1a (between Channels 4 and 14) is 650 km (1820 km vs. 1170 km; these are the approximate distances at which two observations in the same channel will become uncorrelated).

Correlations for a typical channel from each of the six groups of Table 1 are shown in Fig. 1b. Prior to interpreting this figure, some exceptions are first noted. The stratospheric channels varied widely in length scale, from about 900 km to well over 2000 km, exceeding the detectable length scale within the observation domain. The same was true of the microwave channels, in

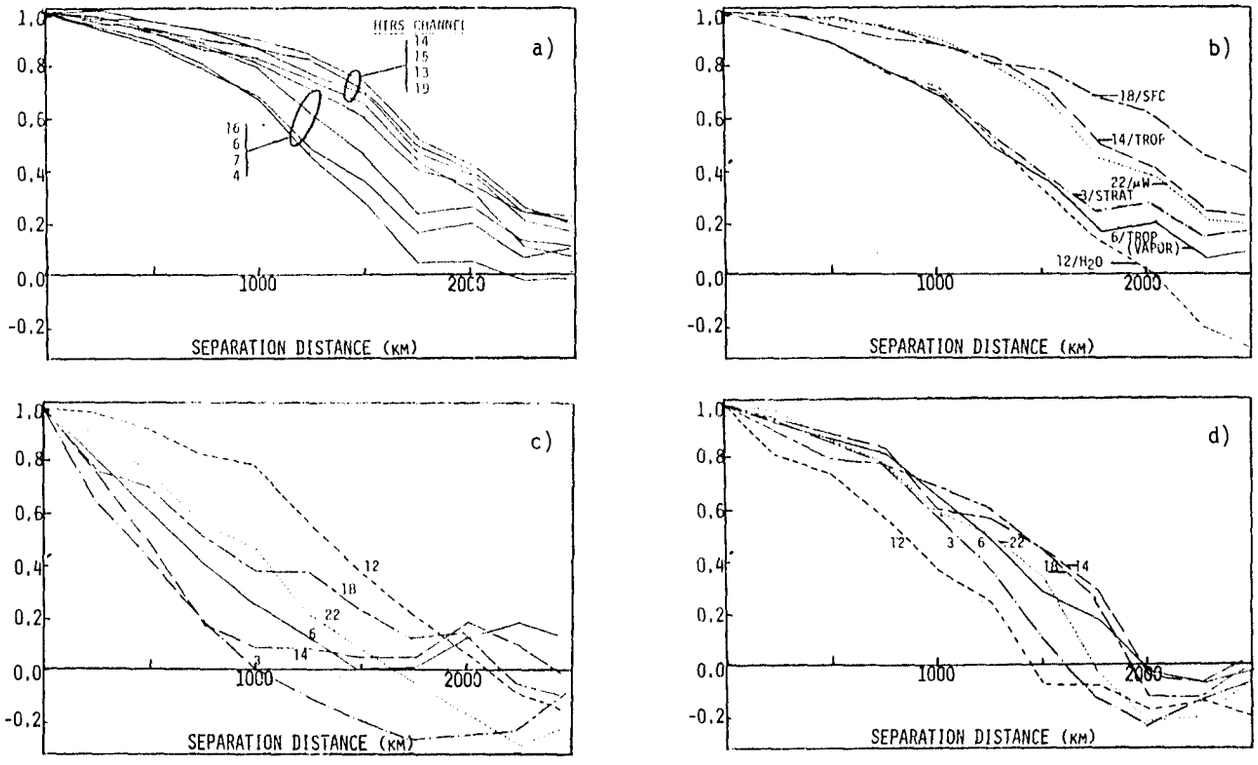

Fig. 1. Individual channel brightness temperature correlation (ordinate) as a function of separation distance between pairs of observations (abscissa). a) For all tropospheric infrared signals and for the entire region. b) For six representative channels and for the entire region. c) As in (b), but for an equatorial strip. d) As in (b), but for a subtropical strip. See text for details and see Table 1 for an explanation of the numbers labeling the several curves.

which unrealistically small length scales occurred in the window and tropopause channels.

Three behaviors appear in Fig. 1b. The highest spatial coherence occurs in surface channels with length scales exceeding 2000 km. Tropospheric signals, insensitive to moisture, possess length scales of about 1800 km, but are nearly identical with surface correlations at distances less than 1300 km. Finally, the stratospheric and moisture sensitive tropospheric channels are similar, with length scales of about 1000 km.

The implication of the first two results is that the scale of the atmospheric system is somewhat larger than the scale of imposed sea surface temperature variation within this part of the tropics. It is likely then that sea surface patterns do not drive directly the most active synoptic systems over the eastern Pacific Ocean.

Connecting the second two results leads to the implication that temperature and humidity variations occur on two diverse scales over the tropical eastern Pacific.

2.2 Geographic Differences

The correlations for each channel were recomputed for two zonal bands, one between 10°S and 15°N (the equatorial section), and the other between 15°N and 30°N (the subtropical section). These subsets, shown in Figs. 1c and 1d, minimize the meridional temperature gradient in two ways: the first separates the tropics from the subtropics, while the second aliases out the north-south separations at scales larger than about 1000 km for each subset. (The distance between 15°N and 30°N is only about 1600 km, so most of the longer separation distances for observations contributing to the correlation coefficient tend to be oriented east-west).

Comparison of Figs. 1b, c and d allow latitudinal differences to be identified. Except for water vapor channels, the apparent scale of tropical systems is reduced in the zonal strips. The integral length scales of the equatorial strip are about 40% of the scales for the entire region. Scales for the subtropical strip are about 75% of scales in Fig. 1b. Thus, for the five channels associated with temperature variation, the dominant variation appears to be associated with the mean meridional temperature gradient. In the equatorial region the integral length scale for tropospheric disturbances is about 600 km. Length scales at the surface are longer, about 850 km. The infrared water vapor channel possesses an integral scale of 1300 km in the equatorial belt, the same as its scale throughout the region. Not only is moisture's coherence about twice as large as that for temperature along the equator, it is not sensitive to meridional variation. In the subtropics, however, the scale of moisture variation is about 750 km, much smaller than equatorial variation. Finally, the scatter in correlation behavior for individual channels within each group is much greater in the equatorial zone than in the other zones.

The first conclusion is that moisture variations are synoptic in nature, and not a result of a mean meridional gradient in moisture. The scale of moisture variation is dominated by

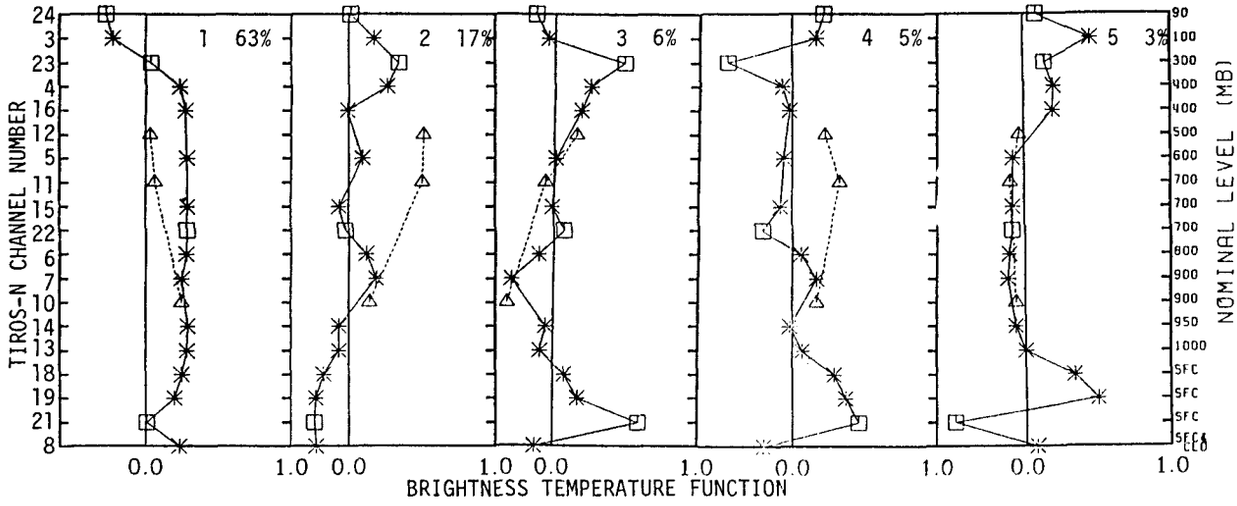

Fig. 2. Eigenvectors of channel brightness temperatures for 23 January 1979 at 00 GMT. The vertical scales are channel number (left) and approximate peak in mb of the weighting function (right). The first eigenvector is at the left and the fifth is at the right. Asterisks are infrared thermal channels, triangles are moisture channels, and squares are microwave channels. The explained variance appears in the upper right hand corner of each individual diagram.

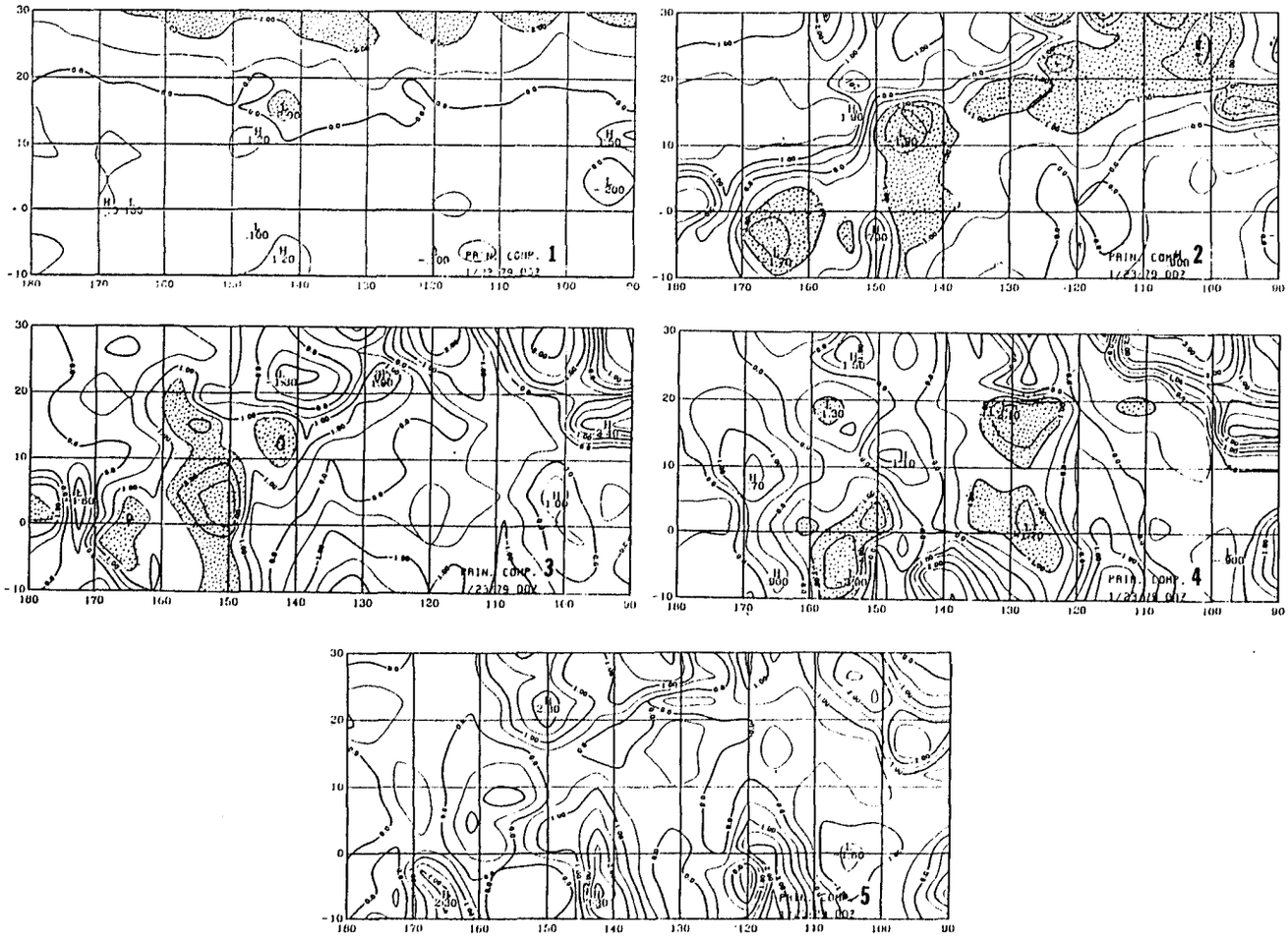

Fig. 3. EOF's, or spatial patterns, for the eigenvectors shown in Fig. 2. Areas shaded for emphasis are explained in the text. The coordinates are latitude (from 10°S to 30°N) and longitude (from 180° to 90°W).

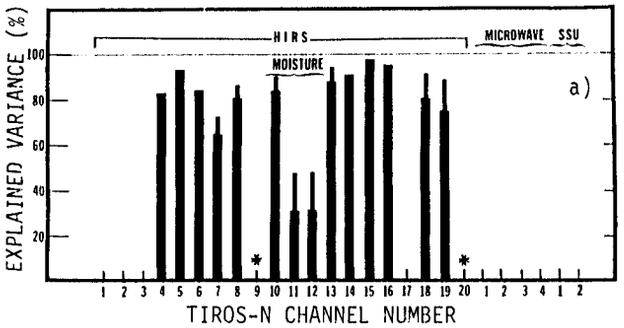

Fig. 4a. Percent variance explained for each TIROS N channel from microwave and stratospheric channels for the same satellite sounding. Heavy lines for linear regression terms; light lines for quadratic regression terms. (not predicted.)*

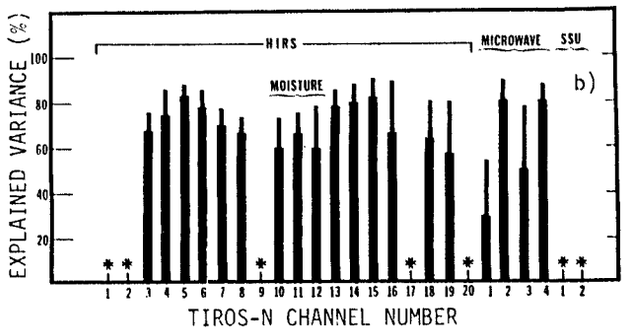

Fig. 4b. As in Fig. 4a, except for prediction from co-located NOAA-5 ITPR channels.

equatorial variation, not by that of the subtropics. On the other hand, temperature variation is controlled strongly by the mean meridional temperature contrast. This contrast occurs primarily in the northern portion of the domain. Equatorial thermal coherance is very small. Finally, the TIROS N moisture channels are truly sensing moisture signals, which vary distinctly from thermal signals, even in the equatorial and subtropical regions.

2.3 Synoptic Differences

Finally correlations were computed for a central Pacific sector between longitudes 140°W and 180° for two different days separated by five days. One day experienced heavy convection along the equatorial section and in the northwest corner of the region. The second day was relatively cloud- and convection-free. In all channels, integral length scales were less for the day with weak synoptic activity, approximately 25% or about 400 km less for the four tropospheric channels of Fig. 1b, including moisture. (The correlation figures are not shown.) The decreases in scale for the surface and stratospheric channels were not significant. The conclusion is that synoptic activity makes the horizontal patterns more coherent and the satellite can detect this organization. The stratosphere and surface do not appear to vary importantly on time scales of a few days.

3. SPATIAL PATTERNS

The horizontal and vertical synoptic patterns in the TIROS channel data were examined through EOF analysis. For a given synoptic time, all the satellite observations over the tropical Pacific region were merged into eigenvectors (vertically-oriented channel brightness temperature patterns) and EOFs (horizontal amplitude patterns of the eigenvectors). EOFs are alternatively called "principal components." This decomposition was done for each synoptic time and the first five eigenvectors for a typical time period appear as Fig. 2. Eigenvector Numbers 3, 4 and 5 varied from day to day, but Eigenvector Numbers 1 and 2 remained stable. Due to a retrival error, the "900 mb moisture signal" is actually a low level thermal signal. Thus, the first eigenvector is unambiguously a mean tropospheric temperature signal, with near zero weight given to the surface microwave signal and the moisture signals. It typically accounts for 60% of the spatial variability of the entire satellite channel data set. The second eigenvector is primarily a moisture signal, accompanied by a weak surface thermal signal; the signs are such that when the troposphere is moist, the boundary layer is warmer than normal. This signal typically explains 15% of the variability. The next three eigenvectors are more complex and less physically interpretable, but typically include large moisture, microwave and surface signals. They can be linked to moisture, cloud, precipitation and surface effects, and typically explain about 5% of the variability each. Thus, the first five EOFs explain over 90% of the variability.

The five EOFs, or principal components, associated with eigenvectors in Fig. 2 are shown in Fig. 3. EOF 1 shows the meridional temperature gradient north of 10°N and the cold trough (cold is shaded) associated with a moisture burst between 150°W and 120°W. EOF 2 shows the moist axis corresponding to the moisture burst (with the wettest areas shaded) and the strong moisture gradient on the northwest flank. Highs in EOF 3 (shaded) generally show contamination by heavy precipitation cores or a warm tropopause. Over land areas surface emissivity dominates the signal. This pattern does not always correspond to cold cloud top temperatures from GOES imagery, suggesting that the GOES signal is not always a good precipitation indicator. EOFs 4 and 5 are more difficult to interpret. They carry a non-meteorological signal along the satellite track in channels MSU 1 and 3, particularly along the equator. This signal has not been discussed in the literature. EOF 4 shows several minima along the burst (shaded), adjusting observations in wet areas which do not have a warm boundary layer. EOF 5, with a warm tropopause and surface, shows a weak maximum along the burst axis.

Most EOF analyses of geophysical data exhibit a gradually decreasing scale in spatial patterns. Except for the first amplitude pattern of mean temperature, the TIROS N data set does not follow this trend. Starting with the moisture pattern, the spatial patterns show a surprising complexity, a result of the atmospheric structure of this portion of the tropics. It is not surprising, then, that the integral length scales of the preceeding section exhibited so much variation or signal.

4. INTERCHANNEL COMPARISONS

Because of regions of missing satellite observations, attempts were made to reconstruct

"bogus" TIROS N channel brightness temperatures from two sources: NOAA-5 (VTPR) observations where no TIROS N observations were available; and TIROS N microwave and stratospheric channels for cloudy/overcast conditions where tropospheric infrared channels were not available. The procedure was statistical, involving a full quadratic response surface regression model.

For the bogus data generated from TIROS N data in cloudy regions, the tropospheric IR channels were predicted by regression, using the available TIROS data (MSU 1, 2, 3, 4; SSU 1, 2; HIRS 1, 2, 3, 17). The model was constructed using over 2500 complete soundings available in clear sky conditions. The model was then applied to overcast regions.

In an analogous model, NOAA-5 VTPR channel data were regressed to predict TIROS N channel brightness temperature. The model was constructed with clear sky TIROS and NOAA soundings colocated within 500 km in space, and 3 hours in time; only 300 colocated soundings were available for model construction.

Figs. 4a and b depict the percentage variance predicted in each channel from the TIROS N microwave and stratospheric channels, and from the NOAA-5 channels, respectively. The heavy lines show the linear terms; the light lines give the improvement by including quadratic terms. Improvements by quadratic terms in excess of 10% were limited to only a few channels in the NOAA-5 model. NOAA-5 predictions were only slightly less accurate due primarily to time and space extrapolation and to the degraded observing capability of the deteriorating NOAA satellite. Generally speaking, about 85% of the variance in each channel can be predicted for the TIROS model, excepting the two tropospheric moisture channels, where prediction is less successful. About 80% of the variance is recovered by the NOAA model, except for the microwave window channel. Because NOAA-5 infrared channels are sensitive to water vapor, their prediction of moisture in clear sky conditions was more successful; since they are, however, all infrared, they will provide no new moisture information in cloudy regions.

5. SUMMARY

Individual channels of TIROS N vary on their own integral length scales. The variation is sensitive to absorber (particularly water vapor and precipitation), to mean meridional atmospheric gradients, and to synoptic signal. This length scale variation, and the strong channel interdependence allow TIROS N channel brightness temperatures to be merged into a few vertical/horizontal structures through EOF analysis. The vertical eigenfunctions and horizontal EOFs can be interpreted synoptically. Finally, the strong channel inter-dependence allows "bogus" channel data to be constructed from partial channel soundings or from different satellites carrying different instruments; however, water vapor channels will remain poorly predicted in cloudy regions.

6. ACKNOWLEDGEMENTS

Paul Dirmeyer, Donna Woolley and Mark Chambers prepared data and figures. The research reported here is supported by the George C. Marshall Space Flight Center, NASA, under Contract No. NAS8-35182.

7. REFERENCES

McGuirk, J. P., and A. H. Thompson, 1984: Transient tropical disturbances within the Pacific Hadley cell. Postprints, 15th Conf. Hurricanes and Tropical Meteor. Miami, Amer. Meteor. Soc., 249-254.

Smith, N. R., A. H. Thompson and J. P. McGuirk, 1986: Moisture bursts over the tropical Pacific Ocean. Paper submitted to Mon. Wea. Rev.

Smith, W. L., H. M. Woolf, C. M. Hayden, D. Q. Wark and L. M. McMillin, 1979: The TIROS-N operational vertical sounder. Bull. Amer. Meteor. Soc., 60, 1177-1187.

P4.6

A GLOBAL COMPARISON OF TOTAL OZONE AND TROPOPAUSE PRESSURE FIELDS

Siegfried D. Schubert and Marie-Jeanne Munteanu

Department of Meteorology
University of Maryland
College Park, MD 20742

1. INTRODUCTION

The existence of a total ozone - weather relationship has been known for many years (see e.g. Dobson et al., 1946; Reed, 1950). However, it is only recently, through the use of satellites, that the spatial and temporal distribution of data has become sufficient to attempt a more comprehensive analysis of this relationship involving spectral decompositions in both space and time.

Several years of high resolution total ozone measurements have been analyzed by Bowman and Kruegar (1985). They provide a global climatology of total ozone including the annual and semiannual harmonics from 4 years of NIMBUS-7 total ozone mapping spectrometer data area-averaged onto a 5° by 5° grid. Meteorological quantities are also being made available on a global basis. With the help of satellite observations, the National Meteorological Center (NMC) now routinely produces global analyses of surface pressure, temperature, winds and geopotential heights.

In the present study we make use of these data sets to study the global distribution of the ozone-weather relationship as it is reflected in the temporal correlation between total ozone and tropopause pressure. This work is an extension of the study by Munteanu, 1982 which provides a detailed case-study analysis of ozone-tropopause correlations over Europe. The Munteanu study also outlines a methodology for applying the observed tropopause-ozone relationship to improve temperature retrievals from satellite measurements.

2. RESULTS

In this section we discuss some preliminary results concerning the geographical distribution of the correlation between daily values of total ozone and tropopause pressure for the transition seasons of 1979-1982. We limit the discussion to spatial scales normally associated with weather systems (medium scale waves): this is accomplished by performing a spherical harmonic decomposition and removing the largest scales defined here as all wave components with total wave number less than or equal to 5.

Figure 1 shows the Northern Hemisphere springtime (MAM) correlation field. The most striking feature of this field is the strong latitudinal dependence with maximum correlations occurring in the middle latitudes of both hemispheres and a rapid drop in the correlations away from these regions. Correlations greater than 0.6 occur throughout the latitude bands 30°-70°N and 30°-50°S. Values greater than 0.7 occur over the North Atlantic, central Asia, off the coast of Asia and the eastern hemisphere of the southern hemisphere middle latitudes. The tropics generally show very weak correlations. Figures 2 and 3 show the variance of the tropopause pressure and total ozone, respectively. A comparison of these maps with figure 1 shows very clearly the strong correspondence between maximum variability associated with the medium scales and the regions of strongest correlation.

Figures 4, 5 and 6 show the analogous fields for the Northern Hemisphere fall (SON). The general features of the correlation field (Fig. 4) are similar to MAM, with maximum correlations exceeding 0.8 in the North Atlantic. However, the band of high correlations in the Northern Hemisphere is generally narrower particularly over North America and the North Atlantic. Note also the much stronger gradient in the correlations immediately to the south. Figure 5 shows that the high correlations are again strongly tied to the regions of high variance in the tropopause pressure and that the restricted distribution in the meridional direction and strong gradients are a reflection of the behavior of the variance field. In contrast, the ozone variance field (Fig. 6) does not show as strong a relationship with the correlation distibution. In fact the region of highest variance over the eastern sector of the Southern Hemisphere lies poleward of both the maximum correlations and the maximum tropopause variance in this region.

Correlations have also been computed for MAM of 1979 using tropopause pressure derived from radiosonde data for stations lying between +/-30° longitude. For this case only 12Z data was used to achieve better collocation in time. The results (not shown) are very similar to those based on the NMC analyses verifying the dependence on latitude as well as the magnitude of the correlations.

3. DISCUSSION

A fairly strong positive correlation (>0.6) between tropopause pressure and total ozone has been found for the medium scale waves for the transition seasons in the middle latitudes of both hemispheres. The regions of maximum correlation are generally associated with regions

of maximum variance in the tropopause pressure and appear to be associated with the major middle latitude storm tracks in both hemispheres. The variance in the total ozone does not always show a strong correspondence with the correlation field. This is particularly true for the SON fields where the maximum in total ozone lies poleward of the correlation maximum in the Southern Hemisphere.

One must keep in mind that the tropopause data is to a certain extend model dependent particularly over the tropics and the Southern Hemisphere. We have attempted to determine the degree of model dependence by examining station data for limited regions and time periods. These results tend to confirm the general features we find using the gridded tropopause data.

We have also examine the extreme seasons and generally find very similar results. A somewhat surprising result is that the summer hemispheres show some of the most extensive areas of high correlation while the winter hemispheres generally exhibit the weakest correlations. The large-scale correlation fields are presently under investigation and a further, more detailed spectral analysis is also being carried out for selected regions to determine the frequency dependence of the correlations.

4. ACKNOWLEDGMENTS

We wish to thank Dr. Kenneth Bowman for providing us with the gridded total ozone data. We also benefited from discussions with Dr. Bowman and Dr. Arlin Krueger. Mr. Dan Iredell provided the expert programming necessary to analyze the station data.

5. REFERENCES

Bowman, K. P., and A. J. Krueger, 1985: A global climatology of total ozone from NIMBUS-7 total ozone mapping spectrometer. J. Geophys. Res., 90, 7967-7976.

Dobson, G. M. B., A. W. Brewer and B. M. Cwilong, 1946: Meteorology of the lower stratosphere. Proc. Roy. Soc. London, A, 185, 144-175.

Munteanu, M.-J., 1983: Study of tropopause height estimate from TOMS ozone data from NIMBUS-7 and from the microwave regression temperature retrieval of simulated brightness temperatures. NASA Technical Memorandum 84983.

Reed, R. J., 1950: The role of vertical motions in ozone-weather relationships. J. of Meteor., 7, 263-267.

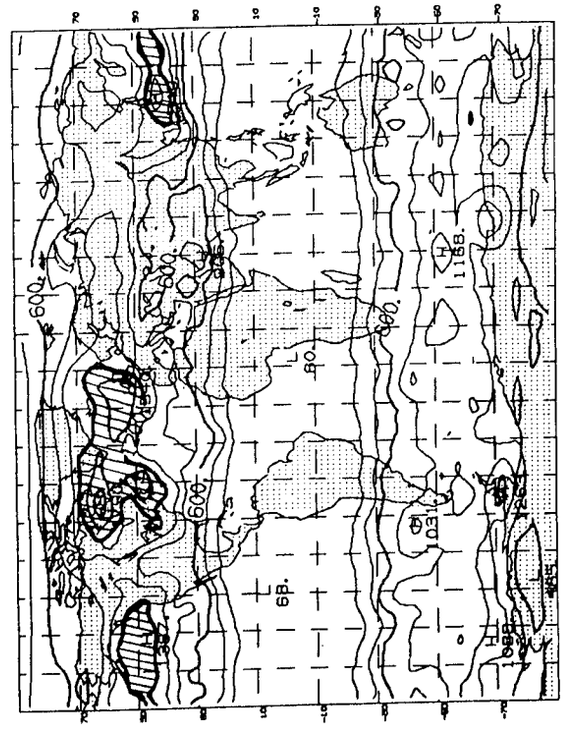

Fig. 2. Same as fig. 1 except for variance of the tropopause pressure. Contour interval is 200mb^2.

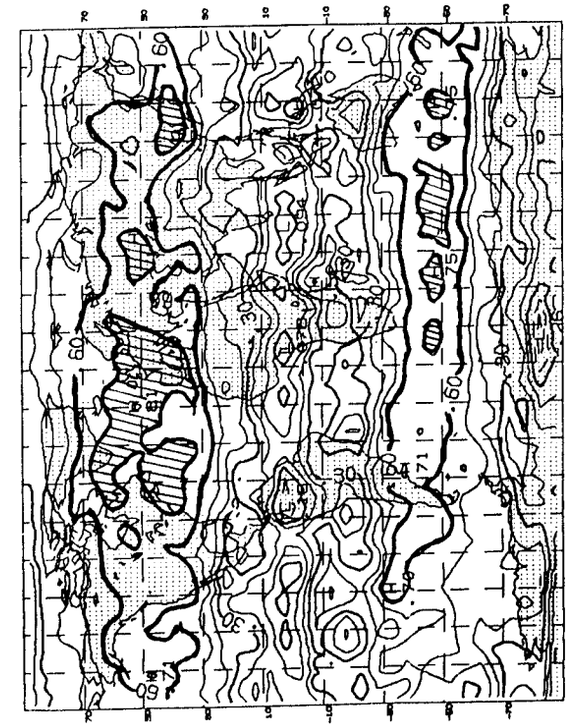

Fig. 1. Correlation between total ozone and tropopause pressure for (MAM), 1979-82. Contour internal is 0.1.

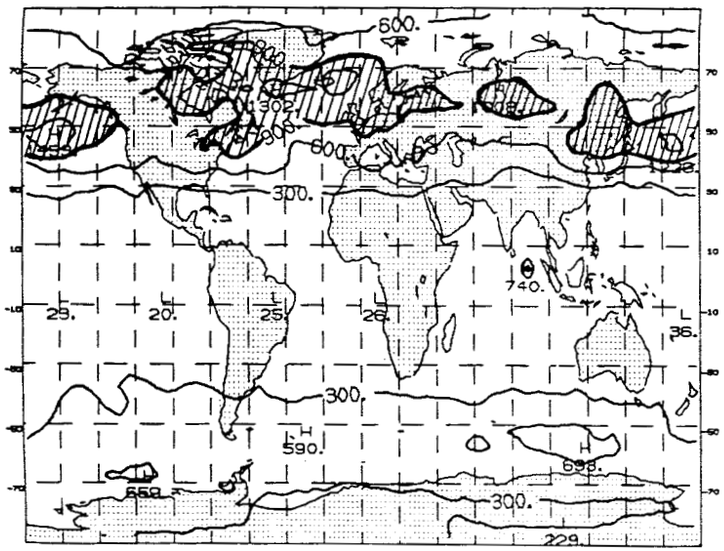

Fig. 3. Same as fig. 1 except for variance of total ozone. Contour interval is 300DU^2.

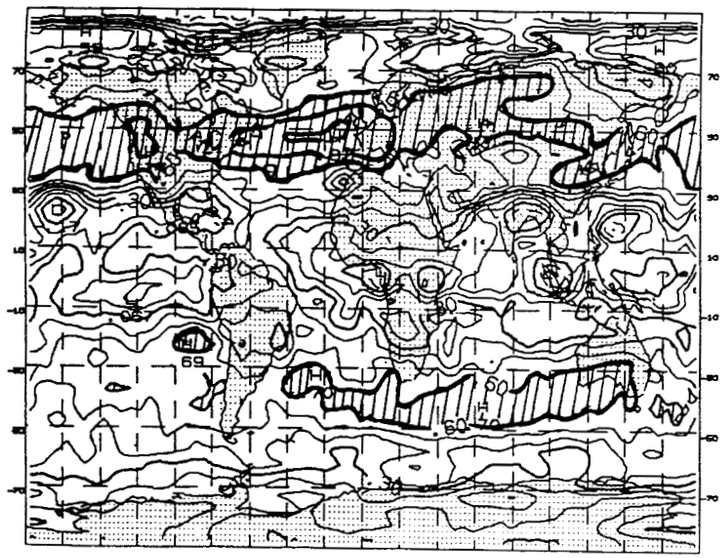

Fig. 4. Same as fig. 1 except for September, October and November (SON).

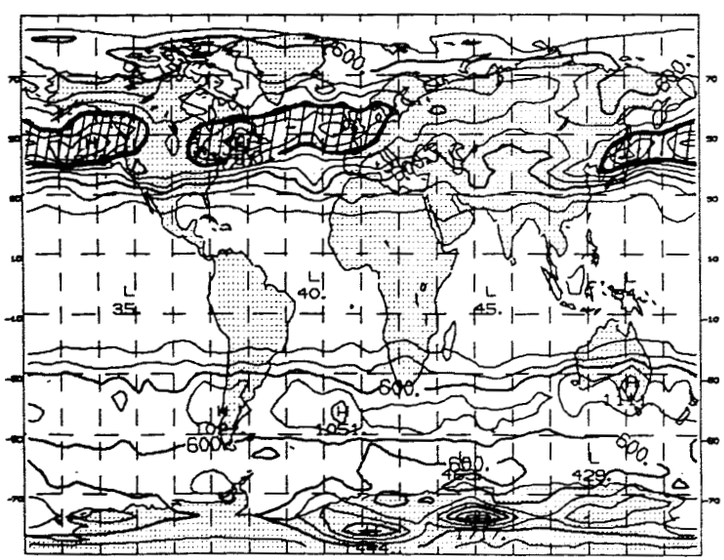

Fig. 5. Same as fig. 1 except for variance of the tropopause pressure and SON. Contour interval is 200 mb^2.

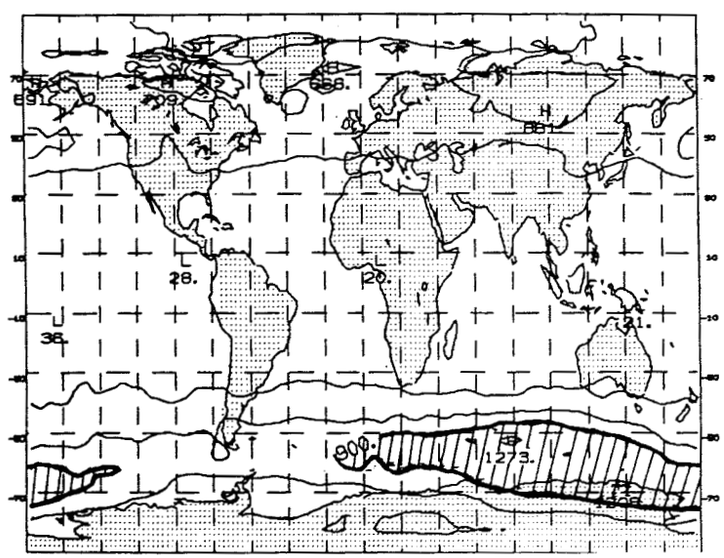

Fig. 6. Same as fig. 1 except for variance of total ozone and SON. Contour interval is 300 DU^2.

COMPARISONS BETWEEN PHYSICALLY RETRIEVED TEMPERATURES FROM NOAA-7 AND NOAA-8 AND CONVENTIONAL ANALYSES OR RADIOSONDE DATA

N.A. Scott[1], N. Husson[1], A. Chedin[1], J.F. Flobert[1], G. Rochard[2] and J. Quéré[2]

[1] Laboratoire de Météorologie Dynamique du CNRS
Ecole Polytechnique, 91128 Palaiseau Cedex, France

[2] Centre de Météorologie Spatiale / EERM
22302 Lannion, France

1. INTRODUCTION

The quality of the instruments aboard the present generation of operational meteorological satellites (The Tiros-N series) and the increasing capability of the so-called physical inversion methods to accurately retrieve atmospheric parameters from the multi-spectral radiative measurements, explain the increasing compatibility of these remote observations with the requirements of most of the present or planned meteorological or climatological programmes, as far as the atmospheric structure (temperature, moisture, cloudiness, etc..) is concerned. This essentially results from the actual taking account of the physical and statistical aspects of the phenomena - very often through a coupling of the various instruments (e.g. infrared and microwave sounders) - which leads :

a) to enter the inversion process with an initial guess close to the final solution,
b) to acquire clear equivalent radiances through an appropriate cloud clearing algorithm, and
c) correlatively to derive high density retrievals even in case of heavy cloudiness.

The 3I (Improved Initialization Inversion) procedure (Chedin et al., 1984 ; Chedin et al., 1985) offers modular answers to these essential points :

a. Retrieval of the initial guess solution through a pattern-recognition type approach. The observed cleared radiances are first used to retrieve the "best" initial guess solution in a statistical sense. The procedure makes use of the "TIGR" (TOVS Initial Guess Retrieval ; see above references) data set. The selected set of observed brightness temperatures is "compared" to each of the computed sets of brightness temperatures and the "closest" is retained.

b. The use of the so-called "ψ-method" (see above references) relying on a coupling of the infrared and microwave channels, to obtain "equivalent clear radiances" in cloudy areas, preserves as far as possible the nominal vertical resolution of the instruments.

c. The basis for the retrieval of the "exact" solution is a maximum probability estimation procedure aimed at minimizing the differences between the brightness temperatures associated with the initial guess and the observed ones. Use is made of the Jacobian associated with the retrieved initial guess, in the "TIGR" data set.

Resulting from a compromise between the spatial resolutions of the two sounders HIRS-2 (infrared) and MSU (microwaves) and from an oversampling along the sub-satellite track, the 3I algorithm produces one retrieval every 100 x 30 km².

Within the frame of the International TOVS Study Conference ITSC, I and II, IRC/IAMAP

Table 1 TOVS case study sets

	Satel.	Date	Orbit	Time	
1	NOAA-7	3/04/82	3586	12:05	(a)
2	NOAA-7	3/04/82	3587	13:45	(a)
3	NOAA-7	3/05/82	3594	14:05	(a)
4	NOAA-7	3/05/82	3595	15:45	(a)
5	NOAA-8	7/06/84		12:	(b)
6	NOAA-7	9/27/83	11664	14:35	(c)
7	NOAA-7	9/29/83	11692	14:11	(c)
8	NOAA-7	11/26/83	12512	15:47	(c)
9	NOAA-7	12/08/83	12681	15:00	(c)
10	NOAA-7	12/08/83	12682	16:43	(c)
11	NOAA-7	12/27/83	12949	14:29	(c)
12	NOAA-7	12/27/83	12950	16:11	(c)
13	NOAA-7	12/28/83	12963	14:17	(c)
14	NOAA-7	12/28/83	12964	15:58	(c)

(a) ITSC I study cases time coincident with the ALPEX IOP
(b) ITSC II study case
(c) Other TOVS study case corresponding to poorly forecasted situations.

held in Austria (August 1983, February 1984), the 3I method has already demonstrated its capability to produce accurate temperature soundings (Le Marshall, 1985). These first encouraging results must however be complemented by further systematic comparisons with either colocated radiosoundings data or operational analyses. Moreover, recent improvements brought to the 3I code (introduction of an air-mass classification scheme ; refinement of the initial guess retrieval procedure) have led us to re-assess its accuracy. This has been done, or is in progress, for several sets of observations as given in Table 1.

The five first sets in Table 1 are considered in the present work. They correspond to the Alpex (Alpine Experiment) IOP (Intensive Observing Period) of March 4-5, 1982 (cases 1 to 4) and to one pass of NOAA-8 over the United States and Gulf of Mexico. The remaining nine situations (NOAA-7 observations) mostly correspond to rather poorly forecasted meteorological situations over Europe. In such cases, the differences between retrievals and operational analyses must be interpreted having in mind the forecast errors, the main purpose being to properly assess the real benefit brought by such remote observations.

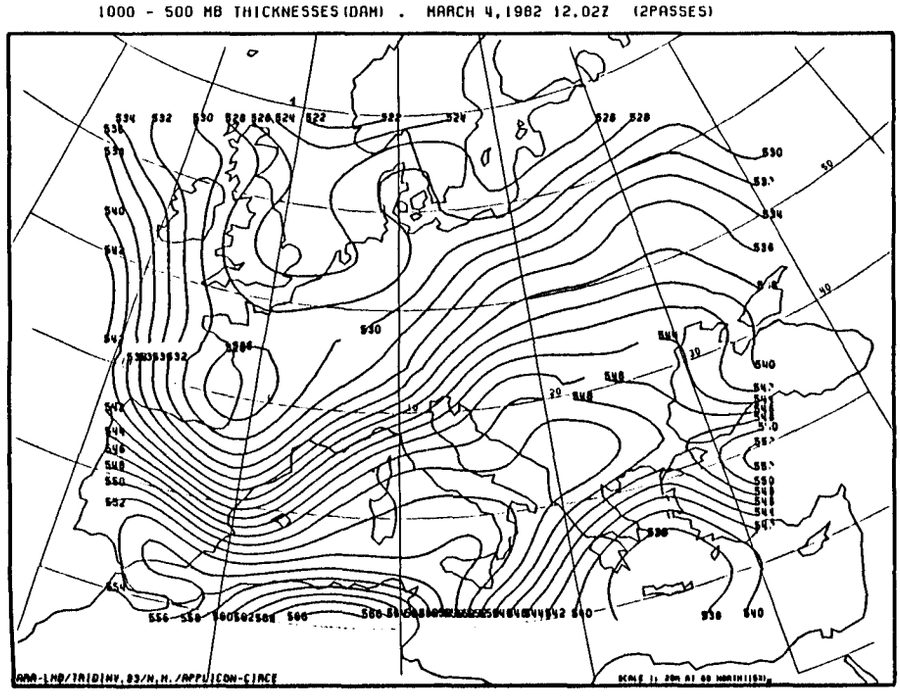

Figure 1

3I retrieved thicknesses iso-lines for the layer 1000-500 mb. Alpex case, March 4, 1982. 3I - ECMWF statistics : bias = -1,6 dam ; rms = 2.8 dam.

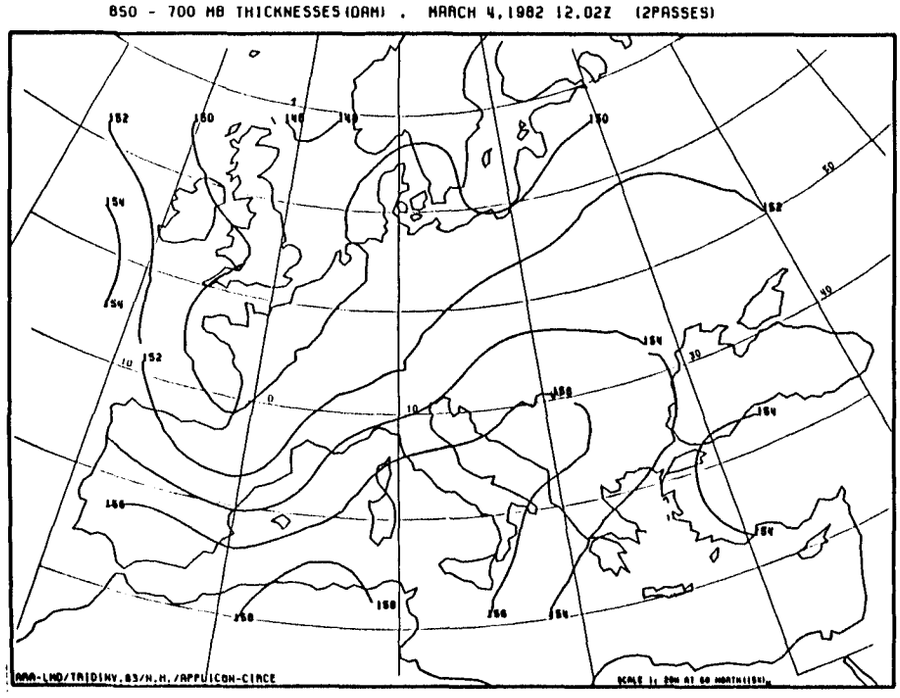

Figure 2

3I retrieved thicknesses iso-lines for the layer 850-700 mb. Alpex case, March 4, 1982. 3I - ECMWF statistics : bias = -0,4 dam ; rms = 0.9 dam.

II. COMPARISONS BETWEEN ECMWF, NMC OR RADIOSONDE DATA AND THE 3I RESULTS

The basic statistics (mean, rms) generated from the atmospheric soundings are given : a) for temperatures at the standard levels ; b) for geopotential thicknesses obtained from the retrieved temperatures by vertical integration.

The observed sets are either RAOB data or analyses from ECMWF or NMC/LFM (Limited Fine Mesh model).

The colocations between RAOB and satellite soundings are accepted within the following constraints : (1°x1°) latitude longitude distance ; 2 hours in time ; if the measure of the temperature is available up to 100 mb and the dew point temperature up to 400 mb. The colocations with the analyses are obtained through a spline interpolation procedure at the satellite sounding points.

II.1 Alpex case

The quality of retrieved products (thermal structure from which geopotential thicknesses and thermal winds may be derived) has been estimated, for the ALPEX IOP mentioned above, qualitatively and quantitatively. On a qualitative point of view, Figs. 1 and 2 which display, respectively, the 1000-500 mb thickness iso-lines and the 850-700 mb thickness isolines, for the two passes of March 4 (day) obtained from the 3I algorithm, may be compared to the corresponding ECMWF (European Centre for Medium Range Weather Forecasts) analyses. Corresponding biases and rms are also given on Figs. 1 and 2.

The agreement is satisfactory. A quantitative assessment of the accuracy of the retrieved products goes through a statistical analysis of the deviations between the retrievals and either radiosonde data or ECMWF thermal (or thickness) fields. The results of this statistical evaluation are reported in Figure 3 which displays the biases and the rms errors obtained when comparing the retrievals to the two sources of data mentioned above. Among the 170 radio-soundings considered covering the day and night passes, only 4.7% (8 items) were rejected and do not enter the statistics. Comparisons with analyses comprise about 2130 3I boxes over a total available of 2235 boxes representing the day time passes, the closest in time from the 12:00Z ECMWF analyses. Table 2 gives similar results for the geopotential heights. These results compare favourably with other similar approaches (see, for example Le Marshall, 1985) and effectively demonstrate the capability of the 3I code to provide accurate products.

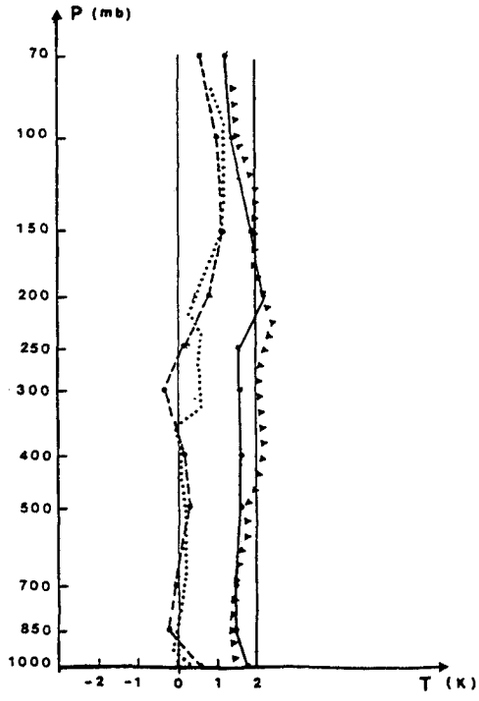

Figure 3

Biases and rms of the deviations between either co-located radiosonde data (biases : ... ; rms : ▸▸▸) or ECMWF analyses (biases : --- ; rms : ——) and the 3I retrieved temperatures.

Table 2

Biases and rms errors for geopotential heights between the 3I retrievals and the ECMWF analyses as observed set. ≈ 2100 items. Alpex case (cases 1 and 2 of Table 1).

Layer (mb)	Mean (m)	rms (m)
1000 - 850	- 3.50	6.95
1000 - 700	- 7.70	14.50
1000 - 500	- 16.50	28.20
1000 - 400	- 23.00	36.20
1000 - 300	- 21.25	38.40
1000 - 250	- 19.80	35.80
1000 - 200	- 21.20	32.50
1000 - 150	- 28.00	36.30
1000 - 100	- 42.50	49.30
1000 - 70	- 51.30	57.50
850 - 700	- 3.80	8.90
700 - 500	- 9.20	16.40
500 - 300	- 7.50	24.30
300 - 100	- 18.00	37.30
100 - 50	- 10.40	14.50

II.2 The NOAA-8 case (June 7, 1984)

Fields of temperature and geopotential heights derived from the 3I algorithm have been compared to both colocated radiosonde data and NMC/LFM (Limited Fine Mesh) analyses. Comparisons with radiosonde data are shown on Fig. 4 (temperatures) or given in Table 3 (geopotential heights). Comparisons with NMC analyses are shown on Fig. 5 (temperature) or given in Table 4 (geopotential heights). In both cases, these figures display the biases and the rms errors as a function of pressure. Two kinds of 3I retrieved temperatures have been considered : the "standard" one as described in the references already quoted and another one referred to as "*satellite-only*". Contrary to the former one for which use is made of operational forecasts of the temperature at 1000 mb and of the surface pressure for the retrieval of the initial guess solution (the forecasts are not assimilated within the retrieval scheme of the final solution itself), the later product, "satellite only", is obtained from the satellite observations only, with no inclusion of operational forecasts in the initial guess solution retrieval scheme. Several comments come out from Figs. 4 and 5. First, the general agreement is satisfactory and the relatively large biases with the colocated radiosonde data seem to be mostly due to the smallness of the sample (about 40 items).

Second, comparisons with analyses (about 900 items) show a very small bias. The larger rms error at 850 mb on Fig. 5 seems to point out a difference between the two fields NMC and 3I. This has been confirmed (Scott et al, 1986) and interpreted in the context of the particular meteorological situation involved.

Third, the rapid increase of the error above 150 mb has also been observed by other authors working, within the frame of the activities of the International TOVS working group, on the same scene (Le Marshall, 1985). Fourth, the impact of the operational forecasts of the temperature at 1000 mb and of the surface pressure for the retrieval of the initial guess appears relatively modest. This conclusion must however be taken with care, since, in the case considered, the temperature field is rather smooth with no important gradients except for one or two restricted areas.

A similar work is in progress for the Alpex case. Results concerning the situations listed in Table 1 will be presented at the time of the conference.

Table 3

NOAA-8 case. Biases and rms errors between retrieved geopotential thicknesses and colocated radiosondes (≈ 40 items).

Layer (mb)	Mean (m)	rms (m)
1000 - 850	- 6.9	11.1
1000 - 700	- 9.8	21.1
1000 - 500	- 6.5	22.2
1000 - 400	- 12.7	25.5
1000 - 300	- 20.1	35.0
1000 - 250	- 24.4	38.9
1000 - 200	- 28.0	39.1
1000 - 150	- 27.1	41.9
1000 - 100	- 70.1	78.5
850 - 700	- 2.8	11.9
700 - 500	- 0.6	10.3
500 - 300	- 12.6	23.4
300 - 100	- 50.9	57.6

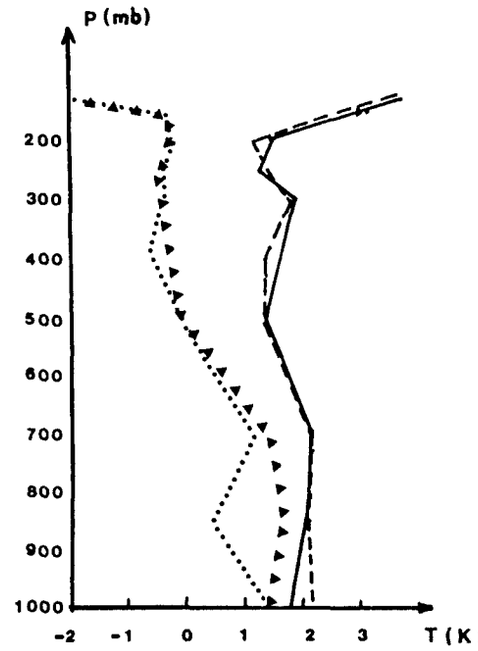

Figure 4

Biases and rms errors for the deviations between 3I retrieved temperatures and colocated radiosonde data. Biases : ... for the "standard" solution ; ▸▸▸ for the "satellite-only" solution. rms : —— for the "standard" solution ; --- for the "satellite-only" solution (≈ 40 items).

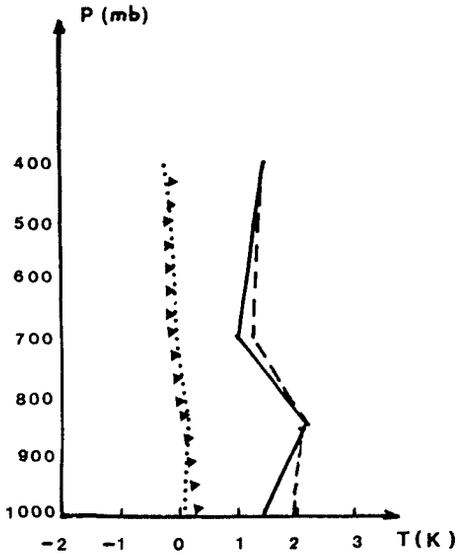

Figure 5

Same as for Figure 4 for comparisons between 3I retrieved temperatures and NMC/LFM analyses (≈ 40 items).

III. CONCLUSION

From these applications to various meteorological situations, the 3I algorithm has demonstrated its ability to retrieve quite accurately meteorological patterns at various scales including mesoscale features. The spatial resolution of 3I, combined with an original way of "de-clouding" the observations even for overcast areas, lead to a high density of retrievals : for the cases considered here, the mean percentage of bad retrievals automatically rejected is around 6%.

The coupling of pure physics with an a priori knowledge of the medium observed extracted from an "educated" data set ("TIGR"), ensures a good spatial coherence. It is worthwile pointing out : a) the fact that the gradients are often stronger on the 3I thickness charts than on the conventional charts, a characteristics confirming our present experience of the 3I code ; b) the usefulness of the chart related to the relatively thin layer 1000-850 mb, a result demonstrating that a satisfactory vertical resolution may be obtained from the remote observations of the Tiros-N series. (Scott et al,1986).

Table 4

Same as Table 3. The observed set is the NMC/LFM analyses (≈ 910 items).

layer (mb)	mean (m)	rms (m)
1000 - 850	0.0	8.8
1000 - 700	- 3.5	18.2
1000 - 500	- 9.0	23.1
850 - 700	- 3.5	11.1
700 - 500	- 7.7	12.4

REFERENCES

Chedin, A., and N.A. Scott, 1984 : Improved Initialization Inversion Procedure. Proc. of the 1st Int. TOVS Study Conference. Igls, Austria. August 1983. A report from the CIMSS, Ed. P. Menzel, p. 14-79.

Chedin, A., and N.A. Scott, 1985 : Initialization of the radiative transfer equation inversion problem from a pattern recognition type approach. Applications to the satellites of the Tiros-N series. Advances in Remote Sensing Retrieval Methods, Academic Press, A. Deepak Ed. To be published.

Chedin, A., N.A. Scott, C. Wahiche, P. Moulinier, N. Husson, G. Rochard, J. Quéré, M. Derrien, 1985 : The 3I procedure applied to the retrieval of meteorological parameters from NOAA-7 and NOAA-8. Proc. of the 2nd Int. TOVS Study Conference. Igls, Austria. February 1985. A report from the CIMSS, Ed. P. Menzel, p. 11-38.

Le Marshall, J.F., 1985 : An intercomparison of temperature and moisture fields from Tiros Operational vertical sounder data. The Technical Proceedings of the 2nd Int. TOVS Study Conf. Igls, Austria, Ed. W.P. Menzel, p. 106-161.

Scott, N.A., A. Chedin, N. Husson, C. Levy, G. Rochard, 1986 : Analysis of NOAA-8 TOVS observations over the central United States for a pre-tornadic situation. Submitted to J. Clim. Appl. Meteor.

P4.8

CONSTRUCTING A COHERENT LONG-TERM GLOBAL TOTAL OZONE CLIMATOLOGY FROM THE BUV, MFR, AND SBUV/TOMS DATA SETS

J. S. Ellis and F. M. Luther

Lawrence Livermore National Laboratory
Livermore, California 94550

1. INTRODUCTION

The backscatter ultraviolet spectrometer (BUV) aboard the NIMBUS 4 satellite provided global ozone data until mid-1977. The Total Ozone Mapping Spectrometer (TOMS) and Solar Backscattered Ultraviolet (SBUV) instrument aboard the NIMBUS 7 satellite began providing global ozone in November 1978. The only satellite derived global total ozone data available between the termination of the BUV data and the startup of the SBUV/TOMS data is that from the Multichannel Filter Radiometer (MFR) instrument aboard the Defense Meteorological Satellite Program (DMSP) series of satellites.

The MFR was a cross track scanning instrument that measured radiance from channels in the 9.6-μm ozone bands, 15-μm carbon dioxide bands, 18- to 30-μm rotational water vapor band, and from the atmospheric "window" near 12-μm. MFR data began in March 1977 and continued until mid-February 1980. Four MFR instruments provided total ozone data over this period. The data from the F1 and F2 instruments span March 25, 1977 through July 10, 1977 and July 10, 1977 through February 16, 1980, respectively. Data from the other two MFR instruments began and terminated within the time period of the MFR F2 data record and are not considered in this study.

In this paper we intercompare the MFR and the SBUV/TOMS data during the data overlap period in order to determine how well the MFR data might be used to represent the SBUV/TOMS and BUV data during the data gap period.

2. THE COMPARISON TECHNIQUE

The DMSP satellite carrying the MFR F2 instrument was in a near polar, sun-sychronous orbit with local daytime overpass time between 8 and 10 AM at the equator on the ascending portion of its orbit. The NIMBUS satellites are also in near polar, sun-synchronous orbits but with a local noon ascending time. The MFR scans cross track so that it produces total ozone measurements at 40 to 120 km resolution (Nichols, 1975). The TOMS also scans cross track to produce total ozone measurements at 50 to 150 km resolution, whereas the SBUV measures ozone in the nadir only at a 200 km resolution (Heath et al., 1978).

We have intercompared TOMS and SBUV ozone data that are within 6 hours of an MFR ozone sample, thus eliminating the MFR ozone data measured during the nighttime descending portion of the orbit from the comparison. We experimented with various limiting distances between the MFR and the other data sample locations extending from 20 km to 400 km and found no improvement in the RMS differences at distances less than 100 km. Our testing was done over various latitude zones and over hundreds of thousands of data points. This point is demonstrated in Fig. 1 for the latitude zone 35N–45N on January 1, 1979. Intercomparison is made between the MFR and the TOMS total ozone measurements at distances of 0-50 km, 50-100 km, 100-200 km, 200-300 km, and 300-400 km. We also compared the MFR data with itself, and the TOMS data with itself at various separation distances beginning with 50-100 km separation in order to see how the data vary with distance for each sensor. Contributions to the RMS difference in these latter two cases come from random error in the measurements, possible systematic error with cross track scan angle, and variation of ozone. Both curves have similar slopes, increasing as separation distance increases, and they each show significantly less RMS difference than the MFR-TOMS intercomparison.

Fig. 2 shows the scatter of the 1103 MFR and TOMS ozone values at the 100 km-or-less separation distance. A wide range of values occurs within this zonal band. The correlation coefficient is 0.88 for the MFR and TOMS data. In Fig. 3 the average of the ozone values in 10 degree latitude-longitude bins for this same latitude zone shows no obvious phase differences at the larger scale or bias between the two data sets. Therefore we selected the 100 km-or-less separation distance for all intercomparisons.

3. THE MFR OZONE RETRIEVAL MODEL

The theory and total ozone retrieval algorithm development for the MFR are discussed in Lovill el al. (1978) and updated in Luther and Weichel (1981). The retrieval algorithms were statistically derived using the method of multiple linear regression. The dependent data used in the statistical regression technique were vertically integrated total ozone from historical ozonesondes (calibrated against the Dobson spectrophotometer), and simulated MFR radiances calculated with a line-by-line radiation code as applied to the atmospheric vertical temperature, ozone, water vapor, cloud, and CO_2 profiles. Retrieval algorithms were developed for each of 11 latitude bands and for each calendar month (132 different algorithms in total) by employing dependent data that were geographically located within each band and that

spanned a two month period centered on the month of interest.

We have selected four days of the MFR and TOMS total ozone data (one day from each season) to evaluate how well the algorithms met their designed capability (Table 1). The linear correlation coefficient as applied to the dependent data set, which gives a measure of the design capability of the algorithm and is the square root of the fractional variance explained by the algorithm, is represented by r' for each month within each of the 11 latitude bands. Linear correlations (r') vary from as low as 0.28 in the tropics, where total ozone has only small temporal and spatial variation (small signal to noise ratio), to as high as 0.90 in the higher latitudes, where total ozone generally shows large temporal and spatial variation (large signal to noise ratio). The percent standard deviation (s) of one day of TOMS total ozone data within each latitude band depicts the spatial variation of total ozone with latitude and with season.

In latitude zones 15S-25S and 50S-70S there are no r' values except in the zone 50S-70S during the month of July. This indicates that the algorithm used within that zone was interpolated from the algorithm in adjacent bands north and south. Interpolation was required when there were insufficient ozonesonde data available in a latitude band for constructing an ozone retrieval algorithm.

Also shown in Table 1 is the linear correlation coefficient (r) between the MFR and the TOMS total ozone data for each of the four days. For the most part the r' and the r values agree quite well. However, there are cases where the r' values are much larger than the r values. If the TOMS total ozone data are taken as a reference standard by which to measure the MFR total ozone algorithm accuracy, then the algorithms in the latitude bands marked with a star are performing below their design capability. Since the objective of this work is to determine how well the MFR total ozone data might perform as a surrogate data set in place of the TOMS/SBUV data during the period between the BUV and SBUV/TOMS data, then using the TOMS data as a reference standard is appropriate. The correlation coefficient is not an absolute measure of how well the MFR and TOMS data sets agree since two data sets can show high correlation yet show large average difference and RMS difference due to biases and differences in wave amplitudes or scaling, respectively. In the next section we examine these latter two differences.

4. INTERCOMPARISON OF THE MFR AND THE SBUV/TOMS OZONE DATA

We have selected data for one month out of each season during the data overlap period of the MFR and SBUV/TOMS ozone data to demonstrate how well they intercompare. Average differences (d) and the standard deviation of the differences (sd), both in percent, for 5 months of data in 10 degree latitude bands (except at the poles where they are 5 degree bands) are shown in Table 2. There are more than 10,000 intercomparisons for each entry in the table except at the northernmost and southernmost entries, which can be as small as 600 intercomparisons. The majority of the differences are negative in sign indicating that the TOMS average ozone is less than the MFR average. The reverse is true only in the northern middle latitudes in January 1979 and 1980 and in the southern tropical to middle latitudes in July and November 1979. The fact that the average difference varies with latitude is undoubtedly partially caused by differences in the 11 MFR ozone retrieval algorithms.

It is surprising that differences are not more nearly equivalent between the two January cases, since the same MFR retrieval algorithms have been used. In fact the differences in January 1980 are more positive by 3% in the southern high latitudes, by 1% in the southern tropics, and by more than 7% in the northern high latitudes than they are in corresponding latitudes in January 1979. The TOMS data increased by a larger amount in the Southern Hemisphere from January 1979 to January 1980 than did the MFR data. In the northern high latitudes the MFR data actually decreased between the two Januaries, whereas the TOMS data increased. Bhartia et al. (1984) found that the TOMS data increased by 0.34 ±0.17% with respect to the Dobson data from the first to the second year of data, which would account for less than 0.5% of the difference.

The standard deviation of the differences (% sd in Table 2) varies by less than 3% at the equator to greater than 9% in the January northern high latitudes. These numbers are about 1.5 times greater than those Bhartia et al. (1984) observed between the TOMS and the Dobson spectrophotometer data.

We have also compared the MFR data with the SBUV total ozone data and the TOMS data with the SBUV total ozone data using the same SBUV data points in both cases. The number of intercomparisons are 10 to 20 times fewer than in the MFR-TOMS intercomparison because of the smaller number of measurements from the non-scanning, nadir looking SBUV instrument. We have elected to show the percent difference of the TOMS minus the SBUV total ozone (Table 3) and use the TOMS data as a transfer standard between the MFR and the SBUV data. The differences in Table 3 vary from 0.4% in the northern tropical latitudes in April to 3% or less in the higher latitudes for all months. Taken together, these numbers do not disagree with the overall 1.7% difference that Bhartia et al. (1984) found. However, there is some indication from Table 3 that this difference is getting larger with time.

Even though the number of intercomparisons in each entry of Table 2 differs by an order of magnitude from the number used in each entry in Table 3, the differences between the MFR and TOMS ozone are essentially the same using either the MFR-TOMS or the MFR-SBUV data (not shown). Therefore, the entries in Table 3 can be subtracted from the entries in Table 2 to show approximately how the MFR and SBUV differ. The differences become smaller for all positive entries and larger for all negative entries in Table 2. Since most of the entries in Table 2 are negative, the MFR-SBUV differences are generally greater than the MFR-TOMS differences.

Table 1. The linear correlation coefficient within latitude zones between MFR and TOMS total ozone on selected days (r), between the historical ozonesonde data and model calculations (r'), and the percent standard deviation of the TOMS total ozone within the latitude zones (s).

Latitude	Jan. 13, 1979 r	r'	s (%)	Apr. 15, 1979 r	r'	s (%)	July 14, 1979 r	r'	s (%)	Nov. 15, 1979 r	r'	s (%)
90N-70N				* 0.39	0.76	5	0.83	0.89	7			
70N-55N	0.89	0.79	17	0.77	0.84	9	0.73	0.79	6	0.81	0.85	13
55N-45N	0.93	0.90	15	0.78	0.86	8	0.71	0.90	6	0.84	0.89	12
45N-35N	0.86	0.87	10	0.80	0.89	12	* 0.52	0.82	7	0.82	0.92	10
35N-25N	0.78	0.78	9	* 0.60	0.82	8	* 0.32	0.69	5	* 0.34	0.83	5
25N-15N	0.55	0.51	5	* 0.36	0.62	6	* 0.32	0.56	3	* 0.06	0.63	3
15N-15S	0.44	0.39	3	0.40	0.28	3	0.72	0.28	5	0.41	0.42	4
15S-25S	0.48	--	3	0.27	--	3	0.58	--	4	0.65	--	4
25S-50S	0.90	0.83	8	0.78	0.84	7	0.88	0.89	13	0.87	0.90	8
50S-70S	0.71	--	6	0.55	--	7	0.79	0.86	12	0.87	--	13
70S-90S	0.65	0.76	4	* 0.55	0.87	4				0.84	0.75	14

5. CONCLUSIONS

From the sample of five months studied, we see that the differences between the MFR total ozone and the TOMS or SBUV total ozone are latitudinally and monthly dependent. The average differences between the TOMS and the MFR ozone vary from -12.4 to +13.3% with differences in the tropical to middle latitudes generally between ±4%. The standard deviation of the differences for the same intercomparison set vary from 2.5 to 10%, the largest values being in the high latitudes.

There are latitude zones in which biases occur between the data sets which can be removed by operating on the MFR ozone data with an appropriate algorithm. The latitude zones in which the standard deviation of the differences are large are more difficult to reconcile with the TOMS data. One possibility for correcting this type of difference is to reconstruct the MFR statistical retrieval algorithms by regressing the MFR radiance data on the TOMS or SBUV total ozone data.

ACKNOWLEDGEMENTS

This work was performed under the auspices of the U. S. Department of energy by the Lawrence Livermore National Laboratory under contract No. W-7405-Eng-48 and supported in part by the National Aeronautics and Space Administration Upper Atmospheric Research Program.

REFERENCES

Bhartia, P. K., K. F. Klenk, C. K. Wong, and D. Gordon, (1984) "Intercomparison of the NIMBUS 7 SBUV/TOMS Total Ozone Data Sets With Dobson and M83 Results," *J. Geophys. Res., 89,* 5239-5247.

Heath, D., A. J. Krueger, and H. Park, (1978) "The Solar Backscatter Ultraviolet (SBUV) and Total Ozone Mapping Spectrometer (TOMS) experiment, in the NIMBUS 7 User's Guide," edited by C.R. Madrid, NASA Goddard Space Flight Center, Greenbelt, Md., 175-211.

Lovill, J. E., T. J. Sullivan, R. L. Weichel, J. S. Ellis, J. G. Huebel, J. A, Korver, P. P. Weidhaas, and F. A. Phelps, (1978) "Total Ozone Retrieval From Satellite Multichannel Filter Radiometer Measurements," Lawrence Livermore National Laboratory, UCRL-52473, 97 pp.

Luther, F. M. and R. L. Weichel, (1981) "Determination of total ozone from DMSP multichannel filter radiometer measurements," Proceedings of the Quadrennial International Ozone Symposium, Boulder, Colorado.

Nichols, D. A., (1975) "DMSP block 5D special meteorological sensor H, optical subsystem," *Opt. Engr., 14,* 284-288.

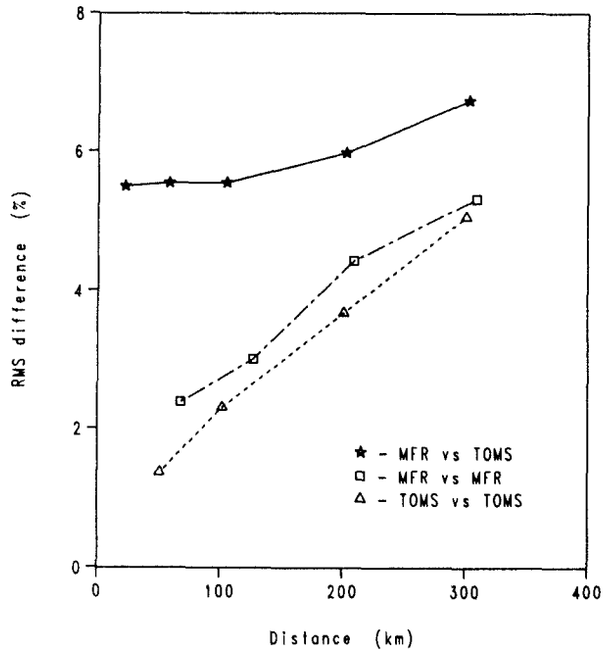

Fig. 1. Variation of the RMS difference in percent of total ozone at various separation distances in the latitude band 35N-45N on January 1, 1979.

Table 2. The average difference (d) and the standard deviation (sd) of the differences of the TOMS minus the MFR total ozone, both in percent of the MFR total ozone, for selected months.

Latitude	Jan. 79		Apr. 79		Jul. 79		Nov. 79		Jan. 80	
	d	sd	d	sd	d	sd	d	sd	d	sd
90N-85N			-4.1	7.6	-4.2	4.2				
85N-75N			-3.6	8.0	-4.9	4.5				
75N-65N	2.8	9.2	0.2	6.6	-7.3	5.0	-0.3	8.7	13.3	10.1
65N-55N	4.1	9.3	-1.0	5.8	-5.9	4.6	0.5	8.2	10.7	9.2
55N-45N	-0.8	7.4	0.1	6.3	-2.1	4.8	-1.2	6.3	0.8	7.8
45N-35N	0.8	6.5	-2.5	7.0	-3.8	6.5	-0.4	5.6	-1.1	7.0
35N-25N	0.0	5.8	-2.2	7.2	-5.4	6.6	-3.1	5.7	-3.6	6.3
25N-15N	-6.3	5.8	-2.3	6.2	-2.2	5.2	-4.1	6.1	-9.4	5.1
15N- 5N	-5.5	3.5	-0.6	3.8	1.8	2.9	-0.6	3.8	-5.9	3.5
5N- 5S	-4.9	2.6	-2.4	3.7	-2.6	3.0	1.2	3.4	-0.8	2.9
5S-15S	-1.2	3.2	-3.5	3.3	-2.8	2.5	3.6	3.1	2.0	3.2
15S-25S	-0.6	4.0	-4.0	3.6	-1.3	3.8	2.6	4.9	2.5	4.4
25S-35S	0.7	3.4	-1.3	4.1	0.0	5.4	2.6	3.6	2.2	3.6
35S-45S	-1.2	3.4	-2.3	3.8	0.3	5.7	0.6	4.1	0.2	4.0
45S-55S	-1.1	4.1	-2.7	5.5	1.7	7.4	2.9	5.7	0.6	4.7
55S-65S	-3.7	4.6	-0.5	8.3	4.1	8.3	3.7	7.4	-1.5	4.7
65S-75S	-7.2	4.0	0.0	7.0	9.9	5.7	-1.6	8.6	-4.9	4.7
75S-85S	-8.9	3.2	-4.7	6.0			-8.2	7.0	-6.4	3.8
85S-90S	-10.6	2.8					-12.4	6.7	-7.4	4.0

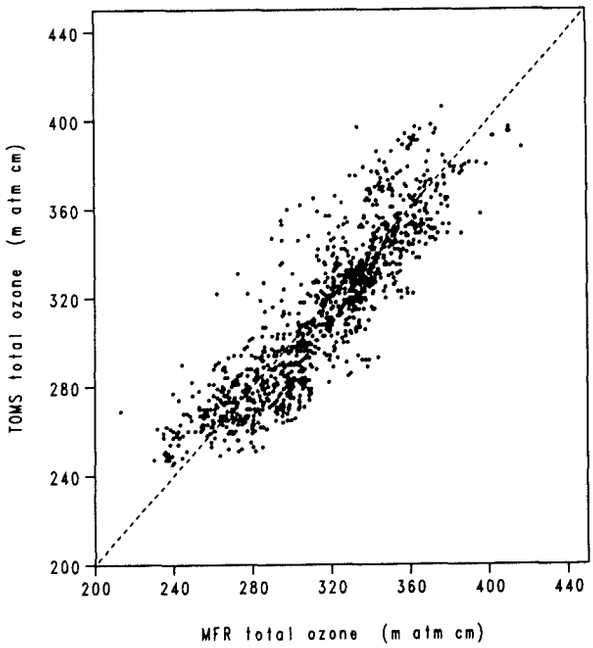

Fig. 2. Scatter plot of the MFR and TOMS total ozone (1103 points at 100 km separation distance) in latitude band 35N-45N on January 1, 1979.

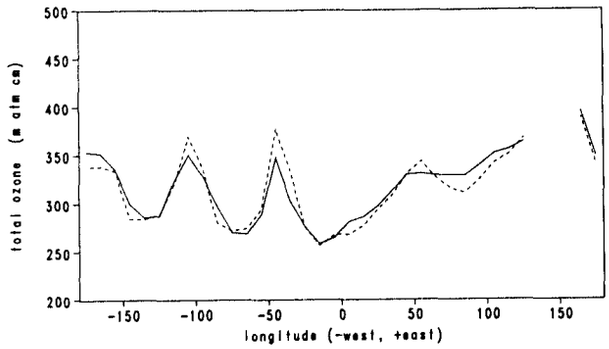

Fig. 3. The 1-by-10 degree latitude-longitude average of the 1103 MFR (solid) and the TOMS (dashed) total ozone data at 100 km separation distance inthe 35N-45N latitude zone on January 1, 1979.

Table 3. The average difference of the TOMS minus the SBUV total ozone as a percent of the MFR total ozone for selected months.

Latitude	Jan. 79	Apr. 79	Jul. 79	Nov. 79	Jan. 80
90N-85N					
85N-75N		2.6	1.7		
75N-65N		1.6	1.8	0.4	
65N-55N	2.6	1.6	1.4	2.2	2.8
55N-45N	1.8	1.7	1.8	2.4	2.4
45N-35N	2.1	1.7	1.4	2.2	2.1
35N-25N	1.8	0.9	0.8	2.0	2.0
25N-15N	1.3	0.4	0.5	2.1	2.3
15N- 5N	1.0	0.4	1.4	2.5	2.0
5N- 5S	1.2	1.4	1.6	2.3	2.2
5S-15S	1.2	1.2	1.4	2.4	2.6
15S-25S	1.0	1.2	1.5	2.1	1.9
25S-35S	1.1	1.5	1.8	2.2	2.0
35S-45S	1.6	1.8	1.7	2.6	2.7
45S-55S	2.2	1.5	1.7	3.0	3.0
55S-65S	1.8	1.5	2.2	3.0	2.8
65S-75S	2.0	1.4	4.2	3.3	2.8
75S-85S	1.1	1.7		1.7	1.6
85S-90S					

IMPACT OF THE INITIAL SPECIFICATION OF MOISTURE AND VERTICAL MOTION ON PRECIPITATION FORECASTS WITH A MESOSCALE MODEL-- IMPLICATIONS FOR A SATELLITE MESOSCALE DATA BASE

Pamela E. Mlynczak

Department of Meteorology
University of Wisconsin-Madison

George R. Diak

Cooperative Institute for Meteorological Satellite Studies
University of Wisconsin-Madison

David D. Houghton

Department of Meteorology
University of Wisconsin-Madison

1. INTRODUCTION

Over the years, a number of regional numerical weather prediction models have been developed in an attempt to forecast not only synoptic scale events, but the mesoscale phenomena that are associated with or even independent of synoptic scale systems. One problem with regional models, however, involves the forecast of precipitation, which is a mesoscale event itself. The onset of precipitation in model forecasts commonly lags behind the observations, even when precipitation is observed at the initial time. To understand the nature of precipitation forecast deficiencies, two key related variables, namely moisture and vertical motion, their initialization in a model, and their evolution during the forecast must be examined. In this study, model simulations with modifications of the initial specifications of moisture and vertical motion will be examined to determine the relative impact of the mesoscale component of each parameter on the subsequent quantative precipitation forecast.

2. MESOSCALE MODEL

2.1 Analysis System

The analysis system and the forecast model have a grid of 51 east-west rows and 61 north-south columns on a Lambert conformal projection, with a horizontal grid increment of 67 km at the standard latitudes of 20 and 50 degrees north latitude. The domain is shown in Fig. 2. The principal characteristics of the analysis system are found in Table 1.

The objective analysis scheme is a version of the analysis system which is used by the Australian Numerical Meteorology Research Centre (ANMRC). This research analysis system was developed from the analysis scheme used operationally by Australia's Bureau of Meteorology (Seaman et al., 1977). The scheme is a combination of the successive correction method (SCM) of Cressman (1959) and the variational blending technique of Sasaki (1958, 1970). The research version contains three-dimensional variational blending of geopotential. Mills (1981) presents a qualitative discussion of the analysis sequence.

Table 1

Principal Characteristics of the Analysis System and Model

Analysis System
Combination of successive correction method and variational blending in three dimensions
Ten pressure levels, p=1000, 850, 700, 500, 400, 300, 250, 200, 150, and 100 mb
Horizontal resolution: 67 km
Fields analyzed or derived at each pressure level: - geopotential height - temperature - dewpoint - horizontal wind components - streamfunction
Forecast Model
Primitive equations model in σ-coordinates
Ten vertical levels at σ=0.09, 0.19, 0.29, ..., 0.99
Horizontal resolution: 67 km
Staggered horizontal grid (Arakawa "C" grid)
Semi-implicit time differencing (Δt=5 min)
Similarity theory surface layer
Stability-dependent vertical diffusion of momentum, heat, moisture above surface layer through depth of boundary layer
Surface shortwave and longwave flux modified by cloudiness
Surface energy balance equation
Large-scale precipitation
Kuo-type convective parameterization
Updated boundary conditions

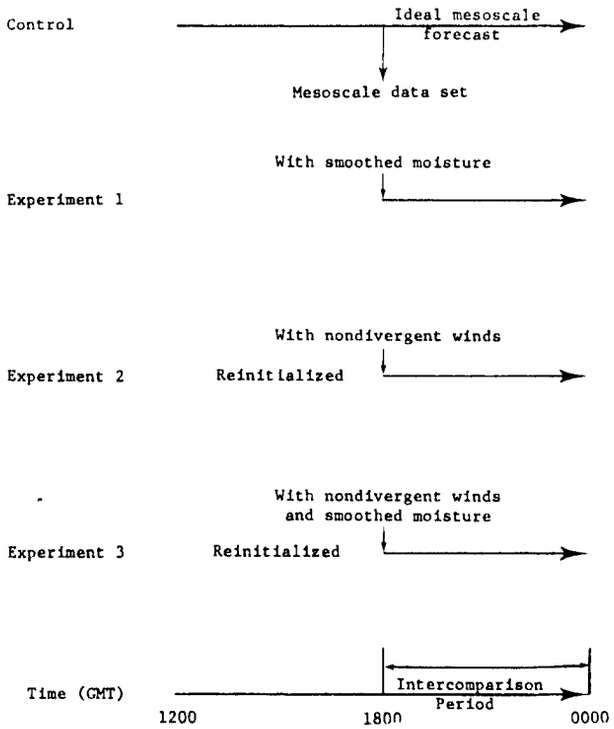

Fig. 1. Schematic summary of experimental design. The duration for each simulation is indicated by horizontal arrows.

2.2 Forecast Model

The forecast model was developed from the Australian Region Primitive Equations (ARPE) model (McGregor et al., 1978). The subsynoptic Scale Model (SSM) of the Space Science and Engineering Center at the University of Wisconsin-Madison used in this study is an adaptation of the ARPE model to the North American region. In this adaptation on Kuo-type convective parameterization (Kuo, 1965, 1974) and a comprehensive planetary boundary layer scheme were incorporated into the model. Also, a finite differencing scheme discussed by Corby et al. (1972) which lessens truncation effects in regions of steep topography has been added. Further characteristics are found in Table 1.

3. EXPERIMENTAL DESIGN

Four simulations are made with the SSM to determine the impact of the initial moisture and vertical motion fields on the evolution of the precipitation forecasts. These are a control forecast 12-hour simulation that begins at 1200 GMT 6 March 1982 and three experiment simulations with modifications to the moisture and vertical motion fields incorporated at 1800 GMT. The experiment forecasts from 1800 GMT are compared to the second half of the control forecast. The experimental design is given in Fig. 1.

The 12-hour control simulation begins at 1200 GMT 6 March 1982 and develops precipitation by 1300 GMT. The model is still producing precipitation at 1800 GMT the time a data set is extracted for use in the three experiments.

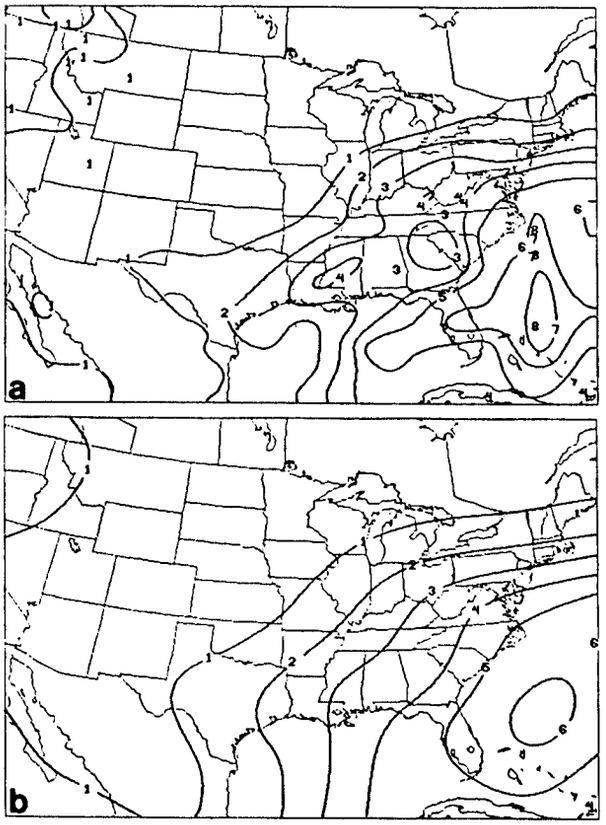

Fig. 2. Mixing ratio from the control forecast at 1800 GMT for the sigma level of 0.69; a) unsmoothed, b) smoothed. Contour interval is 1 g kg^{-1}.

Beginning at this time, changes in the precipitation rates and accumulations due to changes in the initial specifications will be most accentuated. The six-hour control forecast from 1800 GMT 6 March to 0000 GMT 7 March 1972 provides the "ideal forecast"--one that contains mesoscale moisture and vertical motion information from beginning to end.

Experiment 1 is run like the control forecast, except that at 1800 GMT, smoothed moisture fields replace the mesoscale moisture fields in the model. The moisture fields are smoothed to make them representative of fields that would be obtained from analyzed radiosonde data, usually considered to be at the synoptic scale. Fig. 2 shows the original and the smoothed mixed ratio fields for the sigma level of 0.69. Experiment 1 provides the precipitation forecast for the initial state with only a synoptic scale moisture field.

Experiment 2 is like the control forecast except that the initial wind fields are constrained to be nondivergent at 1800 GMT. The nondivergent wind components are derived from the model winds extracted from the control forecast data set and are inserted into the model. All of the other variables remain unchanged. Because the winds are nondivergent, the initial vertical motion is suppressed, particularly away from areas of significant topography (Fig. 3). Experiment 2 shows the effect of a nondivergent initialization of winds on the subsequent quantitative precipitation forecast.

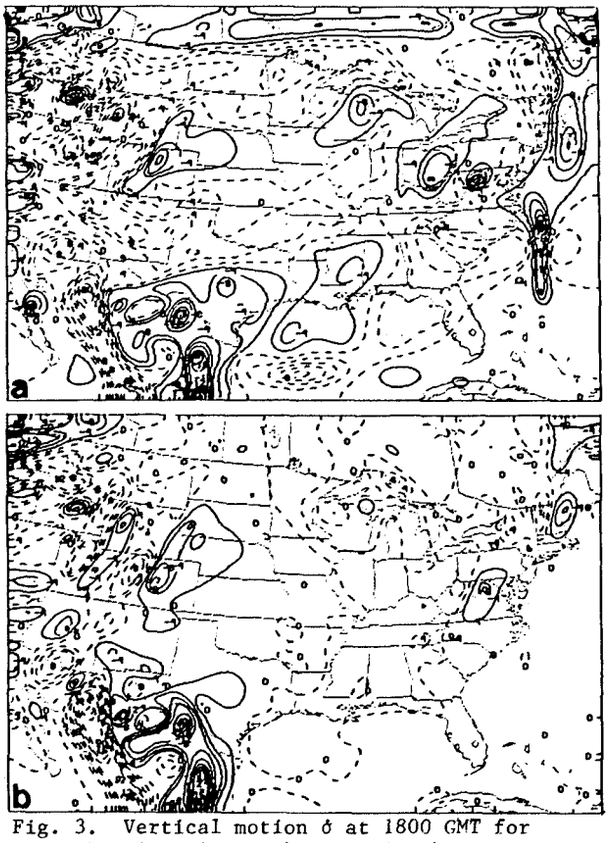

Fig. 3. Vertical motion $\dot{\sigma}$ at 1800 GMT for sigma level of 0.49; a) control, b) experiment 2. Negative values (upward motion) are solid. Contour interval is $2X10^{-6}$ s^{-1}.

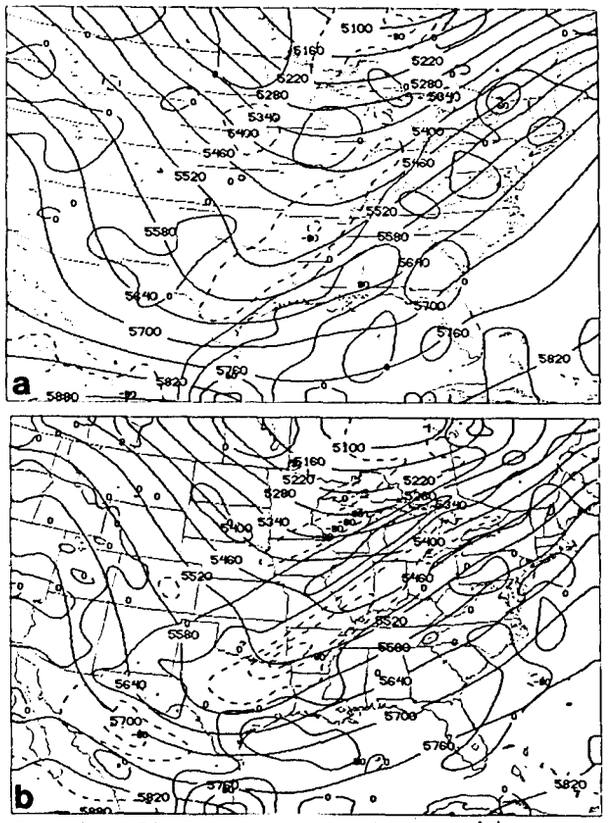

Fig. 4. 500-mb geopotential heights (m) and 500-mb relative vorticity (contour interval $40X10^{-6}$ s^{-1}, negative values dashed) at 0000 GMT; a) observed, b) control.

Experiment 3 is a combination of Experiments 1 and 2, containing both the initial smoothed moisture and nondivergent wind fields. This experiment is the most representative of a forecast beginning with synoptic analyses. It should be noted, however, that mesoscale and synoptic scale information from the six-hour control forecast remained in the height and temperature fields.

4. CONTROL CASE OF 6 MARCH 1982

The purpose of this research to study the changes made to a precipitation forecast due to modifications of the initial moisture and vertical motion fields is achieved by comparing simulation of the three experiments to the control forecast. The performance of the control itself is discussed very briefly here, although its accuracy in terms of the observations is not central to the analysis.

The model performed well at 500-mb level, as shown in Fig. 4. The forecasted trough over the central U.S. is slightly behind that of the analysis, but the intensity is simulated well. The forecast, however, does not capture the short wave trough observed west of Florida. The forecast of mean sea level pressure was excellent, with accurate placement and strength of the features (not shown).

The precipitation forecast from the model was not as satisfactory as the height and mean sea level pressure forecasts. The model's placement of copious rainfall east of Virginia and North Carolina seems accurate, based upon comparing Figs. 5 and 6 with radar maps (not shown). Precipitation output from the model is shown in hundredths of centimeters. The development of the precipitation area over Ohio and Pennsylvania lagged four hours behind the observations, yet the model greatly overforecasted the amounts in this region, producing as much as 2.00 cm (0.75 in.) while the observations were all less than 0.25 in. The model's performance in the Gulf region compared much less favorably to the observations than did the forecast off the East Coast and over the northeastern United States. The precipitation band observed over Louisiana, Mississippi, and Alabama was not forecasted at all. No rainfall greater than 0.25 in. was forecasted over the land. Instead, the model generated precipitation out over the Gulf of Mexico, but not until 1700 GMT. The validity of this feature is questionable because of the lack of verification data; however, satellite imagery did suggest that precipitation had developed here earlier before moving eastward. The forecasted feature, however, remained stationary.

It is unfortunate that the precipitation forecast produced by the control simulation was not more accurate. The purpose of this study, however, is to discuss changes in the forecasts brought about by modifications to the initial conditions. It is expected that the comparisons between the control and the experiments will be meaningful, regardless of the simulation deficiencies in the control forecast.

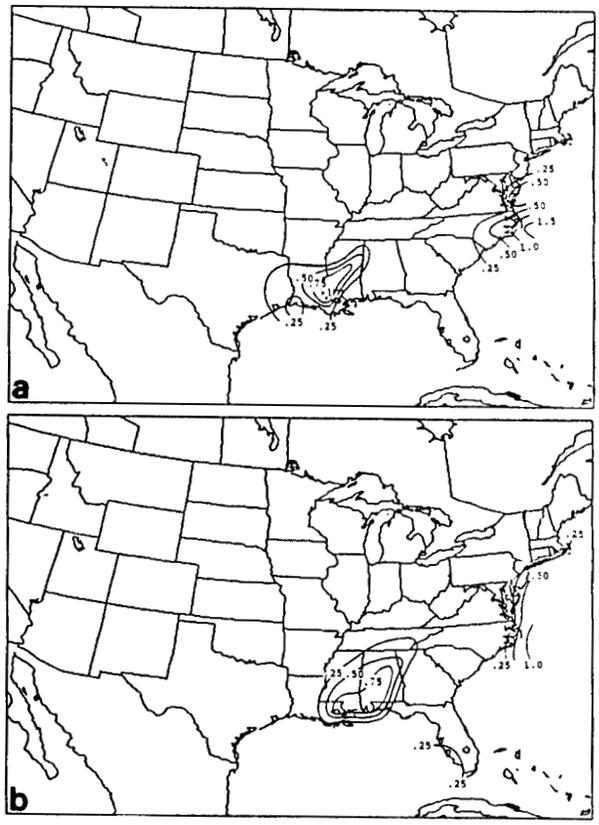

Fig. 5. Six-hour observed precipitation accumulations (in.) ending at (a) 1800 GMT, (b) 0000 GMT.

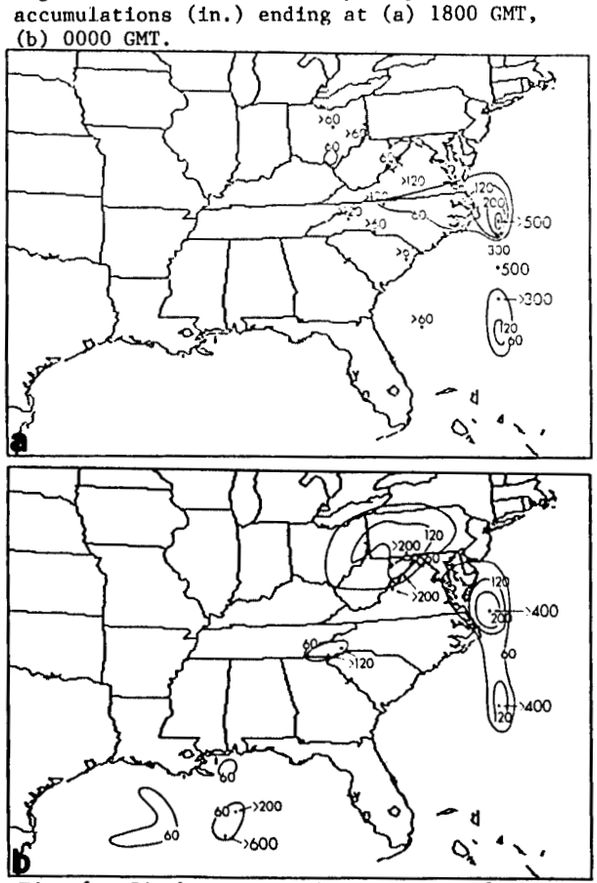

Fig. 6. Six-hour precipitation accumulations (hundredths of cm) from the control forecast ending at (a) 1800, (b) 0000 GMT.

5. EXPERIMENTAL RESULTS AND COMPARISONS

The six-hour precipitation forecasts from 1800 GMT to 0000 GMT of the control and the experiments are compared. To facilitate this comparison, three rectangular domain "boxes" encompassing the major precipitation areas of the control forecast were chosen for analysis (Fig. 7). Area-averaged accumulations, plotted in Fig. 8, were calculated in each box by summing the total accumulations and dividing by the number of grid points.

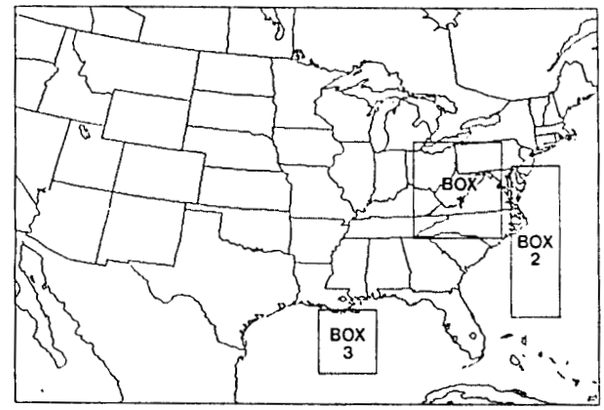

Fig. 7. Areas of precipitation for statistical calculations.

In Experiment 1, accumulations were much lower than those of the control, especially in boxes 2 and 3, where moisture values at 1800 GMT had been reduced by the smoothing process. In these two boxes, accumulations were only 24-30% of the control values. One precipitation maximum was reduced by 50%, and two other maxima found in the control were not forecasted in Experiment 1. Precipitation rates lagged behind the control forecast, and areal coverage was reduced to 68-77% of the control.

The reduced vertical motions of Experiment 2 resulted in lower accumulations that were 40-45% of the control values for the three boxes. Precipitation maxima for this experiment were positioned well when compared to the control, but most maxima were much lower. Area coverage was also reduced, while precipitation rates generally lagged behind the control.

As would be expected, Experiment 3, both lacking initial vertical motion and having lower initial moisture values than the control forecast in the precipitation regions, produced the lowest precipitation accumulations of the three experiments. Fig. 8 reveals that Experiment 3 yielded much lower average accumulations and precipitation rates than the control, with Box 2 having the largest differences. Average accumulations at the end of the forecast were only 4-22% of those from the control forecast, and precipitation covered 6-43% of the control's area of precipitation. This experiment missed completely the precipitation centers over the Atlantic and in the Gulf that were forecasted by the control (Fig. 6b). After beginning with primarily "synoptic scale" conditions, the model was unable to recover in the six-hour period and regenerate the mesoscale fields necessary to

yield detailed precipitation features and higher levels of precipitation accumulation.

An interexperimental precipitation comparison supports the results previously discussed. Comparing the precipitation forecasts between Experiments 2 and 3 shows the effects of smoothing the initial moisture fields, just as done by the comparison between Experiment 1 and the control. Fig. 8 shows that the average accumulations in Experiment 3 were, at most, 50% of the accumulations in Experiment 2. Areas of precipitation were also reduced in Experiment 3. Comparing Experiment 3 with Experiment 1 also showed the effects of suppressing the initial vertical velocities. Again, precipitation accumulations, rates, and areal coverage were reduced significantly. These comparisons are indeed consistent with the comparisons between the control and each experiment.

6. CONCLUSIONS

Four simulations were made with a numerical mesoscale model to determine the effects of suppressing the initial mesoscale information in the moisture and wind fields on the precipitation forecasts. The latter half of a 12-hour control forecast represented an ideal forecast that was "initialized" with fields containing mesoscale as well as synoptic scale structure. The three experiments were degraded versions of this ideal initialization and their forecasts were compared to the control forecast during the period from 1800 GMT 6 March to 0000 GMT 7 March 1982.

The characteristics of the precipitation forecasts of the experiments are not different enough to conclude that either mesoscale moisture or mesoscale vertical velocity at the initial time is more important for producing a forecast closer to that of the control. For example, at the end of the forecast, the average precipitation accumulation over a land area in the smoothed moisture experiment was 67% of the control forecast, while the nondivergent experiment produced accumulations that were 45% of the control. Over the oceans, however, the smoothed moisture experiment produced 24-30% of the control forecast, less than the nondivergent experiment, which produced 40-44% of the control forecast. No general statements can be made about this study, therefore, except to say that degrading one or both of these initial fields produces a drier forecast when compared to the control forecast. First of all, comparisons were made for only a six-hour period, and this may not have been sufficient time for the model to recover from the modifications made. Secondly, these experiments were performed on one case only, with just one model, and as such, generalizations regarding the relative worth of initial moisture and vertical velocities are inappropriate.

This research points out the need for proper initialization of mesoscale moisture and vertical motion information so that more accurate precipitation forecasts may be obtained. Improvement of the data base that is analyzed should be very helpful. More detailed moisture

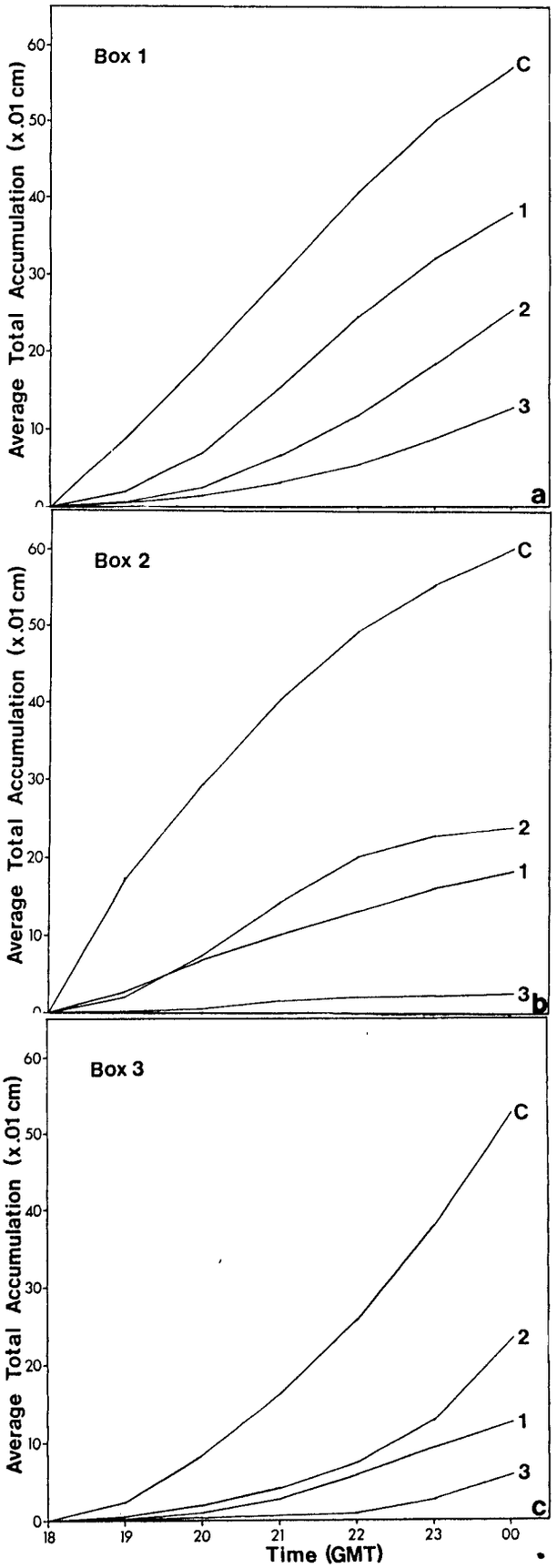

Fig. 8. Area-averaged precipitation accumulations (hundredths of cm) as a function of time for the control forecast (c) and the experiment for (a) Box 1, (b) Box 2, (c) Box 3.

information is available from high-resolution satellite data, satellite cloud and water vapor drift winds would improve the horizontal winds, and thus the vertical motion derived from the convergence/divergence of these winds. Considerable research will be required to determine how to use a satellite mesoscale data to make short-term precipitation forecasts more accurate and timely.

7. ACKNOWLEDGEMENTS

The work of the first author was supported by a National Science Foundation Graduate Fellowship. Computing and data resources were made available through the Cooperative VAS Program with the Marshall Space Flight Center, Control NAS8-34732. The Atmospheric Science Division of NSF provided additional support through Grant ATM-8005369.

8. REFERENCES

Corby, G. A., A. Gilchrist, and R. L. Newson, 1972: A general circulation model of the atmosphere suitable for long period integrations. Quart. J. Roy. Meteor. Soc., 98, 809-832.

Cressman, G. P., 1959: An operational objective analysis system. Mon. Wea. Rev., 87, 367-374.

Kuo, H. L., 1965: On formation and intensification of tropical cyclones through latent heat release by cumulus convection. J. Atmos. Sci., 22, 40-63.

_____, 1974: Further studies of the parameterization of the influence of cumulus convection on large scale flow. J. Atmos. Sci., 31, 1232-1240.

Le Marshall, J. F., W. L. Smith, and G. M. Callan, 1985: Hurricane Debby--an illustration of the complementary nature of VAS soundings and cloud and water vapor motion winds. Bull. Amer. Meteor. Soc., 66, 258-263.

McGregor, J. L., L. M. Leslie, and D. J. Gauntlett, 1978: The ANMRC limited-area model: Consolidated formulation and operational results. Mon. Wea. Rev., 106, 427-438.

Mills, G. A., 1981: An objective limited-area analysis/prognosis experiment using FGGE data in the Australian region. Mon. Wea. Rev., 109, 1898-1913.

Sasaki, Y., 1958: An objective analysis based on the variational method. J. Meteor. Soc. Japan, 36, 875-883.

_____, 1970: Some basic formalisms in numerical variational analysis. Mon. Wea. Rev., 98, 875-883.

Seaman, R. S., R. L. Falconer, and J. Brown, 1977: Applications of variational blending technique to numerical analysis in the Australian region. Aust. Meteor. Mag., 25, 3-23.

ANALYSIS AND FORECAST EXPERIMENTS INCORPORATING SATELLITE SOUNDINGS AND CLOUD AND WATER VAPOR DRIFT WIND INFORMATION

Brian M. Goodman

George R. Diak

Cooperative Institute for Meteorological Satellite Studies
Space Science and Engineering Center
Madison, Wisconsin

Graham A. Mills

Bureau of Meteorology Research Center
Melbourne, Australia

1. INTRODUCTION

The Man-computer Interactive Data Access System (McIDAS) (Suomi et al., 1983) has extensive capability to ingest conventional surface and upper air meteorological data, in addition to satellite-derived data which can be processed and edited in the McIDAS environment. These satellite products routinely consist of temperature and moisture profiles from both orbiting (Smith et al., 1979) and geostationary (Smith, 1983) satellites, as well as cloud drift and water vapor winds derived from geostationary satellite imagery (Mosher, 1979, Stewart et al., 1985), and gradient winds estimated from VAS temperature soundings (Hayden, 1985).

While large amounts of application software exists to analyze and process these data for specific case studies, including advanced objective analysis and numerical weather prediction models (Mills and Hayden, 1983, LeMarshall et al., 1985), no formal mechanism has hitherto existed to perform routine assimilation of these mixed data types with the aim of producing four-dimensional gridded data sets of the primary atmospheric variables which can be used to periodically update limited area forecast models. While most national weather centers use global forecast model products to provide the first guess for the analyses used to initialize their limited area forecast models, there is no reason why an equivalent data assimilation system should not be operated on a limited area domain, provided care is taken in the specification of the lateral boundary conditions. Mills (1981) has demonstrated a stable analysis/forecast cycling system using FGGE data sets over a limited area domain in the Australian region.

The essential phases of data assimilation scheme are a model forecast to the data insertion time, the correction of the forecast fields to fit the observed data (the analysis phase), and an initialization phase to balance the adjusted fields prior to the next forecast stage. Lorenc (1984) lists the following desirable principles of such a scheme: (1) the analysis must fit the observations to within their estimated observational errors; (2) the analyzed fields must be internally consistent, matching the structure, scale, and balance of the atmosphere; and (3) the anlysis must be near the forecast based on earlier observations unless current observations indicate otherwise.

Two further requirements were made. First, the system should be computationally efficient and geographically portable. Second, the system should be as robust as possible, without excessively compromising the quality of the output product. That is, minimal manual intervention should be needed in the operation of the system. This is, however, to some extent at the expense of maintaining maximum detail in the analysis, and a variety of options exist to relax these constraints in development and testing of this system.

It was decided to base the first generation of this system on existing analysis and forecast modules, with which some experience and expertise was available, and to modify these pre-existing components to improve their suitability as assimilation vehicles. The basic modules which are used in the scheme are the three-dimensional variational analysis scheme of R. S. Seaman (e.g. Mills, 1981) and the new Australian Region Primitive Equation (ARPE) model which has been extensively described by Leslie et al. (1985). The interface programs have been extensively modified so that the system should approach satisfying Lorenc's condition (3) above. The range of available options is summarized in Table 1. The basic and incremental assimilation cycles are schematically represented in Figs. 1 and 2, respectively. The analysis scheme, the forecast model, the interface codes, and how they are linked together to perform an assimilation sequence in the McIDAS environment will be discussed in detail in a forthcoming paper.

The assimilation system was initially tested in a case study mode using a mixture of VAS soundings and special network radiosonde data at 1430 and 1730 GMT on March 1982 (Diak, et al., 1986). To adequately test the

Table 1

Options To Be Selected

Data mix:	
Radiosonde	
Special network	
Satellite temperature retrievals/gradient winds (either/or)	
Cloud and water vapor drift winds	
SVCA/buoys	
Assimilation type:	
Basic	
Incremental	
Analysis:	
Weight of geostrophic/gradient wind	
Rejection tolerance	
Minimum pass radii for first pass	
Pre-processor:	
Sigma level disposition	
Divergent or non-divergent winds	
Topography enhancement factor	
Model:	
Timestep	
Boundary conditions	- fixed
	- updated
Initialization	- none
	- free VMI
	- pressure constrained VMI
Physics options	- surface T, T_D prediction
	- convective pptn
	- large scale pptn
	- vertical diffusion

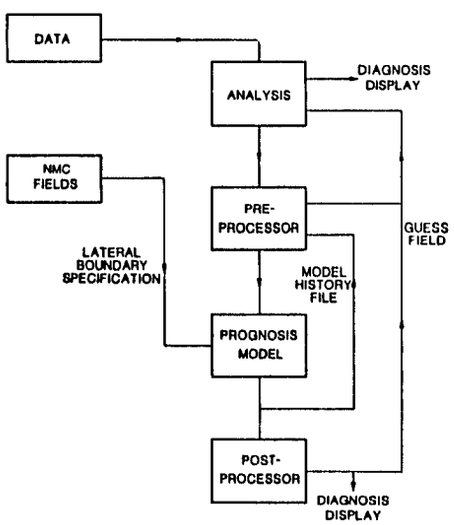

Fig. 1. Basic (or cold start) case study configuration.

assimilation system using data from more extended periods of time, advantage was taken of CIMSS support of the National Hurricane Center to assimilate radiosonde, buoy, VAS temperature and dewpoint (Smith, 1983) and gradient wind data (Hayden, 1985), and cloud drift and water

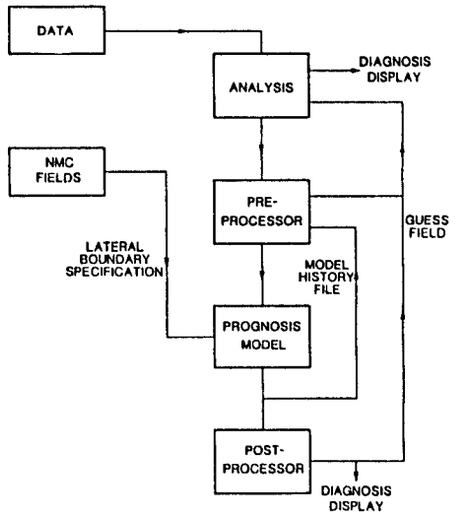

Fig. 2. Incremental assimilation sequence configuration.

vapor motion winds (Stewart, et al., 1985). A 12 hour assimilation interval run at 00 and 12 GMT was performed in a quasi-real-time mode from 12 GMT on 8 October 1985 to 12 GMT on 18 October 1985. No VAS or cloud and water vapor drift winds were available during the weekend. For convenience, the domain was chosen to be the same as the March 6 assimilation: 26x31 grid with a 125 km grid spacing centered on longitude 95W and between latitudes 20 and 50N.

A significant amount of day-to-day fluctuation was noted during this period of time, and some interesting situations did occur. For example, at 12 GMT on day 283, the initialization makes very large changes to almost all fields, and clearly there was considerable imbalance in the initial state, which was then followed by the largest 1000-500mb thickness errors in any of the 12-hour forecasts (Fig. 3). It was encouraging, at this stage of development of the system, to find that this did not destabilize the system. There is a considerable degree of oscillation in the skill of the 1000-500mb thickness forecasts based at 12 GMT and those based at 00 GMT. The cause of this may be due to the differing mixes of satellite and conventional data at the different times, or may be due to more subtle factors needing further investigation.

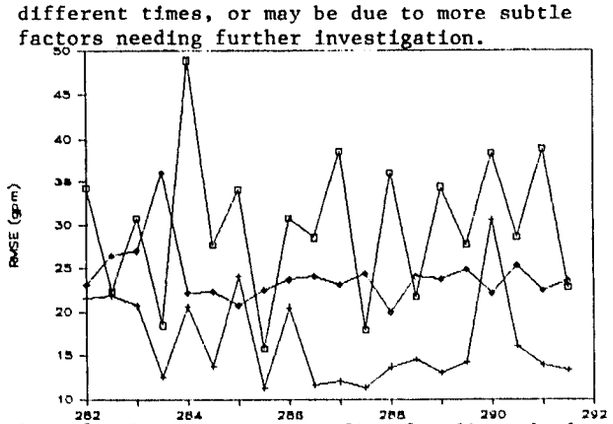

Fig. 3. Root-mean-square fit of radiosonde data 1000-500 mb thickness to assimilation cycle analyses, initialized fields, and 12 hour prognoses at 12-hour intervals from 00 GMT 9 October 1985 (day 282) to 12 GMT 18 October 1985 (day 291).

When looking at the RMS vector errors in Fig. 4, it must be remembered that the wind fields input to the prognosis model are non-divergent increments added to the model forecast wind fields, and thus the RMSVE statistics have a greater magnitude than would be expected from a scalar analysis of wind components. The RMSVE of the radiosonde data to these wind fields are also included for comparison, and are substantially lower than the statistics for the winds used for model initiation.

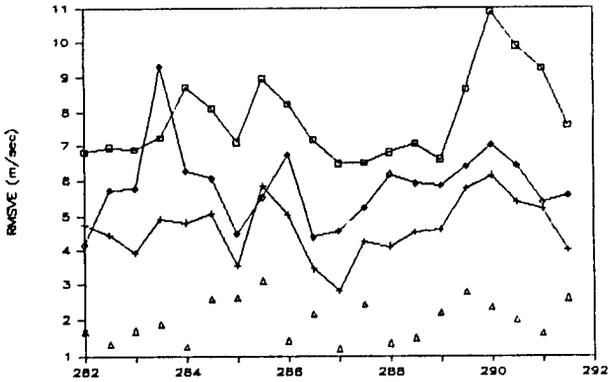

Fig. 4. Root-mean-square vector error at 500 mb of 12-hour prognoses, analyses with non-divergent wind increments, analyses with divergent wind increments (triangles), initialized fields, and 12-hour prognoses at 12-hour intervals from 00 GMT 9 October 1985 (day 292) to 12 GMT 18 October 1985 (day 291).

To a large extent, Lorenc's condition (3) is met by correcting the first guess forecast in the anlysis. Of equal desirability is that information from the prognosis model which is not resolved by the observations or the analysis scheme be preserved through the analysis (correction) and initialization phases of the assimilation. One such field is the vertical motion structure. The 500 mb omega field ($\partial p/\partial t$) were compared before the analysis and after initialization at each data insertion time and, in general, the major features and structure were preserved which was very encouraging. Two examples for the 12-hour forecast vertical motion and the after initialization vertical motion at 00 GMT 10 October and 00 GMT 16 October 1985 are shown in Fig. 5. In each case, it is clear that substantial continuity of these fields has been preserved, even though there has been significant changes to the prognosis fields during the analysis. These patterns are quite typical of the synoptic sequence during this period, with an area of upward vertical motion toward the northwest of the grid, associated with an advancing trough, and another weaker, alongated southwest-northeast area of upward motion which has propagated southeastward in association with the eastward passage of the preceeding middle latitude trough.

This period was not synoptically very active. A powerful anticyclonic circulation covered the southeastern part of the U.S. throughout the entire period, with a sequence of advancing troughs which entered the analysis domain from the west and northwest and were forced northward by the anticyclone as they moved eastward. The assimilation sequence clearly demonstrates a synoptic continuity

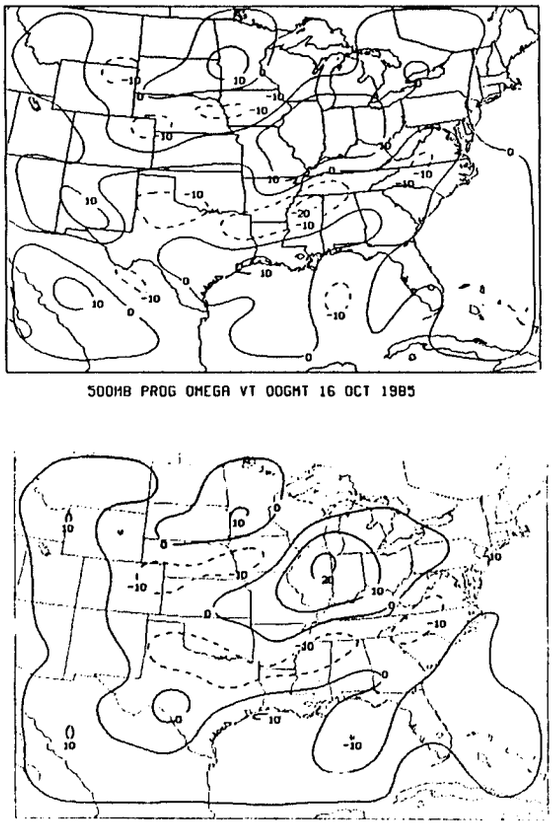

Fig. 5. Before analysis and after initialization 500 mb vertical motion ($\partial p/\partial t$) fields at 00 GMT 16 October 1985 (units mb/hr).

throughout the entire assimilation period for all variables, as would be expected from a robust analysis/prognosis system. Figure 6 shows an example of four assimilation analyses of 500 mb heights and winds for the two-day period 00 GMT 15 October to 12 GMT 16 October 1985.

Development of a functional, stable assimilation system is being continued in a delayed real-time mode in association with the special GALE observing networks at 12 and 6 hour analysis/prognosis assimilation cycles, and in a quasi-real-time mode on a 3 hour assimilation interval during the special observing periods.

2. ACKNOWLEDGEMENTS

Much of the work on VAS and satellite wind assessment has been funded through the NASA Marshall Space Flight Center Contract NAS8-34732.

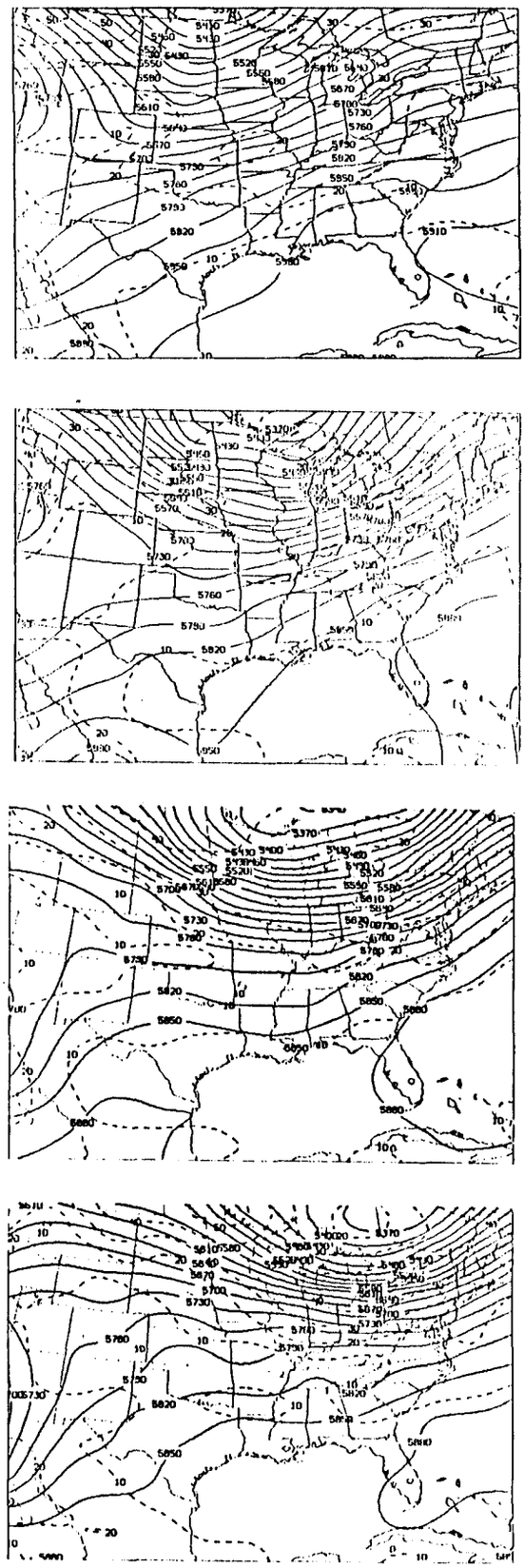

Fig. 6. 500 mb geopotential height/isotach patterns from 00 GMT 15 October 1985 to 12 GMT October 1985.

3. REFERENCES

Diak, G., S. Heikkinen and J. Bates, 1986: The influence of variations in surface treatment on 24-hour forecast with a limited area model, including a comparison of modelled and satellite-measured surface temperatures. Accepted by Mon. Wea. Rev.

Hayden, C. M., 1985: Estimating the wind field from VAS temperature soundings. Submitted to J. Clim. Appl. Meteor.

LeMarshall, J. F., W. L. Smith and G. M. Callan, 1985: Hurricane Debby - An illustration of the complementary nature of VAS soundings and cloud and water vapor motion winds. Bull. Amer. Meteor. Soc., 66, 268-263.

Leslie, L. M., G. A. Mills, L. W. Logan, D. J. Gauntlett, G. A. Kelly, J. L. McGregor and M. J. Manton, 1985. A high resolution primitive equations NWP model for operations and research. Aust. Meteor. Mag., March 1985.

Lorenc, A. C., 1984: Data assimilation by repeated insertion into a forecast model - principles, practice, problems and plans. ECMWF Seminar/Workshop. Data assimilation systems and observing system experiments with particular emphasis on FGGE. Vol. 2, pp. 181-214.

Mills, G. A., 1981: An objective limited area analysis/prognosis experiment using FGGE data in the Australian region. Mon. Wea. Rev., 109, 1898-1913.

Mills, G. A. and C. M. Hayden, 1983: The use of high horizontal resolution satellite temperature and moisture profiles to initialize a mesoscale numerical weather prediction model - severe weather event case study. J. Clim. Appl. Meteor., 22, 649-663.

Mosher, F. R., 1979: Cloud drift winds from geostationary satellites. Atmos. Tech., 10, 53-60.

Smith, W. L., 1983: The retrieval of atmospheric profiles from VAS geostationary radiance observations. J. Atmos. Sci., 40, 2025-2035.

Smith, W. L., H. M. Woolf, C. M. Hayden, D. Q. Wark, and L. M. McMillin, 1979: The TIROS-N operational vertical sounder. Bull. Amer. Meteor. Soc., 60, 1177-1187.

Stewart, T. R., C. M. Hayden and W. L. Smith, 1985: A note on water vapor wind tracking using VAS data on McIDAS. Bull. Amer. Meteor. Soc., 66, 1111-1115.

Suomi, V. E., R. Fox, S. S. Limaye and W. L. Smith, 1983: McIDAS III: A modern interactive data access and analysis system. J. Clim. Appl. Meteor., 22, 766-778.

P4.13

GLOBAL SURFACE WIND AND FLUX FIELDS FROM MODEL ASSIMILATION OF SEASAT DATA

R. Atlas[1], A. J. Busalacchi[2], E. Kalnay[1], S. Bloom[3]

NASA/Goddard Space Flight Center
Greenbelt, MD 20771

and

M. Ghil
Department of Atmospheric Sciences and
Institute of Geophysics and Planetary Physics
University of California, Los Angeles, CA 90024

1. INTRODUCTION

Surface fluxes of heat, moisture and momentum between the oceans and atmosphere play a major role in the formation, movement and modification of water and air masses, and in the development and intensification of storms near coasts and over the open ocean. The determination of these fluxes is extremely important for numerical modeling and diagnostic studies of these and other atmospheric and oceanic phenomena and for numerical prediction on a variety of time scales. However, such determinations have been limited to a large extent by the lack of adequate observations of even the most fundamental meteorological variables over the oceans. For example, conventional reports of surface wind by ships are often of poor accuracy, cover only very limited regions of the world's oceans and occur at irregular intervals in time and space.

Due to these deficiencies, analyses of surface wind often misrepresent atmospheric flow over large regions of the global oceans and this contributes to the poor calculation of wind stress, and sensible and latent heat flux in these areas. As a result, most determinations of these fields have primarily been concerned with long-term means. But even the generation of these climatological fields requires considerable smoothing and extrapolation from data-dense to data-sparse areas.

With the launch of the Seasat satellite in June of 1978, a new data source for surface winds became available. On board the satellite was a scatterometer, referred to as SASS, which measured radar backscatter from centimeter scale capillary waves. By means of a geophysical algorithm, these measurements were used to infer surface wind velocity. This geophysical algorithm provided a unique wind speed but up to four possible wind directions, called aliases. Thus before this data could be utilized in meteorological analysis or diagnostic or numerical studies, this ambiguity in wind direction had to be removed.

Both objective and subjective methods have been developed to remove the ambiguity in SASS winds (i.e. dealias the SASS data). As a joint project between the Jet Propulsion Laboratory (JPL), the Atmospheric Environment Service (AES) of Canada, the University of California at Los Angeles (UCLA), and the Goddard Laboratory for Atmospheres (GLA), subjective dealiasing procedures were developed and used to globally dealias SASS data for a fifteen day period from 0000 GMT 6 September to 0000 GMT 20 September 1978 (Peteherych et al., 1984). In subjective dealiasing, meteorological analysts manually choose the correct wind direction in an iterative procedure using pattern recognition techniques. They attempt to insure kinematic consistency and consistency with other data, such as ship reports and cloud imagery. Such procedures are described in more detail by Wurtele et al. (1983) and Baker et al. (1984). Several alternative methods for objective dealiasing, described by Hoffman (1982, 1984), Baker et al. (1984) and Yu and McPherson (1984) have been developed. These all make use of an atmospheric model forecast and conventional and other satellite observations to objectively remove the ambiguity in the SASS winds.

At GLA, we have recently applied a version of the objective scheme described by Baker et al. (1984) to dealias the complete 96-day global SASS data from 0000 GMT 7 July 1978 to 0000 GMT 10 October 1978. This data has been assimilated using the GLA analysis/forecast system to produce global gridded surface wind fields at 6 h intervals. In addition, as a by-product of the assimilation process, global gridded fields of wind stress and sensible and latent heat fluxes were generated. In this paper, we present the methodology used to produce these fields, and show some preliminary comparisons between the flux fields obtained here by model assimilation of SASS data with previously published climatological fields. The most important features of the fields, such as large areas of consistently high or low heat fluxes and cyclonic or anticyclonic wind stresses, are analyzed for their physical and synoptic agreement with atmospheric circulation features

[1] Laboratory for Atmospheres
[2] Laboratory for Oceans
[3] University Space Research Associate

above and ocean circulation features below. The effect of SASS winds is evaluated through comparisons of model assimilations with and without these data.

2. Data Assimilation System

In this study, we used the GLA analysis/forecast system to objectively dealias the SASS surface winds, assimilate all available conventional and satellite data, and generate global gridded fields of surface wind, wind stress, and sensible and latent heat fluxes. This system was originally developed for the assimilation of First GARP Global Experiment (FGGE) data and was previously used in studies of the impact of FGGE data (Halem et al., 1982) and of SASS data (Baker et al., 1984) on large-scale atmospheric analysis and numerical weather prediction. It has also been used in a limited assessment of global ocean surface wind and stress fields for a 15-day period (Kalnay and Atlas, 1986). In this latter investigation, the previously mentioned subjectively dealiased SASS data set from 6-20 September 1978 was utilized.

The version of the GLA analysis/forecast system used in the current study differs from that of earlier investigations in that it contains a fully objective dealiasing procedure (without an option for subjective enhancement) and there is no balancing between the sea level pressure and surface wind fields. This system, like other four-dimensional data assimilation systems in use at operational centers, uses a 6h atmospheric model forecast integrated from a previous objective analysis as a first guess for the next analysis. All available conventional and satellite data within +/- 3h of the analysis time are then used to correct the first guess at each model grid point. The forecast model, objective analysis scheme and methods used to dealias the SASS data and compute surface fluxes are described briefly in the following subsections.

2.1 Forecast Model

The model used in the data assimilation cycle is the GLA Fourth-Order General Circulation Model (GCM) with a horizontal resolution of 4° latitude by 5° longitude and nine levels in the vertical. This model has been described in detail by Kalnay et al. (1983).

Six prognostic variables are used: the zonal and meridional winds, temperature and specific humidity in the free atmosphere, surface pressure and ground temperature. The governing equations for all of the prognostic variables are written in flux form and are solved by using fourth-order finite differencing in space and the Matsuno (Euler-backward) scheme for integration in time.

A sixteenth-order Shapiro (1970) filter is applied every 2 h on the sea level pressure, potential temperature, and wind fields. In this way, wavelengths longer than four grid lengths, which would otherwise be grossly misrepresented by the finite differences, are filtered out while they are still infinitesimal. This filtering avoids the accumulation of energy that would otherwise occur at the short-wave cutoff.

Shallow water experiments indicate that this scheme conserves potential enstrophy to a high degree of accuracy (Kalnay-Rivas and Hoitsma, 1979) and long integrations with the GLA fourth-order model have demonstrated very good skill in simulating January and July climatology (Kalnay et al., 1983). In addition, the use of the Euler backward time scheme during the model integration damps most of the gravity waves, with the result that the vertical motion fields are well correlated with synoptic patterns.

The model contains a complete range of sub grid scale physical parameterizations. The surface fluxes of heat, moisture and momentum over the ocean are modeled using bulk aerodynamic equations:

$$F_H = \rho\, c_p\, D_R\, (T_g - T_s)$$

$$F_L = \rho\, L\, D_R\, (q^*_g - q_s)$$

$$\underset{\sim}{F_M} = \rho\, D_R\, \underset{\sim}{V_s}$$

where ρ is the density, D_R is an air/surface interaction coefficient, c_p is the specific heat of air, L is the latent heat of evaporation, $\underset{\sim}{V_s}$ is the wind at the top of a surface shear layer, T_s and T_g are the respective temperatures at the top of the shear layer and the ocean surface, and q_s and q^*_g are the specific humidity at the top of the shear layer and the saturation specific humidity at the ocean surface, respectively. For a neutral atmosphere, the drag factor D_R is the product of a bulk drag coefficient (C_D) and the wind speed near the surface ($W = |\underset{\sim}{V_s}|$). However, when the entire PBL becomes stable or unstable, corrections dependent on the temperature difference across the surface layer ($\Delta T = T_g - T_s$) are made to D_R as follows:

$$D_R = \begin{cases} C_D\,(W + \Delta T^{1/2}), & \text{for an unstable PBL.} \\ \dfrac{C_D W^3}{W^2 - 7\Delta T}, & \text{for a stable PBL.} \end{cases}$$

Note that these corrections enhance D_R for unstable conditions, while they decrease D_R for stable conditions.

The value of T_g (and therefore q^*_g) over the ocean is specified in this model using climatological values, but T_s is calculated through a process that involves the matching of fluxes across the shear layer - mixed layer interface. The details of this computation are discussed at length in Kalnay et al. (1983). A similar process is followed to obtain q_s. $\underset{\sim}{V_s}$ is calculated by the extrapolation of the winds to the surface from the bottom two levels of the model.

2.2 Objective Analysis and Dealiasing Scheme

The objective analysis scheme described by Baker et al. (1984) was used in this study to dealias the SASS data and produce gridded surface wind fields. In this scheme, zonal and meridional wind components, geopotential height and relative humidity are analyzed on mandatory pressure surfaces. The 6h model forecast provides a first guess for these fields at 300 mb and at sea level, where pressure and temperature are also analyzed. The first guess for the other levels is obtained from the model first guess, modified by a vertical interpolation between the two closest completed analyses. Vertical consistency is maintained through static stability constraints. The analysis at each level is performed with a succes-

sive correction method (SCM) modified to account for differences in the data density and the statistical estimates of the error structure of the observations.

SASS data, obtained from the Atmospheric Environment Service of Canada, were objectively dealiased as a part of the objective analysis at each synoptic time. For this purpose, an iterative procedure consisting of three passes through the SASS data was utilized.

In the first pass, the least ambiguous SASS reports (those with one or two aliases) are dealiased, while in the second and third passes the more ambiguous three or four alias reports are dealiased. The first guess for the first pass is provided by the GLA model's 6 h forecast for the surface wind which is bilinearly interpolated to each SASS wind location from the four model grid points surrounding it. One alias (i.e. unambiguous) reports, which occurred fifteen times during the 96 days period, are accepted if their directions are within 165° of the first guess. For two alias reports (comprising 5.4% of the AES SASS data), the solution closest to the first guess is chosen if it is also within 75° of the first guess.

After the first pass, the dealiased SASS vectors and available ship winds are analyzed using the previously mentioned SCM. The resulting surface wind analysis is then used to provide the first guess for the second pass through the SASS data. Three or four vector solutions (comprising 10.5% and 84.1% of the total SASS data respectively) are considered in the second pass if the two closest aliases to the first guess are within 75° of one another. Of these, the solution closest to the first guess is chosen if it is also within 30° of it. The dealiased SASS winds from the first and second passes and available ship data are then reanalyzed using the SCM to provide a first guess for the third pass through all remaining SASS reports. In this pass, the solution within 75° and closest to the first guess is selected. All of the dealiased SASS and ship surface wind observations are then included in the final surface wind analysis and influence the model's next 6 h forecast and the computation of surface fluxes.

3. EVALUATION OF DEALIASED WIND FIELDS

A detailed evaluation of dealiased SASS winds was performed in order to assess the uncertainty in the selected wind directions. To this end, comparisons were made among the subjectively dealiased winds of Peteherych et al. (1984), the GLA objectively dealiased winds, which were generated using the method described in the previous section, and objectively dealiased winds which were also generated at GLA using the direct minimization method of Hoffman (1982, 1984). It should be noted that none of the dealiased fields can be considered as ground truth, as considerable uncertainty exists in each of the methods. It is also difficult to verify against conventional observations because of differences in representativeness of the conventional and satellite data and because the SASS dealiasing methods make use of these observations. Therefore, in order to actually verify the GLA objective method used in this study, a limited dealiasing experiment using simulated Seasat data was also performed.

3.1 Comparison of Objectively and Subjectively Dealiased Winds

For the period from 0000 GMT 6 September to 0000 GMT 20 September 1978, 340,686 SASS winds were subjectively dealiased while 305,422 winds were objectively dealiased using the GLA scheme. The decreased number of objective winds was due primarily to the coarse resolution of the model used and the decision to not dealias in situations where any model gridpoints surrounding a SASS report were located over land or ice. In addition, in some situations none of the aliases are sufficiently close to the first guess to be selected. 266,769 reports were common to both the subjective and GLA objective data sets; of these, the chosen directions agreed in 73% of the cases. A regional breakdown of the agreement between these fields showed little difference between the Atlantic, Indian and Pacific Oceans. However, significant variations between different latitude bands were observed. The best agreements were found in the Southern Hemisphere tropics (78%) where fairly consistent southeasterly trades predominate, and in the Northern Hemisphere extratropics (76%) where relatively large amounts of conventional data are available. Somewhat poorer agreement (69%) was found in the Northern Hemisphere tropics and middle latitudes in the Southern Hemisphere. The lowest agreement (57%) occurred in high latitudes of the Southern Hemisphere, where both methods are probably poorest due to the lack of auxiliary data and difficulties in modeling and analysis over and near Antarctica.

The global results were also evaluated in terms of speed and directional differences. 13% of the subjective and GLA objective winds were found to differ by more than 60°. But the vast majority of these were at relatively low wind speeds. Only 3% of the winds differed by more than 60° and had speeds greater than 10 m sec^{-1}.

Comparisons between the Hoffman objectively dealiased winds and the subjective winds (for a more limited sample of 21,995 cases) gave similar results. The global agreement was 71%; 15% of the winds had directional differences greater than 60°; 4% had directional differences greater than 60° and speeds greater than 10 m sec^{-1}. The GLA objective and Hoffman objective winds agreed 88% of the time.

A limited number of subjective comparisons of the dealiased winds revealed generally good agreement but also showed a tendency for more substantial differences near atmospheric fronts and cyclone centers. In such areas, the subjectively dealiased winds appear to be superior, probably because of its use of satellite imagery.

Fig. 1 presents an example of subjective and GLA objective winds near the famous Queen Elizabeth II storm (Duffy and Atlas, 1986) on 11 September 1978. In this case, there is excellent agreement between the dealiased fields although differences are evident in the location of the wind shear line in the northeast portion of the SASS swath and the objective scheme was not able to dealias one SASS report near the cyclone center. For some cases and regions the agreement is substantially poorer than in this case.

3.2 Comparison of Time-Averaged Analyses

In addition to the instantaneous compari-

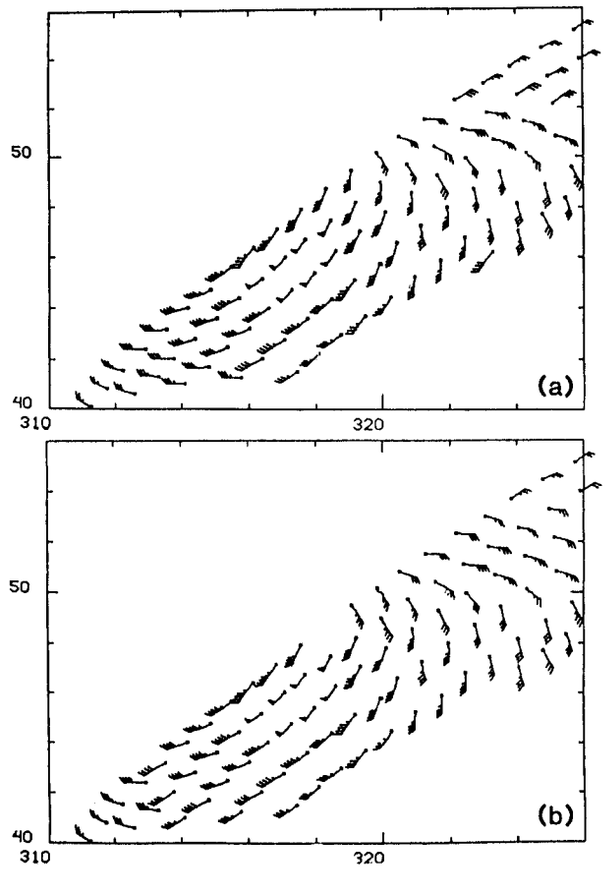

Fig. 1 Subjectively dealiased (a) and objectively dealiased (b) SASS winds in the vicinity of the QEII storm at 0215 GMT 11 Sept. 1978.

sons of dealiased winds, comparisons of time-averaged analyses using these data, for the period from 6-20 September 1978, have been made. Fig. 2 shows analyses of the curl of the wind stress for the tropical Pacific, in which either subjective or GLA objective dealiased winds were assimilated. Excellent agreement between the analyses using either dealiased data set can be seen, with the largest differences located near the west coast of South America. These fields are in good qualitative agreement with the climatological field published by O'Brien and Goldenberg (1982) for the same region.

3.3 Verification Using Simulated Seasat Data

In an attempt to verify the GLA objective dealiasing procedure, ambiguous SASS winds and other types of conventional and satellite data were simulated using the advanced simulation system described by Atlas et al. (1985). The SASS data were then objectively dealiased using the GLA analysis/forecast system and verified against the known correct solutions.

65,094 dealiased winds were verified over a four-day period under the conditions of this preliminary simulation experiment. 84% of these were found to be correct; 7% had directional errors greater than 60°. A regional breakdown of the verifications showed the dealiasing over the Atlantic Ocean to be 89% correct while the Indian and Pacific Oceans were somewhat less accurate (83% correct). The poorest results (72% accuracy) were found in high latitudes of the Southern Hemisphere in agreement with the real data comparisons.

4. GLOBAL FLUX FIELDS

4.1 Wind Stress

Fig. 3 presents the monthly mean wind stress fields for July-September 1978 obtained from the GLA model assimilation of all available data, including the objectively dealiased SASS surface winds. Comparisons of these fields with previously published climatologies (e.g. Han and Lee, 1983) reveals good general agreement. The GLA fields show most of the large ocean basin features. But substantial differences from the long-term climatologies are also present. In particular, the GLA fields show more structure; the exact locations of centers of cyclonic and anticyclonic wind stress are different and the GLA fields show areas of cyclonic and anticyclonic wind stress which are not present in the climatologies.

Some of the differences are because the GLA fields are for a single year as opposed to the climatologies, which are averages over many years. Other differences are almost certainly due to the unprecedented amount and coverage of surface wind data provided by the Seasat satellite.

In order to determine the reasonableness of the GLA fields where they differed from climatologies, subjective comparisions with sea-level pressure anomaly fields were performed. In every case examined, the sea-level pressure anomalies were in agreement with the analyzed anomalies in wind stress.

4.2 Sensible and Latent Heat Fluxes

Figs. 4 and 5 present the monthly mean sensible and latent heat flux fields for July-September 1978, obtained from the GLA model assimilation using Seasat data . These have been compared with corresponding climatological fields derived by Esbensen and Kushnir (1981). The basin-scale distribution of the model derived sensible heat flux is similar to the pattern of the sea-air temperature difference (not shown), that is influenced by the global pattern of sea-surface temperature (SST). The large-scale pattern of surface wind speed serves to modify these patterns and together they determine the magnitude structure of the sensible heat flux. For the majority of the oceanic expanse, the sensible heat flux is broadly positive, i.e., a heat flux from ocean to atmosphere. Regionally, the largest values are in the tropics and subtropics of the winter hemisphere, and are associated with significant sea-air temperature differences and wind speeds. Negative or small positive sensible heat fluxes are present in the cool water regimes of high latitudes and the coastal upwelling areas along the west coast of continents. The GLA sensible heat fluxes have significant differences with climatological sensible heat fluxes in both magnitude and regional structure.

The sensible heat fluxes of the Pacific Ocean for July to September, 1978 reflect small positive sea-air temperature differences over most of the ocean. The larger values northeast

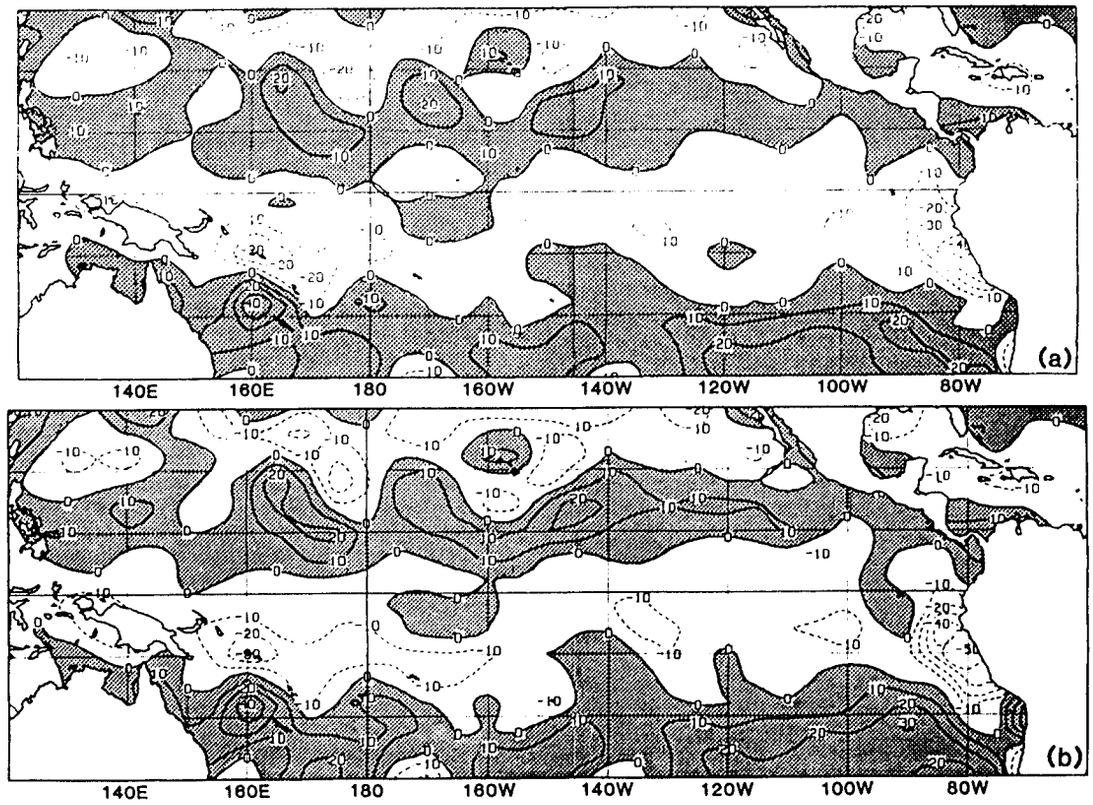

Fig. 2 Average wind stress curl (N m^{-3}) for the period 0000 GMT 6 Sept. to 0000 GMT 15 Sept. 1978 from GLA model assimilation of (a) subjectively dealiased winds, and (b) objectively dealiased winds.

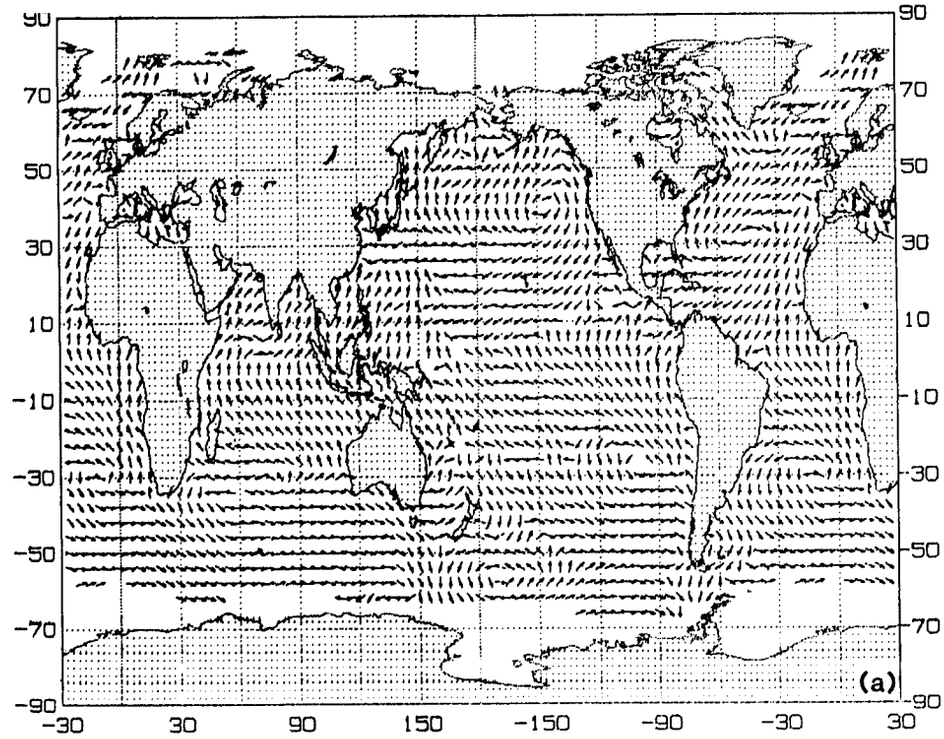

Fig. 3a Monthly mean wind stress directions from the GLA assimilation using SASS winds for July 1978.

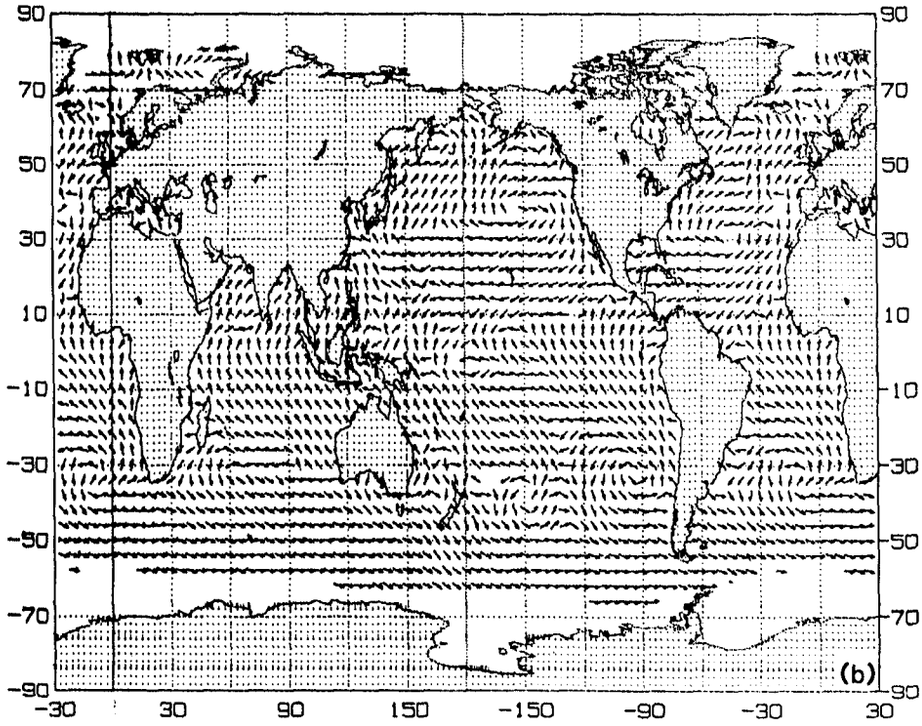

Fig. 3b Same as Fig. 3a for August 1978.

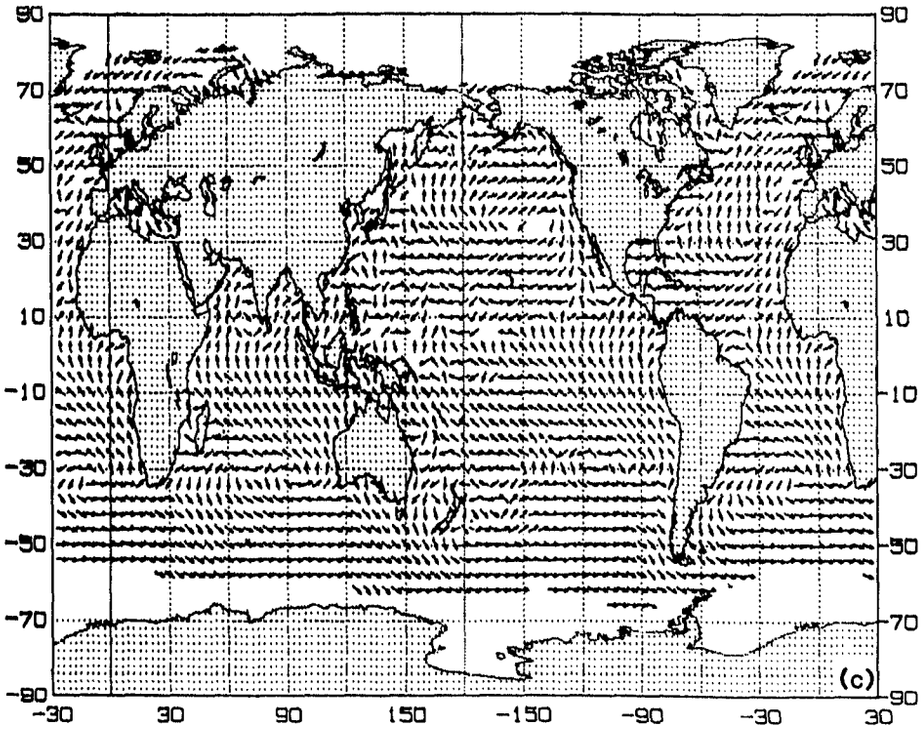

Fig. 3c Same as Fig. 3a for September 1978.

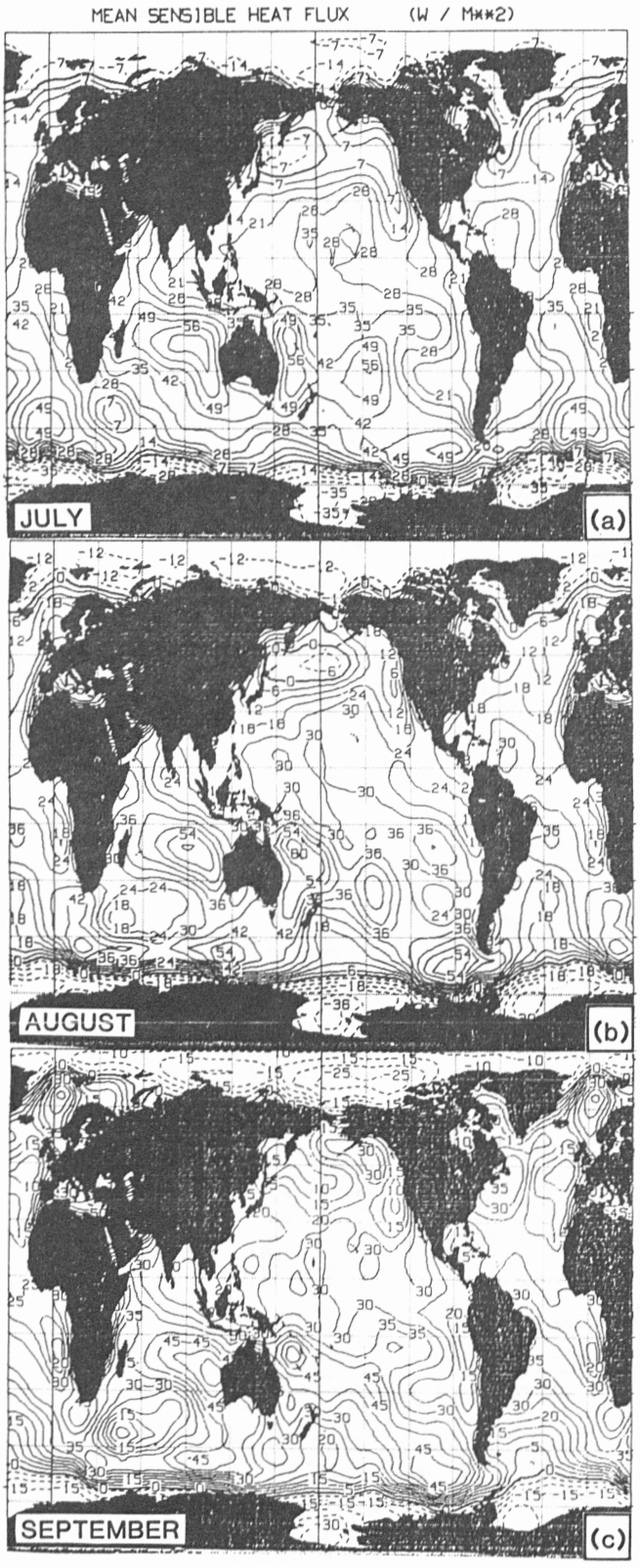

Fig. 4 Monthly mean sensible heat flux (W m^{-2}) fields from GLA assimilation using SASS winds for July-Sept. 1978 (a-c).

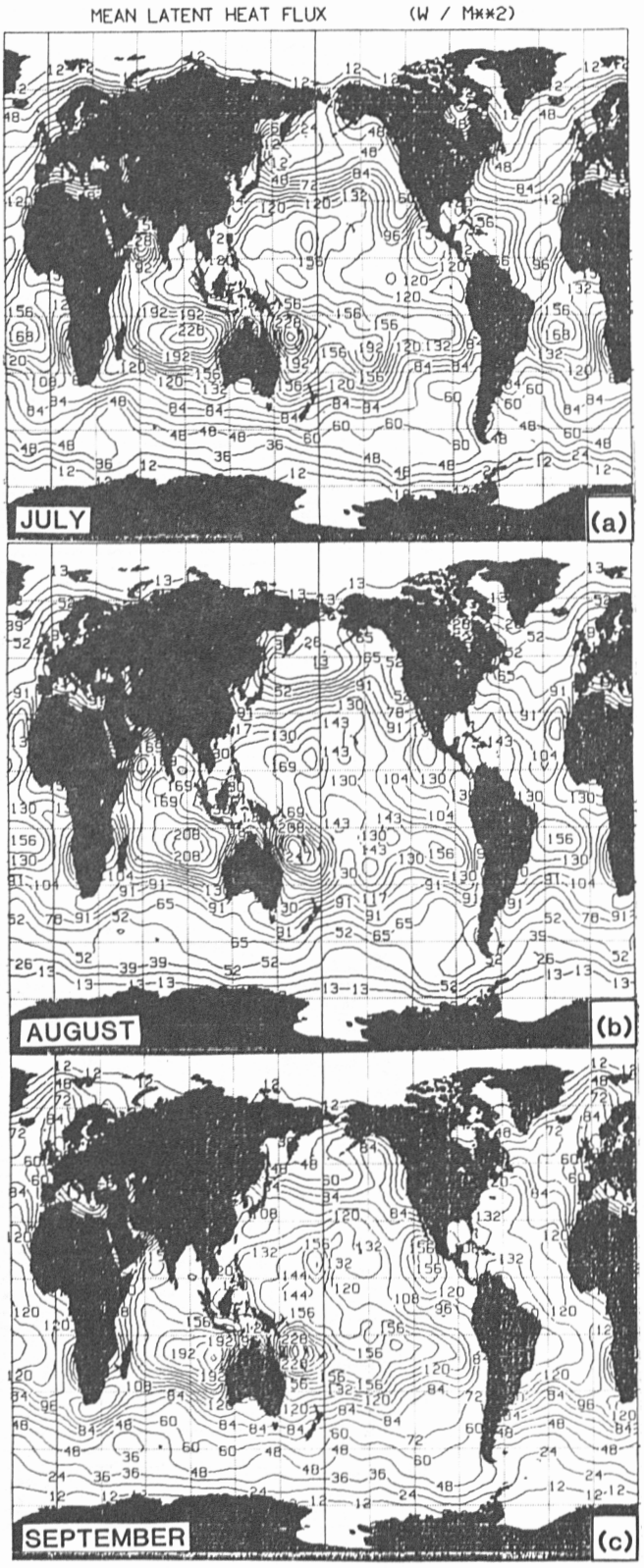

Fig. 5 Monthly mean latent heat flux (W m^{-2}) fields from GLA assimilation using SASS winds for July-Sept. 1978 (a-c).

of Australia and in the central South Pacific are induced by 3-4°K temperature differences and strong winter trade winds. Low sensible heat fluxes are present in the upwelling zones of western North and South America where warm continental air comes in contact with the cool waters of the Oyashio off northeast Asia. The magnitude of the fluxes derived from the model assimlation using SASS winds is several times greater than indicated by the climatology for these months. In addition, there is little indication of reduced or negative sensible heat fluxes in the region of the cold water equatorial tongue as in the climatology.

The most notable feature of the sensible heat flux fields for the Indian Ocean is the area of large upward heat transfer northwest of Australia that is influenced by significant temperature differences and southwest trades present during the austral winter. The minimum heat flux southeast of the Cape of Good Hope is the result of a localized, near-zero temperature difference. Besides the prevalent differences in magnitude with respect to climatology, one particularly significant discrepancy is the increase in sensible heat flux northwest into the Arabian Sea. Normally, this is a region of negative sea-air temperature differences as a result of the coastal upwelled cool water driven by the southwest monsoon of the summer months. In the present analysis the temperature difference is always positive in the Arabian Sea.

The large-scale structure of the model derived latent heat flux fields is similar to the patterns of the sensible heat flux, but with magnitudes several times greater. The largest latent heat fluxes are in the low latitudes of the Southern Hemisphere representative of increased evaporative heat losses during the austral winter. Generally lower values are found poleward in each hemisphere. Synoptic-scale structure often corresponds to specific features in the ocean and wind fields. The computed latent heat fluxes are in much better agreement with climatology, in terms of magnitude and spatial distribution, is than are the sensible heat fluxes.

The fields of latent heat flux for the Pacific Ocean during July to September are characterized by minima at high latitudes and in the upwelling regions offshore North America where the vertical gradient of specific humidity is small. High latent heat fluxes are present in the tropics where the humidity difference is comparatively large. Extreme releases of latent heat are indicated northeast of Australia, and are associated with a significant humidity difference and locally strong southeast winds. One discrepancy with climatology, consistent with that for the sensible heat flux, is the absence of a depression of the latent heat flux over the cold water tongue of the eastern equatorial Pacific.

The distribution of latent heat fluxes for the Atlantic Ocean is similar to the Pacific Ocean in that large fluxes are characteristic of the tropics and subtropics in areas of significant wind speed and/or humidity difference. One such area is the tropical South Atlantic which is under the influence of increased. Trades during the austral winter. Reduced latent heat fluxes are present at higher latitudes, and in particular within the cold water regions of the Labrador and Benguela Currents. Also evident is an increase in the latent heat flux over the Gulf Stream from June to September indicative of an increase in evaporation as the fall season approaches.

Within the Indian Ocean the largest latent heat flux is located northwest of Australia, coincident with the maximum of the sensible heat flux, in a region of seasonally strengthened southeast trades. An increase of the latent heat flux into the Arabian Sea is related to the southwest monsoon and the concomitant increase in wind speed. The magnitude of the Arabian Sea latent heat flux is noted to decrease from July to September consistent with the eastward advected influx of cool water from the coastal upwelling to the west.

4.3 Effect of Data

An important question with regard to the model-derived analyses of fluxes, presented in the preceding subsection, is to what extent are these fields being determined by the available data? To answer this question, an assimilation cycle with no data (i.e. a long model forecast) was generated for July 1978 and then compared with the fields determined by model assimilation of SASS winds and all other conventional and satellite data.

Figs. 6 and 7 show the monthly mean forecast latent heat flux field for July and the differences between this field and that obtained using all available data. As can be seen, data has had a large effect in constraining the model integration and the magnitude of the flux maxima are determined by data. On the other hand, the forecast field (Fig. 6) is in good qualitative agreement with the analysis (Fig. 5a) indicating that models may provide a useful means to fill in data gaps.

The specific effect of SASS data (not shown) was also evaluated. It was found to have a large effect on the model-derived flux fields.

5. SUMMARY

The entire 96-day period of Seasat scatterometer data has been objectively dealiased using the GLA analysis/forecast system and global gridded fields of wind stress and sensible and latent heat fluxes were produced as a by-product of the data assimilation process.

The GLA objectively dealiased winds were compared with the subjectively dealiased winds of Peteherych et al. (1984) and with objectively dealiased winds using the method of Hoffman (1982, 1984). The GLA objective method was also verified using simulated Seasat data. Time-averaged analyses of wind stress using either subjectively or objectively dealiased winds were found to be in excellent agreement in most regions.

Monthly mean analyses of wind stress and latent heat flux agreed reasonably well with climatological fields and known atmospheric and oceanic features. The sensible heat flux fields differed substantially from climatology. But in a limited number of subjective comparisons with observed atmospheric features (not shown here for reasons of brevity), the instantaneous fields were found to be reasonable.

6. ACKNOWLEDGEMENTS

The authors gratefully acknowledge the support of NASA Headquarters Oceanic Processes Program for this work. We also wish to thank S. Peteherych for providing the AES SASS data, and P. Woiceshyn, M. Wurtele, S. Peteherych and

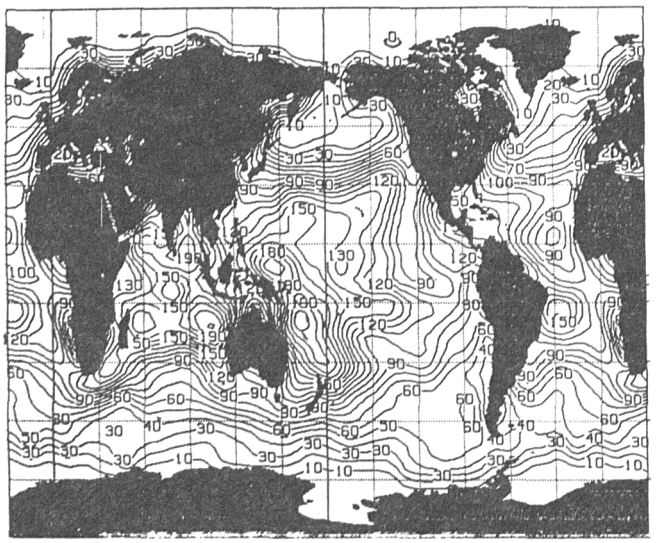

Fig. 6 Monthly mean latent heat flux (W m^{-2}) field for July from a GLA model forecast.

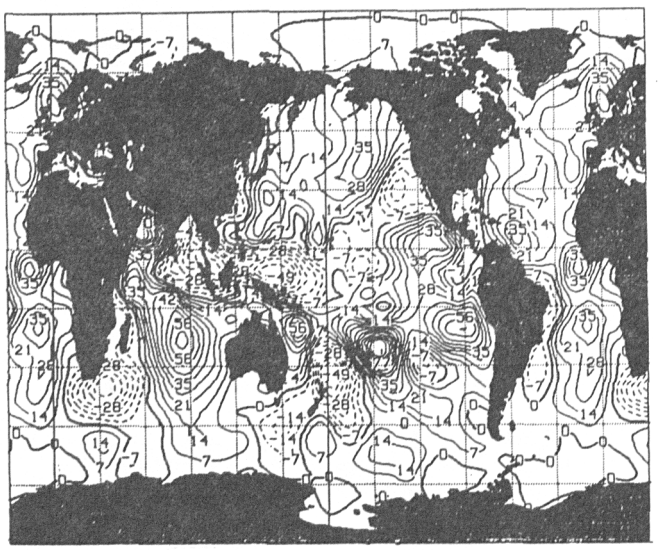

Fig. 7 Effect of data on GLA latent heat flux (W m^{-2}) analysis for July 1978.

D. Boggs for providing the subjectively dealiased winds. Discussions with W. E. Baker, R. Hoffman, J. C. Jusem, J. Woollen, S. Peteherych, P. Woiceshyn, M. Wurtele, E. Harrison and D. Chelton contributed to this work. Diagnostic and Programming support were provided by R. Rosenberg, J. Ardizzone, J. Terry, M. Heiser and G. Brin. M. Wells typed the manuscript.

7. REFERENCES

Atlas, R., E. Kalnay, J. Susskind, W. E. Baker, and M. Halem, 1985: Simulation studies of the impact of the impact of future observing systems on weather prediction. Proceedings of Seventh Conference on Numerical Weather Prediction.

Baker, W. E., R. Atlas, E. Kalnay, M. Halem, P. M. Woiceshyn, and D. Edelmann, 1984: Large-scale analysis and forecast experiments with wind data from the Seasat-A scatterometer. Journal Geophys. Res., 89, 4927-4936.

Duffy, D. and R. Atlas, 1986: The impact of Seasat-a scatterometer data on the numerical prediction of the QEII storm. Accepted by J. Geophys. Res.

Esbensen, S. K., and Y. Kushnir, 1981: The heat budget of the global ocean: An atlas based on estimates from surface wind observation, REP. 29, Climatic Research Institute, Oregon State.

Halem, M., E. Kalnay-Rivas, W. Baker, and R. Atlas 1982: An assessment of the state of the atmosphere as inferred from the FGGE satellite observing system during SOP-1. Bull. Amer. Soc. Meteor., 63, 407-426.

Han, Y.-J. and S.-W. Lee, 1983: An analysis of monthly wind stress over the global ocean. Mon. Wea. Rev., 111, 1554-1566.

Hoffman, R. N., 1982: SASS wind ambiguity removal by direct minimization. Mon. Wea. Rev., 110, 434-445.

Hoffman, R. N., 1984: SASS wind abmiguity removal by direct minimization. Part II: Use of smoother and dynamical constraints. Mon. Wea. Rev., 112, 1829-1852.

Kalnay-Rivas, E., and D. Hoitsma, 1979: The effect of accuracy, conservation and filtering on numerical weather forecasting, paper presented at the Fourth Conference on Numerical Weather Prediction. Am. Meteorol. Soc., Silver Spring, MD.

Kalnay, E., R. Balgovind, W. Chao, D. Edelmann, J. Pfaendtner, L. Takacs and K. Takano, 1983: Documentation of the GLAS Fourth Order General Circulation Model. NASA Tech. Memo 86064.

Kalnay, E. and R. Atlas, 1986: Global analysis of ocean surface wind and wind stress using the GLAS GCM and Seasat scatterometer winds. Accepted by J. Geophys. Res.

O'Brien, J. J. and S. B. Goldenberg, 1982: Atlas of Tropical Pacific Wind Stress Climatology. Florida State Unversity.

Peteherych, S., M. G. Wurtele, P. M. Woiceshyn, D. H. Boggs, and R. Atlas, 1984: First global analysis of Seasat scatterometer winds and potential for meteorological research. Frontiers of Remote Sensing of the oceans and Troposphere from Air and Space Platforms, 575-586.

Wurtele, M. G., P. M. Woiceshyn, S. Peteherych, M. Borowski, and W. S. Appleby, 1983: Wind direction alias removal studies of Seasat scatterometer derived wind fields. J. Geophys. Res., 87, 3365-3377.

APPLICATION OF SATELLITE DATA TO THE VARIATIONAL ANALYSIS OF THE THREE DIMENSIONAL WIND FIELD

Barbara A. Chance and Gary L. Achtemeier
Climate and Meteorology Section
Illinois State Water Survey, Champaign, IL 61820

1. INTRODUCTION

A hybrid mesoscale vertical velocity algorithm, which is a variational mesh of two independent methods, is developed. The two methods used are the kinematic and adiabatic methods (Pettersen, 1956). The relative weights accorded to the two schemes are deduced from digital GOES data. The cloud top temperature data are used to determine cloud top heights, and the visible brightness data provide an estimate of cloud thickness. The adiabatic method receives greatest weight in layers not influenced by diabatic heating: clear regions and above the tropopause. The kinematic method is assigned greatest weight near the surface and in cloudy regions. This algorithm is tested with the SESAME I case period data set.

2. KINEMATIC AND ADIABATIC METHODS: STRENGTHS AND WEAKNESSES

The two methods selected to be constituents of the vertical velocity algorithm are the kinematic and adiabatic methods. Each method depends on different atmospheric parameters and has strengths and weaknesses in various layers of the atmosphere.

The kinematic method is based on the conservation of mass principle. Solving for ω, the vertical component of velocity in pressure coordinates, this becomes symbolically,

$$\int_{\omega}^{\omega+\Delta\omega} d\omega = -\int_{p}^{p+\Delta p} (\partial u/\partial x + \partial v/\partial y)\, dp \qquad (1)$$

Here, u is the zonal velocity component and v is the meridional component.

This method vertically integrates divergence through the domain. The errors in the horizontal divergence sum upward from the bottom of a column and can become very large at the top. To alleviate this problem, an O'Brien correction method can be utilized (O'Brien, 1970). This correction technique uses mass continuity and an estimate of vertical velocity at the top of the column as constraints. From these constraints weighted adjustments are determined and applied to the vertically integrated divergences. This approach forces the velocity at the top of the column to a preset value and can transfer errors from the low troposphere into the upper troposphere and stratosphere. These errors can become unrealistically large near and above the tropopause.

The second method, the adiabatic method, takes into account other atmospheric data. Mathematically, this method has the form

$$\omega = \frac{\partial T/\partial t - (-V\cdot\nabla T)}{s} \qquad (2)$$

where $\partial T/\partial t$ is the temperature tendency, $-V\cdot\nabla T$ is the horizontal thermal advection, and s is the static stability parameter.

Advantages of the kinematic method are that 1) it is based on the simple principle of mass continuity, and 2) only knowledge of the horizontal wind field is required, ie. no additional processes such as heating are involved. Disadvantages of the kinematic method are that 1) the method is very sensitive to data errors and data interpolation, and 2) vertical integration causes errors to accumulate at the top of a column.

Advantages of the adiabatic method are that 1) additional information about the atmosphere is incorporated into the calculation and 2) there is no need to impose boundary conditions. Disadvantages of the adiabatic method are that 1) it can only be used where the flow is nearly adiabatic, 2) it requires frequent temperature observations so that temperature tendency can be accurately estimated, and 3) it becomes unstable for nearly adiabatic layers where the static stability parameter approaches zero.

From these strengths and weaknesses, it is expected that the adiabatic method would give better results in layers away from the surface, in clear areas, and near and above the tropopause. The kinematic method would perform better in layers near the surface and in deep cloudy areas.

The kinematic method is very sensitive to the scheme chosen to approximate the horizontal divergence field. To demonstrate that spurious divergence values are introduced by numerical procedures, a non-divergent, analytic stream function is employed. This function is described on a Cartesian grid by

$$\varphi = By + Ae^{-\alpha} \quad \text{, where} \qquad (3)$$

$$\alpha = a(x-x_o)^2 + b(y-y_o)^2$$

The quantities A, B, a, and b are constants, and x_o and y_o are the coordinates of the center of the grid.

The u- and v-components of horizontal velocity are determined from differentiating the stream function. These expressions for a Cartesian grid are

$$u = -\partial\varphi/\partial y = -B + 2bA(y-y_o)e^{-\alpha}$$
$$v = \partial\varphi/\partial x = -2aA(x-x_o)e^{-\alpha} \qquad (4)$$

For the work presented here, a square grid is chosen to be thirty grid space units (gsu) on each side. The values for the constants are selected as follows.

A = -166.7	a = b = 0.03125
B = -10.0	$x_o = y_o = 15$

Divergence of the horizontal velocity field is approximated by using a second-order, finite difference scheme on a staggered grid. Since the given analytic field is non-divergent, the values calculated with the finite difference scheme are actually the truncation error of the scheme. If this non-zero value of divergence is assumed to exist throughout a layer in the atmosphere, then from the conservation of mass principle, a corresponding vertical component of motion must be present. Hence, erroneous values of vertical motion can be introduced from the use of a finite difference scheme to calculate divergence.

The result of objectively analyzing ϕ -, u-, and v-fields with a variation of the Barnes (1973) scheme is demonstrated. The data points are provided in either a regular or random spacing. The Barnes scheme is used to objectively analyze observations onto a 30 gsu by 30 gsu grid. This version involves an exponential weighting of the twelve closest data points to perform the analysis.

From the analyzed u- and v-fields, the divergence field is calculated. The same finite difference scheme as before is employed. Again, it is certain that the divergence field is identically zero. Thus, any non-zero values are due to the data interpolation and finite difference approximations. In all cases, this erroneous divergence is assumed to be constant over a 1 km layer, and a corresponding w is calculated. As a measure of the inaccuracy in w, the root-mean-square (RMS) error is determined for each case.

Effects of finite differencing and objectively analyzing a data field are demonstrated by performing these numerical manipulations on a known field. Cases were run for six regularly-spaced data meshes. The data spacings range from 2 gsu (225 data points) to 8 gsu (16 data points). Only the 4 gsu data spacing is presented here. Four cases were run using a randomly-spaced data mesh. Each case has a different data point distribution, but each contains 20 points. Only two cases are presented in this work.

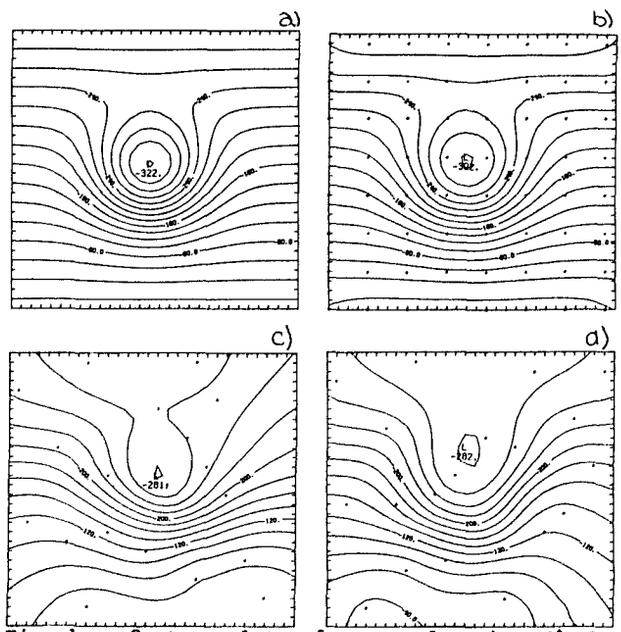

Fig. 1. Contour plots of stream function, ϕ for a)original field and for b), c), and d)objectively analyzed fields.

A contoured plot of the non-divergent, analytic stream function is shown in Fig. 1a. A minimum is present near the center (origin) of the field, and the field is symmetric with respect to a vertical line (y-axis) passing through the origin. If 1 gsu is allowed to equal 100 km, then the units for ϕ are m^2/s.

Appearing in Figs. 1b, 1c, and 1d are contoured plots of ϕ after the Barnes objective analysis scheme is performed. Fig. 1b uses a regularly-spaced (4 gsu spacing) data mesh consisting of 64 data points. Figs. 1c and 1d use randomly-spaced data meshes each made up of 20 points.

The objective analysis produced from the regularly-spaced data mesh shows an excellent recreation of the ϕ contour pattern. The symmetry is maintained, but the magnitude of the minimum has been reduced by about 6% and the contours have been slightly distorted near the corners. This distortion appears since the objective analysis routine must search out farther to find the 12 closest data points for a corner grid point than for an interior grid point.

The objective analysis utilizing the randomly-spaced data points does not produce the high quality result as seen above. Here, the contour patterns display a tilt and have lost their symmetrical structure. For both cases, the magnitude of the minimum has decreased by about 12% to 13%.

Although not shown, w-fields were constructed for each case. These fields were calculated by using the analyzed u- and v-fields and by applying a finite difference scheme to approximate the derivatives. Recall that the given stream function is non-divergent so that according to mass continuity, w should be identically zero.

As a measure of error of the ϕ- and w-fields, bar charts of RMS error are shown in Fig. 2. For a grid spacing of 100 km, the units of RMS error for ϕ are m^2/s and for w are cm/s.

As expected, Fig. 2a shows that the RMS errors in ϕ for a regularly-spaced data mesh increase as the data density decreases. For the randomly-spaced data mesh, the RMS errors in ϕ appear in Fig. 2b. These values show that other factors such as data distribution must be significant when performing an objective analysis.

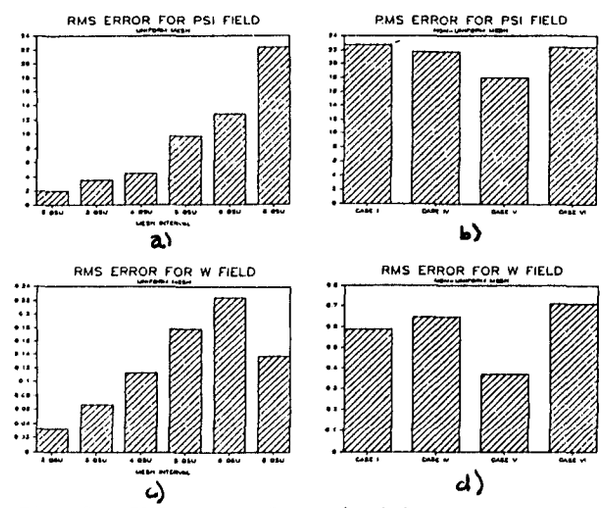

Fig. 2. RMS errors for w (cm/s).

The RMS errors in w for regularly-spaced and randomly-spaced data meshes are exhibited in Figs. 2c and 2d, respectively. Fig. 2c shows that the RMS error values increase as the data density decreases, except for the 8 gsu mesh. Here, the data spacing has approached the size of the disturbance. Therefore, the objective analysis scheme only reconstructs the basic state zonal flow which is constant and non-divergent.

In both figures, the RMS errors in w are significant with values up to 0.22 cm/s for a regularly-spaced grid and up to 0.7 cm/s for a randomly-spaced grid. Considering the w-fields for each case, extrema as large as 2 to 3 cm/s are common.

3. VARIATIONAL APPROACH

The variational algorithm for calculating vertical motion combines satellite data with conventional data. The conventional data are assigned weights according to their relative measurement accuracies. The satellite data are used to determine weights assigned to the independent, adiabatic estimate of vertical motion. The data are adjusted by a least squares approach that requires mass continuity to be satisfied.(Achtemeier et al , 1984)

The quantities to be minimized are contained in the function I, written for a nonlinear, sigma vertical coordinate.

$$I = \Pi_1(u-u^o)^2 + \Pi_1(v-v^o)^2 + \Pi_2(\dot{\sigma}-\dot{\sigma}^o)^2 + 2\lambda m \tag{5}$$

Here, Π_1 and Π_2 are the assigned weights, u^o and v^o are observed data, $\dot{\sigma}^o$ is the adiabatic estimate of vertical motion, λ is the Lagrange multiplier and m is the constraining continuity equation in sigma coordinates. Symbolically,

$$m = \int(\partial u/\partial x + \partial v/\partial y)\,d\sigma + \dot{\sigma} - \dot{\sigma}_o + \int F\,d\sigma \tag{6}$$

where $\dot{\sigma}_o = \dot{\sigma}$ at the surface and F is a function including the surface vertical velocity and factors to transform the equation to a Lambert conformal map image projection.

Subjecting I to the Euler-Lagrange operations and setting the results to zero, allows the quantities u, v, and $\dot{\sigma}$ to be minimized.

$$\delta u = \Pi_1(u-u^o) - \partial\lambda/\partial x \int \delta\sigma = 0 \tag{7}$$

$$\delta v = \Pi_1(v-v^o) - \partial\lambda/\partial y \int \delta\sigma = 0 \tag{8}$$

$$\delta\dot{\sigma} = \Pi_2(\dot{\sigma}-\dot{\sigma}^o) + \lambda = 0 \tag{9}$$

If it is assumed that $\Pi_1 = \Pi_1(\sigma)$ and $\lambda = \lambda(x,y)$, then Eqs. 7 and 8 can be differentiated and combined with 9 to solve for λ . Here, λ is expressed in the form of a Helmholtz equation:

$$\nabla^2\lambda - a\lambda + H = 0 \tag{10}$$

where H contains forcing terms and

$$a = (\Pi_2 \int \delta\sigma \int \Pi_1^{-1} d\sigma)^{-1}$$

Under certain simplifications, the O'Brien method of calculating corrected vertical velocities is a special case of the above formulation.

To test this new variational algorithm data is selected from SESAME case period I (12Z 10 April 1979 to 12Z 11 April 1979). This data set is chosen because of its three-hour frequency, its large data density, and its vast documentation. The frequent data collection is helpful in obtaining accurate estimates of temperature tendency. A larger data density provides more information to be supplied to the objective analysis scheme. And, good documentation allows results of the vertical velocity algorithm to be compared to several other published results.

The data are provided every three hours by the standard and supplemental rawinsonde stations within the SESAME network. These data points are interpolated at ten levels onto a 24 gsu by 20 gsu gridded, Cartesian field with one gsu equal to 100 km. The ten levels lie between the surface and the 100 mb pressure level and are oriented along a terrain following coordinate system from the surface to the 700 mb level and along pressure surface coordinates above 700 mb.

To serve as initial fields for the vertical velocity algorithm, w-fields are calculated using each method, kinematic or adiabatic, separately. These w-fields are determined at each three-hour interval. The kinematic w values are initially adjusted with the O'Brien correction technique to require the vertical velocity to vanish at the top of the column.

Examples of the initial fields of w are presented in Fig. 3. The fields are calculated using either the kinematic method (Figs. 3a and 3c) or the adiabatic method (Figs. 3b and 3d). Layers 6 and 9, corresponding to 450 mb and 150 mb, respectively, are displayed. These layers are chosen to give examples of each method's applicability. For reference, areas of cold cloud tops indicated by an infrared satellite image are noted as well as precipitation areas determined from radar echoes.

According to Moore and Fuelberg (1981), the synoptic conditions for 12 GMT 10 April 1979 are as follows. At the surface, the eastern half of the U.S. is experiencing cool and dry conditions. A ridge is positioned over the Great Lakes, and a deep low pressure system is located at the Colorado-Wyoming border. There is warm, moist air over southern Texas with a dry line developing in western Texas. At 700 mb, southwesterly flow has brought dry air to overlie the moist air at the Red River Valley. An amplifying wave extending from Washington to New Mexico appears at 300 mb

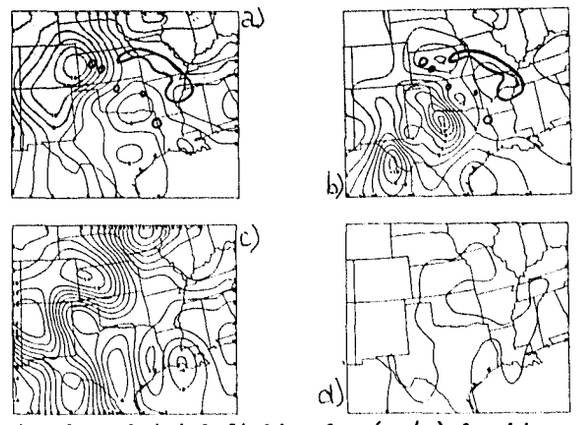

Fig. 3. Initial fields of w (cm/s) for kinematic method at a)450 mb and c)150 mb and for adiabatic method at levels b)450 mb and d)150 mb. All fields for 12Z 10 April 1979.

along with a weakening short wave over the Midwest. Also at 300 mb, there is a jet streak over northern Mexico.

The kinematic w-field at 450 mb is displayed in Fig. 3a. It shows a large region of intense, upward vertical motion in the western half of the grid, and significant sinking motion in the Mississippi Valley. This shows good agreement with the synoptic pattern. The infrared and visible satellite images at 1230 GMT show a nearly clear area over the northeast corner of Oklahoma and the southeast corner of Kansas. The w-field exhibits values between 0 and -2 cm/s in this region.

Fig. 3b shows the w-field at 450 mb determined by the adiabatic method. This field has an intense maximum over the Red River Valley and minimum over southwest Texas. These extrema result from strong thermal advection. Warm air advection is present at the Red River Valley while cold air advection is occurring at southwest Texas.

For the 150 mb level, the kinematic w-field and the adiabatic w-field appear in Figs. 3c and 3d, respectively. This level is known to lie near or above the tropopause where the atmosphere is stable. In stable layers, it is expected that the vertical motion is nearly zero. Here, the adiabatic w-field produces a better representation of this property.

4. SUMMARY

Typically, mesoscale vertical velocities are estimated by the kinematic method. This is a simple method based on the conservation of mass principle. It states that the change in vertical motion throughout a layer is due to the horizontal divergence in that layer. Therefore, to accurately calculate vertical motion, a proper estimate of horizontal divergence is required.

Horizontal divergence is commonly found by using a finite differnce scheme on gridded horizontal velocity fields. The wind velocity data suffer from intrinsic errors due to instruments and to unresolvable phenomena whose scales are smaller than the station spacing. The inaccuracies become compounded from errors introduced by objectively analyzing the sparse, irregularly-spaced data onto a gridded field. Further error is created from the use of a finite difference scheme on the velocity fields.

The use of the new variational algorithm helps to reduce errors introduced by numerical techniques utilized in the kinematic method. By combining this method with the adiabatic approach sole reliance upon kinematic method for determining vertical motions is removed. Results from the variational meshing of the three dimensional velocity fields will be presented at the conference.

ACKNOWLEDGEMENTS

This research was sponsored by the National Aeronautics and Space Administration through Contract NAS8-34902 and by the Universities Space Research Association through Contract NAS8-35530.

REFERENCES

Achtemeier, G. L., Ochs, H. T. and S. Q. Kidder: A diagnostic numerical model for the application of satellite data for the study of global weather systems. Reprints, Conference on Satellite Meteorology/Remote Sensing and Applications 25-29 June 1984, p. 260.

Barnes, S. L., 1973: Mesoscale Objective Map Analysis Using Weighted Time-Series Observations. ERL NSSL-62, NOAA Technical Memorandum, Norman, Oklahoma, 60 pp.

Moore, J. T. and H. E. Fuelberg, 1981: A Synoptic Analysis of the First AVE-SESAME '79 Period. Bull. Am. Meterol. Soc. , 62 , 1577-1590.

O'Brien, J. J., 1970: Alternative Solutions to the Classical Vertical Velocity Problem. J. Appl. Meteorl. , 9 , 197-203.

Pettersen, S., 1956: Weather Analysis and Forecasting , Vol. 1, New York, McGraw-Hill, 428 pp.

PREPARATION OF SATELLITE SOUNDINGS FOR INSERTION IN A VARIATIONAL OBJECTIVE ANALYSIS MODEL

Stanley Q. Kidder and Gary L. Achtemeier

Climate and Meteorology Section
Illinois State Water Survey
Champaign, Illinois

1. INTRODUCTION

Satellite soundings have been available for many years. Still they are not routinely used over land areas largely because they have different characteristics than rawinsonde soundings. A variational analysis model under development at the Illinois State Water Survey (Achtemeier et al., 1986) offers a means for blending satellite and conventional soundings in a way which preserves the information content of both data sources. However, model performance improves if the input data are "prepared" before model insertion.

We investigated four ways to prepare satellite soundings for insertion into the variational analysis model: (1) determining and removing biases, (2) determining standard errors of the satellite temperatures to assist in the assigning of weights in the model, (3) converting layer mean temperatures (the form in which the satellite soundings are supplied on tape) to level temperatures (which are required in the variational analysis model), and (4) determining what action to take to correct for the non-synoptic nature of the satellite data. These are discussed in the following three sections.

2. BIASES AND WEIGHTS

The accuracy of satellite soundings from the Tiros Operational Vertical Sounder (TOVS) has been investigated several times (e.g. Phillips et al., 1979; Schlatter, 1981; Gruber and Watkins, 1982). However, the comparisons change with time both because the retrieval algorithms are occasionally updated and because the retrieval coefficients are regularly updated. In addition, there are a number of ways to compare satellite soundings with "truth." Because gridded data are required as input for the model, we needed to know the bias of TOVS temperatures with respect to objectively-analyzed rawinsonde data. None of the previous studies of TOVS biases used precisely this standard of comparison. Schlatter compared the Tiros-N soundings with NMC Final Analyses; others have compared the satellite soundings with "co-located" rawinsonde observations. We decided, therefore, to recalculate the biases.

The case study on which the variational analysis model was first run is 10-11 April 1979. To do the calibration study, we acquired operationally-retrieved Tiros-N TOVS soundings and rawinsonde data data for the period 26 March through 11 April 1979. This is the same period (plus three days) analyzed by Schlatter (1981). Layer mean virtual temperatures, derived from rawinsonde thicknesses, each 12 hr for the period 0000 GMT 26 March through 1200 GMT 11 April 1979 were objectively analyzed on a 21 x 21 grid (260 km grid spacing at 45°N) covering most of North America (Figure 1). Biases were estimated by calculating the difference between satellite-estimated mean virtual temperatures and rawinsonde values interpolated in both time and space from the analyses to the satellite data.

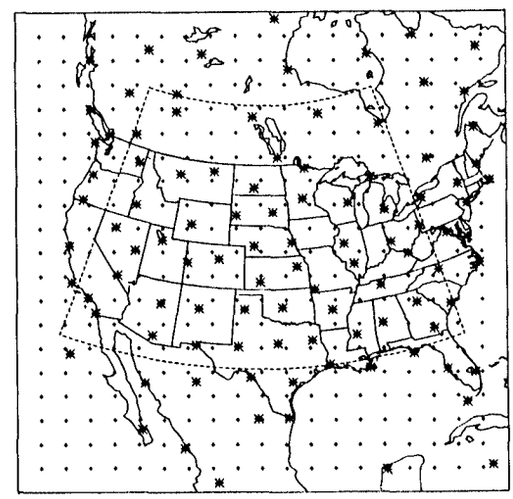

Fig. 1. Asterisks indicate the location of the 101 rawinsonde stations used to construct the objective analyses for comparison with satellite soundings. The dashed line encloses the satellite soundings (this is the same area used by Schlatter, 1981). Note that the satellite soundings are well within the boundaries of the rawinsonde objective analysis area, thus edge effects should be minimal.

Figure 2 shows the 12-hr average biases as a function of time for each layer. The dashed lines represent the mean biases for the periods 26 March through 8 April and 10-11 April. The three sounding types (clear, partly cloudy, cloudy) were kept separate. The error bars represent 95% confidence intervals assuming that the biases are normally distributed about the 12-hr mean, which proved to be a good assumption upon examination. Two aspects are disturbing: (1) For a large number of points the error bars do not include the mean represented by the dashed line. Only one in 20 points should not include the mean if the long term average is representative. (2) There seems to be a 24-hr oscillation, which indicates that daytime and nighttime biases may be different. That this is the case is not surprising since the atmosphere varies diurnally but the operational TOVS retrieval scheme is essentially the same for both day and night soundings.

The next step was to separate day and night soundings and to calculate the mean biases for the period 26 March through 8 April. These results are plotted in Figure 3 and listed in Table 1. Again, the error bars represent 95% confidence intervals. It is clear that biases for day and night soundings are statistically different for clear and partly cloudy soundings, and at most levels for cloudy soundings. Schlatter's results are plotted for comparison. Because Schlatter did not separate day and night soundings, his biases tend to split the difference between the day and night biases. In the upper troposphere, Schlatter's biases tend to be smaller than the biases calculated with respect to rawinsonde analyses. It is important to note that if the biases are not properly removed by time and by sounding type, objectively-analyzed fields of satellite temperatures can have variations of several degrees due solely to biases.

An additional kind of bias was also investigated. The operational TOVS retrieval algorithm is statistical. It assumes that the bottom of the sounding is at (or near) 1000 mb. This assumption is not valid over elevated terrain. An attempt to correct this problem is made in the operational retrieval scheme, but there remains the possibility that a bias in the low levels is created in the processes. Discussions with C. Hayden (NOAA/NESDIS, Madison, WI) indicated that the TOVS temperatures would most likely be too cold. We therefore correlated the deviations of the satellite temperatures from the rawinsonde analyses with terrain height. No useful correlation was found. The cold bias over elevated terrain seems to be a negligible in comparison with other errors in this analysis.

Also listed in Table 1 are the standard deviations of the biases. If the biases are properly removed, the standard deviations become the potential RMS errors. These are plotted in Figure 4 along with RMS errors published by Schlatter. Note that his RMS errors tend to be larger than the potential RMS errors. This is due in part to the fact that Schlatter treated day and night soundings together and partly because he did not remove the mean. The weights to be assigned to the Tiros-N data are proportional to the standard deviation to the -2 power.

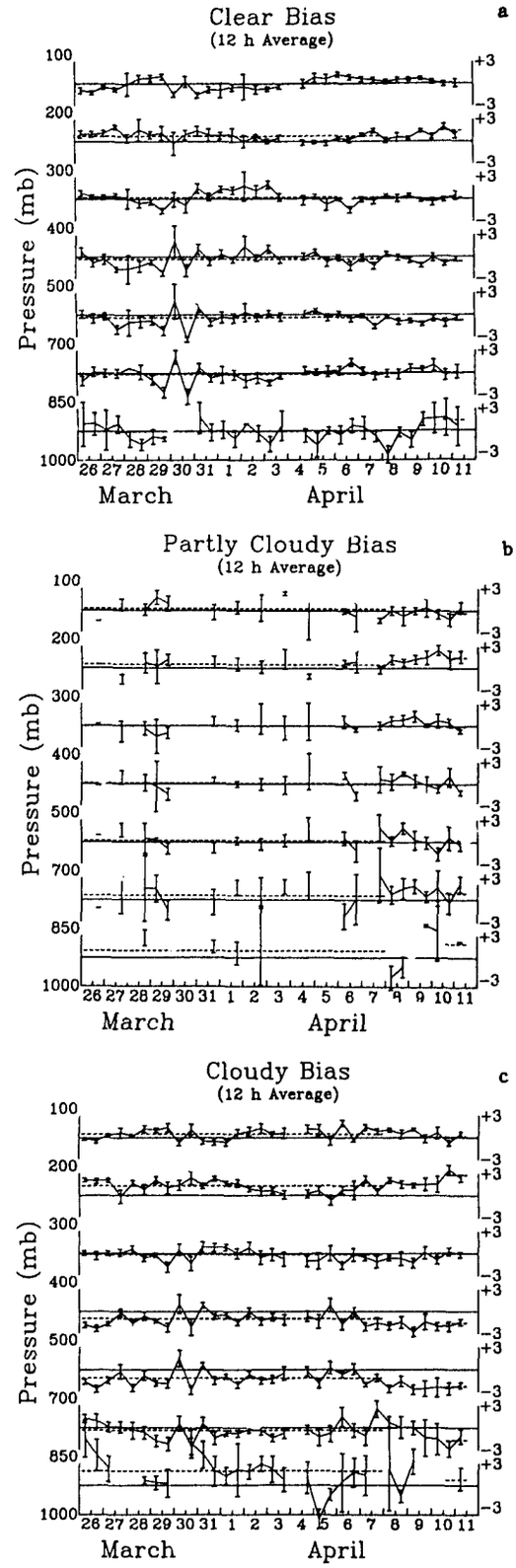

Fig. 2. 12 h average biases of satellite soundings: (a) clear soundings, (b) partly cloudy soundings, (c) cloudy soundings. The error bars represent the 95% confidence interval. Dashed lines represent the average of the biases. The temperature scale on the right is in kelvin.

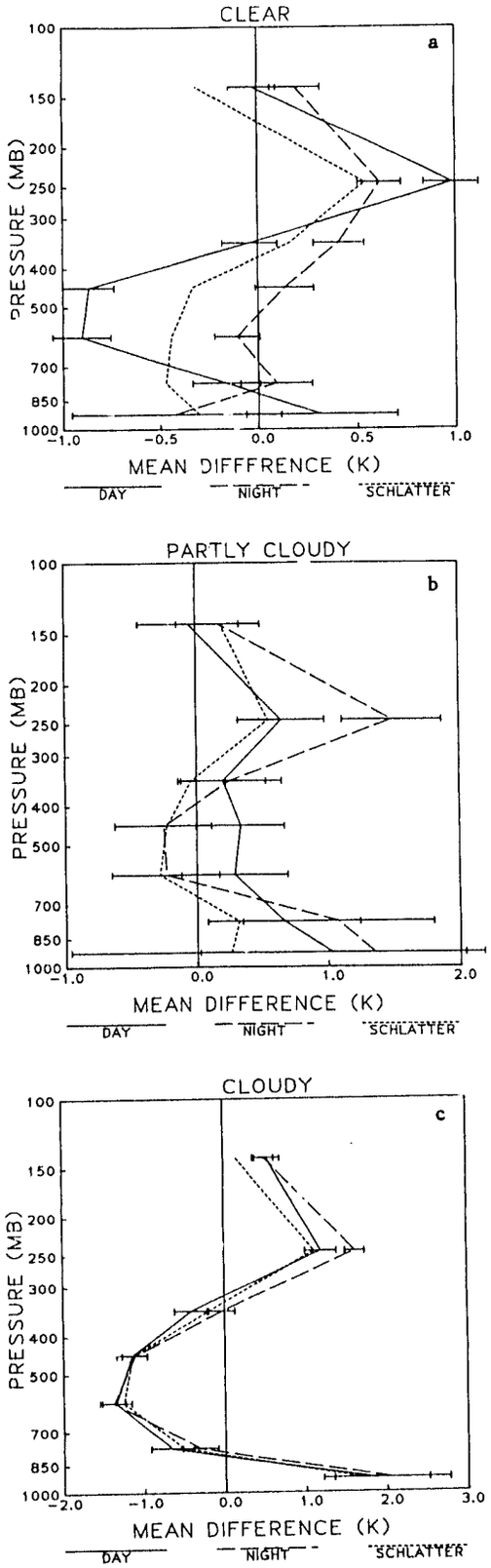

Fig. 3. Average biases for the period 26 March through 8 April 1979: (a) clear soundings, (b) partly cloudy soundings, (c) cloudy soundings. Day and night biases have been kept separate. The biases published by Schlatter (1981) are plotted for reference. The error bars represent the 95% confidence interval.

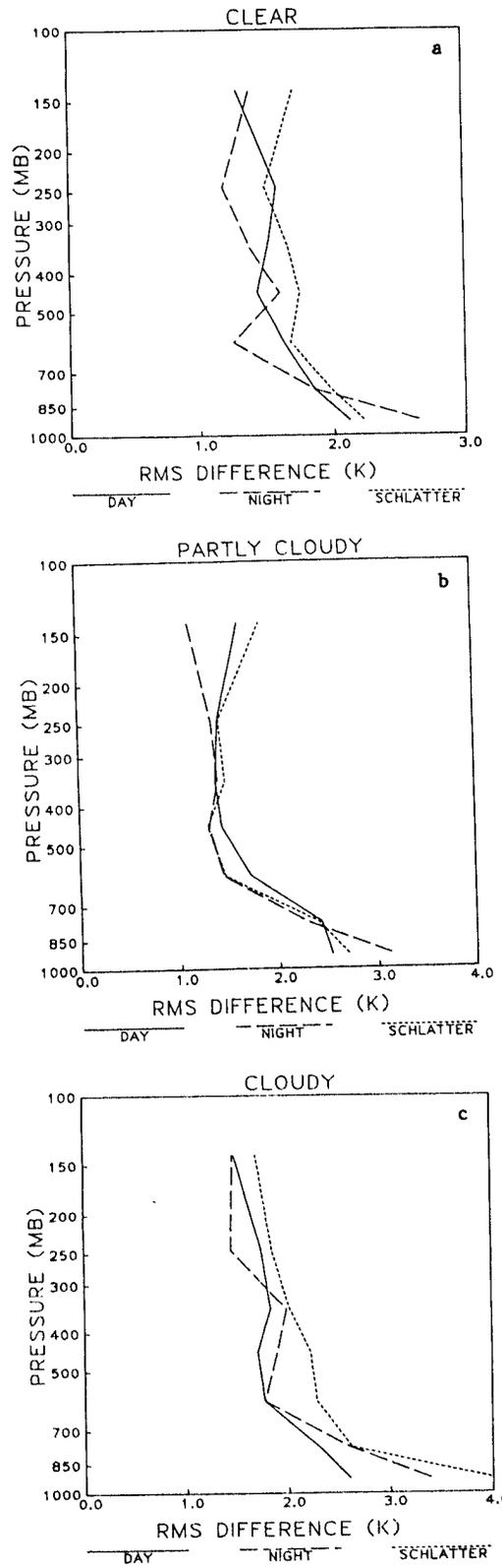

Fig. 4. RMS errors in the satellite temperatures: (a) clear soundings, (b) partly cloudy soundings, (c) cloudy soundings. Day and night soundings are separate. Note that the mean biases were removed before calculation of the RMS errors (see text). Schlatter's results are plotted for comparison.

Table 1

Biases and standard deviations of Tiros-N layer mean virtual temperatures (K).

Layer(mb)	Day			Night		
	Clear	Partly Cloudy	Cloudy	Clear	Partly Cloudy	Cloudy
			Biases			
200-100	-0.02	-0.05	0.54	0.19	0.18	0.51
300-200	0.98	0.65	1.20	0.61	1.49	1.62
400-300	-0.04	0.20	-0.41	0.41	0.26	-0.02
500-400	-0.87	0.33	-1.14	0.14	-0.25	-1.11
700-500	-0.90	0.29	-1.35	-0.10	-0.23	-1.37
850-700	-0.16	0.67	-0.65	0.09	1.08	-0.31
1000-850	0.32	1.03	1.87	-0.42	1.35	2.06
			Standard Deviations			
200-100	1.29	1.63	1.48	1.38	1.12	1.47
300-200	1.57	1.40	1.74	1.18	1.34	1.45
400-300	1.50	1.37	1.83	1.38	1.40	1.99
500-400	1.43	1.43	1.70	1.59	1.30	1.89
700-500	1.62	1.72	1.77	1.25	1.44	1.77
850-700	1.84	2.42	2.31	1.84	2.28	2.60
1000-850	2.11	2.52	2.60	2.64	3.12	3.39

3. LEVEL TEMPERATURES

Operationally-retrieved TOVS soundings are supplied on tape as layer mean virtual temperatures. The variational model requires virtual temperatures at specified levels. Since the layer mean temperatures are essentially the arithmetic mean of the temperature at the top and bottom of the layer, the layer mean temperatures can be converted to level temperatures, *if the temperature at one level is known*. We attempted to recover the 400 mb temperature by assuming that the lapse rate between 500 and 300 mb is constant. Examination of the rawinsonde data used above reveals that this is reasonable. At first we assumed that the 400 mb temperature is simply the average of the 300-400 and the 400-500 mb mean layer temperatures. A check with rawinsonde data revealed that the 400 mb temperatures estimated in this manner are too cold on the average by 0.65 K. A check using the U.S. Standard Atmosphere (1962), also showed that the 400 mb temperature estimated in this way should be 0.65 K too cold.

To correct this problem, the equations which describe a constant lapse rate atmosphere (Hess, 1959) were incorporated in a subroutine which calculates a corrected 400 mb temperature, given the average and the difference between the layer mean temperatures for the 300-400 and the 400-500 mb layers. When this method was tested using the rawinsonde data from 26 March through 11 April (over 3200 observations) the mean of the difference between the corrected and actual 400 mb temperatures was 0.00 to within 2.77 K (95% confidence level). Since this method proved to be accurate, it was used to decompose the Tiros-N mean layer temperatures into level temperatures before insertion into the variational analysis model.

4. NON-SYNOPTIC CORRECTION

Satellite soundings are not made at synoptic times. If one wants to use satellite soundings in analyses at synoptic times, a correction for atmospheric changes between the time of satellite observation and synoptic time should be considered. We decided to investigate the ability of simple horizontal temperature advection to correct the temperatures. The idea would be to use the winds and objectively-analyzed rawinsonde temperatures at the synoptic time to calculate the advective rate of change of temperature. This rate could be applied to the satellite temperature for the time period between the satellite sounding and the synoptic time. We checked the utility of this idea by correlating the 3-hr temperature change with the advective temperature change for the AVE/SESAME data for 10-11 April 1979. The correlation coefficients, as shown in Table 2, are low.

A second attempt involved the calculation of geostrophic temperature advection (see Wallace and Hobbs, 1977), in which the change of wind with height is assumed to be due to the thermal wind (proportional to layer mean temperature gradient). The layer mean temperature advection is simply the scalar product of the temperature gradient and the layer mean wind. This approach avoids objectively analyzing the temperature, and it estimates the time rate of change of the layer mean temperature (which is more applicable to the satellite data), but the correlation between observed and calculated 3-hr temperature change did not improve.

Apparently a correction to satellite temperatures based on temperature advection is too simple. This is not entirely surprising since a rather severe storm system passed over the rawinsonde network during 10-11 April. Processes other then synoptic-scale temperature advection were probably important. A correction for the non-synoptic nature of satellite soundings will have to be made with a more complicated scheme, such as that of Lewis *et al.* (1983) in which potential vorticity is conserved.

Table 2

Correlation coefficients between advective temperature change and observed temperature change over a 3 hr period.

Level (mb)	Correlation Coefficient
850	.20
700	.27
500	.02
400	.04
300	.09
200	.11
100	.04

5. DISCUSSION

As a result of this work, all of the satellite soundings used in the variational analysis model were debiased using separate biases for day and night soundings, and separate biases for the three sounding types. The corrected mean layer temperatures were converted to level temperatures before insertion. No corrections were made for terrain height or for non-synoptic timing. The standard deviations of the satellite-estimated temperatures were used in assigning weights in the model.

Acknowledgement. This work was supported by the National Aeronautics and Space Administration under Grant NAS8-34902.

REFERENCES

Achtemeier, G.L., H.T. Ochs III, S.Q. Kidder, and R.W. Scott, 1986: Evaluation of a multivariate variational assimilation of conventional and satellite data for the diagnosis of cyclone systems. Preprints: Second Conference on Satellite Meteorology/ Remote Sensing and Applications.

Gruber, A., and C.D. Watkins, 1982: Statistical assessment of the quality of TIROS-N and NOAA-6 satellite soundings. Mon. Wea. Rev., 110, 867-876.

Hess, S.L., 1959: Introduction to Theoretical Meteorology. Holt, Rinehart and Winston, New York, 362 pp.

Lewis, J.M., C.M. Hayden, and A.J. Schreiner, 1983: Adjustment of VAS and RAOB geopotential analysis using quasi-geostrophic constraints. Mon. Wea. Rev., 109, 2058-2067.

Phillips, N., L. McMillin, A. Gruber, and D. Wark, 1979: An evaluation of early operational temperature soundings from TIROS-N. Bull. Amer. Meteor. Soc., 60, 1188-1197.

Schlatter, T.W., 1981: An assessment of operational TIROS-N temperature retrievals over the United States. Mon. Wea. Rev., 109, 110-119.

U.S. Standard Atmosphere, 1962: U.S. Government Printing Office, Washington, D.C.

Wallace, J.M., and P.V. Hobbs, 1977: Atmospheric Science: An Introductory Survey. Academic Press, New York, 390-396.

P4.16

EASTERN PACIFIC MODEL IMPACT STUDY (EPAC) AT THE NATIONAL METEOROLOGICAL CENTER

Anthony J. Mostek and David A. Olson

National Meteorological Center
Camp Springs, Maryland

NMC Activities - Eastern Pacific Exercise (EPAC) 1984-86

1. INTRODUCTION

The National Meteorological Center (NMC) has conducted a modelling study for the past four years which has attempted to assess the impact of remote VISSR Atmospheric Sounder (VAS) retrievals upon the Limited Fine Mesh (LFM) numerical model (O'Lenic, 1984). The Eastern Pacific Model Impact Study (EPAC) was made possible through the installation of a remote workstation linked to the Man-computer Interactive Data Access System (McIDAS) based at the University of Wisconsin - Madison (Suomi et al., 1983). The purpose of the NMC VAS assessment activities is to provide quality control of the satellite retrievals and transmit the VAS soundings to the NMC data base on the NOAA Central Computer Facility in real-time; and to develop initial analyses and model forecasts both with and without VAS data to produce quantitative comparisons and subjective evaluations of the with and without VAS cases. The basic concept of the EPAC effort seems logical and straightforward, but the operational implementation of the experiment is another matter, as will be displayed at Williamsburg and reported here. The VAS retrievals are centered over the data void of the eastern Pacific and are available between December and early March. For the EPAC 1984-85 season, the analyses and forecasts were done in real-time for the operational model runs and then forecasts and analyses were compared to those generated without VAS data. However, as a result of the unforeseen events near the end of the 1984-85 season, the 1985-86 EPAC effort reverted back to a case study mode of operations. This report presents the findings of both the 1984-85 and 1985-86 (only initial results) EPAC studies. For information on the retrieval algorithm the reader is referred to Smith and Woolf, 1984 and Hayden and Schreiner, 1984.

2. EXPERIMENTAL DESIGN AND IMPLEMENTATION

During the 1984-85 season, the LFM, the Regional Analysis and Forecast System (RAFS) were run operationally for selected cases. The remote soundings are analyzed to establish whether VAS observations can help fill the data void left by current polar orbitting sounders of the NOAA series. However, the need for VAS over the eastern Pacific at 00 GMT is no longer a strong requirement since NOAA 9 data generally arrives in time for this analysis and model run. From 12 December 1984 through 8 March 1985, VAS retrievals for EPAC were generated for the 1200 GMT forecast run and beginning in February retrievals for 0000 GMT were also prepared. Meteorologists from the Heavy Precipitation Unit (HPU) and the Techniques Development Group (TDG) provided monitoring and editing of the VAS retrievals for vertical and horizontal consistency and for agreement with west coast radiosondes. The VAS fields were compared with the general synoptic pattern as depicted by the LFM 12-hour forecast and by cloud motions in the satellite imagery. The VAS retrieval coverage extended from 55 to 29 N latitude composed of two dwell sounding swaths (down from three the previous EPAC season). East/west coverage remained the same extending out to 155 W longitude from the west coast. For EPAC 1985-86, the area was expanded south (to 24 N latitude) and further east to provide some retrievals over the northern Gulf of Mexico. Many significant features were missed during 1984-85 with no data south of 30 N, since a strong north/south jet stream was often present along the west coast which on occasion reached down to Baja California. Duplicate runs of the LFM were done for 13 cases (1984-85) and for 10 cases (December 1985) when significant changes occurred in the initial analysis over the Pacific as a result of the satellite retrievals. Several missing days (no VAS retrievals available) occurred during these last two seasons. Missing data were generally the result of problems at Wallops Island ground station, or when the satellite is scheduled for rapid scan operations, or when communications between the University of Wisconsin, the World Weather Building and the NOAA Central Computing Facility (NCCF) were interrupted.

3. DATA UTILIZATION

For the last two EPAC seasons, height data from the VAS retrievals were generally of high enough quality for operational use, although some editing (both deletion of bad retrievals and reinsertion of deleted soundings) was required. Editing seldom eliminated more than approximately 10-20% of the observations. EPAC 1984-85 ran smoothly until 0000 GMT retrievals began to be inserted into the model runs. On 13 February 1985, VAS retrievals of poor quality were inserted into the LFM, which caused a spurious cutoff low to be generated in the 36- and 48-hour forecasts near

the Baja California coast (Fig. 1). For the rest of EPAC 1984-85, only one more model run was conducted in real-time for 1200 GMT on 20 February 1985, when another spurious wave was generated. The LFM forecasts were compared to the LFM and RAFS which were run without VAS data and which did not generate the unexpected wave. Post processing of several LFM runs in late February and early March 1985 did not reveal any serious problems as indicated by the statistics in Table 1. Detailed analyses of the entire VAS processing procedure by Advanced Satellite Products Program (ASPP) revealed that a problem occurred with heating in the filter wheel of the VAS instrument, which introduced a bias into the VAS retrieval calculations. ASPP has provided corrective measures in the VAS retrieval algorithm and changed the scheduling of the VAS instrument to alleviate this problem. Nevertheless, EPAC 1985-86 was conducted under a case study mode of operation to determine not only whether the VAS retrieval bias problem has indeed been corrected but also to ensure that all data processing procedures were operating in a reliable fashion required by NMC operations. Initial results from EPAC 1985-86 indicate that the bias problems have not been completely eliminated. A cold bias has been apparent in the 700 to 500 mb layer for several cases, and seems to be increasing as the EPAC season moves into late January and early February. However, this cold bias does vary from one day to the next, and does not always show up. The ASPP group is monitoring the bias problem and a full report will be ready by May. Latest indications are that not all of the VAS retrieval bias can be attributed to the GOES-6 filter wheel heating problem, and that some of the deviations may be a function of the VAS instrument itself.

As opposed to the previous 1983-84 EPAC season when high pressure dominated the height field across lower latitudes, many significant features were missed because retrievals seldom reached 30 N latitude (due to the sounding field-of-view window of 11 pixels by 11 lines which results in a gap along the southern edge of the dwell sounding swath). The critical restriction imposed by clouds which prevent soundings especially in active cyclonic systems will remain. However, many retrievals can still be generated near the edge of these systems even in partly cloudy areas. A new requirement for the 1985-86 season allows the NMC forecaster/analyst to interactively produce retrievals to fill in gaps left by the automatic sounding procedure especially in those areas of active weather. However, as a result of the tight time constraints associated with editing and transmitting the VAS retrievals in real-time, only a few soundings have been generated at NMC, mostly to generate VAS retrievals over radiosonde sites for comparison between VAS and radiosonde.

VAS derived winds, both cloud and water vapor drift, were not introduced into the models during the 1984-85 season. However, during EPAC 1985-86 a two week test was conducted during the first half of December to derive satellite winds at 0000 GMT which will be used in the RAFS to evaluate the impact of high density cloud and water vapor winds over the eastern Pacific on the analysis and forecast system. On the two critical failure days in February 1985, the LFM analysis system ignored good aircraft winds in favor of the biased VAS retrieval heights which in several areas were 90 degrees out of phase. Therefore, the EPAC wind study will focus on the RAFS. Satellite winds will include tracked, water vapor tracked, and possibly VAS gradient winds. Results of case studies using the RAFS system are expected by the summer of 1986.

4. RESULTS

The findings of EPAC 1984-85 and 1985-86 generally concur with those of the previous seasons (O'Lenic, 1984), with some notable exceptions. VAS retrieval heights over a limited area of the eastern Pacific do not consistently produce a significant positive impact on the forecast of the LFM, even when there was a change introduced into the initial analysis field by the VAS data. In most cases during the 1984-85 season the differences were too small or any positive impact in one area of the model domain was counteracted by just as great a negative impact in another region. However, during December 1985, 10 cases were run using the LFM with and without VAS retrievals and significant impact was readily apparent from most of the cases. However, the impact was again unpredictable with just as many negative cases as positive (Figs. 3 and 4). Note how on the 6 December 1985 case (Fig. 4) the NoVAS LFM already generated an extremely poor forecast, especially over the northwestern U.S. However, the addition of VAS data not only did not improve the forecast, but actually increased the errors already in the model forecast. Then, on 17 December 1985, the opposite affect was seen as the LFM was dramatically improved with the addition of VAS data (Fig. 4).

The statistics (Table 1) for EPAC 1984-85 are for the most part inconclusive. However, the S1 and RMS differences between VAS and NoVAS are in the noise level because the NoVAS LFM scores are already very good, which makes improvement difficult. In addition, the 12-hour global model forecast, which is used as a first guess by the retrieval algorithm, already contains satellite retrievals from the NOAA polar orbitters. Comparisons of the VAS retrievals with the polar orbiter soundings generally show the VAS retrievals being a little colder at middle levels, with generally good agreements at other levels. The major exception to the inconclusive statistics found in Table 1 occurs with the 17 January 1985 case when the overall S1 score for the 110 North American stations improved from 34.5 for NoVAS to 29.5 for VAS. However, the counteracting pattern was again present as the strong positive impact across the East 73 stations (33.5-NoVAS and 26.3-VAS) was slightly offset by the West 37 stations (37.8-NoVAS and 39.1-VAS). However, in this one case the positive impact was overwhelming. As shown by the difference plot in Figure 4, the 48-hour LFM forecast with

VAS generated a much deeper trough over the eastern half of North America. The 90 meter differences produced by the VAS data that were centered over Illinois and Indiana were all in the right direction and verified much closer to the actual analysis than the NoVAS forecast. The changes in the LFM forecast can be followed from 12 through 48 hours as a steadily progressing pattern beginning over the northern Plains. This case is still quite perplexing since the changes in the initial analysis are all over the eastern Pacific off the west coast and do not readily explain the resultant impact on the forecasts downstream over the eastern half of North America. Another confusing aspect also arises since the RAFS with VAS data produced a slightly worse forecast than the LFM with NoVAS. (The archive tape was lost for this case and no rerun was done for the RAFS.) This situation clearly points to the need for further detailed study of the RAFS.

Other major findings from both EPAC 1984-85 and 1985-86:

1) LFM can be impacted negatively by bad height data as occurred with the introduction of biased VAS retrievals on 13 and 20 February 1985 and again for four of the cases in December 1985.

2) the LFM (Cressman) analysis will draw for height data over wind data even when the observations are inconsistent.

3) VAS data can be displayed, edited and transmitted in time for the operational model runs, when EXPERIENCED forecasters and analysts are available. An appropriate combination of automated string commands allow for increased speed and efficiency in the display and editing functions.

4) Communications between McIDAS and the NOAA Central Computing facility (NCCF) must be improved which is planned for the EPAC 1986-87 when the new VAS Data Utilization Center (VDUC) system will be installed at the World Weather Building. The VDUC will have direct access to the NCCF via a high-speed microwave link.

5) All future model assessment efforts both for VAS retrievals and winds will focus on the NGM, which should be fully operational by EPAC 1986-87. EPAC 1986-87 will also act as a benchmark for establishing the operational capabilities of the new VDUC system.

Future plans beyond EPAC 1986-87 will address the following:

1) Supplying the RAFS with VAS thickness and precipitable water retrievals over the Pacific, Atlantic and Gulf of Mexico at both 0000 and 1200 GMT all year long. Two GOES satellites should be available to provide extended coverage. An investigation is underway to determine whether EPAC requirements can be merged with support provided to the National Severe Storms and Hurricane Centers.

2) One VAS data assimilation is clearly not enough as shown by studies such as Gal-Chen et al., 1985. NMC is already developing plans for multiple satellite data assimilation into the model analysis and forecasting systems.

3) NMC is addressing the issue of improved data assimilation schemes for the RAFS, including a Newtonian nudging technique which should help increase the efficiency of incorporating the satellite data.

We would like to thank the staff at the University of Wisconsin and the ASPP team, who were most cooperative, and responded quickly to our suggestions and needs. In particular, Anthony Schreiner was very helpful and provided assistance on a daily basis. The automated retrieval and editing functions were enhanced and checked to provide additional capabilities. The VAS retrieval display function was revised several times by Anthony Siebers to meet the ever changing needs of the World Weather Building editing and monitoring team. We would also like to thank Dennis Deaven from the Development Division at NMC for providing reruns of the LFM in a timely fashion.

5. REFERENCES

Gal-Chen, T. 1983: Initialization of mesoscale models: The possible impact of remotely sensed data. Mesoscale Meteorology, Theories, Observations, and Models, D.K. Lilly and T. Gal-Chen, Eds., Reidel, 157-171.

Hayden, C.M., and A.J. Schreiner, 1984: Real time meteorological application of the geostationary satellite sounder on GOES-6: battling the computer, code and clock. SPIE, VOL 481, Recent Advances in Civil Space Remote Sensing, 100.

O'Lenic, 1984: Results of experimental numerical forecasts using temperature profiles from geostationary satellite. Proceedings of SPIE Symposium East, April 29 - May 9, 1984, Crystal City, VA.

Smith, W., and H. Woolf, 1984: Improved vertical soundings from an amalgamat of polar and geostationary radiance observations. Conf. on Satellite Meteor./Remote Sensing and Appl., Clearwater Beach, FL. AMS, pp. 45-48.

Suomi, V.E., R. Fox, S.S. Limaye, W.L. Smith, 1983: McIDAS III: A modern interactive data access and analysis system. J. Clim. Appl. Meteor., 22, 766-778.

FIGURES ARE NOT AVAILABLE AT THIS TIME BUT WILL BE AVAILABLE AT THE CONFERENCE.

EPAC 84-85

VAS-----NoVAS COMPARISON--48 Hour

500 MB HEIGHT FIELD (METERS)

	INITIAL TIME	S_1 NoVAS	S_1 VAS	MEAN NoVAS	MEAN VAS	RMS NoVAS	RMS VAS	
NA 110	DEC 17	23.0	23.7			32.7	35.7	(36 Hour)
	DEC 19	35.0	35.9			36.2	41.4	
	DEC 20	24.8	25.2			54.8	54.2	
	DEC 21	21.4	21.9			58.9	66.4	
	JAN 8	35.8	35.8			41.0	36.6	
	JAN 16	36.2	38.1			46.0	51.2	
	JAN 17	34.5	29.5	-5.3	-30.8	66.8	67.3	
	FEB 8	38.3	37.3			51.8	47.6	
	FEB 27*	34.2	36.6			38.7	41.2	
	FEB 28*	33.5	31.3	-5.0	- 4.8	45.3	44.7	
	MAR 1*	34.2	36.6	9.4	16.2	38.7	41.2	
	MAR 3*	37.2	38.0	31.1	28.4	50.4	50.1	
	MAR 8*	32.5	34.6	-19.5	-14.8	42.3	42.6	
WNA 37	DEC 17	27.0	31.2			32.0	39.5	(36 Hour)
	DEC 19	40.7	42.6			39.7	46.1	
	DEC 20	30.0	29.2			74.4	71.4	
	DEC 21	33.0	31.5			86.9	93.1	
	JAN 8	54.3	50.7			46.3	37.7	
	JAN 16	41.9	45.6			47.5	55.3	
	JAN 17	37.8	39.1	-65.3	-75.9	80.2	93.3	
	FEB 8	31.2	32.7			37.7	48.1	
	FEB 27*	45.0	43.7			47.3	45.9	
	FEB 28*	44.3	42.0	7.8	7.9	64.3	66.3	
	MAR 1*	45.0	43.7	29.9	29.0	47.3	45.9	
	MAR 3*	62.2	66.7	53.5	49.1	75.2	77.2	
	MAR 8*	48.3	55.2	-33.3	-16.7	63.1	60.1	
ENA 73	DEC 17	21.5	21.0			33.0	33.7	(36 Hour)
	DEC 19	33.0	33.6			34.4	38.9	
	DEC 20	22.7	23.6			41.6	43.1	
	DEC 21	17.0	18.3			39.0	48.7	
	JAN 8	28.5	29.8			37.9	36.0	
	JAN 16	34.2	35.3			45.3	49.0	
	JAN 17	33.5	26.3	24.2	-8.5	59.1	49.8	
	FEB 8	42.2	39.8			57.4	47.3	
	FEB 27*	29.7	33.7			34.0	38.8	
	FEB 28*	30.0	27.9	-11.0	-10.8	32.8	29.5	
	MAR 1*	29.7	33.7	- 0.0	10.3	34.0	38.8	
	MAR 3*	27.5	26.9	20.6	18.7	32.9	29.8	
	MAR 8*	26.2	26.0	-13.2	-13.9	28.2	31.6	

*These cases were run in post real-time mode.

Table 1

FOREST FIRE MONITORING USING THE NOAA SATELLITE SERIES

M.D. Flannigan

Canadian Forestry Service
Petawawa National Forestry Institute
Chalk River, Ontario, Canada K0J 1J0

T.H. Vonder Haar

Department of Atmospheric Science
Colorado State University
Fort Collins, CO 80523

1. INTRODUCTION

Forest fires can pose a serious threat to communities, property, and valuable timber every year. In Canada, during the period 1973-82, there was a yearly average of 9,200 fires which burned 2.1 million hectares (ha) (Ramsey and Higgins, 1985) and cost $100 million to control. During that 10-year period, fires that were larger than 200 ha, which made up 3% of the total number of fires, were responsible for 97% of the area burned. Fire control agencies try to detect the fire as soon as possible after ignition and take appropriate action. If the action required is to extinguish the fire, the smaller the fire the easier the task. Detection is achieved by aircraft reconnaissance, observations from manned fire towers, and by the general public.

The ability to monitor forest fires by satellite has been possible for over two decades now. LANDSAT imagery has been used to calculate area burned in the Northwest Territories, Canada, at the end of a fire season. The LANDSAT satellites with a resolution of 30-80 m range would be ideal for fire monitoring were it not for the 18-day gap between passes over the same area. The Geostationary Operational Environmental Satellite (GOES) which has excellent temporal resolution, with imagery every half hour, has some drawbacks. First, the infrared resolution of 7 kilometers (km) at the subsatellite point makes it impossible to detect small fires; second, GOES VISSR has only one infrared channel, thereby eliminating the possibility of a multispectral approach.* It is, however, possible to detect fires indirectly by using the GOES visible channel to spot smoke plumes from the larger fires. This is because the resolution of the visible channel is considerably better (0.9 km at nadir). The National Oceanic and Atmospheric Administration (NOAA) satellites, with a resolution of near 1 km at nadir along with a pass every 12 hours over the same location, appear best equipped to monitor forest fires. Also, the NOAA satellites have multiple infrared channels which facilitate multispectral techniques. The National Weather Service has used the infrared channels from the NOAA satellites since 1981 to help identify forest fires in the western United States (Matson et al., 1984).

The technique of fire monitoring described in this report uses satellite data to monitor forest fire location and size and could be used to complement existing detection systems. Remote areas of North America, which include large segments of Canada's boreal forest, are ideally suited for fire monitoring by satellite because reports of fire detection by conventional means are usually slow and scarce.

2. THE ADVANCED VERY HIGH RESOLUTION RADIOMETER

The Advanced Very High Resolution Radiometer (AVHRR) has been on board NOAA satellites since 1979. The NOAA satellites were designed to operate in a near polar, sun synchronous orbit with a nominal altitude of 833 km. The orbital period is 104 minutes, which results in 14.2 orbits per day. The AVHRR provides one visible channel, one near-infrared channel, and two or three infrared channels. Table 1 from Kidwell (1984) shows the spectral interval and the Instantaneous Field of View (IFOV) for the AVHRR channels. The IFOV of each channel is approximately 1.4 milliradians leading to a resolution of 1.1 km at the subsatellite point for an altitude of 833 km. The AVHRR is a cross-track scanning radiometer with a scan rate of 360 scans per minute covering an angle of ±55.4° from the nadir, equivalent to a swath width of 2,600 km. Data is digitized onboard the spacecraft with a total of 2,048 samples per scan per channel. A more complete description of the NOAA satellite

---

* Future GOES-I,J,K satellites will have multispectral capabilities as does the present VAS experiment on GOES.

series and the AVHRR can be found in Schwalb (1978, 1982) and Kidwell (1984).

Table 1. Bandwidth and IFOV of the AVHRR

Ch. #	Bandwidth (micrometers) NOAA-6, -8	NOAA-7, -9	IFOV (mrad.)
1	.58 - .68	.58 - .68	1.39
2	.725 - 1.10	.725 - 1.10	1.41
3	3.55 - 3.93	3.55 - 3.93	1.51
4	10.5 - 11.5	10.5 - 11.3	1.41
5	Ch. 4 Repeated	11.5 - 12.5	1.3

3. DATA

The satellite and forestry data were selected for the Slave Lake Forest Region for the period June 12 to June 21, 1982 to take advantage of a rapidly changing forest fire situation. On June 12 only a few small forest fires were burning in the Slave Lake Forest Region. By June 21, there were over 30 fires burning out of control, with some fires larger than 20,000 ha. The Slave Lake Forest Region, as shown in Figure 1, extends from latitude 54.5°N to 57.5°N and from longitude 113°W to 117°W.

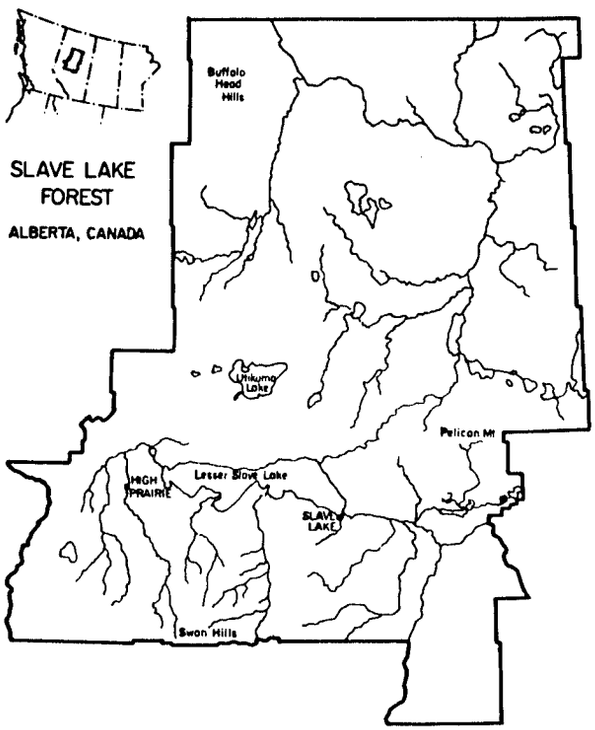

Fig. 1. Slave Lake Forest Region

NOAA-7 AVHRR data were obtained through the Atmospheric Environment Service (AES) from the ground station in Edmonton, Alberta. Data were retrieved from two passes a day from June 12 to June 21, 1982 unless the data were not saved or were at a large viewing angle from nadir. The ascending orbit (northbound equator crossing) for NOAA-7 is in the afternoon, while early morning passes are southbound. The AVHRR data recorded by the Edmonton ground station included channels 2, 3, and 4. The data has 2,048 samples per scan per channel, of which a few samples at the beginning and end are for calibration. The data for the infrared channels were calibrated according to to the procedure described by Lauritson et al. (1979). The data has full spatial resolution of 1.1 km at nadir.

The forest fire data were supplied by the Alberta Forestry Service for the period June 12-22, 1982. They are in the form of daily reports which, by forest region, list the name, location, size (acres), and status of the fire. Almost all fires in this case study were ignited by lightning. The size of the fire was estimated via aircraft reconnaissance, usually in the late afternoon or early evening.

4. FIRE MONITORING TECHNIQUE

Dozier (1981) showed that it was possible to use a multispectral approach to detect subpicture element (pixel)-sized elevated heat sources. He used data from AVHRR channels 3 and 4 to find the temperature of the elevated heat source and percentage of the pixel covered by the hot target. Matson and Dozier (1981) used this approach to detect steel mills in the midwestern United States. The multispectral technique developed by Dozier was used in this study to find the area and temperature of the forest fire within a pixel.

The fire monitoring technique is a result of the differences in the radiometric response of the AVHRR Channels 3 and 4. AVHRR channel 3 is very sensitive to high temperature sources. Figure 2 shows that, as temperature increases, the wavelength of the maximum value of the blackbody radiance shifts toward smaller wavelengths. Using this figure, a forest fire at 500°K compared with the unburned forest at 300°K, will produce a greater fractional contribution to the radiance sensed for Channel 3 than for Channel 4. Figure 3 shows integrated Planck radiances for NOAA-7 Channels 3 and 4. This figure shows the Channel 3 curve has a greater slope than Channel 4; thus, high temperatures for Channel 3 will make a greater contribution to the total radiance sensed. It follows that forest fires or any elevated heat sources are easier to detect on Channel 3 imagery.

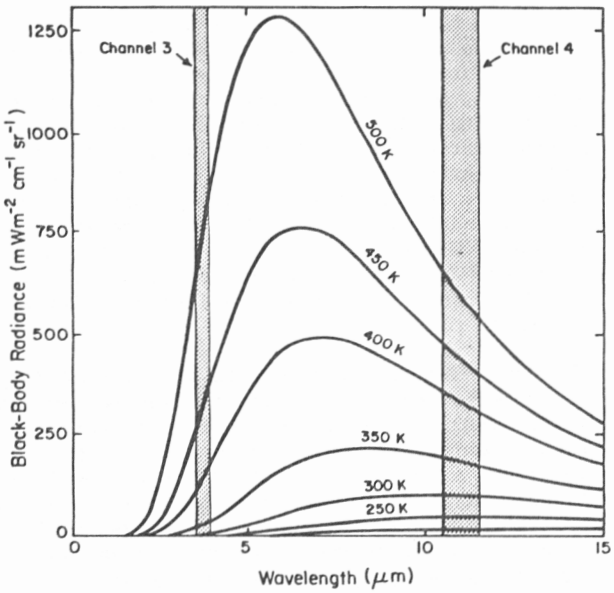

Fig. 2. Planck Radiances for Temperatures from 200° to 500°K.

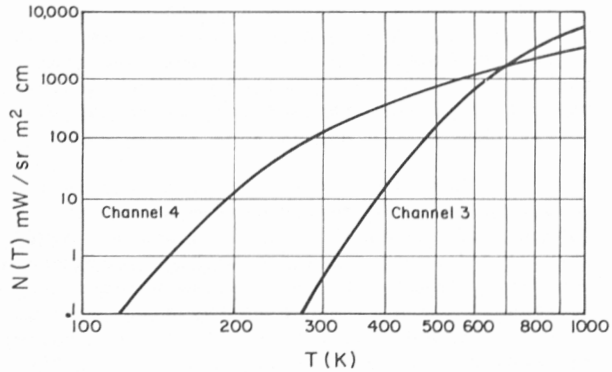

Fig. 3. Integrated Planck radiances for NOAA-7 AVHRR Channels 3 and 4.

To calculate fire size and temperature within a pixel, let $N_3(T)$ and $N_4(T)$ represent NOAA-7 Channels 3 and 4 radiances sensed by the satellite. A pixel may be composed of an elevated heat source, in this example a forest fire at temperature T_f, which occupies portion p of the pixel (where $0 \leq p \leq 1$). The remaining portion (1-p) of the pixel is covered by forest with a background temperature T_b. Therefore, the radiances sensed by the radiometer can be written as follows for Channel 3 and Channel 4:

$$N_3(T_3) = pN_3(T_f) + (1-p)\ N_3(T_b) \qquad (1)$$

$$N_4(T_4) = pN_4(T_f) + (1-p)\ N_4(T_b) \qquad (2)$$

where $N_3(T_3)$ and $N_4(T_4)$ are known. If T_b is known, then p and T_f can be found by solving the two equations. This technique will not determine the location of the fire within the pixel. One limitation of this method is that the Channel 3 sensor will saturate at 322°K. Fortunately, saturation will only occur when the fire is intense or covers a significant portion of the pixel.

Figure 4 shows a sample NOAA-7 AVHRR Channel 3 image from June 19, 1982, 2110 GMT. The image covers an area of about 360,000 km² (600 km x 600 km). The enhancement scale is such that black is hot and white is cold.

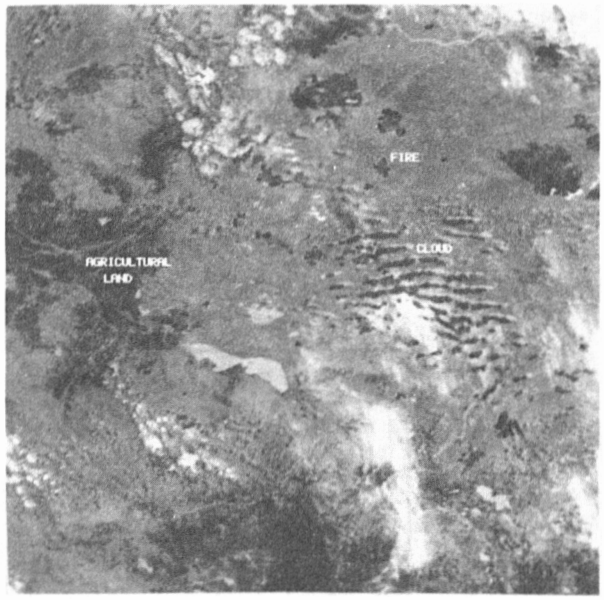

Fig. 4. NOAA-7 AVHRR Channel 3, June 19, 1982, 2110 GMT.

Traditionally, Channel 3 imagery has not been used during daylight hours due to the reflection of solar radiation. This solar contamination is evident in figure 4 as some clouds appear very warm. Even though the relative intensity of solar radiation in the AVHRR channel 3 range (3.55 - 3.93 μm) is small, the reflection from clouds can compare to the radiation emitted by cloud tops. The reflected radiation is dependent upon the albedo of the illuminated surface. The albedo of clouds in the 3.5-4.0 μm region is high and pixels with some cloud are contaminated. Therefore, cloud-contaminated pixels were eliminated through a cloud discrimination technique based on the spatial coherence method of Coakley and

Bretherton (1982). The reflectivity of a typical hardwood leaf in the 3.0-4.0 μm range was shown by Lee (1978), based on data from Gates (1965), to be zero. Wong and Blevin (1967) found reflectances of plant leaves in the 3.0-4.0 μm region are less than .05 for the majority of leaves. From the above information the amount of solar radiation reflected by the forest was considered insignificant. Therefore, Channel 3 imagery was used during daylight hours to monitor the forest.

Detecting fire in a pixel was accomplished through a temperature differencing technique. The effective infrared temperature of each cloud-free pixel was calculated for both Channels 3 and 4. If the calculated temperature exceeded the mean background temperature of the forest and if the Channel 3 temperature was greater than that of Channel 4 by a critical value, it was assumed that fire was present. The threshold value of the temperature difference was 8°K for night passes, and 10°K for day passes. After this technique was applied to the region of interest in the image, contiguous pixels with fire present were grouped together as one fire. The fire area in any given pixel was calculated by the multispectral approach (Dozier, 1981) except when a pixel was surrounded by other fire pixels. In such a case it was assumed the pixel was totally burned over.

5. RESULTS

Verification of fire identification for two class sizes are shown: Class 1 included fires 40 ha or less, and Class 2 was for fires over 40 ha. During the 10-day period June 12 - June 21, a total of 355 fire observations were reported by the Alberta Forest Service. Many of these were repeated observations of the same fire in several satellite passes. For example, if the same fire was present for three passes it was counted as three fire observations. Table 2 displays the total fire observations for class type and for day and night cases, as well as unobstructed fire observations. Cloud and smoke were responsible for obstructing the satellite view in many cases. Table 3 shows the number of fire identifications made by satellite for those fire observations that were not obscured.

Table 2. Total fire observations by class and time of pass

	Class 1 (≤ 40 ha)	Class 2 (> 40 ha)	Total
Day	66 (16)	117 (62)	183 (78)
Night	73 (20)	99 (49)	172 (69)
Total	139 (36)	216 (111)	355 (147)

The ( ) number indicates those fire observations which were unobstructed for satellite viewing.

Table 3. Unobstructed fire observations identified by satellite.

	Class 1 (≤ 40 ha) (%)	Class 3 (> 40 ha) (%)	Total
Day	9/16 (56)	59/62 (95)	68/78 (87)
Night	9/20 (45)	41/49 (84)	50/69 (73)
Total	18/36 (50)	100/111 (90)	118/147 (80)

The results from table 3 show that 80% (118/147) of the unobstructed fire observations were identified. However, only 33% (118/355) of total fire observations were identified, with almost 59% (355-147/355) unavailable for satellite viewing due to obscuration by cloud or smoke. The results also show that afternoon passes had a higher per cent of fires identified 87% (68/78) than morning passes 73% (50/69). The better performance of fire identification during afternoon passes was not surprising as fires generally burn more vigorously due to lower relative humidities, higher temperatures, and stronger winds at that time of day. As one would expect, a higher percentage of larger fires (Class 2) were identified. Fires as small as 0.5 ha were also properly identified by this technique.

As evident from the results, a significant number of fires were obscured by smoke and/or cloud. During a major forest fire outbreak vast quantities of smoke were to be anticipated. Thus this fire monitoring system was tested under difficult conditions. On the other hand, fire monitoring would be most beneficial in this kind of situation. Cloudiness was also a problem, particularly with the development of afternoon cumulus.

Forest fire area was calculated for each fire observation. The technique tended to overestimate the size of small fires and underestimate the size of large fires. A more detailed account of forest fire area calculation is given in Flannigan (1985).

6. DISCUSSION

The automated fire monitored system described here has two inherent weaknesses. A fire may go undetected because, (1) the temperature difference between Channels 3 and 4 is below the threshold, and (2) thin cloud or smoke may be obscuring the fire. Automated monitoring could be improved by visual inspection. The image analyst could verify new fires and scan for any undetected fires. It would not be necessary to monitor all forested areas every day during the fire season. Using the Canadian Forest Fire Danger Rating System (Canadian Forestry Service 1984, Van Wagner and Pickett 1985) which evaluates fire danger and predicts fire behaviour, close forest fire monitoring is warranted only in forested regions with a high fire danger rating.

Problems with fire identification can be dependent on the type of fire. A surface fire can be very difficult to detect as the forest canopy can effectively block the view of the satellite. We have assumed that an entire pixel was composed of a constant background or fire temperature. Actually, the pixel could be composed of fire, smoldering burned over forest, smoke, water, small clouds, as well as unburned forest.

7. CONCLUSIONS

The fire monitoring system described in this study has some limitations, the most serious being obscuration of fires by smoke and cloud. Despite these limitations, the system identified most unobstructed fire observations in the Slave Lake Forest Region during a major fire outbreak.

Fire monitoring over remote areas of the forest has been hindered by the cost and logistics of spatial and temporal coverage. Use of this fire monitoring system would enable the detection of fire location and size over large areas of forest.

8. REFERENCES

Canadian Forestry Service. 1984. Tables for the Canadian Forest Fire Weather Index System. Environ. Can., Can. For. Serv., For. Tech. Rep. 25 (4th ed.).

Coakley, J.A., Jr.; Bretherton, F.P. 1982. Cloud cover from high-resolution scanner data: detecting and allowing for partially-filled fields of view. J. Geophys. Res. 87: 4917-4932.

Dozier, J. 1981. A method for satellite identification of surface temperature fields of subpixel resolution. Remote Sens. Environ. 11: 221-229.

Gates, D.M. 1965. Radiant energy, It's receipt and disposal. In Agricultural Meteorology, ed. P.E. Waggoner. American Meteorological Society, Boston.

Flannigan, M.D. 1985. Forest fire monitoring using the NOAA satellite series. M.S. thesis, Colorado State Univ., Fort Collins, Colorado, 59 p.

Kidwell, K.B. 1984. NOAA Polar Orbiter Data (TIROS-N, NOAA-7, NOAA-7, and NOAA-8) User's Guide. NESDIS.

Lauritson, L.; Nelson, G.J.; Porton, F.W. 1979. Data extraction and calibration of TIROS-N/NOAA radiometers. NOAA Tech. Mem. NESS-107.

Lee, R. 1978. Forest microclimatology. Columbia University Press, New York.

Matson, M.; Schneider, S.R.; Aldridge, B.; Satchewll, B. 1984. Fire detection using the NOAA-series satellites. NOAA Tech. Mem. NESDIS 7.

Matson, M.; Dozier, J. 1981. Identification of subresolution high temperature sources using a thermal IR sensor. Photogrammetric Engineering and Remote Sensing 47: 1311-1318.

Ramsey, G.S.; Higgins, D.G. 1986. Canadian forest fire statistics 1981-83. Environ. Can., Can. For. Serv., Petawawa Nat. For. Inst., Inf. Rep. (In press).

Schwalb, A. 1978. The TIROS-N/NOAA A-G Satellite Series. NOAA Tech. Mem. NESS-95.

Schwalb, A. 1982. Modified version of the TIROS N/NOAA A-G Satellite Series (NOAA E-J) - Advanced TIROS N (ATN). NOAA Tech. Mem. NESS-116.

Van Wagner, C.E.; Pickett, T.L. 1985. Equations and FORTRAN program for the Canadian Forest Fire Weather Index System. Can. For. Serv., For. Tech. Rep. 33.

Wong, C.L.; Blevin, W.R. 1967. Infrared reflectances of plant leaves. Aust. J. Biol. Sci. 20: 501-508.

REMOTELY SENSED ALBEDO OF SNOW-COVERED LANDS

David A. Robinson

Lamont-Doherty Geological Observatory
of Columbia University
Palisades, NY 10964

1. INTRODUCTION

Snow cover is an important variable of the climate system. The accurate forecasting of local daily temperatures, regional climatic anomalies and the location and strength of cyclonic systems relies, in part, on knowledge of the distribution and state of regional snow cover (Dewey, 1977; Kukla, 1979; Namias, 1981; Walsh et al., 1982; Foster et al., 1983; Robinson, 1984a; Walsh and Ross, 1986). Snow-covered land exhibits major differences from snow-free ground due to snow's low heat conductivity, high thermal emissivity, low vapor pressure and high shortwave albedo.

The high albedo of snow permits the recognition of snow-covered land in shortwave satellite imagery. This task is often difficult, however, as the albedo of snow-covered land varies considerably as a function of the type and density of vegetative cover, the physical properties and depth of snow and the continuity of snow cover. Automated analyses of multi-spectral satellite imagery have shown to be promising (Kunzi et al., 1982; Bunting and D'Entremont, 1982; Tsonis, 1984). Nevertheless, an interactive analysis of satellite data on an image processor by an observer familiar with the studied area is still the optimal method of retrieving information on snow-covered regions.

In the following, examples of albedo variations of both fresh and aging snow cover are examined using a combination of remotely-sensed aircraft and satellite data. For the purpose of this discussion, only clear-sky albedo values are discussed.

2. DATA

2.1. Aircraft measurements

Surface albedo (0.28-2.80μm) was measured over typical middle latitude surface types under a variety of snow-covered conditions. Data were gathered over southeastern New York and northern New Jersey from aircraft equipped with wingtip-mounted hemispheric pyranometers. At the flight altitude of approximately 200m, 90% of the reflected signal came from an area of approximately 0.50km^2. The confidence limit of flight albedos is ±4% of the calculated value (Robinson and Kukla, 1984).

2.2. Satellites

Surface albedo was estimated over full and partly snow-covered lands from Defense Meteorological Satellite Program (DMSP) and NOAA Advanced Very High Resolution Radiometer (AVHRR) imagery, having resolutions of 2.7km and 1.1km, respectively. Albedo was determined by analysing clear-sky scenes on a digital image processor. The brightness of the scene was converted to surface albedo by linear interpolation between bright and dark snow-covered or snow-free targets with known albedos. Shine and Henderson-Sellers (1983), using a radiative transfer scheme, have shown that this approach works well with DMSP imagery because of the wide spectral range (0.4-1.1μm) of the DMSP sensor.

Albedos so calculated from DMSP imagery may be up to 0.10 too low or 0.05 too high (Robinson and Kukla, 1985). The range is larger for the narrow band (0.6-0.7μm) AVHRR imagery. These error ranges are relatively small compared to the dramatic differences in surface albedo due to contrasting types and densities of vegetation and varying snow conditions.

3. FRESH SNOW COVER

The albedo of surfaces which are covered with fresh snow varies due to the type and density of vegetative cover and the depth of snow. The latter is exemplified in table 1, which presents aerial albedo data gathered over fresh snow-cover on two days where only the snow depth differed. On February 10 only 10-15cm of snow covered the fields and forests, while on the 14th of February 40-50cm of snow lay on the ground. Ground measurements of the albedo of pure snow on both dates were between 0.78 and 0.83. Albedo on the 10th was from 0.03-0.12 lower than on the 14th. Representative differences were 0.03-0.06 over forests, 0.05 over grassy meadow, 0.06-0.08 over developed areas, and 0.12 over shrubby grassland and cultivated fields. These differences were due to the presence of grass, bushes, crop and forest litter, rocks, rooftops, etc., which were buried on the 14th, but protruded through the pack on the 10th. In general, differences caused by varying depth are significant when less than 15 to 20cm of snow covers the ground.

The impact of vegetation on the surface albedo varies markedly over land covered by fresh snow. Figure 1 shows the potential

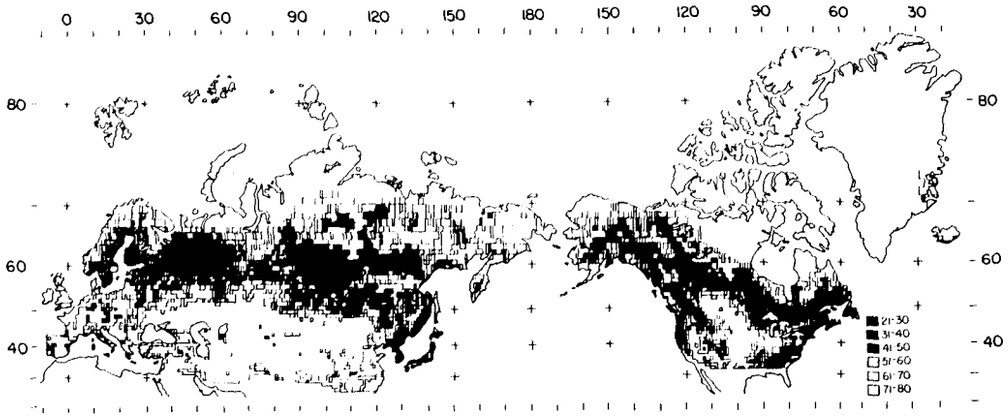

Fig. 1. Maximum surface albedo of Northern Hemisphere land with the potential of developing seasonal snow cover. Cells, measuring 1° x 1°, are marked in 0.10 increments. (from Robinson and Kukla, 1985)

Table 1. Surface albedo with differing depths of snow cover over sites representing a variety of middle latitude surfaces. On Feb. 10, 1983 the snow cover was 3 days old and 10-15cm deep. Over the same sites on Feb. 14, 1983 the top 30-40cm of the cover was 2 days old and the entire pack was 40-50cm deep. The albedo of the snowpack on both dates was between 0.78 and 0.83. For a further description of sites see Robinson and Kukla (1984).

Surface	Albedo Feb. 10	Feb. 14	14th-10th
mixed forest	0.16	0.19	0.03
deciduous forest	0.25	0.31	0.06
shrubby grassland	0.48	0.60	0.12
grassy meadow	0.67	0.72	0.05
cultivated fields	0.68	0.80	0.12
suburban residential	0.40	0.48	0.08
industrial	0.51	0.57	0.06

maximum surface albedo of seasonally snow-covered Northern Hemisphere lands. Data were gathered in selected clear-sky scenes of DMSP imagery where visual inspection showed the presence of deep and stable snow cover over several consecutive days. In areas where deep snow was not found in the several years of imagery analysed, albedo was inferred. These areas were mostly located in portions of arid and semiarid southern Asia, where albedo inference is simplified by the general absence of tall or dense vegetation (Robinson and Kukla, 1985).

There is a broad zone of relatively dense forests masking the underlying snowpack in Eurasia and North America. In Eurasia, the areally averaged albedo is 0.36 over the boreal forest zone between 60° and 65°N. It rises to 0.76 over the short grassy tundra further north.

4. AGING SNOW COVER

When assessing the albedo of an aging or dissipating snow cover other factors, in addition to vegetation and depth, come into play. These include the physical properties of the snow and the areal continuity of the cover.

As the snowpack ages, the grain size increases, the surface gets dirty and eventually the pack becomes wet. As a result, the albedo continually decreases. At depths less than approximately 10cm, the underlying surface begins to influence the reflected signal. Ground measurements of an originally 50cm deep snowpack over a short grassy field showed albedo falling by 0.29, from 0.83 to 0.54, over a 13 day period (Fig. 2). While the snow was slushy by the 13th day, no grass blades had yet protruded through the pack.

The physical condition of the snowpack impacts on the albedo of all snow-covered surfaces. Aerially-measured albedos from 25 sites, including field, forest and developed areas, on a day with 10-15cm deep 3 day old snow (Feb. 10) were approximately 20% greater than at the same sites with identical snow depth but with the snow 9 days old (Feb. 22) (Fig. 3). The albedo of the uninterrupted snowpack was approximately 0.80 on the 10th and 0.60 on the 22nd.

Over lightly-vegetated regions with snow present, the largest decreases in surface albedo occur not from physical changes in the snowpack but from the exposure of bare ground. The latter may result from melt or deflation. In figure 4, brightness histograms measured from AVHRR images show the changing proportion of snow-covered and snow-free surfaces as snow dissipated over approximately 100,000km^2 of farmland in the central U.S..

Histogram 1 shows the area in March 1976, when all of the approximately 90 climate stations in the area measured over 15cm of fresh

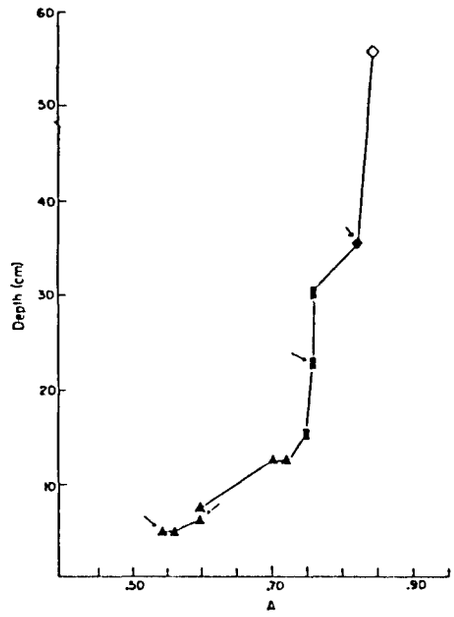

Fig. 2. Midday albedo of a complete snowpack over a short grassy field at the Lamont Observatory (41°N) from Feb. 13-25, 1983. Albedo is shown with a diamond for 1-3 day old snow (open diamond: dry, Feb. 13 and 14), squares 4-6 days old, triangles 7 days or more old. Solid symbols indicate a wet snowpack. Datum from Feb. 20 is missing. Arrows point to cases where global atmospheric transmissivity was below 40%. (after Robinson, 1984b)

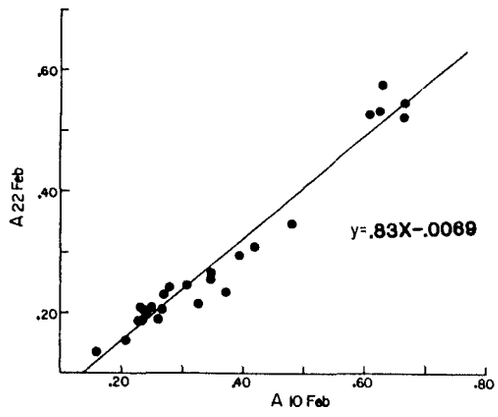

Fig. 3. Snow depth-age-albedo relationships. The albedo of a site on Feb. 10, 1983 is plotted against the albedo of the identical site on Feb. 22, 1983. Both days had clear skies and the same snow depths at forest and field test sites. Snow on the 10th was 3 days old and dry with an albedo of 0.78. Snow on the 22nd was 10 days old and wet with an albedo of 0.60. The regression equation has a correlation of 0.96. (after Robinson and Kukla, 1984).

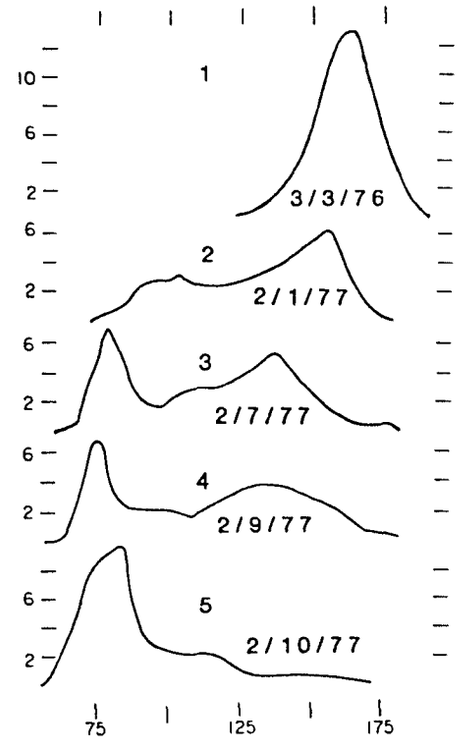

Fig. 4. Brightness histograms with different snow-cover conditions over central U.S. farmland. Vertical axis shows the number of processor pixels (x 10^3) with a particular brightness (horizontal axis). (after Robinson and Kukla, 1982)

snow cover on the ground. A single high brightness peak corresponded to an albedo of about 0.70. The February 1, 1977 histogram (2) quantifies the brightness distribution over the region when a snow cover was 7 days old. Some bare ground had begun to appear, giving the histogram a bimodal character. Regional albedo was approximately 0.40. Compared to histogram 1, the bright peak is shifted towards the dark end, probably due to a combination of decreasing albedo of aging snow and subresolution patches of bare ground. Some 80% of the stations in the region reported snow cover on the 1st. At these stations the average depth was 10cm.

In subsequent days (histograms 3-5), the amount of snow-free ground began to exceed that of snow-covered ground and regional albedo decreased from about 0.30 to 0.20. By the 10th, the single dark peak on the histogram (5) indicates that the surface was mostly snow free, with only subresolution snow patches probably present. These broadened the peak and skewed it towards brighter values. On this date, 50% of the stations reported snow cover, with the depth averaging 4cm.

5. CONCLUSIONS

Regions where snow is present exhibit a wide range of surface albedo due to variations in the type and density of vegetation and the depth, physical properties and continuity of the

snowpack. At present, the most accurate way to assess the winter surface albedo on regional to continental scales is through the analysis of shortwave satellite imagery in an interactive manner on an image processor by an observer familiar with the studied area.

6. ACKNOWLEDGMENTS

This work was supported by NSF grant ATM 83-18676 and Air Force grant AFOSR 86-0053.

7. REFERENCES

Bunting, J.T. and R.P. d'Entremont, 1982: Improved cloud detection utilizing Defense Meteorological Satellite Program near infrared measurements. Air Force Geophysics Lab. Environmental Research Papers, 765, 91pp.

Dewey, K.F., 1977: Daily maximum and minimum temperature forecasts and the influence of snow cover. Mon. Wea. Rev., 105, 1594-1597.

Foster, J., M. Owe and A. Rango, 1983: Snow cover and temperature relationships in North America and Eurasia. J. Cli. Appl. Met., 22, 460-469.

Kukla, G.J., 1979: Climatic role of snow covers. in: Sea Level, Ice and Climatic Change, IAHS Publ. 131, 79-107.

Kunzi, K.F., S. Patil and H. Rott, 1982: Snow-cover parameters retrieved from Nimbus-7 Scanning Multichannel Microwave Radiometer (SMMR) data. IEEE Transactions on Geoscience and Remote Sensing, GE-20, 452-467.

Namias, J., 1981: Snow covers in climate and long-range forecasting. in: Snow Watch 1980, Glaciological Data, GD-11, World Data Center A for Glaciology, 13-26.

Robinson, D.A. and G. Kukla, 1982: Remotely sensed characteristics of snow covered lands. in: (Keydel, W., ed.) 1982 IEEE International Geoscience and Remote Sensing Symposium Digest, WA-1, 2.1-2.9.

Robinson, D.A., 1984a: Spring snow dissipation in Alaska. in: The Potential Effects of Carbon Dioxide-Induced Climatic Changes in Alaska, The Proceedings of a Conference, Fairbanks, Alaska, April 1982, U. Alaska Miscellaneous Publication 83-1, 124-128.

Robinson, D.A., 1984b: Anthropogenic Impact On Winter Surface Albedo. Doctoral thesis, Columbia Universtiy, 384pp.

Robinson, D.A. and G. Kukla, 1984: Albedo of a dissipating snow cover. J. Cli. Appl. Met., 23, 1626-1634.

Robinson, D.A. and G. Kukla, 1985: Maximum surface albedo of seasonally snow-covered lands in the Northern Hemisphere. J. Cli. Appl. Met., 24, 402-411.

Shine, K.P. and A. Henderson-Sellers, 1983: Cryosphere-cloud interactions near the snow/ice limit: sensitivity testing of model parameterizations. Final report of NSF grant ATM 80-18898, University of Liverpool, 158pp.

Tsonis, A.A., 1984: On the separability of various classes from the GOES visible and infrared data. J. Cli. Appl. Met., 23, 1393-1410.

Walsh, J.E., D.R. Tucek and M.R. Peterson, 1982: Seasonal snow cover and short-term climatic fluctuations over the United States. Mon. Wea. Rev., 10, 1474-1485.

Walsh, J.E. and B. Ross, 1986: Snow cover, cyclogenesis and cyclone trajectories. in: Snow Watch 1985, Glaciological Data, World Data Center A for Glaciology, in press.

THE EFFECT OF HURRICANE GLORIA ON SEA SURFACE TEMPERATURE PATTERNS

William G. Pichel, Robert A. Warner, Barbara A. Banks

National Environmental Satellite, Data, and Information Service, NOAA
Washington, D.C.

CDR Craig S. Nelson

National Meteorological Center, NWS, NOAA
Washington, D.C.

1. INTRODUCTION

Hurricane Gloria, one of the largest storms of the twentieth century, made successive landfalls at Hatteras Island, North Carolina and Long Island, New York on September 27, 1985. Gloria skirted the Atlantic seaboard and caused considerable damage on land, but also dramatically altered sea surface temperatures in the Middle Atlantic Bight, in the wake of the storm. The effects of hurricane Gloria on ocean surface conditions are assessed by analyzing changes in sea surface temperature patterns as depicted in (1) satellite infrared (IR) images and (2) operational satellite-derived, multi-channel sea surface temperature (MCSST) analyses.

2. HURRICANE GLORIA

The National Hurricane Center's preliminary report on hurricane Gloria (Lawrence, 1985) is summarized below. As indicated in Fig. 1, this severe storm affected weather over a substantial portion of the North Atlantic Ocean during the last two weeks of September 1985.

Gloria began as a low-level circulation on September 16, 1985 near the Cape Verde Islands. By September 22, the storm had crossed the Atlantic and reached hurricane strength. As Gloria passed to the north of the Bahama Islands on September 24, the hurricane's central pressure fell below 950 mb and observed upper level winds exceeded 46 m/s. The next day, Gloria's central pressure dropped to a minimum of 919 mb, and based on reconnaissance aircraft data, the maximum sustained surface wind speed was estimated at 65 m/s. Gloria then veered to the north and began to weaken.

On September 27, the hurricane's center passed over Hatteras Island, North Carolina, then moved just offshore, skirting the coasts of Virginia, Maryland, Delaware and New Jersey. In a coincident infrared satellite image of this region (Fig. 2) Gloria is located just south of the entrance to Chesapeake Bay. During this period, the strongest winds (43-46 m/s), associated with the northeast quadrant of the hurricane, remained over open water. Wind speeds

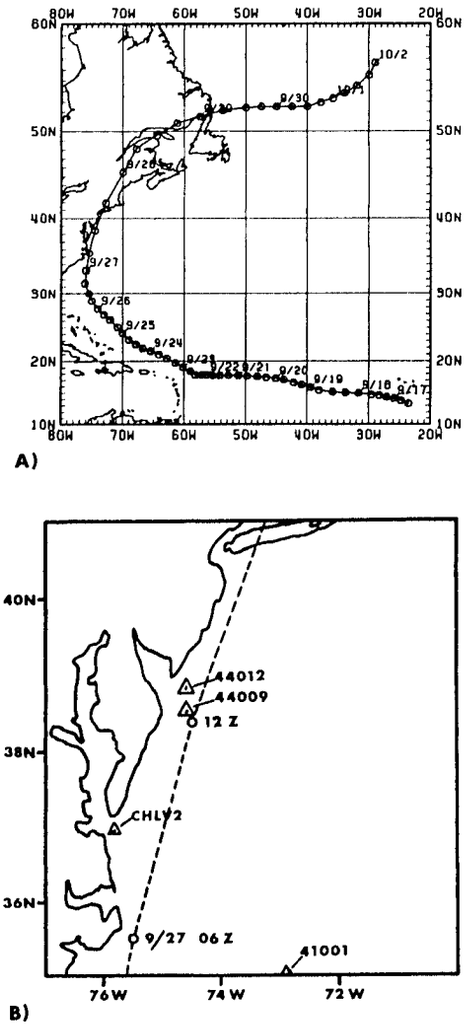

Figure 1. Track of hurricane Gloria: 1) over the North Atlantic Ocean, 17 September to 2 October 1985, and b) over the Middle Atlantic Bight, 27 September 1985.

observed at land stations and at coastal meteorological buoys were not as high. For example, at Cape Point, North Carolina, maximum sustained winds were approximately 33 m/s and reported hourly observations from the NDBC buoys (41001, 44009, CHLV2, see Fig. 1) did not exceed 35 m/s. However, the automated station at Diamond Shoals Light reported sustained winds greater than 40 m/s (Lawrence, 1985). Colder sea surface temperatures (SST) were recorded at each of the coastal buoys after Gloria moved through the area. Although the absolute change in SST at each buoy was not large, it is worth noting that rapid decreases in SST (0.5°C to 1.0°C) were observed at three of the four buoys after Gloria passed (Fig. 3).

Hurricane Gloria made its second landfall on Long Island, approximately ten hours after the initial landfall in North Carolina. Gloria continued on a north-northeast track and became extratropical over Maine on September 28.

From North Carolina to Massachusetts, storm surge tides ranged from two to four meters above predicted astronomical tides. Coastal flooding, although serious in the Outer Banks of North Carolina, was moderated by the coincidence of peak storm surge and low tide. Gloria was the largest storm tracked by the National Hurricane Center since it began monitoring hurricanes in the early 1950's. However, Gloria was not excessively devastating because (1) the main storm surge nearly coincided with low tide, (2) the northeast quadrant passed offshore, and (3) Gloria weakened as it passed over colder water north of the Gulf Stream (Botzum and Garner, 1985).

3. SATELLITE DATA

During the past three years, significant advances have been made in the methods used to derive ocean surface temperatures from operational environmental satellites (Strong and McClain, 1984). These improvements have enabled the routine production of relatively high resolution and accurate satellite-derived SST analyses. The effects of hurricane Gloria on the ocean surface temperature structure can be assessed by using satellite thermal-infrared images and objective analyses of satellite-derived SST measurements.

3.1 Satellite Imagery

The satellite images (Fig. 2 and 6) are enhanced grey-scale representations of infrared-channel scanner data derived from the Advanced Very High Resolution Radiometer (AVHRR) carried on the TIROS-N series of NOAA polar-orbiting environmental satellites. The current satellite in the series is designated NOAA-9 and is the one used to derive the images and analyses depicted here. The AVHRR is a multi-spectral scanner, measuring visible and infrared radiation in five spectral bands at a ground resolution of 1.1 km (Schwalb, 1979; Schwalb, 1982). The images show the variation in the amount of infrared radiation upwelling from the earth's surface in the 10.3-11.3 um spectral bands. The amount of radiation observed is proportional to the temperature of the radiating surface, but is altered by absoption and reemission of radiation by atmospheric constituents, principally water vapor.

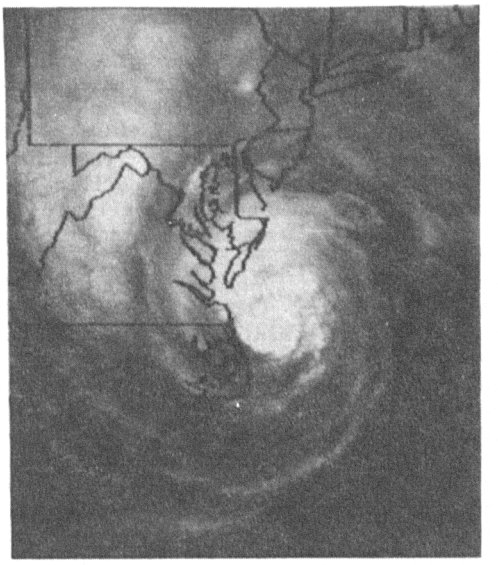

Figure 2. NOAA-9 satellite infrared image of hurricane Gloria, shortly after landfall on Hatteras Island (September 27, 1985). The image depicts temperature as grey-shades, with the warmest regions shown in black and the coldest in white. The coldest clouds are located near the storm's center.

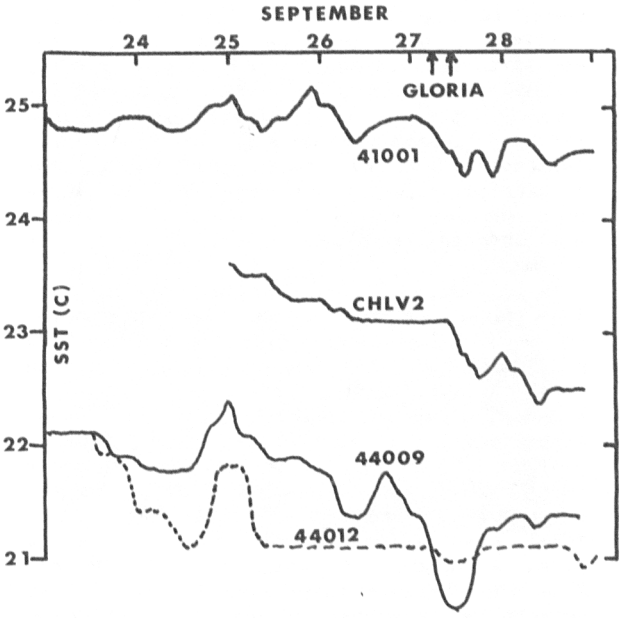

Figure 3. Time series of sea surface temperature at NDBC moored buoys 41001, 44009, 44012 and the Chesapeake Light C-MAN station.

3.2 Multi-Channel SST

To correct for atmospheric effects and derive a quantitative measure of SST, two or more infrared channels are employed. Each channel is affected somewhat differently by the atmosphere, and the difference between the amount of radiation sensed in different channels is a measure of this atmospheric effect. To measure SST, theoretical multi-channel equations are derived using a seasonally and geographically diverse set of atmospheric temperature and moisture profiles, in conjunction with the spectral-response functions of the AVHRR channels (McClain, 1981). These equations are adjusted to minimize the differences between the SSTs calculated with the theoretical multi-channel equations and closely matched drifting buoy SST measurements. The resulting multi-channel SST (MCSST) equations, one for daytime data and one for nighttime data, are used operationally to calculate SST observations (i.e., time and location tagged SST measurements) of 8 km resolution in cloud-free areas. Visible channel thresholds, IR channel relationships, and data uniformity checks are employed to detect clouds before calculating SST. Details of the MCSST algorithms may be found in McClain et al. (1985). In general, the resulting satellite-derived MCSST observations have RMS differences between 0.5°C and 0.7°C when compared to screened buoy observations (Strong and McClain, 1984).

3.3 SST Analysis Technique

An automated objective analysis is used to produce the grid point SST fields shown in Fig. 4 and 5. The input to the analysis program is a set of satellite-derived MCSST observations covering a time period of 3 to 4 days. The output from the program is a mapped field of sea surface temperatures on a 14 km (1/8-degree latitude-longitude) rectangular grid for a particular geographic region. A single pass analysis scheme is used. Grid points are updated with new observations one at a time.

Initially, a rectangular search area is defined which surrounds the grid point to be modified. The distance between the grid point and the boundary of the search area in any cardinal direction varies as a function of the thermal gradient in that direction. This distance varies from a minimum of 45 km for a gradient stronger than 3°C/100 km to a maximum of 75 km for a gradient weaker than 1°C/100 km. Each MCSST observation in the search area is given a weight, W, where $W = 100/D^2$ and D is the distance (expressed in grid units) between the observation and the grid point being updated. All observations within 0.33 grid units (about 4.6 km) of the grid point are given the same weight. Computed weights vary from 3.43 for an observation which is 75 km away from the grid

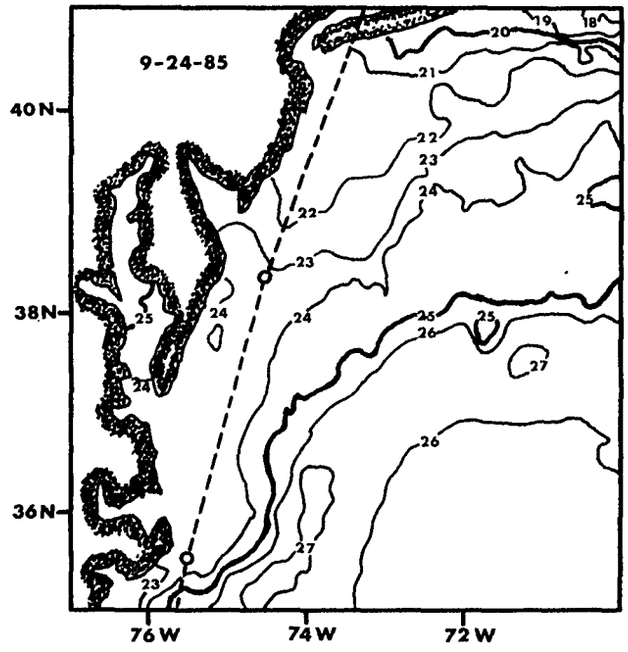

Figure 4. Satellite-derived, 14 km grid, sea surface temperature (SST) analysis for the Middle Atlantic Bight, based on multi-channel data for September 24, 1985.

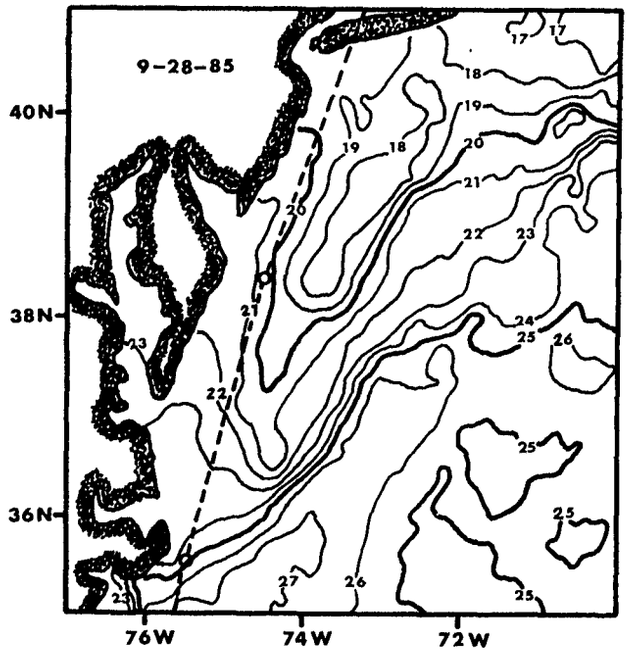

Figure 5. Satellite-derived, 14 km grid, sea surface temperature (SST) analysis for the Middle Atlantic Bight, based on multi-channel data for September 28, 1985.

point to 918.3 for an observation closer than 4.6 km. A weighted average SST is then calculated by using all observations within the search area.

To complete the analysis procedure, the grid point temperature calculated in the previous analysis is replaced by a weighted average of this old grid point temperature and the weighted average of the new MCSST observations. If the sum of the weights of the new observations is greater than the weight of the old grid point temperature, the old grid point temperature is given a weight of zero. If no new observations occur within the search area, the old grid point temperature is retained and its weight is halved. Recent comparisons (Strong, 1986, personal communication) indicate that when satellite observations are available to update the field, RMS differences between buoy temperatures and the nearest analyzed field grid point temperatures have the same 0.5°C to 0.7°C range as do the direct matches between individual satellite observations and buoy temperatures.

4. SURFACE TEMPERATURE EFFECTS

Patterns of SST as derived from satellite data prior to Gloria's passage through the Middle Atlantic Bight are shown for the region between North Carolina and Long Island in Fig. 4. The warm surface manifestation of the Gulf Stream can be seen east of Cape Hatteras as 27°C water located at approximately 36°N, 74°W. Surface thermal gradients north of the Gulf Stream are not notably strong; however, the temperatures decrease steadily to the north, reaching a minimum of 20°C just to the south of Long Island.

The hurricane's passage significantly altered the surface temperature patterns, which can be seen by comparing the SST patterns after Gloria's passage (Fig. 5) with those before (Fig. 4). An elongated pool of relatively cool, 18°C water appears east of Gloria's central track, in the region of maximum winds associated with the northeast quadrant of the storm. In a strip parallel to and 50 km to 100 km east of Gloria's central track, the surface temperature decreased by as much as 4°C. A comparison of the analyzed SST field (Fig. 5) with the observed coastal buoy temperatures (Fig. 3) shows reasonable agreement (i.e., differences of approximately 0.5°C) which suggests that the cold tongue and strong thermal gradients are real features induced by the passage of hurricane Gloria and not artifices of the MCSST retrieval algorithms or the analysis procedures. Further supporting evidence may be found in the few available expendable bathythermograph (XBT) profiles taken in this region before and after Gloria. These data (not shown) not only show a 3°C decrease in SST, but also suggest that the entire water column from the surface to about 40 m cooled by as much as 2°C.

An enhanced, infrared image of the Middle Atlantic Bight (Fig. 6) taken after hurricane Gloria moved to the north clearly shows the "cold" features which are associated with the storm. In this image, the Gulf Stream is located in the lower right quadrant. Upwelled (mixed) cool water can be seen as a bright band stretching diagonally through the center of the image. In general, this image shows the same features as the SST analysis displayed in Fig. 5. However, the resolution of the image is greater than that of the analysis, and therefore, much finer structure can be seen. Regions associated with upwelling typically exhibit the filamentous patterns evident in this image. A warm-core eddy and apparent entrainment of cool water by the Gulf Stream are other features which can be seen in the image but which are not captured in the objective analysis.

5. HISTORICAL COMPARISONS

The surface temperature pattern which became evident after Gloria's passage is not substantially different from that seen during Octobers of previous years. Figure 7 shows time series of sea surface temperature at one location (39.5°N, 73.0°W) in 1983, 1984, and 1985, as derived from objective analyses of satellite SST observations. From September 24 to October 24, the temperature decreased 3°C in 1983 and 5°C in 1984. Both changes are comparable to the 4°C decrease evident on September 27, 1985. Of course, in previous years, the temperature decrease was spread out over a much longer period.

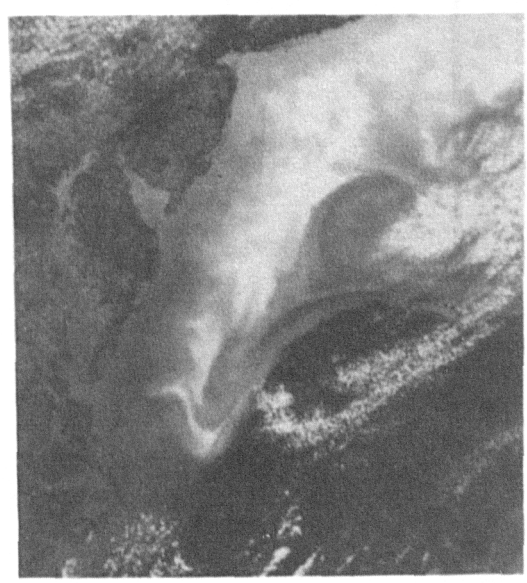

Figure 6. NOAA-9 satellite infrared image after the passage of hurricane Gloria (September 28, 1985). The image depicts temperature as grey shades with the warmest regions shown in black and the coldest in white. The area of coverage extends from Cape Hatteras to Long Island.

Studies of other hurricanes show surface temperature effects similar to those observed during the passage of hurricane Gloria. Leipper (1967) found a 1°C to 5°C decrease in SST in the Gulf of Mexico due to upwelling and mixing after hurricane Hilda in 1964. Bates and Smith (1985) found a 1°C to 3°C decrease in SST to the right of the storm track in the Gulf of Mexico with the passage of hurricane Alicia in 1983. Our results are further corroborated by Stramma and Cornillon (1986, in press) who studied 13 hurricanes in the western North Atlantic between 1981 and 1984, and found maximum cooling (up to 3.5°C) well to the right of the storm track (approximately 70 km).

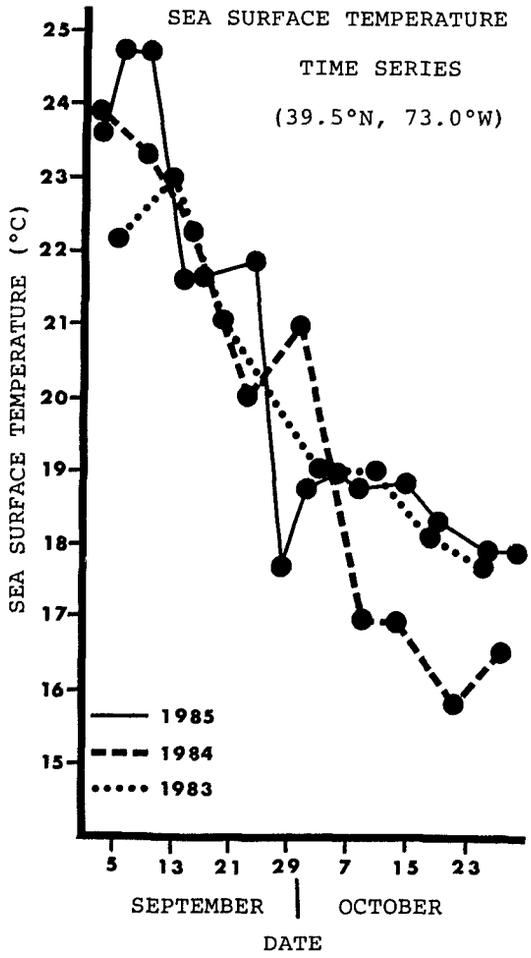

Figure 7. Time series of sea surface temperature (SST) at 39.5°N, 73.0°W during September and October 1983, 1984, and 1985. Data were obtained from 14 km analyzed fields of MCSST observations.

6. CONCLUSIONS

Operational SST analyses, which use satellite data, are now of sufficient accuracy and resolution that they can be used to monitor the detailed effects of a hurricane passage on sea surface temperature patterns. In the wake of hurricane Gloria, it is probable that significant upwelling and mixing cooled surface waters by as much as 4°C. The maximum cooling occurred 50 km to 100 km to the east of the track, associated with the maximum surface winds in the northeast quadrant of the storm. These surface temperature effects are readily observable in infrared satellite images and in 14 km analyses of satellite-derived multi-channel SST observations.

7. ACKNOWLEDGMENT

The authors would like to thank Krishna Tadepalli for his assistance in preaparing the satellite images.

8. REFERENCES

Bates, J.J., and W.L. Smith, 1985: Sea Surface Temperature; Observations from Geostationary Satellites. J. Geophys. Res., 90, 11609-11618.

Botzum, J.R., and D. Garner, 1985: Weather and Climate Report, Vol. 8, Washington, D.C.

Lawrence, M.B., 1985: Preliminary Report: Hurricane Gloria, 16-27 September 1985. Internal report, National Hurricane Center, NWS, NOAA Coral Gables, Florida, 12 pp.

Leipper, D.F., 1967: Observed Ocean Conditions and Hurricane Hilda, 1964. J. Atmos. Sci., 24, 182-196.

McClain, E.P., 1981: Multiple Atmospheric Window Techniques for Satellite Derived Sea Surface Temperatures. Oceanography from Space, Plenum, 73-85.

McClain, E.P., W.G. Pichel, and C.C. Walton, 1985: Comparative Performance of AVHRR-Based Multichannel Sea Surface Temperatures. J. Geophys. Res., 90, 11587-11601.

Schwalb, A., 1979: The Tiros-N/NOAA A-G Satellite Series. U. S. Dep. Commer., NOAA Tech. Memo. NESS-95.

Schwalb, A., 1982: Modified Version of the TIROS-N/NOAA A-G Satellite Series (NOAA E-J) Advanced TIROS-N (ATN). U.S. Dep. Commer., NOAA Tech. Memo. NESS-116.

Stramma, L., and P. Cornillon, 1986: Satellite Observations of Sea Surface Cooling by Hurricanes. J. Geophys. Res., in press.

Strong, A.E., and E.P. McClain, 1984: Improved Ocean Surface Temperatures from Space - Comparison with Drifting Buoys. Bull. Amer. Meteorol. Soc., 65, 138-142.

GLOBAL RADIATION ESTIMATION: A COMPARISON BETWEEN SATELLITE AND CONVENTIONAL METHODS

Elisabete Caria Moraes
Fausto Carlos de Almeida

Instituto de Pesquisas Espaciais - INPE
São Paulo, Brazil

1. INTRODUCTION

The need to substitute and supplement the not-so-good conventional global radiation network around the world has motivated several researchers to look to satellites as a new operational tool for global radiation measurements. For Brazil, due to its large territory, satellite methodologies seem the most appropriate, both economically and logistically.

To test the satellite methodology, we set up a specific field test experiment, where global, direct and diffuse radiation were all gathered in three different wavelength bandpasses, using conventional filters on an Eppley pyranometer. The data presented in this study were gathered from April 27 to May 09, 1985 in São José dos Campos, São Paulo, Brazil (Lat 23°14'S; Long 45°51'W; Alt 644m), using automatic data sampling and storage equipment. The data recorded on diskettes including pressure measurements, were checked and calibrated, according to the instruments' constants and amplifier gains. A bench test was performed to intercalibrate the radiometric instruments. Other observations such as temperature, dew-point, wind direction, cloud cover, and the existence of particulate matter, were manually logged. To complete the data base, visible channel GOES images were digitally received and recorded on magnetic tape.

Three different model categories are used in this comparison. The so-called "semi-direct" model, category based on sunshine hours (e.g., Ångström, 1924; Bennett, 1964); the "indirect-conventional" model, based on conventional, no-radiation meteorological surface observations (e.g., Brooks, 1959; Archer, 1964; Schulze, 1976); and the satellite model (e.g., Gautier et al, 1980).

The referenced models will be used in this paper. They were chosen for the study based on their representativeness for each model category defined, always keeping in mind a possible operational use. Other models could have been tested, but the idea was to set up and compare, results from conventional and satellite methodologies, to measure global solar incident radiation.

2. INSTANTANEOUS OBSERVATIONS

Intercomparisons among instantaneous pyranometer observations, and the model category results are shown in Figure 1a and b.

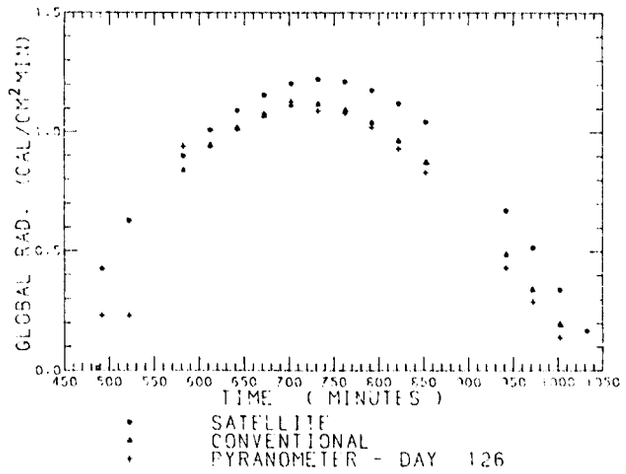

(a)

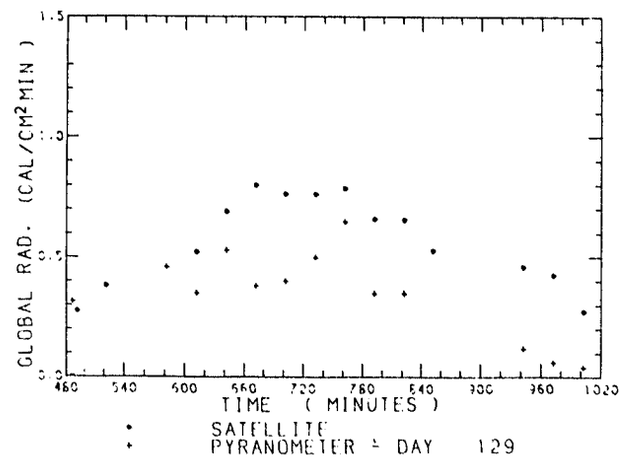

(b)

Fig. 1. Instantaneous observation. (a) clear sky during all day, (b) cloud cover during all day.

Figure 1a shows a typical result for clear skies. The so called "indirect-conventional" model, used by Brooks (1959) for the direct radiation component and Archer (1964) for the diffuse component of the global radiation, correlates well with the pyranometer observations (r=0.98). Note that this good agreement depends upon the adjustment of the dust parameter on Brooks' (1959) direct radiation model. In our case, the adjustment resulted in a value of 6.1, which differs from Schulze's (1976) suggested maximum of 3.0. The larger error (about 50%) for the diffuse component model does not add significantly to the actual global radiation result, due to its small contribution (15%).

The satellite model overestimates the pyranometer observations, with larger errors for days with variable cloud cover (Figure 1b). The probable cause of this overestimation is the distinct cloud coverage existent in the sun-pyranometer and the satellite-pyranometer paths. Also, the morning/afternoon error differences presented for both conventional and satellite models, in all cases studied (Figure 1a) are a result of the rise of aerosol concentration during the day, due to the heavy industrial activity in the region. Both models work with fixed scattering parameterizations.

We found, as Taylor and Stowe (1984) also verified, that for angles larger then 60 degrees, satellite estimates should not to be used.

Note that in comparing satellite estimates to surface pyranometer observations, a wavelength bandpass conversion has to be performed, i.e., while the visible channel of the GOES satellite "sees" the 0.55 to 0.75μm window, the shortwave pyranometer observation sees a much wider window (0.28 to 2.8μm).

A top-of-the-atmosphere (no absorption or scatter) bandpass conversion had to be assumed for the data used in this study, due to problems in the data acquisition system. This conversion tends to overestimate the satellite results, due to absorption and scattering outside the visible channel, which affects the pyranometer data, but is not incorporated in the broadband simulated satellite estimation. Also note that in Figure 1b (julian day 129) results for the conventional model are not shown because Brooks' (1959) direct component model is only valid for clear skies.

3. INTEGRATED DAILY OBSERVATIONS

Table 1 shows results of applying the Bennett (1964) model to our data. Except for days 118 and 120, which were variable cloudy days with clear skies near noon, the errors varied from +0.42 to -8.90. Our analysis suggests that this model for daily radiation can be much improved, if hourly weights are used.

Table 2 presents results showing small errors of the indirect-conventional model (Brooks, 1959; Archer, 1964). As previously mentioned, these results are heavily dependent on the dust parameter adjustment of the Brooks' (1959) direct-component model.

Table 1

Semi-direct model, daily totals of global solar radiation (experiment of April-May/85)

Julian Day	Semi-direct ($cal\ cm^{-2}\ dia^{-1}$)	Pyranometer ($cal\ cm^{-2}\ dia^{-1}$)	Relative error (SD-P)/P %
118	350.51	218.71	+60.26
119	327.56	354.56	-7.62
120	252.60	191.80	+31.70
124	283.94	282.76	+0.42
125	351.73	349.40	+0.66
126	394.01	411.28	-4.20
127	394.65	401.36	-1.67
129	135.04	148.23	-8.90

Average relative error (except 118 and 120) = 3.91%
σ = 13.30

Table 2

Indirect-conventional model, solar radiation integrated daily (experiment of April-May/85)

	GLOBAL		
Julian Day	Estimated ($cal\ cm^{-2} dia^{-1}$)	Pyranometer ($cal\ cm^{-2}\ dia^{-1}$)	Relative error (E-P)/P
114	364.22	375.99	-3.13
117	139.20	148.38	-6.18
118	145.21	145.92	-0.48
119	163.45	168.21	-2.83
124	234.43	253.92	-7.68
125	212.83	209.70	1.49
126	385.45	381.27	1.10
127	370.45	372.24	-0.48
128	223.93	220.53	1.54

Average relative error = 2.77%
σ = 6.54

Table 3 presents results of the satellite model, for zenith angles smaller than 60 degrees. For clear skies or thin cirrus cover (day 118, 126, 127 and 128), the average relative error was less than 14%. For the other cases, where variable cloud cover existed, the error increased to about 35%. Again, the need to take into consideration the possible differences in sky conditions for individual satellite-pyranometer (reflected) and sun-pyranometer (incident) paths, is made clear.

By comparison, for an independent set of data, gathered in Balboa, Panama (Klein and Goldberg, 1978) during April-May, 1976, the error in assuming top-of-the-atmosphere conversion values, when comparing satellite and surface pyranometer observations, was about 5%.

Table 4 shows the relative errors for the satellite estimates versus pyranometer observations, applying this 5% correction, for situations of clear skies (afternoon of day 125, day 126 from 10 am up and morning of day 127). In order to check the trend of the error, Table 4 also shows results for corrections applied to the direct reflection coefficient of the satellite model. We have tested some values of

the coefficient which we feel represent continental regions better than the ones determined for oceanic regions by Paltridge (1973). Each correction indicates, by itself, smaller errors in the global radiation estimation than by satellite methods.

Table 3

Global solar radiation in the band of the satellite excluding $\theta > 60^{o}$

Julian Day	Satellite Model (cal cm^{-2} dia^{-1})	Pyranometer (cal cm^{-2} dia^{-1})	Relative Error (S-P)/P %
118	23.455	20.745	13.06
119**	71.319	59.955	18.95
120*	5.775	4.161	38.79
124**	67.215	52.227	28.70
125**	66.740	48.075	38.82
126	76.676	67.410	13.75
127	75.015	66.675	12.51
128	42.013	36.345	15.60
129*	36.556	24.720	47.88

* Situation with cloud cover during day

** Period with cloud cover

Table 4

Daily totals for situation of clear sky obtained by the analysis with the satellite model (with and without modifications)

Julian Day	Relative error of the analysis		
	Original (%)	With modification 5% in the pyranometer observation (%)	With modification in the parameter (direct reflection coefficient ($\alpha \propto 0.03$)) (%)
125	18.29	12.66	14.11
126	18.76	13.11	15.03
127	11.36	6.06	7.46

Figure 2 illustrates an intercomparison of the three estimators, against the pyranometer observations. Note that the indirect-conventional model offers the best results, surely due to the dust factor adjustment. The satellite model overestimates the results by about 14%, and the semi-direct (sunshine type) model is not consistent from day to day.

A more complete discussion can be found in Moraes and Almeida (1986) and Moraes (1986).

4. CONCLUSIONS

Considering the model categories tested, the semi-direct model was shown to be the least desirable of the three models, although it is widely used in meteorology, agriculture and related areas.

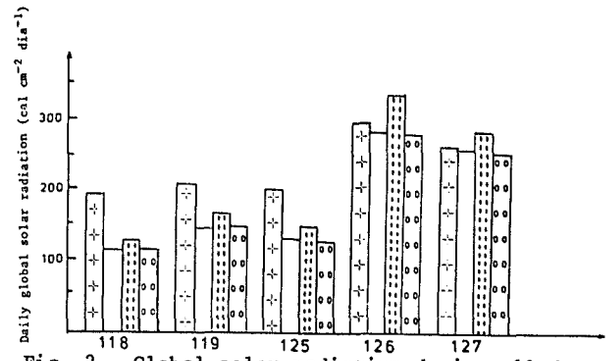

Fig. 2. Global solar radiation during all day (partial areas).

- semi-direct model
- indirect conventional model
- satellite model
- direct model

The indirect-conventional model showed the best result, due to the adjustment of the dust parameter to the data base used. One of the problems in using this methodology to estimate global solar radiation reaching the ground, is its validity for only clear skies, and its dependence on obtaining pressure, precipitable water and "dust" concentration on a routine basis.

Aerosol concentration and gases are the most important factors defining radiation variability, for clear skies. This variability during the day is evident in the instantaneous estimations obtained with the satellite methodology (Figure 1) where it clearly shows a larger attenuation in the afternoon. It is also interesting to recall that the dust factor adjustment has shown consistently larger values for the afternoon compared to the morning hours.

When using satellites to infer global solar radiation reaching the ground, the estimations should involve zenith angles less than 60 degrees.

The data analyzed in our study have shown that the most efficient manner to estimate global solar radiation, either instantaneous or integrated daily values, is through the use of satellites. Data from geostationary satellites offer good spatial and temporal resolution and together with the available models work for clear as well as cloudy skies.

A better understanding of radiation-cloud interaction processes in the atmosphere, together with the acquisition and integration of a good data base, where digital images and spectral radiation measurements are simultaneously obtained, will certainly consolidate the use of satellites as a radiation monitoring "network" worldwide.

This study will continue extending its coverage to other regions, seasons and time spans, trying to test integrated monthly data.

Studies of this type can also help to develop remote sensing techniques to ascertain pollution concentration trends and surface instrumentation calibration.

5. REFERENCES

ÅNGSTRÖM, A.K. Solar and atmospheric radiation. *Quart. J. Roy. Met. Soc.*, 50:121, 1924.

BENNETT, I. Monthly maps of mean daily insolation for the United States. *Sol. Energy*, 9(3):145-152, 1965.

BROOKS, F.A. An introduction to physical microclimatology. Davis, University of California, 1959.

GAUTIER, C.; DIAK, C.R.; MASSE, S. A simple physical model to estimate incident solar radiation at the surface from GOES satellite data. *J. Appl. Met.* 19(8):1005-1012, 1980.

KLEIN, W.H.; GOLDBERG, B. Solar radiation measurements/1976-1977. Smithsonian radiation biology Laboratory, Rockville, MD, 1978.

MORAES, E.C. Comparação entre métodos de estimativa da radiação solar: satélite e convencional. Unpublished. Ms. Thesis, Instituto de Pesquisas Espaciais, 1986.

MORAES, E.C.; ALMEIDA, F.C. Estimativa da radiação solar (satélite e convencional) para abril e maio de 1986. In press, Instituto de Pesquisas Espaciais, 1986.

PALTRIDGE, G.W. Direct measurement of water vapor absorption of solar radiation in the free atmosphere. *J. Atm. Sciences*, 30(1): 156-160, 1973.

SCHULZE, R.E. A physically based method of estimating the total solar radiation from suncards. *Agric. Met.*, 16(2):85-101, 1976.

TAYLOR, V.R.; STOWE, L.L. Reflectance characteristics of uniform earth and cloud surfaces derived from NIMBUS-7 ERB. *J. Geop. Research*, 89(D4):4987-4996, 1984.

P4.23

HAIL SIZE DIAGNOSIS FROM HRPT DATA

J.M. Bullas

Special Projects Office
AES Western Region
Edmonton, Alberta

INTRODUCTION

Research into relationships between satellite data and severe weather has been ongoing for many years. It is known that a correlation exists between thunderstorm height as measured by radar, the tropopause and hail occurrence (Donaldson, 1960 and Bonner and Kemplar, 1971). Reynolds (1979) found a relationship between the occurrence of large hail and cloud tops colder than the tropopause, using GOES data. Several researchers, including Adler (1985) have investigated the structure of severe storms using GOES and NOAA HRPT imagery data.

An HRPT ground receiving station is operated by AES, Western Region, which results in the full AVHRR dataset being available in 1 km horizontal resolution. A routine was written to calibrate the 11 u (Band 4) thermal data into temperature and extract and contour cloud-top temperatures.

This data was correlated with actual hail data from the Alberta Hail Project in an effort to find an operationally useful warning mechanism for hail occurrence from the HRPT data. This paper will describe the results.

THUNDERSTORM - TOP TEMPERATURES

The methodology of calibrating Band 4 (11 u) imagery into temperature is well known (Lauritson, 1979) and will not be discussed here, except to say that no moisture absorption correction was attempted, as thunderstorm tops are well above the significant moisture layers. The procedure for locating tops bears mention.

The imagery data was sectorized and radiance data extracted on a "coarse" grid (25Km spacing) by the nearest-neighbor technique. The highest radiance values (lowest temperatures) below -40°C. were located. A fine-mesh grid (2Km spacing) was centered on the coldest radiance values and the coldest temperature value was extracted and located from the raw data. The data was also contoured (Fig 1), and cold cores were confirmed visually. The fine-mesh grid was moved to other cold cores and the procedure repeated. In most cases, the cold cores were restricted to the upwind side of the storm although other cold cores were accepted in complex and merging storms. In this way, temperature data was extracted only from active updraft areas.

The cases were pre-selected by scanning AVHRR imagery for thunderstorms with identifiable updraft areas.

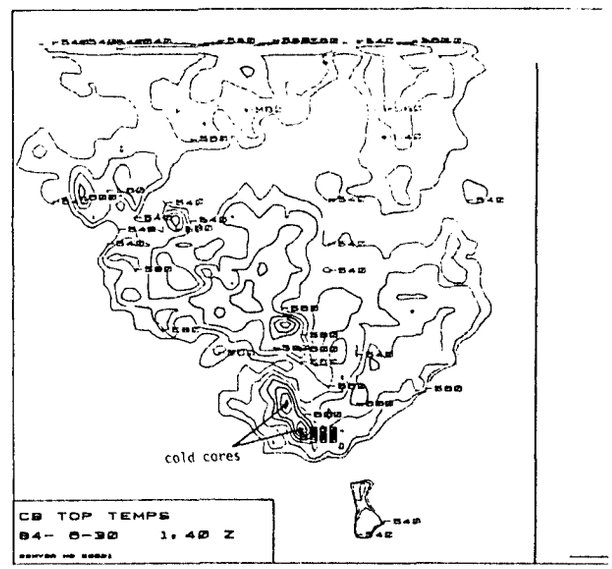

FIG. 1 Example of contoured thunderstorm - top temperature output.

HAIL DATA

In general, data on hail occurrence and especially hail size is difficult to obtain. Fortunately a network of volunteer observers is maintained by the Alberta Hail Project as part of their summer field program. Fig 2 shows the network. In addition, data collected from the Alberta Weather Centre as part of their severe weather program was used. This data was obtained primarily from weather watcher calls, newspaper accounts, surface weather observations and the climate observation network.

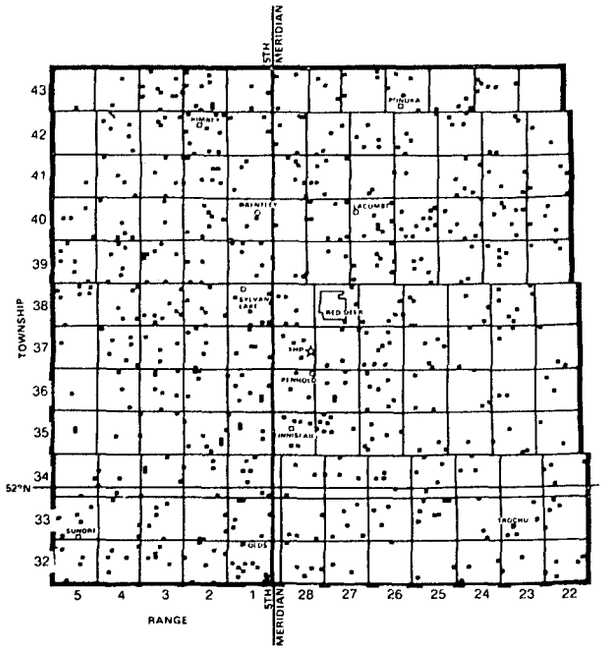

FIG. 2 The Alberta Hail Project collection network. Reprinted with permission. (Alberta Research Council, 1984)

In mapping the hail data to the particular updrafts from which the cloud-top temperatures were extracted, a number of uncertainties had to be overcome:

i) Hailswath time

The data collected was not time-tagged. Although it is possible that two or more thunderstorms might pass over a given location in the course of an afternoon/evening, it was assumed that any hail reported was associated with the thunderstorm observed at analysis time at that location.

ii) Errors in navigation of AVHRR data

These errors were of the order 5 - 10 km.

iii) Hailswath location

It was assumed that hailswaths were located close to the active updraft regions, but could occur on any flank. This led to an uncertainty in position of the order 5 - 10 km on the average. This uncertainty when combined with ii) above led to a potential location error of 10 - 20 km. Therefore, any hailswath within 20 km of the location of a cold core was assumed to be the correct one. (For operational purposes this would be sufficiently precise for a warning).

iv) Hail size distribution

In a given hailswath, a range of sizes is often reported. In addition, the hail being supported by a given updraft can remain in the storm for some time and be deposited downstream of the cold core. Therefore, the following algorithm was used to determine "reported" hail size:

Isolated Report - Size reported used

Range of sizes - Maximum size reported within 30 km of cold-core location was used if more than one report of that size was received; otherwise the average of that report and the next largest size reported was used. (This was done to reduce overestimation of size due to one possibly exaggerated report).

HAIL SIZE AND TEMPERATURE GRADIENT

Problems were encountered in defining a representative gradient, as the gradient was found to be highly variable around a cold core (Fig 3). Therefore, no correlations were attempted.

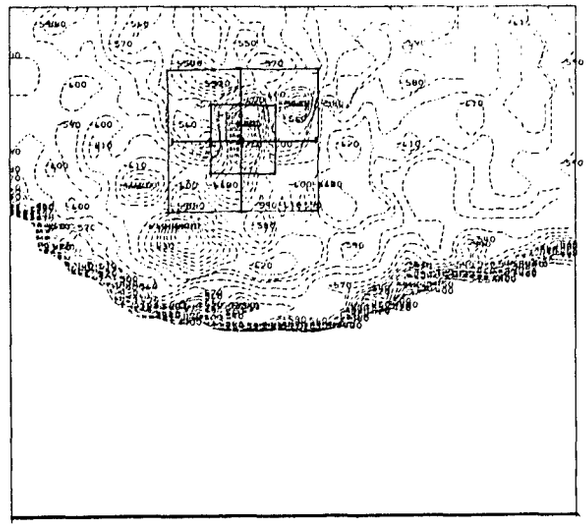

FIG. 3 Temperature structure of the upwind side of a storm. The grid boxes are centered on a cold core. The gradient calculated is highly dependent on grid length and direction.

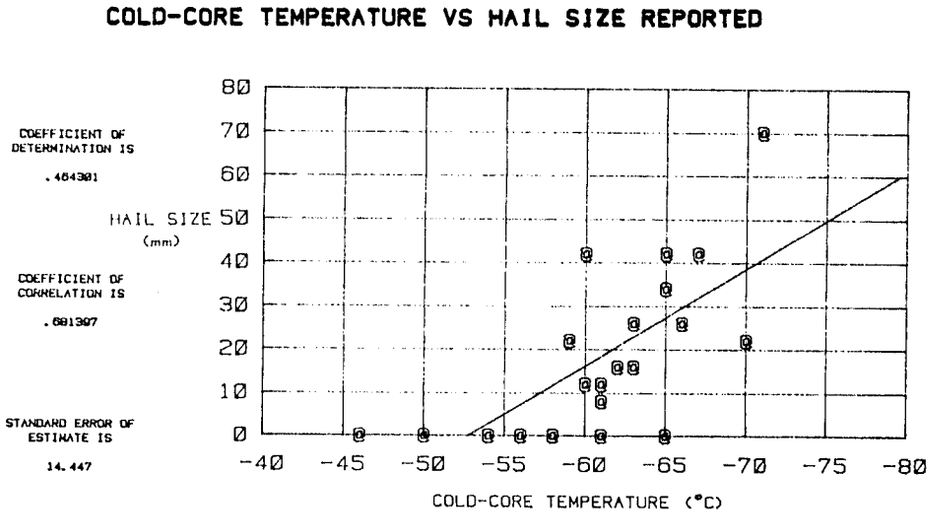

FIG. 4 Plot of reported hail size vs the minimum temperature of the cold core.

HAIL SIZE AND COLD-CORE TEMPERATURE

Fig 4 shows the relationship between reported hail size and cold core temperature. The correlation coefficient is .68, with a standard error of estimate of 14.5 mm.

The fact that the correlation is not especially good is not surprising, as there is no unique relationship between cloud top temperature and updraft energy due to variables such as tropopause height and the thermal structure of the troposphere. This is illustrated in Fig 5

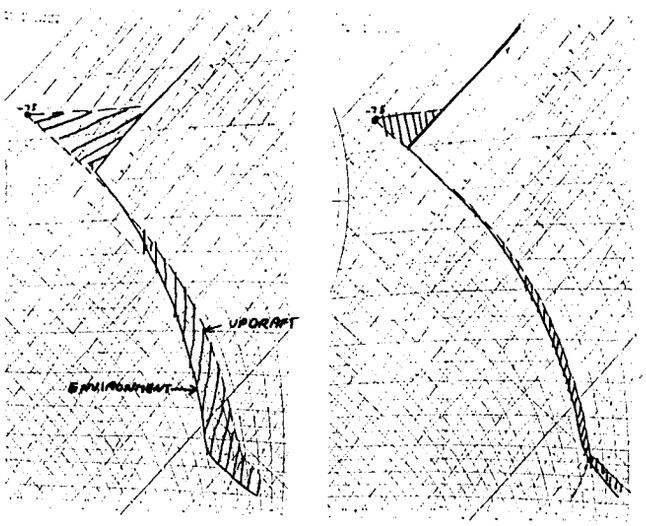

FIG. 5 Two storm updraft curves, energy balanced, with -75°C tops. The storm on the left has a much higher updraft energy.

with the aid of a tephigram. Depending on the value of the parcel wet-bulb potential temperature, and the tropopause height, there are an unlimited number of updraft energy curves which can result in a particular updraft equilibrium temperature.

From the graph (Fig 4), however, it was noted that hail was reported in 16 out of 18 cases of thunderstorm - top - temperatures equal to or colder than -60°C. On the other hand, hail was reported in only 1 out of 6 cases where the thunderstorm - top - temperature was warmer than -60°C. (Climatologically, the tropopause temperature in Alberta in the summer months is above -60°C. Therefore storms with cold cores below -60°C are usually penetrating the tropopause and therefore have an appreciable updraft velocity.)

These statistics suggest a possible cold-core temperature threshold for hail occurrence in Alberta.

HAIL SIZE AND TROPOPAUSE PENETRATION

Fig 6 shows the relationship found between hail size and tropopause penetration. Tropopause penetration is defined in terms of T (trop) - T (cloud).

where T (Trop) - Tropopause Temperature
T (Cloud) - Thunderstorm-Top Temperature (cold cores)

TROPOPAUSE PENETRATION vs HAIL SIZE REPORTED

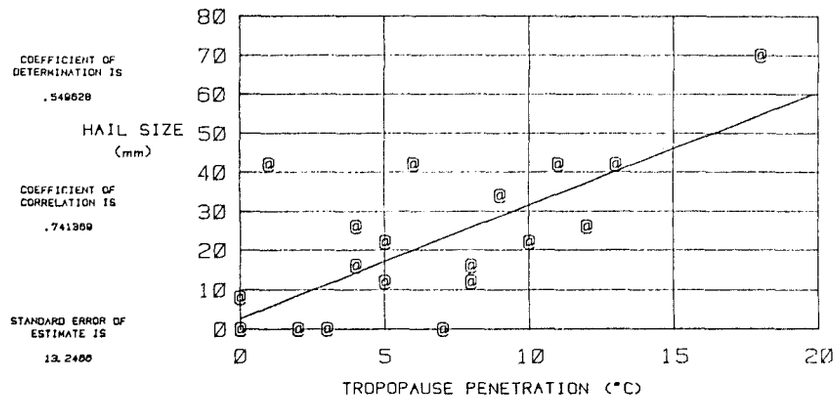

FIG. 6 Plot of reported hail size vs the tropopause penetration (^{o}C).

When the temperature of the tropopause is taken into account in this way, a better correlation to hail size is observed but the stratification between hail/no hail is removed. Large hail occurred at almost any value of penetration but tended to occur with higher values of T(trop) - T(cloud).

One possible explanation of the variance observed lies in the structure of the upper atmosphere and the way the updraft energy is distributed vertically in the storm. Fig. 7 shows updraft curves with the same updraft penetration but different updraft energy. Tropopause penetration does not, therefore, give a true indication of updraft velocity at equilibrium.

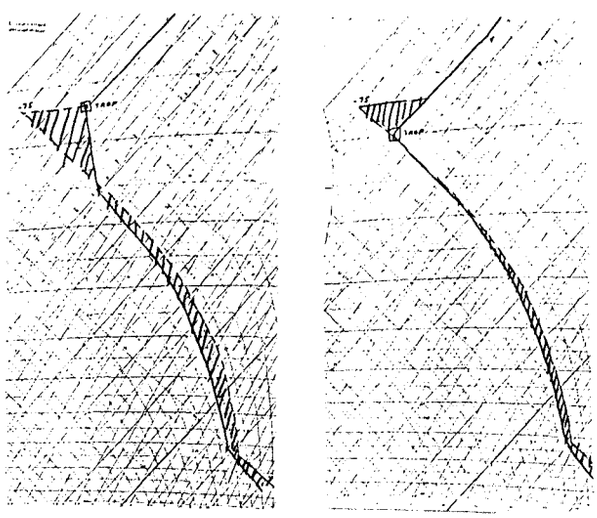

FIG. 7 Two updraft curves with equal tropopause penetration (^{o}C). The storm on the left has much higher updraft energy. This energy is converted to potential energy below the tropopause due to the warm layer just below the stratosphere.

A second possible explanation for the variance lies in the energy distribution in the storm itself. When latent heat is released below the hail growth region of a storm, a greater updraft velocity will exist at that level, than in storms where an equivalent amount of energy is released above it. Therefore, the temperature structure of the lower troposphere is also important. Fig. 8 illustrates this relationship.

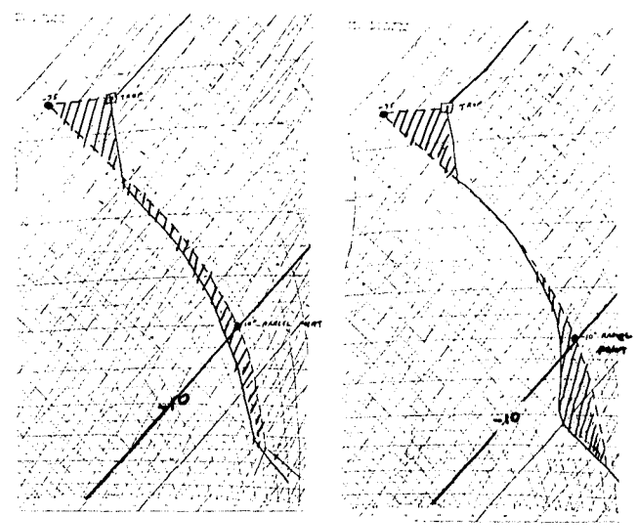

FIG 8 Two storms having the same tropopause penetration (^{o}C), and the same overall total latent heat release. The storm on the right should have a higher updraft velocity at -10°C parcel temperature (Hail growth region).
REF. Foster and Bates (1976)

DIAGNOSED HAIL SIZE

In an effort to eliminate uncertainies in diagnosis and obtain a better correlation, a simple parcel model was employed to take into account the variation in tropospheric structure. Using the nearest radiosonde observation (in time and space), an updraft curve (theta W) was found by iteration which resulted in the observed cold-core top temperature when latent heat release was equated to potential energy at the top of the storm (energy-balance). No entrainment or dissipation terms were considered, as these terms were to be eliminated statistically, and not explictly. This procedure resulted in a unique solution of updraft velocity for the energy and buoyancy distribution. Given the updraft curve, the method of Foster and Bates (1956) was used to derive the hail size which could be supported by the given updraft. This was given the term "Diagnosed Size".

The relationship of Diagnosed Hail Size to actual hail size reported is shown in Fig 9.

The diagnosed hail size is smaller than reported size, possibly due to turbulent energy dissipation in the upper troposphere. This results in lower updraft velocities at equilibrium, and a higher value of cold-core temperature than a simple parcel model would predict. Mixing of the cold cores in the stratosphere with warm stratospheric air is also a possibility (Roach, 1967).

Potential sources of dispersion in the distribution would be:

(i) Representativeness of radiosonde data.

The upper-air data network in Alberta is relatively sparse, and the sampling frequency is 12-hourly. A nearest- neighbour technique would not, therefore, necessarily give representative environmental data. A space-and-time interpolation technique might be better.

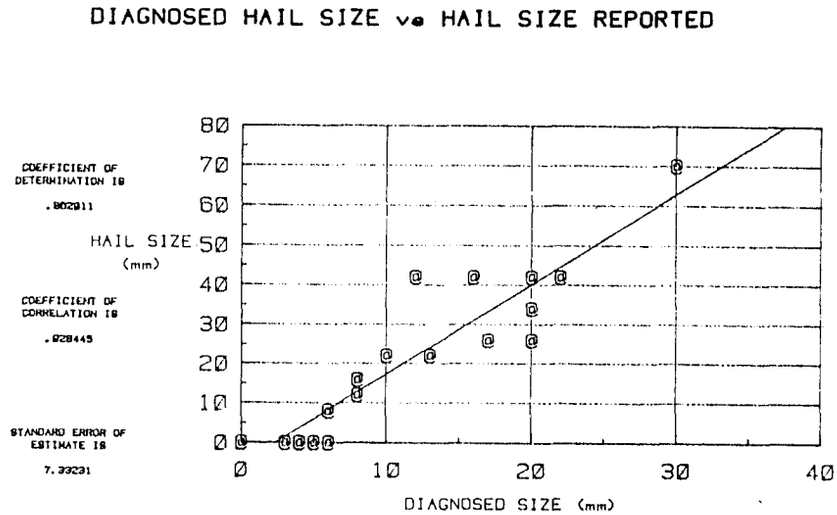

FIG. 9 Plot of reported hail size vs hail size diagnosed by the algorithm.

The coefficient of correlation is .93, the co-efficieint of determination is .86, and the standard error of estimate is 7.33 mm.

In all of the cases where the algorithm diagnosed a "0" hail size, the size reported was less than 6mm. In all cases of large hail diagnosis (>15 mm), large hail occurred.

The least squares linear regression equation (prediction equation) yields:

Hail size = 2.274 Diagnosed size - 5.345

ii) Errors in mapping hail reported to updrafts

The algorithm used to reduce uncertainty in mapping hail size reported to updrafts is not rigorous or all- inclusive.

iii) Entrainment and Energy Dissipation

These effects may not be linear with respect to updraft velocity.

(iv) Sampling frequency

At the time of observation, the cold cores may have been expanding (rising) or collapsing (sinking). This would potentially give rise to random sampling errors in cold-core temperatures relative to updraft velocity.

FUTURE WORK

At the time of writing, the diagnosis routine was being fully computerized. A test of the prediction equation is planned for the summer of 1986 using independent data in near-real time.

SUMMARY AND CONCLUSIONS

A good correlation was found between predicted hail size by the model used and actual reports. Correlations with cloud-top temperature per se and tropopause penetration were not as good, although a potentially useful threshold of -60 C was suggested from the cloud-top Temperature/Hail Size plot.

ACKNOWLEDGEMENTS

The author would like to thank Mr. W. Wilkie of the Alberta Hail Project (Alberta Research Council) for the invaluable hail data. An acknowledgement is also owed to Mr. C. Schneider who developed the computer programs and extracted data while working in the department as a summer student.

REFERENCES

Adler, R.F., and M.J. Markus, 1985: Objective detection of severe thunderstorms using GOES IR observations. Preprints, 14th Conference on Severe Local Storms.

Alberta Research Council, 1984: Alberta Hail Project Field Program-1984. Alberta Research Council, Natural Resources Division.

Bonner, W.D. and S.E. Kemplar, 1971: Broadscale relations between radar and severe weather reports. Preprint, 7th Conference on Severe Local Storms, AMS, pp 140-147.

Donaldson, R.J., 1960: Radar method for identification of severe thunderstorms. Preprint, Conference On Severe Local Storms, AMS, 28 pp.

Foster, D.S. and F.C. Bates, 1956: A hail forecasting technique B.A.M.S., Vol. 37, No. 4.

Lauritson, L., G.J. Nelson and F.W. Porto, 1979: Data extraction and calibration of TIROS-N/NOAA radiometers, NOAA Technical Memorandum NESS 107.

Reynolds, D. W., 1979: Observations and detection of damaging hailstorms from geosynchronous satellite digital data. Preprints, 11th Conference on Severe Local Storms, AMS, 181 pp.

Roach, 1967: On the nature of the summit areas of severe storms in Oklahoma. Quart. J. Roy. Meteor. Soc., 93, 318-336.

OPERATIONAL ESTIMATIONS OF HAIL DIAMETER FROM VAS-DERIVED VERTICAL SOUNDING DATA

Preston W. Leftwich, Jr.

National Severe Storms Forecast Center
National Weather Service, NOAA
Kansas City, Missouri 64106

1. INTRODUCTION

Severe local storm watches are issued by the National Severe Storms Forecast Center (NSSFC) located in Kansas City, Missouri. A tornado or severe thunderstorm watch describes an area that will be threatened by these storms during its valid period. With the exception of watches issued in conjunction with tropical cyclones, each message will contain an estimate of the diameter of the largest hailstones expected to form in the watch area during the valid period. An example of an abbreviated severe local storm watch message, designed for rapid dissemination, is shown in Figure 1.

In the past, several objective techniques were devised to estimate hail size from vertical sounding data. As far back as 1953, Fawbush and Miller developed a nomogram that related the dimensions of "positive area" to hailstone size. This work was later revised by Miller (1975). Foster and Bates (1956) took a more physical approach by equating the terminal velocity of a falling hailstone to the vertical velocity of a rising parcel derived from buoyancy. Prosser and Foster (1966) outlined a sounding analysis procedure designed for an electronic computer. This procedure, which included a hail size estimate obtained via the Foster and Bates method, was used routinely for several years at the NSSFC with rowinsonde data at 0000 and 1200 GMT. However, Doswell et al. (1982) documented that this procedure exihibited little skill in distinguishing a "small hail" from a "large hail" environment, and it rarely predicted a hail potential larger than one inch. Lack of routine success of such a technique was mainly attributed to the often unrepresentative nature of rawinsonde soundings that differ greatly in time and/or space from the development of thunderstorms that produce hail.

In an earlier study, Leftwich (1984) documented that useful predictive information resided in the traditional parameters extracted from rawinsonde soundings, provided data were close in space (within 100 km) and time (within 2h) of the hail event.

Although some biases have been observed in direct comparison of VISSR Atmospheric Sounder (VAS) data with conventional rawinsonde data (Jedlovec, 1984), prospects of increased time and space resolution (Uccellini et al., 1982) supported attempts to utilize these data for operational sounding analysis and estimation of hailstone size. In the current study, hail size estimates were computed via a one-dimensional model for parcel lifting from both VAS- derived vertical soundings and conventional rawinsonde soundings. The following sections describe the preliminary experiments.

2. HAIL SIZE ESTIMATION

A one-dimensional model for parcel lifting provides the basic objective procedure for hailsize estimation. This model was originally formulated for the McIdas computer system for utilization in rawinsonde sounding analysis. Recently, this model was implemented on the Centralized Storm Information System (CSIS) at the NSSFC. To begin, a parcel is assigned temperature and moisture values equal to averages from the lowest 150 mb of the sounding. Next, the Convective Condensation Level (CCL) is calculated. An initial upward velocity of 5 m/s is given to the parcel, and it is forced to its level of Free Convection, if it exists.

```
MKC AWW Ø116Ø4
WW 117 TORNADO KS MO IL  Ø117ØØZ - Ø123ØØZ
AXIS..8Ø STATUTE MILES EITHER SIDE OF LINE..
15S TOP - 15ENE STL
HAIL SURFACE AND ALOFT..3 INCHES.  WIND GUSTS..75 KNOTS.
MAX TOPS TO 52Ø. MEAN WIND VECTOR 26Ø45.
REPLACES WW  115..KS MO .
REPLACES WW  116..MO IL .
```

Fig. 1. Example of a tornado watch (short version issued by the NSSFC. Note the estimate of maximum expected hail diameter at the surface and aloft.

Table 1. Times (GMT) of VAS-derived vertical sounding data utilized in this study are denoted by an "X" for each case.

DATE	1118	1318	1418	1718
2 MAY 1984		X		
14 MAY 1984	X	X	X	X
13 JUN 1984	X	X	X	X
11 MAY 1985	X		X	
20 MAY 1985	X		X	X

The model continues to lift the saturated parcel, computing the parcel's temperature and pressure every 10 mb. Entrainment of environmental air is parameterized (Ruprecht, 1971) to be 80% in 400 mb, as a default value.

For each 10 mb layer the parcel's change in kinetic energy can be expressed (Haltiner and and Martin, 1957) by:

$$\Delta KE = R_d (\bar{T}_{vp} - \bar{T}_{ve}) \ln (p_1/p_2) \quad (1)$$

and $$w_2^2 = w_1^2 + 2 R_d (\bar{T}_{vp} - \bar{T}_{ve}) \ln (p_1/p_2) \quad (2)$$

where w_1 and w_2 are the parcel's initial (at p_1) and final (at p_2) vertical velocity, and $\bar{T}_{vp}$ and $\bar{T}_{ve}$ are the layer mean vertical temperatures for the parcel and environment, respectively.

The terminal velocity, V_T, of a spherical hailstone (Matson and Huggins, 1980) can be expressed as:

$$V_T = (4\rho_h g / 3\rho_a C_d)^{1/2} D^{1/2} \quad (3)$$

where ρ_h and ρ_a are the densities of the hail and air, respectively, g is the acceleration of gravity. C_d is a drag coefficient for hail, and D is the diameter of the hailstone. An updraft strong enough to support a hailstone assumes a balance between (2) and (3). Equating these and solving for D gives the following equation:

$$D = 3\rho_a C_d w_2 / (4\rho_h g) \quad (4)$$

Equation (4) is used to compute the hailstone diameter when the parcel acquires a temperature of -10°C. This value is the estimated hailstone size.

Establishment of an environment conducive to hail production can be a complex interaction of various scales of motion, temperature and humidity (Wilson, 1980). For these reasons, estimates of hail size from this procedure are conditional upon whatever atmospheric processes that are dominant allowing a strong thunderstorm to form. This procedure does not directly address the question of whether or not thunderstorms will form.

3. CASE STUDIES

Selection of the first five cases for this study was based mainly on the availability of archived VAS-derived (Smith, 1983) sounding data. The sounding data were provided for the times listed in Table 1 by the National Weather Service's Advanced Satellite Products Project located in Madison, Wisconsin. Rawinsonde data were compiled from archive tapes kept at the NSSFC. Reported hail sizes were found in Storm Data. Two cases, 14 May 1984 and 20 May 1985, are discussed in the following sections. Details of other cases will be included in the conference presentation.

a. 14 May 1984

As depicted in Figure 2, an east-west cold front extended across northern portions of Mississippi, Alabama, Georgia and South Carolina to the North Carolina coast at 1200 GMT on 14 May 1984. This front moved slowly southward during the day. A severe thunderstorm watch was in effect across eastern Alabama and central Georgia during the afternoon. Large hail up to 5.1 cm in diameter was reported in central Georgia during the afternoon. Locations of hail size estimates from rawinsonde and VAS soundings, along with reported hailstone sizes are plotted in Figure 2. Hail diameters corresponding to the indicated letters and numbers are listed in Table 2. VAS sounding data at 1418 and 1718 GMT produced large hail estimates in central and southern Georgia that were not indicated by 1200 GMT rawinsonde data at Appalchicola (AQQ), Waycross (AYS) or Athens (AHN). Large hail sizes were computed from 1200 GMT rawinsonde data at Centreville (CKL) and Savannah (SAV). The largest reported hailstone was 5.1 cm near Eatonton in central Georgia. Increasing hail sizes from the one-dimensional model as later VAS data were used produced a trend that would complement conventional subjective estimates based solely on atmospheric stability.

b. 20 May 1985

Hail up to the size of a tennis ball (6.4 cm in diameter) fell in southern Oklahoma during the early evening of 20 May 1985. At 1200 GMT, a quasi-stationary front lay across western Texas northward into Kansas. A wind shift line was evident across northern Texas. As small surface lows moved northeastward, the frontal position shifted eastward across Oklahoma during the day. Hail up to 4.4 cm in diameter was reported in north central Texas during the morning. A tornado watch covered parts of northern Texas and southern Oklahoma during the afternoon and evening.

Hail size estimates from rawinsonde data at 1200 GMT were just over 2.5 cm at Amarillo (AMA) and Oklahoma City (OKC), but were much lower at the stations farther south. VAS soundings gave estimated diameters of 4.8 cm near the Red River (Figure 3) at 1418 GMT and

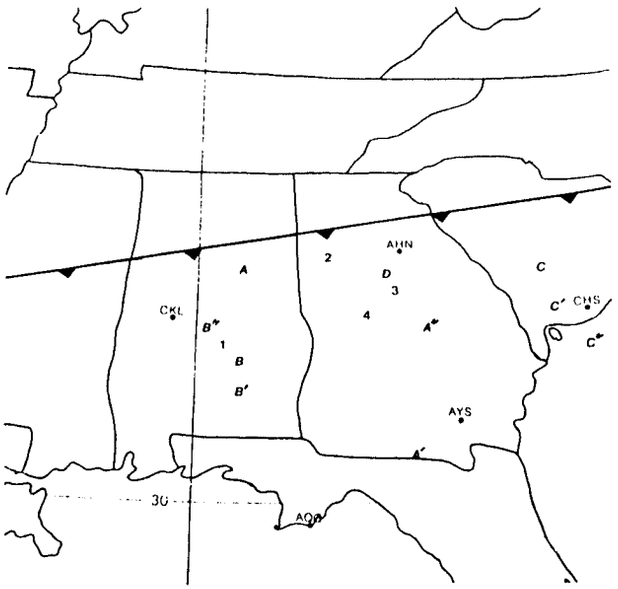

Fig. 2. Estimated and observed hail sizes for 14 May 1984. Values are listed in Table 2. Frontal position is shown for 1200 GMT.

Table 2. Data for Fig. 2.

LOCATION	SOURCE/DATE/TIME(GMT)	HAIL DIAMETER(CM)
CKL	RAOB/14/1200	7.1
AQQ	RAOB/14/1200	0.8
AYS	RAOB/14/1200	0.0
AHN	RAOB/14/1200	1.3
SAV	RAOB/14/1200	2.0
A"	VAS/14/1118	2.3
B"	VAS/14/1118	1.5
C"	VAS/14/1118	1.0
A′	VAS/14/1418	6.4
B′	VAS/14/1418	5.6
C′	VAS/14/1418	5.0
A	VAS/14/1718	6.9
B	VAS/14/1718	8.1
C	VAS/14/1718	6.6
D	VAS/14/1718	6.9
1	REPORT/14/2058	1.9
2	REPORT/14/1855	4.4
3	REPORT/14/2020	5.1
4	REPORT/14/2035	4.4

6.4 cm in southern Oklahoma at 1718 GMT. In this case, the estimates from VAS soundings were good estimates of the 6.4 cm hail stones reported in southern Oklahoma later in the day. Data for each location and time denoted in Figure 3 are listed in Table 3.

Table 4 lists estimates from both VAS and rawinsonde (RAOB) data and reported hail diameters. These are estimates that were closest in time and space and preceded the events. The capability to produce large (greater than 2.5 cm) was exhibited by the one-dimensional model with both types of data. VAS data produced an excellent estimate on 20 May 1984, but produced large overestimates on 2 May 1984 and on 14 May 1984 (near Montgomery, Alabama). In general, estimates from RAOB data were lower than observed values. the estimate from RAOB data on 11 May 1985 was very close to an observed value. Root-mean-square errors (RMSE) for these cases were 2.6 cm and 5.4 cm for VAS data and RAOB data, respectively. Better quantitative estimates will be required for proper operational utility. However, lower RMSE

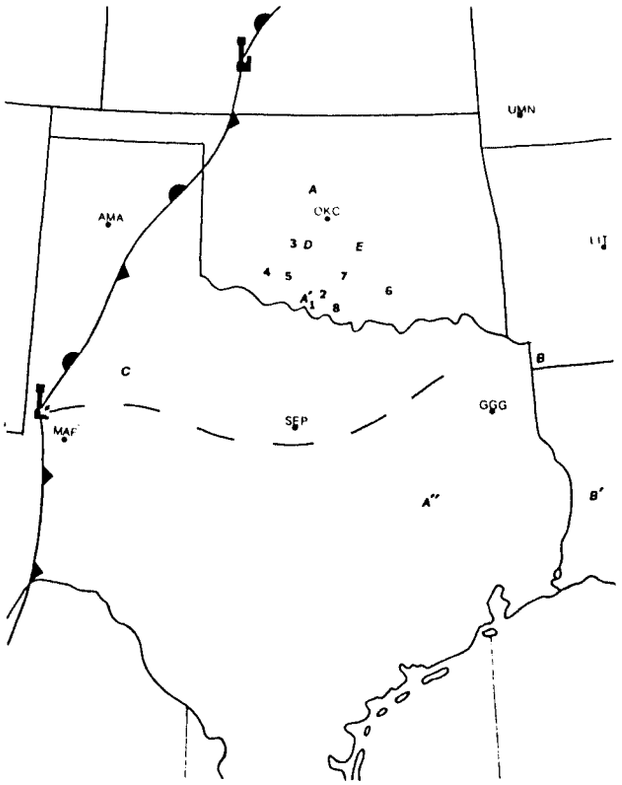

Fig. 3. Estimated and observed hail sizes for 20 May 1985. Values are listed in Table 3. Frontal position is shown for 1200 GMT.

errors than RAOB data and proper reflection of trends in hail potential encourage continued efforts with both the one-dimensional model and VAS vertical sounding data in development of an objective technique for hail size estimates.

Table 3. Data for Fig. 3.

LOCATION	SOURCE/DATE/TIME(GMT)	HAIL DIAMETER(CM)
AMA	RAOB/20/1200	3.3
OKC	RAOB/20/1200	2.8
MAF	RAOB/20/1200	0.3
SEP	RAOB/20/1200	1.5
GGG	RAOB/20/1200	1.3
LIT	RAOB/20/1200	0.3
UMN	RAOB/20/1200	1.3
AMA	RAOB/21/0000	1.3
OKC	RAOB/21/0000	3.0
MAF	RAOB/21/0000	3.6
SEP	RAOB/21/0000	7.6
GGG	RAOB/21/0000	2.5
LIT	RAOB/21/0000	0.8
UMN	RAOB/21/0000	3.3
A"	VAS/20/1118	5.1
A′	VAS/20/1418	4.8
B′	VAS/20/1418	3.0
A	VAS/20/1718	6.4
B	VAS/20/1718	4.6
C	VAS/20/1718	6.9
D	VAS/20/1718	5.8
E	VAS/20/1718	6.4
1	REPORT/20/1830	1.9
2	REPORT/20/1900	2.5
3	REPORT/20/2135	4.4
4	REPORT/20/2143	4.4
5	REPORT/20/2212	4.4
6	REPORT/20/2310	4.4
7	REPORT/21/0030	4.4
8	REPORT/21/0115	6.4

Table 4. Hail size estimates (cm) from VAS and rawinsonde (RAOB) data and observed (OBS) hail diameters (cm). Magnitudes of errors (cm) are given in parentheses. Estimates are closest in time and space that preceded the events. Root-mean-square error (RMSE) is given for each data type.

DATE/STATE	VAS	RAOB	OBS
2 MAY 1984/OK	1.3(5.7)	1.3(5.7)	7.0
14 MAY 1984/AL	8.1(6.2)	7.2(5.2)	1.9
14 MAY 1984/GA	6.9(1.8)	1.3(3.8)	5.1
13 JUN 1984/CO	8.4(1.8)	0.8(9.4)	10.2
11 MAY 1985/IA	2.8(1.6)	4.3(0.1)	4.4
20 MAY 1985/OK	6.4(0.0)	3.0(3.4)	6.4
RMSE	2.6	5.4	

4. SUMMARY AND CONCLUSIONS

Hail size estimates were obtained via use of VAS vertical sounding data in a one-dimensional model for five large hail events during 1984 and 1985. Estimates were made for the same five cases from conventional rawinsonde data. When estimates closest in time and space to the hail events were compared with observations, VAS sounding data produced lower root-mean-square errors than did the rawinsonde data. The one-dimensional model exhibited the capability to produce large diameter estimates with both types of data. Reflection of trends of increasing hail potential after the rawinsonde data cycle appeared to be more consistent than quantitative estimates with the current formulation of the algorithm used to calculate hail size.

These preliminary results encourage continued efforts with the one-dimensional model and VAS sounding data in development of an operational objective aid for the SELS forecaster. More cases will be considered to better document characteristics of hail size estimates for various synoptic situations.

5. ACKNOWLEDGEMENTS

The author thanks Roney Sorensen of the Advanced Satellite Products Project, NWS, in Madison, Wisconsin for his help in extracting VAS sounding data from archive tapes. D. Andy Edman and William D. Hirt, NSSFC, provided assistance in setting up data files in the CSIS computer. April D. Laufer prepared the manuscript.

6. REFERENCES

Doswell, C.A., J.T. Shaefer, D.W. McCann, T.W. Schlatter and H.B. Wobus, 1982: Thermodynamic Analysis Procedures at the National Severe Storms Forecast Center. Preprints, Ninth Conf. on Weather Forecasting and Analysis, Seattle, Amer. Meteor. Soc., 304-309.

Fawbush, E.J. and R.C. Miller, 1953: A Method of Forecasting Hailstone Size at the Earth's Surface. Bull. Amer. Meteor. Soc., 34, 235-244.

Foster, D.S. and F.C. Bates, 1956: A Hail Size Forecasting Technique. Bull. Amer. Meteor. Soc., 37, 135-141.

Haltiner, G.J. and F.L. Martin, 1957: Dynamical and Physical Meteorology. McGraw-Hill Book Company, New York, New York. 470 pp.

Jedlovec, G.J., 1984: A Statistical Evaluation and Comparison of VISSR Atmospheric Sounder (VAS) Data and Corresponding Rawinsonde Measurements. NASA Technical Memorandum 82575, 11 pp.

Leftwich, P.W., 1984: Operational Experiments In Prediction of Maximum Hailstone Diameter. Preprints, Tenth Conference on Weather Forecasting and Analysis, Clearwater Beach, Amer. Meteor. Soc., 525-528.

Matson, R.J. and A.W. Huggins, 1980: the Direct Measurement of Sizes, Shapes and Kinematics of Falling Hailstones. J. Atm. Sci., 37, 1107-1125.

Miller, R.C., 1975: Notes on Analysis and Severe Storms Forecasting Procedures of the Air Force Global Weather Central. Air Weather Service Technical Report 200 (REV), Headquarters, Air Weather Service, 190 pp (approximately).

Prosser, N.E. and D.S. Foster, 1966: Upper Air sounding Analysis By Use of An Electric Computer. J. Appl. Meteor., 5, 296-300.

Ruprecht, E. 1971: Enhancement as a Factor On Shower Development. Contributions to Atmos. Physics, 44, 1-16.

Smith, W.L., 1983: The Retrieval of Atmospheric Profiles From VAS Geostationary Radiance Observations. J. Atm. Sci., 40, 2025-2035.

Storm Data, 1984: National Climatic Data Center, Asheville, N.C., Vol 26, No. 5 (May), 45 pp.

Storm Data, 1985: National Climatic Data Center, Asheville, N.C., Vol 27, No. 5 (May), 66 pp.

Uccellini, L.W., R. Peterson, D. Chester, A. Mostek, and T.H. Lee, 1982: Use of VAS for Analysis of a Prethunderstorm Environment. VISSR Atmospheric Sounder (VAS) Research Review, NASA Conference Publication 2253, 9 pp.

Wilson, G.S. 1980: Thunderstorm Environment Interactions Determined with Three Dimensional Trajectories. NASA reference Publication 1054. Marshall Space Flight Center, Alabama. 163 pp.

P4.25

DEEPENING RATE OF EXTRATROPICAL CYCLONES ESTIMATED FROM DIVERGENCE OF UPPER LEVEL CLOUD DRIFT WINDS

Gary Ellrod

Satellite Applications Laboratory (NOAA/NESDIS)
Washington, DC

1. INTRODUCTION

The rapid intensification of oceanic extratropical cyclones continues to be a major problem for the marine forecaster. These storms, often referred to as "bombs" due to the explosive nature of their development can produce heavy precipitation, a rapid increase in winds and high seas. They are difficult to forecast because numerical prediction models usually fail to capture them, or at least do not portray the severity with which they occur. This is partially due to the sparcity of data over the oceans, both surface ship reports and upper air observations.

Rapidly deepening mid latitude storms have been defined as those whose central pressure falls at least 24 mb in 24 hours (Sanders and Gyakum, 1980). The storms often develop near strong sea surface temperature gradients (such as those of the Gulf Stream). This is not always the case, however, as evidenced by the presence of these storms in the central and eastern Pacific where ocean temperature gradients are much weaker. They normally develop about 400 nm downstream from a short wave 500 mb trough, within or just poleward of the jet stream.

Attempts to identify explosive cyclogenesis in satellite imagery have led to some cloud pattern characteristics which have been of some use to forecasters in diagnosing rapid development (e.g., Böttger et al., 1975; Junker and Haller, 1980; Smigielski and Ellrod, 1985). Among the most important are: (1) the cloud pattern evolution of the rapidly intensifying storms proceeds at a much faster rate than that of average storms - they often evolve from the prestorm open wave to a tightly wound spiral in less than 24 hours (for example, see Jager, 1984). (2) They are characterized by a leaf shaped cloud mass which expands rapidly as development proceeds. (3) A pronounced dry slot, indicative of a rapidly sinking jet stream usually develops on the upstream edge of the cloud mass, which by this time is assuming the well known comma shape.

Within the past several years, satellite sounding data from the VAS (VISSR Atmospheric Sounder) has been evaluated for its utility in initializing numerical forecast models in oceanic areas (e.g., O'Lenic, 1982). One difficulty with VAS data however, is that it can only be obtained in relatively cloud-free regions, thus minimizing its usefulness in the region of rapid storm development. Remote soundings can be obtained in cloudy regions using the TOVS (TIROS Operational Vertical Sounder) microwave instrument. The gradient winds derived from the TOVS data are less accurate however, due to the relatively poor resolution of the sensor (Velden et al., 1984).

A source of data that has not been evaluated extensively in analyzing mid latitude ocean storms is upper level cloud drift winds. This paper describes preliminary attempts at using cloud drift wind data for independently estimating the deepening rate of oceanic cyclones.

2. BASIC APPROACH

The factors affecting the change in surface pressure at a point are described by the pressure tendency equation:

$$\left.\frac{\partial p}{\partial t}\right)_0 = \underbrace{-g\int_0^H \rho \nabla_H \cdot V\, dz}_{A} \underbrace{- g\int_0^H V \cdot \nabla \rho\, dz}_{B} \qquad 2.1$$

where term A is the net horizontal divergence, term B is the net horizontal density advection in the atmospheric column which has a depth H. The pressure falls in advance of a surface low center are caused by both warm advection and divergence aloft. Near the center of the low however, the divergence is believed to be more important since the thermal advection diminishes (Palmén and Newton, 1969).

Regions of upper level divergence are normally associated with the left front or right rear quadrants of isotach maxima embedded within the jet stream core (jet streaks). A jet streak is thought to have played a major role in the development of the President's Day east coast storm of 1979 (Uccellini et al., 1984). It has also been shown that there is a linkage between upper level jet streaks and the intensification of the low level jet (Uccellini and Johnson, 1979). Such an increase in the low level flow would also enhance the low level warm advection (term B) in advance of a developing low.

Cloud track winds obtained from cirrus motion provide an opportunity to analyze the upper level divergence patterns over developing oceanic lows. Although it is not possible to obtain the total divergence (term A) from cloud drift winds,

it is possible that an empirical relationship can be found between the upper level divergence and the intensification rate of a surface low. The approach that will be taken in this study is to determine: (1) if such a relationship exits using radiosonde data over the central and eastern U.S. where surface data is dense, (2) determine if this relationship is valid for oceanic storms analyzed using cloud wind data, and (3) if not, make the necessary adjustments. So far, only step (1) has been accomplished to any extent.

It is hoped that several cases can be obtained during the GALE (Genesis of Atlantic Lows Experiment) project to be conducted from January through March, 1986 (Dirks et al., 1986).This project will provide unusually dense surface and upper air data near the mid Atlantic coast of the U.S. for the purpose of studying cyclogenesis and coastal fronts. Included in the data sets will be VAS retrievals, cloud track winds and winds derived from the 6.7 μm water vapor channel.

For the technique to be useful, some assumptions must be made:

(1) Cloud drift and water vapor wind data are comparable in accuracy to radiosonde winds. This is difficult to determine since radiosonde data has its own inherent errors. Previous studies (Hubert and Whitney, 1971; Mosher, 1978; Stewart et al., 1985) have indicated that these winds are reasonably accurate, however. The RMS vector differences are typically 5 to 10 m sec^{-1}.

(2) The upper divergence must remain nearly steady state through the subsequent 6 and 12 hour period. Some changes are bound to occur with time but it is expected that they will be gradual in most cases.

(3) Deepening mechanisms for oceanic storms are similar to those over land. It has been suggested that thermal advection effects are more important for ocean storms. If so, a new relationship would have to be obtained.

3. DATA ANALYSIS

The cloud drift winds to be used are generated on the McIDAS (Man Computer Interactive Data Access System) located at the University of Wisconsin, Madison (Suomi et al., 1983) by personnel of the NESDIS Development Laboratory. The data are accessible at any of the remote terminals such as the one at the World Weather Building in Camp Springs, Maryland.

For any data set (radiosondes, surface data, etc.), conventional analyses such as divergence and vorticity, for example, can be contoured and overlayed on satellite images. The analysis technique used on the McIDAS is similar to that described by Barnes (1964). Examples of a complete wind set in the western Atlantic and the divergence analysis derived from this wind set are shown in Figures 1 and 2.

The standard pressure level chosen for the radiosonde analyses required for the dependent data set was 300 mb. This level was chosen since it is close to the height of the winter tropopause and there are fewer cases of missing winds than at higher levels. The maximum computed divergence within the upper air stations which enclosed the location of the surface low was normally used. In some cases, divergence values near the midpoint in a gradient region were selected when it was considered to be more representative of conditions over the surface low. These data were then compared to the 6 hour and 12 hour pressure change of the low centers.

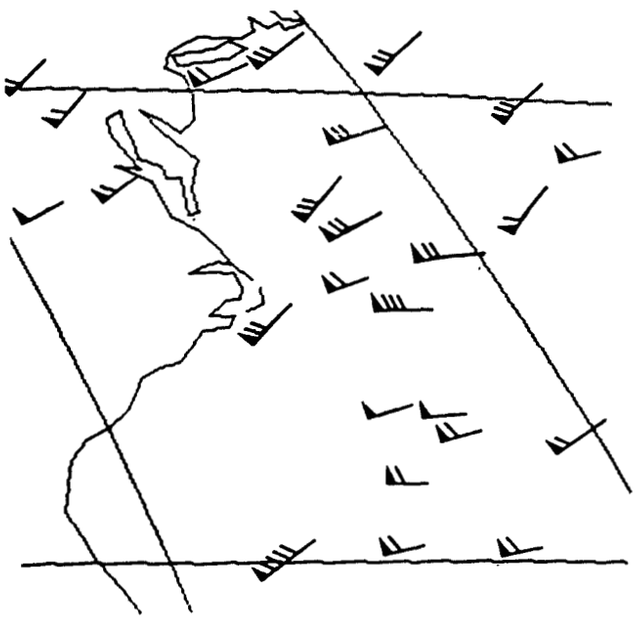

Figure 1. Combined cloud drift wind and water vapor wind data set for 23 January 1986 at 0900 GMT for high levels (200-400mb).

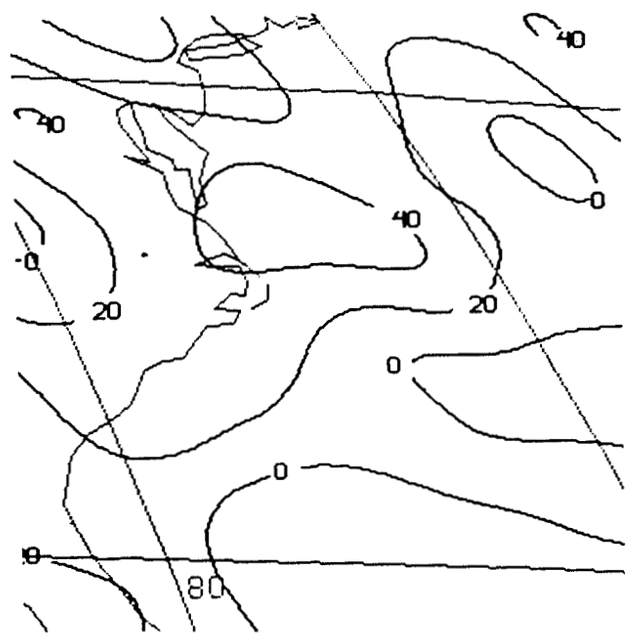

Figure 2. Divergence ($x10^{-5}$ sec^{-1}) analysis derived from winds shown in Figure 1.

4. PRELIMINARY RESULTS

Based on more than a dozen cases over the eastern U.S., a plot of divergence aloft determined from McIDAS versus 6 hour and 12 hour pressure change is shown in Figures 3 and 4. A nearly linear relationship is indicated. The few cases of rapidly deepening lows were mostly associated with very large divergence aloft ($\geq 80 \times 10^{-5}$ sec^{-1}).

The actual application of the above relationship to oceanic cases using cloud wind data sets has been attempted in only a few cases. Two of the cases involved wind data produced for the eastern Pacific (EPAC) experiment (Hayden and Schreiner, 1984) in order to evaluate the impact of processed VAS data on operational numerical forecasts. In both EPAC situations, surface deepening occurred in conjunction with divergence aloft, but surface data were not sufficient to determine the magnitude with much accuracy.

In a case over the western Atlantic (shown in Figure 5) a low center was located south of Nova Scotia at 0900 GMT on 28 January, 1986. The cloud wind divergence analysis showed a maximum of +80 near the location of the surface low. The low center moved rapidly northward into eastern Canada during the day and had deepened about 13 mb by 2100 GMT.

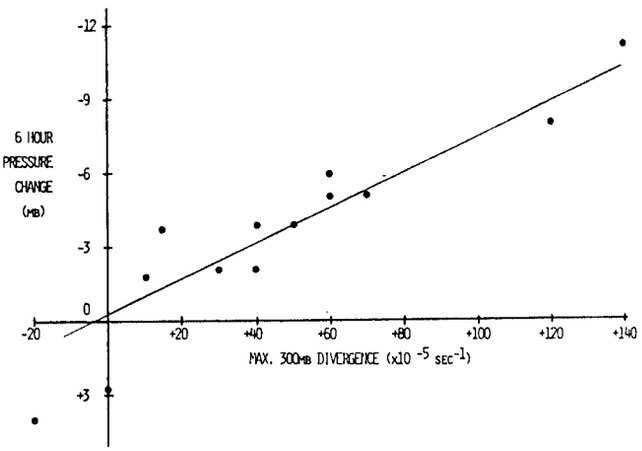

Figure 3. Six hour change in surface pressure versus 300mb divergence derived from radiosonde data for extratropical lows over the U.S. east of the Rockies.

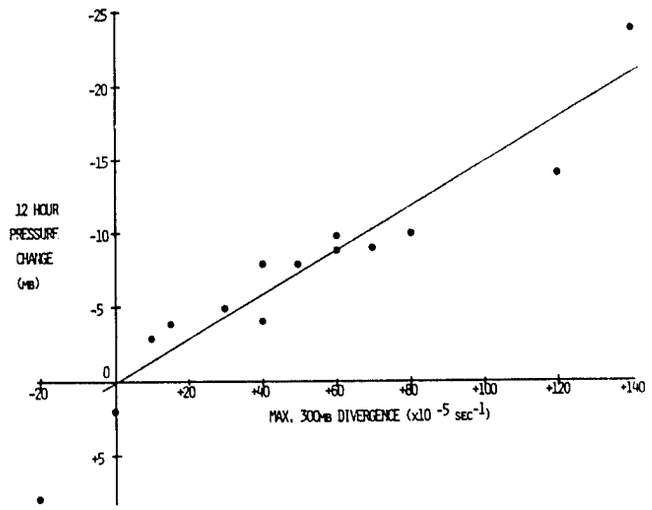

Figure 4. Same as Figure 3 except for twelve hour pressure changes.

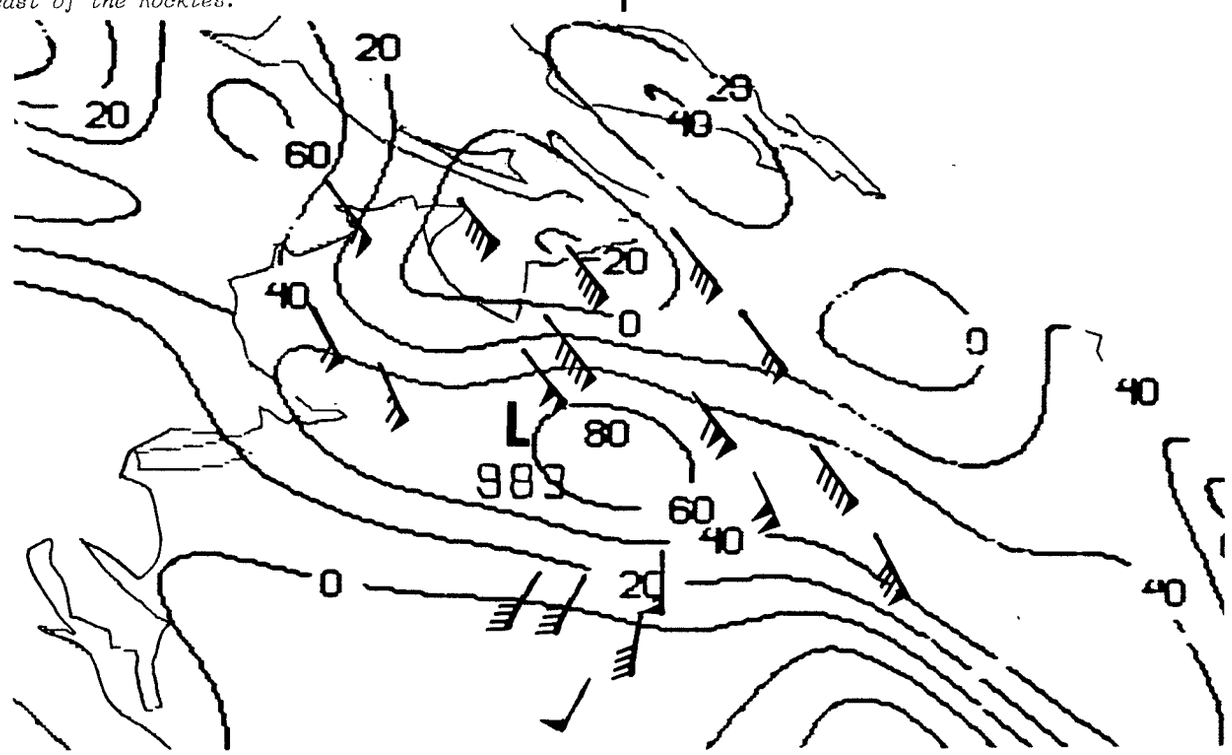

Figure 5. Cloud drift winds and divergence analysis for 0900 GMT, 28 January, 1986.

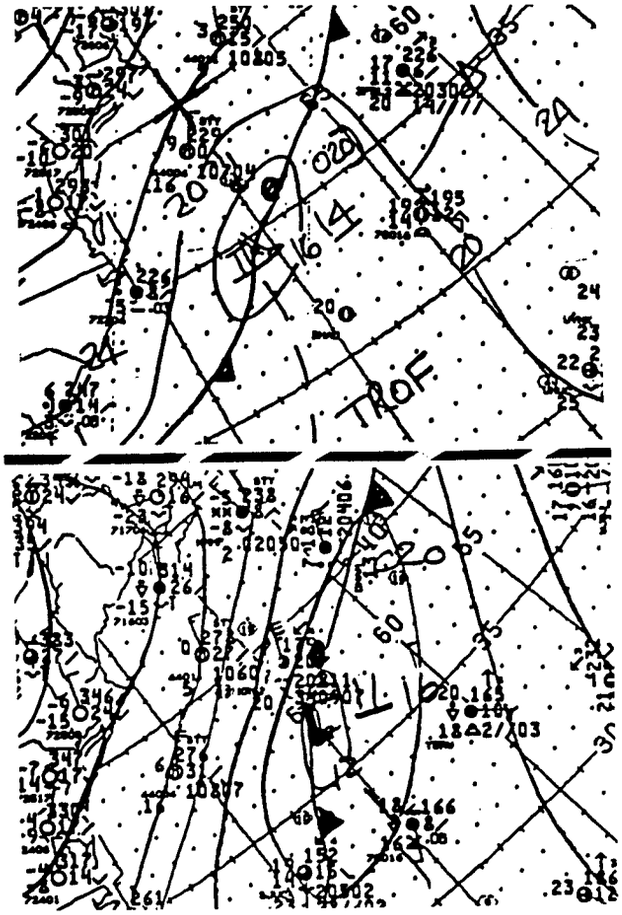

Figure 6. Surface analysis for 0000 GMT 24 January 1986 (top) and 1200 GMT 24 January, 1986 (bottom).

In a few situations where divergence maxima existed (both over land and water), surface lows developed along baroclinic zones where no surface low existed before. This suggests another possible application - diagnosing the location of future storm development. The case shown in Figures 1 and 2 is an example. A cold front was moving slowly eastward off the coast on the morning of 23 January 1986. By 0000 GMT 24 January (12 hours later), a weak low had formed near 35N 70W (Figure 6), just east of the maximum divergence area that morning. The surface pressure fell about 4-6 mb in that period. By the next morning, the low had deepened further and gale force winds were being reported north of the center. The Limited-area Fine-mesh (LFM) Model was fairly accurate in its forecast of this system while the Spectral and Nested Grid Model (NGM) were not.

5. CONCLUDING REMARKS

A means of estimating the deepening rate of cyclones using cloud drift winds has been described. Further case studies are needed to determine if there is any operational application for this approach.

The technique described is not envisioned as a replacement for numerical prediction models over the oceans, but rather a means of checking the accuracy of the models using an independent source of data. When the numerical models are not in agreement, it could also help a forecaster decide which one has the best solution for the particular situation he is faced with.

6. REFERENCES

Barnes, S. L., 1964: A technique for maximizing details in numerical map analyses. J. Appl. Meteor., 3, 396-409.

Böttger, H., M. Eckardt, and U. Katergiannakis, 1975: Forecasting extratropical storms with hurricane intensity using satellite information. J. Appl. Meteor., 14, 1259-1265.

Dirks, R., et al., 1986: GALE Operations Plan, January 1986, Boulder, CO.

Hayden, C. M. and A. J. Schreiner, 1984: Real time meteorological applications of the geostationary satellite sounder on GOES-6: battling the computer, code and clock. Society of Photo-Optical Instrumentation Engineers, Vol. 481, 100-107.

Hubert, L. F. and L. F. Whitney, 1971: Wind estimation from geostationary satellites. Mon. Wea. Rev., 99, 665-672.

Jager, G. L., 1984: Satellite indicators of rapid cyclogenesis. Mariners Weather Log, 28, 1-6.

Junker, N. W. and D. J. Haller, 1980: Estimation of surface pressure by satellite cloud pattern recognition. Proc. Eighth Conference on Weather Forecasting and Analysis, June 1980, Denver, Amer. Meteor. Soc., 119-122.

Mosher, F. R., 1978: Cloud drift winds from geostationary satellite. Atmos. Tech., 10, 53-60.

O'Lenic, E., 1982: Evaluation of the Effect of VAS data on some NMC analyses and forecasts. NMC Office Note 253, April 1982.

Palmén E. and C.W. Newton, 1969: Atmospheric Circulation Systems. Academic Press, New York, pp 133 -136.

Sanders, F. and J. R. Gyakum, 1980: Synoptic-dynamic climatology of the "bomb". Mon. Wea. Rev., 108, 1589-1606.

Smigielski, F. D. and G. P. Ellrod, 1985: Surface cyclogenesis as indicated by satellite imagery. NOAA Tech Memo NESDIS 9, Dept. of Commerce, Washington, DC, 30 pp.

Stewart, R.S., C.M. Hayden and W.L. Smith, 1985: A note on water vapor winds tracking using VAS data on McIDAS. Bull. Amer. Meteor. Soc., 66, 1111-1115.

Suomi, V. E., R. Fox, S. S. Limaye and W. L. Smith, 1983: McIDAS II: A modern interactive data access and analysis system. J. Clim. Appl. Meteor., 22, 766-778.

Uccellini, L. W., P. J. Kocin, R. A. Petersen, C. H. Wash, and K. F. Brill, 1984: The President's Day cyclone of 18-19 February 1979: Synoptic overview and analysis of the subtropical jet streak influencing the precyclogenetic period. Mon. Wea. Rev., 112.

Uccellini, L. W. and D. R. Johnson, 1979: The coupling of upper and lower tropospheric jet streaks and implications for development of severe convective storms. Mon. Wea. Rev., 107, 682-703.

Velden, C.S., W.L. Smith and M. Mayfield, 1984: Application of VAS and TOVS to tropical cyclones. Bull. Amer. Meteor. Soc., 65, 1059-1067.

P4.26

CLASSIFICATION OF SATELLITE IMAGES OF EXTRA-TROPICAL CYCLONES OVER THE OCEAN BY MEANS OF COMPUTERIZED PATTERN ANALYSIS

Craig R. Burfeind and James A. Weinman

Department of Meteorology
University of Wisconsin-Madison 53706

I. Introduction

Currently, there are many regions over the oceans, where no surface or upper-air data are measured by conventional methods. Although upper-air temperature and humidity soundings can be obtained from infrared and microwave measurements from satellite-borne radiometers, the surface pressure is not at present being measured operationally using these methods. Accurate surface-pressure measurements are needed to obtain good weather forecasts.

Attempts have been made to manually assign quantitative parameters to large-scale vortices observed in satellite weather images. Troup and Streten (1972) devised a cyclone classification scheme according to developmental stage by means of an objective set of rules applied to a satellite picture to classify the cyclone. The surface-pressure field was statistically derived using the cyclone class and the climatology for that class. Guymer (1978) used both the large-scale shape and small-scale features to derive several meteorological parameters. This analysis was conducted by a human analyst. Such analysts may become less attentive after looking at many such satellite pictures.

No previous attempts have been made to automatically classify cyclone images or to derive meteorological parameters from satellite images by means of computer analysis. This study is a first attempt to automatically classify cyclones over the ocean. Once an objective technique for obtaining parameters from the shape, size, and orientation is devised, a regression scheme using climatology can be applied to the data without concern for errors induced by subjective biases. This paper presents an automatic satellite-image classification technique that places cyclones into five classes which are comparable to the five classes defined by Troup and Streten (1972) (see Figure 1).

The algorithm presented here classifies oceanic extratropical cyclones into one of these five classes, locates the cyclone center and the appropriate fronts, and derives a set of objective parameters that describe the size, shape and orientation of the storm system. All this is done without manual intervention.

The technique can be divided into four steps:

1) The image of the cyclone is extracted from the GOES hemispheric picture by means of the McIDAS image display system (Suomi et. el., 1983). This is done so that analyses can be done on only the extratropical cyclone in question. This procedure uses the position of the 24 hour LFM forecast cyclone-center as an approximate indicator to initiate the search for the cyclone.

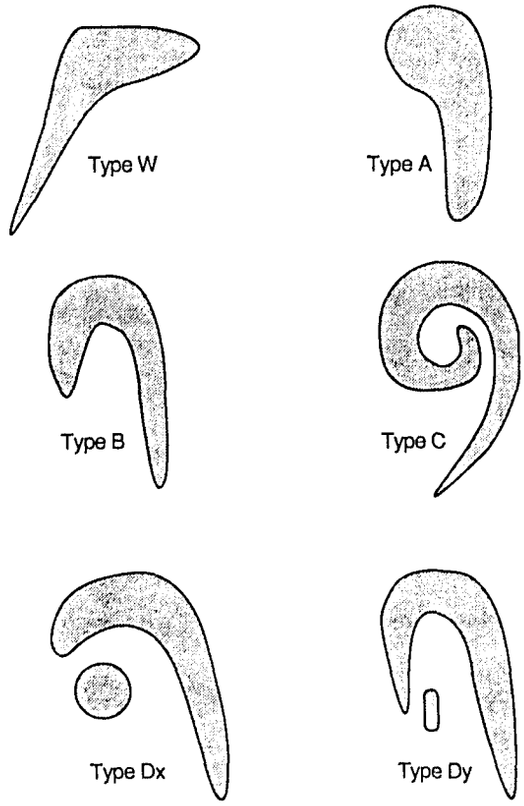

Figure 1: Schematic diagram of the six cloud pattern classifications defined by Troup and Streten (1972).

2) The cyclone is placed into one of five classes. In order to do this, objective parameters that describe the appearance of the system are calculated and used to determine the cyclone type.

3) The center of rotation is located using the cyclone class and the visible image.

4) The fronts are located using the class, the cyclone center, and the visible image as input information.

Fifteen cases are analyzed in this study. Their time of observation, location, and original spatial resolution are summarized in Table 1.

II. Preprocessing of GOES Visible and Infrared Images of Extratropical Cyclones

At any given there are numerous cyclone systems in various stages of

Data Set	Date	Time (GMT)	Latitude (deg)	Longtitude (deg)	Resolution (km)
1	4-6-84	19:45	25-60N	125-170W	16X16
2	12-9-83	20:46	25-50N	130-160W	16X16
3	4-5-84	19:45	20-40N	120-235W	16X16
4	4-20-84	19:45	25-60N	130-170W	16X16
5	4-13-84	19:45	25-60N	125-150W	16X16
6	3-3-85	20:00	35-60N	120-150W	16X16
7	3-22-85	20:01	30-50N	125-165W	16X16
8	2-2-84	20:45	15-40N	145-170W	16X16
9	3-29-84	20:45	30-65N	130-170W	16X16
10	2-3-84	20:46	25-45N	155-180W	16X16
11	2-22-84	20:45	25-50N	130-175W	16X16
12	2-26-84	20:46	20-50N	125-150W	16X16
13	11-13-84	19:00	25-45N	130-150W	16X16
14	11-15-84	20:00	25-50N	120-140W	16X16
15	3-2-84	20:45	15-45N	140-170W	16X16

Table 1 : Data set number along with time and location of observation, and spatial resolution for each data set.

development over the oceans. In order to simplify the analysis, the extratropical cyclones are examined one at a time. This is done by extracting a single cyclone from the the GOES hemispheric picture. Because image analysis is computationally intensive, one desires to analyze an image which has the fewest number of pixels possible.

The position of the low-pressure center predicted by the 24 h LFM forecast is used as the first guess to locate the cyclone center. An area with dimensions of 5120 km in the latitudinal direction and 3840 km in the meridional direction with a pixel resolution of 16 km by 16 km is extracted from the full-disk visible and infrared pictures to produce images consisting of 320 pixels in the east-west direction, and 240 pixels in the north-south direction. These images, both visible and infrared, are extracted from GOES pictures so that the center of the cyclone is one-third of the distance from the northern edge to the southern edge and one-half of the distance between the eastern and western edges of the 320 X 240 image. These 320 X 240 pixel images are then remapped into a Mercator projection with the same number of pixels. This procedure is applied to both the visible and the infrared images to remove large shape distortions caused by the location of the storm relative to the GOES satellite location. This also allows all pictures to be analyzed in the same projection, which is important in the derivation of a single technique for classifying storms at different latitudes. Finally, the 320 X 240 pixel images are degraded by averaging over 8 X 6 pixel boxes to produce images consisting of 40 X 40 pixels each having a resolution of 128 km by 96 km.

The size of extratropical cyclones can vary over an order of magnitude; it is, therefore, desirable to scale all cyclone images so that an image can be created in which all possible cyclones cover approximately the same area in the 40 X 40 pixel image. To produce this image, smaller cyclones are enlarged by a greater factor than larger cyclones. The resolution will be different for each cyclone picture. This area normalization is important so that only one classification and location scheme needs to be developed, instead of having an analysis which depends upon the size of the cyclone.

The normalization process uses many digital image processing techniques, including brightness normalization, threshholding to produce a binary image, spatial filtering to reduce noise, and extraction from the original full resolution visible image to produce the normalized image. From the normalized image, the angle of orientation, along with various size parameters are determined for the cyclone's image. Brightness normalization is performed to correct for limb darkening produced at large solar zenith angles.

III. Classification of the Degree of Development of Extratropical Cyclones Using the Visible Image

The classification of the cyclone's degree of development is achieved by determining several features of the cyclone images, which are then used as indicators to classify the cyclone type. In order to identify the properties of the cyclone image, the scaled cyclone image must be further simplified.

A decision tree structure (see Figure 2) is used to classify the extratropical cyclones. At each node of the tree, one feature is used to determine whether the cyclone fits a certain class. If so, it is classified and the procedure is complete. Otherwise, the next feature is extracted and another decision takes place.

The first feature which is needed to classify cyclone systems is the orientation angle of the major axis of the elliptical approximation of the original visible image. The original image is fit to an ellipse so this analyses can be completed. The angle of orientation is taken to be zero if the major axis of the ellipse is oriented along an east-west line and 90 degrees if the cyclone's major axis is along a north-south line. This angle is used to determine if a cyclone is in the wave stage as opposed to a more developed cyclone. Cyclones with smaller angles

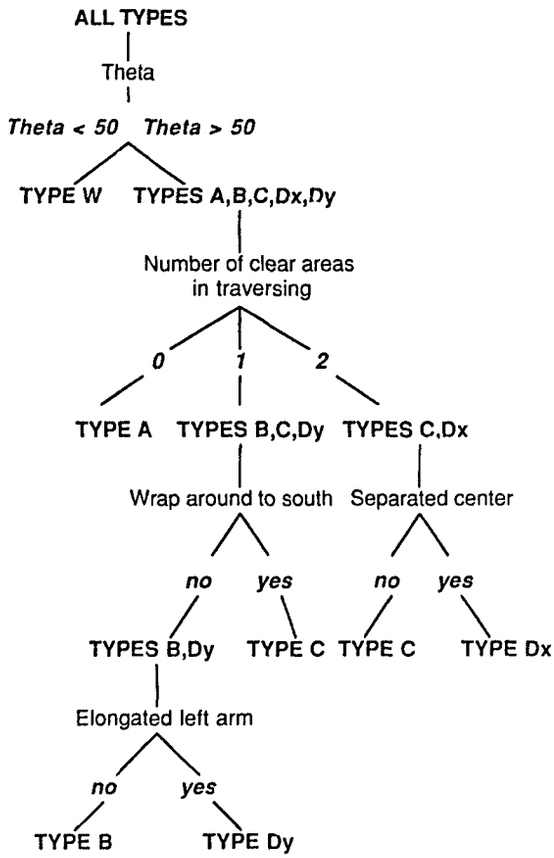

Figure 2 : Decisison tree structure for classifying cyclones.

are thus classified as wave-stage cyclones (denoted W). It is found empirically that a cutoff of 50 degrees best separates wave-stage cyclones from the other types of cyclones.

The remaining features are derived from an image which is a subset of the scaled visible image. A high-resolution image which consisists of the center core of the cyclone system is extracted from the original Mercator visible image. The center point and the size of this high-resolution center section is determined from the centroid of the degraded scaled image. Similer degradation is again applied to the scaled image to produce a noise-free, binary image of the center spirals of the system. This final image is used for cyclone classification.

The pattern-analysis algorithm searches for dry tongues by looking for the first continuous, horizontal string of pixels with a value of 200 on the east edge of the picture. From this continuous string, it searches towards the west until it finds a clear area. It then continues to search towards the west for a cloudy area and repeats the same procedure again, each time counting the number of pixels in the clear area. When a clear area is located, the program searches towards the south to determine whether the cyclone has begun to wrap up. A cyclone is considered to have wrapped up if there are at least two pixels extending toward the east from the southwestern arm of the system. This procedure yields two features--the number of clear slots and an indication as to whether the cyclone has wrapped up.

The binary image is used to classify the cyclones which did not fall into the W class, by looking for the dry tongue. If no dry tongue is present, then the cyclone is classified as a type A. If a dry tongue is present, the algorithm searches to the south to determine whether the cyclone has begun to wrap up or checks for two slots of dry air between the edges of the entire cyclone, thus indicating that the cyclone has wrapped around itself a second time. If either of these features are present, the cyclone is classified as a type C; otherwise, it is classified as a type B.

At this point all cyclones which can be classified as W, A, B, or C have been classified. Also, the algorithm has saved certain reference points on the image for later use in determining the cyclone center. In order to classify the types D_x and Dy, the program checks types B and C to see if they are not actually of type D, since all type D's would have been included in the classification of type B or C up to this point.

First a check is made to determine whether the wrapped-around cloud band of a type B or C is connected to the main cloud band. The segmented image is used to determine if the cloud band is continuous by comparing the label on the center spiral region with the label on the frontal band. If the labels are the same, the cloud band is continuous and the cyclone classification is left unchanged. If the regions have different labels, the cyclone system is classified as a type D_x. If the center spiral is disconnected from the main cloud band, it is classified as a dissipating cyclone.

Secondly, type B cyclones are checked to determine if the cloud band to the west, which has not wrapped around is elongated. This is done by comparing the lengths of the western arm and the eastern arm associated with the cold front.

IV. Location of the Cyclone Center

A different technique for locating the cyclone center is used for each of the five classes. Using points saved previously as starting locations, the program moves predetermined distances from these locations to determine the cyclone center.

This section of the program takes as input the three locations on the spirals: the location of the southwestern edge of the dry tongue, the center of the northern edge of the cloud band which is wrapped around to the south, and the western edge of the cloud band which has wrapped around a second time to the east of the second dry tongue.

For type W cyclones, the cyclone

center is located where the thickest bulge is found in the band of cloudiness, or where the curvature of the cloud bands changes sign. In either case, this is where the cloud band is thickest in the east-west direction. The same procedure that is used for type W cyclones is also used for type A cyclones. The only difference is that the classification of type A cyclone uses the entire image and not only the high-resolution center section. For type B cyclones, the point located at the southwestern edge of the dry tongue is used as a starting point for locating the cyclone center. This point is also used for type Dy. It was empirically determined that the center of the cyclone should be placed at the point one pixel to the south of the point saved in the above procedure. If the cyclone is determined to be a type Dy, then the cloud band is searched to find the southern-most tip of the western cloud leg of the type Dy. It is this point that is given as the cyclone center in type Dy cyclones. For type C cyclones, two possibilities exist. The first is that the cyclone has only begun to wrap around to the south, but has not started to form the second dry tongue. The second is that it has begun to wrap up, thus forming a second slot of dry air as the cyclone is traversed form east to west. For the first case, the algorithm begins searching from the point on the northern edge of the band which has wrapped to the south towards the northeast until it has located the northeastern-most edge of the cloud band. The cyclone center is placed two pixels to the west of this point, which corresponds to the vertex of the spiralling band. In the second case, the cyclone center is placed one pixel to the north of the point which is defined as the western edge of the cloud band which has begun to wrap around a second time to the east. This once again places the center at the vertex of the spiralling cloud band. If the cyclone is classified as a type D_x, then the cloudy area closest to the center of rotation is located. This cloudy area is disconnected from the main cloud structure as indicated above. The centroid of this region is determined and is taken to be the cyclone center.

V. Location of the Front

The final analysis done by this algorithm is to roughly locate the cold front, or the occluded front. In the case of the type W system, the warm front is also located. It should be pointed out that for dissipating cyclones (type D's) no front is located.

The original Mercator visible image is the starting point in the frontal analysis. A binary image is created from this image. A filter is placed over this binary image to remove the noise and rough edges while retaining the general shape of the frontal cloud bands. The front is determined by moving away from the center of rotation in predetermined directions until the frontal cloud bands are located. These points are marked and saved. After all points which make up the front are located, the front is smoothed by placing a running mean through the points.

VI. Results

The relative area of the cyclone cloud (Table 2) shows no strong correlation to the type of cyclone. This indicates that any cyclone type can vary in size. The value of theta changes as the cyclone matures. Small angles are noted in developing cyclones since the cold air is still to the north and has not begun to sweep southward to overtake the warm air. As the cyclones develop, larger angles are found as the tilt of the system becomes more negative due to the southward sweeping cold air. description of the cyclone system.

Data	Type	Area Str ($x10^3$ km)	Connect	Theta (deg)
1	C	92.77	1.00	87.1
2	C	54.95	1.00	139.5
3	B	34.76	1.00	97.3
4	DX	92.77	0.94	100.5
5	B	105.71	0.99	74.4
6	C	93.58	1.00	106.9
7	W	78.68	1.00	33.6
8	B	82.43	1.00	101.3
9	A	108.52	1.00	75.6
10	A	42.57	1.00	93.1
11	W	96.76	1.00	33.0
12	DY	104.27	1.00	101.7
13	DX	38.86	0.71	74.2
14	DX	79.64	0.93	114.9
15	B	88.61	1.00	94.7

Table 2 : Cyclone classification and features for each data set.

A comparison of the results of this study with the results obtained from human analysts was performed. Six meteorologists, all of whom have had experience in analyzing satellite imagery or a strong synoptic meteorology background, analyzed the 15 cases to locate the low pressure center and the fronts. The mean low pressure center location and the mean frontal position along with the standard deviation for each of the 15 data sets were calculated for the six analyses.

Table 3 displays the distance between the cyclone center found by the computer algorithm and the mean center location found by the analysts. Along with these values, the standard deviation for the human analysts and the ratio of the computer's distance from the mean to the human analysts' standard deviation is tabulated. Except for one very bad case (data set 4), the results show that the computer analysis is within one standard deviation half of the time and always

Data Set	Subjective Std. Dev. (km)	Objective Dist. from Mean (km)	Ratio Dst from Mn Std dev
1	177	37	0.21
2	91	155	1.70
3	151	183	1.21
4	104	407	3.91
5	276	141	0.51
6	98	161	1.64
7	178	258	1.45
8	254	217	0.85
9	444	614	1.38
10	N/A	N/A	N/A
11	187	136	0.73
12	701	1086	1.55
13	70	32	0.46
14	202	101	0.50
15	343	268	0.78

Table 3 : Comparison of standard deviation of low pressure center position for a group of human analysts versus distance from the mean for the computer algorithm.

within two standard deviations. These results also show that the cases in which the computer algorithm had difficulty in locating the center and the fronts, the human analysts also produced a wide range of results.

Table 4 gives the same parameters for the frontal position. The computer algorithm did poorly on data sets 9 and 15, while the distances for the remaining cases are approximately equal to one standard deviation or less.

Overall, the computer algorithm showed the poorest results for type A cyclones, especially data set 9. This is due to the lack of large-scale structure encountered in type A cyclones when compared to the other types. Since the computer needs structure to serve as a guide in locating features of the extratropical system, it was unable to perform as well for these cases. Also, if more type A cyclones would be analyzed and used as training sets for the computer algorithm, performance might be improved.

The computer seemed to yield the best analysis on type C cyclones. This is mainly due to the structure associated with the spiralling center of rotation. The algorithm is able to locate many reference points on the spiralling cloud bands to use in identifying the low pressure center. Type C cyclones, especially data set 1, also show well defined and narrow frontal cloud bands which make the associated frontal position easy to locate.

These pattern analyses were conducted on an IBM AT-99 personal computer equipped with an 80287 coprocessor chip and 512 kb of random access memory. The

Data Set	Subjective Std. Dev. (km)	Objective Dist. from Mean (km)	Ratio Dist from Mn Std dev
1	143	44	0.31
2	86	24	0.28
3	75	80	1.07
4	N/A	N/A	N/A
5	125	312	2.50
6	118	91	0.77
7	151	141	0.93
8	114	41	0.36
9	170	1273	7.49
10	N/A	N/A	N/A
11	185	49	0.26
12	N/A	N/A	N/A
13	N/A	N/A	N/A
14	N/A	N/A	N/A
15	77	136	1.77

Table 4 : Comparison of standard deviation of frontal position for a group of human analysts versus the average distance from the human frontal position mean for the computer algorithm.

extended "Turbo-Pascal" software system was used for programming these algorithms. The entire analysis took approximately 3 minutes from beginning to end for each cyclone. While the personal computer is in no way overburdened by these procedures, the analysis could be performed much more rapidly on a minicomputer equipped with a parallel array processor.

VII. Summary

An algorithm was developed that objectively analysed synoptic-scale satellite images depicting various stages of development of extratropical cyclones. The images were analyzed to assign a category to the cyclone based on its stage of development. Once classified, the rotation center and the fronts associated with the cyclone were located.

This classification scheme along with the parameters derived from the satellite images may ultimately used to empirically derive surface-pressure fields. Thus, the surface-pressure field could be derived from the large-scale features of the extratropical cyclone images. This would be similar to the work done by either Nagle and Hayden (1971) or Troup and Streten (1972). This technique would be especially useful over data-sparse regions of the oceans, where little surface-pressure data are available.

This study demonstrates that pattern analysis techniques may permit the development of rapidly executed, objective computer-assisted analyses of satellite images. These analaysea are able to distinguish cyclones in any of their stages of development. It is realized that not all cyclone shapes will be analyzed correctly, but as more cyclones are analyzed, the program can be improved to accomodate the more complicated cloud shapes associated with various cyclone systems. This is only the beginning of the "learning" stage for the computer algorithm. It is evident that the program can become much more precise as more satellite images are analyzed.

REFERENCES

Guymer, L.B., 1978: Operational Application of Satellite Imagery to Synoptic Analysis in the Southern Hemisphere. Technical Report #29, Commonwealth Bureau of Meteorology, Melbourne, AUtralia, 83 pp.

Kelly, G.A.M., 1978: Interpretation of Satellite Cloud Mosaics for Southern Hemisphere Analysis and Reference Level Specification. Monthly Weather Review, 106, 870-889.

Nagle R.E. and C.M. Hayden, 1971: The Use of Satellite-Observed Cloud Patterns in Northern Hemisphere 500-mb Numerical Analysis. NOAA Technical Report, NESS 55, U.S. Department of Commerce, Washington D.C., 25 pp.

Suomi, .V.E, R. Fox, S.S. Limaye and W.L. Smith, 1983:McIdas III: A Modern Interactive Data Access and Analysis System. Journal of Climate and Applied Meteorology, 22, pp. 766-778.

Troup A.J. and N.A. Streten, 1972: Satellite Observed Southern Hemsiphere Cloud Vortices in Relationship to Conventional Observations. Journal of Applied Meteorology,11, pp. 909-917.

ON RAINFALL RATE DELINEATION IN THE MIDLATITUDES FROM THE GOES IMAGES

by

A.A. Tsonis

Department of Geological and Geophysical Sciences
The University of Wisconsin-Milwaukee

1. INTRODUCTION

The estimation of rain from the Geostationary Orbiting Environmental Satellite (GOES) visible and/or infrared imagery has received during the past fifteen years much attention. A comprehensive review of rain area estimation from satellites up to 1981 was gathered by Barrett and Martin (1981). In general, the majority of the techniques can be divided in mono-spectral methods, (Scofield and Oliver (1977), Griffith et al. (1978) and Stout et al. (1979), for example) and bi-spectral methods (Lovejoy and Austin (1979) and Tsonis and Isaac (1985), for example). Although the rain area delineation from the GOES images is progressively improving attempts to relate the cloud brightness (visible information) and/or the cloud top temperature (infrared information) to the rainfall rate have not been very successful. Part of the problem lies in the fact that high cloud brightness values or low cloud temperatures can in fact result from nonraining clouds. Lately, Wu et al. (1985) presented a rather sophisticated method for classification of the satellite derived rain area into light and heavy rain areas. Their approach makes use of the textural and spectral properties of the visible and infrared fields of, mainly, tropical storms. It seems, however, that textural properties would not serve as good discriminators for rainrates in the midlatitudes where in general less convection is available. Tsonis (1984) observed that in some nonconvective cases texture by itself may not even be able to discriminate between rain and no rain. The present study presents some preliminary results of a different approach which could be used to delineate some rainrate information from the GOES images in the midlatitudes, and to differentiate between convective and nonconvective precipitation

2. DATA

The satellite data used in this work are GOES East visible (0.54-0.70 μm wavelength) and thermal infrared (10.5-12.6 μm wavelength) images. The temporal resolution of the satellite data is 30 minutes and the spatial resolution is 4 x 4 km. It should be noted at this point that the true resolution of the sensed infrared images is 8 x 8 km. From these images 4 x 4 km resolution images have been constructed for a better resolution equivalence between the infrared and visible data. The intensity range of the visible image is 0-63 and that of the infrared is 0-255.

The analysis of the data was restricted to the area in Ontario, Canada, which is covered by the C-band Woodbridge weather radar indicated by the circle in Fig. 1. Table 1 gives a summary of the satellite and radar data used in this study. The third column indicates the type of precipitation (C for convective and N-C for nonconvective). For more details on the data see Tsonis (1984) or Tsonis and Isaac (1985).

Table 1 Summary of the data used in this study

Date	Period (GMT)	Type of Precipitation
27 July 1982	1230-1900	N-C
28 July 1982	1400-2200	C
3 Aug. 1982	1200-2300	N-C
2 May 1983	1730	C
6 June 1983	1230-1730	N-C
27 June 1983	1430-2200	N-C,C
4 July 1983	1230-2330	C
21 July 1983	1730-2300	C
29 July 1983	1330-2330	N-C
13 May 1984	1330-1900	N-C
23 May 1984	1300-2200	N-C,C

3. METHOD

This work is based on the method and results of instantaneous rain area delineation in the midlatitudes from GOES imagery reported in Tsonis and Isaac (1985). Their method is composed of two parts: a technique for the discrimination between raining and nonraining clouds and a scheme for the delineation of the rain area. Although some restrictions apply, the delineation of the rain area from the raining clouds is based on some optimimum visible threshold (V_o) which varies according to the day, time and type of precipitation. Hereafter any rain area determined by the Tsonis and Isaac method will be denoted as $R_{V_o}(x,y)$.

The novelty of the above method is that it is oriented toward instantaneous rain area delineation using only a visible and an infrared image and thus it does not require radar data or life history knowledge. The main conclusion of Tsonis and Isaac (1985) is that the visible images contain more information about the areal extent of precipitation in the midlatitudes compared to the infrared images except in cases of strong convection. In such cases some optimum infrared threshold (I_o) can be as effective as V_o. In nonconvective cases or in cases of weak convection any infrared threshold fails to delineate the rain area satisfactorily but in contrast V_o does not fail (for more details see

Tsonis and Isaac (1985).

These observations will be extended here for the purpose of inferring rainrate information from a visible and an infrared image. The method to be employed involves the concept of the degree of matching between two two-dimensional patterns $P_1(x,y)$ and $P_2(x,y)$. The degree of matching between any two patterns $P_1(x,y)$ and $P_2(x,y)$ can be determined by their cross-correlation which is expressed mathematically as follows:

$$\gamma = \frac{1}{NS_1S_2} \iint (P_1(x,y) - \overline{P}_1)\,(P_2(x,y) - \overline{P}_2)\,dxdy \quad (1)$$

(a) γ is the cross-correlation between $P_1(x,y)$ and $P_2(x,y)$ $(0 \leq \gamma \leq 1)$

(b) $N = \iint dxdy$ is the area of integration which must contain both patterns

(c) $P_1(x,y)$ and $P_2(x,y)$ are the spatial distributions of the patterns under consideration

(d) $\overline{P}_1, \overline{P}_2$ are the average value of the fields $P_1(x,y)$ and $P_2(x,y)$ over the area N, i.e.:

$$\overline{P}_1 = \iint P_1(x,y)dxdy/N$$

(e) S_1, S_2 are the standard deviations of $P_1(x,y)$ and $P_2(x,y)$ over N, i.e.:

$$S_1 = [\iint (P_1(x,y) - \overline{P}_1)^2\, dxdy/N]^{1/2}$$

Let us now assume that a scheme is devised which simply delineates the rain area using a single infrared threshold (I). Given an infrared image, starting with some low threshold one can produce a series of rain areas by raising at each step the infrared threshold. Apparently, by raising the threshold the resulted rain area will become smaller and smaller. Let us denote these areas as $P(x,y,I)$.

In view of the foregoing facts, in cases of strong convection there will exist some $I = I_o$ for which $R(x,y,I_o) \simeq R_{Vo}(x,y)$. Under this condition, for $P_1 = R_{Vo}(x,y)$ and $P_2 = R(x,y,I_o)$, γ should be high. In addition, for $I > I_o \Rightarrow R(x,y,I) < R(x,y,I_o)$ and for $I < I_o \Rightarrow R(x,y,I) > R(x,y,I_o)$. Therefore, it follows that for $I \neq I_o$ the cross-correlation between $R(x,y,I)$ (for any I) and $R_{Vo}(x,y)$ will be lower than the cross-correlation between $R(x,y,I_o)$ and $R_{Vo}(x,y)$. If we denote as $\gamma_{Vo,I}$ the cross-correlation between $R_{Vo}(x,y)$ and $R(x,y,I)$ it should be expected that $\gamma_{Vo,I}$ as a function of I would present a maximum for $I = I_o$. The above can be visualized in Fig. 1. On the left hand side $R_{Vo}(x,y)$ indicates the rain area delineated by the optimum visible threshold according to the Tsonis and Isaac (1985) method from the satellite information on 2 May 1983 at 1730 GMT. The radar data indicates moderate to heavy precipitation at this time. On the right hand side of Fig. 1 rain areas determined by four different single infrared thresholds are shown. The cross-correlation between $R_{Vo}(x,y)$ and each one of $R(x,y,I)$ is also indicated. As can be seen from Fig. 1, $R(x,y,I)$ decreases in size as I increases, whereas the degree of matching between $R(x,y,I)$ and $R_{Vo}(x,y)$ (from equation (1)) increases attaining a maximum value for $I = I_o \simeq 184$. In nonconvective cases $R(x,y,I)$ (for any I) may deviate significantly from $R_{Vo}(x,y)$ and therefore $\gamma_{Vo,I}$ may not a) be as high and/or b) may not vary as a function of I in a similar fashion.

Therefore, the study of $\gamma_{Vo,I}$ may be beneficial in inferring rainfall rates or in discriminating between convective and nonconvective precipitation.

4. RESULTS

Figure 1 shows $\gamma_{Vo,I}$ as a function of I for nine selected cases which represent convective and nonconvective cases of various rainfall intensities. The classification into light, moderate and heavy rainfall corresponds to the radar rainfall rate intervals $0 \leq R \leq 2$ mmh^{-1}, $2 < R \leq 8$ mmh^{-1} and $R > 8$ mmh^{-1}, respectively. First, let us concentrate on the cases of 2 May 1983 at 1730 GMT and 4 July 1983 at 2230 GMT, which represent convective cases of (as indicated by the radar) moderate to heavy rainfall. In both cases $\gamma_{Vo,I}$ increases as I increases attains a maximum value (pointed by an arrow) for I = 184 and I = 196, respectively, and then decreases (because for higher I's, $R(x,y,I) \rightarrow 0$). Note that the observed maximum value of the cross-correlation is in both cases very high. Similar behavior can be observed in the case of 29 July 1983 at 1400 GMT, which represents a nonconvective case of predominantly moderate precipitation. Here again, $\gamma_{Vo,I}$ increases as I increases and attains a maximum value for I = 196. However, the magnitude of the maximum in this case is not as high. In all other cases (which represent either cases of weak convection or nonconvective cases) $\gamma_{Vo,I}$ decreases constantly as I increases.

From the available data 27 different cases were studied. Fourteen of those cases were convective cases, seven of which were associated with moderate to heavy rainfall and seven with light to moderate rainfall. The remaining cases were nonconvective cases, six of which were associated with predominantly moderate rainfall, four with light to moderate rainfall and three with light rainfall. Two or more cases from the same day were included in the sample only if there were at least three hours apart. This restriction on one hand limits the size of the sample to be studied but on the other hand minimizes the degree of dependancy in the sample. In all cases of moderate to heavy rainfall (convective or not) $\gamma_{Vo,I}$ increased with I and attained a maximum value for some I. However the magnitude of this maximum cross-correlation was, on the average, higher for the convective cases where it was found to range between 0.68 and 0.92 (mean value equal to 0.87). The corresponding range for the nonconvective cases was 0.52 - 0.72 (mean value equal to 0.64). For all cases of light to moderate rainfall (convective or not) $\gamma_{Vo,I}$ decreased as I increased. In view of the discussion above these findings do not come as a surprise and in a way they confirm the fact that the infrared images are not as effective as the visible images for rain area delineation in the

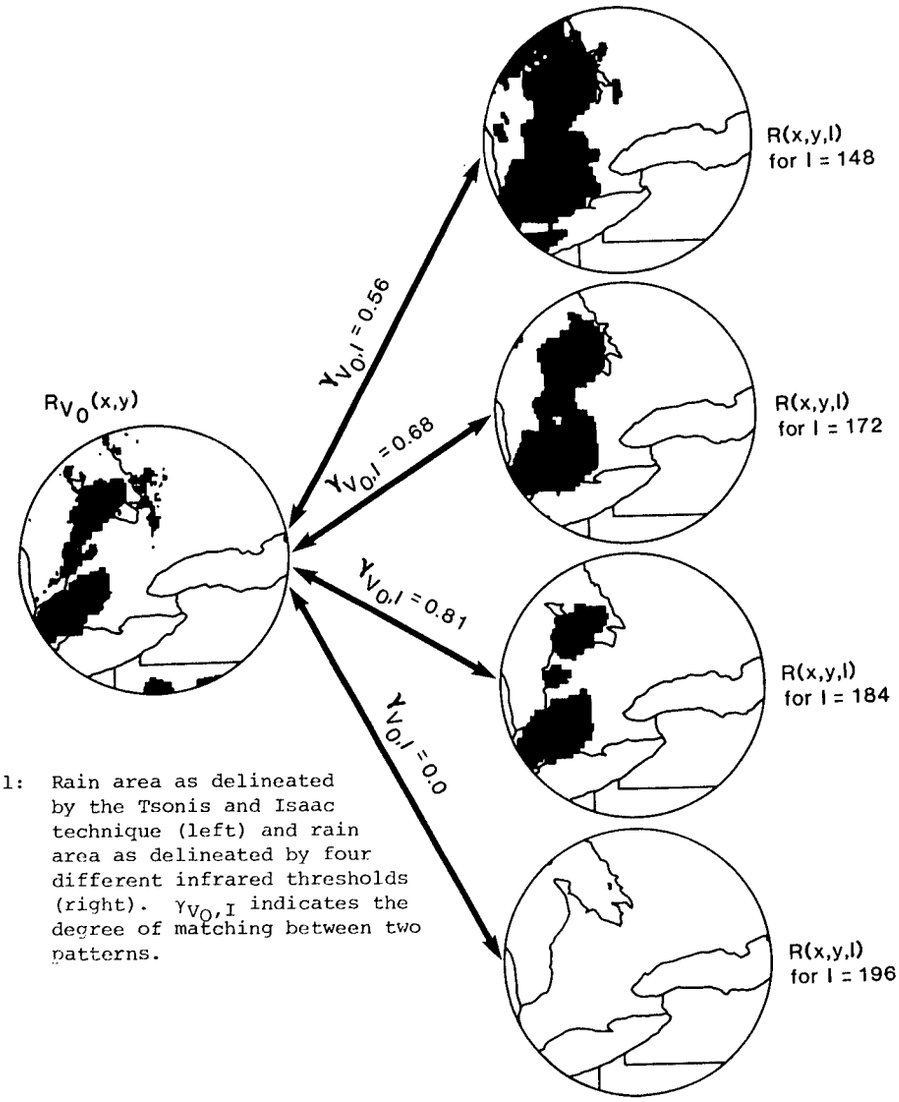

Fig. 1: Rain area as delineated by the Tsonis and Isaac technique (left) and rain area as delineated by four different infrared thresholds (right). $\gamma_{V_0,I}$ indicates the degree of matching between two patterns.

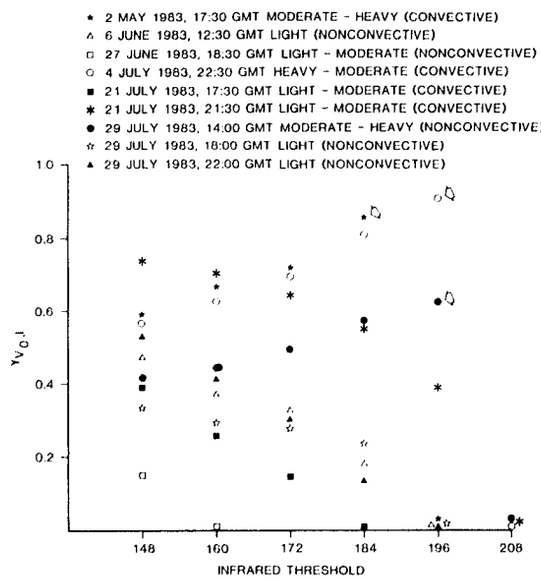

Fig. 2: $\gamma_{V_0,I}$ as a function of the infrared threshold for various precipitation types and intensities.

midlatitudes in cases of weak or no convection. However, they point out that 1) the behavior of $\gamma_{Vo,I}$ as a function of I may be useful in extracting some information of rainfall intensity and 2) in cases of moderate to heavy rainfall the magnitude of the maximum $\gamma_{Vo,I}$ may be a good discriminator between convective and nonconvective rainfall.

5. CONCLUSIONS

This study made use of the Tsonis and Isaac (1985) technique for rain area delineation in the midlatitudes using GOES data and presented an approach that may assist in the extraction of some rainrate information and the discrimination between convective and nonconvective cases. Both these problems are of great importance to researchers that would like to improve and maximize rainfall information from satellite imagery. The results of this study are still preliminary. Their clarity, however, suggests that further analysis and the accumulation of larger sample statistics, and their extension to larger areas should be encouraged.

REFERENCES

1. Barrett, E.C. and D.W. Martin, 1981: The Use of Satellite Data in Rainfall Monitoring. Academic Press, New York, 340 pp.

2. Griffith, G., W.L. Woodley, P.G. Grube, D.W. Martin, J. Stout and D.N. Sikdar, 1978: Rain estimation from geosynchronous satellite imagery - visible and infrared studies. Mon. Wea. Rev., 106, 1153-1171.

3. Lovejoy, S. and G.L. Austin, 1979: The delineation of rain areas from visible and IR satellite data for GATE and midlatitudes. Atmos-Ocean, 17, 77-92.

4. Scofield, R.A. and V.J. Oliver, 1977: A scheme for estimating convective rainfall from satellite imagery. NOAA Tech. Memo. NESS 816, 47 pp.

5. Stout, J.E., D.W. Martin and D.N. Sikdar, 1979: Estimating GATE rainfall with Geosynchronous Satellite Images. Mon. Wea. Rev., 107, 585-598.

6. Tsonis, A.A., 1984: On the separability of various classes from the GOES visible and infrared data. J. Climate Appl. Meteor. 23, 1393-1410.

7. Tsonis, A.A. and G.A. Isaac, 1985: On a new approach for instantaneous rain are delineation in the midlatitudes using GOES data. J. Climate Appl. Meteor., 24, 1208-1218.

8. Wu, R., J.A. Weinman and R.T. Chin, 1985: Determination of rainfall rates from GOES satellite images by a pattern recognition technique. J. Atmos. Oceanic Technology, 2, 314-330.

P4.28

EFFECTS OF CONVECTIVE TYPE CLOUDS ON HEAVY SNOW AS VIEWED BY GOES SATELLITE IMAGERY

Samuel K. Beckman

Satellite Field Services Station
National Severe Storms Forecast Center
Kansas City, Missouri 64106

1. INTRODUCTION

The purpose of this paper is to demonstrate the usefulness of operational half-hourly near-real time GOES IR satellite imagery in following convective type clouds (generally with a report of thunder) which move northward into the colder baroclinic environment and produce heavy snow (termed "snowburst" in this paper). The intent of this paper is not to discuss various heavy snow forecast techniques. It is assumed that the necessary parameters are in place and the forecaster knows in advance where the liquid/frozen dividing line is located. Observations of many different snow cases by satellite imagery at the SFSS (Satellite Field Services Station) have shown the 850mb 0C isotherm and 500-1000mb thicknesses around 540dm to be very valuable in delineating the liquid/frozen precipitation line over the central United States. The added vertical motion and deepening of the moist layer by the convective type clouds result in a rapid snow increase with likely, brief, accumulations of 2 to 3 inches (25-80 mm) per hour.

There has been little information published on a direct link between thunder and snow occurrences. A short paper by Curran and Pearson (1971) examined proximity soundings for snow with thunderstorms. Their study, which looked at only 3 hr surface observations for three seasons, found just 76 reports of thunder with snow. RAOBS close to these occurrences showed a deep moist layer and rather high instabilities. A later paper by Galway and Pearson (1981) presents the envelopes of tornado outbreaks and heavy snow relative to the mean surface low track but do not mention any possible relationships in the frontal zone between these two events. Parmenter (1972) was one of the first to study winter cloud patterns in satellite imagery and noted the more significant precipitation (rain/snow) was associated with convective type clouds poleward of the upper jet in the northeast quadrant of east coast cyclones. The polarorbiting satellite imagery used in the study limited observations to only twice a day. Recently, Kocin, et. al. (1985) demonstrated the ability of a mesoscale numerical forecast model to simulate a convective snowburst in the Washington, D.C. - Baltimore, Md areas. They found that the three-hourly output from these models is a valuable aid to forecasters in understanding and predicting mesoscale phenomenon.

The past few years meteorologists at the Kansas City SFSS have found near real-time operational GOES visible and IR satellite imagery to be a valuable tool to help explain heavy snowbursts in winter precipitation events. The imagery have been most useful in identifying and tracking convective-type clouds. The thunder initially associated with these clouds may continue to be heard at the time of heavy snow, well into the cold air. However, this may not always be the case. It will be shown in this paper that continuity in the half hour GOES imagery indicates that the clouds producing the snowburst may have been originally associated with thunder but the mechanism generating thunder weakened as the clouds moved northward into the colder air mass.

The thunderstorms generally form in a marginally unstable, but moist, air mass near or south of the cold front. Positive vorticity advection with a mid-tropospheric shortwave trough and moderate to strong low/mid level warm air advection are found to be necessary ingredients for the convective type cloud development. There have been enough of these events documented in the GOES satellite imagery during the past couple of years to indicate it is a common rather than a rare occurrence and there is a definite link between snowbursts and convective type clouds. The different cases also suggest a seasonal and possible diurnal trend.

Thunder and heavy snow events have been observed most often during the early and late parts of the cold season (Oct., Nov., Mar., Apr.) over the Northern Plains and Upper Mississippi Valley. During this time of year, there is ample low-level warm air advection and strong dynamics in the cold air aloft to generate sufficient vertical motion and instability for thunder. In the middle of the cold season (late Dec. into early Feb.), thunder accompanying heavy snow is infrequent except in unusually strong

deepening systems when adequate moisture and instability are present. The prime area for this to occur is from Arkansas northeast into the Middle Mississippi and Lower Ohio Valleys. Some of the record breaking heavy snow with storm totals as high as two feet (600 mm) have occurred during the past few years in these cases. An example will be presented in the next section. Since the prime function of the Kansas City SFSS is to interpret GOES satellite imagery over the central United States, all cases are from this area.

2. PRESENTATION OF CASES.

Three examples will be presented. The first will describe an early season ice and snow episode when thunder was reported with ice pellets and freezing rain but not with the heavy snow event. The next two examples will show joint thunder and heavy snow occurrences. Both are typical cases; One with a shortwave trough over the Northern Plains and the other with a deepening storm in a frontal zone over the Mid-Mississippi and Lower Ohio Valleys. The cases are introduced from the perspective of the operational forecaster by showing how the cloud features can be monitored in the continuous near real-time GOES imagery.

A. Event of 30 Nov. - 1 Dec. 1985.

During the afternoon of 30 November 1985, a stationary front lay from the Lower Great lakes to west Texas (Fig. 1). There was a strong thermal contrast across the front with surface dew point temperatures reaching the mid 50'sF (10 to 15C) into southeast Oklahoma and central Arkansas while just north of the front the surface temperatures rapidly decreased below freezing.

By 2100 GMT (Fig. 2a), a line of thunderstorms developed along the west edge of low level moisture ahead of a cold front in east Oklahoma. Because of the low sun angle, the Cb tops were well defined in visible imagery (Fig. 2b). The cells expanded northward across extreme east Kansas during the next couple of hours. Thunder and moderate intensity ice pellets (a mixture of frozen rain/snow which is colloquially called sleet in some parts of the United States) were reported in the Kansas City area at 2300 GMT (A, Fig. 2c).

An analysis of 0000 GMT upper air data via CSIS (Centralized Storm Information System; Anthony et. al.,1982) indicated a combination of mid-tropospheric positive vorticity and warm air advection were contributing to upward vertical motion across Missouri and Iowa. The 850mb and 700mb warm air advection were both maximized over Missouri and Iowa (Fig. 3a,b). Although rather weak, 500mb positive absolute vorticity advection was present over this area (Fig. 3c). The vorticity advection was strongest at the 400mb level (Fig. 3d).

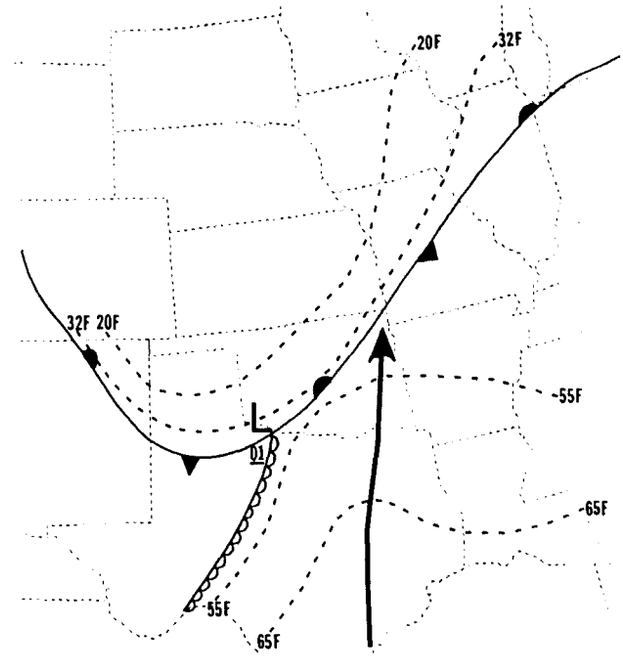

Fig. 1. Surface analysis for 2100 GMT, 30 Nov. 1985. Dash lines are isodrosotherms; Dotted lines isotherms.

Although thunder was not heard at any of the regular reporting stations north and east of Kansas City, the very cold cloud tops, which were associated with the earlier thunder, could be tracked in the satellite imagery during the evening across northern Missouri into central and east Iowa (Fig. 2d-f). Moderate snow with rates of around 1 inch (25 mm) per hour began near the leading edge of very cold cloud tops (black or around -60C) along and north of the 850mb 0C isotherm (dash line in Fig. 2d). Snowbursts with accumulations of 2 inches (50 mm) per hour were reported near the back edge of coldest cloud top temperatures. Snowfall totals were 4-6 inches (100-150 mm) in a band from just south of Des Moines (A) to just east of Waterloo (B, Fig. 2f).

B. Event of 19 Oct. 1982.

As frequently the case during the fall and spring, the first few polar outbreaks produce a variety of precipitation as the weather changes from thunderstorms and rain to ice and snow. In this example, thunder was reported with the moderate and heavy intensity snow in the frontal zone ahead of a shortwave trough moving eastward into the north and central plains. One of the first visible satellite images showed well-defined convective cloud tops in east and central Nebraska (fig. 4a). Moderate snow was occurring from north central Nebraska into eastern South Dakota. Thunder was reported in a band to the south from south central through northeast Nebraska.
The colder thunderstorm tops were well marked in the IR imagery from Grand Island to Norfolk (A-B, Fig 4b).

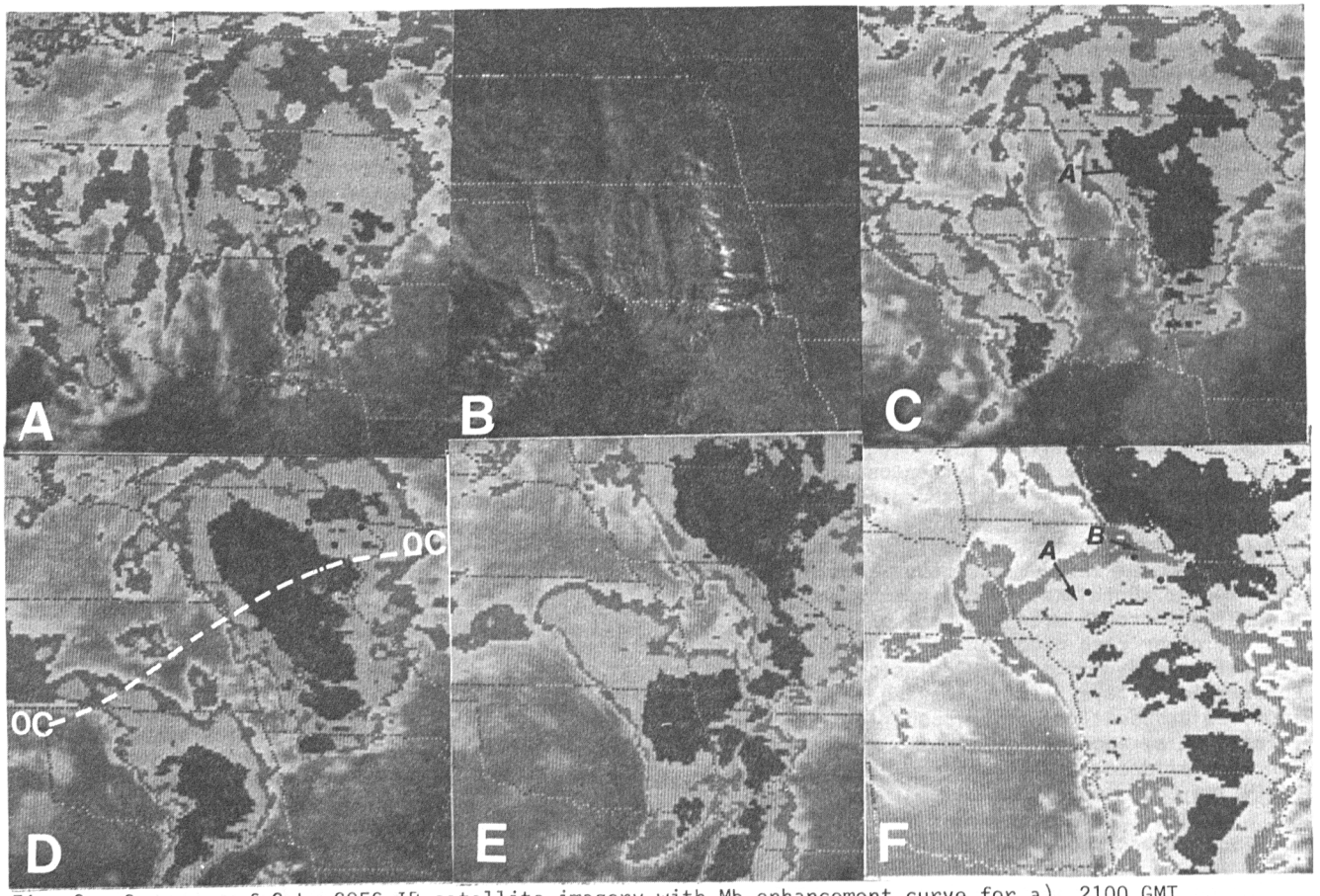

Fig. 2. Sequence of 2 km GOES IR satellite imagery with Mb enhancement curve for a) 2100 GMT b) 2130 GMT (visible) c) 2300 GMT d) 0100 GMT e) 0300 GMT f) 0600 GMT.

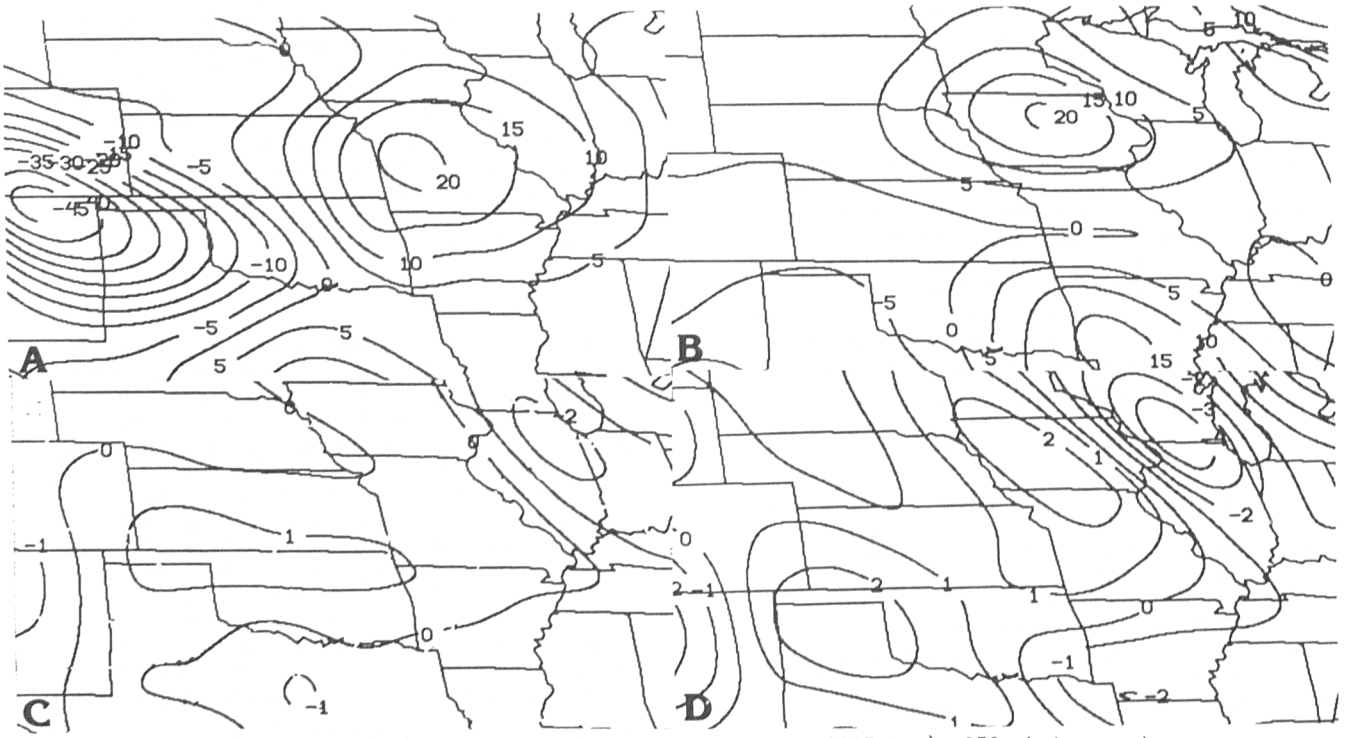

Fig. 3. CSIS analyzed upper air parameters for 0000 GMT, 1 Dec. 1985. a) 850 mb temperature advection (°C per 24hr) b) 700 mb temperature advection (°C per 24hr) c) 500 mb absolute vorticity advection d) 400 mb absolute vorticity advection.

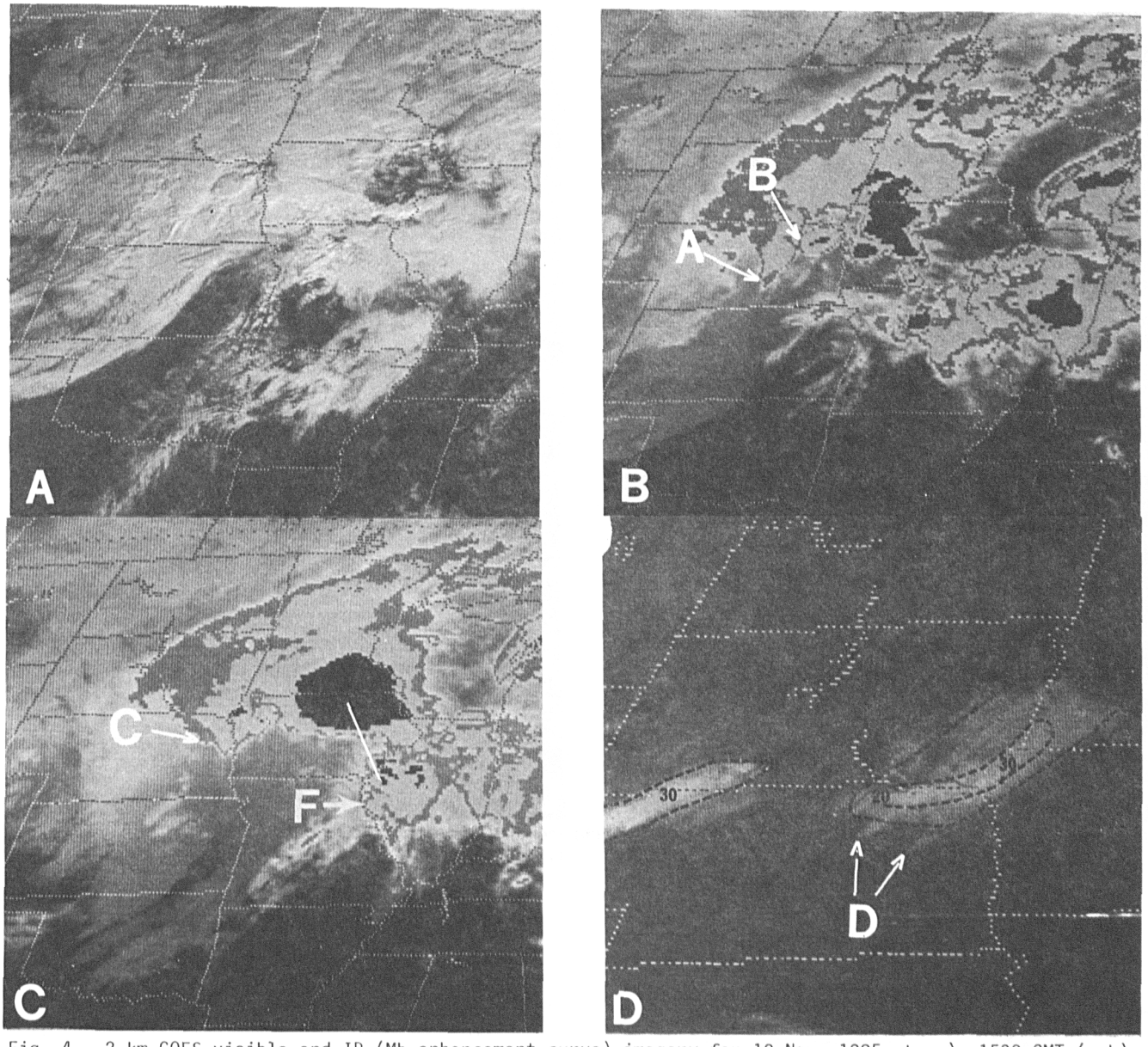

Fig. 4. 2 km GOES visible and IR (Mb enhancement curve) imagery for 19 Nov. 1985 at a) 1530 GMT (vsb). b) 1600 GMT (IR). c) 1900 GMT (IR). d) visible imagery at 1900 GMT, 21 Nov. 1985.

During the next three hours the thunderstorms developed northeastward into the southeast corner of South Dakota and northwest Iowa (Fig. 4c). The thunder was accompanied by brief moderate and heavy snowbursts which accumulated at the rate of 2 inches (50 mm) per hour. The snow was very wet and heavy resulting in many reports of broken tree limbs and power failures especially from the Norfolk area (C) northeastward. The band where the heaviest snow occurred was well defined in visible imagery a couple of days after the clouds cleared (Fig. 4d). Surface temperatures were around freezing when the initial snow fell and some melting undoubtedly occurred after that time. A couple of remaining narrow snow streaks (D) were probably associated with thunderstorm clusters which redeveloped discontinuously eastard. The clusters then slipped eastnortheast along a favorable thickness gradient over the same area resulting in the band of heavy snow. A cluster of thunderstorms in western Illinois moved northeast and aided snow increase later in the evening over northern Wisconsin.

C. Event of 30 - 31 Jan. 1982.

Beginning the evening of the 30th, thunderstorms developed in the low-level moist tongue (> 8 g/kg at 850mb) near the low-level jet (> 50kt, 25 m s^{-1}) over western Louisiana and central Arkansas. The LFM initialized a 22 unit absoulte vorticity maximum in west central Texas. The geostrophic temperature advection charts at 850 and 700mb (Fig. 5) showed a large area of positive warm air advection from the Lower Mississippi into the Ohio and Tennessee Valleys with strong (>6°C h^{-1}X10^{1}) centers near the mouth of the Ohio and Tennessee rivers.

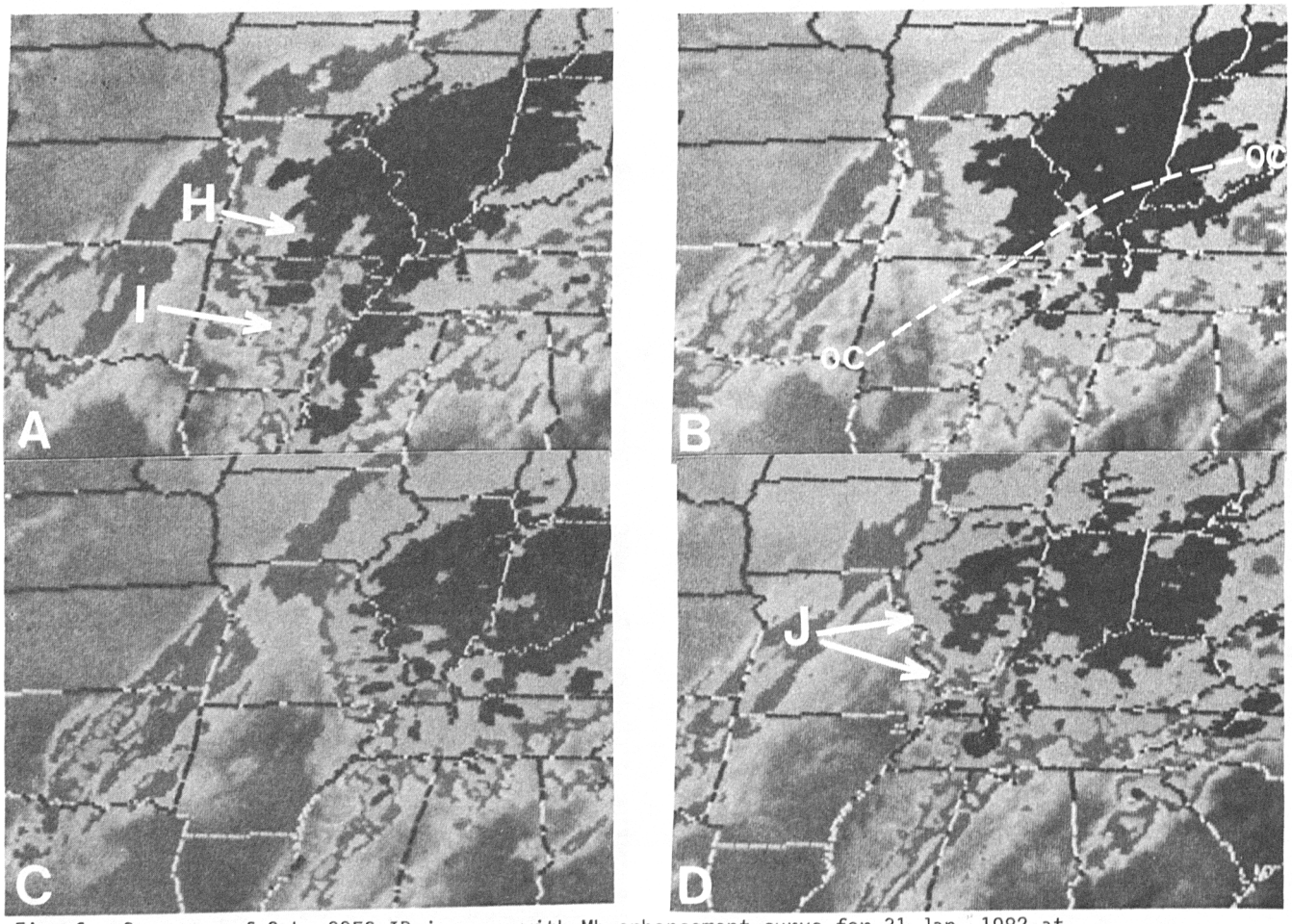

Fig. 6. Sequence of 2 km GOES IR imagery with Mb enhancement curve for 31 Jan. 1982 at a) 0515 GMT. b) 0700 GMT. c) 0900 GMT. d) 1030 GMT.

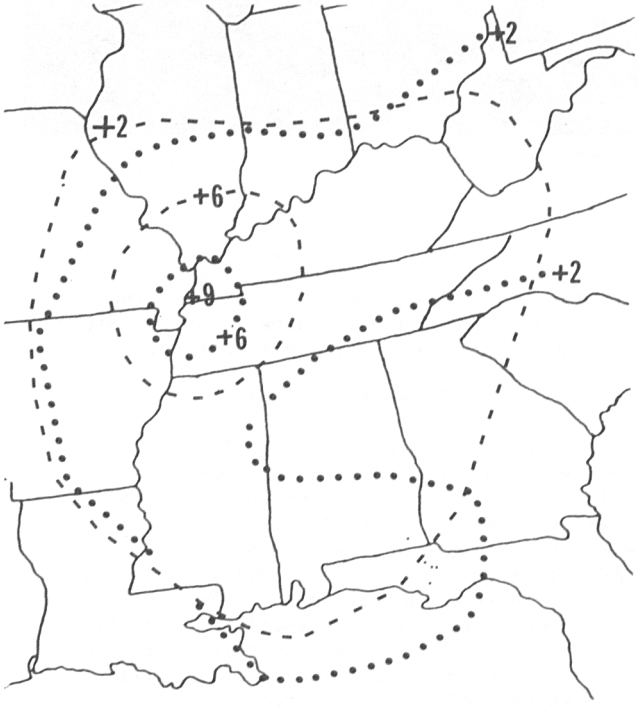

Fig. 5. Geostrophic temperature advection for 0000 GMT, 31 Jan. 1982 at 850 mb (dash) and 700 mb (dot).

By midnight local time (Fig. 6a), a surface wave was developing in eastern Arkansas. A line of thunderstorms was well defined in satellite imagery along the Mississippi River from St. Louis to east Louisiana. Moderate rain was falling from southeast Missouri and southern Illinois southward with thunder and heavy snow reported just to the north in east central Missouri and south central Illinois. A second line of thunderstorms was also developing at this time from south central Missouri into central Arkansas (H-I). Although there are no regular hourly surface reporting stations over this area at this time of night, thunder with moderate to heavy rain and snow should be expected based on what was known to be occurring in the line to the east.

Thunder and heavy snow showers were reported as the second line moved east into the St. Louis area between 0700 and 0900 GMT (Fig. 6b,c). The dash line is the 850 mb 0C isotherm. Snowfall rates of 2-3 inches (50-80 mm) occurred during this time with storm totals of 12 to 22 inches (300-550 mm) in a band from south central Missouri eastnortheast across south central Illinois into central Indiana. The snow decreased to

light intensity with the passage of the west edge of enhanced clouds (J, Fig. 6d) across Illinois during the morning. The thunder accompanying the snow undoubtedly contributed to the heavy accumulations which virtually paralyzed the area.

3. SUMMARY.

This paper has demonstrated the usefulness of near real-time GOES IR and visible satellite imagery to monitor local areas of heavy snow. The snowbursts are related to convective-type clouds which are usually accompanied by thunder. Snowfall rates of 2-3 inches (50-80 mm) per hour are common. The GOES satellite imagery is most useful over sparce reporting areas, especially at night, when a number of stations close.

The air mass in these cases is very moist with strong low and mid level warm air advection across the frontal zone ahead of an approaching mid-tropospheric shortwave trough. The thunder develops in the marginally unstable air on the north end of a widespread thunderstorm line or area which reaches across the below freezing temperatures near the surface. There have been enough cases during the past few years to suggest further study on a diurnal tendency and possible more direct link to the establishment of the low-level jet. If short range numerical output from a mesoscale model were available as described by Kocin et. al. (1985), this information could supplement the forecast routine.

4. REFERENCES.

Anthony, R.W., W.E. Carle, J.T. Schaefer, R.L. Livingston, A.L. Siebers, F.L. Mosher, J.T. Young and T.W. Whittaker, 1982: The Centralized Storm Information System at the NOAA Kansas City complex. Preprints. 9th Conf. Wea. Fcstg. and Analysis, Amer. Meteor. Soc., Seattle, Wa. 40-43.

Carr, F.H., and J.P. Millard, 1985: A composite study of comma clouds and their association with severe weather over the Great Plains. Mon. Wea. Rev., 113, 370-387.

Curran, J.T. and A.D. Pearson, 1971: Proximity soundings for thunderstorms with snow. Preprints. 7th Conf. Severe Local Storms, Kansas City, Mo, Amer. Meteor. Soc. 118-119

Galway, J.G. and A.D. Pearson, 1981: Winter tornado outbreaks. Mon. Wea. Rev., 109, 1072-1080.

Kocin, P.J., L.W. Uccellini, J.W. Zack, and M.L. Kaplan, 1985: A mesoscale numerical forecast of an intense convective snowburst along the east coast. Bull. Amer. meteor. Soc.,66, 1412-1424.

Parmenter, F.C., 1972: Use of satellite data in east coast snowstorm forecasting. NOAA Tech Memo NESS 33 U.S. Dept. of Commerce, 21pp.

Scofield, R.A. and L.E. Spayd Jr., 1984: A technique that uses satellite, radar and conventional data for analyzing and short-range forecasting of precipitation from extratropical cyclones. NOAA Tech Memo NESDIS 8 U.S. Dept. of Commerce, 51pp.

A CUMULUS CLOUD FIELD OBSERVED BY LANDSAT THEMATIC MAPPER

Ross N. Hoffman and Ronald G. Isaacs

Atmospheric and Environmental Research, Inc.
Cambridge, MA 02139-3758

1. INTRODUCTION

A considerable effort has been devoted to characterizing the spatial properties and spectral signatures of terrestrial clouds. These efforts have been hampered by the scarcity of sufficient observational data sets. A unique opportunity to investigate the retrieval of cloud properties is thus afforded by the high resolution, high quality, multispectral, calibrated data sets available from the Landsat 4 Thematic Mapper (TM). These data are currently archived by EOSAT. We have begun a study of the determination of cloud properties from TM data by combining a spatial coherence scene model with other cloud parameter retrieval methods. This report focuses on the scene model. The TM has seven spectral bands, which in principle allow cloud amount, height, phase and thickness to be retrieved. Cloud particle size may also be retrievable. The scene model accounts for partial beam filling, identifies homogeneous areas in the scene, and effectively composites the entire scene for ensuing cloud parameter retrievals.

Landsat 4 was placed into orbit in July 1982. The TM was designed to achieve finer spatial resolution, sharper spectral separation, improved geometric fidelity, and greater radiometric accuracy and resolution than previous sensors (see Table 1). The Landsat series of satellites has been designed primarily to view the earth's surface rather than the earth's clouds. This is in contrast to meteorological operational satellite systems, such as the polar-orbiting NOAA and DMSP satellites and the geosynchronous GOES satellites, which are designed primarily for meteorological purposes. A major difficulty in this regard is that clouds are so reflective in the visible that they often saturate the TM sensor. Nevertheless, it is obvious that the Landsat images display a considerable amount of information relevant to meteorology.

2. LOCAL UNSATURATED STATISTICS

The effects of saturation in the visible channels 1-5 make the interpretation of sensitive statistics difficult. Therefore, we calculated some local statistics in which the various sample sums are replaced by sums all over all unsaturated pixels. For statistics involving two channels, all sums are replaced by sums over pixels which are unsaturated for both channels. We term such statistics unsaturated statistics. Examination of some of the local unsaturated statistics lead us to new approach to the problem which we call scene modeling. We used data from LANDSAT TM scene for August 30, 1982, path 15, row 38, south of Cape Hatteras. Scene center is N 31° 44' by W 78° 54', sun elevation angle is 53, and sun azimuth angle is 122. This scene shows scattered maritime cumulus. Local unsaturated means, standard deviations, and correlations in counts for all channels were calculated for subscenes (1 km^2) in area (33 × 33 pixels). Further details are reported by Hoffman et al. (1985). In particular, three subscenes -- denoted 1A, 1B, and 1C, which were chosen to be cloudy, clear, and partly cloudy -- will be referred to further.

Table 1. Comparison of LANDSAT TM and other current imaging sensors.

	TM (Engel and Weinstein, 1983)	MSS	AVHRR (NOAA, 1981)
Spacecraft	LANDSAT 4	LANDSAT 4	TIROS/NOAA
Orbit	Polar	Polar	Polar
Wavelength (μm)			
Channel 1	0.45-0.52	0.50-0.60	0.58-0.68
2	0.52-0.60	0.60-0.70	0.725-1.1
3	0.63-0.69	0.70-0.80	3.55-3.93
4	0.76-0.90	0.80-1.10	10.5-11.3
5	1.55-1.75		11.5-12.5
6	10.30-12.50		
7	2.08-2.35		
Resolution at Nadir (m)			
Visible	30	82	1100
IR	120		1100

In brief, the outstanding local statistical characteristics of the Hatteras Scene, when the effects of saturation are removed, are the following:

1) There are distinctive mean spectra for the ocean and clouds.

2) There is very little variability of the observed ocean spectra.

3) In cloudy parts of the scene, there is very little variability for the thermal

channel indicating nearly constant cloud top heights, but a large variability in the visible and NIR channels remains. These channels are extremely well correlated in such cases.

4) Along the cloud-ocean boundary, all channels are highly correlated. The thermal channel is somewhat less well correlated with the others.

3. MODELING THE SCENE

3.1 A Simple Scene Model

We will show that the following simple model accounts for the features enumerated at the end of the last section. We model the observed radiances in terms of the ocean and cloud spectra, the cloud fraction and a geometric factor. The algorithm described here retrieves these quantities from the observations. For the moment, we ignore the effects of saturation (see Section 3.2).

The model for the thermal channel includes contributions to the emitted radiation from the ocean and cloud each weighted by their fractional coverage, i.e.,

$$R_{in} = (1 - f_n)B_i + f_n A_i \qquad (1a)$$

where R_{in} = observed radiance in channel i at pixel n,
B_i = sea surface radiance in channel i,
A_i = cloud radiance in channel i,
f_n = cloud fraction at pixel n.

A_i and B_i include the atmospheric contribution to radiance. In this section, all radiances will be normalized radiances, i.e., R = 0 or 1 corresponds to a recorded digital count of 0 or 255, respectively. The A_i and B_i are also defined in terms of these units.

In the visible and NIR channels, radiation is reflected or backscattered by the clouds. These processes are affected by the cloud geometry because real clouds are neither flat nor infinite in horizontal extent. Therefore, we include a geometric factor γ in our model of these channels,

$$R_n = (1 - f_n)B_i + f_n(1 + \gamma_n)A_i \ . \qquad (1b)$$

We will relate γ_n to the cloud top incidence angle although the retrieved value of γ_n is probably also influenced by the effect on multiple scattering of the distance of pixel n from the cloud edge.

To relate γ_n to the cloud top geometry, note that the amount of solar radiation intercepted by each pixel depends on how the cloud is oriented. As can be seen in Fig. 1, the ratio of the solar flux striking the inclined cloud to that striking a horizontal cloud is

$$\frac{I + A}{A} = 1 + \frac{\tan i}{\tan a}$$

where a, the elevation angle of the sun, is almost uniform over the scene, but i, the inclination angle of the cloud, varies from pixel to pixel. Since the cloud is probably close to a Lambertian reflector, the simplest model, given above, is used for these channels.

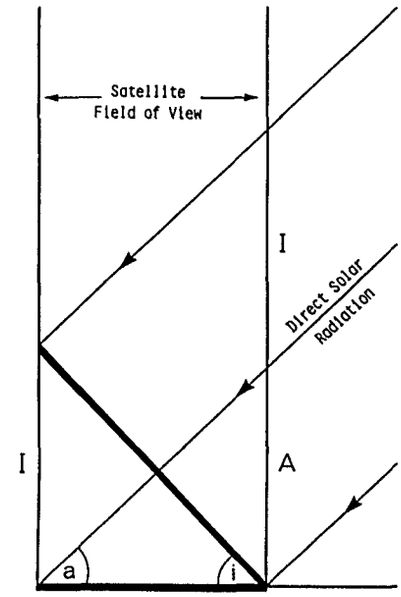

Fig. 1. Geometric factor due to cloud inclination angle i.

Although we will explore the ability of this simple model to explain the scene in some detail, we first note some of its deficiencies.

a) Cloud top height varies, so cloud top temperature should change with cloud top height. Our model assumes cloud top and sea surface temperatures are constant. We could formulate the problem so that these properties vary smoothly or depend on cloud fraction.

b) The effective inclination angle i is probably different for the NIR channels and for the visible channels since the correlations between these groups of channels are not as high as within these groups.

c) Cloud shadows should affect the sea surface radiance observed in the visible. Also sea state and sunglint are potential problems. More complex models might be formulated but should explain a significant part of the variance unexplained by the simpler model.

3.2 Constraints

When we fit model (1) by our nonlinear least squares method, we must constrain the solution to be physically realizable, eliminate multiple solutions where possible,

and account for the effect of sensor saturation.

We require that cloud fraction satisfy $0 < f_n < 1$. This is accomplished by using x_n as an independent variable which is not constrained, and defining

$$f_n = \frac{1}{2}(1 - \cos x_n).$$

For the reflective bands, we do have one degree of freedom in choosing the A_i and γ_n, because in the model the cloudy contribution is always proportional to $(1 + \gamma_n)A_i$. To eliminate the multiplicity of solutions implied by this degree of freedom, we constrain our solution as described below by our definition of S_γ.

Saturation effects must be included in our model. If R_{in}, as calculated from the above model, is greater than one, it must be reset to one. For the purpose of minimization, a continuous, infinitely differentiable approximation to this piecewise linear function is used to calculate the saturated value R^*_{in} (that is, the modeled value which includes saturation effects) as

$$R^*_{in} = 1 + \exp(-R^p_{in})(R_{in} - 1). \qquad (2)$$

In work presented here, p = 50, which yields very close agreement with the piecewise linear function.

3.3 Optimization Methodology

Since our model is nonlinear, it must be fit by an iterative least squares procedure. The number of free parameters is large, O(2N), where N is the number of pixels. Therefore, we use a conjugate gradient minimizer. We must also provide some reasonable initial estimates of the parameters.

We fit our model by determining A_i, B_i, x_n, and γ_n to minimize the total sum of squares,

$$S_T = \mu_R S_R + \mu_\gamma S_\gamma$$

where the sum of squares due to lack of fit of model (1) is

$$S_R = \sum_i \mu_i S_i$$

and the sum of squares due to the geometric factor is

$$S_\gamma = \mu_{\gamma 2} S_{\gamma 2} + \mu_{\bar{\gamma}} S_{\bar{\gamma}} .$$

The component sums of squares are

$$S_i = \sum_n w_n \left(R^*_{in} C_{max} - C_{in}\right)^2$$

$$S_{\gamma 2} = \sum_n \tilde{w}_n f_n \gamma_n^2$$

$$S_{\bar{\gamma}} = \left[\sum_n \tilde{w}_n f_n (\gamma_n - \gamma_0)\right]^2 .$$

The weight factors μ are constants which reflect the importance of the component sums of squares. The μ may be tuned to adjust the fit.

In the above expressions, R^*_{in} is the modeled radiance for channel i at pixel n obtained from (1) and (2), w_n is the weight associated with pixel n, $\tilde{w}_n$ is the area associated with pixel n, C_{max} is the saturation value of the instrument, and C_{in} is the observed counts for channel i at pixel n. In this work, w_n and $\tilde{w}_n$ are always both taken to be unity. Note that S_γ removes the degree of freedom associated with the γ_n which was discussed above. Ordinarily, $\gamma_0 = 0$.

The conjugate gradient algorithm requires estimates of the gradient, i.e., the vector of partial derivatives of S_T with respect to the independent variables A_i, B_i, x_n, and γ_n. Previous experience (Hoffman, 1982, 1984) suggests that finite difference approximations of the gradient are inefficient. We have, therefore, developed software to calculate the exact analytical partial derivatives. This is straightforward but requires extensive use of the chain rule.

3.4 Initial Estimates

The conjugate gradient algorithms also requires an intial estimate of A_i, B_i, x_n, and γ_n. We found in preliminary experiments that the conjugate gradient method converged slowly, and that, for the sake of efficiency, a good initial estimate is desirable. The approach we have taken to accomplish this is to solve a series of linear least squares problems using the current estimates of some parameters to refine the estimates of the same or other parameters.

4. ONE-DIMENSIONAL SIMULATION STUDY

To test our method and to provide by way of example some insight into our results, we conducted a one-dimensional simulation study. For this purpose, we simulated radiances (in digital counts) by using Eqs. (1a) and (1b), adding measurement error and then resetting values greater than the saturation value to 255. For the results shown here, the added errors were zero mean uncorrelated Gaussian noise with standard deviations of 10 counts for the reflective channels and 2.5 counts for the thermal channel. The simulated radiances (scaled by C_{max}) for channel 3 (a representative reflective channel) and channel 6 (the thermal channel) are shown in Fig. 2. The abscissa in these plots is $x_n = (n - 1)\Delta x$ with $\Delta x = 30$ m. The values of A_i and B_i are given in Table 2 and f_n and γ_n are shown in Fig. 3. Values of γ_n for $f_n = 0$ ($x_n < 1500$) are arbitrary. The corresponding retrieved values, after 300 iterations, are shown in Fig. 4. Fig. 5 shows the fit for channels 3 and 6. Since there are no horizontal

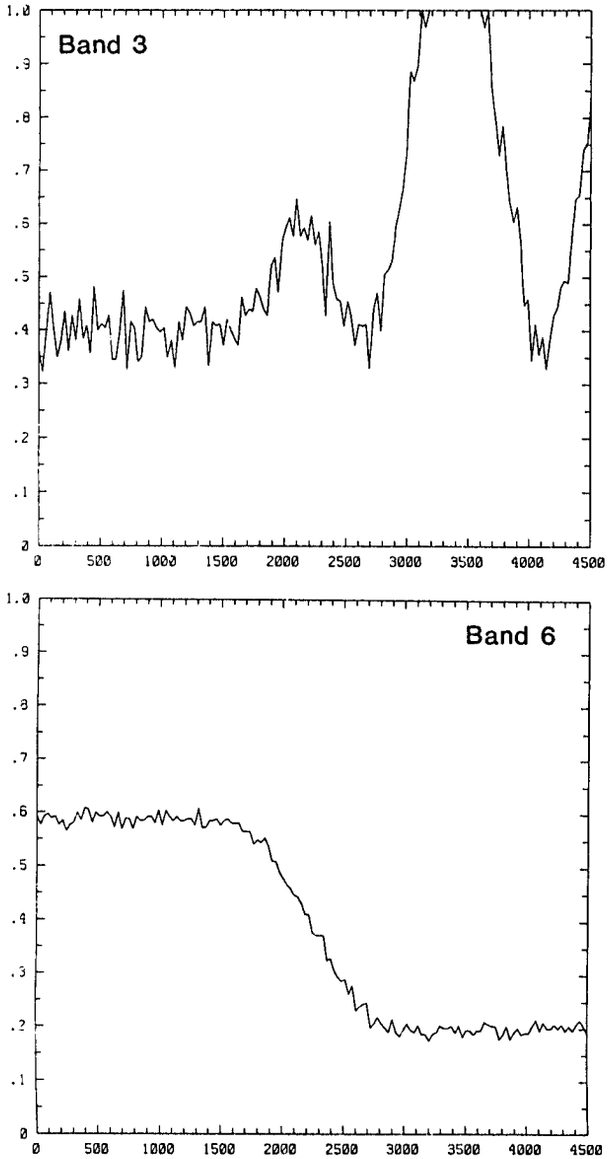

Fig. 2. Simulated, scaled, 1-D radiances for channels 3 and 6 with observational errors added.

Table 2. Values of parameters A_i, B_i (multiplied by 255) for the 1-D simulation study.

i	True A_i	True B_i	After 300 Iterations A_i	After 300 Iterations B_i	Optimal Reset A_i
1	250	150	224	149	249
2	225	125	204	127	226
3	200	100	179	101	199
4	175	75	157	74	175
5	150	50	134	50	149
6	50	150	47	153	47
7	125	25	114	22	127
S_T	184522		75169		

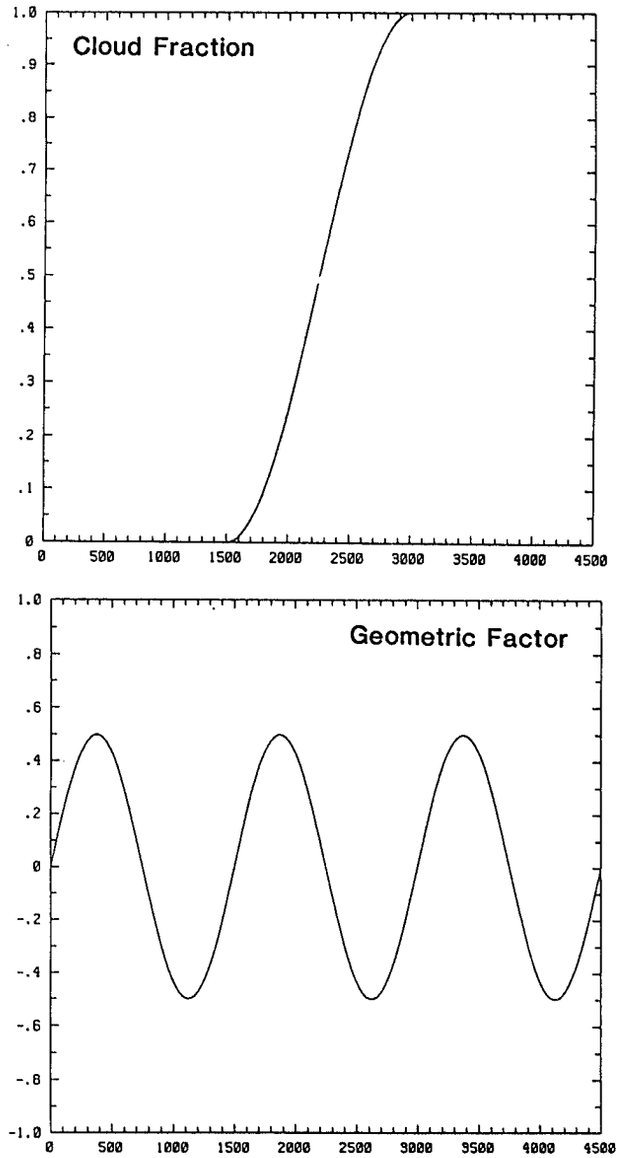

Fig. 3. Cloud fraction (f_n) and geometric factor (γ_n) used to simulate 1-D data.

homogeneity constraints, the fit is noisy but somewhat less noisy than the original data in the reflective channels. The retrieved values of A_i and B_i are also shown in Table 2. The cloud spectra (i.e., the A_i) do not agree as well as hoped. This results because the geometric constraint is not precisely correct. If γ_n and A_i are reset to give a best fit to the true A_i, very good agreement is obtained (last column of Table 2).

5. RESULTS

We have only performed initial real data testing of our method. The results presented here are limited to Subscene 1C. These data are shown in Fig. 6 for channels 3 and 6.

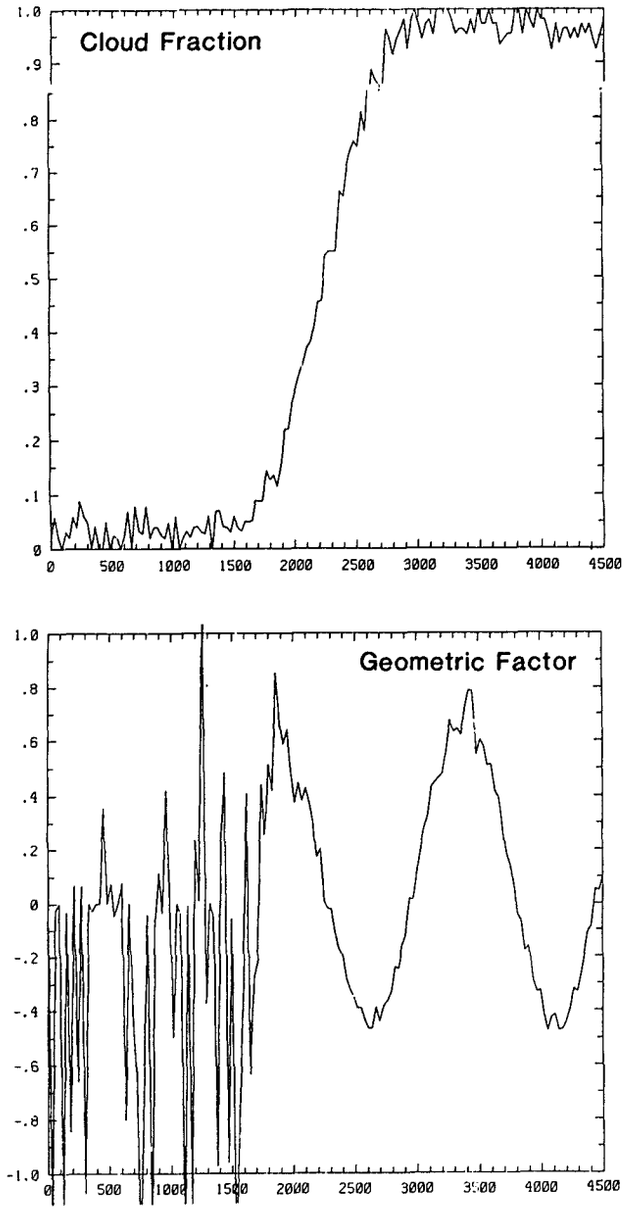

Fig. 4. Retrieved values of cloud fraction (f_n) and geometric factor (γ_n) after 300 iterations.

The overall fit obtained is quite good. The fit in channel 6 corresponds to an rms error of about 2 counts. The fits in the other channels correspond to errors which range from 7 to 12 counts in an rms sense. The final values of the parameters A_i and B_i are shown in Table 3, and the final values of f_n and γ_n are plotted in Figure 7. The spectra obtained differ somewhat from the local average spectra in subscenes 1A and 1B. In part, these discrepancies may be due to viewing angle.

More detailed discussion of these results is given in Hoffman et al. (1985). Note that the objective function, S_T, used by Hoffman et al., has been improved upon slightly in this work. Small changes to the

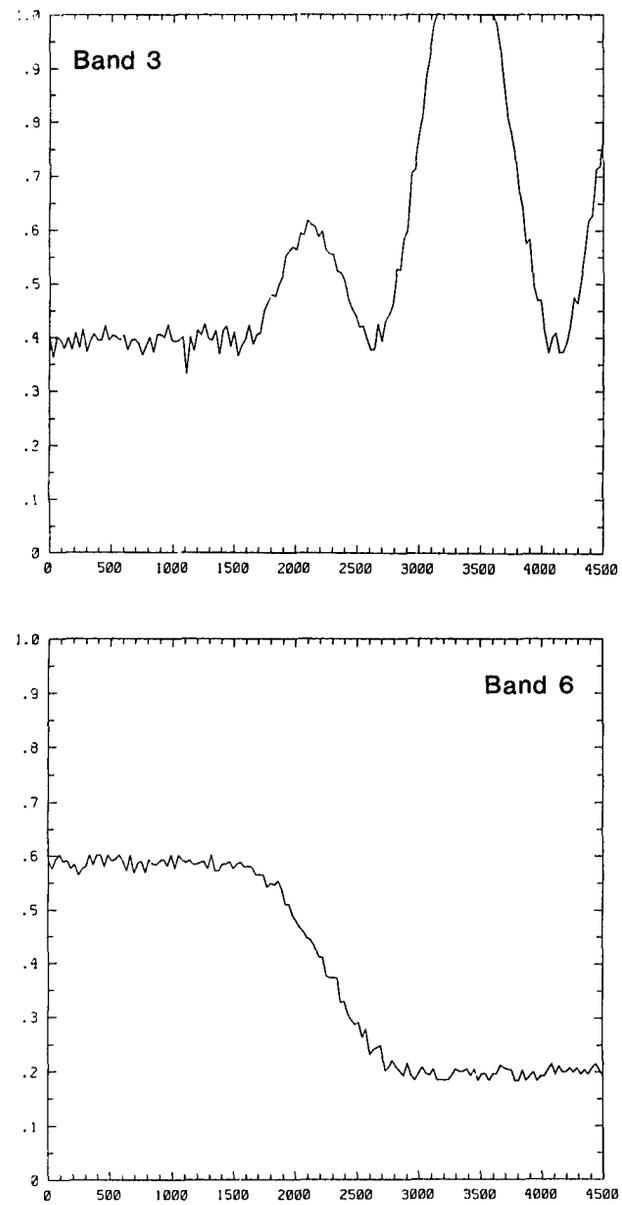

Fig. 5. Optimal fit of scaled radiances for bands 3 and 6.

results described in this section are expected when the improved version is applied.

6. REFERENCES

Engel, J. L. and O. Weinstein, 1983: The Thematic Mapper-An Overview, IEEE Trans. Geosc. Remote Sensing, GE-21, pp. 258-265.

Hoffman, R. N., 1982: SASS wind ambiguity removal by direct minimization. Mon. Weather Rev., 110, 434-445.

Hoffman, R. N., 1984: SASS wind ambiguity removal by direct minimization. II. Use of smoothness and dynamical constraints. Mon. Weather Rev., 112, 1829-1852.

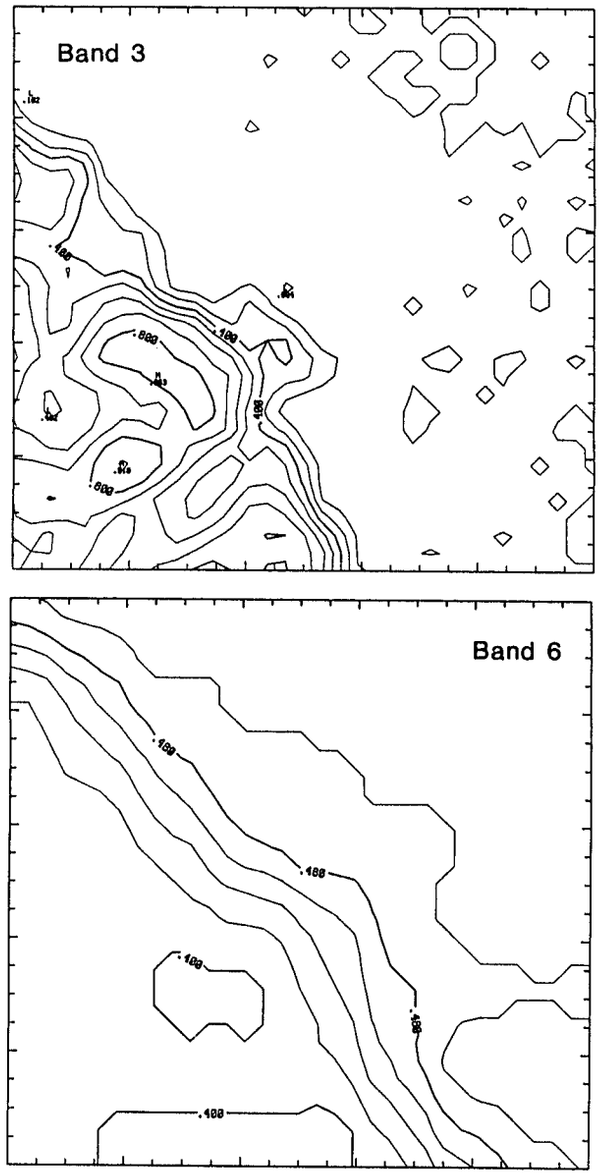

Fig. 6. Normalized radiances (i.e., counts divided by the saturation value) observed for subscene 1C. The contour interval is 0.1 for band 3 and 0.02 for band 6.

Table 3. The value of the parameters A_i and B_i after 100 iterations.

i	A_i	B_i
1	1.132	0.329
2	0.527	0.092
3	0.614	0.062
4	0.491	0.023
5	0.664	0.000
6	0.373	0.507
7	0.383	0.000

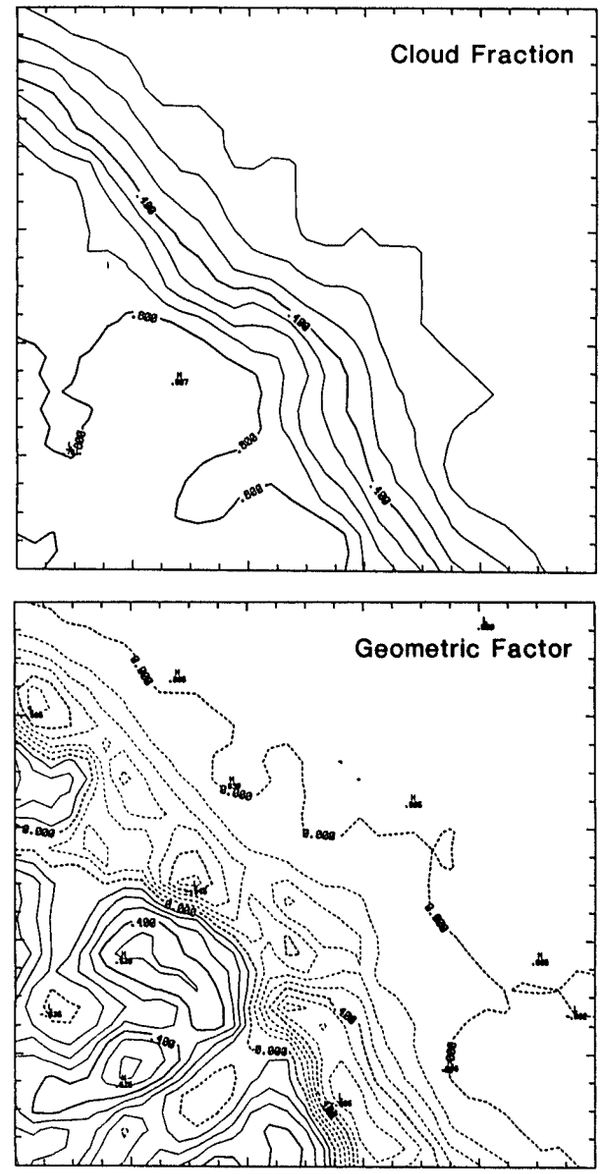

Figure 7. Derived parameters for subscene 1C. Contour interval is 0.1.

Hoffman, R. N., R. G. Isaacs, and L. D. Petro, 1985: Determination of cloud properties from satellites. Final report for NASA contract NAS5-28633. Atmospheric and Environmental Research, Inc., Cambridge, MA, 65 pp.

NASA, 1982: Landsat Data Users Notes (No 23), U. S. Geological Survey. EROS Data Center, Sioux Falls, SD.

NOAA, 1981: NOAA polar orbiter data (TIROS-N and NOAA-6) users' guide. NOAA-EDIS-NCC-SDSD. Washington, DC.

7. ACKNOWLEDGMENTS

This work was supported by the NASA SBIR program through contract NAS5-28633.

SATELLITE RAINFALL RETRIEVAL BY LOGISTIC REGRESSION

Long S. Chiu
Applied Research Corporation
8201 Corporate Drive, Suite 920
Landover, Maryland 20785

and

Benjamin Kedem
Department of Mathematics
University of Maryland
College Park, Maryland 20742

1. INTRODUCTION

The retrieval of meteorological quantities from satellite observations is based on covariate information such as radiometric measurements or physical quantities derived from them. The covariate information is influenced by factors other than the desired meteorological variable. The situation is further complicated by the different resolutions of the different sensors. It is useful to identify important covariates for the prioritization of transmission of data and to ascertain the possibility of on board processing.

Accurate measurement of tropical rainfall is crucial for the advancement of our understanding of the large-scale dynamics of the ocean/atmosphere system. An account of rainfall monitoring techniques from satellites is given by Barrett and Martin (1981). A satellite mission for the monitoring of tropical rainfall has been proposed to NASA (Theon et al 1986). Three instruments are proposed for the mission: a radar, an Advanced Very High Resolution Radiometer (AVHRR) and a microwave instrument, possibly an Electrically Scanning Microwave Radiometer (ESMR). The expected outcome from this mission is at least three years of rainfall data derived from concommitant covariate observations.

In the following a logistic model that can effectively accommodate covariate information, but which has not been used in the context of rainfall estimation, is described. A major difference between linear regression and logistic regression is that the former technique maximizes the variance explained while in logistic regression a likelihood function, or probability of an event, is maximized. The output from such a model is the distribution of rainrate categories from which standard errors can be estimated. The significance of the covariates can be tested rather readily. An example of the logistic model is given for the scenario of the proposed tropical rainfall monitoring mission from which microwave observations and fractional rain area measurements may be available.

2. THE LOGISTIC MODEL

The logistic model is useful in determining the relationship between the distribution of a random variable and a set of covariates. It has been applied in various forms in reliability testing and the analysis of survival data (Cox and Oakes, 1984). A detailed treatment of the logistic model is given by Cox (1970). We are interested in the relationship between rainfall rate averaged over an area R and $\underline{t}$, the vector of covariate variables related to R. For the event $R \geq R_0$, the logistic model is given by

$$P(R \geq R_0) = [1 + \exp(-\underline{b}'\underline{t})]^{-1}$$

where $P(R \geq R_0)$ is the probability that the rainfall rate R exceeds R_0 and

$$\underline{b} = (b_0, b_1, b_2, \ldots, b_k)$$

is a vector of constants. From n observations of R, the b's can be estimated by the method of maximum likelihood. Let R_0 be fixed so that the a binary variable Y can be defined as

$$Y = \begin{cases} 1 & R \geq R_0 \\ 0 & \text{otherwise} \end{cases}$$

The logistic model becomes

$$P(Y = 1) = [1 + \exp(-(b_0 + b_1 t_1 + \ldots + b_k t_k))]^{-1}$$

where the t's are covariate variables. We assume $Y_1, Y_2, \ldots, Y_n$ are conditionally independent given the covariate information. Then the likelihood function $L(\underline{b})$ is given by

$$L(\underline{b}) = \prod_{i=1}^{n} [\exp(\underline{t}_i'\underline{b})]^{Yi} / [1 + \exp(\underline{t}_i'\underline{b})]$$

and the asymptotic covariance matrix is given by

$$(-E(\partial^2 \log L(\underline{b}) / \partial b_i \, \partial b_j))^{-1}$$

where E is the expected value. To test the significance of the regression coefficients, we use the likelihood ratio test

$$\lambda = -2 \log L_0/L_1$$

where L_1 is the maximized likelihood under the full model and L_0 is the maximized likelihood under the hypothesis that the some of the regression coefficients are zero. If q of the b's are assumed to vanish, then λ follows asymptotically a chi-square distribution with q degrees of freedom.

3. A SCENARIO

We consider the scenario when concommitant observations of microwave temperature and fractional rain area are available. The rainfall data collected during the phase I of GATE are used. The basic data are radar-estimated rainrates on 4 by 4 km^2 pixels and measurements are made at 15 minute intervals. From the basic data, temperature and fractional rain area data for the scenario are generated as follows.

We assume that the microwave instrument measures the temperature over an area of 32 by 32 km^2 (i.e. 8 by 8 pixels) which is the unit area for our scenario. To calculate a mean temperature over the 32 by 32 km^2 box, a simple relation between the rainrate (r) and temperature (T_R)

$$T_R(r) = T_{av}(1-x) + T_s \varepsilon x + (1-\varepsilon)T_{av}(1-x)x \quad (1)$$

where T_{av} is the average temperature of the atmospheric column (=270K), T_s is the surface temperature (=290K), ε is surface emissivity (=0.5), $x=\exp(-\tau)$ is optical thickness, is used. τ is approximated as $\tau = 0.2r$, with r in mm/hr. The dependence of τ on the height of the rain column is ignored in this case. A functional relation between R and T_R is shown in fig. 1. From the rainrate at each pixel, a microwave temperature is computed. The microwave temperatures are then averaged over the 32 by 32 km^2 box to yield the average temperature (T). The fractional rain area (F) is obtained by dividing the number of pixels with rainrate in excess of 1 mm/hr by 64. The box averaged rainrate (R) is obtained by averaging the rainrates over the 64 pixels. Fig. 1 shows the scattered diagrams of R versus T. The fact that $T_R(R)$ is greater than T follows from Jenssen's Inequality (Feller, 1966). Fig. 2 shows the relationship between F and R. The strong correlation between R and F is also noted by Lovejoy (1980) for the phase III of GATE for the whole GATE area. Also included in our analysis are fractional rain area with rainrates in excess of 20 mm/hr (F_1). The data have been extracted from a 32 by 32 km^2 grid box in the center of the GATE area. Characteristics of the time series are summarized in table 1. Data from another box located approximately 100 km to the south of the first is used for validation.

Table 1. Characteristics of the time series

Variable	mean	s.d.	minimum	maximun
R (mm/hr)	.44	1.48	0.0	17.5
T (K)	151.5	16.67	145.0	263.1
F	.072	.17	0.0	1.0
F_1	.006	.03	0.0	.47

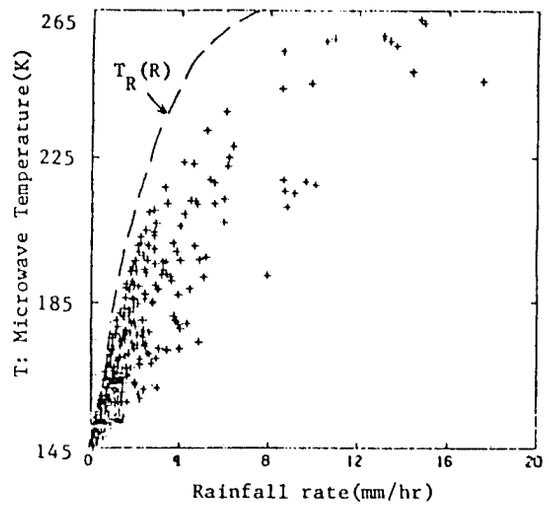

Fig. 1. Scatter diagram of rainfall rate over the box (R) and microwave temperature (T). The dashed curve shows that functional relationship between T_R and R.

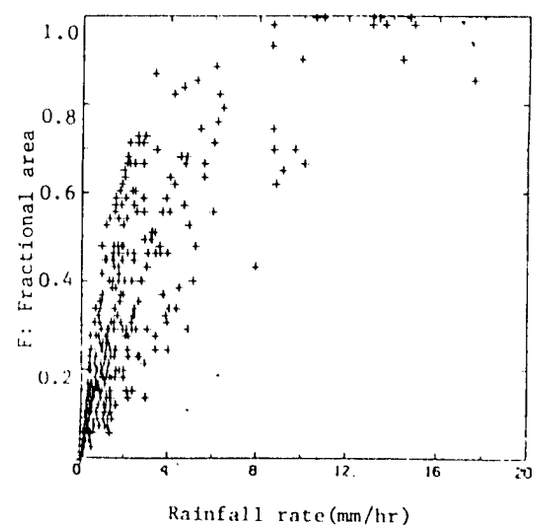

Fig. 2. Scatter diagram of rainfall rate (R) and fractional rain area with rainrates in excess of 1 mm/hr (F).

4. RESULTS

The full logistic model is of the form

$$P(R>1)=[1+\exp-(b_0+b_1F+b_2F_1+b_3T+b_4T_L)]^{-1}$$

where R, F, F_1 and T are rainrate, fractional area with rainrate in excess of 1 mm/hr, fractional area with rainrate in excess of 20 mm/hr and the temperature over the 32 by 32 km^2 box. T_L is T lagged at 1 time unit (i.e. 15 minutes). A total of 10 different models have been run and the regression coefficients are presented in table 2. The maximum log likelihood ranges from -309.6 for a model with F_1 as the only regressor (model 10) to -28.6 for the full model (model 1). From the table, important covariates can be identified. For illustration purposes, we consider models 1 and 8. The hypothesis we want to test is

$$H_0: b_2 = b_3 = b_4 = 0$$

The likelihood ratio test yields

$$\lambda = -2\ [-159.1+28.6] = 260$$

and the 5% significance level of $\chi^2(3)$ is 7.81. Hence H_o is rejected. To see if covariate T_L contributes to the estimation, the hypothesis H_1: $b_4 = 0$ is tested. To do this, we compare model 1 and 2 and obtain the λ value of $-2[-30.1+28.6] = 3$. The 5% level for $\chi^2(1)$ is 3.8 and H_1 has to be accepted. In this way, it is readily seen that b_1, b_2, b_3 are highly significant.

The goodness of the model is tested by applying it to the validation time series which is taken from an area to the south of the center of GATE (see section 3). Model 2 is adopted for validation, i.e. we use

$$P(R>1mm/hr)=[1+\exp-(-207.8-61.7F+307F_1+1.34T)]^{-1}$$

The values of F, F_1 and T taken from the location designated for validation are substituted in (2) and the probability calculated. We defined as a goodness of fit criterion the mean square error

$$MSE = 1/n\ \Sigma_{i=1}^{n}\ (P(Y_i=1) - Y_i))^2$$

This is 0.005 for the prediction using model 2. It can be seen from fig. 3 that the prediction matches the observations very well.

Table 2. Regression Coefficients for Different Logistic Models

parameter	F	F_1	T	T_L		
regression coeff.	b_0	b_1	b_2	b_3	b_4	maximized log likelihood
model						
1	-217.7	-66.8	309.8	1.33	0.077	-28.6
	(46.9)	(16.7)	(61.0)	(.30)	(.046)	
2	-207.8	-61.7	307.0	1.34	---	-30.1
	(44.8)	(16.0)	(59.4)	(.29)		
3	-17.7	16.6	249.7	---	0.071	-62.8
	(4.34)	(3.2)	(31.4)		(.028)	
4	-7.27	22.5	240.5	---	---	-65.9
	(.68)	(2.4)	(29.3)			
5	-166.2	-62.8	---	1.10	---	-76.2
	(18.5)	(8.6)		(.12)		
6	-48.1	---	---	.33	-.035	-115.0
	(3.46)			(.04)	(.027)	
7	-47.9	---	---	.29	---	-116.1
	(3.4)			(.02)		
8	-4.9	21.0	---	---	---	-159.1
	(.27)	(1.4)				
9	-34.9	---	---	---	.21	-188.1
	(2.1)				(.01)	
10	-3.1	---	249.3	---	---	-309.6
	(.12)		(19.5)			

The s.d.s of the coefficients appear in parentheses

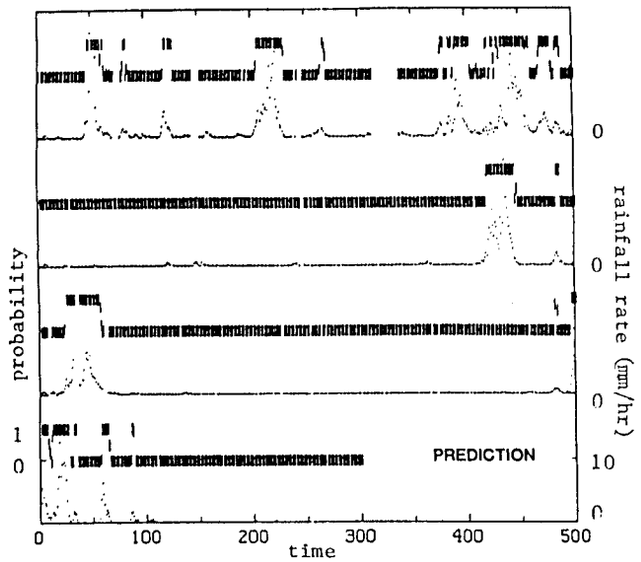

Fig. 3. Time series of predicted probability of exceeding 1 mm/hr and observed rainrate in another location.

5. DISCUSSION

In our example, the microwave temperature data, which integrates the effect of partially filled non-uniform field of view of the microwave sensor, are not independent since they are derived from a rainrate-temperature relationship but in the presence of T, the addition of T_L as a regressor does not improve the model significantly. This can be seen by comparing the maximized likelihood in models 1 and 2 and models 6 and 7. The interpretation is that most of the information is contained in T and the addition of T_L adds redundant information. In the absence of T, the inclusion of T_L improves the model as the maximized log likelihood is increased from -65.9 (model 4) to -62.8 (model 3). This increase is significant by the log likelihood ratio test.

The relationship between average rainrate and fractional rain area has strong implications for rainfall estimation. From infrared imagery, Arkin (1979) accounted for a large fraction of the rainfall variance by considering the number of pixels below a threshold temperature. Implict is the assumption that convective rainfall, which is in the heavy rainrate portion of the rain spectrum, is produced in deep cumulus clouds. How important the heavy rainrates are in determining the total rainfall can be examined by considering F_1. If we compare the maximized log likelihood in model 8 and 10, we see that model 8, with fractional low rainrates (>1 mm/hr) area as the only regressor is better than model 10 which uses only F_1 in the maximum log likelihood sense. If both are used, a significantly better model is obtained (model 4).

In this report, the potential of logistic models in rainfall estimation is demonstrated. We plan to extend our analysis using actual satellite observations such as the ESMR measurements taken on board the NIMBUS V satellite.

6. REFERENCES

Arkin, P. A., 1979: The Relationship Between Fractional Coverage of High Cloud and Rainfall Accumulations during GATE over the B Scale, Mon. Weath. Rev., 107, 1382-1387.

Barrett E. C. & D. W. Martin, 1981: The Use of Satellite Data in Rainfall Monitoring, Academic press, New York, NY, 10003, 340pp.

Bras, R. L. & I. Rodriguez-Iturbe, 1976: Net Work Design for the Estimation of Areal Mean of Rainfall Events, Water Resources Res., 12, 1185-1195.

Cox, D. R., 1970: The Analysis of Binary Data, Methsen, London.

Cox, D. R. & D. Oakes, 1984: Analysis of Survival Data, Chapman and Hall, New York, NY, 10017, 201pp.

Feller, W., 1966: An Introduction of Probability Theory and its Application, Vol 2, Wiley, New York, NY, 626pp.

Lopez, R. E., J. Thomas, D. O. Blanchard & R. L. Holle, 1981: Estimation of Rainfall over an Extented Region Using only Measurements of the Area Covered by RADAR Echoes, 21st Conf. on Radar Meteorology, Amer. Meteor. Soc., Calgary, Canada.

Lovejoy, S., 1981: The Remote Sensing of Rain, Ph.D. thesis, Dept. of Physics, McGill University, Montreal, Canada, 102pp.

Theon, J., G. N. North, T. Wilheit & O. Thiele, 1986: Tropical Rainfall Monitoring Mission Workshop Report, NASA, Nov., 1985, Calverton, Maryland. (To be published)

THE CHARACTERIZATION OF CUMULIFORM CLOUD FIELDS USING SPACE SHUTTLE PHOTOGRAPHY

J.W. Snow and D.D. Grantham
Air Force Geophysics Laboratory
Hanscom AFB, MA 01731

E. M. Tomlinson
Air Weather Service, USAF
Los Angeles AFS, CA 90009

J.H. Willand
Systems and Applied Sciences Corp.
Lexington, MA 02173

1. SOURCE OF DATA

Among the geophysical experiments being conducted during space shuttle missions, the CLOUDS experiment, under sponsorship of the U.S. Air Force, has as its broad purpose research on Earth's cloudiness and as a particular objective the quantification of the apparent cloud amount, S, as a function of the angle at which a cloud field is viewed, the "view angle" ζ. At the minimum view angle, the vertical, $\zeta = 0$, the apparent cloud cover is the true cloud cover C, i.e., $S(0) = C$; at all other angles $S(\zeta) > C$. (It is here recalled that the range of values for cloud cover (and for S) is $0.0 < C < 1.0$.)

Series of photographs are made of fixed cloud scenes as the orbiting space shuttle passes overhead ($\zeta \approx 0$) and then retreats from them. The entire series requires not more than 3 minutes to complete, thus the cloud field itself is unchanged. The angle at which the scene is viewed, however, varies through a large portion of its possible range, $0 < \zeta < 90°$. Photogrammetric analysis yields S and ζ for each photograph in the series. S is the fraction of a fixed area on the Earth's surface which is "white." (Additional details concerning the analysis are contained in Snow et al, 1985.)

The scope of the present discussion is limited to single-layer cumuliform cloud populations. The three particular CLOUDS series discussed are from the subtropics and all contain single-layer cumuliform clouds of the low base-height type. Specific information on each location is contained in Table 1.

Using these data a physically realistic model for cumuliform cloud populations is developed and applied. For such cloud fields the model permits the cloud cover C to be determined from a single measurement S at known ζ.

2. IDEALIZED CLOUD POPULATION MODELS

Idealized cloud populations are made up of regularly spaced clouds all having the same size and shape. There are two genera of simple 3-dimensional cloud population models: Type A -- those having clouds of constant vertical thickness, z = constant, and Type B -- those with clouds having variable z. The distinction is apparent in the form of the S versus ζ relationship. Type A has $S \sim (1 + \tan \zeta)$ and Type B has $S \sim \sec \zeta$. The simplest cases of each type are cubes for Type A and spheres for Type B. Mathematically, the $S(\zeta)$ relationships for these simplest models are:

$$S_c(\zeta) = C(1 + \tan \zeta) \qquad (1)$$

$$S_s(\zeta) = C \sec \zeta \qquad (2)$$

where the meaning of the subscripts is cube model and sphere model, respectively. (The development of all models presented here is contained in Snow and Grantham (1986)).

More generally, the thickness of the idealized cloud, z, is allowed to be different from their horizontal dimension, y. This is most readily accomplished by parameterizing the cloud thickness in terms of horizontal dimension, namely

Table 1

Space shuttle CLOUDS photographic series of single-layer cumulus clouds

Location	Abbrev.	Latitude (°N)	Area Analyzed (Sq km)	Underlying Surface	Month/ Year	Local Solar Time
Cape Canaveral, Florida	CCO	28	2200	offshore	01/85	mid-afternoon
Baja California Sur, Mexico	BCS	25	4400	land	01/85	early afternoon
Northeastern Dominican Republic	NDR	19	4000	land	09/84	late morning

$\beta = z/y$, the ratio of maximum vertical dimension of the cloud to the horizontal dimension in the plane in which ζ is measured, which is called the thickness parameter.

Introduction of β into Eq (1) results in the more realistic rectangular solid model

$$S_r(\zeta) = C(1 + \beta \tan \zeta) \qquad (3)$$

which was first published by Lund in 1965. (It should be noted that "viewing angle" as used in Lund (1965) is $(90° - \zeta)$ in present notation.)

The linear regression of the BCS values of $S(\zeta)$ versus $\tan \zeta$, plotted in Figure 1, determines $C^* = 0.318$ and $\beta = 0.226$. The regression provides a first estimate for C (* indicates an estimated C-value) and for β . It is evident from the systematic overestimation of S for $\zeta < 45°$ and underestimation for $\zeta > 45°$ in Figure 1 that a more complete model is needed.

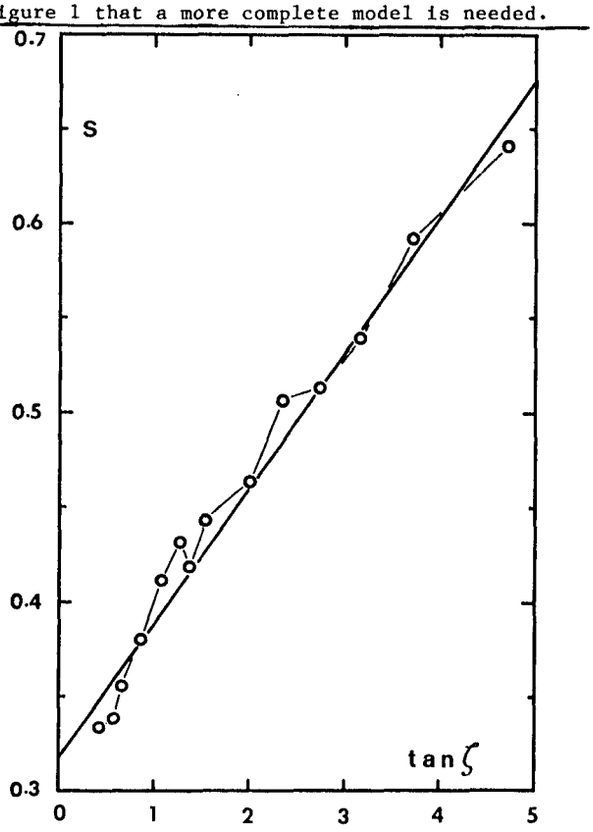

Figure 1. Apparent cloud cover S versus tangent of view angle. Bold line results from least-squares linear regression using rectangular solid model, intercept is cloud cover estimate $C^*=0.318$, slope is thickness parameter multiplied by C^*. Data, plotted as open circles with light connecting lines, are from space shuttle CLOUDS photographs of cumulus clouds over Baja California Sur.

Before considering any other models an important characteristic which any useful model must have is here discussed. At the vertical angle $\zeta = 0$ (the nadir angle as seen from above), there cannot be a discontinuity in the apparent cloud cover, i.e. the rate of change in S with ζ must be continuous and, in fact, $dS/d\zeta = 0$ at $\zeta = 0$, because there $S = C$, a constant. The only way this condition can be met by the rectangular solid model, Eq (3), is for $\beta = 0$ which degenerates the model into the useless 2-dimensional case, $S(\zeta) = C \neq f(\zeta)$. The sphere model, Eq (2), in spite of its restriction to the single value $\beta = 1$, does conform to the $dS/d\zeta = 0$ at $\zeta = 0$ condition, as does any model having a view angle functionality of $\sec \zeta$.

It is common observation that cumulus clouds have flattened bases and bulbous tops. A model which incorporates both variable thickness and flattened base is the hemisphere. The equation for this cloud morphology is

$$S_h(\zeta) = \frac{C}{2} (1 + \sec \zeta) \qquad (4)$$

which can easily be understood if the totality of the cloud is treated by portions. The half toward the direction of view acts like half of a horizontal disk and contributes a constant amount to S for all values of ζ, specifically C/2. For treatment by portions, the forward half must always be attached to the half away from the direction of view. The away-half interrupts the view as a halved hemisphere, i.e. a quarter-sphere which has its plane vertical surface perpendicular to the direction in which ζ is measured. It should be noted that the thickness parameter for the quarter-sphere, like the whole sphere, is $\beta = 1$. That two terms appear in Eq (4) is thus explained. Multiplication of the cross-sectional area of the away-half which is perpendicular to the direction of view by $\sec \zeta$ gives the portion of a horizontal surface which is masked by the quarter-figure. (For the complete development, refer to Snow and Grantham (1986)). The hemisphere model accommodates the important condition of $dS/d\zeta = 0$ at $\zeta = 0$, but no flexibility in β is possible.

In addition to variable thickness and flattened bases, more realistic morphologies can be studied using the technique of linear combination of portions applied in the hemisphere case. The morphology of typical cumulus clouds can be described as that of domed cylinders. The simplest domed cylinder consists of a hemisphere of radius r positioned on top of a cylinder of diameter $y = 2r$ and of height z. Mathematically, the model is

$$S_m(\zeta) = \frac{C}{2} (1 + \sec \zeta + B \tan \zeta) \qquad (5)$$

where B is the thickness parameter of the cylindrical base portion of the cloud multiplied by $8/\pi$ and the subscript signifies domed cylinder.

Any of these idealized models can be fitted by the least-squares linear regression method to actual measurements made from the CLOUDS photographic series. The most extensively analysed series to date, the 14-member BCS data set, is the one primarily used in model testing. Linear regression provides estimates for two parameters by way of the intercept A_0 and the slope A_1. In the case of the cube model the intercept is C^* and the slope is βC^*. In Table 2A are given these values for the rectangular solid and other models which result from regression on the BCS data set. All entries in the rectangular solid column have been explained, except the last.

The statistic used to quantify the goodness-of-fit provided by any model to the data used in the regression is

$$Q = \frac{10^3}{N} \sum (S_j - S)^2/S_j \qquad (6)$$

where S is the apparent cloud cover measured at viewing angle ζ and S_j is the value predicted

Table 2

Comparative cumulus cloud population models

A. BCS Data Set

	Rectangular Solid	Sphere	Hemisphere	Domed Cylinder($\pi/8$)	Single Layer Cumulus
A_o	0.3181	-1.0993	-1.4948	-1.4986	-1.3845
A_1	0.0719	0.4222	0.6138	0.4493	0.3738
C*	0.318	0.333	0.343	0.305	0.324
β	0.226	1.000	0.500	0.893	---
ν	---	0.422	0.614	0.449	0.374
Q	0.431	0.357	0.558	0.258	0.272

B. CCO Data Set

	Rectangular Solid	Sphere	Hemisphere	Domed Cylinder($\pi/8$)	Single Layer Cumulus
A_o	0.5248	-0.6347	-0.9168	-0.8618	-0.8159
A_1	0.0668	0.2863	0.4238	0.2817	0.2483
C*	0.525	0.530	0.536	0.513	0.525
β	0.127	1.000	0.500	0.893	---
ν	---	0.286	0.424	0.282	0.248
Q	0.980	0.624	0.958	0.645	0.482

C. NDR Data Set

	Rectangular Solid	Sphere	Hemisphere	Domed Cylinder($\pi/8$)	Single Layer Cumulus
A_o	0.2265	-1.3825	-1.9347	-1.9548	-1.7910
A_1	0.0870	0.5973	0.8567	0.6404	0.5338
C*	0.226	0.251	0.262	0.221	0.241
β	0.384	1.000	0.500	0.893	---
ν	---	0.597	0.857	0.640	0.534
Q	0.902	0.709	1.294	0.557	0.431

A_o & A_1 - Linear regression coefficients
C* - Cloud cover estimate
β - Thickness parameter
ν - Exponent, equal to A_1
Q - Goodness-of-fit statistic

from the model j at angle ζ. N is the number of prediction-measurement pairs, i.e. the number of ζ-values over which the summation is performed. Since Q is basically the common chi-squared statistic divided by N, the smaller its value the better the fit.

From Table 2 it is evident that the sphere model provides a better approximation to the 14 BCS measurements (and to the other data sets) than the rectangular solid model. However, an explanation of the two regression parameter is needed. Eq (2) is linearized by taking the logarithm of both sides, specifically $\ell n\ (S) = A_o + A_1\ \ell n\ (\sec \zeta)$. At $\zeta = 0$ the inverse natural logarithm provides the cloud cover estimate, $C^* = e^{A_o} = 0.333$. The question arises as to the non-unity value of A_1 for all models except the first. In the present case $A_1 = 0.4222$. (To simplify notation, $A_1 \equiv \nu$ and $e^{A_o} \equiv \alpha$.) The phenomenon of multiple-masking must be explained in order to understand the value of ν.

By multiple-masking is meant that a portion of a horizontal surface concealed from view by one particular cloud is also masked from view by another cloud. Whenever the view angle exceeds some critical value, ζ_c, the value of S will be too large unless compensation is made for the fact that some portion of the horizontal surface is being excluded from view by clouds more than once. The rectangular solid model performs this compensation by suggesting an unrealistically small value for β. (For the BCS series $\beta < 1/4$.) The sphere, hemisphere and all other models discussed perform the compensation primarily by assigning a value of $A_1 < 1$. Linear regression thus results in Eq (2) taking on the form $S_s(\zeta) = C \sec^{\nu} \zeta$. (For the BCS series $\nu = 0.422$.)

Allowing compensation for multiple-masking to be performed in this manner improves the goodness-of-fit as the Q-value for the sphere model indicates. Extension to the hemisphere and the domed cylinder models gives $C^* = \alpha 2^{\nu}$. The hemisphere model regression on the BCS series results in the largest cloud cover estimate of any model $C^* = 0.343$. The large Q-value associated with the hemisphere model indicates that it is the poorest idealization of the actual cloud populations. Up to this point, the sphere model has provided the best approximation to the data, in spite of the fact that it does not allow any freedom in regard to the thickness parameter.

Discussion is now completed of the domed cylinder model, Eq (5). The model is the only instance where the idealized cloud morphology is not completely defined by the equation, i.e., B is not a-priori specified. In order to investigate this more realistic cloud model it is instructive to assign a value to B which results in a particularly simple expression, specifically $B = 1$ (meaning that the thickness parameter for the cylindrical portion of the cloud is $\pi/8$ and for the entire cloud it is $\pi/8 + 1/2 = 0.893$). With $B = 1$, it is evident that the domed cylinder model is the linear combination of constant, spherical and rectangular portions. From Table 2 it is seen that the addition of the cylindrical section below a hemisphere considerably improves the fit to the BCS or any other data set from that of the hemisphere alone.

However, the critical condition that $dS/d\zeta = 0$ at $\zeta = 0$ is violated by the domed cylinder model except when $B = 0$, in which case Eq (5) degenerates back into the hemisphere model. Yet the Q-values in Table 2 support the possibility of $B > 0$, which in effect allows the $(\tan \zeta)$ term to contribute. If series approximations to the trigonometric functions are substituted into the differentiated form of Eq (5), two solutions for B are obtained, specifically $B = 0$ and $B = \zeta$. Allowing the latter, the resulting version of the domed cylinder model is

$$S_u(\zeta) = \alpha(1 + \sec \zeta + \zeta \tan \zeta)^{\nu} \quad (7)$$

where the compensation for multiple-masking resulting from linear regression is anticipated by the presence of the exponent ν. The subscript u signifies that Eq (7) is the single-layer cumulus model.

In the final column of Table 2A are given the quantities resulting from linear regression for the BCS data set. The cloud cover is intermediate in value between the sphere and the domed cylinder. Although Q is somewhat larger than for the domed cylinder model, it is recalled that no data exists below ζ = 23 1/2° from the BCS series. Before the true value of the single-layer cumulus model can be appreciated it must be applied to a data set having information at small ζ.

Model development and testing is here summarized before proceeding to the two other data sets. The domed cylinder, Eq (5), provides the best approximation to the BCS data. However, it cannot accommodate the necessary conditions that $dS/d\zeta = 0$ at $\zeta = 0$ without allowing $B = f(\zeta)$. By so doing, the optimum model for single layer cumulus is obtained, Eq (7). In Figure 2 is shown the BCS data and $S_u(\zeta)$ parameterized by the final column of Table 2A.

3. REGRESSIONS FOR OTHER DATA SETS

Four of a series of space shuttle cloud photographs of stunted cumulus clouds forming offshore of Cape Canaveral and under an atmospheric inversion have been analysed and the data appear in Figure 2. The results of regression for the rectangular solid, the sphere, the hemisphere, the domed cylinder and the single-layer cumulus model are given in Table 2B. The domed cylinder model regression, again, was performed using B = 1. From Table 2B it is evident that the domed cylinder model, while coming close, cannot provide a better approximation than the sphere model for this field of stunted cumulus clouds. The first data point of the series is at ζ = 5 1/2° and given such low view angle data the single-layer cumulus model demonstates its true capability. A substantially lower Q-value than any other model is obtained when B is allowed to vary with ζ. Using the final column in Table 2B in Eq (7) provides the CCO solid curve plotted in Figure 2.

The third data set, also given in Figure 2, is for trade-wind cumulus clouds forming over a large island. The regression results are presented in Table 2C, the NDR data set. Again, the single-layer cumulus model provides the best fit to the data. $S_u(\zeta)$, parameterized from the final column of Table 2C, also appears in Figure 2.

4. APPLICATION TO SATELLITE CLOUD COVER MEASUREMENTS

In the present development, the regression on any of the three space shuttle data sets has provided the value for the exponent ν directly. However, the situation of single measurements (ζ_1, S_1), provided routinely by meteorological satellites, would require an estimation of the value of ν if a model such as Eq (7) were to be used in the estimation of C. If the world's cumulus cloud populations were categorized by their ν-values, then such a single measurement would be sufficient to ascertain the cloud cover. Future research may provide for such an approach but at present such categorization is very inadequate if not totally lacking.

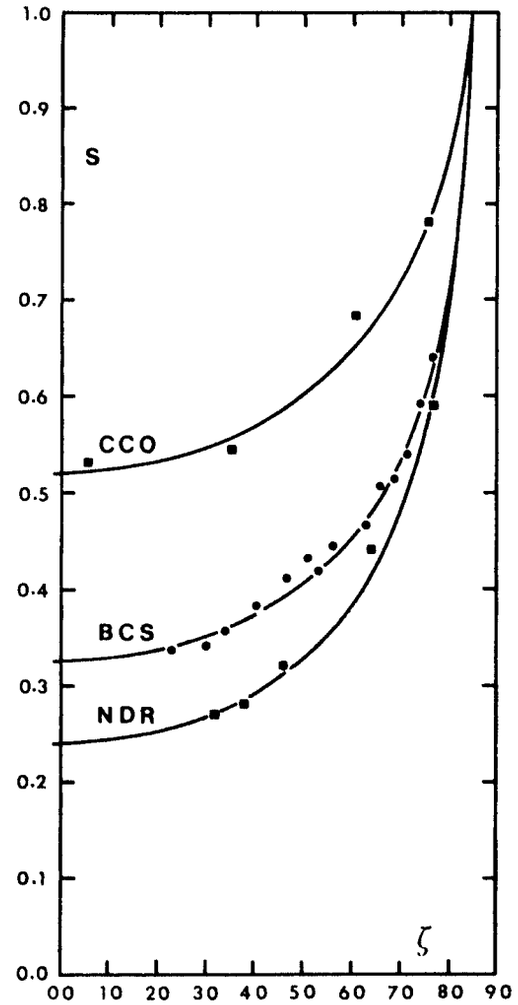

Figure 2. Apparent cloud cover S versus view angle ζ for cumuliform cloud fields offshore of Cape Canaveral (CCO), over Baja California Sur (BCS), and over northeastern Dominican Republic (NDR). Solid curves result from the single-layer cumulus model. Data from space shuttle CLOUDS photographs are plotted as bold symbols. (Photographs by astronauts Steven A. Hawley and Gary E. Payton.)

A second approach is to use adjacent measurements, (ζ_1, S_1) and (ζ_2, S_2), assuming that that both are viewing basically the same cloud field. The determination of ν is then straightforward and once evaluated, C is calculated from the model equation. For the single-layer cumulus model ν would be computed from

$$\nu = \ln (S_1/S_2) \Big/ \ln \left(\frac{1 + \sec \zeta_1 + \zeta_1 \tan \zeta_1}{1 + \sec \zeta_2 + \zeta_2 \tan \zeta_2}\right) \quad (8)$$

However, the assumption of uniform cloud field is limiting, especially for small cloud populations and at large ζ-values. Furthermore, the precision of the ν-determination varies with the difference $(\zeta_2 - \zeta_1)$, meaning that the closest measurements result in the greatest uncertainty in ν.

A third approach might be to use measurements made at different spectral wavelengths, S and S', but at the same ζ to infer ν.

Quite apart from these speculations, if a simulator is worth employing then a very large amount of the inherent variation in the phenomenon modeled must be contained within the model itself. In the present application, this means that if ν changes markedly from one cumulus cloud population to another, such idealized cloud population models are of very limited applicability. Inspection of Table 2 does indeed suggest that ν varies widely.

It is reemphasized that ν is the primary mechanism by which multiple-masking is handled in models of form similar to Eq (7). The range of values for the exponent is $0.0 < \nu < 1.0$. If multiple-masking does not occur for any values of ζ, then $\nu = 1.0$; if multiple-masking is absolutely dominant then $\nu = 0.0$, a condition to be approached at the highest values of C. In fact it may be anticipated that cloud amount is the physical quantity principally governing the value of ν, when C is large, ν is small and vice versa. The simplest, yet consistent alternatives are $\nu \sim (1 - C)$ and $\nu \sim 1/C$. From the information in Table 2, the former is not tenable whereas the latter is very well confirmed, particularly when applied to the single-layer cumulus model. The resulting relationship for the three data sets is

$$\nu = (0.127)/C \qquad (9)$$

It is the product νC which is nearly constant from one cumulus field to another and not ν itself.

What is needed to provide C, given a single set (ζ_1, S_1) is Eq (9) along with the model, Eq (7). Introducing Eq (9) into Eq (7) and linearization through logarithms gives

$$C^* = \ln^{-1}[\ln(S) - \frac{0.127}{C^{**}} \ln (1/2(1 + \sec \zeta + \zeta \tan \zeta))] \qquad (10)$$

where C^{**} is the previous value of C^* in the iteration process required to solve Eq (10). When $C^* = C^{**}$, out to however many decimal places deemed appropriate, then $C = C^*$.

The proof of worth for the single layer cumulus model remains to be determined by extensive application to other cumulus cloud scenes. The value 0.127 may undergo some refinement but the form of Eq (10) is promising. A preliminary assessment can be made using the same information which was employed in developing the model. In applying Eq (10) to the data contained in Figure 2 and listed in Table 3, the number of iterations for 3 decimal-place precision is approximately 4 for $\zeta < 45°$ and 10 for $\zeta > 45°$. The initial value C^{**} is the actual measurement itself, S. In Table 3 are contained values of C^* determined from Eq (10) using single measured values of S from the BCS, CCO and NDR series. The value obtained from linear regression on the entire series with the model is entered at the bottom of each column for comparison. No individual value departs from the regression value by more than 0.04, which for cloud cover is well within the uncertainties in cloud cover determined by any other means.

It is concluded that the model developed and tested with series of space shuttle photographs of cumuliform clouds may be useful in estimating cloud cover C from single measurements of S made within a visible channel by meteorological satellites.

Table 3
Comparison of cloud cover values estimated by cumulus model compared with value from linear regression on whole data set.

ζ	S	C^*
BCS		
23 1/2	0.334	0.318
30 1/2	0.338	0.310
34 1/2	0.355	0.318
41	0.380	0.327
47 1/2	0.412	0.338
52	0.432	0.340
54	0.418	0.317
57	0.443	0.327
64	0.464	0.301
67	0.507	0.322
70	0.513	0.293
72 1/2	0.539	0.286
75	0.592	0.308
78	0.641	0.291
Regression Value		0.324
CCO		
5 1/2	0.532	0.531
35	0.544	0.507
60 1/2	0.682	0.556
76	0.780	0.521
Regression Value		0.525
NDR		
32	0.270	0.238
38	0.280	0.234
46	0.320	0.249
64	0.440	0.273
77	0.600	0.245
Regression Value		0.241

5. FURTHER CHARACTERIZATION

Various space shuttle CLOUDS photographs have been digitized and analysed to produce the probability density functions for the clear and the cloudy lengths occurring in cumuliform cloud scenes. The results of these analyses are presented in Session 4, Satellite Meteorology and Applicatons, of the Conference.

REFERENCES

Lund, I.A., 1965: Estimating the probability of clear lines-of-sight from sunshine and cloud cover observations. J. Appl. Meteor., 4, 714-722.

Snow, J.W., J.T. Bunting, R.P. d'Entremont, D.D. Grantham, K.R. Hardy, and E.M. Tomlinson, 1985: Space shuttle cloud photographs assist in correcting meteorological satellite data. EOS Trans. Am. Geophys. Union, 66, 489-490.

Snow, J.W., and D.D. Grantham, 1986: Variation of cumuliform cloud amount with view angle. AFGL, Technical Report (to be published).

AN INTERMITTENT WAVE PACKET MODEL OF RAIN AND CLOUDS

J. Wilson,
Meteorology dept.,

S.Lovejoy, D. Schertzer,
Physics dept.,
McGill University,
845 Sherbrooke st. west,
Montreal, Que.,
CANADA

1 Introduction

It is becoming increasingly obvious that a fundamental obstacle to exploiting remotely sensed data is our inability to account for the extreme variability of the phenomena over wide ranges in scale. We believe that the best way to overcome the difficulties is to explicitely model the fields themselves in order to investigate their radiative properties. This point of view has been extensively discussed elsewhere (e.g. Lovejoy and Schertzer (1985) and .Lovejoy and Schertzer (1986) in this volume) and has already lead to an interesting model of visible radiative transfer including comparison with satellite data (Gabriel et al, 1986).

Lovejoy and Mandelbrot (1985) and also Schertzer and Lovejoy (1985) have convincingly argued that the two basic ingredients required for realistic stochastic cloud and rain models are:
a) the strong intermittency characterized by hyperbolic distributions e.g. $Pr(\Delta R > \Delta r) \approx (\Delta r/\Delta r^*)^{-\alpha}$ where Pr is probability, ΔR the fluctuations of rain rate where α the hyperbolic exponent and Δr^* is the distribution-width
p) scaling: $\Delta r^*(\lambda \Delta x) = \lambda^H \Delta r^*(\Delta x)$ where λ is the varying scale ratio and H, the scaling exponent, Δx is the distance between the two points.

A number of scaling fractal models have been developed for the purpose of simulating remotely sensed fields. Existing models include non-intermittent models of topography (Mandelbrot 1975, Fournier et al 1982, Voss 1983) and strongly intermittent models of rain and cloud fields (Lovejoy and Mandelbrot 1985, Lovejoy and Schertzer 1985). These models are geometrical: they display certain aspects of the observed fields, and in some cases (e.g. the atmosphere) certain aspects of the equations (e.g. scale invariance). A problem of fundamental importance is therefore to relate the model assumptions to the underlying dynamical processes.

In this paper we consider the problem of simulating rain and cloud fields both of which are obviously highly turbulent and chaotic. It is then natural to formulate the problem in turbulent terms. Most phenomenologies of turbulence are based on the dynamical interaction of structures at different scales, conveniently represented by spherical shells in Fourier space. A particularly interesting class of models are the "spherical shell" models (e.g. Siggia 1977,78) where the basic structures are packets of waves defined by disjoint annulii in Fourier space with each packet interacting only with neighboring packets. A limitation of existing spherical shell models is that the number of degrees of freedom (e.g. the number of independant structures at a given scale) does not increase with wavenumber. Our stochastic intermittent wave packet model has the advantage of enabling us to easily increase the number of degrees of freedom in any desired way. Intermittency is modelled by modulating wave packet amplitudes by a hyperbolic random variable (exponent α).

This intermittent wave packet model is therefore close to the phenomenological turbulent formalism. It is interesting to note that earlier real-space models discussed in Lovejoy and Mandelbrot (1985), Lovejoy and Schertzer (1985) can be obtained as special cases. The detailed properties of this model will be discussed elsewhere.

2 Results and zoom

The basic wave packet shapes used here are two-dimensional gaussians of varying amplitude and phases, and of equally probable random signs. Choosing the hyperbolic exponent α to be 5/3 and constructing the spectrum in order to obtain a horizontal scaling exponent H_E of 1/2 accordingly to

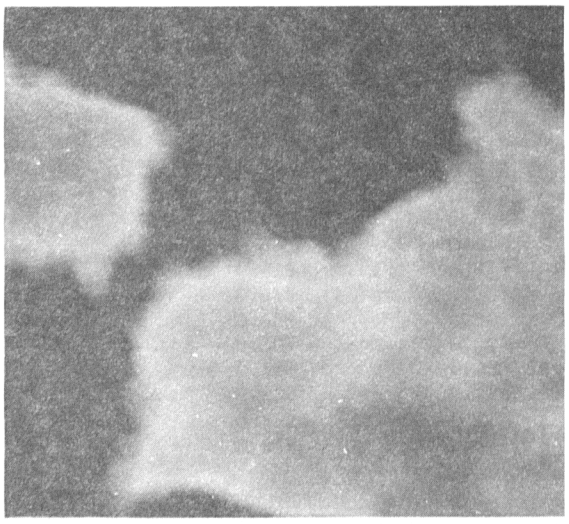

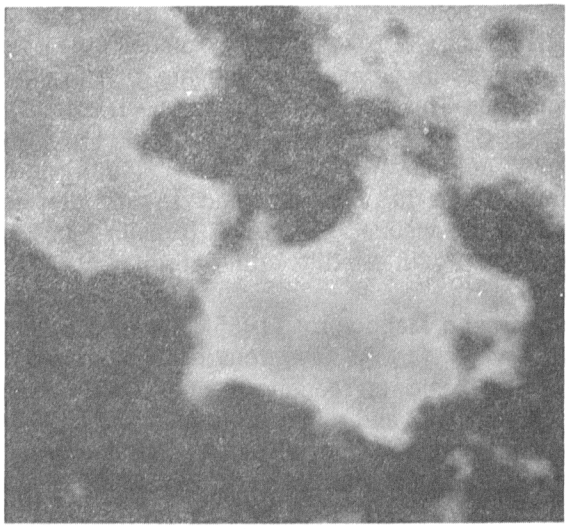

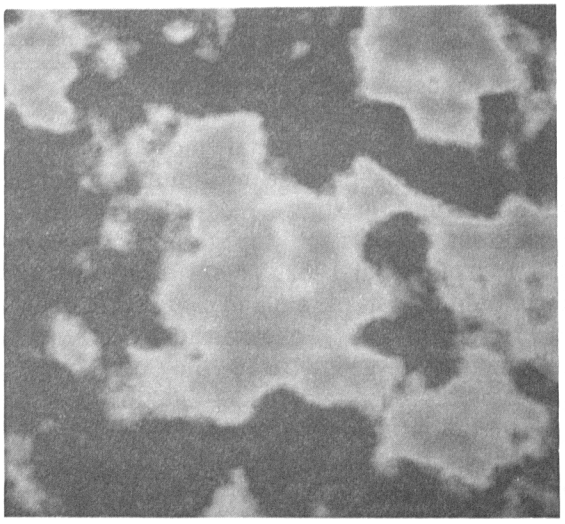

Fig. 7

Fig. 8

observations, we proceed to the sum at a given scale K (the discretization is in wave number). For a two-dimensional implementation we must have a fixed number of random wave packets realisations per wave number step in order to obtain, after doing the sum up to scale K, a number of degrees of freedom which is increasing as the square of the spanned wave number. And repeating similarly for all the scales to be considered in the entire mesh we finally get the complete Fourier field. The remaining step is the numerical fast fourier transform execution that should take advantage from the fact that the physical field is real.

The field cannot readily represent a rain rate spatial distribution due to the presence of either positive or negative regions. But to do so we use a histogram analysis of the field determine a threshold value $V_T(\%_c)$. in order to achieve a spatial coverture percentage $\%_c$, then lower values are reset to zero and the remaining higher ones are believed to represent the rain rate field. The quantity $R_{PPI}(\underline{x}) = \log(V_{phys}(\underline{x}) - V_T)$ for $V_{phys}(\underline{x}) > V_T$ and 0 otherwise can be interpreted using a grey scale as the rain rate on a PPI scope. Alternatively one can use linear color scales to mimic crudely the appearance resulting from multiple scattering processes in the following way. Starting for 0 values from a sky-type blue, each R G B components are driven separately with properly chosen positive slopes to obtain a bright white at approximatively 10% of the field maximum value, this will occur near the edge of the cloud enhancing its contour, and after the R G B components are decreased together slowly on a grey scale up to the maximum field value giving the usual impression created by the multiple scattering taking place in the thick part of a cloud. The resulting pictures are strikingly realistic. Now we will look at the zoom simulation for $\lambda = 2^n$ (n=0,...,7) where the pictures were made using such linear grey scales.

The actual simulation is based on a complementary use of Fourier and real spaces. Because wave packets are defined either in Fourier space or in physical space, one can take great advantage from the fact that characteristic lengths of gaussian wave packets defined as one standard deviation are simply related between the two spaces (well-known uncertainty relationship):

$$\Delta x_{1STDV} = \frac{\text{linear mesh}}{2\pi} \frac{1}{\Delta K_{1STDV}}$$

therefore if we create the small physical stochastic structures up to a cut-off scale in the real space (doing half of the work in the physical space), the remaining greater structures can be supplied in Fourier space working on the correspondingly missing small wave numbers. Because the most computational work concerns the treatment of the biggest packets (high wave numbers in Fourier space and large physical scales in real space), this method is clearly economical. Note that consistency requires a common scale discretization which was done linearely in wave number for both parts of the procedure. This gave us the first image of our zoom simulation (see figure 1) using 2.5×10^5 packets on a 512X512 pixels grid.

The first zoom by a factor 2 was performed on the left upper corner of this image (see figure 2 the zoom is centered at 128,128) dedoubling simply each pixels in each x and y direction. In the actual simulation after few consecutive zooms the problem of ghosty squares in the field arose. They were remnents of the square patterns produced by the first zoom. To escape from that we choose to smooth locally the field, performing an arithmetic mean between each pixels and its direct neighbors. Alternatively one may choose to zoom in applying an adequate interpolation scheme to create each new inner pixels rather than simply dedoubling the older ones. But one should be aware from the fact that this can likely modify the spectrum and eventually

break the scaling which is not more desirable. The inner scale chosen to be $\Delta x_{1STDV} = 3$ doubles then to 6 and we only need to feed in the more refined missing structures. As an evidence working directly in the real space is more suitable to supply efficiently those small structures. The same procedure is maintained for zoom #2 up to the seventh except that now the window to be enlarged is taken at the exact center (256,256 for the zoom center coordinates, see figures 3, 4, 5, 6, 7 and 8).

Conclusion

This intermittent wave packets stochastic model may serve not only to simulate or calibrate remotely sensed data such as rain and cloud fields but it may also be applied to temperature and velocity fields. Furthermore Lovejoy and Mandelbrot (1985) have shown that the fractal sum of pulses which belongs to the same formalism, can be used to simulate time-evolving sequence of rain rate fields under the hypothesis of frozen turbulence from Taylor where the time axis acts exactly the same way as another spatial dimension. Moreover we already mentionned interesting applications to the multiple scattering problem (Gabriel et Al 1986). We hope however that our more general Fourier space approach can be linked more closely to spherical shell models of turbulence because they share similar phase space decomposition.

References:

Gabriel, P., S. Lovejoy, G.L. Austin, D. Schertzer, 1986: Radiative transfer in extremely inhomogeneous fractal clouds, 6th conf. of rad. trans. (accompanying volume).

Fournier, A., D. Fussell, L. Carpenter, 1982: Computer rendering of stochastic models. Comm. of the ACM, 371-84, 6.

Lovejoy, S., D. Schertzer, 1985: Generalised scale invariance and fractal models of rain. Wat. Resour. Res. 1233-50, 21.

Lovejoy, S., B. Mandelbrot, 1985: Fractal properties of rain and a fractal model. Tellus 209-232, 37A.

Lovejoy, S. D. Schertzer, 1986: Scale and dimension dependence in the detection and calibration of remotely sensed atmospheric phenomena. (in this volume).

Mandelbrot, B., 1975. Stochastic models for the earth's relief, the shape and fractal dimension of coastlines, and the number-area rule for islands. Proc. Nat. Acad. Sci. USA, 2825-28, 72.

Siggia, Eric D. 1977: Origin of intermittency in fully developed turbulence. Phys. Rev. A, 1730-50, 15.

Siggia, Eric D. 1978: Model of intermittency in three-dimensional turbulence. Phys. Rev. A 1166-76, 17.

Voss, R.F., 1983: Fourier synthesis of gaussian fractals: 1/f noises, ladscapes and flakes. Preprints Siggraph conf., Detroit, 1-21.

PRECIPITATION ESTIMATION USING PASSIVE MICROWAVE RADIOMETRY AT 92 AND 183 GHz: AIRCRAFT RESULTS

Ida M. Hakkarinen
General Software Corporation
Landover, MD 20785

Robert F. Adler
Laboratory for Atmospheres
NASA/Goddard Space Flight Center
Greenbelt, MD 20771

1 INTRODUCTION

Space-borne remote sensing techniques for the estimation of precipitation amount and and intensity have been developed over the last two decades using satellite data at visible, infrared and microwave frequencies. Many of these methods are based upon empirical relationships between cold and/or bright clouds in satellite imagery and ground truth from radar or rainfall networks. The microwave techniques offer a more physically-based method, since the upwelling radiation is affected by scattering and absorption processes related to the microphysical characteristics of the ice particles and rain drops in the clouds.

1.1 Microwave Precipitation Estimation: Satellite Methods

Barrett and Martin (1981) provide a comprehensive review of satellite techniques for the estimation of rainfall over both land and ocean. In the microwave frequency ranges, the emissivity of the background surface is an important factor to consider. The ocean is radiometrically "cold" in the microwave region; providing a uniform background. Land surfaces have large and highly variable microwave emittance properties, posing a complication for the interpretation of observations of precipitation over land. Savage and Weinman (1975) demonstrated that scattering processes of hydrometeors at 37 GHz are strong enough to provide at least a qualitative estimate of rainfall over land. Spencer, et al. (1983a) showed that statistically significant correlations existed between 37 GHz T_B's from the Scanning Multichannel Microwave Radiometer (SMMR) on Nimbus-7 and rain rates (RR) estimated from manually digitized WSR-57 PPI photographs. The T_B - RR relationship was approximately linear up to rain rates of 40 $mmhr^{-1}$

Spencer, et al. (1983b) reported very cold SMMR temperatures at 37 GHz which coincided temporally and spatially with the occurence of heavy thunderstorm rainfall. Spencer and Santek (1985) have pointed out the feasibility of mapping the global distribution of intense convection with passive microwave methods by comparing SMMR data over land with a climatology of surface-observed thunderstorm days for June-August.

1.2 Microwave Precipitation Estimation: Aircraft Observations

The utilization of aircraft-mounted sensors for remote observations of precipitation permits greater spatial and temporal resolution than provided by current satellites, as well as the capability of directing the aircraft to specific target areas. Aircraft experiments are also usually a step in the process of research and development leading to new satellite sensors.

Theoretical calculations of Savage (1976) showed that at microwave frequencies above 90 GHz, the scattering effects of ice associated with convective rainfall have a large enough effect to produce brightness temperatures much colder than either land or ocean background temperatures. Observations of a variety of precipitation regimes made from a Navy aircraft with a multi-frequency radiometer at 14, 19.3, 22.2, 31.3 and 89.5 GHz demonstrated that the 89.5 GHz channel was able to distinguish even light rainfall over both land and water backgrounds. (Hollinger, et al., 1978).

Wilheit, et al. (1982) published results from airborne observations of rain cells associated with a decaying tropical storm over water. In addition to an imaging radiometer at 19.35 GHz, the aircraft carried a fixed-view radiometer operating at 183 $\pm$ 1.2, $\pm$ 5, and $\pm$ 9 and 92 GHz. Extremely low T_B's (~140 K) were noted in the high-frequency channels in association with heavy convective precipitation. Modeling results by Wilheit, et al. (1982) showed that these extremely cold temperatures could be attributed to the scattering of upwelling radiation from precipitation-sized ice particles in the upper part of the clouds. Hakkarinen et al. (1982) and Hakkarinen and Adler (1984) presented preliminary results from a scanning version of the high-frequency radiometer which showed that areas of very cold T_B were related to the more intense convective areas of thunderstorm cells.

The purposes of this paper are: 1) to present comparisons of aircraft microwave sensor and radar imagery showing the relationships between patterns and gradients of T_B and echo intensities and 2) to compare observed T_B's with theoretical calculations of Wu and Weinman (1984) and Szejwach, et al. (1986) for similar frequencies.

2 DATA AND METHODOLOGY

2.1 Advanced Microwave Moisture Sensor (AMMS)

a) Instrument Description

The AMMS is a four-channel passive microwave imaging radiometer which has been flown on NASA high-altitude research aircraft. Three channels at 183 GHz observe at sidebands of $\pm$ 2, $\pm$ 5 and $\pm$ 9 GHz. Because of the near symmetry of the water vapor absorption band at this frequency, the two

bands received by each channel are equivalent. The fourth channel at 92 GHz observes radiation in the sidebands of 90-91 and 93-94 GHz. This large frequency spread is not a problem since this is in a broad window region of the atmospheric absorption spectrum. After every six scans, the radiometer views a heated (+60°C) and cooled (-20°C) calibration load for ten samples. These points are used to construct the linear curve for radiance versus brightness temperature. The calibration accuracy is approximately 5 K (Wilheit, et al., 1982).

The radiometer views ± 45° from nadir across track about the roll axis of the aircraft in a series of 50 equal steps. From a nominal aircraft altitude of 18 km, the ground resolution of the AMMS is 350 m (700 m) for the 183 (92) GHz channels. During the 1981 field experiment, the instrument operated in a non-scanning mode at periodic intervals for water vapor sounding retrievals. Images shown from this experiment will have blanked areas where this "stare" mode occured. Further information about the instrument is found in Gagliano and McCheehy (1981).

b) AMMS Imagery

Images of the scene are produced by sequencing successive scan lines of data. The distance between adjacent scan lines is a function of the rotation rate of the reflector and the aircraft ground speed. The distance between data points composing a scan line is a geometric function of the viewing angle and the target altitude. Differences in across-track and along-track resolutions produce a distorted image which is corrected for by a linear remapping algorithm during image analysis. The AMMS images have been remapped to user-specified heights and pixel sizes, normally chosen to compare with estimated cloud heights and resolutions of the visible/infrared airborne radiometer.

c) Area-averaged Brightness Temperatures

Average T_B's were calculated for clearly identifiable cold features using a 1 km by 1 km box centered on the coldest point of the feature through the use of interactive image analysis software (Ku, 1982). Minima in T_B were also noted. These values were used to compare with the radar data.

2.1 Radar Data

a) PPI Photographs

For all the cases except the 1981 field experiment, the ground-based radar data were low-level PPI photographs from operational National Weather Service WSR-57 radars. The data consisted of the standard video integrator and processor (VIP) levels of 1 to 6. The photographs were scaled to match maps on which the flight track of the aircraft and swath width of the AMMS imagery were plotted. The maximum VIP levels corresponding most closely in time and space with the AMMS features were paired by an analyst. The median value of rain rate using the Marshall-Palmer Z-R relationship was selected for each VIP level as the radar-derived rain rate for that point.

b) Digital Radar Data

During the Montana Cooperative Convective Experiment (CCOPE), digital radar data were collected from various radars. We used the data from the 10-cm Skywater radar located near Miles City, MT for comparison with the aircraft data. Computer software programs (Heymsfield et al., 1983) were used to generate constant altitude PPI (CAPPI) and range-height indicator (RHI) images. Navigation data from the aircraft were used to map the aircraft location onto the radar imagery. Maximum reflectivity values for areas which matched AMMS feature locations were converted to median rain rates.

3 RESULTS

3.1 Imagery Comparisons

a) Case 1: Evolution Of An Oceanic Squall Line

On the afternoon of 17 September 1979, a squall line formed off eastern Florida near Palm Beach and remained quasi-stationary during the next several hours. The NASA aircraft made several passes over this line along the major axis of the convection. Figure 1 shows a comparison of nearly simultaneous AMMS 92 GHz data and radar data. The microwave images are qualitatively similar to the radar echoes, with areas of lower T_B tending to coincide with higher VIP levels. The areas of colder T_B expand in size with time and the gradients tighten, indicative of an increase in the storm intensity. There are several elongated regions which are warmer than the background ocean T_B (260-264 K). Huang and Liou (1983) have shown theoretically for upwelling radiation at 85.5 GHz that T_B is a double-valued function for rain rate over an ocean surface. At low rain rates, T_B increases with increasing rain rate. Once the rain drops become large enough in size or precipitation ice forms, T_B decreases with increasing RR as the scattering process dominates emission and absorption. Thus, the AMMS appears to be detecting shallow convection (no ice layer) with light rain (T_B<266 K) as well as deeper convection which has an ice layer above heavier rain. It should also be noted that one-to-one matches between radar echoes and low T_B values are not obvious in all cases.

b) Case 2: Convection Over Land (Montana)

Figure 2 shows a portion of AMMS and digital radar data obtained for a flight track on 31 May 1981 in eastern Montana over developing thunderstorm cells. The 183 ± 9 and 92 GHz channels show a large convective tower with minimum T_B=135 K to the left of nadir and several smaller towers to the right of nadir at 20:08 GMT. The radar data shown are CAPPI's for 2 and 6 km above ground level (AGL). CAPPI's were generated at 1 km intervals for AGL heights of 2 to 12 km. The 6 and 7 km CAPPI's most closely matched the AMMS data in shape and location of features, implying that the microwave sensor is responding to mid-level reflectivity cores rather than precipitation at the ground. An interesting feature of the 183 GHz data is the region of colder temperatures along nadir one minute later which is not as strongly highlighted in the 92 GHz channel. This difference may be due to the differing sensitivity of the two

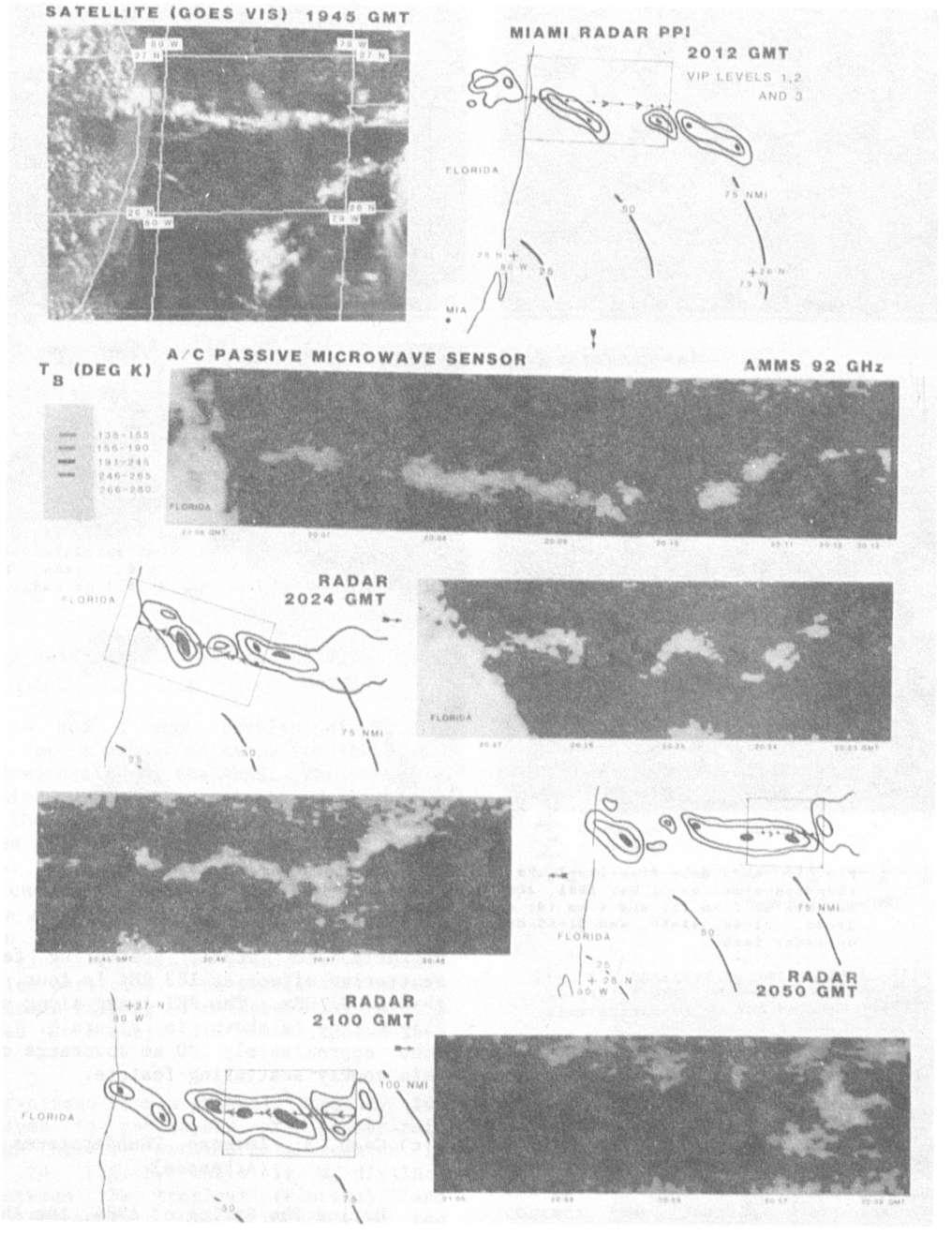

Fig. 1. Satellite, radar and microwave views of a Florida squall line on 17 September 1979. The radar VIP levels corresond to median rain rates of 1.5, 8, and 19 $mmhr^{-1}$.

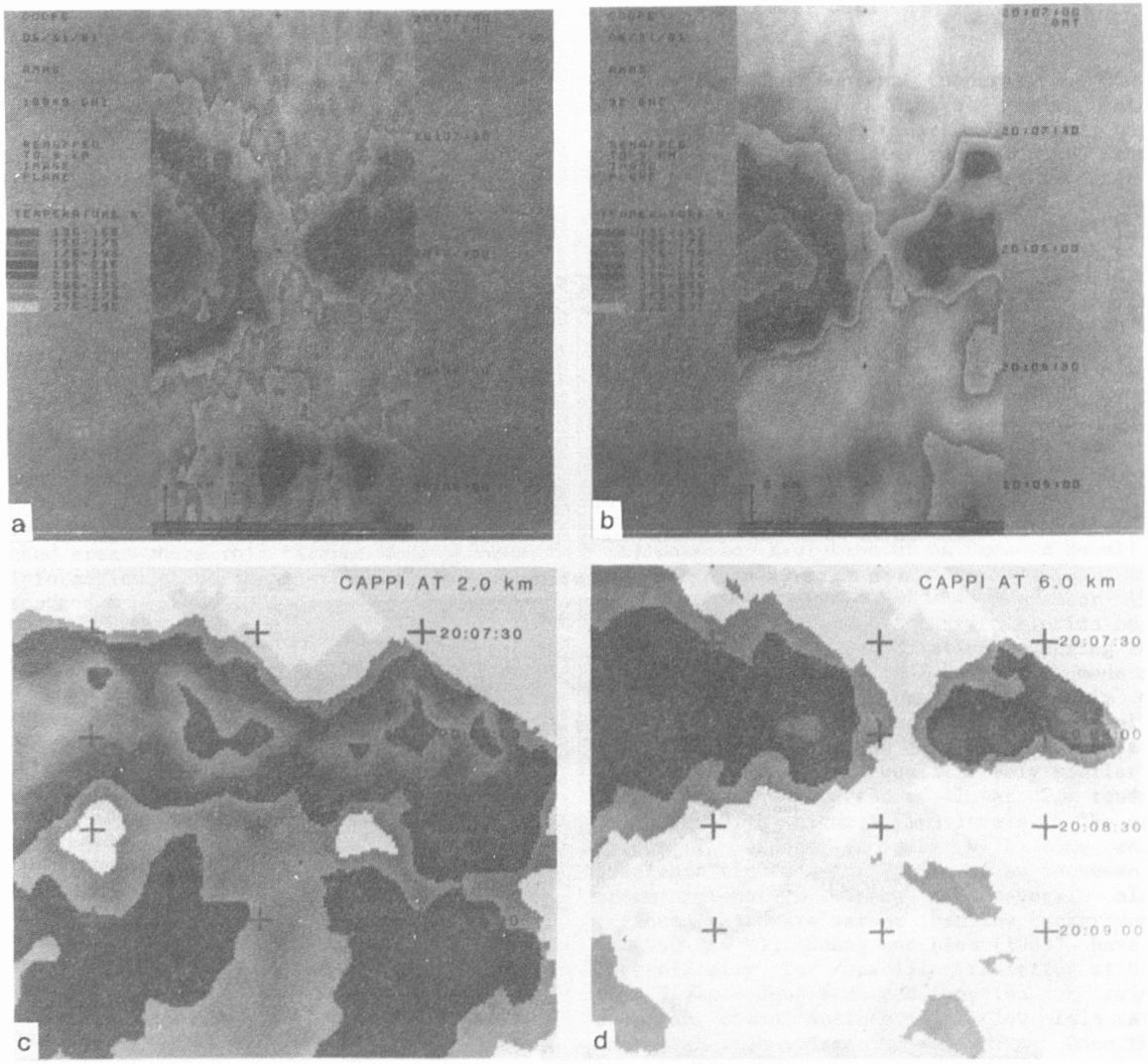

Fig. 2. AMMS data from 183±9 GHz (a) and 92 GHz (b) channels for Montana thunderstorms on 31 May 1981, 2007-2009 GMT. Concurrent radar CAPPI's for heights of 2 km (c) and 6 km (d) show reflectivity levels of 0-10, 11-20, 21-30, 31-40, 41-50, and 51-60 dBZ. Cursors denote position of AMMS swath on radar image.

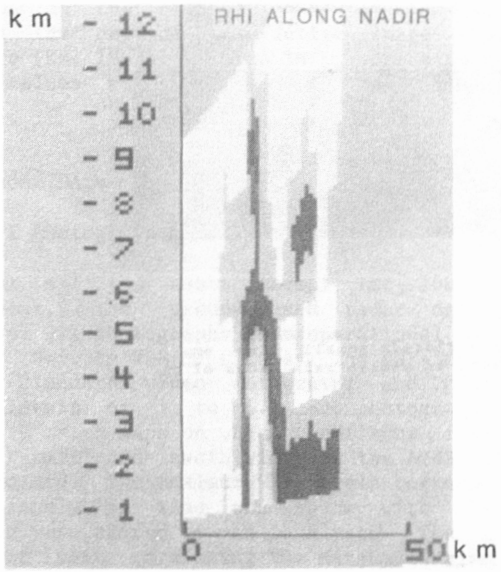

Fig. 3. Radar RHI along nadir for flight line shown in Fig.2.

channels to weakly scattering features. The scattering effect at 183 GHz is four times larger than at 92 GHz. The RHI image along nadir for this flight line is shown in Figure 3. The elevated echo approximately 30 km downrange corresponds to this weakly scattering feature.

c) Case 3: Intense Thunderstorms Over Land (Arkansas)

During the Spring of 1984, the AMMS overflew a line of intense thunderstorms in Arkansas. Images from the visible and microwave channels of the aircraft sensors from a flight line on 7 May are shown in Figure 4, along with a low-level PPI from the Little Rock, AR radar. Clouds which appear convective in the visible image have corresponding cold features in the microwave channels. During this flight day, T_B's as cold as 70 K were observed in all four channels of the AMMS. For this particular pass, maximum low-level VIP values of 4 were associated with these convective cells. Note, however, that precise matches between AMMS cold points (A,B,C) and an individual low-level echo are not always evident.

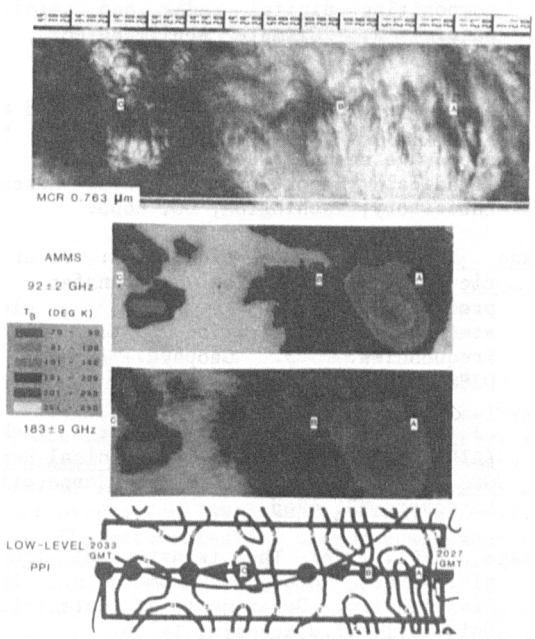

Fig. 4. Aircraft visible and microwave images of Arkansas thunderstorms on 7 May 1984 compared with ground-based radar. VIP levels correspond to median rain rates of 1.5, 8, 19, and 38 mmhr^{-1}.

3.2 T_B Versus Rain Rate: Comparison With Model Results

Figures 5 and 6 show results of T_B - RR observations for a number of cases for the 92 and 183 ± 9 GHz frequencies of the AMMS. These values were calculated using the process described in Section 2. The discrete rain rate values are median values for rain rates corresponding to VIP levels 1 to 5. Also shown on the plots are the theoretical curves calculated by Wu and Weinman (1984). These authors used a radiative transfer algorithm to compute radiances emerging from precipitating clouds containing liquid water, mixed phases, and ice particles. The vertical structure of tropical clouds raining at different intensities was determined in a subjective manner, based upon observations.

The observations show a general tendency for lower T_B values to correspond with higher rain rates, although there is considerable scatter in the data. In Fig. 5, there is a distinct difference between the tropical (Florida) and mid-latitude (Arkansas) observations, with the latter points showing a more rapid decrease in T_B with increasing RR. Szejwach et al. (1986, this volume) have simulated this climatological difference by using a combination of a cloud model and a radiative transfer model. The dissimilarities are primarily due to the differences in depth of the precipitation ice layer, which is related to environmental temperature and moisture conditions. These observational results strongly support the necessity for incorporation of environmental information into precipitation estimation techniques using microwave observations.

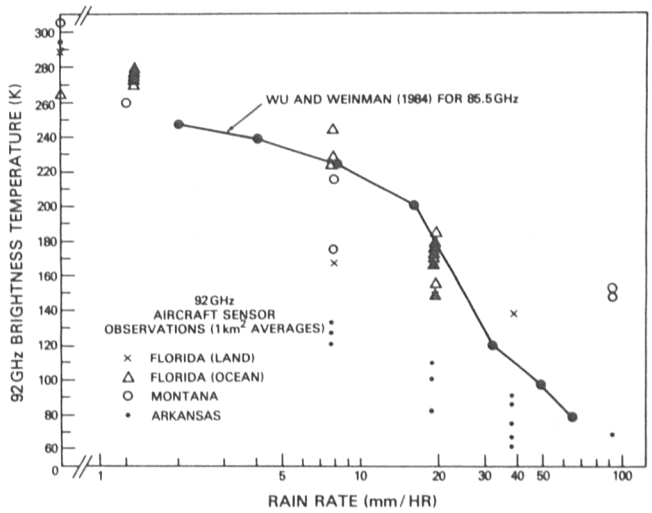

Fig. 5. Observed T_B versus rain rate values for the AMMS 92 GHz channel compared with theoretical calculations of Wu and Weinman (1984) for 85.5 GHz.

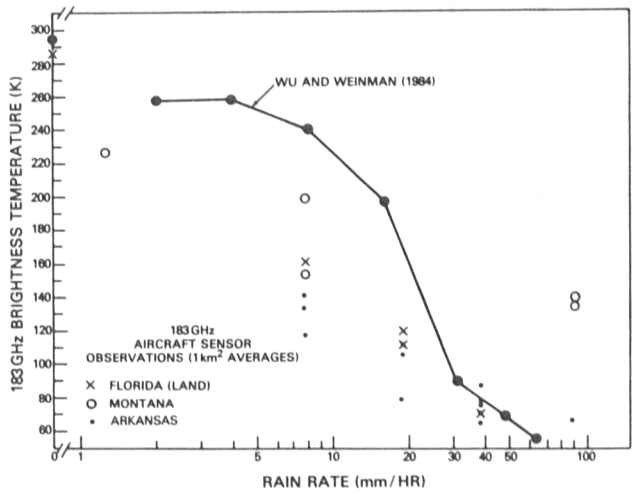

Fig. 6. Observed T_B versus rain rate values for the 183±9 GHz channel compared with theoretical calculations of Wu and Weinman (1984).

The behavior of the observations from the Montana case is puzzling. The slope of the T_B - RR line falls between that of the Florida and Arkansas cases. Even with surface rain rates as high as 90 mmhr^{-1}, average T_B values were no colder than 150 K. Assuming that the instrument calibration is correct, one possible explanation for the discrepancy is that the environmental conditions on this day (a low freezing level and a relatively low, warm tropopause) inhibited the development of a deep layer of precipitation-sized ice in the clouds. Investigation of this point is underway using the cloud model - radiative model calculations.

4 SUMMARY

Observations of convective precipitation from an airborne microwave radiometer operating at 92 and 183 GHz showed that areas of T_B much colder

than atmospheric temperatures are positively correlated with regions of high radar reflectivity. The patterns and gradients of T_B were similar in appearance to the radar echoes. Precise matches between AMMS and radar features occurred more often with mid- to upper-level reflectivity echoes than with the low-level data. This confirms the numerical results of Wu and Weinman (1984), who presented vertical profiles of weighting function for upwelling radiances of 85.5 and 183 GHz which showed that the greatest contribution from the atmosphere at these frequencies came from the upper 3 to 5 km of a cloud containing ice hydrometeors.

Comparison of spatially-averaged (1 km by 1 km) T_B with low-level rain rates showed an inverse quasi-logarithmic relationship, with lower T_B's indicative of higher rain rates. The slope of the T_B - RR curves varied with geographical location. This contrast was attributed to the differing local climatological conditions.

T_B values as low as 70 K were found in clouds which were producing heavy thunderstorm rainfall. These results are in agreeement with those of Spencer et al. (1983b), who found unusually cold 37 GHz T_B values in areas of heavy convective rain.

The frequencies of 92 and 183 GHz have potential applications on a geosynchronous passive microwave imager/sounder for the global monitoring of precipitation and severe storm intensity. The ground resolution from geostationary altitude of a 183 GHz channel with a 4 m antenna would be approximately 20 km.

In the shorter term, analysis of these aircraft observations may provide insight regarding data from the 85.5 GHz channel of the upcoming SSM/I instrument which is due to be launched on an Air Force satellite during 1986.

5 REFERENCES

Barrett, E.C. and D.W. Martin, 1981: The Use of Satellite Data in Rainfall Monitoring, Academic Press, 340pp.

Gagliano, J.A. and J.J. McCheehy, 1981: Advanced microwave moisture sounder (AMMS) for WB-57F CCOPE mission. Tech. report for Project A-2904, Georgia Institute of Technology, 40pp.

Hakkarinen, I.M., E.B. Rodgers and M.C. McCumber, 1982: The evolution of Florida thunderstorms on 23 September 1979 as observed by an airborne passive microwave radiometer. Preprints Conf. on Cloud Physics, Chicago, IL, Amer. Meteor. Soc., 504-507.

Hakkarinen, I.M. and R.F. Adler, 1984: Observations of deep convection from an airborne high-frequency (92 and 183 GHz) passive microwave radiometer. Preprints Conf. on Satellite Meteorology/Remote Sensing and Applications, Clearwater Beach, FL, Amer. Meteor. Soc., 216-221.

Heymsfield, G.M., K.K. Ghosh and L.C. Chen, 1983: An interactive system for compositing digital radar and satellite data. J. Climate Appl. Meteor., 22, 705-713.

Hollinger, J.P., R.M. Lerner, B.E. Troy and M.M. Wisler, 1978: Joint services 5D-2 microwave scanner definition study. NRL Technical Report 3807. Naval Research Laboratory, Washington, DC, 66pp.

Huang, R. and K.-N. Liou, 1983: Polarized microwave radiation transfer in precipitating cloudy atmospheres: application to window frequencies. J. Geophys. Res., 88, D3885-D3893.

Ku, J.-L., 1982: AOIPS Aircraft Package (AIRPAK) User's Guide. Technical Report GSC-TR8207, General Software Corporation, Landover, MD, 49pp.

Savage, R.C., 1976: The transfer of thermal microwaves through hydrometeors. Ph.D. Dissertation, Department of Meteorology, University of Wisconsin, 147pp.

Spencer, R.W., D.W. Martin, B.B. Hinton and J.A. Weinman, 1983a: Satellite microwave radiances correlated with radar rain rates over land. Nature, 304, 141-143.

Spencer, R.W., W.S. Olson, W. Rongzhang, D.W. Martin, J.A. Weinman and D.A. Santek, 1983b: Heavy thunderstorms observed over land by the Nimbus-7 Scanning Multichannel Microwave Radiometer. J. Climate Appl. Meteor., 22, 1041-1046.

Spencer, R.W. and D.A. Santek, 1985: Measuring the global distribution of intense convection over land with passive microwave radiometry. J. Climate Appl. Meteor., 24, 860-864.

Szejwach, G., R.F. Adler, I. Jobard and R.A. Mack, 1986: A cloud model-radiative transfer model combination for determining microwave T_B-rainrate relations. Preprints 2nd Conf. on Satellite Meteorology/Remote Sensing and Applications, Williamsburg, VA, Amer. Meteor. Soc. (this volume).

Wilheit, T.T.,Jr., A.T.C. Chang, J.L. King, E.B. Rodgers, R.A. Nieman, B.M. Krupp, A.S. Milman, J.S. Stratigos and H. Siddalingaiah, 1982: Microwave radiometric observations near 19.35, 92 and 183 GHz of precipitation in Tropical Storm Cora. J. Appl. Meteor., 21, 1137-1145.

Wu, R. and J.A. Weinman, 1984: Microwave radiances from precipitating clouds containing aspherical ice, combined phase, and liquid hydrometeors. J. Geophys. Res., 89, D7170-D7178.

REMOTE SENSING OF HYDROLOGICAL VARIABLES FROM THE DMSP MICROWAVE MISSION SENSORS

R. G. Isaacs, Y.-Q. Jin, G. Deblonde, R. D. Worsham, and L. D. Kaplan

Atmospheric and Environmental Research, Inc.
840 Memorial Drive, Cambridge, Massachusetts 02139

1. INTRODUCTION

Satellite observations of hydrological variables are essential to provide comprehensive initial states and improve the physical parameterizations of related moist processes in numerical weather prediction (NWP) models (Kaplan et al., 1983). The meteorological sensor complement of the Defense Meteorological Satellite Program (DMSP) spacecraft of the 1990s will include the SSM/T microwave temperature sounder, the SSM/T-2 millimeter wave moisture sounder, and the SSM/I microwave imager. Data from these microwave mission sensors are potentially applicable to the retrieval of a number of hydrological variables including atmospheric water vapor profiles, clouds, precipitation, and surface moisture (e.g., snow cover, soil, moisture, and vegetative moisture). This paper reports the recent results of our ongoing study to develop unified retrieval techniques to obtain these variables based on simulations of the microwave mission sensor data products.

2. THE DMSP MICROWAVE MISSION SENSORS

The instrumental characteristics of the SSM/T microwave temperature sounder, the SSM/T-2 millimeter wave moisture sounder, and the SSM/I microwave imager are summarized in Table 1. These three sensors will provide a total of nineteen channels of information extending from the microwave to the millimeter wave spectral regions.

Notably, the fields of view of these sensors will not all be colocated. The SSM/I, in particular, is a conically scanning microwave radiometer with a constant scan angle of 45 deg looking aft of the subsatellite point. This geometry results in a local scene zenith angle of about 54 deg. Both the SSM/T and SSM/T-2, in contrast, are cross-track scanning sounders. Furthermore, there is a considerable difference between the fields-of-view (FOV) of each sensor. For the SSM/I, FOVs differ for each frequency. Spatial filtering techniques should be applicable. For these and other reasons, exploiting the complete data sets to be available from this ensemble of sensors will not be straight forward.

Further information regarding these sensors can be found in Isaacs et al. (1985a) and Isaacs and Barnes (1985).

Table 1
Microwave Mission Sensor Characteristics

Instrument	Frequency (GHz)	Polarization (H or V)	FOV (km)	Response
SSM/T	50.5	H	180	surface
	53.2	H	180	T at 2 km
	54.35	H	180	T at 6 km
	54.9	H	180	T at 10 km
	58.825	V	180	T at 16 km
	59.4	V	180	T at 22 km
	58.4	V	180	T at 30 km
SSM/I	19.35	H and V	50	surface
	22.235	V	50	water vapor
	37.0	H and V	25	clouds, rain
	85.5	H and V	12.5	clouds, snow
SSM/T-2	90.0	V	50	surface
	150.0	V	50	surface
	183.31±1	V	50	water vapor
	183.31±3	V	50	water vapor
	183.31±7	V	50	water vapor

3. REMOTE SENSING APPLICATIONS

In the following sections, applications of the microwave mission sensor data to the remote sensing of water vapor profiles, precipitation, integrated water vapor, cloud liquid water, soil moisture, and surface type are discussed. All retrievals are based on the use of simulated sensor data.

3.1 Water Vapor Profiles

Water vapor profile retrievals were obtained in simulation from six selected sets of brightness temperatures calculated for 14 of the channels listed in Table 1, above. The six sets used various combinations of available channels from among the microwave mission sensors and are listed in Table 2. Spatial registration among FOVs of different sensors was not considered. Sets 1 and 3 consisted of the SSM/T-2 channels excluding and including the window channel at 90 GHz, respectively. Set 2 consisted of the four temperature channels from the SSM/T which peak lowest in the atmosphere. Sets 3, 4, and 5 include the complete SSM/T-2 channel set (i.e., set 3) with the addition of SSM/T temperature channels alone, SSM/I imager channels alone, and both SSM/T and SSM/I channels together.

Table 2
Selected Channel Subsets for Water Vapor Retrievals

Set #	1	2	3	4	5	6
Frequency	SSM/T-2	4 Chan	5 Chan	9 Chan	10 Chan	14 Chan
183±7	X		X	X	X	X
183±3	X		X	X	X	X
183±1	X		X	X	X	X
90.0			X	X	X	X
150.0	X		X	X	X	X
50.5		X		X		X
53.2		X		X		X
54.35		X		X		X
54.9		X		X		X
19.35H					X	X
19.35V					X	X
22.235V					X	X
37.0H					X	X
37.0V					X	X

Simulated sensor brightness temperatures were calculated for each channel set and atmospheric profile using the radiative transfer equation (Waters, 1976):

$$T_B = T_{B1} + \{\varepsilon\ T_s + (1-\varepsilon)T_{B2}\}\ \exp(-\tau) \qquad (1)$$

where T_{B1} is the upward emission from the atmosphere alone, ε is the surface emissivity = (1-R), R is the surface reflectivity, T_s is the surface temperature, T_{B2} is the downward emission from the atmosphere plus the attenuated cosmic background emission, and τ is the total opacity of the atmosphere along the line of sight. The quantities T_{B1} and T_{B2} are line integrals along the sensor line of sight given by:

$$T_{B1} = \int_o^H T(z)\ \gamma(z)\ \exp\ [-\int_z^H \gamma(z')\ dz']dz, \qquad (2)$$

$$T_{B2} = T_c\ e^{-\tau} + \int_o^H T(z)\ \gamma(z)\ \exp[-\int_o^z \gamma(z')\ dz']dz. \qquad (3)$$

Here H is the effective height of the atmosphere (taken as 50 km), $\gamma(z)$ is the total extinction profile equalling the sum of gas absorption and cloud attenuation, and T_c is the cosmic background temperature. Millimeter wave cloud attenuation properties used in the simulation were from Falcone et al. (1979).

Vertical moisture profile retrievals were obtained from independent samples of simulated sensor brightness temperatures using a statistical inversion technique. The scheme chooses, in a statistical sense, the most probable combination of atmospheric and surface properties which produces the set of measured radiometric data values. An individual retrieval of the absolute abundance of water vapor (molecules cm^{-2}) in six layers corresponding to 0-200, 200-300, 300-500, 500-700, 700-850 mb, and 850-1000 mb, respectively, from n channel brightness temperatures was obtained from

$$\hat{u} = D\hat{t}, \text{ with } D = (UT^t)(\hat{T}^*\Lambda^{*-1}\ \hat{T}^{*t}), \qquad (4)$$

where $\hat{u}$ is a vector giving an estimate of the profile of integrated water vapor in each of the six layers, $\hat{t}$ is a vector whose components are n brightness temperatures, U_{rs} is water vapor at six levels for s atmospheric samples (r=6), T_{ns} are brightness temperatures for n channels for s samples, $\hat{T}^*$ are selected eigenvectors of TT^t, and Λ^* is a diagonal matrix whose elements are corresponding eigenvalues.

Retrieval accuracy was assessed by comparing inferred layer water vapor abundances to those in the actual profiles and evaluating the fractional root mean square (RMS) error over the ensemble of retrievals. The RMS error for each layer k evaluated over the set of N = 100 independent soundings was defined as:

$$RMS(k) = \frac{1}{\bar{u}(k)}\ \{N^{-1} \sum_{j=1}^{N} [\hat{u}(k,j)-u(k,j)]^2\}^{1/2}, \qquad (5)$$

where $\hat{u}(k,j)$ and $u(k,j)$ are, respectively, the retrieved and actual water vapor amounts for the kth layer and j^{th} sounding and $\bar{u}(k)$ is the layer mean value. For comparison, the same statistic was evaluated assuming the mean of the ensemble as the best estimate climatological retrieval for each sounding, i.e. by replacing $\hat{u}$ by $\bar{u}$ itself.

Over the tropical ocean for the sample set investigated, water vapor profile retrieval results in clear cases are encouraging. All of the sample channel sets (except number 2) tested in simulation provide retrievals with less than 15 percent fractional RMS error in the lower troposphere (below 700 mb) and between 20 and 30 percent in the middle troposphere (between 300 and 700 mb). These retrieval accuracies may be compared with that of climatological variance for these layers, 28 to 38 percent and 55 percent, respectively (see Figure 1).

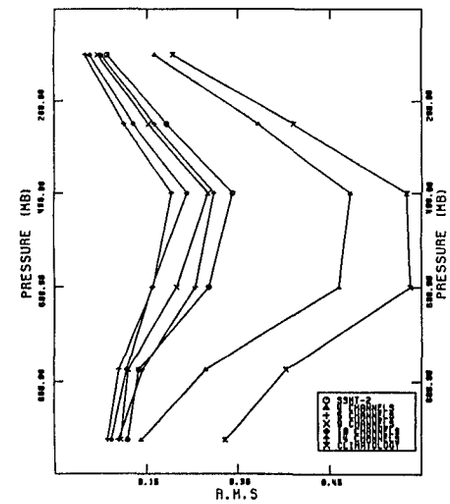

Fig. 1. RMS error DMSP mission sensor channel sets, clear cases over the ocean.

Set number 2, which consists of four SSM/T temperature channels does provide some skill over climatology in the lower atmosphere. The best retrievals are obtained using all 14 channels (set 6). Inclusion of either the SSM/T or SSM/I channels (sets 4 and 5, respectively) provide an improvement over the SSM/T-2 channel set alone.

These results can be compared to those obtained based on simulation of the HIRS-2 infrared

sounder using the same atmospheric profile data sets. Results are shown in Figure 2 for various combinations of temperature and water vapor sounding channels (from Kaplan et al., 1985).

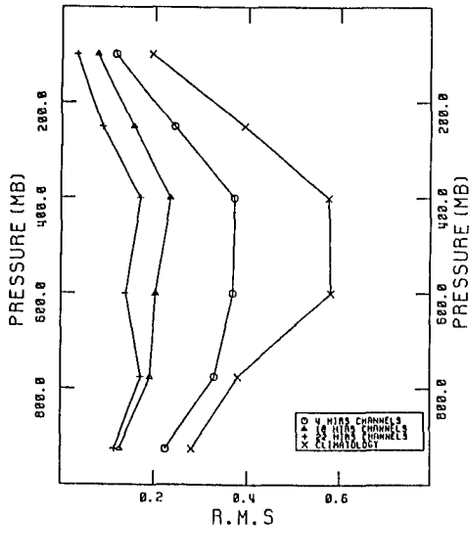

Fig. 2. RMS errors for HIRS-2 water vapor retrieval (clear cases).

While the statistical method provides an efficient retrieval calculation, the results are occasionally not physically realistic. A simple step would be to determine whether the statistical retrieval is consistent with the observed channel brightness temperatures. If the residuals are sufficiently large, the statistical first guess can be adjusted or rejected. Using the calculated residual values and an appropriate relationship between the change in water vapor profile and changes in channel brightness temperatures, we have formulated a physically-based correction to the statistical first guesses. The desired relationship is based on a perturbation form of the radiative transfer equation (see Smith et al., 1984):

$$\delta T_B^{\,j} = \sum_{i=1}^{M} \alpha_i \left\{ \int_0^{P_s} \phi_i(p) \frac{\partial T}{\partial p} \frac{\partial \tau^j}{\partial U} \right\} \qquad (6)$$

where U is integrated water vapor, τ^j is the transmittance function for the jth channel, and ϕ_i is an appropriate set of empirical orthogonal functions (EOFs) derived from the ensemble of atmospheric profiles. The number of EOFs used is small to help filter out noise and keep calculations to a minimum. The unknown α_i coefficients provide the necessary adjustments to the integrated water profile, $\delta U(p)$, consistent with brightness temperature residuals $\delta T_B^{\,j}$, and are obtained by inverting (6). Once the α's are known:

$$\delta U(p) = \sum_{i=1}^{M} \alpha_i \phi_i(p). \qquad (7)$$

The results of this approach using the SSM/T-2 channels alone are shown in Figure 3. There is an improvement in the RMS error near the surface.

The effect of cloud on the simulated millimeter wave moisture retrievals is dramatic. For cloudy cases over the ocean, for example, the RMS fractional error for the SSM/T-2 instrument (Figure 4), is increased by a factor of one half. Based on the results of our retrieval simulations

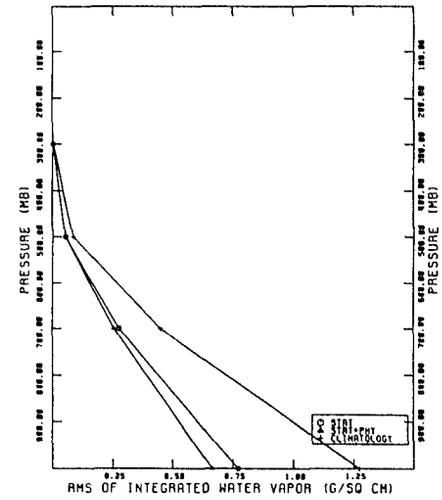

Fig. 3. Results of physical adjustment of statistical first guess retrieval.

it is evident that millimeter wave vertical moisture profile retrievals in the presence of clouds will be degraded in quality in comparison to those obtainable in clear situations and that suitable treatment of cloud will be necessary. Further details can be found in a report by Isaacs and Deblonde (1985).

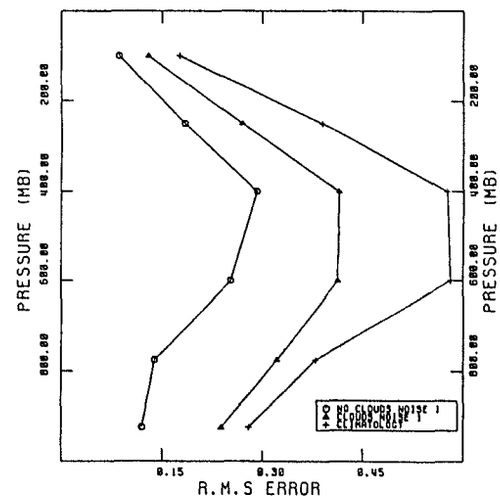

Fig. 4. RMS error, SSM/T-2 instrument, cloudy vs. clear, over the ocean.

3.2 Precipitation

The SSM/I microwave imager will provide some capability to infer precipitation, limited, however, by such factors as the lack of global coverage over much of the globe, lack of sensitivity to higher rainfall rates, and the inability to treat subresolution rain cells. A statistical retrieval scheme, similar to that described above, has been suggested for the SSM/I data in order to quantify precipitation.

Prior simulation studies were performed to support the development of a priori statistics relating channel brightness temperatures to various characteristics of precipitation. Notably, a number of physical processes were neglected in that work. These include: (a) the gradient of temperature within the precipitating layers, (b) anisotropic multiple scattering (important at higher rainfall rates and frequencies), and the vertical structure of the precipitation (e.g., the existence of glaciated layers of vertical gradients in rainfall rate).

To investigate the effect of neglect of these processes on the simulation of sensor brightness temperatures and inference of rainfall rates, a detailed radiative transfer model based on the Gaussian quadrature method has been employed. Details of this model are contained in the paper by Jin and Isaacs (1985). Simulated brightess temperatures as a function of rainfall rate from this model are illustrated in Figure 5.

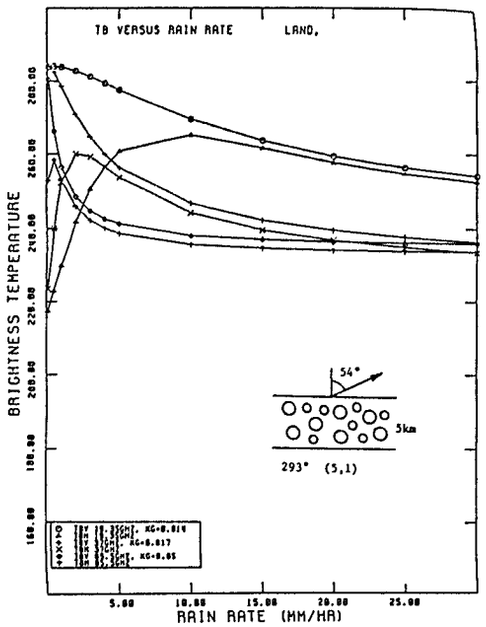

Fig. 5. Brightess temperature as a function of rainfall rate for SSM/I. (Lapse rate -6 K/km)

Using this model, the effect of neglecting particular physical processes in the model simulation of SSM/I brightness temperature was investigated. The results are summarized in Table 3. Processes listed include specification of a realistic temperature gradient, treatment of scattering anisotropy, and treatment of the existence of a top ice layer. Also included is treatment of the field-of-view problem, i.e., assumption that the precipitation is beam filling when it is not. The beam filling assumption leads to an overestimate of brightness temperature (denoted by a plus) when over the ocean and an underestimate (denoted by a minus) when over land.

Table 3
The Effect of Neglecting a Physical Process in the Model Simulation of SSM/I Brightness Temperatures

(+) denotes an overestimate (i.e., simulated brightness temperature is greater than true brightness temperature) and (-) denotes an underestimate (i.e., brightness temperature is less than actual brightness temperature).

Physical Process	Background Ocean	Background Land	Note
1. Temperature gradient, rain rate:			
(a) low	(-)	(-)	1
(b) high	(+)	(+)	1
2. Scattering anisotropy	(-)	(-)	2
3. Existence of top ice layer	(+)	(+)	2
3. Field of view	(+)	(-)	3

Notes:

1 All frequencies
2 Higher frequencies (i.e., 85.5 GhZ, V, and H)
3 Assumption that precipitation fills the field of view.

3.3 Surface Modeling

Appropriate radiative models of earth surface types can provide an understanding of the sensitivity of microwave sensors to variations in hydrological variables such as soil moisture, snow, and vegetative moisture content. We have applied two distinct modeling approaches: that based on wave theory for random discrete scatterers and that based on radiative transfer theory for continuous random media. The former approach is applied to modeling the ocean surface, sea ice, and snow, while the latter is applied to both soil and vegetation. Surface types modeled are summaried in Table 4. Further details can be found in Isaacs et al. (1985b).

Table 4
Surface Model Types and Modeling Approaches

Model	Surface Type	Modeling Approach
1	Calm ocean	Dielectric slab
2	Rough ocean	Random discrete scatterers
3	FY sea ice	Random discrete scatterers
4	MY sea ice	Random discrete scatterers
5	Dry snow	Random discrete scatterers
6	Wet snow	Random discrete scatterers
7	Land	Dielectic slab
8	Wet soil	Continuous random medium
9	Vegetation	Continuous random medium

Using these surface simulation models, surface types can be identified based on simulated brightness temperatures evaluated at 19.35 GHz. While gross classifications such as the distinc-

tion between land and ocean can be made based on ephemeris data and static surface data bases, many surface types are dynamically variable. These include snow cover, vegetation, and sea ice, for example. It would be of interest to identify simple algorithms applicable to the SSM/I which would abet surface type discrimination based on the sensor incident brightness temperatures themselves.

Simulated brightness temperatures at 19.35 GHz for both vertical and horizontal polarizations were evaluated corresponding to those surface types described above. These values were plotted against one another to determine whether a cluster analysis approach could be used for surface type identification. The results are promising and are illustrated in Figure 6. Plotted are individual simulations corresponding to a number of oceanic (calm, rough, multiyear, and first year sea ice) and land (dry and wet snowpack, vegetation, and wet soil) surface types. Multiple points for individual surface types (ocean, soil, and vegetation, for example) correspond to variations in related surface parameters such as surface temperature and moisture values and atmospheric temperature and water vapor profiles corresponding to tropical, midlatitude, and arctic models. Notably, results indicate that over land it should be possible to distinguish between vegetation, soil, and snow at least to first order. Limitations are introduced by the tendency of clusters characteristic of specific surface types to overlap at boundaries when, for example, vegetative cover or snow is so optically thin that it cannot be distinguished from the underlying soil. Over the ocean there should be little difficulty discerning sea ice of various ages from the ocean surface. Additional modeling at other frequencies and for a broader domain of surface and atmospheric parameters is required to establish the validity of this approach on a firmer basis.

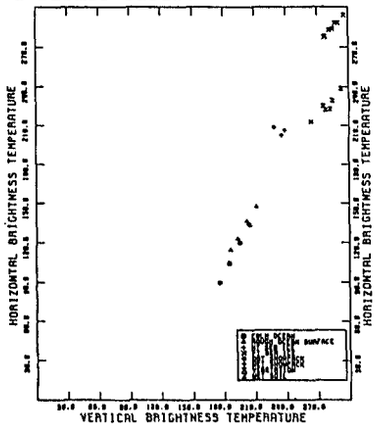

Fig. 6. Scatter diagram of polarized brightness temperatures for different surface types and atmospheres. Freq. = 19.35 GHz, zenith angle = 54°.

3.4 Integrated Water Vapor and Cloud Liquid Water Content

The uncertain effects of water vapor absorption and attenuation due to the presence of clouds will degrade the determination of the surface properties such as soil moisture (SM) obtained from data at a single frequency such as 19.35 GHz. In order to circumvent this problem, additional brightness temperature data at other frequencies which are more sensitive to atmospheric effects can be used to supplement the retrieval process. An additional benefit of this multispectral approach is the opportunity to retrieve information on atmospheric parameters of interest such as total integrated water vapor (TIWV) and cloud liquid water content (CLWC). In this section, the three quantities cited above are retrieved from a set of simulated polarized brightness temperature data calculated at 19.35, 22.235 (V only), 37.0, and 85.5 GHz using the D-matrix retrieval approach described in Section 3.1.

Retrievals were based on SSM/I brightness temperatures simulated for a set of two hundred tropical radiosonde profiles. Soil emissivities as a function of soil layer temperature and moisture content were calculated at 22.235 and 37.0 GHz to supplement the calculations at 19.35 GHz using the radiative transfer theory approach described in Section 3.3. Values at 85.5 GHz were assumed to be unity. Soil temperatures and moisture contents were assigned to each radiosonde profile. Soil temperatures were assumed to be equal to the radiosonde air surface temperature and moisture content values were assigned using a random normal distribution. This process provides appropriate emissivities at each desired SSM/I frequency.

Atmospheric properties to complete the simulation were obtained from the radiosonde data set. Total integrated water vapor (in precipitable centimeters) was calculated for each sounding and a Monte Carlo approach was implemented to assign clouds. For each radiosonde, a cloud type model was randomly assigned using a uniform probability distribution. Cloud models were chosen from those described by Falcone et al. (1979). The cloud liquid water content (in g/cm^2) for each cloud model was assigned to the corresponding profiles. In the presence of clouds, the impact on retrieval results of assuming water vapor saturation within the cloud layer was investigated. This was accomplished by creating simulated data sets both with and without saturated cloud layers.

Retrieval results are presented in Figures 7 and 8. The root mean square error (RMS) and fractional unexplained variance (FUV) are shown in Table 5.

Table 5
Multispectral Statistical Retrieval Results for Soil Moisture (SM), Total Integrated Water Vapor (TIWV), and Cloud Liquid Water Content (CLWC)

Model	Parameter	RMS	FUV
No clouds	SM	0.152	0.057
	TIWV	0.226	0.461
Clouds (saturated)	SM	0.221	0.119
	TIWV	0.211	0.415
	CLWC	0.394	---

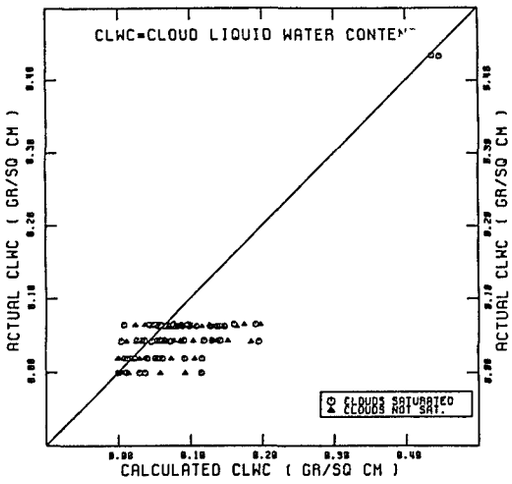

Fig. 7. Scatter diagram of actual versus retrieved cloud liquid water content.

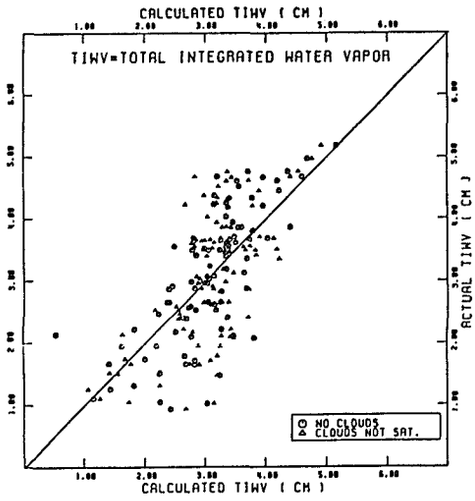

Fig. 8. Scatter diagram of actual versus total integrated water vapor.

4. CONCLUSIONS

The multispectral response of simulated sensor incident brightness temperatures to realistic variations in water vapor, cloud, precipitation, and surface moisture is illustrated. Using simulated data, the DMSP microwave mission sensor package is shown to have some skill in retrieving these quantities, especially when a multispectral approach is taken. There are difficulties, however, including the apparent effect of beam filling cloud on water vapor retrievals.

5. ACKNOWLEDGEMENTS

This work is sponsored by the Air Force Systems Command, Air Force Geophysics Laboratory, under contracts F19628-83-C-0027 and F19628-84-C-0134.

6. REFERENCES

Falcone, V. J., L. W. Abreu, and E. P. Shettle, 1979: Atmospheric attenuation of millimeter and submillimeter waves: Models and computer code. AFGL-TR-79-0253.

Isaacs, R. G., and J. C. Barnes, 1985: Tactical application of DMSP microwave temperature sounder (SSM/T) and imager (SSM/I) data. Scientific Report No. 3. Atmospheric and Environmental Research, Inc. AFGL TR-85-0094, 80 pp.

Isaacs, R. G. and G. Deblonde, 1985: Water vapor profile retrievals at 183 GHz: Land vs. ocean and clear vs. cloudy. Scientific Report No. 4. Atmospheric and Environmental Research, Inc. AFGL TR-85-0095, 86 pp.

Isaacs, R. G., G. Deblonde, R. D. Worsham, M. Livshits, 1985a: Millimeter wave moisture sounder feasibility study: The effect of cloud and precipitation on moisture retrievals. Atmospheric and Environmental Research, Inc. AFGL TR-85-0040, 60 pp.

Isaacs, R. G., Y.-Q. Jin, and G. Deblonde, 1985b: DMSP microwave imager (SSM/I) simulation and retrieval studies: Precipitation, soil moisture, and cloud liquid water. Scientific Report No. 5. Atmospheric and Environmental Research, Inc., 166 pp.

Jin, Y.Q., and R.G. Isaacs, 1985: Thermal radiative transfer for inhomogeneous nonisothermal atmospheric precipitation and statistical retrieval of related parameters. International Geoscience and Remote Sensing Symposium, Oct. 7-9, 1985, Amherst, MA, pp. 351-356.

Kaplan, L. D., R. N. Hoffman, R. G. Isaacs, R. D. Rosen, D. A. Salstein, and W.-C. Wang, 1983: Outlook for improved numerical weather prediction using satellite data with a special emphasis on the hydrological variables. Atmospheric and envornmental Research, Inc., AFGL-TR-83-0305, 195 pp.

Kaplan, L. D., R. G. Isaacs, R. D. Worsham, and G. Deblonde, 1985: Advanced moisture and temperature sounder (AMTS) study. Final report, NASA Contract NAS5-27629, NASA Goddard Space Flight Center, Greenbelt, MD 20771, 73 pp.

Smith, W. L., H. M. Woolf, and A. J. Schreiner, 1984: Simultaneous retrieval of surface and atmospheric parameters, a physical and analytically-direct approach. Paper presented at the Workshop on Advanced Retrieval Methods, October, Williamsburg, VA (in press).

Waters, J. W., 1976: Methods of Experimental Physics, 12, Part B, Academic Press, pp. 142-176.

P4.40

STRATOSPHERIC LIMB RADIANCE SIMULATIONS FOR THE HCL CHANNEL OF CLAES

J. L. Mergenthaler and J. B. Kumer

Lockheed Palo Alto Research Laboratory
Palo Alto, California

1. INTRODUCTION

The CLAES instrument (Cryogenic Limb Array Etalon Spectrometer), currently being constructed for deployment on the NASA Upper Atmospheric Research Satellite (UARS), will measure spectral earth limb infrared emission at approximately 0.2 to 0.7 cm^{-1} resolution in regions between 3.5 and 12.7 μm from which profiles of temperature, pressure, and concentrations of stratospheric chemical constituents will be inferred (Roche, 1985). A major sink of stratospheric chlorine, HCl is to be detected through its emissions in the vibrational fundamental (P2) line at 2843.62 cm^{-1} (Kumer and James, 1982). In this work the earthlimb radiance at the HCl detector array has been simulated in order to specify and optimize the free spectral range for the etalon used in this spectral region and to select sampling positions which facilitate the recovery of HCl profiles.

Section 2 discusses considerations which enter into the limb radiance computation of each contributing specie. Section 3 presents CLAES data earth limb radiance simulations for tangent heights of 15 to 55 km for daytime and nighttime conditions. Section 4 discusses these simulations as they pertain to HCL retrievals. Section 5, the conclusion, is a brief summary of our most important results.

2. DATA SIMULATION

The major contributors to the earth limb radiance in the neighborhood of 2843.6 cm^{-1} for tangent heights from 15 to 55 km are HCl, CH_4, Mesospheric OH and aerosol. Simulation of the earth limb radiance for each of these species has special problems and are not amenable to calculation by a "canned program" such as AFGL's FASCODE.

2.1 HCl

The non-LTE behavior of the HCl emission in the 1-0 band has been discussed by Kumer and James. Briefly, they find that the resonant scattering of sunlight will increase the daytime emission of stratospheric HCl up to several times the thermal emission depending on altitude. Their estimated emission rates and altitude profiles of non-LTE effects are used in this simulation.

2.2 OH

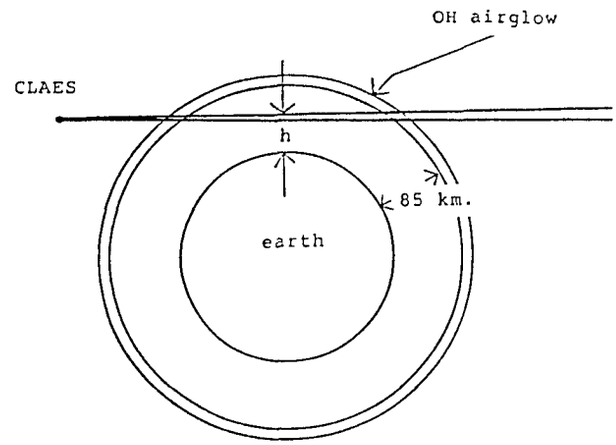

Figure 1. Geometry of CLAES earth limb measurement.

Figure 1 demonstrates the viewing geometry of the limb measurement. The line of sight at tangent height, h, appropriate for viewing the stratosphere passes through the region of OH chemiluminescent emission arising primarily from the reaction, $H + O_3 \rightarrow OH\ (v < 10) + O_2$ (Bates and Niclolet, 1950). The near-IR spectrum of earth limb emission of OH has been measured by Nadile et al. (1977) during the Air Force Geophysics Laboratory (AFGL) sponsored Spectral Infrared Experiment (SPIRE). A typical sample of nighttime earth limb spectrum of the fundamental, $\Delta v = 1$, band with maximum at 2.9 μm (3450 cm^{-1}) and the first overtone, $\Delta v = 2$, band with maximum at 1.6 μm (6250 cm^{-1}) are shown by Stair et al. (1985). The low resolution of the SPIRE data, approximately 25 cm^{-1}, washes out the detailed spectral structure of the OH bands by smearing individual vibration-rotation lines together. The higher CLAES resolution of approximately 0.6 cm^{-1} will be capable of resolving the spectral structure detecting weaker emission lines located among OH lines. This analysis is based on nighttime observations taken during a vertical scan on the earth limb with tangent height ranging from 81 km to 88 km which crossed the region of the maximum in OH emissions. This particular data was selected because it has the greatest amount of OH emission at the HCl line position of the data available and approximates a "worst case" analysis. Utilization of nighttime data takes advantage of the nocturnal maximum in OH chemiluminescent emission and absence of the daytime solar pumped ν_3 band of H_2O and

ν_3 fluorescent CO_2 components which appear around 3700 cm^{-1} (Sharma, et al. 1981). The limb radiance at wavenumber, ν, arising from a particular vibration-rotation transition, (v', j', Ω'> v", j", Ω"), is given by Equation 1. We define as N (v') as the column number density of molecules in state v' integrated through the earth's limb along the line of sight. A is the Einstein coefficient for spontaneous emission, and Q(T), the rotational partition function at rotational temperature T. The E (j', Ω') is the molecular rotational energy above vibrational ground state specified by v', Ω'. Partition functions are tabulated by Goldman(1982).

$$R(\nu) = (hc\nu/4\pi)\, N(v')\, (2j'+1)(A/Q(T)) \times \exp(-E(j', \Omega')/kT) \quad (1)$$

Energy levels, line postions, and intensities for OH are available through the AFGL Atmospheric Trace Gas Compilation (Rothman, et al., 1982) for vibrational levels up to v = 9 and j = 15.5. It was assumed that associated rotational levels are in thermal equilibrium with rotational temperature of 200 K.

The measured SPIRE $\Delta v = 1$ band from 2.5 μm (4000 cm^{-1}) to 3.7 μm (2700 cm^{-1}) was divided into thirteen 100 cm^{-1} wide intervals. The N (v') have been determined by a least squares fit to the SPIRE data and substituted into equation 1 to compute individual line earth limb radiances. The N(v) fit to the $\Delta v = 1$ OH band reconstructs the original 13 rectangle representation to better than 6.0% RMS accuracy. Stair et al. (1985, ibid.) shows the nighttime contribution of OH chemiluminescence to earth limb radiance as a function of viewing tangent height from approximately 100 to 45 km in their Figure 30. An extrapolation of this data to lower altitudes provides a factor with which to scale the magnitude of OH radiance to the desired tangent height.

2.3 Aerosol

Measurements of the daytime aerosol earth limb radiance profile at wavelengths short of 2.4 μm were extrapolated from shorter wavelengths to the region of interest using an an extrapolation formula based on a Mie theory computation using the AFGL Background Stratospheric size distribution. This is the closest approximation to a direct measurement at the HCl wavelength (3.517 μm) available. The aerosol component of earth limb radiance consists of thermal emission and scattering from the direct solar beam, upwelling reflected solar radiation, and earthshine. As far as HCL retrievals are concerned, it is important to analyze the spectral structure imposed on the aerosol component by atmospheric molecular absorption. In general the limb radiance due to scattering out of the direct solar beam and thermal emission is fairly "unstructured." However, scattering of upwelling radiation is highly structured by the water vapor and methane in the lower atmosphere.

The data yields an approximation to the total daytime earth limb radiance and of course no detailed spectral information can be derived directly from it. Scaling formulae have been derived to approximate the fraction of the total radiance attributed to each component. The ratio of sun light scattered from the direct solar beam to scattering of reflected sun light has been approximated by assuming that the earth-atmosphere system has a reflectivity of 0.1 at 3.5 μm. For example, the ratio of scattered solar radiation to scattered thermal earthshine was estimated by assuming a blackbody temperature of 300 K for the earth during the summer. The ratio of solar scattered to direct thermal emission of the aerosol was computed using an aerosol single scattering albedo computed from the AFGL Background Stratospheric size distribution using a temperature profile from a standard midlatitude atmosphere. These assumptions are sufficient to establish the nominal contributions from each component of the aerosol radiance. FASCODE has been used to study the structure and magnitude of the upwelling earthshine and albedo radiance using a summertime model with about 3.0 cm of precipitable water. The spectrum of upwelling earthshine was computed by combining transmission and emission spectra with a 300 K surface of emissivity 0.9. Of course upwelling radiation depends on highly variable quantities like surface temperature, cloud cover, surface reflectivity, and tropospheric water vapor. For example, extensive cloud cover could reduce the upwelling thermal radiance by an order of magnitude or an expansive cloudless desert could enhance the albedo and thermal radiation several hundred percent over these estimates.

2.4 CH_4

The target HCl emission at 2843.62 cm^{-1} is mixed with a contribution from CH_4 lines. To determine whether non-LTE effects are important in the $\nu_2 + \nu_4$, ν_3, and $2\nu_4$ bands in this region the laser excitation experiment results of Hess and Moore (1976) were employed. Their data indicates that the quenching times for these vibrational states are on the order of 10 μsec-torr in a variety of gases. Comparing this to the natural radiative lifetimes of the strongest of these bands, ν_3, the ratio of solar resonant scattering to thermal emission will be less than 2% for altitudes less than 45 km and less than 8% for altitudes less than 50 km. In this work FASCODE results for CH_4 are uncorrected for resonant scattering. These non-LTE effects, though not of great importance for the purposes of this work will be given further consideration in our retrieval analysis.

3.0 SIMULATIONS OF CLAES DATA

High resolution and the ability to sample at specified positions on and about the HCl feature are achieved by the CLAES optical system by means of a tiltable etalon proceeded by a blocker filter which transmits in the spectral neighborhood (~15 cm^{-1} FWHM) surrounding the HCl feature(see James and Kumer, Poster 4.43). A schematic diagram of the CLAES HCl transmission function is shown in Figure 2.

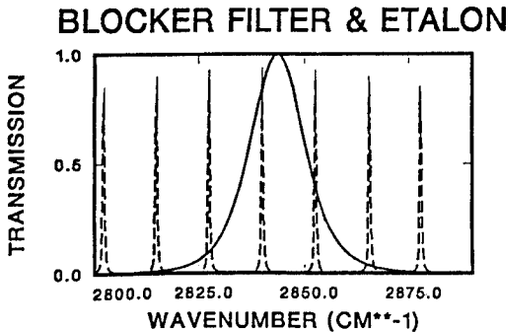

Figure 2. Transmission functions of the CLAES etalon and blocker filter for the HCl channel.

In this instance the blocker filter is wide enough to transmit radiance which has passed through several etalon transmission peaks spaced one free spectral range apart across the blocker filter. As the etalon is tilted, the transmission peaks shift relative to the blocker filter allowing the spectrometer to scan across the blocker filter region as shown in Figure 3.

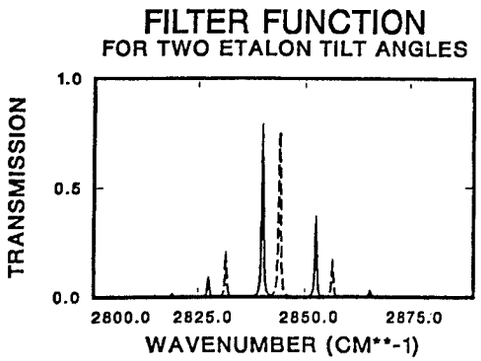

Figure 3. HCl channel filter function resulting from the blocker filter and etalon combination. The the dashed and solid lines show the effect of etalon tilting.

One major goal of this work was to specify a etalon thickness or free spectral range which would isolate the radiance from individual constituents, particularly HCl, as much as possible. Within constraints imposed by strength requirements an FSR of 12.6 cm^{-1} was found to be optimum. This etalon model provided the least overlap of the target HCl line with best separation of constituents.

Figures 4 through 11 depict the altitude profile of the CLAES simulated data for day and night for altitudes of 15, 30, 40, and 55 km. These tangent heights have been selected because they conform roughly to the bottom and top of the image on the three detector HCl array. The wavenumber scale attached to these simulations corresponds to the etalon transmission peak nearest the center of the blocker filter at 2843.6 cm^{-1}. The spectra appear strange to someone familiar with this region as emission lines transmitted by other transmission peaks are included. Figure 4 depicts the simulated nighttime earth limb radiance at 15 km. The region of the probable NER (noise equivalent radiance) for the instrument has been sketched in. Note that our target HCl line is approximately four times our highest estimate for the NER and is heavily blended with the OH P7.5 doublet in the 5-4 sub-band centered at 2842.2 cm . The most prominent feature in the CH spectrum is the large CH_4 ($\nu_2 + \nu_4$) combination band line at 2847.7 cm^{-1}. Corresponding to this feature in the aerosol spectrum is a dip associated with earthshine absorption and the absorption of radiation as it propagates out to space. In the daytime, Figure 5, several changes are apparent. The intensity of OH chemiluminescence decreases to an estimated one third due to the depletion of O_3 by photodissociation (Llewellyn 1979). On the other hand, HCl emission is increased by resonant solar scattering. However, it is noted that the scattering of sunlight increases the aerosol component to exceed the HCl emission by a factor of 50 or so. The absorption of aerosol-scattered light by CH_4 actually dominates the gaseous thermal emission at 2847.7 cm leaving a depression in the sum of these components. This 15km data is somewhat indicative of the data which will be gathered by the lower HCL detector. The high level of interference from aerosol CH_4, and OH and the additional likelihood of seeing high level clouds in this detector render the recovery of HCl from the lower detector problematical.

Figure 5 depicts the nighttime simulations for a tangent height of 30 km corresponding to the lower edge of the middle detector. In this case the aerosol component has dropped to the level of the NER and the CH_4 component has dropped to about twice the HCl radiance. The nighttime recovery of HCl is feasible in this case although averaging may be needed to raise the signal to noise in these measurements. The daytime 30 km simulations, Figure 6, appear promising for HCl recovery since there is less structure on the aerosol components as well as a relatively enhanced HCl emission.

Figures 7 and 8 show the night and day simulations near the top of the middle detector at 40 km. Figure 9 is the nighttime 55 km simulation. In this case the HCl radiance has fallen to the level of the NER. However, this is the upper part of the top detector and should be weighted accordingly when simulating the data from the entire

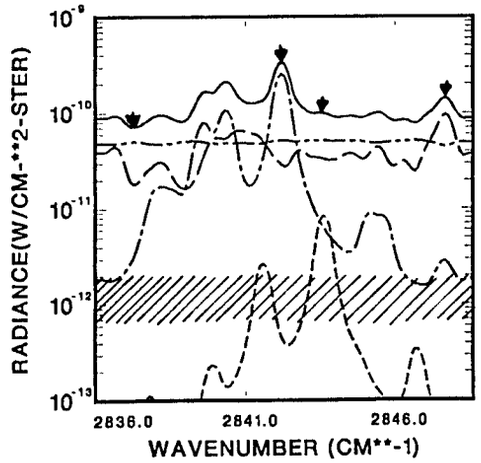

Figure 4. The nighttime earth limb simulation of CLAES data at 15 km. Four contributing species and their sum are shown. HCl (----), OH (—·—·), CH_4 (———), aerosol (—··—··), and their sum (———). The cross hatched segment of the estimated NER of the CLAES instrument in the HCl channel. Projected sampling points are indicated by arrowheads.

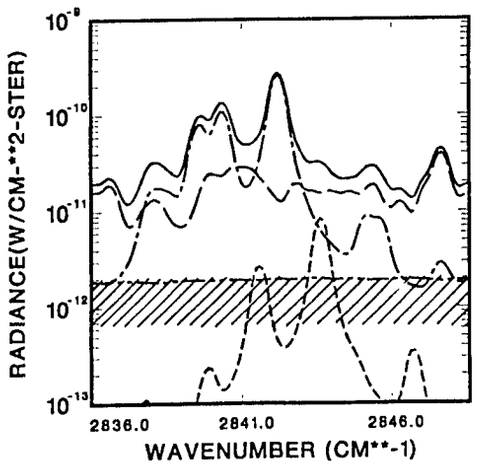

Figure 6. The nighttime earth limb simulation of CLAES data at 30 km. Legend is the same as Figure 4.

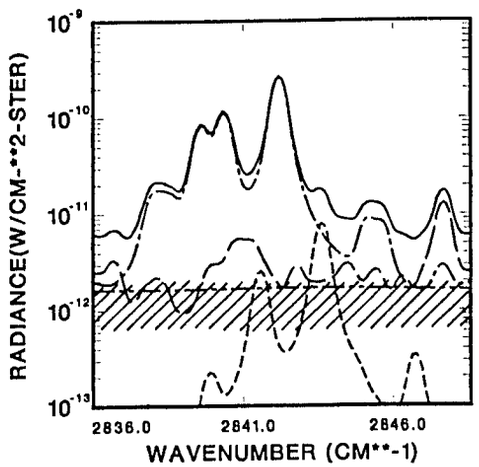

Figure 8. The nighttime earth limb simulation of CLAES data at 40 km. Legend is the same as Figure 4.

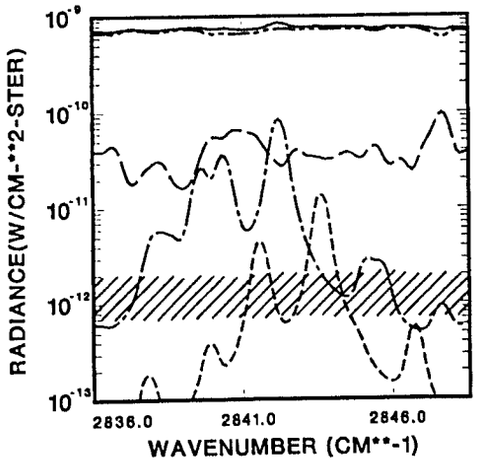

Figure 5. The daytime earth limb simulation of CLAES data at 15 km. Legend is the same as Figure 4.

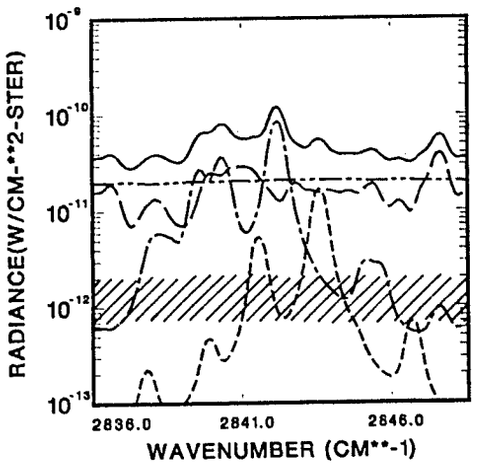

Figure 7. The daytime earth limb simulation of CLAES data at 30 km. Legend is the same as Figure 4.

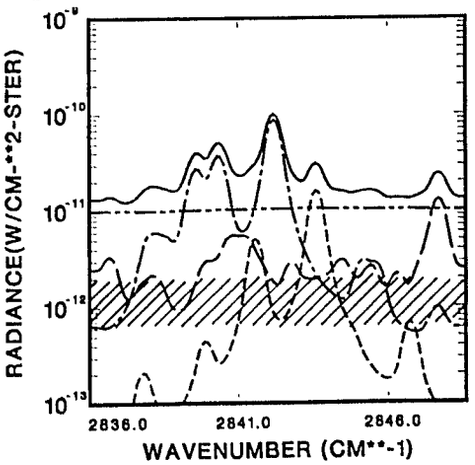

Figure 9. The daytime earth limb simulation of CLAES data at 40 km. Legend is the same as Figure 4.

upper detector. In the daytime at 55 km, Figure 10, the solar resonant scattering

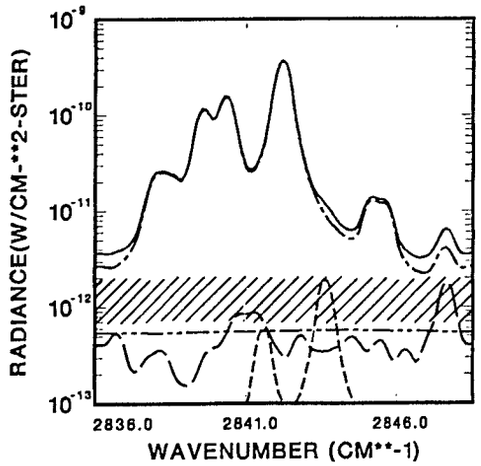

Figure 10. The nighttime earth limb simulation of CLAES data at 55km. Legend is the same as Figure 4.

increases the HCl signal to about five times the NER.

4.0 IMPLICATIONS FOR HCL REMOTE SENSING

In the interest of efficient data acquisition four points or etalon tilt angles have been selected to sample the HCL spectrum. These points are: the target HCl line at 2843.6 cm^{-1}; the OH doublet peak at 2842.2 cm^{-1}; the CH_4 peak at 2847.7 cm^{-1} and the relative window at 2837.1 cm^{-1}. Atmospheric pressure and temperature will be remotely sensed through another channel using the CO_2 Q branch at 791.2 cm^{-1}. These measurements should contain enough information to isolate the contribution from HCl. There are many potential error sources which are illuminated by this simulation and must be evaluated in the design of a retrieval algorithm. For example the Non-LTE emission of OH makes it difficult to assess the contributions from other OH lines from the measurement of 2842.2 cm^{-1} doublet. From the simulations it appears that other OH lines contribute at the HCl line position in a significant manner only at nighttime at high altitudes. This may not present a serious problem in practice since SPIRE OH data was chosen with what appears to be a higher than normal amount of emission at 3.5 μm.

The aerosol radiance component is increasingly uncertain with increasing altitude. The "window" measurement at 2837.1 cm^{-1} should help provide the magnitude of aerosol contribution while the very strong aerosol component appearing in the lower detector may provide the spectral structure. The middle detector corresponds with tangent heights from 28 to 42 km and the top detector with 42 to 57 km. The daytime simulated spectrum show the HCL line to be a factor of five or so above the maximum estimated NER on the middle detector and slightly lower on the

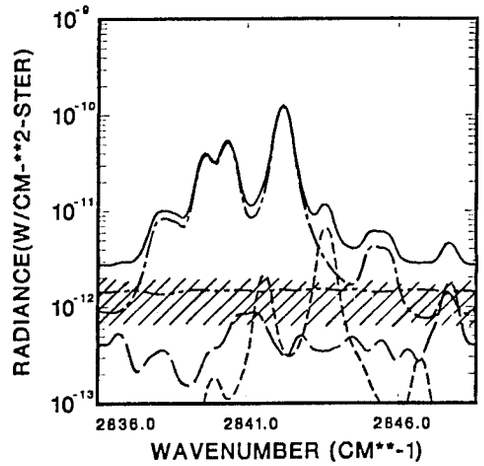

Figure 11. The daytime earth limb simulation of CLAES data at 55 km. Legend is the same as Figure 4.

upper detector. This S/N =~4 or 5 on a "point" to "point" basis should provide good precision for producing daily zonal averages. Data at a point here should be understood as the data obtained on each 65 second cycle, ie each ~380 km along the CLAES observational earth limb track. During a day ~64 such points will be obtained in an average 10 degree zonal belt at a given local time. Hence, the theoretical daily zonal average HCl mixing ratio S/N that can be derived for such a belt at given local time is S/N ~5*SQRT(64) =~ 40. Practically one might expect to achieve 5 << S/N < 40 for such an average.

5. CONCLUSION

Our simulations of earth limb spectra indicate that the HCl (P2) feature should be observable in the earth limb emission spectrum. In practice, CLAES is projected to sample the earth limb spectrum at four points near the primary HCl feature: the CH_4 line at 2847.7 cm^{-1}, the center of the OH doublet at 2842.2 cm^{-1}, the relative 'window' at 2837.1 cm^{-1} which may be dominated an aerosol component, and the HCl line center at 2843.6 cm^{-1} . The results of this study indicate that the selection of an etalon with an FSR = 12.6 cm^{-1} optimally avoids interference from OH emission lines blended with the HCl feature by adjacent transmission peaks.

An assessment of the accuracy with which HCL radiance can be isolated from the other components of the signal requires a numerical study of error propagation in the retrieval algorithm.

ACKNOWLEDGEMENT

This work supported by NASA contract NAS5-27757.

REFERENCES

Baker, D. J., 1978, Studies of atmospheric infrared emissions. AFGL-TR-78-0251, Air Force Geophysics Laboratory, Hanscom AFB, Massachusetts.

Bates, D. R., and Nicolet, M., 1950, The photo-chemistry of Atmospheric water vapor. J. Geophys. Res., 55, 301.

Goldman, A., 1982, Line parameters for the atmos-pheric band system of OH. Appl. Opt., 21, 2100.

Hess, P., and Moore, C. B., 1976, Vibrational energy transfer in methane. J. Chem. Phys., 65, 2344.

Kumer, J. B., and James, T.C., 1982, Non-LTE calculation of HCl earthlimb emission and implication for detection of HCL in the atmosphere. Geophys. Res. Lett., 9, 860.

Llewellyn, E. J., Long, B. H., and Solheim, B. H., 1978, The quenching of OH in the atmosphere. Planet. Space Sci., 26, 525.

Nadile, R. M., Wheeler, N. B., Stair Jr., A. T., Frodsham, D. C., and Wyatt, L. C., 1977, SPIRE--Spectral Infrared Experiment. SPIE, Vol. 24 -Modern Utilization of Technology III, 18.

Roche, A. E., 1985, Cryogenic Limb Array Spectro-meter (CLEAS), Upper Atmospheric Research (UARS) Mission, ed. S. Reber, NASA Publication #430-1003-001.

Rothman, L. S., Goldman, A., Gillis, J.R., Gamache, R. R., Pickett, H. M., Poynter, R. L., Husson, N. and Chedin, A., AFGL trace gas compilation: 1982 version. Appl. Opt., 22, 2100.

Sharma, R., Nadile, R.M., Stair Jr., A.T., and Gallary, W., 1981, Earth limb emission analysis of spectral infrared rocket experiment (SPIRE) data at 2.7 micrometers. SPIE, Vol. 304 - Modern Utilization of Technology VII, 139.

Stair, A. T. Jr., Sharma, R. D., Nadile, R. M., Baker, D. J. and Grieder, W. F., 1985, Observations of limb radiance with limb cryogenic spectral infrared experiment (SPIRE)". J. Geophys. Res. (in Press).

P4.41

QUALITY INDICATORS FOR TRACE GAS CONCENTRATIONS DETERMINED FROM EARTHLIMB EMISSION SPECTRA

W. G. Uplinger and J. B. Kumer

Lockheed Palo Alto Research Laboratory

3251 Hanover Street, Palo Alto, CA. 94304

1. INTRODUCTION

The CLAES instrument (Cryogenic Limb Array Etalon Spectrometer) will be deployed on the NASA Upper Atmosphere Research Satellite (UARS), scheduled for an October 1989 launch on the space shuttle. The ten instruments on board the UARS will greatly increase our knowledge of the chemistry, dynamics, and energy balance of the stratosphere and mesosphere. With an altitude of 600 km and orbit inclination of 57 Deg., the UARS covers the entire range of local solar angles in about 33 days. CLAES has an array of 20 detectors which look at the earth's limb between 10 and 60 km., in 8 narrow (~10 cm^{-1}) bands between 3.5 and 12.63 μm. The 14 orbits per day allow coverage up to 80 Deg. latitude. Atmospheric temperature and the mixing ratio of 11 different gases will be retrieved from spectral radiance measurements in the 8 spectral regions at resolution 0.2 to 0.7 cm^{-1}. The measured spectra are compared to calculated spectra based on assumed mixing ratios for the various gases. A linear, least squares fit of the spectra of the various gases to the measured data provides a new estimate of the mixing ratios for each gas. This article will discuss different techniques which indicate the quality of the retrieved mixing ratios. A key to retrieval from noisy data is the Singular Value Decompostion (SVD). Use of the SVD with simulated data and radiance measurements from a ballon floating at 30 km. will be discussed.

2. SIMULATED DATA

Computer runs have been made simulating measured CLAES spectral data. Among the effects included are detector noise, atmospheric radiation leaking through the blocking filter wings, telescope thermal emission, earth radiation scattered off the main telescope mirrors (BRDF), A/D conversion, errors in knowledge of the etalon postion, errors in knowledge of the spectroscoptic line parameters, and errors in the fast algorithms for atmospheric radiation. Figure 1 shows an example of CLAES spectral radiance at 22.5 km. tangent altitude, with the various components included. Detector noise is not a component, but is included as a reference level for the signal-to-noise of the components. Mixing ratios of the various gases are retrieved by a least squares fit of the components to the simulated data, which has the appropriate noises imposed.

3. SINGULAR VALUE DECOMPOSITION

A standard least squares fit of the components to noisy data is often unstable, due to components lying below the noise level, or two or more components being nearly linearly dependent. Use of the Singular Value Decompostion (SVD) can often reduce these problems. A brief discussion of the application of SVD analysis follows, based on Long (1983) and Lawson and Hanson (1974). The least squares problem can be written as

$$Ax = b \qquad (1)$$

where x are the unknown least squares coefficients and b is the noisy data matrix. Any real, rectangular matrix A can be decomposed as

$$A = USV^T \qquad (2)$$

where A is an mxn matrix, U is an mxm orthogonal matrix, V is an nxn orthogonal matrix, and S is a diagonal matrix with n values. The diagonal elements of S are the non-negative singular values s_i. Equation (1) can be written as

$$A = s_1R_1 + s_2R_2 + s_3R_3 + \ldots + s_nR_n \qquad (3)$$

where R is composed of the rows and columns of U and V. It can be shown that the sum of the elements squared of R_i is equal to 1.0. The contribution of each term in equation (3) is therefore proportional to the singular value s_i. Similarly, the inverse of matrix A can be written as

$$A^{-1} = s_1^{-1}R_1^T + s_2^{-1}R_2^T + \ldots + s_n^{-1}R_n^T \qquad (4)$$

Note that the term with the smallest singular value contributes the most to the inverse. This is the reason for the instability of least squares problems. Small singular values occur when there are components which are almost linearly dependent. The existance of linear dependence can be found in the last column of the matrix V. The sum of these elements squared is 1.0. The existance of positive and negative values near 1.0 indicates a linear dependence given by these elements. Reliability of the least squares coefficients, σ_i, is proportional to the square root of the diagonals of the covariance matrix C. The scaling factor is usually the square root of the mean square fit to the data. When σ_i is large compared to x_i, the component is often less than the

noise or is linearly dependent with another component. Stability of the inverse of matrix A is usually improved by truncating matrix A, deleting terms associated with singular values less than the noise. The least squares problem is solved exactly, but for a slightly different matrix. A sudden decrease in the size of the singular values as the order increases may also indicate singular values which can be discarded. Fewer singular values means that the fit to the data is not quite as good, but this may be compensated for by a greater stability of the fit. Chapter 23 of Lawson and Hanson (1974) contains a discussion of these and other techniques for determining a reliable least squares fit.

4. EXAMPLE

Application to simulated CLAES spectral radiance in the region 775 to 785 cm^{-1} will be used to demonstrate some of these techniques. Figure 1 shows the spectral radiance at 22.5 km tangent altitude, one of the 18 altitudes used in this study. The singular values versus order are shown in Figure 2 for all 18 altitudes. The noise level shown in Figure 1, 1.0E-09, is below the singular values at the lowest altitudes, but is very important at the highest altitudes. The sudden drops in singular values at orders 6 and 8 is also seen in the stability of the retrieved mixing ratios at the highest altitudes. If a gaseous spectral radiation lies below the expected noise, no retrieval should be possible. Figure 3 shows the mean signal-to-noise ratios as a function of altitude, for each of the different gases. The values of σ_i calculated from the covariance matrix correspond inversely to the signal-to-noise ratios in Figure 3. The altitudes where a component drops below the noise also show a decrease in singular value at high orders. Finally, Figure 4 shows the error in a preliminary retrieved mixing ratio for $ClONO_2$, whose mixing ratio decreases rapidly above 30 km and below 20 km. The expected error in knowledge of etalon position is assumed. Retrieval is seen to be impossible at altitudes where the signal-to-noise ratio is poor.

In this retrieval example the relative values of the spectral line parameters are assumed to be known to within 1 %. If these parameters are known less precisely the retrieval precision will degrade from what is shown. Our preliminary applications to actual data are briefly described below in Section 5. These preliminary applications do not achieve the precision shown on figure 4. One of several reasons for this result is that we are using the spectral parameters on the 1982 version of the AFGL tape. These parameters are not relatively precise to within 1 %. As an extreme example two of the strongest lines in the region 780.2 to 780.6 cm^{-1} appear to have relative line strength error of approximately 40 % on the 1982 AFGL tape.

Discussion with practicing laboratory spectroscopists indicates that it is possible to measure the relevant line parameters to within 1 % precision relative to the strongest line in the region for the more important species such as O3 and CO2. Spectroscopic data with the specified precision are necessary (but not sufficient) to achieve the precision of $ClONO_2$ retrieval that our study suggests is possible from the data that we expect to obtain in the CLAES mission.

5. DENVER UNIVERSITY DATA

In order to test the usefullness of the SVD against real data, some spectral radiance data from a balloon floating at 30 km, and looking down at 19 km tangent altitude, were kindly provided by Dr. Aaron Goldman at Denver University. These preliminary data were degraded to CLAES resolution, and the SVD was used with FASCOD1 to give the best fit to an assumed temperature and mixing ratio profiles for O3, CO2, ClONO2, H2O, and aerosol. Figure 5 shows the fit in the spectral region 778 to 783 cm^{-1}. The fit is good, considering that there was no attempt made to tune the temperature or mixing ratio profiles. Also, since these data are preliminary, they are still subject to revision by Dr. Goldman.

6. CONCLUSIONS

Computer simulations indicte that the Singular Value Decomposition (SVD) provides a stable method of solving least squares problems associated with high resolution atmospheric spectral radiance. Problems with closeness of fit, signal-to-noise ratios, linear dependence, and covariance matrices are all reflected in the SVD analysis.

7. ACKNOWLEDGEMENTS

Thanks to Dr. Aaron Goldman of Denver University for providing preliminary, high resolution, atmospheric radiance balloon data. These data were obtained by Denver University and the work was supported by AFOSR under the Atmospheric Science Project 2310 and performed as part of AFGL Task 2310g1.

This work supported by NASA contract NAS5-27752.

8. REFERENCES

Lawson, C. L., and R. J. Hanson, 1974: Solving Least Squares Problems. Engle Cliffs, N. J., Prentice-Hall Inc.

Long, C., 1983: Visualization of Matrix Singular Value Decompostion. Mathematics Magazine, 56, 161-167.

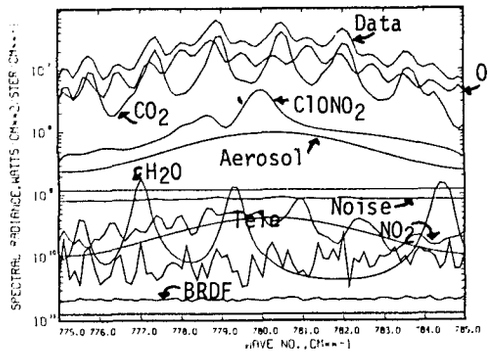

Figure 1 CLAES Spectral Radiance at 22.5km

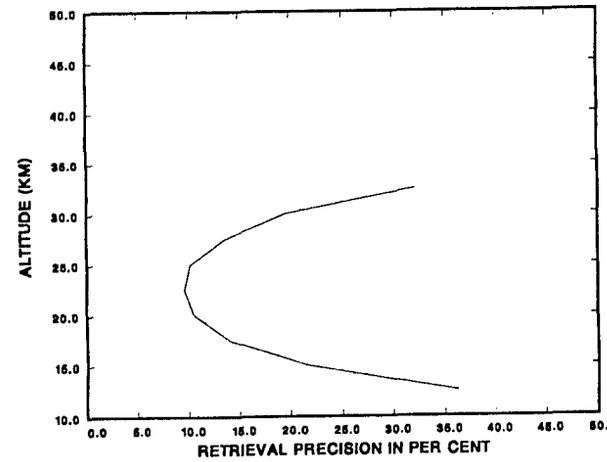

Figure 4 Estimated $ClONO_2$ Retrieval Precision

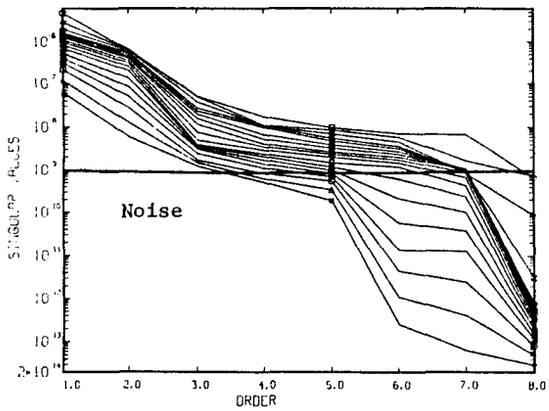

Figure 2 Singular Values vs Order for 18 Tangent Altitudes from 12.5 to 55km

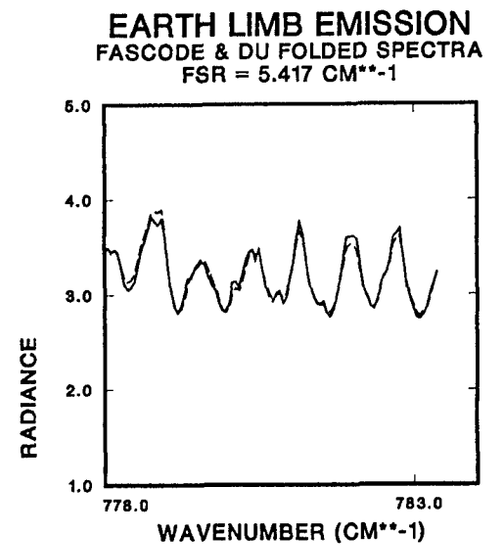

Figure 5 Fit with SVD of FASCODE Calculations to Denver University data

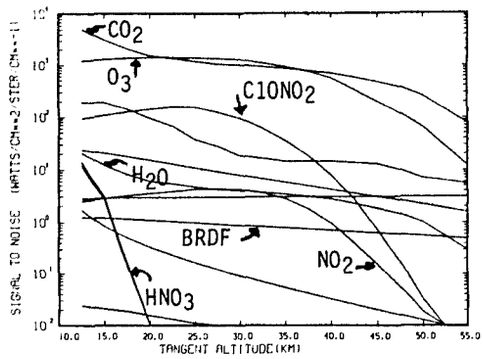

Figure 3 CLAES Signal-to-noise Ratio for Each Component

SENSITIVITY OF PROPOSED NEW AVHRR CHANNEL FILTERS TO AEROSOLS, WATER VAPOR AND VIEWING ANGLE FACTORS

C. G. Justus and M. V. Paris

Georgia Institute of Technology
Atlanta, Georgia

1. INTRODUCTION

The current AVHRR channels 1 (0.55-0.7 μm) and 2 (0.7-1.0 μm) are used, among other purposes, to determine aerosol parameters over water targets, and vegetation index over land targets. The sensitivity of proposed new filters (with channel 2 narrowed to 0.84-0.87 μm) for measurement of these parameters is examined by using the spectral model of Justus and Paris (1985) to simulate radiances along an AVHRR scan line. Effects of satellite viewing angle changes across the sensor scan and of a variety of surface directional reflectances for vegetation targets are examined. Plots of current and proposed channel 1 and 2 filter factors (Dr. Larry Stowe, private communication) are illustrated in Figure 1.

As a possible improvement in snow/cloud discrimination, it has also been proposed that the AVHRR channel 3 (3.7 μm) filter be replaced by a channel 3A (1.6 μm) filter during daylight periods. The initial version of the spectral model accounted for scattering and absorption processes, but not thermal emissions by the surface or within the atmosphere. Since the model was designed to accommodate absorption and scattering processes for wavelengths up to 4.0 μm, the addition of a reflective-IR absorption-emission radiative transfer routine (described by Justus, 1985) allows simulation of either daytime or nighttime values for AVHRR channel 3. Some comparisons of simulations of channel 3 and 3A values are also presented.

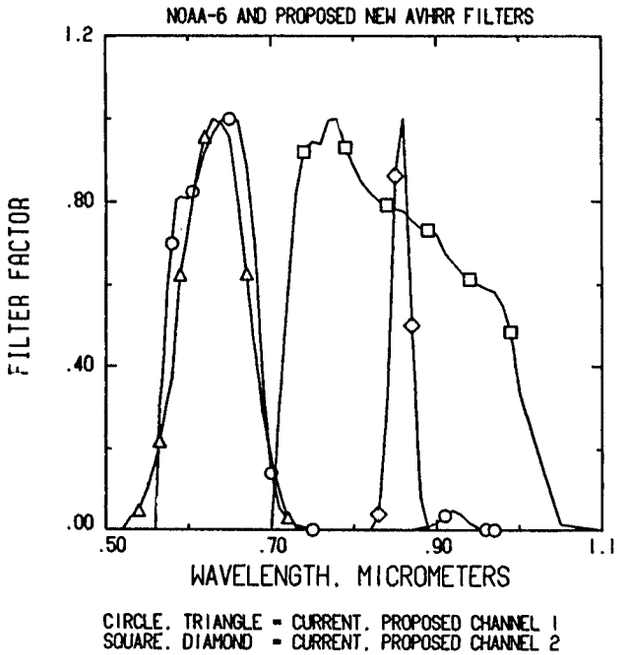

Fig. 1. Filter factors for current and proposed AVHRR filter factors.

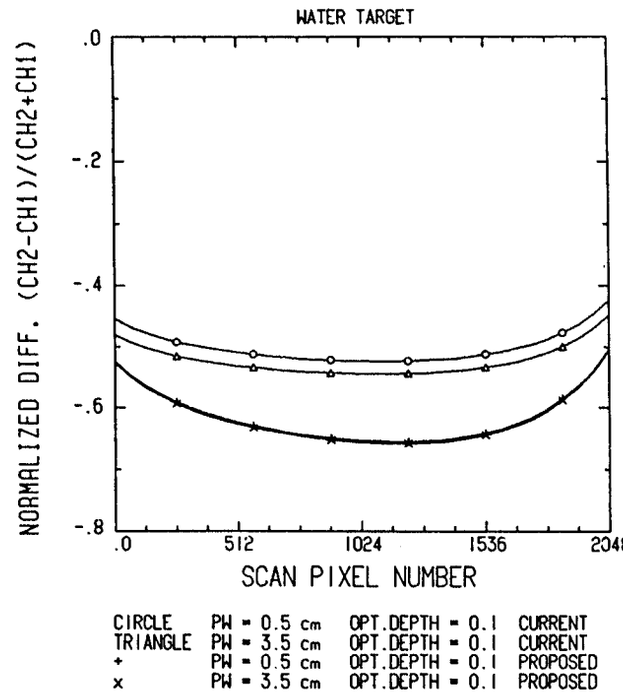

Fig. 2. Simulated effects of water vapor on normalized reflectance difference over a water target for current and proposed channel 1 and 2 filters.

2. SIMULATION RESULTS

2.1 Channels 1 and 2

Simulations of AVHRR channel 1 and 2 scan data (as characterized by the normalized reflectance difference) are illustrated in Figures 2-5. These figures show the sensitivity of the present and propsosed filters to interference effects

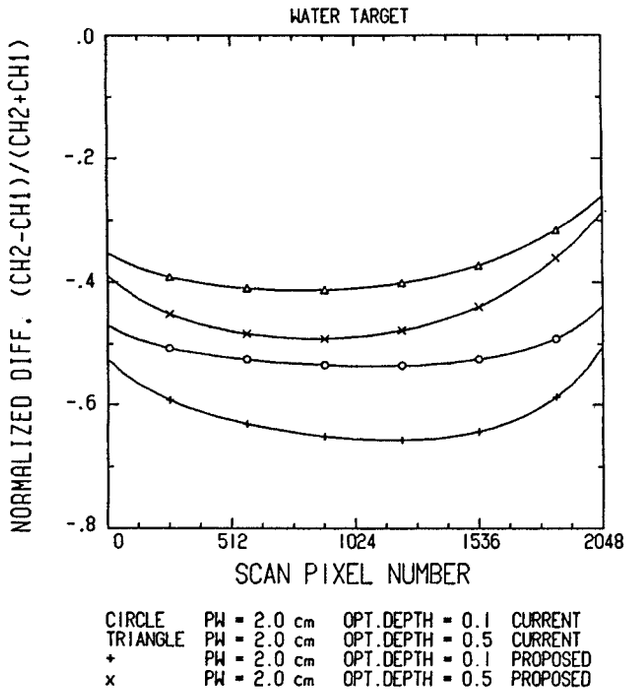

Fig. 3. As in Figure 2 for the effects of aerosol optical depth.

precipitable water and aerosol optical depth for water targets (Figures 2-3) and for vegetation targets (Figures 4-5). The new filters are significantly less sensitive to water vapor interference, since the narrower new channel 2 includes no significant water vapor absorption bands. The new filters are more sensitive to aerosol effects over water (i.e. aerosol parameters will be better detectable) and have about

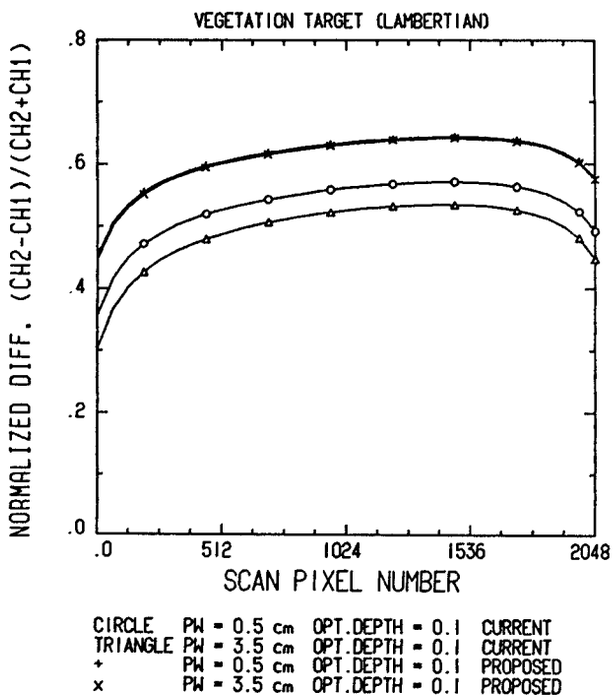

Fig. 4. As in Figure 2 for a vegetation target (Lambertian surface).

the same or less sensitivity to aerosols for the vegetation target. However, somewhat larger limb "brightening" and "darkening" effects are noted for the new filters than for the current ones.

The effects of surface directional reflectance factor on channel 1 and channel 2 reflectances at the top of the atmosphere are shown in Figures 6 - 8. Surface directional reflectance factors used are: (1) Lambertian, (2) results from a canopy model (supplied by Prof. John Norman), and (3) empirical data of Kriebel (1977) for surfaces of pasture land, savannah, bog and coniferous forest. All of the simulations assume the same spectral reflectance values for a vegetation surface as used for Figures 2-5. Figures 6 and 7 are for the current AVHRR channel 1 and 2 filters, while Figure 8 is for the proposed new channel 2 filter. The sensitivity to surface directional reflectance is almost the same for the current channel 1 and the proposed new filter (results not shown). For channel 2, the new filter is somewhat more sensitive to variations in surface directional reflectance, especially on the backscatter (pixel 0) side of the scan.

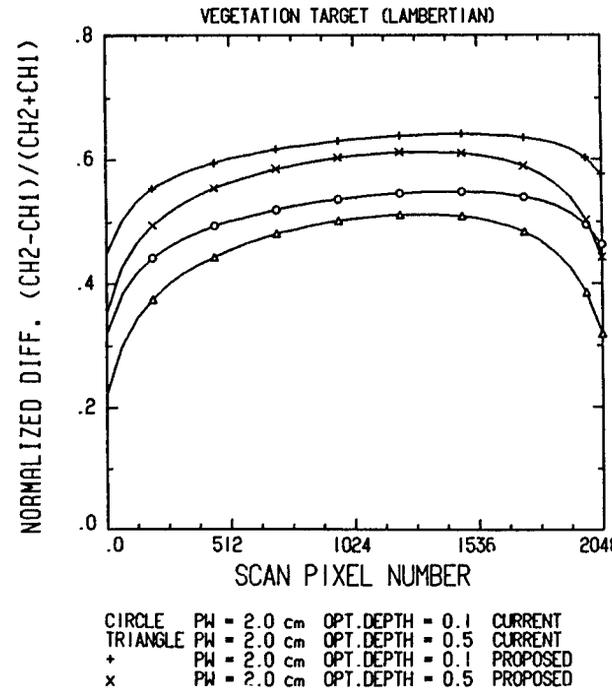

Fig. 5. As in Figure 2 for a vegetation target (Lambertian surface), effects of aerosol.

With the proposed changes in the channel 2 filter removing the interference effects of water vapor, measurement of aerosol parameters for water targets should be considerably improved over the use of the present filters.

2.2 Channels 3 (3.7 μm) and 3A (1.6 μm)

Figure 9 illustrates the results of simulations of the upwelling radiance at the top of the atmosphere for a scan line from AVHRR channel 3 over various (Lambertian) target surfaces, including both optical depth 4 and optical depth 64 clouds layers. All surfaces are assumed to be at 0°C. Although there is some discrimination between the snow surface (which has essentially zero reflectance in this wavelength range) from

soil, vegetation and clouds, the effects of thermal emission tend to lessen the contrast if, as shown in Figure 10, snow at one temperature is compared to a colder (high) cloud surface.

Cloud reflectances used in these simulations are computed with a delta-Eddington subroutine in a model that includes a cloud layer between clear layers above and below (Paris and Justus, 1985).

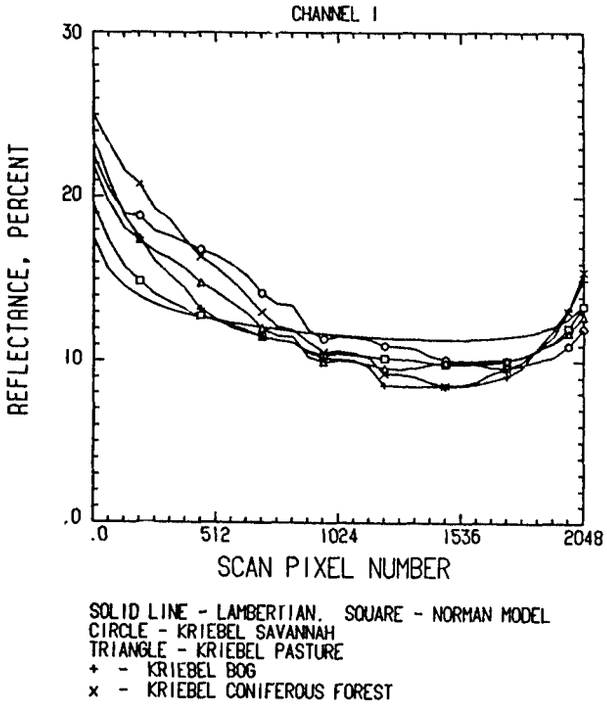

Fig. 6. Effects of various surface directional reflectance factors on channel 1 top-of-atmosphere reflectance (all assuming vegetation surface spectral reflectance).

The contrast between snow and other surfaces is much better for the spectral range of the proposed new AVHRR channel 3a, shown in Figure 11. In this case the snow surface appears essentially "black" because of its very low reflectance, with no interference from surface thermal emission at these wavelengths. The channel 3a radiance from thick clouds is noticeably larger than that for soil and vegetation, although this channel offers little contrast between thin clouds and these surfaces. Notice the different pattern of limb brightening and darkening for channel 3a shown by Figure 11, compared with only limb darkening for channel 3, illustrated in Figures 9 and 10.

REFERENCES

Justus, C. G. (1985): "Satellite Data, Model, and Ground-Truth Studies at AVHRR Visible, Near-IR, and Reflective-IR Wavelengths", Quarterly Report under NOAA Cooperative Agreement NA84AA-H-00010, October.

Justus, C. G. and M. V. Paris (1985): "A model for solar spectral irradiance and radiance at the top and bottom of a cloudless atmosphere", J. Clim. Appl. Meteorol, 24, 193-205.

Kriebel, K. T. (1977): "Reflection Properties of Vegetated Surfaces: Tables of Measured Spectral

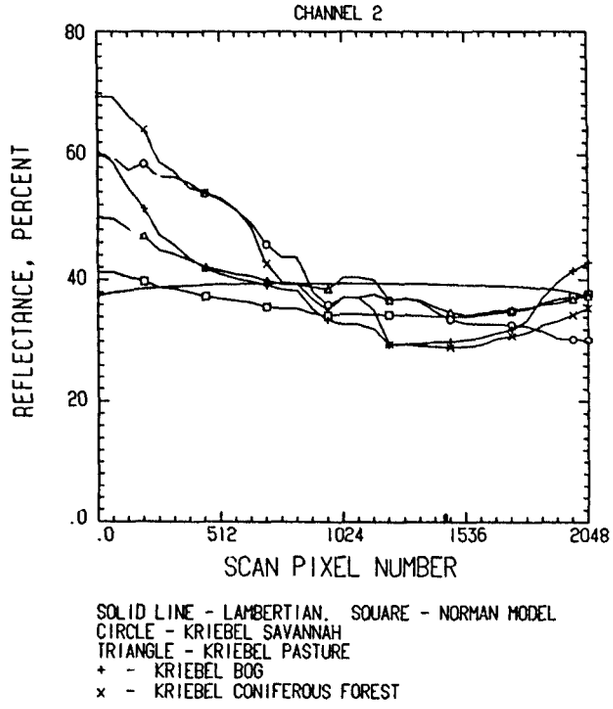

Fig. 7. As in Figure 6 for current channel 2 filter.

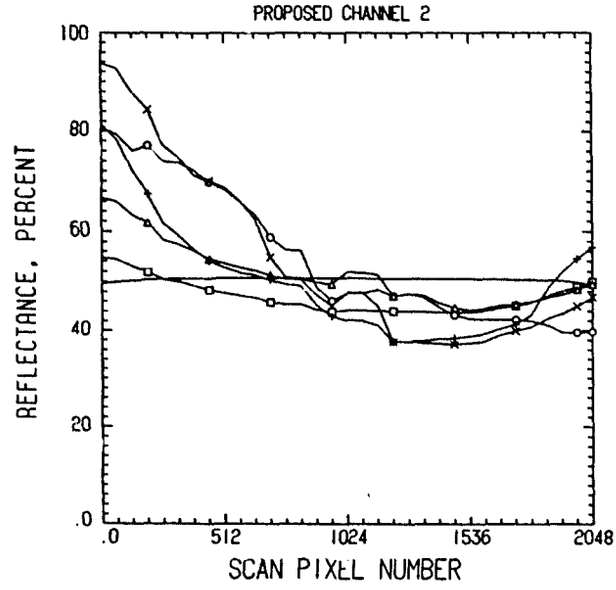

Fig. 8. As in Figure 6 for proposed channel 2 filter (0.84 - 0.87 μm).

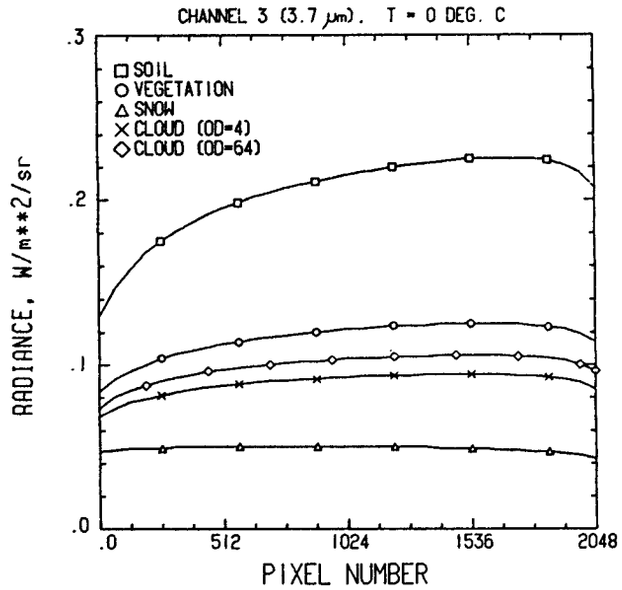

Fig. 9. Simulated channel 3 (3.7 μm) scans for various surfaces at 0° C temperature.

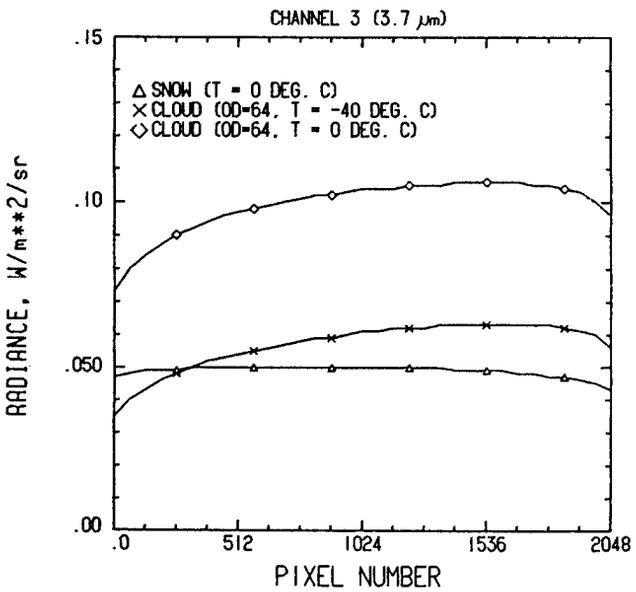

Fig. 10. Reduction in channel 3 snow/cloud contrast caused by a colder cloud temperature (high clouds).

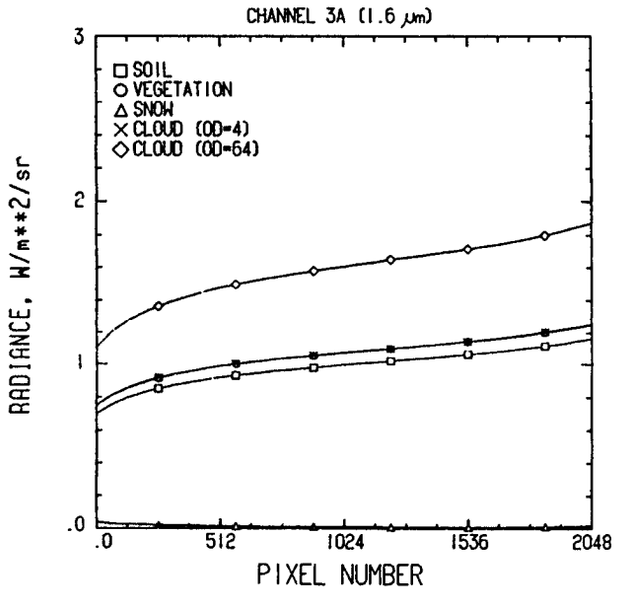

Fig. 11. Simulated channel 3A (1.6 μm) scans.

Biconical Reflectance Factors", Meteorological Institute, University of Munich, Number 29, September.

Paris, M. V. and C. G. Justus (1985): "Vicarious Calibration of GOES VISSR with Surface Observations of Cloud Transmittance", Proc. 2nd Conf. on Satellite Meteorology/Remote Sensing and Applications, May 12-16, Williamsburg, VA.

P4.43

CLAES BLOCKER FILTER REJECTION REQUIREMENTS

T.C. James, J.B. Kumer, A.E. Roche, L.W. Sterritt and W.G. Uplinger

Lockheed Palo Alto Research Laboratory
3251 Hanover Street, Palo Alto, Ca. 94304

INTRODUCTION

The CLAES (Cryogenic Limb Array Etalon Spectrometer) will be deployed on the NASA Upper Atmosphere Research Satellite (UARS) scheduled for autumn 1989 launch. The CLAES will obtain earthlimb spectra at resolution less than or equal to 0.5 cm^{-1} in 9 carefully selected narrow (of the order of 10 cm^{-1}) regions that are located in the relatively broad range 3.5 to 12.6 μm. The measurements will be obtained at altitude resolution of 2.5 km from 10 to 60 km. The measurements will be repeated every minute to obtain horizontal resolution of 500 km. The measurements will be used to determine temperature and pressure and the species O3,H2O, N2O, CH4, CF2Cl2, CFCl3, CCl4, HNO3, N2O5, ClONO2, HCl, NO, and NO2 globally.

The CLAES is shown schematically in figure 1. Solid Hydrogen is utilized to cyrogenically cool optics, spectrometer, and focal plane to the temperatures shown. The cooler is sized to support the mission in excess of 18 months duration. Each of the 9 blocker filters have full width at half max (FWHM) in the range 8 to 14 cm^{-1}. Light that passes through a given blocker filter is further reduced in spectral width by a factor of 20 to 40 by passing through the the serially mounted etalon as shown in figure 2. A programmable tilt angle range of 0 to 22.5 degrees is sufficient to scan the etalon transmission peak throughout the transmission range of the blocker filter. Thus high resolution spectra are obtained simultaneously on each element of a 20 element Si:Ga PC detector array that is vertically oriented to obtain coverage over the altitude range as shown in figure 3. An additional array of 3 large detector elements (as indicated on figure 1) in which vertical resolution is a sacrifiaced to enhance signal/noise is utilized specifically for the HCl measurements that are to be made in the 3.52 μm region. Specific spectral regions covered by the blockers and etalons, and measurements to be made in each region are shown in figure 4.

The main intent of this article is to describe the details of the calculation of out of band spectral rejection requirements for the blocker filters. For a particular blocker which is centered within an etalon bandpass we calculate the signal to be expected when a particular etalon transmission peak is centered at the central wavelength of the blocker filter. This signal arising from single etalon transmission peak is then compared with the total signal arising from all of the other transmission peaks within the etalon bandpass and all of the radiation from the entire spectrum outside of the etalon bandpass. The blocker filter design must be such that the total out of band signal is less than the signal from the etalon peak centered at the blocker wavelength. In most cases this value was taken to be an out of band contribution of the order of 1 percent or less.

Our method of calculation was made by choosing a specific model to represent the blocker filter behavior and an approximate model to represent the reflectivity of the etalons. We also required an approximate analytical representation of the detector response as a function of wavelength. The radiance calculations were made with the LOWTRAN 5 code developed at AFGL. In the following sections we briefly describe the models we have used for each component of the calculation, namely: Radiance Calculation, Blocker Filter Model, Etalon Model, and Detector Response.

RADIANCE CALCULATION

LOWTRAN 5 calculated limb radiance for various assumed atmospheric conditions and specified tangent altitudes. The calculations are made in 5 cm^{-1} intervals and are spectral averages over 5 cm^{-1} intervals. In our calculations we used a tropical atmospheric model. Figure 5 shows a plot of atmospheric radiance over a portion of the spectrum for limb viewing at tangent altitudes of 15, 35, and 55 km. From results such as this we can calculate the spectral signal arising from any spectral bandpass and compare this with the signal arising from the etalon peak centered at the central wavelength of the blocker filter. In order to make this comparison it is first necessary to take into account the relative response of the detector as a function of wavelength.

DETECTOR RESPONSE

THE CLAES Detectors are Si:Ga detectors. These detectors have a maximum response near 15 microns and have a rapid cut-off in response for wavelengths longer than about 17 microns. For wavelengths shorter than about 12 microns the response falls off with decreasing wavelength but the drop is not as rapid as it is at the longer wavelengths. In our calculations we have chosen the approximate representation shown in figure 6. Between 3 and 20 μm this figure can be represented by the analytical expression:

$$R = 0.0302 \exp(-0.28\lambda) \; ; \; \lambda < 12.5$$

$$R = 1 \; ; \; 12.5 \leq \lambda \leq 17.5 \qquad (1)$$

$$R = 2.15 \times 10^{23} \exp(-3.07\lambda) \; ; \; \lambda > 17.5$$

While any actual detector would not have responsivities which wouldd fall precisely on the curve represented by these equations as shown in figure 6, this representation is qualitatively correct and considered to be adequate for the blocker filter calculations described in this article.

BLOCKER FILTER MODEL

The blocker filters are assumed to be three period filters with a transmission given by

$$T_F = \left[\frac{1}{1 + a^2 \sin^2 (2\pi x)} \right] \qquad (2)$$

where

$$a^2 = \frac{4R}{(1-R)^2} \quad \text{and} \quad x = \left(\frac{\nu - \nu_o}{\delta}\right)$$

Typical values of a^2 and δ were determined by fitting some existing filter transmission spectra which were obtained from OCLI (Optical Coating Laboratory Inc.) We found that a 5 cm^{-1} bandpass filter could be fitted like equation 2 if the value of a^2 was 35.7 and δ = 184 cm^{-1}. In the calculations described in this article we assumed that the value of a^2 = 35.7 is typical of what we could expect for all of the filters. The expressions of equation 2 would not provide a suitable filter without additional blocking. These filters would have a minimum transmission at $\delta/4$. The actual filters will have to contain additional coatings to suppress all but their central transmission peak. Our calculations were done by assuming that the filters will behave as given by equation 2 for $|\nu-\nu_o| < \delta/4$. Beyond these minima, the blocking is assumed to be at or below certain levels which are prescribed by the requirement that all out of band blocking limits the out of band signal to some prescribed value which is determined by our calculations.

We had been supplied with sample spectra of narrow bandpass filters made by OCLI which were illustrative of the narrowest FWHM that could be expected in various spectral regions. From these comparisons it seemed as though a FWHM of about one half percent of the central wavelength was about as good as could be expected. Using this as a guideline, we did calculations using FWHM of 15 cm^{-1} for the HCl blocker #1, 10 cm^{-1} for blockers 2 and 3, and 5 cm^{-1} for all of the other blockers. The actual FWHM of the individual filter differs somewhat from these model calculations but does not have any significant effect on the rejection requirements which we specify.

ETALON MODELS

Spectral resolution and scanning capabilities are provided by four Fabry-Perot etalons consisting of Silicon substrates with reflective coatings designed for operation in several wavelength bands in the 3.5 to 12.9 μm region. In the region where the reflectivity of the coatings is high, the etalon spectrum consists of a series of narrow transmission peaks. The separation of the peaks is the free spectral range (FSR) and is given by

$$\Delta\nu_s = 1/2nd \ (cm^{-1}) \qquad (3)$$

The FWHM of the transmission peaks is related to the FSR and the reflectivity of the coatings by

$$\Delta\nu_F = \Delta\nu_s / F \qquad (4)$$

where F is the reflective fineness given by

$$F = \pi R^{1/2}/(1-R) \qquad (5)$$

The basic principle of the CLAES instrument is to use a Fabry Perot etalon in conjunction with suitable blocking filters to measure radiance in a narrow region $\Delta\nu_F$. Spectral scanning is achieved by tilting the etalons so as to change the angle of incidence of the collimated input beam. This produces a shift in the wavelength at which the transmission peaks occur.

For highly reflective coatings the transmissiion peaks are narrow and the transmission spectrum consists of the Airy function

$$T = \frac{1}{1 + \frac{4R}{(1-R)^2} \sin^2 (2\pi\chi)} \qquad (6)$$

where R is the reflectivity of the coating and

$$X = (\nu-\nu_o) / (2) \ (FSR) \qquad (7)$$

The transmission between the peaks has a minimum value of

$$T_{min} = \frac{(1-R)^2}{(1+R)^2} \qquad (8)$$

which is quite small for highly reflective coatings.

In calculating the signal arising from the various etalon transmission peaks we have multiplied the radiance (in watts/cm^2-sr-cm^{-1}) by the area of the peak(in cm^{-1}). The total area of a given peak depends on the reflectivity of the coating. Integrating from one minimum through the peak to the other minimum(through one free spectral range) gives a value related to the free spectral range and reflectivity by the expression:

$$A_E = \int_{-\frac{FSR}{2}}^{\frac{FSR}{2}} T d\nu = (FSR)\left(\frac{1-R}{1+R}\right) \qquad (9)$$

In doing our calculations we used a nominal free spectral range of 10 cm^{-1} and a reflective finnesse of 40 corresponding to a reflectivity of 92.5%. This yields an area of 0.389 cm^{-1} for the etalon peaks near the design wavelength. At other wavelengths where the reflectivity of the coatings is falling off there will be a corresponding increase in the FWHM and area of the peaks. The contribution of individual etalon transmissioin peaks was calculated by approximating the reflectivity of the coatings by a step like function. Figure 7 gives an illustration for one of the etalons. Slightly different step like functions were used for other etalons. We were guided in this choice by knowledge of the reflectivity of coatings for several different etalons which we had on hand. Outside the bandpass of the etalons we assumed that the reflectivity dropped to zero. This actually overestimates the amount of radiation transmitted outside the bandpass of the etalon. The Silicon substrates have a reflectivity of about 30% which would result in a transmission of about 54% based on equation 9.

METHOD OF CALCULATION

The basic procedure used to determine the blocking requirements is to calculate the magnitude of the signal in the main etalon peak centered at the center of the blocker filter with the signal from other wavelength regions and set the blocking requirements so that the signal from outside of the etalon bandpass is less than one percent of the signal from the main etalon peak. LOWTRAN 5 produces values of the limb radiance $R\lambda$. This radiance is then multiplied by the relative response of the detector $D\lambda$. Within the etalon bandpass the signal occuring in various etalon transmission peaks is given by

$$\text{Signal} = R_\lambda D_\lambda T_F A_E \qquad (10)$$

where T_F is the blocker filter transmission at the particular etalon peak A_E is the effective area of that etalon peak in cm^{-1}. T_F is given by equation 2 for values of $|\nu-\nu_o| \leq \delta/4$ and set equal to some constant value for $|\nu-\nu_o| > \delta/4$. This constant value is then adjusted for various wavelength intervals to insure that the total out of band signal meets the rejection requirements. A_E is given by equation 9. At frequencies beyond the minimum in the blocker filter where a constant (or series of constant) transmission is assumed, the signal for a given interval is given by

$$\text{Signal} = \int_{\lambda_1}^{\lambda_2} T_F A_E D_\lambda R_\lambda d\lambda = T_F\left(\frac{1-R}{1+R}\right) \int_{\lambda_1}^{\lambda_2} R_\lambda D_\lambda d\lambda \qquad (11)$$

where r is the reflectivity of the etalon between λ_1 and λ_2.

An additional point which is not evident on looking at figure 5 is the presence of a large amount of radiance in the visible and near infrared which arises from solar scattering by aerosols. This signal must also be taken into account in specifying the blocking requirements. For wavelengths less than 1.4 μm this radiation is rejected by choosing Ge as the material for the filter substrates.

The HCl measurement poses some additional difficulties in that the signal is quite weak. In this case it is not meaningful to spec the blocking to be less than one percent of the signal as this is an amount which is less than the NER. For this particular case the specs have been chosen to decrease the out of band signal to less than 1/4 NER. In order to meet the blocking requirements it has also been necessary to introduce an additional filter with an infrasil substrate which effectively blocks all of the radiation at long wavelengths.

Blocking required at long wavelengths can be relaxed considerably due to the presence of a refractive re-imager made of ZnS and ZnSe. This is effective in blocking radiation beyond about 14.5 μm except for two small regions near 15 and 18.5 μm where at low temperatures the ZnS has peaks in the transmission spectrum which allow for considerable transmission and require blocking. In some cases the blocking requirements can be met by the coating design alone. In other cases the blocking can only be met by choosing a suitable filter substrate to help in the long wavelength blocking.

RESULTS

In the limited amount of space available it is not possible to list all of the individual blocking requirements. Table 1 lists the results for a few of the blocker filters and compares the design goals with the theoretical design results obtained by OCLI. Although the blocking requirements are quite severe in some wavelength regions, OCLI has been able to meet these requirements in their design. The HCl filter has been built and meets specs. Additional filters are in the coating stage as of this writing. No major drawbacks in the construction of additional filters are anticipated at this time.

ACKNOWLEDGEMENT

This work was supported by NASA contract NAS5-27752.

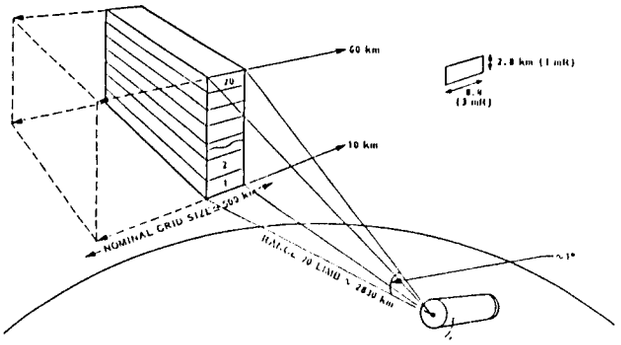

Fig. 3 Diagram of the CLAES viewing geometey showing a limb projection of CLAES vertically oriented focal plane. The spectrum in each blocker region is taken each minute.

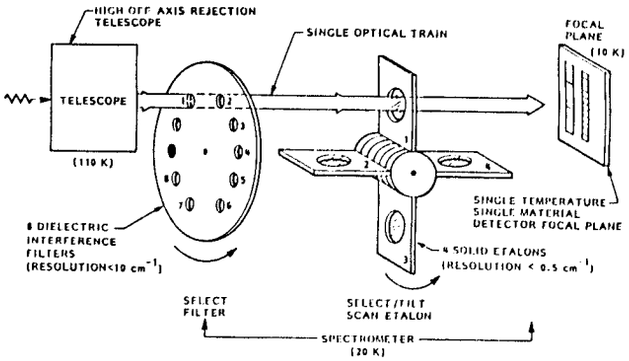

FIG. 1 Functional Diagram of CLAES.

ETALON OPERATIONAL RANGE (cm^{-1})		BLOCKING FILTERS		
		WAVELENGTHS (cm^{-1})		FWHM (cm^{-1})
E①	2703-3030	B1	2843	14
E②	1538-1960	B2	1897	10
		B3	1605	10
E③	1149-1369	B4	1257	10
E④	763-943	B5	925	8
		B6	879	8
		B7	843	8
		B8	792	8

Fig. 4a Spectral regions covered by the etalons and blocking filters.

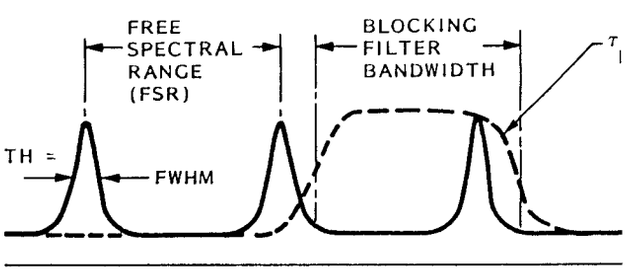

Fig. 2 Diagram illustrating the isolation of a single etalon transmissiion peak by the blocker filter. In practice the tail of the blocker filter tranmits several adjacent etalon transmission peaks.

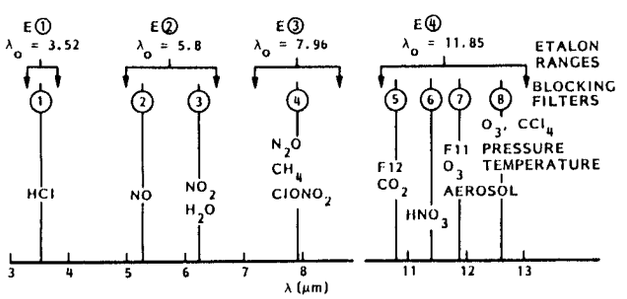

Fig. 4b Graphical representation of the etalons and blockers and the species to be measured in each blocker region.

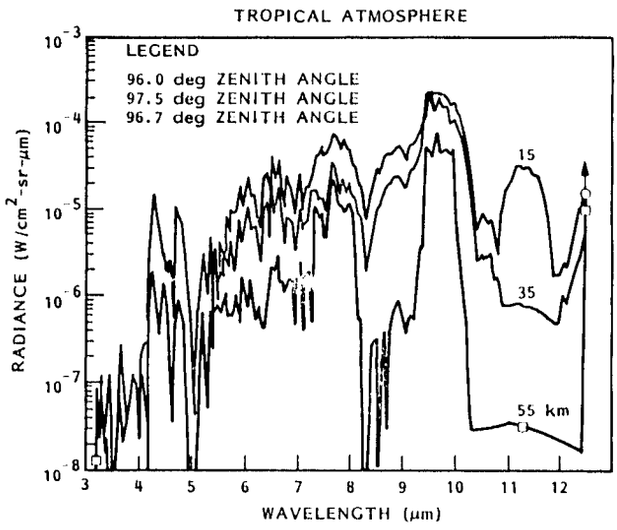

Fig. 5 Plot of LOWTRAN 5 limb radiance between 3.5 and 12.5 μm. In the calculations it was necessary to compute the radiance from 1.5 to 20 μm. This graph is just illustrative of the type of output obtainable from LOWTRAN 5.

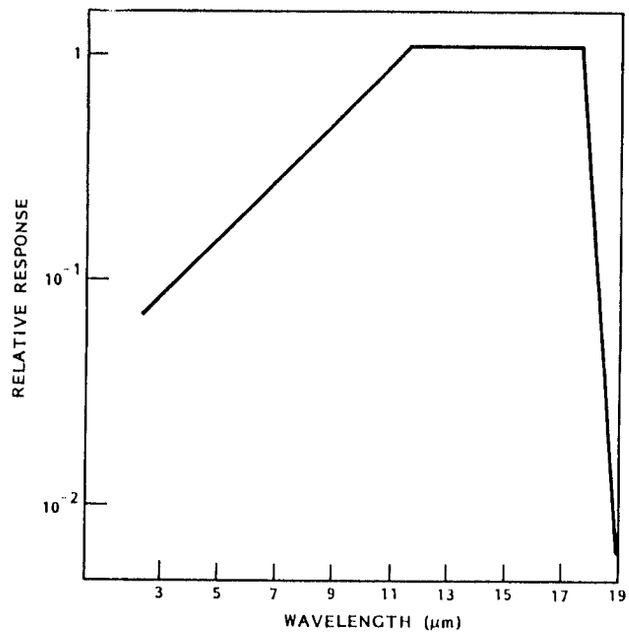

Fig. 6 Relative response of the detectors vs. wavelength.

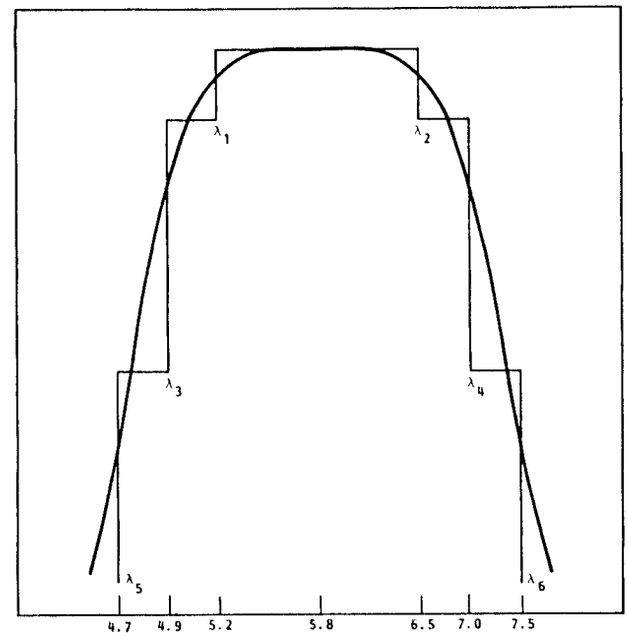

Fig. 7 Illustration of the approximation of the etalon reflectivity vs. wavelength. The various steps depicted correspond to reflectivities of 92.5%, 85%, 60%, and zero for wavelengths outside the limits.

12.63 UM FILTER

WAVELENGTH	REQUIREMENTS	OCLI DESIGN
1.40 TO 1.50	1.0(-3)	5.89(-9)
1.50 TO 2.00	7.0(-5)	4.13(-8)
2.00 TO 2.50	3.0(-4)	1.70(-7)
2.50 TO 3.00	1.0(-3)	9.31(-7)
3.00 TO 4.00	7.0(-3)	2.11(-7)
4.00 TO 5.40	5.0(-4)	5.64(-7)
5.40 TO 6.41	1.0(-3)	2.42(-5)
6.41 TO 7.54	1.5(-5)	2.13(-9)
7.54 TO 8.23	6.0(-6)	3.05(-8)
8.23 TO 8.58	7.5(-4)	1.93(-6)
8.58 TO 9.26	2.5(-5)	2.72(-8)
9.26 TO 9.95	5.0(-6)	1.10(-6)
9.95 TO 10.81	3.5(-5)	7.42(-6)
10.81 TO 11.93	1.2(-6)	2.56(-7)
13.40 TO 14.30	4.5(-6)	2.16(-6)
14.30 TO 14.80	1.0(-4)	9.85(-7)
14.80 TO 15.40	5.0(-6)	1.35(-7)
15.40 TO 18.00	NONE REQUIRED	
18.00 TO 19.00	1.0(-2)	4.59(-5)

11.38 UM FILTER

WAVELENGTH	REQUIREMENTS	OCLI DESIGN
1.40 TO 1.50	4.20(-4)	1.74(-4)
1.50 TO 2.00	2.80(-5)	2.42(-6)
2.00 TO 2.50	1.00(-4)	1.53(-7)
2.50 TO 3.00	2.50(-4)	7.58(-9)
3.00 TO 4.00	9.10(-4)	4.07(-8)
4.00 TO 10.00	2.00(-7)	9.19(-8)
10.0 T0 10.81	1.20(-5)	6.11(-7)
12.00 TO 12.82	3.6(-6)	2.87(-6)
12.82 TO 19.00	1.0(-6)	1.97(-7)

5.27 UM FILTER

WAVELENGTH	REQUIREMENTS	OCLI DESIGN
1.40 TO 4.75	1.00(-6)	1.05(-6)
4.74 TO 5.04	2.40(-5)	9.51(-6)
5.52 TO 5.88	9.00(-6)	9.56(-7)
5.88 TO 6.25	3.00(-6)	9.53(-7)
6.25 TO 6.67	2.00(-6)	1.21(-6)
6.67 TO 7.52	2.00(-6)	1.97(-6)
7.52 TO 8.10	2.00(-2)	1.60(-5)
8.10 TO 9.39	7.00(-1)	3.25(-5)
9.39 TO 10.01	7.00(-2)	2.93(-2)

7.995 UM FILTER

WAVELENGTH	REQUIREMENTS	OCLI DESIGN
1.40 TO 1.50	6.70(-4)	1.83(-6)
1.50 TO 2.00	4.80(-5)	3.05(-6)
2.00 TO 2.50	2.20(-4)	1.21(-5)
2.50 TO 3.00	7.80(-4)	6.90(-6)
3.00 TO 4.00	5.00(-3)	2.77(-5)
4.00 TO 5.40	4.00(-5)	3.22(-6)
5.40 TO 5.70	2.00(-4)	3.36(-6)
5.70 TO 6.10	9.00(-4)	5.38(-9)
6.10 TO 7.59	2.00(-5)	1.30(-5)
8.35 TO 8.69	3.00(-4)	7.86(-6)
8.69 TO 9.52	1.30(-5)	3.29(-7)
9.52 TO 19.00	8.00(-7)	1.70(-6)

Table 1. This table gives illustrations of the blocking requirements for several blocker filters. It also lists the design performance which has been obtained by OCLI in their theoretical design.

RESULTS FROM 1984 AIRBORNE DOPPLER LIDAR WIND MEASUREMENTS

Jeffry Rothermel

Universities Space Research Association Research Associate
ED43, Atmospheric Sciences Division
NASA/Marshall Space Flight Center
Huntsville, Alabama 35812

1. INTRODUCTION

The past decade has seen considerable advancement in the application of the Doppler technique to laser radar (lidar). Lidar wind measurement systems have evolved from ground-based arrangements to those operated from aircraft with fixed pointing systems. More recently an Airborne Doppler Lidar System (ADLS) was developed which incorporated the flexibility of a scanning system (Bilbro et al., 1984). The resulting system permitted the reconstruction of a two dimensional horizontal wind field with a resolution of roughly 300 m. The ADLS was field tested in the summer of 1981 aboard the NASA/Ames Convair 990, Galileo II. These flights resulted in extensive data sets on atmospheric phenomena such as boundary layer flows, gust fronts, and terrain effects.

The 1981 flight test program confirmed the feasibility of the ADLS concept, but revealed the need for improvements to increase the capabilities of the system. Moreover, analysis of the wind data indicated that some of the more serious deficiencies could be overcome with modest system revisions. It was found that the data rate that information was available from the CV 990 inertial navigation unit (INU) was not adequate to ensure that the lidar beam pointing was independent of aircraft attitude. Accordingly, an INU dedicated to the lidar system was mounted directly onto the optical table. In order to use the attitude information a new control system was developed which allows the scanner to respond more rapidly to the roll and pitch of the aircraft and, additionally, provides much more flexibility in beam pointing and increased system reliability. Up to 15 different scan angles, chosen from any plane within the 20 degree capability of the scanner, can be used in each scan pattern. The chosen angles will remain fixed in space as long as the aircraft roll does not cause the scanner limit to be reached. Operations in 1981 and subsequent data analysis showed the need for real-time display of data to guide the operation of the experiment in progress. A flexible, real-time display system was included in the new control system, allowing the display (in color) of the line-of-sight signal intensity or velocity. With timely information on the operation of the system, a response could be made either to adjust the system or change the aircraft flight track.

This report describes observations made with the revised system during research flights in the summer of 1984.

2. SYSTEM DESCRIPTION

A detailed description of the system that was flown in 1981 is given by Bilbro et al. (1984). Modifications to the system for the 1984 flights have been described above. Briefly, an 8 Watt, continuous wave carbon dioxide laser is operated in a master-oscillator, power-amplifier configuration at a wavelength of 10.6 microns. An electro-optic modulator forms a train of 330 m long pulses that are amplified and expanded to a diameter of 24 cm. The pulses then pass through two rotatable germanium wedges that allow scanning anywhere within a 20 degree cone normal to the aircraft fusilage. Once the pulses enter the atmosphere, they are scattered in all directions by naturally-occurring aerosols in the diameter range of 1 - 10 microns. The receiver measures the Doppler-shifted radiation scattered back along the axis of illumination. The signal processor extracts three spectral parameters (Lee and Lee, 1980), as illustrated in Fig. 3 of Bilbro et al. (1984). The mean frequency shift is related to the mean aerosol line-of-sight velocity, while the intensity is related to the backscattered power. The spectral width relates to the spread in velocities in the measurement volume.

The scanner position is controlled so that the scans will fall within planes that may be inclined at angles subject to the scanner limits. Within each plane the scanner motion, combined with the aircraft motion, produces a network of ground-relative velocity measurements taken from two different viewing angles. During post-processing, the resulting vector velocity can then be calculated for the plane by solving two simultaneous equations obtained from an intersecting fore and aft measurement.

3. DESCRIPTION OF EXPERIMENTS

Two research flights were performed to measure the flow around Mt. Shasta, California, an isolated mountain approximately 3 km above the surrounding terrain. The flight tracks were long racetrack patterns aligned generally along the wind direction and were run at several different altitudes. Scan patterns were chosen to give forward and aft look angles in the horizontal plane and in planes inclined several degrees above and below the horizon to yield the wind at aircraft altitude and to attempt to see the vertical structure of the wind flow pattern.

Figure 1 shows post-processed, forward scan radial velocities, measured at three elevation angles (-1, -2, and -3 degrees), from an altitude of 2998 m. The acquisition of a meaningful velocity estimate requires the presence of sufficient aerosol so that the volume backscatter is above a minimum value determined by the system sensitivity. It is apparent that windward of the mountain the backscatter was below the limit of detectability of the ADLS. On the leeward side the area of velocity estimates spreads out in a "V"-shaped pattern behind the peak, indicating that the

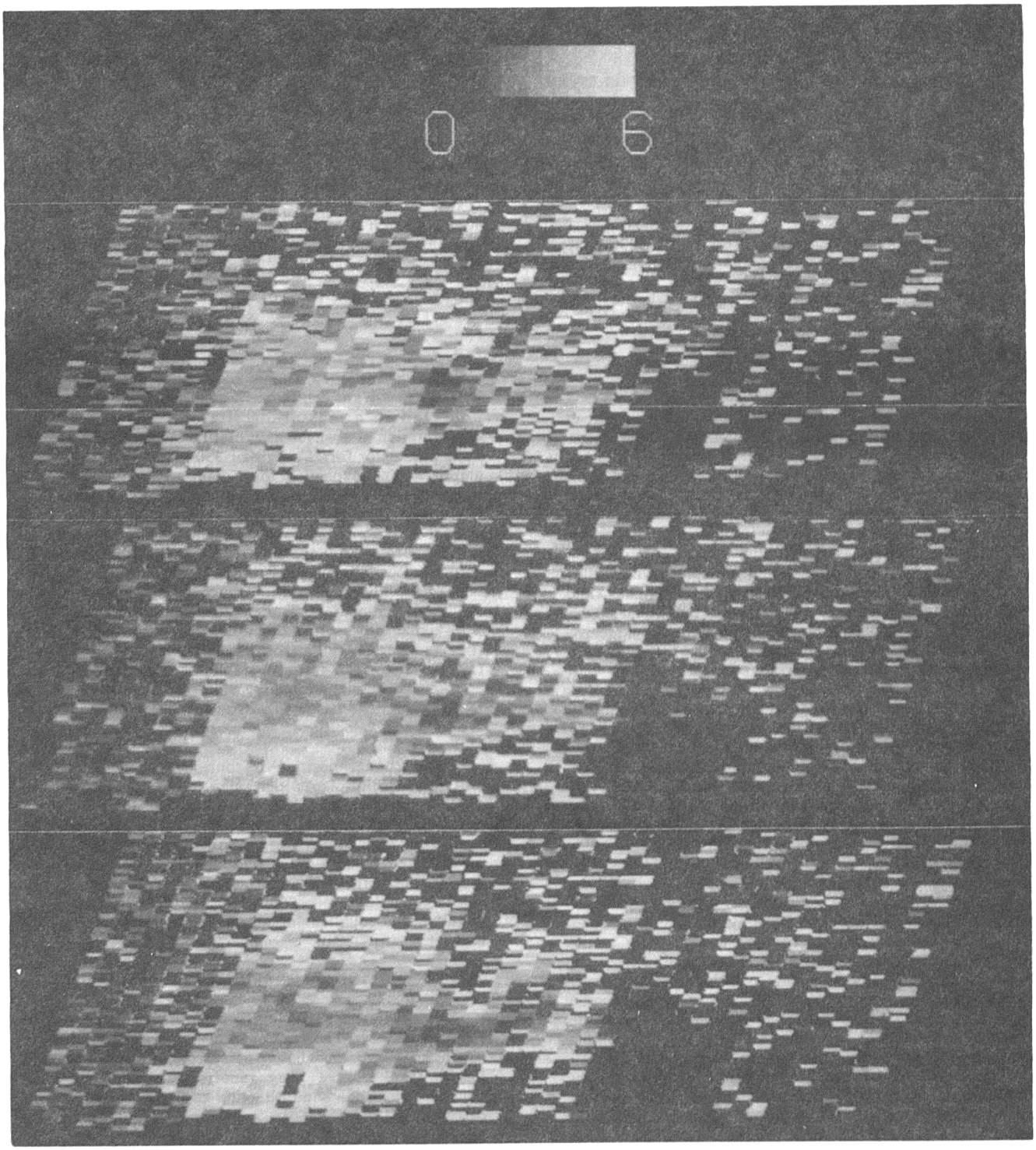

Figure 1. Forward scan radial velocities (m s^{-1}) measured at -1 (top), -2 (middle), and -3 degrees elevation at 2998 m altitude. "V"-shaped pattern in velocity field downwind of Mt. Shasta, California indicates that three-dimensionality of flow had brought a large amount of backscatterers up from a lower level.

three-dimensionality of the flow had brought a large amount of aerosols up from a lower level. Wave-like velocity variations are present. Also evident are false returns in front of the mountain due to a weak, pre-pulse tail that produced small negative velocities.

One research flight was conducted just downstream of the Carquenez Strait in the Sacramento River Valley. The flight tracks were chosen to be near the top of the boundary layer in a direction normal to the flow. Thus the extent of the flow divergence would be shown as the air spills through the strait from the San Francisco Bay area into the Central Valley. Scan patterns were chosen to give the wind at aircraft altitude and the vertical structure down to the surface.

Figure 2 shows forward and aft scan radial velocities at elevation angle -3 degrees from an altitude of 738 m. The lower left and lower right hand corners of the images correspond to the beginning and ending times indicated by the dots near the bottom of the topographic map (2236 and 2247 GMT, respectively). The results show the general turning of the wind as it diverges upon entering the Central Valley. Evidence of the flow can be found (from data not shown here) as far east as Sacramento. A region of weak out-bound velocities is present in front of the Black Hills, as are ground returns from the base of the Hills. The collocation of ground hits in the fore and aft radial velocity fields is strong evidence that the aircraft attitude was being properly taken into account. Scans from other elevation angles (not shown) show the speed of the flow through the strait to decrease with height. Evidence that the flow overrides the Montezuma Hills is apparent at shallower elevation angles, as are wave-like velocity variations in front of the Black Hills.

The aircraft made repeated passes by the Carquenez Strait; consequently, the lidar scanned toward the east into the Central Valley as the aircraft moved into position for the next pass. Returns over the valley indicated that wave-like velocity variations persisted within an area from one pass to the next. Clear-air convection cells are present everywhere and can be seen, from different scan elevations, to tilt in response to the vertical wind shear. In some areas the cells appear to be aligned with the wind.

The measurements made during this research flight are unique and are of particular interest to air pollution meteorologists concerned with the behavior of the flow into the Central Valley.

4. CONCLUSION

The findings of the 1984 flight experiments with the ADLS demonstrated the success of the modifications in correcting the major error sources present in the 1981 flights. The result, along with improved operational procedures, has been to yield more accurate wind fields and better response to changing weather opportunities.

The wind measurements described here are being analyzed by MSFC personnel and by groups that helped to plan the flights. It is expected that the results of these analyses will be of meteorological significance in addition to their importance in demonstrating the effectiveness of the Doppler lidar as a remote sensor.

5. ACKNOWLEDGEMENTS

The work described here is based upon the efforts of many people. Their affiliations are: NASA Headquarters Mesoscale Research Project, NASA Marshall Space Flight Center, NASA Ames Research Center, Lassen Research, Desert Research Institute, Raytheon Corp., Univ. Tennessee Space Inst., Univ. Colorado, Univ. California at Irvine, California Air Resources Board, Univ. California at Davis, and Pennsylvania State Univ. This work was also partially supported by the Universities Space Research Association under contract NAS8-34010.

6. REFERENCES

Bilbro, J. W., G. H. Fichtl, D. E. Fitzjarrald, M. Krause, and R. W. Lee, 1984: Airborne Doppler lidar wind field measurements. Bull. Amer. Meteor. Soc., 65, 348-359.

Lee, R. W. and K. A. Lee, 1980: A poly-pulse-pair signal processor for coherent Doppler lidar. Paper presented at a topical meeting on Coherent Laser Radar for Atmospheric Sensing, Aspen, Colo., July 1980.

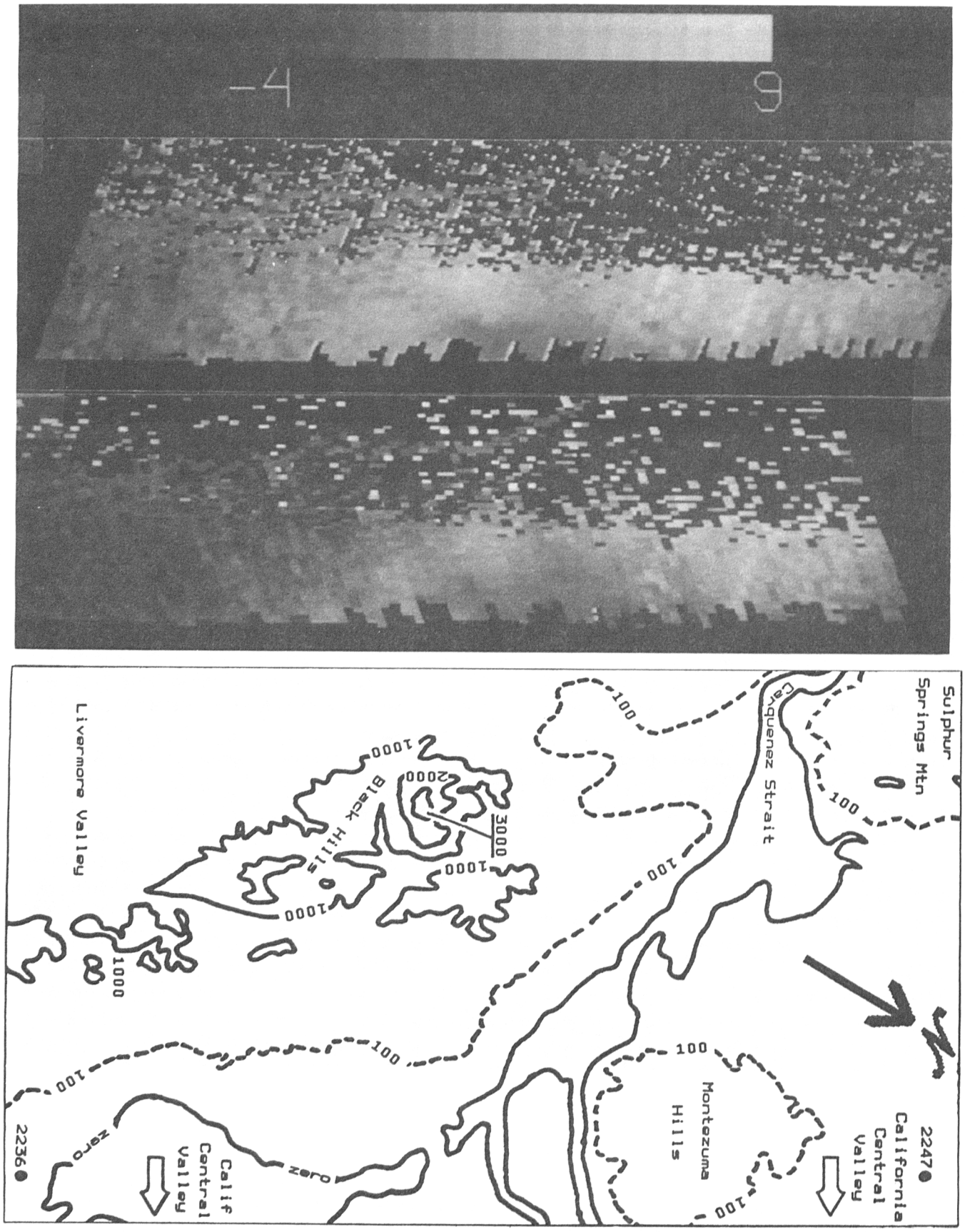

Figure 2. Forward and aft scan radial velocities (m s^{-1}) at elevation angle -3 degrees at 738 m altitude. Lower left and lower right hand corners of images correspond to beginning and ending times indicated by dots near bottom of topographic map (2236 and 2247 GMT, respectively). Figure shows behavior of flow as air spills through Carquenez Strait from San Francisco Bay area into California Central Valley. Note collocation of ground returns from base of Black Hills.

use the data from one of these reports to illustrate the effect of scattering contribution to out of band transmission.

3.2 Example of scattering effects on OBR

On figure 3 is shown an experimental set up that NOSC personnel used to measure out of band transmittance in 3 geometries in which the filter subtends 1/2 cone angles of 11.2, 43 and 90 degrees as seen by the detector. The results obtained in this experiment for a sample filter are shown on figure 4. To first order the out of band transmittance scales as the solid angle of the detector field of view that is subtended by the filter.

Similar effects are documented in the series of reports cited above for a large number of filters. Stierwalt and associates postulate that these effects are the result of scattering within the interference coatings due to globular structures that occur within the coating. Scanning electromicrograph (SEM) photographs of the filters coatings taken by NOSC personnel clearly show the presence of such globules. The scattering degradation of OBR was found to vary by orders of magnitude within the set of sample filters. NOSC personnel found a positive correlation between the number of globules present in the coating as determined by the SEM data and the severity of the scattering effect.

Figure 5 illustrates that the out of band scattering contribution to transmittance into the acceptance cone of 1/2 angle THETA/2 through a filter at a focal plane is equivalent to the out of band scattering contribution to transmittance through a filter that subtends a 1/2 angle THETA/2 detector field of view as illustrated by figure 3. The filters in the CLAES are mounted in the former geometry.

Scattering will not contribute to out of band transmittance in the case where the acceptance cone 1/2 angle THETA/2 = 0. In this case the out of band transmittance may be designated by T. For the case THETA/2 > 0 the out of band transmittance may be designated by T + Ts where Ts is the scattering contribution.

3.3 Scattering effect for dual wedged filters

Referring back to the dual wedged filter configuration shown on figure 2 we designate the out of band transmittance of filter number 1 into 1/2 angle THETA/2 = 0 by T1 and that of filter number 2 into 1/2 angle THETA/2 = 0 by T2. To simplify the discussion we designate the out of band transmittance of filter number 1 into 1/2 angle THETA/2 > 0 by T1 + TS AND for filter number 2 by T2 + Ts. For further simplification the scattering contribution Ts is assumed to be identical for filters number 1 and 2. Neglecting multiple scattering effects the transmittance through the dual wedged filter configuration is approximated by

$$T = (T1+Ts)*(T2+(1+N)*Ts) \qquad (3)$$

As expected equation (3) reduces to equation (2) in the no scattering limit Ts = 0. A brief qualitative argument to support the form of equation (3) follows. A fraction (namely T1 + Ts) of the incident light is transmitted through filter number 1 into the acceptance cone of light that will be focussed onto the detector. At initial incidence on filter number 2 a fraction (namely T2 + Ts) of the remaining light is transmitted through filter number 2 into the acceptance cone. On each internal reflection off filter number 2 an additional fraction Ts is scattered into the acceptance cone. It is assumed that the light walks out the open end of the wedge configuration after N internal reflections off filter number 2. The value of N is 3 or less for the CLAES configuration where the wedge angle is Larger than 12 degrees.

4. DESIGN CONSIDERATIONS, CLAES APPLICATION

Usually a filter designer works to satisfy a set of blocking specifications in the out of band region. For example ,the long wavelength wing blocking specifications for the CLAES blocker filter centered at 10.8lum are shown on figure 6. The filter designer needs to produce design transmittances T1 and T2 for filters number 1 and 2 such that transmittance as given by equation (3) is less than the blocking specifications. To conservatively account for scattering the designer must use a value for Ts that he believes will be somewhat larger than what will be characteristic of the filter to be built.

In the case of the CLAES filters it was planned to use substrates, coating materials and procedures similar to those that were used in the building the LIMS filters that had band passes shortward of 13um (namely the HNO3, O3, H2O and NO2 filters). To first order one would expect that out of band scattering similar to that measured by NOSC personnel for these LIMS filters would also apply to the CLAES filters. Inspection of the LIMS filter out of band scattering data that was reported by NOSC personnel indicated that Ts = 1.E-6 would be representative of a typical short wave (ie., less than 13UM)

LIMS like filter if it were to be utilized in the CLAES f5 beam. In order to produce a conservative design, with high probability of achieving the required rejection the ten times larger value Ts = 1.E-5 was used for purposes of designing the CLAES filters.

Next a procedure to find the appropriate values T1 and T2 might go as follows. The designer inputs a set of high and low index layer thicknesses for the coatings on each side of the filter element substrate into the design code and the code outputs the design transmittance. The designer uses this technique for each of the elements in the dual wedged filter configuration (as shown on figure 2) in order to produce designs for T1 and T2.

Using these design values T1 and T2, and the value for Ts the designer tests T as computed by equation (3) against the the blocking specifications. If the specifications are not satisfied the designer modifies the coating designs, and thereby the computed T1 and T2 for the elements number 1 and 2. The designer tests the revised design against equation (3) to see if the blocking specifications are satisfied. The process is repeated until a design that satisfies spec is produced.

The final designs T1 and T2 and the transmittance of the wedged system as computed by equation (3) with Ts = 1.E-5 are compared against the long wave wing blocking specifications for the CLAES 10.81um filter on figure 7.

It is interesting to note that a designer could ignore scattering and produce a design transmittance via equation (2) (namely, T = T1*T2) for the filter system that would appear to satisfy the blocking specifications. Since scattering is not accounted for in such a design the likelyhood that blocking specifications would be satisfied in practice is left to chance. The transmittance computed by equation (3) with Ts = 1.E-5 and by equation (2) which ignores scattering are compared against the long wave wing blocking specifications for the CLAES 10.81um filter on figure 8. In the region 11.38 to 12.9um for example the transmittance computed by equation (3) just barely satisfies specifications in the integrated sense, but when computed by equation (2) which ignores scattering is orders of magnitude within specification. The effect of including scattering negates what would look like several orders of magnitude margin to a designer that ignores scattering.

ACKNOWLEDGEMENT

This work supported by NASA contract NAS5-2772.

REFERENCES

Arrington, D.C., Internal Report of the Naval Electronics Laboratory Center (now Naval Oceans Systems Center (NOSC)), "Geometrical Effects on Out-of-band Leakage of Low Temperature Band Pass Filters"

Stierwalt, D.L., Internal Report of the Naval Electronics Laboratory Center (now Naval Oceans Systems Center (NOSC)), "Geometrical Effects on the Out-of-band Transmittance of Interference Filters"

Stierwalt, D.L., Interim Report on Naval Oceans Systems Center (NOSC) work on Space and Missile Systems Organization MIPR No. FY76167700382, "Optical Filter Measurements", 10 August 1977.

Stierwalt, D.L., Interim Report on Naval Oceans Systems Center (NOSC) work on Space and Missile Systems Organization MIPR No. FY76167700382, "Optical Filter Measurements", 7 September 1977.

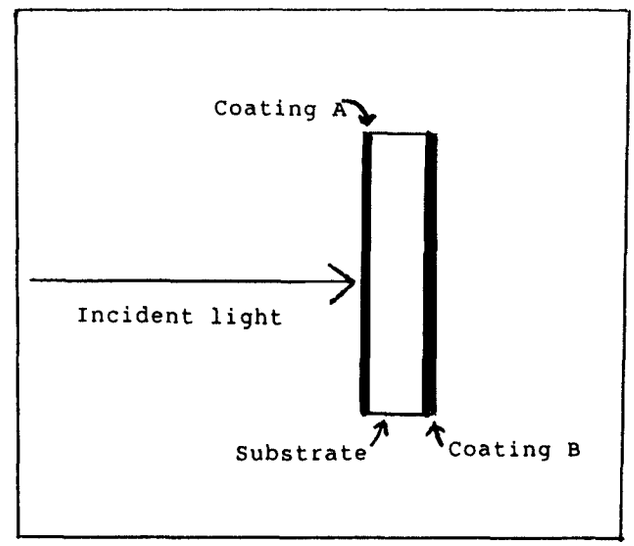

Figure 1 Filter construction schematic.

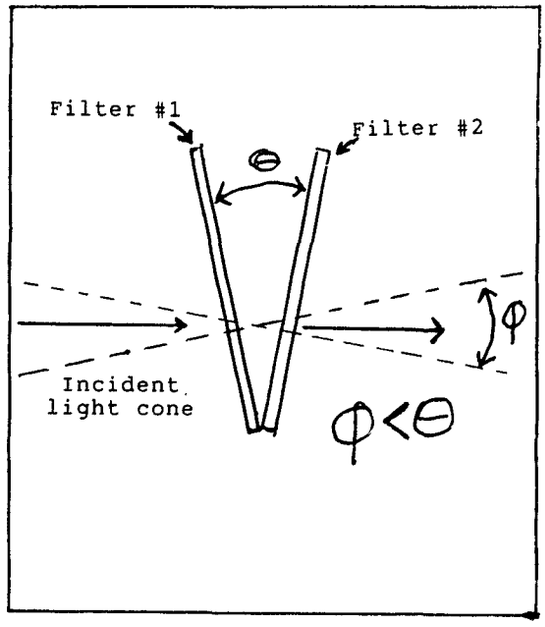

Figure 2 Schematic of dual filter configuration with beam angle φ and with wedge angle $\Theta > \varphi$.

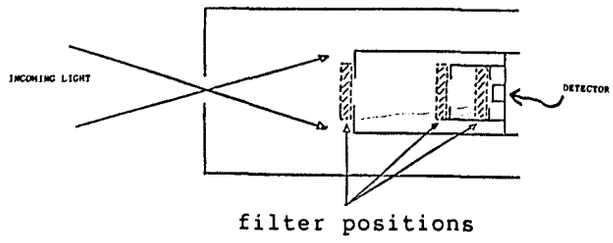

Figure 3 The filter subtends THETA/2 = 11.2, 43 & 90 degrees of detector FOV.

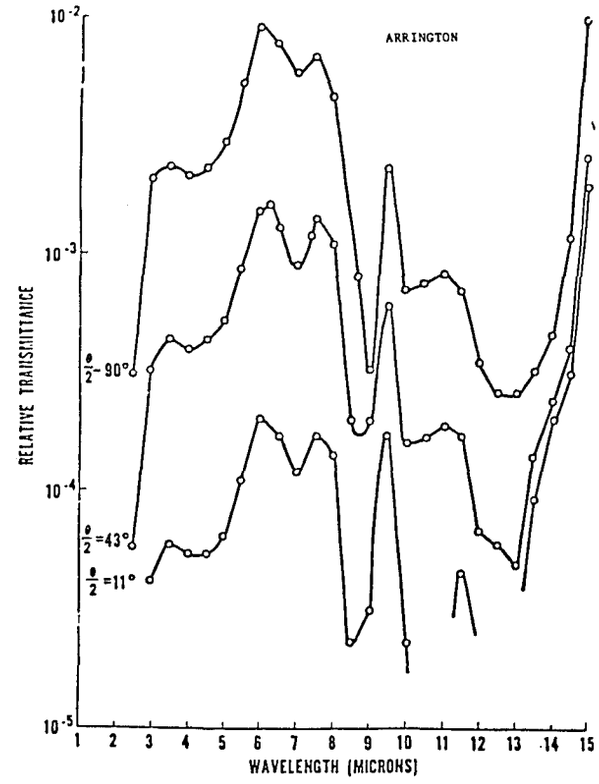

Figure 4 Results for the geometries that are shown on figure 3

FOR CLAES CASE D^2 AREA DETECTOR IMAGE AREA SCATTERS $I\,D^2 \int_0^{\theta/2} d\alpha\, 2\pi\alpha\, f(\alpha)$

ONTO D^2 AREA DETECTOR

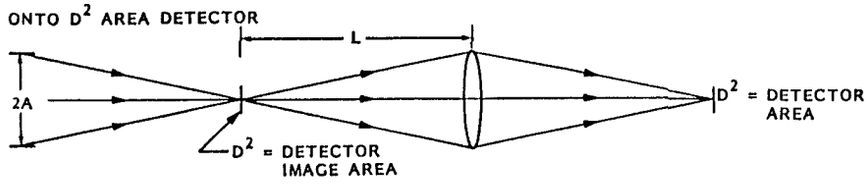

FOR THE STIERWALT CASE AN ELEMENT OF AREA $2\pi a da$ SCATTERS $F(\alpha)$ INTO SOLID ANGLE D^2/L^2; HENCE, TOTAL SCATTERINGS ON D^2 AREA DETECTOR IS $S = I \int_0^A da\, 2\pi a\, f(\alpha)$ (D^2/L^2), BUT SINCE $\alpha = a/L$, THEN $S = I\,D^2 \int_0^{\theta/2} d\alpha\, 2\pi\alpha\, f(\alpha)$, WHICH IS IDENTICAL TO THE CLAES CASE ABOVE. THE IRRADIANCE I AND DIMENSIONS A, $\theta/2$, AND L ARE THE SAME IN BOTH CASES.

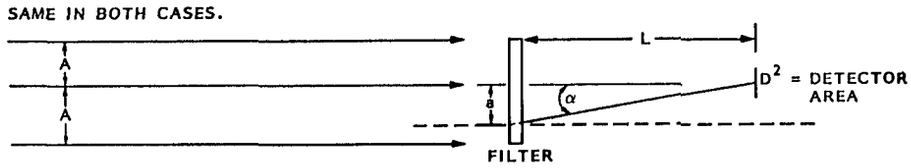

Figure 5 CLAES and Stierwalt scattering geometry equivalence for angle THETA

Figure 6 LONG WAVE BLOCKING SPECS

CLAES 10.81um filter

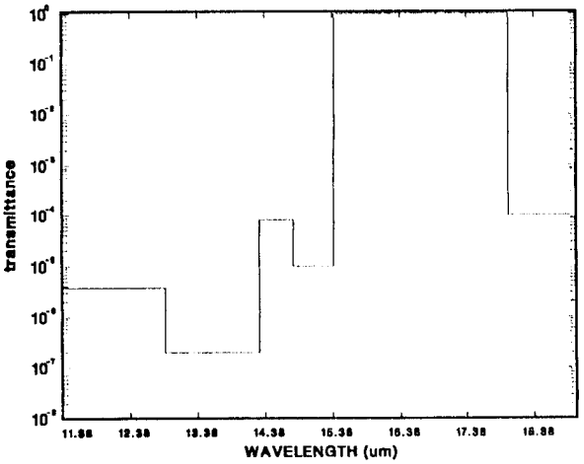

Figure 7 T1, T2, T & BLOCKING SPECS

T computed for Ts=1.E-5

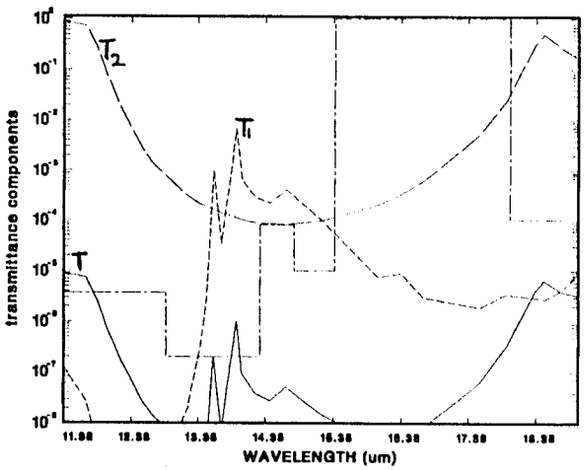

Figure 8 BLOCKING & T FOR 2 CASES

cases Ts=1.E-5 & 0.0

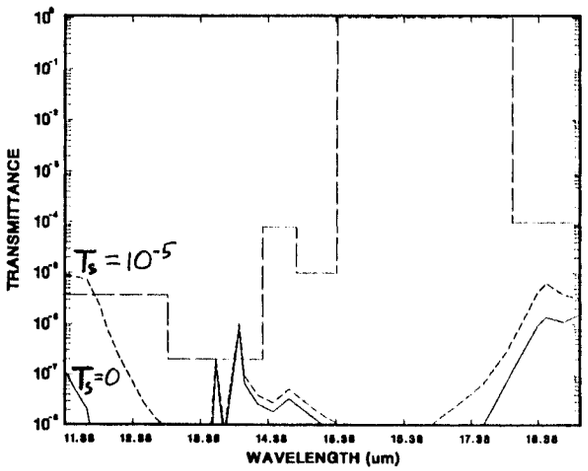

VICARIOUS CALIBRATION OF GOES VISSR WITH SURFACE OBSERVATIONS OF CLOUD TRANSMITTANCE

M.V. Paris and C.G. Justus

Georgia Institute of Technology
Atlanta, Georgia

1. INTRODUCTION

Although satellite sensors are calibrated before launch and in some cases can be calibrated in orbit, some operational sensors require calibration adjustments which can most easily be done vicariously using surface measurements and inferred radiances at satellite position. We have developed a method of vicarious calibration of the GOES Visible and Infrared Spin Scan Radiometer (VISSR) visible sensor using simultaneous satellite and surface observations under overcast cloud conditions via a radiative transfer model for a cloudy atmosphere.

The model calculates irradiances at the top and bottom of an atmosphere consisting of an upper and lower clear layer with a middle cloudy layer. Figure 1 is a schematic diagram of the form of the model. Clear-sky effects include absorption by ozone, water vapor, the uniformly-mixed gases and aerosols; and scattering by air molecules and aerosols. Modified Beer's Law relationships are used to determine clear-sky effects. Cloud optical effects are calculated using the delta-Eddington method.

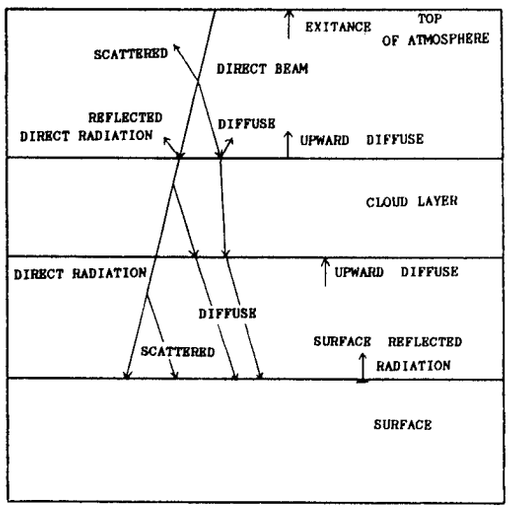

Fig. 1. Schematic diagram of the spectral model.

The calibration procedure uses simultaneous GOES VISSR counts and global surface irradiances. The model is used to find a cloud optical depth which reproduces the observed surface irradiance. The top-of-atmosphere exitance for this cloud optical depth is then converted into radiance using empirically-derived bidirectional reflectance factors (Taylor and Stowe, 1984). The resulting directional radiance is compared to observed satellite counts to provide a calibration of the instrument.

The surface measurements of irradiance which we used were taken at the Georgia Tech Solar Energy Meteorology Research and Training Site (SEMRTS) during late 1982 and 1983. The resulting model upward radiances were compared to simultaneous satellite measurements taken over the Atlanta area.

2. MODEL DESCRIPTION

The model calculates irradiances in 145 spectral intervals from 0.29 to 4.0 μm. Clear-sky transmissivities are calculated by using extinction coefficients for each absorber or scatterer in each spectral interval. This gives a total transmissivity for direct radiation within a clear layer. Reflectances are determined by assuming that a certain fraction of the scattered direct radiation is scattered into the backward hemisphere. Diffuse transmissivities are calculated by using effective air masses which represent an integration over the hemisphere. The clear-sky part of the model has been described in Justus and Paris (1985).

Transmissivities and reflectivities for direct and diffuse radiation are calculated separately for the cloud by using two sets of boundary conditions to solve the Eddington form of the radiative transfer equation. One set of boundary conditions assumes direct radiation only incident at cloud top; the second set assumes no direct but an arbitrary diffuse radiation incident at cloud top. The delta-Eddington method (Joseph et al., 1976) requires three parameters, cloud asymmetry factor, single-scattering albedo and cloud optical depth. These may be found for theoretical clouds by using an assumed drop size distribution and performing Mie calculations. We used optical parameters of

Newiger and Bahnke (1981), which were found by Mie calculations for an assumed cloud drop size distribution. A regression was used to interpolate for the spectral intervals in the model.

3. MODEL CALCULATIONS

The model calculations made use of the Georgia Tech SEMRTS Hourly Data Base (HDB). The HDB includes measurements of irradiance and meteorological conditions at the Georgia Tech site as well as certain weather service data from the Atlanta airport and other locations. Measurements taken at the site include broad-band total, diffuse and direct irradiances and long wavelength (>630 nm) total and direct irradiances. Temperature, dewpoint, barometric pressure and other meteorological measurements are also included at the site. The Atlanta airport data include cloud type and cloud amount in up to four layers. Ozone and precipitable water measurements are interpolated from weather service measurements taken at sites near Atlanta. The visible and infrared satellite counts from the VISSR instruments are also merged into the HDB.

The HDB includes most necessary data to run the model. Certain assumptions must be made, such as aerosol optical depth at 500 nm and the distribution of precipitable water within the atmosphere; however, these parameters have a relatively small effect on the final results. The most important parameter is cloud optical depth. This was found by using a regression on measured global transmissivity and the cosine of the solar zenith angle. Using several months' data, a regression which gave satisfactory agreement between model results and measurements was found.

The computer model was modified to access the HDB's, which are stored in a monthly format. Certain criteria had to be met for the model to perform calculations for a given hour. These included the presence of total opaque cloud cover in one layer, a percent sunshine of less than one, sun elevation greater than 10 degrees and the presence of data for certain meteorological parameters. In the 1983 HDB's, 221 hours met all criteria. Of these, 168 also had valid satellite visible counts.

Further comparisons of model exitances based on measured irradiances were made to compare estimated VISSR-band as well as broad-band radiances to observed satellite counts.

4. RESULTS AND DISCUSSION

Calculated exitances for the 168 hours with satellite visible counts are compared to the raw instrument counts in Figure 2. The model values have a quadratic relationship, which is the form of the satellite instrument calibration.

Figure 3 is a second comparison between model broad-band exitances and counts. Data used in this comparison are from a longer period than those used in Figure 2. Figure 4 shows VISSR-band model exitances compared to instrument counts. The larger difference between the nominal calibration curve and the best-fit curve in Figure 3 is the result of the different spectral reflectances of the broad-band and VISSR-band spectra.

The rms error about the least-squares regression line in Figure 4 is 13%. The error is reduced to 11% if the outlying points shown as circles are eliminated.

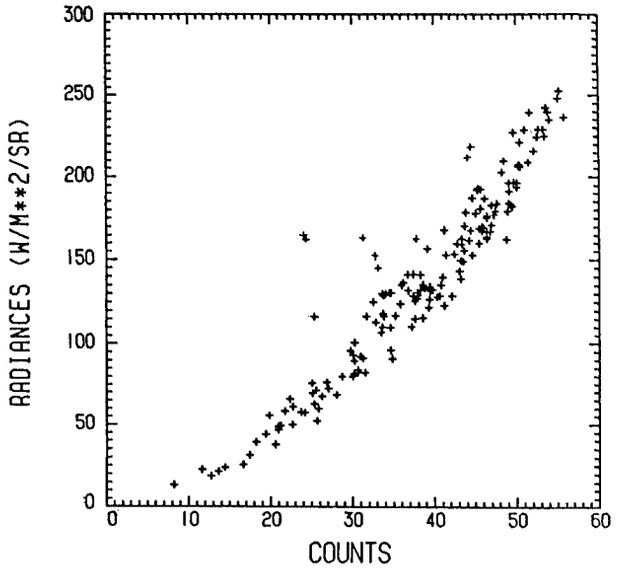

Fig. 2. Model broad-band exitances versus VISSR visible counts.

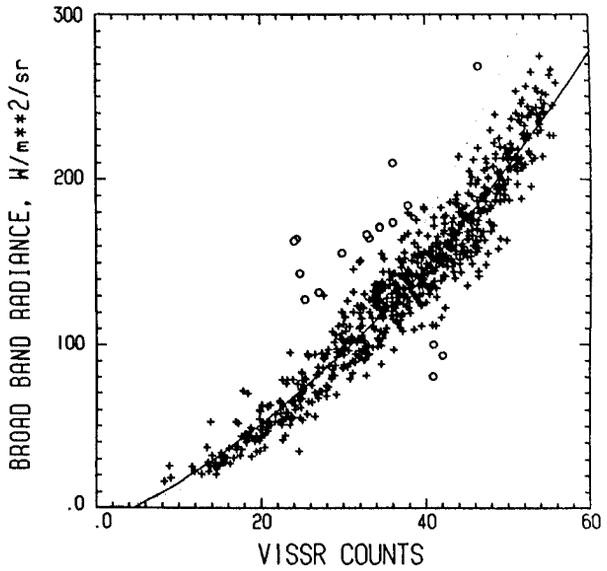

Fig. 3. Similar to Fig. 2. Solid line is nominal satellite calibration curve. Dotted line is best-fit regression to model data.

We used the nominal instrument calibration to convert counts to radiances and scaled for the difference between the spectral response of the instrument and the model broad-band calculations shown in Figure 2. We found the expected linear relationship with an rms error of 16.4% of the model mean of 137.3 $W/m^2/sr$ (Fig. 5). When nine outlying points were removed from the data, we found an rms error of 12.5% of the mean of 135.6 $W/m^2/sr$.

Some error may be introduced into the model calculations through the determination of cloud

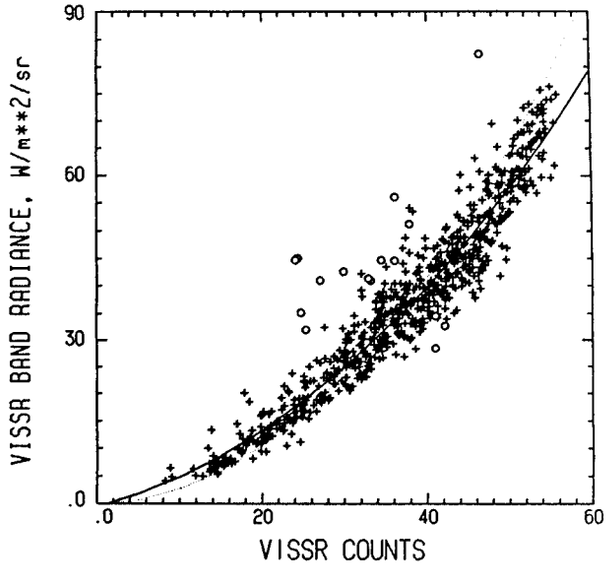

Fig. 4. Model VISSR-band exitances versus satellite counts. Solid line is nominal calibration and dotted line is regression to model data.

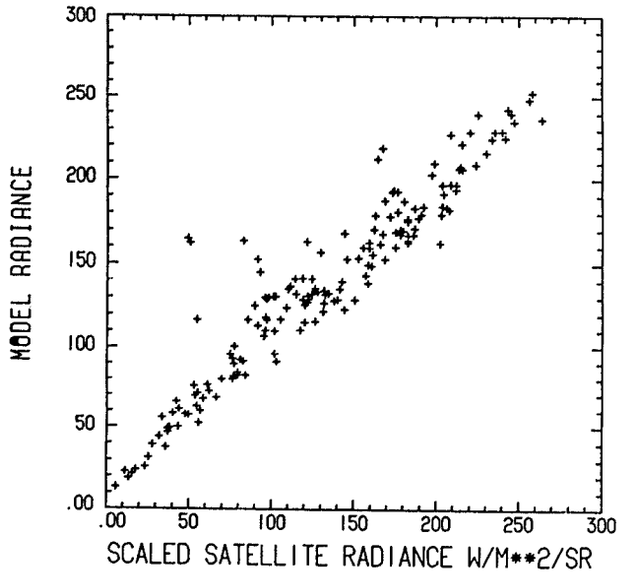

Fig. 5. Scaled model exitances versus satellite-measured radiances. Satellite radiances are produced from the nominal calibration of the VISSR instrument.

optical depth. Although there may be errors in setting other optical parameters, cloud optical depth is the most significant. In principle it would be possible to match measured irradiances to any accuracy desired. Having done so, any errors in the model should then appear in differences between measured and modeled top-of-atmosphere radiances.

The two major sources of error in the upward irradiances, and thus the radiances, are errors in setting the model parameters and errors in the conversion between nondirectional irradiances and directional radiances. Errors in model calculations should be relatively small. Clear-sky effects are small compared to the effects of the cloud layer; thus the cloud calculations are more important. The zenith angles and optical depths in the calculations are within the range of validity of the Eddington method (Wiscombe and Joseph, 1977). Although errors in setting cloud optical parameters can produce some errors in the upward irradiances, it appears that the major source of error is in the conversion to radiances.

The bidirectional reflectance factors are empirically derived from satellite measurements and are thus averages. However, model calculations have indicated that cloud top geometry can influence radiances even for the same gross cloud optical depth (Wendling, 1977). Information in the HDB indicates the presence of multiple cloud layers and changing cloud-top heights during some of the hours for which model calculations were made, despite the official reports of only a single layer of cloud at that time. The bidirectional reflectance factors cannot take cloud-top structure into account for individual cases.

Despite this source of error, the rms error of the model-satellite radiances is comparable to a comparison between the GOES-2 instrument (an earlier version of the GOES instrument in this comparison) and a second satellite (Nimbus-7) (Minnis and Harrison, 1984). Their comparison between satellite instruments yielded an overall rms error of 14%.

5. CONCLUSION

The model we have developed reproduces measured surface irradiances and, through the use of empirical bidirectional reflectance factors, produces upward directional radiances of sufficient accuracy for calibration of operational satellite sensors. Errors introduced by assumptions about cloud optical effects and other optical effects appear to be small compared to errors from the conversion of nondirectional model irradiances into directional radiances. Despite these sources of error, the model produces results with an error similar to direct comparison between instruments on two satellites. The spectral resolution of the model also provides the opportunity to make comparisons between model results and satellite observations in the same spectral region, rather than relying on broad-band observations and calculations alone.

Joseph, J.H., W.J. Wiscombe and J.A. Weinman (1976): "The Delta-Eddington Approximation for Radiative Flux Transfer", J. Atmos. Sci., 33, 2452-2459.

Justus, C.G., and M.V. Paris (1985): "A Model for Solar Spectral Irradiance and Radiance at the Bottom and Top of a Cloudless Atmosphere", J. Clim. Appl. Meteor., 24, 193-205.

Minnis, P., and E.F. Harrison (1984): "Diurnal Variability of Regional Cloud and Clear-Sky Radiative Parameters Derived from GOES Data. Part III: November 1978 Radiative Parameters", J. Clim. Appl. Meteorol., 23, 1032-1051.

Newiger, M., and K. Bahnke (1981): "Influence of Cloud Composition and Cloud Geometry on the Absorption of Solar Radiation", Contrib. Atmos. Phys., 54, 370-382.

Taylor, V.R., and L.L. Stowe (1984): "Reflectances of Uniform Earth and Cloud Surfaces Determined from Nimbus-7 ERB", J. Geophys. Res., 89, 4987-4996.

Wendling, P., (1977): "Albedo and Reflected Radiance of Horizontally Inhomogeneous Clouds", J. Atmos. Sci., 34, 642-650.

Wiscombe, W.J., and J.H. Joseph (1977): "The Range of Validity of the Eddington Approximation", Icarus, 32, 362-377.

COMPARISON OF DIURNAL CHARACTERISTICS OF STRATOCUMULUS CLOUDS OVER CALIFORNIA AND SOUTH AMERICA COASTS USING GOES SATELLITE DATA

Chi-Fan Shih
T. H. Vonder Haar

Department of Atmospheric Science
Colorado State University
Fort Collins, CO 80523

1. INTRODUCTION

Although it is well known that low stratocumulus clouds occur persistently during the summer over the Eastern Pacific near the California (CA) and South America (SA) coasts, little is known about their diurnal characteristics. Early work by Minnis and Harrison (1984) studied broad area characteristics of diurnal variation.

To describe the diurnal temperature variations of these two climatologically important cloud bands, we collected hourly GOES-6 data for 48 hours during August 25-27, 1985 over two areas near CA (115°-130°W, 25°-40°N) and SA (75°-90°W, 0°-15°S) at 8 km (infrared) and 2 km (visible) resolution (Figure 1). The results of the first 24 hour data is presented here, and a more complete comparison based upon more days will be presented at the conference.

2. ANALYSIS

Although our data covered a 15°x15° area for both CA and SA cases, we decided to choose 2.5°x2.5° subareas as our target regions. For this study, four target regions were chosen (Table 1). In order not to be confused by upper level clouds above the stratocumulus, we displayed all hourly satellite images on our Interactive Research Imaging System (IRIS) to choose our target regions so that they were not covered by any extensive cold clouds (infrared temperature < 275°K). As the results will show, our target regions are covered mainly by the stratocumulus. On a few occurrences, thin high clouds do exist in our target regions with relatively warm temperatures (about 0° to -5°C). These thin high cloud pixels were discriminated from other low cloud pixels by checking their infrared temperatures. If their infrared temperatures are colder than the background temperature by 13°C (as used by Minnis and Harrison, 1984), these pixels were not included in the following cloud-top temperature computation. The background temperatures were obtained from compositing the maximum temperatures of GOES-6 images for two weeks. These background temperatures are now regularly derived at CSU under the International Satellite Cloud Climatology Project (ISCCP) (Schiffer and Rossow, 1983).

To compute the regional mean cloud-top temperature, we used the standard GOES infrared - temperature conversion table, which is:

IR Temperature = 330 - (CT/2) for CT < 176
IR Temperature = 418 - CT for 176 ≤ CT < 255

where IR = infrared, CT = brightness count

With the conversion table, we obtained the infrared temperature of each pixel inside a target region without correction for atmospheric effects. The regional mean cloud-top infrared temperatures and standard deviations are then computed as generally defined. Current results are plotted in Figure 2.

3. DISCUSSION

In Figure 2, the regional mean cloud-top infrared temperatures over the California coastal area were ploted against the GMT time. The local midnight and noon time are indicated on top of the diagram. The one-day mean cloud-top temperatures were also added as the horizontal lines. The cloud-top IR temperature clearly varies diurnally for both target regions. Compared with June through September observations of cloud-top temperatures (Neiburger, et al., 1961) and numerical modeling studies (Wakefield and Schubert, 1978), our daily mean cloud-top infrared temperatures (9.6°C for CA1 and 11.5°C for CA2) agree very well with theirs (8-10°C for Neiburger, et al., and 10-12°C for Wakefield and Schubert). More strikingly, if we assumed that cold cloud-top temperature corresponds to high cloud-top altitude and warm cloud-top temperature corresponds to low cloud-top altitude, we found the diurnal change of our cloud-top IR temperature is in phase with the diurnal change of cloud height of stratocumulus (Schubert, 1976). However, our current results are only from one day's data. To make sure that our current results are representative, we will extend our research for a longer time period. With this in mind, it is interesting to see that in Figure 2b, the diurnal changes of cloud-top temperature over South America have two warming peaks during the 24-hour period for both SA1 and SA2 regions. Although the maximum temperature difference of SA1 and SA2 (3.3°C) within this day is not as large as that over California

(3.5°C), we can clearly note the semi-diurnal nature in Figure 2b which suggests a major and a minor warming of cloud-top temperatures. This double warming of cloud-top temperature, if it exists, will suggest a different characteristic of South America stratocumulus from California stratocumulus. It is also interesting to note for these two target regions the double warming that happened near local midnight and noon.

4. SUMMARY

One day's GOES hourly images of California and South America stratocumulus were analyzed to compute the diurnal variations of cloud-top infrared temperatures. Our observational results agree well with numerical modeling results, despite that no correction for atmospheric effects was applied to our cloud-top temperaure computation. The overlying dry subsiding atmosphere is a likely reason. It is also noted in our current results that the South America stratocumulus has a double warming during 24 hours, occurring at about local midnight to local noon. Further composite studies are underway to confirm our current findings. We believe that better understanding of the phenomenology of these key extensive cloud regions will aid a number of climate diagnostic and modeling studies.

5. ACKNOWLEDGEMENTS

We thank Loretta Wilson for typing and layout of the manuscript. This research has been supported by the Climate Dynamics, Atmospheric Sciences, NSF grant ATM-8401229.

6. REFERENCES

Minnis, P., and E. F. Harrison, 1984: Diurnal variability of regional cloud and clear-sky radiative paramters derived from GOES data. Part II: November 1978 cloud distributions. J. Climate Appl. Meteor., 23, 1012-1031.

Neiburger, M., D. A. Johnson and C. W. Chien, 1961: Studies of the structure of the atmosphere oer the eastern Pacific Ocean in summer. I: The inversion over the eastern North Pacific Ocean. Univ. Calif. Publ. Meteor., 1, 1.

Schiffer, R. A., and W. B. Rossow, 1983: The International Satellite Cloud Climatology project (ISCCP): The first project of the World Climate Research Programme. Bull. Amer. Meteor. Soc., 64, 779-784.

Schubert, W. H., 1976: Experiments with Lilly's cloud-topped mixed layer model. J. Atmos. Sci., 33, 436-446.

Wakefield, J. S., and W. H. Schubert, 1978: Numerical simulation of Eastern North Pacific stratocumulus. Atmos. Sci. Paper No. 294, Dept. Atmos. Sci., Colorado State Univ., Fort Collins, CO 80523

Table 1. The geographical locations of 4 target regions.

NAME	LATITUDE	LONGITUDE
CA1	125W,122.5W	37.5N, 35.0N
CA2	130W,127.5W	30.0N, 27.5N
SA1	90W, 87.5W	0.0S, 2.5S
SA2	90W, 87.5W	7.5S. 10.0S

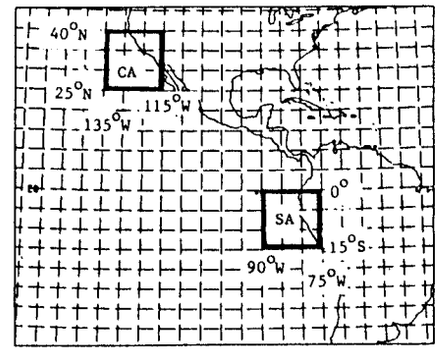

Figure 1. The study areas over which the GOES-6 satellite data was collected for 48 hours during August 25-27, 1985.

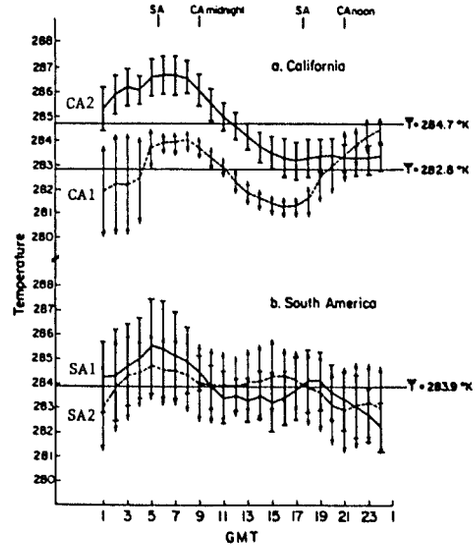

Figure 2. The regional hourly mean cloud-top infrared temperatures of 4 target regions versus time (GMT). Regions CA1 and CA2 are plotted in (a), while SA1 and SA2 are displayed in (b). The local midnight and noon time are marked on top of both diagrams.

A METHOD TO DETERMINE SURFACE ALBEDO FROM METEOSAT OBSERVATIONS OVER AFRICA

E. Ruprecht and G. Nacke
Institut für Meereskunde, Universität Kiel
F. R. Germany

1. INTRODUCTION

The surface albedo is a parameter which strongly affects the earth/atmosphere energy budget. Through its dependency on the vegetation it reacts very sensitively to anthropogenic activity. Therefore it stands as an important climate factor and is needed for diagnostic studies and climate modelling. Its global distribution and interannual variations are hardly known and can be derived only from satellite observations. In this study a method is developed to calculate the surface albedos of Africa with the observations of the geostationary satellite METEOSAT. The aim is to produce albedo maps of the whole African continent and to study the seasonal and interannual variations of the albedo of the southern Sahelzone in W-Africa.

The method needs two steps:

1. determine clear sky radiances,
2. convert the clear sky radiances into surface albedos.

Here only the first step will be discussed because this is the main task of the whole study. The method will be demonstrated on the area of 0° - 18° E, 12° - 26° N, subdivided into 2° x 2° subareas, with the observations from June 1983.

2. DETERMINATION OF CLEAR SKY RADIANCES

For determination of the clear sky radiances a 2-dimensional histogram is constructed from the two-channel observations (VIS and IR) of METEOSAT. Then a cluster analysis is applied to the histogram. The asymmetric GAUSSIAN cluster-analysis developed by Simmer et al (1982) is used. It fits to each maximum within the histogram Gaussian distribution functions, which define each cluster by the standard deviation and the radiances of the maximum. The last ones are called characteristic parameters of each cluster: R_i (= Reflectivity), TB_i (= Brightness Temperature). The scattering of the data around the cluster centre exists because of natural variability, observational errors and mixed scenes within the field of view. The cluster parameters R_i, TB_i are used for the further steps. In order to eliminate the cluster of cloudy pixels from the one of cloud free pixels a minimum technique is applied. After the cluster analysis is performed from all histograms of one subarea for a whole month, the warmest cluster is determined for each pixel. The corresponding VIS count (for each pixel) yields the minimum picture. This minimum technique has two advantages compared to other methods: first, the cluster parameters give an integrated value of the radiances which eliminates small errors; second, based on the warmest cluster it leads to an elimination of the radiances from cloud shadows and thin cirrus.

Fig. 1 gives the minimum picture at noon during June 1983 and for comparison an almost cloud free VIS image of the same area at June 5, 1983. The minimum picture portrays the dominant surface features of this area very well e.g. dark rocks of the Tibesti (right edge) and Ahaggar (upper edge) mountains, lake Tshad (lower right corner). The minimum picture provides the basic data for the clear sky radiances. The question arises, however, whether it shows representative values or whether the scatter is large. This scatter is studied, an example is given in Fig. 2. For one of the centre subareas of Fig. 1 (4th line, 5th column) all analysed clusters are shown which appear during June 1983. Those to the left repre-

sent clusters of cloudy pixels. The four encircled groups characterize the four dominant surface types of this subarea from dark rocks (of the Air Mountains) to bright sand.

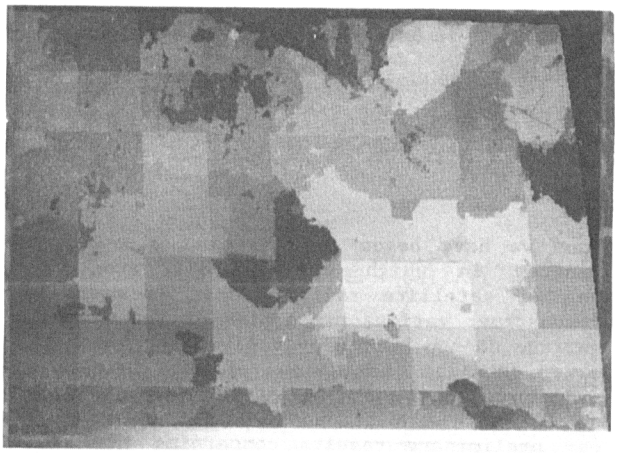

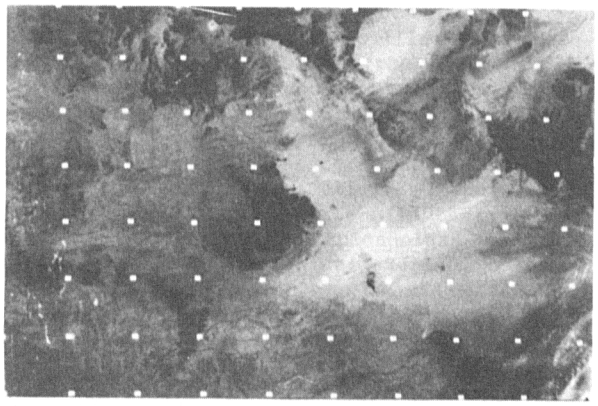

Fig. 1: Satellite images from the VIS channel observation of METEOSAT
below: June 5, 1983 Slot 23, 11^{30} GMT
above: Minimum picture June 1983, geographical area 0° - 18° E, 12° - 26° N.

The mean quadratic deviation from the minimum VIS count is calculated for each region of a subarea, which is defined by all pixels with the same VIS radiance in the minimum picture. These deviations correspond to the sizes of the encircled areas in Fig. 2. The minimum radiances and their mean quadratic deviations are then used to calculate the surface albedo and its scatter.

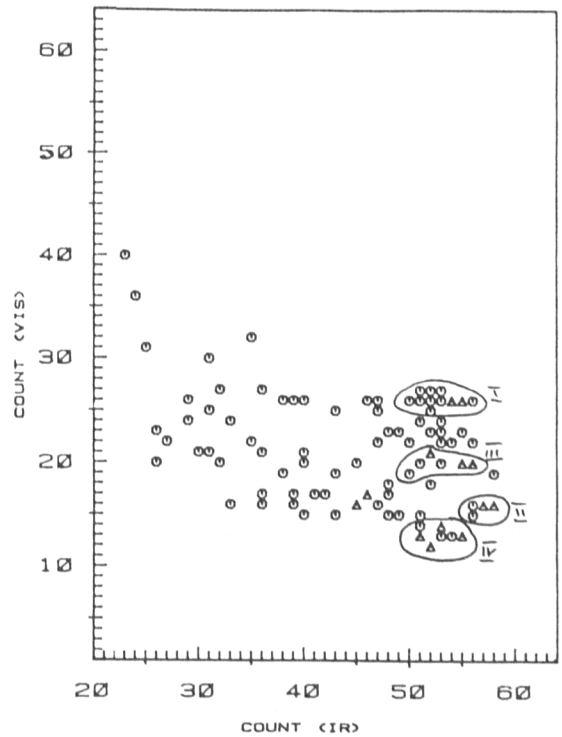

Fig. 2: Distribution of all cluster parameters which are determined from the subarea (4/5) in the center of Fig. 1. The points encircled and numbered (I - IV) represent the dominant surface types at the subarea. (O = 1 cluster, Δ = 2 clusters).

3. CONCLUSION

The study has shown, that our cluster algorithm can be applied for the localisation of different surface types. The minimum picture based on the warmest clusters portrays the dominant features of the surface in the southern Sahelzone. Now the method will be applied to study seasonal and interannual variations of the surface properties.

REFERENCES

Simmer, C., E. Raschke and E. Ruprecht, 1982: A method for determination of cloud properties from two-dimensional histograms. Annalen Meteor. NF, 18, 130 - 132.

5.3

MONITORING THE SPRING - SUMMER SURFACE ENERGY BUDGET TRANSITION IN THE GOBI DESERT USING AVHRR GAC DATA

Eric A. Smith

Department of Meteorology and
Supercomputer Computations Research Institute
Florida State University
Tallahassee, FL 32306

Elmar R. Reiter

Department of Atmospheric Science
Colorado State University
Fort Collins, CO 80523

1.0 Introduction

An investigation of the transition between spring and summer seasons of the surface energy budget in the Gobi desert has been carried out by Smith et al (1985). The previous study was based on a data set obtained at a desert edge site in Gansu province, P.R.C. The field program was conducted during the spring and summer periods of 1984. The site coordinate is (38° 52' N; 100° 29' E) at an elevation of 1525 meters. The site is located approximately 20 km to the south of the village of Zhangye which is situated near the Hei-He river, one of the many river systems which drain the northern Tibet Plateau into the arid regions of the southwest flank of the Gobi desert in western Gansu province. The site is indicated by the pointed finger symbol in the Landsat-2 photograph shown in Figure 1. The Qilian Shan Range, to the south of the village of Zhangye, contains mountain peaks ranging between 4500-5500 meters.

The Gobi desert is a large arid region of Northern China, oriented principally from east to west from 110°E to 118°E. It is bounded to the north by the Mongolian Plateau, to the south by the Yellow river drainage system, and to the west by Qilian Shan Range of the Quinghai-Xizang (Tibet) Plateau. The surface geomorphology of the site location is consistent with conditions all along the desert lowlands to the north of the Plateau in Gansu province. The surface consists of course sand grains and small pebbles with occasional rock outcroppings and very sparse scrub vegetation.

It is important to note that desert-edges and semi-desert regions are of principal concern to the International Satellite Land Surface Climatology Project (see ISLSCP (1983) and Rasool and Bolle (1984)). This emphasis has arisen from the deteriorating condition in the African Sahel and the now chronic problem of drought and desertification taking place over the Sahara desert's southern boundary - see Nicholson (1983). By the same token, desertification has occurred in the Gobi desert in recent years; Luk (1983) has reported a steady transformation of the Maomasu desert in the Central Gobi between 1953-1976.

It is useful to determine the degree to which the seasonal cycle can be monitored remotely as means of estimating how well we can expect to monitor interannual changes. Thus we have begun to carry out a research program in which operationally available weather satellite radiance data is used to reconstruct various properties of the diurnal surface energy budget over sites for which we have detailed estimates of the complete radiation, heat, and moisture exchange process. In this short paper, we present some of our preliminary results concerning the 1984 summer period for which we have already carried out the detailed surface analysis.

2.0 Preliminary Analysis of the 1985 Gobi Summer Period

The satellite measurements used in the preliminary study were collected by the AVHRR imaging radiometer flown on the NOAA-7 operational polar orbiter. We have used the Global Area Coverage (GAC) reduced resolution measurements which we obtained from the National Environmental Satellite and Data Information Service (NESDIS) -- see Kidwell (1985) for a detailed explanation of GAC data and the standard calibration procedures. A brief explanation as to why we chose the sun-synchronous twice-a-day NOAA polar orbiter satellite over a geosynchronous platform is in order (for this site INSAT provides 24 hour coverage). First of all, the 1984 INSAT geostationary data, which we have obtained under the auspices of the INDO-US Science and Technology Exchange Program, consist only of twice-a-day images. Furthermore, the Gobi site is beyond the limb of the daytime VIS-IR pair available in the INDO-US INSAT data tapes. Considering these factors, the NOAA-7 data is preferred for this particular investigation. In addition the NOAA-7 AVHRR instrument incorporates a near-IR shortwave channel (0.725-1.1 μm), a 3.7 micron weak window channel (3.55-3.93 μm), as well as the split window (10.3-11.3 and 11.5-12.5 μm) and the standard visible channel (0.58-0.68 μm).

Since the additional channels are helpful in discriminating moisture changes, which is important to this particular analysis, we are able to perform a variety of calculations that are not possible with a standard VIS-IR radiometer. This advantage in part outweighs the disadvantage of not having continuous monitoring of the diurnal cycle, although the ideal data set would be based on a 5-channel radiometer flown in a geosynchronous configuration.

In Figure 2 we illustrate the diurnal surface energy budget obtained at the Gobi site during the July 3-18 summer period. The instrumentation and methodology for this result is found in Smith et al (1985). In our present analysis we have extracted AVHRR-GAC radiance information in 0.5 x 0.5 degree grids, where the lower left hand grid corner conforms to the coordinate of the surface measurement where we obtained the result in Fig. 2. The pixels in these grids are then compiled into the following set of parameters:

$$T = \overline{(CH4 + CH5)/2}$$

$$R = \overline{CH1}$$

$$D45 = \overline{(CH4 - CH5)/CH4} \qquad (1)$$

$$D43 = \overline{(CH4 - CH3)/CH4}$$

$$D41 = \overline{(CH2 - CH1)}/(\overline{(CH2 + CH1)/2})$$

where CH1, CH2, CH3, CH4 and CH5 represent calibrated unnormalized albedos and equivalent black body temperatures. T and R represent temperature and reflectance parameters; D45 and D43 represent differential temperature parameters; and D21 represents a differential albedo parameter. The bars on the R.H.S. expressions in equation 1 indicate that all pixels within the 0.5 x 0.5 grid boxes are averaged. The averaging procedure improves the signal to noise ratio and is intended to produce satellite parameters representative of conditions around the site in question.

Results of the preliminary analysis are presented in Tables 1-2 and Figures 3-5. In Table 1 the daytime-pass satellite parameters for days 193-200 (July 11-18) are denoted along with daytime maximum values of upward flux emission temperature ($EBBT\uparrow_s$), surface soil temperature (ST), surface air temperature (AT), surface mixing ratio (w) and surface relative humidity (RH). A representative noontime broad-band surface albedo is also given (ALBSUR). The latter parameters have been derived from the surface monitoring station which was located at the Gobi site. Table 2 provides the nighttime parameters with the exception of R, D21, and ALBSUR which are not defined at night. There has been no attempt to match the time of the satellite pass to the points on the diurnal surface curves; the tabulated surface parameters are the day-night extremes of the diurnal signals.

Figure 3 illustrates the correspondence between satellite estimated window temperature (T) and reflectence (R), and radiative properties of the surface ($EBBT\uparrow_s$ and SURALB which is denoted by TOT in Fig. 3). Figure 4 illustrates the relationship between the soil temperature minima and nightime minima of AT and $EBBT\uparrow_s$ along with T (from the satellite). Figures 5a-b provide scatter plots of the daytime D45 and D43 parameters in conjunction with the surface mixing ratio (w) and the temperature difference $T=EBBT\uparrow_s - T$. Figure 5c provides a scatter plot of the D21 parameter and w and R=R - ALBSUR.

3.0 Discussion

The results shown in Tables 1-2 and Figures 3-5 demonstrate various important relationships concerning the feasibility of retrieving the amplitudes of the diurnal surface energy budget processes. The following preliminary conclusions are based on the tacit assumption that within a regional scale satellite scene (order 1000km square) there is a surface "tie down" monitoring station providing a continuous time series of surface energy budget parameters. The properties of the larger scale scene are presumed to be reasonably homogeneous with respect to the monitoring site in terms of surface boundary conditions (e.g. vegetative index and topography), but not necessarily atmospheric conditions.

These initial results demonstrate that:

For Daytime Conditions

1) There appears to be good correlation between D45 and w and T suggesting that the actual radiative emission temperature can be recovered in spite of moisture fluctuations.
2) The D43 parameter is somewhat less well-behaved due to contributions from both emission and solar backscatter in channel 3.
3) There appears to be good correlation between D21 and w and R suggesting that a representative noontime surface albedo can be recovered. The directional reflectance properties would have to be modeled -- as seen in Fig. 3 the shape of R as a function of solar zenith angle is not generally sinusoidal.
4) The relationship between surface ST and $EBBT\uparrow_s$ can be obtained by parameterizing with a single moisture parameter (e.g. w).

For Nighttime Conditions

1) There is a nearly constant relationship between minimum ST, minimum AT, minimum $EBBT\uparrow_s$, and T at night. The average temperature interval is 2^oC between each parameter (see Fig. 4) for a variety of moisture and temperature conditions. This suggests that the AVHRR nighttime window temperature can be used to reconstruct the upwelling infrared radiation flux, the surface air temperature and the surface skin temperature without resorting to multiple-channel information.
2) The D45 parameter does not appear to resolve moisture fluctuations.
3) The D43 parameter possibly could be used in a binary role to discriminate between wet and dry conditions.
4) The relative humidity parameter may be adequate for parameterizing the difference in upward/downward emission temperatures ($EBBT\uparrow_s - EBBT\downarrow_s$) needed in the calculation of surface net infrared flux (L^*_s).

The above points will be expanded on in conference. This paper is concluded by conjecturing on the issue of how to treat sensible and latent heating. It is presupposed that these terms cannot be retrieved directly. However, it is possible to proceed with a calculation of total conductive flux by applying the residual method to

parameterized estimates of Q^*_s and S and then incorporate a Bowen ratio derived at the monitoring site to the regional scale scene. This approach has its shortcomings if there are large soil moisture gradients across the regional scale scene, however, it would generate a first order separation of mean sensible and latent heating if the "tie down" coordinate is chosen appropriately.

4.0 Acknowledgements

The authors would like to express their appreciation to Greg Hunolt of the National Environmental Satellite and Data Information Service for the timely acquisition of the AVHRR-GAC data. The authors also express their appreciation to Mr. Kyung-Whan Oh for assisting with the computer processing. The manuscript was expertly prepared by Anna Nelson of the FSU Department of Meteorology. This research was funded under NASA grant NAGW-601 and NSF grant ATM-8514184. Computer support was provided by the FSU Supercomputer Computations Research Institute.

5.0 References

ISLSCP, 1983: Development of the implementation plan for the International Satellite Land-Surface Climatology project (ISLSCP). Prepared by a committee of specialists representing COSPAR, IAMAP, and the United Nations Environmental Programs, Document printed by the National Center for Atmospheric Research, Boulder, CO, 97 p.

Kidwell, K.B., 1985: NOAA polar orbiter data (TIROS-N, NOAA-6, NOAA-7, and NOAA-8) Users Guide. Technical Report, NOAA-NESDIS, Washington, D.C. 4 chapters, 5 appendicies.

Luk, S.H., 1983: Recent trends of desertification in Maowusu desert, China. Environ. Conservation, 10, 213-224.

Nicholson, S.E., 1983: Sub-Saharran rainfall in the years 1976-80: Evidence of continued drought. Mon. Wea. Rev. 111, 1646-1654.

Rasool, S.F., and H.J. Bolle, 1984: ISLSCP: International Satellite Land-surface Climatology Project. Bull. Amer. Meteor. Soc., 65, 143-144.

Smith, E.A., E.R. Reiter, and Y.Gao, 1985: Transition of surface energy budget in the Gobi desert between spring and summer seasons. Sub. to J. Clim. Appl. Meteor. for publication.

Table 1: Daytime Satellite Parameters and Surface Parameter Maxima during July 11-18.

	T(K)	R(%)	D45(x10)	D43	D21	ALBSUR(%)	$EBBT\uparrow_s$(K)	ST(K)	AT(K)	w(gm/kg)	RH(%)
193	298	29	+10.5	-5.6	-7.6	27	308	304	296	8.0	40
194	301	26	+ 9.6	-5.2	-7.2	27	315	308	299	7.5	30
195	299	25	+ 6.4	-4.5	-2.0	26	305	300	296	5.5	30
196	308	20	+ 1.9	-2.8	+0.5	27	316	310	301	4.0	15
197	311	21	+ 3.1	-2.6	+0.9	27	319	312	305	4.0	12
198	301	24	+ 2.5	-3.7	-0.7	26	308	304	300	5.0	18
199	310	23	+ 4.1	-2.9	+0.4	27	319	313	304	4.5	14
200	304	28	+ 6.2	-4.9	-8.6	26	314	309	298	8.5	35

Table 2: Nighttime Satellite Parameters and Surface Parameter Minima during July 11-18.

	T(K)	D45(x10)	D43(x10)	$EBBT\uparrow_s$(K)	ST(K)	AT(K)	w(gm/kg)	RH(%)
193	283	+2.0	-2.0	285	289	287	12.0	95
194	284	-1.8	-1.5	288	291	290	9.5	60
195	284	+2.2	-2.7	287	290	289	13.0	90
196	285	-1.7	-18.5	286	291	290	8.0	40
197	284	+1.9	-15.7	285	291	288	8.5	45
198	287	+1.4	- 3.9	291	295	293	8.0	37
199	(MISSING -		MISSING)	286	291	290	8.5	43
200	285	+1.6	+1.4	287	292	290	11.0	57

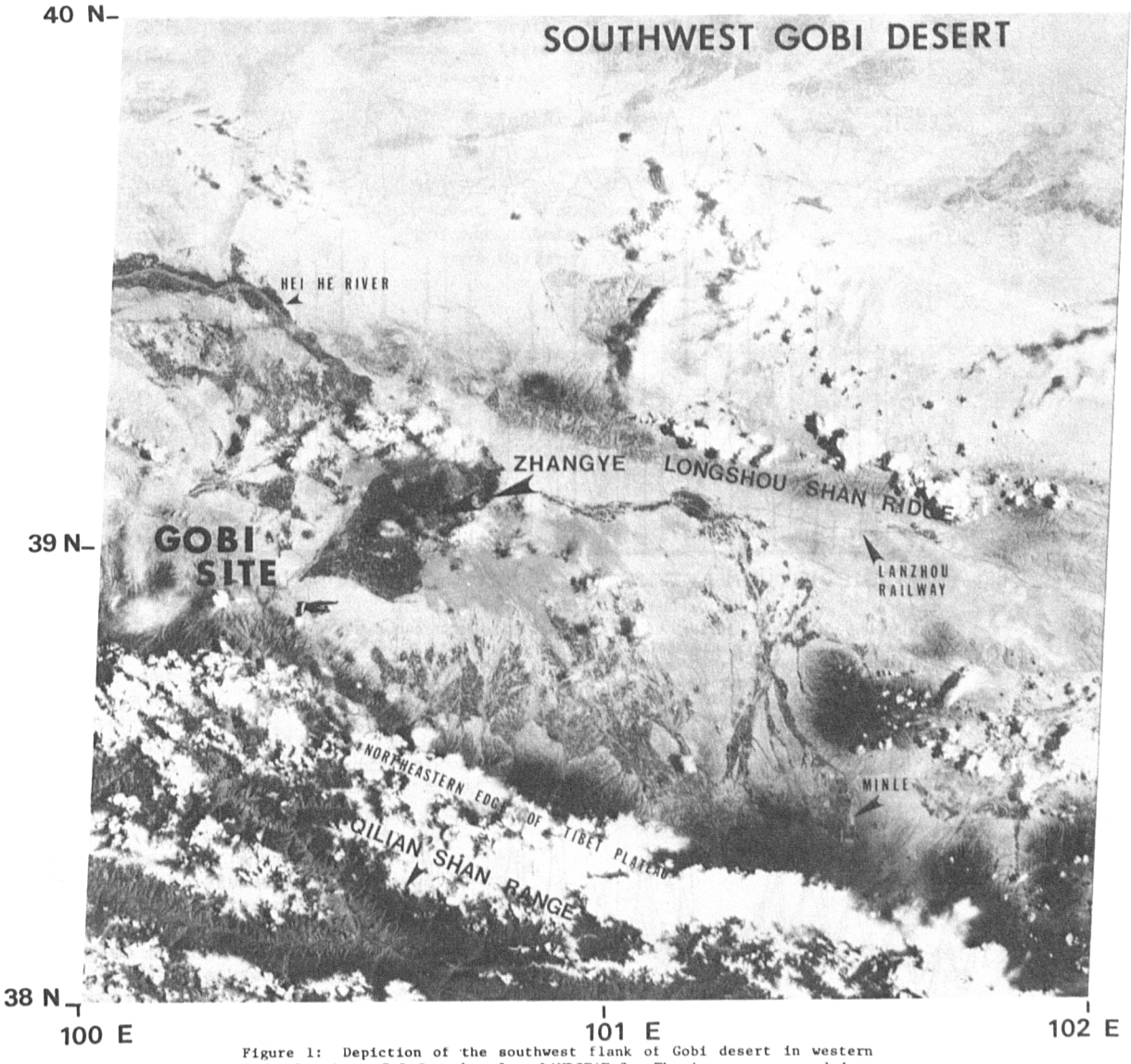

Figure 1: Depiction of the southwest flank of Gobi desert in western Gansu Province, P.R.C. taken from LANDSTAT-2. The image was recorded on 28 June, 1977, at 9:55 solar time utilizing VIS-RED channel 5 (0.6-0.7 μm). The pointing finger symbol indicates the position of the measurement site. To the immediate south of the measurement site is the leading edge of the northern edge of the Tibet plateau.

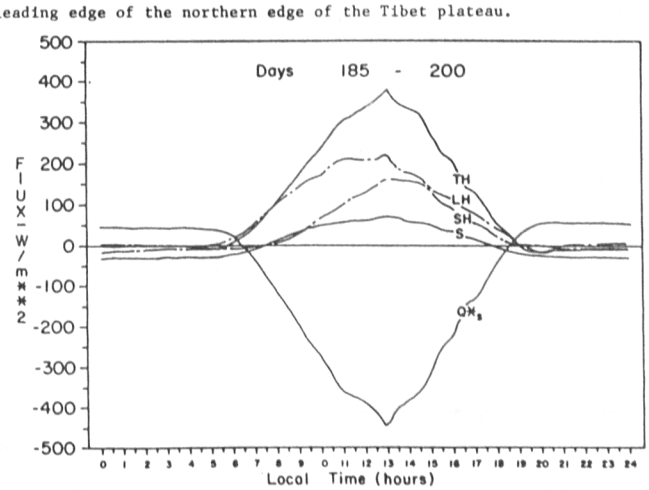

Figure 2: Diurnal surface energy budget process during the July 3-18 summer period at Gobi desert site. The diurnal cycles of net radiation (Q^*_s), storage (S), sensible heat flux (SH), latent heat flux (LH), and total conductive heat flux (TH) are indicated.

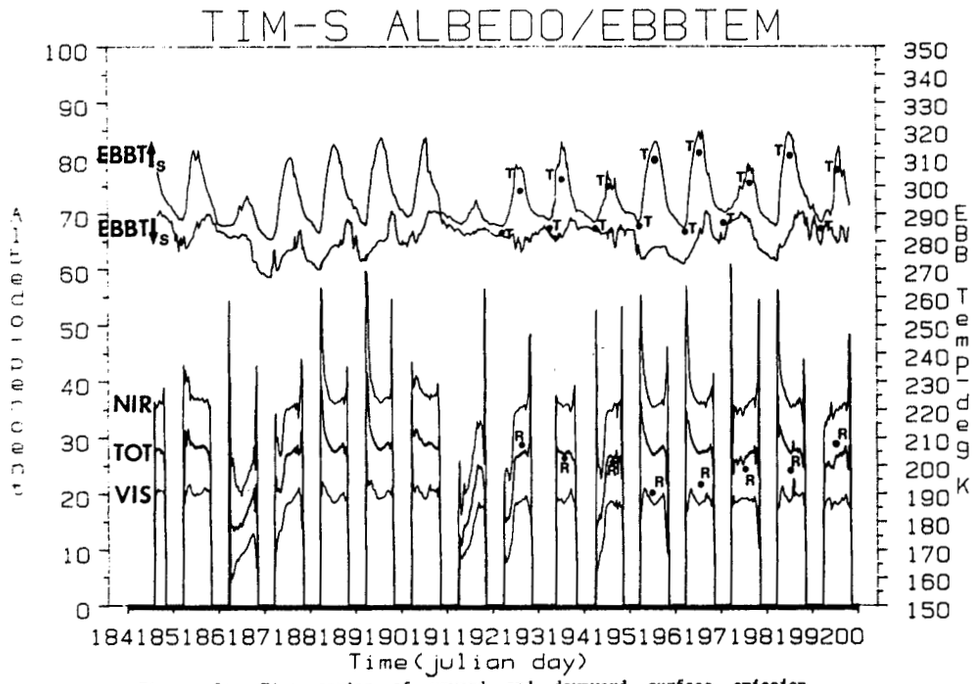

Figure 3: Time series of upward and downward surface emission temperatures ($EBBT\uparrow_s$ and $EBBT\downarrow_s$) along with near-infrared (NIR), visible (VIS) and total solar (TOT) surface albedo at Gobi site from July 3-18. The satellite window temperatures (T) and spectral reflectances (R) for the day and night passes during July 11-18 are indicated in conjunction with min-max conditions of $EBBT\uparrow_s$ and noontime TOT.

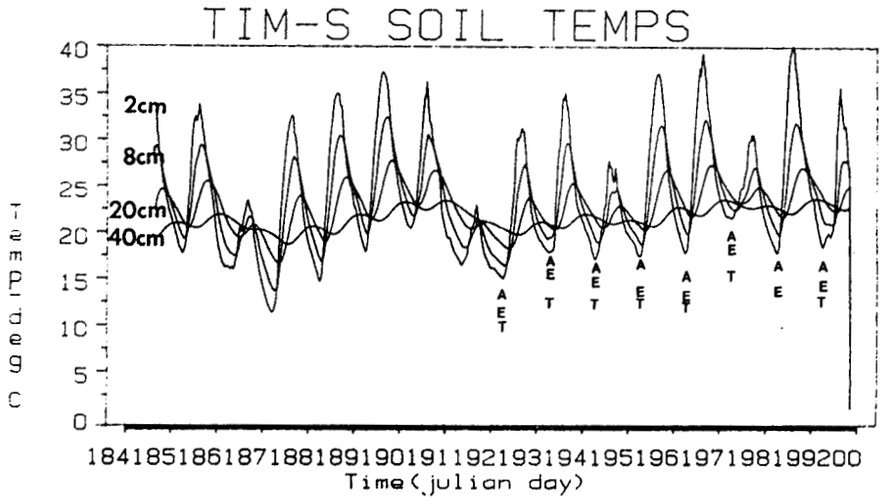

Figure 4: The sub-surface soil temperature cycles at Gobi site during same period as in Fig. 3. The nighttime minima of air temperature (A), emission temperature ($EBBT\uparrow_s$), and satellite window temperature (T) during July 11-18 are indicated in conjunction with the nighttime minima of 2 cm soil temperature.

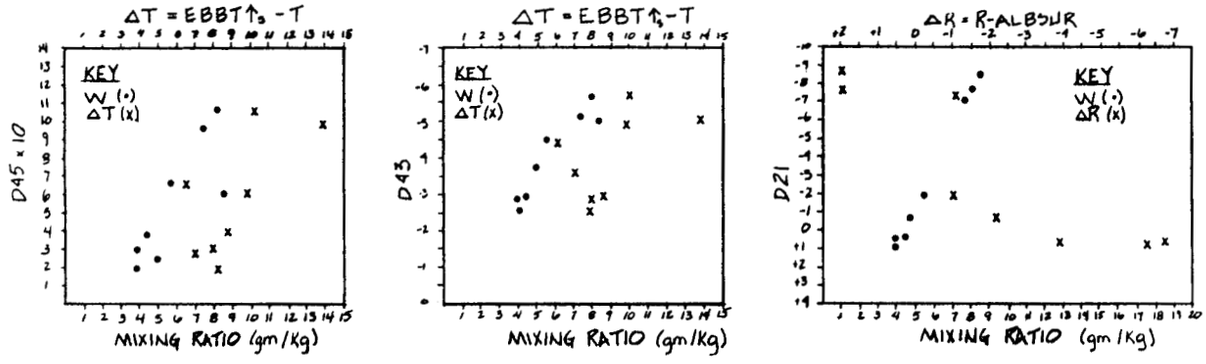

Figure 5a-c: a) Scatter plot of daytime D45 with w and T (left);
b) Scatter plot of daytime D43 with w and T (middle);
c) Scatter plot of daytime D21 with w and R (right).

5.4

Estimating Dust Optical Depth from the Radiative Temperature difference of 11 μm and 3.7 μm channels

Steven A. Ackerman
and
Stephen K. Cox

Department of Atmospheric Science
Colorado State University
Fort Collins, CO 80523

1. INTRODUCTION

Each year surface observations suggest that large quantities of dust are transported out of the deserts of the world. These dust outbreaks can produce environmental hazards, especially along major transportation routes. Since surface observations are generally sparce, it is often difficult to locate the orgin as well as the movement of a dust outbreak . The optical thickness of the dust layer is an important parameter affecting the transfer of radiant energy in the earth's atmosphere. Dust optical depth is generaly observed using a sun-photometer (Volz, 1970) and is reported in terms of turbidity (optical depth at 0.5 μm). The number of sun-photometer measurements are extermely limited. The disadvantage of surface observation horizontal resolution can be overcome with the aid of satellite data. For example, Carlson 1979 and Norton et al., 1979 have incorported satelliete measurements in the visible to monitor dust outbreaks as well as to estimate dust optical depth. This research uses IR satellite measurements to track a dust outbreak and to derive values of the dust optical depth.

2. THEORY

The methodology uses the radiative temperature difference between 3.7 μm and 11 μm in the presence of a dust layer. The single scattering albedo (ω_0), volume extinction coefficient (K_{ext}) and asymetry parameter (g) were calculated (Table 1) from Mie theory assuming the size distribution given by Norton et. al. (1980) and an index of refraction of Patterson (1981). These parameters were then used in a doubling model and the upwelling radiances were converted to brightness temperatures. The difference between these temperatures ($\Delta T = T_{3.7} - T_{11}$) is shown in figure 1 as a function of turbidity for a satellite viewing angle of 8°. Since optical depth is a function of wavelength, results are given as a function of optical depth at λ=0.5μm. This is the most common wavelength for measuring atmospheric dust loading. The ratio of K_{ext} at 3.7 and 11 μm to K_{ext} at 0.5 μm is given in Table 1. For simplicity water vapor absorption has been neglected; due to the dry atmospheres involved this neglect of water vapor absorption should not affect the conclusions. To aid in the interpretation of the results dust layer reflectance, transmittance and emittance at the two wavelengths are shown in figure 2.

TABLE 1. Single scattering properties of the dust layer at 3.7 and 11 μm.

	3.7 μm	11 μm
ω_0	.9869	.4162
g	.6507	.5038
$KEXT_\lambda$ / $KEXT_{0.5}$	.77	1.07

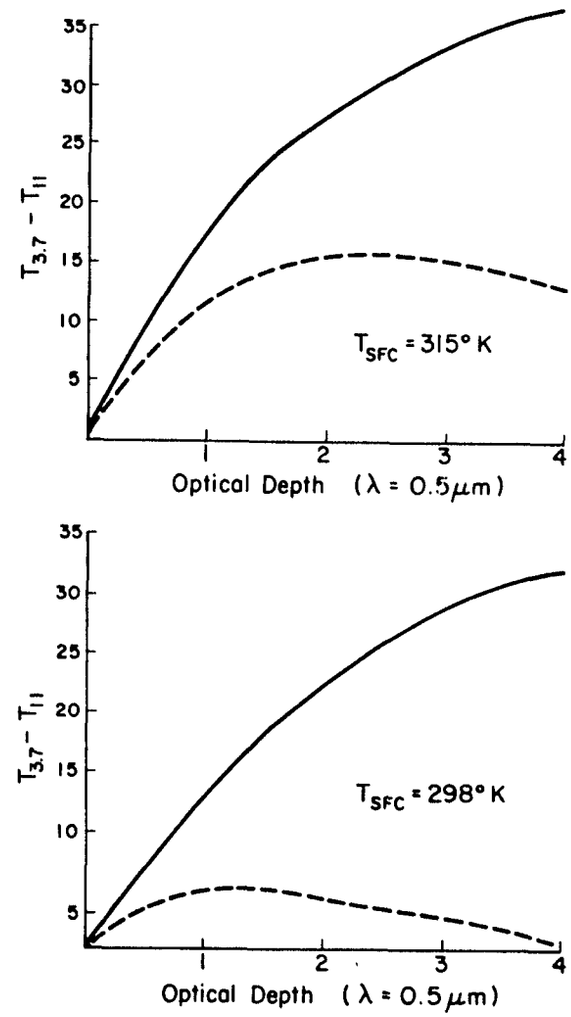

Figure 1. Radiative temperature difference ($\Delta T = T_{3.7} - T_{11}$) as a function of turbidity for a satellite viewing angle of 8° and a solar zenith angle of 0°.

Fiqure 1a. represents the case of a dust layer over lying a desert surface with a surface temperature of 315° K, the solid line includes solar reflectance (solar zenith angle of 0°) while the dashed does not. The upwelling 3.7μm radiation is significantly augmented by reflection of solar energy by the dust layer. Even without the inclusion of solar reflection the 3.7 μm temperature is still larger than the 11 μm temperature, despite reflection of the surface upwelling radiance at the dust layer base. The 3.7 μm emittance is small even for large optical depth, thus the upward radiance is largely determined by the transmittance of the surface radiance and reflection of the downward solar component. In the 11 μm radiance, the reflectance is always small. Thus for small dust optical depths the major contribution is from the surface and as the dust layer optical thickness increases, emission by the dust layer itself becomes important. The transmission is always greater at 3.7 μm, thus ΔT is, for this case, always positive. For the case of a surface inversion (e.g. over the desert at night) one may expect negative ΔT.

Figure 1b represents the case of a dust layer overlying an ocean surface with a surface temperature of 298° K. The dashed line excludes the solar component and can be considered the nighttime case. Again there is a large contribution from solar reflectance. For the night case the maximum ΔT ≈ 5°, which peaks at $\tau \approx 1.3$. For optical depths greater than 1.3 ΔT decreases with increasing τ. The 3.7 μm radiance decreases with increased τ due to the decrease in the transmitted surface radiance; while the 11 μm radiance also decreases with increasing τ the rate of decrease changes as the dust layer emittance increases. This nightime curve suggests that retrieval of dust optical depth using these two wavelengths would be least sensitive at night. Given the indices of refraction of dust, it may be more appropriate to chose two wavelengths in the 8-12 μm window where there are still large variations in complex index of refraction.

3. OBSERVATIONS

Before inquiring into the effects on ΔT of atmospheric temperature and moisture profiles, the vertical distribution of the dust loading and the surface radiative properties, it is instructive to compare satellite measurements with surface observations. Unfortunately, coincident satellite and sun-photometer measurements were not available to demonstrate the method. However since visibilty is often related to mass concentration for airborne soil particles (Patterson and Gillete 1977), surface observations of visibilty were compared with the satellite measurements. Observations of the TIROS-N AVHRR's channel 3 (3.58-3.97 μm) and channel 4 (10.53-11.45 μm) were used in the study. The equatorial crossing times of the TIROS-N are 0300 (descending) and 1500 (ascending) LT. The data was mapped by Smith and Graffy (1982) onto a uniform grid with a resolution of 15 points per degree latitude or longitude. The scheme of Lauritson et. al. (1979) was used to convert raw digital data to window temperatures.

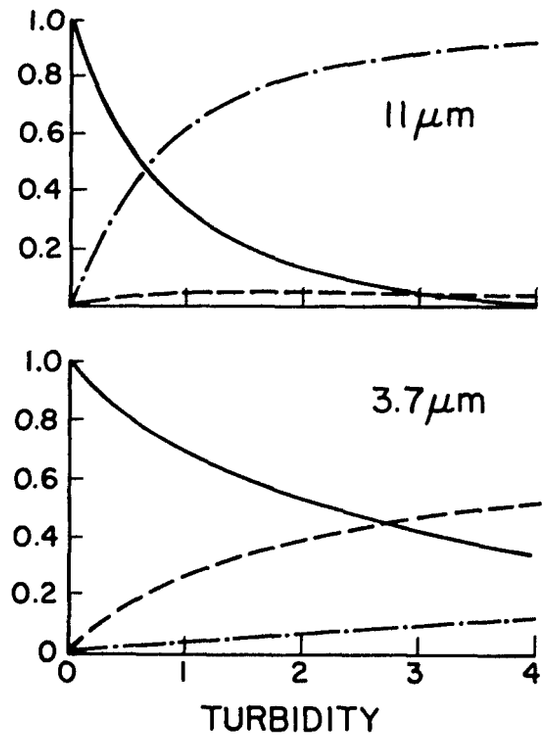

Figure 2. Dust layer transmittance (solid), reflectance (dashed), and emittance (dot-dashed) at wavelengths of 3.7 and 11 μm.

Figure 3 depicts a large scale dust outbreak observed over the Saudi Arabian Peninsula in late June 1979. Each station plot includes information on wind speed and direction, temperature, dew point depression, cloud cover, present and past weather, visibility, pressure and 24 hour pressure tendency (WMO,1974). Lines of constant visibility (in km) are analysed as solid lines. Regions of low visibility are generally associated with large optical depths. Figure 3 also depicts the satellite radiative temperature differences (dashed lines) as well as the surface observations. The dust outbreak region is cloud free. Large temperature differences measured by the satellite are well correlated with regions of low visibility.

4. SUMMARY

Using a doubling model the brightness temperature difference (ΔT) between 3.7 μm and 11 μm radiation was investagated as a function of dust optical depth at a wavelength of 0.5 μm. The spectral radiances are largest during the day when the ΔT's are enhanced by reflection of incident solar flux. This technique would therefore work best during the day, though nighttime application may still be possible.

The feasibilty of tracking dust outbreaks, as well as inferring the dust layer optical depth, is demonstrated by comparing satellite observations with surface estimates of visibility.

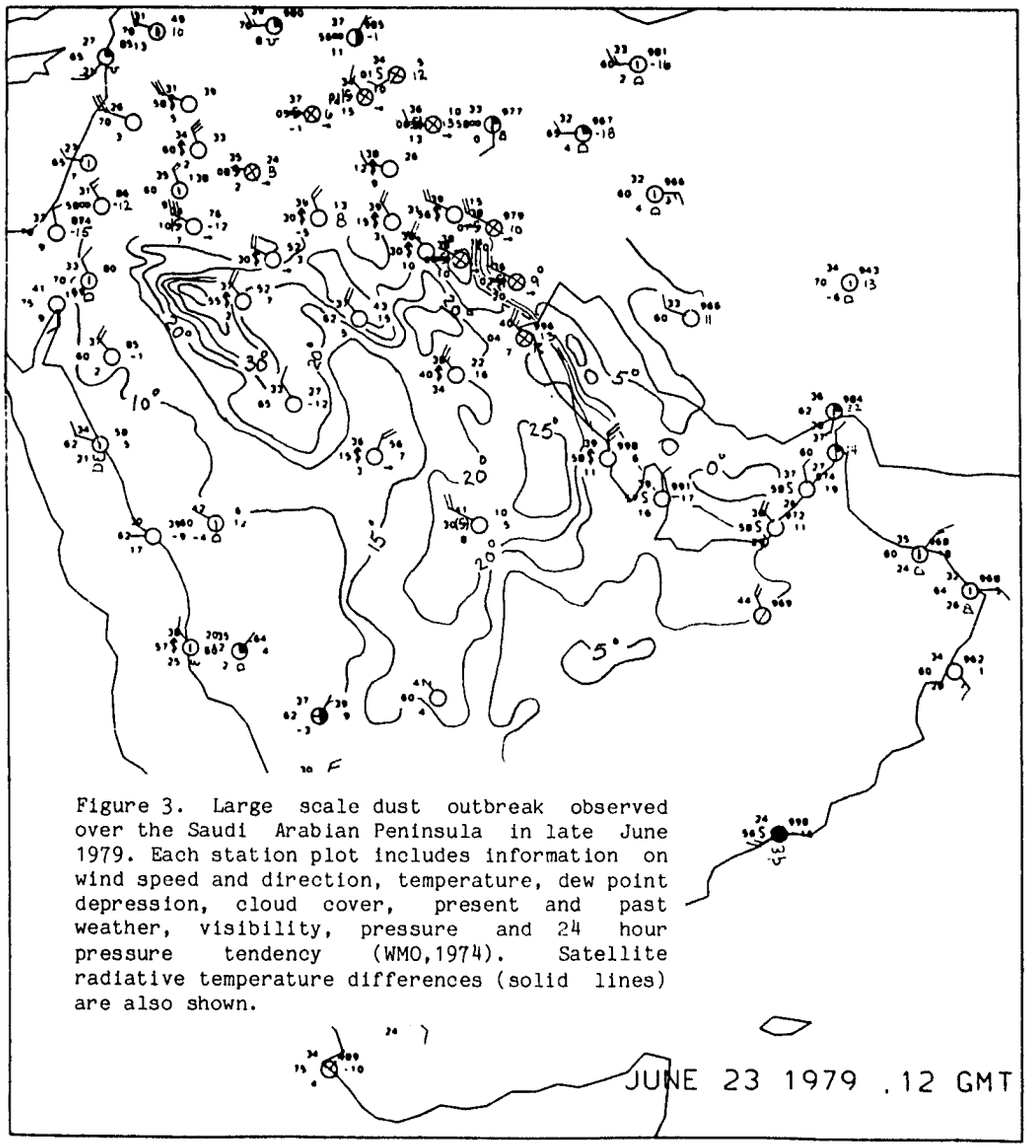

Figure 3. Large scale dust outbreak observed over the Saudi Arabian Peninsula in late June 1979. Each station plot includes information on wind speed and direction, temperature, dew point depression, cloud cover, present and past weather, visibility, pressure and 24 hour pressure tendency (WMO,1974). Satellite radiative temperature differences (solid lines) are also shown.

5. REFERENCES

Carlson, T.N., 1979: Atmospheric turbidity in Saharan dust outbreaks as determined by analyses of satellite brightness data, Mon. Wea. Rev., 107, 322-335.

Lauritson, L., G.J. Nelson and F.W. Portr, 1979: Data extraction and calibration of TIROS-N/NOAA radiometers. NOAA Tech. Memo. NESS 107, NOAA-NESS, Washington, DC, 58 pp.

Norton,C., F.R. Mosher, B. Hinton, D.W. Martin, D. Santek, and W. Kuhlow,1980: A model for calculating desert aerosol turbidity over the oceans from geostationary satellite data, J. Appl. Meteorol., 19, 633-644

Patterson, E.M., 1982: Optical properties of the crustal aerosol: Relation to chemical and physical characteristics. J. Geophys. Res., 86, 3236-3246

Patterson, E.M. and D.A. Gillette, 1977: Measurements of visibility vs. mass-concentration for airborne soil particles. Atmos. Envir., 11, 193-196.

Smith, E.A. and J. Graffy, 1982: A TIROS-N AVHRR digital data set for analysis of the 1979 southwest summer monsoon. Special Report, Dept. Atmos. Sci., Colorado State University, Fort Collins, CO 15 pp., 617 plates, 41 tables.

Volz, F.E., 1970: Spectral skylight and solar radiance measurements in the Caribbean: Maritime aerosols and Sahara dust. J. Atmos. Sci., 27, 1041-1047.

WMO, 1974: International Codes, WMO-306, Manual on Codes, Vol. 1

5.5

SATELLITE MEASUREMENTS OF PHYSICAL PROPERTIES OF SAHARAN DUST

Tae Young Lee
Applied Research Corporation
8201 Corporate Drive
Landover, MD 20875

Robert S. Fraser
Laboratory for Atmospheres
Goddard Space Flight Center
Greenbelt, MD 20771

Yoram Kaufman
University of Maryland and
Laboratory for Atmospheres
Goddard Space Flight Center

1. INTRODUCTION

The Saharan dust flowing over the Atlantic Ocean may have climatic consequences through its radiative interaction with both short and long wave radiation. The study by Randall et al. (1984) suggested that Saharan dust heating can produce a narrowing and intensification of Intertropical Convergence Zone and a weakening of trade winds. The impact of Saharan dust can be evaluated only when its physical properties are well known.

Many investigations have been made concerning the physical properties of Saharan dust such as long range transport (Prospero and Carlson, 1972; Prospero et al., 1981), size distributions (Schutz and Jaenicke, 1974), refractive index (Volz, 1973; Patterson et al., 1977; Carlson and Caverly, 1977), etc. Although such studies result in a significant advances in our knowledge of Saharan dust, there are still many uncertainties in its physical properties.

Due to the relative simplicity in analysis of satellite data and their wide areal coverage, satellite measurement is an efficient approach to obtain such information. Researchers have been using satellite images to obtain aerosol optical depth (Griggs, 1975; Fraser, 1976; Mekler et al., 1977; Koepke and Quenzel, 1979), to track the aerosol over the land and ocean (Carlson, 1979; Fraser et al., 1984), and to estimate the aerosol absorption (Otterman et al., 1982; Kaufman and Fraser, 1985).

In this report, the physical properties of Saharan dust are obtained from AVHRR and VISSR images. The techniques of Fraser (1976) and Kaufman and Fraser (1985) are used to derive the aerosol optical depth, mass and single scattering albedo. These properties are derived for the region extending from the west coast of Africa to the Barbados Island for the period of June 21-25, 1984. Satellite measured optical properties are comparied to aircraft measurement taken near the Barbados Island at the same period. Remote measurement of thermal properties is also discussed in this report.

2. OPTICAL DEPTH

The Saharan dust optical depth is derived from satellite measurements of the radiance of sunlight scattered from the earth and its atmosphere. VISSR radiance is calibrated by comparing sensor voltages with computed radiance of sunlight scattered from an ocean-atmosphere system (Fraser and Kaufman, 1986). The method of deriving optical depth from satellite measured radiance is given in Fraser et al. (1984). The method requires a table of radiance as a function of optical depth and view angles. For this purpose, the radiance is computed with a radiative transfer model of the ocean-atmosphere system (Ahmad and Fraser, 1982). Two different dust particle size distributions are used in the computations. Near Barbados Island we used size distribution measured by Talbot et al. (1985) for the period of June 21-26, 1984. For the region just off the west coast of Africa, we employed a desert dust storm model of WMO (1983) which is based on the measurements of Schutz and Jaenicke (1974) and Jaenicke and Schutz (1978). The surface is assumed to be a rough ocean with surface wind speed of 7.5 m/s. Atmospheric gas absorption and Rayleigh scattering are also considered. Satellite images for June 6, 21, and 25, 1984 are selected for this report.

The aerosol mass is related to the optical thickness by computing the ratio of the mass to the extinction coefficient, using the size distribution measured from aircraft and Mie theory. Satellite derived aerosol masses are compared to the aircraft measurements in Table 1. The table shows a fair agreement between the satellite and aircraft measured aerosol mass.

Table 1: Comparison of satellite derived and aircraft measured mass of Saharan Dust in units of gm^{-2}.

	AVHRR	VISSR	Aircraft
6-21-84	0.31	0.37	0.31±0.05
6-25-84	0.27	----	0.23±0.05

Satellite derived optical depth at λ = 0.63 μm of Saharan dust just off the west coast of Africa is shown in Figure 1. The optical depths are generally between 1.0 and 2.0 and reach up to 2.5. This amount of Saharan dust can significantly affect the energy budget of aerosol layer (Fouquart et al., 1984). The Saharan dust optical depth near Barbados Island ranges from 0.1 to 0.7.

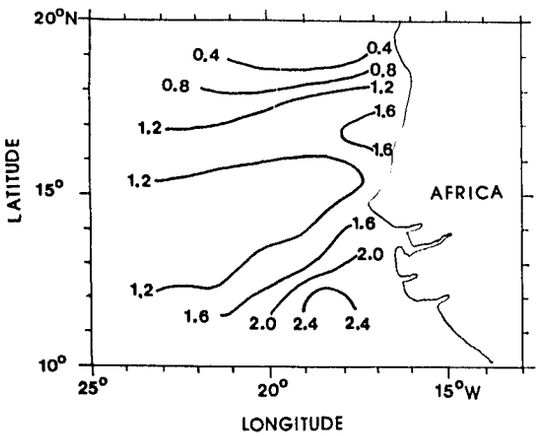

Figure 1 Vertical aerosol optical thickness measured at λ 0.63μm by AVHRR on 6 June 1984, 1635GMT.

The Angstrom exponent α is also derived using the AVHRR radiances of two channels (0.63 and 0.83 μm) (Table 2). The α value just off the west coast is smaller than near Barbados Island, indicating a decrease in the relative number of large particles with passage over the Atlantic ocean. This trend and the values of α are in very good agreement with Prospero et al. (1976) in which α increases from 0.3 at Senegal to 0.9 at Miami. The above results are also in good agreemet with other measurements of Saharan dust (Carlson and Caverly, 1977; Cerf, 1980; Fouquart et al., 1984).

Table 2: Average Angstrom exponent α derived from AVHRR data.

	α	Location
6-06-84	0.11	just off the west coast of Africa
6-21-84	0.70	Barbados
6-21-84	0.33	Barbados

3. AEROSOL ABSORPTION

The effect of aerosol on climate depends on its absorption of sunlight. The method of determination of aerosol absorption is described in Kaufman and Fraser (1985). The satellite derived single scattering albedo is 0.96. We are not aware of direct measurements of aerosol of single scattering albedo of Saharan dust by collecting samples and measuring at least two of their three coefficients of absorption, scattering and extinction. Fouquart et al. (1984), however, estimated the albedo of single scattering from measurements of flux divergence of solar radiation in the Saharan dust layer. Their values range from 0.92 to 0.99. Since the wavelength dependence of the albedo of single scattering is not known reliably, these values can not be compared exactly with the satellite values at λ = 0.63 μm.

4. THERMAL PROPERTY

Since the Saharan dust is appreciably colder than the ocean, because it generally is located above the trade wind inversion, its thermal effect is directly detectable from satellite (e.g. reduction of brightness temperature by Saharan dust). From AVHRR images used in this report, up to 6 degree of brightness temperature reduction by Saharan dust is detected (Figure 2). One distinctive thermal effect of Saharan dust is found in the variation of $\Delta T(=T_{11}-T_{12})$ with dust optical depth. T_{11} and T_{12} are brightness temperatures for 11 and 12μm. Figure 3 shows a relationship between ΔT and optical depth. ΔT decreases with increase of Saharan dust amount. Since the water vapor absorbs radiation more at 12μm than 11μm, ΔT for thin clouds shows the opposite trend given by dust. The trend in this figure, therefore, is a good indication of a thermal effect of Saharan dust. Figure 3 suggests that Saharan dust absorbs more at 11μm than at 12μm and, with a large amount of dust, T_{12} becomes larger than T_{11}. Theoretical calculations assuming the refractive index of Volz (1973) give partial agreement with Figure 3. The refractive index for 11 micron is m = 1.82 - 0.30i and for 12μm, m = 1.77 - 0.16i. The partial agreement may be due to the uncertainties in the refractive index and the vertical distribution of Sahran dust.

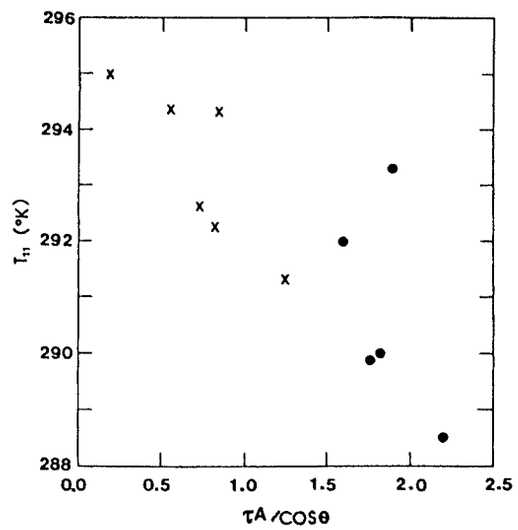

Figure 2 Apparent temperature measured by AVHRR in the 11μm band as a function of the aerosol optical thickness along a slant path where θ is the zenith angle between a local vertical and the line-of-sight to AVHRR. X denotes observation near Barbados Island on 6-21-84; o denotes observation near Africa on 6-6-84

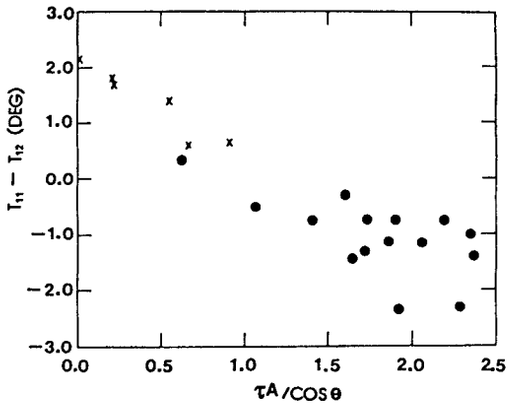

Figure 3 Temperature difference in 11μm and 12μm bands as a function of aerosol optical thickness along a slant path. The symbols are the same as in Figure 2.

5. CONCLUSION

Physical properties of Saharan dust are obtained from VISSR and AVHRR images. They are derived over the region off the west coast of Africa and near Barbados Island. Optical depth ranges from 0.3 to 2.4 off the west coast of Africa and 0.1 to 0.7 near Barbados Island. The average Angstrom exponent α ranges from 0.11 just off the west coast of Africa to 0.33 - 0.70 near Barbados Island. Satellite derived single scattering albedo is 0.96. A thermal effect of Saharan dust is to absorb more at 11 μm than at 12μm.

6. REFERENCES

Ahmad, Z. and R. S. Fraser, 1982: An iterative radiative transfer code for ocean-atmosphere system. J. Atmos Sci., 29, 656-665.

Carlson, T. N., 1979: Atmospheric turbidity in Saharan dust outbreaks as determined by analysis of satellite brightness data. Mon. Wea. Rev., 107, 322-335.

Carlson, T. N. and R. S. Caverly, 1977: Radiative characteristics of Saharan dust at solar wavelengths. J. Geophys. Res., 82, 3141-3152.

Cerf, A., 1980: Atmospheric turbidity over West-Africa. Contributions to Atmospheric Physics, 53, 3, 414-429.

Fouquart, Y., A. Cerf, B. Bonnel, M. Chaoui-Roquai, L. Smith and J. C. Vanhoutte, 1984: Size distribution and optical properties of Saharan aerosols during ECLATS. In Aerosols and Their Climatic Effects, edited by A. Deepak and H. Gerber, A. Deepak publishing, 35-62.

Fraser, R. S., 1976: Satellite measurements of mass of Sahara dust in the atmosphere. Appl. Opt., 15, 2471-2479.

Fraser, R. S. and Y. J. Kaufman, 1986: Calibration of Satellite sensors after launch. Accepted, Appl. Opt.

Fraser, R. S., Y. J. Kaufman, and R. L. Mahoney, 1984: Satellite measurements of aerosol mass transport. Atmos. Environ., 18, 2577-2584.

Griggs, M., 1975: Measurements of atmospheric aerosol optical thickness over water using ERTS-1 data. J. Air. Pollution. Control Assoc., 25, 622-626.

Jaenicke, R. and L. Schutz, 1978: Comprehensive study of physical and chemical properties of the surface aerosols in the Cape Verde Islands region. J. Geophys. Res., 83, 3585-3599.

Kaufman, Y. J. and R. S. Fraser, 1985: Remote sensing of aerosol absorption. Proceedings of the International Radiation Symposium, Perugia, ITALY, edited by Fiocco, 16-19.

Koepke, P., and H. Quenzel, 1979: Turbidity of the atmosphere determined from satellite: Calculation of optimum viewing geometry. J. Geophys. Res., 84, 7847-7855.

Mekler, Y., H. Quenzel, G. Ohring and I. Marcus, 1977: Relative atmospheric aerosol content from ERTS observations. J. Geophys. Res., 82, 967-970.

Otterman, J., R. S. Fraser and O. P. Bahethi, 1982: Characterizations of tropospheric desert aerosols at solar wavelengths by multi-spectral radiometry from Landsat, J. Geophys. Res., 87, 1270-1278.

Patterson, E. M., D. A. Gillette, and B. H. Stockton, 1977: Complex index of refraction between 300 and 700nm for Saharan aerosols. J. Geophys. Res., 82, 3153-3161.

Prospero, J. M. and T. N. Carlson, 1972: Vertical and areal distribution of Saharan dust over the Western Equatorial North Atlantic Ocean, J. Geophys. Res., 77, 5355-5365.

Prospero, J. M., T. N. Carlson, D. Savoie, and R. T. Nees, 1976: Atmospheric turbidity measurements during GATE. Univ. Miami Technical Report, TR76-6.

Prospero, J. M., R. A. Glaccum and R. T. Nees, 1981: Atmospheric transport of soil dust from Africa to South America, Nature, 289, 570-572.

Randall, D., T. Carlson, and Y. Mintz, 1984: The sensitivity of a general circulation model to Saharan dust heating. In Aerosols and their Climatic Effects, edited by A. Deepak & H. Gerber, A. Deepak Publishing, 123-132.

Schutz, L., and R. Jaenicke, 1974: Particle number and mass distributions above 10^{-4}cm radius in sand and aerosol of the Sahara Desert. J. Appl. Meteor., 13, 863-870

Talbot, R. W., R. C. Harriss, E. V. Browell, G. L. Gregory, D. I. Sebacher, and S. M. Beck, 1985: Distribution and geometry of aerosols in the tropical North Atlantic troposphere - Relationship to Saharan dust. Submitted to J. Geophys. Res.

Volz, F. E., 1973: Infrared optical constants of ammonium sulfate, Saharan dust, volcanic Pumice and Flyash. Appl. Opt., 12, 564-567.

WMO (1983): Report of the Experts Meeting on Aerosols and their Climatic Effects (Williamsburg, VA, 28-30 March 1983), World Climate Research Programme, Report No. WCP-55, Published by the World Meteorological Organization, Dec. 1983.

AEROSOL CHARACTERIZATION WITH DUAL-WAVELENGTH RADIANCE MEASUREMENTS

Philip A. Durkee

Department of Meteorology
Naval Postgraduate School
Monterey, CA 93943

1. INTRODUCTION

New radiometers on meteorological satellites have made it possible to detect variations of aerosol particles within the atmosphere. Most of the published techniques use radiance measured in a single wavelength band. In this paper, radiance values from visible and near-infrared wavelength bands are used to provide information about particle size distribution and composition.

Single-wavelength measurements of upwelling radiance contain information about the total aerosol optical depth of the atmosphere. This total optical depth is determined by the scattering characteristics of the aerosol distribution. As size distribution and composition of particles vary within the atmosphere, scattering efficiency, and thus total optical depth changes.

Changes occur not only at a single wavelength, but the wavelength dependence on scattering is also altered when size distribution and composition vary. A change in particle size from small to large will shift the spectral scattering dominance toward longer wavelengths. Therefore, if scattering is measured at multiple wavelengths, information about particle size is included in the upwelling radiance.

Previous studies have shown that single-wavelength radiance measurements are related to aerosol optical depth (Griggs ,1975; Hindman, et al., 1984; and Durkee, et al., 1986). This paper discusses the potential for deriving aerosol-type information from dual-wavelength radiance measurements. Both modeled and observed aerosol distributions will be examined. The aerosol models focus on the expected variations due to changes in particle type, changes in relative humidity, and changes in particle-production thru wind speed variation. Observed variations in aerosol distributions are presented from simultaneous aircraft-measured particle characteristics and satellite-detected upwelling radiance.

2. WAVELENGTH-RATIOS

The upwelling radiance measured at the satellite is determined by the scattering characteristics of the atmosphere. These include scattering by molecules and particles. The scattering ability of the atmosphere is described by the scattering optical depth, and may be written as the sum of the molecular and aerosol optical depths. In this paper, scattering effects of molecules have been calculated separately and subtracted from the total radiance.

Following the development of Durkee (1984), a ratio can be formed with the single scattering solution for satellite-detected upwelling radiance, L, applied at two wavelengths:

$$\frac{(L/F_0)_{\lambda_1}}{(L/F_0)_{\lambda_2}} \approx \frac{(\omega_0 P(\theta)\tau_A)_{\lambda_1}}{(\omega_0 p(\theta)\tau_A)_{\lambda_2}} \qquad (1)$$

where F_0 is the incident solar irradiance, μ is the cosine of the satellite zenith angle, w_0 is the single scattering albedo, $p(\theta)$ represents the single scattering phase function, and τ_A represents the aerosol optical depth. According to (1) the wavelength-ratio of satellite-dependent terms will have high values when the aerosol-dependent terms exhibit large variation with wavelength.

The wavelength variation of the right side of (1), the aerosol-dependent terms, is dominated by the variation of τ_A. Variation of τ_A results from changes in the particle size distribution. A size distribution with more large particles will scatter better at longer wavelengths. That is, broad size distributions will exhibit less scattering variation with wavelength and narrow distributions will produce greater wavelength-variation of scattering.

Particle composition determines the amount of absorption and therefore the value of w_0 for the distribution. This aerosol-dependent term varies much more slowly with wavelength variation than τ_A.

Particle size distribution primarily, and particle composition secondarily determine the value of $p(\theta)$. At single

scattering angles typical of sun-earth-satellite geometries, $p(\theta)$ decreases with increasing wavelength. This is due to the increase in forward scattering (and decrease in backward scattering) as wavelength increases with respect to particle size. Although the variation of this parameter with wavelength is in the opposite sense of τ_A variations, its magnitude is small. Therefore, the total value of the ratio (1) will be greater than one.

3. MODEL AEROSOL DISTRIBUTIONS

3.1 Rural vs Marine Distributions

Figure 1 shows the size distributions for the Shettle and Fenn (1979) marine and rural aerosol models. The rural model has many more small particles than does the marine model. This difference produces a significantly different spectral variation of the scattering properties of the two models. Table 1 lists the values of τ_A (using a 1 km thick layer), w_o, and $p(\theta)$ from Shettle and Fenn (1979) models of marine and rural aerosols. The parameters are given at a red-visible (0.6328 microns) and near-infrared (0.86 microns) wavelength. Also provided in Table 1 are the wavelength-ratios (red/near-IR) of τ_A, w_o, $p(\theta)$, and the total for the aerosol-dependent terms. The largest individual ratio is for τ_A, due to the difference in size distributions. The total wavelength-ratio of the aerosol-dependent terms is almost 50% greater for rural aerosols than for marine aerosols. These values show that rural particle distributions should produce greater values of the satellite-dependent ratio according to (1).

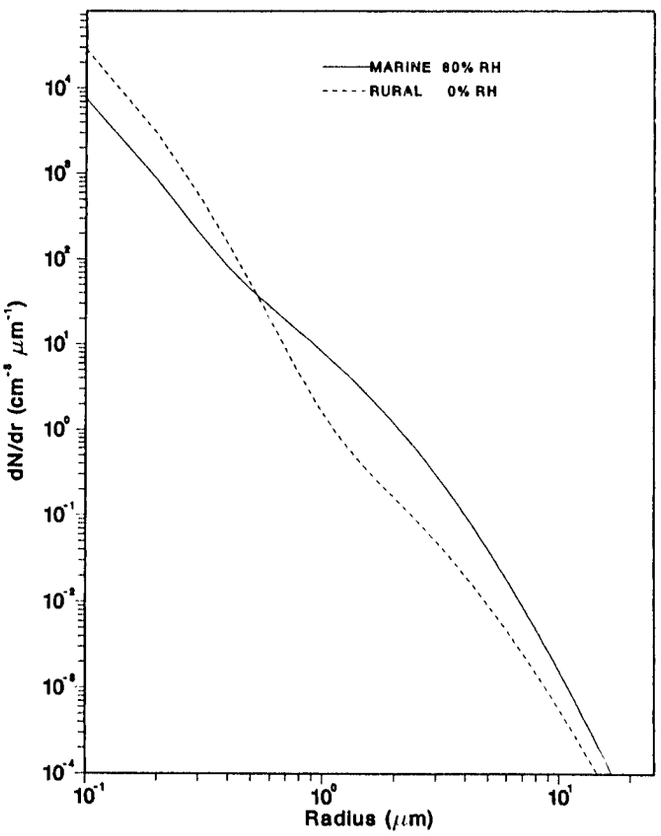

Figure 1. Size distributions from Shettle and Fenn (1979) marine and rural aerosol models.

3.2 Wind Speed Variations

The particle size distribution is shaped by the generation and removal mechanisms acting on it. Breaking waves on a wind-roughened sea is an important production mechanism for marine particles. This mechanism increases primarily the numbers of large particles (radius > 0.5 microns). The slope of the marine distribution is, therefore altered by variations in wind speed.

To test the effect of this variation on the wavelength-ratios in (1), the marine distribution (80% RH) of Shettle and Fenn (1979) was altered for wind speed change according to Lovett (1978). The resulting size distributions are shown in Figure 2. Notice the decrease in negative slope with increasing wind speed. The wavelength-ratio changes from 1.062 for no wind speed variation to 1.014 and 0.988 for a 5 and 10 m/s wind speed increase. This variation is considerably smaller than the variations due to particle types outlined in Table 1.

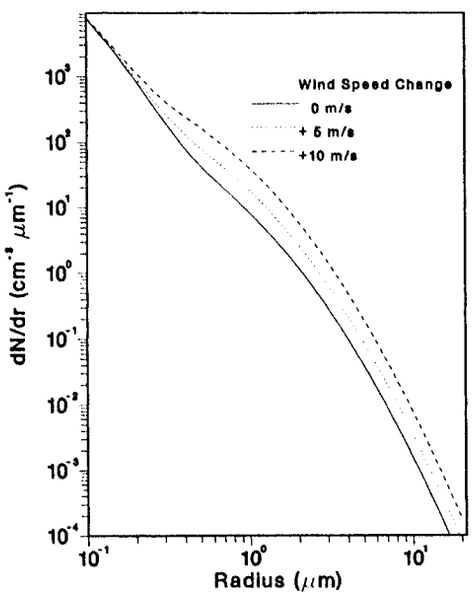

Figure 2. Size distributions resulting from changes in wind speed. The marine aerosol model from Shettle and Fenn (1979) is the base distribution and is altered according to Lovett (1978).

Table 1. Aerosol-dependent parameters for marine and rural models from Shettle and Fenn (1979) at 0.6328 and 0.8600 microns wavelength. Wavelength-ratios (red-visible/near-infrared) of the parameters are also given.

	Marine @ 80% RH		Rural @ 0% RH	
Wavelength	0.6328	0.8600	0.6328	0.8600
τ_A	0.2142	0.1998	0.1329	0.0854
w_o	0.9940	0.9930	0.9415	0.9003
$p(\theta=120°)$	0.0890	0.0900	0.1849	0.1998
τ_A-ratio	1.072		1.556	
w_o-ratio	1.001		1.046	
$p(\theta)$-ratio	0.989		0.925	
Total ratio	1.062		1.506	

3.3 Relative Humidity Variations

Another way to vary the shape and composition of the size distribution is by varying relative humidity. Figure 3 shows marine size distributions at 70, 80, and 99% RH. Again, the shape of the distributions change. Table 2 lists the wavelength-ratios for relative humidities of 70, 80, and 99%. The wavelength-ratios decrease with increasing relative humidity. Note that all of the values are considerably smaller than the wavelength-ratio for the rural case described above.

4. OBSERVED AEROSOL DISTRIBUTIONS

To investigate the relationship between wavelength-ratios of satellite-dependent terms and aerosol-dependent terms, a set of near-simultaneous aircraft and satellite measurements have been analyzed. The data were collected off the coast of southern California during the period 20 September thru 6 October 1982.

The aircraft measured aerosol particle size distributions, collected particles for composition analysis, and measured state variables such as temperature and relative humidity. These sets of measurements are more fully described in Durkee, et al. (1986).

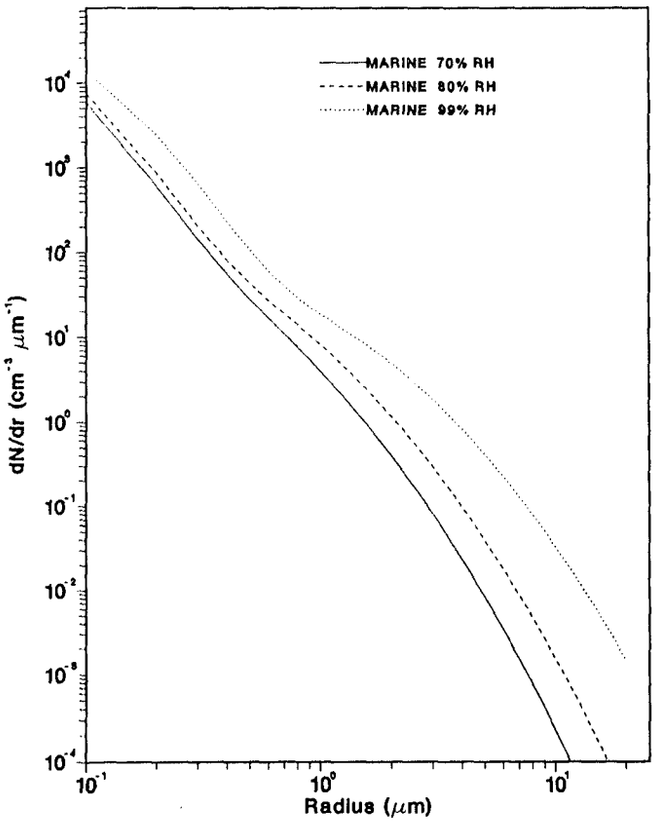

Figure 3. Size distributions resulting from changes in relative humidity.

Table 2. Aerosol-dependent parameters for marine models (70, 80, and 99% RH) from Shettle and Fenn (1979) at 0.6328 and 0.8600 microns wavelength. Wavelength-ratios (red-visible/near-infrared) of the parameters are also given.

	70% RH		80% RH		90% RH	
Wavelength	0.6328	0.8600	0.6328	0.8600	0.6328	0.8600
τ_A	0.1063	0.0909	0.2142	0.1998	0.9977	0.9732
w_o	0.9877	0.9846	0.9940	0.9930	0.9986	0.9985
$p(\theta=120°)$	0.1149	0.1059	0.0891	0.0900	0.0535	0.0668
τ_A-ratio	1.170		1.072		1.025	
w_o-ratio	1.003		1.001		1.000	
$p(\theta)$-ratio	1.086		0.989		0.801	
Total ratio	1.275		1.062		0.821	

Particle size distribution measurements were made with an ASSP (Axially Scattering Spectrometer Probe). The probe measured particle sizes and numbers during vertical spirals from 100 to about 1500 meters above the ocean surface. Aerosol optical depth was calculated from the particle measurements and at the satellite sensor's mean wavelength weighted by its spectral response function. Within the boundary layer, the index of refraction was assumed to follow the Shettle and Fenn (1979) marine model. Above the boundary layer, particles were assumed to behave as a mixture of marine, and rural types. The mixture of the particle types was derived from the analysis of Hindman, et al. (1985). A mixture of 30% marine and 70% rural optical properties from Shettle and Fenn (1979) best approximated the measured particle properties.

Satellite data from two systems were used in this study. The NOAA-7 AVHRR (Advanced Very High Resolution Radiometer) and the NIMBUS-7 CZCS (Coastal Zone Color Scanner) measured upwelling radiances at red-visible and near-infrared wavelengths. Table 3 lists the spectral bands of the AVHRR and CZCS instruments.

A distinct change in the vertical distribution of aerosols occurred during the experiment. During the first half of the experiment, the extinction values above the marine boundary layer were 10 times higher than during the second half of the experiment. These high extinction values resulted from particles of radius less than 1 micron. Sub-micron sized particles were found in numbers two orders of magnitude higher before 26 September than after. Also, the relative humidity above the boundary layer was typically less than 30%. Therefore, the relatively high upper-level extinction during the first half of the experiment (prior to 26 September) was due to higher total numbers of small particles ($r < 1$ micron) and not due to particle size increase with relative humidity.

A Precipitating cold front passed through the area on 26 September. The post-frontal air mass contained very few particles and accounts for the absence of upper-level particles after the middle of the experiment.

Figure 4 is a time series of the wavelength-ratios from the satellite-dependent and aerosol-dependent terms during the 2-week period of the experiment. The open squares and circles represent the AVHRR and CZCS satellite-dependent ratios. The solid triangles represent the aerosol-dependent ratios calculated from the aircraft measurements. Both the aerosol- and satellite-dependent ratios show a decrease after the exchange of air masses resulting from the frontal passage on 26 September. This confirms the variation expected from the discussion in section 3.1.

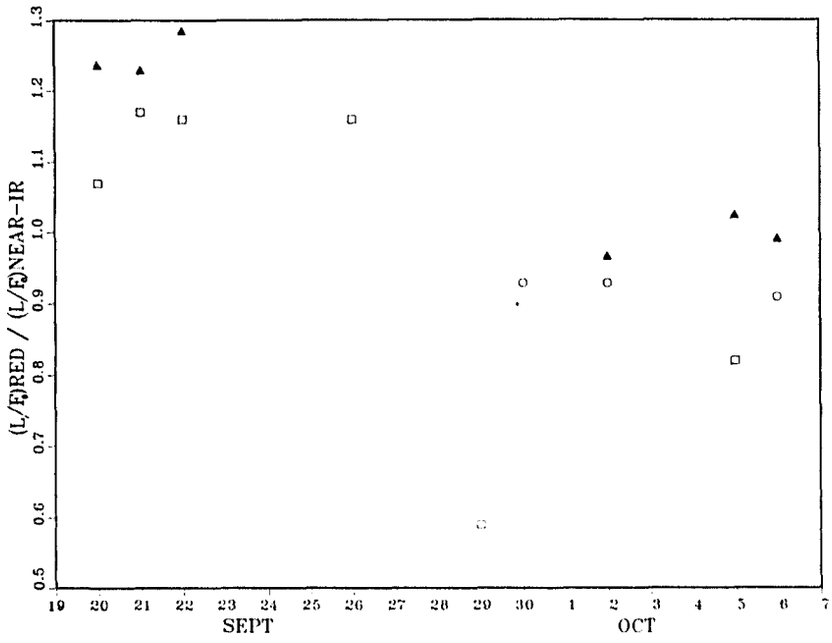

Figure 4. Time series of the wavelength-ratios from the satellite-dependent and aerosol-dependent terms during the 2-week period of the experiment. The open squares and circles represent the AVHRR and CZCS satellite-dependent ratios respectively. The solid triangles represent the aerosol-dependent ratios calculated from the aircraft measurements.

Table 3. Spectral intervals of the CZCS and AVHRR red-visible and near-infrared channels.

CZCS	
Channel 4	0.66-0.68 micrometers (red-visible)
Channel 5	0.70-0.80 micrometers (near-infrared)
AVHRR	
Channel 1	0.58-0.68 micrometers (red-visible)
Channel 2	0.72-1.10 micrometers (near-infrared)

5. CONCLUSIONS

This study has shown that typical variations of aerosol particle size distributions result in significant variations in spectral scattering characteristics. For rural-to-marine variations the wavelength variation is significant in the red-visible to near-infrared wavelength region. Wind-speed and relative humidity variations result in smaller wavelength variations than aerosol-type variations.

A set of observations showing dramatically changing particle distributions have been analyzed. As the size distributions changed from rural to mostly marine in shape, the satellite-dependent and aerosol-dependent wavelength-ratios decreased as predicted by the analysis of the model distributions.

Future efforts will document these effects around other frontal passages thru southern California. Some of these cases will be ready for presentation at this conference. These techniques are potentially useful wherever distinct changes in the shape of particle size distributions occur. Studies of these other regimes are also in progress.

6. ACKNOWLEDGEMENTS

Much of this work was done while the author was at Colorado State University and in collaboration with the Naval Ocean Systems Center. Drs. E. E. Hindman, D. R. Jensen and T. H. Vonder Haar are thanked for their contributions to this work. The study was sponsored in part by ONR Contract No. N00014-79-C-0793 and NOSC Contract No. N66001-84-C-0186 administered through the Research Institute of Colorado, Ft. Collins, CO. Support was also received from the Naval Postgraduate School Foundation Research Program.

7. REFERENCES

Durkee, P. A., 1984: The relationship between marine aerosol particles and satellite-detected radiance. Ph.D. Dissertation, and Atmospheric Sciences Paper No. 380, Colorado State University, Fort Collins, CO, 80523.

Durkee, P. A., 1986: The relationship between marine aerosol particles and satellite-detected radiance. J. Geophys. Res., in press.

Hindman, E. E., P. A. Durkee, W. Kuenning, 1985: Physical, chemical and optical properties of aerosol particles detected in satellite images. submitted to J. Rech. Atmos.

Hindman, E. E., P. A. Durkee, P. C. Sinclair and T. H. Vonder Haar, 1984: Detection of marine aerosol particles in coastal zones using satellite imagery. Intl. J. Remote Sensing, 5, 577-586.

Griggs, M., 1975: Measurement of atmospheric aerosol optical thickness over water using ERTS-1 Data. J. Air Pollut. Control Assoc., 25, 622-626.

Griggs, M., 1983: Satellite measurements of tropospheric aerosols. Adv. Space Res., 2, 109-118.

Lovett, R. F., 1978: Quantitative measurement of airborne sea-salt in the North Atlantic. Tellus, 30, 358-364.

Shettle, E. P., and R. W. Fenn, 1979: Models for the aerosols of the lower atmosphere and the effects of humidity variations on their optical properties. AFGL-TR-79-0214 Air Force Geophysics Laboratories, Hanscom AFB, MA.

A GLOBAL-SCALE MODEL OF AEROSOL BACKSCATTER AT CO_2 WAVELENGTHS FOR SATELLITE-BASED LIDAR SENSORS

David A. Bowdle

Universities Space Research Association
Atmospheric Sciences Division
NASA Marshall Space Flight Center
Huntsville, Alabama

1. INTRODUCTION

This paper describes the status of a global-scale model of background aerosol backscatter cross-sections at CO_2 wavelengths. The modelling work is being performed in support of feasibility studies for NASA's prospective satellite Doppler Lidar Atmospheric Wind Sounder (LAWS), which is intended to provide global-scale wind profiles in the troposphere and lower stratosphere (e.g., Huffaker et al, 1984).

The current goal of the model development effort is to describe typical backscatter cross-sections for "clean" background conditions in remote areas and in the middle and upper troposphere, where new global-scale wind measurements are especially important. Future versions of the model will also describe the spatial/temporal distribution of background conditions. The entire model development effort is designed to provide critical inputs to the LAWS design as early as possible.

The model emphasizes aerosol backscatter properties at CO_2 wavelengths, especially 9.11 micrometers, which is currently the most promising design wavelength for LAWS. However, the basic modeling approach described below may be used to derive background aerosol optical properties at other wavelengths of interest in the CO_2 wavelength band or from the ultraviolet to the middle infrared. The results of this kind of model can also be applied to design studies for any ground-based, airborne or spaceborne lidar system which uses atmospheric aerosols as a backscatter target for the measurement of some other primary atmospheric quantity, such as trace species concentrations with DIfferential Absorption Lidar (DIAL).

2. MODEL

2.1 Model Needs

For lidar systems such as LAWS and DIAL, the accuracy of the retrieved primary variable deteriorates sharply as the return signal strength approaches a system-specific threshold. For signals well below threshold, the retrieval is dominated by system noise. For signals well above threshold, the retrieval is typically dominated by other parameters, such as wind sampling statistics in the case of LAWS (Huffaker et al, 1984).

When the threshold backscatter for a given lidar system is comparable to atmospheric background backscatter levels, the performance capability of the system is obviously in question. Since this condition appears to hold for LAWS (Huffaker et al, 1984), realistic LAWS design studies will require accurate characterization of the spatial, temporal, and possibly spectral distribution of global aerosol background backscatter values.

Information is also needed on the frequency of occurrence and the general spatial/temporal distribution of targets with high backscatter values. For example, high backscatter is expected to prevail in the planetary boundary layer, continental plumes, water clouds, and volcanic debris clouds. However, as the discussion above indicates, the enhanced backscatter from these targets is not expected to significantly improve wind retrieval accuracy. Thus, details of backscatter distributions within these targets, and details of the aerosol physiochemical factors which determine the spatial, temporal, and spectral variability of backscatter values for these targets, are neglected in this model.

This approach is valid for longer wavelengths, including CO_2 wavelengths, outside of dense water clouds. For shorter wavelengths, where aerosol scattering and absorption losses may be significant even in moderate haze layers (e.g., Prospero et al, 1983), these details need to be considered.

2.2 Model Strategy

The research methods required to characterize global-scale backscatter values in background conditions differ radically from methods which are adequate for characterizing high aerosol loading, such as in conventional studies of aerosol effects on climate, passive remote sensing, and air pollution. Four key elements are involved in this novel model development strategy.

First, background aerosol features and parameters are sought which have a small variance on global spatial and temporal scales, on the basis of both empirical evidence and theoretical considerations. These quantities can then be extrapolated beyond the limited spatial/temporal domains of the field programs in which they are identified. By contrast, conventional methods generally assume, usually implicitly but occasionally explicitly, that no such features exist.

Second, aerosol data bases which have global-scale spatial or temporal coverage are sought to quantify the background aerosol conditions. Special precautions are often necessary to extract the background signature. By contrast, conventional methods often extrapolate to the global-scale from small data sets, with very limited spatial and temporal coverage. Conventional anaytical methods also utilize statistical methods (such as indiscriminate linear averaging) which are heavily biased against background aerosol populations.

Third, suitable aerosol covariates (tracers, or surrogates) are sought which are already observable on a truly global scale. Data sets are sought to establish the degree of correlation between aerosols and their covariate(s), and also to determine the spatial/temporal distribution of the covariate(s).

Fourth, the model concept is being used to develop a sound scientific basis for advanced backscatter research to fill in key gaps in the data base for the comprehensive global background model. In particular, preliminary model predictions are used to design an appropriate data base for verification of the background aerosol concept. The

resulting data base requirements are then used to design a complete measurement program, including specification of sensor capabilities and sampling requirements.

The model framework described below concentrates on the first three elements of this model development strategy.

2.3 Model Concept

This study assumes the existence of a universal global background tropospheric airmass, with very low concentrations of aerosols and water vapor. Similar background conditions were postulated by Junge (1963) and studied by numerous workers (e.g., Charlson et al, 1974). The background aerosol population is assumed to consist of two primary species: a sub-micrometer sulfate component, with relatively uniform concentrations, and a somewhat more variable micrometer-sized crustal component (Parrington and Zoller, 1984). The molecular form of the sulfate and crustal components and the degree of internal mixing between these components are free parameters unless the data indicate otherwise.

In this model, background conditions are assumed to be produced by nearly complete removal of moisture and aerosols from rising airmasses in large-scale storm systems. Airmasses that have been scrubbed in this manner retain their pristine condition in the middle and upper troposphere until they accumulate new aerosols by sedimentation from overlying aerosol layers (e.g., dust plumes) or by direct mixing with aerosol-laden air (e.g., from the convective boundary layer). The dry removal times for micrometer-sized and smaller particles added by either of these processes are typically longer than airmass residence times, even at high altitudes in the troposphere (Prospero et al, 1983). Thus, a background air parcel which becomes "contaminated" in this way loses its background classification until it is once more scrubbed by precipitation or diluted by other background parcels.

As the above discussion shows, this airmass approach essentially involves a Lagrangian (parcel following) analytical frame of reference. As Sections 2.4 and 2.5 show, the Lagrangian reference frame is much more powerful for this model application, and also much less susceptible to sampling biases, than the more conventional Eulerian reference frame, where air parcels are classified on the basis of their current position.

2.4 Model Parameters

In the Lagrangian reference frame, typical values of background aerosol backscatter cross-sections at a given altitude are assumed, to first order, to be invariant in space and time, and to be statistically distinct from backscatter populations which are derived from major aerosol sources. Implementation of this assumption reduces the variance in tropospheric backscatter for the model data base from six or more orders of magnitude to slightly over one order. It allows background aerosol measurements at any location on the globe to be incorporated into the model data base. It also excludes from the data base occasional episodes of high aerosol loading at sites which are otherwise characterized by background aerosol populations.

Furthermore, typical values of the background backscatter mixing ratio (defined here as the backscatter cross-section at a given altitude normalized by the atmospheric density at that altitude) are assumed to be invariant (again to first order) throughout the depth of the troposphere. The second assumption removes a systematic bias of about a factor of three or four between the surface and the tropopause. It allows background aerosol measurements at any altitude in the troposphere to be incorporated into the model data base. And once again, it excludes from the data base episodes of high aerosol loading at altitudes which are generally characterized by background conditions.

2.5 Model Capabilities

The Lagrangian model reference frame therefore provides a sound theoretical basis for ongoing backscatter research in support of LAWS. It provides an objective basis for screening existing aerosol data sets and for analyzing suitable data with standard statistical methods. It provides a means of optimizing new backscatter measurement programs and objectively analyzing the resulting data. It also provides a rationale for extrapolating to a true global scale from aerosol data sets which were obtained at diverse times and locations on smaller spatial and temporal scales.

The model reference frame also provides a means for improved understanding of the global-scale life-cycles of atmospheric aerosols. In this reference frame, departures from a well-mixed background airmass should be interpretable in simple physical terms, such as enhanced mixing, increased aerosol emissions, and modified removal mechanisms.

3. DATA BASE

3.1 Data Selection

The aerosol data base for the background model includes carefully-selected measurements from a wide variety of sensors and sensor platforms. Included are measurements of aerosol backscatter at CO_2 wavelengths, with ground-based pulsed and airborne continuous wave (cw) Doppler lidars; aerosol optical properties at shorter wavelengths; aerosol concentrations and size distributions, with optical particle counters; and aerosol composition, from high volume filter samplers.

First preference is given to aerosol data sets with one or more of the following characteristics: a) data obtained with several different kinds of aerosol sensors; b) data which span a wide range of wavelengths or particle sizes; c) data which represent global scale spatial or temporal coverage; or d) data which involve minimal spatial and temporal averaging during data collection, processing, and analysis. Where aerosol data with high spatial or temporal resolution are considered essential, preference is given to data sets with readily accessible raw data. These selection criteria are relaxed for direct backscatter measurements at CO_2 wavelengths, since data of this kind are relatively rare.

3.2 CO_2 Backscatter Measurements

The major pulsed lidar data are obtained from the complete three-year archive for NOAA's Wave Propagation Laboratory (WPL) at Boulder, Colorado (Post, 1984). Also included are the complete one-year archive from NASA's Marshall Space Flight Center (MSFC) at Huntsville, Alabama (Rothermel and Jones, 1985), and published data summaries from NASA's Jet Propulsion Laboratory (JPL) at Pasadena, California (Menzies et al, 1984).

The major cw lidar data are obtained from the entire three-year archive for the Royal Signals and Radar Establishment (RSRE) lidar over the United Kingdom, Gibraltar, the eastern and northern Atlantic Ocean, and Boulder, Colorado (Foord et al, 1983). Also included are data sets from the MSFC cw lidar over much of the continental United States (Jones et al, 1984).

3.3 Aerosol Optical Measurements

Direct measurements of aerosol scattering extinction at 0.45, 0.55, 0.70, and 0.85 micrometers are obtained from NOAA's multiwavelength integrating nephelometer at the Geophysical Monitoring for Climatic Change (GMCC) station on Mauna Loa Observatory (MLO), Hawaii (Bodhaine, 1983). The GMCC archive includes over eleven years of nephelometer data. A wide variety of

supporting information is also available for this site (Bodhaine, 1983), including other aerosol, air chemistry, and meteorological parameters.

Global measurements of total aerosol extinction at 1.0 micrometer are obtained from NASA's Stratospheric Aerosol and Gas Experiment (SAGE I) and Stratospheric Aerosol Measurement (SAM II) satellites (Kent and McCormick, 1984). These data are obtained by the limb occultation technique. The SAM II sensor has been operational since 1978; the SAGE I sensor was operational from 1979 to 1981.

Backscatter values at CO_2 wavelengths are determined from direct measurements of these aerosol optical properties using conversion factors from the literature (e.g., Kent et al, 1983).

3.4 Aerosol Microphysical Measurements

Measurements of aerosol size distributions are obtained from the Global Atmospheric Measurement Experiment for Tropospheric Aerosols and Gases (GAMETAG) over the central and southern Pacific Ocean (Patterson et al, 1980). These measurements were obtained in summer 1977 and spring 1978. Backscatter values at CO_2 wavelengths, as well as aerosol optical properties at other wavelengths, are determined for background GAMETAG data using standard Mie scattering computations (Patterson, private communication).

Measurements of sulfate aerosol in the upper troposphere and lower stratosphere are obtained from NASA's Global Air Sampling Program (GASP) (Papathakos and Briehl, 1981). Measurements of background dust concentrations over the central Pacific Ocean are obtained from the Sea Air Exchange (SEAREX) surface stations (Uematsu et al, 1983). In addition, measurements of sulfate and crustal aerosol are obtained from the MLO surface station (Parrington and Zoller, 1984).

3.5 Water Vapor Measurements

Where possible, airborne measurements of aerosol parameters are compared with simultaneous measurements of atmospheric water vapor concentrations from standard dew point monitors. If this kind of moisture data is not available, comparisons are made with nearby rawinsonde soundings.

3.6 Data Analysis

Each datum entry in a given aerosol data set is expressed in mixing ratio form. Typical (geometric mean) background values of the mixing ratio parameter are then determined for that data set, either by a priori stratification when supplementary information is available, or by a posteriori statistical decomposition otherwise.

Statistical analysis of multiple vertical profiles for a given type of aerosol measurement initially employs stratification by altitude. Advanced analysis involves compositing all of the profile data, in mixing ratio terms, into one comprehensive data set. Statistical analysis is then performed on this composite data in the same manner as for other data subsets.

Several types of data display techniques are used in this phase of the analysis to increase the detectability of the background aerosol population under visual examination. These techniques include standard time-height cross-sections, stacked histogram cross-sections, and diurnal vs seasonal or seasonal vs annual cross-sections, depending on the spatial and temporal coverage of the data. The results of the visual examinations are then used to initialize the statistical analyses.

Model data which do not involve direct backscatter measurements at CO_2 wavelengths are converted to CO_2 backscatter using the methods described in Sections 3.3-3.5 . A composite background CO_2 backscatter population is then developed from all of the data sets in the model data base. The composite results are extended over the entire globe using the "universal global background" assumption, and over the entire troposphere using the "well-mixed" assumption. Uncertainty limits are indicated for the composite, including the effects of real spatial and temporal variations and uncertain conversion factors. This analysis terminates the first phase of the global backscatter modeling effort.

4. RESULTS

4.1 Backscatter Estimates

Preliminary surveys have already been made on most of the aerosol data base for the global backscatter model. Detailed analysis has been performed on several segments of the data. Preliminary findings are summarized below.

The key finding of this study thus far has been the identification of strong evidence for a universal global background aerosol population. Current results indicate background backscatter values ranging from about 2×10^{-11} to 2×10^{-10} m^{-1} sr^{-1} at CO_2 wavelengths, regardless of location, altitude, season, year, global volcanic activity, and method of measurement.

Typical (geometric mean) background values cover a somewhat narrower range. Tentative values range from about 3×10^{-11} to 8×10^{-11} m^{-1} sr^{-1}. Typical values decrease slightly with altitude, consistent with the "well-mixed background" hypothesis. Typical values generally differ by less than a factor of two or three from one data set to another.

However, the uniformity of these background estimates does depend critically on the statistical methods which are used to extract the estimates. Backscatter estimates from conventional methods, which tend to indiscriminately determine arithmetic means, geometric means, or medians for an entire data set, are typically higher than those determined here by factors of two to ten or more. These discrepancies result from the susceptibility of the conventional methods to biases in sampling, data acquisition, and data processing.

Background optical properties for atmospheric aerosols at shorter wavelengths are somewhat more uniform than at CO_2 wavelengths. Apparently, optical properties at the shorter wavelengths are less sensitive to variations in trace quantities of micrometer-sized dust in the aerosol population.

4.2 Data Gaps

Several significant uncertainties remain in this phase of the modelling effort. For example, the general validity of the "well-mixed background" hypothesis needs to be rigorously validated with objective statistical tests. The estimates of typical background backscatter values need to be improved. The causes of small variations in typical backscatter values need to be investigated. The degree of correlation between aerosol content and moisture content needs to be established. The spectral dependence of background backscatter values at CO_2 wavelengths needs to be determined. Finally, the molecular composition and morphology of background aerosol populations need to be established.

Many of these uncertainties can be evaluated with more detailed analysis of the current model data base. The necessary analysis is underway, and the results of the updated version of the model will be presented.

More important, additional information is needed on the frequency of occurrence of background conditions, and on the spatial and temporal variability of the frequency of occurrence. Other types of aerosol or aerosol surrogate data, with true global-scale coverage, will be required to

provide this information. This type of study is beyond the scope of the initial phase of the modeling effort.

5. CONCLUSIONS

Strong evidence has been found for a "universal" global background tropospheric aerosol population. Typical background backscatter values at CO_2 wavelengths appear to be about 3×10^{-11} to 8×10^{-11} m^{-1} sr^{-1}. Background signatures are evident in most aerosol data sets which have global-scale coverage in space or time. However, in several data sets, particularly those with biased sample populations, special precautions are necessary to extract representative background aerosol parameters.

The model results will have important implications for the design of the LAWS system, or any other lidar system that uses atmospheric aerosols only as a backscatter target for the measurement of some other atmospheric quantity. The results can also be used as a baseline for studies of changes in natural or anthropogenic aerosol emissions.

6. ACKNOWLEDGEMENTS

This study was carried out by Universities Space Research Association for the National Aeronautics and Space Administration, Marshall Space Flight Center, under Contract NAS8-35919. Support under this contract is gratefully acknowledged.

Several individuals and research groups -- M. J. Post (NOAA WPL), J. Rothermel (USRA), J. M. Vaughan (RSRE-UK), B. Jones (NASA MSFC), B. Bodhaine (NOAA GMCC), G. Kent (IFAORS), and E. Patterson (Ga. Tech) -- generously provided copies of their aerosol archives for this modeling study. Their cooperation is also gratefully acknowledged.

7. REFERENCES

Bodhaine, B. A., 1983: Aerosol measurements at four background sites. J. Geophys. Res., 88, 10,753-10,768.

Charlson, R. J., W. M. Porch, A. P. Waggoner, and N. C. Ahlquist, 1974: Background aerosol light scattering characteristics: nephelometric observations of Mauna Loa Observatory compared with results at other locations. Tellus, 26, 346-360.

Foord, R., R. Jones, J. M. Vaughan, and D. V. Willets, 1983: Precise comparison of experimental and theoretical SNRs in CO_2 laser heterodyne systems. Appl. Opt., 22, 3787-3795.

Huffaker, R. M., T. R. Lawrence, M. J. Post, J. T. Priestly, F. F. Hall, Jr., R. A. Richter, and R. J. Keeler, 1984: Feasibility studies for a global wind measuring satellite system (WINDSAT): analysis of simulated performance. Appl. Opt., 23, 2523-2536.

Jones, W. D., L. Z. Kennedy, J. W. Bilbro, and H. B. Jeffrys, 1984: Coherent focal volume mapping of a cw CO_2 Doppler lidar. Appl. Opt., 23, 730-733.

Junge, C., 1963: Large scale distribution of condensation nuclei in the troposphere. J. Rech. Atm., 1, 185-190.

Kent, G. S., and M. P. McCormick, 1984: SAGE and SAM II measurements of global stratospheric aerosol depth and mass loading. J. Geophys. Res., 89, 5303-5314.

_____, G. K. Yue, U. O. Farrukh, and A. Deepak, 1983: Modeling atmospheric aerosol backscatter at CO_2 laser wavelengths. 1: aerosol properties, modeling techniques, and associated problems. Appl. Opt., 22, 1655-1665.

Menzies, R. T., M. J. Kavaya, P. H. Flamant, and D. A. Haner, 1984: Atmospheric aerosol backscatter measurements using a tuneable coherent CO_2 lidar. Appl. Opt., 23, 2510-2517.

Papathakos, L. C., and D. Briehl, 1981: NASA Global Atmospheric Sampling Program (GASP) data report for Tape VL0015, VL0016, VL0017, VL0018, VL0019, and VL0020. NASA Tech. Mem. 81661, 69-82.

Parrington, J. R., and W. H. Zoller, 1984: Diurnal and longer-term temporal changes in the composition of atmospheric particles at Mauna Loa, Hawaii. J. Geophys. Res., 89, 2522-2534.

Patterson, E. M., C. S. Kiang, A. C. Delaney, A. F. Wartburg, A. C. D. Leslie, and B. J. Huebert, 1980: Global measurements of aerosols in remote continental and marine regions: concentrations, size distributions, and optical properties. J. Geophys. Res., 85, 7361-7376.

Post, M. J., 1984: Aerosol backscattering profiles at CO_2 wavelengths: the NOAA data base. Appl. Opt., 23, 2507-2509.

Prospero, J. M., R. J. Charlson, V. Mohnen, R. Jaenicke, A. C. Delaney, J. Moyers, W. Zoller, and K. Rahn, 1983: The atmospheric aerosol system: an overview. Rev. Geophys. Space Phys., 21, 1607-1629.

Rothermel, J., and W. D. Jones, 1985: Ground-based measurements of atmospheric backscatter and absorption using coherent CO_2 lidar. Appl. Opt., 24, 3487-3496.

Uematsu, M., R. A. Duce, J. M. Prospero, L. Chen, J. T. Merrill, and R. L. McDonald, 1983: Transport of mineral aerosol from Asia over the North Pacific Ocean. J. Geophys. Res., 88, 5343-5352.

5.8

THE EFFECT OF LOCAL ADVECTION ON THE INFERENCE OF SOIL MOISTURE FROM THERMAL INFRARED RADIANCES

Peter J. Wetzel

Goddard Laboratory for Atmospheres
NASA/Goddard Space Flight Center, Greenbelt, MD 20771

and

Robert H. Woodward

General Software Corporation
Landover, MD 20785

1. INTRODUCTION

In a variety of scientific disciplines accurate areal soil moisture information is required in order to answer current research questions. Many of these questions relate to the energy and water balances of snow-free land surfaces. The basic link between the hydrological cycle and the surface energy budget of land surfaces is the moisture content of the soil. As such, its measurement is important to the study and understanding of many biogeophysical processes taking place on the earth's land surfaces. As man accelerates his uncontrolled modification of surface properties, concern has increased about the feedbacks that these modifications may have, both short and long term, on weather, climate, water supplies, crop production, biochemical cycles, and the ecological balance of the biosphere. In this context, even broad area-averaged soil moisture information could have a large impact on many current research problems.

It is the purpose of this paper to explore, for one five-day case study period, the degree to which the GOES-VISSR infrared data can be used to infer area-averaged soil moisture. In an analysis presented by Wetzel et al. (1984; hereafter WAW), an extensive set of model runs was used to identify the variables which are significant to the soil moisture estimation problem. In this study the chosen variables are transformed so they may be incorporated into a multiple linear regression. Then the actual observations, rather than a simplified model, are used to determine the relationship between soil moisture and GOES-IR radiance.

2. BACKGROUND

Some of the results of the modelling work reported in WAW form the basis for the present study. They presented a series of sensitivity tests which led to the identification, from among a number of GOES-observable signatures in the surface temperature wave, of the mid-morning temperature change. The tests further showed that the effects of wind speed and vegetation cover on the chosen parameter are large enough that they must be measured, and a correction for their effects must be included. The salient conclusion to be drawn from the sensitivity tests is that, in the absence of factors such as cloud cover, temperature advection, and large variations in soil properties across a case study site, the mid-morning change in skin temperature, ΔT, is primarily dependent only on variations in soil moisture, vegetation, and wind speed. Based on a limited set of model runs, WAW concluded that low level temperature advection could be neglected in some cases, however advection has been included in this study.

WAW found that linear regression provided an excellent fit to the data when the natural logarithm of the surface geostrophic wind ($\ln V_g$) and the square of the soil moisture deficit,

$$m = (1-W/W_{fc})^2 \qquad (1)$$

were used as the independent variables. The soil moisture variables W and W_{fc} are the actual and field capacity values of bulk available root zone soil water content, assuming W=0 at the wilting point. The functional form of m indicates that the morning temperature change is most sensitive to changes in soil moisture when the soil is relatively dry.

Based on the results presented above, we seek a statistical algorithm for estimating soil moisture using linear regression between the variables ΔT, m, $\ln V_g$ and some measure of vegetation.

3. DATA REQUIREMENTS AND SOURCES

The study area incorporates the eastern two thirds of the state of Kansas and an adjacent section of Nebraska (Fig. 1). The area has a rather uniform flat surface which slopes gently downward from west to east. In conjunction with an east-west gradient of mean annual precipitation, there is a general increase in vegetation density (Fig. 1, see below for further discussion) as one moves form west to east. The exception to the overall longitudinal uniformity of the study area is a region of irrigated cropland along the Platte river in southern Nebraska

The period chosen for study is 24-29 July, 1978. During these six days, skies over the study area were mostly clear, and no precipitation was observed. However, on 22 and 23 July, a significant rainstorm had deposited as much a 138 mm of precipitation over northern Kansas and southeastern Nebraska. At the same time, southern Kansas received little or no precipitation, so a strong gradient of soil moisture existed across the study site.

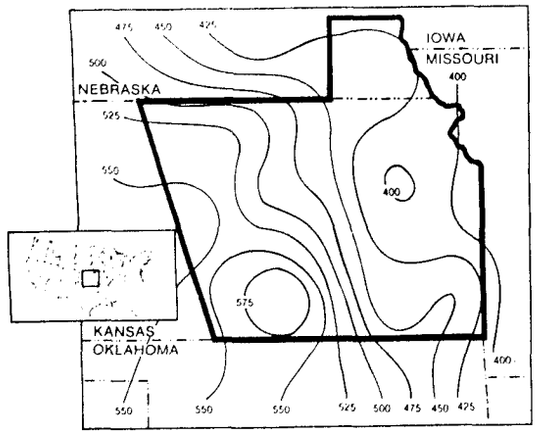

Fig. 1. Map of the study area, enclosed by the heavy solid line, with an analysis of the normalized difference vegetation index (NDVI) obtained from TIROS-N data. Units of the vegetation index are arbitrary, with smaller values indicating greater coverage by green vegetation.

For each of the six days of the case study, GOES-VISSR infrared data were obtained at half hour intervals from just after sunrise to shortly before noon. All infrared images were ground-registered to within one pixel (~10 km). Vegetation information for the study area shown on Figure 1, was obtained from TIROS-N AVHRR data. The data are in the form of a normalized difference vegetation index (NDVI) which is the ratio of the difference to the sum of the reflectances of the 0.55-0.68 μm visible and 0.725-1.10 μm near infrared channels. The numbers shown on Fig. 1 are arbitrary units with smaller values corresponding to greater amounts of vegetation.

In addition to the satellite derived parameters described above, a number of in situ meteorological measurements are required. These are 1) the surface geostrophic wind, 2) mid-morning shelter temperature, humidity, station pressure and wind data, and vertical profiles of temperature and humidity, which are used to correct the satellite measured skin temperature for atmospheric effects, and 3) daily rainfall data, which are used in combination with a simple hydrological model (see below) to compute ground truth soil moisture. The shelter temperature, station pressure, and wind data were subjectively analyzed to produce fields of potential temperature advection. Potential temperature is appropriate because there is a significant variation in surface elevation across the study area.

4. DATA PROCESSING AND ANALYSIS

a). GOES-VISSR Data

The raw digital infrared images from GOES were used to generate morning skin temperature change maps. Visible channel images were used as an aid to eliminate cloud contaminated regions. Subtraction of the appropriate images then produced maps of two hour mid-morning temperature change. Two such images were produced for each day of the study, using the 1330, 1400, 1530, and 1600 GMT data. The two images were then averaged to produce the final uncorrected surface temperature change data set.

These data were then further processed to account for the effects of atmospheric water vapor using a radiation flux algorithm for the GOES window channel developed by Chesters (1984). The absolute calibration between the GOES radiance and a reference surface temperature is a matter of some uncertainty, as discussed by Chesters (1984). However, since our technique requires only corrected temperature differentials, a calibration is not needed.

b). Computation of Soil Moisture

An antecedent precipitation index (API) is used, in lieu of actual soil moisture measurements, as the verification standard, or "ground truth" in this study. For a given day i:

$$API_i = P_i - R_i + k(API)_{i-1}. \qquad (2)$$

The previous day's API is modified by precipitation P, runoff R, and a seasonally varying depletion coefficient k. The depletion coefficient is specified as a sinusoidal function with a period of one year and with maximum and minimum values of 1.0 and k_{min} on 15 January and 15 July respectively. Runoff is assumed to occur only when API exceeds the root zone saturation value W_{sat}, at which time all additional precipitation is assumed to runoff. The saturation soil water content is given by

$$W_{sat} = 10mm/(1-k_{min}) \qquad (3)$$

Finally, the relationship between API and the moisture parameter m, to be used in the linear regression (eq. 1) is given by

$$m = [1.064-1.33(API/W_{sat})]^2 \qquad (4)$$

This assumes that $W_{fc} = 0.8\ W_{sat}$ and that the wilting point occurs at $API = 0.06\ W_{fc}$.

c). Objective analysis and regression.

Fields of all variables (corrected ΔT, NDVI, $\ln V_g$, m, and advection) were analyzed objectively to remove small scale "noise" and to place all variables on a common grid for statistical analysis. The objective analysis scheme used is a modified Barnes scheme. A grid interval of 0.3 degrees latitude and longitude was selected for the final analysis because it represented a satisfactory compromise between reduction of noise and retention of detail.

A two step linear regression procedure was then applied to the gridded data. The two step approach is advisable to infer soil moisture from the data set since, in the physical cause-and-effect relationship, ΔT is actually the predictand. The first step preserves this relationship to the maximum extent by regressing all variables except m against ΔT. The result is a linear equation for estimated morning temperature change $\Delta T'$ based on the wind speed, vegetation, and advection at each point. In the second step the temperature change residuals ($\Delta T - \Delta T'$) are regressed against m producing an equation for the estimated soil moisture, m'.

5. RESULTS AND DISCUSSION

Before generating the regression equations for this case, preliminary experiments were performed to establish the optimum value of k_{min} (eq.3). In these experiments, API was computed based on a number of selected values of k_{min}. For each value, the regression described above was run, neglecting advection and using the raw, unsmoothed (i.e. no objective analysis) data at each raingauge site. Results, presented in Figure 2 show that for this case, k_{min} = 0.92 produces the highest coefficient of determination between m and the morning temperature slope residuals.

For each of the five days of the case study with usuable data (24, 25, 27, 28, and 29 July 1978) a quasi-independent statistical test was performed. In these tests, the day in question was treated as an independent data set. The two step regression equation was performed on the remaining four days, and the resulting regression coefficients were used to estimate m on the independent day. Results of these tests are presented in Figs. 3-7.

On 24 July (Fig. 3), a day on which scattered cloud cover somewhat reduced the amount of data, major differences between the estimated and observed fields occurred over north central Kansas, where the estimated soil moisture was too dry, and in the southwestern part of the study area where the satellite estimate shows a tongue of wet soil, which was not observed, extending eastward from west central Kansas. The strong gradient of m across central and northeastern Kansas was estimated to be somewhat weaker than observed. The regression indicates that 70% of the variance in m is accounted for by the variables used. Advection on this day was rather weak, as winds in the study area were light or parallel to the isotherms.

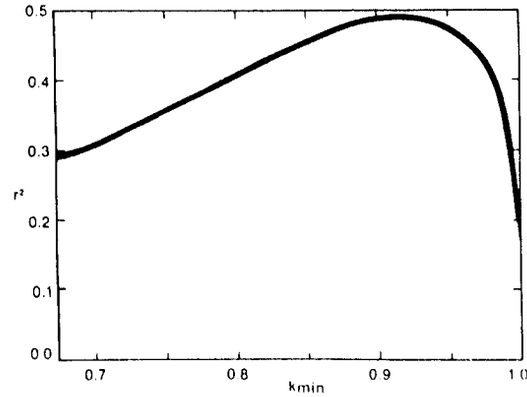

Fig. 2. Results of the two-step linear regression comparing GOES-estimated soil moisture with the API estimate at all raingauge sites in the study area. Plotted curve relates the resulting coefficient of determination, r^2, to the value of k_{min} used in computing API.

The estimated moisture field on 25 July (Fig. 4) is dominated by an area of dry soil in southeastern Kansas. The location of the center of driest soil agrees well with the observations but the dryness extends too far to the northwest into an area that is observed to be quite moist. There is also a net underestimate of soil moisture on this day which is most evident in north central Kansas. This is in an area where strong southwesterly winds were blowing warm dry air from dry soil over a region of cool wet soil. We feel it is likely that the difference is caused by a serious underestimate of the local warm advection over this sharp soil moisture gradient. Because of the coarse resolution of the surface data, the potential temperature analysis (Fig. 4e) necessarily cannot resolve such sharp local gradients.

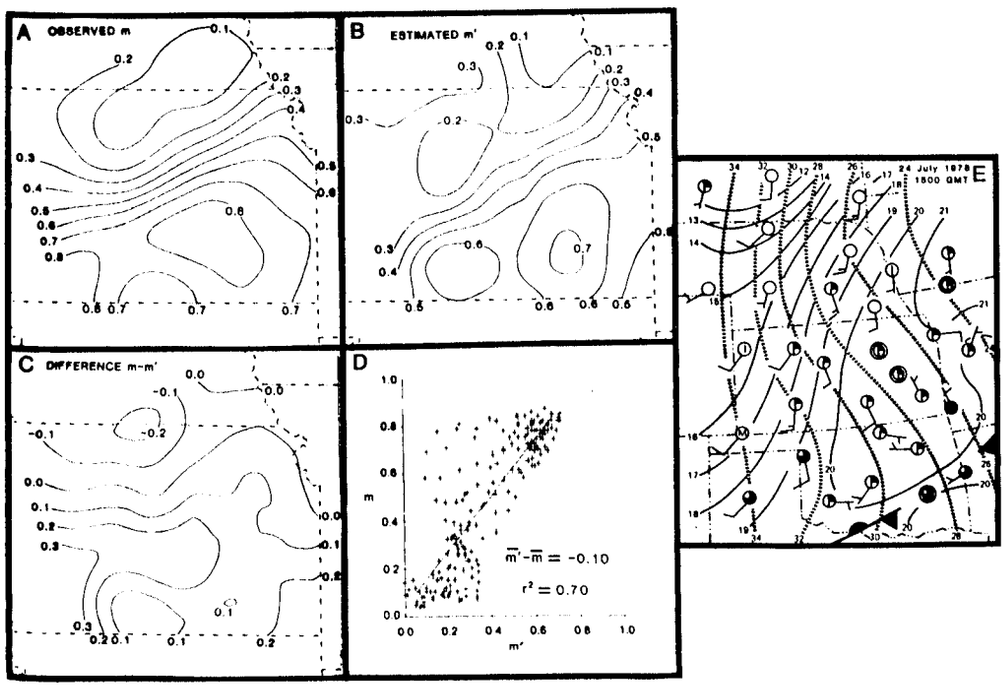

Fig. 3. Evaluation of the soil moisture estimate for 24 July, 1978: a.) The observed field of m, based on the API computed from raingauge data; b.) the estimated field, m', using GOES-IR data in a two step linear regression; c.) the difference field, m - m'; d.) scatter plot of the data from all objective analysis grid points in the study area; e.) surface pressure (mb - 1000), wind (full bar = 5m/s), cloud cover and potential temperature (C) for 1500 GMT, 24 July 1978.

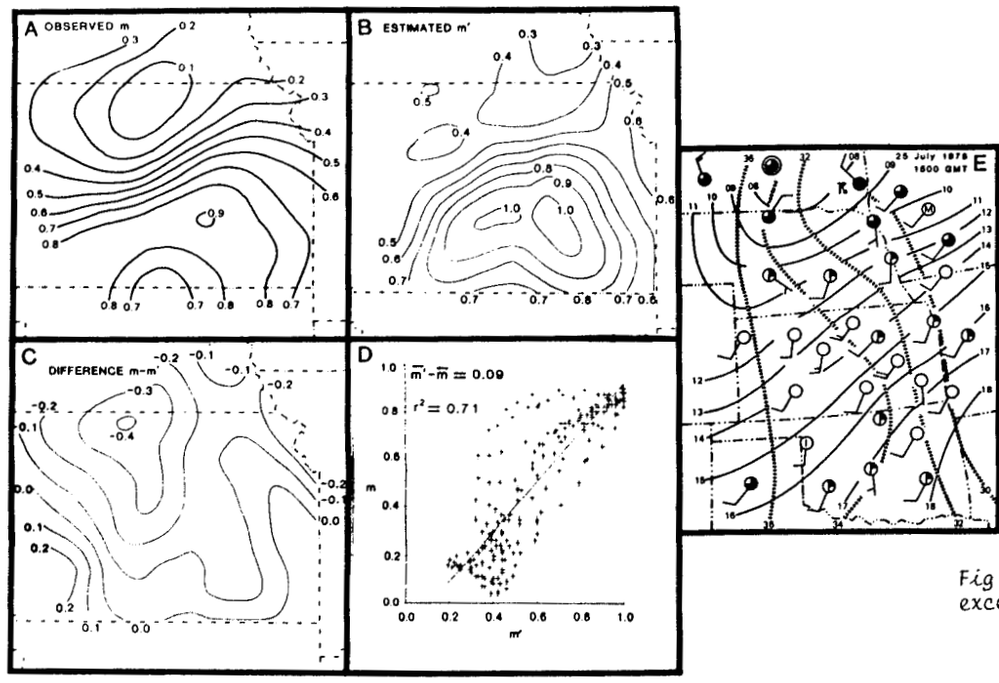

Fig 4. Same as Fig. 3, except for 25 July, 1978.

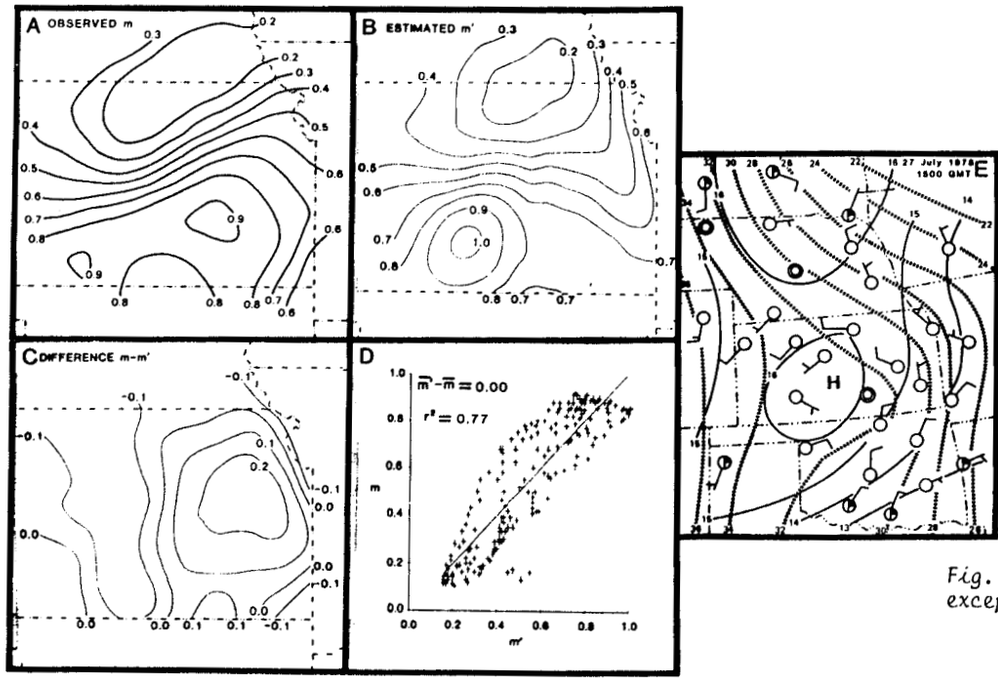

Fig. 5. Same as Fig. 3, except for 27 July, 1978.

On 27 July (Fig. 5) a tongue of moist soil on the estimated map extends southward through eastern Kansas. The observations do not display this feature. This may again be a result of an underestimate of the local cold advection as air flows across the sharp moisture gradient from wet to dry soil. The dry soil is estimated to extend somewhat too far northward into north central Kansas. The result of this pair of anomalies on 27 July is that the strong gradient of soil moisture across northern Kansas is improperly oriented in the estimated field. Nevertheless, the value of r^2, at 0.77, ties 28 July for the highest of the five case study days.

The quasi-independent test results for 28 July appear on Fig. 6. On this day most of the features in the observed API field are estimated well. The greatest differences are due to an extension of the region of wet soil too far south into western Kansas in the estimate, and an underestimate of soil moisture in southern Nebraska. A small positive bias is probably due to underestimated warm and dry advection.

Only the southern half of the study area was free of clouds on 29 July. Since this area contained only drier soils, there is a very narrow range in the data (Fig. 7), and it is more

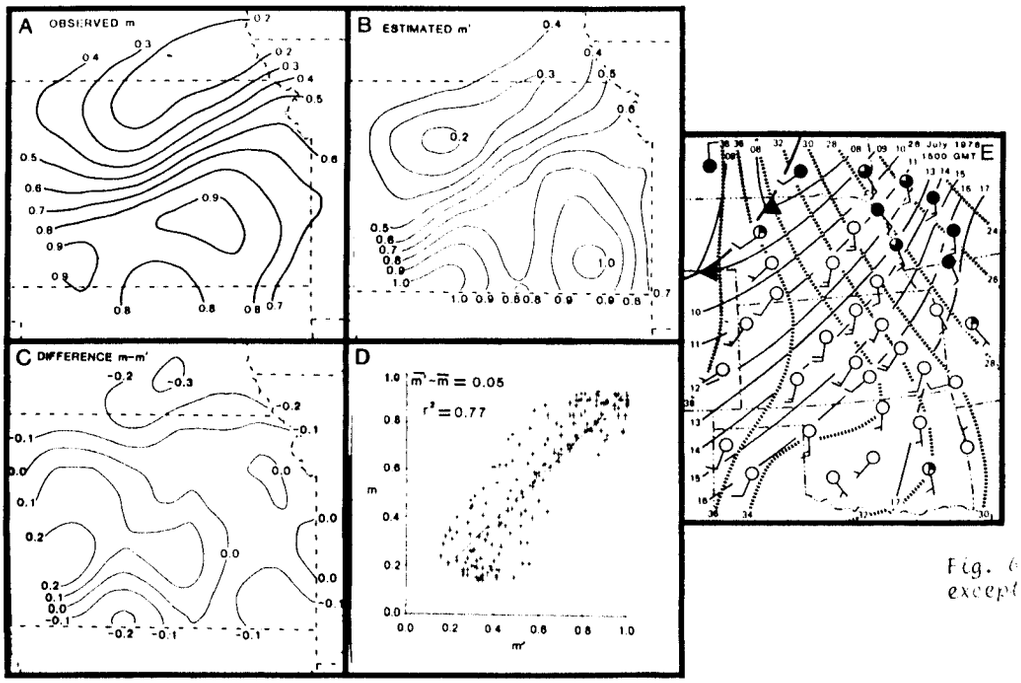

Fig. 6. Same as Fig. 3, except for 28 July, 1978.

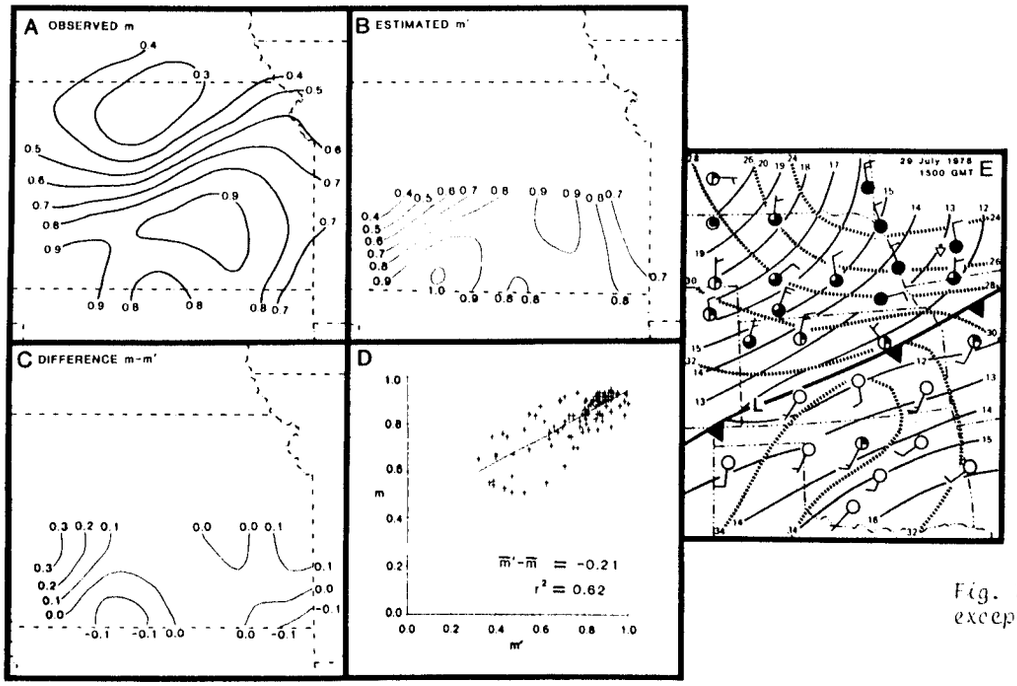

Fig. 7. Same as Fig. 3, except for 29 July, 1978.

difficult to establish a clear relationship. As a result, the coefficient of determination is somewhat lower on this day. However, the quasi-independent estimate does indicate dry soil in the region where it is in fact driest. The large negative bias is probably caused by a serious underestimate of the cold advection immediately behind the cold front which was entering the northwestern part of the data region.

Finally, in order to determine the accuracy with which a weekly value of soil moisture could be determined during a rain-free period, the five daily quasi-independent estimates of m were averaged at each grid point. These results are compared with the five day mean observed soil moisture in Fig. 8. All of the main features of the observed field are reproduced in the estimated map. The value of r^2 rises to 0.85 for the five day mean, with an RMS error of 1.7%, however there is a tendency to overestimate m when the soil is wet and underestimate it when the soil is dry. The largest differences between the two fields exceed 20% in north central Kansas and in the extreme southwestern corner of the study area. In light of this, it appears that by combining several days of infrared data, it is possible to unambiguously distinguish at least four categories of soil moisture, or to generate a soil moisture index which is accurate to within 20 to 25 percent.

The results presented above are in good agreement with results presented by Carlson et al.

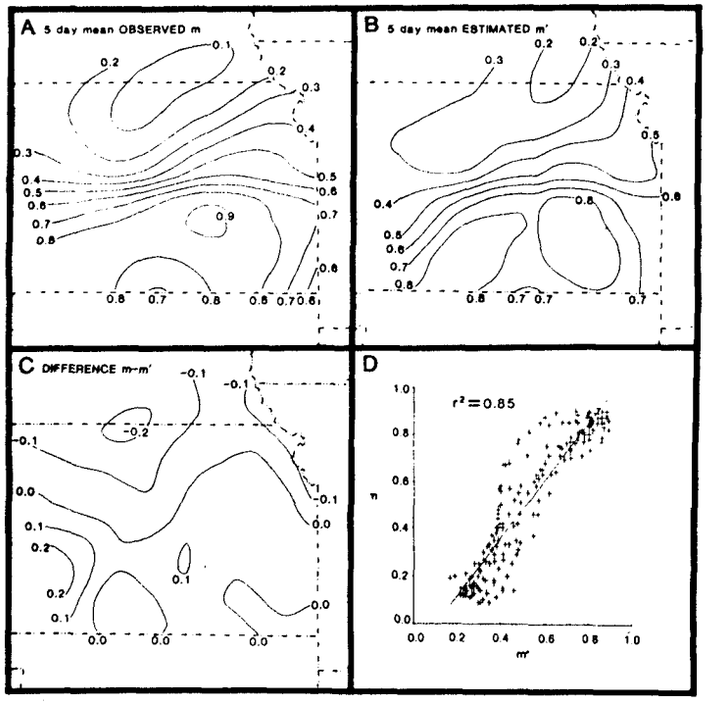

Fig. 8. Same as Fig. 3 (a-d), except using values of m and m' averaged over the five days of the case study.

Table 1. Partial correlation coefficients for each individual variable in the multiple linear regression using ΔT as the dependent variable, and in the two step regression used to predict m.

Predictand / Independent variable	ΔT	m
ΔT	--	0.87
m	0.87	--
NDVI	0.72	-0.60
Advection	0.56	-0.57
ln V_g	-0.04	-0.05

(1984). In the present study the average coefficient of determination for all case days is 0.71, compared to 0.49 for Carlson et al. (1984). In our study, when advection is not included as a variable in the regression, the average value of r^2 deteriorates to 0.57. Thus Carlson's neglect of advection may be the major cause of the difference between the two studies.

The relative impact of the individual variables is tabulated in Table 1. The most surprising result is the lack of importance of wind speed. The general dependence of surface temperature on wind speed is inherent in the surface energy balance equation, so the relative lack of importance here must be considered an anomaly. We attribute it to the fact that there is an insufficient range of wind speed in the five day sample used. Nearly all geostrophic winds were between 5 and 10 m/sec. the relationship between NDVI and ΔT is strong because it has a physical cause and effect basis, whereas one would expect little physical link between current soil moisture and vegetation cover. On the other hand the slightly greater correlation between advection and m than between advection and ΔT can be explained physically. The flow of air across the sharp soil moisture boundaries in the study area is a significant contributor to the local surface temperature advection.

6. Conclusions

Results show good agreement between estimated and observed regional scale soil moisture features. It is shown that a depletion coefficient of 0.92 produces an API which is best correlated with soil moisture as inferred from GOES thermal infrared data. When all the individual daily soil moisture estimates during the case study period are averaged at each point and compared to the average observed soil moisture, the data correlate at $r^2 = 0.85$. This implies that the algorithm is capable of distinguishing at least four categories of soil moisture.

The technique described here is tested on a single five day case study. Clearly a larger body of data from other locations and seasons is required before the technique can be applied universally. The effects of differing soil types, surface albedo, and atmospheric haze and aerosols also have not been considered. Other problems which may have significant impact on this study include the use of vegetation data from a year other than the study year, the use of API as the soil moisture "ground truth" data set, and the fact that there was not a wide range of observed surface geostrophic winds during the study period. It is expected that planned additional case studies will help to clarify the importance of these problems.

REFERENCES

Carlson, T. N., F. G. Rose and E. M. Perry, 1984: Regional scale estimates of surface moisture availability from GOES infrared satellite measurments. Agron. J., 76, 972-979.

Chesters, D. 1984: Calculations of atmospheric transmittance in the 11 μm window for estimating skin temperature from VISSR infrared brightness temperatures. NASA Tech. Memo. 86105, 35pp.

Wetzel, P. J., D. Atlas, and R. H. Woodward, 1984: Determining soil moisture from geosynchronous satellite infrared data: A feasibility study. J. Clim. Appl. Meteor., 23, 375-391.

SOIL MOISTURE ESTIMATES FROM SATELLITE INFRARED TEMPERATURES AND THEIR RELATION TO SURFACE MEASUREMENTS

Toby N. Carlson

The Pennsylvania State University
University Park, PA 16802

1. INTRODUCTION

Spatial and temporal variations in soil moisture are reflected by variations in the surface temperature. Exact measurements of the soil moisture using remote measurements of thermal infrared temperatures of the surface are possible, in theory, but very difficult to make in practice because of the enormous complexity of the ground surface, especially in the presence of vegetation. Our approach is to invert a time-dependent, initial-valued, one-dimensional boundary layer model in conjunction with measured surface temperatures to obtain the surface energy balance, a soil moisture parameter, called the moisture availability, and the thermal inertia. For the theory behind the model, the reader is referred to papers by Carlson and Boland (1978) and Carlson et al. (1981; henceforth referred to as CM). Similar models have been used to obtain soil moisture values from satellite infrared measurements by Wetzel et al. (1984) and Price (1982) in the United States and by Taconet et al. (1986a,b; henceforth referred to as OT) and Abdellaoui et al. (1985) in France and by Nieuwenhuis et al. (1985) in Holland. Recently, modelers have begun to treat vegetated surfaces by including parameters that govern the fluxes between the soil/plant/atmosphere system. The vegetation component in both the CM and OT are nearly identical, being based on an earlier version by Deardorff (1978), but simplified and streamlined by Bernard et al. (1986) using data for sorghum.

The purpose of this paper is to report some of the recent results showing agreement between moisture values calculated with the model using satellite infrared temperatures as input and ground-based measurements of related parameters.

2. RESULTS

2.1 Soil Moisture Versus Antecedent Precipitation as Measured by GOES

Twenty days of satellite images were analyzed for a period during the summers of 1978 and 1980 over Kansas. The region and dates were chosen because of the extreme drought conditions that were affecting a wide region of the midwest extending from Kansas to Texas. We reasoned that if the infrared method was viable it should prove so under conditions of great horizontal variation in soil moisture and rainfall. Accordingly, the parameter called moisture availability (M) was determined over a region a few hundred kilometers on a side using GOES daytime and nighttime infrared temperature measurements (Carlson et al., 1984). The vegetation model was not used for this study.

Moisture availability is defined as the ratio of evaporation to potential evaporation and is also equal in the model to the ratio of soil water content (θ) over a layer near the surface to the value of soil water at field saturation (θ_{fs}). Thus, M varies from 0 (for perfectly dry surfaces) to 1.0 for saturated surfaces. In the example shown in Fig. 1, the vegetation model was not used to derive the results. Consequently, the prairie surface is treated as bare soil. Contours of M in Fig. 1 closely reflect the surface temperature over the region of Kansas on the afternoon of the 14th of July, 1980. There is an overall similarity on all the days between the M field and antecedent precipitation, which is effectively a running mean of the rainfall. Low values of M (0.12-0.25) in the south correspond roughly to low rainfall and high values in the north to higher rainfall totals. The correlation between the log of M and the antecedent precipitation is about 0.7 for all cases. A similar relation was found by Flores and Carlson (1985) for scenes over Texas on three days during the same month of July, 1980.

2.2. AVHRR Images and Surface Measurements Made Over France

During a field measurement program conducted over the Beauce region of France (near the town of Voves) by scientists at two French national laboratories (INRA, CRPE), there occurred a remarkable increase in the surface sensible heat flux during a period of drying. Although the drying trend had been continuing a couple of weeks, the increase (measured by both the SAMER method of Itier (1981) and by sodar) began just after the 6th of July and was most abrupt between the 11th and 14th (Fig. 2).

Heat flux values derived from the CM and OT models (using the same set of initial conditions) using afternoon temperatures (approximately 1400 sun time) from NOAA AVHRR as input also show a similar trend, although the version of CM with bare soil was less able to capture the increase in sensible heat flux with time.

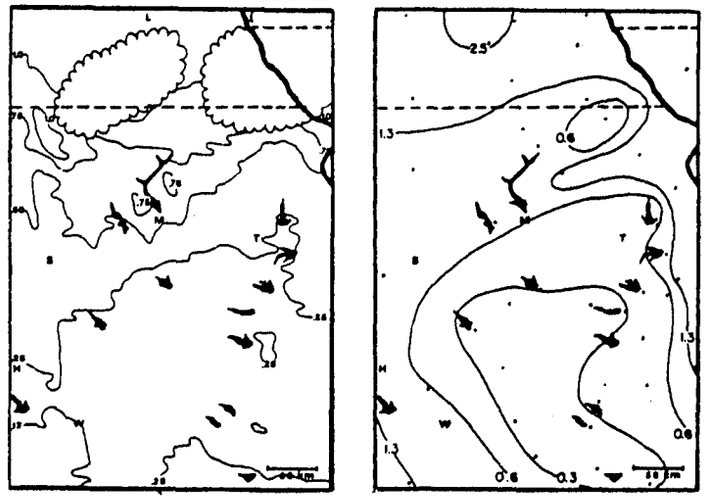

Fig. 1. Moisture availability (M) analysis over a portion of eastern Kansas and Nebraska for 14 July 1980 based on surface temperature measurements for a pair of GOES images (left). Dark, irregular shapes are bodies of water, including the Missouri River near upper right. Scalloping denotes regions obscured by cloud. Antecedent precipitation for 14 July 1980 is shown on the right. Dots indicate location of rainfall measurement stations.

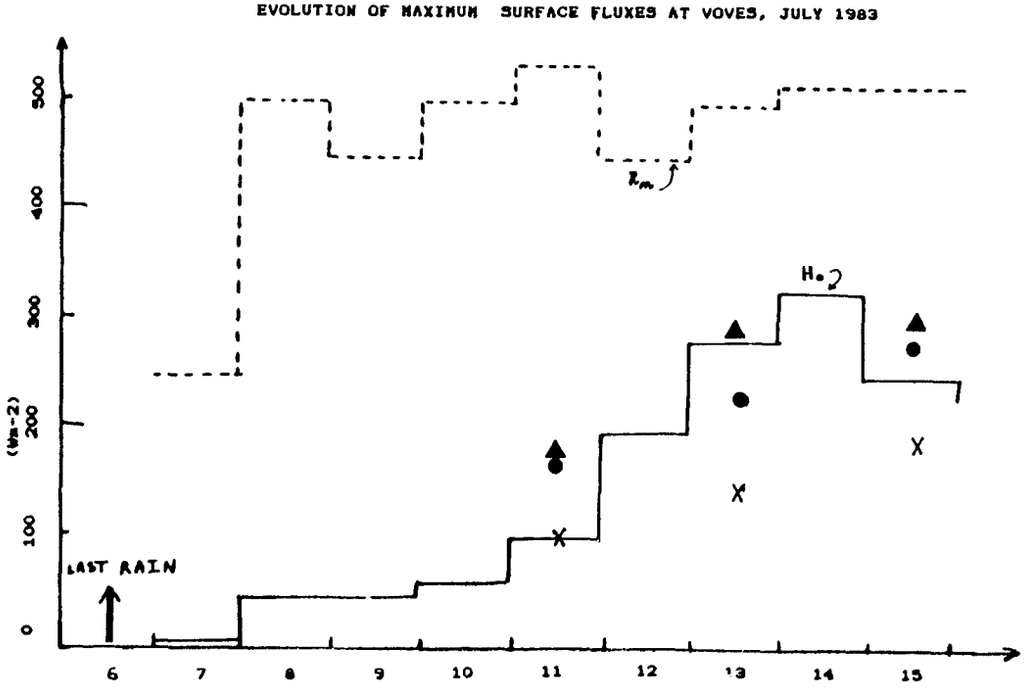

Fig. 2. Evolution of maximum net radiation (top curve dashed) and maximum surface sensible heat flux (bottom curve; in wm^{-2}) for Voves during during a period in July 1983. The last rainfall before the end of the record occurred on the 6th of July. Symbols refer to maximum heat flux values determined from the models using AVHRR data as surface temperature input: the CM for bare soil (X), the CM for vegetation (●) and OT for vegetation (▲).

Soil water content (θ) measured with a neturon probe near the Voves site continued only up until the 12th of July. Averages of 0 over four depths (Fig. 3) show a decreas at all levels down to about 40 cm below the ground; the most rapid drying, of course, occurred in the top 30 cm, where levels of water content were approaching the wilting point of the soil (approximately 0.15 cm3/cm3; field saturation was about 0.35 cm3/cm3).

Model results also show a corresponding decline with time in soil water content, although more precipitiously than the measurements made earlier in the period suggest. Curiously, although the model

water contents pertain to the vegetation parameterization, the bare soil valued for CM were virtually identical to those shown in Fig. 3. These values correspond to very low moisture availability (approximately 0.2 on the 15th), which are comparable to those in the dryer parts of the Kansas image of Fig. 1. The puzzling fact here is that the surface measurements seem unassailable and are supported by the model results. At the same time it is to be noted that the wheat crop over which these measurements were made did not appear to be highly water stressed.

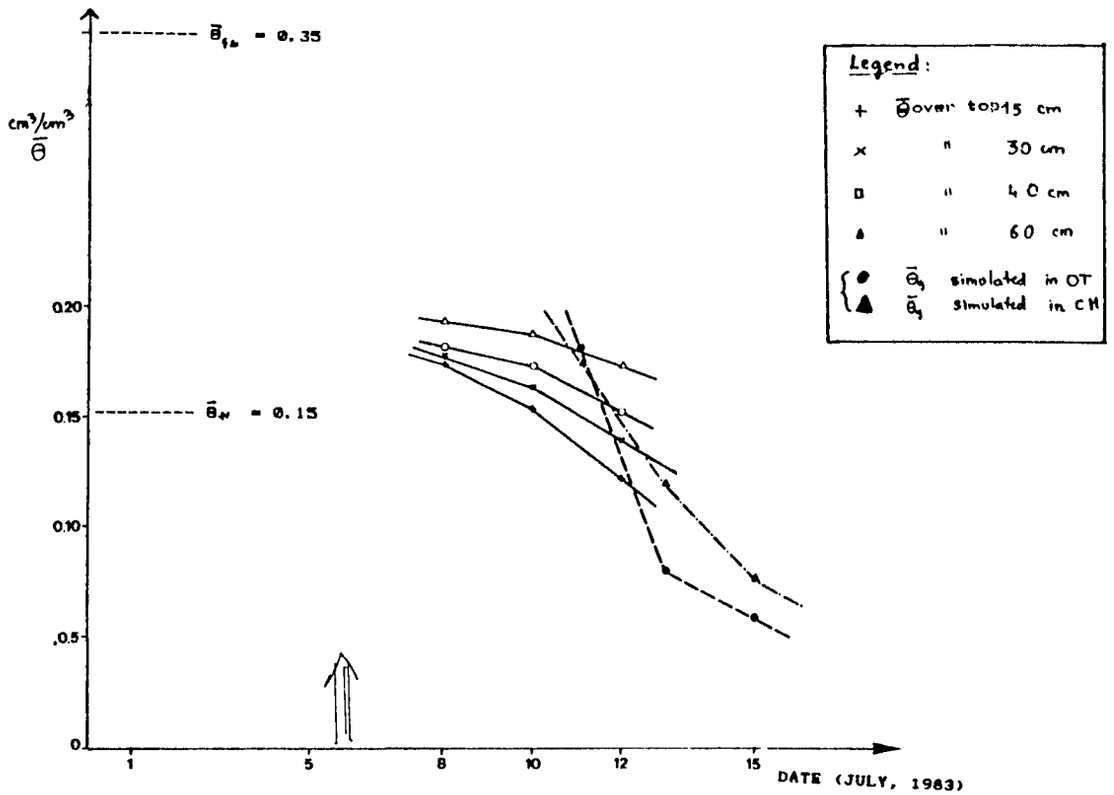

Fig. 3. Measured (solid lines) soil water content (cm3/cm3) versus time for averages over four vertical soil depths as given in the key. Soil water content (θ) determined from the model using the 1346 GMT AVHRR surface temperature measurement is shown by the dashed and dot-dashed lines, respectively, for the OT and CM. The vertical arrow denotes the last rainfall during the period.

3. CONCLUSION

Infrared temperatures measured with the aid of satellite can reflect large spatial and temporal changes in soil moisture but not enough is known and the parameterization sufficiently undeveloped to arrive at a completely consistent measure of the real soil water content or the soil depth over which it applies.

4. REFERENCES

Abdellaoui, A., F. Becker and E. Orlory-Hechinger, 1985: Use of metwosat for mapping thermal inertia and evapotranspiration over a limited region of Mali. Submitted to J. Clim. and Appl. Meteor.

Bernard, R., J.L. Hatfield and M. Vauclin, 1986: Test of an evapotranspiration model for diurnal and seasonal behavior of sorghum fields under various water availability conditions. Submitted to Boundary Layer Meteo.

Carlson, T.N., J.K. Dodd, S.G. Benjamin, J.N. Cooper, 1981: Remote estimation of surface energy balance, moisture availability and thermal inertia. J. Appl. Meteor., 20, 67-87.

Carlson, T.N., F.G. Rose, E.M. Perry, 1984: Regional-scale estimates of surface moisture availability from GOES satellite. J. Agronomy, 76, 972-979.

Carlson, T.N. and F.G. Boland, 1978: Analysis of urban-rural canopy using a surface heat flux/ temperature model. J. Appl. Meteor., 17, 998-1013.

Deardorff, J.W., 1978: Efficient prediction of ground surface temperature and moisture with inclusion of a layer of vegetation. J. Geophys. Res., 83, 1889-1904.

Flores, A.L. and T.N. Carlson, 1985: Estimacion de parametios del suelo dombinado imagenes digitales de GOES en un modelo de copa limite. Meteorologica (Argentina) (in press).

Itier, B., 1981: Une méthode simple pour la measure de l'evapotranspiration reélle á l'échelle de la parcelle. Agronomie, 10, 869-876.

Nieuwenhuis, G.J.A., E.H. Smidt and H.A.M. Thunmissen, 1985: Estimation of regional evapotranspiration of arable crops from thermal infrared images. J. Remote Sensing, 6, 1319-1334.

Price, J.C., 1982: Estimation of regional scale evapotranspiration through analysis of satellite thermal-infrared data. IEEE Transactions on Geoscience and Remote Sensing, GE-20, 286-292.

Taconet, O., R. Bernard and D. Vidal-Madjar, 1985: Evapotranspiration over an agricultural region using a surface flux/temperature model based on NOAA-AVHRR data. J. Clim. Appl. Meteor. (in press).

Taconet, O., T.N. Carlson, R. Bernard, D. Vidal-Madjar, 1986: Evaluation of a surface/vegetation model using satellite infrared surface temperatures. Submitted to J. Clim. Appl. Meteor.

Wetzel, P.J., P. Atlas and R. Woodward, 1984: Determining soil moisture from geosynchronous satellite infrared data: A feasibility study. J. Appl. Meteor., 23, 375-391.

CORRELATIONS BETWEEN REMOTELY MEASURED SOIL WATER CONTENT AND SURFACE TEMPERATURES FOR THE BEAUCE REGION, FRANCE

Eileen M. Perry
The Pennsylvania State University
University Park, PA 16802

1. INTRODUCTION

Soil water content has been shown to be highly correlated with radiometric surface temperatures, and a number of studies have demonstrated that the surface temperature increases as the substrate soil water content decreases. (See Hatfield et al. (1983) and Carlson (1984) for a summary of articles on this research.) As part of a study to model the available water in the unsaturated zone using thermal infrared data, this paper is a first look at some aircraft measurements that show a correlation between microwave measured soil water content and radiometric surface temperatures.

During an experiment held in the summer of 1983 near Voves, France, active microwave and thermal infrared measuraments were made during the early afternoon aboard a French aircraft flying a grid pattern over a flat, agricultural region south of Paris called the Beauce. The vegetation consisted mainly of wheat and corn, with some stands of trees. The infrared sensor was a Barnes PRT-5 radiometer which has a measurement accuracy to within .5 degrees celsius. The active microwave measurements were taken with the ERASME scatterometer (5.35 GHz (FM-CW) with an incidence angle of eleven degrees for minimizing the effects of roughness and therefore maximizing the accuracy of soil water measurement. Calibration missions of the microwave measurements were performed with reference to in-situ measurements of soil water content; the correlation coefficient was .89 between the microwave back scatter coefficients and the ground measurements of the soil water content in the first ten centimeters. Accordingly, soil water content was converted directly from backscattering cross section to soil water content. The scatterometer and radiometer were mounted so that the two instraments were taking measurements of the same ground area simultaneously, five measurements per second, with each having a surface sampling area of approximately 40 meters squared. The average flight altitude was about 400 meters.

Data was collected during July and September of 1983; the dates in July were 8 and 12 July during a period of drying following a 6 July rainfall episode; the September dates were the 20, 23, 26, 28 and 29 September following a 19 September rainfall episode. Data segments along two of the aircraft legs were selected to discuss because they represent alternately the poorest and best correlation of surface temperatures with microwave-derived soil water content measurements, respectively on 8 July (1:45 LT) and 26 September (3:45 LT).

To examine the data through time and perform some descriptive statistics, a statistics/graphics package (SAS) was used to plot the microwave and thermal IR data, and to perform correlations between them. Figure 1 shows a plot of the temperature resonse as the sensor was flown over a west to east transect near the town of Voves on 8 July. Figure 2 shows a plot of the soil moisture values measured along the same transect. In order to gain a simple visual comparison between the temperature and microwave measurements, the two lines are overlain on the same plot, using a cubic spline to fit the points (see figure 3). Note the inverse relation between the microwave backscatter and the surface temperature at the points where the sensor was flown over road surfaces (A, B, D, L, M, N on figure 3) which are very dry and have a high surface temperature. Figure 4 is a transect flown on 26 September, over approximately the same area as in figure 3. Note that for the same roads (points B, D, L, M), the data again show that a low soil water content correlates with a high surface temperature. However, for the 26 September case, this inverse relation is demonstrated over the entire transect. For both of the cases, the subset area labelled on figures 3 and 4 were plotted to show the variations of the microwave and thermal infrared response on a field basis (see figures 5 and 6).

2. RESULTS AND DISCUSSION

The first and most important observation is the poor correlation between the microwave backscatter coefficients and the thermal infrared measured temperatures for the 8 July case (shown in figure 3). The correlation coefficient for the entire data segment is .3459. The correlation between these same data types is -.7795 for the 26 September case, which is what would be expected given previous research. Possible explainations (not yet confirmed) for this lack of correlation of the vegetated 8 July case are:

i) For the July case, the plants may be in effect "integrating" the available water because they are using the water at depth (in the root zone). If the surface temperature was being influenced by the amount of water available at a depth of perhaps 45 cm or more, and the variability of this soil water content is not as great as that at 0-10 cm (being measured by the microwave), there would be a difference in the variability of the surface temperature and the microwave measurements. This difference in variability could decrease the correlation between the remotely measured temperature and soil moisture for any given point.

ii) There could be a difference in the "measurement depths" between the July and September cases. For the July case, the thermal infrared sensor is measuring temperatures that are largely influenced by the water available to the plants in the root zone (much deeper than 10 cm), while the microwave backscatter coefficients are most highly correlated with the top ten centimeters. For the September case, with nearly bare soil conditions, the thermal infrared temperatures are more influenced by the soil water content near the surface, and the microwave backscatter coefficients are again most correlated with the soil water content in the first ten centimeters.

iii) If the stomates were closed for some reason other than lack of available water, the plant temperatures measured by the thermal infrared sensor could be much higher that what would be expected for a given soil water content.

Another observation is the possible lack of a significant correlation between remotely measured soil water content and surface temperatures within an individual field. For one corn field (field 10) there is a correlation coeffient of -.326 for 8 July and -.484 for 26 September. For the forest stand (field 7), the correlations are +.403 for 8 July and -.18 for 26 September (see Table I).

Finally, it can be seen from figures 5 and 6 that there is a greater variation of microwave backscatter coeffiecients than surface temperature . This would tend to support the idea that the variability of soil moisture is greater in the surface layers of the soil.

Table 1. CORRELATION COEFFICIENTS BETWEEN TEMPERATURE AND SOIL MOISTURE

DATE	FIELD COVER	SURFACE TEMPERATURE	MICROWAVE	N	CORREL.
8 July	all data (mixed cover)	29.7 +/- 1.98	-2.10 +/- 2.26	9165	-.004
	segment 3 (mixed)	30.1 +/- 1.98	-1.87 +/- 1.77	1004	.346
	segment 3 subset (mixed cover)	30.4 +/- 1.15	-.660 +/- 1.52	218	-.170
	field 10 (corn)	29.1 +/- .308	-.051 +/- .984	68	-.326
	field 7 (woods)	29.2 +/- 1.07	-2.80 +/- 1.23	29	.403
26 Sept.	all data (mixed cover)	31.3 +/- 2.79	-3.98 +/- 2.82	7556	-.712
	segment 3 (mixed)	31.4 +/- 3.02	-3.15 +/- 2.82	926	-.780
	segment 3 subset (mixed cover)	30.8 +/- 2.92	-2.94 +/- 2.69	232	-.722
	field 10 (stubble)	26.8 +/- .537	.258 +/- .755	73	-.484
	field 7 (woods)	32.4 +/- .538	-4.61 +/- .642	24	-.181

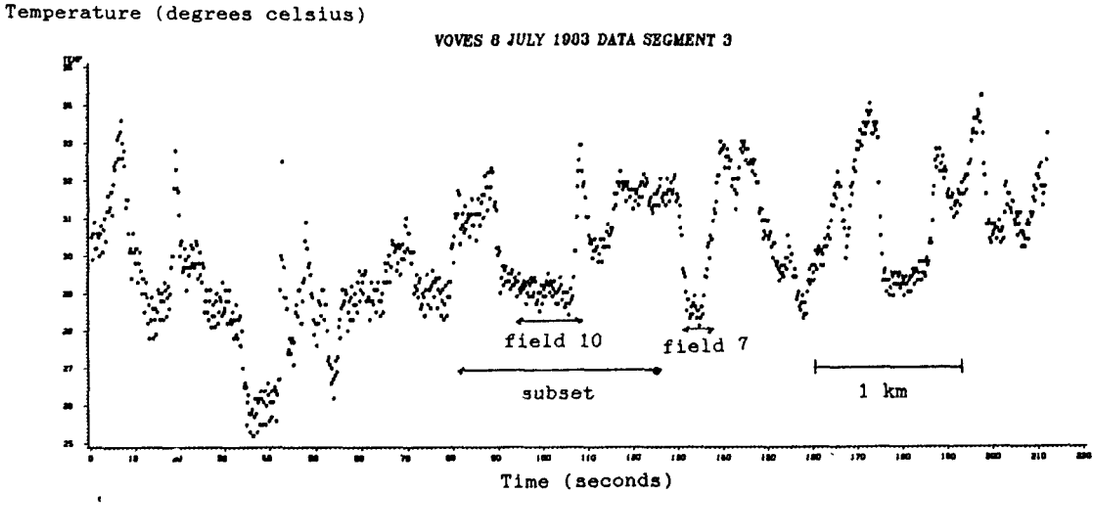

Figure 1. West to east tranverse showing the thermal infrared response. Time of day approximately 1:45 LT Note locations of fields 10 and 7, and the location of the subset to be examined later.

Temperature (degrees celsius) - - - - -
Soil water content (cm**3/cm**3 x 10**2) ————

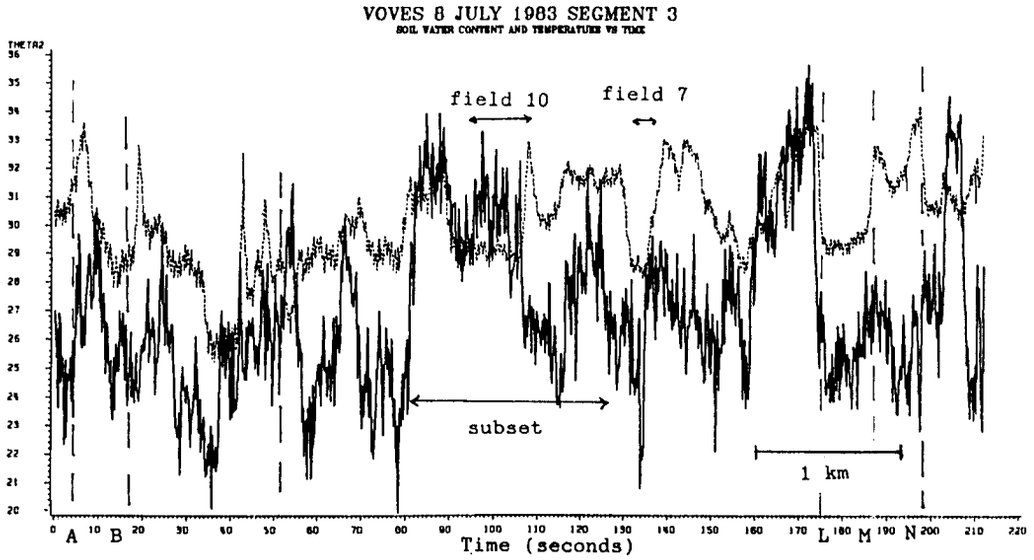

Figure 3. Combined plot for soil water content and temperature. Note the inverse relation of the responses for roads (points A,B,D,L,M,N).

Soil water content (cm**3/cm**3)

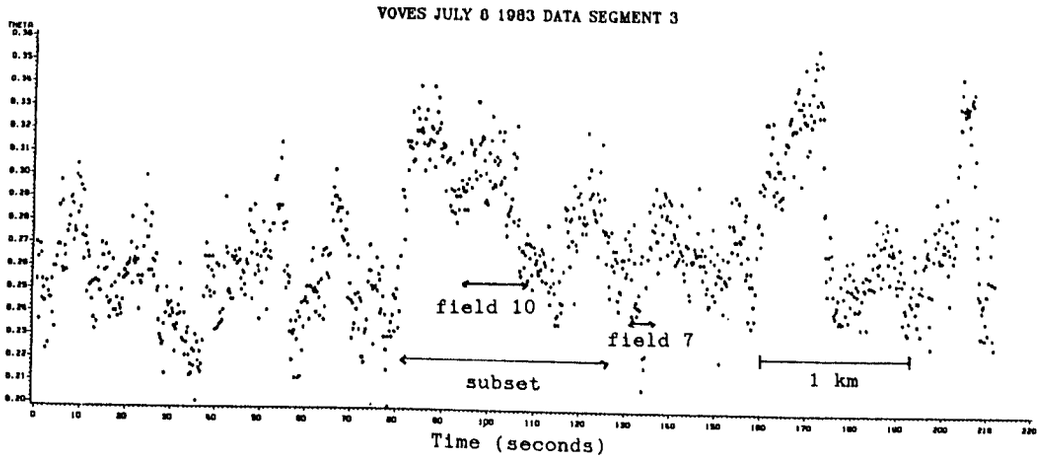

Figure 2. Soil water content measured with active microwave, same transverse as in figure 1.

Temperature (degrees celsius) - - - - - - -

Soil water content (cm**3/cm**3 x 10**2) ———

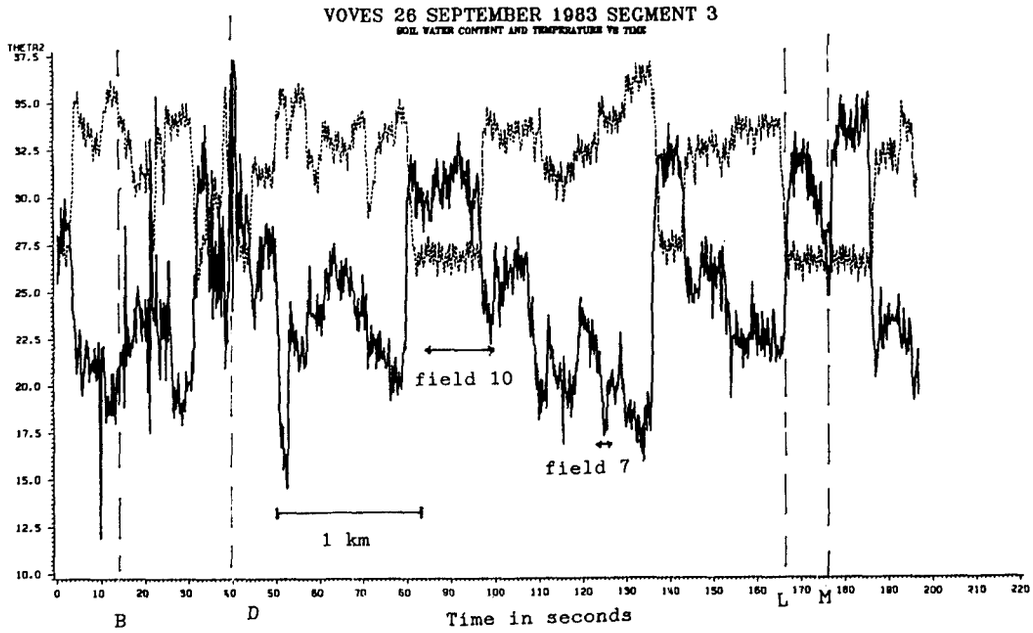

Figure 4. Combined remotely measured soil water content and surface temperature for approximately the same transect as in figure 3, ' data taken on 26 September at approximately 3:45. Note the inverse relation of the microwave and temperature responses. The road locations are the same as in figure 3.

Temperature (degrees celsius) - - - -

Soil water content (cm**3/cm**3) ———

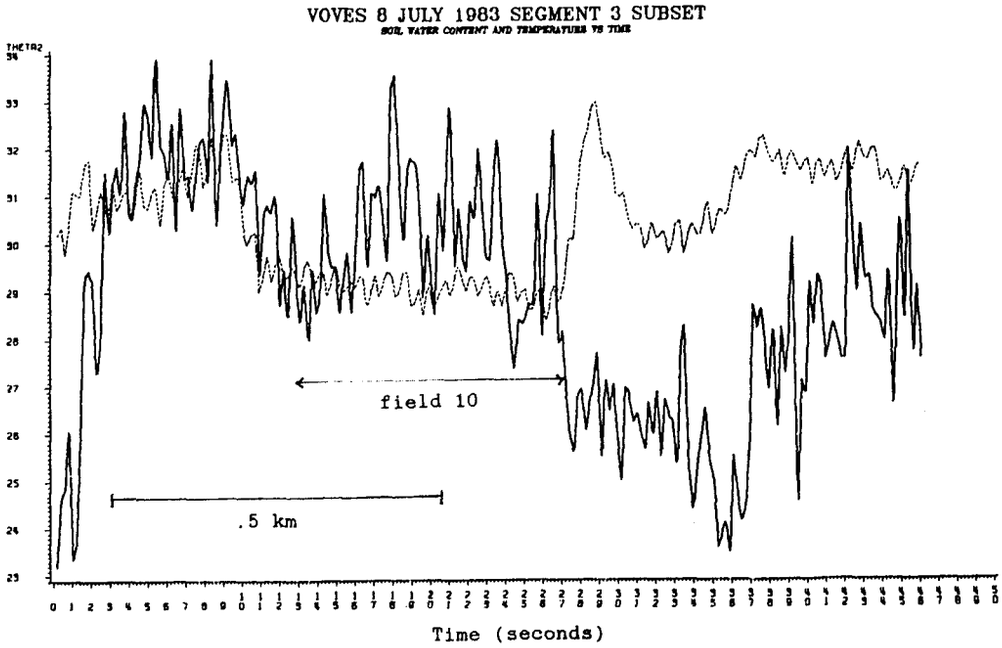

Figure 5. Combined temperature and soil water content responses for the subset of data segment 3. Note that the variation for soil water content within a field is much greater than the variation of temperature.

Temperature (degrees celsius) - - - - -

Soil water content (cm**3/cm**3) ———

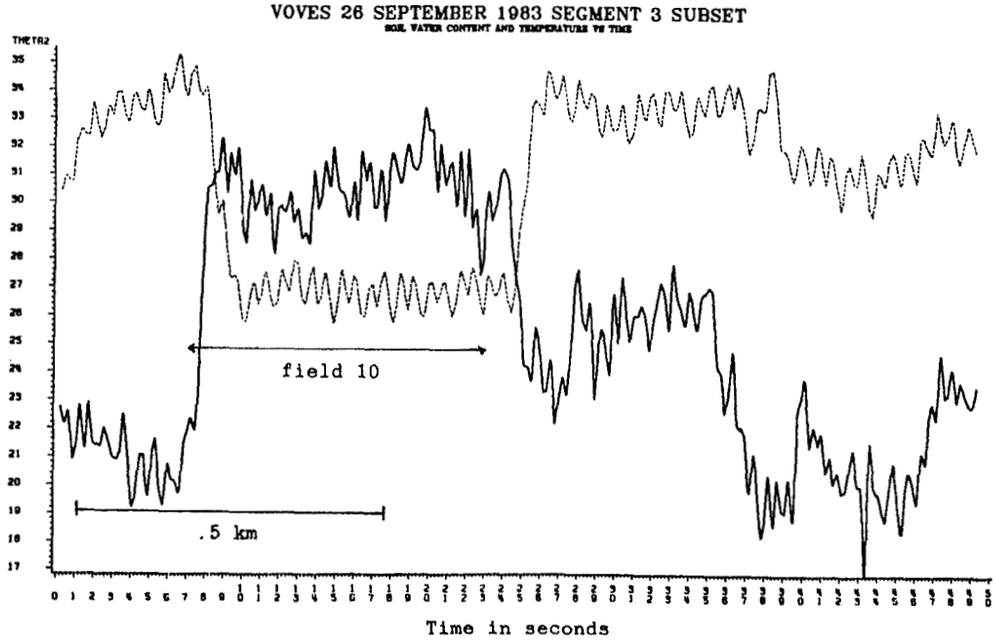

Figure 6. Combined temperature and soil water content for the subset of data segment 3, for the 26 September case. Note again the greater variability of the soil water content measured by the microwave.

3. CONCLUSION

The data analyzed so far has indicated a strong negative correlation between remotely sensed soil water content and surface temperatures for the near bare soil conditions of 26 September, while for the same area on 8 July there is little correlation between the remotely sensed soil water content and surface temperature.

4. REFERENCES

Barnes Engineering Company (no date): Bulletin 14-315D, product description of the Model PRT-5 radiation thermometer.

Bernard, R. and D. Vidal-Madjar, 1983: ERASME: Diffusiometre heliportable en bande C. Application a la mesure de l'humidite des sols. Proceedings of EARSeL/ESA Symposium on remote sensing applications for environmental studies, ESA SP-188, July 1983, pp. 59-64.

Carlson, T.N., 1984: Regional scale estimates of soil moisture availability and thermal inertia using remote thermal measurements, in Interpretation of thermal infrared data. J. Price (ed.), Harwood Academic Press, Remote Sensing Rev., pp. 197-247.

Hatfield, J.L., A. Perrier and R.D. Jackson, 1983: Estimation of evapotranspiration at one time of day using remotely sensed surface temperatures. Agricultural Water Management, 7, 341-350.

5.11

NIMBUS-7 SMMR MULTISPECTRAL PASSIVE MICROWAVE CORRELATIONS WITH AN ANTECEDENT PRECIPITATION INDEX*

Gregory D. Wilke

Air Force Global Weather Central,
Offutt AFB, NE 68005

Marshall J. McFarland

Texas A&M University,
College Station, TX 77843

1. INTRODUCTION

The purpose of this study was to use dual-polarized, passive microwave brightness temperatures to infer surface soil moisture. This research involved correlation analysis between Nimbus 7 Scanning Multichannel Microwave Radiometer (SMMR) passive microwave brightness temperatures and an antecedent precipitation index (API). The API used in this study was calculated from climatological precipitation observations. In this respect, the API can be used to infer soil moisture (Blanchard et al., 1980). Three transformations of both the vertical and horizontal components of the polarized brightness temperatures were used to account for varing aspects of terrain, vegetation, and atmospheric conditions.

Quantitative soil moisture amounts are a necessary input into crop growth stage models. Several hydrologic parameters can be obtained through remote sensing to arrive at a soil moisture estimation. Burgy (1974) lists thirteen parameters which can be measured or inferred through remote sensing. Hughes Aircraft Company in Denver and their subcontractor Environmental Research and Technology, with Dr. Ken Hardy as the principle investigator, developed algorithms for inferring hydrologic parameters using simulated DMSP/SSMI passive microwave data.

Passive microwave brightness temperatures are a function of the moisture content of the emitting layer. This relationship is basically a function of the high dielectric constant of water, and the relatively low constant for air and dry soil. The dielectric properties of a substance determines the electromagnetic wave propagation characteristics of that substance. The dielectric constant of the air, water and soil mixture determines the soil emissivity. An increase in volumetric water content results in an increase in the dielectric constant and a decrease in emissivity.

In the microwave region (approximately 1-50 cm), the Rayleigh-Jeans' approximation of Planck's radiation law can be applied to non-blackbodies. When using this approximation, we assume that the product of Planck's constant and the velocity of light is much less than the product of Boltzman's constant and the blackbody temperature. This assumption is valid only in the microwave region and allows us to neglect all second and higher order terms in a Maclaurin Series expansion of the exponent in Planck's radiation law. This approximation shows that the intensity of the observed emission, or brightness temperature, is essentially proportional to the product of the surface temperature and the emissivity of the emitting layer (Wilke and McFarland, 1984). Advantages of passive microwave approaches include the ability to penetrate non-precipitating clouds and light vegetation. Disadvantages include rather course resolution (12 km) and relatively little soil penetration (2 cm). The temperature of the emitting layer can be estimated through meteorological observations or inferred through passive microwave measurements. The limited areal coverage of conventional meteorological surface temperature observations can be supplemented with satellite observations to arrive at a global database. This database can then be used to calculate the surface soil moisture depletion coefficient of a simple soil moisture model, such as the API.

* AMS Journal of Climate and Applied Meteorology Article, Feb 1986.

The SMMR instrument responds primarily to surface moisture, however the response is influenced by both attenuation and scattering within the intervening medium. The primary causes of atmospheric attenuation and scattering are due to water vapor and oxygen. Surface attenuation and scattering is primarily the result of vegetation and terrain. Since the passive microwave response is a composite of the entire foot print, all measurements will have some influence from vegetation and roughness. While these influences affect the microwave response in different ways, they both result in decreasing the signal received by the radiometer.

2. METHODOLOGY

This investigation involved an analysis of SMMR brightness temperature data collected between 25 Oct 1978 and 10 Nov 1979. The study area included Kansas, Oklahoma, and the Panhandle of Texas. This analysis involved seasonal trends, a visual image of the entire study area which illustrated any large scale patterns, and an areal analysis over seven 20 x 20 km case study grid cells. The areal analysis was used to indicate vegetative and terrain influences. The 10 channel brightness temperatures and several combinations of these brightness temperatures were correlated with the API using regression analysis in monthly, bi-monthly, and annual series.

3. DATA

The data used in this investigation involved Nimbus 7-SMMR passive microwave data, surface observations from more than 500 stations within the study area obtained from the National Climatic Data Center, and calculated API values. The SMMR data covered 25 Oct 1978 to 10 Nov 1979 with repetitive coverage over the study area every 2 to 3 days. The average satellite overpass time was approximately 1100L and 0100L for day and night passes respectively. Data included both vertical and horizontal polarized brightness temperature components in five wavelengths; 0.81, 1.36, 1.66, 2.80, and 4.54 cm. In addition, GOES satellite imagery was used to delineate clouds in the case study analysis. National Weather Service weather radar summary charts were used to locate precipitating clouds. United States Geological Survey topographic and land-use maps were used in conjunction with reported crop statistics, from the state crop and livestock reporting services, to select and evaluate case study grid cells.

The Antecedent Precipitation Index is a very simple soil moisture model which can utilize the low resolution passive microwave data. The form of the API used in this study is

$$API(i) = API(i-1) * k + P(i)$$

where API(i) is the API value for day i, API(i-1) is the previous day's value, k is a fractional moisture depletion coefficient, and P(i) is the effective precipitation for day i. The depletion coefficient was selected to be a simple sinusoidal curve using observations from February and August 1979 to approximate the annual maximum and minimum temperature values. Blanchard et al. (1980) found that an approximate sinusoidal curve which represented inverted mean daily temperature represented the seasonal changes in k. They found that the inverted mean daily temperature curve was very similar to the inverse of a curve of mean monthly Penman potential evapotransportation calculations. The effective precipitation was computed by rasing the observed precipitation to a power of 0.891, suggested by Blanchard et al. (1980)

4. TRANSFORMATIONS

Transformations or combinations of the polarized brightness temperatures can reduce the error involved with the passive microwave observations. Newton (1977) showed that increasing the sensor's viewing angle from nadir to near 50 degrees increased the vertically polarized brightness temperature component and decreased the horizontal component. The mean of these components was shown to be nearly independent of viewing angle. Normalized brightness temperatures, the brightness temperature divided by the effective temperature of the emitting layer, was used by Mo et al. (1980). They found this parameter to be closely related to soil moisture. Subsequent investigations which used this normalized brightness temperature included Mo and Choudhury (1980), Wang et at. (1981), Njoku and O'Neill (1982), McFarland and Harder (1983), and Wilke and McFarland (1984). McFarland et al., (1984) found that the majority of the variance in the linear regression model correlating API and the 1.66 cm passive microwave brightness temperature from Nimbus 7 SMMR could be explained by three indicies. These were: horizontally polarized normalized brightness temperature (Th / T), polarization difference (Tv - Th), and normalized polarization difference [Tv - Th / 0.5 (Tv + Th)].

5. ANALYSIS AND DISCUSSION

The sensitivity of the passive microwave sensor response in each wavelength is largely determined by the amount and type of atmospheric attenuation. The atmospheric attenuation for each wavelength is shown in Figure 1. The 0.81 cm wavelength is quite sensitive to cloud water content and snow. The 1.36 cm wavelength can be used to detect the presence of atmospheric water vapor. The 1.66 and 2.80 cm wavelengths respond to surface moisture while both the 2.80 and 4.54 cm wavelengths can give an indication of the amount of surface vegetation.

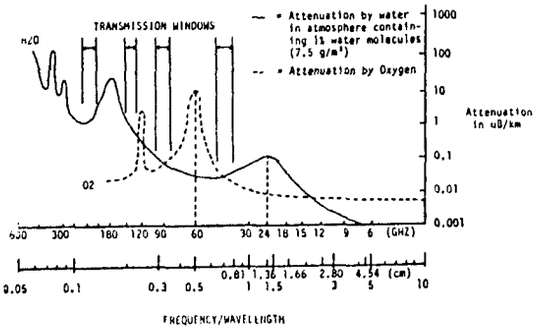

Fig. 1. Atmospheric attenuation of microwave radiation from water vapor and oxygen.

10 May was selected as the dominant case study day. Photographs were taken of images from all ten SMMR brightness temperature channels to provide a qualitative data analysis. The brightness temperatures ranged from approximately 230K to 270K, with the shorter wavelengths having the colder temperatures. Photographs of these images are given in Figures 2 and 3. The horizontal wavelength data had a greater temperature range which provided more information for pattern recognition. The resolution degradation associated with the longer wavelength data was very evident, however previous work by Newton et al. (1982) and McFarland and Harder (1983) showed that lower resolution data did not result in a loss of soil moisture sensitivity.

The GOES satellite imagery for 10 May indicated thunderstorms over most of the western half of the study area. The weather radar summary chart indicated a squall line with areas of heavy precipitation located NE - SW across the center of the study area. The climatic data showed that the area of maximum precipitation was located along the squall line, with a secondary maximum from SW Kansas northeast to the Kansas-Nebraska border. The corresponding 10 channels of SMMR imagery show the brightness temperature attenuation was primarily a result of atmospheric water vapor, rain droplets or surface moisture.

The effect of the atmosphere is clearly visible on the shorter wavelength horizontally polarized imagery. The precipitation area associated with the squall line is the area of greatest attenuation on the 0.81 cm imagery, while the precipitation area west of the squall line is the location of greatest attenuation on the longer wavelength data. It is probable that at the time of the Nimbus-7 overpass, the area of greatest surface moisture is the area west of the squall line, and the area having the greatest atmospheric moisture is along the squall line. The shorter wavelength data would have a greater degree of attenuation in the presence of atmospheric moisture than the longer wavelength data. The imagery showed that as the wavelength increased, the effect of the atmosphere became less pronounced. This imagery suggests that the optimum SMMR channel to use to sense surface moisture is the 2.80 cm horizontally polarized channel. The patterns on both the 2.80 and 4.54 cm channels were very similar, however the degraded resolution was quite apparent on the longer wavelength data.

The correlation analysis on the transformed brightness temperature values was done using data from six predominantly agricultural grid cells. The analysis was initially done for April and September, since a large percentage of the ground is essentially bare during most of these months. The correlation coefficients were compared using the Fisher's Z' transformation described by Brooks and Carruthers (1953). The correlation coefficient from the horizontally polarized normalized brightness temperature (Th / T) and the API for these months ranged from 0.84 to 0.90 for April, and 0.64 to 0.72 for September. These correlation coefficients were then compared using the Fisher's Z' transformation. The 1.66 cm data had the largest correlation coefficient for both months, but it was not significantly greater at the 0.05 level.

The polarization difference transform (Tv - Th) correlation coefficient ranged between 0.77 and 0.91 for April, and between 0.61 and 0.87 for September. The correlation coefficients from the 1.36 and 1.66 cm data were lower than the values from the horizontally polarized normalized brightness temperature transform for both months. The correlation coefficient from the 2.80 cm data was the largest, but not significantly different from either the April 0.81 or 4.54 cm data, at the 0.05 level. The September 2.80 cm correlation coefficient was significantly greater than the other values at the 0.05 level.

The correlation coefficient of the normalized polarization difference [Tv - Th /0.5 (Tv + Th)] transform ranged between 0.73 and 0.91 for April, and between 0.60 and 0.87 for September. The 2.80 cm data again had the largest correlation coefficient, with the 1.36 cm data having the lowest correlation. The April 2.80 cm correlation coefficient was not significantly larger than the other correlation coefficients, however the September value was significantly larger at the 0.05 level.

This analysis indicates that the strongest correlation was found between the polarization difference transform of the 2.80 cm wavelength SMMR brightness temperatures and the API. However, the correlation coefficients were so close that any of these transforms could be used independently to estimate the API over bare soil without the need of a surface temperature estimate.

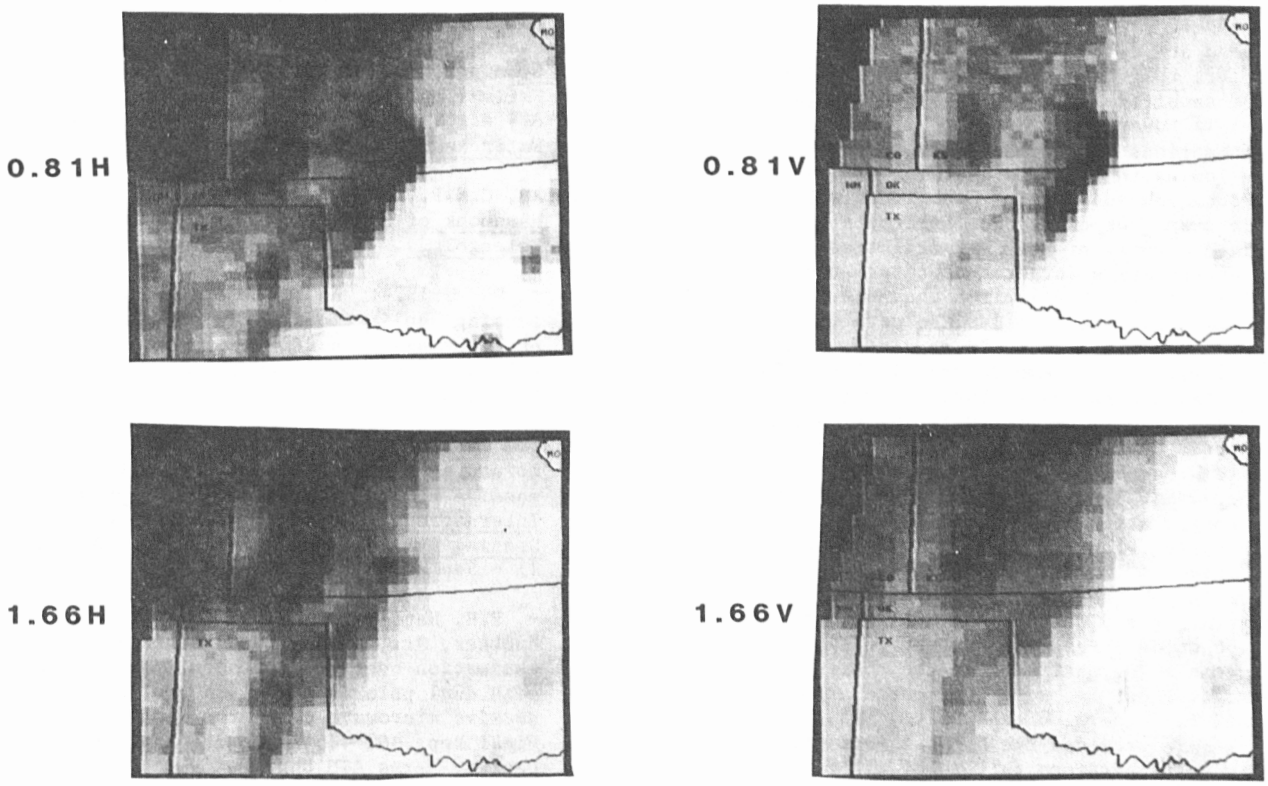

Fig. 2. SMMR Brightness temperature images for 0.81 and 1.66 cm horizontal and vertical polarizations for 10 May 1979. The 0.81 cm horizontal polarization temperatures range from 270K as a light tone to 230K as a dark tone.

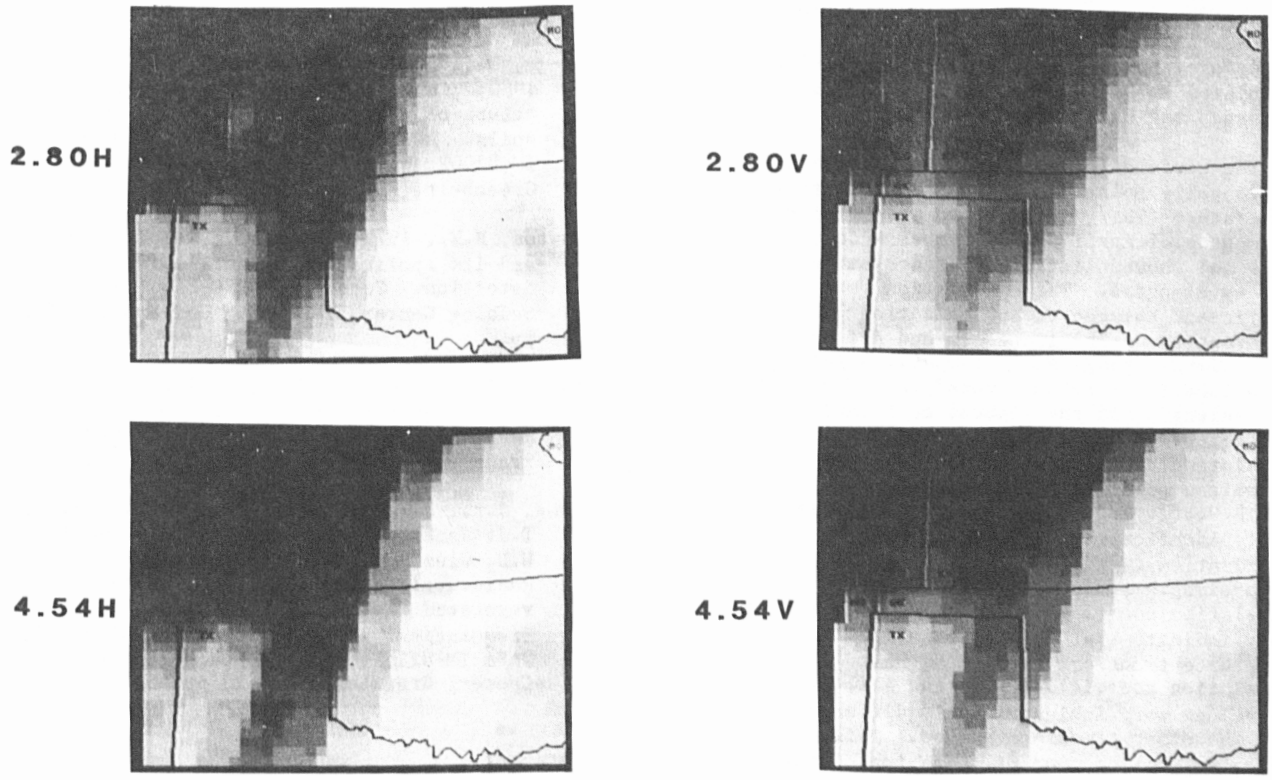

Fig. 3. SMMR brightness tmperature images for 2.80 and 4.54 cm horizontal and vertical polarizations for 10 May 1979.

6. CONCLUSIONS

There are certain environmental parameters that each microwave channel will be most sensitive to. Simultaneously using several microwave responses or transformations of the microwave responses will allow us to create a decision tree which can reduce inherent errors associated with the microwave response. The horizontally polarized channel of the SMMR brightness temperatures has a larger temperature range than the vertically polarized channels. Using the horizontally polarized data provided a greater pattern recognition over an areal brightness temperature display. The coldest brightness temperatures corresponded with areas of maximum precipitating clouds at the shorter wavelengths (0.81 and 1.36 cm), and with areas of maximum surface moisture at the longer wavelengths. The 0.81 cm imagery was strongly attenuated in the presence of precipitating clouds. The 1.36 cm imagery can be used to indicate clouds, while the 0.81 cm imagery can distinguish between precipitating and non-precipitating clouds. The 1.66 cm data responded better to the surface moisture pattern than the shorter wavelengths, but had a smaller correlation with API than the 2.80 or 4.54 cm data. The 2.80 cm data provided the highest resolution brightness temperature pattern of all five wavelengths. The horizontally polarized channel had a greater temperature range than the vertically polarized channels making the 2.80 cm horizontally polarized channel the overall best channel for determining the surface moisture pattern. The 4.54 cm data responded quite well to the surface moisture and had the least effect from the intervening atmosphere, however the degraded resolution associated with the longer wavelength data decreased the usability of this data.

The correlation coefficients between the horizontally polarized normalized brightness temperature (Th / T) transform and API for the months of April and September were very large and showed little difference among the five wavelengths. The correlation coefficient between the polarization different (Tv - Th) transform and API had both a larger range and a slightly higher value than the previous transform. The 2.80 cm wavelength had the highest correlation coefficient of the five wavelengths. The correlation coefficient between the normalized polarization difference [Tv-Th/0.5(Tv+Th)] transform and API were nearly identical to those from the polarization difference transform. The 2.80 cm wavelength again had the highest correlation coefficient. The results of this study indicate that the polarization difference transform had the highest correlation coefficient with the API, however the values were insignificantly different from the other transform values. This indicates that any one of these transforms could be used to estimate the API over bare soil without the need for an additional surface temperature estimate.

REFERENCES

Blanchard, B.J., M.J. McFarland, T.J. Schmugge, and E. Rhoades, 1980: Estimation of surface soil moisture with API algorithms and microwave emission. Water Resource. Bull., 17, 767-773.

Brooks, C.E.P., and N. Carruthers, 1953: Handbook of Statistical Methods in Meteorology. H.M.S.O., London, 410 pp.

Burgy, R.H., 1974: An assessment of remote sensing applications in hydrologic engineering. Rep HEC-RN-4, Contr DACW05-74-C-0034, Burgy and Associates, Davis, CA, 61 pp.

McFarland, M.J., and P.H. Harder, 1983: Crop moisture conditions assessment with passive microwave radiometry, Preprints International Geoscience and Remote Sensing Symposium, San Francisco, CA, Aug 31 - Sep 2.

-----, P.H. Harder III, G.D. Wilke and G.L. Huebner, Jr., 1984: Crop moisture estimation over the southern Great Plains with dual polarization 1.66 centimeter passive microwave data from Nimbus 7. Final Rep. RSC-4854. Remote Sensing Center, Texas A&M University, 142 pp.

Mo, T., and B.J. Choudhury, 1980: Diurnal variation of microwave brightness temperature of soils, Report under NASA contr. NAS 5-24350, CSC/TR-80/6003, Computer Sciences Corporation, Greenbelt, MD, 46 pp.

-----, T.J. Schmugge, and B.J. Choudhury, 1980: Calculations of the spectral nature of the microwave emission from soils. AGRISTARS Rep. SM-GO-04018, NASA TM-82002, Goddard Space Flight Center, Greenbelt, MD, 66 pp.

Newton, R.W., 1977: Microwave remote sensing and its application to soil moisture detection. Tech. Rep. RSC-81. Remote Sensing Center, Texas A&M University, 500 pp.

Njoku, E.G., and P.E. O'Neill, 1982: Multifrequency microwave radiometer measurements of soil moisture. IEEE Trans. Geosci. Rem. Sens., GE-20, 468-475.

Wang, J.R., J.E. McMurtrey, III, E.T. Engman, T.J. Jackson, T.J. Schmugge, W.I. Gould, W.S. Glazar, and J.E. Fuchs, 1981: Radiometric measurements over bare and vegetated fields at 1.4 GHz and 5 GHz frequencies. AGRISTARS Rep. SM-G1-04113, NASA TM-82151, Goddard Space Flight Center, Greenbelt, MD, 23 pp.

Wilke, G.D. and M.J. McFarland, 1984: Multispectral passive microwave correlations with an antecedent precipitation index using the Nimbus-7 SMMR. Tech. Rep. RSC-141. Remote Sensing Center, Texas A&M University, 125 pp.

-----, and M.J. McFarland, 1986: Correlations between Nimbus-7 scanning multichannel microwave radiometer data and an antecedent precipitation index. J. Climate and Appl. Meteor., 25, 227-238.

MONTH-TO-MONTH VARIABILITY OF OCEAN-ATMOSPHERE LATENT HEAT FLUX AS OBSERVED FROM THE NIMBUS MICROWAVE RADIOMETER

W. Timothy Liu

Jet Propulsion Laboratory
California Institute of Technology
Pasadena, CA 91109

1. INTRODUCTION

Evaporation from the ocean is an important component of the hydrological cycle, supplying most of the water vital to the human habitat. Evaporation also affects climate variation because it carries latent heat. In the past, large-scale latent heat flux has been compiled with meteorological reports from ships. Over vast areas of tropical and southern oceans, these data are at best able to delineate long-term means; not enough ship data exist to resolve the month-to-month variation. Spaceborne sensors have the potential of providing adequate coverage.

The warming events in the tropical Pacific, known as El Niño, have far-reaching economical and ecological consequences. The 1982-83 episode (Gill and Rasmusson, 1983), with its record intensity, provided an interesting case for ocean-atmosphere interaction study and a clear signal to test the sensitivity of spaceborne sensors. The Scanning Multichannel Microwave Radiometer (SMMR) on the satellite Nimbus-7 provided global coverage during that time. With the measurements by this sensor, monthly-mean latent heat fluxes were computed using the method suggested by Liu (1984) and Liu and Niiler (1984). These results were then compared with <u>in situ</u> measurements.

In this paper, preliminary results of the comparison are presented with some examples of the flux variation in the tropical Pacific derived from SMMR data. More comprehensive results will be published in the near future.

2. FLUX TECHNIQUE

The conventional method of estimating large-scale moisture flux is by bulk parameterization, in which the flux is related to measurements made on ships - the sea surface temperature (T_s), the wind speed (U) and the dew point temperature (T_d) measured at a reference level. The basic form is

$$E = \rho C_E U (Q_s - Q) \qquad (1)$$

where E is the moisture flux, ρ is the surface air density, Q_s and Q are the saturation mixing-ratio at T_s and T_d, respectively. The latent heat flux (LE) is the product of the moisture flux and the latent heat of vaporization L. There are a number of statistical (e.g., Anderson and Smith, 1981) and physical (e.g., Liu et al., 1979) models to evaluate the transfer coefficient C_E.

A number of spaceborne sensors are designed to measure U and T_s. No satellite sensor can measure Q, but a number of studies (e.g., Alishouse, 1983; Chang et al., 1984) demonstrated that the spaceborne microwave radiometer could measure the total water vapor in an atmospheric column (W) with accuracy comparable to those derived from radiosonde soundings. The key to the technique of estimating latent heat flux from spaceborne sensors is the relation between Q and W. Liu (1984), using radisonde reports from Bermuda, found that the first empirical orthogonal function described 65% of the variance of the twice-daily humidity soundings and 97% of variance of the monthly-mean soundings. The results suggested that one parameter (W or the humidity at any level) is adequate in predicting monthly-mean Q. In this study, a global Q-W relation, determined by Liu (1986) from 17 years of humidity soundings at 46 ocean stations, is used to derive monthly-mean Q from monthly-mean W measured by SMMR. The transfer coeffient is assumed to have a constant value of 1.2×10^{-3}.

3. DATA

SMMR geophysical parameters from January 1982 to October 1983 were obtained from Goddard Space Flight Center (GSFC). From these data, monthly mean U, W, and T_s over 2° latitude by 2° longitude areas were extracted. Data from equatorial moorings and from global ship of opportunity were used in the evaluation. The mooring data came from three buoys consecutively deployed at 95°W on the equator from January 1982 to March 1983 as part of the Equatorial Pacific Ocean Climate Studies. Scaler monthly mean wind speeds and sea surface temperatures were formed from data sampled at 15 min intervals. The ship data were archived at National Climatic Data Center as Tape Deck (TD) 1129. Three parameters - U, T_s, and T_d - were

extracted after the application of a quality control procedure described by Liu and Niiler (1985).

4. EVALUATION

In studies of climate change, the usefulness of a sensor is often judged on its sensitivities to annual and interannual variability. In Fig. 1, the temporal variations in surface level wind speed and in sea surface temperature, as measured at buoys moored at 0°, 95°W, are compared with those measured by Nimbus SMMR over an area bounded by 2°N, 2°S, 94°W and 96°W, from January 1982 to April, 1983. The period covers a strong interannual warming event (starting July 1982) superimposed on the annual cycle. Considering the difference in areal coverages, SMMR tracked the temporal variation well. There are obvious systematic differences, part of which may be due to vertical gradients in wind speed and ocean temperature. The SMMR winds are referenced to a 19.5 m height, but the buoy winds are measured at 3.8 m. The radiometer measures the skin temperature of the oceans while buoy thermometers were located about 1 m below the surface.

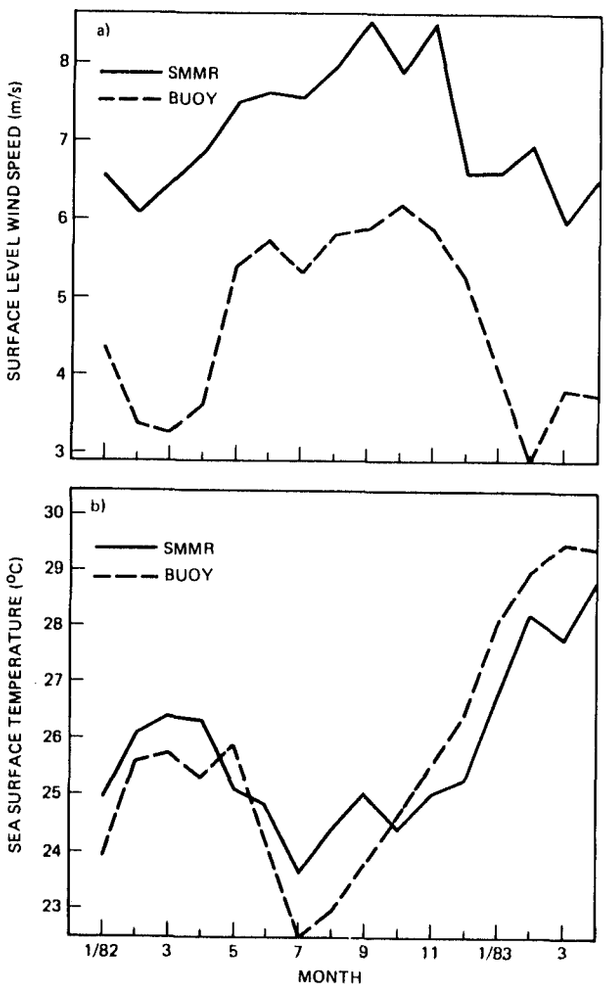

Fig. 1 Temporal variation of monthly-mean (a) wind speed and (b) sea surface temperature, measured at buoys moored at 95°W on the equator and those measured by Nimbus/SMMR averaged over an area bounded by 2°N, 2°S, 94°W and 96°W.

There are no good *in situ* measurement to serve as an evaluation standard for LE. The quality of routine meteorological reports from merchant ships is demonstrated in Fig. 2. The ship data, TD 1129, were searched to locate all pairs of ships within an hour and 10 nautical miles (18.5 km) of each other. Latent heat fluxes were computed from each pair and compared. Data between June and August, 1982, are shown in Fig. 2. Of the 1304 pairs, the mean and standard deviation of the difference are 45 and 71 W/m^2, respectively. Corresponding values for 1005 pairs found during December, January and February, 1982, are 57 and 87 W/m^2. Despite the poor quality of ship data, they provide the only reference to evaluate latent heat flux computed from satellite data.

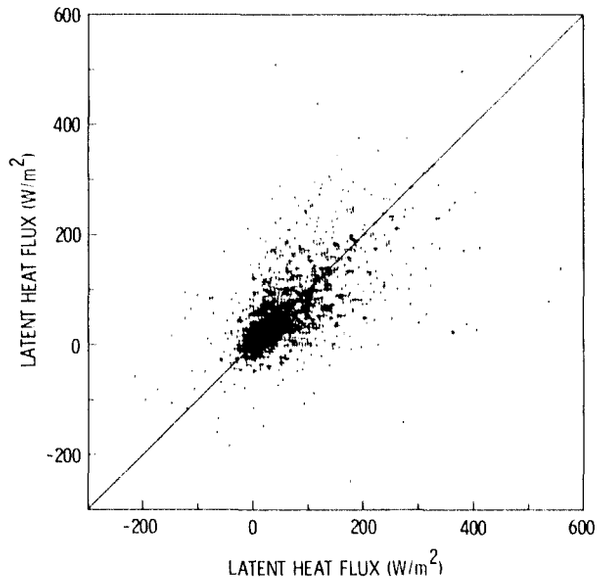

Fig. 2 Comparison of latent heat fluxes computed from reports of two ships within an hour and 18.5 km of each other during June-August 1982. Solid line represents perfect agreement.

Fig. 3 shows the comparison of LE computed from SMMR data and those computed from ship reports for a typical month, June 1982. Each point is a monthly average over a 2°x2° area. Only those areas with more than 10 ship reports during the month were compared. Fig. 4 shows the locations of these 2°x2° areas. In coastal areas, there were ship reports, but no satellite data because of land-contamination of sensor signals. Over most of the tropical and southern oceans, there were satellite data, but not enough ship reports. The difference between satellite and ship measurement of a parameter was found to depend not only on the parameter but also on other parameters measured by the same sensor ("cross-talk" between channels).

The absolute accuracy of satellite data may change due to sensor drifts or algorithm improvement. In long-period application of satellite data, calibration with stable *in situ* measurements is often required. Although ship data are not ideal, they are the only data available with long historical records covering reasonable range of conditions. A subset of the

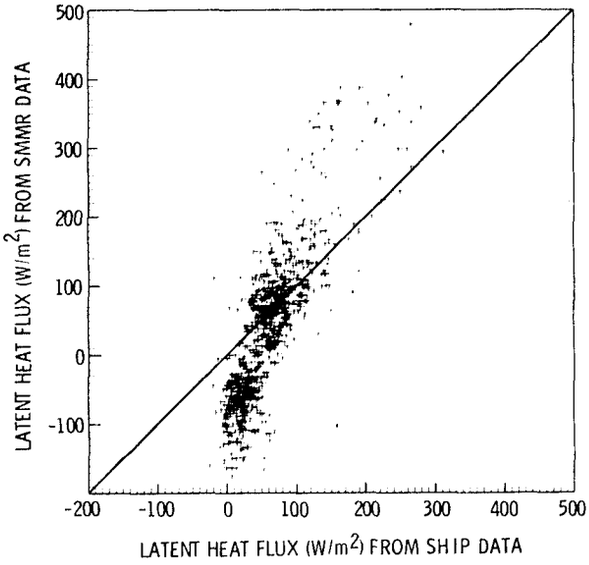

Fig. 3 Comparison of latent heat fluxes computed from ship reports with those computed from official Nimbus/SMMR geophysical parameters for June, 1982. Each point is a 2°x2°-monthly mean. The solid line represents perfect agreement.

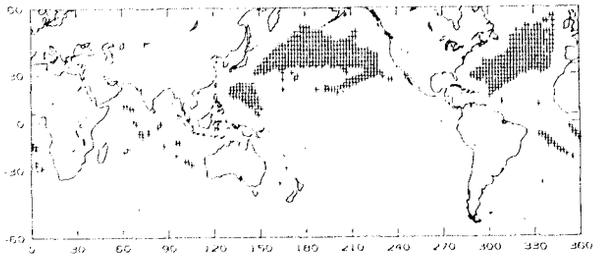

Fig. 4 Locations of 2°x2° areas selected for the comparisons in Fig. 3 and 5.

ship data was used to calibrate SMMR data in this study. Statistical relations were established to describe the systematic differences. With wind speed, for example, the difference in wind speed $\delta U = U' - U''$ was expressed as:

$$\delta U = C_1 + C_2 U' + C_3 U'^2 + C_4 T_s' + C_5 W'$$

where single primed parameters are SMMR measurements and double primed parameters are ship measurements. The coefficients C were determined from four months of data in 1982 (January, April, July, and October) using only monthly-2°x2° means in areas with more than 10 ship reports. A forward stepwise regression technique (Draper and Smith, 1981) was used and only those terms with coefficient passing the 0.05 significant level test were included. Similar relations were derived for T_s and Q. Before Q' were computed with the relation of Liu (1986), W' were adjusted to radiosonde data at a few locations in the Pacific. Heat fluxes computed from the corrected SMMR data were compared with those from ship data in Fig. 5. The data range is about 400 W/m^2 and the scatter is 28.7 W/m^2. At least part of the scatter is caused by noisy ship data.

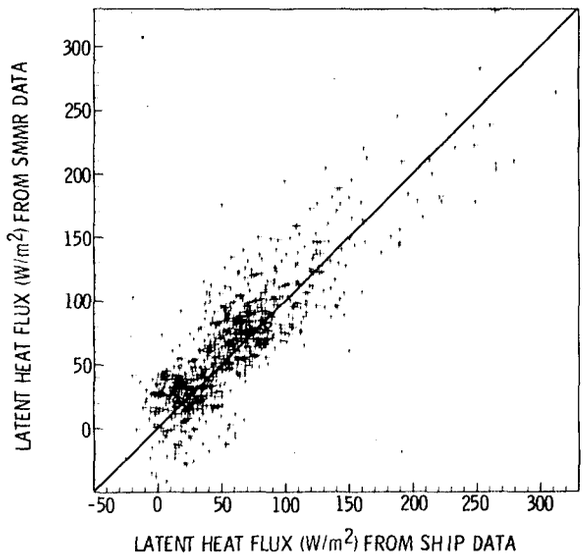

Fig. 5 Same as Fig. 3 except for recalibrated Nimbus/SMMR parameters.

5. FLUX VARIATION

The evolution of the distribution of LE and related parameters in the tropical Pacific during the 1982-83 period were described by the SMMR data. Fig. 6 and 7 show the temporal-zonal variations of T_s and their anomalies. The critical pool of warm water as defined by the 29°C isotherm moves eastward from a region west of the date-line to the Galapagos. In the east, the anomalies remain greater than 3°C for almost a year. The anomalies were computed using climatology by Reynolds (1982). The information given by SMMR agrees closely with what we learned from operational data (Gill and Rasmusson, 1983).

Fig. 8 shows the distribution of U, humidity difference $(Q_s - Q)$, and LE for February, 1982, before the onset of El Nino. The Intertropical Convergence Zone (ITCZ) near the equator and the South Pacific Convergence Zone to the southwest are marked by low U. The distribution of LE follows the distribution of the humidity difference. Similar distributions for April, 1983, towards the final phase of the episode, are shown in Fig. 9. For most of the tropical Pacific, the humidity difference is very uniform. There is only one zonally oriented belt of very low U near the equator with strong wind speed gradients north and south of it. The distribution of LE, in this case, appears to be dominated by the distribution of U.

The time rate of change of T_s $(\delta T_s/\delta t)$ depends on the balance of heat advected into the upper ocean and the heat exchange with the atmosphere. In areas where the influence of ocean dynamics is weak and the variability of other components of ocean-atmosphere heat exchange (radiation and sensible heat fluxes) are relatively small, $\delta T_s/\delta t$ would be governed by LE. The temporal-zonal variations of $\delta T_s/\delta t$ are shown in Fig. 10a. The rate was computed as the gradient of the linear regression on three consecutive months of T_s. Fig. 10b shows the corresponding variations in LE. Both are com-

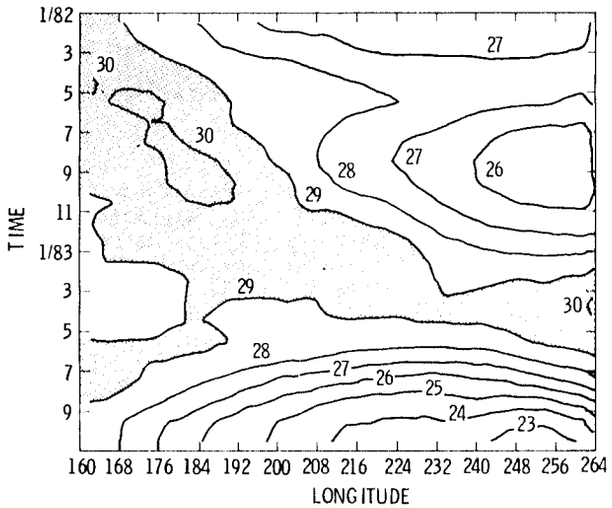

Fig. 6 Temporal-zonal variation of 4°x4°-mean sea surface temperature centered on the equator. Isotherms are in degrees Celsius.

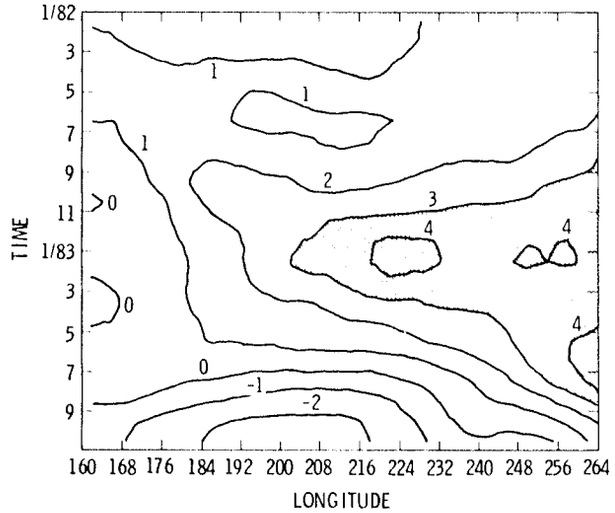

Fig. 7 Same as Fig. 6 except for sea surface temperature anomalies.

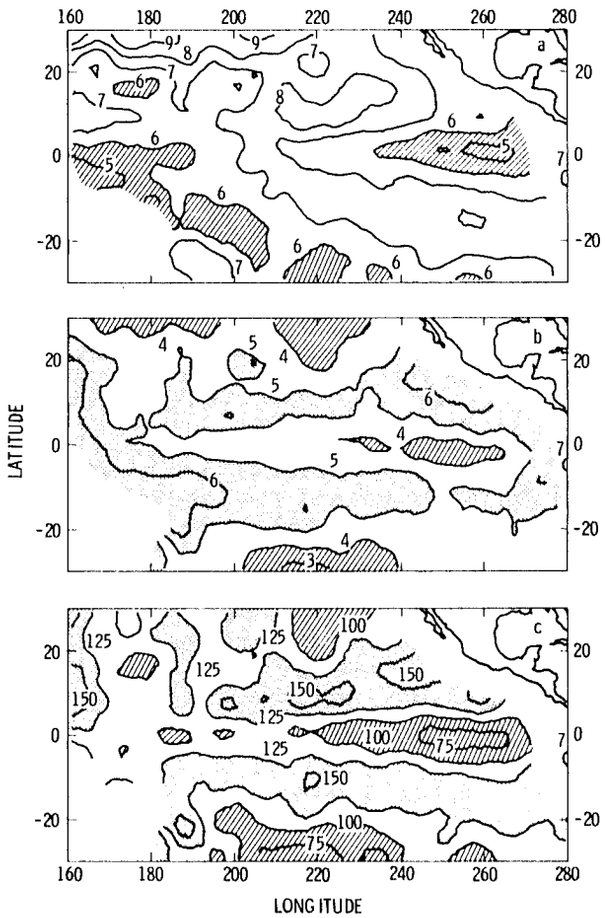

Fig. 8 Distribution of mean (a) wind speed, (b) humidity difference, and (c) latent heat flux for February 1982. Contour intervals are in m/s, 10^{-3}, and W/m^2, respectively.

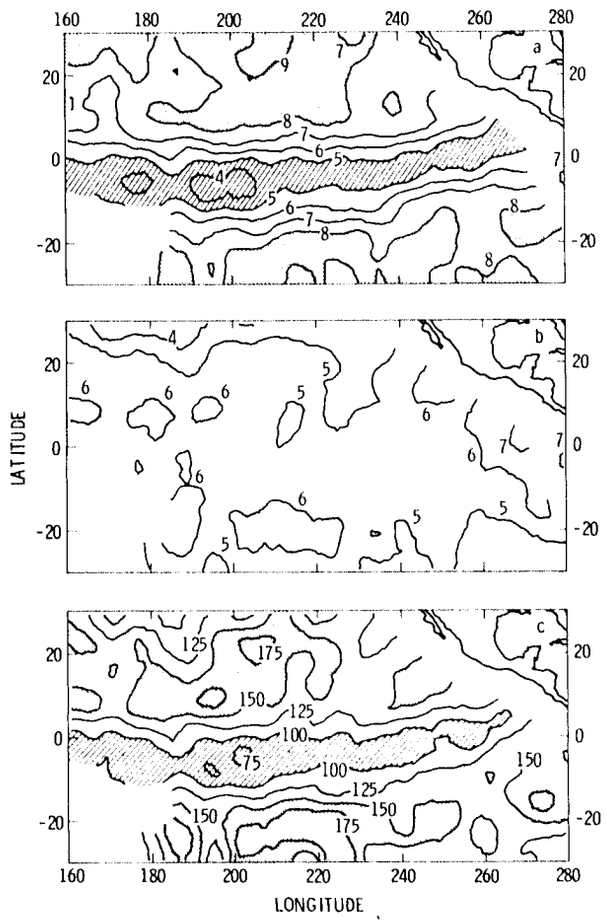

Fig. 9 Same as Fig. 8 except for April 1983.

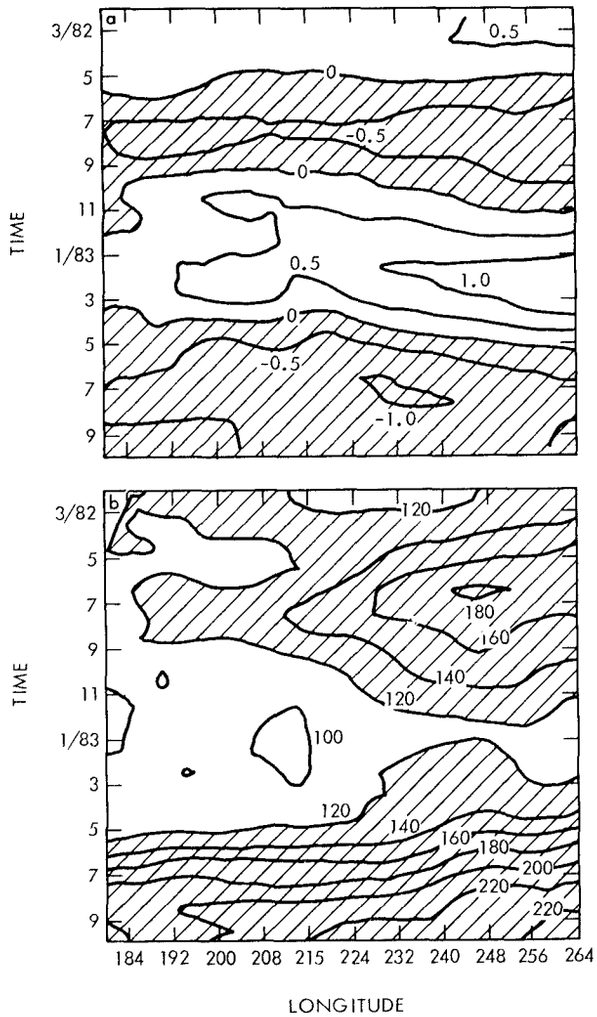

Fig. 10 Temporal-zonal variation of 4°x4°-mean (a) time rate of change of sea surface temperature and (b) latent heat flux, centered on 10°S. Contour intervals are in °C/month and W/m^2, respectively.

puted as 4°x4°-monthly means centered on 10°S from SMMR data. The patterns of high LE are very well related to patterns of T_s cooling and the patterns of low LE are related to T_s warming. The figures demonstrate that LE is a dominant factor in the change of T_s in this region. At the equator or near an atmospheric convergence zone, ocean currents and cloud variability have stronger influences and the relation between LE and $\delta T/\delta t$ are not expected to be as prominent.

6. CONCLUSION

The results demonstrate that spaceborne microwave radiometers measure monthly mean latent heat flux to within 30 W/m^2 of those derived from ship reports. Due to the lack of a good evaluation standard, the absolute accuracy could not be ascertained, but satellite measurements could, at least, be useful in extrapolating information on LE both in space and in time. The Nimbus/SMMR was found to be useful in describing the month-to-month variability of LE and related parameters during the 1982-83 El Niño.

A research project is underway to estimate the net ocean-atmosphere heat exchange (radiative and latent heat flux) over tropical oceans using satellite data (Liu and Niiler, 1985).

7. ACKNOWLEDGMENTS

Dr. Paul Hwang of the Goddard Space Flight Center kindly helped in acquiring the Nimbus/SMMR data and Dr. David Halpern of University of Washington generously made the equatorial mooring data available. This study was performed at the Jet Propulsion Laboratory, California Institute of Technology, under a contract with the National Aeronautics and Space Administration.

8. REFERENCES

Alishouse, J.C., 1983: Total precipitable water and rainfall determinations from the SEASAT Scanning Multichannel Microwave Radiometer. J. Geophys. Res., 88, 1929-1935.

Anderson, R.J. and S.D. Smith, 1981: Evaporation coefficient for the sea surface from eddy flux measurements. J. Geophys. Res., 86, 449-459.

Chang, H.D., P.H. Hwang, T.T. Wilheit, A.T.C. Chang, D.H. Staelin, and P.W. Rosenkranz, 1984: Monthly distributions of precipitable water from the NIMBUS 7 SMMR data. J. Geophys. Res., 89, 5238-5334.

Draper, N.R. and H. Smith, 1981: Applied Regression Analysis, 2nd Edition, John Wiley & Sons, New York, Chapter 6.

Gill, A.E. and E.M. Rasmusson, 1983: The 1982-83 climate anomaly in the equatorial Pacific. Nature, 306, 229-234.

Liu, W.T., K.B. Katsaros, and J.A. Businger, 1979: Bulk parameterization of air-sea exchanges of heat and water vapor including the molecular constraints at the interface. J. Atmos. Sci., 36, 1722-1735.

Liu, W.T., 1984: Estimation of latent heat flux with Seasat-SMMR, a case study in N. Atlantic. Large-Scale Oceanographic Experiments and Satellites, C. Gautier and M. Fieux eds, Reidel Press, Dordrecht, 205-221.

Liu, W.T. and P.P. Niiler, 1984: Determination of monthly mean humidity in the atmospheric surface layer over oceans from satellite data. J. Phys. Oceanogr., 14, 1451-1457.

Liu, W.T. and P.P. Niiler, 1985: Tropical Ocean and Global Atmosphere (TOGA) Heat Exchange Project - A Summary Report. JPL External Publication 85-49, Jet Propulsion Laboratory, Pasadena.

Liu, W.T., 1986: Statistical relation between precipitable water and surface level humidity over global oceans. Mon. Wea. Rev., submitted.

Reynolds, R., 1982: A Monthly Averaged Climatology of Sea Surface Temperature. Tech. Rep. NWS 31, Nat. Oceanic Atmos. Admin., Silver Springs.

OBSERVATION OF EL NINO BY THE NIMBUS-7 SMMR

P.H. Hwang, D.S. MacMillan[1], C.C. Fu[1], S.T. Kim[1], Daesoo Han[1], P. Gloersen

NASA/Goddard Space Flight Center, Greenbelt, Maryland 20771

1. INTRODUCTION

Since October 1978, the Scanning Multichannel Microwave Radiometer (SMMR) on the Nimbus-7 satellite has been in continuous one-day on/one-day off operation. The instrument is described in the Nimbus-7 User's Guide by Gloersen and Hardis (1978). It measures microwave radiation from the earth's surface and the surrounding atmosphere at five frequencies (6.6, 10.7, 18, 21, and 37 GHz) in both the horizontal and vertical polarizations. These brightness temperatures are used to infer several geophysical parameters over the oceans: sea surface temperature (SST), water vapor, sea surface windspeed, and sea ice concentrations. This is done by using physical models that describe how brightness temperatures depend upon these geophysical parameters. The 6.6 and 10.7 GHz channels are the most sensitive to surface quantities (SST and surface windspeed); whereas, the 18, 21, and 37 GHz channels are more sensitive to atmospheric moisture contents such as integrated water vapor and liquid water (see e.g., Wilheit and Chang, 1980). Since the spatial resolution of the instrument is proportional to wavelength, the resolutions for the SST, windspeed, and water vapor retrieval algorithms described in the next section are 156 km, 98 km, and 60 km respectively.

There are several advantages of using SMMR to retrieve geophysical parameters. First, microwave remote sensing can be done both day and night through non-precipitating clouds in contrast to infrared/visible remote sensing such as with the AVHRR. This is particularly a problem during the 1982-83 El Nino period when AVHRR gave a low estimate of SST because of the presence of El Chichon aerosols (Strong, 1983). The second advantage is that SMMR covers the whole globe in six calendar days while there are few ship or buoy surface data available in the tropical and southern ocean. A third is that the Nimbus-7 SMMR has a seven year history of measurements. This history consists of the geophysic parameters and the brightness temperatures used to derive them. SMMR is the only instrument which measures water vapor contents and surface windspeed before, during, and after the El Nino period.

In this paper we assess the quality of SMMR-derived SST, water vapor, and windspeed and study these parameters to improve our understanding of the El Nino event of 1982-1983. Our object is to demonstrate consistency between SMMR retrievals and other observations made during the El Nino period. In Section 2, a description of the data which we have analyzed is given. Section 3 consists of an analysis of the SST, wind speed, and water vapor retrievals during El Nino. We describe the features of the anomaly fields for these parameters. The connections between these fields are examined. In addition we find that our anomaly fields are qualitatively consistent with outgoing longwave radiation (OLR) anomaly fields and wind vector anomaly fields.

2. DATA DESCRIPTION

To study El Nino, we computed the anomaly fields for SST, water vapor, and windspeed. The calculation of SST was done with a retrieval algorithm which was discussed by Wilheit et al. (1984). The water vapor retrieval algorithm was discussed by Rosencranz (1982). Fine tuning of this algorithm which uses the 18, 21, and 37 GHz channels is described by Chang et al. (1983). Fu and Hwang (1983) developed the surface windspeed algorithm with the 10 and 37 GHz channels.

For each month in the period January 1982 - December 1983, monthly mean anomaly fields were computed. A climatological monthly mean was subtracted from each monthly average in this period to get the monthly anomaly. For SST, we have used the long-term climatology developed by Robinson (1976). Since no such climatology exists for wind or water vapor, 3-year monthly averages (1979-1981) of these parameters derived from SMMR were computed.

Three representative monthly anomaly maps of the Pacific region are shown in Figures 1-3. These maps were produced by averaging SMMR data into a $2^{\circ} \times 2^{\circ}$ grid. It should be noted that SST in Figure 1 is not retrieved closer than 600 km from the land. Near land boundaries there is land contamination in

[1]SASC Technologies, 5809 Annapolis Road, Hyattsville, Maryland 20784

radiance measurements arising from the antenna sidelobes. This is especially true in the 6.6 GHz channels, which are the primary source of SST information.

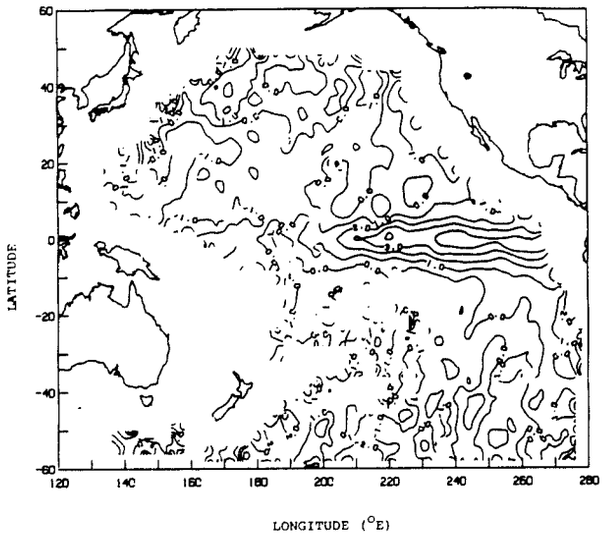

Figure 1. Monthly mean sea surface temperature anomaly (°C) in November 1982.

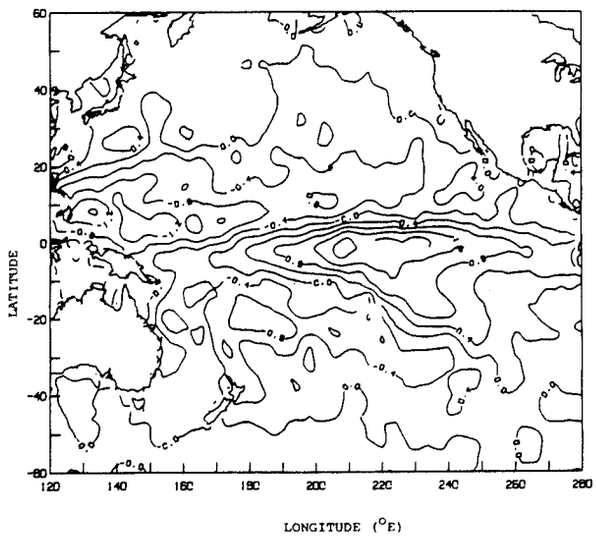

Figure 2. Monthly mean water vapor anomaly (gm/cm^2) in January 1983.

We have also constructed time-longitude cross sections in Figures 4, 5, 7 for each anomaly field averaged over the 5°S-5°N latitude band. These maps illustrate the evolution of the anomalies. The water vapor anomaly in Figure 5 was computed only up to June 1983. After this date, the behavior of the SMMR 21 GHz channels changed significantly, resulting in abnormally low water vapor estimates. An alternative method of retrieval will be used to obtain water vapor after that date.

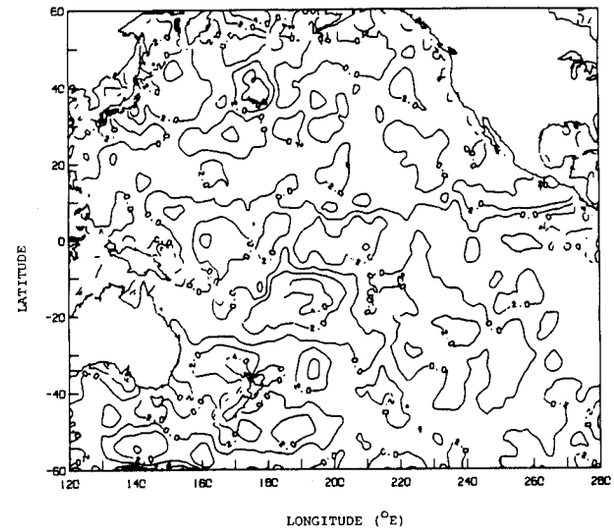

Figure 3. Monthly mean surface windspeed anomaly (meters/sec) in November 1982.

3. ANALYSIS

SMMR observations show that the onset of the El Nino sea surface warming began as early as May-June 1982 along the coast of South America. This can be seen in the longitude-time cross section in Figure 4. This warming spread westward to produce a peak of 3.5°C at 240°E in November 1982. A secondary warming appeared along the South American coast from May-September 1983. The anomaly retrieved by SMMR was between 4.5 and 5°C at 270°E. It is clear from Figure 4 that the anomaly is higher between 270°E and the coast of South America.

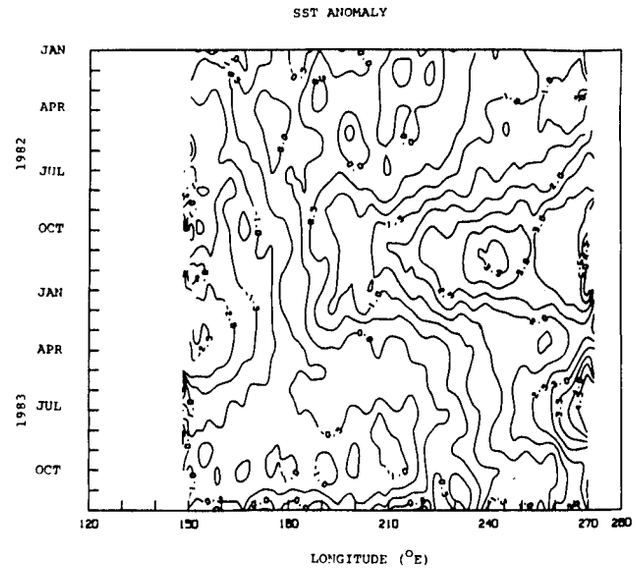

Figure 4. Time-longitude cross section of the sea surface temperature anomaly field (°C) for the latitude band 5°S-5°N from January 1982 to December 1983.

In response to SST warming a positive water vapor anomaly (Figure 5) began to develop along the equator in June 1982 just west of the dateline. This anomaly moved eastward to peak at 1.6 gm/cm^2 in December 1982 and January 1983 at about 220°E. This positive anomaly was accompanied by the development of negative anomalies to the west, north, and south. In a normal (non-El Nino) year, there is a large amount of water vapor in the western Pacific region centered around 140°E and relatively less water vapor further east from 180°E - 270°E. However, one can see the reduction of water vapor in the region from 120°E - 140°E in Figure 5 which began in June 1982 and reached a minimum of -1.2 gm/cm^2 in January 1983 (Figure 2). In general, the water vapor anomalies that we see are similar to those found by Prabhakara et al. (1985).

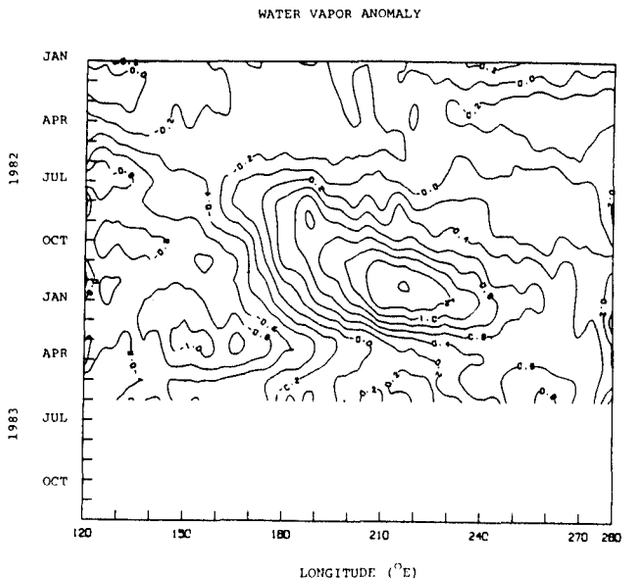

Figure 5. Time-longitude cross section of the water vapor anomaly field (gm/cm^2) for the latitude band 5°S-5°N from January 1982 until June 1983.

Qualitative agreement of water vapor anomalies and OLR anomaly maps can easily be seen. The positive (negative) anomalies in water vapor correspond closely to the negative (positive) anomalies in OLR which indicate above (below) average cloudiness and rainfall. For January 1983, the water vapor anomaly field in Figure 2 resembles the OLR anomaly field (Ardanuy and Kyle 1986) in Figure 6 obtained from the ERB instrument also on the Nimbus-7 satellite. Specifically, there is a strong positive OLR anomaly north of Indonesia at 130°E along with a large negative water vapor anomaly. The maximum positive anomaly in water vapor in the central Pacific (210°E) coincides with a strong negative OLR anomaly center. There is a similar correspondence between anomaly centers that lie to the north and south of this point. The eastward movement of the water vapor (Figure 5) and OLR anomaly centers suggests that the convective zone of the western equatorial Pacific also shifted eastward as the El Nino peaked.

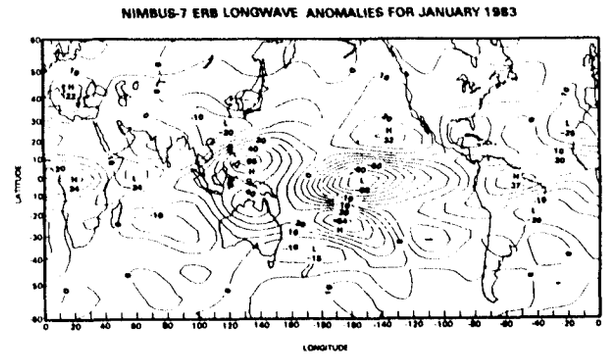

Figure 6. Monthly mean anomaly (W/m^2) of the outgoing longwave radiation for January 1983 from measurements made by the Nimbus-7 ERB instrument. (From Ardanuy and Kyle (1986)).

In the time-longitude cross section of windspeed in Figure 7, one can see that a negative windspeed anomaly appears about July 1982 at the dateline and progresses eastward. Its maximum value is -2.5 m/sec in the period October 1982 to January 1983 at 210°E. There are positive anomalies to the south (+4 m/sec) and to the west and north of this negative anomaly. This can be seen in Figure 3 for November 1982.

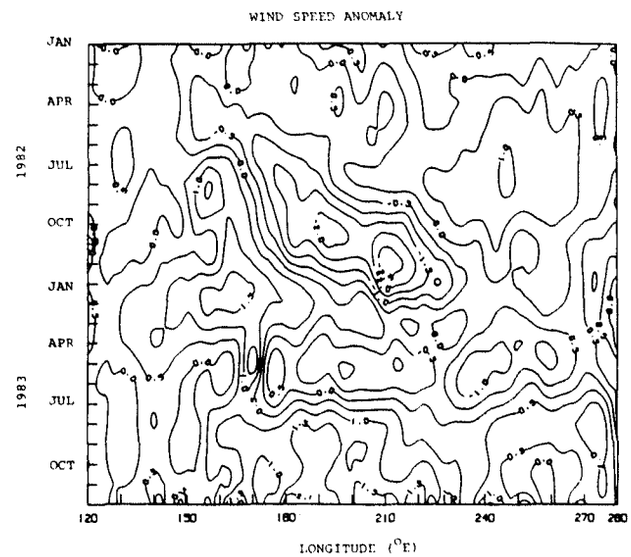

Figure 7. Time-longitude cross section of surface windspeed anomaly field (meters/sec) for the latitude band 5°S-5°N from January 1982 until December 1983.

When considering the windspeed anomalies, one must remember that there is no wind direction information. A sign change in the westerly component of the wind vector, (i.e. a shift from easterly to westerly) can correspond to a small change in the windspeed anomaly. This explains why negative windspeed anomalies are seen in the central Pacific. In July and August 1982, the mean wind velocity had a westerly component to the west of the dateline after having reversed direction in June 1982 (NOAA Climate Analysis Center (CAC) (1983), Rasmusson and Wallace (1983)). The growth of this anomaly at 850 mb is shown in Figure 8 from CAC (1983). It corresponds closely to the negative anomaly that is seen in Figure 7 for windspeed.

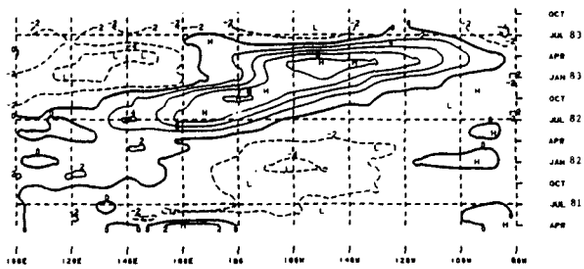

Figure 8. Time-longitude cross section along the equator (5°N-5°S) of the 850 mb zonal (westerly) wind anomaly. Units are meters/sec. (Reproduced from CAC (August 1983)).

Comparisons of SST, water vapor, and wind speed anomaly fields provide some correspondences. An important correlation is that between SST and water vapor anomalies. The anomalously warm SST (Figures 1, 4) in the central and eastern Pacific promote increased convection which then transports more water vapor into the atmosphere (Figures 2, 5). The negative windspeed anomaly in Figure 7 between 180°E and 230°E corresponds in Figure 5 to the large positive water vapor anomaly in the same place. In addition, there is a large negative water vapor anomaly of -.8 gm/cm^2 and a positive windspeed anomaly of 4-5 m/sec at (20°S, 200°E) in November 1982 (Figure 3). A well-defined region of negative water vapor anomalies (-1.2 to -.4 gm/cm^2) extends from Indonesia across the Pacific to Mexico (see Figure 2 for January 1983). This corresponds to a similar region of positive windspeed anomalies in December 1982 and January 1983. The 1000 mb anomalous vector wind field in the CAC (1983) for January 1983 shows that there is an anomalous low-level convergence into a region below the equator at about 190°E-230°E. This region coincides with the area where the maximum water vapor anomaly is seen.

The time series behavior of the central Pacific water vapor and windspeed anomalies is similar to the Southern Oscillation index (difference of the anomaly pressures between Tahiti and Darwin, Australia) and the 850 mb trade wind index (easterly anomaly from 180°E-220°E) reported by the CAC (1983). These indices move into the negative phase of their oscillations in May-June 1982, peak in December 1982 - January 1983, and return to zero June 1983. Though the time series is not explicitly plotted, this behavior (with opposite sign) is evident particularly for the positive water vapor anomaly that develops between 180°E and 230°E (Figure 5). Therefore, it should be useful to define water vapor and windspeed anomaly indices as additional measures of the Southern Oscillation.

4. CONCLUDING REMARKS

The SMMR data set provides a continuous historical record of SST, water vapor and surface windspeed starting in November 1978 with which to study the mechanism of El Nino. We are using this record to study the onset of El Nino including the years prior to 1982. In this paper, attention has been focused on the El Nino phenomenon in the equatorial Pacific region from 120°E to the South American coast. However there are other regions, for example in the Atlantic and Indian Oceans, where there is significant anomalous behavior. Though the discussion here has been qualitative, it provides a picture of the evolution of El Nino as reflected in the relationships of SST, atmospheric water vapor content, and surface windspeed.

5. ACKNOWLEDGEMENTS

The authors would like to thank Dr. Hyo Duck Chang for helpful discussions and Ms. Cherrie Johnson for typing and editing the manuscript.

6. REFERENCES

Ardanuy, P.E., and H.L. Kyle, 1986: El Nino and outgoing longwave radiation: observations from Nimbus-7 ERB. Mon. Wea. Rev, 114, In press.

Chang, H.D., P. Hwang, T.T. Wilheit, A.T.C. Chang, D.H. Staelin, and P.W. Rosencranz, 1983: Monthly distributions of precipitable water from the Nimbus 7 SMMR Data. J. Geophys. Res., 89(D4), 5328-5334.

NOAA, 1983: Climate Diagnostics Bulletin NOAA. Climate Analysis Center, Washington, D.C.

Fu, C.C. and P. Hwang, 1983: Sea surface wind speed observed by the Nimbus-7 SMMR. EOS, Transactions, American Geophysical Union, 64(45), 732.

Gloersen, P., and L. Hardis, 1978: Scanning multichannel microwave radiometer (SMMR) experiment. Nimbus-7 User's Guide. C.R. Madrid, Ed., NASA/Goddard Space Flight Center, Greenbelt, Maryland, 213-245.

Prabhakara, C., D.A. Short, B.E. Vollmer, 1985: El Nino and atmospheric water vapor: observations from Nimbus-7 SMMR. J. Climate Appl. Meteor., 24, 1311-1324.

Rasmusson, E.M. and J.M. Wallace, 1983: Meteorological aspects of the El Nino/Southern Oscillation. Science, 222, 1195-1202.

Robinson, M., 1976: Atlas of North Pacific Ocean monthly mean temperature and mean salinities of the surface layer. Reference Publication 2, Naval Oceanographic Office, Washington.

Rosencranz, P.W., 1982: Inversion of data from diffraction limited multiwavelength remote sensor. 2. Nonlinear dependence of observables on the geophysical parameters. Radio Sci., 17, 245-256.

Strong, A.E., 1983: Satellite derived sea surface temperature errors due to the El Chichon aerosol cloud. Tropical Ocean-Atmosphere Newsletter, No. 18, 14-15 (available from JISAO, University of Washington AK-40, Seattle, Washington).

Wilheit, T.T., and A.T.C. Chang, 1980: An algorithm for retrieval of ocean surface and atmospheric parameters from the observations of the scanning multichannel microwave radiometer (SMMR). Radio Sci., 15, 525-544.

Wilheit, T.T., J. Greaves, J. Gatlin, D. Han, B.M. Krupp, and A.S. Milman, 1984: Retrieval of ocean surface parameters from the scanning multichannel microwave radiometer on the Nimbus-7 satellite. IEEE. Trans. Geosci. Remote Sensing, GE-22, 133-143.

6.1

PATTERN RECOGNITION ANALYSIS OF SATELLITE DATA FOR TROPICAL CYCLONE MOTION AND INTENSITY FORECASTS

Herbert Hunter, Edwin Nunez, Llyle Barker

Nichols Research Corporation
Huntsville, Alabama

Ed Rodgers

Laboratory for Atmospheres
NASA Goddard Space Flight Center
Greenbelt, Maryland

1. INTRODUCTION

It is generally accepted that the large-scale circulations in the troposphere surrounding a tropical cyclone act as the steering current for the storm and are best approximated by mid-tropospheric winds. However, since these circulations are often not accurately described, forecasting tropical cyclone motion is a difficult task, particularly for storms that are undergoing recurvature. This is because rawinsondes are too widely spaced in areas where storms usually exist and operational analysis methods are inadequately tuned in sparse data regions. Better definition of the initial tropical cyclone environment is needed to improve motion forecasts. Satellite measurements are a major potential data source.

This study evaluates the usefulness of GOES IR and TOVS measurements from satellites for tropical cyclone motion forecasting. This satellite data: 1) can be related to the atmospheric circulation surrounding the storm, 2) are available for a sufficiently large number of cyclones to derive statistical models, and 3) can be obtained operationally. The satellite infrared measurements of cloud areas and clear regions provide an indicator of the position and the strength of the large-scale circulation features surrounding a tropical cyclone (Shenk and Rodgers, 1978) and, therefore, are related to the middle tropospheric flow. These circulation features include baroclinic zones in the westerlies, tropical convection systems (e.g., ITCZ), cirrus associated with jet streams and clear areas associated with subtropical and midlatitudinal anti-cyclones. Furthermore, infrared measurements of the tropical cyclone's central dense overcast (CDO) may be related to storm motion since a relationship has been demonstrated between storm intensity and motion. The relationship was suggested by Rossby (1948). He indicated that larger and more intense storms have a tendency to accelerate northward more rapidly than smaller and weaker storms due to a large radius of maximum surface winds and therefore, a large β effect.

A relationship between the CDO characteristics and future changes in storm intensity has been demonstrated by Gentry et. al. (1980). They found that there is a relationship between the storm maximum wind speed at a future time and satellite measured equivalent blackbody temperatures (T_{BB}) of the storm's CDO. Latent heat release (LHR), which is essential to the maintenance and intensification of tropical cyclones at the later stages of development (Palmen and Riehl, 1957, and Riehl and Malkus, 1961), can be inferred from the areal extent and height of the CDO as measured from infrared sensors.

It would be even more desirable to have a direct measurement of the middle tropospheric circulation from satellite data. A nearly direct estimate can be made from cloud motions, determined from geosynchronous satellite image sequences, mostly at the 950 and 200 mb levels in the tropics. In the midlatitudes, the middle tropospheric circulation can be derived from the mass field through the thermal wind relationship using satellite-derived temperature profiles. Chan et. al. (1980) have derived the temperature gradients and, therefore, vertical wind shear profiles around 13 tropical cyclones by using the Nimbus-6 Scanning Microwave Spectrometer (SCAMS) measurements. These measurements were used to indicate whether in 24 hr. a tropical cyclone moved to the left or right, or not at all, from its present course with about an 80% certainty. The TOVS sounding products offer the opportunity to obtain moisture and mean layer temperature profiles from the surface to 200 mb. These products also provide cloud cover, ozone and cloud free 11m radiation fields which were evaluated in this study.

An objective empirical analysis technique was employed to investigate the extent to which satellite obtained measurements of a tropical cyclone and its environment can be used to predict cyclone motion. A similar approach has been successfully used with Nimbus-5 microwave data to estimate future tropical cyclone intensity from inferences of the rainfall rate distribution in areas within and immediately surrounding a cyclone (Hunter et. al., 1981). Similarly, cyclone motion has been estimated from IR derived cloud top temperatures from NIMBUS and NOAA polar orbiting satellites (Hunter et. al. 1984). The data in the present study were examined alone and in conjunction with other readily available non-satellite climatological and persistence

variables for each storm. These predictors are similar to those used in the National Hurricane Center (NHC) CLIPER model. In this study, these will be referred to as the (Nichols Research Corporation) NRC CLIPER predictors. The performance obtained using the NHC CLIPER model will be compared and major differences between the NRC and NHC CLIPER performances will be related to differences in the models.

This paper will describe how the satellite derived data were processed to optimize their possible predictive value, the technique that was used in developing the regression algorithms, and the results of testing these algorithms using the Lachenbrach and Mickey (1968) U-method independent test procedure.

Homogeneous (i.e., identical observations) data sets are used for the comparisons presented. These comparisons include: 1) a comparison of the NHC and NRC CLIPER model performance, 2) a comparison of the NHC CLIPER performance and official forecast performance, 3) a comparison of the NRC CLIPER with the NRC CLIPER plus satellite fields, and 4) a comparison of NRC CLIPER forecasts with satellite only forecasts.

2. DATA DESCRIPTION AND SAMPLING METHODS

The satellite data used in this study was obtained from the GOES IR (11 micron) channel and the TOVS archived data described by Gibson (1984) and Kidwell (1983). The GOES data was supplied in a gridded format and was navigated using the data supplied on the tapes. The gridding for the GOES data provided a resolution of 4 km which was considerably higher than the 150 km utilized in this study. Thus, each of the grid point values in this study was obtained by averaging 9 adjacent points. The TOVS data products are supplied in an ungridded format, where the latitude and longitude of each observation is supplied along with the measured values and computed data products. Since these points are at different earth locations for each data set and have a variable resolution, it was necessary to develop a gridding program which interpolated between the nearest available data to obtain the desired 195 grid points. The number of data points available within the region covered by the grid range from approximately 150 to 1000. Due to the variable resolution of this data, in some places a grid point represented the averaging of a number of nearby points whereas in other regions, the grid required interpolation over distances sometimes larger than the distance between two grid points.

The grid used in this study is shown in Fig. 1 and extends for a distance of 1950 nmi in latitude and 2250 nmi in longitude. A spacing between the grid points in both a latitude and longitudinal directions is 150 nmi. The center of the storm is always placed 7½° north and 12½° west of the southeast grid corner. The grid is always oriented so that north is at the top.

In addition to the gridded satellite measurements, there are 14 non-gridded primarily CLIPER derived predictors which are appended to the satellite data for the satellite plus CLIPER analyses and which, when used by them-

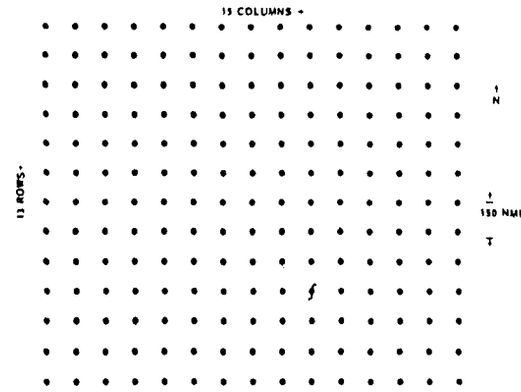

FIGURE 1. SPACIAL SAMPLING GRID USED FOR EACH OF THE SATELLITE FIELDS EVALUATED. NOTICE THAT THE GRID SAMPLES A LARGER REGION TO THE NORTH AND WEST OF STORM CENTER.

selves, constitute the NRC CLIPER model. These 14 non-gridded variables are described in Table 1 below.

TABLE 1. DEFINITION OF 14 NONGRIDDED VARIABLES

VARIABLE NUMBER	VARIABLE NAME (SYMBOL)
1)	MAXIMUM WIND AT OBSERVATION TIME (V_0)
2)	NORTH LATITUDE AT OBSERVATION (LAT_0)
3)	WEST LONGITUDE AT OBSERVATION TIME ($LONG_0$)
4)	DAY OF THE YEAR (FOLDED BETWEEN END POINTS OF 1 MARCH AND 31 SEPTEMBER) (DAY)
5)	RATIO OF HIGH LEVEL TO LOW LEVEL MOISTURE (RMOS)
6)	CHANGE IN MAXIMUM WIND OVER PREVIOUS 12 HR (AV)
7)	CHANGE IN NORTH LATITUDE OVER PREVIOUS 12 HR (ALAT)
8)	CHANGE IN WEST LONGITUDE OVER PREVIOUS 12 HR (ALONG)
9)	AVERAGE SPEED OVER PREVIOUS 12 HR (SPD)
10)	DIRECTION OF MOTION AT OBSERVATION TIME (DOM)
11)	SIN OF THE DIRECTION OF MOTION AT OBSERVATION TIME (SIN (DOM))
12)	COS OF THE DIRECTION OF MOTION AT OBSERVATION TIME (COS (DOM))
13)	BINARY EARLY VERSUS LATE SEASON (H(EARLY))
14)	BINARY DAY VERSUS NIGHT (H(DAY))

Data was obtained from a total of 120 observations of five 1979, five 1981, and four 1982 tropical cyclones. Fig. 2 shows the tracks of the storms used in this study. The symbols

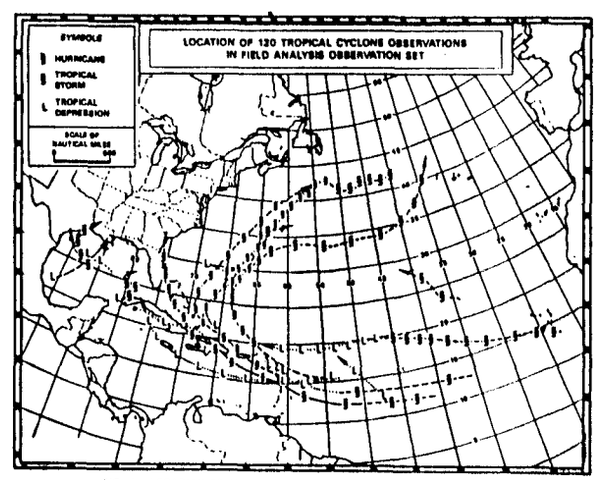

FIG. 2. LOCATION OF 120 TROPICAL CYCLONE OBSERVATIONS IN FIELD ANALYSIS OBSERVATION SET

for hurricanes, tropical storms and tropical depression show the 120 observations used in this study.

3. EMPIRICAL METHOD

The objective empirical analysis method used to derive and test the algorithms has been described by Hunter (1976). The approach has been used in many other studies including Shenk et. al. (1973) and Hunter et. al. (1981, 1984).

The general concept of the approach is to take a data set from the original high-dimensional data space and transform it to a lower-dimensional optimal analysis space. The data vectors resulting from sampling the 195 grid points in the high-dimensional data space are transformed into an ordered optimal coordinate system defined by the Karhunen-Loeve expansion (Andrews, 1972). Regression algorithms are then developed in the lower-dimensional optimal analysis space using an improved independent eigenscreening technique. This technique is related to the classical screening regression technique but differs in that the screening uses independent data rather than dependent data for screening evaluation. The screening decision is based on the independent test results using the U-method of Lachenbrach and Mickey (1968). Another advantage of using the lower-dimensional optimal analysis space is that the orthogonality of the eigenvector space eliminates redundance problems, and, therefore, reduces the complexity and cost of the more classical screening regression techniques.

Since the transformation to the analysis space is orthogonal and the inverse is know, the algorithm can be transformed back to the original data space. The original data space is the gridded satellite data field in Fig. 1. Thus, the way in which each grid point of the data vector contributes to the forecast algorithm can be shown pictorially by inverting the original sampling procedure and mapping the amount of contribution of each grid point.

The forecast algorithms were developed using both the 14 non-gridded variables shown in Table 1 and the gridded data from the: 1) moisture, 2) 500 mb temperature, 3) 200 mb temperature, 4) 11μ cloud free, 5) ozone, 6) cloud cover, and 7) GOES 11μ fields. Fig. 3-4 show examples of the average of some of these fields.

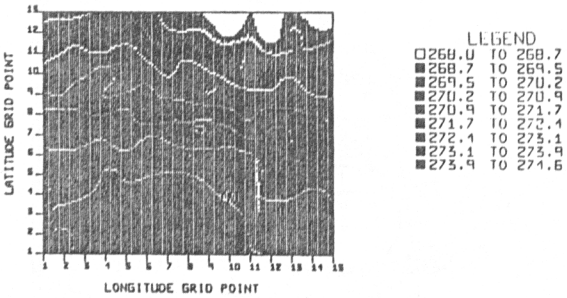

FIG. 3. AVERAGE OF TOVS 500 MB TEMPERATURE FIELD

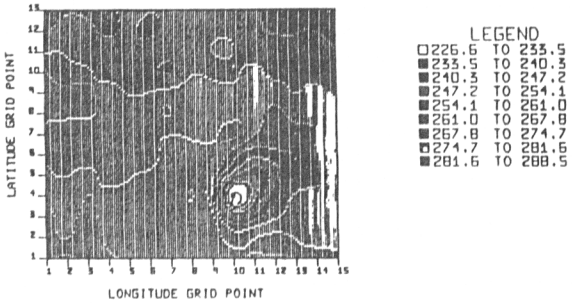

FIG. 4. AVERAGE OF GOES IR FIELD - HURRICANES

The 14 non-gridded descriptors were biased (i.e., weighted) such that the variation explained by the 14 non-satellite variables is approximately that explained by the 195 satellite measurements. This resulted in the leading terms of the eigenvector expansion explaining almost all of the variation in the non-satellite variables, and any redundant variation in the infrared values. The remainder of the variation that is explained by the satellite fields is contained in the higher order eigenvector.

To test the performance of these forecast algorithms, a storm-out independent test procedure similar to Lachenbrach's (1968) U-method was used. This procedure consists of removing the infrared and non-satellite information for a given storm from the dependent data, redeveloping the regression algorithms, and then independently testing the performance of these algorithms with the given storm. This procedure is repeated sequentially, omitting different storms as independent test cases until all the available storms that were used to develop the algorithms were also used for independent test cases. This procedure was used to maximize the number of observations available for developing each algorithm.

4. COMPARISON OF CLIPER MODELS

The NRC-CLIPER model differs from the well-known NRC-CLIPER model in at least four significant ways: 1) the NHC-CLIPER model was derived using a significantly larger sample of cyclones than the NRC model; 2) the NHC-CLIPER model uses information obtained over a period of 18 hrs. prior to the forecast time, whereas the NRC-CLIPER model only uses information obtained up to 12 hrs. prior to the forecast time; 3) the NHC model uses intensity, speed, direction, and cross-products of these parameters as predictors, while the NRC-CLIPER model uses intensity, speed, direction, Cartesian position and change of position; and 4) the NHC model, when derived from best track data, uses a calculated speed of the cyclone which in order to provide a "best track model" of the forecaster's estimate is based on information only available 6 hours <u>after</u> the forecast time.

Table 2 compares the performance of these CLIPER algorithms based on best track data as archived by Asheville and as archived by the National Hurricane Center, as well as on operational positions as archived by the National Hurricane Center. Comparison of the third and fourth columns on Table 2

TABLE 2. COMPARISON OF NRC & NHC CLIPER

OBSERVATIONS USED:	NHC/NRC COMMON SET					
MODEL USED:		NRC CLIPER	NHC CLIPER	NHC CLIPER	NHC CLIPER	NRC CLIPER
DATA SOURCE:		ASHEVILLE BEST TRACK		NHC-BT	OPERATIONAL	OPERATIONAL
COLUMN TITLE:	NO CASES	AVG ERROR	AVG ERROR	AVG ERROR	AVG ERROR	AVG ERROR
12-HR. FORECAST						
VECTOR AVG (KM)	99	89.9	45.7	45.7	109.4	113.2
ΔLAT (KM)		56.9	35.3	35.5	75.3	70.2
ΔLONG (KM)		69.6	29.1	28.7	79.3	88.8
24-HR. FORECAST						
VECTOR AVG (KM)	92	181.8	123.3	122.7	206.2	212.8
ΔLAT (KM)		113.2	84.0	84.0	140.2	122.0
ΔLONG (KM)		141.9	90.2	89.4	161.2	174.3
48-HR. FORECAST						
VECTOR AVG (KM)	79	387.7	334.2	334.4	419.7	427.9
Δ LAT (KM)		213.1	221.4	223.3	277.6	232.6
Δ LONG (KM)		323.9	260.4	248.9	314.8	359.2
72-HR. FORECAST						
VECTOR AVG (KM)	65	593.4	617.7	617.1	679.3	669.1
Δ LAT (KM)		307.7	402.6	404.8	435.6	315.2
Δ LONG (KM)		507.4	468.5	465.8	521.3	590.2

shows that, for the application to the best track data, the NHC has significantly smaller errors than the NRC-CLIPER forecast for all 12 and 24 hr. forecasts and for the longer period longitude forecasts. However, the comparison of the same two models using operational data, which is shown in the last two columns of Table 2, shows that a large portion of this difference disappears and, in fact, the vector errors for these two models are nearly identical for all four forecast periods. Since the NHC-CLIPER model's use of data 6 hours after the forecast is only applicable to the best track data, it seems likely that this difference between the two models will explain the majority of the difference in the performance shown on the forecast utilizing the best track data. Fig. 5 provides further justification of this hypothesis. This figure replots the errors shown in columns 3 and 4 of Table 2 as a function of time since the latest information utilized in preparing the forecast. When this is done, both the NHC and NRC-CLIPER snow very similar results, except that, in general, the NRC-CLIPER has smaller errors for the latitude forecast and the NHC-CLIPER has smaller errors for the longitude forecast. It is anticipated that these relatively small differences are due to the first three differences between the models discussed above.

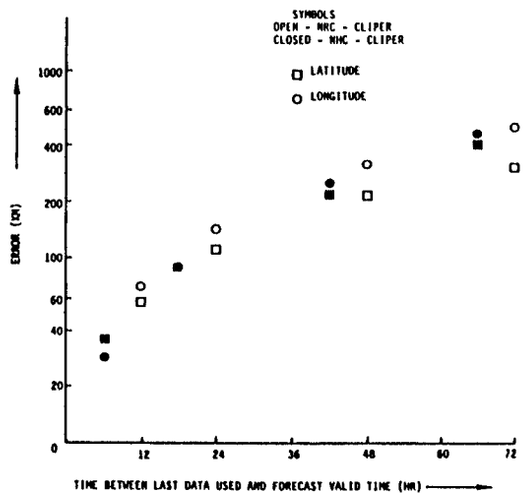

FIGURE 5. COMPARISON OF NRC & NHC CLIPER USING BEST TRACK DATA

By comparing columns 4 and 5 of Table 2, one sees that there is very little difference between the Asheville and the NHC archived data. This is not surprising, since the Asheville archived data are based on the NHC data. Similarly, columns 5 and 6 of Table 2 show the effect of using operational data as compared to best track data. These effects are also very similar to those which have been previously observed.

A comparison between the vector errors of the NRC and NHC-CLIPER models, for a common set of observations, is presented in the left-hand side of Table 3. In addition, a comparison of the NHC-CLIPER model and the official forecast errors, for a set of 223 observations over the 1973-1977 time period, is shown. This comparison is taken directly from the NOAA report FCM-R2, 1982. Table 3 shows that the NRC and NHC-CLIPER models produce essentially the same vector errors and that the NHC-CLIPER model produces slightly greater error than the official forecast for the 12-48 hr. forecast and slightly smaller errors for the 72 hr. forecast. Thus, it seems reasonable to conclude that the official forecast vector errors are approximately 4-10% less than the NRC-CLIPER models errors for the 12-48 hr. position forecast and approximately 5% larger than the NRC-CLIPER errors for the 72 hr. forecast.

TABLE 3. COMPARISON OF CLIPER AND OFFICIAL PERFORMANCE (FORECASTS PREPARED USING OPERATIONAL DATA) AVG POSITION ERROR (KM)

MODEL USED / DATA SET / FORECASTS	NRC - CLIPER	NHC - CLIPER		OFFICIAL
	NRC/NHC - COMMON (99 - OBSERVATIONS)		1973-77 NHC (223 OBSERVATIONS)	
12HR POSITION	113	109	102*	98*
24HR POSITION	213	206	228*	209*
48HR POSITION	420	420	500*	481*
72HR POSITION	669	679	683*	718*

*REF: DEPT. OF COMMERCE/NOAA REPT FCM-R2-1982; "REVIEW OF FEDERAL RESEARCH AND DATA COLLECTION PROGRAM FOR IMPROVING TROPICAL CYCLONE FORECASTING", JAN. 1983

5. COMPARISON OF SATELLITE AND CLIPER MODELS

Table 4 presents a comparison of forecast errors utilizing CLIPER only models, satellite only models and models using combinations of the satellite fields and CLIPER variables. Performances shown on Table 4 are homogeneous since they are based on the same observations from 1979, 81, and 82, which constitute the field analysis set. The truth and CLIPER variables were derived from the Asheville best track data. Columns 2 and 3 of this table compare the performance of the NRC-CLIPER models with the performance of a model developed using the total moisture, the 500 mb temperature, and the 200 mb temperature satellite fields. It can be seen that for the 12, 24, and 48 hrs. forecasts, the CLIPER only model has slightly smaller errors than the satellite only model. These differences are larger for the 12 hr. forecast and become relatively small by the time the forecast period has increased to 48 hrs. For the 72 hr. forecast, the satellite only model has a significantly smaller longitude error and just a slightly larger latitude error than the CLIPER only model.

TABLE 4. COMPARISON OF CLIPER AND SATELLITE FIELD PERFORMANCE

OBSERVATIONS USED:	FIELD ANALYSIS SET										
MODEL USED:	NRC CLIPER	SATELLITE ONLY	SATELLITE + CLIPER	TOT MOISTURE + CLIPER	T500 + CLIPER	T200 + CLIPER	11μ + CLIPER	OZONE + CLIPER	CLD CVR + CLIPER	GOES-IR (11 μ) + CLIPER	BEST
DATA SOURCE:	ASHEVILLE BEST TRACK										
COLUMN TITLE: COLUMN NUMBER:	2	3	4	5	6	7	8	9	10	11	12
12-HR. FORECAST											
VECTOR AVG (KM)	83.3	117.2	73.6	72.4	74.2	76.6	75.0	77.6	75.3	81.0	71.6
Δ LAT (KM)	52.4	65.1	47.6	48.3	47.4	49.9	47.9	50.9	47.1	51.7	47.1
Δ LONG (KM)	64.7	97.4	56.2	53.9	57.1	58.1	57.7	58.6	58.7	62.3	53.9
24-HR. FORECAST											
VECTOR AVG (KM)	173.5	209.0	151.0	158.4	151.7	165.3	159.3	162.0	161.8	166.9	149.6
Δ LAT (KM)	105.1	120.8	90.2	92.8	93.5	97.2	94.8	98.9	92.9	101.6	90.2
Δ LONG (KM)	138.0	170.5	121.1	128.4	119.4	133.7	128.0	128.3	132.5	132.6	119.4
48-HR. FORECAST											
VECTOR AVG (KM)	405.4	411.8	299.2	326.9	300.9	331.1	342.5	331.4	336.1	325.7	290.1
Δ LAT (KM)	214.7	223.3	183.9	194.7	168.7	180.3	201.1	186.5	186.5	191.9	168.7
Δ LONG (KM)	343.9	346.0	236.0	262.6	249.1	277.7	277.2	274.0	279.6	263.2	236.0
72-HR. FORECAST											
VECTOR AVG (KM)	632.8	584.1	532.0	518.6	453.4	529.1	524.4	533.0	562.2	496.5	451.8
Δ LAT (KM)	289.4	297.0	277.2	273.5	250.7	267.8	249.5	247.7	281.7	287.1	247.7
Δ LONG (KM)	562.7	503.0	454.1	440.6	377.8	456.3	461.2	472.0	486.5	405.1	377.8

Column 4 shows the performance when the CLIPER data and the satellite data from the three fields are combined into the model. As would be expected, all of the forecast errors for the satellite plus CLIPER are smaller than the forecast errors for either the CLIPER only or the satellite only models.

6. EVALUATION OF INDIVIDUAL SATELLITE FIELDS

Columns 5-11 of Table 4 present the forecast errors produced by models which are based on the combination of CLIPER plus a single satellite field. The seven fields considered are: total moisture, 500 mb temperature, 200 mb temperature, 11 micron cloud free, ozone, cloud cover, and the GOES IR which is also an 11 micron radiometer. Column 12 presents the smallest forecast error for the latitude and longitude obtained using any of the CLIPER plus satellite models. The vector average is that which would be obtained by utilizing the smallest latitude and longitude errors shown.

On comparing the individual fields plus CLIPER in Table 4, one would expect that each field would have forecast errors smaller than the CLIPER only presented in column 2, but larger than or equal to the satellite plus CLIPER presented in column 4. This is satisfied within the uncertainty of these numbers for all of the forecasts except the 48 hr. latitude and the 72 hr. forecasts. This suggests that more terms should have been retained in the eigenvector representation for the development of these forecast algorithms. However, because the number of training cases was limited to 120, it was not feasible to obtain additional terms in the eigenvector expansion. In order to do this, it would be necessary to increase significantly the number of training cases utilized, both to develop the eigenvector expansion and to develop the regression algorithms. Thus, we have compelling evidence suggesting that a maximum of three satellite fields cannot be exceeded with the training set available at this time. Consequently, a major objective of the analysis presented in columns 5-12 will be to assist in selecting the best fields to use for each parameter to be forecasted and each forecast period. Note that it is not necessary to use the same fields for each period parameter to be forecasted. For example, for the 12 hr. latitude forecast, cloud cover produces the smallest error with the 500 mb temperature; 200 mb temperature and 11 micron cloud free fields provides close seconds. Thus, the forecast of the 12 hr. latitude would probably include a cloud cover field whereas for the 12 hr. longitude the smallest error occurs when the total moisture field is used. Thus, one would anticipate that the total moisture field would be one of the fields utilized in any algorithm to forecast a 12 hr. longitude. Similarly, for the 72 hr. latitude forecast, the ozone, 11μ cloud free and 500 mb temperature fields have the smallest error and would probably be used utilized for the forecast. For the 72 hr. longitude forecast, the 500 mb temperature has by far the smallest forecast errors and it is not clear which additional fields should be added to it at this point.

Upon comparing the forecast errors based on utilizing the best of the satellite fields in combination with the CLIPER (column 12), with the CLIPER model presented in column 2, the improvements for the 12 and 24 hr. forecasts range from 10 to 16% and for the 48 and 72 hr. forecasts from approximately 15-30%. Thus, the addition of the satellite data provides these improvements relative to the CLIPER model. In section 4, we showed that the CLIPER model was only slightly inferior to the official forecast for the 12-48 hr. forecast, and slightly superior for the 72 hr. forecast. Thus, the approach presented in this paper, in combination with the additional information available from satellite data, offers the potential for relatively modest improvements in the short period forecasts, but improvement of 30-35% for the forecast of the 48-72 hr. positions of Atlantic hurricanes. Because of this potential, plans have been made to evaluate algorithms derived using these techniques at the National Hurricane Center during the 1986 hurricane season.

REFERENCES

Andrews, H.C., 1972: Introduction to Mathematical Techniques in Pattern Recognition, Wiley-Interscience, 242 pp.

Chan, J.C.L., W.M. Gray, and S.Q. Kidder, 1980: Forecasting tropical cyclone turning motion from surrounding wind and temperature fields. Mon. Wea. Rev., 108, 778-792.

Gentry, R.C., E. Rodgers, J. Steranka, W.E. Shenk, 1980: Predicting tropical cyclone intensity using satellite measured equivalent blackbody temperature of cloud tops. Mon. Wea. Rev., 108, 445-455.

Gibson, Jannie, 1984: GOES Data Users' Guide, National Oceanic and Atmospheric Administration, National Environmental Satellite, Data, and Information Service, Washington, D.C.

Hunter, H.E., 1976: Effect of mechanical cooling devices on ambient salt concentration. EPA Report, 133 pp. [NTIS 600/3-76-034].

Hunter, H.E., E.B. Rodgers, and W.E. Shenk, 1981: An objective method for forecasting tropical cyclone intensity using Nimbus-5 electrically scanning microwave radiometer measurements. J. Appl. Meteor., 20, 137-145.

Hunter, H.E., E.B. Rodgers and W.E. Shenk, 1984: An objective method for forecasting tropical cyclone motion using Nimbus and NOAA-2 infrared measurements. J. Climate and Appl. Meteor., 23, 668-678.

Kidwell, K.B., 1983: NOAA Polar Orbiter User's Guide, National Oceanic and Atmospheric Administration, National Environmental Satellite, Data, and Information Service, Washington, D.C.

Lachenbrach, P.A., and M.R. Mickey, 1968: Estimation of error rates in discriminate analysis. Technometrics, 10, 11-17.

National Oceanic and Atmospheric Administration, 1982: Review of Federal Research and Data Collection Programs for Improving Tropical Cyclone Forecasting. FCM-R2-1982.

Palmen, E., and H. Riehl, 1957: Budget of angular momentum and energy in tropical cyclones. J. Meteor., 14, 150-159.

Riehl, H., and J. Malkus, 1961: Some aspects of Hurricane Daisy, 1958. Tellus, 13, 181-213.

Rossby, C.G., 1948: On displacement and intensity changes of the atmospheric vorticities. J. Mar. Res., 7, 175-187.

Shenk, W.E., and E.B. Rodgers, 1978: Nimbus 3/ATS 3 observations of the evolution of Hurricane Camille. J. Appl. Meteor., 17, 458-476.

Shenk, W.E., H.E. Hunter, F.V. Menkello, R. Holub, and V.V. Salomonson, 1973: The estimation of extratropical cyclone parameters from satellite radiation measurements. J. Appl. Meteor., 12, 441-451.

FORECASTING THE MAXIMUM RAINFALL IN TROPICAL CYCLONES

James B. Lushine

NOAA, NWS, National Hurricane Center
Miami, Florida

1. INTRODUCTION

At the National Hurricane Center (NHC), forecasting the heavy rainfall associated with landfalling tropical cyclones has been an imprecise task. A rule of thumb (ROT) developed by Kraft in the 1960s (Hebert, personal communication) originally intended to forecast the maximum rainfall in inches for hurricanes affecting the U.S. Gulf of Mexico coast, takes the form of 100 divided by the speed of translation (SOT) of the hurricane in knots. This ROT has been operationally applied to other Atlantic basin tropical systems and was used as the basis for maximum rainfall estimates in public advisories issued by the NHC for many years. Beginning in the mid 1970s, a technique using weather satellite cloud top temperature data has been used at the NHC to forecast operationally tropical cyclone rainfall for coastal locations up to 36 hours in advance. The technique entitled the Griffith-Woodley rainfall technique (GWRT), Waters (1975), used satellite infrared (11 micron) cloud top temperature data to estimate the area rainfall averaged over the tropical cyclone cloud canopy. Woodley modified the original technique to include a "core" rainfall intended to simulate the maximum rainfall normally located near the inner core of the tropical cyclone. This was done by apportioning the rainfall into a theoretical distribution whereby 50% of the total area average rainfall occurs in the coldest 10% of the cloud top area. This apportionment was taken after radar studies by Woodlye (1975). This modified GWRT has been automated and used operationally at the NHC since 1977.

2. RULE OF THUMB VERIFICATION

To test the ROT, maximum rainfall measurements for tropical storms and hurricanes affecting the coastal sections of the United States east coast and Gulf of Mexico were taken from the National Hurricane Research Project Report No. 3 (1956) for data from 1900 through 1955 and from individual sotrm reports from 1956 through 1984. In addition, two tropical cyclones that affected portions of the Caribbean Sea were included. To calculate the SOT of these same tropical cyclones, the track data from the publication, Tropical Cyclones of the North Atlantic Ocean (1978), were used for data from 1900 through 1977 and individual storm reports from 1978 through 1984. The SOT was usually calculated by averaging over a 24 hour period from 12 hours prior until 12 hours after cyclone landfall. A total of 230 cases were obtained.

The 230 cases were stratified by intensity, by location of landfall, and by decade of occurence. Table 1.

	ALL TROPICAL CYCLONES	ALL HURRICANES	ALL TROPICAL STORMS	GULF OF MEXICO HURRICANES	FLORIDA HURRICANES	U.S. EAST COAST HURRICANES
NUMBER	230	131	99	79	58	52
AVG MAX RAIN	10.6"	11.3"	9.6"	12.1"	11.2"	10.1"
STAN DEV	5.8"	5.3"	6.2"	5.8"	4.3"	4.0"
AVG SOT	10.5 KT	10.1 KT	11.0 KT	10.0 KT	9.9 KT	10.4 KT
STAN DEV	4.8 KT	4.4 KT	5.2 KT	4.7 KT	3.9 KT	4.7 KT
FORMULA	111/SOT	114/SOT	107/SOT	122/SOT	111/SOT	105/SOT

ALL TROPICAL CYCLONES

YEARS	1900-1909	1910-1919	1920-1929	1930-1939	1940-1949	1950-1959	1960-1969	1970-1979
NUMBER	28	25	21	33	39	29	24	22
AVG MAX RAIN	8.4"	9.1"	10.9"	11.2"	11.5"	11.4"	10.5"	9.8"
STAN DEV	3.8"	5.8"	4.4"	4.9"	7.2"	4.2"	5.8"	8.4"
AVG SOT	10.4 KT	10.0 KT	12.3 KT	10.1 KT	10.1 KT	11.6 KT	9.5 KT	11.4 KT
STAN DEV	4.8 KT	3.2 KT	5.9 KT	4.0 KT	3.8 KT	6.1 KT	4.4 KT	5.9 KT
FORMULA	88/SOT	91/SOT	134/SOT	118/SOT	116/SOT	137/SOT	100/SOT	112/SOT

Table 1. Stratification of tropical cyclones

For all 230 tropical cyclone cases, all but two of which were United States landfalling tropical cyclones, the average maximum observed rainfall in coastal locations was 10.6 inches and the average SOT was 10.5 knots. This yields a formula of 111/SOT. In the following discussion, keep in mind that the numerator in the formula is a measure of the wetness of a tropical cyclone not related to the SOT, since the denominator is always the SOT. The two factors which would affect the wetness of a cyclone are its size and/or its overall rainfall rate. Comparing tropical cyclones of tropical storm versus hurricane intensity, the 131 hurricane cases are slightly wetter than the 99 cases of tropical storms with a difference in the numerator of 114 versus 107. When looking at the location of landfall stratification it is seen that the 79 cases of hurricanes making landfall in the Gulf of Mexico coast of the U.S. are slightly wetter than the 58 cases of those affecting Florida or the 52 cases affecting the U.S. east coast. In fact, the formula for hurricanes affecting the U.S. Gulf of Mexico during the entire twentieth century is 121/SOT rather than the ROT 100/SOT developed by Kraft and used for so many years at the NHC.

The tropical cyclones were broken down into decade of occurence excluding the incomplete 1980s to see if any differences were noted that might relate to a change in rainfall observation accuracy over the years or in the ability to post-track tropical cyclones. Little difference in the average SOT for any particular decade was noted, indicating that tropical cyclone post-tracking for U.S. landfalling tropical cyclones has shown little change in overall accuracy during the twentieth century. In the area of maximum rainfall observations, it is noted that values of wetness were somewhat lower in the first two decades of the twentieth century compared to the remainder of the decade (90 in the period from 1900-1919 versus an overall average of 111) indicating that rainfall observations may have been either less accurate or fewer in number early in this century. As a sidelight, a further strati-

fication of all 230 cases was made by month of occurence(not shown). Excluding May and November of which there was an insignificant number of cases, the average maximum rainfall was greatest in the month of July (13.3 inches versus an overall average of 10.8 inches) owing to a slower average SOT in that month. Excluding the SOT as a factor the average wetness was greatest during the month of October with a value of 129 in the numerator.

A regression equation of the maximum observed rainfall and that predicted by the original ROT was developed for all 230 cases. Figure 1 shows the plotted data and the second order curve best fitted to the least squares regression equation.

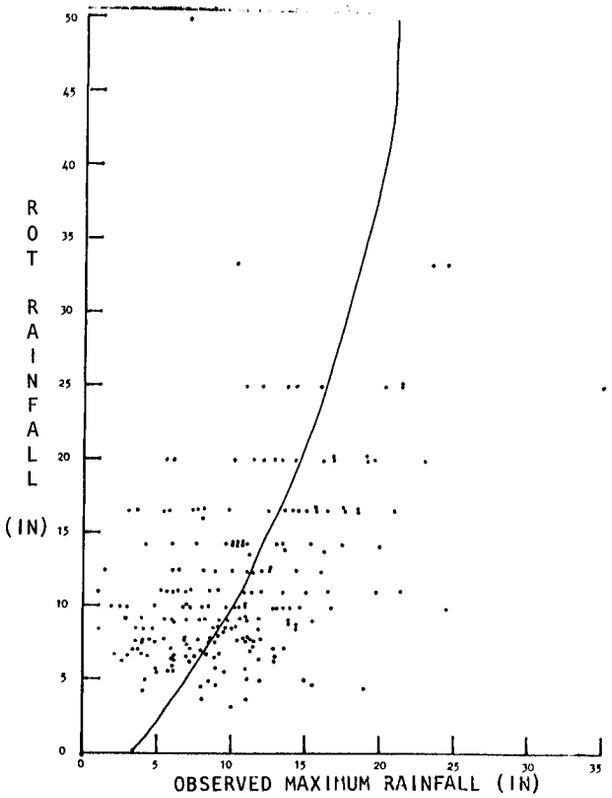

Fig. 1. Observed maximum rainfall versus ROT derived rainfall for 230 cases and best fit curve.

The salient points are: a linear fit produced a correlation coefficient of 0.50 which is significant at the 99% confidence level. It showed a reduction of variance of 25% and a standard error of estimate of +/- 5.0 inches. A second order polynomial fit reduced the variance only an additional 1%.

3. SATELLITE TECHNIQUE VERIFICATION

Satellite core rainfall estimates have been operationally made at the NHC with the modified GWRT since 1977. The operational procedure has been to forecast the core rainfall beginning approximately 36 hours prior to predicted landfall and at 6 hour intervals thereafter until landfall occurs. Cases were examined in which forecasts of the maximum rainfall were made at 36, 30, 24, 18, 12, and 6 hours prior to landfall. A time 24 hours prior to landfall was chosen for verification based on the fact that it was the longest time period prior to landfall which had a sufficient number of cases. From the operational estimates, 14 cases were obtained in which a 24 hour forecast of the maximum rainfall was made. To provide a verification of the technique itself, excluding the error inherent in making a 24 hour forecast of the SOT, the best track estimates of the SOT made in the same manner described above for the ROT cases were used in place of the operational estimates of the SOT. This also allowed a direct comparison between ROT and satellite estimates. Table 2 lists the names, dates, landfall locations, observed maximum rainfall and 24 hour satellite forecasts of maximum rainfall for these 14 cases.

NAME	DATE OF LANDFALL	LOCATION OF LANDFALL	OBS MAX RAINFALL	24 HOUR SATELLITE FORECAST RAINFALL
H. ANITA	2 SEP 1977	S TX/NE MEX	9.2"	11.3"
H. BABE	5 SEP 1977	LA	9.9"	10.0"
H. GRETA	19 SEP 1978	BELIZE	8.9"	9.6"
H. BOB	11 JUL 1979	LA	7.4"	10.9"
T.S. CLAUDETTE	24 JUL 1979	TX/LA	45.0"	52.0"
T.S. ELENA	1 SEP 1979	TX	5.6"	12.5"
H. DAVID	3 SEP 1979	FL	11.1"	13.7"
H. DAVID	5 SEP 1979	GA/SC	9.9"	10.0"
H. FREDERIC	13 SEP 1979	AL/MS/LA	10.5"	12.1"
H. ALICIA	18 AUG 1983	TX	10.7"	10.2"
T.W. BARRY	20 AUG 1983	P.R.	3.3"	5.5"
T.S. BARRY	25 AUG 1983	FL	2.8"	7.0"
H. DIANA	13 SEP 1984	NC	13.7"	19.1"
T.S. ISIDORE	27 SEP 1984	FL	5.6"	10.7"

Table 2. 14 cases for verifying satellite maximum rainfall forecasts.

A regression equation was derived for this data and is presented in figure 2.

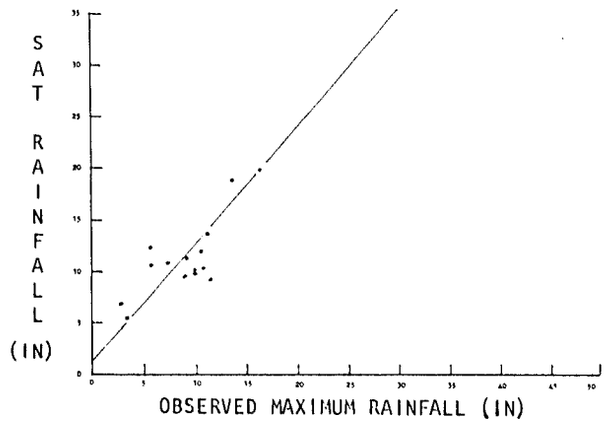

Fig. 2. Observed maximum rainfall versus 24 hour forecasts of rainfall made from GWRT.and best fit.

The best fit was a straight line with a correlation coefficient of 0.98 which is significant at greater than the 99% level of confidence. A reduction of variance of 96% with a standard error estimate of +/- 2.2 inches was found.

4. COMPARISON OF ROT AND GWRT METHODS

To compare the skill of the satellite technique against the ROT, a homogeneous data set was compiled for the 14 cases available from the satellite verification test. Figure 3 shows the ROT data plotted for the same 14 cases used in verifying the satellite technique.

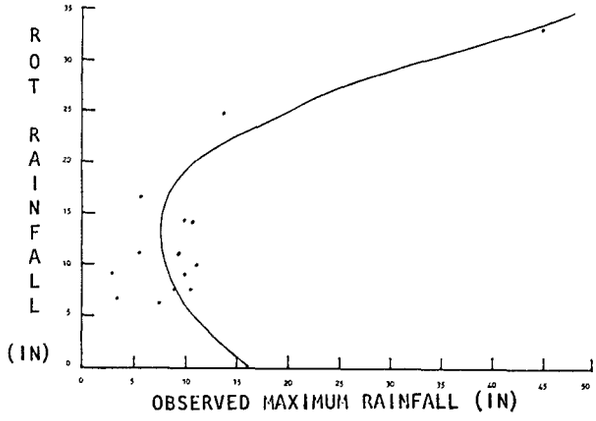

Fig. 3. Observed maximum rainfall versus ROT derived rainfall for 14 cases used in Figure 2.

The ROT for this homgeneous sample showed a correlation coefficient with observed rainfall of 0.89 significant at the 99% level for a linear best fit with a reduction of variance of 80%. Using a second order polynomial fit, an additional reduction of variance of 8% was accomplished. Finally, the data from both techniques in the homogeneous sample are plotted together (Fig. 4) and a statistical correlation between the two was made.

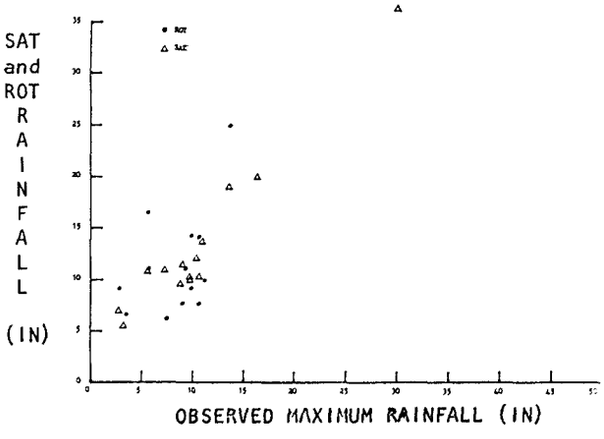

Fig. 4. Observed maximum rainfall versus rainfall forecasted from both the ROT and the GWRT for a homogeneous sample of 14 cases.

It was found that a large intercorrelation between the two techniques was present (0.86 correlation coefficient). Stepwise screening regressions showed that the ROT is a redundant predictor when combined with the satellite technique. Therefore, the satellite technique is superior to the ROT.

5. CONCLUSIONS AND FUTURE WORK

Two methods for operationally forecasting the maximum coastal rainfall in Atlantic tropical cyclones have been tested. Both techniques showed skill in predicting observed maximum rainfall amounts. When the methods were intercompared, the satellite technique produced superior results to those of the rule of thumb.

Additional modifications were made to the GWRT in the 1980s to include among other things a one dimensional profile of the rainfall amounts normal to the track of the tropical cyclone. Verification of this profile is underway both in the United States and in other countries of the Atlantic hurricane basin.

6. ACKNOWLEDGEMENTS

Thanks go to Arthur Pike and Charles Neumann of NHC for help with the statistics.

7. REFERENCES

Neumann, C.J., G.W. Cry, E.L. Caso, B.R. Jarvinen 1978: Tropical Cyclones of the North Atlantic Ocean, 1871-1980, National Climatic Data Center, Asheville, N.C. 174 pp.

Schoner, R.W. and S. Molansky, 1956: Rainfall Associated with Hurricanes (and Other Tropical Disturbances): National Hurricane Research Project Report No. 3, Washington, D.C., 305 pp.

Waters, M.P. III, C.G. Griffith and W.L. Woodley, 1977: Use of digital geostationary satellite imagery for real-time estimation of hurricane rain potential in landfalling storms. Volume of Conference Papers, 11th Technical Conference on Hurricanes and Tropical Meteorology of the American Meteorological Society, Boston, Ma, 198-203.

Woodley, W.L., A.R. Olsen, A. Herndon and V. Wiggert, 1975: Comparison of gage and radar methods of convective rain measurements, J. Appl. Meteor., 14, 909-928.

6.3

Analysis of Mesoscale Air Masses with VAS Retrievals

Raymond M. Zehr

RAMM Branch, NOAA/NESDIS
Cooperative Institute for Research in the Atmosphere
Colorado State University
Fort Collins, Colorado

1.0 Introduction

Vertical profiles of temperature and humidity derived from satellite radiances measured by VAS (VISSR[1] Atmospheric Sounder) became available as a research tool in 1980 (Smith, et al., 1982). More recently, VAS retrievals have been used for operational forecasting at the National Severe Storms Forecast Center (Wade, et al., 1985) and as input to mesoscale numerical models (Cram and Kaplan, 1985). During the PRE-STORM[2] program, VAS retrieval information was available in real-time to aid research scientists (Green and Weaver, 1985).

This paper illustrates how VAS retrievals can be used to diagnose the mesoscale environment and enhance our ability to forecast mesoscale convective systems (MCS). A case study is presented with VAS data sets collected over the central Great Plains in 1984 in support of the AIMCS[3] project. VAS retrievals identify pertinent characteristics of several mesoscale air masses which play an important role in the evolution of mesoscale convective systems. Analyses of VAS-derived thermodynamic parameters are shown to be valuable tools in assessing convective potential of mesoscale air masses.

2.0 Mesoscale Air Mass Analysis

VAS retrievals at approximately 80 km resolution were available at intervals varying from one to three hours during a 24-hour period for both 21-22 June 1984 and 14-15 July 1984. (The 14-15 July 1984 case study will be presented at the conference, but not in the preprint paper due to lack of space.) The retrieved temperatures and dew points were computed at the ASPP[4] at University of Wisconsin and transmitted to CIRA for additional computations and analysis. The technique described by Smith (1983) was used to generate the retrievals.

Initial research efforts with VAS retrievals involved analyses of geopotential heights and thicknesses. Weak gradients provided little useful information on mesoscale features. It was found that superposition of temperature and dewpoint vertical profiles to see differences and similarities provided a better method for identifying mesoscale features. IBM-PC software allowed a quick comparison among retrievals. Similar adjacent retrievals were grouped to define an area of a particular air mass. This analysis with VAS retrievals alone revealed ill-defined boundaries or transition zones which separated areas with relatively uniform retrieval profiles. Differences in water vapor and temperature at various levels and their influence on convective instability provided the basis for differentiating between air masses. Along most of the boundaries, the temperature or dew point difference between air masses extended only through a specific layer rather than the entire depth of the troposphere. Therefore, for this procedure, "air mass" was defined as a homogeneous vertical profile of air masses through the troposphere.

Figure 1 shows an example of the mesoscale air mass analysis for 2318 GMT, 21 June 1984. The "blocky" areas are air masses as defined by the VAS retrievals. The more precise locations of boundaries separating air masses are based on analysis of conventional observations and satellite images. Four independent VAS data sets during the period 1948 GMT, 21 June, to 0418 GMT, 22 June, identify air masses with similar characteristics to those at 2318 GMT. The time continuity among analyses lends credence to the analysis for a given time period.

Table 1 briefly describes the characteristics of each air mass. The mesoscale influences are evident when the analysis in Figure 1 is compared with the conventional surface analysis in Figure 2. Of the features in the synoptic-scale surface analysis (Figure 2) only the trough line which corresponds to the boundary between air masses 1 and 2 is included in the mesoscale air mass analysis. (The warm front in Iowa and Missouri likely corresponds to the eastern edge of

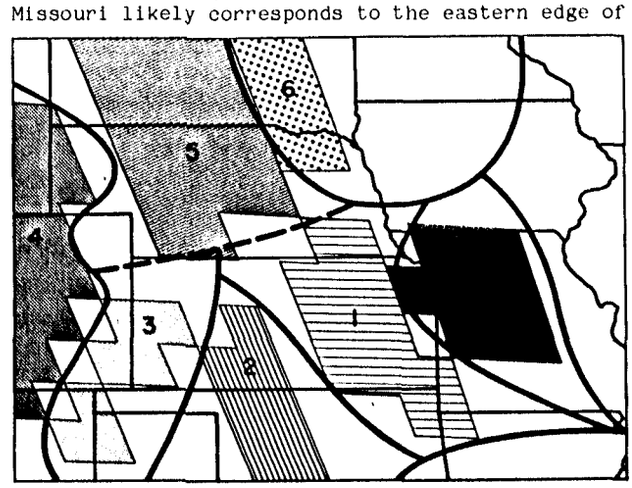

Figure 1. Mesoscale air mass analysis at 2318 GMT, 21 June 1984. The shaded regions depict the area covered by VAS retrievals within each air mass. Upper tropospheric boundaries are indicated by dashed lines, while lower layer boundaries are shown by solid lines.

[1] VISSR — Visible and Infrared Spin Scan Radiometer
[2] PRE-STORM — Preliminary Research Experiment - Stormscale Operational and Research Meteorology
[3] AIMCS — Airborne Investigations of Mesoscale Convective Systems
[4] ASPP — Advanced Satellite Products Project

Table 1

Mesoscale Air Mass Characteristics

No.	Description	Surface Temperature (°F)	Surface Dew Point (°F)	Average 500mb Temperature (°C)
1	capped, very moist	83-88	70-75	-8
2	hot, moist	93-97	62-67	-7
3	hot, dry	88-97	48-62	-8
4	very warm, very dry	82-92	35-48	-11
5	warm, moist, cold aloft	83-92	62-70	-12
6	rain cooled, subsidence	65-81	62-68	-12
7	cool, very moist	78-82	68-72	-8

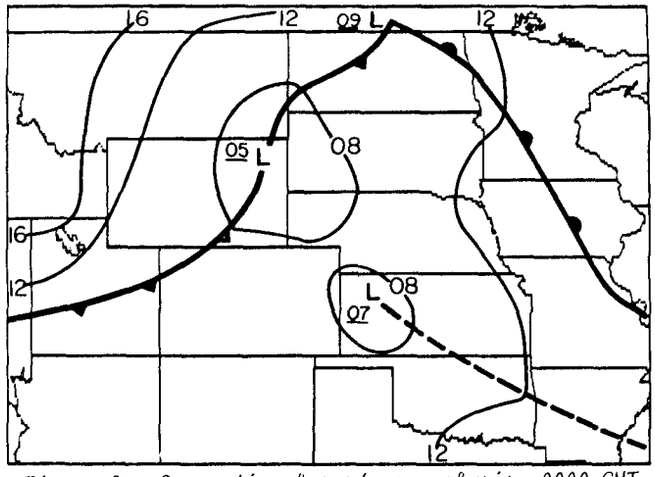

Figure 2. Conventional surface analysis, 0000 GMT, 22 June 1984.

air mass 7, but this was out of the area of interest.) The conventional surface and upper air data summarized in Table 1 reveals limited information about the convective potential of each air mass. The VAS profiles reveal characteristics unique to each air mass type which have important implications to the development and evolution of mesoscale convective systems. Figure 3 depicts the air mass differences across several boundaries with plots of VAS retrievals representative of different air mass pairs. Several radiosonde observations assigned to the air mass at their location are plotted as corresponding pairs in Figure 4. The VAS-detected air mass differences in Figure 3 are similar to the differences measured by radiosondes in Figure 4.

Air mass 6 (Figure 1) has been modified by evaporative cooling and subsidence in response to a mesoscale convective system located in southern Iowa. An arc cloud line (Purdom, 1973) seen in the visible satellite image (Figure 5) is aligned along a portion of the boundary between air masses 5 and 6. Figure 3a shows the VAS detected differences between the two air masses, showing a cooler and drier air mass in the rain-cooled air. Figure 4a shows radiosonde observations at Omaha, NB before and after passage of the outflow boundary. Note that the cool air is confined to a very shallow layer (600 m) at the surface, and the air layer above it is warm and dry having undergone adiabatic descent. The VAS retrievals, therefore, sometimes correctly indicate a warm, dry boundary layer in a rain cooled air mass despite the cool, moist surface observations, due to lack of vertical resolution. However, in this case, VAS indicated a cooler and drier air mass in the rain-cooled air mass.

The boundary between air mass 5 and air masses 1 and 3 is located along an upper-level front in the 300-500 mb layer. An analysis of VAS 400-mb temperature (not shown) depicts the associated temperature gradient. The upper troposphere temperature difference as measured by VAS retrievals is shown in Figure 3b. Air mass 5 is also determined to be several degrees cooler in the upper troposphere by the radiosonde (Figure 4b). The higher lapse rate through the mid-troposphere has important implications to the convective potential of the air mass as will be shown in Section 4.0 of this paper.

Air mass 1 is referred to in Table 1 as "capped". A strong inversion is measured by the radiosonde at around 880 mb (see Figure 4c). Although VAS does not indicate an inversion, a significant smaller lapse rate below 700 mb is measured by VAS in air mass 1 compared with air mass 2 (see Figure 3c). The low level moisture in air mass 1 is very high so that potential instability is high, however the air mass is unfavorable for initiation of convection without strong forcing. The high lapse rates in air mass 2 along with the moist boundary layer is conducive to intense convection. Note that air mass 1 remains completely clear at 2315 GMT (Figure 5), while deep convective clouds were developing in air mass 2.

During the afternoon of 21 June 1984, a severe thunderstorm formed in northwest Kansas along the boundary between air masses 1 and 3 (see Figure 1, and the satellite image, in Figure 5). During the evening hours, this activity evolved into a mesoscale convective system in central and eastern Kansas. A larger MCS developed in eastern Montana and propagated into western North Dakota. Another MCS formed in northeast Colorado. Each of these were supported by air mass 5. The IR satellite image in Figure 6 shows the eastern Kansas system near the time of its maximum extent. Additional details of this case study with regard to surface analysis enhanced with visible and IR satellite images, is given in a paper by Weaver, et al., 1985.

3.0 VAS -- Radiosonde Comparisons

The statistical correlation of vertical profiles from VAS and radiosondes, both for temperature and dew point has been well documented (Jedlovec, 1984). It is likely that the soundings plotted in Figure 3 are typical of that population. Note that although the VAS profiles lack vertical resolution, the key features which determine convective potential, i.e. low-level moisture and lapse rate both in the cloud layer and sub-cloud layer are sufficient to differentiate the air mass types. This evaluation led to the development of the procedure described here where VAS retrievals are used as a tool for mesoscale analysis. Furthermore, the results suggest that quantitative VAS-derived bulk thermodynamic parameters (see Section 4.0) may be valuable in forecasting mesoscale convective systems as well as synoptic-scale convective events and other types of convection.

Figure 3. Air mass differences as indicated by VAS retrievals, 2318 GMT, 21 June 1984.

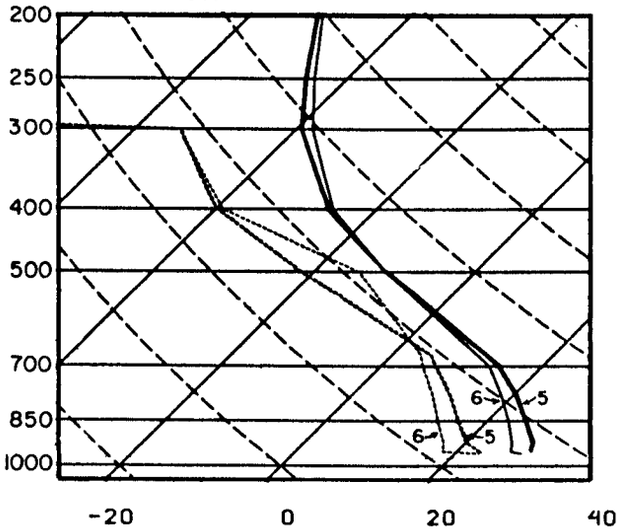

a. Air masses 5 and 6, outflow boundary.

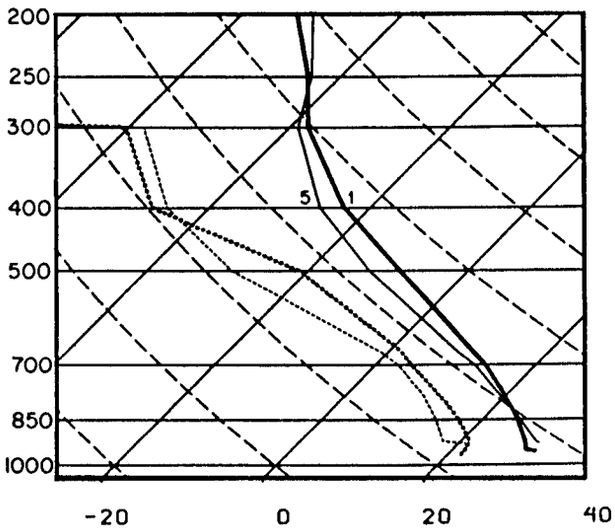

b. Air masses 1 and 5, upper-level front.

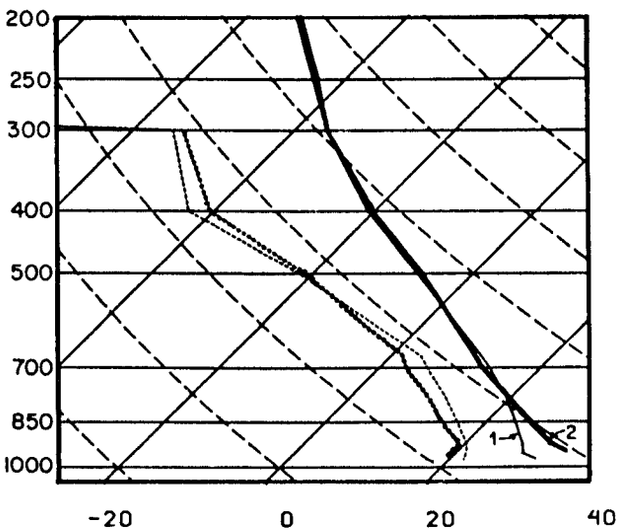

c. Air masses 1 and 2, boundary in central Kansas.

Figure 4. Air mass differences corresponding to those in Figure 3, as indicated by radiosonde observations.

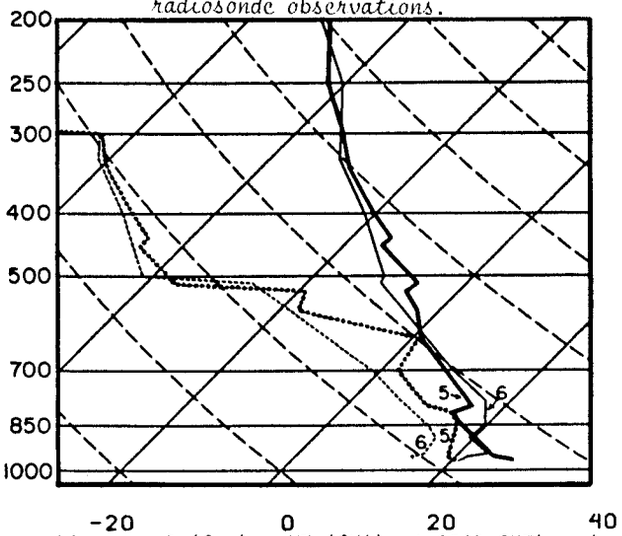

a. Air mass 5 (Omaha, NE (OMA) at 2315 GMT) and air mass 6 (OMA at 0300 GMT), outflow boundary.

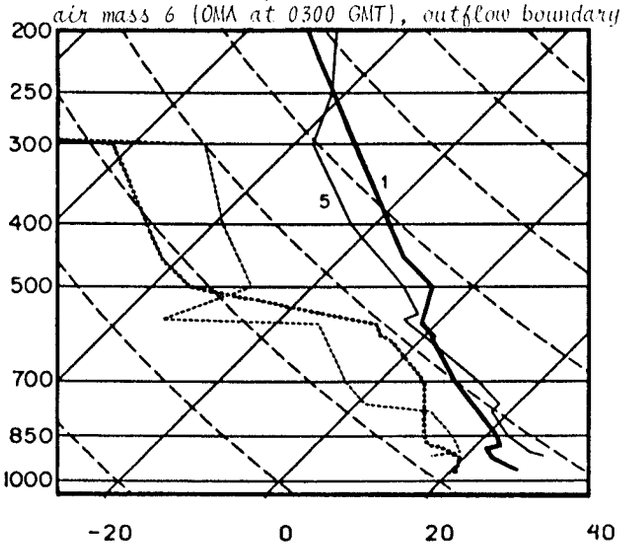

b. Air mass 1 (Monett, MO (UMN)) and air mass 5 (North Platte, NE (LBF)), 2315 GMT, upper-level front.

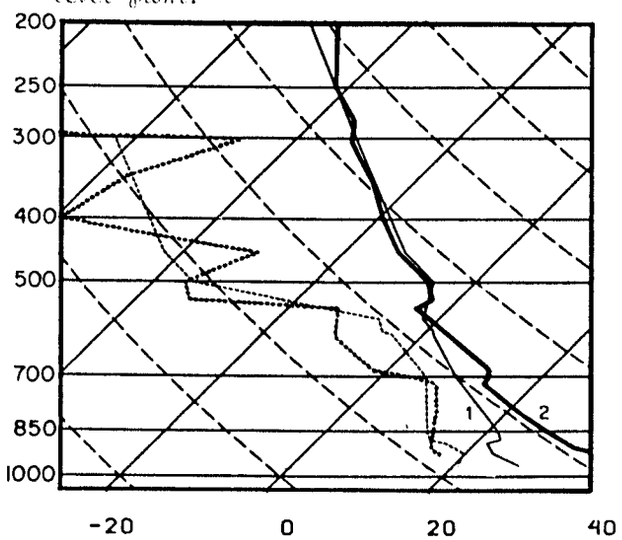

c. Air mass 1 (UMN) and air mass 2 (Dodge City, KS (DDC)), 2315 GMT, boundary in central Kansas.

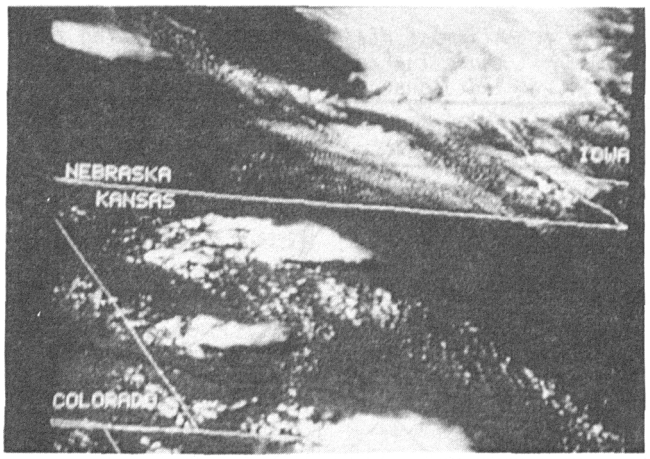

Figure 5. Visible satellite image, 2315 GMT, 21 June 1984.

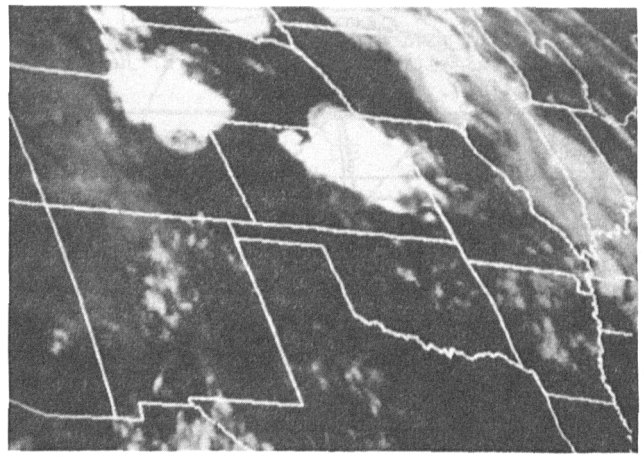

Figure 6. Infrared satellite image, 0530 GMT, 22 June 1984.

Caution is advised when comparing radiosonde and VAS soundings. It is important to be aware that although each data source is interpreted as a "vertical" profile of temperature and humidity, the sampling methods are vastly different. The radiosonde gives a point source measurement over a 30-45 minute ascent through the troposphere along a non-vertical path. VAS, on the other hand, samples a relatively large volume of air at a skewed viewing angle from geostationary altitude. For optimum mesoscale analyses, the two data sources should be complementary and not competitive. For example, VAS provides information on time changes and horizontal air mass extent not available from radiosondes. The location and magnitude of mesoscale horizontal temperature and moisture gradients can be specified by VAS. However, VAS cannot resolve fine vertical resolution structure such as the height of inversions and frontal surfaces. Since a radiosonde gives a point measurement, a question of representative area is associated with each observation. The VAS information may help define uniform regions or air masses for which a radiosonde observation is valid.

4.0 VAS-Derived Thermodynamic Parameters in Mesoscale Analysis and Forecasting

Mesoscale convective systems derive most of their energy from the convective available potential energy (CAPE) of the pre-storm environment. CAPE is measured by integrating the positive temperature difference between a sub-cloud layer parcel displaced upward under adiabatic constraints with no entrainment, and the environmental temperature. This energy source, often referred to as buoyant energy (B) or "positive area", is easily computed from sounding data. Additionally, "negative areas" which must be overcome by lifting (N) or heating (H) in order to realize the buoyant energy, can also be computed (see Figure 7). Assuming that each of the air masses in Figure 1 have characteristic values of derived thermodynamic parameters and that they can be reliably measured by VAS, suggests a new and valuable mesoscale analysis tool. An analysis of the thermodynamic parameters allows convective potential to be estimated on mesoscale space and time scales.

A sounding analysis program was available to run on each individual VAS retrieval. The program outputs a wide variety of parameters which are then plotted and analyzed (Purdom, et al., 1985). Figure 8 shows analyses of B and N for 2318 GMT, 21 June 1984. These two parameters are graphically defined in Figure 7. Each are computed according to the "parcel method". The average temperature and dew point in the lowest one kilometer define the parcel. These two quantities (computed as potential temperature and mixing ratio), along with the lapse rate in the convective cloud layer (between LFC and EL), determine the positive area, B. Similarly, the parcel definition along with the lapse rates below the level of free convection (LFC) determines the "negative area", N, which is a measure of the energy required to lift a parcel to its LFC.

The analyses in Figure 8 illustrate how B and N are related to specific air mass

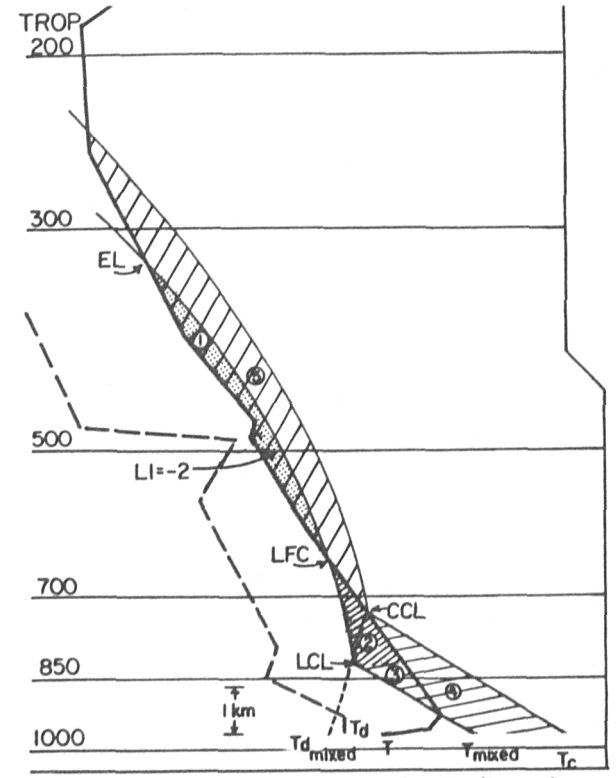

Figure 7. Skew-T, log-p diagram illustrating bulk thermodynamic parameters computed from VAS retrievals.
1. *positive area, B, available buoyant energy*
2. *negative area, N, between LCL and LFC*
3. *negative area, N, between surface and LCL*
4. *heating area, H, heat energy needed to reach convective temperature*
5. *positive area, B_{CCL}, available buoyant energy with convective temperature*

characteristics. Large values of positive area (B) are associated with the very high dewpoints in the lowest kilometer of air mass 1, and also the high cloud layer lapse rates (cool mid-and upper troposphere) in air mass 5. The regions which are dry in the lowest kilometer have low positive areas. The maximum negative area (N) values are found in air masses 1, 6 and 7 due to the more stable lapse rates in the lower layer.

5.0 Diurnal Variation of Thermodynamic Parameters

During the early morning hours, when an inversion is often present in the lowest kilometer, B values are very low and frequently zero due to the cool parcel temperature. However, the air mass may be conditionally unstable with high B values after the boundary layer undergoes diurnal heating. The convective temperature (T_c) and lowest kilometer dew point define a parcel, with positive area (B_{CCL}) computed by parcel ascent from the convective condensation level (CCL). Additionally, the heat energy (H) which must be added to attain convective temperature is computed. Therefore, as the boundary layer is heated, N and H approach zero, and B approaches B_{CCL}. These quantities are defined graphically in Figure 7. Of course, advective and dynamic processes often modify air masses, as diurnal heating occurs, but at least B_{CCL} allows an assessment of afternoon convective potential from morning soundings, while B values may not.

An example taken from the PRE-STORM data sets illustrates the predictive capability of B_{CCL} from morning soundings. The analysis of B_{CCL} at 1418 GMT on 12 May 1985 is shown in Figure 9. At this time, B values are less than 1000 Jkg^{-1} over most of the area (not shown). Figure 10 shows the analysis of B during the early afternoon (1918 GMT). Note that the B_{CCL}=2000 Jkg^{-1} line in Figure 9 is nearly coincident with the B=2000 Jkg^{-1} line in Figure 10, five hours later. Thus in the absence of strong advection, the B_{CCL} analysis in the morning gives a prediction of the afternoon analysis of B.

6.0 Summary

The VAS-derived "positive area" analysis (Figure 8a) identified a maximum of convective available potential energy in regions where nocturnal MCS's occurred. In addition, the initial development occurred in an area with relatively low N values. The analysis of N also identified a region, air mass 7 in northern

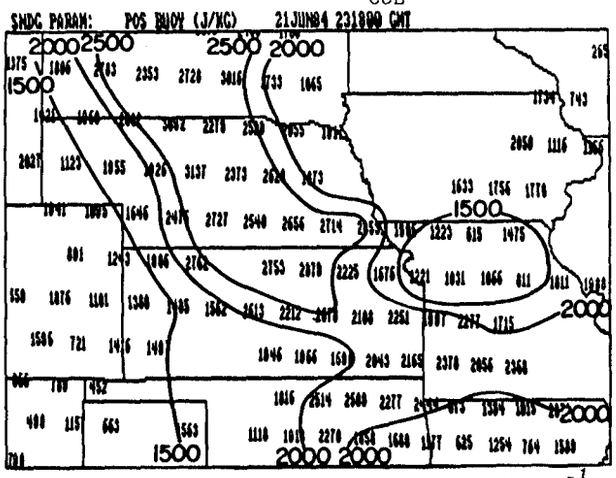

Figure 8a. VAS-derived positive area, B ($J\ kg^{-1}$), 2318 GMT, 21 June 1984

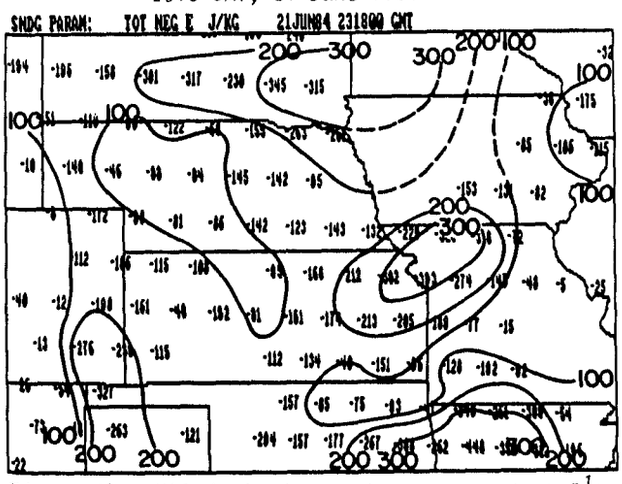

Figure 8b. VAS-derived negative area, N ($J\ kg^{-1}$), 2318 GMT, 21 June 1984

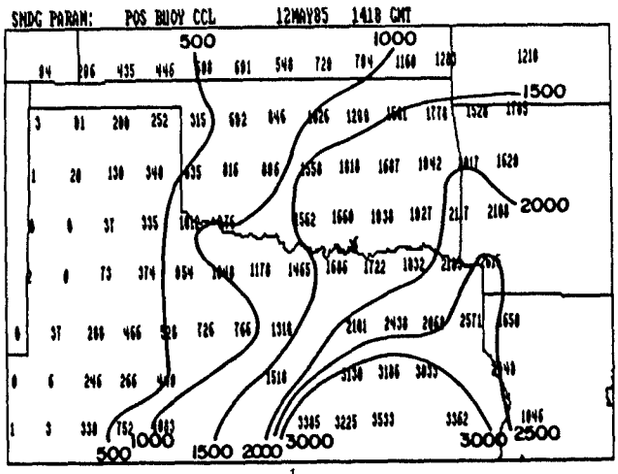

Figure 9. B_{CCL}, ($J\ kg^{-1}$), positive area computed with convective temperature, 1418 GMT, 12 May 1985.

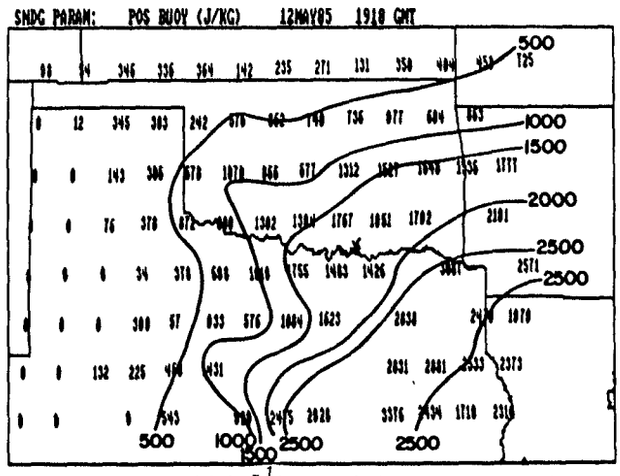

Figure 10. B, ($J\ kg^{-1}$), positive area computed with lowest kilometer average temperature, 1918 GMT, 12, May 1985.

Missouri, which was unfavorable for thunderstorm development even though surface dewpoints were very high. It appears that the nocturnal MCS in eastern Kansas derived some of its energy from air mass 1, which had high "positive area" but was slightly capped and therefore unfavorable for initial thunderstorm development. Additional research work is needed to assess the forcing needed to overcome VAS-derived negative areas. Since boundary layer structure and dynamics are very different at night, it is quite likely that afternoon situations must be approached in a different manner than nighttime situations.

Although a number of questions remain unanswered as to the applicability of VAS-derived parameters to forecasting MCS's, several preliminary forecast aids can be stated. These are based on case studies from 1984, as well as experience gained in the real-time test of VAS-derived products during PRE-STORM in 1985.

The following "rules of thumb" are proposed for using VAS-derived thermodynamic parameters to forecast mesoscale convective systems:

1. Maxima of B and B_{CCL} identify favored regions for MCS's. However, they are not necessarily favorable for initial development of convection.

2. Areas with $B_{CCL} > 1000$ Jkg^{-1} where T_c, N or H are minimum are favored regions for thunderstorms to develop.

3. Although B > 1500 Jkg^{-1} occurs frequently, B > 750 Jkg^{-1} is sufficient for deep convection.

4. MCS's do not occur in: 1) regions with $T_c > 35°C$, and 2) regions with $B_{CCL} < 500$ Jkg^{-1}.

Various synoptic-scale meteorological conditions and mesoscale features have been documented which are used to forecast the development of mesoscale convective systems (Maddox, 1983; Rodgers, et al., 1984). Some of these forecast techniques require a careful re-analysis of routinely available data with emphasis on the mesoscale (Doswell, 1982). VAS retrievals offer a new data source with mesoscale space and time scales to supplement other data sources for optimum mesoscale air mass analysis.

With the anticipated operational use of VAS and the added capabilities of future GOES (I, J and K), further development of forecast techniques utilizing VAS-derived thermodynamic parameters, is needed. Additional refinements of information available from VAS, particularly in measuring temperature and moisture in the sub-convective cloud layer may also prove invaluable to the applicability of VAS to mesoscale convective systems.

7.0 Acknowledgements

The research for this paper has been supported by NOAA Grants NA84AA-D-00017 and NA84AA-H-00020. The author would like to thank Sallie Varner for manuscript preparation, and Debra Lubich and Bob Green for their expertise with computer analysis and plotting routines. Jim Purdom and John Weaver provided many helpful comments pertaining to research goals and preparation of this paper.

8.0 References

Cram, J.M. and M.L. Kaplan, 1985: Variational assimilation of VAS data into a mesoscale model; assimilation method and sensitivity experiments. Mon. Wea. Rev., 113, 467-484.

Doswell, C.A., III, 1982: The operational meteorology of convective weather. Volume I: Operational mesoanalysis. NOAA Technical Memorandum, NWS NSSFC-5, 131 pp.

Green, R.N. and J.F. Weaver, 1985: Use of a personal computer workstation for short range forecasting: a case study. Preprints, 14th Conference on Severe Local Storms, Indianapolis, IN, AMS, Boston, MA.

Jedlovec, Gary J., 1984: A statistical evaluation and comparison of VISSR Atmospheric Sounder (VAS) data and corresponding rawinsonde measurements. NASA Technical Memorandum 82575. NASA/MSFC, Alabama, April.

Maddox, R.A., 1983: Large-scale meteorological conditions associated with mid-latitude, mesoscale convective complexes. Mon. Wea.Rev., 111, 1475-1493.

Purdom, J.F.W., 1973: Meso-highs and satellite imagery. Mon. Wea. Rev., 101, 180-181.

Purdom, J.F.W., R.N. Green, J.F. Weaver, R.M. Zehr and D.A. Lubich, 1985: Satellite data support to the PRE-STORM Operations Center, May - June 1985. CIRA Paper No. 3, Cooperative Institute for Research in the Atmosphere, Colorado State University, Ft. Collins, CO, 75 pp.

Rodgers, D.M., D.L. Bartels, R.D. Menard and J.H. Arns, 1984: Experiments in forecasting mesoscale convective weather systems. Preprints, 10th Conf. on Weather Forecasting and Analysis, Clearwater, FL, AMS, Boston, MA, 486-491.

Smith, W.L., 1983: The retrieval of atmospheric profiles from VAS geostationary radiance observations. J. Atmos. Sci., 40, 2025-2035.

_____, V.E. Suomi, F.X. Zhou and W.P. Menzel, 1982: Nowcasting applications of geostationary satellite atmospheric sounding data. Nowcasting, K.A. Browning, Ed., Academic Press, New York, 123-135.

Wade, G.S., A.L. Siebers and R.W. Anthony, 1985: An examination of current atmospheric stability and moisture products retrieved from VAS measurements in real-time for the NSSFC. Preprints, 14th Conf. on Severe Local Storms, Indianapolis, IN, AMS, Boston, MA, 105-108.

Weaver, J.F., R.M. Zehr and J.F.W. Purdom, 1985: Mesoscale analysis of low-level temperature and water-vapor distribution based on surface and satellite observations. Preprints, 14th Conf. on Severe Local Storms, Indianapolis, IN, Amer. Meteor. Soc., Boston, MA.

6.4

AN OBJECTIVE COMPARISON OF SEVERE LOCAL STORM PREDICTORS DERIVED FROM VAS TEMPERATURE AND DEW POINT PROFILES

David H. Kitzmiller

Techniques Development Laboratory
Office of Systems Development
National Weather Service, NOAA
Silver Spring, Maryland 20910

1. INTRODUCTION

Judging the potential for the occurrence of severe local storms several hours in advance requires a knowledge of the middle and upper troposphere's temperature, moisture, and winds. Static instability and vertical wind shear characterize the severe thunderstorm environment. A large number of indices involving temperature and humidity stratification and wind shear have been applied to this forecasting problem (see, for example, Miller, 1972). Prior to the development of satellite sounding systems, rawinsondes were the primary source of the observations needed to define these parameters.

Since 1981, the National Environmental Satellite, Data and Information Service (NESDIS) has produced vertical profiles of temperature and moisture retrieved from measurements of the Visible and Infrared Spin Scan Radiometer Atmospheric Sounder (VAS). This sounding system (described by Smith et al., 1981) is carried aboard later versions of the Geostationary Operational Environmental Satellite (GOES). During the spring and early summer months, a number of stability indices derived from VAS profiles are forwarded in near real time to the National Severe Storms Forecast Center (NSSFC) for assessment by forecasters. The results of this investigation have been summarized by Anthony and Wade (1983), Anthony and Leftwich (1984), and Wade et al. (1985).

The National Weather Service's Techniques Development Laboratory (TDL) is investigating possible uses for these satellite sounding products in developing objective probabilistic short-range forecasts of thunderstorms and severe local storms. The focus of this report is the initial phase of this research, in which we evaluated and compared the information content of several severe storm predictors. We show which indices and combinations of indices contain the most reliable information on severe storm potential.

2. VAS DATA USED IN THE STUDY

The VAS temperature and dew point profiles used in this study were prepared in real time by personnel of the NESDIS Advanced Satellite Products Project in Madison, Wisconsin. The profiles were prepared during the period March-July in 1984 and 1985. Operations with VAS were often precluded by rapid-interval scanning for visible and infrared images and by computer difficulties, so that retrievals from only 77 days in this period are available. The dataset contains soundings from VAS observations at 1100, 1300, 1400, and 1700 GMT. Retrievals were made over the continental United States east of the Rocky Mountains.

The profiles were retrieved via a physical regression algorithm in which temperature and humidity are computed simultaneously (Smith and Woolf, 1984). This algorithm differs substantially from earlier schemes so that data prepared prior to 1984 were not employed in this investigation. The new algorithm constrains the sounding surface temperature and dew point to match hourly surface observations in order to improve the accuracy of the retrievals at lower levels.

While the VAS instrument was designed to monitor changes in atmospheric temperature and moisture over time, its ability to detect such changes is presently impaired by mechanical problems. Menzel and Schreiner (1985) have reported on the failure of the servo mechanism that initially maintained a constant VAS filter wheel temperature. Changes in the filter wheel temperature can cause unrealistic fluctuations in the retrieved mid-tropospheric temperatures over the course of the day. However, we found very few cases in which the 500-mb temperature changed by more than 10 K during the 1400-1700 GMT period. Our results show no degradation in the information content of several stability indices between 1100 and 1700 GMT. Also, the 3-h change of the 500-mb temperature and dew point appear to contain valid information on changes in stability. While mechanical difficulties with the VAS instrument have some effect on the accuracy of the retrievals, existing errors do not appear to overwhelm the ability of VAS to detect changes in the atmospheric state.

3. PREDICTORS INVESTIGATED IN THE STUDY

Our interest centered on a number of empirically-formulated and physically-based stability indices. The empirical predictors are simple linear combinations of temperature and dew point at several vertical levels. Physically-based indices are computed by applying the laws of thermodynamics applied to ascending air parcels.

The empirically-formulated K stability index is defined:

$$K = (T_{850} - T_{500}) + DP_{850} - (T_{700} - DP_{700})$$

where T and DP refer to temperature and dew point in degrees Celsius, and the subscripts refer to the pressure level in millibars. The K index was originally developed to indicate general thunderstorm potential. Charba (1979) modified the K index by replacing the 850-mb temperature and dew point with the mean value of the surface and 850-mb values. This modified K index is symbolized as MK.

Another empirical index, more commonly used in severe storm prediction, is the Total Totals index, defined:

$$TT = (T_{850} - 2T_{500}) + DP_{850}$$

Charba (1979) also introduced a modified Total Totals index (MTT) by averaging the 850-mb and surface temperature and dew point.

Two physically-based stability parameters in common use are the Showalter and lifted indices. The Showalter index is the difference between the ambient 500-mb temperature and the temperature of a parcel lifted to 500 mb from the 850-mb level. The rising parcel is assumed to cool adiabatically until it reaches its lifting condensation level (LCL), and pseudoadabatically thereafter. The lifted index is computed in a similar manner, except that the parcel is lifted from the surface. In unstable situations, the parcel's temperature is greater than the environment's at 500 mb, and the index is negative.

The Showalter and lifted indices make use of temperature data at two vertical levels. Recently, several researchers have introduced new parameters that use data from all available levels. One such index is the change in kinetic energy (DKE) realized by a surface parcel rising from its lifting condensation level to the 400-mb level. This term is formulated:

$$DKE = -R \int_{p_0}^{p_1} (T' - T)\, d\ln p$$

where T' is the parcel temperature, T is the environmental temperature, p the pressure, and R the gas constant for dry air. We take the lower limit of integration (p_0) to be the lifting condensation level, and p_1 to be the equilibrium level or 400 mb, whichever is lower. In unstable environments, DKE is positive and large.

We have tested another predictor, DTMAX, which we define as the largest difference between the temperature of a surface parcel rising to its equilibrium level and the ambient temperature. This temperature excess may occur at any level, while the lifted and Showalter indices show only the excess at the 500-mb level. In this experiment, we allow no negative values for DTMAX or DKE. Since the depth of the convectively unstable layer may be associated with severe storms, we also tested as a predictor the pressure difference between the LCL and the equilibrium level; this term we refer to as DPTH.

We computed these predictors from both the 1700 and 1100 GMT soundings to assess the differences in their magnitude and information content caused by diurnal temperature and moisture changes. To facilitate our statistical comparison between the stability indices and subsequent severe storm occurrences, we mapped the predictor data onto a uniform grid. Each of the predictors was computed at the VAS profile locations, then interpolated to an 80-km polar stereographic grid via a two-pass Barnes (1973) analysis scheme.

The average spatial separation of the soundings in clear areas is approximately 100 km, but the sounding density varies greatly due to cloud gaps. Because the final analysis may contain unrealistic features within data gaps, we eliminated from consideration all grid points that are more than two grid increments from the nearest sounding. Approximately 15% of all grid blocks were lost in cloud gaps. We hope to overcome this problem in future by using a continuous first guess field (from a model forecast or rawinsondes) for the objective analysis.

4. SEVERE LOCAL STORM REPORTS

Reports of tornadoes, surface hail $\geq$ 2 cm in diameter, and convective wind gusts $\geq$ 93 km h^{-1} or wind damage are routinely collected and edited at the NSSFC. We tabulated these reports for each hour and for each block of the 80-km grid on which the variables were analyzed for easy comparison with the predictor values. A severe storm was considered to occur when at least one of these convective phenomena was observed within the grid block during the period from 2000 to 0000 GMT.

The reports forwarded to us by NSSFC for the 1985 season had not yet been edited to remove duplicate reports. However, since any number of storm reports within a grid block define a severe event, we do not expect that using the unedited data will impact our results.

5. OBJECTIVE ASSESSMENT OF THE PREDICTORS' INFORMATION CONTENT

To judge the ability of the predictors to indicate severe storm potential, we used the computed information ratio (IC) developed by Holloway and Woodbury (1955). The abbreviation IC was adapted from Keller and Smith (1983), to avoid possible confusion with the common abbreviation for infrared radiation. In a form similar to that below, the IC was also used by Lund and Wohl (1955) in experiments in statistical weather forecasting, and by Keller and Smith in a comparison of convective stability indices derived from rawinsonde profiles and satellite retrievals. The IC measures a predictor's relative ability to forecast the occurrence and nonoccurrence of a particular event. In our application of the IC, the predictor is stratified into a number of classes, and the number of cases with and without severe storms in each class is tabulated. If there are k classes, and if the predictand is divided into two categories (as it is here), the information ratio is defined:

$$IC = 1 - \frac{\sum_{i=1}^{k} E_i \ln E_i - S_i \ln S_i - O_i \ln O_i}{N \ln N - M \ln M - P \ln P}$$

where i is the index of the predictor class,
E_i is the number of cases in class i,
S_i is the number of severe cases in class i,
O_i is the number of nonsevere cases in class i,
N is the total number of cases,
M is the total number of severe cases, and
P is the total number of nonsevere cases.

The range of the IC is zero to one. If the predictor has no predictive information (the relative frequency of severe events is identical in all classes), then the IC vanishes. If the predictor has perfect information (all severe events fall into a limited number of classes that have no nonsevere events), then the IC is one.

A prime reason for introduction of the IC as a verification measure is that the IC is not adversely affected by a nonlinear relationship between the predictor and predictand, as is the linear correlation coefficient. As noted by Charba (1979) and by Reap and Foster (1979), stability indices often have a nonlinear relationship to severe local storm relative frequency. In many cases, the linear correlation coefficient of such indices does not reveal their true predictive potential.

In practice, the nonlinearity between the predictor and predictand may be dealt with by performing a mathematical transformation of the original stability indices to ensure a linear relationship to the predictand relative frequency, which is determined empirically from the dependent data sample. The transformed predictor then corresponds to the observed relative frequency for any given value of the original stability index. The main advantage in using the IC lies in its ability to directly estimate the predictive potential of the stability indices without resorting to the time-consuming linearization process described above.

6. RESULTS OF SINGLE PREDICTOR TESTS

We considered predictor values and severe storm reports over the region from the Great Plains to the Appalachian Mountains in evaluating the predictor information content. Approximately 33,500 individual cases were available for consideration in computing values of IC (77 days times 542 grid blocks, minus missing blocks due to cloudiness). Each of the predictors described in section 3 was stratified into 15 categories, with at least 900 events in each category. The values of IC for each predictor at 1100 GMT and 1700 GMT are listed in Table 1.

In general, the best predictors at 1700 GMT are physically-based and dependent on surface observations. The lifted index has a larger IC than the Showalter index, and the K and Total Totals indices have a larger IC when modified by surface temperature and dew point. It appears that the surface observations, which have high absolute accuracy, add predictive information. Two "bulk" indices that depend on temperature data at all levels between the surface and equilibrium level, DTMAX and DKE, have the largest IC of all. In their study of satellite-derived convective indices, Keller and Smith (1983) used a substantially different definition of the severe storm predictand. We note, however, that they found an IC of 0.101 (or 101 in our scale for Table 1) for the Showalter index derived from rawinsonde soundings, and 125 for the same index derived from 1500 GMT NOAA-6 satellite soundings. These values are comparable to those found in this study.

Table 1. Computed information ratio (IC) of various convective stability indices. Predictors are indices derived from 1100 and 1700 GMT VAS retrievals, and the predictand is the occurrence of severe local storms during the period from 2000 to 0000 GMT. The IC is multiplied by 1000.

Predictor	IC at 1700 GMT	IC at 1100 GMT
K index	100	99
MK index	109	106
TT index	76	75
MTT index	78	84
Showalter index	101	96
Lifted index	121	90
DKE	125	80
DTMAX	133	86
DPTH	89	55
Maximum expected random IC	10	10

The information content of many of the predictors is considerably less at 1100 than at 1700 GMT, as might be expected. The magnitude of most of the physically-based indices is strongly dependent on surface temperature, which of course undergoes radical changes between morning and afternoon. The IC values for DTMAX and DKE are much lower in the morning, while those for K and MK are only slightly lower.

The value of IC will tend toward zero for an infinite data sample if there is no relationship between predictor and predictand. If the data sample is limited, however, random influences can result in appreciable values of IC. It is possible to estimate the greatest IC that might occur strictly by chance (Lund and Wohl, 1955). Holloway and Woodbury (1955) state that the numerator of the expression for IC is distributed as one-half "chi-squared" with (k-1)(n-1) degrees of freedom, where k is the number of predictor classes and n is the number of predictand classes. The denominator is constant for any given sample of predictand data. The maximum expected random IC at the 99% confidence level is shown in Table 1. There is clearly very little likelihood that the IC values for any of the predictors could have occurred by chance alone.

The results of this portion of the experiment indicate that DTMAX possesses the greatest predictive information at 1700 GMT, while the MK index possesses the most information at 1100 GMT. Figures 1a and 1b show the observed severe local storm relative frequency as a function of these two predictors. Though the frequency values are low, it should be remembered that the verification grid blocks cover only 6400 km^2 and that only a portion of the day is considered. Furthermore, few active storm days are included in our sample, since on such days VAS operations are precluded by use of the GOES for rapid-interval scanning. Consequently, the observed severe storm relative frequency within the sample is only 0.8%.

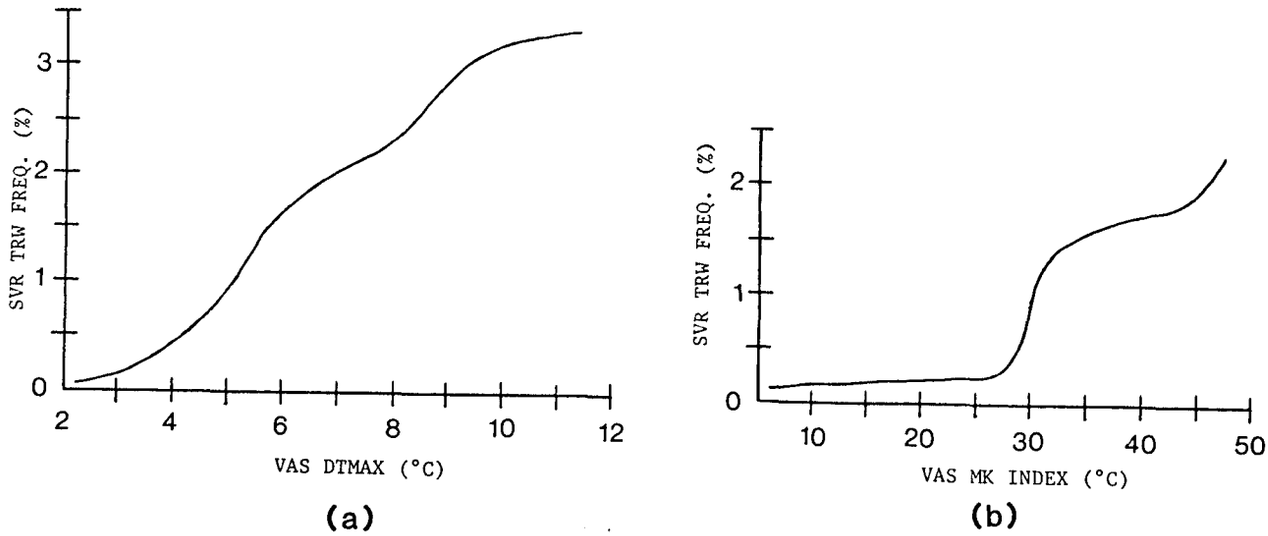

Figure 1. Observed severe local storms relative frequency during the period 2000-0000 GMT as a function of (a) 1700 GMT DTMAX and (b) 1100 GMT MK index.

7. INFORMATION CONTENT OF PREDICTOR COMBINATIONS

Earlier work with VAS soundings (Keller and Smith, 1983; Anthony and Leftwich, 1984) showed that substantial information about severe storm potential is gained when several other factors are considered along with static instability. For example, strong 500-mb winds appear to enhance severe storm likelihood indicated by a large negative lifted index. Therefore, we examined the influence of additional predictors upon the severe storm probability potential by DTMAX and the MK index alone. These predictors include surface variables, VAS-derived winds and vertical wind shear, and climatic severe storm frequency.

Many investigators have documented the importance of surface variables, such as moisture divergence, in determining the location of thunderstorm formation. Charba (1979) also found that surface equivalent potential temperature (Θ_e) advection is associated with severe storm development. We used Charba's (1979) Cressman-type scheme to objectively analyze surface temperature, dew point, winds, and surface pressure. Reap and Foster (1979) and Charba (1984) showed that climatic frequency is a highly useful predictor when combined with a stability index. We used a 24-h severe storm relative frequency derived from reports from 1974 to 1983.

Keller and Smith (1983) showed that parameters from VAS-derived gradient winds, including the 850-mb and 500-mb windspeed and the sine of the angle between the 850-mb and 500-mb winds, are useful predictors of severe storms. We included these terms as well as the total precipitable water in our tests.

Upper-level cooling and drying have often been associated with severe storms. Our dataset permitted us to compute time rates of change of several variables directly. Therefore, we computed the change in dew point and temperature at 500 mb between 1400 and 1700 GMT for use as predictors. The brightness temperature in VAS channel 10 (6.7 microns) has often been used to track dry mid-tropospheric air (see Anthony and Wade, 1983). We computed the 3-h change of this brightness temperature as another measure of mid-level drying. Finally, the 3-h change in Showalter index was used to indicate thermodynamic destabilization.

In combining these variables, we derived histograms of severe storm relative frequency as a function of two predictors at the same time. The frequency values are stored in the form of a table, and forecast probabilities may be obtained from the table by interpolating to the necessary predictor values. This procedure was described by Panofsky and Brier (1965), and it was used by Keller and Smith (1983) and by Charba (1984) in creating severe storm predictors. The IC is computed using the formula given earlier; the predictor categories now depend on the stratification of two variables at once.

Each of the variables was combined with the MK index for 1100 GMT data, and with DTMAX for 1700 GMT data. The resulting IC values appear in Table 2. Combining DTMAX and surface moisture divergence or Θ_e advection yields the greatest IC for 1700 GMT observations. The combination of MK and surface Θ_e advection or 850-mb windspeed gives the most predictive information at 1100 GMT. Among the time-change predictors, the Showalter index change appears to be the most useful. Since the time change of the Showalter index adds predictive information to DTMAX, it is apparent that the VAS can accurately detect changes in dew point and temperature despite its present mechanical problems.

Figures 2a and 2b show the severe storm relative frequency for the DTMAX-moisture divergence combination and for the MK-Θ_e advection combination. As shown in Fig. 2a, the combination of moisture divergence and DTMAX delineates regions containing severe storm probabilities as high as 6.8%. Severe storm potential increases as both

Table 2. Computed information ratio (IC) for various predictors in combination with DTMAX (1700 GMT data) and with MK index (1100 GMT data). The predictand is the occurrence of severe local storms during the period 2000-0000 GMT. Time-change predictors were not available at 1100 GMT. The IC is multiplied by 1000.

Predictor	1700 GMT	1100 GMT
500-mb windspeed	184	147
850-mb windspeed	170	153
Sine of wind shear	172	145
Precipitable water	169	125
24-h climatological relative frequency	176	142
Sfc moisture divergence	196	147
Sfc Θ_e advection	183	159
3-h 500-mb temperature change	167	
3-h 500-mb dewpoint change	164	
3-h Ch. 10 brightness temperature change	167	
3-h Showalter change	174	
Maximum expected random IC	43	43

Among the 1700 GMT stability indices, the temperature excess parameter DTMAX had the largest computed information ratio (IC). Physically-based parameters that depend upon surface observations of temperature and moisture had the greatest values of IC. Among the 1100 GMT predictors, the K index modified by surface data (MK) had the largest IC. The predictive value of some parameters such as DTMAX was much lower at 1100 GMT than at 1700 GMT.

Several other variables derived from VAS soundings, surface observations, or climatic frequencies were examined for their ability to enhance the predictive information in DTMAX and MK. The largest values of IC were those for a combination of DTMAX and surface moisture divergence at 1700 GMT, and MK and surface equivalent potential temperature advection at 1100 GMT.

Our results with the 1700 GMT VAS data illustrate the value of combining timely surface observations with all available satellite-derived information on the vertical temperature structure. An accurate portrayal of the low-level atmosphere is important since predictors such as DTMAX and DKE are sensitive to details in the temperature structure that can inhibit or enhance thunderstorm development. Severe storm occurrence is evidently dependent upon features such as low-level moisture convergence that can be diagnosed from the combined surface and satellite data.

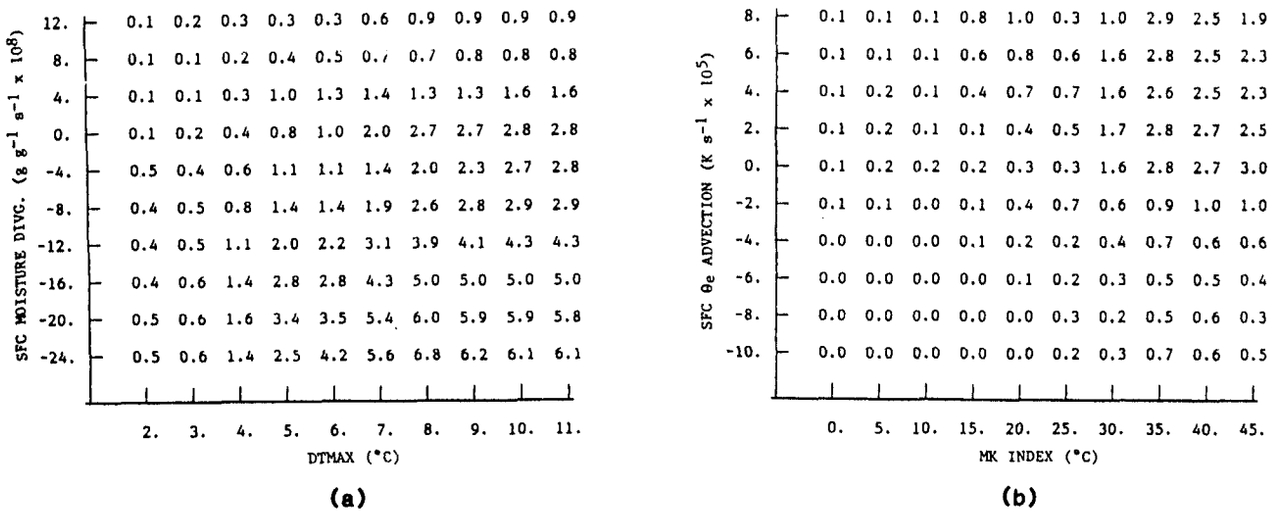

Figure 2. Observed severe local storm relative frequency during the period 2000-0000 GMT, in percent, as a function of (a) DTMAX and surface moisture divergence at 1700 GMT and (b) MK index and surface equivalent potential temperature advection at 1100 GMT.

moisture convergence and instability increase. The relative frequency distribution shown in Fig. 2b shows that severe storm potential is not a monotonic function of MK or of Θ_e advection. We found that severe storm frequency actually decreases slightly for very large values of most stability indices.

8. SUMMARY AND CONCLUSIONS

We have tested several convective stability indices derived from VAS temperature and moisture retrievals for their ability to measure severe local storm potential. The indices were computed from VAS observations taken at 1100 and 1700 GMT, while the severe storm events were observed during the subsequent period 2000-0000 GMT.

When forecasting afternoon convection from morning (1100 GMT) soundings, predictors such as the MK and Showalter stability indices appear to be good choices since they are less sensitive to details in the vertical temperature structure, which can change radically from morning to afternoon. Predictors such as these have traditionally been used by operational forecasters to forecast thunderstorms in many parts of the country.

In a broader context, our results would tend to support the conclusion of Stone (1985) that potential instability is important in defining general areas in which severe storms may occur. However, to accurately define local areas of severe storm occurrence a knowledge of existing

dynamical forcing is required on fairly small time and space scales.

In the future, we will test more combinations of severe storm predictors, and we will examine predictors of general thunderstorm occurrence. The final goal of this study is the incorporation of VAS predictors into TDL's operational short-range thunderstorm and severe local storm probability guidance.

9. ACKNOWLEDGMENTS

I wish to thank Dr. W. Paul Menzel and Messrs. Geary Callan, Roney Sorensen, Anthony Siebers, and Gary Wade for supplying the VAS retrievals and for answering dozens of questions. I also wish to thank Dr. Jerome P. Charba for his suggestions and for supplying the surface data analyses used in this study. In addition, I wish to express my graditude to Mr. Ronald M. Reap and Dr. Wayne E. McGovern for their continued guidance in the development of this effort and to Mrs. Belinda Howard for typing the manuscript.

REFERENCES

Anthony, R. W., and G. S. Wade, 1983: VAS operational assessment findings for spring 1982-83. Preprints 13th Conference on Severe Local Storms, Tulsa, Amer. Meteor. Soc., Boston, J23-28.

_____, and P. W. Leftwich, Jr., 1984: Operational VAS applications in identifying regions with potential fore severe thunderstorm development. Preprints 10th Conference on Weather Forecasting and Analysis, Clearwater Beach, Amer. Meteor. Soc., Boston, 358-364.

Barnes, S.L., 1973: Objective map analysis using weighted time-series observations. NOAA Technical Memorandum ERL NSSL-62, National Oceanic and Atmospheric Administration, U.S. Department of Commerce, 60 pp.

Charba, J. P., 1979: Two to six hour severe local storm probabilities: An operational forecasting system. Mon. Wea. Rev., 107, 268-282.

_____, 1984: Two-to-six hour probabilities of thunderstorms and severe local storms. NWS Technical Procedures Bulletin No. 342, National Oceanic and Atmospheric Administration, U.S. Department of Commerce, 14 pp.

Holloway, J. L., and M. A. Woodbury, 1955: Application of information theory and discriminant function analysis to weather forecasting and forecast verification. Technical Report 1, Contract No. 551(07), Institute for Cooperative Studies, University of Pennsylvania, Philadelphia, 85 pp.

Keller, D. L., and W. L. Smith, 1983: A statistical technique for forecasting severe weather from vertical soundings by satellite and radiosonde. NOAA Technical Report NESDIS 5, National Oceanic and Atmospheric Administration, U.S. Department of Commerce, 35 pp.

Lund, I. A., and E. W. Wohl, 1955: An objective system for preparing operational weather forecasts. Air Force Surveys in Geophysics No. AFCRCTN-55-219, Air Force Cambridge Research Center, Bedford, Massachusetts, 7 pp.

Menzel, W. P., and A. J. Schreiner, 1985: Effects of filter wheel temperature excursions on VAS radiative transfer calculations. Memorandum for the Record dated 30 April, 1985, National Oceanic and Atmospheric Administration, U.S. Department of Commerce, 8 pp.

Miller, R. C., 1972: Notes on analysis and severe-storm forecasting procedures of the Air Force Global Weather Central. Air Weather Service Tech. Rep. 200 (Rev.), U.S. Air Force, 102 pp. [NTIS AD 744 042].

Panofsky, H. A., and G. W. Brier, 1965: Some applications of statistics to meteorology. The Pennsylvania State University, University, Park, 224 pp.

Reap, R. M., and D. S. Foster, 1979: Automated 12-36 hour probability forecasts of thunderstorms and severe local storms. J. Appl. Meteor., 18, 1304-1315.

Smith, W. L., V. E. Suomi, W. P. Menzel, H. M. Woolf, L. A. Sromovsky, H. E. Revercomb, C. M. Hayden, D. N. Erickson, and F. R. Mosher, 1981: First sounding results from VAS-D. Bull. Amer. Meteor. Soc., 62, 232-236.

Smith, W. L., and H. M. Woolf, 1984: Improved vertical soundings from an amalgamation of polar and geostationary radiance observations. Preprints Conference on Satellite Meteorology/Remote Sensing and Applications, Clearwater Beach, Amer. Meteor. Soc., Boston, 45-48.

Stone, H. M., 1985: A comparison among various thermodynamic parameters for the prediction of convective activity: Part II. NOAA Technical Memorandum NWS ER-69, National Oceanic and Atmospheric Administration, U.S. Department of Commerce, 14 pp.

Wade, G. S., A. L. Siebers, and R. W. Anthony, 1985: An examination of current atmospheric stability and moisture products retrieved from VAS measurements in real-time for the NSSFC. Preprints 14th Conference on Severe Local Storms, Indianapolis, Amer. Meteor. Soc., Boston, 105-108.

6.5

RESULTS OF THE PROFS REAL-TIME VAS PRODUCT ASSESSMENT

Daniel Birkenheuer[1] and John S. Snook[2]

National Oceanic and Atmospheric Administration
Environmental Research Laboratories
Environmental Sciences Group
Program for Regional Observing and Forecasting Services
Boulder, Colorado 80303

1. INTRODUCTION

The Program for Regional Observing and Forecasting Services (PROFS) has been improving a prototype workstation developed in 1981 to study mesoscale nowcasting (Reynolds, 1983; Schlatter et al., 1985; Haugen et al., 1984; Birkenheuer, 1983). Forecast exercises using the workstation have been conducted in the past (Schultz, et al., 1985). The latest forecasting exercise was conducted from 15 May through 23 August 1985 to study severe weather nowcasting. For the first time, the workstation incorporated both satellite products and applications from the VISSR Atmospheric Sounder (VAS) together with a set of conventional and advanced data sources (Table 1). (A detailed listing can be found in Wunderlich, 1985.)

PROFS has operated a satellite mode A and mode AA groundstation since the fall of 1984, enabling the preparation and presentation of visible, infrared (IR), and VAS image products for real-time operation at the workstation. The national and northern hemispheric products in Table 1 were remapped to a polar stereographic projection; the regional and local products were remapped to a Lambert conformal projection centered over Colorado. All products were accessed through a mouse-driven menu system. Three Ramtek color graphic terminals were used, two for image display and one for the menu. 512 x 512-pixel images were available in 4- and 8-frame loops. Imagery was degraded to 256 x 256-pixel resolution for 16- and 32-frame loops. Zoom, loop rate, graphic overlays, and the color-enhancement curve were all user selectable.

The 1985 real-time VAS assessment objectives, procedures, daily log, and initial findings are detailed in Birkenheuer and Snook (1985). Briefly, the assessment consisted of a review of products and meteorological conditions from the previous day prior to a daily discussion of that day's weather events attended by the forecasters, exercise participants, and visitors. Discussion topics included damage reports, watches and warnings issued, chase team observations, and product utility. Significant observations relevant to VAS product use were demonstrated and addressed by the forecasters and the VAS assessment team. The observations and conclusions of this paper were acquired from this work and a follow-up case study.

2. VAS PRODUCT GENERATION

VAS images are received in the satellite projection (line and element) and then remapped into the desired map projection producing a 512 x 512 pixel-image product. The remapped regional scale image is digitally smoothed using a 9-point filter. Filtering does not contribute information, but serves to make the image more asthetically pleasing by reducing high-frequency spatial perturbations more evident in smaller scale imagery. The local scale VAS image is a subset of the VAS regional scale product, and pixels are replicated to fill in the smaller scale image. The image is color enhanced for display using a look-up table (color table). Each pixel in the 512 x 512 image is an 8-bit brightness count that references the color table relating the 256 possible 8-bit values (ranging from 0 to 255) to a specific color and intensity. VAS workstation products have specific color tables designed to highlight product features.

Workstation products are generated by either an automatic scheduled process or as an application initiated by the forecaster. Scheduled products are created immediately upon ingest of all required data and appear automatically at the workstation. In contrast, application algorithms are operated by the forecaster. Application algorithms are necessary because computing resources are limited (CPU constraints), and it is desirable for some routines to be forecaster interactive.

2.1 Scheduled VAS Image Products

VAS image products generated in-house included: 1) a linear-enhanced 6.7 μm water vapor image; 2) a "split-window" low-level water vapor image; and 3) a convective stability image derived from the two former products.

The 6.7 μm image is computed using the equation:

$$\text{Brightness count} = 1105. - 4.25\ T_B\ (6.7), \qquad (1)$$

where T_B (6.7) is the 6.7 μm band brightness temperature in Kelvin, and the computed brightness count is constrained between 0 and 255.

Table 1. Major Workstation Product Classifications

Product	Scales+	Freq. (min)
VISSR visible	L*/R/N/H	30/30/60/180
VISSR IR	L/R/N/H	30/30/60/180
*VAS Split Window	L/R/N	30/30/60
*VAS Stability	L/R/N	30/30/60
*VAS 6.7	L/R/N	30/30/60
SAO	R	60
PROFS Mesonet	L	5
Den RAOB Skew-T	V	720
Profiler products	V	60
MAPS Analyses	N	720
MAPS Forecasts	N	720
MAPS/LFM Grids	N	720
AFOS	N	720
NCAR Doppler Radar (CP-2)	L	5 & 10
NEXRAD Algorithms	L	5
WSR-57 PPI	L	5
NCAR x-Band	L	5

+ Scales are: H = Northern Hemisphere Polar Stereographic
N = National Scale (48 States) Polar Stereographic
R = Regional Scale Lambert Conformal (Colorado and portions of surrounding states)
L = Local Scale Lambert Conformal (Eastern Colorado)
V = Vertical Scale

* During Rapid Interval Scanning Operation (RISOP) VISSR visible is available at 5 min. intervals, and VAS data are not available.

The split window image is generated from a differential absorption technique using the 11- and 12 μm VAS bands. The split window algorithm (Chesters et al., 1983) requires an input temperature representative of the boundary layer and brightness temperatures from the two VAS bands. The boundary layer temperature is assigned a constant temperature for all product scales. Using a variable input temperature supplied by other data sources (e.g. the Denver profiler) gave more inconsistent results than simply using a constant value regardless of airmass temperature or geographical location. Since the imagery was only used qualitatively to establish water vapor distribution in the preconvective environment, this approach was presumed to be satisfactory.

Low-level water vapor information is contaminated in cloudy areas because liquid and/or frozen water obscures emmissions in the 11 and 12 μm bands. The algorithm compares the two VAS bands (the "split window") and the input boundary-layer temperature to establish the presence of clouds. Any pixel for which a cloud is indicated is flagged and blacked out in the final imagery. Clouds appear as dark areas representing empty space in the data field.

The stability product is assembled by: 1) inverting the 6.7 μm image by converting each 8-bit pixel to its bit complement, 2) normalizing the brightness counts of the inverted 6.7 μm and the split window products to span 0 to 16, and 3) multiplying both together to produce a new hybrid image having brightness-count values ranging from 0 to 255. This is similar to the technique described in Petersen et al. (1984). The stability product enhances areas of convective instability: upper-level dryness from 6.7 μm imagery atop low-level moisture from split window imagery. The product inherits the problems present in the parent imagery (e.g. cloud and fog contamination from the split window product). The product can only be used qualitatively since it is generated from two normalized products. Cloudy regions are blacked out, indicating areas void of good data.

2.2 VAS Application Products

The PROFS workstation offers both graphic and image VAS application products. There are two graphic application products, Composite Skew T and VAS Region Plot. These algorithms use processed VAS-derived temperature and water vapor soundings received from the University of Wisconsin--Madison to provide horizontal and vertical thermodynamic information. In addition, two other VAS application products integrate VAS and conventional satellite data, producing image products.

2.2.1 Graphics

The Composite Skew T application combines VAS, microwave ground-based radiometer (profiler), and Radiosonde Observation (RAOB) soundings from any available time period on the same Skew T - Log p diagram. In addition, positive and negative buoyant energies, precipitable water (integrated from the water vapor sounding) and lifted index are computed and listed for each color-coded sounding. The display enables comparison of the different data sources and trend analyses for a given sensor.

VAS Region Plot generates plots of precipitable water, lifted index, positive and

negative buoyant energies, isobaric fields of temperature, dew point temperature, dew point depression, relative humidity, geopotential height, wind speed, and wind direction. Wind data are derived from an analyzed geostrophic field generated from the VAS thermal profiles. The wind information is processed at Madison and transmitted with the sounding data. The plots can be superimposed over any regional-scale image or displayed individually. By displaying computed values at the location of the sampled information, the user can infer the quantitative field. Objective analyses of data are avoided until better quality control is available, since analyzed erroneous data can easily destroy what would otherwise be a usable graphic.

2.2.2 Images

The PROFS workstation has application programs capable of producing two combined VAS images: Infrared (IR)/6.7 and IR/VIS/6.7. The combined images were available late in the exercise as applications. The images would normally be cumbersome to obtain because the user must initiate and await product generation. However, since both applications use scheduled products instead of raw data as the input source, generation time is considerably reduced. The IR/6.7 image merges conventional cloud imagery from the VISSR IR data with the 6.7 image by replacing 6.7 μm pixels with VISSR IR pixels wherever cloud tops are colder than -35° C. To distinguish between the two bands, a color table is used with black and white enhancement for the 6.7 portion of the image and color enhancement for the IR cloud-top temperatures. The product gives the forecaster information from both IR and 6.7 μm bands simultaneously. Thus, clear air motion in the vicinity of clouds can be observed and related to storm structure and intensification.

The second application image is a combined IR/VIS/6.7 image, similar to that described by Petersen et al., 1984. Each instrument or band is assigned a different color: IR is green, visible is red, and 6.7 is blue. The Ramtek display used in the PROFS workstation is not capable of directly accessing gun intensity; instead, a color table scheme is used to simulate mixing colors. The IR/VIS/6.7 color table permits all color combinations of discrete intensity values that utilize 216 of the 256 possible color-enhanced brightness counts. The color table index is formulated in base 6 by the equation:

$$\text{Brightness count} = (6^2)r + 6g + b, \qquad (2)$$

where variables r, g, and b each range from 0 to 5, representing the intensities of the red, green, and blue guns respectively. This approach only approximates the desired effect since each channel's measurement is constrained to 6 possible levels. However, the method produces color combinations with the same significance as cited by Petersen et al. 1984. The product indicates cloud level (high or low) as well as the moisture content of clear air.

3. RESULTS FROM 1985 SUMMER EXERCISE

The 6.7 imagery was found to be the most informative VAS imagery studied. Many forecasters elected to begin the day's weather briefing by showing national scale loops of 6.7 imagery. They found this to be an effective overview prior to focusing on the Colorado area. Half-hour loops of 6.7 imagery were used at the regional scale to detect short waves and nowcast their movement. This helped determine the arrival time of supportive upper-level dynamics to better forecast the onset of convection. Often, many convective ingredients were present except for a triggering mechanism to initiate storm formation. Loops of 6.7 imagery frequently showed when the suppressive conditions would switch over and favor convective development. Color tables were used to enhance moist and dry zones indicative of synoptic-scale dynamics. Proper color enhancement made it much easier to detect and track these features.

The 6.7 imagery is capable of displaying mesoscale features as well. Figure 1 shows a developing dry region behind (west of) a convective cell. This is evidence of compensating subsidence in response to strong updrafts within the storm. The dry region develops as drier air moves down from higher levels.

The quality of the split window imagery was dependent on the available moisture. When precipitable water amounts exceeded about 1.8 cm, the product was more reliable. Cloud and fog contamination adversely affected the imagery, causing false moist and dry readings to occur. The dual-display workstation aided in the interpretation of the imagery since split window products could be simultaneously displayed and compared to both visible and IR imagery.

Moisture boundaries, detected by the 6.7 and split window imagery, were also significant during the summer exercise. Boundaries have been shown to be important in mesoscale processes. Common examples are fronts, dry lines, and outflow boundaries. The latter are often observed with Doppler radar (Wakimoto, 1982). An example of an important upper-level moisture boundary is found in the case study in Snook and Birkenheuer, 1986. A dry intrusion (boundary) was observed moving from the southeast into eastern Colorado where the split window imagery and SAO reports showed a deep, moist boundary layer. When the dryness aloft reached the location of the low-level moisture, convection occurred, producing a mesoscale convective complex (MCC) over eastern Colorado. The MCC later moved into southern Nebraska producing flash floods.

Convective stability imagery was plagued by problems inherited from the parent imagery, primarily cloud and fog contamination from the split window product. In a few cases, the image indicated potentially unstable regions where later convection occurred, but the false alarms far outnumbered the successes. Product reliability can be improved with a better parent precipitable water image.

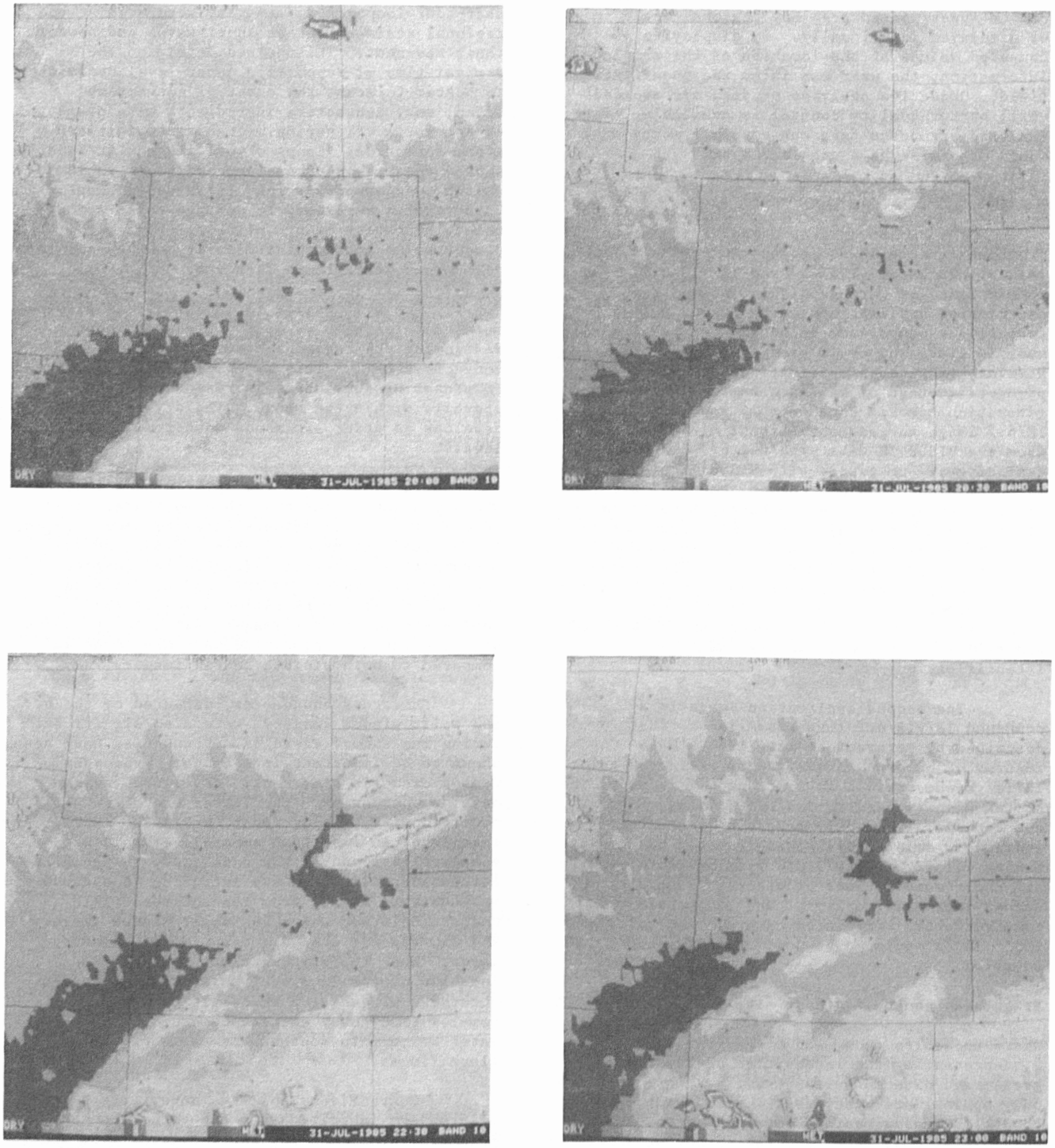

Figure 1. Development of subsidence west of a convective cell. The four 6.7 μm images recorded 31 July 1985 at 2000, 2030, 2230, and 2300 GMT show a thunderstorm developing in an area of relatively uniform moisture. By 2230 GMT the storm in NE Colorado had developed a noticeably dry region to the west, most likely due to drier air from above descending and warming. The storm produced flooding and tornadoes. The cell in Nebraska did not develop this feature and was not as intense.

Bulk parameters derived from the quantitative VAS soundings were more useful than the individual thermal profiles. In one case, values of lifted index, precipitable water and buoyant energies enabled forecasters to identify a region in northwest Kansas and southwest Nebraska as a potential storm-producing area on 9 July 1985 (Figure 2.) The VAS data provided forecasters a 5-hour lead time to convective development.

Precipitable water values obtained from integrating the VAS soundings supported the split window imagery in clear areas. Composite Skew T comparisons of the Denver RAOB data with VAS soundings near Denver showed the VAS thermal soundings in agreement with RAOB measurements, including a surprisingly good representation of weak, summertime low-level inversions. RMS difference errors for VAS thermal soundings and the Denver RAOB are on the order of 1 to 2 Kelvins. The VAS moisture profiles rarely coincided with the RAOB moisture sounding. The differences in precipitable water values computed from integrated Denver RAOB and nearest clear VAS moisture profiles (always within 100 km), showed the VAS profiles to be drier. The mean precipitable water difference (RAOB - VAS) was 0.5 cm with a standard deviation of 0.3 cm. Despite this, relative differences in VAS precipitable water over both time and space were significant and qualitatively useful.

Both VAS retrievals and derived imagery had mixed results over mountainous areas. Low brightness temperatures over the mountains often caused the split window algorithm to flag these areas as cloudy. In soundings, the surface pressure and surface height were usually reasonable. Geopotential heights derived from the thermal soundings caused errors in the PROFS Mesoscale Analysis and Prediction System (MAPS), a mesoscale objective analysis and forecast model (see Benjamin et al., 1985). Instead of using the absolute heights in the model, a new approach using geopotential gradients will be attempted.

Differences between the VAS soundings derived over Denver and the Denver RAOBs may be explained by Denver's proximity to the mountains, since the data incorporated into a VAS sounding may be influenced by mountainous terrain. Reliability of VAS retrievals may be better at locations well east of the mountains than around Denver.

Finally, the local-scale imagery was the least used by forecasters and will likely be dropped in the future. Most VAS imagery had 16-km resolution, and half-hour loops of 16-km imagery on the local scale was too coarse in time and space. This led to noisy images and loops in which the movement of features was discontinuous.

4. POST-EXERCISE RESULTS

The 6.7 μm imagery displays little useful information in cloudy regions. The combined IR/6.7 image provides the same level of detail as the usable portion of the 6.7 image and is more informative in cloudy areas because it shows IR cloud top temperatures. Thus, the combined image has more utility than the 6.7 image alone and is a good replacement for the 6.7 image. With suitable color table selection, the combined product could be made with color-enhanced 6.7 or color-enhanced IR, leaving the remainder of the image in gray scale.

Forecasters desired a higher degree of quantitative information in the split window imagery, resulting in a search for a replacement. One candidate is an image derived from the quantitative VAS soundings and the Multi Spectral Image (MSI) data. Linear regression coefficients are derived from the processed precipitable water

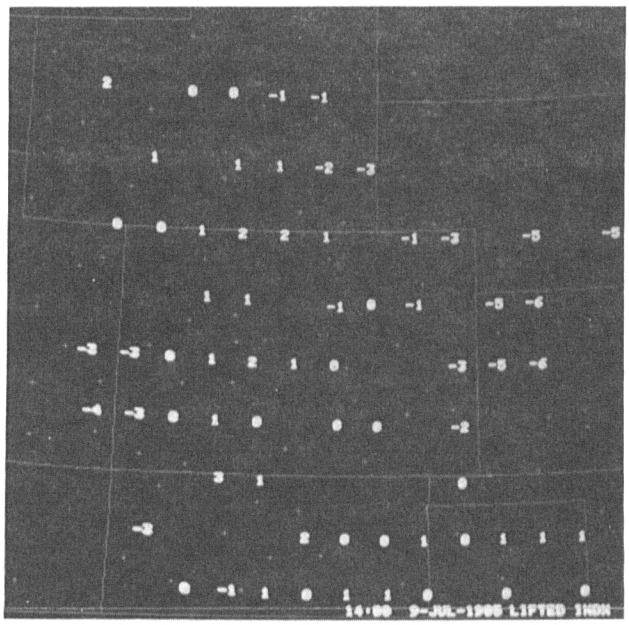

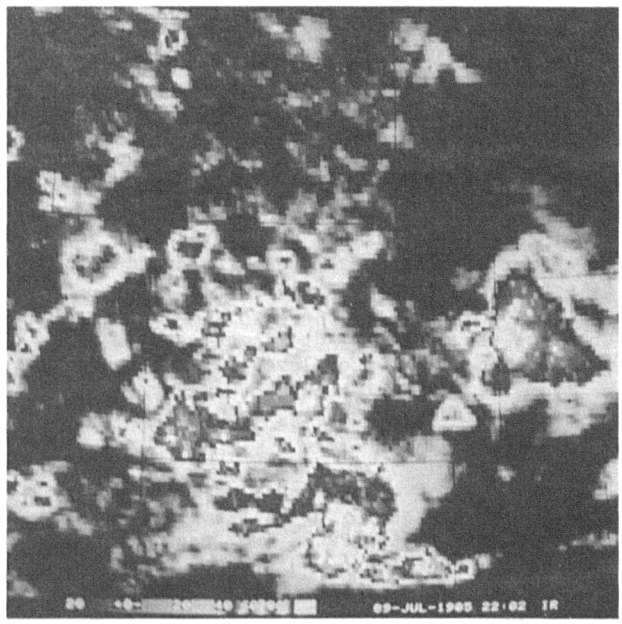

Figure 2. The mesoscale utility of derived VAS soundings. A cluster of unstable lifted index values ranging from -5 to -6 appeared at 1400 GMT on 9 July 1985 in northwestern Kansas and southwestern Nebraska. A storm developed in the area 5 hours later and persisted through 2200 GMT, as shown in the VISSR IR image. The short-range utility of VAS sounding data is clearly evident in this case.

values, received as part of the processed VAS soundings and VAS brightness temperatures from which the soundings were produced. The coefficients are then used to derive a precipitable water image from the various MSI bands. The advantage of the regression method is that it is free from any dependence on climatology, diurnal heating effects, and it can incorporate more VAS radiance information. Testing is now underway to determine whether the product is worthwhile.

5. SUMMARY

Results from the PROFS 1985 summer exercise show that VAS products are a necessary part of a modern automated meteorological workstation. Loops of 6.7 imagery were found to be most useful along with bulk parameters derived from the VAS soundings. Data utility improved with appropriate color representation. Early morning VAS quantitative data and imagery were useful for short range forecasting, but the nowcast application of VAS information requires further study. Cloudiness, which is considered noise in some images and an obscuring phenomenon in others, and mountainous terrain, remain the most serious problems.

6. ACKNOWLEDGEMENTS

We wish to thank Barbara McGehan and Jim Ramsay for the secretarial and technical support in preparing this manuscript. The research was made possible by funding from the NOAA Operational VAS Assessment Project.

7. REFERENCES

Benjamin, S. G., R. S. Lieberman, T. W. Schlatter, and R. G. Rasmussen, 1985: Preliminary tests of a regional objective analysis and short-range numerical forecasting system. Preprints, Seventh Conference on Numerical Weather Prediction, Montreal. AMS, Boston, 440-443.

Birkenheuer, D., 1983: Advanced technologies impact on short term forecasts. Preprints, Ninth Conference on Aerospace and Aeronautical Meteorology, Omaha. AMS, Boston, 68-72.

Birkenheuer, D., and J.S. Snook, 1985: A review of the VAS assessment during the 1985 PROFS summer exercise, NOAA Tech. Memorandum (in press).

Chesters, D. C., L. W. Uccellini, and W. D. Robinson, 1983: Low-level water vapor fields from the VISSR Atmospheric Sounder (VAS) "split window" channels, J. Climate Appl. Meteor., 22, 725-743.

Haugen, D. A., D. Birkenheuer, R. F. Bunting, M. C. McCoy, and G. M. Williams, 1984: An evaluation of the PROFS 1982 real-time forecast experiment, NOAA Tech. Report ERL-427-ESG1, Boulder, Colo. 21 pp.

Petersen, R. A., L. W. Uccellini, A. Mostek, and D. A. Keyser, 1984: Delineating mid- and low-level water vapor patterns in pre-convective environments using VAS moisture channels. Mon. Wea. Rev., 112, 2178-2198.

Reynolds, D. W., 1983: Prototype workstation for mesoscale forecasting. Bull. Amer. Meteor. Soc., 64, 264-273.

Schlatter, T. W., P. Schultz, and J. M. Brown, 1985: Forecasting convection with the PROFS system: comments on the summer 1983 experiment. Bull. Amer. Meteor. Soc., 66, 802-809.

Schultz, P., M. C. McCoy, R. E. McGowan, T. W. Schlatter, and J. S. Wakefield, 1985: The first experiment in forecasting cool-season weather with the PROFS system. NOAA Tech. Memo. ERL ESG-16, (PB85 230605), 25pp. [Available from NOAA, PROFS Program Office, 325 Broadway, Boulder, Co. 80303.]

Snook, J. S., and D. Birkenheuer, 1986: Utilization of VAS data in PROFS' 1985 forecasting exercise. Preprints, Eleventh Conference on Weather Forecasting and Analysis, Kansas City. (In press).

Wakimoto, R. M., 1982: The life cycle of thunderstorm gust fronts as viewed with Doppler radar and rawinsonde data. Mon. Wea. Rev., 110, 1060-1082.

Wunderlich, S., 1985: Real-time 1985 system requirements document (unpublished manuscript). [Available from NOAA, PROFS Program Office, 325 Broadway, Boulder, Co. 80303.]

[1] Contract with Colorado State University Research Foundation and The Cooperative Institute for Research in the Atmosphere Ft. Collins, CO 80523

[2] Contract with T. S. Infosystems, Inc., Lanham, Md. 20706.

DETECTION OF MOUNTAIN-INDUCED MESOSCALE WAVE STRUCTURES WITH HIGH RESOLUTION MOISTURE IMAGERY

Gary J. Jedlovec
CIMSS, Univ. of Wisc.
Madison, Wisc.

W. Paul Menzel
NOAA/ASPP
Madison, Wisc.

Gregory S. Wilson
NASA/MSFC
Huntsville, Al.

Robert J. Atkinson
General Electric Co.
Huntsville, Al.

1. INTRODUCTION

Radiosonde observations near the surface and aloft often detect pressure, temperature, and wind patterns associated with large scale atmospheric wave features which govern our daily weather conditions. The detection of small scale waves such as gravity and bouyancy oscillations however, usually require special observations to measure the perturbations directly. These waves need not always be measured or sensed directly and their observable signatures (i.e., clouds) can be detected in visible photography or satellite imagery.

The detection of mountain and lee wave structures is often done by observing cloud signatures in regions where vertical oscillations are forced by terrain. Satellite observations of these small scale clouds are possible with high resolution visible sensors. Direct observation of wind and thermodynamic parameters is achieved by instrumented aircraft, lidar, and radar measurements. From these observations, quantitative information is available about mountain and lee waves, their formation and three dimensional structure. However, because a moist environment is not necessary, many wave features may go undetected by these conventional measurements because of the absence of clouds.

During one of the flights of the Multispectral Atmospheric Mapping Sensor (MAMS) on a NASA U2 high altitude aircraft in 1985, wave features were found in water vapor channel imagery in close proximity to the Sierra Nevada mountains of California (Fig. 1). Visible channel imagery from the flight was examined for cloud features but none were found. This paper presents evidence that the waves in the imagery reflect changes in the vertical temperature and moisture distribution produced by the vertical oscillations. These features on the downwind or lee side on the mountains are called lee waves.

2. BACKGROUND

2.1 Instrument Characteristics

The MAMS is a multispectral scanner capable of producing high resolution imagery in visible and infrared bands with detailed spectral resolution. Table 1 summaries the characteristics of the instrument and its spectral bands. The MAMS is flown on a NASA U2/ER2 at an altitude of 20km providing a resolution cell of 50-100m on the ground.

Table 1

MAMS: The Multispectral Atmospheric Mapping Sensor

Provides high resolution visible and IR scanning capabilities from a high altitude aircraft platform.

Scan rate	6.25 or 12.50 rps
Instantaneous field-of-view	2.5 or 5.0 mrad
Ground resolution (nadir,19.8km)	50m or 100m
Total field-of-view	86°
Roll correction	±15°
Calibration sources	IR, 2 controllable bbs
Pixels per scan line	716

Spectral Bands

Channel	Wavelength (microns)	Spectral Region	Single Sample Noise(1) 2.5/5.0@6.25rps
1	.42 - .45	blue	1.0
2	.45 - .52	blue/green	.5
3	.52 - .60	green	.4
4	.60 - .62	yellow/orange	.5
5	.63 - .69	red	.5
6	.69 - .75	red/near IR	.4
7	.76 - .90	near IR	.4
8	.90 -1.05	near IR	.4
9	6.20 - 6.90	water vapor	.40/.20
10	10.32 - 12.02	window (cold)	.15/.10
11	10.32 - 12.02	window (warm)	.15/.10
12	12.20 - 12.56	water vapor	.75/.40

(1) NEΔT ($mw/ster/m^2/cm^{-1}$) for 1-8, NEΔT (°C) for 9-12.

The width of the entire cross track field-of-view is 40km, providing detailed resolution over a relatively large area.

Eight channels of the instrument are used to separate the visible and near-infrared radiation into narrow bands which sense reflected solar energy from the earth's surface and clouds. The three infrared channels (one of which is redundant) cover selected regions where infrared emission from the earth and atmosphere are of interest. These bands

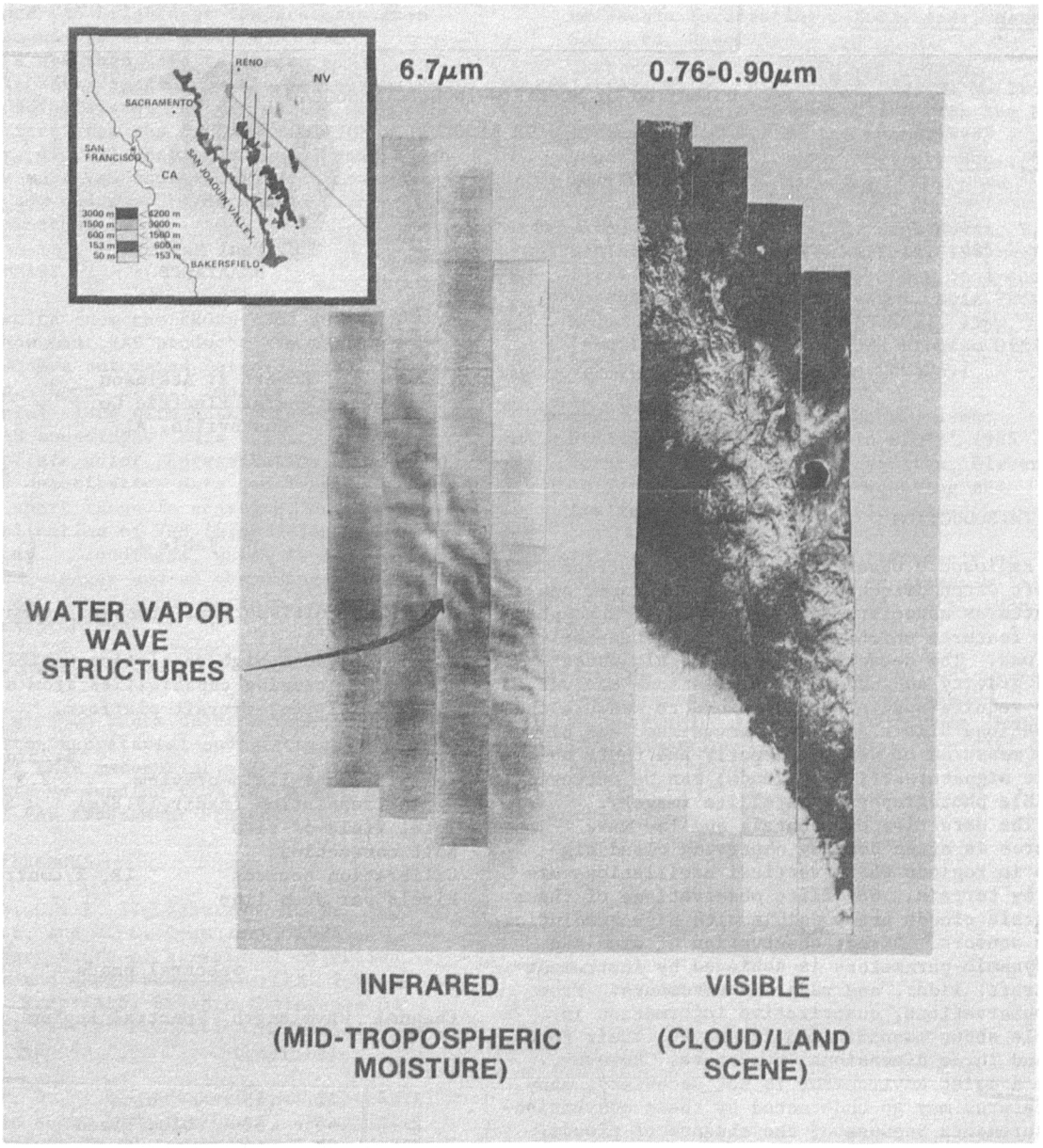

Figure 1. MAMS water vapor and visible channel composite imagery from four adjacent flight tracks on 22 January 1985 from 1942-2109 GMT. The inset shows the major terrain features of the Sierra Nevada mountains over which the imagery was collected.

include the mid-tropospheric (channel 9, 6.5 microns) and low-tropospheric (channel 12, 12.3 microns) water vapor region, and a window region (channel 10/11, 11 microns) where the atmosphere is relatively transparent. The 11 and 12 micron bands form what has become known as the split window channels (Chesters et al., 1983). Further details about the instrument and spectral bands may be found in Jedlovec et al. (1986).

2.2 Structure of Lee Waves

Stationary waves such as mountain or lee waves are a local phenomena which may have significant effect on local weather conditions because of their associated cloud patterns and wind distributions. They may also feedback to the larger scales of motion. The presence of either mountain or lee waves is due to vertical oscillations of air parcels as air is forced over the mountain. Mountain waves usually consist of one vertical oscillation of the flow pattern between two mountain peaks and are mainly governed in size by the spacing of the ridges. Lee waves, although forced by mountains, are not restricted in size to one or two vertical oscillations as with the mountain waves. In fact, the overshooting of the downward flow (the restoring force is gravity) on the lee side of the obstacle produces vertical oscillations which may extend for many wavelengths downstream.

The water vapor image in Fig. 1 shows wave structures in the lee of the Sierra Nevada mountains. Three or four waves are discernable, each having an estimated wavelength of 15-20km. The waves extend away from the face of the mountain range for about 70km and along the face for at least

120km. The waves appear somewhat irregular, possibly due to variations in the mountain peaks, tangental distortion from the scanner geometry (Jedlovec et al., 1986), limb brightening (due to increased water vapor path length at the edges of the flight track), as well as other unknown causes.

The nature of the vertical oscillation producing lee waves was studied in detail by Brunt(1927) who derived a set of equations which can be used to describe this flow pattern. From Brunt's work, a simple vertical oscillation in the atmosphere has a period given by

$$\tau = \frac{2\pi}{\left[\frac{g}{T}(\Gamma_d - \gamma)\right]^{1/2}} \qquad (1)$$

where

- γ is the environmental lapse rate,
- Γ_d the dry adiabatic lapse rate,
- g the gravitational acceleration, and
- T the environmental temperature.

An air parcel moving horizontally with a velocity of V and under this vertical oscillation will complete one cycle over a distance of

$$\lambda = v\tau = \frac{2\pi v}{\left[\frac{g}{T}(\Gamma_d - \gamma)\right]^{1/2}}. \qquad (2)$$

Upon examining this equation, it becomes apparent that the horizontal wavelength (λ) is governed by the wind speed and atmospheric stability. Strong winds and low stability favor long wavelengths, while weak winds and strong stability favor shorter ones.

A number of investigators have studied lee waves by observing their visible signatures and with direct measurements of temperature and wind velocity. Atkinson (1981) presents a fairly extensive review of this research. The characteristics of these waves vary from occurance to occurance but representative values are presented below. The wavelengths of lee waves range from 2-70km but most occurances are in the range of 5-20km. The wavelengths tend to increase with height and seem to be related to the mean wind speed. Corby (1957) performed a linear regression of wind speed on wavelength and suggested that a high enough correlation existed for the wavelength to be determined from the wind speed alone.

Another feature which is of interest is the wave amplitude, defined as the vertical distance between the peak and trough of a streamline. This is more difficult to determine from the cloud itself and requires a number of special measurements of the wind field. From the available empirical data, these wave amplitudes are typically about 1km but amplitudes of 7km have been measured. The larger amplitudes may occur when the wavelength closely matches the size of the obstacle forcing the wave.

From these studies, it appears that two parameters control the appearance and size of lee waves; namely, stability and wind. Of course the obstacle (mountain) is necessary to initiate the vertical oscillation and may have some control over the wave amplitude. Stability and wind are also important parameters in (1), however, the importance of stability in determining wavelength seems less important than indicated by (2). A typical environmental temperature and wind profile would consist of layers of varying stability and an absence of horizontal wind shear. In the lowest layer, the atmosphere would be neutral with a strong layer of stability aloft. This stable layer is necessary for the formation of the waves and should occur near the level of the mountain peak. A layer of weaker stability usually exists above this level. The flow should be perpendicular to the mountain at all levels and increase in speed with height. Significant horizontal shear reduces the liklihood for the development of lee waves.

2.3 Atmospheric Conditions

In the previous section, the atmospheric conditions required for the development of lee waves were summarized. Although they are local conditions, they are governed by the large scale atmospheric patterns. Thus, a discussion of the large scale features on 22 January 1985 corresponding to the MAMS observations is necessary. The upper air data (Fig. 2) exhibited a pronounced ridge of high pressure over the eastern Pacific ocean and over the northwestern portion of the U. S. A trough was positioned over the central part of the country with a portion of it hanging back into Utah and the southern portions of Nevada and California. This set up a [illegible] flow pattern from the northeast [illegible] muc[illegible] [illegible]e Sierra Nevada mountains.

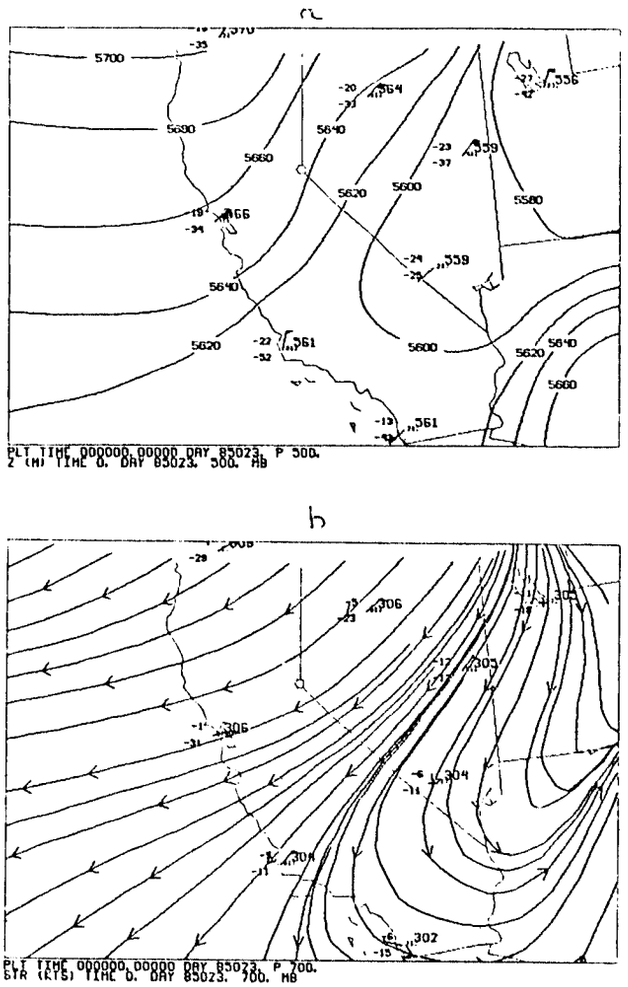

Figure 2. a) 500mb rawinsonde station plots and height analysis, and b) 700mb plots and streamlines for 23 Jan 1985 at 0000 GMT. Plots and analyses are in their standard units.

The region of interest (the Sierras) is in a data void region of the rawinsonde observing network. However, since only 3h difference exists between the MAMS and radiosonde observations, and given the stationarity of the weather systems, a reasonable estimation of the temperature, moisture, and wind profile may be available from the upwind sites. For this reason, data from two Nevada locations is presented in Fig. 3. A moderate to strong inversion exists around 700mb in both soundings. The atmosphere is quite dry above and below this level. The nearly saturated layer at the level of the inversion indicates a shallow layer of clouds. Clouds are not observed over the Sierras so the actual dewpoint will be somewhat colder. The winds are weaker at 72486 but both profiles indicate flow from the mortheast without much directional shear with height. From these diagrams, it seems reasonable to assume that conditions would be favorable for lee waves over the Sierras.

3. DISCUSSION

Although Fig. 1 was briefly discussed in previous sections, further discussion seems appropriate at this time. The MAMS 6.5 micron and visible/near-infrared channel imagery is displayed from four adjacent flight tracks on 22 January 1985. The data were collected from 1942-2109 GMT over the plateau region of Nevada, the Sierra Nevada mountains and the central valley of California as indicated by the inset map. The peaks of the Sierras climb to about 4000m and drop sharply to the southwest. Each flight track is about 40km wide making the entire ground distance of the west-east extent 160km. The north-south extent is roughly 400km. For display purposes, the resolution has been degraded to about 400m.

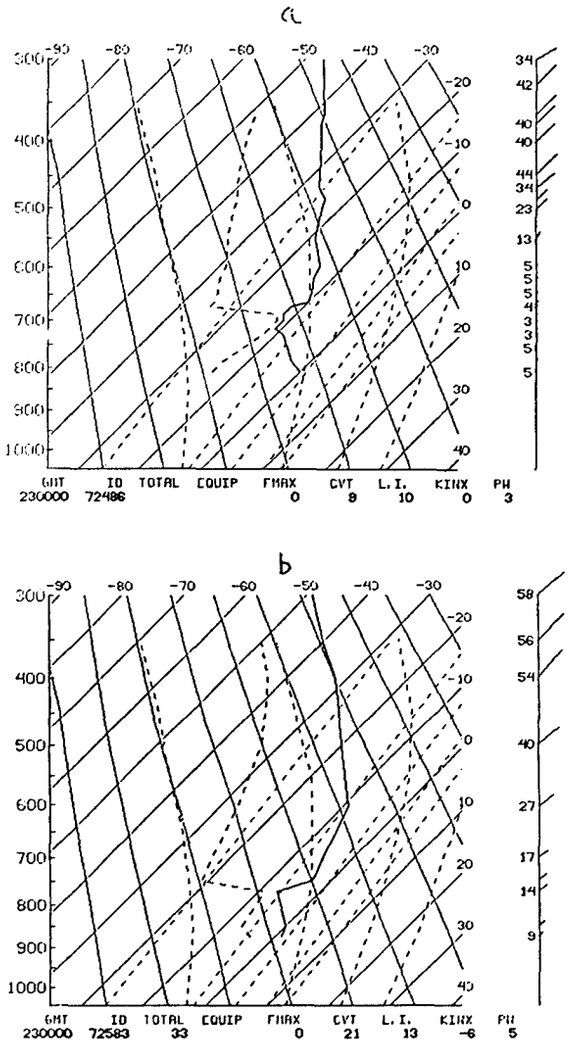

Figure 3. SkewT-LogP diagrams for two Nevada rawinsonde sites a) 72486, and b) 72583 at 0000 GMT 23 Jan 1985. Winds are plotted in knots.

Many very small scale features are apparent in the water vapor imagery. In the center of this imagery, alternating bright (cold/moist) and dark (warm/dry) features exist in wave-like patterns. They are orientated in a northwest-southeast direction parallel to the mountains. It is not posible to determine the position of the waves with respect to the position of the mountains from this image alone. The accompanying flight tracks of visible data capture the cloud/land features at the same instant as the water vapor imagery. Therefore this data can be overlaid and used to determine the exact position of the waves. Several landmarks are visible in the scene, the best being the quasi-circular Lake Mono in the right hand flight track. The bright regions in the lower portion of the visible image are fog and low clouds over the central valley. The bright areas in the center represent snow in the mountains above the 2400m level. Thus the snow region can be used to outline the major mountain features. From this and the terrain map, it is clear that most of the water vapor wave features reside on the downwind side of the mountains where surface elevations are below 2000m. It should also be noted that no clouds are present in the visible imagery over this region.

The estimated wavelengths of these waves (described in section 2.2) can be compared to that obtained from (2) or estimated from the mean tropospheric wind speed. The environmental lapse rate, temperature, and wind speed used in (2) is somewhat arbitrary. A value of γ of 0°K/km (T=250°K), and V of 10 m/s, yields 3.2 km, a rather short wavelength. Since the wave structures occupy more than a single level in the vertical, it may be more appropriate to uses values representative of a layer of the atmosphere. Using values from the 800-400mb layer (T=250°, γ= 6.5, and V=20), a wavelength of 10.7 km is obtained. This is somewhat less than the estimated length of 15-20km. As previously mentioned, Corby (1957) used an empirical relationship between wind speed and wavelength with a good correlation. The linear fit of his data (wavelength versus wind speed) produced a slope of roughly 0.45. For a mean environmental wind speed of 20m/s, a wavelength of 9km is predicted. In either case, a stronger wind speed would be needed to match the one estimated from the water vapor imagery. Considering that the actual wind profile over the Sierras is somewhat uncertain, these calculations are relatively close to the estimates from the observed data.

It is much more difficult to estimate the amplitude of these lee wave features without direct in situ measurements. However, the next section describes an approach to estimate the amplitude by simulating the MAMS water vapor channel radiances.

4. RADIATIVE TRANSFER SIMULATIONS

The water vapor image presented in Fig. 1 represents energy emitted by atmospheric water vapor somewhere in the mid-troposphere. The procedure to determine this layer or level has been the subject of investigation by researchers for many years. In the case of cloud height determinations using window channel radiances, the altitude of the cloud can be estimated by comparing the measured blackbody temperature to a local rawinsonde. The water vapor signal does not come from a single level but actually a layer of the atmosphere (Jedlovec, 1984), and depends on the amount, vertical distribution, and temperature of the vapor itself. It is unclear whether blackbody temperatures in this channel can be used directly to infer a mean height from which the signal originates.

In an attempt to estimate the amplitude of the lee waves observed in Fig. 1, several approaches were considered. Table 2 presents the observed blackbody temperatures measure in the peaks and troughs of the lee wave features. Typical values indicate a 6° temperature difference from the peak to the trough of the wave. It is difficult to use one of the soundings in Fig. 3 to directly infer the levels of the peak and trough of the lee waves. It may be reasonable to assume that the level of the neutral point of the wave is 246°K (-27°C) and the peak and trough occuring at the level of their measured temperature (Table 2), however. If this is done, the estimated wave amplitude is about 1km. While this is consistent with the amplitudes of a typical lee wave, it depends heavily on the lapse rate of the sounding used. Because of the lifting of the lower level inversion by the mountains, a smaller lapse rate of temperature probably existed over the Sierras, producing a greater vertical amplitude for the lee wave.

Another approach to estimate the lee wave amplitude used a composite of the two soundings in Fig. 3. From the composite sounding, MAMS water vapor channel radiances were simulated (McMillan and Fleming, 1976; Fleming and McMillan, 1977; and Weinreb and Neuendorffer, 1973). In order to obtain a representative profile in both the peak and trough of the waves, the inversion layer near 700mb and the accompanying moisture distribution were raised and lowered adiabatically in increments of 1 km. Blackbody temperatures were computed from the channel radiances. Temperature differences of 6°K were observed (similar to the measure values from Fig. 1) as well as the appropriate blackbody temperatures when the inversion was at 2 and 6km level for the trough and peak, respectively. This 4km vertical amplitude, while larger than most lee wave amplitudes, is more consistent with the level of the mountain peaks which produce them.

Table 2

Observed and simulated blackbody temperatures for the lee waves. Units are in degrees°K.

Observed Blackbody Temperatures	mean	extreme
Wave peak	243.5	242.0
Wave trough	249.5	251.0

Simulated Blackbody Temperatures (4km)	
Wave peak	243.9
Wave trough	249.5

5. CONCLUSIONS

The above work has presented evidence for the existence of lee waves in the absence of clouds using high resolution MAMS moisture imagery. Although verifying measurements do not exist, an evaluation of wind profiles and stability in the surrounding region support the existence of these waves. Estimations of the horizontal wavelengths of the observed lee wave features are not inconsistent with those from previous studies. The estimated vertical amplitude, although less certain, seems realistic for the setting. Further work is necessary to more accurately determine this vertical amplitude.

Acknowledgements. This work was performed in part by the lead author while affiliated with several organizations. Support from the Universities Space Research Association through a NASA contract and from the Space Science and Engineering Center at the University of Wisconsin was appreciated. Mr. John Arvesen of NASA/Ames and Jeff Myers also contributed in the collection and data reduction of the MAMS flight data. Their efforts are also appreciated.

REFERENCES

Atkinson, B. W., 1981: Meso-scale Atmospheric Circulations. Academic Press, New York, 495p.

Brunt, D., 1927: The period of simple vertical oscillations in the atmosphere. Q. J. Royal Meteor. Soc., 53, 30-31.

Chesters, D., L. W. Uccellini, and W. D., Robinson, 1983: Low-level water vapor fields from the VISSR Atmospheric Sounder (VAS) "split window" channels. J. Climo. Appl. Meteor., 22, 725-743.

Corby, G. A., 1957: Preliminary study of atmospheric waves using radiosonde data. Q. J. Royal Meteor. Soc., 83, 49-60.

Fleming, H. E., and L. M. McMillan, 1977: Atmospheric transmittance of an absorbing gas. 2. A computationally fast and accurate transmittance model for slant paths at different zenith angles. Appl. Opt., 16, 1366-1370.

Jedlovec, G. J., W. P. Menzel, G. S. Wilson, R. J. Atkinson, and J. Arvesen, 1986: The Multispectral Atmospheric Mapping Sensor (MAMS): Instrument description and data quality. (in press).

Jedlovec, G. J., 1984: Mesoscale analysis of 6.7μm image data from the VISSR Atmospheric Sounder (VAS) for several case studies. Preprints, Conf. on Satellite/Remote Sensing and Appl. AMS, Boston, 185-190.

McMillan, L. M., and H. E. Fleming, 1976: Atmospheric transmittance of an absorbing gas: A computationally fast and accurate transmittance model for absorbing gases with constant mixing ratios in inhomogeneous atmospheres. Appl. Opt., 15, 358-363.

Wienreb, M. P., and A. C. Neuendorffer, 1973: Method to apply homogeneous-path transmittance models to inhomogeneous atmospheres. J. Atmos. Sci., 30, 662-666.

APPLICATIONS OF SATELLITE METEOROLOGY IN SUPPORT OF SPACE SHUTTLE OPERATIONS

B. F. Boyd, T. M. Myers, and C. S. Funk

Office of the Staff Meteorologist
Eastern Space and Missile Center
Patrick Air Force Base, Florida

1. INTRODUCTION

The United States Air Force (USAF) Air Weather Service's Detachment 11 of the 2nd Weather Squadron is tasked to provide meteorological and environmental support to the USAF Eastern Space and Missile Center (ESMC), the National Aeronautics and Space Administration's (NASA) Kennedy Space Center (KSC), and the Department of Defense (DOD) Manager for Space Shuttle Support Operations. They provide weather support to the Cape Canaveral Air Force Station (CCAFS), Patrick Air Force Base (PAFB), KSC, and the entire Eastern Test Range (ETR); primarily through the Cape Canaveral Forecast Facility (CCFF). The CCFF is a 24-hour-a-day forecasting and observing operation. As part of its normal support, it provides specialized forecasts for all missile and space launches from the ETR/KSC and weather services for recovery forces. By far, the launch, landing, and ground operations of the Space Shuttle require the most precise weather support. Most aspects of Space Shuttle operations are sensitive to one or more meteorological parameters. As the Shuttle proved itself in its early missions (Table 1) and became operational with a significant increase in the number of scheduled missions (Table 2), it was evident that weather and weather support would become critical elements in achieving and maintaining the higher launch rate.

TABLE 1

SHUTTLES LAUNCHED BY YEAR

YEAR	TOTAL LAUNCHED
1981	2
1982	3
1983	4
1984	5
1985	9

TABLE 2

PROJECTED SHUTTLE LAUNCHES BY YEAR

YEAR	TOTAL LAUNCHES
1986	17
1987	23
1988	24

To deal with this problem, NASA and the USAF, at the local level, formed a joint Meteorological Systems Modernization Program (MSMP). This group is co-chaired by the Technology Projects Office of the KSC and the Office of the Staff Meteorologist of the ESMC. Through the efforts of the MSMP, and joint funding by the Air Force and NASA, several improvements in meteorological systems were accomplished, allowing better utilization of satellite data. The key improvement was the Meteorological Interactive Data Display System (MIDDS).

2. THE METEOROLOGICAL INTERACTIVE DATA DISPLAY SYSTEM (MIDDS)

To assist the forecaster with the problems of integrating data from various sources and producing mission support products which use all of the available data in an internally consistent manner, the MIDDS was developed under contract with the Space and Science Engineering Center (SSEC). The MIDDS (Young, 1985) consists of an IBM 4341 computer with appropriate peripherals and workstations in supporting a variation of the Man Computer Interactive Data Access System (McIDAS) software (Suomi, 1983). The system provides integration of the data sources available to the CCFF into a single data base where the various types of data can be melded and displayed together for forecaster use. It also provides growth for new data sources and allows for a significant increase in applications. Utilization of the MIDDS over an 18 month period has been presented previously by Kolczynski, Myers, and Boyd (1985, 1986, 1986). To better understand weather impacts to the Shuttle, one must look at Shuttle operations and weather constraints.

3. SHUTTLE OPERATIONS

There are many aspects to Shuttle operations that are much more susceptible to weather than the casual observer might realize.

3.1 Launch and Landing.

The relative low frequency of flight might lead one to think the most optimal times for launch as related to weather are easily attained. Just the opposite is true. Actual launch times are rigidly controlled by the orbital mechanics of the particular payloads and to some extent with other orbiting vehicles. In the extreme case, Mission 51-G had only a four minute launch window. Although most missions are not that restrictive, all have fairly limited launch periods. Within those limited launch windows there may be a much smaller optimal launch period. Once launch is accomplished, Return To Launch Site (RTLS) and Transatlantic Abort Landing (TAL) are also fixed. Abort Once Around (AOA) and normal End of Mission (EOM) are somewhat more flexible, but those opportunities are also very restrictive at any given site, with normally not more than two opportunities per day. For a launch to be completed, weather for a RTLS must also be acceptable. The climatological chances for a successful launch vary at the ETR by time of day and month as illustrated by Figures 1 and 2. Each figure represents a combination of all meteorological parameters with current flight constraints (see paragraph 4). Each also shows the effect of lowering the crosswind component from the current constraints of 10 and 15 to 5 and 8 knots.

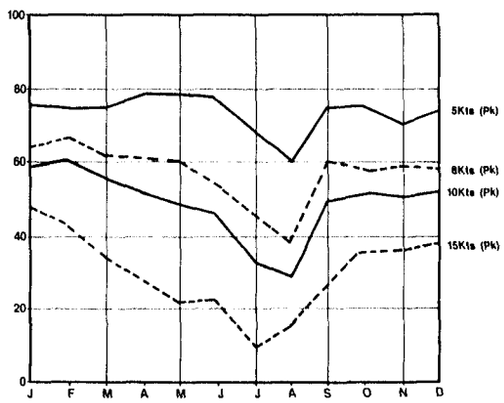

Fig. 1. Percent Probability No Go 1400L

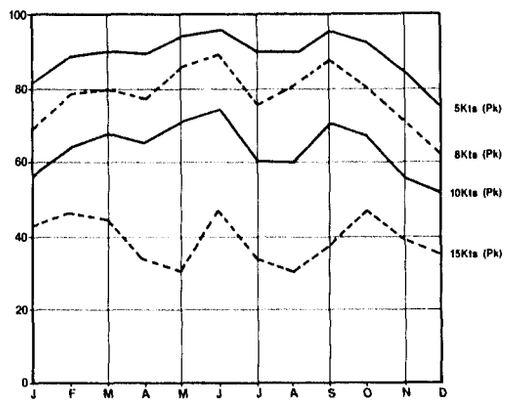

Fig. 2. Percent Probability No Go 1400L

3.2 Prelaunch Processing.

Although launch and landings are the most visible Shuttle operations, there is much to be accomplished between flights. When a payload is returned from outer space aboard the orbiter, the vehicle is towed back along the tow road to one of the Orbiter Processing Facilities (OPFs). In the OPF the payloads are removed, the payload bay is reconfigured for the next mission, broken tiles are repaired, brakes are fixed, etc. Once the orbiter is ready, it is towed to the Vehicle Assembly Building (VAB) where it is put in an upright position and stacked on top of the Mobile Launch Platform. There it is mated with the Solid Rocket Boosters (SRBs) and the External Tank (ET). Once this process is complete the entire Mobile Launch Platform is transported along the crawlerway 4.1 miles to Launch Complex 39A, typically a 6 to 8 hour trip during which the vehicle is vulnerable to weather. The Mobile Launch Platform, along with the vehicle, is left on the pad after the crawler pulls out from underneath it. The vehicle is launched from the Mobile Launch Platform. Any loss of production during this processing cycle may well impact launches when the number of processing days are condensed due to more frequent launches. The single largest loss of processing time is due to thunderstorms. Loss of production time due to lightning occurrences has been a problem since the origin of the space program at the ETR. (Gibbons, et al, 1985)

4. SHUTTLE WEATHER CONSTRAINTS

As shown in Table 3, weather impacts nearly all facets of Shuttle operations from rollover and rollout to final recovery of the Shuttle at end of mission. This table clearly illustrates the sensitivity of Shuttle operations to the environment and the subsequent impact of forecast support in maintaining Shuttle launch schedules.

TABLE 3

STS WEATHER SENSITIVITIES

Temperature, Winds, Precipitation

Temperature less than 31°F or greater than 99°F.

Precipitation forecast or occurring from the start of external tank loading through launch.

Ice accumulation greater than 1/16 inch on the external tank.

Surface winds (measured at 60 feet above natural grade) greater than 34.4 knots (peak) or 22.6 knots (steady state) from any azimuth (lift off).

Prelaunch surface winds greater than 49 knots steady state while on the pad.

Upper air wind shears outside vehicle load limits.

Flightpath (Nominal or RTLS)
Severe Weather Constraints
(to protect the vehicle from lightning strikes)

Cannot be within 2NM above or 5NM horizontal distance of the anvil associated with a thunderstorm.

Cannot be through any cloud (convective or layered) from which precipitation (including virga) is observed.

Cannot be through clouds in the dissipating stage which have detected lightning by the electric field mill network within 15 minutes prior to launch.

Cannot be through any cloud if a 1,000 volt per meter or greater ground level electric field contour encompasses launch (or landing) site.

Offshore Crew Recovery Area Constraints
(from launch pad to 50NM in the Atlantic)

Surface wind greater than 25 knots.

Ceiling less than 500 feet.

Visibility less than 0.5NM.

Seas greater than 8 feet.

Solid Rocket Booster (SRB)
Recovery Area Constraints

Sea state greater than sea state code 3 (3-5 feet moderate waves).

Visibility less than 1.5NM.

Landing Constraints
(RTLS and EOM)

Ceiling less than 10,000 feet (8,000 feet if Microwave Landing System (MLS) available).

Visibility less than 7 statute miles (5 statute miles if MLS). Final launch decision relies on slant range evaluation by weather reconnaissance flights along the return to launch site path at KSC and reentry profile at Edwards AFB or White Sands.

Surface wind component (including gusts) greater than 25 knots headwind, 20 knots crosswind (lakebed), 15 knots crosswind (runway), 10 knots crosswind (EOM), or 10 knots tailwind.

Any precipitation (RTLS), or precipitation within 50NM (EOM at KSC).

Turbulence greater than light to moderate.

Range Safety Constraints

The ESMC Office of Range Safety also has restrictions under the following weather conditions, due to tracking and blast damage considerations:

Ceiling less than 1,600 feet.

Visibility less than 5 statute miles.

Blast due to destruct sequence resulting in predicted fatality probability values greater than one per hundred thousand will result in hold or scrub.

Shuttle Ferry Flight
(Edwards AFB to KSC)

If the Shuttle lands at Edwards AFB instead of the Kennedy Space Center, the following weather constraints apply to the return flight of the NASA B-747 Shuttle Carrier Aircraft:

Flight conducted daylight hours only.

No flight through visible moisture.

Flight level temperature must be greater than 15°F.

No turbulence greater than moderate.

Crosswinds must be less than 15 knots for takeoff and landing.

Take-off runway ambient air temperature must be less than 92°F.

5. A CASE STUDY

Weather has impacted the Shuttle in various ways over the history of the program. A general overview is contained in Table 4.

TABLE 4

WEATHER IMPACTS
(THROUGH DEC 85)

MISSION	IMPACT
STS-3	EOM diverted to WSSH and delayed 1 day (Mar 82)
STS-7	EOM diverted to Edwards vice KSC (Jun 83)
STS-8	Launch delayed 17 minutes by thundershowers (Aug 83)
41-C	EOM diverted to Edwards due to KSC weather (Apr 84)
41-D	SCA flight delayed 1 day due to tropical storm Diana (Aug 84)
51-A	Launch delayed 1 day by windshears (Nov 84)
51-C	Delayed due to cold temperature impacts on ET fueling (Jan 85)
51-D	Held to end of launch window by clouds and showers (Apr 85)
51-D	Landing delayed 1 orbit due to showers. Landed with maximum crosswind at KSC (Apr 85)
SCA	Orbiter Columbia TPS damaged by precipitation during transit to KSC (Jul 85)

51-I Launch delayed 1 day by electrically active convective clouds (Aug 85)

61-C Weather (clouds) hold to near end of window, then aborted due to vehicle problem (Dec 85)

5.1. Mission 61A Background.

A recent case where the use of satellite data via the MIDDS prevented a weather impact was Mission 61A, 30 October 1985. Tropical Storm Juan had dominated the weather along the Gulf states and Florida for several days prior to launch, requiring a detailed metwatch during prelaunch processing as well as the launch itself. In the 48 hours prior to launch a number of operations occurred which are weather sensitive such as: loading of the external tank, last minute payload work, and work along the exposed service structures. Forecasters at the Cape Canaveral Forecast Facility (CCFF), using the MIDDS looping capability of GOES imagery and incorporating wind tower and lightning detection data were able to minimize the impact of the transient squall line feeder bands of Tropical Storm Juan resulting in a nominal launch countdown. Figures 3 thru 6 show daily accumulated rainfall for the southeast, and the eastward movement along the Gulf coast of the rainfall maximum through 30 October (NOAA, 1985). Figures 7 and 8 show the 1200 GMT position of Juan on 30 October.

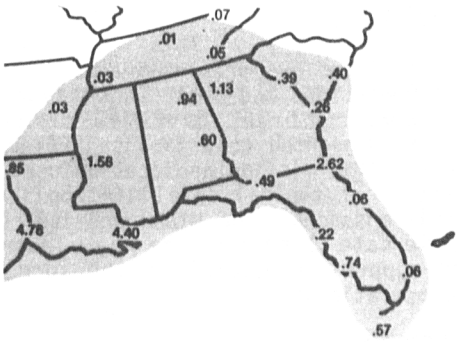

Fig. 3. 24 Hour Precipitation Totals for 28 Oct 85.

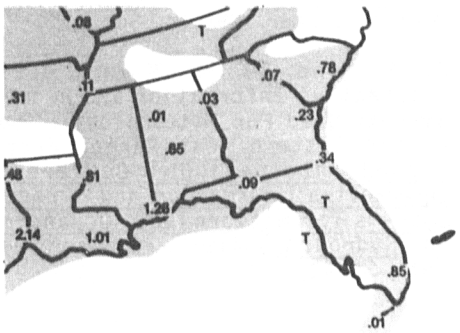

Fig. 4. 24 Hour Precipitation Totals for 29 Oct 85.

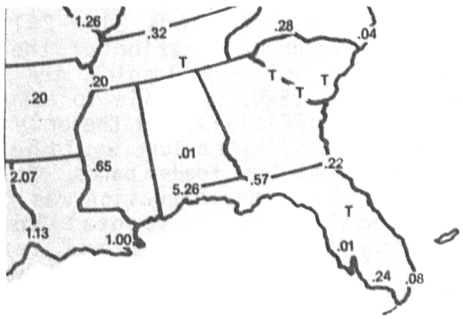

Fig. 5. 24 Hour Precipitation Totals for 30 Oct 85.

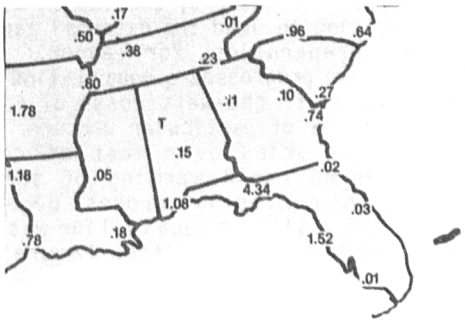

Fig. 6. 24 Hour Precipitation Totals for 31 Oct 85.

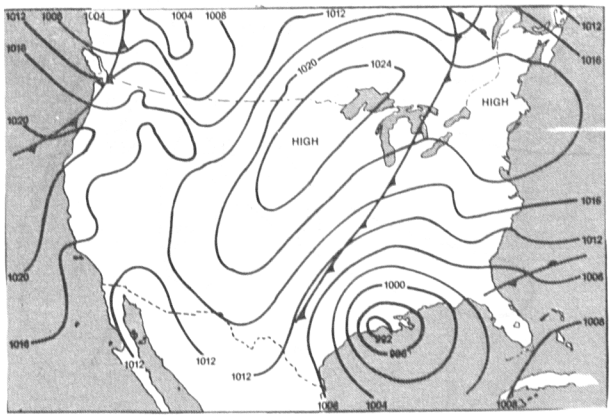

Fig. 7. Surface Weather Map at 0700 EST, 30 Oct 85.

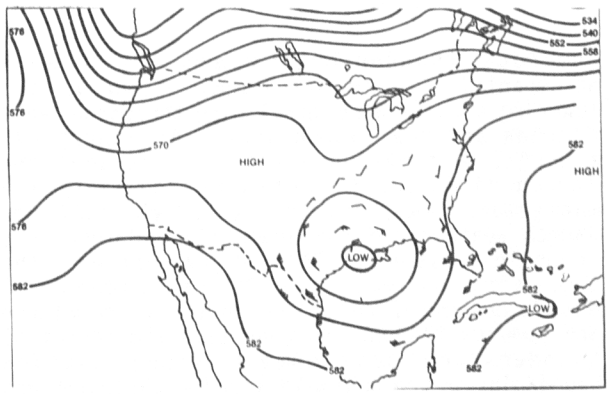

Fig. 8. 500-Millibar Height Contours at 0700 EST, 30 Oct 85.

5.2. Mission 61A Weather Support.

At the launch minus 24 (-24) hours briefing, through utilization of the MIDDS graphic analysis and image looping, the Shuttle Weather Officer (SWO) was able to assure the launch control officials that the only direct impact of Tropical Storm Juan would be in the form of the squall line feeder bands. On launch day, the local weather situation was further complicated by a weak frontal boundary approaching north Florida and forecast temperatures in excess of 80°F contributing to the already unstable environment. At launch -8 hours the launch director was briefed of the possibility of intermittent rainshowers and thunderstorms during the launch window (1700-2000 GMT). Looking at the most current near realtime satellite imagery on the closed circuit television system and forecast guidance by the Shuttle weather forecasters, the launch director made the decision to load the external tanks and begin final preparations for launch. As the launch countdown progressed a squall line in the Gulf of Mexico off the west coast of Florida presented an area of particular concern. After sunrise, clear skies over most of central Florida allowed rapid warming of the land surface and the convective process began. By 1600 GMT (1100 EST) the squall line was along the west coast of Florida (see Figure 9 for clouds as depicted by the MIDDS).

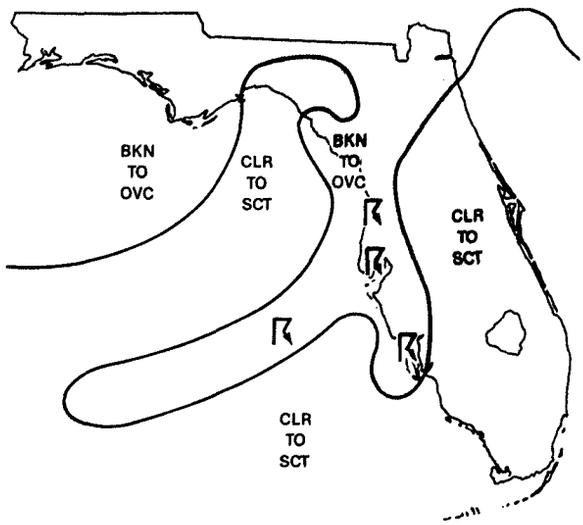

Fig. 9. Cloud Depiction 1600, 30 Oct 85.

Numerous thundershowers and rainshowers accompanied the feeder band. Cumulus and towering cumulus were developing throughout east Florida and the launch area. At launch -45 minutes, a conference was held between the launch director, flight director, mission management team, and the SWO at the CCFF for launch weather and the Spaceflight Meteorology Group in Houston for TAL and AOA weather. The SWO, using the available GOES rapid scan data, displayed the developing thunderstorm pattern and cumulus fields. He discussed the threat of thunderstorm development along outflow boundaries in the unstable local environment and suggested a GO as early in the launch window as possible. As the 1700 GMT opening of the launch window approached, so did the thunderstorms. At 1700 GMT on 30 October, (Figure 10), STS 61-A was launched successfully from Pad 39A at the Kennedy Space Center. According to the official NASA release, despite a tropical storm threatening the Gulf coast states and Florida for several days, the "countdown was uneventful and ascent to orbit normal".

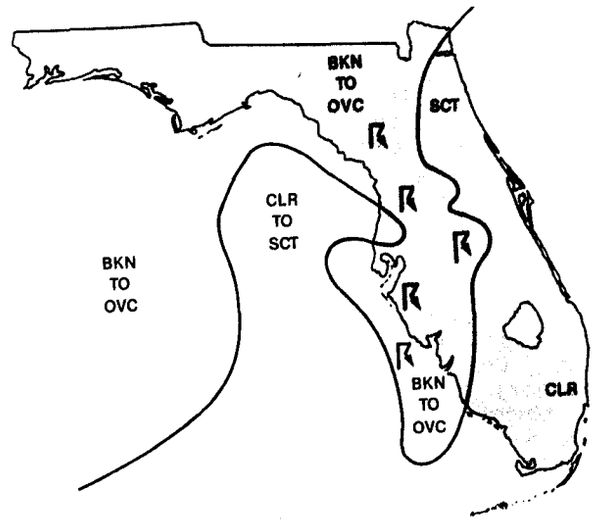

Fig. 10. Cloud Depiction 1700, 30 Oct 85.

6. SUMMARY

This paper has presented a background to Shuttle operations and their sensitivities to the weather. A brief overview of weather impacts was presented to establish the impacts, and one specific mission application used as an illustration of typical satellite applications to Shuttle missions. The MIDDS and its readily available satellite data are key elements of weather support essential to the successful Shuttle operations.

7. REFERENCES

Boyd, B. F., J. E. Erickson, and T. M. Myers, (1985): Modernization of Weather Support to the Space Transportation System, Preprints Second International Conference on the Aviation Weather Systems, Montreal, Amer. Meteor. Soc., 233-237.

Boyd, B. F. and T. M. Myers, (1986): Interactive Information and Processing Systems Used For Meteorological Support to the Eastern Test Range, Preprints Second International Conference on Interactive Information and Processing Systems for Meteorology, Oceanography, and Hydrology, Miami, FL, Amer. Meteor. Soc., 36-42.

Court, A. and J. F. Griffiths, (1982): "Thunderstorms: A Social, Scientific, and Technological Documentation", Vol 2, Thunderstorm Morphology and Dynamics, E. Kessler, Ed. NOAA/ERL

Gibbons, W. C., B. F. Boyd, and W. Jafferies, (1986): Lightning at Kennedy Space Center (Paper AIAA-86-0023 presented at the AIAA 24th Aerospace Sciences Meeting, Reno, NV, 6-8 Jan 86).

Kolczynski, E. F., T. M. Myers, and B. F. Boyd (1986): Meteorological Range Support Requirements and Implications for the Future of Shuttle Operations (Paper AIAA-86-0095 presented at the AIAA 24th Aerospace Sciences Meeting, Reno, NV, 6-8 Jan 86).

Myers, T. M. and B. F. Boyd, (1985): Status Report on the Applications of the Meteorological Interactive Data Display System to Space Shuttle and Range Support at the Kennedy Space Center and Cape Canaveral AFS, Preprints Conference on Aerospace and Range Meteorology, Huntsville, AL, Amer. Meteor. Soc., 73-80.

NOAA, (1985): "Daily Weather Maps, Weekly Series, October 28-November 3, 1985", National Meteorological Center, National Weather Service.

Suomi, V. E., R. Fox, S. S. Limage, and W. L. Smith, (1983): McIDAS III: A Modern Interactive Data Access and Analysis System, J. of Climate and Appl. Meteor., 22, 766-778.

Young, J. T., C. Norton, R. Uram, R. Oehlken, R. Fox, D. Wade, T. Whittaker, J. Benson, and J. Rueden, (1985): The Meteorological Interactive Data Display System, Preprints Second International Conference on the Aviation Weather System, Montreal, Amer. Meteor. Soc., 334-339.

Development of Mesoscale Forecast Products from Satellite Microwave Sounding Data

James F.W. Purdom[1,2], Donald W. Hillger[1], Thomas H. Vonder Haar[1,3], Carl A. Johnson[4], Debra A. Lubich[1] and Patrick Laybe[1]

Cooperative Institute for Research in the Atmosphere
Colorado State University
Fort Collins, CO 80523

1.0 INTRODUCTION

The purpose of this brief paper is to point out some of the new and exciting work underway at CIRA using polar orbiting microwave sounder brightness temperature data. This work is part of our continuing effort to use satellite data to aid in the analysis of regional and mesoscale meteorological phenomena. The results to be presented below are a continuation of CIRA studies concerning the March 28, 1984 Carolina tornado outbreak (Purdom, 1985; Hillger, et al., 1985). Those studies utilized GOES image data along with TIROS infrared sounding data to diagnose the mesoscale state of the atmosphere that locally supported that tornadic storm's development and evolution. The area covered by TIROS microwave data used in this case is shown in Figure 1. The information presented below will focus more on the regional scale uses of the TIROS microwave data, the results point to the tremendous potential of innovative uses of a type data that has been around for some time.

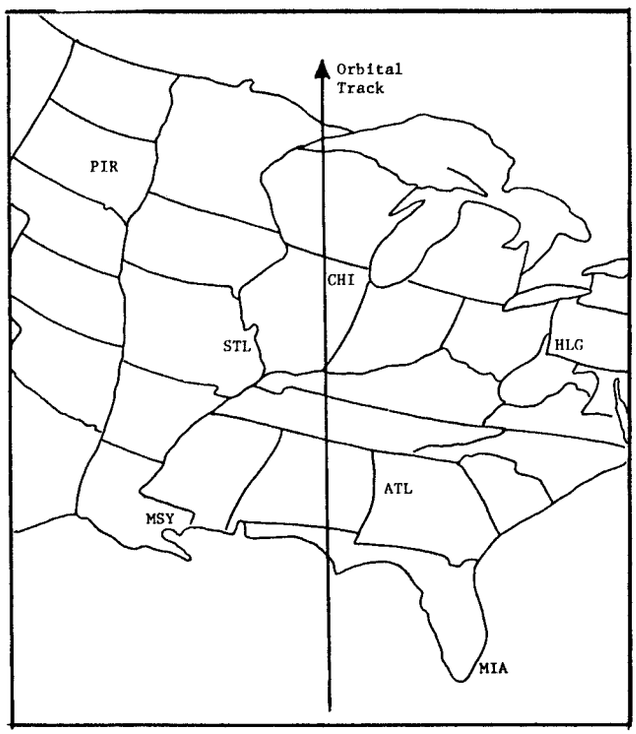

Figure 1. Area covered by TIROS microwave data at ≈2100 GMT, March 28, 1984

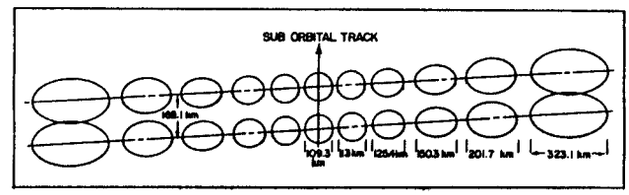

Figure 2. MSU scan patterns projected on earth.

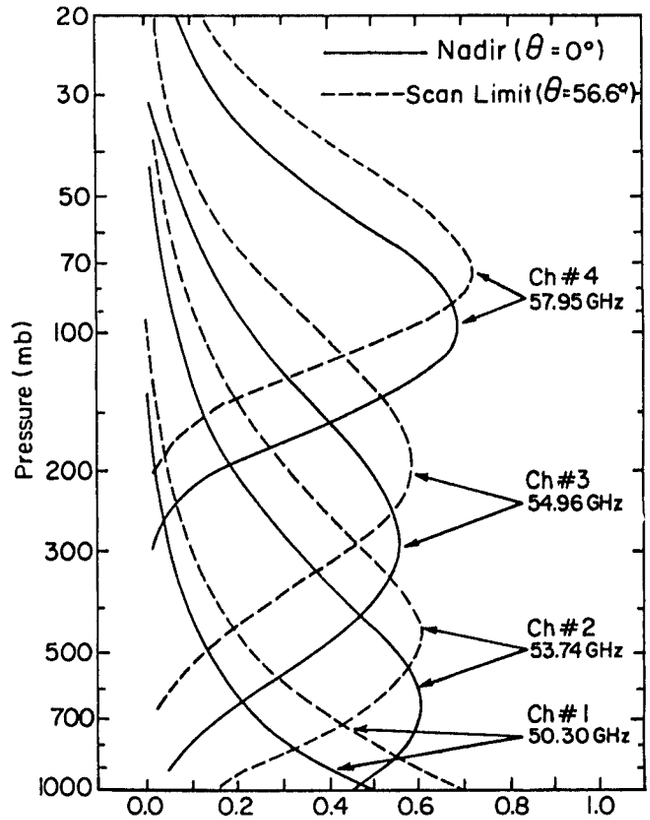

Figure 3. Weighting functions calculated for nadir and scan limit positions for the TIROS-N/NOAA Microwave Sounding Unit (MSU).

[1]Cooperative Institute for Research in the Atmosphere, CSU/NOAA

[2]Regional and Mesoscale Meteorology Branch, NOAA/NESDIS

[3]Department of Atmospheric Science, Colorado State University

[4]Program for Regional Observing and Forecasting Services, NOAA/ERL

2.0 MICROWAVE DATA

During the past several years, microwave sounding data have been routinely available from a variety of meteorological satellites. Those data are generally accessible as brightness temperatures centered on various latitude/longitude locations or as derived soundings from the various microwave channels over an area. Their use as an image product (similar to conventional visible and infrared imagery) has been very limited. This is for a variety of reasons, foremost perhaps being the data's relatively poor horizontal and vertical resolution as well as the effects of limb darkening. Figures 2 & 3 illustrate those problems: note that as the instrument's observations move from nadir toward scan limit that both the horizontal resolution decreases and the temperature weighting functions for each of the channels peak higher in the atmosphere. The limb darkening effect is graphically illustrated in Figure 4, which is a depiction of the MSU's channel 2 with the horizontal resolution of the elements all displayed at the same size. In Figure 4, T_1 is the warmest region, while T_3 (on the limb in relation to T_1) is several degrees cooler. T_2 is also cooler than T_1, this is due to the south to north temperature decrease one normally observes at mid-latitudes in the Northern Hemisphere troposphere. As with T_1 vs T_3, T_4 is several degrees cooler than T_2 due to the limb effect. An image of Figure 4, even when smoothed as shown in Figure 5, makes little sense. An appropriate question is: "Are there simple ways to treat MSU brightness temperature data so that meaningful meteorological products may be obtained?"

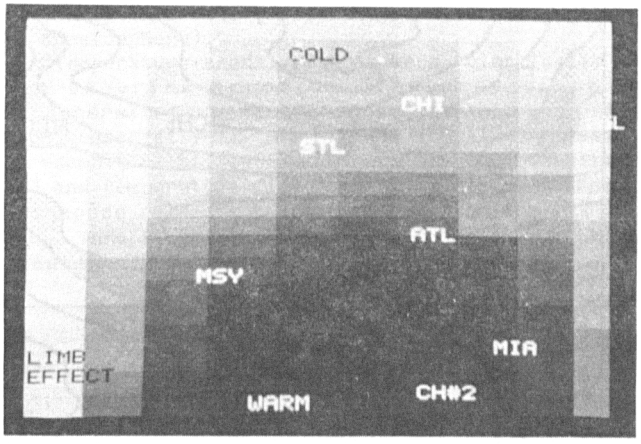

Figure 4a. Brightness temperature data from NOAA-7 MSU Channel 2 for 2100 GMT, March 28, 1984.

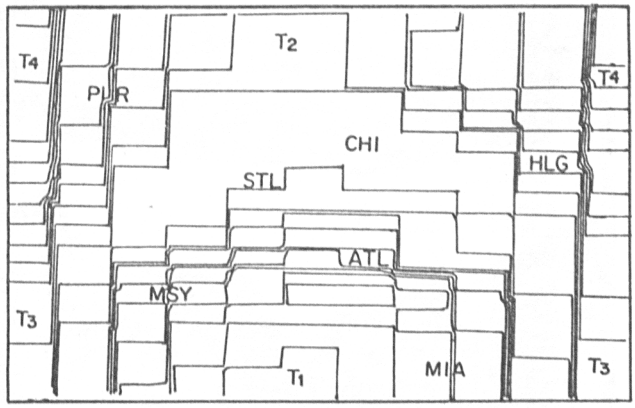

Figure 4b. Isolines of brightness temperature data for 4a.

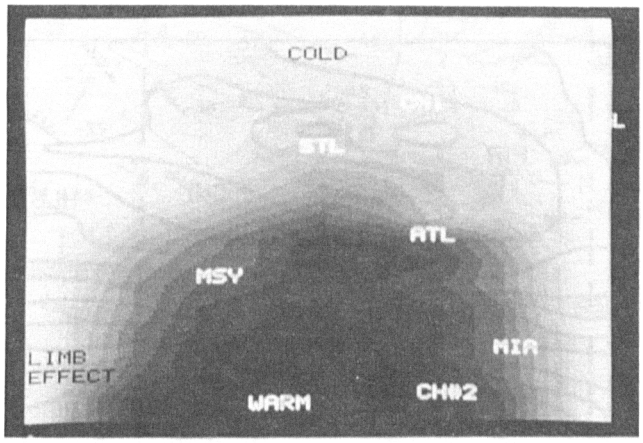

Figure 5a. Smoothed image of Figure 4a.

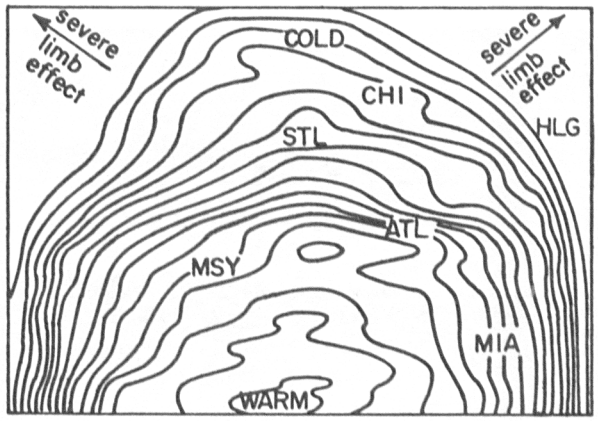

Figure 5b. Isolines of brightness temperature data in Figure 5a.

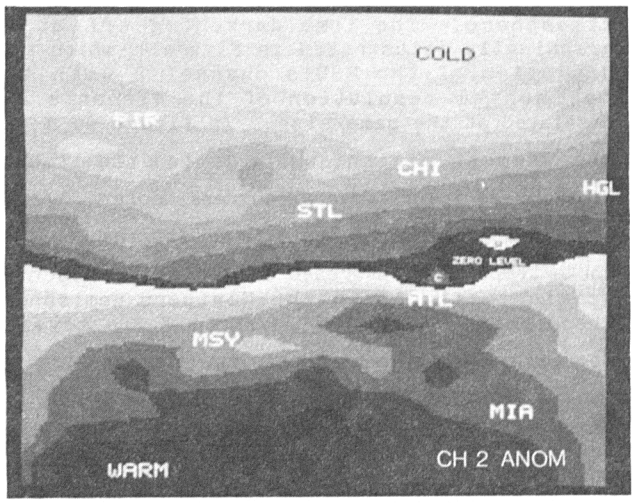

Figure 6a. Smoothed anomaly field for Figure 4 (troposphere). Black area across the center of the image is zero anomaly level.

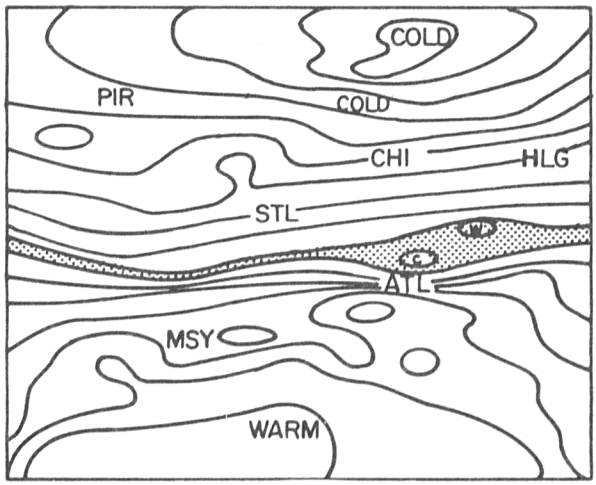

Figure 6b. Isolines of brightness temperature data for 6a. Shaded area is zero anomaly level.

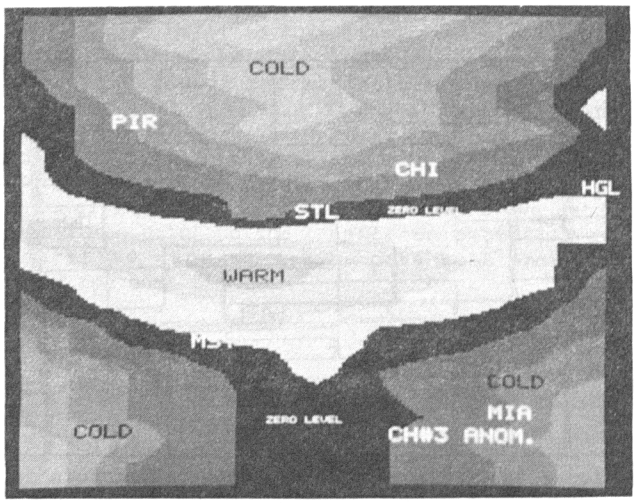

Figure 7a. Smoothed anomaly field for Channel 3 (tropopause). Black area is zero anomaly level.

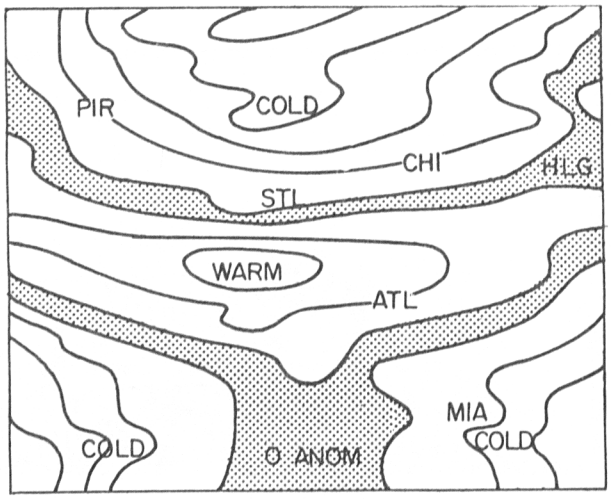

Figure 7b. Isolines of brightness temperature data for 7a. Shaded area is zero anomaly level.

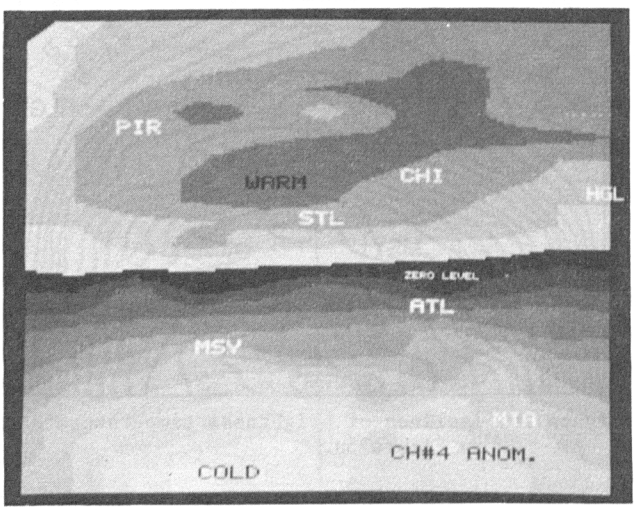

Figure 8a. Smoothed anomaly field for Channel 4 (stratosphere). Black area is zero anomaly level.

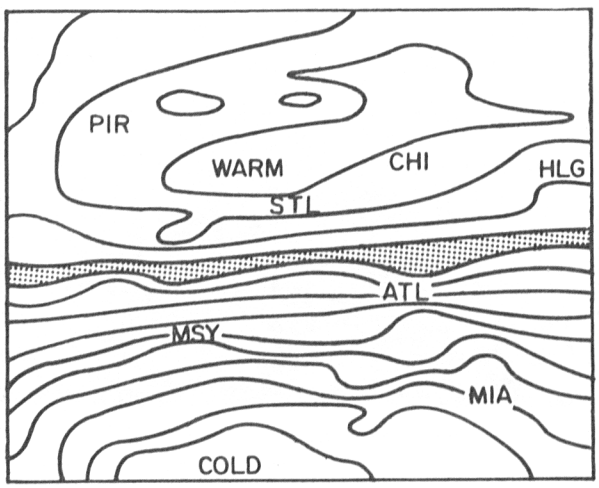

Figure 8b. Isolines of brightness temperature data for 8a. Shaded area is zero anomaly level.

3.0 DEVELOPMENT OF A MICROWAVE IMAGE PRODUCT

The answer to the above question appears to be yes. There are two underlying reasons for this that will only be mentioned briefly here. They are: 1) At the frequencies (wavelengths) observed by the MSU, the Rayleigh-Jeans radiation law is applicable and thus the brightness temperatures from the MSU relate directly to the thickness of the layer being observed; and 2) Adjacent volumes observed along scan line and scan track by MSU channels 2, 3 and 4 are well correlated with respect to their mean temperatures. With these thoughts in mind, a useful image product may be derived by producing an anomaly field for each channel. The anomaly field is produced by separately averaging each column's brightness temperature for each scan angle over the image area and subtracting that average temperature from each individual observation's brightness temperature at that scan angle. The result for Figure 4, shown as a smoothed image in Figure 6, effectively eliminates the limb effect and at the same time provides a very useful product: a south to north anomaly field of the mean temperature of the middle troposphere. Figures 7 and 8 are also mean temperature anomaly fields, in this case for channel 3 (near the tropopause) and channel 4 (in the stratosphere).

Temperature anomaly fields were "classically" used to bring important features of the atmosphere's temperature structure into sharper focus, especially in jet stream situations (see for example Riehl, 1962). Figure 9 shows both the wind and temperature field at 300 mb derived from rawinsonde releases taken 3 hours after the TIROS pass. That figure should be referred to in the discussion below. The anomaly fields shown in

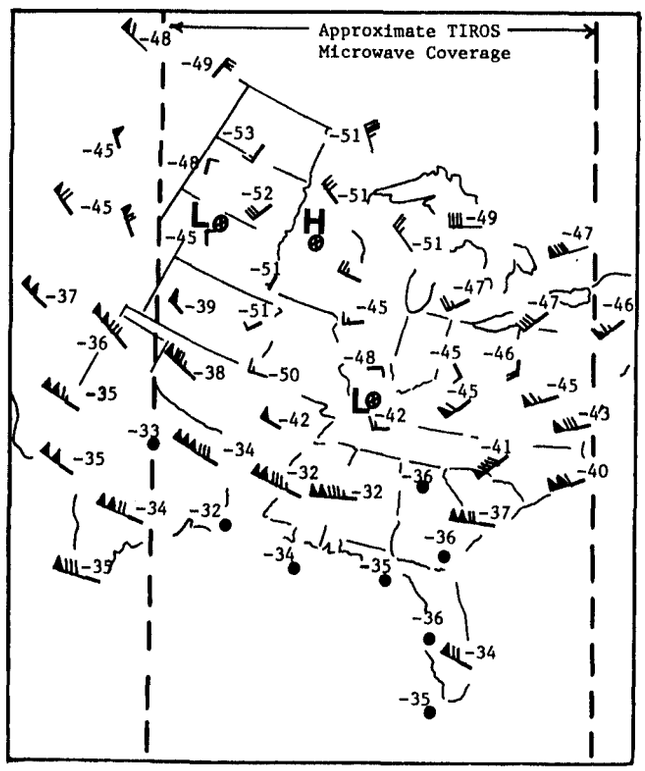

Figure 9. 300 mb winds and temperatures for 00Z March 29, 1984.

Figures 6, 7 and 8 graphically depict certain features known to be associated with jet streams. For example, Figure 6 shows the mean temperature in the troposphere changing from warm to cold as we go from south to north, with the zero anomaly in close proximity to the jet axis. A similar feature is shown in the stratosphere's mean temperature field, Figure 8, however the warm anomaly is on the poleward side of the jet and the cold anomaly equatorward: this reversal of the horizontal temperature gradient with height is as one should expect. Figure 7, the anomaly field near the tropopause, is slightly more difficult to analyze. However, there is evidence of a warm anomaly in the base of the upper trough to the north of the jet axis: this is often observed in strong jet stream situations.

There are many other features of interest in the images that are regional and mesoscale in nature. For example, in Figures 6 and 8 note the wave like structure in the anomaly fields between New Orleans (MSY) and Atlanta (ATL). The warm anomaly in Figure 7 between Saint Louis (STL) and MSY would indicate the western wave structure may be associated with the major trough. What about the wave appearance near ATL? The small cold region in Figure 6 just northeast of the L in ATL is due to precipitation contamination by the major storm: Is the small warm anomaly to its northeast evidence of subsidence, perhaps showing up as a type of convective response?

4.0 HIGHER RESOLUTION MICROWAVE SOUNDINGS

As was shown in Figures 4 and 5, a smoothed field derived from raw microwave brightness temperature data makes little sense for image aplications. However, it is apparent that the smoothed field in Figure 5 provides data at a "higher resolution" than the blocky field in Figure 4. An appropriate question is: "Can smoothed data as shown in Figure 5, but for all the channels, be used to help produce higher spatial resolution microwave soundings?" If this is the case, then through appropriate smoothing, the microwave data could be used more effectively to supplement mesoscale infrared soundings from TIROS and VAS. This has very important implications for the field of mesoscale meteorology.

An initial step toward answering this question is under investigation at CIRA using structure function analysis (as is done for VAS data in the paper by Hillger, et al. elsewhere in these proceedings). If the reader is unfamiliar with the use of structure functions, or how to interpret their results, we suggest they refer to the above mentioned paper before proceeding.

Figures 10, 11 and 12 are structure function analyses for unsmoothed MSU channels 2 (troposphere), 3 (near tropopause) and 4 (stratosphere) respectively. The "a" portion of each of those figures is for each scan angle in a north-south direction, while the "b" portion is for each east-west scan line. The reason the structure functions for each channel were not done isotropically (radially) from each point was because it was felt that a combination of the limb effect and north to south temperature gradient would complicate the interpretation.

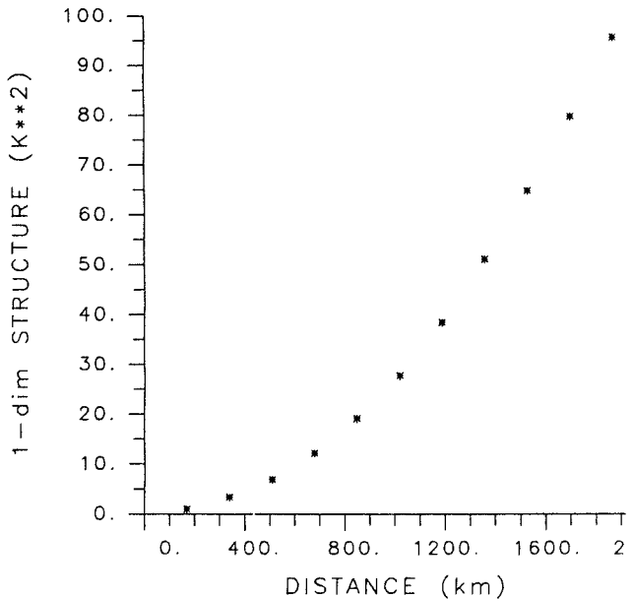

Figure 10a. MSU-2 (N-S) structure.

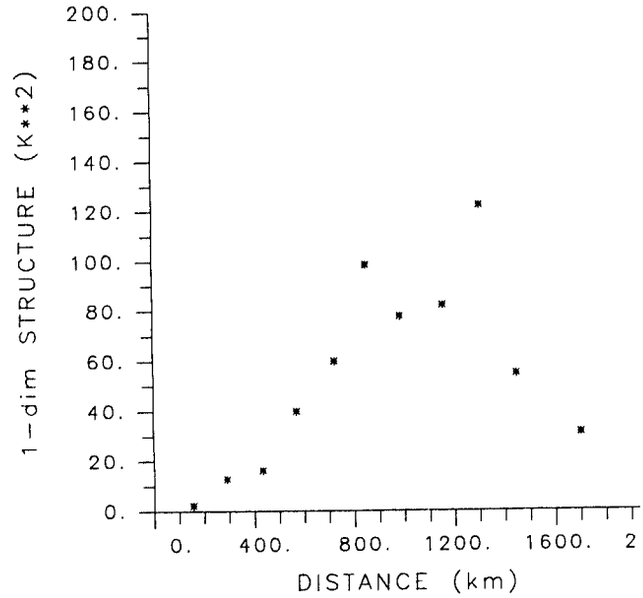

Figure 10b. MSU-2 (E-W) structure.

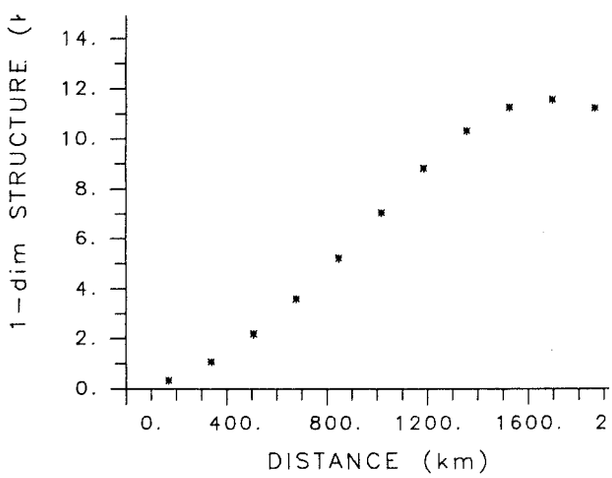

Figure 11a. MSU-3 (N-S) structure.

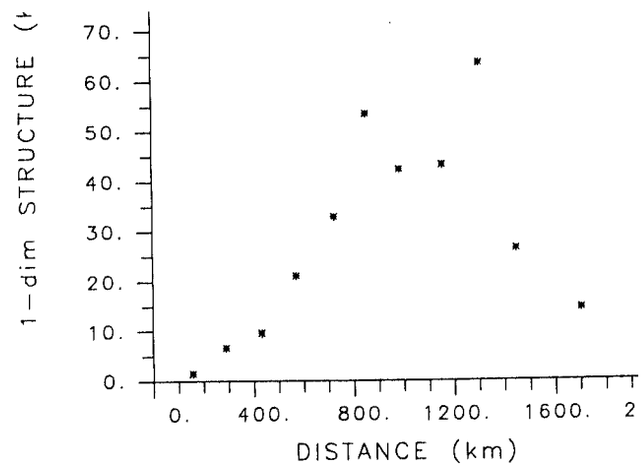

Figure 11b. MSU-3 (E-W) structure.

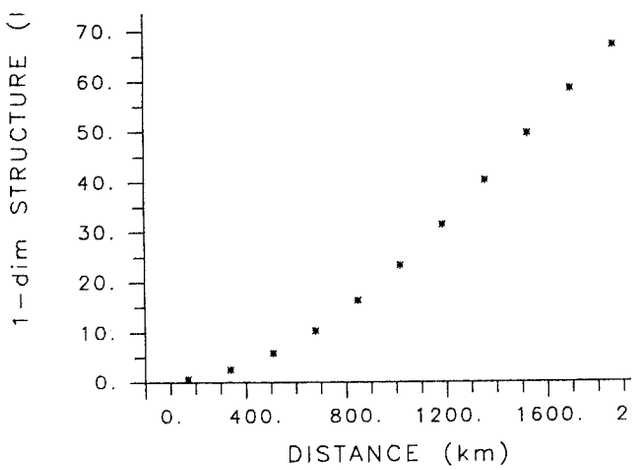

Figure 12a. MSU-4 (N-S) structure.

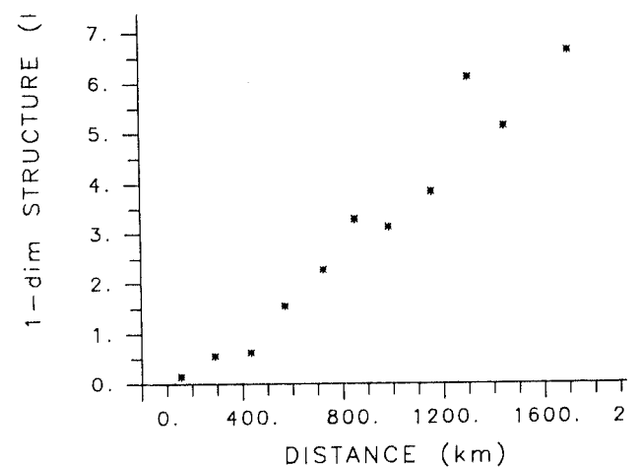

Figure 12b. MSU-4 (E-W) structure.

Inspection of Figures 10-12 reveal some interesting facts. Noise may be determined for each of the channels by extrapolation of their structure function curves to zero separation. The noise in Kelvins may then be determined by dividing by two and taking the square root of that value. Each data point along the structure curve may then be thought of as a combination of the noise plus information concerning the temperature gradient. The noise plus gradient information (in Kelvins) at the minimum separation distance for each channel is given in Table 1 below.

Table 1

MSU Channel	Noise + Gradient (Kelvin) and Signal-to-Noise (dimensionless)
2	0.71 K and 9.6 S/N
3	0.41 K and 8.6 S/N
4	0.59 K and 7.2 S/N

The values in Table 1 may be thought of as the maximum noise since they over estimate the noise due to the gradient contribution. Only noise would remain if zero separation were attainable. Through deblocking the data and performing structure function analyses, improvements in (reductions of) noise are being realized. For example for MSU Channel 2, a smoothing by a factor of 2 results in a noise of 0.34 K and a signal to noise ratio of 18.8. This strongly indicates that higher spatial resolution soundings with low noise may be obtained by smoothing the various MSU channel data! Comparing Figure 13 with Figure 10a graphically illustrates this point.

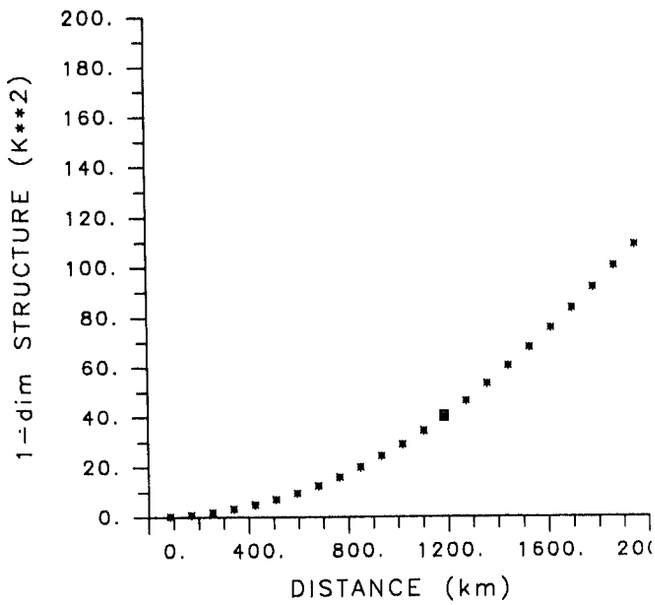

Figure 13. MSU-2 (N-S) structure for data smoothed by a factor of 2.

Inspection of Figures 10-12 while referring to Figures 4-8 point out some interesting features. Figure 10a shows larger structure values as distance increases, a result of the north to south temperature gradient evident in Figures 4, 5 and 6. Figure 10b has a structure which indicates an east to west wave in the thermal field - obviously this is showing us the limb effect on either side of nadir. Figure 11a has a leveling off in structure as distances become large - in this particular case with strong relative warming near north to south image center this should be expected. As in Figure 10b, the limb effect in Figure 11b (note this is for the raw Channel 3 data, not Figure 7) shows up as a wave. Figure 12a shows the north to south temperature gradient, while Figure 12b shows little limb effect. This decrease in limb effect is a reflection of a more homogeneous temperature structure in the stratosphere.

5.0 CONCLUSIONS

Work underway at CIRA is showing strong potential uses for microwave data for both image and sounding applications in regional and mesoscale applications. Future work at CIRA will focus on the utilization of image products for a variety of meteorological situations including those that lead to the development of severe storms, winter storms and hurricanes. Work with the data for sounding applications will focus on blending the higher resolution (smoothed) microwave data with TOVS and VAS infrared sounding data to produce satellite soundings for regional and mesoscale applications.

6.0 ACKNOWLEDGEMENTS

We would like to thank Sallie Varner for the preparation of the text. Research support was provided for this work through NOAA Grants NA84AA-H-00020 and NA85RA-H-05045.

7.0 REFERENCES

Hillger, Donald W., James F.W. Purdom, and Thomas H. Vonder Haar, 1986: The use of structure function analysis to estimate noise levels and the potential resolution of satellite measurements. Preprints, 2nd Conf. on Satellite Meteorology/Remote Sensing and Applications, Amer. Meteor. Soc., Williamsburg, PA, 12-16 May.

Hillger, D.W., J.F.W. Purdom, and T.H. Vonder Haar, 1985: An analysis of various mesoscale air masses for 28 March 1984 using NOAA-7 TOVS. Preprints, 14th Conf. on Severe Local Storms, Amer. Meteor. Soc., Indianapolis, 29 Oct.-1 Nov., 36-39.

Purdom, J.F.W., 1985: The application of satellite sounding and image data to the Carolina tornado outbreak of 28 March 1984. Preprints, 14th Conf. on Severe Local Storms, Amer. Meteor. Soc., Indianapolis, 29 Oct.-1 Nov., 276-279.

Riehl, Herbert, 1962: Jet streams of the atmosphere. Technical Report No. 32. Department of Atmospheric Science, Colorado State University, Ft. Collins, CO. 117 pp.

Upper-Tropospheric and Lower-Stratospheric Dynamics Associated with Tropical Cyclones as Inferred from Total Ozone Measurements

Edward Rodgers
Laboratory for Atmospheres
NASA/Goddard Space Flight Center
Greenbelt, MD 20771

John Stout and Joseph Steranka
General Software Corporation
Landover, MD 20785

1. Introduction

Total ozone associated with western Atlantic and Pacific tropical cyclones at various stages of development was analyzed for the purpose of monitoring the lower-stratospheric and upper-tropospheric mass adjustment processes associated with the tropical cyclone and its environment. The analysis is based on the total ozone measurements from the Nimbus-7 Total Ozone Mapping Spectrometer (TOMS). Monitoring the total ozone may improve the understanding of 1) how the lower stratosphere and upper troposphere cause or respond to tropical cyclone structure changes and 2) why tropical cyclones rapidly intensify.

In examining the total ozone within and surrounding the tropical cyclone, the storm was partitioned into four specific regions: 1) the environment; 2) the moat (cloud-free region surrounding the storm's central dense overcast (CDO); 3) the CDO; and 4) the eye. Tropical Cyclone Allen (1-9 August 1980) will be used to discuss the total ozone features that are typical of other western Atlantic and Pacific storms. Since the Joint Typhoon Warning Center (JTWC) is the only group that systematically collects eye information for all tropical cyclones, western Pacific storms will be emphasized in the discussion of the eye total ozone distribution.

2. Nimbus-7 TOMS

TOMS, which was launched in October 1978 on Nimbus-7 into a sun-sychronous polar orbit, uses six wavelengths from 312.5 to 380 nm to separate the effects of ozone absorportion, molecular scattering, and surface (including cloud) albedo. From these wavelengths and measurements of cloud amount and height, total ozone is determined from TOMS to be within 2% relative to the ground- based observations (Shapiro et al., 1982).

The TOMS is designed to scan at 35 angular steps perpendicular to the orbital path, which is repeated every 8 seconds with a 50 x 50 km instantaneous field-of-view (IFOV) at nadir; the 35 angular steps produce a 2800 km swatch of data that is contiguous between swaths at the equator and overlapping near the poles. Since total ozone is estimated using the ultraviolet spectrum, observations are only obtained during local noon.

3. Total Ozone and Tropopause Relationship

Since ozone may be considered a passive tracer in the lower stratosphere and ozone gradients are strongest just above the tropopause, fluctuations of total ozone are primarily due to variations of tropopause height caused by vertical and horizontal advection (Reed, 1950). For example, the combination of upper-tropospheric cold air advection from higher latitudes and subsidence within the lower stratosphere may lower the tropopause locally and, thereby, increase the amount of total ozone. Cold air advection will both lower the height of the tropopause as well as advect air from higher latitudes where ozone is more abundant. Lower-stratospheric subsidence, on the other hand, will lower the tropopause height through adiabatic warming and turbulent mixing and will subside ozone-rich stratospheric air from above. Continuity requires that the horizontal convergence of more ozone-rich air from above in the column will, thereby, increase the total ozone as the bottom of the column lowers in height. Thus, as the tropopause lowers in height, the total ozone in the column increases. Conversely, upper-tropospheric warm air advection and lower-stratospheric ascent increase the tropopause height and decrease total ozone. This negative correlation between total ozone and tropopause height was first documented by Meethan (1937).

However, as pointed out by Shapiro et al. (1982) and Sechrist et al. (1986), this negative relationship between tropopause height and total ozone does not always exist. This is particularly true in regions where a transverse circulation associated with jet streaks are found. Within these jet streaks, the dynamically forced mass circulation associated with these jet streaks may include a transverse circulation below the jet in the upper troposphere that is in an opposite circulation to what is found above the jet in the lower stratosphere. This would imply either lower-stratospheric ascent (subsidence) above upper-tropospheric subsidence (ascent) depending on what region of the jet streak is being examined. Therefore, the negative correlation between tropopause height and total ozone may not necessarily occur.

From these findings, it is expected that TOMS-measured total ozone within and surrounding tropical cyclones may give information concerning the storm's structure and intensity change. In the following section, the distribution of total ozone will be examined and related to storm structure and intensity change.

4. Results

To best delineate the common features that have been observed in the total ozone within and surrounding a tropical cyclone of hurricane intensity, Fig. 1 shows the TOMS-measured total ozone pattern associated with Hurricane Allen at 1800 GMT 8 August 1980. During this period, Allen was in the western Gulf of Mexico moving westward and intensifying with its maximum winds increasing from 65 to 78 m s^{-1} in a 12-h period. The figure depicts the total ozone that was gridded every 1° latitude and 1.25° longitude and contoured every 5 Dobson Units (DU's) interval (solid line), cloud albedo of 40 and 80% (dashed line), and Allen's location (shown as hurricane symbol). Regions of interest will be discussed as outlined in the introduction.

a. Allen's environment

Since total ozone patterns appear to be reflecting the mass adjustment processes near the tropopause level that are associated with the upper-tropospheric and lower-stratospheric circulation, upper- tropospheric wind associated with heights and horizontal divergence fields (Figs. 2 and 3, respectively) were compared to total ozone patterns seen in Fig. 1. The height and wind fields were observed 6 h earlier at 1200 GMT 8 August 1980. Winds were obtained from both rawinsonde observations and observations of cirrus tracers from the GOES satellite. Considering the 6-h time difference between the observations of total ozone and the height and wind observations and the fact that the tropopause increases with height toward lower latitudes, the following are large-scale

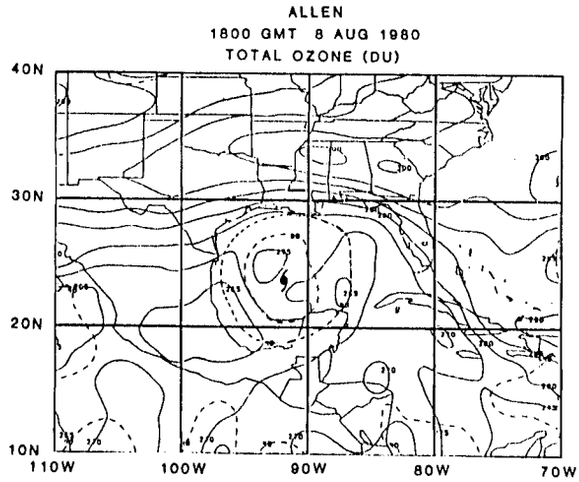

Fig. 1. *TOMS-observed total ozone contoured every 5 DU (solid lines) and cloud reflectivity at 40 and 80 percent (dashed lines) for 1800 GMT 8 August 1980. Allen's center depicted by hurricane symbol.*

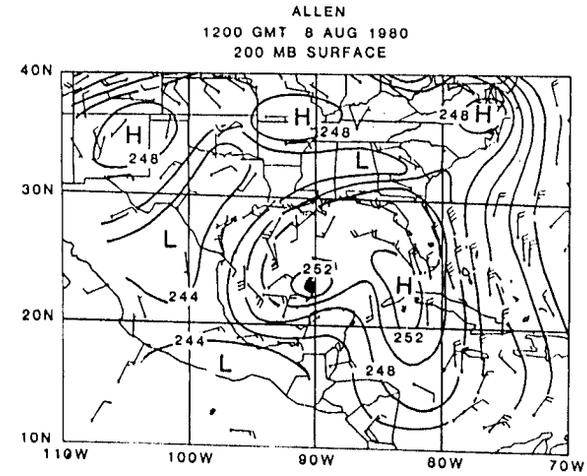

Fig. 2. *Upper-tropospheric winds (wind barbs in m s^{-1}) and 200 mb geopotential heights (12XXX0 m) for 1200 GMT 8 August 1980. Allen's center depicted by hurricane symbol.*

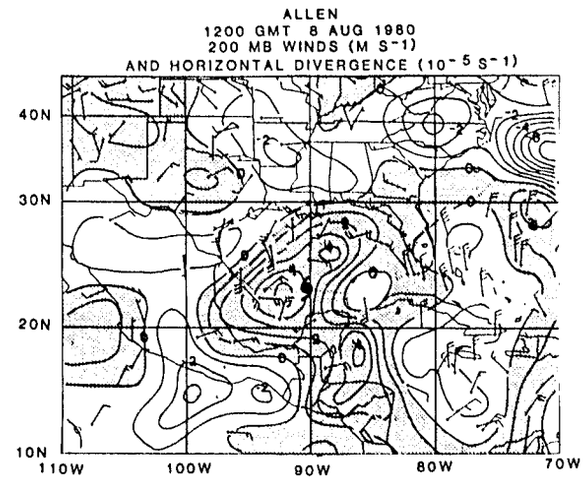

Fig. 3. *Upper-tropospheric winds (wind barbs in m s^{-1}) and derived upper-tropospheric horizontal divergence (10^{-5} s^{-1}). Shaded area is horizontal divergence. Allen's center depicted by hurricane symbol.*

environmental features observed in Figs. 1-3 that are common in all three fields:

- o Ridge of high total ozone that stretches north of Allen from North Carolina westward to Texas and southward through Mexico appears to be associated with lower upper-tropospheric heights and horizontal convergence.
- o Allen's outflow jet corresponds to large total ozone gradient north and east of the storm.

o High total ozone east of Florida corresponds with the lower upper-tropospheric heights and horizontal convergence that is associated with the exit region of Allen's outflow jet.

If it can be assumed that the changes in topography in the upper-tropospheric geopotential height fields reflect changes in topography in the tropopause, the observation within Allen's environment basically supports the negative correlation between total ozone and tropopause height that was first observed by Meethan (1937) and documented by Reed (1950). From these observations, it appears that upper-tropospheric heights surrounding tropical cyclones could be monitored using TOMS. Since Holland and Merrill (1984) have suggested that the upper troposphere forces rapid intensification of tropical cyclones, the TOMS analysis may be used to examine this hypothesis. For example, upper- tropospheric disturbances such as the tropical upper-tropospheric troughs (TUTT's) can be monitored for their strength and location in order to better determine their affect on tropical cyclone structure changes (i.e., initiation and strength of outflow jets, enhancement of convection) and, thereby, possibly predicting whether the system will rapidly intensify. Since the TOMS measurements imply height rather than thickness as derived from infrared and passive microwave sounders and since the TOMS measurements are apparently not cloud contaminated, the TOMS will be of particular value in monitoring these shallow TUTT's.

To demonstrate the feasibility of using TOMS data to monitor upper-tropospheric waves within Allen's environment and to assess how these waves affect storm intensity change, the time change in total ozone and storm intensity was examined. Fig. 4 shows a smoothed longitude and time distribution of total ozone anomalies (derived by subtracting a mean field for a given day from the actual observation) for Tropical Cyclone Allen for the period 1-9 August 1980 (left panel). Total ozone anomalies were used to acquire a more representative temporal change in total ozone. These anomalies were averaged for a 10° latitudinal band centered on Allen's center and extending 16° longitude east and west of the storm's center. High total ozone anomalies depict upper-tropospheric troughs, while low total ozone anomalies depict ridges. The right panel of the figure shows Allen's maximum winds at a 6-h interval during the 9-day period.

The figure suggests that Allen encountered two troughs on its westward movement toward Texas (dashed line depicts the approximate trough location). The first encounter was prior to 1200 GMT 5 August 1980 and the second encounter was prior to 1800 GMT 7 August 1980. It appears that as Allen came within 4° latitude of the axis of the troughs, the maximum winds began to increase. Once Allen passed through the base of the trough, maximum winds decreased. Upper-tropospheric interaction, however, was not evident during Allen's reintensification on 8 August. It should be pointed out that on 5 August, Allen passed just south of Hispaniola, which may have also contributed to its weakening.

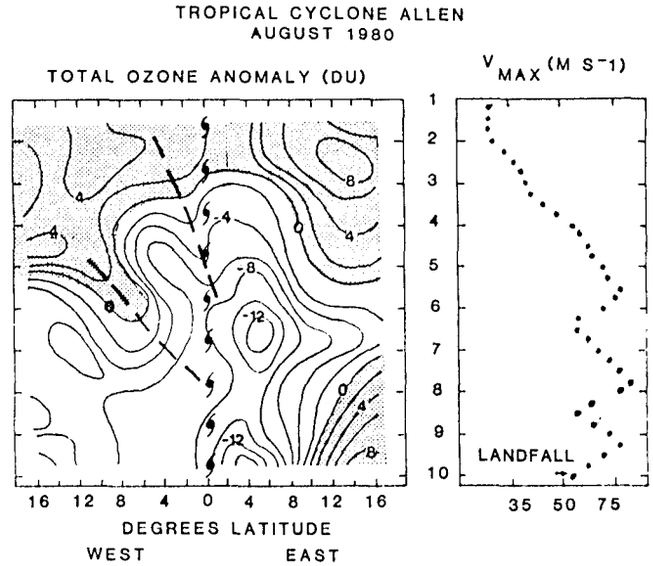

Fig. 4. *Left panel delineates the time/longitude contour of total ozone anomalies (DU) averaged over a latitudinal zone 5° latitude north and south of a latitude passing through Allen's center and extending east and west of the center by 16° longitude for the period 1-9 August 1980. Shaded areas are positive total ozone anomalies. Hurricane symbol depicts Allen's center and observation time. Dashed line locates base of trough. The right panel depicts maximum winds (m s^{-1}) for Allen observed at 6-h intervals for the same period.*

b. Allen's moat region

The moat region of the storm is cloud free due to upper-tropospheric horizontal convergence between the outflow and the basic current and subsequent upper- and middle-tropospheric subsidence. The low total ozone observed south and west of Allen (Fig. 1) can best be explained using the argument given by Shapiro et al. (1982) and Sechrist et al. (1986) for the jet streaks. In the moat region, where subsidence exists below the tropopause, rising motion will be found above the tropopause, thereby giving low total ozone superimposed upon the dry upper troposphere. Fig. 4 shows the time change of total ozone in the moat region approximately 4° latitude east and west of the center. Minimum ozone is most evident east of the center, which appears to decrease as Allen's outflow became more established.

It can be seen in Figs. 5, 6, and 7, which depict the total ozone (at full spatial resolution), cloud reflectivity, and THIR-derived cloud top heights, respectively, at 1800 GMT 8 August that the region of minimum ozone is found on the CDO edge where upper-tropospheric horizontal convergence (Fig. 3) is evident. The cloud edge delineates the upper-tropospheric subsidence, while the lower total ozone infers lower-stratospheric ascent.

c. Allen's CDO region

As can be observed again in Figs. 5, 6, and 7, in Allen's CDO (delineated by cloud reflectivity and pressure heights greater than 80 percent and 150 mb, respectively), the low total ozone (less than 270 DU, area A) near and east of the center appears to be associated with Allen's high tropopause as inferred from the cloud heights. Cloud heights in this area were estimated, using a satellite stereographic technique (Rodgers et al., 1983), to be greater than 16.5 km. Higher total ozone amounts (greater than 280 DU in Fig. 5, area B) northwest of the center correspond to cloud

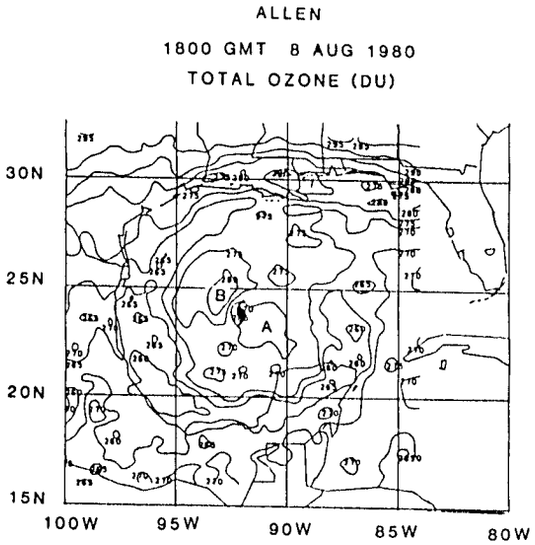

Fig. 5. *TOMS-observed total ozone at full resolution contoured at 5 DU interval for 1800 GMT 8 August 1980. Allen's center depicted by hurricane symbol. Regions A and B are referred to in the text.*

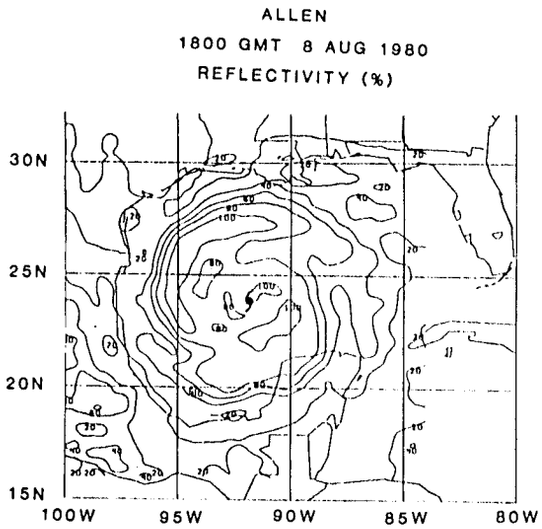

Fig. 6. *Cloud and surface reflectivity contoured at 20 percent for 1800 GMT 8 August 1980. Allen's center depicted by hurricane symbol.*

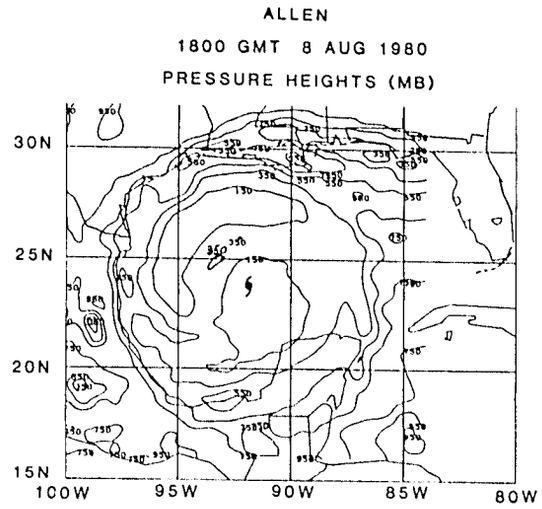

Fig. 7. *Cloud height (mb) inferred from THIR (T_B) and regional standard atmospheric lapse rates contoured at 150 mb for 1800 GMT 8 August 1980. Allen's center depicted by hurricane symbol.*

reflectivity and heights less than 80 percent and 350 mb, respectively. It appears that subsidence in this region is occurring within both the upper troposphere and lower stratosphere. Ozone-rich stratospheric air is descending as it is advected cyclonically around Allen's western convective region (note the upper-tropospheric cyclonic outflow near Allen's center in Figs. 2 and 3). The CDO northwest of the center that has high total ozone amounts greater than 275 DU (Figs. 1 and 5) may be due to both the intrusion of ozone-rich stratospheric air and lower tropopause height. Tropopause heights as inferred by the satellite stereographic-derived cloud heights were 1.5 km lower than what was found in the convective region near and southeast of Allen's center.

To examine how the total ozone is being influenced by Allen's upper-tropospheric dynamics above the CDO, a time/longitude depiction of Allen's total ozone anomalies together with Allen's CDO reflectivity and THIR-inferred cloud top heights is seen in Fig. 8. The parameters were sampled using the same method that was followed to construct Fig. 4. The only difference was that the data were sampled every 0.5° longitude along a latitude 4° west to east across the storm's center using the full spatial resolution of TOMS. No latitudinal averaging was performed in constructing these figures. Points of interest that can be gleamed from this figure are as follows:

- o Within the CDO region (cloud heights and reflectivity are greater than 150 mb and 80 percent, respectively), total ozone decreases from +12 DU to -8 DU on 6 August. This decrease in total ozone is most likely in response to the increase in the tropopause height.

- o Low total ozone anomalies near the edge of the CDO are in response to ascending lower-stratospheric air within the moat region (see Section 4b).

- o Increased total ozone 2° longitude east and west of Allen's center on 8 August is associated with cyclonic intrusion of ozone-rich stratospheric air.

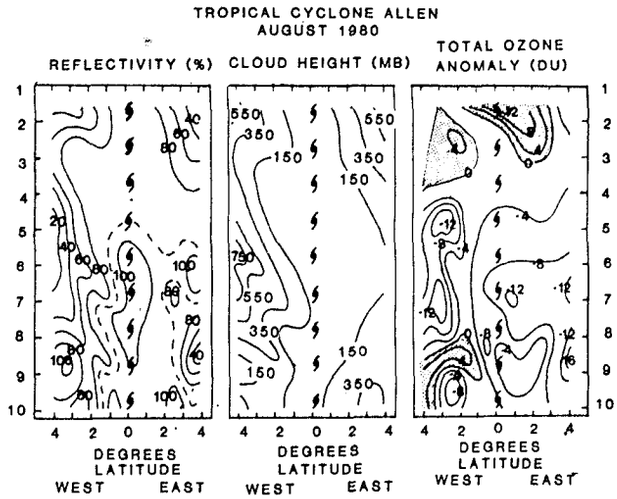

Fig. 8. *Time/longitude contour of cloud reflectivity (percent) (first panel), cloud height (mb) (second panel), and total ozone anomalies (DU) (third panel) for a latitudinal line 4° longitude east and west passing through Allen's center for the period 1-9 August 1980. Hurricane symbol depicts Allen's center and observation time.*

From this figure, it is interesting to note that the evolution of total ozone over the CDO does not necessarily reflect the changes in Allen's CDO, except where strong upper-tropospheric forcing is occurring. Thus, it appears, at least for the Allen case, that high opaque clouds are not contaminating the TOMS measurements.

d. Allen's eye

During U-2 flights over Hurricane Ginny (October 1964), Penn (1965) observed a somewhat larger concentration of ozone within the top of the eye. Ozone- rich air within the eye of Allen, however, was not observed with TOMS even though Allen was a more intense storm. Although Allen had an eye during most of its mature stage, Allen's small eye size (diameter was approximately 20 km) could not be resolved by the TOMS (large IFOV particularly off nadir) and, therefore, the sensor was not able to substantiate Penn's (1965) observations. However, because of the availability of eye information from JTWC, eyes associated with western Pacific tropical cyclones were examined instead. To eliminate the scan angle problem in these observations, the storms were chosen so that the center fell within ±10° of nadir (earth latitude). The difference between total ozone at the center of the eye and the average total ozone for a ring 1° latitude from the center was compared to the size of the eye and to the intensity of the storm. No relationship was found between eye size and total ozone difference (difference between high total ozone in the eye and less total ozone outside the eye). However, considering the TOMS IFOV problem, there was some suggestion (correlation coefficient of 0.44) that storm intensity may be related to the total ozone difference. It can be speculated that the strength of the subsidence within the eye which could be related to the strength of stratospheric intrusion also may be related to storm intensity. It had been noted by Edson (1984) in his comparison of composite radiosonde data for western Pacific storms that the difference between rapidly intensifying (≥42 mb/ 24 h) tropical cyclones, moderate intensifying (18-35 mb), and steady state systems was that the rapidly intensifying systems had greater cyclonic inflowing lower-stratospheric air near the center than the other systems. Thus, eyes that are rich in total ozone may indicate that the tropical cyclone may be rapidly intensifying.

5. Conclusions

It appears from this qualitative study that TOMS-measured total ozone may present important information about the geostrophic adjustment processes within tropical cyclones and their environment. This may indicate both storm structure change and possibly future intensity changes. However, to completely appreciate what the TOMS-measured total ozone is implying about the tropical cyclone and its environment, it would be desirable to do further work in comparing upper-tropospheric and lower-stratospheric mass and wind fields with total ozone by using both aircraft in situ measurements and model simulations.

6. References

Edson, R., 1984: Synoptic scale view of the differences in tropical cyclone intensity vs. strength change. Preprints, 15th Technical Conference on Hurricanes and Tropical Meteorology, Amer. Meteor. Soc., 56-57.

Holland, G. J., and R. T. Merrill, 1984: On the dynamics of tropical cyclone structure changes. Quart. J. Roy. Meteor. Soc., 110, 723-745.

Meetham, A. R., 1937: The correlation of the amount of ozone with other characteristics of the atmosphere. Quart. J. Roy. Meteor. Soc., 63, 289-307.

Penn, S., 1964: Ozone and temperature structure in a hurricane. J. Appl. Meteor., __, 212-216.

Reed, R. J., 1950: The role of vertical motions in ozone-weather relationships. J. Meteor., 7, 263-267.

Rodgers, E. B., R. A. Mack, and A. F. Hasler, 1983: A satellite stereoscopic technique to estimate tropical cyclone intensity. Mon. Wea. Rev., 111, 1600-1610.

Sechrist, F. S., R. A. Petersen, K. F. Brill, A. J. Krueger, and L. W. Uccellini, 1986: Ozone, jet streaks and severe weather. Preprints, 2nd Conference on Satellite Meteorology/Remote Sensing and Applications, Amer. Meteor. Soc.

Shapiro, M. A., A. J. Krueger, and P. J. Kennedy, 1982: Nowcasting the position and intensity of jet streams using satellite-borne total ozone mapping spectrometer. Nowcasting, K. A. Browning, Ed., Academic Press, London, 256 pp.

OZONE, JET STREAKS, AND SEVERE WEATHER

F. S. Sechrist[1], R. A. Petersen[2], K. F. Brill[3],
A. J. Krueger[2], and L. W. Uccellini[2]

[1]Department of Earth Sciences, Millersville University, Millersville, PA 17551.

[2]Laboratory for Atmospheres, NASA/Goddard Space Flight Center, Greenbelt, MD 20771.

[3]General Software Corporation, Landover, MD 20785.

1. Introduction

While upper-atmospheric photochemical ozone production is maximized over low latitudes in summer, ozone reaches its peak concentrations at high latitudes in spring. Since ozone is highly subject to atmospheric transport processes, it can be used as a valuable tool for tracing air motions along the jet stream, not only at large scales, but, as we shall show, at smaller scales as well.

A thorough review of early work relating ozone amount to pressure systems, fronts, upper-air patterns, tropopause height, upper-air isotach gradients, and other factors is provided by Reed (1955). Unfortunately, the ability to fully exploit ozone's potential as a diagnostic tool by these and subsequent studies had been restricted to very limited observations. The launch of the Nimbus-7 satellite on October 24, 1978, however, has greatly enhanced our observational capabilities. Placed in a local-noon-midnight sun-synchronous orbit, the satellite system includes a sensor capable of measuring the worldwide distribution and variations of total ozone at local noon on a spatially continuous basis. This Total Ozone Mapping Spectrometer (TOMS) is described in detail by Heath et al. (1975) and has been used for the analysis of jet streaks and tropopause folds (Shapiro et al., 1982; Uccellini et al., 1985).

In this paper, some preliminary studies will be presented with the following objectives: First, an attempt will be made to relate and synthesize TOMS data with conventional radiosonde analyses and with mid-tropospheric moisture data available from the VISSR (Visible Infrared Spin-Scan Radiometer) Atmospheric Sounder (VAS) onboard the Geostationary Orbiting Environmental Satellite (GOES). Second, case studies will be described which relate the potential vorticity structure of the upper troposphere to the total ozone distribution as measured by TOMS. This effort complements numerous other studies since the early 1950's which used balloon and aircraft measurements of ozone and should further our knowledge of stratospheric-tropospheric exchange processes on the synoptic scale. Concomitant with the potential vorticity studies, we shall relate smaller-scale features of the ozone and potential vorticity distributions to the vertical circulations in the vicinity of jet streaks. Third, cyclogenesis, frontogenesis, and the formation of severe weather outbreaks will be related to jet streaks and their characteristic ozone signature. The last objective will lead to the development of a schematic, conceptual model relating the position and structure of jet streaks to specific signatures in the ozone concentration fields.

2. Background

From the earliest measurements of ground-level ozone concentrations, it was deduced that since there was insufficient ozone at the surface to explain the observed extinction of the ultraviolet solar radiation, high ozone concentrations must exist at much higher levels of the atmosphere. Subsequent continuous measurements showed that the total columnar ozone in the atmosphere underwent significant day-to-day variations at individual stations. Moreover, these changes were highly correlated with weather systems. Some of the relations between total ozone and various types of weather systems will be briefly reviewed below.

Dobson et al. (1927) showed that maximum positive deviations of daily surface ozone values from the monthly means were generally found in the clear air to the rear of surface low pressure systems. Maximum negative deviations were found to the rear of surface high pressure systems.

Reed (1950) was the first to recognize how both advection and vertical motion could alter the ozone distribution in upper-level trough and ridge systems. When ozone-rich stratospheric air subsides, continuity requires the horizontal convergence of more ozone-rich air from above to take its place. Thus, the total ozone in a vertical column increases as the bottom of the column moves to lower levels. In addition, the ozone in the bottom portion of the column tends to persist because it is then protected from destructive ultraviolet solar radiation reactions. Reed concluded that troughs should be relatively ozone-rich, while nearby ridges would be relatively poor in ozone amount.

Reed (1955) also pioneered the concept of the folded tropopause, whereby a thin wedge of stratospheric air descends deep into the troposphere in the vicinity of jet cores. He also established the relation between air of stratospheric origin and large values of potential vorticity—the negative product of absolute vorticity and the static stability. Danielsen (1968) later produced the first figure which explicitly related large values of ozone and potential vorticity to the tropopause fold. Implicit in Danielsen's work was the need for a consistent relation between the fold and an accompanying jet core. Since then, numerous authors have established that unique vertical circulations are associated with the jet core and thereby with the fold as well.

Uccellini and Johnson (1979) reviewed the direct and indirect circulations associated with jet streaks and then related these vertical circulations to a severe weather outbreak. Generally, an indirect circulation in the troposphere occurs in the exit region of jet streaks, while a direct circulation occurs in the entrance region. The patterns of vertical circulation about the jet streak also can be significant to ozone studies if they are extended to include the region above, as well as below, the jet streak (see Fig. 1). In this case, continuity requires that subsidence be found above the areas of tropospheric ascent. This would suggest that the left front quadrant of a jet streak be characterized by cloudiness beneath the streak and by large values of ozone and potential vorticity above the streak.

It is our purpose to test these theoretical considerations involving jet streak vertical circulations on a number of other severe weather cases. Also, we shall determine if a signature related to the upper-level forcing of these tropospheric circulations is evident in the TOMS imagery and if these data have operational potential. The remainder of this paper will address these topics using a case study approach.

3. Case Study of 20 July 1981

Since details of the synoptic situation and related convective developments are presented in Petersen et al. (1984), only a brief description is given here. This summertime case is characterized by a relatively strong baroclinic short wave at 500 mb. The trough line extended from Minnesota southwestward toward Texas at 1200 GMT 20 July 1981. At that time, a well-defined 50 m s^{-1} jet streak on the west side of the trough was oriented in a northwest-southeast direction. This wave with its accompanying jet streak propagated southeastward during the day to a position near the Illinois-Indiana border.

At the surface, a rather large but diffuse low pressure center was located over the Great Lakes at 1200 GMT. From this center, a developing cold front extended westward into central Colorado. A secondary cold front moved from the U.S.-Canada border southeastward into southern Wisconsin by 0000 GMT 21 July 1981.

Before 1800 GMT 20 July 1981, convective cells in the Midwest had developed in the vicinity of the cold front over eastern Nebraska, in Minnesota, and in Wisconsin. These southeastward-moving storms were moderate in intensity and were relatively short-lived. After 1800 GMT, however, an area of extremely intense convective development occurred over central Missouri and eventually spread over most of Illinois by 2300 GMT.

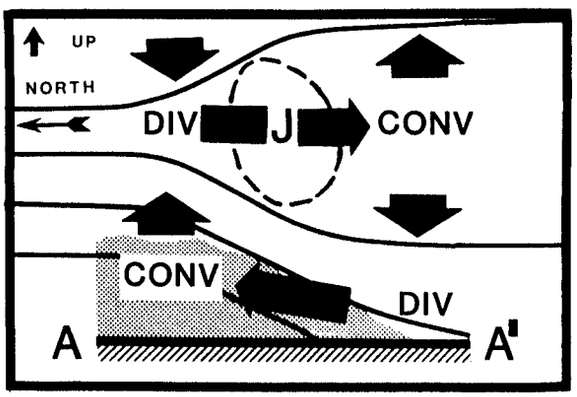

Fig. 1. *Schematic vertical cross section through the front quadrants above and below a simple jet streak. Shading indicates areas of enhanced tropospheric moisture.*

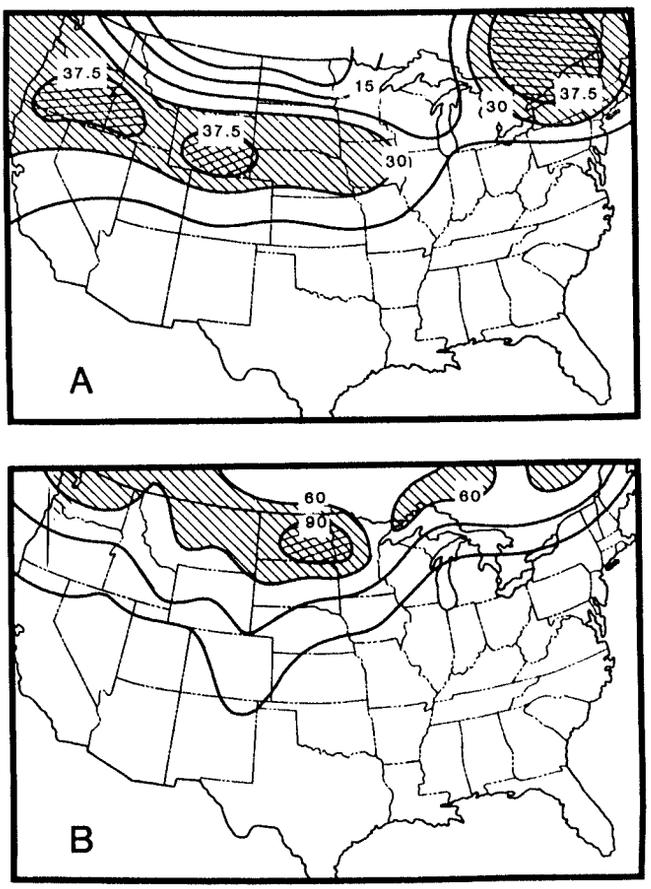

Fig. 2. *Analysis of (A) isotachs (m s^{-1}) and (B) potential vorticity (10^{-6} K mb^{-1} s^{-1}) on the 342 K isentropic surface for 1200 GMT 20 July 1981.*

a. Potential vorticity

To locate the level of maximum winds within this jet streak, isentropic analyses were generated by an objective analysis scheme developed by Petersen (1986). An isotach analysis at the level of the jet streak was generated for the 342 K isentropic surface. From this, the absolute vorticity was found and combined with the static stability to give the distribution of potential vorticity shown in Fig. 2. The maximum values of potential vorticity lie in an area centered over the Dakotas, in a region corresponding to the left front quadrant of the jet streak.

b. Total ozone amount

Fig. 3 shows the distribution of total ozone in Dobson Units (DU) as determined from the TOMS instrument for 1710 GMT 20 July 1981. Recall that previous investigators have established that high values of potential vorticity characterize air of stratospheric origin. Since the left front quadrant is hypothesized to have subsidence above the level of the jet streak, one could expect the total ozone, also of stratospheric origin, to have high values there also.

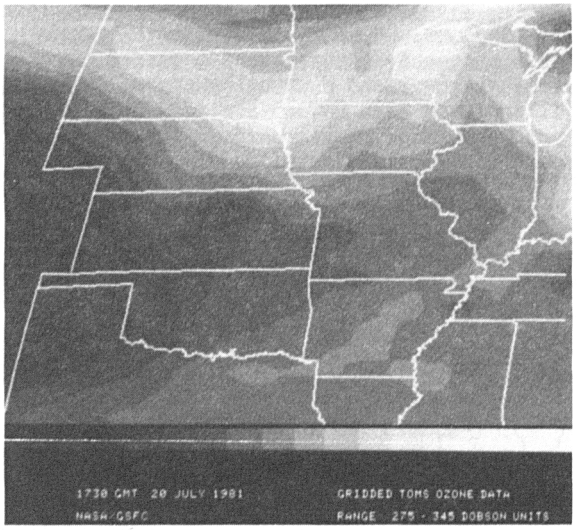

Fig. 3. *Total ozone data for 1730 GMT 20 July 1981. Range: 275-345 Dobson Units, with lighter features representing higher values of ozone.*

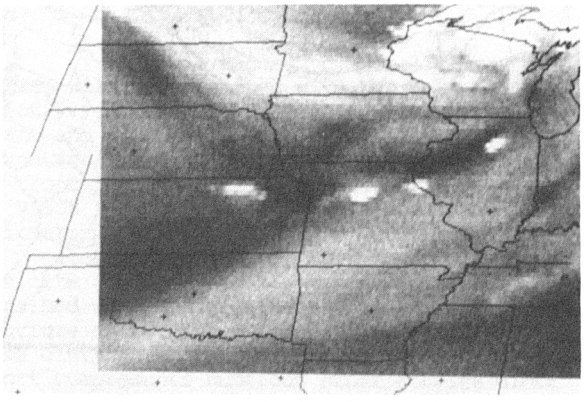

Fig. 4. *Mid-level water vapor (VAS channel 10) data for 1800 GMT 20 July 1981, with lighter features representing greater mid-tropospheric moisture.*

Inspection of Figs. 2 and 3 together shows that there is a striking subjective coincidence between the location of the maxima of potential vorticity and ozone as measured by TOMS. For example, note that the location of the highest values of potential vorticity in south-central South Dakota is nearly coincident with the largest values of ozone found in extreme southeastern North Dakota. The slight difference could be attributed to the time differential in data acquisition, keeping in mind the slow progression of the jet streak.

Evidently, the sinking of the stratospheric air over the left front quadrant of the jet streak is sufficient to enrich both the ozone and the potential vorticity concentrations in this region. This result provides strong support for the motions deduced to be above the jet streak as shown in Fig. 1.

c. VAS mid-level moisture data

Since TOMS data are available only once daily, it remains to be investigated if TOMS observations can be related to (and inferred from) features found in the temporally continuous 6.7 micron VAS moisture information, and if these data also support the jet streak circulation model of Fig. 1. Imagery from the 6.7 micron, mid-level water vapor channel of VAS are presented in Fig. 4. The darker areas of this figure show the location of mid-level dryness. The lighter or white regions show higher amounts of mid-tropospheric moisture and, most likely, cloudiness. In the region of the Dakotas, two obvious features reveal themselves. First, the orientation of the moisture pattern in this area agrees with the orientation of the total ozone shown in Fig. 3. Second, a large moisture gradient separates the very dry air from the cloudy region.

The obvious similarity of the ozone and moisture analyses in this case are in good agreement insofar as the vertical circulation of jet streaks is concerned, with the sinking and ozone enrichment in the upper atmosphere above the left front quadrant, while ascent and cloudiness are apparent below that quadrant in the tropospheric moisture data.

These results provide extremely good qualitative agreement between the three independent observing systems, viz., RAOBS, TOMS, and VAS. This agreement also enhances the credibility of the jet streak circulation model.

4. Case Study of 10 April 1979

To ascertain the degree to which other severe weather cases show the same relationships between ozone, potential vorticity, and jet streaks, another case study was undertaken. The case selected was the Wichita Falls tornado outbreak of 10 April 1979. This case was chosen, not only because of the

severity of the weather, but also because of the availability of three-hourly rawinsonde data and nearly synchronous (within one hour) observations of ozone with TOMS. Detailed synoptic descriptions of the Wichita Falls storms are given by Kocin et al. (1982). For our purposes, it is sufficient to discuss only the relation of the distributions of potential vorticity and ozone to the severe weather.

Fig. 5 gives the potential vorticity analysis for the 330 K isentropic surface at 1800 GMT on the tenth. The largest values occur over New Mexico and are associated with the position of the upper-level trough. Ahead of this large maximum, a secondary maximum of potential vorticity extends into western Oklahoma and central Texas. It is this secondary maximum which agrees best with the location of the left front quadrant of the jet streak. Note also that, as in the previous case, the severe weather again occurs southeast (to the right) of the secondary maximum.

The total ozone distribution for nearly the same time (1700 GMT) is given in Fig. 6. Again, we see good agreement between the potential vorticity distribution and the total ozone pattern. The primary maxima are over New Mexico and the secondary maximum forms a ridge protruding southward into central Texas.

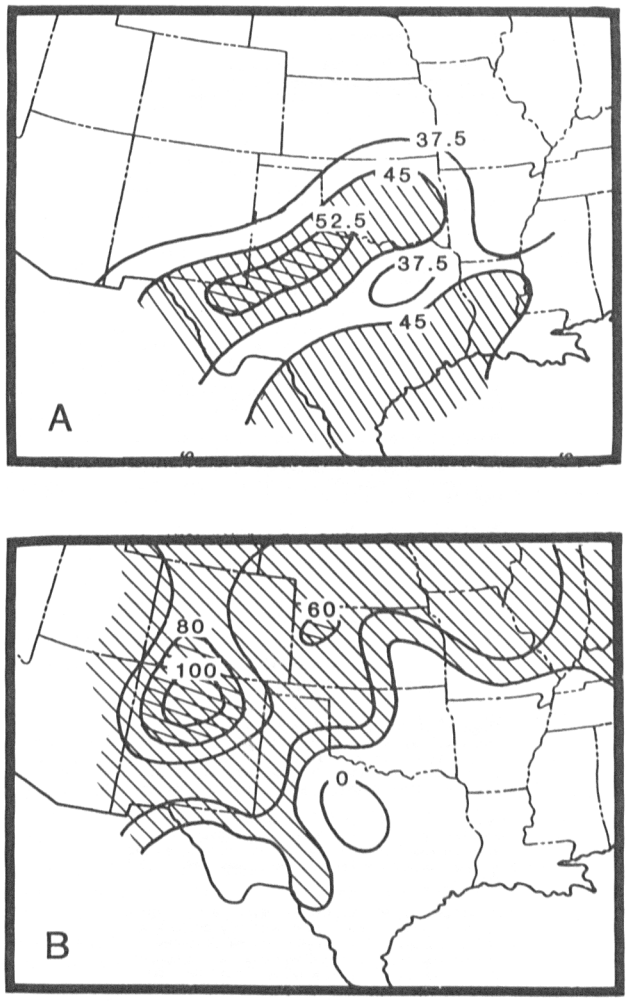

Fig. 5. *Analysis of (A) isotachs and (B) potential vorticity on the 330 K isentropic surface for 1800 GMT 10 April 1979. Units are same as in Fig. 2.*

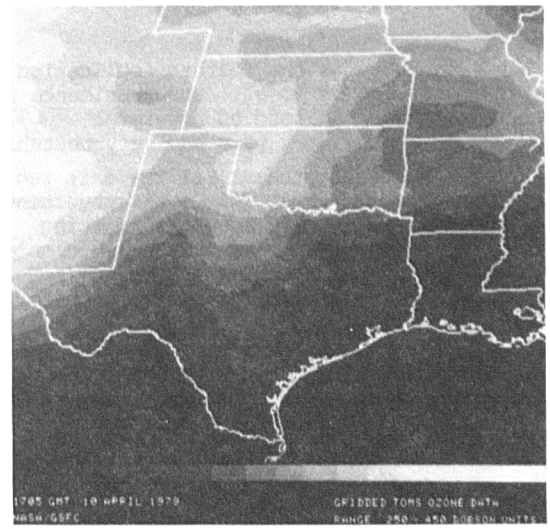

Fig. 6. *Total ozone data for 1705 GMT 10 April 1979. Range: 250-450 Dobson Units, with lighter features representing higher values of ozone.*

Finally, note that minimum values of ozone appear in the area to the south of Wichita Falls, corresponding to the right front quadrant of the jet streak and the minimum of potential vorticity. As in the previous case, these features are located just to the southwest of the severe weather that occurred later that day. This consistent relationship between ozone, potential vorticity, and severe weather points to the possible operational utility of ozone distribution signatures for diagnosing the jet streak's influence on the development of severe weather.

5. A Jet Streak-Ozone Model

From the case studies presented in this paper, an effort was made to relate the horizontal total ozone amount to the distribution of potential vorticity. Since larger values of both these variables are characteristic of stratospheric air, it became clear that they had to be related, not only to each other, but to the vertical circulations around jet streaks. By the very nature of a jet streak, one must expect relatively large values of potential vorticity in its left front quadrant. This is precisely what has been found.

The above characteristics have been incorporated into a simple jet streak-ozone model presented in Fig. 7. The main features of the schematic are: (a) the primary ozone maximum appears in the region of strongest cold advection and subsidence west of the main trough; (b) the secondary ozone maximum is associated with the left front quadrant of the jet streak and is produced by subsidence above the level of the streak; and (c) a relative minimum of ozone south and to the right of the jet streak. It is hypothesized that this minimum occurs because of the ascent above the level of the jet streak, in the same region of the jet streak (right front quadrant) where the

characteristic clear tongue of a cyclone is produced by subsidence below the level of the jet streak.

There is one further implication of the jet streak-ozone model. The subsidence in the clear tongue can lead to low-level convergence in the very warm and very unstable air to the right (southeast) of the exit region of the jet streak. This low-level convergence can, in turn, serve as a low-level forcing mechanism to produce upward vertical motion and destabilization which would enhance the severe weather so characteristic of the warm sector of a developing mid-latitude cyclone.

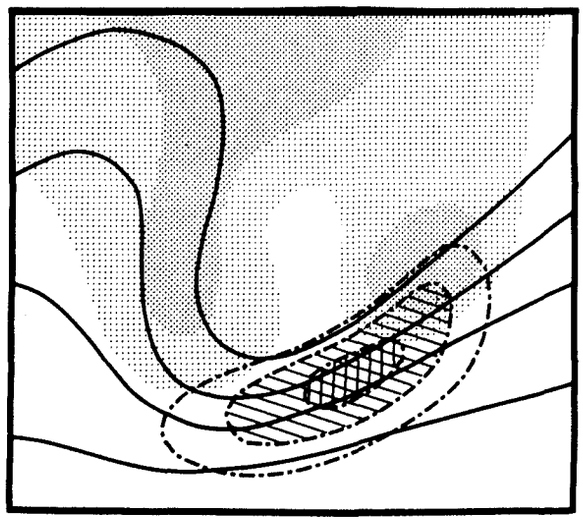

Fig. 7. *Jet streak-ozone schematic model showing typical 300 mb contours (solid lines), isotachs (dashed lines), and areas of ozone concentration (hatching).*

6. Summary and Conclusions

The case studies presented in this study suggest a unique distribution of ozone, potential vorticity, and vertical motion relative to jet streak vertical circulations. Primary maxima of ozone and potential vorticity are associated with cold advection and subsidence in the main upper-air trough as already shown by Reed (1955). The secondary maxima of the three quantities diagnosed in this study, however, appear in the left front quadrant of a jet streak, indicating the importance of transverse, secondary circulations induced by jet streak above the level of maximum winds in further modifying the potential vorticity and ozone structures. The fact that the model deduced here is in good agreement with the wind field and ozone analysis of Shapiro et al. (1982) further substantiates the validity of the hypothesis.

The traditional notion of an indirect circulation in the exit region of the jet streak must be expanded to include a thermally direct cell above the jet to explain the above observations (see Fig. 1). Due to the vertical circulations present at high levels above a jet streak, ozone values tend to be large in the left front quadrant of a jet streak. By the same argument, the ozone values are small above the right front quadrant. Under the jet streak, an indirect thermal circulation gives rise to cloudiness under the left front quadrant and to a clear area under the right front quadrant. Mid-level moisture patterns from the VAS 6.7 micron channel show patterns consistent with these conclusions and thereby complement these results. The subsidence in the clear area may, in turn, produce low-level convergence in the very warm, moist and unstable air to the right of the jet core exit region. It is in this area, to the right of the clear area, that the most severe weather forms.

The agreement between the results from three highly independent observing platforms (balloon-borne radiosondes, the TOMS instrument on Nimbus 7, and the VAS instrument aboard GOES) suggests that data from these observing systems can be combined to better diagnose the evolution of jet streaks and trough systems. The total ozone amounts measured by the TOMS instrument are extremely valuable for detecting the various quadrants of a jet streak. Isolation of the jet streak quadrants then permits identification of the area in which severe weather is most likely to occur. The potential value of temporally continuous geosynchronous TOMS data in this regard becomes clear.

7. References

Danielsen, E. F., 1968: Stratospheric-tropospheric exchange based on radioactivity, ozone and potential vorticity. J. Atmos. Sci., 25, 502-518.

Dobson, G. M. B., D. N. Harrison, and J. Lawrence, 1927: Measurements of the amount of ozone in the earth's atmosphere and its relation to other geophysical conditions, II. Proc. Roy. Soc., London, A114, 521-541.

Heath, D. F., A. J. Krueger, H. A. Roder, and B. D. Henderson, 1975: The solar back-scatter ultraviolet and total ozone mapping sprectrometer (SUBV/TOMS) for Nimbus G. Opp. Eng., 14, 323-331.

Kocin, P. J., L. W. Uccellini, and R. A. Petersen, 1982: The role of jet streak coupling in the development of the 10-11 April 1979 Wichita Falls tornado outbreak. Preprints, Twelfth Conference on Severe Local Storms, San Antonio, Amer. Meteor. Soc, 560-563.

Petersen, R. A., L. W. Uccellini, A. Mostek, and D. A. Keyser, 1984: Delineating mid- and low-level water vapor patterns in pre-convective environments using VAS moisture channels. Mon. Wea. Rev., 112, 2178-2198.

Petersen, R. A., 1986: Three-dimensional objective analysis using a detailed isentropic cross-sectional procedure. Accepted by Mon. Wea. Rev.

Reed, R. J., 1950: The role of vertical motions in ozone-weather relationship. J. Meteor., 7, 263-267.

Reed, R. J., 1955: A study of a characteristic type of upper-level frontogenesis. J. Meteor., 12, 226-237.

Shapiro, M. A., A. J. Krueger, and P. J. Kennedy, 1982: Nowcasting the position and intensity of jet streams using a satellite-borne total ozone spectrometer. Nowcasting, K. A. Browning, Ed., Academic Press, London, 256 pp.

Uccellini, L. W., and D. R. Johnson, 1979: The coupling of upper and lower tropospheric jet streaks and implications for the development of severe convective storms. Mon. Wea. Rev., 107, 682-703.

Uccellini, L. W., D. Keyser, K. F. Brill, and C. H. Wash, 1985: The Presidents' Day cyclone of 18-19 February 1979: Influence of upstream trough amplification and associated tropopause folding on rapid cyclogenesis. Mon. Wea. Rev., 113, 962-988.

TROPICAL STORM FLOSSIE AND THE ARK ROYAL STORM

S. Peteherych

Atmospheric Environment Service
Downsview, Ontario, Canada

A.F. Davies

Consultant
Downsview, Ontario

G. Muttitt
Consultant
White Rock, British Columbia

G.F. Cunningham
JPL, California Institute of Technology
Pasadena, California

1. INTRODUCTION

As a result of being involved in two Seasat validation workshops - GOASEX I Workshop (cit, 1979) at JPL, January, 1979, and GOASEX II (cit, 1980), Pasadena, it was obvious that the plotted scatterometer maps contained patterns that were related to well-known meteorological features such as high and low pressure centers. A study performed as part of the Seasat-Jasin Workshop (Woiceshyn et al. 1981) demonstrated the ability of marine analysts to select the correct wind directions under "Worst-case Conditions", (i.e. no ship, land or satellite imagery). Subsequent publications demonstrated the utility of using Seasat scatterometer data in regional weather forecasting (Peteherych et al. 1981a, b). Wurtele et al. (1982) proposed a methodology for selection of the correct wind direction. Alishouse (1983) found good argument between Seasat SMMR observations of precipitable water vapour and surface RAOB observations as well as between satellite rain rate and surface rain gauges.

The Ark Royal storm occurred on September 16 and 17 1978, north of Scotland. It received its name from the naval vessel which, along with many other ships, was buffeted by this unusually violent storm.

By supplementing conventional land, marine, upper air data and satellite imagery with SEASAT Scatterometer (SASS) winds and Scanning Multichannel Microwave Radiometer (SMMR) moisture data, it was possible to illustrate how the Ark Royal Storm evolved from tropical storm Flossie (Figs. 1a, 1b, 1c; Figs. 2a, 2b, 2c). For purposes of this presentation, as long as the storm is a tropical storm it will be called Flossie. When the tropical storm becomes an extratropical storm it will be called the Ark Royal storm.

2. THE DATA

In addition to a good set of conventional ship and land data, this study includes SEASAT scatterometer winds (100 km spacing) and column abundances of SMMR water vapour, liquid water and rain rate observations. Units for water vapour were g/cm^2. Rain rate is given in millimetres per hour. The SMMR water vapour contours are shown in Figs. 3a, 3b, and 3c.

The analyses of liquid water and rain rate are not shown as they were sub-synoptic in scale, and charts of much larger scale would be needed to show them. The liquid water reports showed a series of maxima along the cold side of the water vapour moist tongue (0000 GMT September 15) ranging from 222 to 313 milligram per square centimetre. The rain rate maxima were virtually coincident with the liquid water maxima, with values ranging from 5.0 to 7.8 millimetres per hour. The rain rate maxima were observed to be along or as much as 200 km on the cold side of the surface warm front.

The SASS windspeeds were derived from scatterometer return signals using the SASS 1 algorithm developed at Jet Propulsion Laboratory. The units for wind speeds are metres per second.

3. ANALYSES

The isobaric and frontal surface charts, isotachs and streamlines of the SASS winds, and contours of water vapour are shown in the analyses at 24 hour intervals (0000 GMT September 15, 0000 GMT September 16 and 0000 GMT September 17), (Figs. 1a, 1b, 1c; Figs. 2a, 2b, 2c; Figs. 3a, 3b, 3c).

This paper is based on analyses performed independently by two of the authors, and then by consensus with a third, which included analyses of synoptic data at 6 hr. intervals, streamline and isotach analyses of all SEASAT orbits 1144 to 1187, and analyses of all three moisture parameters from the SMMR data. Upper air charts (500 mb) were used for this study.

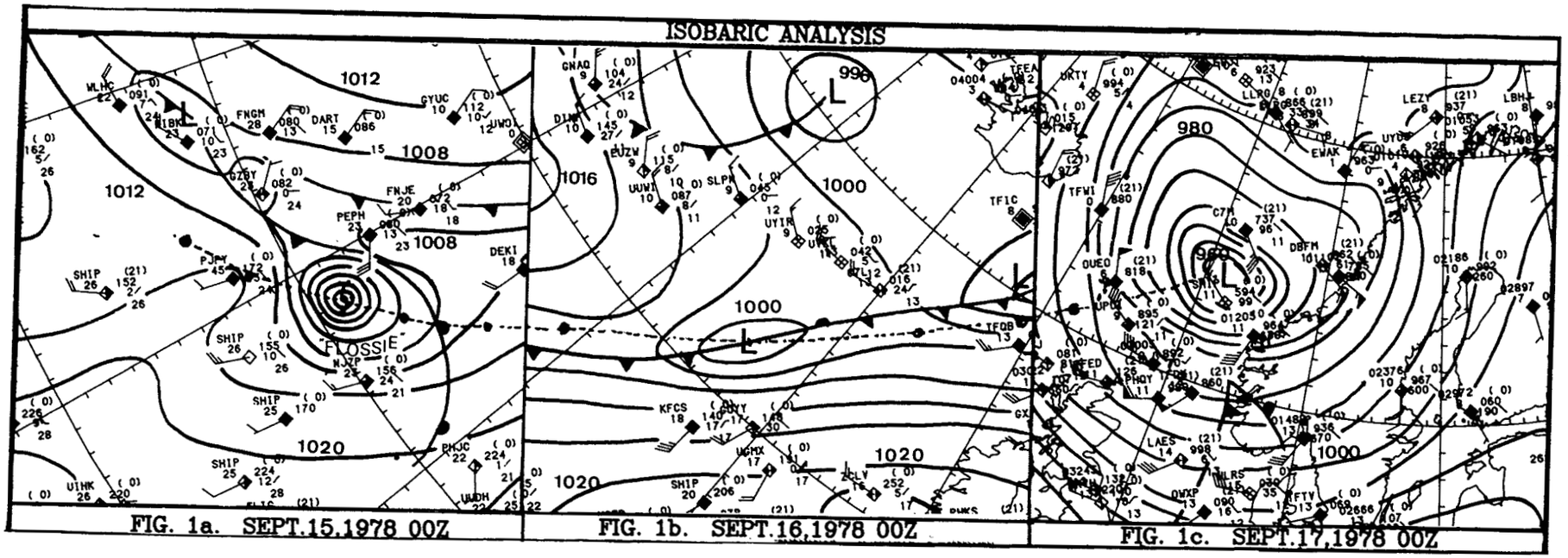

FIG. 1a. SEPT.15,1978 00Z

FIG. 1b. SEPT.16,1978 00Z

FIG. 1c. SEPT.17,1978 00Z

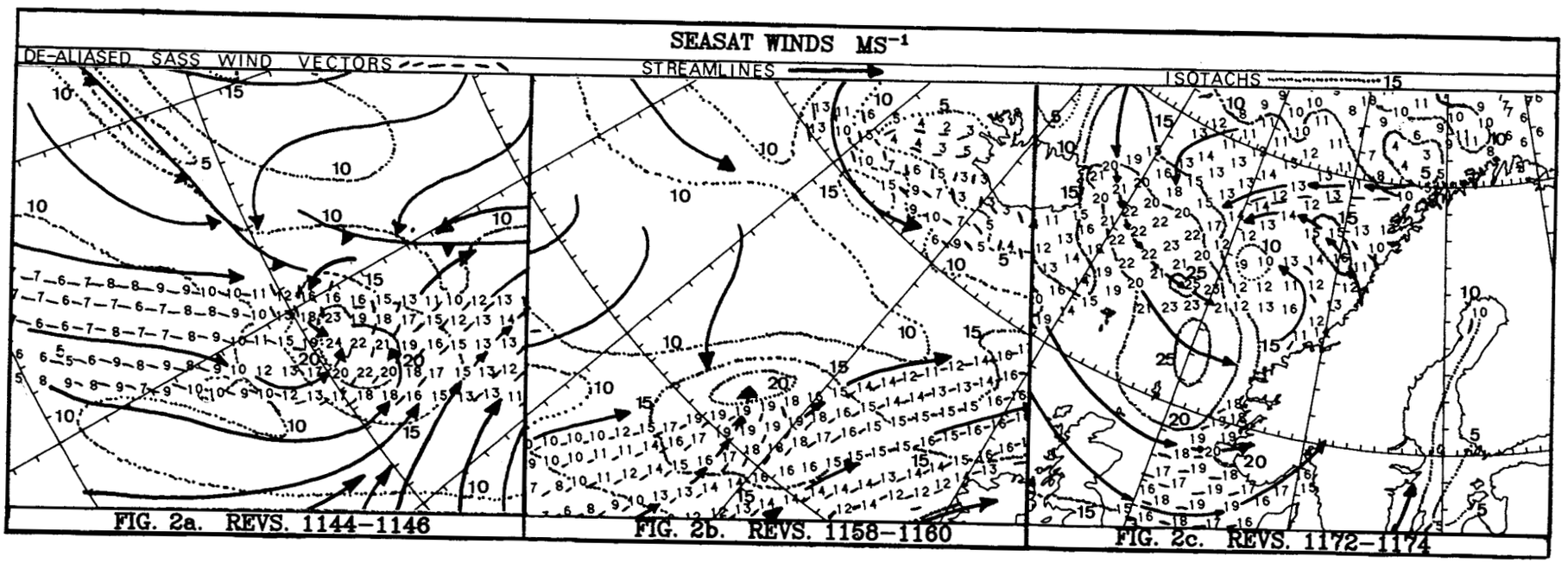

FIG. 2a. REVS. 1144-1146

FIG. 2b. REVS. 1158-1160

FIG. 2c. REVS. 1172-1174

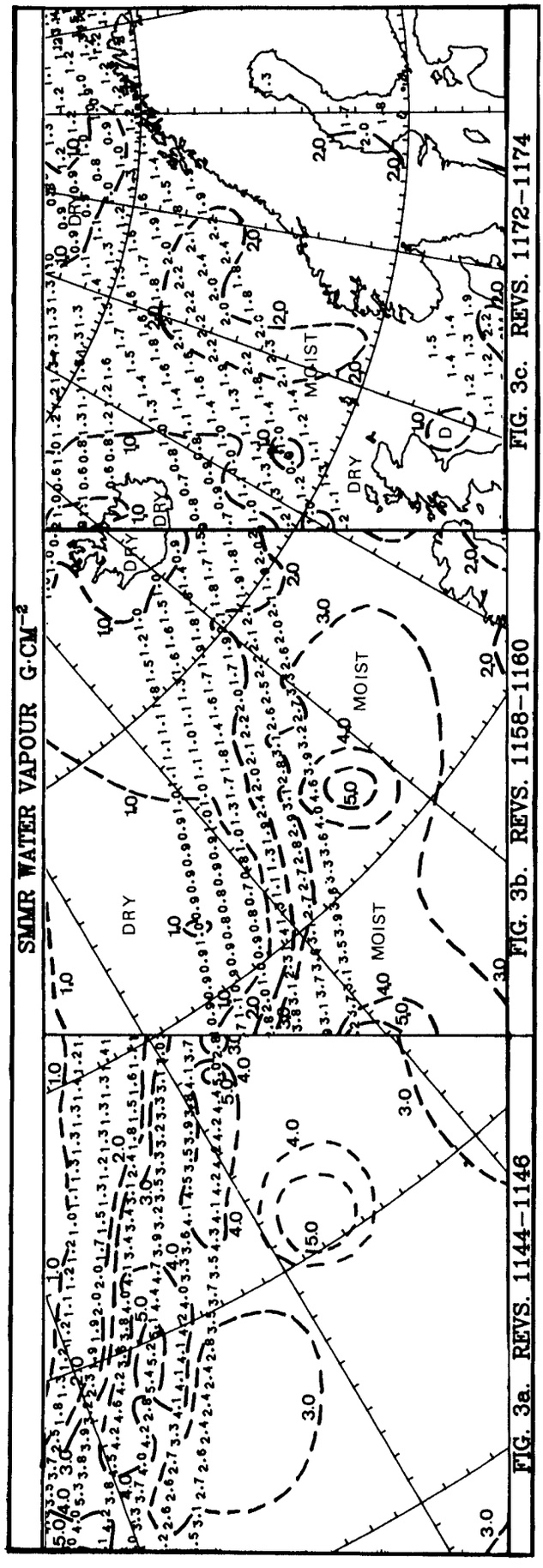

4. METEOROLOGICAL COMMENTS

Tropical storm Flossie was moving northeastward at slightly more than 50 km/h when it passed through 41.5°N 37.5°W; i.e., 1300 km southeast of Newfoundland, at 0000 GMT September 15. It passed through a transitional phase to become an extratropical storm at 1800 GMT, September 15, when the center was coincident with the southeastward moving maritime cold front at 47.5°N 30.5°W. It then accelerated to a speed in excess of 100 km/h as a stable wave which initially weakened by 4 mb in 12 h. After 1600 GMT, September 16, however, a number of surface and upper air factors combined to produce 20 mb deepening in 12 hours. These included the low level injection of very cold air from Greenland and Iceland, a vigorous short wave aloft, the strengthening of the thickness ribbon and jet stream, and the release of latent heat due to lifting of the warm air along the front. This warm air contained up to 5400 mg/cm^2 of water vapour. The deepening continued at a rate of 1 mb/h until 0006 GMT September 17 with the storm attaining a maximum depth of 958 mb. The low, then completely occluded, changed direction and moved directly eastward along latitude 64.5°N toward central Norway, filling to 970 mb by 1800 GMT September 17.

5. CONVENTIONAL WIND REPORTS

Apparently due to good information about the expected motion of Flossie, ships avoided the forecast track of the storm, to such an extent that from 0000 GMT September 15 to 0000 GMT September 16 only 25 synoptic hour ship reports near the storm were received, the closest at a distance of 150 km from the center, the remainder from 200 to 500 km. At 0000 GMT September 16 an elongated area parallel to the front, 3000 km in length and about 800 km in width, was completely without ship reports. As a result, the strongest winds reported prior to 1200 GMT September 16 were 35 knots. At 1200 GMT September 16 the Ark Royal storm appeared at 59.0°N 10.0°W 300 km northwest of the Hebrides, with at least 10 ships experiencing winds in excess of 60 knots. Winds of this strength were experienced over an expanding area for the following 36 hours.

6. SEASAT SCATTEROMETER WINDS

During the 36 hours before the emergence of the Ark Royal storm, the SASS winds considerably increased the information about the frontal wave and tropical storm from which it developed.

There were 144 SASS reports within 500 km of the low during that time, as compared with 25 conventional reports.

The closest conventional report was 150 km from the center at 0600 GMT September 15 showing a speed of 32 knots, while 12 of the SASS reports were within 0 to 150 km of the center, and showed speeds of 20 to 29 m/s (39 to 56 knots). Where conventional and SASS reports were coincident they were almost identical, so the emphasis here is not on the superiority of either, but on the fact that the SASS winds supplemented the conventional winds in areas where ship data was not available.

The scatterometer winds near the storm center were obtained from 6 SEASAT orbits 1145, 1150, 1151, 1159, 1163 and 1164.

Descending orbits 1145 at 0100 GMT September 15 and 1159 at 0100 GMT September 16 passed directly over the center of Flossie and the transitional wave. Ascending orbit 1150 passed on the east side of Flossie and orbit 1151 passed on the west side of Flossie at 0800 September 15 to 1000 GMT September 15, passing orthogonally across the associated front, and overlapping orbit 1145 thus providing information about the location of the storm, as well as a highly detailed record of the changes in winds at the surface, and of moisture aloft over a 7 to 9 hr interval. There were 130 such reports within 500 km of the front. Similar statements are true of orbits 1163 and 1164 at 0800 September 16 to 1000 GMT September 16 which bracketed the Ark Royal storm as well as overlapping and updating orbit 1159.

The SASS winds at 0100 GMT September 15 showed a typical distribution of winds around a tropical storm with speeds from 15 to 29 m/s within a 400 km radius, and the maximum wind about 50 km from the center. At 0100 GMT September 16 the distribution of the winds was asymmetric, with a sharp drop to 10 m/s to the northwest (in the cold air), while the radius of winds in excess of 15 m/s in the warm air had increased to 500 km.

At 0000 GMT September 17 in the occluded Ark Royal phase, there were winds in excess of 15 m/s over an area 1200 km x 1600 km, in the west and southwest quadrants of the storm, and with maximum speeds of 31 m/s, 500 km southwest of the center. (Fig. 2c).

7. SCANNING MULTICHANNEL MICROWAVE RADIOMETER DATA

7.1 Water Vapour

The SMMR water vapour data defined, in detail, the distribution of moisture over the north Atlantic during the 48 hour period.

At 0100 GMT September 15, a tongue of moisture extended from a maximum of 5434 mg/cm^2 about 1000 km southwest of Flossie northward along the maritime front with values in excess of 4000 mg/cm^2, and then eastward with values of 3000 mg/cm^2 all the way to northern Scotland. Steep gradients along the front had water vapour amounts decreasing at 10 mg/cm per km to values less than 2000 mg/cm^2 200 km into the cold air.

The tongue of moisture moved southeastward at 27 km/h during the following 24 hours. The maximum of water vapour associated with Flossie moved northeastward at an average speed of 60 km/h. The tongue of 3.0 g/cm^2 values extended to northern Scotland.

A dramatic change in this pattern occurred just after 0600 GMT, September 16, when the 4000 mg/cm^2 maximum formerly associated with Flossie arrived over the Hebrides, while dry air with values less than 1000 mg/cm^2 moved rapidly eastward behind it, pinching that maximum off from the original moist tongue 1500 km to the southwest.

By 0000 GMT September 17 the only evidences of the moist maximum were values slightly over 2000 mg/cm^2 near the occluded Ark Royal low center, and along the front which by that time extended southward across the North Sea and English Channel to the Bay of Biscay. This suggests that about 2000 mg/cm^2 of water vapour had been converted to rain in about 12 h, at the rapidly deepening center. The latent heat released would have been a significant factor in the extreme development of the low.

7.2 Liquid Water and Rain Rate

The SMMR reports of these two parameters showed a series of maxima of about 150 to over 300 mg/cm^2, and 5 to 8 mm/hr respectively, generally where the moist tongue would have experienced maximum lift at the front. These features were highly detailed on a sub-synoptic scale. The maximum values of liquid water and rain rate of 246 mg/cm^2 and 6.5 mm/hr were observed at the low center at 1200 GMT September 16 dropped to values of 44 and 0.2 respectively by 0000 GMT September 17. It may also be noted that 2.0 g/cm^2 of water vapour converted to rain would produce approximately 2 cm of liquid rain per square cm at the surface. At the reported maximum rate of 6.5 mm/h, it would take 3 hours for this to happen.

8. METEOROLOGICAL SUMMARY

Conventional land and marine and upper air data, when supplemented by scatterometer winds and SMMR moisture data, indicate that the intense development of the Ark Royal storm was due to the phasing of a number of factors: A relatively modest tropical storm became a rapidly moving stable wave when it was picked up by a vigorous upper short wave and surface cold front. It then received strong dynamic and thermodynamic support for development, from such factors as the release of large amounts of latent heat due to the transport of typical tropical moisture values to high latitudes, the injection of cold, dry air from Greenland and Iceland, and additional factors not dealt with in this report such as convective development, the increase in the thickness gradient, the high level jet, and the associated thermal and vorticity advection patterns.

ACKNOWLEDGEMENT

Norbert Driedger, who provided the computer support to produce the data for analysis and figures, deserves a special thanks for his contribution to this paper.

REFERENCES

Alishouse, J.C.; Total precipitable water and rainfall determinations from the SEASAT scanning multichannel microwave radiometer. J. Geophys. Res., 88(C3), 1929-1935, 1983.

CIT. California Institute of Technology, Seasat Gulf of Alaska Workshop I Report (GOASEX I): Volume 1, Jet Propulsion Laboratory, Report #622-101, April 1979.

REFERENCES

CIT. California Institute of Technology, Seasat Gulf of Alaska Workshop II Report (GOASEX II) Jet Propulsion Laboratory, Workshop Report #622-107, January, 1980.

JPL Seasat-Jasin Workshop: Woiceshyn, P.M.; S. Peteherych, M.G. Wurtele, W. Appleby and M. Borowski. SASS Wind Direction Ambiguity Removal Subpanel Report JPL Report #622-220, April, 1981.

Peteherych, S.; W.S. Appleby, P. Woiceshyn, J. Spagnol and L. Chu. Application of Seasat Scatterometer Wind Measurements for Operational Forecasting. Final report, Seasat Commercial Demonstration Program, February, 1981a.

Peteherych, S.; P.M. Woiceshyn, W. Appleby, L. Chu, J. Spagnol and J.E. Overland. High Resolution Marine Meteorological Analysis Utilizing Seasat Data. In: Oceanography from Space, Vol. 13. F.J.R. Gower, Ed., May, 1981b.

Peteherych, S., A.F. Davies, 1985: Measurements and Applications of ocean winds and atmospheric parameters from spaceborne scatterometer and passive microwave radiometer. Report on the International Workshop on Offshore Winds and Icing.

Wurtele, M.G., P. M. Woiceshyn, S. Peteherych, M. Borowski and W.S. Appleby, April 30, 1982. Wind Direction Alias Removal Studies of Seasat Scatterometer-Derived Wind Finals. J. Geophys. Res. 87, C5.

EFFECTS OF DATA RESOLUTION ON SATELLITE CLOUDINESS ESTIMATION

Chi-Fan Shih
G. Garrett Campbell
T. H. Vonder Haar

Department of Atmospheric Science
Colorado State University
Fort Collins, CO 80523

1.0 INTRODUCTION

Since meteorological satellites became available in the 1960s, processing and storing satellite data of high spatial and temporal resolutions has been a difficult job. Users normally choose to process data of reduced sizes (either sampled or averaged down) to get around the large data volume problem. We address this data resolution problem by comparing the histograms and variances of data sets of the same origin but with different resolutions. Several case studies will be presented at the conference, some of which are discussed below.

2.0 DATA

At the Department of Atmospheric Science, Colorado State University, we have a Direct Readout Satellite Earth Station (DRSES) which receives GOES-6 transmission routinely. On August 26, 1985 we collected two satellite images covering the California coast (40°-25°N, 130°-115°W), and South America (0°-15°S, 90°-75°W) as our test data set. The spatial resolution of this test data is 2 km for the raw visible data and 8 km for the raw infrared data. Using the raw data, we made two levels of degrade visible data by averaging 4x4 (or 8x8) visible pixels into one pixel using the following formula:

$$\text{Degrade Pixel Count} = \left(\sum_{1}^{N} \text{Count}^{2}/N \right)^{0.5}$$

where N is the number of pixels averaged. The 4x4 and 8x8 area-averaged data are named degraded A and degraded B data. To investigate the different effects of data resolution between a uniform cloud field and a non-uniform cloud field, we chose four target regions of different cloud conditions (Table 1).

3.0 ANALYSIS

To simulate the sampling of the International Satellite Cloud Climatology project (ISCCP)(Schiffer and Rossow, 1983), we sampled the raw infrared data every 3 pixels of every scan line for form level 1 reduced data. A further sampling of every 3 pixels of every 3 scan lines were used to make level 2 reduced data. For the visible data, sampling of every 6 pixels of every 4 scan lines was done to make level 1 data. Level 2 visible data was further sampled every 4 pixels of every 4 scan lines of level 1 visible data. The reduced infrared and visible data will have the same spatial resolution. We then calculated the averages, variances and skewness of a target region of 2.5^{o}x2.5^{o} in size. Each target region is further divided into 25 small 0.5^{o}x0.5^{o} boxes. Their statistics were computed for all levels of infrared and visible data. This means that for every 2.5^{o}x2.5^{o} region, we had one set of regional and 25 sets of subregional statistics. Tables 2 and 3 list out the regional statistics of 4 target regions. For simplicity, the subregional statistics will not be presented here.

Table 1. The geographical locations of target regions and their cloud conditions.

NAME	LATITUDE/LONGITUDE	CLOUD CONDITION
CA1	130W, 127.5W 40N, 37.5N	uniform low cloud with a little thin cirrus
CA2	130W, 127.5W 37.5N, 35N	uniform low cloud with an up-side down V clear sky
SA1	90W, 87.5W 5S, 7.5S	half filled with unfiorm low cloud and half filled with shallow convection
SA2	85W, 82.5W 2.5S, 5S	deep convection, high clouds with low cloud below

4.0 DISCUSSION

Tables 2 and 3 summarize the statistics of the infrared and visible data of 4 target regions. In Table 2 we found that the regional mean, variance and skewness of all 4 regions are well represented by the sampled subsets. Compared to the other regions, the SA2 region lost some statistical information with sampling. This is not surprising because, as mentioned in Table 1, the cloud conditions of SA2 are the most complicated among all 4 regions, while the other regions are mostly covered by uniform low clouds (visually determined from the warm cloud top temperature of infrared images) with some clear sky or little thin cirrus clouds. Thus, sampling data of regions having complicated cloud conditions will lose some statistical information which exists in the original data. This effect can be seen in Figure 1, as the histograms of sampled 1 and 2 data become more blocky than the original data. However, the major peaks of sampled data stayed at about the

same brightness level (the x-axis) as in the original data. This means that only sampled data retains the first order statistical characteristics well, but not necessarily the high order statistical information such as the variance and skewness, which depends on the cloud condition. A further comparison of mostly clear with a few clouds conditions of a $2.5^{o}x2.5^{o}$ region is underway to see if the findings of regions of mostly clear sky with few clouds are different.

Unlike the infrared data, the GOES visible data has very high spatial resolution and sometimes an area-averaging technique is used to reduce the size of the visible data. Compared with original data, area-averaged data is more smooth and thus less variance. This effect shows up in both Table 3 and Figure 2 as the brightness counts of area-averaged data has a narrower range horizontally. Another effect of area-averaging is to shift the low end of the energy spectrum (low brightness counts) to a higher end (high brightness count) as shown in Figure 2. Nevertheless, the sampling effects on the infrared data still apply here and the combining effect of sampling and averaging the visible data will increase the loss of high order statistical information. This smoothing effect is clearly displayed in Figure 3, in which the variance of 25 subregions of SA1 is plotted using the variance of original data as the x-axis and A1 (quantized level A with sampling level 1, Figure 3a), B1 (defined as A1, Figure 3b) as the y-axis. As the area-averaging goes from level A (Figure 3a) to B (Figure 3b), we can see its corresponding variance values become smaller. Also notice that in Figure 3a the points are scattered along a diagonal line of slope 1, while in Figure 3b the points are widely scattered under the lower half of that diagonal line. Their skewness diagrams (not shown here) show a similar pattern. One implication of this finding is if variance or skewness of a target region is used in a cloud algorithm or in other applications, care must be taken to insure the correctness of the results if using data of reduced resolution.

Table 2. The summary of regional statistics of all target regions of infrared data.

Region Name		Original	Sampled Level 1	Sampled Level 2
CA1	N*	1476	491	55
	MEAN**	25.4	25.4	25.4
	VAR	4.0	4.0	3.6
	SKEW	-3.3	-3.3	-0.6
CA2	N*	1616	539	58
	MEAN**	26.1	26.1	26.1
	VAR	1.2	1.2	1.2
	SKEW	1.1	1.1	1.3
SA1	N*	3607	1208	140
	MEAN**	27.8	27.8	27.8
	VAR	0.8	0.8	0.8
	SKEW	0.6	0.5	0.6
SA2	N*	3524	1160	130
	MEAN**	20.1	20.0	19.8
	VAR	20.0	19.8	19.7
	SKEW	10.9	11.2	14.2

* N is the number of pixels.
** Unit is proportional to radiance (W/M**2/STER).

Table 3. The summary of regional statistics of all target regions of visible data.

Region Name		Original	Sampled Level 1	Sampled Level 2	Degraded A Sampled Level 1	Degraded B Sampled Level 2	Degraded A Sampled Level 1	Degraded B Sampled Level 2
CA1	N*	11785	491	55	491	55	491	55
	MEAN**	33.5	32.0	32.3	31.9	31.7	31.8	32.1
	VAR	130	120	118	95	93	84	73
	SKEW	-838	-878	-764	-652	-674	-500	-540
CA2	N*	12874	491	58	539	58	539	58
	MEAN**	30.7	29.0	28.6	28.7	28.6	28.8	28.8
	VAR	83	72	63	63	69	52	63
	SKEW	-488	-467	-329	-441	-472	-395	-545
SA1	N*	28686	1208	140	1208	140	1208	140
	MEAN**	121.0	116.9	117.8	116.6	117.5	115.7	116.8
	VAR	4541	4510	4333	4039	4073	3748	3858
	SKEW	-82729	-83353	-88155	-56235	-72197	-36717	-56122
SA2	N*	28146	1160	130	1160	130	1160	130
	MEAN**	122.8	120.3	122.1	118.7	119.4	117.9	118.6
	VAR	3664	3534	3856	3260	3355	3185	3287
	SKEW	86723	82691	100709	79127	88098	80445	82406

* N is the number of pixels.
** Unit is proportional to radiance (W/M**2/STER).

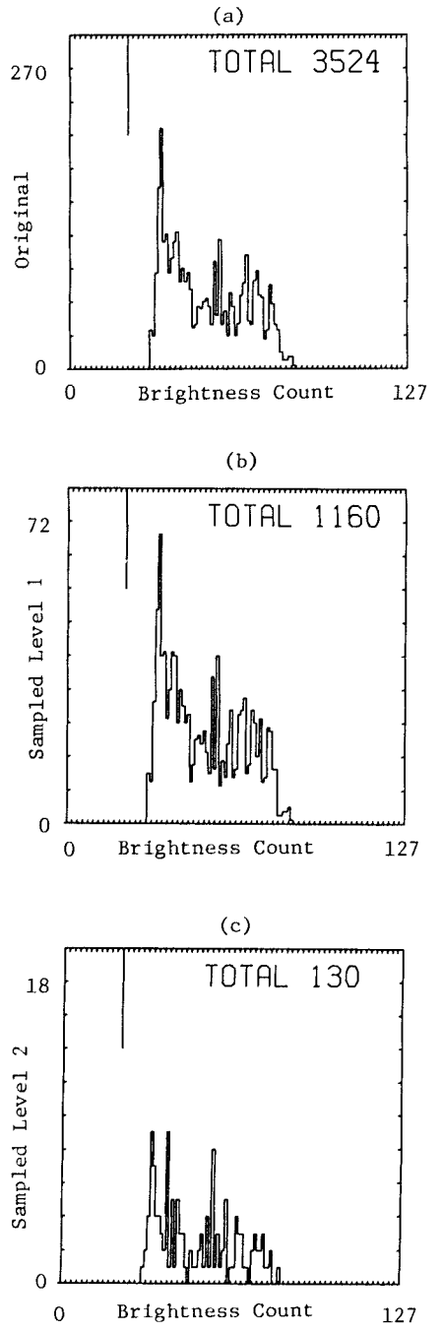

Figure 1. Histograms of infrared data over SA2 region for original (a), sampled level 1 (b), and sampled level 2 (c) resolution. The long tickmark on the top of each diagram is the relative infrared background brightness count for reference.

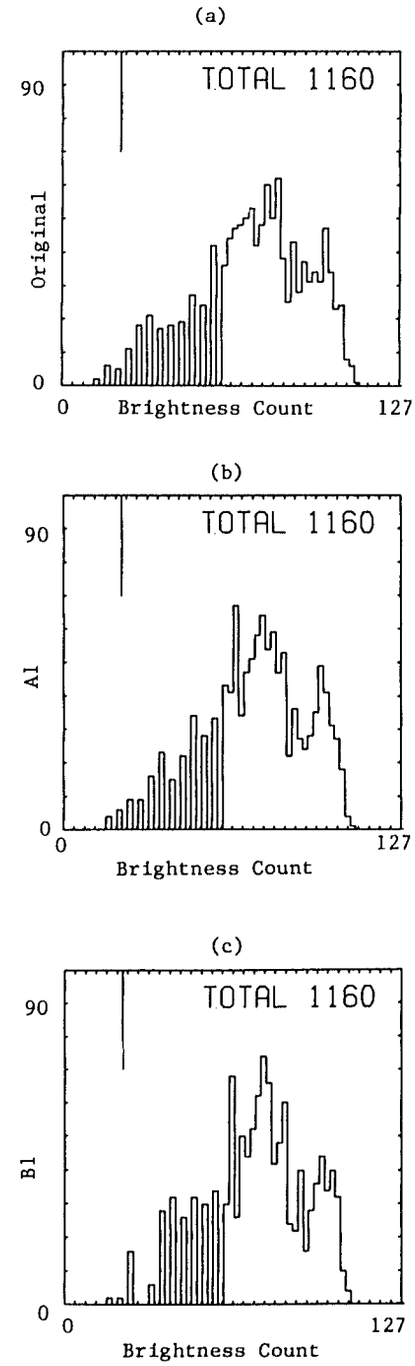

Figure 2. Histograms of sampled level 1 visible data over SA2 region for original (a), degraded level A (b), and degraded level B (c). The long tickmark on the top of each diagram is the relative visible background brightness count for reference.

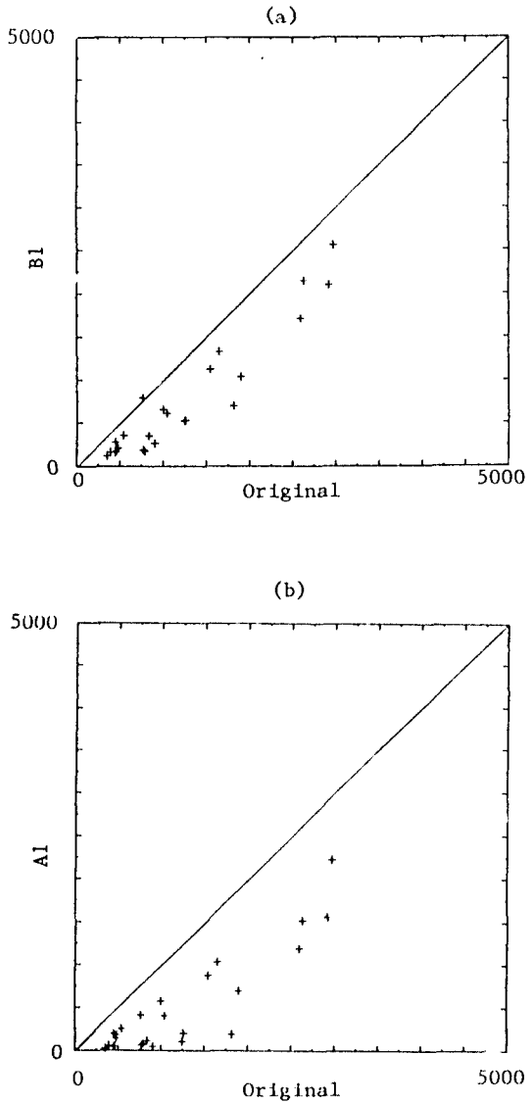

Figure 3. Correlative diagrams of sampled level 1 variance of degraded level A (a) and of degraded level B (b) versus the original data for 25 subregions of SA1.

5.0 SUMMARY

Using GOES 2 km visible and 8 km infrared digital data, we computed the statistics of 4 target regions of original and reduced resolution. We also looked into the effects of area-averaging high resolution visible data on its regional statistics. As it turns out, if a target region is covered with uniform clouds, sampling of the infrared data does not change its statistics compared to that of the original data. But if the cloud condition becomes complicated, the sampled data will begin to lose its high order statistical information. Similar findings also apply to the sampling effects of visible data. And the area-averaged visible data loses its high order statistical information faster compared to the sampled data. Further tests of data resolution effects on mostly clear target regions, as well as their effects on estimated cloudiness, will be presented at the meeting.

6.0 ACKNOWLEDGEMENTS

We thank Loretta Wilson for typing the manuscript. This research has been supported by the Climate Dynamics, Atmospheric Sciences, NSF grant ATM-8401229.

7.0 REFERENCES

Schiffer, R. A., and W. B. Rossow, 1983: The International Satellite Cloud Climatology project (ISCCP): The first project of the World Climate Research Programme. Bull. Amer. Meteor. Soc., 64, 779-784.

7.2

NEIGHBOR-TO-NEIGHBOR OBJECTIVE SATELLITE ANALYSIS FOR THE DETERMINATION OF SURFACE AND CLOUD MEAN RADIATIVE PROPERTIES

S.K. Cox, S. A. Ackerman and T.H. Vonder Haar
Department of Atmospheric Science
Colorado State University

1. INTRODUCTION

Clouds play a major role in determining the radiative properties of the earth's atmosphere and surface, and are thus a significant component of the earth's climate. The effects of clouds on the energy budget within and at the boundaries of the atmosphere are functions of cloud amount, cloud optical properties and the cloud top and base height. Studies of the effect of clouds on the radiative energy budget have taken two approaches: modeling studies and observational studies. For the later case it is essential that an objective scheme for deriving cloud properties be used.

Recently Rossow et al. (1984) have compared six different cloud detection schemes using the same satellite radiation measurements. All the methods worked well for some cloud types or climate regimes, and did poorly for other situations. All the algorithms require accurate estimates of the clear-sky radiance. While satellite time composites can account for mean spatial variations of clear-sky radiance, the time variation of these parameters poses a particular problem to cloud detection algorithms. This paper presents a simple objective analysis scheme to identify uniform radiative features. Under the assumption that variations in the measured radiance of a given surface type (e.g. cloud or ground) is small compared to the radiance difference between types, one can easily identify different surface types. Thus the technique is potentially very useful in estimating clear-sky radiances as well as mean cloud radiances and cloud amount. The technique is referred to as the neighbor-to-neighbor (NTN) method.

2. ANALYSIS TECHNIQUE

The NTN methodology is straight forward and simple. It consists of displaying radiances of adjacent samples (pixels) in a given satellite scan in a two dimensional histogram. The histogram, which consists of the number of occurrences in which a given radiance in pixel I was followed by a radiance in the pixel I+1, is then analyzed using a cluster technique (Debois et al. 1982).

In the applications which follow, the NTN was applied to digital data from the TIROS-N multichannel Advanced Very High Resolution Radiometer (AVHRR) (Hussey, 1979; Schwalb, 1978). Global Area Coverage (GAC) data (Kidwell, 1979) for channel 1 (552-.904 μm), channel 2 (.71-1.02 μm), channel 3 (3.58-3.97 μm) and channel 4 (10.52-11.45 μm) were used in the retrieval technique. The resolution of the GAC data is approximately 8 km at nadir. Equatorial crossings are 0300 and 1500 mean solar time.

a. MEAN CLEAR-SKY AND CLOUD RADIANCES

Examples of the resulting two-dimensional histogram for the four channels of the TIROS-N are shown in figures 1a-d. The analysis was conducted over the Arabian Sea on 23 June 1979 for the region 15° N to 18° N and 64° E to 67° E. A research flight mission was conducted over this same region as part of the summer monsoon experiment (Smith et al., 1980). Observers onboard the aircraft observed the existance of an altostratus/altocumulus cloud deck whose top was located at approximately 6.7 km. The data analyzed from the aircraft mission are compared with NTN retrievals.

In figure 1, the data arrays were normalized to the maximum count in the array and contours were drawn at 0.1 intervals. Values along the matrix diagonal are the number of occurrences in which the radiance of pixel I equals the radiance of pixel I+1. Thus uniform features are readily decernible in this type analysis. In this case an estimate of clear-sky radiances (shown as mean surface temperature and reflectance) can be obtained from a cluster (or threshold) analysis of the appropiate histogram. It is important to note here that in searching for the cluster center of gravity one need only search along the diagonal. The NTN analysis retrieves surface visible and near infrared (NIR) reflectances of 8.5 and 6 percent respectively, which compare well with the aircraft observations of visible (.28-.7 μm) and NIR (.7-2.8 μm) broadband albedoes of 7 and 4 percent respectively. The retrieved 11 μm radiative temperature is 291° K while the 'cleaner' 3.7 μm window temperature is 300° K which is in excellent agreement with the aircfart measured surface temperature of 299° K.

A NTN analysis can also be used to estimate the mean radiative properties of the cloud layer. The aircraft research flight mission conducted over this region measured a cloud mean radiative temperature of 284° K, compared to a 11 μm NTN retrieval of 281° K. It is difficult to retreive a representative spectral reflectance owing to the wide scatter in the histograms. This dispersion is due to physical processes (nonlinear dependence of the satellite measured radiance with cloud cover, cloud albedo, surface albedo, sun-satellite geometry, and the finite structure of the the cloud) and is inherent in any cloud retrieval technique. Similarly, owing to the physical nature of the 3.7 μm channel (Arking and Childs, 1985), it is difficult to retrieve a representative value for the cloud layer; however, the combination of channels 3 and 4 can be quite useful in describing mean cloud radiative properties.

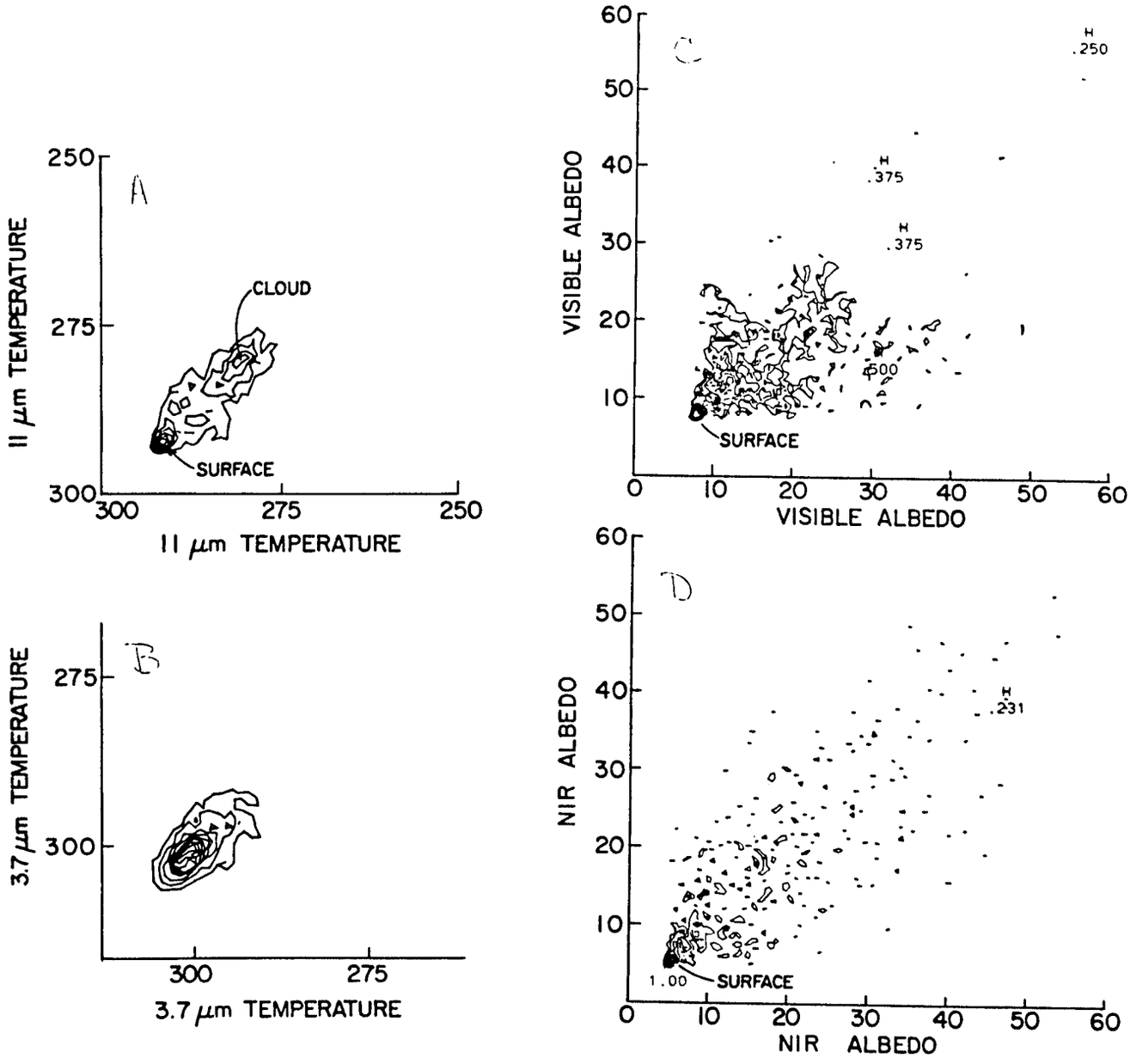

Figure 1. Neighbor-to-Neighbor analysis of TIROS-N AVHRR data for the region 15° N to 18° N and 64°E to 67°E on 23 June 1979

b. Total Cloud Cover

After determing those pixels associated with the surface using the cluster analysis, estimates of the total cloud cover can be made using a the threshold technique or by counting the total number of pixels not in the surface cluster. The disadvantage of using the above cloud amount analysis is that it does not account for partially filled field of views (FOV). The NTN can, under certain conditions, account for partially filled FOV. For example, consider a satillte viewing an area with a single homogeneous cloud layer with areal coverage F, mean planck radiance N_{cld} with an emittance ε_{cld}, and a surface mean radiance of N_{sfc} with an emittance of 1.0. Then the radiance measured at the satellite (neglecting IR reflection) is

$$N_m = N_{sfc} - \varepsilon_{cld} * F * (N_{sfc} - N_{cld})$$

The cluster analysis of the mean surface radiance provides N_{sfc} as well as those pixels associated with the surface. The effective cloud radiance ($\varepsilon_{cld} * N_{cld}$) is obtained from cluster analysis of the mean cloud radiance where it is assumed that the FOV is entirely filled with cloud (i.e. F=1). Now if one assumes that other radiance measurements arise from unfilled FOV's one can solve equation 1 for a total effective cloud cover ($\varepsilon_{cld} * F$).

3. SUMMARY

An objective method is presented for analysis of satellite radiometric data for the estimation of cloud cover and surface and cloud mean radiative characteristics. The major advantage of the neighbor-to-neighbor technique is that it is a simple yet accurate analysis routine for estimating uniform radiative features. The method of analysis for determining mean radiative surface parameters requires a search in one-dimensional space, e.g. along the histogram diagonal. While only analysis of one scene was presented, additional analysis indicates that the NTN (by itself) is best applied to layered type cloud systems when cloud cover estimation is required. Complex cloud structures result in the merging of clusters making the NTN cloud cover analysis difficult.

Due to the simplicity of the technique, the NTN can be combined with other cloud retrieval techniques. For example, the NTN can be used to identify uniform radiative features, surface type can then be identified by comparison with specified threshlold values. In this way, it is possible to estimate clear-sky radianes at a particular time, an essential parameter in any cloud detection algorithm. The methodology may also be used in deriving climatological surface and cloud mean radiative properties.

4. REFERENCES

Arking, A. and J. D. Childs, 1985: Retrieval of Cloud Cover Parameters from Multispectral Satellite Images. J. Climate Appl. Meteor., 24, 322-333.

Coakley, J.A., Jr. and F.P. Bretherton, 1982: Cloud cover from high-resolution scanner data: Detecting and allowing for partially filled fields of view. J. Geophys. Res., 87, 4917-4932.

Desbois, M., G. Seze and G. Szejwach, 1982: Automatic classification of clouds on METEOSAT Imagery: Application to high-level clouds. J. Appl. Meteor., 21, 401-412.

Hussey, W.J., 1979: The TIROS-N/NOAA operational satellite system. Technical Report, National Environmental Satellite Service, NOAA, Dept. of Commerce, Washington, D.C., 35 pp.

Kidwell, K.B., 1979: NOAA polar orbiter data (TIROS-N and NOAA-6) users' guide - Preliminary version. Technical Report, National Climatic Center, NOAA, Dept. of Commerce, Washington, D.C.

Schwalb, A., 1978: The TIROS-N/NOAA A-G satellite series. NOAA technical memo, NESS 95, NOAA-NESS, Washington, D.C., 75 pp.

7.3

VALIDATION OF NIMBUS-7 CLOUD AND SMMR DATA

by

P. H. Hwang

NASA/Goddard Space Flight Center, Greenbelt, MD 20771

and

H. Y. M. Yeh, D. S. MacMillan, and C. S. Long

SASC Technologies, 5809 Annapolis Road, Hyattsville, MD 20784

1. INTRODUCTION

The earth's cloudiness and moisture exterts a profound influence on the budgets of solar and thermal radiation, and thus on the net radiation in the earth-atmosphere sytem. The presence of clouds and moisture affects the atmospheric heating through reflection, absorption and emission of radiation, and the surface heating through modification of the solar and infrared fluxes reaching the ground. The evolution and distribution of cloud and moisture fields when coupled with radiative processes are found to be the most significant factors in the energetics and general circulation of the atmosphere (e. g. Ohring and Clapp, 1980; Liou and Zheng, 1984).

In recent years, the availability of global satellite data has stimulated the development of many techniques for visible, infrared and microwave remote sensing of cloud, moisture and other geophysical parameters (e. g. Rossow et. al., 1985; Yeh et. al., 1985; Prabhakara et. al., 1982; Chang and Milman, 1982; and Chang et. al., 1984). The visible and infrared instruments obviously are more sensitive to the presence of any type of clouds, however, quickly become opaque when a thick or multiple-layered clouds are present within field-of-view (FOV). On the other hand, cirrus and stratoform clouds are virtually transparent to microwave frequency. Microwave radiometry, however, has the advantage of measure vertically integrated water vapor and liquid water content in the atmosphere and surface characteristics in cloudy conditions.

Although different frequencies of instruments are used to measuring different parameters in the atmosphere, all the atmospheric parameters are related. For instance, it is known that the distribution of water vapor is highly dependent upon the tropospheric dynamics associated with the circulation features in the atmosphere. The water vapor content is usually expected to be closely related to the cloud amount present in the atmosphere. In the past, the relation between radiosonde relative humidity profiles and observed cloud amount have been derived from synoptic data (Smagorinsky, 1960; Ricketts, 1973), although Ricketts comments that the relation is rather indefinite. Problems were also encountered with GATE data where the diagrams of observed relative humidity versus cloud amount showed a high degree a scatter (Slingo, 1980). This is because the radiosonde only observes a single point which is not necessarily representative of the large horizontal area covered by an observer's field-of-view. For instance, in situtations with partial cloud cover the relative humidity profile is dependent on whether the radiosonde ascends through clear or cloudy area. Consequently little quantitative relationship can be obtained from ground based observations. In contrast to the conventional surface observations, the measurements from present satellites provide large spatially-contiguous distributions of cloudiness and moisture content. The availability of six years of continuous Nimbus-7 satellite data presents an excellent opportunity for studying the relationship between clouds and the governing parameters, such as water vapor content, of general circulation models.

The liquid water content and rainfall over the oceans, acting as a source of energy to drive the atmospheric circulation through the release of latent heat, also play an important role in the weather systems (Gill, 1980). It is desirable to validate the Scanning Multichannel Microwave Radiometer (SMMR) derived liquid water content (LWC) in order to accurately map the global LWC distribution. Because of the high spatial variability of atmospheric LWC, the verification of satellite derived LWC by comparing with in situ observations will encounter difficulties similar to the cloud-water vapor problem mentioned above. We therefore, validate the values of LWC by a comparison with the Nimbus-7 cloud data for the same target areas.

Recently, the anomalous sea-surface temperature (SST) in the equatorial ocean has become an important subject in climate and weather studies because of its association with large changes not only in the equatorial atmosphere but also midlatitude circulation. The coherence of the fluctuations in SST and other meteorological parameters is shown by Philander (1985). It can readily be explained that large-scale motion in the tropical atmosphere corresponds primarily to a direct thermal circulation. During El Nino periods, the increasing area of high sea surface temperature enhances the release of latent heat to the atmosphere and subsequently drives the instability of an atmospheric circulation. In this validation study, we compare the SST retrieved from SMMR data to the Air Force surface temperature data available from the three dimensional (3-D) nephanalysis archive. Both SST data sets are averaged into the same spatial resolution for direct comparison.

In summary, the purpose of this paper is to

validate the quality of Nimbus-7 LWC and cloud data. The investigation is conducted by comparing regional distributions of WV and LWC during July 1979 with the cloud distribution for the same month. Furthermore, the SMMR derived SST is also compared with the Air Force SST. The initial results show that the SST derived from SMMR corresponds closely to the Air Force data, and the WV and LWC are strongly related to the Nimbus-7 cloud amount.

2. DATA BASE

Starting in April 1979 for THIR and November 1979 for SMMR, more than six years of continuous data have been archived from Nimbus-7 satellite measurements. The Nimbus-7 cloud data set is generated from Temperature-Humidity Infrared Radiometer (THIR) 11.5 micron radiances together with Total Ozone Mapping Spectrometer (TOMS) UV reflectivities, climatological temperature lapse rate from Subtarget Area Geographical Season (STAGS) data by NOAA/NCC, and concurrent surface temperature information from the Air Force 3-D nephanalysis archive. The Nimbus-7 cloud-MATRIX (CMATRIX) tape contains 117 parameters including daily and monthly average daytime and nighttime values of cloud amount and radiances as well as their variances in space and time in the resolution of Earth Radiation Budget (ERB) target area (TA), approximately (500 km)^2.

The SMMR flown on board the Nimbus-7 satellite is a 10-channel microwave radiometer delivering orthogonally polarized antenna temperatures at five frequencies, 6.6, 10.7, 18, 21 and 37 GHz (Gloersen and Hardis, 1978). Each of these 10 channels is sensitive in a different manner to various geophysical parameters. In general, the lowest two frequencies are more sensitive to the surface characteristics such as sea surface temperature and surface wind, while the highest three frequencies are mainly designed for the retrieval of atmospheric parameters: water vapor and liquid water content over the oceans. A multiple regression technique was initially applied to obtain the SMMR retrieval algorithms under non-precipitating conditions over the ocean (e. g. Wilheit and Chang, 1980). Further tuning of the algorithm was then carried out by comparing with the in situ measurements. The retrieved data of WV, sea surface wind speed, SST and surface snow/ice are stored in the Nimbus-7 SMMR PARM tapes, which contain values of 19 parameters. The SST information is only retained for the descending (midnight) orbits due to the more serious calibration errors in daytime. These calibration errors, apparently caused by solar driven temperature gradients within the SMMR, have latitudinal and seasonal dependence, and can differ between the Northern and the Southern Hemisphere (Prabhakara et. al., 1983). The effect of the calibration errors on other parameters is less significant and has been taken into consideration in the retrieval algorithms.

3. INTERCOMPARISON BETWEEN NIMBUS-7 CLOUD AND SMMR DATA

It is recognized that the most active weather systems over the globe often occur in the tropics. The spectacular instances of interannual variability in the ocean, such as El Nino events, have profound consequences for climate and the ocean ecosystem. Therefore we have selected July 1979 monthly average cloud and SMMR measurements over 18°N - 18°S covering important regions of heating like the Intertropical Convergence Zones (ITCZ) and South Pacific Convergence Zone (SPCZ) for a satellite measurement initial validation study. The Nimbus-7 cloud data is originally designed to independently detect the presence of clouds in ERB subtarget area (STA), approximately (160 km)^2. The cloud information is then further averaged into ERB TA, and stored in CMATRIX tapes. The spatial resolutions of SMMR derived parameters, stored on PARM tapes are (60 km)^2 for WV and LWC, and (156 km)^2 for SST. For this paper, we have averaged the available SMMR measurements into ERB TA. Since the SMMR parameters are not retrieved over land, only TA in ocean are utilized in the case studies. Total of 543 TA is examined to determine the relationship of cloud information and the SMMR measurements.

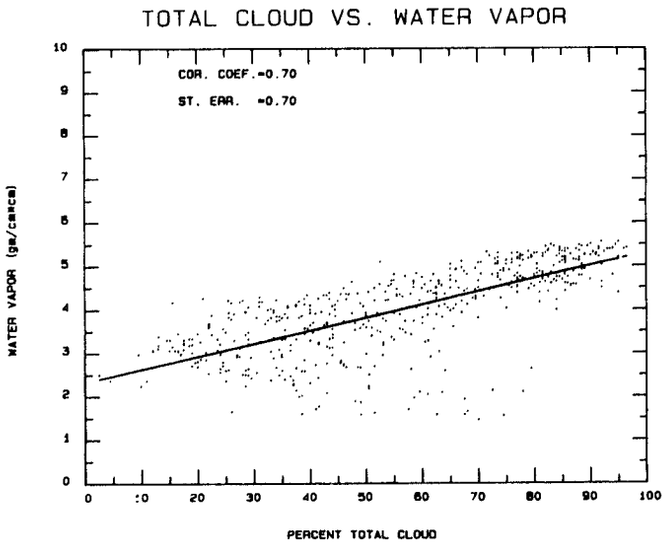

Figure 1 Scatter diagram of Nimbus-7 total cloud amount versus SMMR derived water vapor content in a column. The quantities of total cloud amount and water vapor are averaged to ERB TA for direct comparison. Total of 543 TA is used for study.

We first carry out a statistical analysis of Nimbus-7 total cloud amount, WV and LCW. Fig. 1 it shows that the total cloud amount and WV retrieved from SMMR data are reasonably well correlated with correlation coefficient = 0.70 and standard error of estimate = 0.70 gm/cm^2. Note that Nimbus-7 cloud information is retrieved over the entire globe twice a day; but global coverage for SMMR derived parameters requires about six calendar days. The technique for WV retrieval over oceans was based on an experience with data from the multispectral microwave radiometers on board the Nimbus-5 and 6 satellites (e. g. Staelin et al., 1976; Chang and Wilheit, 1979). The rms error of

the water vapor retrieval in this study is about 0.21 g/cm^2, which is comparable to the values reported by Wilheit and Chang (1980) and Prabhakara et. al. (1982). The Nimbus-7 cloud data has also been statistically compared with analyst estimates derived from independent, concurrent GOES satellite images and conventional meteorological reports (Stowe et. al., 1984). The Nimbus-7 cloud amount closely corresponding to the analyst estimate with correlation coefficient equal 0.96 and 11% rms for water areas. As mentioned earlier, Slingo (1980) encountered the problems with GATE data in correlating radiosonde relative humidity and surface observed cloud amount. In our colocated data analysis, a positive relationship was found. This is expected since an abundance of WV in the atmosphere, in general, fosters the environment for the cloud formation as atmospheric circulation theory has suggested (Palmen and Newton, 1969). When there is convergent air motion in the lower layers of the atmosphere, a vertical veolocity is induced which can increase the vertical transport and thereby the water vapor content. Such a situation rapidly leads to a convectively active atmosphere forming clouds and precipitation. On the other hand, when there is divergent motion in the lower layers the accompany subsidence brings down drier air from above. This dry air tend to dissipate the existing clouds or prevent the formation of clouds.

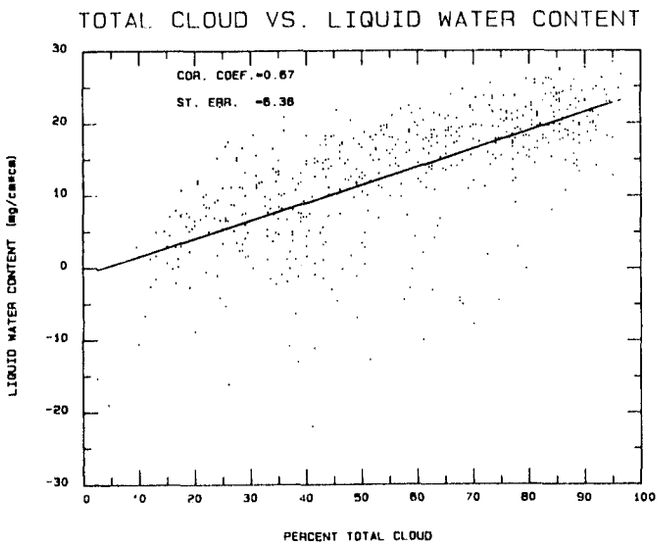

Figure 2 Scatter diagram of Nimbus-7 total cloud amount versus vertically integrated liquid water content derived by SMMR data. The quantities of total cloud amount and water vapor are averaged to ERB TA for direct comparison. Total of 543 TA is used for study.

In Figure 2, we compare the Nimbus-7 total cloud amount versus vertically integrated LWC derived by SMMA data for the same target areas. The retrieval of nonprecipitating liquid water is based on a linear regression method discussed by Wilheit et. al., (1977). The basic formula of the algorithm is deriving a set of linear regression coefficients from an ensemble of models that represent the calculated brightness temperature corresponding to different vlues of the LWC. In the absence of rain, Wilheit et. al. estimated that the LWC can be retrieved with an accurancy of 4 mg/cm^2. A comprehensive evaluation for the algorithm by comparing with in situ data is, however, not available so far. The accuracy estimation is still in process as part of this validation effort. It is shown in Figure 2 that some of the computed LWC have negative values. This may be because of a systematic bias in the LWC algorithm itself. Some low values or even negative values of LWC values corresponding to large percentage of total cloud amount may be due to the presence of high thin cirrus which is transparent to SMMR instruments, or the overestimation of low cloud amount by Nimbus-7 cloud algorithm. Since low altitude clouds usually have weak infrared radiance contrast with the surface, the TOMS reflectivity at 0.38 micron is utilized to help detect the existence of low clouds in Nimbus-7 cloud algorithm. The complexity of merging THIR and TOMS data may have resulted in somewhat overestimating the total cloud amount, especially the low level clouds. In general, however, two parameters are quite well correlated, with correlation coefficient = 0.67 and 6.38 mg/cm^2 standard error of estimate, considering the uncertainty of the atmospheric compositions and the problems of remote sensing techniques. It is desirable that the values of LWC be further by compared with the colocated total cloud amount when the six years of Nimbus-7 satellite data is utililzed for the validation. Any systematic bias of the LWC product can then be removed in the final tuning.

The comparison between Air Force surface temperature and SMMR drived SST as shown in Figure 3, demonstrates high correlation of two measurements with correlation coefficient equal to 0.94 and 0.74^{o}K standard error of estimate. The SMMR SST is calculated from the calibrated brightness temperature in 156 km resolution measured during descending orbits in sevenof the

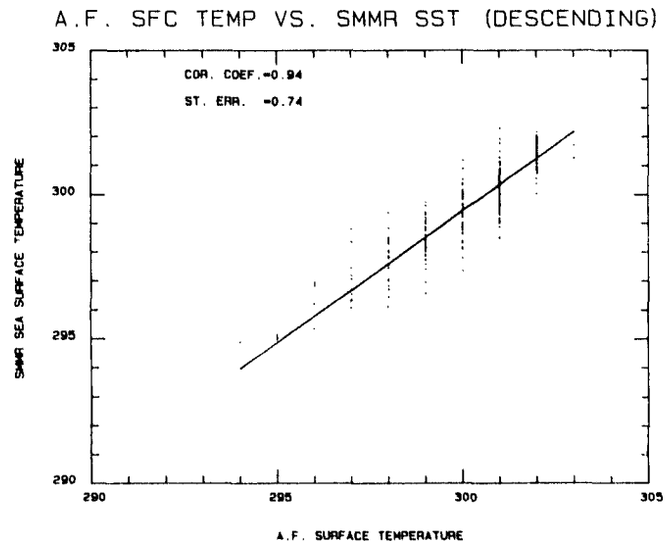

Figure 3 Comparison between Air Force surface temperature and SMMR derived sea surface temperature for descending (midnight) orbits. All data sets are average to ERB TA for intercomparison.

ten SMMR channels. Briefly, the major sources of the SMMR SST are the 6.6V and H channels, whereas the corrections for windspeed information comes primarily from the 10.7 H and V channels, and the correction for atmospheric opacity is derived from 18.0H and V and 21.0H channels. The SMMR SST has been compared with climatology. For 1979-1982, the monthly rms differences between SMMR SST and climatology range between 1.3-1.5°C. Air Force surface temperature, as a parameter in 3-D nephanalysis archive, is obtained by combining satellite data and surface-based reports on a time scale of 3 hour. Both of SMMR SST and Air Force data have been averaged to ERB TA for direct comparison.

4. CONCLUSION

In this preliminary validation of Nimbus-7 cloud data and SMMR measurements, we found that the total cloud amount is reasonably well correlated to the SMMR derived WV and LWC. In general, values of WV and LWC increase with the total cloud amount, except that about 5% of data samples show low values of WV and LWC correspond to high percentage of total cloud average. The discrepancies may be due to (1) the presence of thin cirrus or stratoform clouds, which are transparent to the microwave frequencies, or (2) somewhat overestimation of Nimbus-7 total cloud amount, especially low level clouds which heavily rely on TOMS measurements. The SMMR SST has also been compared with Air Force surface temperature archive, and shows good correlation between two measurements.

It is obvious that the data sample size of this experiment, based on one month of satellite measurements, maynot large enough to draw a distinctive conclusion for the validation. Further effort utilizing the six years of available Nimbus-7 cloud data and SMMR measurements is desirable, and to further quantify the relationship between cloud amount and WV and LWC.

ACKNOWLEDGEMENTS

The authors would like to thank Ms. D. Robinson for editing and typing the manuscript, and Mr. E. Suhari for preparing the final format of the paper.

REFERENCES

Chang, A. T. C., and A. S. Milman, 1982: Retreival of ocean surface and atmospheric parameters from multichannel microwave radiometric measurements. IEEE Trans. Geos. Remote Sensing, GE-20, 2, 217-224.

Chang, H. D., P. H. Hwang, T. T. Wilheit, A. T. C. Chang, D. H. Staelin and P. W. Rosenkranz, 1984: Monthly distributions of precipitable water from the Nimbus-7 SMMR data. J. Geophy. Res., 89, D4, 5328-5334.

Gill, A. E., 1980: Some simple solutions for heat induced tripical circulation. Quart. J. Roy. Met. Soc., 106, 447-462.

Gloersen, P. and L. Hardis, 1978: Scanning Multichannel Microwave Radiometer (SMMR) experiments. Nimbus-7 User's Guide, Madis (Ed.), NASA/Goddard Space Flight Center, Greenbelt, MD.

Liou, K. N. and Zheng, 1984: A numerical experiment of the interactions of radiation, clouds and dynamic processes in a general circulation model. J. Atmos. Sci., 41, 9, 1513-1535.

Ohring, G. and P. Clapp, 1980: The effect of changes in cloud amount on the net radiation at the top of the atmosphere. J. Atmos. Sci., 37, 2, 447-454.

Palmen, E. and C. W. Newton, 1969: Atmospheric Circulation System, Academic Press, New York, pp. 379-386.

Philander, S. G. H., 1985: El Nino and La Nina. J. Atmos. Sci., 42,23, 2652-2662.

Prabhakara, C., H. D. Chang and A.T. C. Chang, 1982: Remote sensing of precipitable water over the ocean from Nimbus-7 microwave measurements. J. Appl. Meteor., 21, 1, 59-68.

Prabhakara, C., I. Wang, A. T. C. Chang and P. Gloersen, 1983: A statistical examination of Nimbus-7 SMMR data and remote sensing of sea surface temperature, liquid water content in the atmosphere and surface wind speed. J. Climat. Appl. Meteor., 22, 2023-2037.

Ricketts, J. N., 1973: An investigation into a relationship between upper air relative humidity and cloud cover, Met. Mag., 102, 146-153.

Rossow, W. B., F. Mosher, E. Kinsella, A. Arking, M. Desbois, E. Harrison, P. Minnis, E. Ruprecht, G. Seze, C. Simmer and E. Smith, 1985:ISSCP Cloud Algorithm Intercomparison. J. Climat. Appl. Meteor., 24, 9, 877-903.

Slingo, J. M., 1980: A cloud parameterization scheme derived from GATE data for use with a numerical model. Quart. J. R. Met. Soc., 106, 747-770.

Smagorinsky, J., 1960: On the dynamical prediction of large-scale condensation by numerical methods. Amer. Geophy. Union, Geophy. Monogr., No. 5, 71-78.

Yeh, H. Y. M., T. H. VonderHaar and K. N. Liou, 1985: Cloud paramenters and temperature profile retrieval from infrared sounder data. J. Atmos. Sci., 42, 22, 2360-2370.

Wilheit, T. T. and A. T. C. Chang, 1980: An algorithm for retrieval of ocean surface and atmospheric parameters from the observations of the Scanning Multichannel Microwave Radiometer. Radio Sci., 15, 525-544.

Wilheit, T. T. and A. T. C Chang, M. S. V. Rao, E. B. Rodgers and J. S. Theon, 1977: A satellite technique for quantitatively mapping rainfall rates over oceans. J. Appl. Meteor., 16, 551-560.

SATELLITE AND SURFACE BASED REMOTE SENSING OF SIERRA NEVADA WINTER STORMS: APPLICATIONS TO WEATHER MODIFICATION

David W. Reynolds

U.S. Bureau of Reclamation
Auburn, California

1. INTRODUCTION

During the past three winter seasons, the Sierra Cooperative Pilot Project (SCPP), a weather modification research program operated by the Bureau of Reclamation (Reynolds and Dennis, 1986), has employed a combination of remote and in situ measurement systems near the Sierra Nevada mountains in an effort to determine when and where the best opportunities might exist in cold winter orographic clouds for precipitation increases by glaciogenic seeding.

Out of all the necessary kinematic and microphysical requirements that need to be met before seeding can produce increases in precipitation, Supercooled Liquid Water (SLW) is the most critical. Knowing when it will exist, and for how long will generally determine when cloud seeding will take place.

The application of a dual wavelength scanning microwave radiometer (Hogg et al, 1983) to winter orographic cloud seeding has greatly enhanced our abilities to detect SLW and its frequency and duration of occurrence. This because the instrument can operate 24 hours a day providing fairly unambiguous SLW measurements in all but rain or at cloud temperatures above 0 °C.

SCPP has concentrated its observations over the American River Basin (ARB) (outlined by heavy line in Fig. 1) and specifically to a small fixed target region in the upper northeast corner of the ARB (outlined by dashed line Fig 1). Within this region, a high altitude observatory has been established at Kingvale (KGV). This site contains the dual channel radiometer, Ka band radar, a rawinsonde station, a ground microphysics laboratory and several digital precipitation gages. Other key observations are made at Sheridan where a 5 cm digital weather radar and rawinsonde site are located. A 5 cm Doppler radar provided by the National Center for Atmospheric Research has been made available in alternate years and located at either Sheridan or near Auburn as shown in Fig. 1. This paper will emphasize the remote sensing data collected at KGV, the Sheridan rawinsonde data taken at 3-hourly intervals, and GOES-W satellite imagery collected every 30 min at the Auburn forecast office through a direct link to the Redwood City Satellite Field Service Station.

With the above measurement systems, we have begun to resolve at what stage in a storms life-cycle liquid water may be occurring. The evidence supports the shallow warm-topped orographic cloud as providing the extensive long lasting SLW that can be utilized by cloud seeding to increase snowfall. These results support the earlier work of Ludlam (1955), Grant and Elliott (1974), Hobbs (1975), Hill (1980) and Rauber and Grant (1986).

This paper will try to briefly document the meteorological conditions conducive to the production of SLW over the Sierra Nevada barrier and show how through the use of GOES satellite imagery (Reynolds et al, 1978) suitable conditions can be forecast several hours ahead of time to allow the seeder aircraft, ground based sampling equipment and the cloud physics aircraft the time necessary to achieve operational readiness for conducting a cloud seeding research mission.

2. SYNOPTIC CONTROLS

Through analysis of Sheridan rawinsonde time cross sections, three distinct cold front types can be associated with the lowering and warming of cloud top over the Sierra Nevada. Fig. 2 (from Marwitz, 1984) shows conceptually the structure of these three cold front types. The first is the more classic Norwegian cold front with the well known westward sloping with

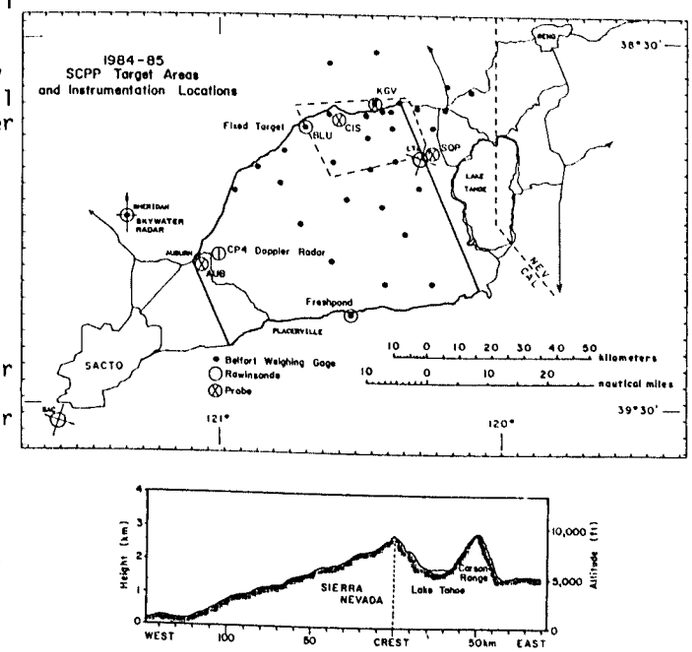

Fig. 1. a) Layout of SCPP instrumentation with main experimental area outlined and b) elevation transect over the American River Basin.

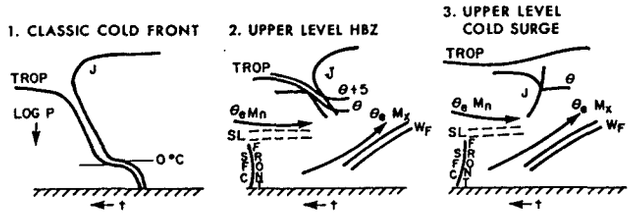

Fig. 2. Schematic of a classic cold front, upper level Hyper Baroclinic Zone (HBZ) and upper level cold surge. (After Marwitz, 1984) Symbols discussed in the text.

height frontal surface (type of front also called anafront, Bergeron, 1937). The next two types are of the katabatic type (warm, dry air descending down surface frontal slope, Bergeron, 1937) or as Browning and Monk (1982) call it, a split front.

Each appear to give rise to SLW over the barrier once either the surface cold front passes or the upper level front passes (Heggli and Reynolds, 1985). An example of each of the three types will be given in the following sections along with corresponding satellite images and liquid water traces from the radiometer located at the Kingvale high altitude observatory.

3. CASE STUDIES

3.1 Mar 26-27, 1985

Fig. 3 is a time cross-section of θ_e from the Sheridan rawinsonde during the passage of a more classic cold front. The key features of interest are the warm-front (WF) or stable layer, enhanced by existing cold air over the Sierra Nevada, which is overrun by the warm moist conveyor belt of high θ_e air in the prefrontal airmass. Note this high θ_e air is lifted by the frontal band (anafront) followed by a rapid descent in the tropopause height and drying in the lower troposhere as indicated by the cloud tops rapid descent after frontal passage. Note the relationship between the passage of the upper

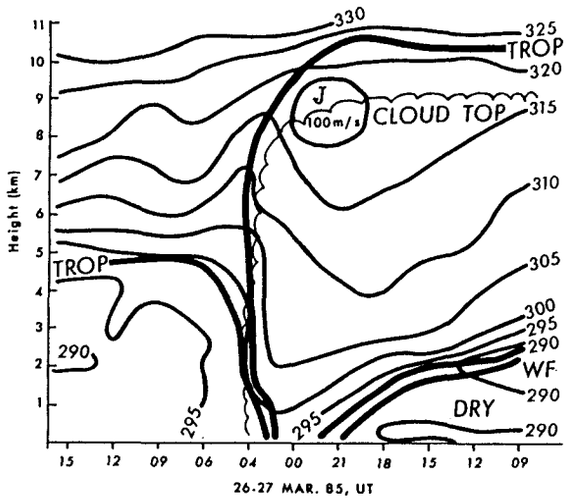

Fig. 3. Time cross section of θ_e from the Sheridan rawinsonde, (J)-upper jet, (WF)-warm front, with cloud top (scalloped), based on relative humidity, annotated.

jet and descent of the higher clouds. This relationship will be emphasized later.

Fig. 4 and Fig. 5 are the 0200 Gmt and 0400 Gmt GOES enhanced infrared images showing the location of the surface front with respect to the upper cloud edge. The Kingvale (KGV) remote sensing site is annotated on each image. It appears from the surface analysis that the Sierra Nevada have a distinct influence on the surface front by slowing its southward progress such that it tends to align itself near the back edge of the higher clouds (first gray-scale enhancement -30 °C) near the barrier but moves out ahead of the higher clouds near the coastline for this case.

The surface front and back edge of the higher clouds pass through KGV just after the 0400 Gmt image. Fig. 6 shows the temporal trace of both liquid water (30.5 GHZ) and precipitable water (20.5 GHZ) from the dual channel microwave radiometer which was operated entirely in the zenith pointing mode during this period. The heaviest precipitation period began at 1500 Gmt on the 26th and ended at 0500 Gmt on the 27th. This precipitation was initiated by the abundant ice crystals coming from the colder reaches of the cloud as shown on the satellite images. However, once these colder clouds moved past Kingvale to where the ice crystal trajectories could no longer deplete the low level condensate produced by the lift up the barrier, the liquid water concentrations in the remaining shallow orographic cloud increased rapidly after 0500 Gmt as shown in Fig. 6. Note, however, that in this particular case the liquid water trace is quite variable due to the convective nature of the cloud being produced in the post frontal air mass.

3.2 Feb 24, 1984

Fig. 7 is the time cross-section of θ_e from the Sheridan sounding centered upon the passage of an upper-level Hyper Baroclinic Zone (HBZ) or split front. The cross-section shows that the upper level frontal characteristics are similar to a classic cold front. The difference is that at about 600-700 mb (3-4 km) the front splits with a very dry intrusion (θ_e Mn) and stable layer (SL) overriding the shallow moist zone or conveyor belt. This high θ_e air (θ_e Mx) is forced over the barrier giving rise to a shallow, neutrally stable orographic cloud that is maintained until the surface katabatic type cold front passes at 2000 Gmt when the air becomes fully mixed and the latent instability is released by the orographic uplift giving higher but more variable liquid water amounts.

Figs. 8 and 9 are the 1215 Gmt and 1515 Gmt enhanced GOES infrared images during the passage of the upper front. One can see upon close examination that the high clouds (again note relationship to upper jet passage) continue to move through KGV but a fairly warmed topped orographic cloud and surface frontal boundary remains in the central Sacramento Valley trailing out through the San Francisco Bay region. It appears that a part of the reason for the slowing down of the surface front is its response to the barrier induced low level jet (Parish, 1982) which blows from SE to NW, parallel to the barrier at about 1 km AGL and impedes the southward progress of this front along the foothills.

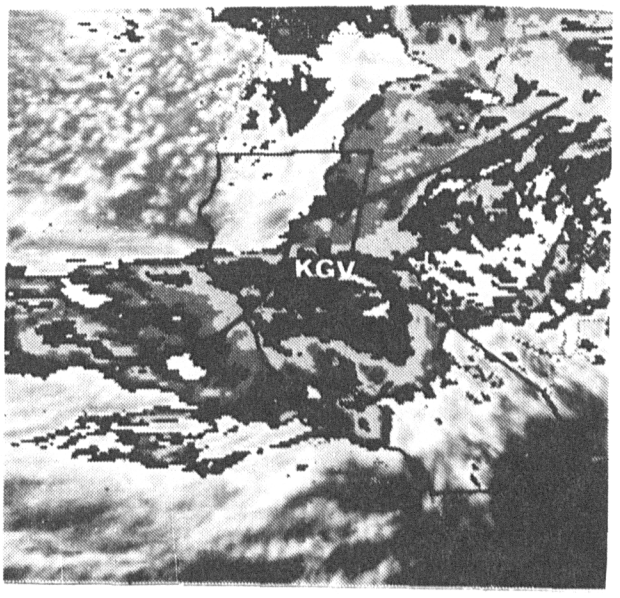

Fig. 4. 0200 Gmt GOES enhanced infrared image showing California, Kingvale observatory (KGV) and position of surface front. Enhancements begins at -30 °C.

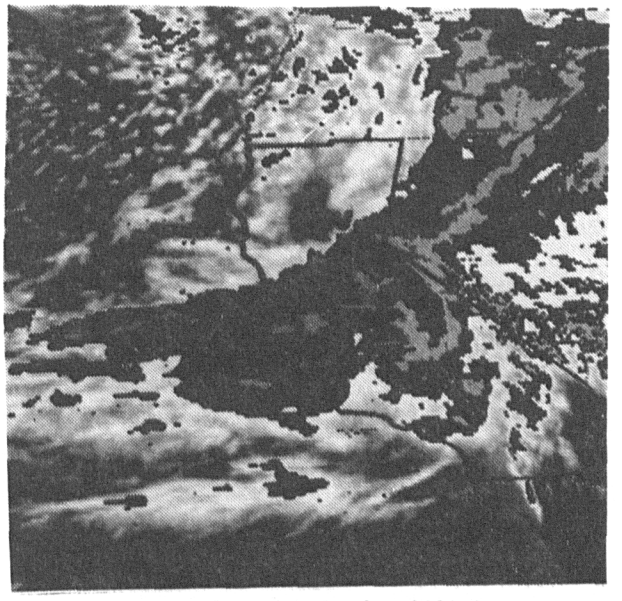

Fig. 5. Same as Fig. 4 only for 0400 Gmt.

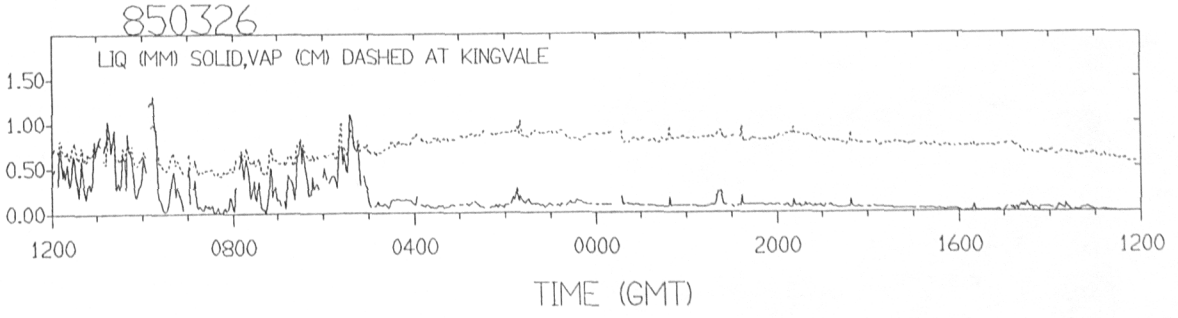

Fig. 6. Temporal plot of liquid water (solid line) and precipitable water (dashed) from the Kingvale vertically pointing radiometer during the passage of a cold front on Mar. 26-27, 1985. (1 mm of liquid water through a cloud depth of 1 km equates to an average concentration of 1 gm/m^3.)

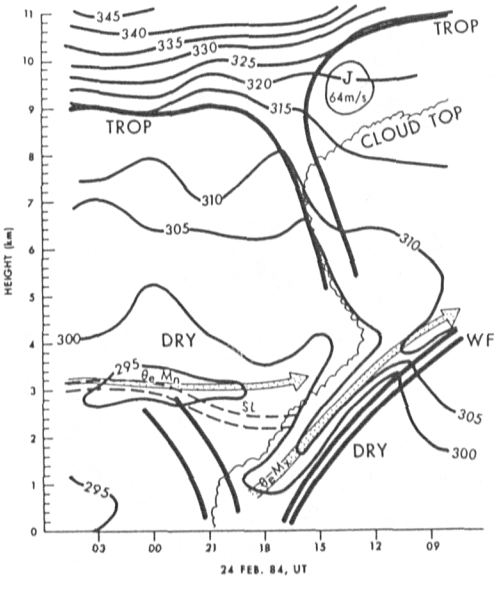

Fig. 7. Time cross section of θ_e from the Sheridan rawinsonde showing passage of an upper level HBZ and surface Kata-front. Cloud top is annotated by scalloped line.

The remaining orographic cloud is well depicted in Fig. 10, a 1 km resolution visible sector taken at 1645 Gmt. Cloud top temperatures (CTT) are all above -30 °C (CTT measured by KGV rawinsonde = -10 °C) as noted by the lack of gray scale enhancement around the KGV site.

Fig. 11 is the corresponding temporal plot of cloud water and precipitable water from the KGV radiometer. Note that the liquid water tends to increase substantially once the upper front passes, with small amounts of liquid water evident through the period of the shallow orographic cloud. This particular day the main precipitation fell after the upper-level front passed during the period of the shallow orographic cloud (1500-2100 Gmt). Even though CTTs were fairly warm (-10 °C) a significant ice enhancement process was occurring naturally in the cloud probably due to a Hallet-Mossop (Mossop, 1985) type process, competing for the available liquid water. As drying and mixing continue, convection increases after 2100 Gmt until surface heating subsides and liquid water begins to diminish.

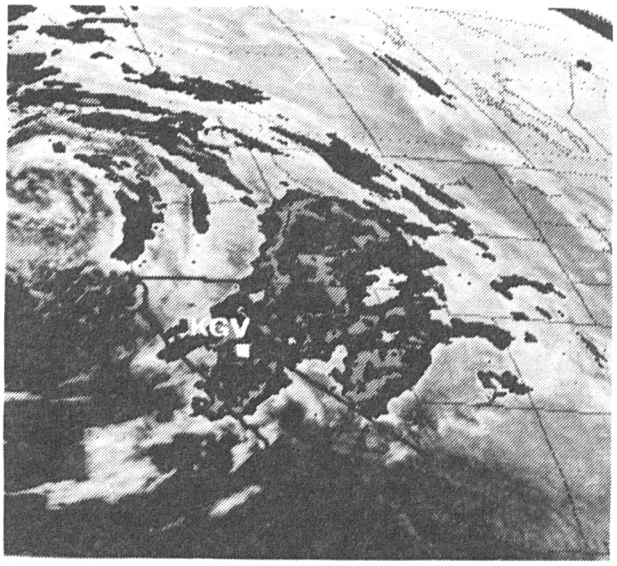

Fig. 8. 1215 Gmt, Feb. 24, 1984, GOES enhanced infrared image showing California and Kingvale (KGV) radiometer site. Enhancement begins at -30 °C.

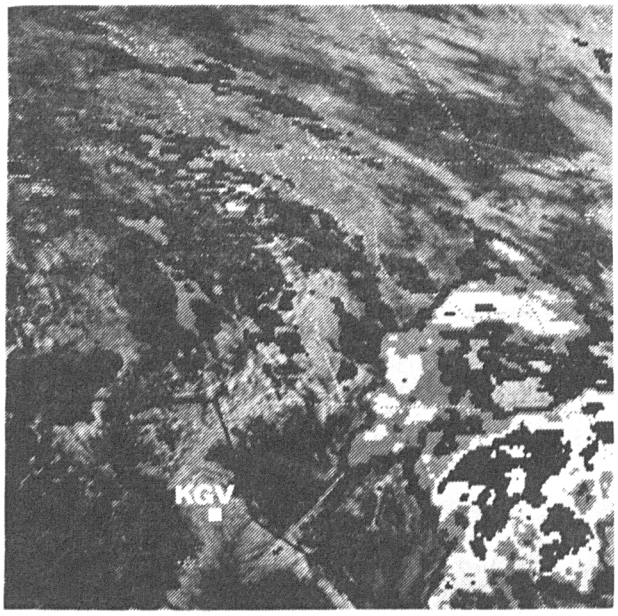

Fig. 10. Visible GOES satellite image for 1645 Gmt. Clouds with top temperature colder than -30 °C are gray-scaled.

Fig. 9. Same as Fig. 8 only for 1515 Gmt.

3.3 Jan 20-21, 1984

The final case study is an example of another type of split-front, one that Hobbs (1978) has called an upper-level cold surge. Fig. 12 is the θ_e time-height profile from the Sheridan sounding. Unfortunately the 0000 Gmt sounding as well as the 09, 12, and 1500 Gmt soundings were missing but the passage of the upper level system was well documented. Here the upper front is tilted in the opposite direction from the previously described upper fronts and appears to be much weaker kinematically. Note how tropopause height changes very little with the passage of the upper front. The features noted in the analysis after the upper front are somewhat inferred from satellite images and interpolated sounding information.

Fig. 13 is the enhanced GOES infrared satellite image for 0615 Gmt on 21 Jan, showing the passage of the higher cloud to the east of Kingvale. Again, the upper speed maximum (not shown) passes in close proximity to the rapid drop in cloud top height. The surface kata-front at this time was still located along the California coast as evidence of the rather large time and space separation between the upper and lower frontal boundaries.

For this storm a vertically point Ka band (.86 cm) radar provided by the Desert Research Institute was recording data throughout the passage of the upper front. This is shown graphically in the upper plot of Fig. 14. This plot outlines the cloud as depicted by the radar.

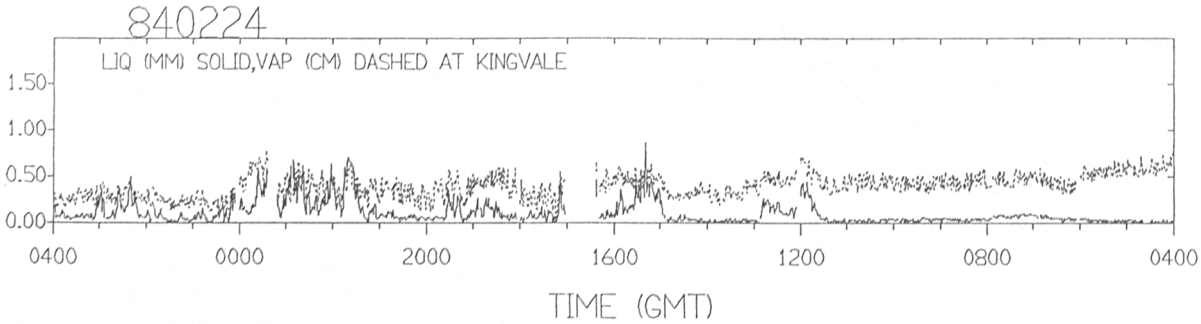

Fig. 11. Temporal plot of liquid water and precipitable water during passage of split front (HBZ) over the Sierra Nevada.

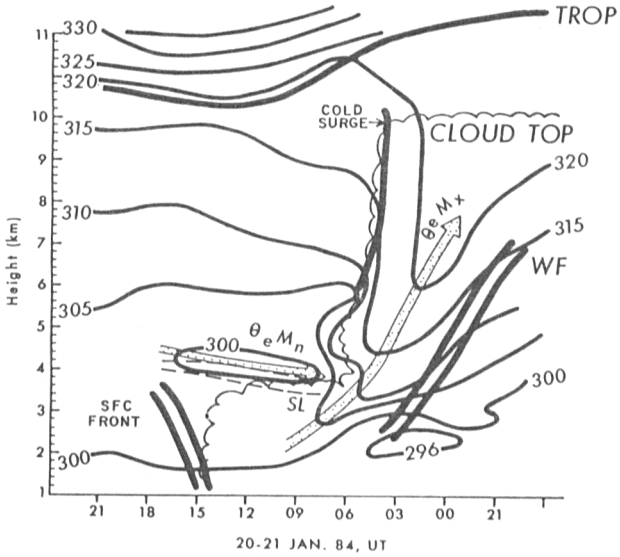

Fig. 12. Time-height profile of θ_e from the Sheridan rawinsonde showing upper cold surge and surface Kata-front. Annotation same as Fig. 7.

Note that the clouds move in aloft as moisture rides up over the warm front, with a gradual descent of moisture and precipitation until very light precipitation begins about 0430 Gmt. The upper frontal passage is well defined by the distinct drop in cloud top, with a very shallow orographic cloud left behind. The liquid water trace again notes the increase in cloud liquid once the higher cloud moves away. Here again, the only measurable precipitation (3rd panel from top in Fig. 14) occurred after the upper front passed in response to higher accretion rates on ice crystals within the shallow cloud (those crystal falling prior to the upper frontal passage consisted of pristine dendrites of very low density).

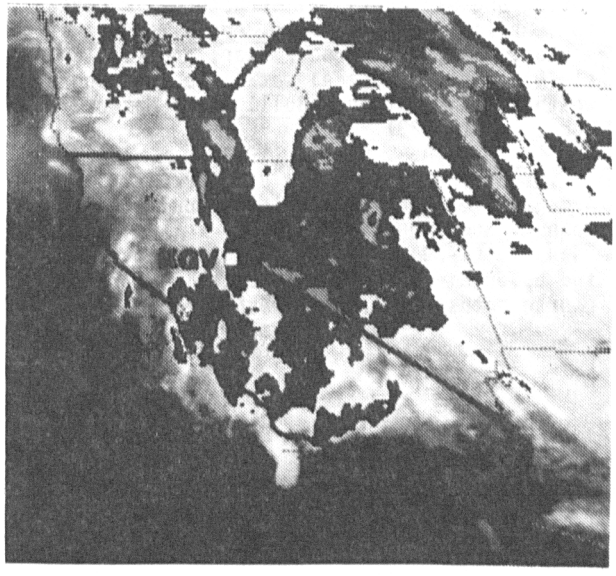

Fig. 13. 0615 Gmt, Jan. 21, 1984, enhanced GOES infrared image showing passage of upper front. Enhancement begins at -30 °C.

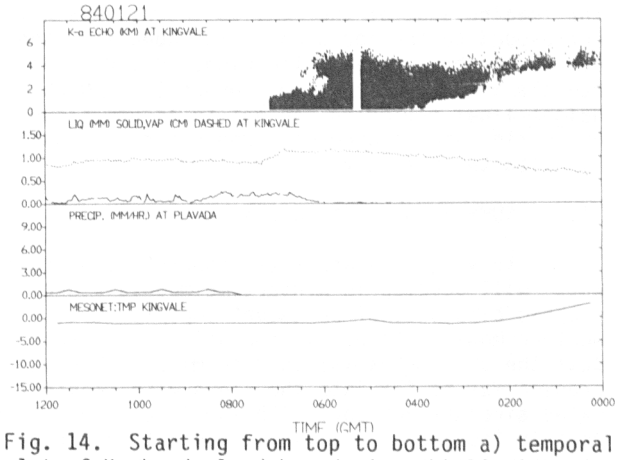

Fig. 14. Starting from top to bottom a) temporal plot of Ka band cloud boundaries, b) liquid and vapor from radiometer, c) precipitation from gage near Kingvale, d) surface temperature at Kingvale.

3.4 Other Forecast Aids

As has been shown in Fig. 2, and in the case studies given, there is a close relationship between the back-edge of the higher clouds and the upper level jet or speed maximum. This is a well documented phenomena (Oliver et al., 1964). However, Weldon (1979) has shown that the relative vorticity field (vorticity being a function of shear and curvature) as depicted on the 500 mb height-vorticity analysis/forecast provided by NMC numerical models, will correspond to the position of the upper-level wind maximum in that this is the boundary between cyclonic and anticyclonic shear. By using the 12 or 24 hr height-vorticity prog chart one might time the arrival of the back-edge of the higher clouds. As an example, Fig. 15 shows the 500 mb height-vorticity analysis from 1200 Gmt 24 Feb. 1984, corresponding to Fig. 8. If one draws a line at

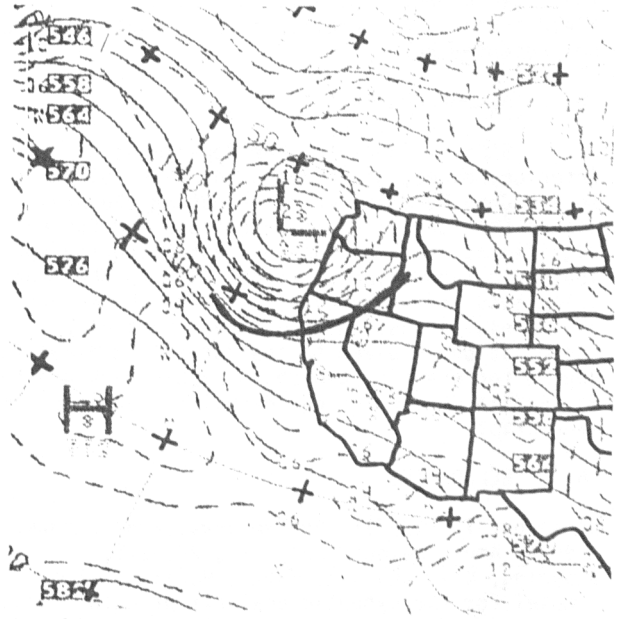

Fig. 15. 1200 Gmt, Feb. 24, 1984, height-vorticity analysis from Limited Fine Mesh model. Proposed upper jet location annotated by heavy lines.

the leading edge of the PVA, as shown, this will correspond to the location of the upper-jet and denote the back-edge of the higher clouds. Note how the wind speed maximum crosses the 500 mb height lines reminding one not to assume cloud boundaries are aligned with upper stream lines but with the "relative" flow field.

4. SUMMARY AND CONCLUSION

Knowing when and where supercooled liquid water will develop in wintertime mountain orographic clouds is of paramount importance to weather modification. In the not too distant past the only mechanism to determine if SLW was present was to fly into the cloud with sophisticated aircraft equipped with sampling probes. In certain instances this liquid was either within cloud systems too vigorous to sample by aircraft, or low down in a cloud below safe flight altitude. However, with the application of the dual-channel microwave radiometer, liquid water can be sampled continuously in all but warm storms where the data is biased. By documenting, through use of the radiometer, when SLW appears, relationships to other measurement systems can be developed.

This paper has tried to show that a rather distinct set of synoptic controls influence the development of SLW and that these controls can be monitored rather well with geostationary satellite imagery. Although other parameters besides SLW influence a clouds seedability, such as competing ice processes, wind speed and direction, etc., the combination of these remote sensing tools along with in situ observations have greatly advanced the knowledge necessary for a viable winter cloud seeding program.

In an effort to document whether the information presented in this paper can be used to accurately forecast the onset of SLW over the Sierra, Flueck and Reynolds (1986) present results of a statistical forecast experiment to test the skill level of forecasters applying these techniques during the SCPP 1985-86 winter field season. For brevity these results will not be presented here.

5. ACKNOWLEDGMENTS

SCPP is funded by the Department of Interior, Bureau of Reclamation. Special thanks to Dr. John Marwitz for contributing the processed Sheridan time cross-sections and for his significant contribution in classifying the various cold front types. Thanks also to the many scientists and technicians, without whose help these results would not have been possible. Appreciation is given to the Bureau's Mid-Pacific Region for drafting and photographic work and to Ms. Bernie Culver for her excellent typing of the manuscript.

6. REFERENCES

Bergeron, T. (1937): On the physics of fronts. Bull. Amer. Meteor. Soc., 18, 265-275.

Browning, K.A. and G.A. Monk (1982): A simple model for the synoptic analysis of cold fronts. Quart. J. Roy. Meteor. Soc., 101, 893-900.

Flueck, J.H. and D.W. Reynolds (1986): A forecast experiment on the prediction of cloud conditions suitable for treatment in the Sierra Nevada. Preprints Tenth Conference on Weather Modification of the Amer. Meteor. Soc., May 27-30, Arlington, VA.

Grant, L.O. and R.D. Elliott (1974): The cloud seeding temperature window. J. Appl. Meteor., 13, 355-363.

Heggli, M.F. and D.W. Reynolds (1985): Radiometric observations of supercooled liquid water within a split front over the Sierra Nevada. J. Clim. Appl. Meteor., 24, 1258-1261.

Hill, G.E. (1980): Seeding opportunity recognition in winter orographic clouds. J. Appl. Meteor., 19, 1371-1381.

Hobbs, P.V. (1975): The nature of winter clouds and precipitation in the Cascade Mountains and their modification by artificial seeding. Part 1: Natural conditions. J. Appl. Meteor., 14, 783-804.

_____ (1978): Organization and structure of clouds and precipitation on the mesoscale and microscale in cyclonic storms. Rev. Geophys. and Space Phys., 16, 741-755.

Hogg, D.C., F.O. Guiraud, J.B. Snider, M.T. Decker, E.R. Westwater (1983): A steerable dual-channel microwave radiometer for measurement of water vapor and liquid in the troposphere. J. Appl. Meteor., 22, 789-806.

Ludlam, F.H. (1955): Artificial snowfall from mountain clouds. Tellus, 7, 277-290.

Marwitz, J.D. (1984): The structure of cold fronts over California. In Cloud Physics Studies in the SCPP, Interim Progress Report 1983-84 to the Bureau of Reclamation. Dept. of Atmos. Sci., Univ. of Wyoming, Laramie, WY 82071.

Mossop, S.C. (1985): The origin and concentration of ice crystals in clouds. Bull. Amer. Meteor. Soc., 66, 264-273.

Oliver, V.J., R.K. Anderson, and E.W. Ferguson 1964: Some examples of the detection of jet streams from TIROS photographs. Mon. Wea. Rev., 92, 444-445.

Rauber, R.M. and L.O. Grant (1986): The characteristics and distribution of cloud water over the mountains of northern Colorado during wintertime storms. Part II: Physical distribution and microphysical structure. Accepted for publication in J. Clim. Appl. Meteor.

Reynolds, D.W., T.H. Vonder Haar, and L.O. Grant (1978): Meteorological satellite in support of weather modification. Bull. Amer. Meteor. Soc., 59, 269-281.

_____ and A.S. Dennis (1986): A review of the Sierra Cooperative Pilot Project. Accepted for publication in the Bull. Amer. Meteor. Soc., June issue.

Weldon, R. (1979): Part IV: Cloud patterns and the upper air wind field. Satellite training course notes, NOAA/NESS, Washington, DC.

7.5

Observations of Arc Cloud Lines Using Research Aircraft Data, Rapid Scan Satellite Data and Doppler Radar Data

Peter C. Sinclair
Dept. of Atmospheric Science

James F.W. Purdom
NOAA/NESDIS/RAMM Branch

Cooperative Institute for Research in the Atmosphere
Colorado State University
Fort Collins, CO 80523

1. INTRODUCTION

The convective storm plays an important role across many scales in meteorology. During the spring and summer months, tornadoes, flash floods, downbursts and severe thunderstorms pose serious threats to life and property throughout the United States. The same "ordinary" thunderstorm that can wreak havoc in the construction industry may at the same time provide much needed water for agricultural purposes.

Understanding the forces that control the development and evolution of deep convection is one of the most important and challenging problems in meteorology today. Prior to satellites, meteorologists were forced to make inferences about the mesoscale from macroscale patterns. However, significant advances in that area have been made using data available from geostationary satellites. Based on analysis of GOES imagery, Purdom (1979) introduced the concept of "convective scale interaction" due to arc cloud lines and discussed their role in controlling the development and evolution of deep convection. That interaction manifests itself as the merger and intersection of thunderstorm-produced arc cloud lines with other convective lines, areas and boundaries (Purdom, 1979). Pertinent conclusions can be summarized as follows:

1. Thunderstorm-produced outflow boundaries (arc clouds) are of primary importance in the formation and maintenance of strong convection;

2. Outflow boundaries may maintain their identity as arc clouds for several hours after the convective array that produced them has dissipated;

3. Deep convective development along an arc cloud line is a selective process - highly favored where two arcs intersect or where an arc moves into a convectively unstable region; and

4. In a weakly forced atmosphere, arc boundary interactions determine the location of the majority of new thunderstorms by the end of the day.

During the summer of 1985 a number of separate, but coordinated, field research programs took place in northeast Colorado's high plains. Measurements were taken by a variety of remote and in situ instrumentation systems including research Doppler radar, special rawinsondes released from mobile rawinsonde units, rapid scan GOES satellite data (at five minute intervals), surface mesonet systems, and a specially instrumented Cessna T207 research aircraft. Previous research by the authors has described the dynamic and thermodynamic character of the air between the base of the cumulus convection observed along the arc cloud line and the top of the density surge line which drives the arc cloud line (Sinclair and Purdom: 1983, 1984). This paper uses in situ data from research aircraft flights to describe the dynamics and thermodynamics of the arc cloud line within the density surge region.

One particular research aircraft flight which will be examined in detail occurred on July 22, 1985. Aircraft penetrations of the density surge line were made at several altitudes between approximately 700 ft/AGL and 4000 ft/AGL. These penetrations were made in an arc cloud line that was over two hours old and far from its parent thunderstorm. Special rawinsondes were also released in the vicinity of this arc cloud line. From the aircraft measurements, wind speeds and circulations within the arc cloud line region are deduced and compared with certain of the special rawinsonde observations and observations from Doppler radar and rapid scan satellite data.

It should be noted that the arc cloud line of July 22, 1985 played an important role in subsequent convective development. When the arc merged with an enhanced convective region near Greeley, Colorado, a large and intense thunderstorm developed (Figure 4).

2. THE EXPERIMENT

2.1 General

The arc cloud line investigations were carried out in the Colorado High Plains during the summer of 1985. Using the Cessna T207 research aircraft, arc cloud line penetrations were made through the density surge line region. For a variety of reasons, including logistics, fuel availability and access to weather information operations were based out of Christman field at Colorado State University. General areas for penetration were chosen using near real time GOES satellite data from the CSU IRIS system and input from the NCAR CP-2 Doppler radar. Once the aircraft reached an area for investigation, decisions concerning penetration points were made visually. Aircraft position was determined from VOR-DME and Doppler navigation systems, and could be cross referenced using visual landmarks such as towns, roads and other ground features.

2.2 Aircraft Observational System

The Colorado State University Atmospheric Research Flight Facility (ARFF) has developed a number of Airborne Atmospheric Data Systems (AADS) for direct measurements of temperature, dew point, pressure, atmospheric constituents and the atmosphere's three dimensional velocity field. These systems have been specially designed for a variety of aircraft for measurements in atmospheric systems ranging in size from mesoscale systems and severe thunderstorms to waterspouts and dust devils (Sinclair, 1974; Leverson, Sinclair and Golden, 1975). A miniaturization of the AADS system was designed and constructed by the ARFF for the Cessna Turbo 207 aircraft used in this experiment (see Figure 1). It is believed that this is the first installation of this type on a light single-engine aircraft.

Figure 1. Cessna Turbo 207 Atmospheric Research Aircraft.

The Cessna T207 aircraft is the largest single-engine (non-turbine) light plane manufactured in the U.S. and consequently it provides maximum volume and payload capabilities at minimum cost. The aircraft is STOL equipped for high accuracy wind and gust measurements and isokinetic air sampling requirements. The gust probe system is mounted in a pod under the left wing and a doppler navigation - wind system is located in a specially designed pod located on the bottom of the fuselage near the tail of the aircraft.

A fast response total temperature sensor is shown mounted on the upper part of the vertical plate on the right wingtip. On the lower part of the plate, a special splitter plate mount houses the Cambridge dew point sensor. The splitter plate provides unobstructed flow past the sensor air ports. The temperature and dew point sensors are mounted on the wingtip to minimize engine effects and contamination and adverse airflow situations at other wing-fuselage locations.

Relatively fine structure of the velocity field (u', v', w') is obtained using a gust probe and gyro reference system that is designed to be independent of the aircraft's sensitivity to atmospheric motions and/or pilot induced motions. Temperature and dew point are continuously recorded using a standard Rosemount fast response total temperature sensor and a Cambridge dew point sensor. In addition to the above measurements, a Doppler wind system provides accurate measurements of ground speed and aircraft drift angle. These data, along with aircraft heading and true airspeed provide mean horizontal wind components ($\bar{u}$, $\bar{v}$). Aircraft position data can be obtained from VOR/DME and LORAN-C stations along with pressure and radar altimeter instrumentation. Accuracy in measurement of the various parameters mentioned above is given in Table 1.

Table 1

Parameter	Relative Accuracy	Absolute Accuracy
Temperature	0.05°C	0.2°C
Dew Point Temperature	0.2°C	0.5°C
u', v'	0.1 $msec^{-1}$	0.5 $msec^{-1}$
w'	0.1 $msec^{-1}$	0.5 $msec^{-1}$
$\bar{u}$, $\bar{v}$	0.5 $msec^{-1}$	1.0 $msec^{-1}$
a/c location	$\pm$0.1 nm	$\pm$0.2 nm

3. MEASUREMENTS AND OBSERVATIONS

Successive penetrations of a well-defined outflow region were accomplished in an open, farming area approximately 60 km southeast of Fort Collins and 50 km northeast of the NCAR Doppler radar (CP-2) near Boulder, Colorado. The outflow, gust front developed along the outflow boundary of a large, intense thunderstorm some 90-100 km to the southeast of the measurement area. The outflow and preceding gust front were propagating to the northwest at approximately 5-7 $msec^{-1}$. In the measurement area, the outflow winds were from approximately 090° to 150°, depending on height above the ground. The penetration headings of 120° and 300° were selected to minimize aircraft drift angles and thereby provide more accurate winds along the outflow axis.

The gust front (GF) penetration measurements at four different levels (9000, 7700, 6700, and 5700 ft MSL) are shown in Figures 2 and 3. The gust front shape and boundary structure in relation to the wind, temperature and moisture fields are indicated by the narrow hatch region which is bounded by the warm, dry air ahead and the cool, moist air behind the gust front zone. NCAR special release rawinsondes (taken at point E in Figure 5) showed similar warm and dry air ahead of the gust front (1703 release) and cool and moist air behind it (1749 release). Several salient features from the aircraft measurements are outlined below:

3.1 Thunderstorm Outflow and Gust Front (GF) Boundary Features (Figure 2)

a. The upper part of the GF is nearly vertical and somewhat narrower than the lower part. In the lower levels the GF is displaced forward of the upper part due to its higher horizontal velocity, i.e. approximately 7 $msec^{-1}$ vs 5 $msec^{-1}$. Since the GF is a considerable distance from the parent storm (90-100 km), the GF translation velocity was probably larger in the first half of its life-cycle than during our measurement phase.

b. Ahead of the GF, relatively warm, dry air is being forced upward in a narrow band, approximately 2-3 km wide. Also, at all levels, there apperas to be a region of sinking motion (or return flow) ahead of this rising warm air current. Similar return flow features have also been noticed near dry thermal and cumulus cloud boundaries.

c. Immediately behind the GF, there is a continuous, upward movement of relatively cool, moist air that appears to form one leg of a long narrow circulating cell of a solenoidal-type circulation. This thermally direct circulation appears to be driven by the significant temperature - density contrast across the GF from warm to cold air. The updraft portion of this cell is somewhat weaker and narrower (1-2 km wide) than that ahead of the GF. However, we feel that it is this circulation that is responsible for transporting low-level moisture upward for subsequent cloud formation or cloud intensification. It is interesting to note that this feature is not the dominant moisture transport mechanism in moist, boundary layer environments such as in the southeast U.S. In those situations we have found the upward moisture transport is ahead of the GF and associated with the relatively warm air.

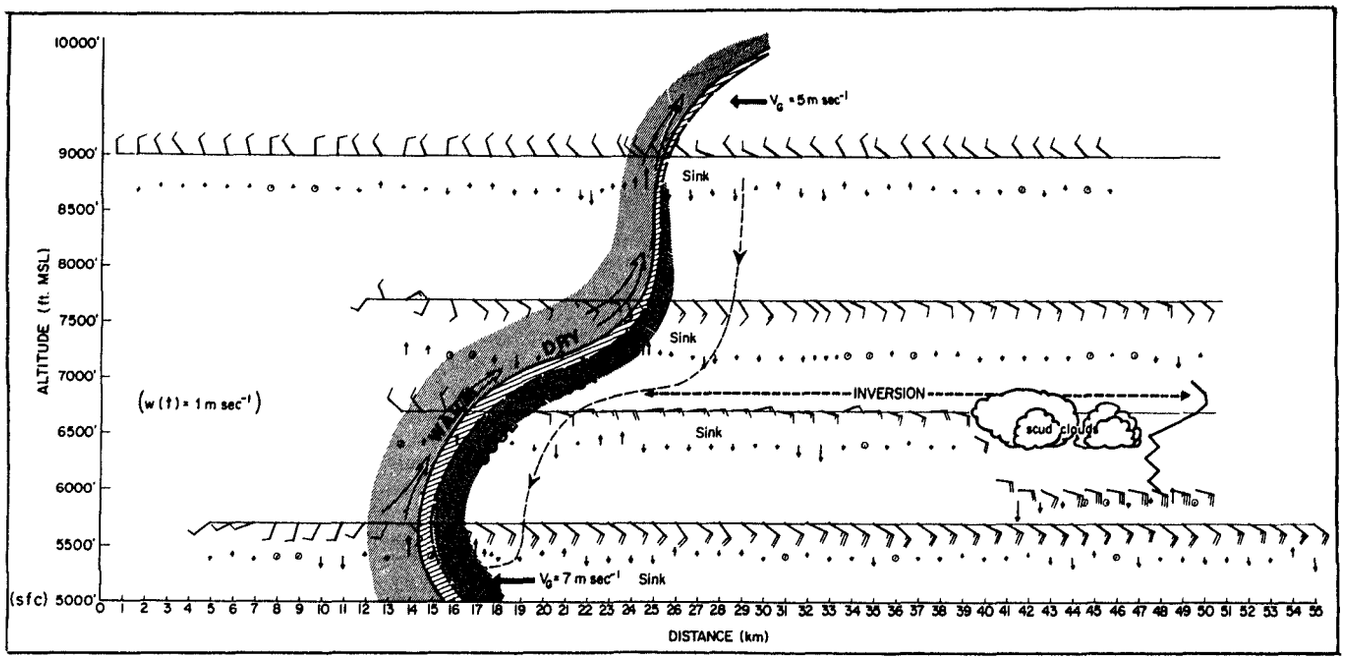

Figure 2: Thunderstorm Outflow and Gust Front (GF) Boundary Features
Aircraft penetrations at four different levels (5700, 6700, 7700, 9000 ft MSL) are shown with the associated winds (horizontal and vertical). Vertical winds (w) are indicated by small vertical arrows placed just below the penetration altitudes (the w magnitude and arrow length relationship is indicated on the diagram). The parent storm precipitation core is located to the right of the GF boundary (hatched zone) at approximately 90-100 km. V_G is defined as the horizontal propagation velocity of the GF boundary. See text for further discussion.

d. The horizontal winds measured by the aircraft Doppler navigation system are entered at 1 km intervals at each flight penetration level. At the 6700 ft level (1700 ft AGL) there is a distinct wind shift (east to northwest winds) as one passes from the cool to the warm air, i.e. right to left in Figure 2. At the lowest level (5700 ft MSL, 700 ft AGL) the wind shift zone is somewhat larger and not as abrupt. At the lower levels the winds normal to the gust front in the advancing cold air are approximately 20 knts at 5700 ft MSL (700 ft AGL) and 13 knts at 6700 ft MSL (1700 ft AGL). With the GF moving at 7 $msec^{-1}$ (13.5 knts) at the lowest level (700 ft AGL), there is consequently some speed convergence in this layer, but it appears to rapidly diminish with height. In contrast to the two lowest levels, the horizontal winds at the two upper levels show no well-marked directional variations through the GF zone. There is, however, some speed increase through and on either side of the GF zone.

e. The low-level cold air layer produces a temperature inversion at middle levels (6400 ft - 6800 ft). The NCAR special rawinsonde taken at 1749 (at E in Figure 5) shows a similar low level inversion structure. The scud clouds encountered in the cold air are capped from further growth by this stable layer. This inversion is schematically shown to the right of the scud clouds - the difference in temperature between the base and the top of the inversion is approximately 2.5°C. The lateral extent of this inversion is shown by the horizontal dotted lines at Z~6700 ft MSL and in the distance interval of 25-50 km.

f. In general, there is weak subsidence in the cold air behind the GF. In addition, the turbulence levels appear to be very low in this region as we experienced very smooth flight conditions at all levels in the cold air - the gust probe data corroborated these observations also.

3.2 Gust Front (GF) Temperature-Moisture Structure (Figure 3)

To depict more clearly the temperature and moisture variations through the GF, temperature and moisture profiles (horizontal) for each level were constructed for each penetration.

a. The temperature profile (solid lines) show in each case a marked temperature drop from the warm to cold air. At the lowest level (5700 ft MSL), this temperature decrease amounts to approximately 5°C (26.1°C to 21.6°C) in 3.5 km distance. At the upper levels this decrease is also abrupt but less intense. At the lowest level (5700 ft MSL), the temperature continues to decrease to 18.1°C at the end of the penetration in the cold air. The upper levels do not show a similar temperature decrease.

b. The moisture profiles (dashed lines) show a similar sharp change through the GF. In this case however, the dew points increase rapidly from the warm air to the rain-cooled moist air behind the GF. The largest variations occur at the two lowest levels where the dewpoints show abrupt changes of 3° to 3.5°C in 1 km.

The temperature and moisture profiles at all levels both confirm the existence of the relatively warm, dry air ahead of the GF and the cool, moist air in the outflow region behind the GF. In addition, the rapid change in the temperature and moisture profiles at successive penetration levels substantiates the shape and width of the GF boundary.

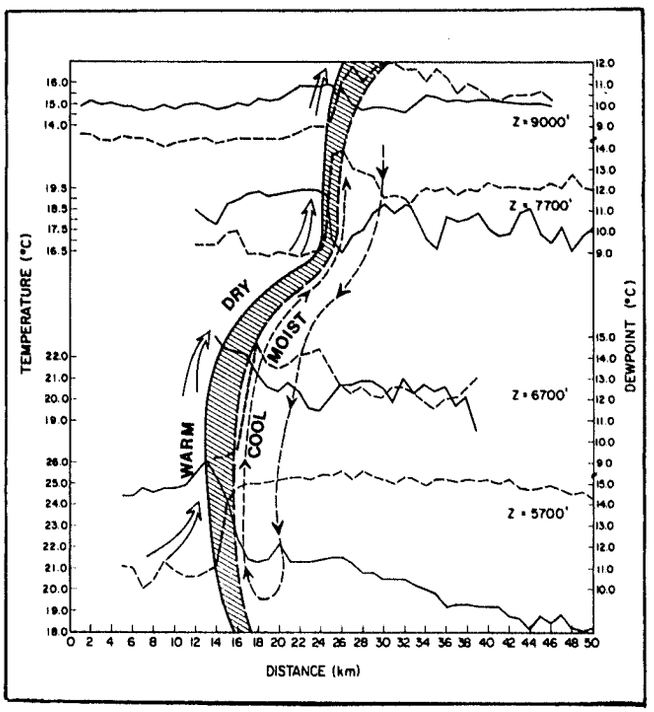

Figure 3: Gust Front (GF) Temperature-Moisture Structure

The temperature-moisture profiles through GF at the four penetration levels (5700, 6700, 7700 and 9000 ft MSL) are shown above. Each set of profiles has its own temperature (°C) and dewpoint (°C) scale on the left- and right-hand ordinates, respectively. The GF is advancing to the left with the parent storm at the 90-100 km location as in Figure 1. See text for discussion of specific structure features.

4. Satellite and Radar Observations

Figure 4a shows the location of the arc cloud line (A) and its parent storm at 1531 Local. This figure shows that the arc cloud line was well formed almost two hours prior to the penetrations mentioned in the previous section. At this time the arc cloud was located approximately 80 km east of the CP-2 radar (see Figure 5) expanding radially outward at a velocity between 5 $msec^{-1}$ (from 90°) and 10 $msec^{-1}$ (from 140°). The cumulus region north of Greeley, at B in Figure 4a, moved slowly southward during the next several hours. When that cumulus region merged with the arc cloud line later in the day, the ensuing convective scale interaction produced large thunderstorm near Greeley, at C in Figure 4b.

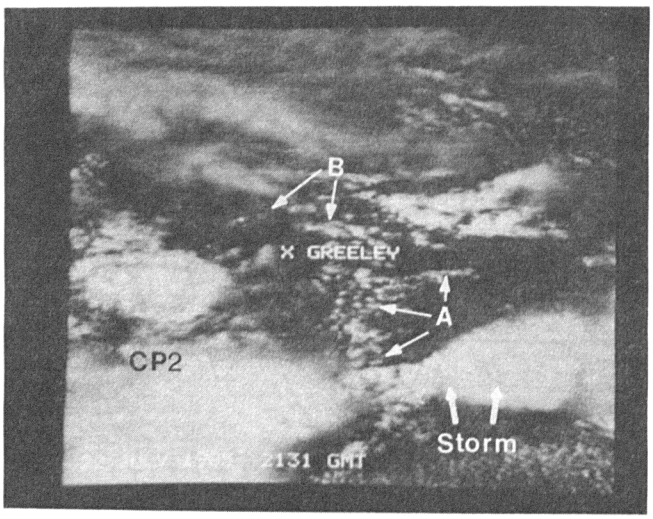

Figure 4a: GOES-Central 1 km resolution visible image for 1531 Local, July 22, 1985. The arc cloud line is shown in location A, with its parent cell approximately 30 km to its south.

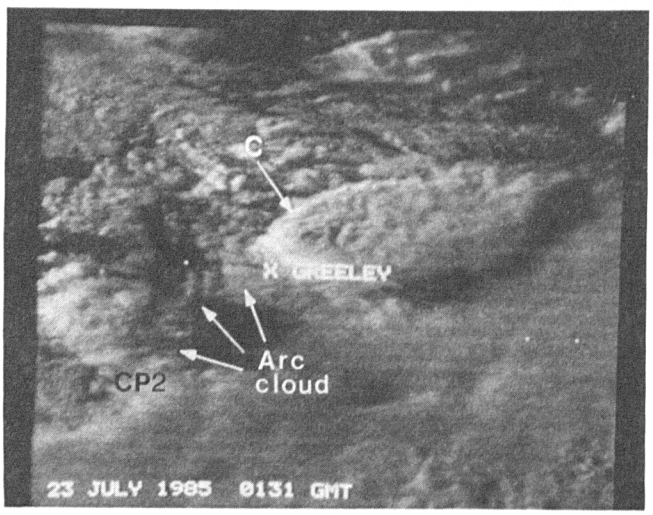

Figure 4b: GOES Central 1 km resolution visible image for 1931 Local, July 22, 1985. The large thunderstorm at C, near Greeley, formed when the arc cloud line, A, merged with the convective region, B, in Figure 4a.

The arc cloud line shown in Figure 4 was tracked by NCAR's CP-2 radar for most of its lifetime. Figure 5 shows its location at 1532 CDT (for comparison with Figure 4) as well as at 15 minute intervals during the time of the aircraft penetrations shown in Figure 3. During those times the boundary was moving toward the CP-2 radar (from A to B) at an average speed of 6.4 $msec^{-1}$. The boundary's motion from C to D averages 7.9 $msec^{-1}$. A line from C to D is parallel to the wind direction found in our lowest two penetrations shown in Figure 3, and the 7.9 $msec^{-1}$ motion of the boundary matches well with the wind speeds measured along those two flight legs. The movement of the northern portion of the arc, in a line parallel to CD, slowed from an average velocity of 7.6 $msec^{-1}$ (F to G) to 5.5 $msec^{-1}$ (G to H). We attribute this decrease in velocity to the arc cloud line's increased distance from its cold air source (parent storm). Point I along the flight track is the location of the aircraft sounding, while point E is the location of the NCAR mobile, sounding releases.

In this particular case, the major portion of the Doppler velocity field associated with the outflow boundary was confined to a one to three kilometer wide portion of the arc. This is the same region that is associated with cumulus cloudiness along the arc in the satellite image, and also in the weak reflectivity fields of the 5 and 10 cm Doppler measurements (0.3 and 0.7 deg. elevation). It should be noted that this reflectivity is too low to be the clouds observed along the arc. In the cool outflow air behind the arc, where skies were clear, the Doppler velocity field was zero except for the dashed area of Figure 5. From the aircraft we observed blowing dust in that region and high wind velocities.

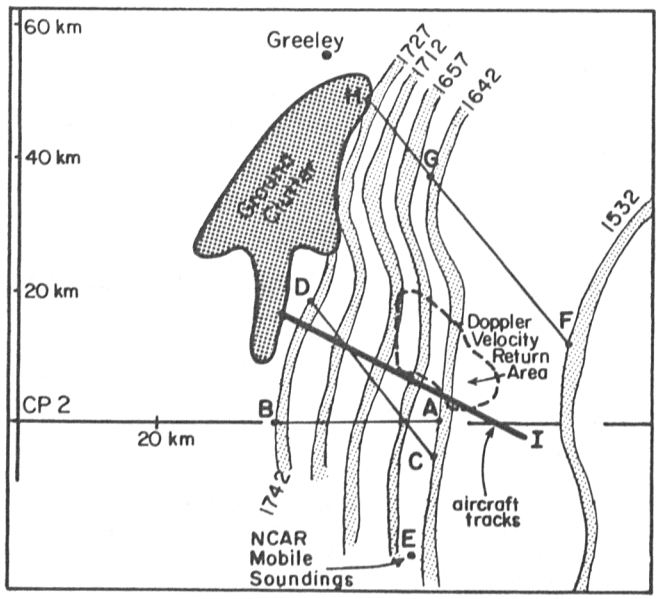

Figure 5: Traces of boundary locations from 0.3° elevation CP-2 reflectivity for the times (local) indicated. The bold dashed line shows the location of the aircraft penetration fligth tracks in Figure 3. Location E shows the release point for the NCAR rawinsondes.

5. Summary and Conclusions

For a number of years, one of our primary goals has been to document, by in-situ measurements, the structure of the thunderstorm outflow region and the associated gust front (GF) boundary at the leading edge of the outflow. As was shown in this case, such boundaries are important trigger mechanisms for new intense convective storms. While these latest aircraft measurements corroborate, in general, our previous results and analyses, they add much more detail and add several new insights as to the GF structure and the adjacent warm-cold air environments:

1. One of the most significant results of this research has been the documentation of an apparent direct or solenoidal circulation immediately behind the GF boundary in the cold air. This circulation we believe pumps the boundary layer moisture, which in this case was enhanced by the parent thunderstorm, to higher levels where it may provide the moisture for subsequent cloud formation and/or intensification. This feature is not so evident in moist environments (S.E. U.S.) where the moisture pathway is in the warm air circulation ahead of the GF.

2. The significant upward motion field is confined to a narrow zone on either side of the GF boundary in the warm-dry and cool-moist circulations (Figure 2). In other outflow locations, the vertical motion is not so well organized except for a general weak subsidence throughout the cool, moist air mass. This subsidence leads to stabilization and clearing, as is evident in Figure 4a, within the cool moist air behind the arc cloud line.

3. Scud clouds formed in the cool air, well behind the GF, are capped by the cool air inversion at approximately 6400 ft to 6800 ft MSL (1400 ft to 1800 ft AGL).

4. Both the temperature and moisture profiles show sharp changes through the GF boundary. These gradients provide part of the driving mechanism for the direct (cool-moist) circulation behind the GF.

6. Acknowledgements

The authors would like to thank Sallie Varner for preparation of the text. We are especially grateful to Jim Wilson and Cindy Muller of NCAR for providing the CP-2 radar data and special rawinsonde data, as well as their valuable input concerning arc cloud line locations and movement. This research was supported in part by NSF Grant #ATM-8420980.

7. References

Leverson, V.H., P.C. Sinclair and J.H. Golden, 1977: Waterspout wind, temperature and pressure structure deduced from aircraft measurements. Mon. Wea. Rev., 105(6), 725-732.

Purdom, 1979: The development and evolution of deep convection. Preprints, 11th Conf. on Severe Local Storms, Kansas City, Amer. Meteor. Soc., 143-150.

Sinclair, P.C., 1974: Severe storm turbulent energy structure. Preprints, Sixth Conf. on Aerospace and Aeronautical Meteorology, El Paso, Amer. Meteor. Soc., 12-14 Nov., 13 pp.

Sinclair, P.C. and J.F.W. Purdom, 1983: The genesis and development of deep convective storms. CIRA Paper No. 1, Cooperative Institute for Research in the Atmosphere, Colorado State University, Ft. Collins, CO, 56 pp.

Sinclair, P.C. and J.F.W. Purdom, 1984: The genesis and development of deep convective storms: A new approach to their prediction and possible modification. CIRA, Cooperative Institute for Research in the Atmosphere, Colorado State University, Ft. Collin, CO, 47 pp.

7.6

ON THE ACCURACY OF CLOUD TRACK WINDS DERIVED FROM METEOSAT-2 IR IMAGES

Johannes Schmetz and Olli Turpeinen

European Space Operations Centre
Robert-Bosch-Str.5, Darmstadt, FRG

1. INTRODUCTION

Cloud track winds are derived routinely in near real-time at the European Space Operations Centre and they are disseminated twice daily for routine use in numerical forecast models. The cloud motion vectors are determined from carefully aligned subsequent infrared (IR: 10.5 - 12.5 μm) images with a cross-correlation technique over segments of 32x32 IR pixels which corresponds to an area of 160x160 km at the sub-satellite point. Only those segments are processed which were classified as containing cloud tracers by two-dimensional histogram analysis. Correlation surfaces are calculated for two subsequent pairs of images (i.e.3 images at half hourly intervals) which allows for a symmetry check of the two corresponding wind vectors.

The height assignment is based on the IR radiance of the cloud pattern and it includes a correction for atmospheric absorption and emission.The black body temperature equivalent to the radiance is converted into a pressure level using vertical temperature profiles of the forecasts from the ECMWF. The satellite's channel in the 6.3 μm water vapour band is employed to correct the height assignment of semi-transparent cirrus cloud. The data are subject to an automatic and manual quality control before dissemination.

The overall impact of the cloud track winds on the numerical forecast is beneficial (e.g.Baede et al,1985). However the tendency of high level cloud track winds to underestimate the wind speed especially in jet stream areas can damage the analysis.

While the speed bias has been noted by several authors (e.g.Bizzari and Sorani 1980; Pierrard,1985) and it is an evident feature of our own routine comparison with radiosondes, so far little attention has been paid to physical explanations and possible ameliorations.

The height assignment of cloud has been identified as a major problem area (e.g. Whitney,1983).

Concerning Meteosat and the present processing scheme it is expected that the use of forecast profiles implies errors and that the assignment to the level of cloud top temperature is a crude assumption for deep convective clouds. The height assignment of jet stream cirrus depends on the performance of semi-transparency correction. Our paper addresses two points:

a) a brief discussion on features of the jet stream leading unrefusingly to an underestimation of the actual wind speed by our automatic cloud track scheme.

b) a sensitivity analysis of the semi-transparency correction for height assignment of cloud which is applied to many high level winds.

2. SPEED OF HIGH LEVEL CLOUD TRACK WINDS

Fig.1 shows the cumulative frequency of winds as a function of wind speed. The data are from a 13 months (January 1984 - January 1985) data set of collocated radiosonde (RAS) and satellite (SAT) measurements. The data sample contains 9684 pairs of high level (<400 hPa) and 2360 pairs of low level (>700 hPa) wind vectors. The solid curves pertain to the RAS and the dashed curves to SAT measurements. An excellent agreement between SAT and RAS is to be observed for low level winds, whereas the high level SAT winds approach the 100% value at a lower speed than the RAS winds. The latter corresponds to a mean bias of 3.3 m/s between RAS and SAT wind speed. Concerning the direction of the winds there is no systematic deviation and both measuring systems agree within 3°. The RMS error of the algebraic direction differences decreases with height.

A wind measurement with a radiosonde can be considered as being a random sampling of the air flow so that a sufficiently large number of measurements represents the true wind. For cloud track winds one can estimate an unbiased wind only if clouds were conservative tracers randomly distributed within and floating with the airflow. However, this postulation is not true.

For instance, in jet areas the major part of cloud is found below the level of maximum wind speed and there are seldom any clouds above that level (e.g.Englandand Ulbricht, 1980). The jet core itselfis also mostly cloud free. The vertical and horizontal wind shear can be as large as 10 m/s per 1 km and 5 m/s per 100 km, respectively. Thus, it is not unreasonable to expect from the present cloudtrack scheme significant under estimations.
Even if there are clouds in the high-speed zone those are not likely to be useful tracers since they are not long-lived enough to be trackable over a period of one hour. Fig.2 is a sketch of the prevailing vertical motions in proximity to a jet stream.
The above is also an explanation for the observation that Meteosat cloud track winds seldom exceed values higher than 60 m/s. In a recent campaign with the UK Meteorological Office (J.Turner, personal communication) some 75 severely underestimated winds were examined in near-real time, including a later classification according to the synoptic situation. Interestingly nearly 40% were classified as either being jet core or winds east of a trough in regions of frontal disturbances.

It should be mentioned that the tendency of cloud track winds to be biased to the low side is not specific to Meteosat cloud track winds (Delsol, 1985).

3 HEIGHT ASSIGNMENT OF SEMI-TRANSPARENT CLOUDS

Cirrus cloud are very often semi-transparent to infrared radiation. It is therefore not feasible to determine the effective emittance and the temperature from measurements in one channel. Since Meteosat observes emitted radiation from cirrus cloud in two channels (IR and WV:water vapour) a combination of both wavelengths allows a correction to be made to observed brightness temperature (Cayla and Tomassini, 1978). The measured radiances L_{IR} and L_{WV} are given by:

$$L_{IR} = L_{IR}^{BG}(1 - \varepsilon_{IR}N) + \varepsilon_{IR}N\, L_{IR}^{c}$$

$$L_{WV} = L_{WV}^{BG}(1 - \varepsilon_{WV}N) + \varepsilon_{WV}N\, L_{WV}^{c} + L_A$$

where L_{IR}^{BG}, L_{WV}^{BG} are the background radiances corresponding to clear sky (highest radiance cluster), L_{IR}^{c}, L_{WV}^{c} are the desired radiances from cloud top with an emittance of 1, N is the fractional cloud amount, and ε_{IR}, ε_{WV} are the actual cloud emittances. L_A is the contribution of the atmosphere above the cloud in the WV band which is only negligible for high level clouds.

Assuming that the products $\varepsilon_{IR}N$ and $\varepsilon_{WV}N$ are equal and neglecting L_A, one can write a linear relation:

$$L_{WV}^{c} = a\, L_{IR}^{c} + b$$

L_{WV}^{c} is then obtained from the additional relationship $L_{WV}^{c} = f(L_{IR}^{c})$ which relates the black-body radiance from cloud top in the two channels. a and b are constants for a given background and cloud scene. This correction is applied operationally to Meteosat cloud track winds (Bowen and Saunders, 1984). Tests are performed before its application: First L_{WV}^{BG} is allowed to vary only by 10% around the theoretical function $f(L_{IR})$.
Second the contrast between the background and the actual cloud radiances must be sufficient, and third no correction is applied if there is no intersection between the straight line and f(L).

Although the semi-transparency correction significantly improves the height assignment of high level cloud the subject cannot be considered as being solved with sufficient accuracy. Fig.3 intends to bring into perspective some limiting factors. The solid curve is the function $L_{WV}^{c} = f(L_{IR}^{c})$ for a black cloud in a mid-latitude summer atmosphere as calculated with a multispectral radiative transfer scheme (Schmetz and Raschke, 1981). Points along the curve denote clear sky and clouds at 2,4,6,7.2,9.2, and 11 km altitude. The dashed line pertains to a semi-transparency correction for an opaque cloud with 50% cloud cover (N=0.5) at 11KM. The dash-dotted line corresponds to a cirrus with $\varepsilon = 0.5$ and N=1, but considering that the relative humidity within the cloud (9-11 km) is 100%. This reduces the water vapour radiance by 2 counts (the radiance to count conversion is linear) and leaves the IR radiance virtually unaffected. As a consequence the intersection occurs at a lower count yielding an overestimation of the actual cloud height by about 1.5 km. Similar magnitudes of cloud misplacement are obtained if the background radiance is varied; for instance, the cross in Fig.3 denotes a clear atmosphere with 100% relative humidity between 9 and 11 km. Fig.3 indicates also that the 6-bit resolution of the WV channel is rather crude, and that the correction depends strongly on the theoretical bispectral function $L_{WV}^{c} = F(L_{IR}^{c})$. One can conclude that cirrus cloud misplacements which could bring the cloud track winds into levels of much higher wind speed are likely to occur. Nevertheless it should be mentioned that the WV channel is a precondition for our automatic and objective processing scheme and it is therefore a tremendous improvement over a single IR channel.

Fig.4 demonstrates that it is justified to assume $\varepsilon_{IR}=\varepsilon_{WV}$; the flux emittance of a CS cloud at the wavelengths 6.3, 10 an 12 μm, is plotted as a function of cloud optical thickness in terms of ice water path. The optical constants are taken from Kinne (1981) and were determined for a modified CS ice column distribution after Heymsfield (Table 1). There is close agreement between the emittance curves and reflectances approach values of 2-3% for thick clouds.

4. FINAL REMARKS

Comparison of Meteosat high level winds with radiosonde winds shows on the mean an underestimation of the wind speed by satellite measurements. The bias can be attributed partly to the non-occurence of long-lived cloud tracers in the high speed areas of a jet. Inaccurate cloud height assignment is believed to increase the apparent discrepancy. While the semi-transparency correction to cirrus cloud is theoretically sound limited factors exist for an operational application. Improvements to the automatic cloud tracking and results from case studies will be discussed during the conference.

References:

Baede, A.,P.Kallberg and S.Uppala,1985, Impact of aircraft wind data on ECMWF analyses and forecasts during the FGGE period, 8-19 Nov.1979, ECMWF Technical Report No.47 85pp

Bizzari,B. and R.Sorani,1980: The accuracy of Meteosat winds over the Mediterranean. Proceedings of the 2nd course on satellite meteorology of the Mediterranean, ESA-SP-159, 65-70

Bowen,R. and R. Saunders, 1984: The semi-transparency correction as applied operationally to Meteosat infrared data. ESA-Journal,8, 125-131.

Cayla, F. and C. Tomassini,1978: Determination de la temperature des cirrus semi-transparents. La Meteorologie, VI, No.6, 73-77.

Delsol,F., 1985. Monitoring the quality of cloud winds from Meteosat and other meteorological satellites. Proceedings of the 5th Meteosat Scientific User Meeting, 28-30 May, 1985, Rome.

England, J and H.Ulbricht, 1980: Flugmeteorologie, Transpress VEB Verlag für Verkehrswesen, Berlin, 403 pp.

Kinne,S.,1981: Einfluss von Eiswolken auf den Strahlungshaushalt der Atmosphäre. Diploma Thesis, FB Geowissenschaften, Universität Hamburg.

Pierrard, M.C.,1985. Intercomparison between cloud track winds and radiosonde winds. Proceedings of the 5th Meteosat Scientific User Meeting.

Schmetz, J. and E.Raschke, 1981: An approximate computation of infrared radiative fluxes in a cloudy atmosphere. Pure Appl. Geophys.,119,248-258

Whitney,L.,1983: International comparison of satellite winds - an update. Adv.Space Res.,2, No.6, 73-77

Table 1: Optical constants for a CS cloud (after Kinne, 1981) in the IR and WV channel. (λ = wavelength; $\tilde{\omega}$ = single scattering albedo; σ = mass extinction coefficient; g = asymmetry parameter).

λ	$\tilde{\omega}$	σ	g
6.3 μm	0.571	0.097m^2/g	0.893
10.0	0.636	0.100	0.898
12.0	0.536	0.095	0.868

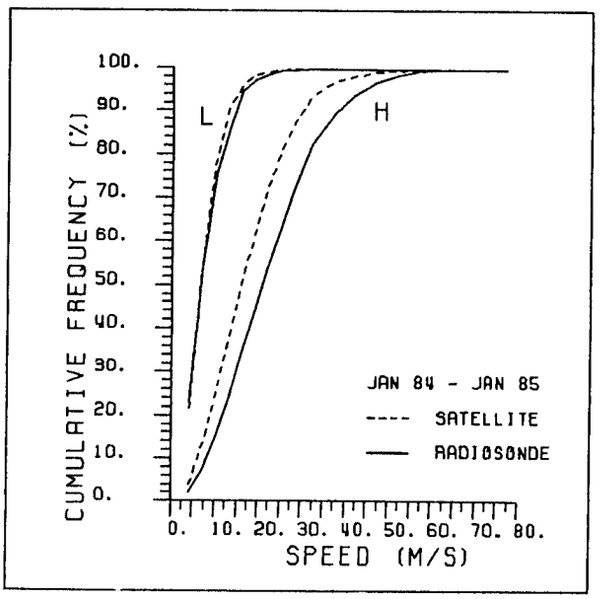

Fig.1: Cumulative frequency of cloud track (----) and radiosonde (——) winds versus wind speed for low level (L) and high level (H) cloud.

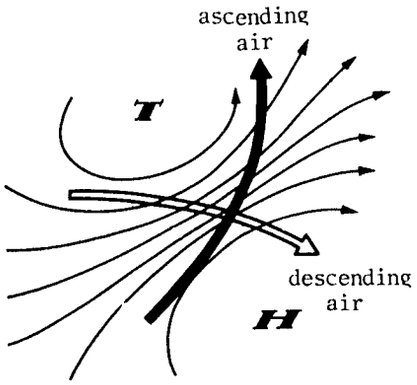

Fig.2: Ascending and descending air in the branches of a polar jet (from England and Ulbricht, 1980).

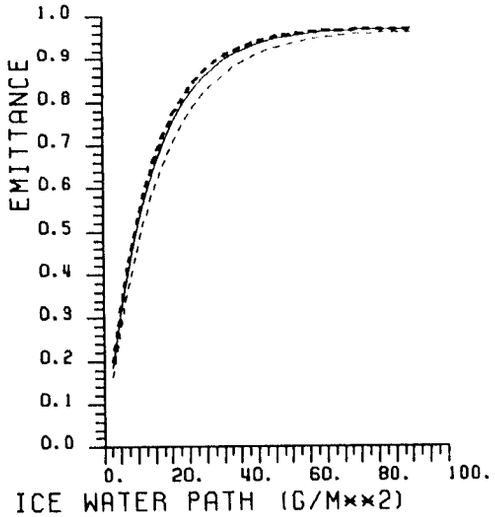

Fig.4: Flux emittance of CS cloud at the wavelengths 6.3 μm (solid), 12.0 μm (upper dashed) and 10.0 μm(lower dashed) as a function of the ice water path.

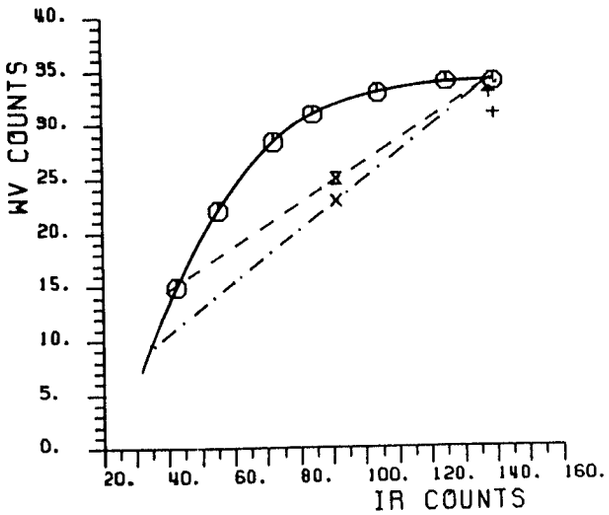

Fig.3: Outline of the semi-transparency correction scheme: The solid curve is the bispectral curve for an opaque cloud at different altitudes. Straight lines pertain to the correction for an opaque cloud with a fractional cloud cover of N=0.5 (dashed), and for a cloud with N=1 and an emittance of 0.5 (dash-dotted).

8.1

SCALE AND DIMENSION DEPENDENCE IN THE DETECTION AND CALIBRATION OF REMOTELY SENSED ATMOSPHERIC PHENOMENA

S. Lovejoy and S. Schertzer

Physics Dept.
McGill Radar Weather Observatory
Ste Anne de Bellevue, Quebec
Canada H9X 1C0

ABSTRACT:

We consider the problem of remotely sensing extremely variable geophysical phenomena. Theoretically, we argue that it can be understood by a symmetry principle called generalised scale invariance (GSI), in which the small and large scales are related by a magnification coupled with a geometrical transformation such as a rotation or compression we empirically investigate GSI in the rain field. Phenomenologically, we show how to construct stochastic, fractal models of extremely variable phenomena. Using radar data, we empirically investigate two basic aspects: the dependence of all statistical properties on both the scale and dimension over which they are averaged. The dimensional dependence of averages is important because we also analyse the global meteorological ground station network and show that -due to inhomogeneities at all scales- it has a fractal dimension of ~1.75 which is considerably less than that of most remote sensing devices (i.e. 2 or 3). This places a limit on the dimensional resolution of the networks and is important when using network data to calibrate satellite or radar detected fields.

1. INTRODUCTION:

A fundamental problem in the remote sensing of geophysical parameters is the extreme variability of the phenomena. Typical symptoms are the existence of sharp gradients, sudden transitions, erratic fluctuations, structures spanning a wide range of scales, apparent statistical non-stationarity, and in some cases, difficulty in obtaining the convergence of high order statistical moments. In physics, particularly in turbulence, these symptoms have long been studied under the rubric "intermittency". It is known for example, that when phenomena are intermittent, that the standard statistical techniques involving the assumption both of the existence of characteristic time and distance scales (hence an exponential fall-off of correlations), and the existence of characteristic amplitudes of fluctuations (hence an exponential fall-off of probability distributions) are inappropriate. Below, following Schertzer and Lovejoy (1985a), we argue that the type of extreme variability encountered in many geophysical

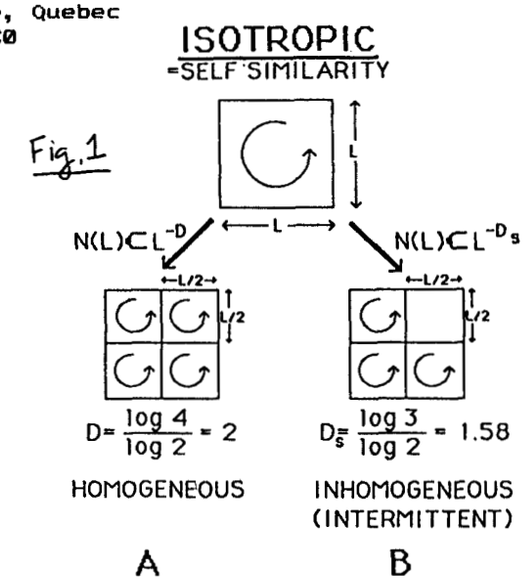

phenomena, (and hence relevant to remote sensing), can be understood in terms of a symmetry principle that we call generalised scale invariance (GSI - Schertzer and Lovejoy (1985b)).

GSI grew out of developments in hydrodynamic modelling in which the variability was consider to arise as a result of a cascade process concentrating energy from one scale to another, while conserving its average value (see e.g. the simple cascade scheme shown in Fig. 1). GSI is a formalism that develops these cascade ideas in two directions.

First, it shows with the aid of a generalised scale changing operator, how anisotropic scale invariance (for example that between the horizontal and vertical directions in the atmosphere, or that associated with surface texture), can be accounted for (and modelled), and second, it leads to a systematic study of the various measures that can be invariant under the action of the scale changing operators. These scale invariant quantities are expected to have a fundamental physical significance, since the ensemble average of their spatial means does not depend on the scale (or dimension of space) over which they are averaged. Conversely, quantities defined by the various powers of the scale invariant quantity are strongly scale dependent. Precisely, the moments $\langle \bar{\epsilon}^h \rangle$ of the density of the invariant (ϵ), where "<.>" indicates statistical, (ensemble) averages decrease with scale for h>1, and increase for h<1.

In hydrodynamics, it is plausible

that flows respect GSI because the governing (Navier-Stokes) equations contain no length scale (above a small inner viscous scale which in the atmosphere is of the order of millimeters), and hence, scale invariant solutions (such as those displaying a Kolmogorov $k^{-5/3}$ energy spectrum) are possible. However, in remote sensing, the exact equations governing the phenomena of interest are seldom known, hence we have only recourse to more general arguments of the type that physicists call symmetry principles. Familiar symmetry principles include the conservation of energy, and matter as well as invariance with respect to translation, rotation and reflection.

Following a standard approach in physics, a system is expected to respect symmetries unless specific ("symmetry breaking") mechanisms can be found. In any case, there is now much evidence (see Table 1) that for many geophysical quantities, over large ranges in scale, no mechanisms exist that are strong enough to break the basic scaling symmetry. Hence, over ranges spanning a small inner, and large outer scale, GSI is likely to be relevant.

2. TECHNIQUES FOR ANALYSING SCALE AND DIMENSION DEPENDENCE:

A wide variety of analysis tools exist for studying the scale and dimension dependence of phenomena, for determining their scaling parameters, as well as the limits of their scaling regimes. Table 1 gives a list of some of the most important methods (as well as some relevant geophysical references) that have been used to study geophysical phenomena over a wide range of scales. They are all capable of determining the inner and outer scaling cutoff, as well as certain scaling parameters. When the phenomena of interest are mono-dimensional, both intense and weak regions scale in the same way, hence there are relatively few parameters involved. Futhermore, the dimension of the space over which the averages are taken is unimportant. In this case, no special care is needed in applying any of these techniques. However, in the general case where the phenomena are multidimensional, direct and indirect dimensional dependencies will be present (and will not necessarily be easy to remove). The main exception is the integral structure function (Lovejoy and Schertzer 1985a) which is specifically designed to seperately study both scale and dimensional dependence.

TECHNIQUES FOR ANALYSING SCALE AND DIMENSION DEPENDENCE

ANALYSIS METHOD		WELL ADAPTED FOR: (STRENGTHS)	ILL-ADAPTED FOR: (WEAKNESSES)	GEOPHYSICAL PHENOMENA STUDIED	REFERENCES
Probability Distributions:	fluctuations	strong intermittency-	multiple dimensions, dimensional dependence	wind, temperature, potential temperature, rain, aerosols	Lovejoy 1981, Schertzer and Lovejoy 1983, Lovejoy and Schertzer 1985, a,b,c
	integrals	strong intermittency		surface reflectivity	Jones and Thomas (1984)
Structure Functions:	fluctuations 2nd order (variance)	simple physical interpretation	strong intermittency, multiple dimensions, dimensional dependence	surface elevation,	Goodchild (1982), Mark and Aronson (1984)
				temperatures	Lovejoy and Schertzer (1985b)
				wind	Gage (1979)
	fluctuations high order	theoretical studies	dimensional dependence	wind tunnel turbulence	Anselmet et Al (1984), Parisi and Frisch (1985)
	integral	scale and dimension dependence		rain	Lovejoy and Schertzer (1985a)
Energy Spectra:		scale dependence,	intermittency, dimensions	Ocean temperatures	Deschamps et Al (1981) (1985d)
				Wind	Nastrom and Gage (1983), Lilly and Petersen(1983)
				surface elevations	Bills and Kobrick (1985)
				texture	Pentland (1984)
Distribution of Areas:		2-D image analysis	physical interpretation	island areas	Korchak (1938), Mandelbrot (1982)
				rain and cloud areas	Lovejoy (1981)
				ice flow areas	Rothrock and Thorndike Thorndike (1983)
				image segments	Peleg et Al (1984)
Area-Perimeter Relation:		2-D image analysis	physical interpretation	islands	Mandelbrot (1982)
				rain and cloud areas	Lovejoy (1982), Cahalan et Al (1984)
Covering by balls:		Direct determination of fractal dimension		phase-space analysis of paleotemperatures	Nicolis and Nicolis (1984)
				analysis of meteorological measuring networks	Lovejoy and Schertzer (1985c,d)

TABLE 1

3. MULTIPLE FRACTAL DIMENSIONS IN REMOTELY SENSED FIELDS

We have recently pointed out (Schertzer and Lovejoy 1983, 1985a, b) and it has since become apparent (Mandelbrot 1985, Parisi and Frisch 1985) that in general, cascades are characterised not by a single D, but rather by a whole series decreasing with intensity (e.g. the energy flux to smaller scale cloud liquid water content, radar reflectivity etc.) actually measured. Hence, if we fix a threshold (T), then the volume of the regions exceeding T scale as $V_T(L) \propto L^{D(T)}$ and D(T) is decreasing function of T. These cascade processes have other interesting properties, such as the divergence of high order statistical moments (Mandelbrot 1974, Lovejoy and Schertzer (1986)), and are currently being studied under the rubric "multiplicative chaos", (Kahane 1986), who showed that the multiple dimension property is generic and that the artificial construction grid shown in Fig. 1 is unnecessary. These results show that mono-dimensional fractal fields are very special cases. In the case of clouds and rain, it is quite plausible that cascade type processes are responsible for the concentration of liquid water into smaller and smaller scales. Indeed, (Lovejoy 1982) showed that over the range of at least 1 km^2 to over $1.2 \times 10^6 km^2$, that these areas have complex perimeters that can be characterised by a fractal dimension $D_p \sim 1.35$. While this result clearly supports the scaling nature of the cloud and rain perimeters, its import is limited for two reasons: first, the dimension of the perimeter is in general not equal to the dimension of the cloud or rain area itself (the D

used here), and it is the latter that is directly related to the physically important water fluxes. Second, only a small range in thresholds T was used. Since then, the multidimensional nature of cascade processes has become apparent, and we no longer expect D_p to be independent of T (Tsonis, private communication, confirms that D_p does in fact decrease as T increases).

Using radar data from the McGill Radar Weather Observatory, we determine $V_T(L)$ for a variety of thresholds T using the so-called "box-counting algorithm" (see e.g. Hentschel and Procaccia 1983), which estimates $V_T(L)$ by the number of boxes (e.g. elementary shapes, size L), required to cover the rain areas with radar reflectivity exceeding T. When this was done, in the horizontal (x,y) plane, using constant altitude radar data (height, 2.5km, with 200 downrange, 375 azimuthal elements), we obtained the log V_T-logL plot shown in Fig. 2a. The straight lines, have correlation coefficients >0.999 for all 9 values of T used. T was incremented by constant factors of $10^{0.4}$ and hence spans a range of a factor $\sim 2\times10^3$ in intensity, while the slope (written $-D_{xy}(T)$ to stress that it refers to horizontal x, y cross-sections) ranged from ~1.7 to 0.25. Only 001% of the points in the sample exceeded the largest T used. Using the rough formula $R=200Z^{1.6}$, with R=rainrate in mm/hr, Z, the radar reflectivity in mm^6/m^3, the maximum corresponds to a rainfall rate of about 50mm/hr.

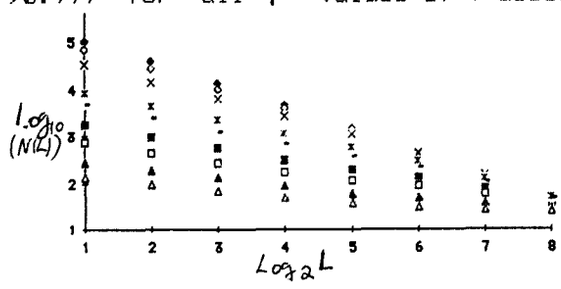

Fig. 2a: N(L) V.S.L for horizontal rain cross-sections for 9 logarithmically spaced intensity thresholds (increasing from top to bottom). The L axis is in units of factors of 2, spanning a factor 2 =128 in scale (the largest scale being roughly 100km). The straight line behaviour indicates scaling (the slope $=-D_{xy}(T)$) and the variation in slope shows the multi-dimensional character of rain.

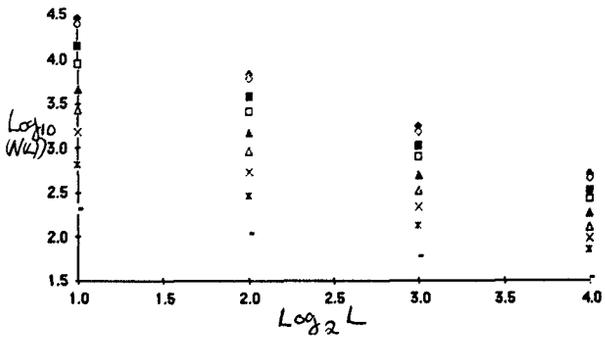

Fig. 2b: Same case as in 2a except now for horizontal and vertical spanning only factor of 8(x,y,z space).

Using the radar data from scans at 8 altitudes between heights of 2.5 and 12.5 km (the entire x,y,z scan is digitised on a 4 bit log scale in a period of roughly 3 minutes), we can similarly estimate $D_{xyz}(T)$ (the dimension of the whole fractal not just an x,y cross-section) for rain volumes in (x, y, z) space (Fig. 2b), although the range in scales is only 8 rather than 128, due to the limited vertical resolution of the radar.

Analysis of the differences in dimension is Fig. 2a and b is very interesting (see Lovejoy, Schertzer and Tsonis 1986), and shows that vertical stratification in rain is precisely of the sort predicted by GSI.

4. STOCHASTIC MODELS OF MONO AND MULTIDIMENSIONAL PHENOMENA:

Stochastic models of geophysical phenomena (Table 2 shows a summary) have been largely based on the addition of large numbers of elementary units (i.e. stochastic integration of various white noises - see Wilson, Lovejoy and Schertzer 1976, this volume for an illustrative example of a cloud model). In remote sensing, the most important use of such models is in the understanding of the scale and dimension dependence of the (non-linear) sensor averages. Such models are therefore likely to be indispensable in the calibration of remotely sensed information. Early models, such as those of terrain (Mandelbrot 1975), Fournier et al (1982), Voss (1983), while differing in details, are all

FRACTAL MODELS OF GEOPHYSICAL FIELDS:

MODEL:		TYPE:	INTERMITTENCY:	PHENOMENA:	REFERENCES:
Fractional Brownian Motion:	real space	additive, mono-dimensional	weak weak	surface relief, streamflow surface relief, hydrology	Mandelbrot (1975) Goodchild (1982)
	Fourier space	additive, mono-dimensional	weak	surface relief, clouds	Voss (1983)
Random mid-point displacement:		additive, mono-dimensional	weak	surface relief	Fournier et Al (1982)
Fractal Sums of Pulses Process:		additive, mono-dimensional	strong	rain and cloud areas, volumes and time series	Mandelbrot (1985), Lovejoy and Mandelbrot (1985)
Scaling Cluster of Pulses Process:		additive, mono-dimensional	strong	rain and cloud areas	Lovejoy and Schertzer (1985)
Cascades, Multiplicative Chaos:		multiplicative, multi-dimensional	strong	turbulent energy dissipation	Novikov and Stewart (1964) Mandelbrot (1974), Schertzer and Lovejoy (1983,1985)
				rain	Lovejoy and Schertzer (1985)

TABLE 2

characterised by weak (gaussian or quasi-gaussian) fluctuations and by a single fractal dimension. More recent models, such as the Fractal Sums of Pulses (FSP) process, or Scaling Clusters of Pulses process (SCP), were specifically designed to have extreme variability (hyperbolic, strong intermittency). Nevertheless, they are still mono-dimensional: i.e. the fractal dimension defined by lines of constant intensity (e.g. in terrain models, lines of constant altitude), is independent of the intensity. Schertzer and Lovejoy 1985b, argue that this monodimensionality is a general feature of additive processes. As pointed out above, the multiplicative processes leading to multiple dimensions are more general, and probably more interesting.

From the perspective of remote sensing, the most immediate manifestation of the difference between mono and multidimensionality, is in the behaviour of spatial and temporal averages. Mono-dimensional fields have statistical properties that depend on the scale over which they are averaged, because, as shown in Fig. 3, the fraction of space (dimension E) occupied by the fractal at scale L is proportional to L^{D_s-E} where D_s is the (unique) fractal dimension. Averages are thus decreasing functions of scale. Multiplicative phenomena have, in addition to scale dependence, dimensional dependence of averages. This may be understood by considering a particular iso-line defined by the threshold T with dimension $D_s(T)$. If the averaging is performed over a sufficiently sparse set (with dimension D_A low enough), then, with probability 1, they will not intersect. The precise condition (as well as the dimension of the intersection set) is shown in Fig. 4. Dimension dependence of statistical

SCALE DEPENDENCE OF MONO-DIMENSIONAL PHENOMENA:

(all iso-lines have same dimension - D_s)

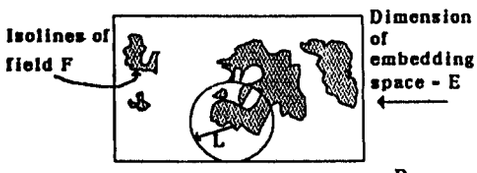

Volume on fractal: $\propto L^{D_s}$

Volume of space available: $\propto L^{E}$

Fraction on fractal: $\propto L^{E+D_s}$

($E>D_s$, hence small for large L)

$$\langle \bar{F} \rangle \sim \left(\text{fraction on fractal}\right) \times \left(\text{Value on fractal}\right)$$

$$\sim \underset{\substack{\uparrow \\ \text{strong scale dependence}}}{L^{E+D_s}} \times f(L)$$

FIG. 3

FIG. 4

THE INTERSECTION THEOREM:

Two sets, dim - D_1, D_2 embedded in a space dim - E, intersect on a set dim - D_I.

Define the *Co-dimension* C-E- D.

THEOREM:
$$C_I = \inf((C_1+C_2), E)$$

Ex. **Intersection in space (E-3) of two planes ($D_1 = D_2 = 2 \Rightarrow C_1 = C_2 = 1$)**

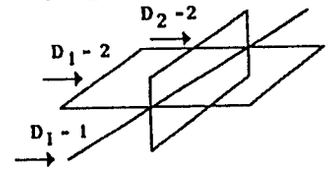

$$C_I = C_1 + C_2 - 2 \Rightarrow D_I = E - C_I - 1$$

FIG. 5

DIMENSIONAL DEPENDENCE OF MULTI-DIMENSIONAL PHENOMENA:

Here, $D_s(T_2) < D_s(T_1)$ for $T_2 > T_1$

Ex.

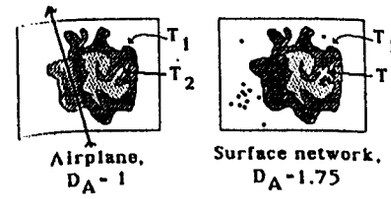

All intense regions with $C_s(T) > D_A$ are not included in averages (prob. = 1). Hence all statistical properties are both scale and dimension dependent.

averages now arises because, whenever the phenomenon is averaged over sets with dimension less than the maximum (E) some intense regions (with low dimension) are excluded, thereby altering the statistical properties (Fig. 5).

Section 5 shows that measuring networks do indeed have D<E (hence they exclude some extreme phenomena), and section 5 directly shown dimensional dependence in the rain field. Among their various uses, an important new one, is using fractal cloud models' for radiative transfer calculations. Preliminary results (Gabriel, Lovejoy, Austin and Schertzer 1986) show that the inhomogeneous distribution of cloud liquid water may explain the optical depth or "albedo" paradox.

5. THE DIMENSION OF INHOMOGENEOUS GEOPHYSICAL NETWORKS AND THE NEED FOR REMOTE SENSING:

The measuring stations of most in situ geophysical networks are spatially distributed in a highly inhomogeneous manner, being primarily concentrated on continents and population centres.

Lovejoy, Schertzer and Ladoy 1986 showed that this inhomogeneity can be simple consequence of the fact that the fractal dimension of the network D_m is less than the dimension (E) of the space in which it is embedded (its maximum possible value). To estimate D_m for a geophysical network (considered here as a set of points), a simple method which has been widely applied to strange attractors was used. For each station in the network, determine the number n(L) of other stations within various radii L of the point, and its average $\langle n(L)\rangle$ over all the stations. If the latter are distributed over a set with dimension D_m, then $\langle n(L)\rangle \propto L^{D_m}$. Scales L over which other (non-algebraic) behaviour occur define the characteristic lengths of the network. Lovejoy, Schertzer and Ladoy 1986 show that $D_m \sim 1.75$ for the 9563 stations in the world meteorological measuring network, over the range ~1 km to ~2000km.

6. CONCLUSIONS:

The first basic point of this paper is that in general, all the statistical properties of the spatial and temporal averages depend in a simple, power law manner on the scales over which they are averaged. Sufficiently small moments increase with scale, whereas, the high moments decrease. The intermediate power where the moments are independent of scale defines scale invariant quantities that are physically significant because they are conserved from one scale to another.

The simplest models of such behaviour are mono-dimensional -the intense and weak regions are characterised by the same fractal dimension. The discussion of these models brings out the second major point: the necessity of developing stochastic models of the sub-resolution scales of remote sensing devices. The understanding of extreme variability requires the developing stochastic fractal models, on the one hand to make the theory more precise, and on the other hand, in order to understand the details of the sampling, averaging and calibration of remotely sensed quantities. The third and last basic point in this paper, is that remotely sensed averages are not only scale dependent, but are also dimension dependent.

Even if we fix the scale, statistical properties will still be different if we compare e.g. averages along a line (D_A=1), or along a plane (D_A=2). The possibility of dimensional dependence is due to the recent discovery of (mathematical) measures with multiple fractal dimensions. Multidimensional phenomena are scale invariant, but with the more intense regions characterised by lower fractal dimensions than the weaker regions. In Section 3 we empirically establish the multiple fractal nature of the rain field by using radar data. Averaging over dimensions less that that of the full space/time in which the phenomena are embedded implies that in general, some of the most intense regions (with the lowest dimensions) will not be included in the averages. As we average over sets with lower and lower dimension, more and more of the intense regions are excluded, thereby modifying all the statistical properties. The significance of the dimensional dependence of averages is underlined by our study (Section 5) of the dimension of the global meteorological observing network. Over the range of at least 1 to ~2000 km the network (regarded as a set of points), has dimension ~1.75 (rather than the value 2 which it would have if it were uniform), indicating a clustering of stations (at all scales) about the various population centres.

This observation puts remote sensing in a new perspective: not only is it necessary in order to increase the density and rate of sampling but also in order to increase their dimension. Many of the analytical tools, models, and theoretical developments outlined in this paper, grew out of recent work in chaos, fractals and especially hydrodynamic turbulence. What these fields have lacked in the past, are copious sources relevant data spanning many orders of magnitude in scale. On the other hand, the remote sensing community has lacked systematic methods for dealing with extreme variability. We believe that it is now possible to end this dichotomy: for the first time, we have not only the quantity and quality of data and the necessary computing capacity, but also a growing variety of methods for systematically analysing and modelling. The consequences will undoubtedly be important for not only remote sensing, but also for turbulent and chaotic systems.

8. ACKNOWLEDGEMENTS:

We greatly benefitted from both discussions and encouragement from Peter Muller and Geoff Austin. We also acknowledge discussions with R. Cahalan, D.K. Lilly, B. Mandelbrot, R. Peschanski, J. Peyreire, M. Rafy. This work was partially supported by the Centre National de Recherches Scientifiques (ATP RA (85,).

9. REFERENCES:

Anselmet, F., Y. Gagne, E.J. Hopfinger, R.A. Antonia, 1984: High order velocity structure functions in turbulent shear flows. J. Fluid Mech., 140, 63-75.

Badi, R., A. Politi, 1985: Statistical description of chaotic attractors: The dimension function. J. of Stat. Phys., 40, 725-750.
Bills, B.G., M. Kobrick, 1985: Venus topography: a harmonic analysis. J. of Geophys. Res., 90 B1, 827-836.
Cahalan, A. Wiscombe, Joseph, 1984: Fractal clouds from LANDSAT imagery. Preprints, NASA, Greenbelt, Ma.
Deschamps, P.Y., R. Frouin, L. Wald, 1981: Satellite determination of the meso-scale variability of the sea-surface temperature. J. Phys. Ocean., 11, 864-870.
Fournier, A., D. Fussell, L. Carpenter, 1982: Computer rendering of stochastic models. Comm. of the ACM, 6, 371-384.
Gabriel, P., S. Lovejoy, G.L. Austin, D. Schertzer, 1986: Radiative transfer in extremely inhomogeneous fractal clouds. Proceedings, 6th Conf. of atmospheric radiation, May 12-16, Williamsburg, Va.
Gage, K.S., 1979: Evidence for a k-5/3 law inertial range in meso-scale two dimensional turbulence. J. Atmos. Sci., 36, 1950-1954.
Goodchild, M.F., 1982: the fractional brownian process as a terrain simulation model.
Grassberger, P., 1983: Generalised dimensions of strange attractors Phys. Lett., 97, 227-230.
Hentschel, H.G.E., I. Procaccia, 1983: The infinite number of generalised dimensions of fractals and strange attractors. Physica, 8D, 435-444.
Jones, J.G., R.W. Thomas, 1984: a statistical model for localised natural features in measure satellite imagery. RAE, Farnborough, Tech. Memo 339.
Kahane, J.P., 1985: Multiplicative chaos. (in preparation).
Kerchak, J., 1983: Deux types fondamentaux de distribution statistique. Bull. de l'Inst. inter. de stat., 3, 295-299.
Lilly, D., K., E.L. Petersen, 1983: Aircraft measurements of atmospheric kinetic energy spectra. Tellus, 35.
Lovejoy, S., 1981: A statistical analysis of rain areas in terms of fractals. Proc. 20th radar conf. AMS, Boston, 476-484.
Lovejoy, S., 1982: The area-perimeter relationship for rain and cloud areas. Science, 216, 185-187.
Lovejoy, S., B. Mandelbrot, 1985: Fractal properties of rain and a fractal model. Tellus, 37A, 209-230.
Lovejoy, S., D. Schertzer, 1985a: Extreme variability scaling and fractals in remote sensing: analysis and simulation. Digital Image processing in remote sensing, P.J. Muller Ed., Francis and Taylor, London, Ch. 14.
Lovejoy, S., D. Schertzer, 1985b: Scale invariance in climatological temperatures and the spectral plateau. Ann. Geophys., (in press).
Lovejoy, S., D. Schertzer, 1986: Scale invariance, symmetries, fractals and stochastic simulations of atmospheric phenomena. Bulletin of the AMS. (in press)
Lovejoy, S., D. Schertzer, 1985c: Generalized scale invariance in the atmosphere and fractal models of rain. Wat. Resour. Res. 1233-1250, 21.
Lovejoy, S., D. Schertzer, P. Ladoy, 1986: Fractal characterization of inhomogeneous geophysical measuring networks. Nature, 43-44, 319.
Lovejoy, S., D. Schertzer, T. Tsonis, 1986: Multiple (elliptical) fractal dimensions in rain (in preparation).
Mandelbrot, B., J.R. Wallis, 1969: Some long-run properties of geophysical records. Wat. Resour. Res., 5, 321-340.
Mandelbrot, B., 1974: Intermittent turbulence in self-similar cascades: divergence of high moments and the dimension of the carrier. J. Fluid. Mech., 62, 331-350.
Mandelbrot, B., 1975: Stochastic models for the earth's relief, the shape and fractal dimension of coastlines, and the number-area rule for islands. Proc. Nat. Acad. Sci. USA, 72, 2825-2828.
Mandelbrot, B., 1982: the fractal geometry of nature. New York, Freeman and Co., 461pp.
Mandelbrot, B., 1984: Fractals in physics: squigs, clusters, diffusions, fractal measures and the unicity of fractal dimensionlity. J. Stat. Phys., 34, 895-930.
Mandelbrot, B., 1985: Fractal sums of pulses and new random variables and functions (available from the author).
Mark, D.M., P.B. Aronson, 1984: Scale-dependent fractal dimensions of topographic surfaces: an empirical investigation, with applications in geomorphology and computer mapping. Math. Geo., 16, 671-683.
Marshall, J.S., W.M. Palmer, 1948: The distribution of raindrops with size. J. Met., 5, 165-169.
Nastrom, G.P., K.S. Gage, 1983: A first look at wave-number spectra from GASP data. Tellus, 35, 383-390.
Nicolis, C., G. Nicolis, 1984: Is there a climate attractor? Nature 311, 529-532.
Novikov, E.A., R. Stewart, 1964: Intermittency of turbulence and spectrum of fluctuations of energy dissipation. Izv. Akad. Nauk. SSSR Ser. Geofiz., 3, 408-412.
Parisi, G., U. Frisch, 1985: A multifractal model of intermittency. Proc. of the inter. school of physics "Enrico Fermi", course 88: Turbulence and predictability in geophysical fluid dynamics and climate dynamics, M. Ghil et al Eds., 84-88.
Peleg, S., J. Naor, R. Hartley, D. Anir, 1984: Multiple resolution texture analysis and clasification. IEEE Trans. on PAMI., 6, 518-523.
Pentland, H., 1984: Fractal based description of natural scenes. IEEE Trans on PAMI, 661-674.
Rothrock, D.A., A.S. Thorndike, 1983: Sea ice flow size distribution. J. of Geophys. Res.
Schertzer, D., S. Lovejoy, 1983: On the dimension of atmospheric motions. Preprint vol., IUTAM symp. on turbulence and chaotic phen. in fluids, 141-144.
Schertzer, D., S. Lovejoy, 1984a: The dimension of atmospheric motions. Turbulent and chaotic phenomena in fluids, Ed. T. Tatsumi, North Holland.
Schertzer, D., S. Lovejoy, 1984b: Les fractales dans l'atmosphere. Sciences et Techniques, 5, 69-72.
Schertzer, D., S. Lovejoy, 1985a: The dimension and intermittency of atmospheric dynamics. Turbulent Shear Flow, 4, 7-33, B. Launder Ed., Springer, New York.
Schertzer, D., S. Lovejoy, 1985b: Generalised Scale Invariance in turbulence. PCH Journal, 623-635, 6
Voss, R.F., 1983: Fourier synthesis of gaussian fractals: 1/f noises, landscapes and flakes. Preprints Siggraph conf., Detroit, 1-21.
Wilson, J., S. Lovejoy, D. Schertzer: An intermittent wave packet model of clouds and rain (in this volume).
Schertzer, D., S. Lovejoy, 1986: Generalised Scale invariance and anisotropic inhomogeneous fractals in turbulence. Fractals in Physics, Pietronero Ed., North-Holland (in press).

Oceanic Rain Retrievals from Satellite Passive 37 GHz Scattering Measurements

Roy W. Spencer
Universities Space Research Association
NASA/Marshall Space Flight Center
Huntsville, Alabama 35812

1. INTRODUCTION

The satellite microwave retrieval of oceanic rain rates has usually exploited the warm emission signal that rain presents in front of the radiometrically cold (reflective) ocean background. This warming was quantified at 19.35 GHz by Wilheit et al. (1977) in what will be referred to here as an "emission" method (Fig. 1). In this technique, as a rain layer becomes increasingly opaque (due to the increased number density and drop size as the rain rate increases), the cold ocean surface becomes gradually obscured.

Unfortunately the emission method has two major disadvantages. First, it is nonlinear due to saturation of the signal at 19 GHz. As a result, various rain rates existing within a single satellite footprint produce an average brightness temperature (T_B) which corresponds to a rain rate with a low bias. Footprints on the order of a few kilometers in diameter are needed to alleviate this problem. Secondly, the single channel emission method can not discriminate between the emissions from non-precipitating clouds and rain. Even though the cloud induced warming is only about 20% to 30% of what rain produces at a given liquid water content at 19 GHz (Fig. 1), the cloud contamination problem is magnified by the proportionately greater number of clouds that do not precipitate.

Here I will outline a method for estimating the degree to which the T_B has been affected by scattering, which at 37 GHz is only due to precipitation size hydrometeors (especially ice). Based upon numerous comparisons between radar derived rain rates and radiances measured by the Nimbus 7 Scanning Multichannel Microwave Radiometer (SMMR), it has been demonstrated that precipitation over land can be estimated based upon the degree to which T_B over land are depressed below the radiometrically warm land background levels (Spencer et al., 1983a ; Spencer et al., 1983b; Spencer, 1984). This correlation is due to the scattering of the upwelling land radiation by, primarily, precipitation size ice hydrometeors which, in turn, are a significant part of the rain formation process.

This technique is not directly transferable to the ocean because the ocean background is already at a lower T_B than most rain system ice canopies could ever achieve. However, because the ocean emitted radiation is highly polarized (e.g. Weinman and Guetter, 1977) while the radiation scattered by the ice is only slightly polarized it is possible to distinguish between the two T_B depressing phenomena when polarization information is used.

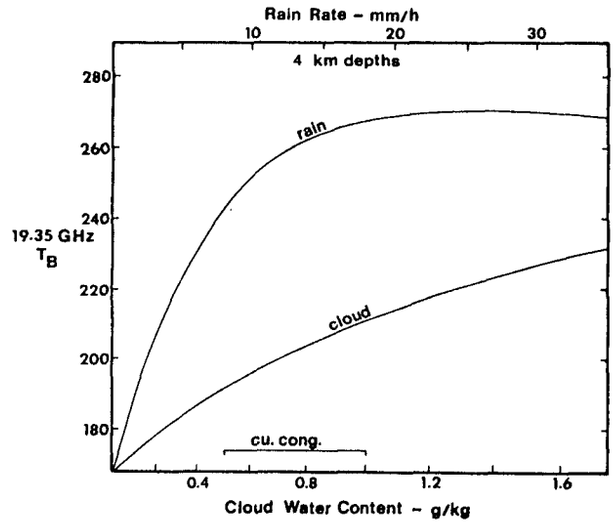

Fig. 1 The 19.35 GHz brightness temperature signature of rain (Wilheit et al., 1977) and cloud with the same liquid water contents over an ocean background.

2. THE SCATTERING METHOD

If we consider the horizontally and vertically polarized brightness temperatures (T_B^h and T_B^v) measured by the SMMR at 37 GHz, and display them as a difference and average, we find that the ocean surface is cold and highly polarized (the point in the lower right hand portion of Fig. 2). The thermal emission by non-precipitating clouds (which do not scatter at 37 GHz), in contrast, is warm and unpolarized. The SMMR data show a well defined trend, as depicted by the solid line in Fig. 2 labeled "emission", indicating various amounts of footprint coverages of clouds with an average "effective radiating temperature" (ERT) of about 273 K. Model calculations indicate that various footprint coverages of cumulus congestus clouds of 7 km vertical extent and 0.50 g/kg cloud water content can explain these observations. Other cloud types can also

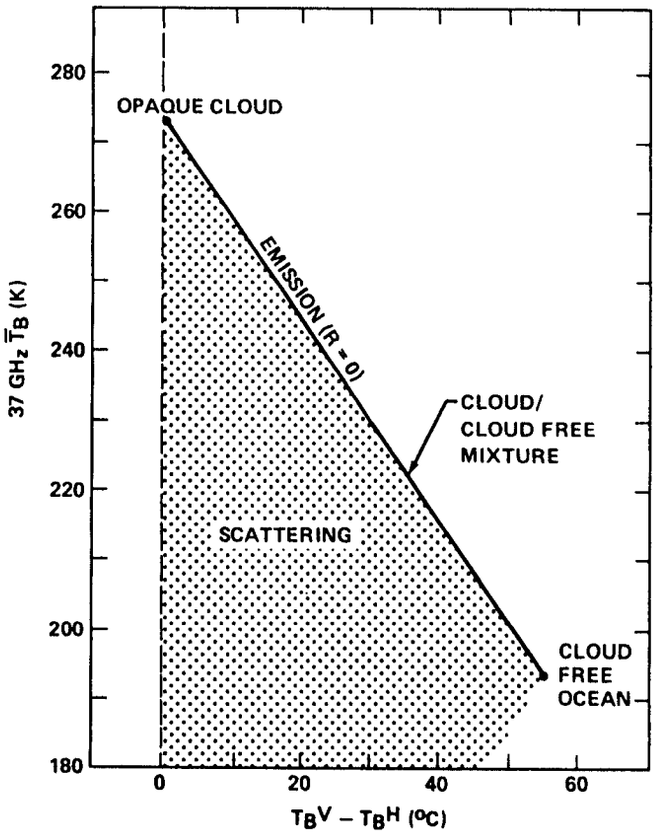

Fig. 2 Bipolarization plot of 37 GHz T_B vs. rain rate illustrating the effects that emission and scattering have on the dual polarized radiances.

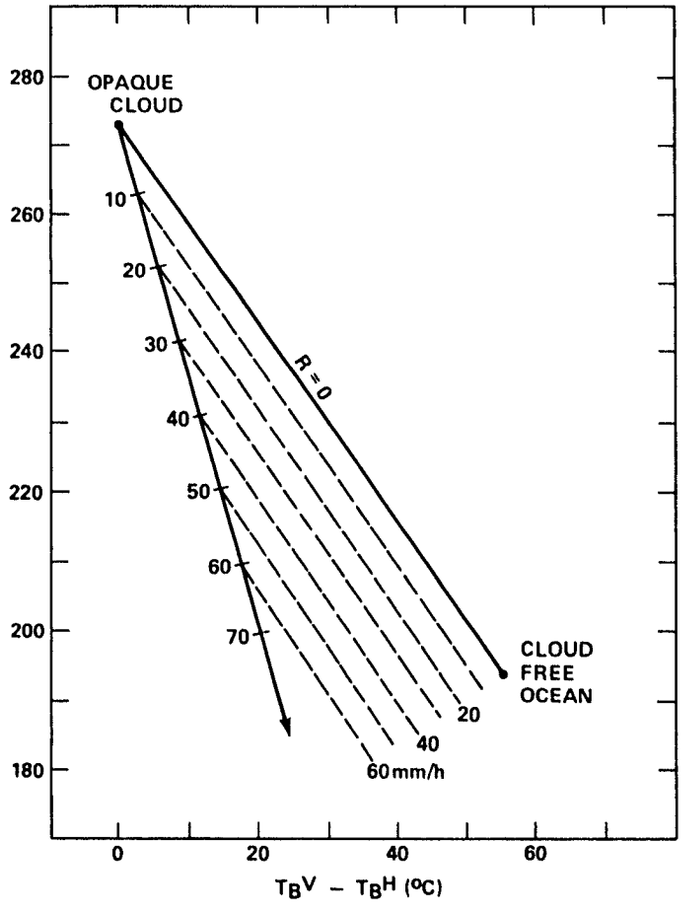

Fig. 3 Bipolarization plot of both the zero rain rate (emission only) line from Fig. 2 and the observed relationship between U.S. summertime WSR-57 radar rain rates and SMMR T_B. From these two lines, a family of rain rate lines result which uniquely assign a footprint average rain rate to a given dual-polarized T_B measurement.

explain these data.

Here we assume that any observations below this emission (zero rain rate) line represent contributions by scattering and thus a non-zero rain rate. Because the average relationship observed over land between SMMR T_B and radar derived rain rates is linear in rain rate, it can be shown analytically that any given satellite observed pair of T_B^h and T_B^V correspond to a unique footprint averaged rain rate (Fig. 3). In terms of the SMMR T_B, the relationship in equation form is

$$R = a(b*T_B^h - T_B^V + c) \qquad (1)$$

where "a" has a value of 2.5 for rain clouds similar to those observed over the U.S. during summer; "b" approximately equals 0.5; and c is approximately 137. Because of the method's linearity, there are no nonlinear "footprint filling" (or, more accurately, "footprint averaging") effects. Also, because the cloud emission effect is removed, and since only precipitation size hydrometeors cause significant scattering at 37 GHz, there is little cloud contamination. There are, nevertheless, limitations which will be discussed later.

3. RADAR TEST OF THE SCATTERING ALGORITHM

The scattering algorithm represented by Fig. 3 and Eq. 1 was tested on a total of five cases where the SMMR and U.S. National Weather Service WSR-57 radars simultaneously viewed convection over the Gulf of Mexico during 1979. This is but a small sample of all cases that would be available for analysis.

The image pairs in Fig. 4 reveal the results of the comparisons. The images indicate considerable similarity between the radar reflectivity

Fig. 4 An independent test of the 37 GHz scattering algorithm with radar and SMMR data from five dates during 1979 over Gulf of Mexico coastal waters. Dates and radars included are (a) 20 April, Galveston, TX and Lake Charles, LA; (b) 11 July, Apalachicola, FL; (c) 17 July, Apalachicola, FL; (d) 27 September, Miami and Key West, FL; and (e) 1 October, Miami, FL. Both SMMR and radar images were low pass filtered to reduce noise in the SMMR data and to reduce the resolution of the radar data consistent with the SMMR resolution (25 km). Only oceanic data within the scans of the radar and SMMR are included. Brightness levels correspond to increments of 4 mm/h, starting at 4 mm/h, with recycling to black at 20 mm/h.

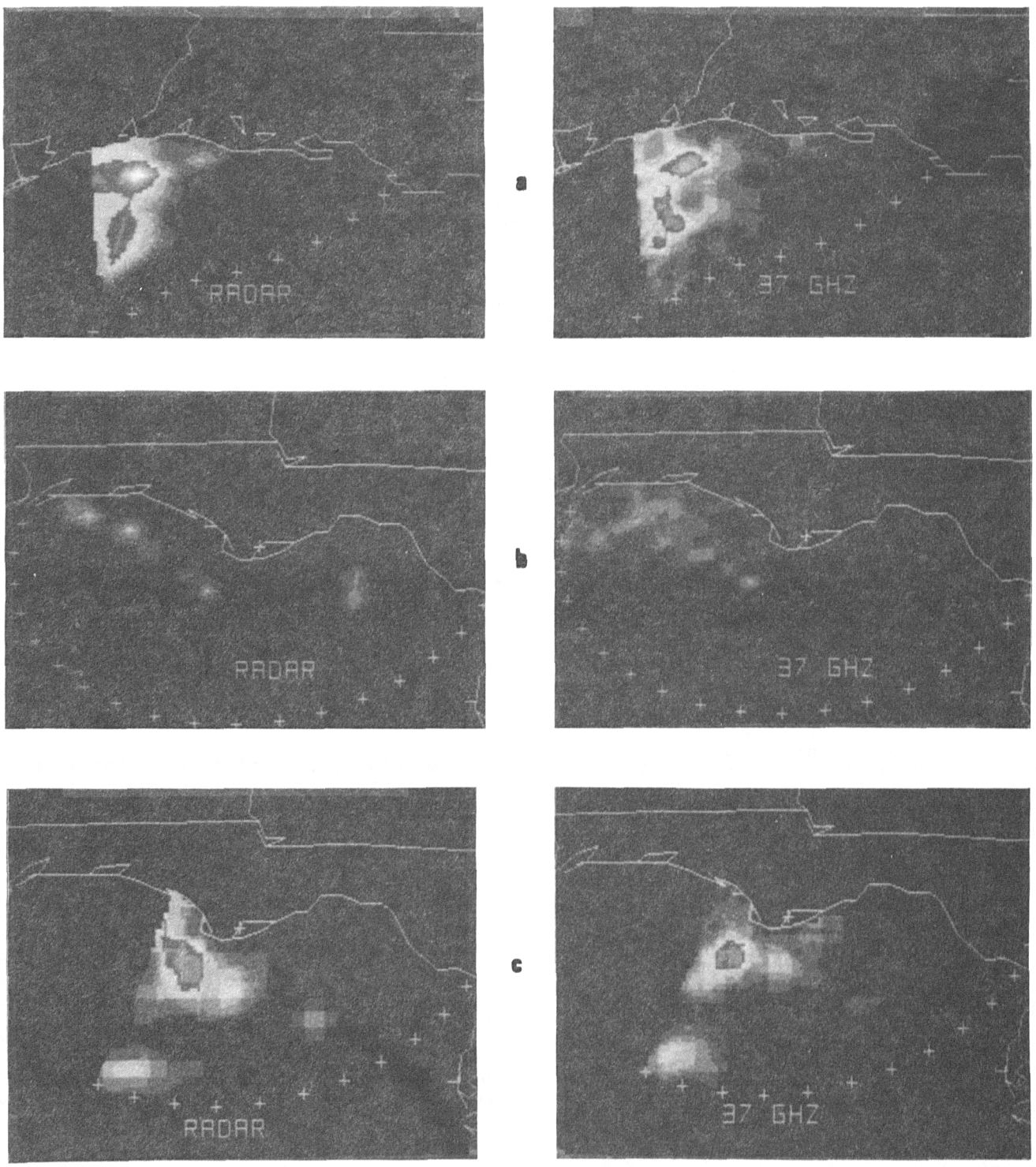

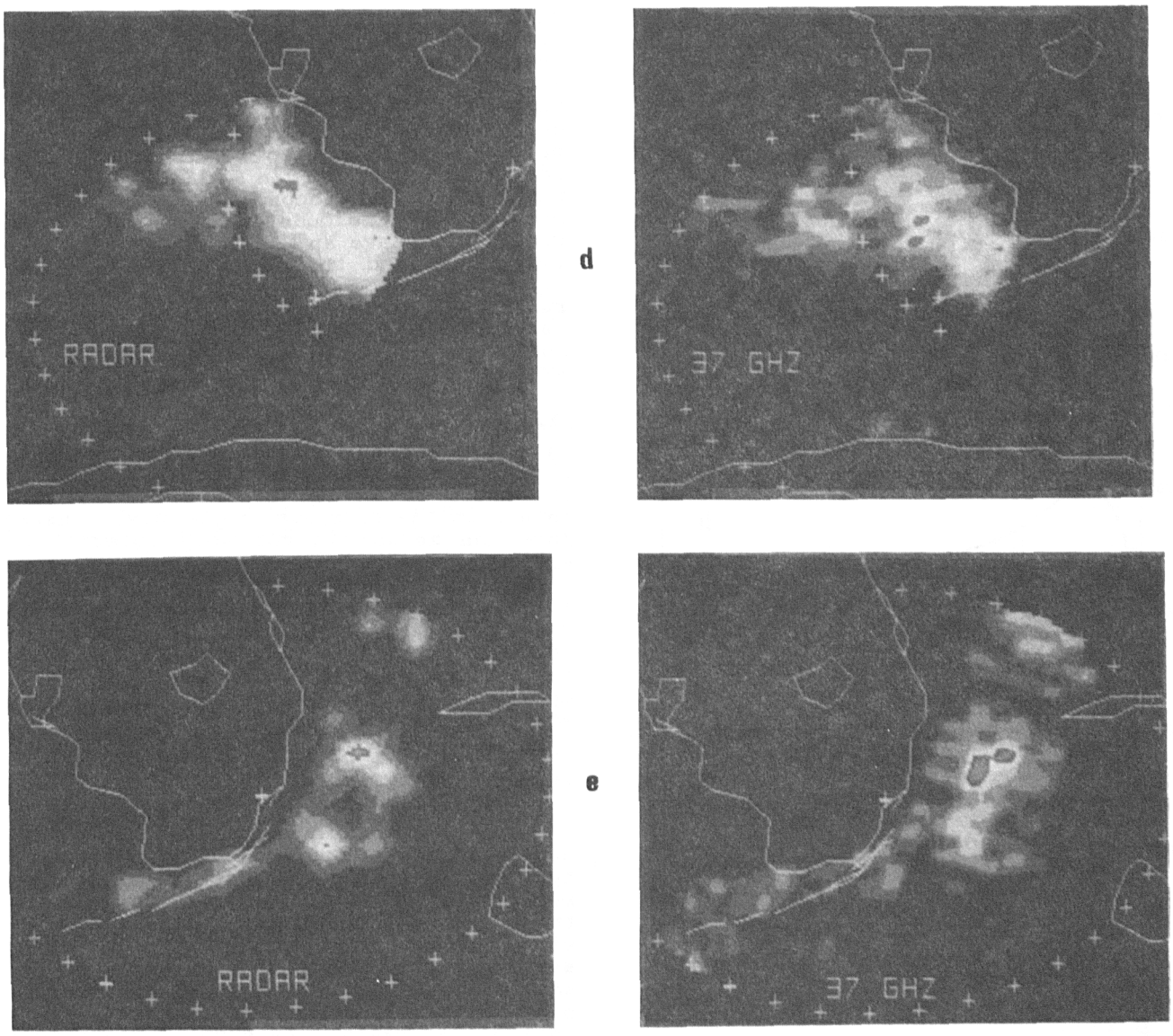

derived rain rates and the radiometer derived rain rates. These images represent an overall 0.90 correlation when the images are sampled within the radar and SMMR scans at 40 km resolution.

4. REEVALUATION OF THE RESULTS OF SPENCER, HINTON, AND OLSON (1983)

Spencer et al. (1983c) showed that the 37 GHz liquid phase plane-parallel models are not adequate to explain the observed relationships they found between radar derived rain rates and SMMR T_B at individual polarizations. However, if we fit the data they presented for one channel (Fig. 5a) and input this relationship into Eq. 1 to obtain a relationship for the other channel (Fig 5b) we find that the trend exhibited by the data is well explained. Therefore, the data presented in the previous study can be explained as a combination of the effects of partial footprint coverage and scattering by ice. It must be emphasized that the two parameter graphs exhibited in Fig. 5 do not replace the three parameter graph in Fig. 3 because it is not possible to deduce the footprint coverage and scattering effects with data from a single channel alone. It would seem that 37 GHz liquid phase algorithms are not suitable for rain rate retrievals unless (1) a warm rain process dominates the precipitation formation and (2) the footprints are sufficiently small to preclude substantial variations in rain rate within the footprint.

5. LIMITATIONS

There are several limitations to using the 37 GHz scattering method by itself for measuring oceanic precipitation rates.

First, the amount of scattering measured at 37 GHz is only a first approximation to the amount of rain

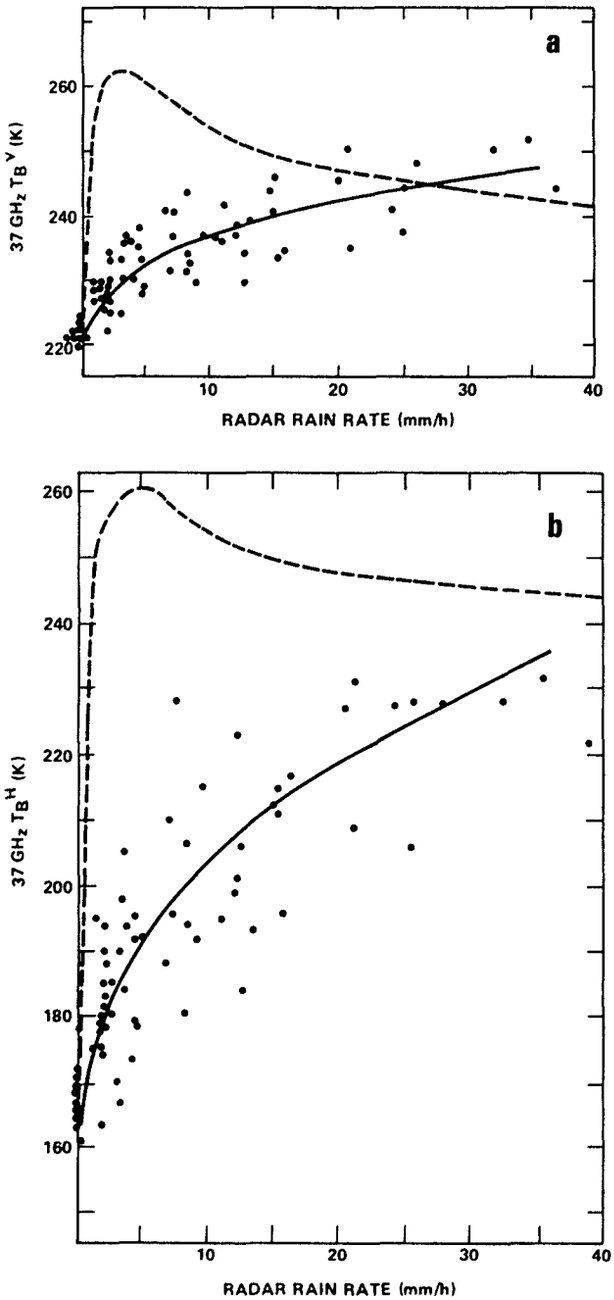

Fig. 5 Application of the 37 GHz scattering method (Fig. 3 or Eq. 1) to the data of Spencer, Hinton, and Olson (1983c). The solid line represents liquid phase plane-parallel relationships. A line was fitted to the observed radar and vertically polarized SMMR T_B data (a), then horizontally polarized T_B were computed through Eq. 1 to arrive at the curve shown through the points in (b). This illustrates that these previously published data can be interpreted in terms of the scattering algorithm, which allows for unfilled footprints and stronger scattering than can be reasonably accounted for with liquid phase models alone.

falling out of the bottom of the cloud. We have already found that tropical rain systems exhibit less scattering than mid-latitude systems. This is probably due to the warmth and relatively weak updrafts associated with tropical convection. This problem would lead to regional biases if the variable "a" in Eq. 1 is kept constant. Secondly, the ERT of non-precipitating clouds can vary. High clouds will have an ERT lower than that of low clouds and thus a greater chance of being misdiagnosed as rain. However, cirrus clouds (even thick ones) have been observed to be essentially transparent over both land and ocean based upon analyses of SMMR 37 GHz data.

Third, the scattering signal at 37 GHz is relatively weak. From Eq. 1 it is evident that, for rain systems like those in the U.S. during summer, a change of 1° in T_B^V leads to a 2.5 mm/h change in the retrieved rain rate. Therefore the method is not very tolerant of errors in the measured T_B.

Despite these limitations, the results demonstrated in Fig. 4 reveal that there is information obtainable concerning the precipitation rate within oceanic rain systems based upon 37 GHz estimates of volume scattering.

6. IMPLICATIONS

The current method is not suggested as a replacement for emission type methods for oceanic precipitation retrievals. Rather, it could supplement those methods, particularly with information on the more intense precipitating systems where the 19 GHz emission method saturates. It should also provide useful microphysical information on rain systems on a global basis. As such it might help give insight into the conditions accompanying ice formation within precipitation systems.

The author also feels that the problems associated with the 19 GHz emission method might be alleviated if lower frequency observations (e.g. at 6 and 10 GHz) were used together. This should allow partial separation between the cloud and rain signals, as well as provide a more linear relationship through a greater dynamic range of rain rates.

ACKNOWLEDGMENTS

Dr. Norman Grody helped in the technique development and provided the radiative transfer code for the cloud calculation in Fig. 1. This research was supported by NASA contract NAS8-34767.

REFERENCES

Spencer, R.W., W.S. Olson, W. Rongzhang, D.W. Martin, J.A. Weinman, and D.A. Santek, 1983a: Heavy thunderstorms observed over land by the Nimbus 7 Scanning Multichannel Microwave Radiometer. J. Climate Appl. Meteor., 22, 1041-1046.

Spencer, R.W., D.W. Martin, B.B. Hinton, and J.A. Weinman, 1983b: Satellite microwave radiances correlated with radar rain rates over land. Nature, 304, 141-143.

Spencer, R.W., B.B. Hinton, and W.S. Olson, 1983c: Nimbus-7 37 GHz radiances correlated with radar rain rates over the Gulf of Mexico. J. Climate Appl. Meteor., 22, 2095-2099.

Spencer, R.W., 1984: Satellite passive microwave rain rate measurement over croplands during spring, summer, and fall. J. Climate Appl. Meteor., 23, 1553-1562.

Weinman, J.A., and P.J. Guetter, 1977: Determination of rainfall distributions from microwave radiation measured by the Nimbus-6 ESMR. J. Appl. Meteor., 16, 437-442.

Wilheit, T.T., A.T.C. Chang, M.S.V. Rao, E.B. Rodgers, and J.S. Theon, 1977: A satellite technique for quantitatively mapping rainfall rain rates over the oceans. J. Appl. Meteor., 16, 551-560.

8.3

MODEL-BASED RETRIEVAL OF TROPICAL CYCLONE RAINFALL RATES USING THE NIMBUS-7 SMMR

William S. Olson

Department of Meteorology/
Space Science and Engineering Center
University of Wisconsin-Madison 53706

1. INTRODUCTION

Methods for inferring the intensity and distribution of hurricane rainfall have for many years been a focus of research efforts in tropical cyclone meteorology. According to most theories, the latent heating mechanism is a critical factor in tropical cyclone genesis/intensification and is responsible for much of the kinetic energy production in mature storms (Palmén and Newton, 1969). Tropical cyclone forecasts might be improved if latent heating distributions could be included in model initialization schemes (Anthes, 1982).

To the present most tropical cyclone rainfall data have been derived from raingauge and radar measurements. Limited spatial coverage is probably the most serious drawback of these measurement systems. Raingauges and land-based radar can provide hurricane rainfall data only if the storm is within reasonable proximity of coastal or island stations. Although aircraft radar can be used to make rainfall measurements in the storm locality, the span of continuous coverage is limited to the aircraft flight time.

Satellite-borne microwave radiometers, including the Nimbus-7 Scanning Multichannel Microwave Radiometer (SMMR), have shown utility in retrieving rainfall distributions and intensities over the oceans (Savage and Weinman, 1975; Wilheit, et al., 1977; Spencer, et al., 1983a) and have the potential for global coverage of storms. However, a main difficulty in the retrieval algorithms so far proposed has been the apparent ambiguity between rain intensity and spatial extent which can lead to several estimates of area-averaged rainfall rate within a SMMR footprint, given a brightness temperature (intensity) measurement in only one channel. This is a particular problem in storms which contain regions of stratiform rainfall, for which the intensity and areal extent of rain may be uncorrelated. Also, the sensitivity of the highest-resolution SMMR channels (37GHz) to variations in rain liquid water content appears to depend upon the relative numbers of rain drops and precipitation-sized ice particles present in the precipitating cloud (Spencer, et al., 1983b).

Tropical cyclones are characterized by both convective and stratiform rain regions. In areas of downdraft or stratiform rainfall significant numbers of ice particles may be present, although the vast majority have diameters less than .5 mm (Black, pers. comm.). These observations suggest that the full multichannel capability of the SMMR should be explored in the context of rain rate retrievals in hurricanes.

2. RETRIEVAL METHOD

A model-based rainfall rate retrieval method which can incorporate any or all of the SMMR brightness temperature measurements is developed in this section. In order to facilitate the multispectral procedure, the SMMR data from each channel are first spline-interpolated to a common cartesian grid at 22.2 km spacing. For each scene of interest a 6° latitude x 6° longitude domain of gridded brightness temperatures is thus created within the SMMR swath boundaries.

At each gridpoint i,j the SMMR-observed brightness temperature in channel m is modeled as

$$TBobs_{mij} = [A_m * TBmod_m(LWC,f)]_{ij} + e_{mij} , \quad (1)$$

where $TBmod_m(LWC,f)$ is the model average brightness temperature in channel m upwelling from a 22.2 km x 22.2 km box centered on the gridpoint, A_m is the antenna spatial response function for channel m, and the notation * indicates the two-dimensional discrete convolution. Each observation is therefore modeled as a weighted average of the high-resolution "data" represented by $TBmod_m$ within the sensor field of view. A_m can be regarded as an analog for the antenna power pattern in the discrete domain. The residual e_{mij} is the error between the modeled and observed brightness temperatures.

The solution of the rain retrieval problem is obtained by minimizing the mean square error between the modeled and observed brightness temperatures as a function of the unknown total cloud liquid water contents LWC_{ij} and cloud filling fractions f_{ij} in all grid boxes:

$$\min_{\substack{LWC_{ij} \\ f_{ij}}} \sum_{i,j} (e_{mij})^2 = \min_{\substack{LWC_{ij} \\ f_{ij}}} \sum_{i,j} (TBobs_{mij} - [A_m * TBmod_m(LWC,f)]_{ij})^2 . \quad (2)$$

All other geophysical parameters are prescribed in the model. The minimization of the mean square error in

Eq. (2) is performed iteratively using a method of conjugate gradients described in Shanno (1978). If the brightness temperature and antenna response models presented below are incorporated into Eq. (2), then the error is typically reduced to near noise level, about 3 K r.m.s., after 10 iterations by the method of conjugate gradients.

Once the fields of LWC and f are determined, the area-averaged rainfall rate for each grid box is computed from

$$\bar{R} = \begin{cases} R(LWCpc)\cdot f\ , & f \leq 1 \\ R(LWCpc)\ , & f > 1 \end{cases} \qquad (3)$$

where the rain rate R is computed assuming the Merceret (1974) hurricane drop-size distribution for a precipitation liquid water content LWCpc. The quantity LWCpc is parameterized

$$LWCpc = \begin{cases} 0\ , & LWC \leq LWCnpc \\ LWC - LWCnpc, & LWC > LWCnpc\ . \end{cases} \qquad (4)$$

Here, LWCnpc is the prescribed maximum liquid water content of non-precipitating cloud; i.e., all cloud liquid water in excess of LWCnpc is considered precipitating water.

3. RETRIEVAL MODEL

The complete derivation of the radiative transfer model for $TBmod_m$ can be found in Olson (1986), and so only the basic features of the model will be described here. A vertical x-z cross-section of the model geometry is presented in Fig. 1. In the vertical the atmosphere is divided into three layers separated by the freezing level h_0 and the cloud top level h. The top of the atmosphere is defined by h_T. Within each of the three layers molecular absorbers are distributed uniformly. The air temperature is assumed to decrease linearly with height. The cuboidal cloud (length and width equal to s) contains precipitating and non-precipitating liquid droplets below h_0, and precipitation-sized ice particles between h_0 and h. Rain drops and ice particles are assumed to be uniformly distributed within their respective domains and are constrained to have the same size distribution. The surface emissivity/reflectivity is expressed as a function of the surface friction velocity according to the parameterization of Wentz (1983).

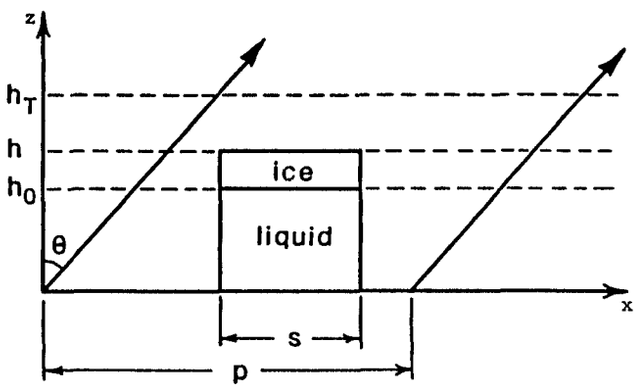

Fig. 1. Cross-section of the radiative transfer model geometry.

The contribution of precipitation-scattered microwave radiances to the source term of the radiative transfer equation is approximated by the 1-dimensional Eddington solution for a horizontally infinite cloud. Radiances upwelling at the SMMR viewing angle θ are numerically integrated over the domain of the grid box (length and width p) and are then normalized by the projected box area $p^2 \cos\theta$ to yield the grid box-averaged upwelling brightness temperature $TBmod_m$.

Note that the cloud filling fraction is defined by

$$f = s^2/p^2 \qquad (5)$$

in the model.

By parameterizing the liquid/ice hydrometeor extinction coefficients and single scatter albedoes as power-law functions of rainfall rate R, the brightness temperature model presented here can be adjusted to agree within approximatey 1 K r.m.s. of precise model formulations in the limit of a horizontally infinite cloud ($s \rightarrow \infty$).

Model output brightness temperatures at 37 GHz in the vertical polarization for a typical hurricane atmosphere are plotted as functions of grid box-averaged rainfall rate for different filling fractions in Fig. 2a. In this figure h = h_0 = 4.8 km, and a non-precipitating cloud with a liquid water content equal to .4 gm/m^3 is assumed at zero rainfall rate. The model output may be compared to the scatter plot of SMMR-observed brightness temperatures vs. box-averaged rainfall rates derived from digital radar coverage of three hurricanes (Fig. 2b). Based upon several model runs, a general consistency between model output and observations was found for h_0 equal to 4.8 km, values of h between 4.8 and 5.8 km, and LWCnpc equal to .4 gm/m^3. Note that most of the observed 37 GHz brightness temperatures corresponding to significant rain rates cluster in the range of model-designated f values between .6 and 1.0, and that there is no obvious correlation between f and $\bar{R}$ in the data. These data features, and the apparent lack of sensitivity of the 37 GHz brightness temperatures to variations in rainfall rate at rain rates

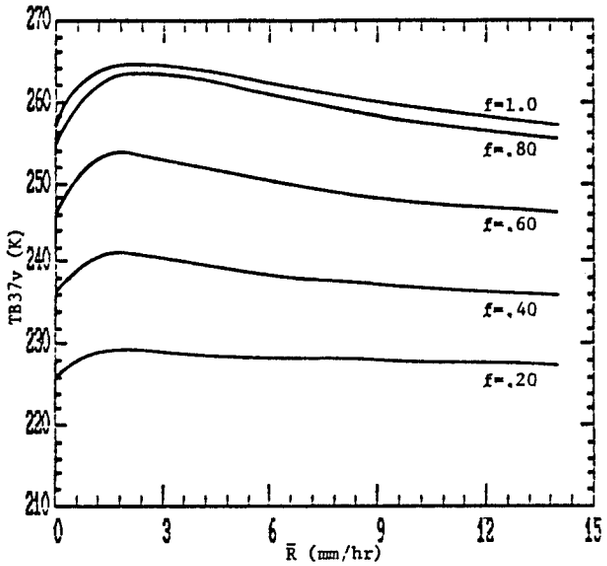

Fig. 2a. Model-computed, 37 GHz vertically-polarized brightness temperatures for various cloud filling fractions versus grid box-averaged rainfall rate.

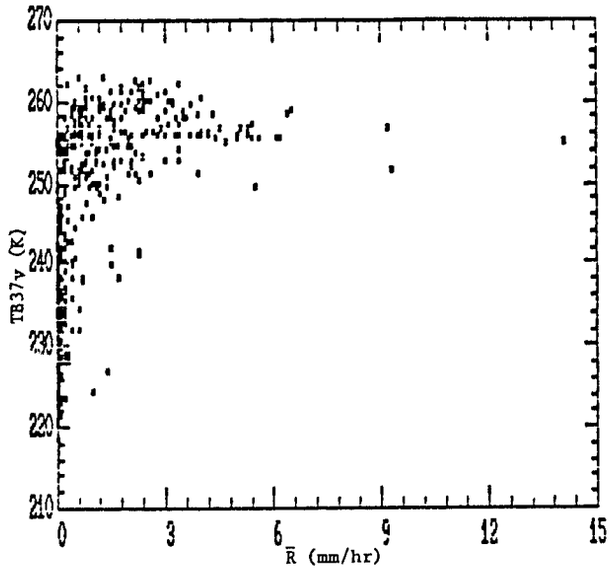

Fig. 2b. SMMR-observed, 37 GHz vertically-polarized brightness temperatures from three hurricanes versus radar-derived, grid box-averaged rainfall rate.

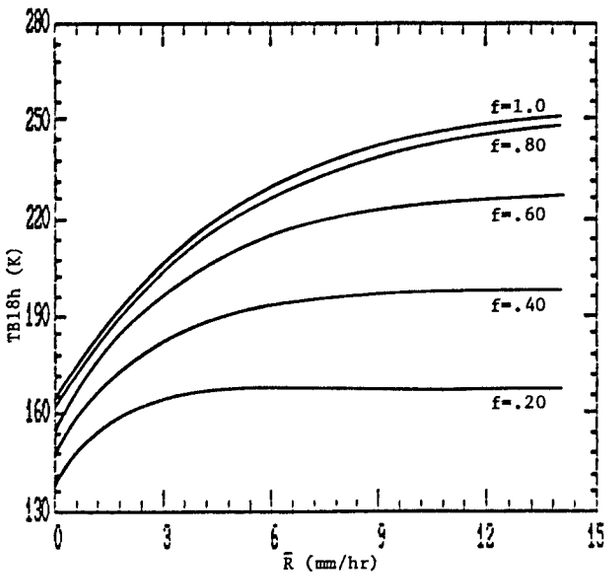

Fig. 2c. Model-computed, 18 GHz horizontally-polarized brightness temperatures for various cloud filling fractions versus grid box-averaged rainfall rate.

greater than roughly 3 mm/hr suggest that more than one channel/frequency is required to obtain a unique estimate of rainfall rate. Additional information could be provided by the 18 GHz channels, for which the model curves of the horizontally-polarized brightness temperature component are shown in Fig. 2c. Note that the brightness temperature sensitivity to rainfall rate extends through a much greater range of rainfall rates for this channel.

The antenna response functions A_m were originally estimated by studying the resolution degradation of synthetic, high-resolution coastline imagery by prospective Gaussian response functions. The degraded imagery was compared to SMMR imagery of actual coastlines with the same contour and brightness temperature dynamic range as the synthetic data. For each channel, the best-estimate Gaussian response function was found to have a half power width nearly equal to the reported mean footprint dimension of the SMMR in that channel (ref. Gloersen and Barath, 1977). As a result, the response functions A_m selected for this study are symmetric, two-dimensional Gaussians with half-power widths equal to the mean footprint dimensions of the Nimbus-7 SMMR.

4. RESULTS

The SMMR rain retrieval method was employed to derive grid box-averaged rain

rates in Hurricane David using data from the Nimbus-7 overpass at 1644Z, 9/3/79 (Fig. 3a). At that time the storm was making its landfall on the eastern Florida coast about 100 km north of Miami. In this particular retrieval, data from only the 37, 21, 18 and 10.7 GHz channels of the SMMR were employed (see Eq. 2). Typical values of h (4.8 km), h_o (4.8 km) and LWCnpc (.4 gm/m^3) were specified in the retrieval model. Coincident WSR-57 radar coverage of David from the Miami station was utilized to produce the adjoining figure (Fig. 3b). In this figure, digital recordings of radar reflectivity were converted to equivalent rainfall rate using the Z-R relationship of Jorgensen and Willis (1982), and were then area-averaged within the SMMR grid boxes. For display purposes both rain fields were median filtered and then thresholded at trace, 2 mm/hr, and 8 mm/hr levels. Land areas including extreme eastern Florida and Andros Island are indicated by a stipple pattern. In Fig. 3b, the range limit of recorded radar data is shown by a range marker.

Overall, the figures indicate reasonable agreement between the patterns and intensities of the SMMR- and radar-derived rain fields. Also the structure of the eyewall and rainbands in the SMMR rain field is consistent with tropical cyclone climatology.

At radar ranges greater than about 140 km, however, the SMMR rain rate estimates appear to be positively biased with respect to the radar measurements (Fig. 4). It is difficult to draw any conclusions based upon the small sample of data presented here, but the probable cause of this discrepancy is the effect of partial radar beam filling by rain, as the beam exceeds the height of the rain layer at long range (NOAA, 1979). If a rain layer height of 4.8 km is assumed, then the Miami radar beam as defined by its half power width would begin to overshoot the rain layer at roughly 146 km range. Beyond this range, only a fraction of the radar beam would be filled by rain, which would result in an underestimate of the rainfall rate based upon the power received by the radar. The plot in Fig. 4 seems to reflect this range-dependent, negative radar bias. The scatter of points seen at long range would indicate rain height variations, which affect beam filling.

5. CONCLUDING REMARKS

Incorporating brightness temperature data from the 37 - 10.7 GHz channels of the Nimbus-7 SMMR, the multispectral, model-based retrieval method presented in this study yields tropical cyclone rain rate estimates which are in reasonable agreement with radar observations. Discrepancies between SMMR and radar rain estimates observed at radar ranges greater than ~140 km suggest that CAPPI (volume scan) radar should be used for

Fig. 3a. SMMR-derived rainfall rates in Hurricane David at 1644Z, 9/3/79. Stippling indicates land areas, where the retrieval method does not apply.

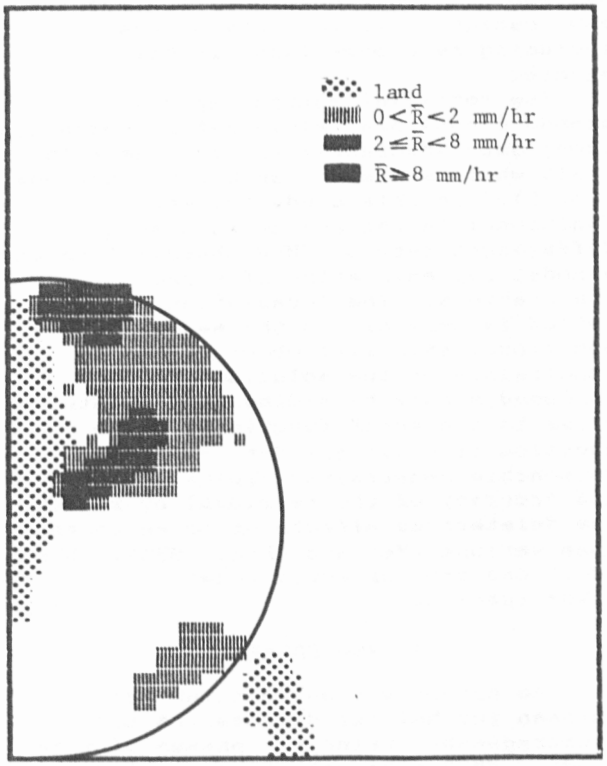

Fig. 3b. Radar-derived rainfall rates in Hurricane David at 1644Z, 9/3/79. A marker indicates the maximum range of the data.

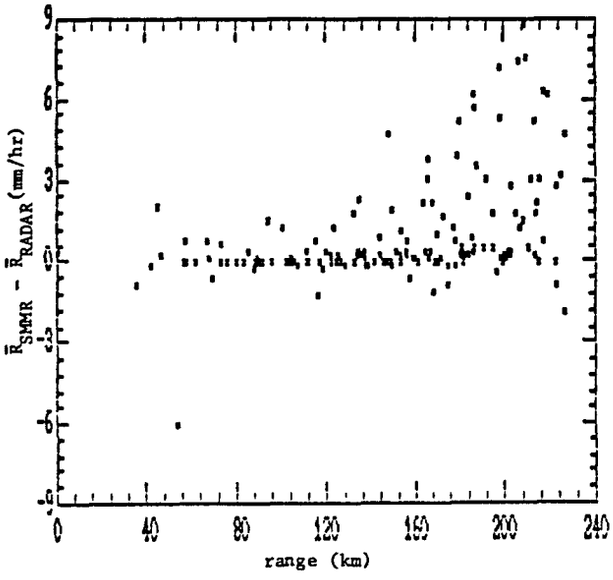

Fig. 4. Difference of SMMR- and radar-derived rainfall rates in Hurricane David (16442, 9/3/79) versus radar range.

retrieval method calibrations in order to avoid radar beam-filling problems.

The focus of this research has been on tropical cyclone rain rate retrievals. Since the retrieval method is model-based, it can be recalibrated for other kinds of precipitation systems, given some notion of the physical structure and environment of those systems. A modification of the model for application to midlatitude storms, including rain over land, is being studied.

The retrieval method employs a standard nonlinear minimization technique (conjugate gradients) to find the rain field which minimizes an error functional (Eq. 2). In this study the error functional is the sum of squared differences between SMMR observations and a model representation of those observations. The formulation of this method is general, in the sense that additional satellite observations or constraints on the solution can be included simply by adding appropriate terms to the error functional. The addition of auxiliary data and/or reasonable constraints typically improves the accuracy of the retrieval by reducing the deleterious effects of noise in the observations (Yeh and Chin, 1985). Such additions are currently under investigation.

ACKNOWLEDGMENTS

The author wishes to thank James Weinman for helpful discussions and encouragement during all phases of this study. SMMR data sets were acquired from Per Gloersen, William Abbott, and Paul Hwang of NASA/GSFC. Radar data in digital form were kindly provided by Frank Marks and Peter Dodge of NOAA/AOML/HRD. This research was supported in part by NRL contract #N00014-86-K-2001.

REFERENCES

Anthes, R.A., 1982: Tropical cyclones-their structure, evolution and effects. Meteorological Monographs, 19, 208 pp.

Black, R.A. (with NOAA/AOML/HRD, 4301 Rickenbacker Causeway, Miami, FL 33149)

Gloersen, P. and F.T. Barath, 1977: A Scanning Multichannel Microwave Radiometer for Nimbus-G and Seasat-A. IEEE J. of Oceanic Eng., OE-2, 172-178.

Jorgensen, D.P. and P.T. Willis, 1982: A Z-R relationship for hurricanes. J. Appl. Meteor., 21, 356-366.

Merceret, F.J., 1974: On the size distribution of raindrops in Hurricane Ginger. Mon. Wea. Rev., 102, 714-716.

NOAA, 1979: Introduction to Weather Radar. U.S. Dept. of Commerce, 70 pp.

Olson, W.S., 1986: Estimation of Rainfall Rates in Tropical Cyclones by Passive Microwave Radiometry. Ph.D. thesis, Dept. of Meteorology, Univ. of Wisconsin, Madison, WI.

Palmén, E. and C.W. Newton, 1969: Atmospheric Circulation Systems. Academic Press, NY, 603 pp.

Savage, R.C. and J.A. Weinman, 1975: Preliminary calculations of the upwelling radiance from rainclouds at 37.0 and 19.35 GHz. Bull. Amer. Meteor. Soc., 56, 1272-1274.

Shanno, D.F., 1978: Conjugate gradient methods with inexact searches. Mathematics of Operations Research, 3, 244-256.

Spencer, R.W., B.B. Hinton and W.S. Olson, 1983a: Nimbus-7 37 GHz radiances correlated with radar rain rates over the Gulf of Mexico. J. Climate Appl. Meteor., 22, 2095-2099.

Spencer, R.W., W.S. Olson, W. Rongzhang, D.W. Martin, J.A. Weinman and D.A. Santek, 1983b: Heavy thunderstorms observed over land by the Nimbus-7 scanning multichannel microwave radiometer. J. Climate Appl. Meteor., 22, 1041-1046.

Wentz, F.J., 1983: A model function for microwave brightness temperatures. J. Geophys. Res., 88, 1892-1908.

Wilheit, T.T., A.T.C. Chang, M.S.V. Rao, E.B. Rodgers and J.S. Theon, 1977: A satellite technique for quantitatively mapping rainfall rates over the oceans. J. Appl. Meteor., 16, 551-560.

Yeh, C.-L. and R.T. Chin, 1985: Constrained optimization for image restoration using nonlinear programming. IEEE Conf. on A.S.S.P., Tampa, FL 4 pp.

A Cloud Model-Radiative Model Combination for Determining Microwave T_B-Rain Rate Relations

Gerard Szejwach[1,2,3], Robert F. Adler[2], Isabelle Jobard[3], and Robert A. Mack[4]

1. Introduction

This paper presents the initial results of using a combination of a cloud dynamical/microphysical model and a microwave radiative transfer model. The objectivies of the work are: 1) to determine the relations among rain rate, cloud and rain water, cloud and precipitation ice, and upwelling radiance at various microwave frequencies under differing climatological conditions and 2) to test the derived relations against aircraft and satellite radiometer data.

The approach is to use the cloud model to produce the vertical distribution of microphysical parameters required as input into the radiative transfer model. The desire is to improve upon the relatively simple cloud structures that have been previously used as input into microwave models, and to determine the variability of the relations as a function of the climatological regime (e.g., tropical vs. mid-latitude).

2. Cloud Model Description

The cloud model used in this study is a slightly modified form of the one-dimensional, time-dependent model of Cheng (1981). The calculations are made for an updraft cylinder of constant radius, r. This updraft radius, which is an input variable, controls the dilution of the cloud by entrainment through a k/r relation similar to that in other one-dimensional models (e.g., Simpson and Wiggert, 1969), where k is the entrainment coefficient, usually set equal to 0.2 for tropical, low shear cases. The cloud can be initiated with a combination of boundary layer temperature perturbation, moisture perturbation, and/or vertical velocity perturbation. The model's dynamical formulation includes the important pressure perturbation effect.

The model's cloud microphysics includes four categories of condensate: cloud liquid water (q_c), rain water (q_p), cloud ice (q_{ci}), and precipitation ice (q_i). The ice parameterization scheme is essentially that of Stephens (1979) [see also Cotton et al. (1982)]. Marshall-Palmer size distributions are used for both the rain water and for the precipitation ice. The cloud ice is assumed to all be at the same size with finite fall velocity.

Because initial model runs did not produce sufficient cloud ice in the 0C to -35C layer, the parameterization of the cloud ice initiation process was modified from that of Stephens. An identical formulation for crystal concentration was used. That is

$$N_{tf} = N_{of} \exp[\beta \Delta T],$$

where N_{tf} is the crystal concentration [m^{-3}], N_{of} is the concentration at 0C, and ΔT is the number of degrees below 0C. In our case, N_{of} was set to $10^4 m^{-3}$ and $\beta = 0.2$, instead of 10^{-2} m^{-3} and 0.6 as in Stephens (1979) and Cheng (1981). This change produced more cloud ice and less cloud water at temperatures 0-35C.

3. Radiative Transfer Model

The basic model used for calculating microwave brightness temperatures is a revision of the model described by Wilheit et al (1982). Modifications concern the capability of handling mixed phase layers and introduction of new and temperature dependent indices of refraction for ice, taken from Warren (1984).
The transfer of horizontally and vertically polarized radiation is computed through an horizontally infinite plane parallel atmosphere which contains a cloud of liquid and ice hydrometeors. The hydrometeors absorb, emit and scatter radiation.

The vertical structure of the cloud is provided by the cloud dynamical model described above. We assume no variation in the horizontal structure at the scale considered for the radiative transfer calculation.

---

[1]Universities Space Research Association.

[2]Laboratory for Atmospheres, NASA/Goddard Space Flight Center, Greenbelt, MD 20771.

[3]Laboratoire de Meteorologie Dynamique, CNRS, France.

[4]General Software Corporation, Landover, MD 20785.

The radiance $I_{\nu,p}$ for a frequency ν and polarization p is computed from Eq.1 .

$$\mu \frac{DI_{\nu,p}}{dz} = k_{\nu,p} (I_{\nu,p} - J_{\nu,p}) \qquad (1)$$

where μ is the cosine of the zenith angle and $k_{\nu,p}$ the extinction coefficient.

The source term $J_{\nu,p}$ is given by

$$J_{\nu,p} (z,\mu,\phi) = [1 - \bar{\omega}_\nu(z)] B_\nu [T(z)]$$

$$+ \frac{\bar{\omega}_\nu(z)}{4\pi} \int_0^{2\pi} \int_{-1}^{1} \underline{P}(\mu,\phi;\mu',\phi') I_\nu(z,\mu',\phi')d\mu'd\phi' \qquad (2)$$

$\bar{\omega}_\nu(z)$ and $\underline{P}(\mu,\phi;\mu',\phi')$ represent the albedo for single scattering and the phase function of an ensemble of spherical particles.

μ,ϕ and μ',ϕ' define the directions of incident and scattered beams of radiation.

B [T(z)] is the Planck function at the frequency ν for the temperature T at level z.

In addition to absorption and scattering by hydrometeors, absorption by molecular atmospheric constituents, water vapor and oxygen is also considered.

The atmosphere is divided into regions Each region is characterized by a uniform distribution of hydrometeors (ice, liquid or both). Several classes of particles can coexist in each region. In this study, the number of classes of ice or liquid hydrometeors present in each region is at most four (two classes of ice and two classes of liquid water).

The number of regions depends on the vertical distribution of hydrometeors provided by the dynamical model. We used a maximum of ten regions, but the model can handle more regions if necessary. Computation of the extinction, scattering, absorption coefficients and phase function is performed according to the Mie theory for each region.

The atmosphere is then divided into 200 layers of equal optical thickness.
The transfer of radiation is computed from the top of the atmosphere down to the surface and back up using an iterative approach.
The surface emissivity, for over ocean models is computed according to Chang and Wilheit (1979). for a surface windspeed of 10 m/s.

The vector representing each of the two Intensities (vertical and horizontal polarization) used in the radiative transfer model has twenty components.

4. Application of Model Combination to Two Climatological Regimes

Upwelling microwave radiance is a function of the physical characteristics of the cloud, not the ground-level rainfall itself. Therefore, since the relations between rainfall rate and cloud characteristics such as cloud depth, ice content, etc., are expected to vary according to location, climatological regime, and even synoptic situation, T_B-rain rate relations must be a function of the convective cloud characteristics. As a first test of the model combination, results were compiled for a tropical-summer situation and a mid-latitude spring (severe thunderstorm) situation. This particular comparison was done for two reasons. First, aircraft microwave radiometer data (92 and 183 GHz) has been correlated to ground-based radar for both regimes (Hakkarinen and Adler, 1986). Second, Adler and Mack (1984) have already compared cloud maximum height-rainfall rate relations for these regimes with a cloud model and observations.

The vertical soundings used as input into the Cheng cloud model are the same as used by Adler and Mack (1984). The Florida sounding is from Miami during the Florida Area Cumulus Experiment (FACE); the mid-west sounding is a modified Oklahoma City sounding for a situation of severe thunderstorms in Oklahoma and Arkansas. For each sounding, a series of model runs is made with updraft radii varying from 0.5 to 7 km. In the Oklahoma case, the entrainment coefficient, k, is increased to 0.5 based on results from Adler and Mack (1984) to roughly account for the effect of shear on the entrainment rate.

For each model run, a time-height profile of pertinent quantities (such as the four classes of condensate) is produced. For this exercise, the time of maximum rain rate at the ground was located, and one vertical profile within ± 10 min of the rainfall rate maximum (R_{max}) and with the largest integrated ice content, was chosen to represent that cloud model run. Because the cloud model confines all its rain to the updraft area, the model R_{max} is divided by 5.0 to compensate for the difference between updraft area and rain area. The basis for this procedure was discussed by Adler and Mack (1984). A summary of the cloud model runs is shown in Table 1.

5. Results and Discussion

Figs. 1 to 4 present the results obtained at various frequencies for the 13 cases presented in section 4. The frequencies were chosen as to be representative of some existing space or airborne radiometers. The two last ones refer to the AMMS instrument(Wilheit et al,1982) The 183+-9 frequency corresponds to the 2 band-channel with center frequencies at 183-9 and 183+9 Ghz.

Table 1. Cloud Model Parameters and Results

Florida							
Updraft radius (km)	1	2	3	4	5	6	7
w_{max} (m s^{-1})	4.8	6.1	7.2	8.0	9.4	10.8	11.0
Z_{max} (km)	5.0	6.5	8.1	10.1	12.3	13.3	13.7
Rainfall rate (mm h^{-1})	7	18	21	27	35	41	46
Integrated ice content (10^4 gm^{-2})	0	0.05	0.23	0.53	0.83	1.07	1.22

Oklahoma						
Updraft radius (km)	2.5	3	4	5	6	7
w_{max} (m s^{-1})	13.3	15.0	17.6	19.5	21.1	22.6
Z_{max} (km)	10.3	11.5	12.3	12.7	12.9	13.1
Rainfall rate (mm h^{-1})	5	10	17	24	31	36
Integrated ice content (10^4 gm^{-2})	0.67	0.99	1.33	1.52	1.60	1.63

The brightness temperature TB is plotted as a function of rainrate R as defined in the cloud dynamical model description. For each figure we present four curves corresponding to the Oklahoma and Florida cases. Solid and dashed curves refer to nadir and 45 degrees view angles respectively. Results at 45 degrees are averaged over the two polarizations in order to simulate the observations of a non polarized radiometer.

5.1 Surface and cloud effects

The points plotted for R=0 correspond to land background and atmospheric conditions taken from the soundings used in the model.

Table 2 presents the brightness temperatures for the Florida case and an ocean background at nadir and 45 degrees viewing angle Results for cloudy atmospheres are also included in Table 2. The clouds contain 0.1 and 0.5 g/m3 of liquid water respectively from the cloud base at 0.5 km to the freezing level. These cloud examples are given to illustrate background TBs in the absence of precipitation.

While the three first frequencies are located in atmospheric "window" regions, the last one lies along an absorption line by water vapor centered at 183.35 GHz.

In the absence of cloud surface emission drives the brightness temperature in the first three channels and since water surfaces have much lower emissivity than ground surfaces, TB can be much lower than the thermodynamic surface temperature in the ocean model. Absorption/emission by atmospheric constituents tends to increase the value of TB. The atmosphere is not polarized and the difference between the horizontal and vertical TBs at 45 degrees is due to the lower surface emissivity for the horizontal polarization.

At 183+-9 GHz, the atmosphere is almost opaque and the atmospheric emission drives the value of TB. No significant difference can be observed between ocean or ground background.

Clouds droplets absorb and emit radiation. Scattering by cloud droplets is totally negligible for all the frequencies considered here. The absorption coefficient is proportional to the liquid content and increases with the square of the frequency. This explains the results observed in Table 2 for all channels. The slight decrease in TB for 183+-9 is due to the fact that when absorption by atmosphere (cloud included) increases, the weighting function peaks at a higher level in the troposphere where the temperature is lower.

Table 2
Brightness temperatures for clear and cloudy atmospheres over Florida (ocean surface)

CASE		FREQUENCY (GHz)			
		19.35	37.00	92.00	183-9
CLEAR	Nadir	173.4	177.7	257.2	281.9
	45 V	209.8	215.5	275.2	279.3
	45 H	157.4	157.5	253.1	273.3
CLOUD .1g/m3	Nadir	189.0	206.2	280.4	280.6
	45 V	222.8	237.8	284.5	278.7
	45 H	178.5	196.5	279.5	278.7
CLOUD .5g/m3	Nadir	212.8	255.3	281.8	277.1
	45 V	241.1	270.6	279.3	276.0
	45 H	208.7	256.2	279.2	276.0

5.2 Precipitation effects

In a first approximation, scattering effects increase with the size of the cloud particles and with the frequency. While liquid drops both scatter and absorb radiation, absorption by ice crystals is negligible at the frequencies considered in this study.

Scattering tends to decrease the value of TB, because part of the radiation emitted by the surface and the lower layers does not reach the top of the atmosphere. If a given layer contains absorbing/emitting particles such as water cloud drops, emission by these particles will attenuate the loss by scattering.

On all four figures (which are for land surface background), we observe a decrease in TB when the rainfall rate increases due to scattering by ice principally and rain to a much lesser extent. As expected the drop in brightness temperature is smaller at 19.35 GHz and at 37 GHz than at the higher frequencies. At 183+-9 GHz, absorption/emission by water vapor will tend to very slightly reduce the loss due to scattering.

We observe a very different behavior between the two meteorological regimes at 37 GHz and above. While TB remains slightly constant for rainfall rates up to about 16 mm/hr for the Florida cases, there is a very rapid decrease in the Oklahoma case. This is due to the fact that the ice content and vertical extent corresponding to a given rainrate are larger in the later case (see also next section).

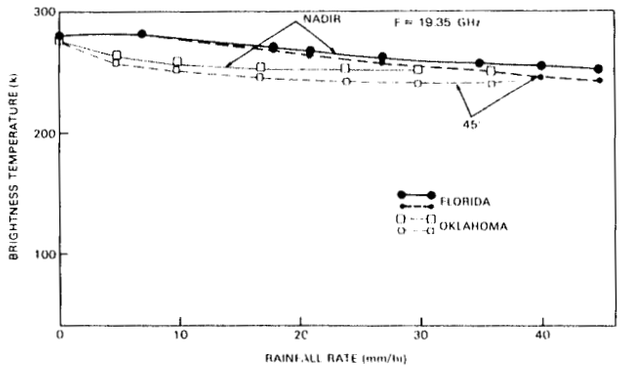

Fig. 1 *Brightness temperature (TB) as a function of rainfall rate (R) based on results from cloud model-radiative transfer model at 19.35 GHz (land surface background).*

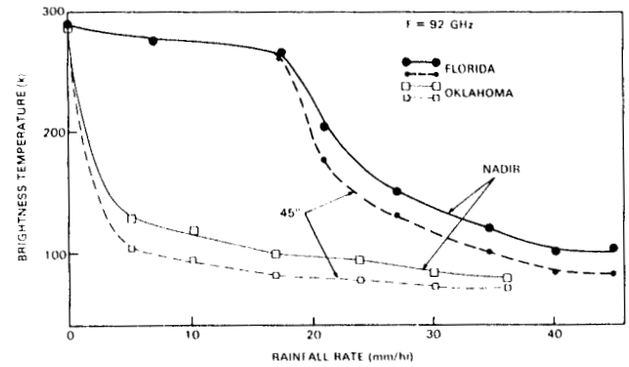

Fig. 3 *Brightness temperature (TB) as a function of rainfall rate (R) based on results from cloud model-radiative transfer model at 92 GHz (land surface background).*

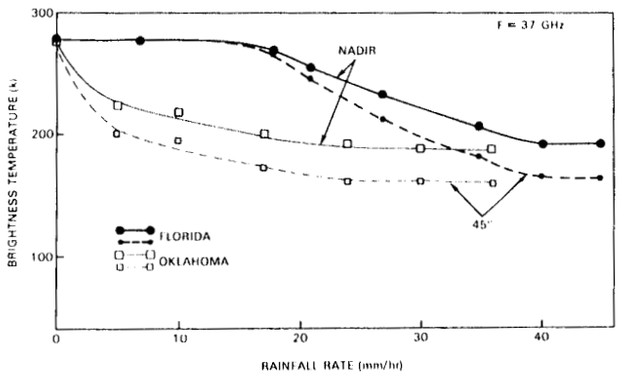

Fig. 2 *Brightness temperature (TB) as a function of rainfall rate (R) based on results from cloud model-radiative transfer model at 37 GHz (land surface background).*

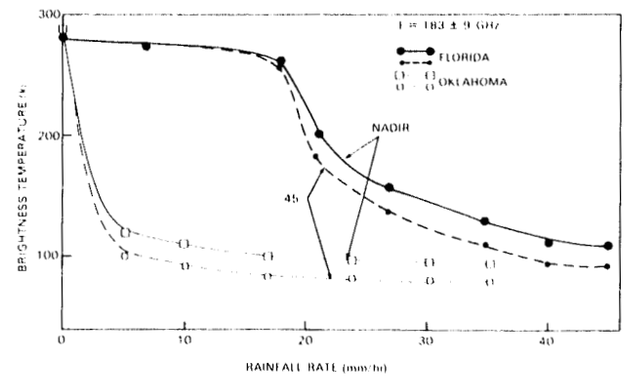

Fig. 4 *Brightness temperature (TB) as a function of rainfall rate (R) based on results from cloud model-radiative transfer model at 183±9 GHz (land surface background).*

It is clear from our results that we can not derive a unique relationship between rainfall rate and brightness temperature for any of our frequencies. The high frequency channels give a good indication of rain/no rain situations for the Oklahoma regime and a good estimate of the rainfall rate in medium to high rain situations in the Florida regime.

Although not shown on Fig.1, which is for land surface background, the 19.35 GHz channel provides an estimate of rain over ocean for light to medium rain rates (Wilheit et al, 1977) (see Table 2 for ocean surface).

These results of course correspond to a field of views totally covered by a uniform precipitating cloud and are therefore suitable for comparison with aircraft measurements.

6. Comparison of 92 GHz Calculations to Aircraft Observations

Hakkarinen and Adler (1984, 1986) have analyzed 92 and 183 GHz aircraft observations in comparison to ground-based radar data. The aircraft microwave instrument is the Advanced Microwave Moisture Sounder (AMMS), a scanning radiometer flown on NASA high-altitude aircraft. The results of the referenced studies indicated that low brightness temperature (TB) features occurred with deep convective features. The patterns and gradients of TB were similar in appearance to radar echoes, although the best matches between AMMS low TB features and radar reflectivity occurred with mid-level radar echoes.

Hakkarinen and Adler (1986) have correlated radar-estimated rain rate with aircraft TB at 92 and 183 GHz. The results are shown in Fig. 5 for 92 GHz along with the cloud model-radiative transfer model results discussed in the previous section. The model combination results compare favorably with the observations. The Florida observations show a less rapid decrease in TB with increasing rain rate in the 0-10 mm/hr range than the Arkansas spring case. At higher rain rates (>10 mm/hr), the Florida observations show a larger decrease in TB with increasing rain rate than the Arkansas observations. This difference translates to an observed TB difference of approximately 100 K at a radar-observed rain rate of 10 mm/hr. The cloud model-radiative model combination correctly simulates these basic differences, although the model-calculated TB magnitudes in the Florida case are too large.

The basic difference in TB between the Florida and Oklahoma model runs is due to the larger depth and concentration of ice in Oklahoma/Arkansas as compared to Florida. This is shown in Table 1, where the Florida run with an updraft radius of 3 km has approximately the same rain rate as the Oklahoma run at 5 km radius, but has an integrated ice content only one-fifth of the Oklahoma case. The physical and dynamical reasons for this are: 1) a lower 0C isotherm in Oklahoma; 2) a greater depth of cloud in Oklahoma (for the same rain rate); and 3) a larger precipitation efficiency in the Florida model storms.

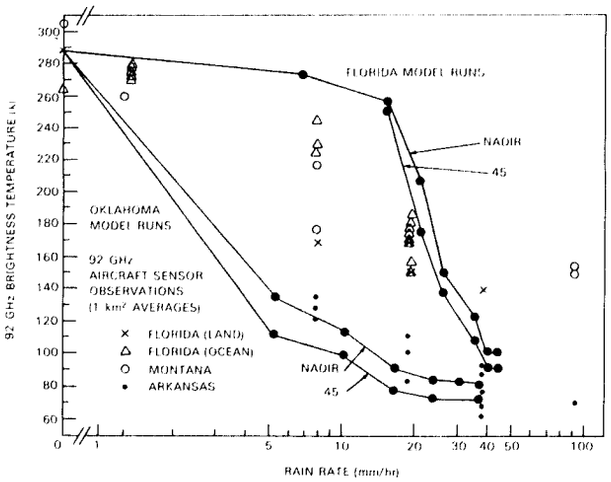

Fig. 5 *Comparison of cloud model-radiative transfer model results with 92 GHz aircraft observations and ground-based radar data from Hakkarinen and Adler (1986).*

7. Conclusions and Future Work

The combination of a cloud dynamical/microphysical model and a microwave radiative transfer model has been accomplished and has been used to explore the relations between rain rate, cloud and rain water, cloud ice, and upwelling radiance at various microwave frequencies (19, 37, 92, and 183 GHz). The focus of the effort is to determine the brightness temperature (TB)-rain rate relations for various microwave frequencies for convective rain under differing climatological (e.g., tropical versus mid-latitude) conditions.

A one-dimensional, time-dependent cloud model is used to generate vertical profiles of cloud water, precipitation water, cloud ice, precipitation ice, and other in-cloud parameters along with ground-level rain rate. The pertinent microphysical parameters for each cloud model run are then used as input into the radiative transfer model. The calculation of TB for each cloud model run completes the TB-rain rate combination.

The cloud model-radiative model combination generates reasonable TB values at all frequencies and indicates the strong differences in TB-rain rate relations between tropical conditions and mid-latitude, spring intense convection. Comparison with 92 GHz aircraft observations was made for tropical (Florida summer) and mid-latitude (Oklahoma spring) conditions, for which rain rate (from radar) and TB [from an aircraft Advanced Microwave Moisture Sounder (AMMS)] are available. The observations show a distinct difference in the TB-rain rate relations between the two regimes, with the Oklahoma observations showing a much more rapid decrease of TB with increase in rain rate from light to moderate rain rates than is observed under tropical conditions. This observational difference is correctly simulated by the cloud model-radiative model combination which produces TB-rain rate curves similar to those from the aircraft data analysis. The tropical-extratropical disparities are shown to be caused by differences in microphysical distributions related to differences in freezing level, depth of the cloud, updraft intensity (related to stability), and storm precipitation efficiency.

These results indicate the need to investigate the variation of TB-rain rate relations under differing climatological conditions, and indicate that the cloud model-radiative transfer model approach can be the basis for precipitation estimation techniques. The model combination approach also shows potential for analysis of convective storm structure when coupled with overflight microwave radiometer data.

In the coming months, additional high-altitude aircraft data will be obtained at 92 and 183 GHz during GALE (Genesis of Atlantic Lows Experiment) and at 18, 37, 92, and 183 GHz during SPACE/MIST (Satellite Precipitation And Cloud Experiment/MIcroburst Severe Thunderstorm project). In both cases, research-quality radar data (including dual polarization data) will be collected to coincide with aircraft observations. This collection of observations will be examined in the context of the cloud and radiative transfer model results such as those shown in this paper. Shortly, three-dimensional cloud models with more sophisticated microphysical parameterization will be incorporated into this effort.

References

Adler, R. F., and R. A. Mack, 1984: Thunderstorm cloud height-rainfall rate relations for use with satellite rainfall estimation techniques. J. Clim. Appl. Meteor., 23, 280-296.

Cheng, C. P., 1981: Numerical simulation of the dynamics, cloud microphysics and radar echo structure of tropical and mid-latitude convection. Ph.D. Dissertation, University of Washington, 217 pp.

Cotton, W. R., M. A. Stephens, T. Nehrkorn, and G. J. Tripoli, 1982: The Colorado State University three-dimensional cloud/mesoscale model-1982, Part II: An ice phase parameterization. J. Rech. Atmos., 4, 295-320.

Hakkarinen, I. M., and R. F. Adler, 1984: Observations of deep convection from an airborne high-frequency (92 and 183 GHz) passive microwave radiometer. Preprints, Conf. on Satellite Meteorology/Remote Sensing and Applications, Clearwater Beach, FL, Amer. Meteor. Soc., 216-221.

Hakkarinen, I. M., and R. F. Adler, 1986: Precipitation estimation using passive microwave radiometry at 92 and 183 GHz: Aircraft results. Second Conf. on Satellite Meteorology/Remote Sensing and Applications, this volume.

Simpson, J., and V. Wiggert, 1969: Model of precipitation cumulus towers. Mon. Wea. Rev., 97, 471-489.

Stephens, M. A., 1979: A simple ice phase parameterization. Atmospheric Science Paper No. 319, Colorado State University, 122 pp.

Wilheit, T. T., A. T. C. Chang, M. S. V. Rao, E. B. Roders, and J. A. Theon, 1977: A satellite technique for quantitatively mapping rainfall rates over the ocean. J. Appl. Meteor., 16, 551-560.

Wilheit, T. T., Jr., A. T. C. Chang, J. L. King, E. B. Rodgers, R. A. Nieman, B. M. Krupp, A. S. Milman, J. S. Stratigos, and H. Siddalingaiah, 1982: Microwave radiometric observations near 19.35, 92 and 183 GHz of precipitation in Tropical Storm Cora. J. Appl. Meteor., 21, 1137-1145.

Wu, R., and J. A. Weinman, 1984: Microwave radiances from precipitating clouds containing aspherical ice, combined phase, and liquid hydrometeors. J. Geophys. Res., 89, D7170-D7178.

FIELD-OF-VIEW EFFECTS IN ESTIMATING PRECIPITATION FROM SATELLITE MICROWAVE RADIANCES

Robert F. Adler
Laboratory for Atmospheres
NASA/Goddard Space Flight Center
Greenbelt, MD 20771

Robert A. Mack
General Software Corporation
Landover, MD 20785

1. Introduction

Theoretical relations between rainfall rate (R) and microwave brightness temperature (T_B) are typically derived by assuming vertical distributions of the pertinent state variables and cloud microphysical parameters for a cloud raining at a certain intensity. A radiative transfer model is then used to calculate the upwelling T_B [see, for example, Wilheit et al. (1977) and Wu and Weinman (1984)]. Recently, Szejwach et al. (1986) have used the output of a cloud model as input to the radiative transfer model. In either case, the approach is inherently one-dimensional (one vertical, no horizontal). However, in the application of such theoretical T_B-R relations to space-borne remote sensing, the horizontal distribution of rainfall and horizontal distribution of microphysical quantities become significant. What is desired for use with the satellite observations is a relation between $\overline{T_B}$ [the satellite-measured average radiance over the FOV (field-of-view)] and $\bar{R}$ (the average rain rate over the FOV). If the relation between T_B and R is non-linear, the retrieval of $\bar{R}$ from $\overline{T_B}$ will not be unique and will be a function of the distribution rain within the FOV. Thus, any algorithm to retrieve rain rate from satellite microwave T_B values must include the effect of the distribution of rain within the FOV.

In this paper, a cloud model is used to generate reasonable convective rain cells which are used to calculate $\overline{T_B}$ and $\bar{R}$ for various microwave frequencies and FOV's; the results of these calculations are compared to radar-based simulations and results from satellite-based studies. A study of the impact of using higher resolution visible and infrared (IR) data to define rain distribution parameters within the microwave FOV is also attempted.

2. Rain Statistics Generated from a One-Dimensional Cloud Model

Adler and Mack (1984) showed that useful rainfall cell characteristics such as R_{max} (maximum rainfall rate), VRR (volume rainfall rate), and A_R (raincell area) could be derived from a one-dimensional cloud model [a modified version of the Simpson and Wiggert, (1969) model]. Table 1 shows the pertinent cloud-model generated quantities for tropical (Florida, summer) conditions for a sequence of model convective cells reaching increasing maximum heights (controlled by the effect of entrainment, which is inversely proportional to the updraft radius). The rain cell area (A_R) was empirically related to updraft area (A_u) by Adler and Mack (1984). That is

$$A_R = 5\ A_u. \qquad (1)$$

The distribution of rain rate within a given cell is given by

$$R = R_{max}\ e^{-2.3(r/r_R)^2}, \qquad (2)$$

where is the radial dimension in a polar coordinate system, r_R is the radius of the assumed circular rain area (i.e., $r_R = \sqrt{A_R/\pi}$). The exponent in Eq. (2) will produce an $R = 0.1\ R_{max}$ at the rain boundary, $r = r_R$.

Table 1. Rain parameters produced by one-dimensional cloud model runs.

	Updraft radius (km)						
	1	2	3	4	5	6	8
Z_{max} (km)	5.6	9.0	12.0	13.5	13.9	14.1	14.4
T_{min} (k)	269.1	247.5	222.8	209.9	206.2	204.7	202.5
W_{max} (m s^{-1})	5.4	8.8	10.2	11.8	13.13	14.2	16.5
R_{max} (mm h^{-1})	7.7	23.7	31.9	41.0	45.7	50.1	54.1
VRR (m^3 s^{-1})	13.2	161.4	487.9	1115.2	1942.1	3070.4	5893.6
PE	0.27	0.60	0.77	0.83	0.86	0.88	0.91

CLOUD BASE = 751 meters (929 mb); T_{cb} = 21.2C; q_s (cloud base) = 17.4 g kg^{-1}

For each rain cell, calculations are attempted for varying fractional coverages (f = 0.1, 0.25, 0.5, 0.75, 1.0). If the rain cell area $A_R \leq f\ A_{FOV}$, multiple, identical rain cells are included in the FOV calculations. If $f\ A_{FOV} < A_R \leq A_{FOV}$, the fraction coverage (f) is adjusted so that $A_R = f' A_{FOV}$. For large cells when $A_R \geq A_{FOV}$, f is set to 1.0 and the rain integration is carried from the center of the idealized rain cell outward until the integration area is equal to A_{FOV}. This represents placing the FOV over the center of the rain cell. Only one size of rain cell is used per calculation.

This procedure generates rain cell characteristics (rain cell size and spatial distribution of rain intensity) which have been compared to observations (Adler and Mack, 1984). Although these characteristics could be generated by the observations themselves, this procedure could be used to generate different characteristics under different climatolgical conditions.

3. Results for 19 GHz

The approach outlined in the previous sections was applied to simulate 19 GHz data. A theoretical curve relating rainfall rate to 19 GHz T_B for a tropical atmosphere (freezing level at 4.5 km) was used based on Wilheit et al. (1977). This is shown as the solid curve in Fig. 1. Each of the points in Fig. 1 is from a calculation for one rain cell type and fractional coverage (f) for a FOV of 30 km (approximately the Nimbus 5 ESMR FOV). Input f's were 0.1, 0.25, 0.5, 0.75, and 1.0. These are represented by the integers (and letters) corresponding to tenths (rounded off in some cases). Intermediate f's (e.g., .4 in Fig. 1) come from the fractional coverage adjustment discussed in Section 2. The letter A represents f = 1.0.

The calculations in Fig. 1 indicate a pattern of $\overline{T_B}$ and $\bar{R}$ to the right of the theoretical curve. This means that use of the theoretical curve will result in underestimates of mean rainfall by a significant amount. This "low bias" effect has been described by previous researchers (Austin and Geotis, 1978; Lovejoy and Austin, 1980). At an intermediate T_B, 220 K, the theoretical curve would give an estimated rain of ~3 mm h^{-1}, while the simulations which take into account the 30 km FOV give $\bar{R}$ values ranging from 4-10 mm h^{-1}. Therefore, the variation in the distribution of rain within the FOV leads to a systematic error (low bias) and a scatter in the distribution of $\bar{R}$ and $\overline{T_B}$ values. With increasing T_B there is also a trend toward larger f. For a FOV to have a $\overline{T_B}$ of $\geq$ 240 K, its fractional coverage (f) must be close to 1.0. At a constant T_B (e.g., 220 K) $\bar{R}$ increases with decreasing f. In other words, of two FOV's having indentical $\overline{T_B}$, one with broad coverage of light rain and one with a smaller f, but with larger maximum rain rate, the latter will have a larger $\bar{R}$. Therefore, if we had some independent estimate of f, a better estimate of $\bar{R}$ could be made.

In order to confirm the cloud model-based simulations concerning $\overline{T_B}$, $\bar{R}$, and f, a second set of simulations using radar data was performed. Using 1 km resolution low-level reflectivity data from the Florida Area Comulus Experiment (FACE) generated as part of another study (Negri and Adler, 1984), $\overline{T_B}$ and $\bar{R}$ fields were constructed with a simulated FOV of 30 km. These are presented in Fig. 2. These radar-based simulations agree well with the cloud-model based one in Fig 1. This is true even to the increase in $\bar{R}$ with decreasing f at constant $\overline{T_B}$.

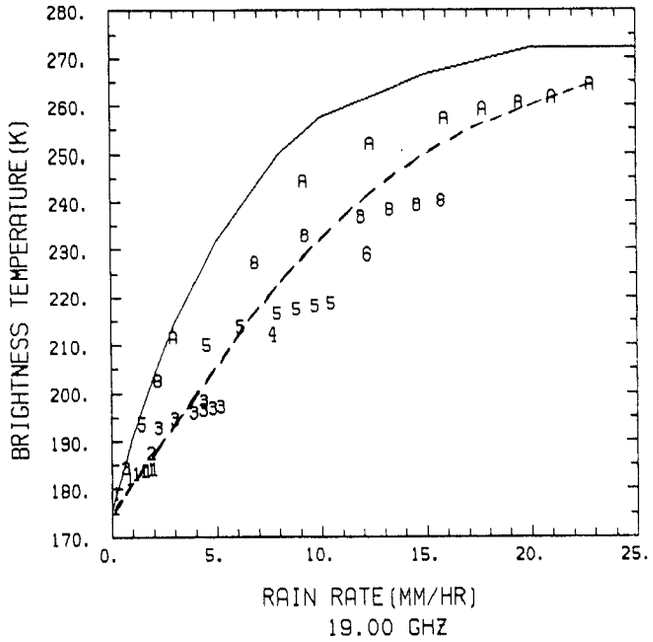

Fig. 1. *Simulated $\bar{R}$ and $\overline{T_B}$ for 19 GHz, 30 km FOV using the cloud model-based rain parameters. The number plotted is f, the fractional rain cover within the FOV in tenths. The symbol A is f = 1.0. The solid curve is the theoretical T_B-R curve. Dashed curve is fitted curve through mid-range values.*

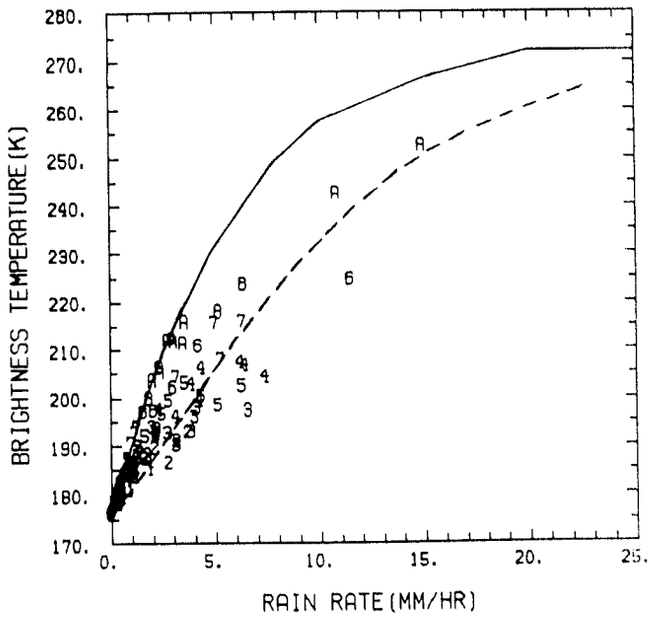

Fig. 2. *Simulated $\bar{R}$ and $\overline{T_B}$ for 19 GHz, 30 km FOV using radar data. The number plotted is f. The dashed curve is same as in Fig. 1.*

If one does not have any independent information as to the rain distribution, or f, in the FOV, a logical choice of a $\overline{T_B}$-$\bar{R}$ relation would be an intermediate curve fitted to the simulated $\overline{T_B}$, $\bar{R}$ data in Fig. 1. Figs. 1,2, and 3 show such an intermediate curve constructed by fitting a curve to the mid-range values of $\bar{R}$ for a sequence of $\overline{T_B}$ values. Also shown in Fig. 3 are the series of $\overline{T_B}$-$\bar{R}$ values generated by Wilheit et al. (1977) from Nimbus 5 ESMR overpasses of the NWS Miami, Flordia, radar. Although the scatter is large, the intermediate curve is a reasonable adjustment to the original theoretical curve. This intermediate curve is very similar to the empirical linear fit of the data that was used by Rodgers and Adler (1981) to successfully estimate tropical cyclone rainfall. Therefore, the cloud model-based approach appears a valid one in estimating the effect of rain distribution on $\overline{T_B}$, $\bar{R}$ relations.

Recently, there has been interest in flying a ESMR-type 19 GHz instrument in a lower orbit (~400 km) as part of the proposed Tropical Rain Measurement Mission (TRMM). Therefore, simulations identical to those in Fig. 1 were done for a 10 km by 10 km FOV. The results in Fig. 4 show a smaller bias, a smaller scatter, but a saturation problem above 15 mm h^{-1}. Although heavy rain may be hard to diagnose, the reduction in bias and scatter, and the increased spatial revolution, make the lower altitude a worthwhile approach.

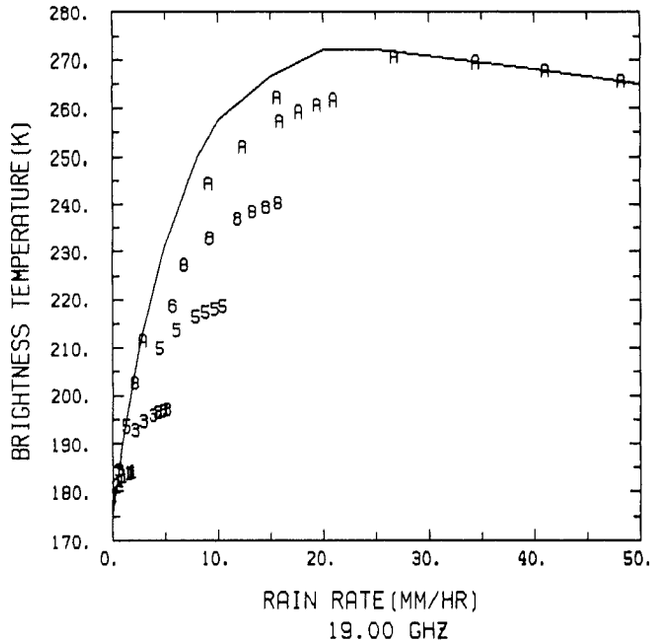

Fig. 4. *Simulated $\bar{R}$ and $\overline{T_B}$ for 19 GHz, 10 km FOV using cloud model-based parameters.*

4. Results at 37 GHz

Figs. 5 and 6 show the results of the cloud model-based FOV simulations for 37 GHz horizontal and vertical polarization, respectively. These calculations are for a water background using the theoretical calculations of Wu and Weinman (1984) (their Table 6) and for the Scanning Multichannel Microwave Radiometer (SMMR) FOV (588 km^2). The results in Fig. 5 indicate that, although the theoretical curve shows a sharp increase in T_B to a maximum at 4 mm h^{-1}, then a more gradual decrease in T_B with increasing R, the FOV simulations show a large scatter of points with a positive correlation between $\bar{R}$ and $\overline{T_B}$. This distribution is in good agreement with the empirical results of Spencer et al. (1983), where SMMR data were compared to ground-based radar observations. Fig. 6 shows the results for the 37 GHz channel (vertical polarization), again in reasonable agreement with the Spencer et al. (1983) data. Therefore, the sharp difference between theoretical curves and satellite data is due, not to errors in the theory, but to the effect of the distribution of rain within the satellite FOV.

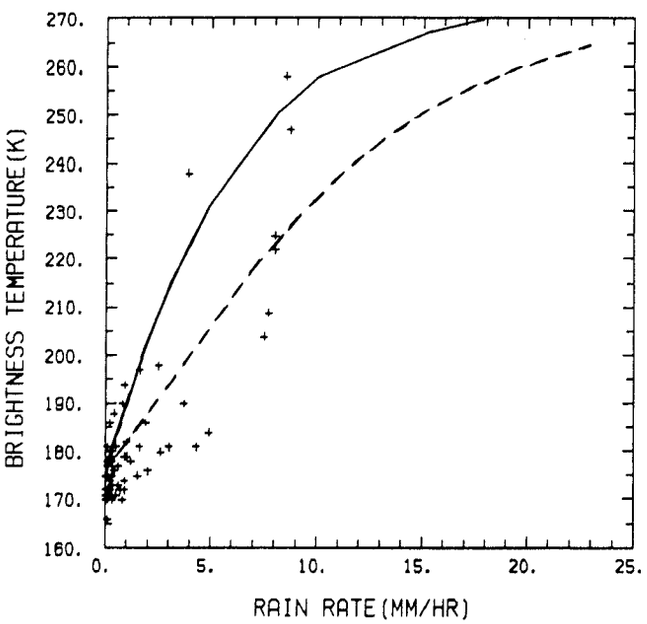

Fig. 3. *Nimbus 5 ESMR data compared to radar observations from Wilheit et al. (1977). Also shown is mid-range curve from Fig. 1 simulations.*

Recently, Spencer (1985) has used both of the polarizations at 37 GHz to derive an over-water rain estimation technique applicable to SMMR data by using a combination of theoretical and empirical approaches. Here we use a very similar approach except no empirical improvement is used. The results of using the theoretical relations at each polarization individually with the cloud-model rain distributions (as shown in Figs. 5 and 6) are compared using the mean T_B of the two polarizations and the ΔT_B difference between the two polarizations as done by Spencer (1985). The results in Fig. 7 show that simulated $\bar{R}$ in the FOV is related to nearly a linear combination of the mean of the two polarizations and the polarization difference. This agrees with the results of Spencer. Fig. 8 shows the same results only with fractional coverage f

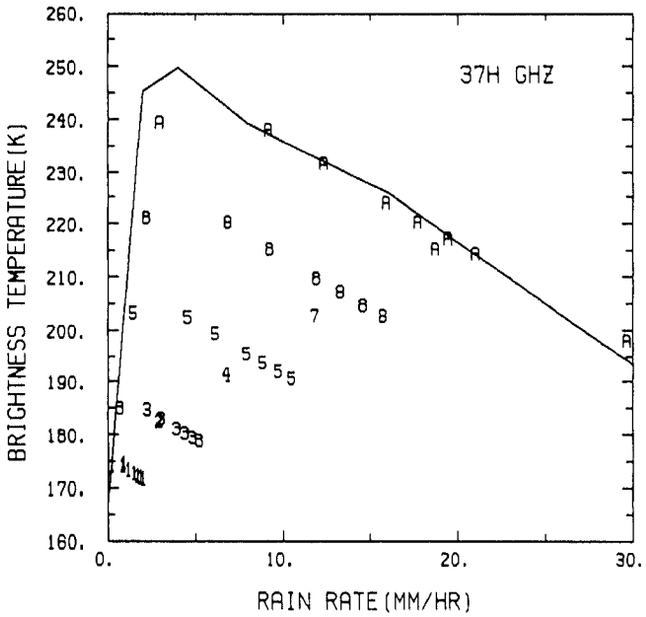

Fig. 5. *Simulated $\overline{R}$ and $\overline{T_B}$ for 37 GHz (horizontal polarization), 588 km^2 FOV for over ocean conditions.*

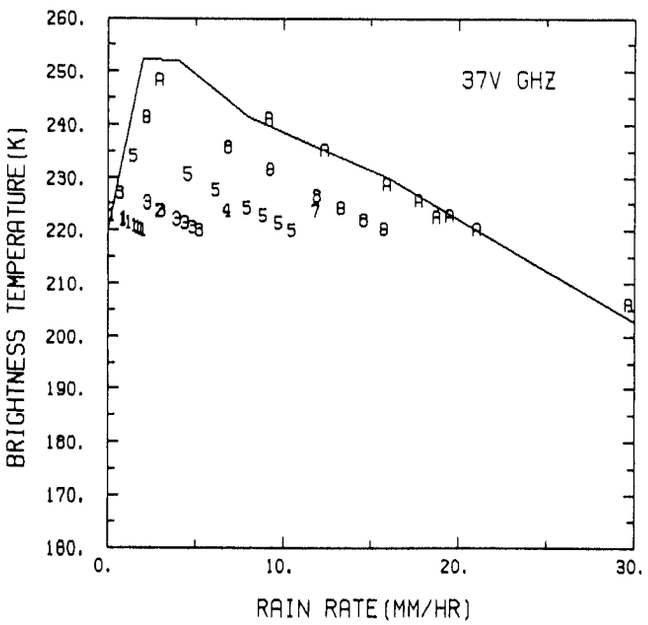

Fig. 6. *Simulated $\overline{R}$ and $\overline{T_B}$ for 37 GHz (vertical polarization), 588 km^2 FOV for over ocean conditions.*

plotted. This confirms that the f is primarily a function of ΔT, while $\overline{T_B}$ (two polarization average) is a function of the mean rain rate within the raining portion of the FOV. Thus, the combination of the mean and the difference results in a good estimate of the $\overline{R}$ for the FOV.

The magnitude of our rainfall rate values differs from those of Spencer (1985) because of his use of the empirical relation to assign the rain rate. Which set of magnitudes is correct is open to question, but the radar reflectivity-rain rate relation used by Spencer in his empirical studies may be producing rain rate magnitudes that are too large. This point needs investigation.

Although the theoretical curves at 37 GHz are distinctly non-linear, the combination of the two polarizations seems to produce rain rate that is an approximately linear function of the mean and the difference. This is because of the piecewise linearity of the individual curves and the breakpoint occurring at a low rain rate magnitude (~3 mm h^{-1}). If a quasi-linear relation exists, the size of the FOV should not significantly change the relation of rain rate to the T_B's. This point was confirmed by doing a separate simulation with a FOV of 1176 km^2 (twice the SMMR FOV). This may be an important point in consideration of these frequencies for future missions.

5. Infrared and Microwave Combined

In Section 3, it was shown that rain retrieval at 19 GHz could be improved with some knowledge about the distribution of rain within the microwave FOV. Higher resolution IR data is a candidate for obtaining that information. Here we have used the simulated 30 km, 19 GHz data from Section 3. To that data, we have added the GOES IR (10 km) data already correlated with the radar data by Negri and Adler (1984). For each simulated microwave FOV, the mean IR T_B [$\overline{T}$(IR)] and standard deviation [σ_{IR}] were calculated.

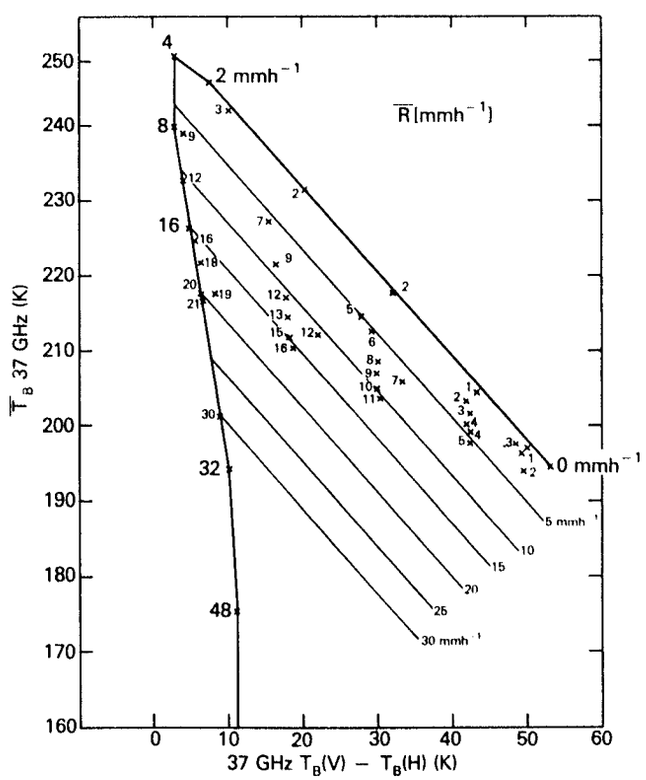

Fig. 7. *Simulated $\overline{R}$, ΔT_B (polarization difference), and $\overline{T_B}$ (polarization average) for 37 GHz (over ocean).*

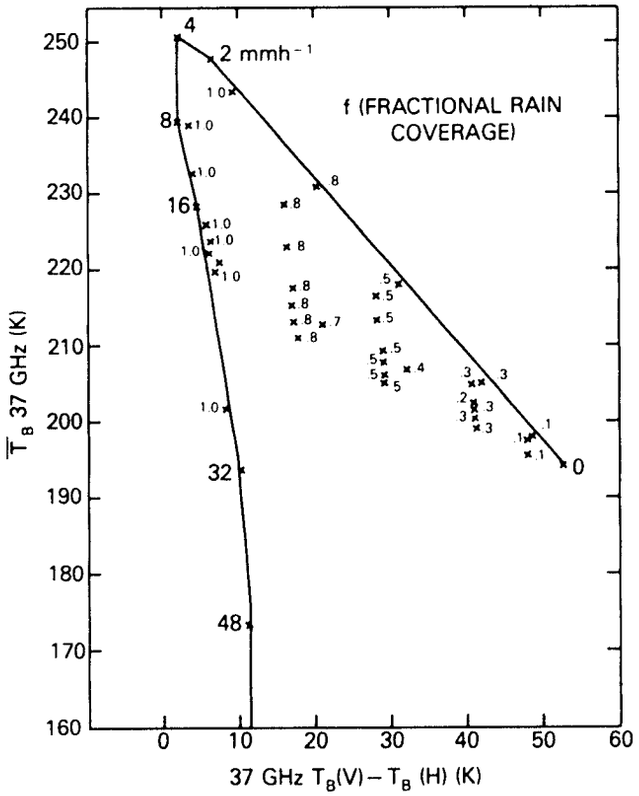

Fig. 8. *Fractional coverage as a function of 37 GHz ΔT_B and $\overline{T}_B$.*

Inspection of the relations among $\overline{R}$, $\overline{T}_B$, and the IR parameters indicated that the IR parameters added information, at least for $\overline{T}_B \leq 200$ K, i.e., where the fractional coverage of rain is usually much below 1.0. For example, although over the entire range of 19 GHz $\overline{T}_B$, there is a strong correlation between $\overline{R}$ and $\overline{T}_B$, over a narrow range of T_B (e.g., 5 K); the scatter in $\overline{R}$ is large enough so that the correlation between $\overline{T}_B$ and $\overline{R}$ approaches zero. For example, in the $\overline{T}_B$ range 190-195 K, the correlation is .22. The question now is: within this limited T_B range, can the IR data provide information on $\overline{R}$? Figs. 9 and 10 show the distribution of T(IR) vs. $\overline{R}$ and σ_{IR} vs. $\overline{R}$, respectively, for the $\overline{T}_B$ range 190-195. These results indicate that for the same T_B (microwave), higher $\overline{R}$ values occur generally with higher T(IR) and σ_{IR} values. These IR parameters are negatively correlated with fractional rain coverage. The correlation ceofficients between $\overline{r}$ and T(IR) and σIR are .46 and .43 respectively. In other words, the IR parameters contain information concerning the distribution of rain with microwave FOV. Only one band (190-195 k) was shown, but the results are simliar for other bands with $\overline{T}_B \leq 200$ k. Above that value the fractional rain coverage is high and the IR parameters show less variation and correlation with $\overline{R}$.

To illustrate the relation of the IR parameters to the microwave and rain parameters, a regression analysis was carried out. With all 339 points included (all with some rain in the radar-simulated FOV), the T_B (microwave) explained 76.2% of the $\overline{R}$ variance, with T(IR) adding only 2.1% when it was added. The σ(IR) parameter did not significantly increase the variance explained. An additional analysis was made for the limited data set of T_B (microwave) $\leq$ 200 k. In this case T_B (microwave) explained 45.8% of the variance. The addition of T(IR) increased the variance explained to 54.0%. For T_B (microwave) > 200 k the variance explained increased only from 60.1 to 60.8% with the addition of the IR data. This reaffirms that the IR data will only make a contribution when the fractional coverage of rain is relatively small.

These preliminary results are similar to those of Smith and Kidder (1978) and point to the use of IR data to aid in microwave rain retrievals. Higher resolution in the IR and use of visible data would probably improve the results.

6. Summary

The rain statistics generated by the one-dimensional cloud model approach were found useful in generating realistic distributions of rain within simulated microwave fields-of-view (FOV's). Application of the approach to a 19 GHz theoretical rain rate (R), T_B relation and a 30 km FOV produces the bias and scatter observed in previous studies and radar simulations presented here. The calculations for 19 GHz also show that the fractional rain coverage (f) of the FOV is correlated with $\overline{R}$ for a constant T_B, with larger f associated with smaller $\overline{R}$.

At 37 GHz, the FOV simulation results for each polarization for a Nimbus 7 SMMR FOV (588 km^2) reproduce similar results to observed distributions for ocean background conditions. A combination of the two

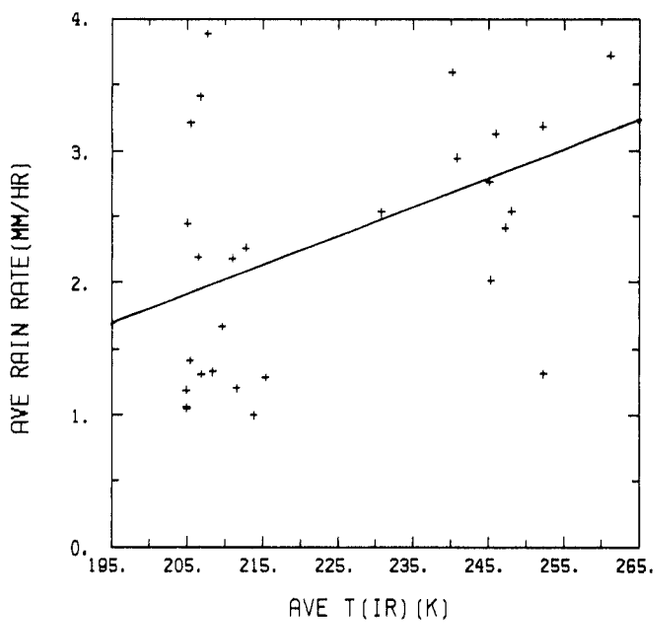

Fig. 9. Distribution of T(IR) versus $\overline{R}$ for T_B (19 GHz) between 190-195 K.

polarizations in general confirms the results of Spencer (1985), except for smaller rain rate magnitudes.

An initial attempt to use IR data to obtain rain distribution information within simulated (from radar) 19 GHz, 30 km FOV's indicate positive results at $\overline{T}_B \leq 200$ K. This may be the first step in combining microwave and IR data for rain estimation.

7. References

Adler, R. F., and R. A. Mack, 1984: Thunderstorm cloud height-rainfall rate relations for use with satellite rainfall estimation techniques. J. Clim. Appl. Meteor., 23, 280-296.

Austin, P. M., and S. G. Geotis, 1978: Evaluation of the quality of precipitation data from a satellite-borne radiometer. Final Report, NASA Grant 5024, 30pp.

Lovejoy, S., and G. L. Austin, 1980: The estimation of rain from satellite borne microwave radiometers. Quart. J. Roy. Meteor. Soc., 106, 255-276.

Negri, A. J., and R. F. Adler, 1984: A new technique to infer convective rainfall from satellite infrared cloud observation. Preprints, Conf. on Satellite/Remote Sensing and Applications, AMS, Clearwater Beach, FL, 58-63.

Rodgers, E. B., and R. F. Adler, 1981: Tropical cyclone rainfall characteristics as determined from a satellite passive microwave radiometer. Mon. Wea. Rev., 109, 506-521.

Simpson, J., and V. Wiggert, 1969: Model of precipitation cumulus towers. Mon. Wea. Rev., 97, 471-489.

Smith, E. A., and S. Q. Kidder, 1978: A multispectral satellite approach to rainfall estimates. Colorado State University (unpublished report).

Spencer, R. W., 1985: A satellite passive 37 GHz scattering based method for measuring oceanic rain rates. J. Clim. Appl. Meteor., accepted.

Spencer, R. W., B. B. Hunter, and W. S. Olsen, 1983: Nimbus 7 37 GHz radiances correlated with radar rain rates over the Gulf of Mexico. J. Clim. Appl. Meteor., 22, 2095-2099.

Szejwach, G., R. F. Adler, I. Jobard, and R. A. Mack, 1986. A cloud model-radiative model combination for determining microwave T_B-rainrate relations. Preprints, Second Conf. on Satellite/Remote Sensing and Applications, Williamsburg, VA.

Wilheit, T. T., A. T. C. Chang, M. S. V. Rao, E. B. Roders, and J. A. Theon, 1977: A satellite technique for quantitatively mapping rainfall rates over the ocean. J. Appl. Meteor., 16, 551-560.

Wu, R., and J. A. Weinman, 1984: Microwave radiances form precipitation clouds containing aspherical ice, combined phase and liquid hydrometeors. J. Geo. Res., 89, 7170-7178.

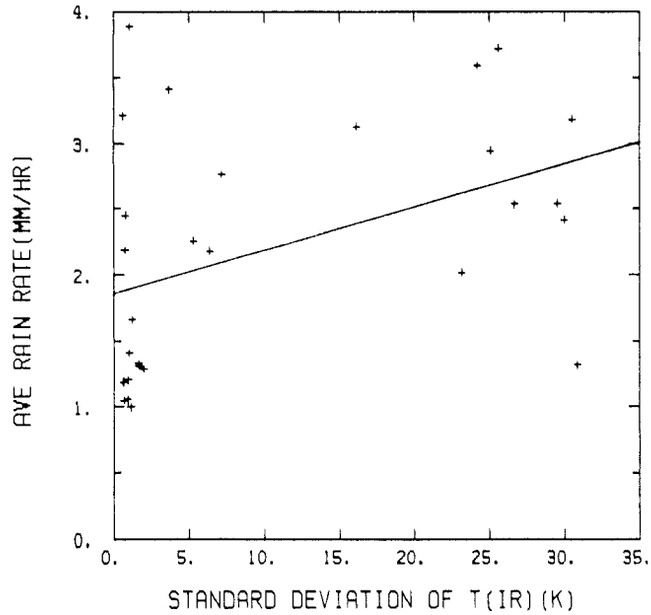

Fig. 10. *Distribution of σ_{T_B} versus $\overline{R}$ for T_B (19 GHz) between 190-195 K.*

INFLUENCE OF SURFACE ROUGHNESS ON MICROWAVE PASSIVE MEASUREMENTS OF RAIN OVER OCEAN

Masaharu Fujita

Radio Research Laboratory
Koganei, Tokyo 184, Japan

1. INTRODUCTION

Global monitoring of rain activity is very important from a viewpoint of the earth's environment, since rain plays an important role in water as well as heat budgets of the earth. For the purpose, some experiments were conducted by means of microwave radiometers onboard the Nimbus and the Seasat satellites (Wilheit et al., 1977; Rodgers and Adler, 1981; Alishouse, 1983) to relate the antenna temperature with rain rate. Although the microwave passive technique has been evaluated to detect rain over land (Rodgers et al., 1979; Rodgers and Siddalingaiah, 1983; Spencer et al., 1983; Spencer, 1984), the algorithm has not yet been established due to relatively large variability of background brightness temperature over land. On the contrary, brightness temperature of ocean background is relatively uniform and low as compared with that of land, so that it is convenient for quantitative measurements of rain from space platforms (Wilheit et al., 1977). Recently, Fujita et al. (1985a) have analyzed the data of an airborne 10 GHz radiometer to show a good correlation with rain rate profiles inferred by a dual-frequency scatterometer onboard the same aircraft over ocean.

Microwave radiometry is also used for remote sensing of ocean surface winds (Nordberg et al., 1969, 1971; Webster et al., 1976; Wentz et al., 1982). In the previous investigations, however, rain and ocean measurements have been examined usually separately, and the rain and the ocean surface roughness due to surface wind have been regarded as an affecting factor for each of their objectives. Wu and Fung (1973) computed brightness temperatures of rain-filled medium over wind-roughened ocean; however, their aim was to evaluate the effect of rain on ocean measurements. In the present article, the influence of ocean surface roughness on quantitative measurements of rain rate by microwave radiometry is examined by a model computation. Two-scale rough surface model developed by Wu and Fung (1972) is used and the equations of transfer of polarized radiation are solved by the method of successive approximation (Fujita, 1985).

2. TWO-SCALE ROUGH SURFACE MODEL

Several models were proposed to characterize a rough ocean surface as reviewed by Fung (1982). Among them, a two-scale rough surface model developed by Wu and Fung (1972) is adopted in the present computation. Although rms height of small irregularities involved in the theory was determined based on experimental results, they gave closed form expressions of differential scattering coefficients of ocean surface due to small irregularities superposed on large undulations. In this case, the differential scattering coefficient is given as follows:

$$\Gamma_{\alpha\beta}(\theta,\psi,\phi)=\Gamma_{\alpha\beta}^{0}(\theta,\psi,\phi)+\langle\Gamma_{\alpha\beta}^{1}(\theta,\psi,\phi)\rangle\ , \qquad (1)$$

$$\alpha,\beta=v,h\ ,$$

where the subscripts α and β denote the polarization states of the incident and the scattered fields, respectively, v and h stand for vertical and horizontal polarization, respectively, and θ and ψ are nadir angles of incidence and scattering, respectively. ϕ is the azimuth angle of scattering. The first term of the right hand side of (1) indicates the differential scattering coeffient due to large undulations and the second term indicates that due to small irregularities averaged over the distribution of the surface normals of the large undulations. Large undulations and small irregularities are both modeled by Gaussian surface height distribution and Gaussian surface correlation. The wind speed dependence of the surface roughness is characterized by their rms slope for large undulations and by their standard deviation and correlation length for small irregularities. These were determined based on the previous experiments. The presence of small irregularities on ocean surface usually causes decrease of the magnitude of its reflection coefficients. To take into account of the influence of small irregularities, the modified Fresnel reflection coefficients were used in their theory. However, they gave only the expressions of the differential scattering coefficients for the scattered field of vertical or horizontal polarization with the incident fields being both vertical and horizontal polarizations. By following their equations and Stogryn (1967), the differential scattering coefficients for four combinations of incident and scattered polarization states are derived and used in the computation. Since the equations are lengthy and complicated, they are not shown here.

The differential scattering coefficients of ocean surface are functions of surface parameters including wind direction as well as nadir and azimuth angles of incidence and scattering. Therefore, when we compute the expected brightness temperature measured over ocean, three-dimensional approach is necessary. However, to solve the equations of transfer of polarized radiation in a scattering medium (rain), three-dimensional approach may be somewhat difficult due to a limitation of computer resources. As a compromize, the differential scattering coefficients are averaged

over azimuth to reduce the problem to be two-dimensional.

The wind speed dependence of rms slope of large undulations is obtained by averaging the results from the expressions by Stogryn (1967), which are given as follows:

$$g_x^2 = 0.003 + 1.92\times10^{-3}w \quad , \tag{2}$$

$$g_y^2 = 3.16\times10^{-3}w \ , \tag{3}$$

where g_x^2 and g_y^2 are the mean-square slopes in the crosswind direction and in the direction parallel to the wind, respectively; w is the wind speed in m/s. The wind speed dependence of the standard deviation and the correlation length of small irregularities averaged over azimuth are calculated from the following wavenumber spectrum given by Masuko et al. (1986) assuming $kl=2$, where k is the wavenumber of microwaves and l is the correlation length:

$$W(K,\phi,U)=4.43\times10^{-5}U^{1.94}(1+0.45U^{0.04}\cos2\phi) \times K^{-4.08} \quad , \quad 7<U<15 \ (m/s), \tag{4}$$

where K is the wavenumber, ϕ is the azimuth angle relative to upwind direction, and U is the wind speed at 19.5-m height. Although the definitions of w and U may be different from each other, they are regarded as the same with each other.

Once the differential scattering coefficients are obtained, we can calculate the emissivities of wind-roughened ocean as follows:

$$\varepsilon_\alpha(\theta) = 1 - \frac{1}{4\pi}\int_0^{2\pi}\int_0^{\frac{\pi}{2}} \{\Gamma_{\alpha\beta}(\theta,\psi,\phi) + \Gamma_{\alpha\alpha}(\theta,\psi,\phi)\}\sin\psi d\psi d\phi. \tag{5}$$

3. NUMERICAL SOLUTION OF THE EQUATIONS OF TRANSFER OF POLARIZED RADIATION

The equations of transfer of polarized radiation are given as follows (Weinman and Guetter, 1977):

$$\frac{dT_\alpha(z,\theta)}{ds} + \gamma_e(z)T_\alpha(z,\theta) = \gamma_s(z)\int_0^\pi \{T_\alpha(z,\theta_i)F_{\alpha\alpha}(\theta,\theta_i) + T_\beta(z,\theta_i)F_{\beta\alpha}(\theta,\theta_i)\}\sin\theta_i d\theta_i + \gamma_a(z)T(z), \tag{6}$$

$$\alpha,\beta = v,h$$

with

$$s = z\cos\theta, \tag{7}$$

where T_v and T_h are the brightness temperatures of vertical and horizontal polarization components, respectively, T is the medium temperature, and γ_e, γ_a and γ_s are extinction, absorption and scattering coefficient of the medium, respectively. $F_{\alpha\beta}(\theta,\theta_i)$, $\alpha,\beta=v,h$, is an element of the phase matrix which describes the intensity of scattered radiance toward θ direction with β-polarized state relative to that of incident radiance from θ_i direction with α-polarized state.

To solve the equations in a scattering medium, the atmosphere is divided into N horizontally stratified slabs of Δz thickness, within each of which the atmospheric parameters are assumed to be constant and uniform. In this situation, the equations can be solved formally, and the downward radiance expressed in brightness temperature within the n-th slab is given as follows (Fujita, 1985):

$$T_\alpha(z',\theta)\big|_n = E_\alpha(z',\theta)\big|_n + \{E_\alpha(\Delta z,\theta)\big|_{n-1} + \sum_{i=1}^{n-2} E_\alpha(\Delta z,\theta)\big|_i \cdot \prod_{j=i+1}^{n-1} A(\Delta z,\theta)\big|_j\}\cdot A(z',\theta)\big|_n \ ,$$

$$\alpha=v,h, \text{ and } \pi\geqq\theta>\frac{\pi}{2} \tag{8}$$

with

$$E_\alpha(z',\theta)\big|_n = \frac{S_\alpha(\theta)\big|_n + \gamma_a\big|_n T\big|_n}{\gamma_e\big|_n} \times \{1-\exp(\gamma_e\big|_n z'\sec\theta)\}, \tag{9}$$

$$A(z',\theta)\big|_n = \exp(\gamma_e\big|_n z'\sec\theta), \tag{10}$$

where the subscript preceded by a vertical bar indicates the slab number, and z' denotes the vertical distance in the n-th slab. $S_\alpha(\theta)$ in (9) denotes the scattering source term corresponding to the first term of the right hand side of (6). No radiances are assumed to be impinging onto the top boundary of the atmosphere; however, it can be easily included by adding its term to (8). By using (8), the boundary conditions at the underlying surface, i.e., wind-roughened ocean surface can be written as,

$$T_\alpha(\Delta z,\psi)\big|_N = \int_{\frac{\pi}{2}}^{\pi}\{T_\alpha(\Delta z,\theta)\big|_N\Gamma_{\alpha\alpha}(\theta,\psi) + T_\beta(\Delta z,\theta)\big|_N \times \Gamma_{\beta\alpha}(\theta,\psi)\}\sin\theta d\theta + \varepsilon_\alpha(\psi)T_o \ ,$$

$$\alpha,\beta=v,h, \quad \frac{\pi}{2}>\psi>0, \tag{11}$$

where $\Gamma_{\alpha\alpha}$ and $\Gamma_{\beta\alpha}$ are the differential scattering coefficients averaged over azimuth as described in the previous section, and ε_α is the emissivity of the ocean surface given by (5): T_o is the ocean surface temperature. Upward polarized radiances can be written as in the same manner with (8) by using (11) as the lower boundary conditions.

In the present numerical technique, at first, angular distributions of polarized radiances in selected discrete directions are computed at the middles of each slab, where scattering due to raindrops is assumed to occur, by putting the scattering source terms at zero. The resulting radiances are used to compute the values of the scattering source terms. Then, upon substituting them into the energy source expression as is given by (9), angular distributions of polarized radiances are again computed. This procedure is repeated until the criterion for convergence is satisfied.

4. MODEL COMPUTATION

The radiometer frequencies are chosen as 10 and 35 GHz aiming to analyze the data obtained by an airborne dual-frequency scatterometer/radiometer system (Okamoto et al., 1982). Height of rain layer is assumed to be 3 km above wind-roughened

ocean, and it is divided into 30 slabs, each having the thickness of 100 m. Vertical profile of rain rate distribution is assumed to be uniform. Extinction, absorption and scattering coefficients of rain are computed by using the Mie scattering theory assuming spherical raindrops, and the modified Marshall and Palmer raindrop size distribution proposed by Olsen et al. (1978). They, in km^{-1}, are related with rain rate R in mm/h by a regression technique as follows:

35 GHz

$$\gamma_e = 0.0502\ R^{1.04}\ ,$$
$$\gamma_s = 0.0112\ R^{1.24}\ , \qquad (12)$$

10 GHz

$$\gamma_e = 1.90\times10^{-3}\ R^{1.29}\ ,$$
$$\gamma_s = 6.10\times10^{-5}\ R^{1.56}\ , \qquad (13)$$

where $\gamma_a=\gamma_e-\gamma_s$. However, the scattering phase matrix is approximated by the Rayleigh one at both frequencies by referring to Savage (1978) and Weinman and Guetter (1977). At the frequencies, the absorption in the atmosphere is essentially due to molecular oxygen, water vapor and liquid water droplets (Wilheit et al., 1977), so that in the present computation only these constituents are taken into account. The model atmosphere is the same with Fujita et al. (1985a). The height of measurements above ocean surface is chosen to be 6 km to simulate an airborne experiment. The polarized radiances are computed at 36 discrete directions by a difference of 5 degrees from 2.5 degrees to 177.5 degrees relative to vertical direction. Assuming the polarized radiances to be constant within each angular range of 5 degrees, scattering integrals due to raindrops as well as at the ocean surface are evaluated by a summation technique. The ocean surface temperature T_o is fixed to be 288 K.

Figure 1 shows the variation of brightness temperature of the ocean surface without rain as a function of off-nadir angle of measurements with wind speed as a parameter. The results for specular ocean, in which Fresnel reflection coefficients are used, are also depicted for comparison. It can be seen that at 10 GHz, brightness temperature is less influenced by the surface wind as compared with at 35 GHz, and that horizontal polarization is more sensitive to wind speed than vertical polarization. The latter trend is more pronounced at larger off-nadir angles than at nadir. The latter result is consistent with Stogryn (1967). It should be added that the wavenumber spectrum given by (4) is assumed to be valid for the wind speed of 4 m/s. In Figures 2 and 3, brightness temperatures are drawn as a function of rain rate at 2.5 and 47.5 degrees of off-nadir angles at 10 GHz and 35 GHz, the parameter of which is wind speed. Although their magnitudes are different from each other in case by case, the brightness temperature generally increases with increase of wind speed. Since at 35 GHz, the brightness temperature is more influenced by surface wind than at 10 GHz, and is a double-valued function with respect to rain rate as computed by Savage and Weinman (1975) and Weinman and Guetter (1977), and as measured by Fujita et al. (1985a), the frequency is not

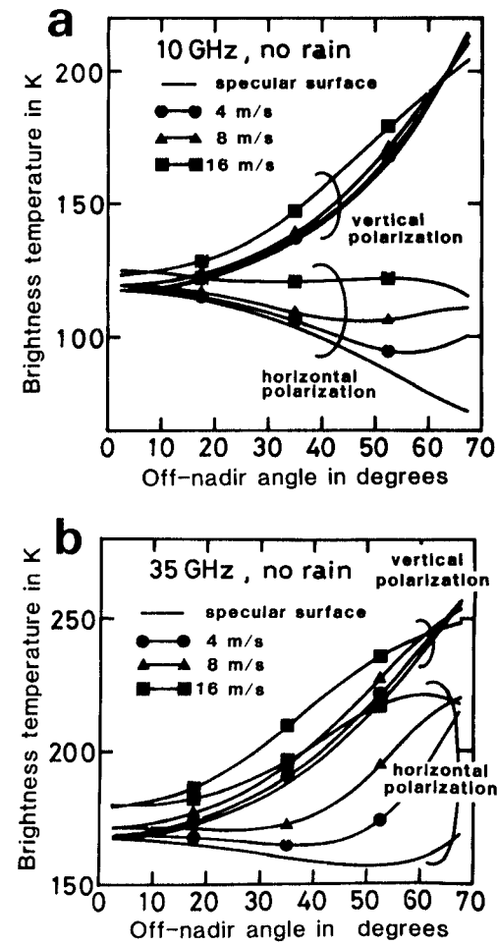

Figure 1. Computed brightness temperature over wind-roughened ocean under no-rain condition. (a) 10 GHz (b) 35 GHz

necessarily suitable for quantitative measurements of rain rate over ocean. Therefore, in the following discussions, only 10 GHz is evaluated concerning with rain rate.

As is expected from Figure 1, the increase of brightness temperature due to surface wind is small at near nadir angle, i.e., 2.5 degrees, than at the off-nadir angle of 47.5 degrees. This suggests to us that nadir-looking configuration is desirable for rain measurements by microwave radiometry over ocean. The relation between the 10 GHz brightness temperature and the rain rate is determined from the results for the specular ocean at the nadir angle of 2.5 degrees by a linear regression, which is given as follows:

$$R = 0.316T_B - 36.62,$$
$$r^2 = 0.9983, \qquad (14)$$

where R is rain rate in mm/h, and T_B is the brightness temperature in K, and r^2 is the determination coefficient. The rain rates are estimated from the computed brightness temperatures under various wind speed conditions by using the relation of (14) and the results are summarized in Table 1. It can be seen that estimated rain rates become larger as

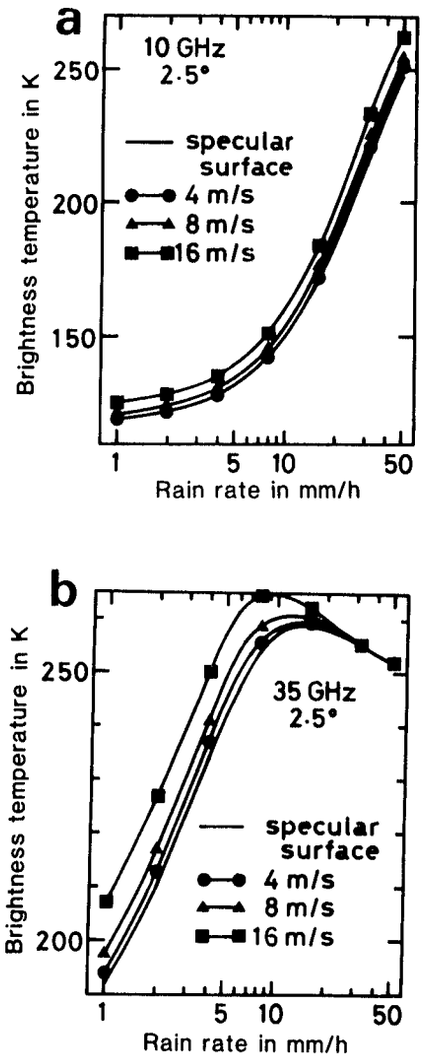

Figure 2. Influence of surface wind on the brightness temperature as a function of rain rate at the nadir angle of measurements of 2.5 degrees. The results for both polarizations are almost the same with each other. (a) 10 GHz (b) 35 GHz

the wind speed increases, and at 16 m/s of wind speed, rain rate is overestimated by 5 mm/h when the assumed rain rate is 16 mm/h or 32 mm/h. It should be noted, however, that the absolute value of brightness temperature may be influenced by calibration of a radiometer as well as due to the variations of surface wind and ocean surface temperature. Additional errors as mentioned above in the brightness temperature may cause more deviation of estimated rain rates than those in Table 1. To reduce partly these effects, the excess brightness temperature, which is the difference between the brightness temperature under raining condition and that under non-raining condition, may be useful (Fujita et al.,1985a). Again the linear regression technique is used to

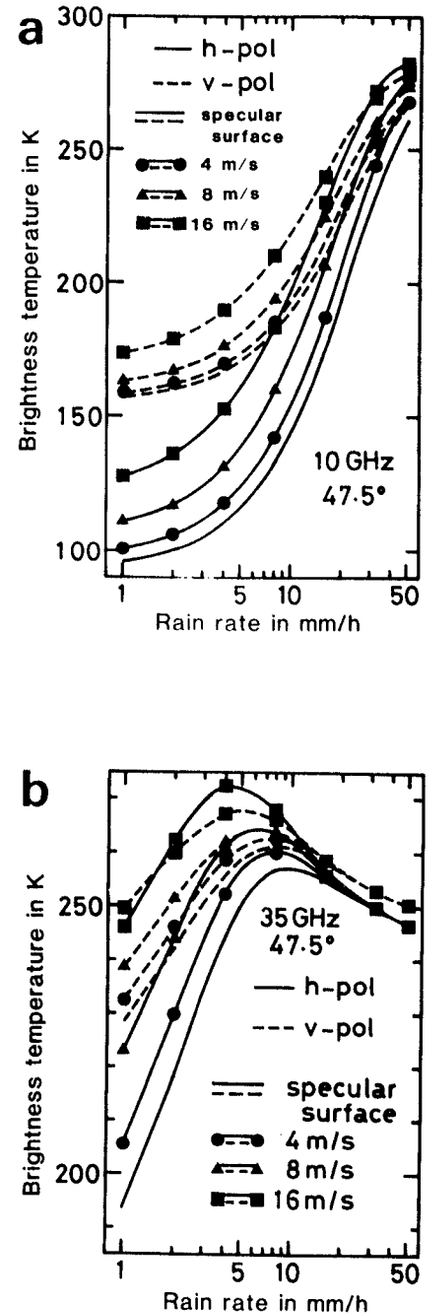

Figure 3. The same as Figure 2 except the nadir angle of measurements of 47.5 degrees. The difference of brightness temperature due to the difference in polarization is clearly seen. (a) 10 GHz (b) 35 GHz

determine the relation between the excess brightness temperature and the rain rate, which is given below:

$$R = 0.316\Delta T_B + 0.441, \quad r^2 = 0.9983, \tag{15}$$

where ΔT_B is the excess brightness temperature in K. The result of rain rate estimation from the excess brightness temperature is listed in Table 2. By comparing Tables 1 and 2, improvements in the estimation accuracy can be seen especially under the high wind speed conditions. When evaluating the excess brightness temperature, however, another problem occurs to determine the brightness temperature under non-raining condition. Reference to the 35 GHz data may be applicable to choose the location over which 10 GHz brightness temperature under non-raining condition is determined. Consideration on this subject in relation to the surface wind condition will be done in a future.

Table 1. Influence of surface wind on the estimation of rain rate from the brightness temperature.

Assumed rain rate	Specular ocean	Wind speed 4 m/s	8 m/s	16 m/s
1	1.0	1.0	1.6	2.9
2	1.8	1.8	2.5	3.8
4	3.7	3.8	4.5	6.0
8	8.0	8.3	9.2	11.0
16	16.9	17.6	18.8	21.3
32	31.5	32.6	34.0	37.0

The unit is in mm/h.

Table 2. Influence of surface wind on the estimation of rain rate from the excess brightness temperature.

Assumed rain rate	Specular ocean	Wind speed 4 m/s	8 m/s	16 m/s
1	1.0	1.0	1.0	1.1
2	1.8	1.9	1.9	2.0
4	3.7	3.9	4.0	4.1
8	8.0	8.4	8.7	9.1
16	16.9	17.7	18.2	19.5
32	31.5	32.7	33.5	35.2

The unit is in mm/h.

5. COMPARISON OF MEASUREMENTS WITH COMPUTED BRIGHTNESS TEMPERATURES

Computed results of brightness temperatures over wind-roughened ocean are compared with the measurements made by an dual-frequency (10 GHz and 35 GHz) airborne radiometer (Fujita et al., 1985a). Since the original aim of the flight experiment was for the measurements of rain, truth data of ocean surface parameters including surface wind were not measured at the time. In addition to them, the off-nadir angle of measurements was restricted to be up to about 30 degrees due to a limitation of the implementation on the aircraft, so that it may be somewhat difficult to assess experimentally the effect of surface wind on brightness temperature. Keeping these restrictions in mind, 35 GHz horizontally polarized brightness temperatures are plotted as a function of path-integrated rain rate together with their theoretical predictions at the off-nadir angle of measurements ranging from 25 to 30 degrees. The theoretical predictions are at 27.5-degree of off-nadir angle. The path-integrated rain rates are obtained by integrating the rain rate profiles inferred by a dual-frequency scatterometer onboard the same aircraft (Fujita et al., 1985b).

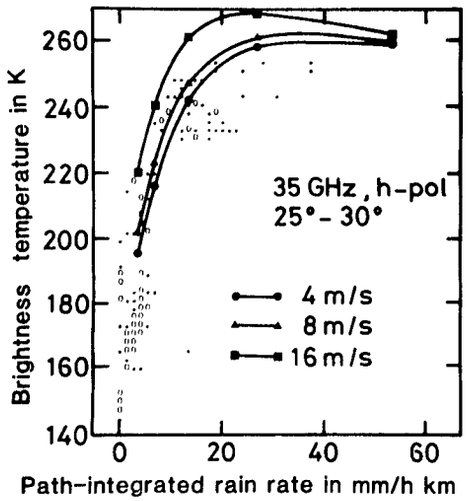

Figure 4. Comparison between the measured (dots and circles) and the computed brightness temperature at 35 GHz over ocean. The polarization is horizontal. The parameter of computation is wind speed. Circles indicate multiple data points.

When the path-integrated rain rate is small, i.e., up to 10 mm/h km, the measurements seem to be consistent with 4 m/s or 8 m/s line. This result may be partly supported by the wind speed measurements of 3-4 m/s made at the coast. However, they become lower than the theoretical predictions when the path-integrated rain rate increases in excess of about 10 mm/h km. When the off-nadir angle of measurements becomes large, reflected radiances at the ocean surface toward a radiometer are not necessarily originated from raindrops covered with an antenna beam. Therefore, if spatial inhomogeneity of rain rate distribution is large, measurements may not agree with theoretical predictions on the assumption of a horizontally stratified rain model. In the present computations, the differential scattering coefficients of the ocean surface are averaged over azimuth, so that the effect of wind direction does not appear in the results. This effect may also cause the difference between the measurements and the theoretical predictions.

The measurements with detailed surface truth data collection are necessary to evaluate exactly the influence of surface wind on brightness temperature of rain over ocean. In addition, three-dimensional treatment of the problem may be worth

for detailed understandings of the influence of surface wind on quantitative measurements of rain rate over ocean.

6. CONCLUDING REMARKS

In the present article, the influence of surface wind on the measurements of rain rate over ocean by microwave radiometry is evaluated by a model computation. As the results, it becomes apparent that the nadir-looking configuration is suitable to minimize the influence of surface roughness due to wind over ocean. In this situation, both polarizations give almost the same brightness temperature. The influence can be more reduced by using the excess brightness temperature for rain rate estimation than by using the brightness temperature itself. At large off-nadir angle of measurements, vertical polarization is less influenced by ocean surface roughness than horizontal polarization.

Combination of a scatterometer and a radiometer may be worth for remote sensing of rain and ocean surface wind simultaneously.

REFERENCES

Alishouse, J.C., 1983: Total precipitable water and rainfall determination from the SEASAT scanning multichannel microwave radiometer. *J. Geophys. Res.*, 88, 1929-1935.

Fujita, M., 1985: Computation of brightness temperature of horizontally stratified rain having a vertical profile. *Proc. 1985 Int. Symp. Antennas Propag.*, 297-300, Aug., Kyoto, Japan.

Fujita, M., K. Okamoto, H. Masuko, T. Ojima and N. Fugono, 1985a: Quantitative measurements of path-integrated rain rate by an airborne microwave radiometer over ocean. *J. Atmos. Ocean. Tech.*, 2, 285-292.

Fujita, M., K. Okamoto, S. Yoshikado and K. Nakamura, 1985b: Inference of rain rate profile and path-integrated rain rate by an airborne microwave rain scatterometer. *Radio Sci.*, 20, 631-642.

Fung, A.K., 1982: Review of random surface scatter models. *Proc. SPIE*, 358 (Applications of Mathematics in Modern Optics), 87-98.

Masuko, H., K. Okamoto, M. Shimada and S. Niwa, 1986: Measurement of microwave back-scattering signatures of the ocean surface using X-band and Ka-band airborne scatterometers. *submitted to J. Geophys. Res.*

Nordberg, W., J. Conaway and P. Thaddeus, 1969: Microwave observations of sea state from aircraft. *Quart. J. Roy. Meteor. Soc.*, 95, 408-413.

Nordberg, W., J. Conaway, D.B. Ross and T. Wilheit, 1971: Measurements of microwave emission from a foam-covered, wind-driven sea. *J. Atmos. Sci.*, 28, 429-435.

Okamoto, K., S. Yoshikado, H. Masuko, T. Ojima, N. Fugono, K. Nakamura, J. Awaka and H. Inomata, 1982: Airborne microwave rain-scatterometer/radiometer. *Int. J. Remote Sens.*, 3, 277-294.

Olsen, R.L., D.V. Rogers and D.B. Hodge, 1978: The aR^b relation in the calculation of rain attenuation. *IEEE Trans. Antennas Propag.*, AP-26, 318-332.

Rodgers, E.B. and R.F. Adler, 1981: Tropical cyclone rainfall characteristics as determined from a satellite passive microwave radiometer. *Mon. Wea. Rev.*, 109, 506-521.

Rodgers, E.B. and H. Siddalingaiah, 1983: The utilization of Nimbus-7 SMMR measurements to delineate rainfall over land. *J. Climate Appl. Meteor.*, 22, 1753-1763.

Rodgers, E.B., H. Siddalingaiah, A.T.C. Chang and T. Wilheit, 1979: A statistical technique for determining rainfall over land employing Nimbus 6 ESMR Measurements. *J. Appl. Meteor.*, 18, 978-991.

Savage, R.C., 1978: The radiative properties of hydrometeors at microwave frequencies. *J. Appl. Meteor.*, 17, 904-911.

Savage, R.C. and J.A. Weinman, 1975: preliminary calculations of the upwelling radiance from rain clouds at 37.0 and 19.35 GHz. *Bull. Amer. Meteor. Soc.*, 56, 1272-1274.

Spencer, R.W., 1984: Satellite passive microwave rain rate measurement over cropland during spring, summer and fall. *J. Climate Appl. Meteor.*, 23, 1553-1562.

Spencer, R.W., B.B. Hinton and W.S. Olson, 1983: Nimbus-7 37 GHz radiances correlated with radar rain rates over the Gulf of Mexico. *J. Climate Appl. Meteor.*, 22, 2095-2099.

Stogryn, A., 1967: The apparent temperature of the sea at microwave frequencies. *IEEE Trans. Antennas Propag.*, AP-15, 278-286.

Webster, W.J., Jr., T.T. Wilheit, B.B. Ross and P. Gloersen, 1976: Spectral characteristics of the microwave emission from a wind-driven foam-covered sea. *J. Atmos. Sci.*, 28, 429-435.

Weinman, J.A. and P.J. Guetter, 1977: Determination of rainfall distributions from microwave radiation measured by the Nimbus 6 ESMR. *J. Appl. Meteor.*, 16, 437-442.

Wentz, F.J., V.J. Cardone and L.S. Fedor, 1982: Intercomparison of wind speeds inferred by the SASS, Altimeter, and SMMR. *J. Geophys. Res.*, 87, 3378-3384.

Wilheit, T.T., A.T.C. Chang, M.S.V. Rao, E.B. Rodgers and J.S. Theon, 1977: A satellite technique for quantitatively mapping rainfall rates over the ocean. *J. Appl. Meteor.*, 16, 437-442.

Wu, S.T. and A.K. Fung, 1972: A noncoherent model for microwave emissions and backscattering from the sea surface. *J. Geophys. Res.*, 77, 5917-5929.

Wu, S.T. and A.K. Fung, 1973: A theory of microwave apparent temperature over the ocean. *NASA Contractor Report CR-2329*, 146pp.

VISIBLE AND INFRARED STRUCTURE OF FLORIDA CONVECTION AND ITS IMPLICATIONS FOR ESTIMATING RAINFALL

Andrew J. Negri
Robert F. Adler

Laboratory for Atmospheres
NASA/Goddard Space Flight Center
Greenbelt, MD 20771

1. INTRODUCTION

It is the intent of this study to explore the relationships between satellite visible (VIS) and infrared (IR) viewed cloudy grid cells and the variability of the precipitation contained therein. Our understanding of these relationships, and the acknowledgement of the limitations of these data, will better enable us to estimate precipitation from space. This is particularly important over the tropical oceans, where knowledge of the rainfall will perhaps imply knowledge of the latent heating and its effects on atmospheric circulation. The advent of microwave remote sensing systems will not render the VIS/IR techniques obsolete. Such data will still be necessary to provide the diurnal variability missing from twice daily observations from low earth orbiters.

This study is similar to that of Arkin (1979) in that it looks at the precipitation characteristics of cloudy grid cells. Time and space scales are 30 min and 32 km, considerably smaller than the 6 h and 5 degree scales employed by Arkin. This study also considers the effect of the visible channel data on the estimation of rainfall. In that respect, it complements the work of Tsonis and Isaac (1985) and Wu et al. (1985).

The objective of this study is to understand the (instantaneous) relationships between cloudiness and rainfall. In this way we may begin to apply what we have learned to improve upon existing techniques and perhaps gain an understanding of the limitations of VIS/IR techniques.

2. DATA

Five days during the second Florida Area Cumulus Experiment (FACE-2) were examined using radar and GOES VIS/IR data. Table 1 contains a list of the dates and available times. The area of study was approx. 250 km on a side, centered in southern Florida (near 26N, 81W). Only data between 50 and 170 km of the WSR-57 radar at Miami were analyzed.

2.1 Satellite Visible Data

The satellite data used are the GOES East visible (0.55-0.70 μm) and infrared (10.5-12.6 μm) channels. Figure 1 (top) is a sequence of four visible images on one case study day, 12 Aug 1978. The resolution is nominally 1 km, and over Florida it is enlarged slightly north-south. In quantitative applications, each visible pixel is corrected for the effect of illumination angle on the perceived brightness. The brightness value of each pixel was multiplied by $1/\sqrt{(\cos Z)}$, where Z is the zenith angle of the sun (see Tsonis and Isaac, 1985). In practice, because of both the small variation in latitude across the region, and the small variation in declination between days, only the hour angle was varied in the computation of Z. This normalization was realistic only through 2200 GMT each day. Raw visible counts are 0-255, however after normalization, some pixels representing sides of clouds or cloud turrets can, late in the day, exceed 255.

Table 1

Data used in this study

DAY	TIMES[1]	# IMAGES	COMMENTS
29 Jul 1978	1800-0000	13	
12 Aug 1978	1600-0030	21	3-15 min images
16 Aug 1978	1800-0000	15	2-15 min images
29 Aug 1979	1630-0030[2]	20	7-15 min images
18 Aug 1980	1630-2300	14	

[1] Visible data to 2200 GMT
[2] No data 2130-2230 GMT

Convection on this day developed about 1600 GMT, between Lake Okeechobee and the east coast. Convection reached a maximum between 2000 and 2200 GMT, with one extensive cloud anvil eventually covering the entire peninsula. Other days were similar in the temporal variation of convection, although rain amounts in the FACE target area (small trapezoid in Fig. 1) varied.

2.2 Satellite Infrared Data

The nominal resolution of the IR data is 8 km, however, due to 50% oversampling in the east-west direction, pixel spacing is approx. 4 km. The data have been converted from IR counts to temperatures via a standard IR calibration (GOES/SMS User's Guide, 1976, NOAA/NASA). Figure 1 (middle) is the corresponding IR data. Contours display the 253, 233 and 213 K isotherms. The 253 K isotherm delineates cloud from no-cloud in this study, a convention used by Griffith et al. (1978).

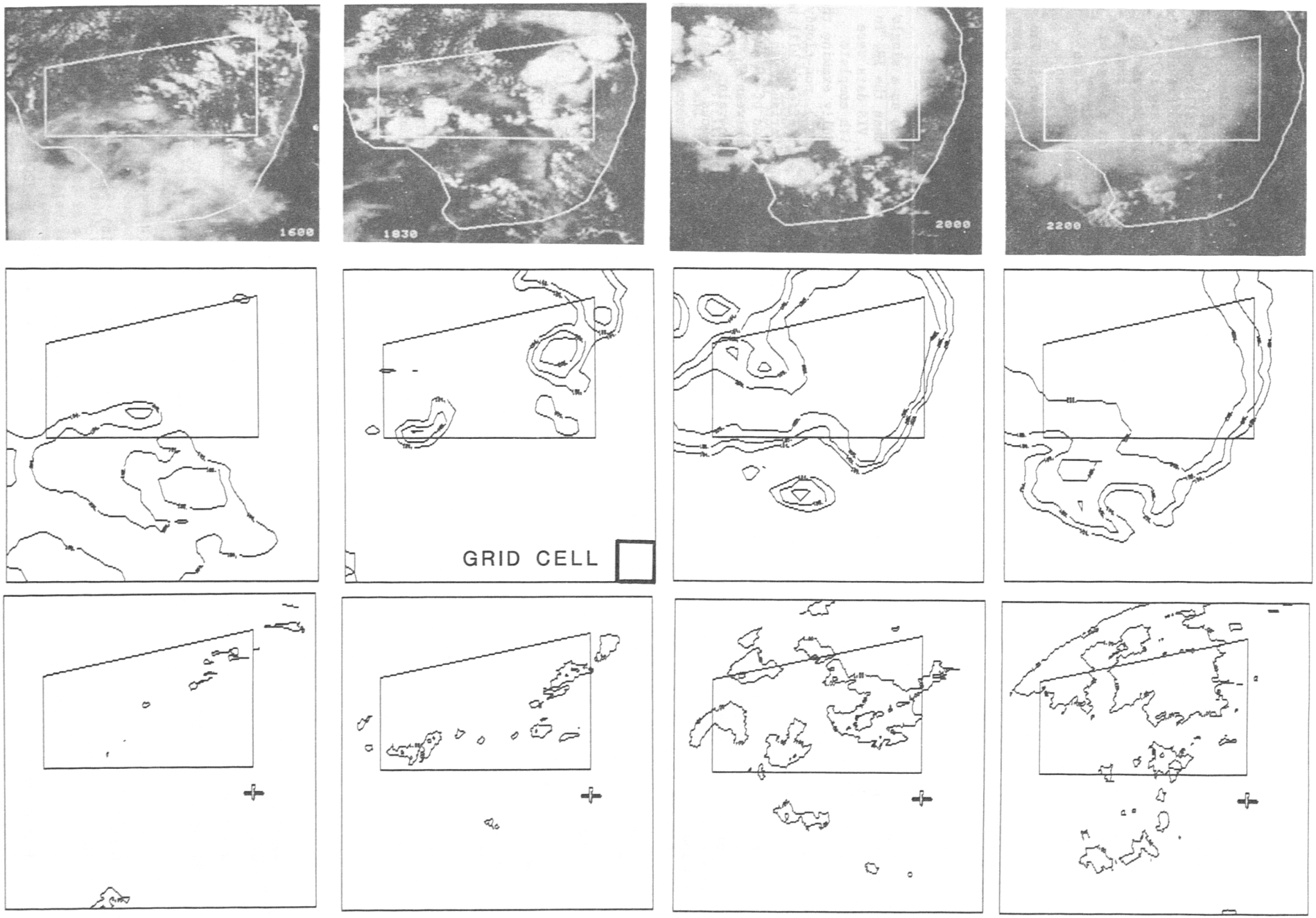

Fig. 1. TOP: Sequence of GOES visible images 1600, 1830, 2000, 2200 GMT 12 Aug 1978. Trapezoid is the FACE target area.
MID: GOES infrared temperatures. Contours are 253, 233, 213 K. Sample grid cell is shown on 1830 GMT image.
BOT: WSR-57 radar data mapped to GOES projection. Contours are 1 and 40 mm/h. Cross marks location of Miami.

2.3 Radar Data

Digital radar data from the WSR-57 radar at Miami were used in this study. A complete description of the radar data is available in Lopez et al., (1984). The 0.5 degree elevation scan coincident with the GOES scan time of Miami was selected (generally no more than a 2 min difference). Reflectivity to rainrate conversion was accomplished using $Z = 300R^{1.4}$ where Z is the reflectivity (mm^6/m^3) and R is the rainrate (mm/h) [Barnston et al., 1981]. Rainrates less than 1.0 mm/h were set to zero, while rainrates greater than 200 mm/h were set to this value. Figure 1 (bottom) displays the corresponding radar data. A threshold of 1 mm/h was used to distinguish rain from no-rain. The 40 mm/h contour is also displayed.

2.4 Averaging Procedure

The radar data were remapped to GOES coordinates in a two-step process. Raw data were first mapped to a cartesian system using RADPAK (Heymsfield et al., 1983). This array was then mapped to GOES coordinates using bi-linear interpolation with nearest neighbor resampling. A constant height of 10 km was used to offset the parallax introduced by the satellite viewing angle.

Full resolution data were averaged (in satellite coordinates) into grid cells 32 x 32 visible pixels (8 x 4 IR pixels). This represents an area of approx. 1024 km^2, varying slightly across the region. A sample grid square is drawn in the 1830 GMT IR panel of Fig. 1.

Table 2 displays the various parameters examined in this study.

3. VARIABILITY OF THE MEAN RAINRATE

Subsequent statistics are stratified into two regimes:

a) grid cells with $F_{253} > 0$ (at least one IR pixel colder than 253 K)

b) grid cells with $F_{253} = 1.0$ (completely cloudy grid cells)

Table 2

Grid cell parameters examined in this study

IR PARAMETERS

T_{mean}: Mean temperature

T_{min} : Minimum temperature

s_T : Standard deviation of temperature

F_{253}, F_{233}, F_{213}: Fraction covered by cloud colder than subscripted temperatures

VIS PARAMETERS

V_{mean}: Mean (normalized) visible count

s_V : Standard deviation of visible counts

RADAR PARAMETERS

R_{mean}: Mean rainrate

3.1 Regression results for single satellite parameters

The satellite parameters in Table 2 were regressed against the mean rainrate [$\log_{10}(R_{mean})$]. To avoid $\log_{10}(0)$, non-raining grid cells were assigned a nominal value of 0.01 mm/h. Figure 2 shows a typical scatterplot, from 12 Aug 1978. While R_{mean} generally increases with decreasing T_{min}, much scatter exists. The plot only shows raining grid cells; there also exist a range of T_{min} for non-raining (but cloudy) cells. T_{min} explained only 27% of the variance of R_{mean}.

Other parameters tested are shown in Table 3. Explained variance is in general low, but more importantly, it is inconsistent from day to day. More variance is explained when the grid cell is completely cloudy (part b), than with incomplete (but non-zero) cloud cover (part a). T_{min} and F_{213} explain the most variance of any IR parameter.

The effect of VIS data (taken as a single predictor) were more inconsistent than the IR. To exclude the effect of the surface, VIS data were taken only from those grid cells with complete cloud cover. Additionally, to carefully examine the "structure" of clouds (in terms of s_V), non-cloudy VIS pixels must be excluded or edge effects will be interpreted as texture. Explained variance was low, (Table 3, part c), with the exception of 29 Aug 1979. The high (0.82) correlation between V_{mean} and R_{mean} is a reflection of rain/no-rain discrimination rather than a continuous estimation

Table 3

Percent explained variance of $\log_{10}(R_{mean})$[1]

	29 Jul 1978	12 Aug 1978	16 Aug 1978	29 Aug 1979	18 Jul 1980
a) IR parameters when $F_{253} > 0$					
T_{mean}	22%	17%	5%	7%	8%
T_{min}	30	27	7	16	14
F_{213}	34	28	3	17	8
s_T	9	1	1	0	1
# obs.	(332)	(522)	(363)	(432)	(371)
b) IR parameters when $F_{253} = 1$					
T_{min}	36%	41%	13%	14%	8%
s_T	19	0	3	1	0
# obs.	(224)	(211)	(57)	(180)	(138)
c) VIS parameters when $F_{253} = 1$					
V_{mean}	17%	32%	0%	67%	9%
s_V	5	1	0	14	0
T_{min} (2)	34	44	8	45	20
# obs.	(93)	(116)	(27)	(70)	(107)

(1) if R_{mean} was 0.0, R_{mean} was set to 0.01 mm/h
(2) reduced data sample 1600-2200 GMT

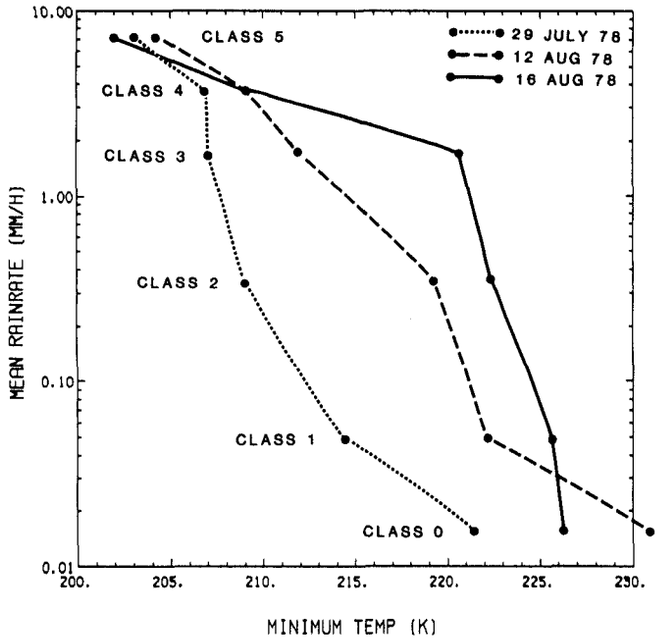

Fig. 3. *Relationships between minimum temperature (K) and classes of mean rainrate (mm/h) for three case study days.*

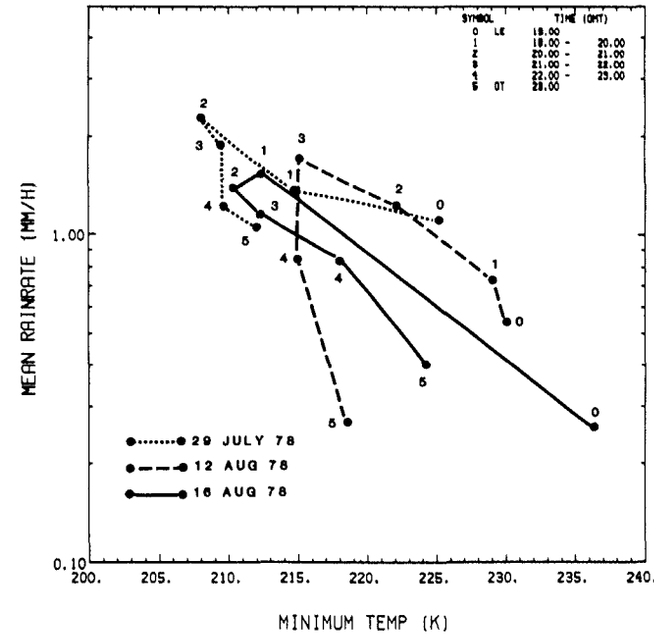

Fig. 4. *Time averages of the minimum temperature (K) and mean rainrate for three case study days, showing the convective cycle.*

Griffith et al. (1978) recognize this asymmetry and incorporate the life history of 253 K defined clouds into their model. The success of this incorporation is arguable; the statistics of Meitin et al. (1981), who use this approach, show consistent underestimates of rain during the first half of each rain event followed by overestimates later in the day. Comparable results for daily rainfall have been obtained from cloud definitions with no life history (Negri et al., 1984).

On 29 July 1978, large areas of stratiform rain produced from extensive convective anvils are evidenced by the 1 mm/h mean R_{mean} and the slow warming of the mean T_{min} after 2100 GMT (see dotted curve in Fig. 4, points 3,4,5). On 16 Aug 1978, the slope of the curve is similar for both the growth and decay phase of the convection, indicating a general relation between T_{min} and R_{mean} might produce realistic estimates.

As was evidenced in Fig. 3, significant variability (10-15 K) existed between days. This is compounded by the variability in T_{min} and R_{mean} on any given day (Fig. 2). Such results indicate the problems faced in using such data to estimate precipitation on this scale.

3.4 Results for two satellite parameters

One parameter estimators, particularly in the IR, can ultimately have only limited success, given the problems of discriminating among active convection, thin (non-precipitating cirrus) and anvil debris. This is compounded by the inherent variability of the data. Thus, a second parameter is sought that will aid in this discrimination. Ideally what is needed is a parameter correlated to rainfall but uncorrelated to temperature, Then, in combination, each parameter can explain rainrate variance separately. Unfortunately, such orthogonal or independent parameters are rare; brighter clouds tend to be higher and thicker, hence colder.

Three parameters were tested in conjunction with T_{min} in a multiple regression with $\log_{10}(R_{mean})$; V_{mean}, s_T and s_V. Table 5 shows the increase in explained variance for each parameter. Results for s_T should be compared to the variance explained by T_{min} in Table 3, part b. Results for the VIS parameters should be compared to the percentages in Table 3, part c.

Results overall are poor. V_{mean}, due to either its low correlation with R_{mean} or its high correlation with T_{min} did not contribute to the explained variance. While results for 29 Aug 1979 show an increase of 24%, this 69% (45% from Tmin) represents only a 2% increase over V_{mean} alone (see Table 3, part c). The visible correlations are strongly influenced by a few points of dark, thin anvil material without rain. This was the only day of the five where a visible threshold might aid in rain/no-rain discrimination.

It was hoped that s_V would be an indicator of cloud structure and thus help pinpoint areas of active convection; this was not found. It is probable that s_V is not uniquely related to the presence of overshooting tops. Identification of such regions is largely a function of sun angle and illumination. Ripples and waves in cirrus anvils may be showing up as "textured" cloud while at times of low sun zenith angle, (i.e. near noon) intense rain is found below relatively "smooth" cloud.

Figure 5 represents an example of this two parameter approach. R_{mean} (in 6 classes) is shown as a function of T_{min} and s_V for completely cloudy grid cells on 12 Aug 1978. A threshold T_{min} would effectively separate rain from no-rain on this day, without the addition of a second parameter. At T_{min} < 210 K, one might expect larger s_V (indicating overshooting tops) to be correlated with R_{mean}. This was not the case. Physically, the "0" points represent cold, cloudy boxes of uniform

of R_{mean} by V_{mean}; i.e. the statistics reflect the fact that 25% of the completely cloudy cells were thin (dark) anvil material with no attendant rain. Section 3.4 will further address the addition of VIS data.

3.2 Discriminant analysis results for single satellite parameters

Rather than estimate a continuous spectrum of R_{mean}, the data were grouped into 6 classes. For each satellite parameter, a mean and standard deviation for each rain class was computed. Results from 12 Aug 1978 are shown in Table 4, with satellite parameter T_{min}. A t-test was performed to see if the means were separable. Results indicate a significant difference in the means between all pairs of rain classes except adjacent classes 1/2 and 3/4. The no-rain class is class "0". The extent to which these results could be used in an estimation scheme on independent data is unclear. A maximum likelihood estimate using the data in Table 4 would assign all observations to either the "0" or "2" class, because they have the highest probabilities of occurence.

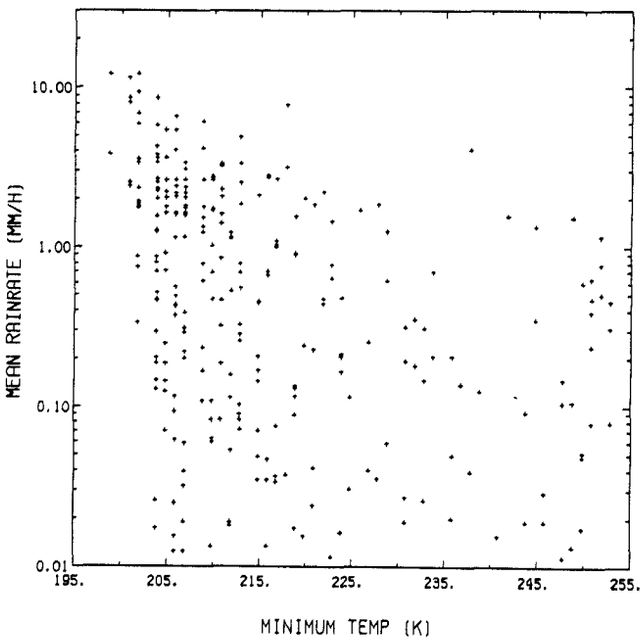

Fig. 2. *Minimum temperature (K) vs. mean rainrate (mm/h) for grid cells 1600-0030 GMT 12-13 Aug 1978. Not plotted, but included in the statistics, are non-raining (but cloudy) grid cells.*

To further complicate any proposed utility, the mean satellite parameters of each class varied from day to day. Figure 3 shows a dramatic difference in the T_{min} - R_{mean} curves for three of the case study days. At high R_{mean} and low T_{min}, only a 3 K variation in T_{min} is seen. This increases to 13 K at lower R_{mean}. This difference is of the same magnitude as the variation between classes on any given day (about 15 K). For example, a T_{min} of 221 K would indicate (in the mean) no rain on 29 July 1978 but an R_{mean} of 2.5-5.0 mm/h on 16 Aug 1978. Temperature profiles were identical on these days, however, there was a deeper layer of moisture on 29 July 1978. Adler and Mack (1984) have investigated the effect of vertical profiles of temperature and moisture on satellite rainfall schemes.

3.3 Effect of convective life cycle

To examine the effect of the convective life cycle, observation pairs (T_{min}, R_{mean}) were stratified into six periods by time of day. For each period, a mean T_{min} and mean R_{mean} were determined. The pattern that emerges is shown in Fig. 4, for 12 Aug 1978 (dashed line), 29 July 1978 (dotted line) and 16 Aug 1978 (solid line). In each case mean T_{min} decreases as mean R_{mean} increases until convective activity is a maximum. After that point, mean R_{mean} decreases, but not along the same curve as in the early stages. For example, on 12 Aug 1978, mean T_{min} increases (warms) 4 K as mean R_{mean} decreases by an order of magnitude. The temperature decrease in the growth cycle on this day was 15 K.

TABLE 4 STATISTICS ON THE SEPARABILITY OF RAIN CLASSES BY MINIMUM TEMPERATURE

NUMBER OF OBSERVATIONS (NUM) IN EACH CLASS, THE MEAN MINIMUM TEMPERATURE (MEAN) AND THE STANDARD DEVIATION (STD) ARE USED IN A ONE-TAILED t-TEST AT SIGNFICANCE LEVEL 0.05. DIFFERENCES IN MEANS ARE SEPARABLE IF TABULAR ENTRIES [$t_{(computed)} - t_{(0.05,a)}$] ARE POSITIVE. SECOND ENTRY IS THE DEGREES OF FREEDOM (a). DATA ARE FROM 1600-0030 GMT 12-13 AUG 1978.

	MEAN RAINRATE (MM/H)					
	< 0.01	0.01 - 0.10	0.10 - 1.00	1.00 - 2.50	2.50 - 5.00	> 5.00
NUM	239.00	63.00	104.00	64.00	36.00	16.00
MEAN	230.90	222.21	218.66	211.94	209.14	204.19
STD	13.94	15.05	15.21	11.27	6.97	4.46
	0	1	2	3	4	5
1	2.664 / 300					
2	5.594 / 341	-0.198 / 165				
3	8.353 / 301	2.665 / 125	1.386 / 166			
4	7.508 / 273	3.207 / 97	1.946 / 138	-0.323 / 98		
5	5.956 / 253	3.011 / 77	2.093 / 118	0.999 / 78	0.888 / 50	

visible texture, i.e anvil cirrus. Such "clustering" of the data in the VIS/IR domain has been noted by Tsonis and Isaac (1985).

4.0 CONCLUSIONS

The variability of the mean rainrate over areas approximately 32 km on a side was examined. Attempts were made to explain this variance in terms of satellite parameters, specifically the minimum grid cell temperature. Explained variance for grid cells with at least 1/32 cloud cover (253 K threshold) varied from 8 to 22%. Results were higher, 8 to 36%, when only completely cloudy cells were considered. On one day (29 Aug 1979) mean visible count explained 67% of the variance, however this was essentially due to a group of data (dark, non-raining cirrus) which has a large impact on the regression.

Classification of the mean rainrate into 6 groups showed little improvement, due to high variability of the satellite parameters both between groups and among days. Results showed dependency on time of day (i.e. convective cycle). This remains a candidate for further study. Significant variability existes between days even for the time averaged rainrate and minimum temperature.

Addition of a second parameter to the regression improved the results slightly (1-8%), with the exception of a 24% increase on the aforementioned 29 Aug 1979 case. This was the only one of five days where the VIS data demonstrated a rain/no-rain discrimination. Results using VIS data are less encouraging than those reported by Wu et al. (1985) and Tsonis and Isaac (1985), who specifically considered rain/no-rain delineation. This discrepancy remains a topic of further investigation. A problem not noted elsewhere in this text was the different calibration of the VIS data between satellites (years) particularly at the high (bright) end. Results overall were discouraging for using VIS/IR data to estimate precipitation rate on these time and space scales.

Table 5

Percent additional variance of $\log_{10}(R_{mean})$ explained by T_{min} and one other parameter

	Parameters when $F_{253} = 1$				
	29 Jul 1978	12 Aug 1978	16 Aug 1978	29 Aug 1979	18 Jul 1980
s_T	6%	2%	8%	5%	1%
V_{mean}	1	0	1	24	0
s_V	1	2	1	8	1

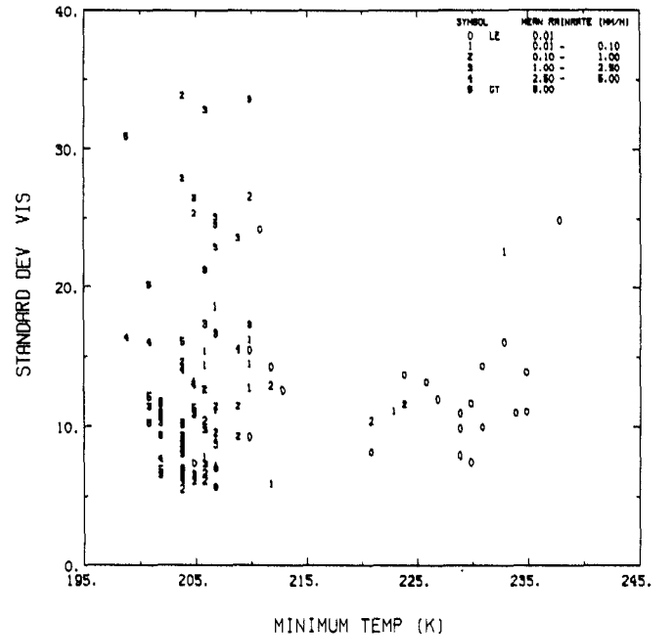

Fig. 5. *Classes of mean rainrate (mm/h) as a function of the minimum temperature (K) and visible standard deviation, for completely cloudy grid cells on 12-13 Aug 1978.*

5.0 REFERENCES

Adler, R. F. and R. A. Mack, 1984: Thunderstorm cloud height-rainfall rate relations for use with satellite rainfall estimation techniques. J. Clim. Appl. Meteor., 23, 280-296.

Arkin, P. A., 1979: The relationship between fractional coverage of high cloud and rainfall accumulations during GATE over the B-scale array. Mon. Wea. Rev., 107, 1382-1387.

Barnston, A. G., W. L. Woodley, and M. Brown, 1981: FACE-2 data reductions and analyses, Part II. NOAA TECH MEMO ERL OWRM-8, U.S. Dept. of Commerce, NOAA, Boulder, CO, 380 pp.

Griffith, C. G., W. L. Woodley, P. G. Grube, D. W. Martin, J. stout, and D. N. Sikdar, 1978: Rain estimation from geosynchronous satellite imagery: visible and infrared studies. Mon. Wea. Rev., 106, 1153-1171.

Heymsfield, G. M., K. K. Ghosh, and L. C. Chen, 1983: An interactive system for compositing digital radar and satellite data. J. Clim. Appl. Meteor., 22, 705-713.

Lopez, R. E., D. O. Blanchard, D. Rosenfeld, W. L. Hiscox, and M. J. Casey, 1984: Population characteristics, development processes and structure of radar echoes in south Florida. Mon. Wea. Rev., 112, 56-75.

Meitin, J. G., W. L. Woodley, and C. G. Griffith, 1981: FACE-2 data reductions and analyses: Part V. Satellite estimated rainfall from a geostationary platform in FACE-2. NOAA TECH. MEMO. ERL OWRM-11, U.S. Dept. of Commerce, NOAA, Boulder, CO, 141 pp.

Negri, A. J., R. F. Adler, and P. J. Wetzel, 1984: Satellite rain estimation: An analysis of the Griffith-Woodley technique. J. Clim. Appl. Meteor., 23, 102-116.

Tsonis, A. A. and G. A. Isaac, 1985: On a new approach for instantaneous rain area delineation in the midlatitudes using GOES data. J. Clim. Appl. Meteor., 24, 1208-1218.

Wu, R., J. A. Weinman, and R. T. Chin, 1985: Determination of rainfall rates from GOES satellite images by a pattern recognition technique. J. Atmos. Ocean. Tech., 2, 314-330.

9.2 PRECIPITATION DISCRIMINATION FROM SATELLITE INFRARED TEMPERATURES OVER EASTERN MONTANA

Mitchell Weiss
Research and Data Systems, Corp.
Lanham, Md. 20706

Eric A. Smith
Dept. of Meteorology
Florida State University
Tallahassee, Fl. 32306

1. INTRODUCTION

Much research has been done on estimating convective rainfall from infrared and visible satellite data. Various studies have shown that convective rainfall from individual thunderstorms can be identified and predicted reasonably well, (Scofield and Oliver, 1977; Griffith et al., 1978; Lovejoy and Austin, 1979; Stout et al., 1979; Wylie, 1979; Griffith et al., 1981; and Whitney, 1982). To accomplish this, many of these studies have considered the physical properties of convective clouds obtained from the cloud top temperature field of infrared images. The proper identification of heavier rain areas in regions of enhanced convection is advantageous since, as seen in Figure 1, it is these rain events which contribute most to the cloud's total volumetric rainfall.

This paper will entail the use of infrared imagery from Geostationary Operational Environmental Satellites (GOES) to properly categorize areas of significant rainfall from light and non rain areas of convective clouds based on a variety of cloud parameters calculated from the cloud top temperature field. The technique of statistical discriminant analysis will be applied to derive and test a series of statistical models consisting of the cloud parameters to identify rainfall. Further discussion of the technique used to categorize rainfall will be given along with a review of the significance and accuracy of the results.

2. TECHNIQUE

This study attempts to statistically correlate various physical parameters derived from the satellite derived cloud top temperature field to different rainrate thresholds in order to more accurately categorize the rainfall representative of higher rain rate events. The optimal combination of cloud parameters was statistically selected to discriminate between raining and non-raining regions of fairly large

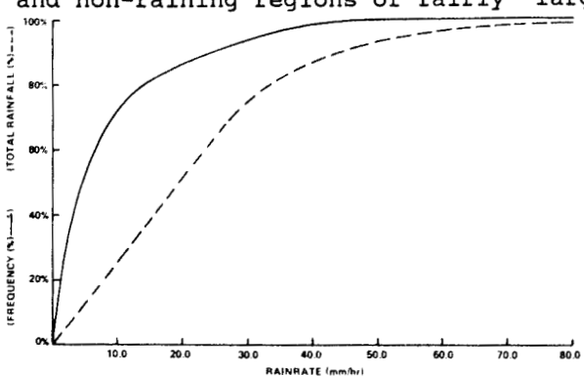

Figure 1. Rain rate frequency and their contribution to the total volumetric rainfall as measured from all the case study days used in this study.

summer season convective systems over the U.S. High Plains.

2.1 Cloud Parameters

Before any cloud parameter calculations were made, a cloud top temperature threshold was selected which defined the convective cloud area. In addition, this temperature threshold eliminated clouds too warm to be considered rain producers. A threshold temperature of 253°K, used in a satellite rainfall estimation study by Griffith et al. (1981) over the U.S. High Plains was used in this study.

A listing and description of all the cloud parameters is given in Table 1. The consensus of many satellite rainfall studies is, that the coldest cloud top temperature (CCTT) is a region of active convection and an area where rainfall is more likely to occur (e.g., Griffith et al. (1978).

The tightest gradient (GRAD) of the cloud top temperature field has been shown by Scofield and Oliver (1977) to occur in the upwind (300 mb level) portion of the cloud, where the convection is most active and where rainfall is likely. The absolute value of gradient was calculated using the basic equation

$$\nabla T = \frac{\partial T}{\partial x}\hat{i} + \frac{\partial T}{\partial x}\hat{j}, \quad (1)$$

where T is the cloud top temperature. The cloud parameter CGRAD aided in evaluating the importance of gradients within the most highly convective cloud regions.

The Laplacian (LAP) of the cloud top temperature field is a measure of the rate of change of the horizontal gradient on a horizontal plane (Zapotocyny, 1981). The Laplacian is potentially a very powerful variable because it offers the possibility of detecting cold convective towers which may be associated with rain without being associated with the CCTT (Whitney, 1982). The basic equation used in calculating Laplacian is

$$\nabla^2 T = \frac{\partial^2 T}{\partial x^2} + \frac{\partial^2 T}{\partial y^2}, \quad (2)$$

where positive values of Laplacian indicate peaks of colder temperatures while negative values indicate valleys of warmer temperatures. As with gradient, the maximum value of Laplacian for the CCTT (CLAP) was calculated.

Other cloud parameters considered were the average cloud top temperature for cloud areas less than or equal to 253°K (AVGCCT), the temperature of the tropopause minus the CCTT (CTSTT), the ratios of the CLAP to CCTT (CLAPDT) and of CGRAD to CCTT (GRADDT). The time change in cloud parameter quantities between images for all 9 variables were calculated except CTSTT (the change over time of CTSTT is the same as CCTT). Scofield and Oliver

Table 1.

List and description of all cloud parameters calculated from the cloud top temperature field.

Cloud Parameter Subscript	Cloud Parameter Description	Physical Relationship to Rainfall
1	CCTT Coldest Cloud Top Temperature	Convectively active cloud region
2	GRAD Largest Absolute Temperature Gradient	In vicinity of cloud updrafts
3	CGRAD Largest Absolute Temperature Gradient of the CCTT	Cloud updrafts associated with the CCTT
4	LAP Largest Temperature Laplacian	Cloud towers within the area of convection
5	CLAP Largest Temperature Laplacian of the CCTT	Coldest most convective cloud towers
6	AVGCCT Average Cloud Top Temperature	Areal extent of the convective region
7	CTSTT CCTT - (Temperature of the Tropopause)	Test for overshooting tops
8	CLAPDT CLAP/CCTT	The physical dependency of of CLAP and CGRAD to CCTT
9	CGRADT CGRAD/CCTT	
10	DEL CCTT The Change Over Time	The variability of convection and/or cloud movement over the past 30 minutes
11	DEL GRAD of Each Respective	
12	DEL CGRAD Cloud Parameter	
13	DEL LAP	
14	DEL CLAP	
15	DEL AVGCTT	
16	DEL CLAPDT	
17	DEL CGRADT	

(1977) demonstrated that a comparison of images 30 minutes apart may indicate either a change in the intensity of the convective system, cloud movement, or a combination of both.

2.2 Statistical Model Calculation

Discriminant analysis is a statistical technique used to select a set of independent variables which optimally discriminate between two or more groups. In this study, rain occurrence acted as the dependent variable and the cloud parameters as the independent variables. This technique is similar to regression analysis except regression attempts to calculate a quantitative estimate of the dependent variable. Neither non-linear analysis nor any special transformations of the independent variables were used. The criteria used to choose the best models were based upon both the percentage of correctly classified and the total number of misclassified rain events.

2.3 Experiments

A series of experiments were used to seek an improved physical interpretation of the statistical method employed. These experiments, outlined in Table 2 essentially modify the dependent variable to account for the difference in the time it takes rainfall representative of rain producing clouds to reach the surface.

Three rain rate thresholds were chosen to help delineate different intensities of rainfall. The rain rate of 1.0 mm/hr was used by Griffith et al. (1978) and in this study to discriminate between rain and no rain occurrence. Rain rate thresholds of 4.0 and 10.0 mm/hr were determined to represent different regimes of rainfall in the convective systems analyzed.

3. DATA

The data chosen for this study were in conjunction with the Cooperative Convective Precipitation Experiment (CCOPE) field project held near Miles City, Montana in the summer of 1981. This site offered an opportunity to study rainfall from summertime convective systems in the High Plains. The case study days of June 12, July 13, and the first storm event of August 2 were chosen to develop the statistical models, and the days of July 11, August 1 and the second storm event of August 2 were used as independent data sets to test these models. These days are all compatible with the type of convective systems targeted by this study. Selection of these days were based on the fact that each convective system was spread over a relatively large area with rainfall occurring in both a large spatial and temporal extent. The constraints of resolution, temporal frequency of the satellite data, and the varying amount of surface station density made the study of small storms too difficult to include.

To verify the occurrence of rainfall, the surface mesonet associated with the CCOPE project was used. The areal density of the CCOPE mesonet is comparable to mesonets in other locations where other satellite rainfall studies have been conducted. The surface mesonet consisted of 96 PROBE (Portable Remote Observation of the Environment) stations and 27 PAM (Portable Automated Mesonet) stations. A thorough quality control analysis was done on both sets of data to eliminate instances of noise (anomalous rain reports). Three different grids, each with a grid spacing of 20 km by 20 km were overlayed on to portions of the surface mesonet. Each grid location served as an independent sample of rainfall verification.

The grids used for the case study days June 12, July 13 and August 2 generally fit the rain gauge density necessary to adequately observe rain areas of a cloud; stated by Silverman (1981) to be 45-80 km^2 per gauge. The grids for these days were overlayed on to the portion of the mesonet where the

Table 2.

The statistical and meteorological considerations involved with modifying the time period of rainfall verification (dependent variable) for each experiment.

Experiment #	Length of Time Period Delay	Statistical Considerations	Meteorological Considerations
1	0 Minutes	The dependent variable is coded 0 (no rain or rain below threshold) and 1 (rainfall above threshold).	Resultant rainfall occurence over the past 30 minutes determined by the cloud top temperature field.
2	10 Minutes	In discriminant analysis the dependent variable can be modified as a means of varying the character of the dependent variable.	Precipitation reaching the ground in association with various features of the cloud top temperature field may occur approximately 10 minutes Grifith (personal communication) after the appearance of the cloud top parameter. This delay may be due to intense updrafts (especially in the developing stage of a storm), strong surface winds and sub-cloud evaporation.
3	30 Minutes	Same as Experiment # 2.	Detecting rainfall over the period following the recognition of convective cloud areas.

combination of PAM and PROBE station were most dense (July 13 used a some what different grid due to missing PAM data). Since rainfall from both July 11 and August 1 occurred over the sparse portion of the mesonet where surface stations were located 20 km apart, each grid contained only one surface station. Due to the lower density of surface stations for the case study days of July 11 and August 1, they were only used as test cases. Since many of the rain events considered in this study occurred after sundown, visible channel measurements of the cloud field were of no value. Infrared imagery were collected from the GOES satellite's Visible and Infrared Spin Scan Radiometer (VISSR) with a resolution of 8 km at the satellite subpoint. Rainfall was classified only for images 30 minutes apart. From each satellite image were obtained independent samples of the cloud top temperature field equal in size to each surface grid location. Accurate navigation, remapping each image to match the projection of the surface grid, and adjustments for paralax (cloud displacement from its actual location as viewed by the satellite) were all essential in processing the satellite data.

4. CLOUD PARAMETER ANALYSIS

Analysis of each surface parameter was undertaken to determine: (1) if each parameter's relationship to rainfall was as expected and; (2) to what degree of discriminatory ability each parameter possesses. In testing their ability to classify, each parameter was compared against each experiment and rain rate threshold by using a box plot. A box plot is an alternative to a scatter plot when the dependent variable is coded into groups. Plotting was done using data limited to those cases used to develop the statistical models.

The colder more convective cloud regions were observed by the parameters CCTT, DEL CCTT, AVGCCT, CTSTT, DEL AVGCCT, CGRAD, CLAP, CGRADT and CLAPDT to discriminate rainfall. The best discrimination coincided strongly with both the heavier rain rate thresholds and with the 10 and 30 minute time delayed rainfall verification. The parameter GRAD however indicated that rainfall associated with the coldest cloud tops might well occur where little gradient is observed. Though cooling cloud top temperature correlated with rainfall occurrence, the parameters DEL GRAD, DEL CGRAD, DEL LAP, DEL CLAPDT and DEL CGRADDT all showed decreases of potentially convective cloud regions as correlating with rainfall consistently over all rain rates and time delays. This may imply that the coldest cloud top temperatures may continue to cool even though other indicators of localized convection have begun to diminish. The cloud parameters LAP and DEL CLAP had such random pattern, they were considered too unreliable to be used for model selection. By not including of these two parameters does not guarantee they are insignificant meteorologically, but only suggests that they are weak classifiers within this data set.

5. STATISTICAL MODEL ANALYSIS

Results from the best statistical models selected for each experiment and rain rate are given in Table 3. The total number of samples used were 166* from the initial storm cases and 147# from the test storm cases.

The most noteworthy results of the 3 experiments were achieved in Experiment 1 at the 10mm rain rate and in Experiment 2 at the 4 and 10mm rain rates. The cloud parameters selected for these statistical models are also very similar. The parameters CCTT and DEL AVGCCT were statistically the most significant predictors of these models followed by DEL GRAD and CTSTT. Selection of these parameters was consistent with their individual behavior with respect to heavier rain rate thresholds and time lags.

(*) One sample was an overly influential outlier, due to a localized heavy shower caused by a small secondary cell. This sample was dropped from the experiments and rainrates where it was determined to be overly influential.

(#) Missing surface data for Experiment 3 resulted in 3 less samples.

Table 3.

The percentage and number of correctly classified samples for both the initial and test data sets for all rain rate thresholds. The subscripts of the cloud parameters (from Table 1) for each tested statistical model are listed in order of predictor significance.

		Experiment #1						Experiment #2						Experiment #3					
		Percent Correct	No Rain		Rain			Percent Correct	No Rain		Rain			Percent Correct	No Rain		Rain		
Initial Data	No Rain	66.2	51		26			66.7	54	27	67.9	55	26	61.3	49	31	62.5	50	30
	Rain	82.0	16		73			69.4	26	59	68.2	27	58	81.2	16	69	81.2	16	69
August 2 Storm #2	No Rain	8.9	3		31			47.2	17	19	44.4	16	20	11.4	4	31	17.1	6	29
	Rain	100.0	0		31			89.7	3	26	93.1	2	27	96.7	1	29	96.7	1	29
August 1	No Rain	29.6	16		38			51.9	27	25	46.2	24	28	38.5	20	32	40.4	21	31
	Rain	100.0	0		18			85.0	3	17	90.0	2	18	94.1	1	16	94.1	1	16
July 12	No Rain	0.0	0		2			0.0	0	5	0.0	0	5	11.1	1	8	11.1	1	8
	Rain	37.5	3		5			100.0	0	5	100.0	0	5	100.0	0	1	100.0	0	1
		Rain Rate Cutoff = 1.0 mm/hour.						Rain Rate Cutoff = 1.0 mm/hour.						Rain Rate Cutoff = 1.0 mm/hour.					
Statistical Model		10, 6, 1, 7, 18						1, 6, 10, 3			1, 10, 6, 8			1, 15, 10, 13			1, 15, 10, 11		
Initial Data	No Rain	82.5	99		21			83.1	98		20			81.5	101		23		
	Rain	71.1	13		32			68.1	15		32			57.1	18		24		
August 2 Storm #2	No Rain	34.9	15		28			60.0	27		18			54.3	25		21		
	Rain	100.0	0		22			90.0	2		18			95.5	1		18		
August 1	No Rain	72.9	43		16			84.5	49		9			75.4	43		14		
	Rain	84.6	2		11			85.7	2		12			91.6	1		11		
July 12	No Rain	25.0	1		3			14.3	1		6			22.2	2		7		
	Rain	100.0	0		6			100.0	0		3			0.0	1		0		
		Rain Rate Cutoff = 4.0 mm/hour.						Rain Rate Cutoff = 4.0 mm/hour.						Rain Rate Cutoff = 4.0 mm/hour.					
Statistical Model		1, 15, 13						1, 15, 11, 7						1, 11, 9					
Initial Data	No Rain	85.5	112	19	84.7	111	20	81.8	108		24			88.1	119		16		
	Rain	61.0	13	21	64.7	12	22	61.8	13		21			48.4	16		15		
August 2 Storm #2	No Rain	55.5	31	25	57.1	32	24	63.0	34		20			84.2	48		9		
	Rain	100.0	0	9	100.0	0	9	100.0	0		11			37.5	5		3		
August 1	No Rain	85.7	54	9	85.7	54	9	92.1	58		5			83.6	51		10		
	Rain	88.8	1	8	77.7	2	7	88.8	1		8			60.0	3		5		
July 12	No Rain	12.5	1	7	12.5	1	7	10.0	1		9			10.0	1		9		
	Rain	100.0	0	2	100.0	0	2												
		Rain Rate Cutoff = 10.0 mm/hour.						Rain Rate Cutoff = 10.0 mm/hour.						Rain Rate Cutoff = 10.0 mm/hour.					
Statistical Model		15, 1, 11, 7			15, 1, 13, 7			1, 15, 11, 7						11, 2, 10, 6, 15, 7					

percentage of correctly classified rain cases at the 10mm rain rate may be due to rain events not associated with a cloud top temperature field, which may have changes during the 30 minutes of time lag.

6. SUMMARY AND CONCLUSION

This study used a statistical discriminant analysis technique to discriminate significant rainfall regions with a low frequency of occurence from both higher frequency light and no rainfall regions in large convective systems over the U.S. High Plains. Cloud parameters derived from the cloud top temperature field as measured by GOES infrared imagery were used as the discriminators. As illustrated in Figure 1, observed rain rates of 10 mm/hr or more contributed to approximately 70 to 75% of the total volumetric rainfall. This study has demonstrated an ability to classify these significant rain events. The highest percentages of correct classifications were 60% and higher when surface rainfall was lagged by 10 minutes at the 4 and 10 mm/hr rain rate thresholds. Using a zero and 30 minute time lag at the 10.0 and 4.0 mm/hr cutoffs respectively produced correct percentages of at least 50%. Overall accuracy was found to increase when raising the rain rate cutoff. It is believed that by using a 10 minute time delay, the rain or no-rain producing areas of the cloud top temperature field become more representative of precipitation occurrence on the ground. Lower accuracy at the 1.0 mm rain rate cutoff compared to the higher rain rate cutoffs indicates that light rainfall may occur too randomly within the cloud to enable adequate classification. The cloud parameters coldest cloud top temperature, and the change over time of the average cloud top temperature, were found to be the best classifiers in this study. These variables demonstrated the importance of active areas of convection in causing rainfall.

Overall there was an improved ability to detect rainfall events when using higher rain rate cutoffs. As recalled from Figure 1, the detection of heavy rainfall events are especially important when considering their contribution to the total volumetric rainfall. Poor no rain classification evidenced by the July 11 case may be attributed to the convective system's rapid development at the time of study. Since the cases used for the initial data were not undergoing such rapid development, the derived models may not have correlated well to this system.

With the exception of July 11, the percentage of correctly classified samples at the 10mm/hr threshold is greater than 50 percent for all 3 experiments however, the presence of both non-rain producing cloud anvils and contamination from convective cloud samples producing light rain may have added some difficulty to the no rain group of classifications.

Comparisons of Experiment 1 and 2 illustrate an overall improvement in rainfall classification when surface rainfall verification is lagged by 10 minutes as seen in Figure 2. This lag time seems to have made the instantaneous observations of the cloud top temperature field more representative of surface rainfall. The 10 minute time lag when combined with the 10 mm rain rate threshold offered the best overall discrimination of rainfall with all correct percentages over 60 percent. These results are noteworthy because the heavier rain episodes can be identified with significant accuracy, even though their frequency of occurrence is low.

More randomness in the percentages of correctly classified samples occurred when trying to classify rainfall lagged by 30 minutes. Results from the 4mm/hr rain rate are consistent with results from Experiment 2 at the 4 and 10mm rain rates in both percentage of correctly classified cases and of two parameters CCTT and DEL GRAD comprising the statistical models. A decrease in the

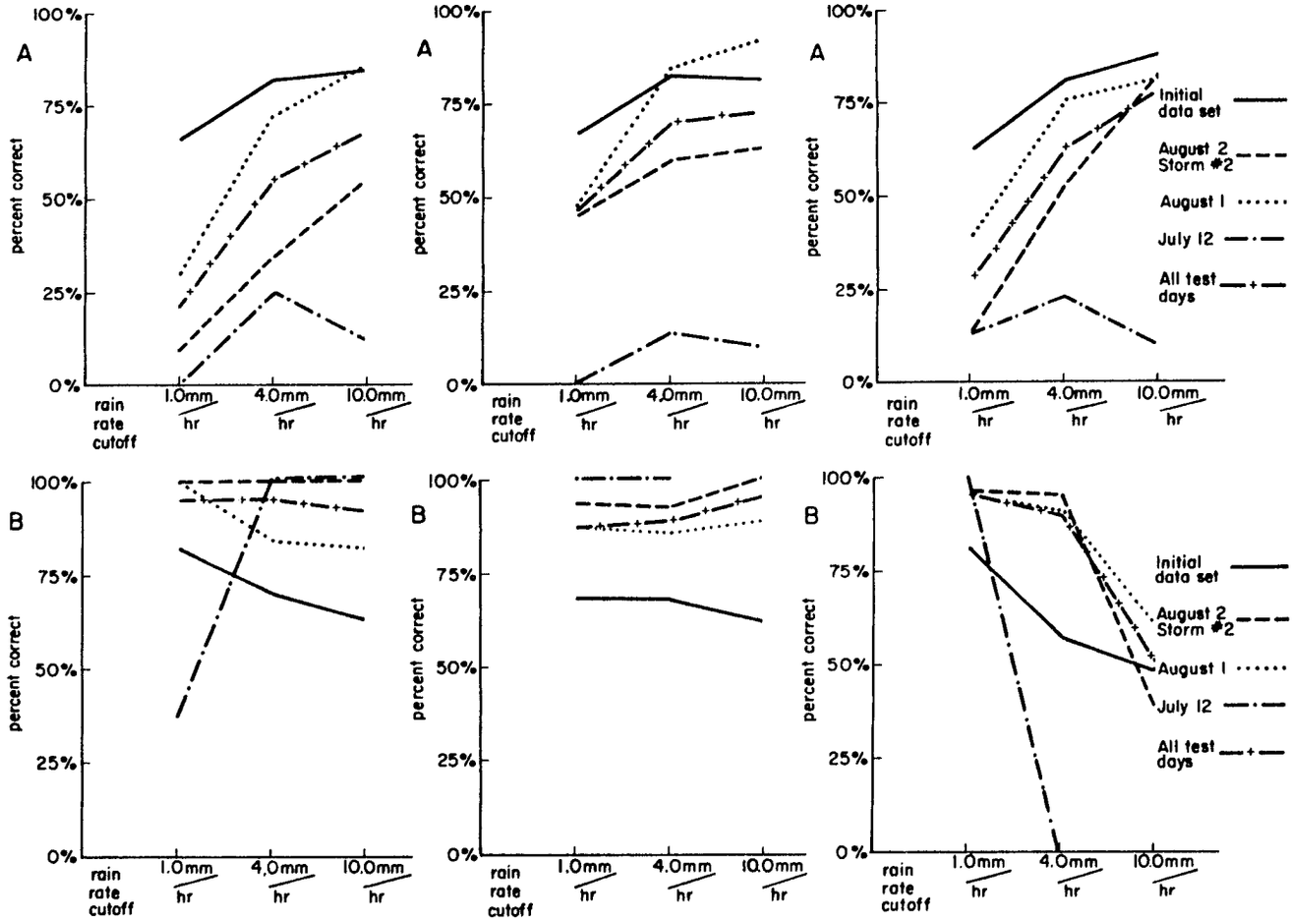

Figure 2. The percentage of samples correctly classified as no rain or rainfall below each rain rate threshold (A) and rainfall at or above each rain rate threshold (B) for all experiments.

The importance of identifying significant rain areas in large convective systesm areas is clearly important. Many studies which try to measure total volumetric rainfall could consider higher rain rate thresholds when trying to pinpoint areas of significant rainfall. This can be especially useful in an area such as the U.S. High Plains, where high cloud bases and sub-cloud evaporation make significant rain areas less frequent but important to detect.

7. ACKNOWLEDGEMENTS

Much thanks go to Thomas H. Vonder Haar for his suggestions and advice during the course of the research at Colorado State University. Appreciation is extended to Research and Data Systems, Corp. for their help in preparing the manuscript. This investigation was supported by National Oceanic and Atmospheric Administration under Contract NA81AA-0-00058.

8. REFERENCES

Griffith, C.G., W.L. Woodley, P.G. Grube, D.W. Martin, J. Stout and D.N. Sikdar, 1978: Rain estimation from geosynchronous satellite imagery-visible and infrared studies. Mon. Wea. Rev., 106, 1153-1171.

_____, J.A. Augestine and W.L. Woodley, 1981: Satellite rain estimation in the U.S. High Plains. J. Appl. Meteor., 20, 53-66.

Lovejoy S. and G.L. Austin, 1979: The delineation of rain areas from visible and IR satellite data for GATE and Mid-latitudes. Atmos. Ocean, 20, 77-92.

Scofield, R.A., and V.J. Oliver, 1977: A scheme for estimating convective rainfall from satellite imagery. NOAA Tech. Memo. NESS 86, 47 pp.

Stout, J.E., D.W. Martin and D.H. Sikdar, 1979: Estimating GATE rainfall with geosynchronous satellite images. Mon. Wea. Rev., 107, 585-598.

Whitney, L.F., 1982: A statistical approach to rainfall estimation using satellite and conventional data. NOAA Tech. Rep. NESS. 89, 50 pp.

Wylie, D.P. 1979: An application of a geostationary satellite rain estimation technique to an extratropical area. J. Appl. Meteor., 18, 1640-1648.

Zapotochy, J.V., D.R. Johnson, and T.M. Whittaker, 1981: The development and testing of methods to infer midlatitude precipitation intensity from geosynchronous satellite infrared data. Scientific Rep. 81-0252 U.S.A.F. Geophysics Laboratory, Hanscom Air Force Base, MA., 82 pp.

STATISTICAL PROBLEMS IN RAINFALL ESTIMATES FROM RAINGAUGE, RADAR AND SATELLITE DATA.

A. Bellon and G. L. Austin

McGill Radar Weather Observatory
Ste. Anne de Bellevue, Quebec
Canada H9X 1C0

1. INTRODUCTION

In this paper, we are concentrating on the relative skill of raingauge and GOES satellite measurements of rainfall over an area of 2.4×10^5 km^2 during daylight hours. The basic strategy consists in the calibration of the satellite information by gauge-calibrated radar data.

A summary of satellite rainfall estimation methods is contained in a book by Barret and Martin (1981) and the references therein. Recently, Wylie and Laitsch (1983) verified daily and monthly point gauge accumulations with a variety of satellite techniques applied over the same area. They concluded that while the increased frequency of satellite images improved the accuracy, schemes including meteorological data and allowing the judgement of a meteorologist achieved a skill only slightly superior to that obtained by a simple automated IR technique. Negri et al (1984) also argued that simpler techniques independent of cloud life history are just as accurate as the life cycle approach of Griffith et al (1978) and Stout et al (1979). We thus believe that the bispectral method of Lovejoy and Austin (1979) combining the visible and IR data in estimating rainfall to be an adequate objective technique applicable to the variety of synoptic situations affecting the middle latitudes.

This research was sponsored by the Canadian Forestry Service in order to determine the usefulness of satellite rainfall estimates over data scarce forested regions. Since the computation of forest fire indices requires a map delineating the areas of dry and wet ground, Van Wagner (1974), a satellite technique which essentially has skill only in delineating the area of rain should satisfy this requirement.

2. RAINFALL MEASUREMENTS BY GAUGE AND SATELLITE

2.1 Raingauge

Hourly reporting gauges are needed to compare satellite or radar rainfall estimates over periods of less than one day (typically four to nine hours as shown in Table 1). The distribution of 167 gauges over or near the area where satellite rainfall estimates are computed, is shown in Fig. 1. With 15% of the gauges unavailable, the effective gauge density of the network over the area of analysis is approximately one gauge per 1900 km^2. In order to derive a gridded rainfall pattern from the point information available at each of the gauge sites it is necessary to use interpolation methods. A simple technique, the Thiessen method, assigns to every unit grid area (I,J) -(4x4) km^2 in size- the amount recorded by the nearest gauge. The result is a pattern of polygons which outline the area of influence of each gauge, creating artificial rainfall gradients which are strongly dictated by the raingauge distribution.

A more desirable method assigns weights to neighboring gauges which are a function of their distance d_i from (I,J). Thus, the relative contribution of gauge i may be expressed by

$$w_i = e^{-d_i/\lambda}$$

where λ is chosen to be 20 km. Eventual comparison with satellite data has revealed that the verification statistics are relatively insensitive with λ, although the worst comparison is obtained with the Thiessen method.

2.2 Satellite

The IR channel at 11.5 μm from GOES provides information on the temperature,

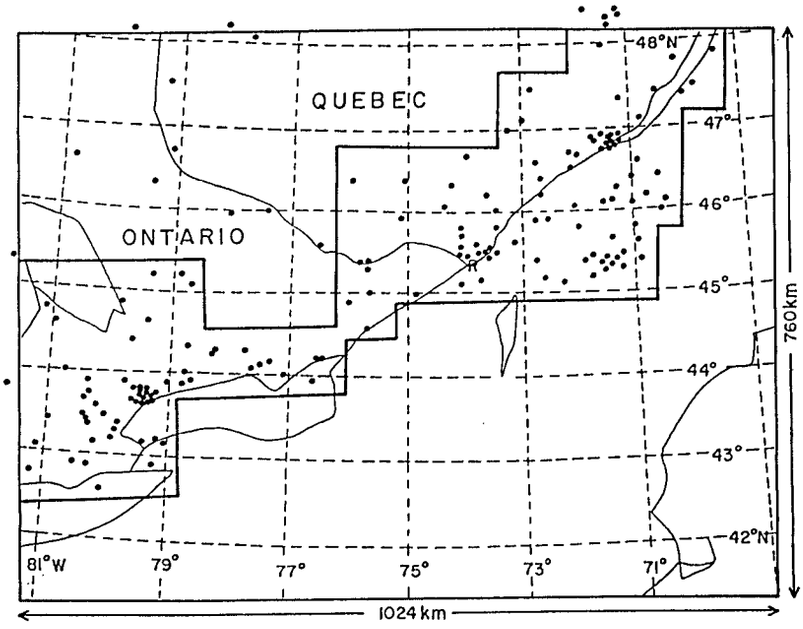

Fig.1: Distribution of Quebec and Ontario hourly reporting gauges over the (1024x760)km^2 area where 4 km resolution satellite rainfall estimates are computed. Verification of those estimates with point gauge measurements or with interpolated gauge fields has been performed only inside the region enclosed by the heavy line. It covers an area of 2.4x10^5 km^2 or 15000 grid areas. The letter "R" indicates the radar location.

and hence the height of the cloud top. The visible brightness at 0.7 μm is related to the thickness of the cloud. Our technique is based on the simple assumption that clouds which are both high and of large vertical extent are more likely to be raining.

In order to eliminate the latitudinal distortion inherent in the raw satellite data, the visible and IR data are remapped at 4 km resolution into a conic projection true at two standard parallels. It is also essential to apply a normalization correction to the visible data, (Cherna et al (1985).

We have derived the rainfall rate as a function of IR and visible satellite data, i.e., R(mm/h) = f(IR,V) where IR is a temperature level in increments of of 5ºC and V is a brightness level of 2 counts. The rainfall rates of four sequences of convective summertime precipitation around Montreal as measured by the McGill radar at a height of 3 km, a resolution of 4 km and within a radius of 180 km have been used as ground truth. For each (IR,V) pair seen by the satellite, the average rainfall rate over the corresponding (4X4) km^2 area measured by the radar has been summed and then divided by the number of occurrences to derive the average satellite rainfall rate. The result is shown in Fig. 2.

It is apparent that high rainfall rates cannot be detected with satellite

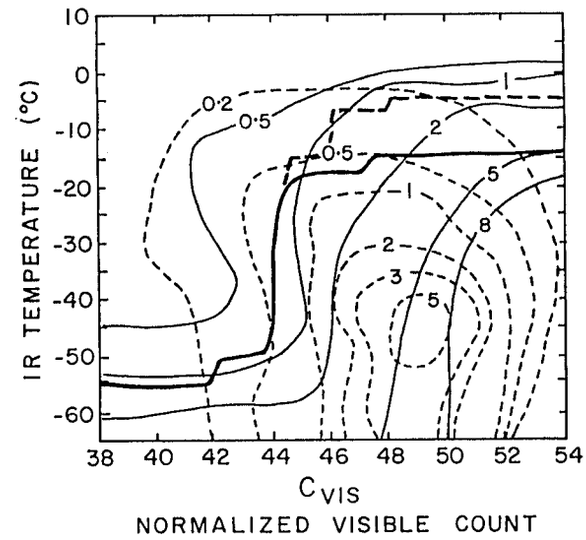

Fig.2: Rainfall rate in mm/h as a function of visible and IR temperatures derived from a comparison of 4 radar sequences of convective weather around the Montreal area (solid lines). The dashed lines are contours of percent rainfall contribution per VIS-IR pair. The heavy line outlines the rain-norain boundary in the binary decision scheme of Method 2. The visible data from the GOES-E satellite which became operational in August 1981 need to be decremented by 10 counts before applying the above relation.

data. A rainfall rate of 8 mm/h is exceeded by less than 1.4% of the data which accounts for only 15% of the total rainfall. For only a negligible number of (IR,V) pairs is R > 12 mm/h. We can state that while high rainfall rates are associated with high (IR,V) pairs, a high (IR,V) pair does not necessarily confirm the presence of high rainfall rates.

Rainfall estimates have been computed from half hourly point GOES measurements using four methods:

#1: The bispectral method of Fig. 2 denoted by R=f(IR,V)

#2: Satellite rain area multiplied by a constant rainfall rate. From Lovejoy and Austin (1979),
R=0 if (IR,V) is outside the satellite rain area (denoted by the heavy line in Fig. 2)
R=7 mm/h if (IR,V) is inside the rain boundary (computed from the training data set).

#3: Rainfall rate computed solely a function of the normalized visible data, i.e., R=f(V)

#4: Rainfall rate computed solely as a function of IR temperature, i.e., R=f(IR).

3. GAUGE-SATELLITE COMPARISONS OF RAINFALL MEASUREMENTS

A total of 14 rainfall sequences have been selected from data since 1980. Their duration and precipitation type are briefly summarized in Table 1.

3.1 Parameters Used for Verification

The percent mean absolute difference (AD) is used to compare each point gauge measurement G_i with the satellite S_i over the (4X4)km^2 grid area that encloses the gauge location. Thus

$$AD_n = 100 \cdot \sum_i \left| S_i - G_i \right| \Big/ \sum_i G_i$$

where the summation is over all the N gauge comparisons of the n'th rainfall sequence. Overestimation or underestimation by the satellite is given by the percent mean difference (D) computed from the above equation by omitting the absolute symbols. The

1	2	3	4	5		6		7			8	9			
#	DATE	GMT	TYPE	N	$\bar{G}$	D		AD			γ	CSI	POD	FAR	CSI
				A	B	A	B	A	B	C		A	B	C	D
1	23- 7-80	1800-2200	C	128	1.37	-16	26	100	144	70	0.402	36	48	42	33
2	9- 7-81	1700-2300	C	130	2.58	-68	50	123	98	93	0.408	49	87	47	66
3	26- 6-80	1700-2300	C	133	2.33	-18	12	79	71	59	0.677	52	73	37	67
4	31- 8-80	1500-2200	C	124	6.40	-25	-33	60	50	47	0.717	71	83	17	70
5	15- 6-80	1900-2300	S	132	2.14	-15	-14	107	80	89	0.348	31	49	54	39
6	20- 6-80	1300-1700	S	126	1.08	-27	-35	91	66	65	0.614	29	38	47	49
7	20- 6-80	1800-2300	S	124	2.06	20	7	122	98	81	0.186	41	60	45	47
8	6- 9-82	1300-2200	S	118	3.43	35	2	70	70	53	0.774	83	88	7	69
9	28- 7-82	1200-2600	S	117	1.53	-62	54	121	112	98	0.429	38	77	57	44
10	22- 6-82	1500-2200	C	123	1.74	-54	-58	95	85	69	0.308	23	31	53	23
11	18- 7-82	1700-2300	C	121	1.40	-30	-18	69	83	52	0.702	70	82	18	56
12	30- 7-80	1500-1900	C	133	0.73	-47	69	108	182	84	0.229	33	38	29	37
13	8- 6-80	1700-2300	S	127	3.16	-75	-70	76	70	69	0.831	44	45	5	51
14	8- 8-82	1500-2100	C	103	2.08	35	43	53	64	32	0.819	82	100	18	77
AVERAGES OR TOTALS				1739	2.29	-25	+3	91	91	69	0.532	49	64	34	52
OVERALL					2.28	-7	-6	85	80	65	0.561	50	68	35	54

Table 1. Statistics from the point gauge-satellite comparisons for each of the 14 rainfall events of the verification sample. (Method 1)

Column

4 : C : convective S: stratiform
5A : N : number of point gauge-satellite comparisons
5B : $\bar{G}$: average rainfall in mm over the N gauges
6A : D : from the N point comparisons
6B : D : from the 15000 grid areas enclosed by heavy line in Fig. 1.
7A : AD : from the N point comparison
7B : AD : from the 15000 grid areas
7C : AD : from the N gauge values verified with the best match in a (3X3) grid area search on the satellite map.
8 : γ : cross-correlation coefficient from the N point comparisons.
9A, B, C CSI, POD and FAR at the 2 mm level for the N point comparisons.
9D CSI at the 2 mm level from the 15000 grid areas.

Critical Success Index (CSI), the Probability of Detection (POD), and the False Alarm Ratio (FAR) for selected rainfall thresholds have also been computed in a manner devised by Donaldson et al (1975).

The cross-correlation coefficient γ is another parameter used in the verification analysis.

3.2 Results

The salient statistics of gauge-satellite comparisons for each rainfall event are presented in Table 1. These are provided for the 1739 comparisons at the gauge locations only, and for the verification over all the (4X4)km^2 grid areas (15000) of Fig. 1 for which a rainfall has been computed by the interpolation method. Each statistic is summarized in terms of the average of the 14 sequence values as well as in terms of its overall magnitude over the 82 hours of data. The total rainfall is only slightly underestimated by the satellite, - 6% or - 7%. The (AD) is 85% for the comparisons over the gauge locations only - column 7A - and reduces to 80% when all the grid areas are considered - column 7B. This result is due in part to the reduction in the standard deviation of the gauge data by the interpolation scheme which generates as ground truth a data set with a variability comparable with that from satellite data.

The correlation coefficient γ for the gauge-satellite comparisons at the gauge locations is given in column 8 while the CSI, POD and FAR scores for a 2 mm threshold are tabulated in column 9A, B and C. The CSI scores for the verification over all the grid areas in column 9D exhibit an improvement similar to the one found with AD.

The dependence of the overall CSI, POD and FAR scores as a function of the rainfall threshold for Method 1 are presented in Fig. 3. These scores are computed from the 1739 gauge-satellite comparisons at the gauge locations. The POD decreases uniformly from a magnitude of 80% at 0.5 mm to 15% at 12 mm, while FAR increses from 30% at 0.5 mm to 75% at 12 mm. As a result, the CSI score decreases in a manner parallel to POD, from a value of 60% at 0.5 mm to 10% at 12 mm. The scores obtained by choosing the best satellite estimate in a (3x3) and (5x5) array centred over the gauge location are also plotted.

Fig. 4 highlights the relative skill in terms of the CSI index of the four satellite rainfall estimation methods introduced in section 2.2. The (AD), (D) and γ scores are also given in the legend. As a basic frame of reference which can be associated with a total absence of skill, curve #5 gives the scores obtained by comparing each of the 14 satellite rainfall accumulations with the remaining 13 raingauge accumulations, the latter being adjusted so as to represent an accumulation interval equal to that of the satellite data. Since the CSI score essentially represents the percentage overlap of satellite and raingauge rainfall contours, and since the rainfall from the 14 available sequences is

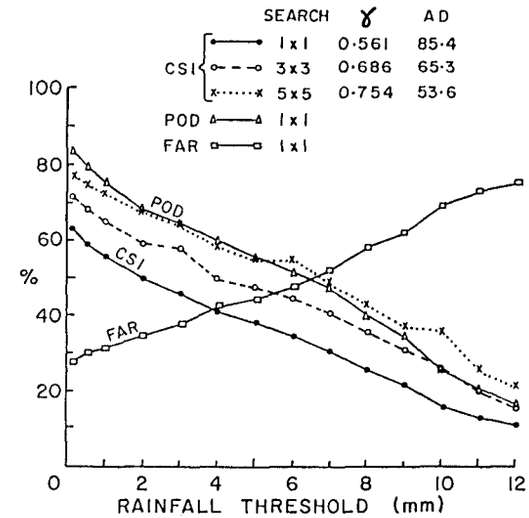

Fig. 3: The dependence of the overall CSI, POD and FAR scores as function of the rainfall threshold and neighborhood search, for the point comparisons with Method 1.

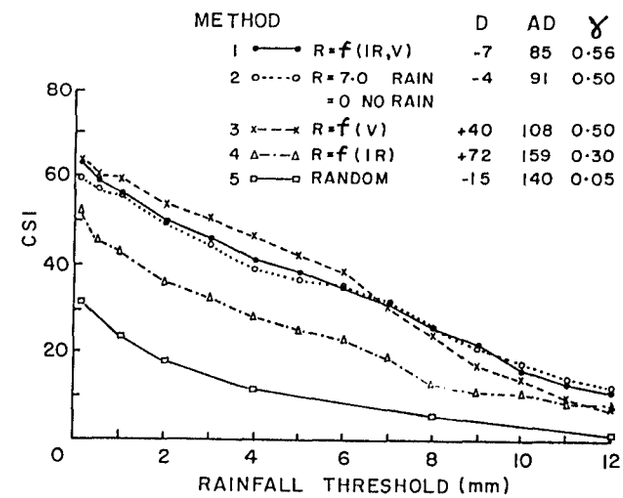

Fig. 4: Relative skill of the point comparisons of four satellite rainfall estimation methods. The fifth curve derived from random gauge-satellite comparisons delimits the level of no skill.

preferentially located along the St. Lawrence Valley, the possibility of chance overlap of the lower isohyets is not negligible, particularly for stratiform rainfall. Thus, CSI scores in excess of 20% at the 1 mm contour are computed, but the fact that γ =0.05 clearly establishes the above procedure as the comparison of random data sets. Figs. 3 and 4 unduly emphasize the poor scores of the satellite data at higher rainfalls. However, when expressed in terms of a ratio with respect with the "no skill" level of curve #5, this relative skill actually increases with rainfall, from a value of 2 at 1 mm to about 3 at R=8 mm.

Since the IR method severely overestimated the rainfall (D=+72%) while this bias is not present in the random verification (D=-15%), the magnitude of AD, which is more adversely affected by overestimation than by underestimation, is larger for the IR method (AD=159%) than for the random comparisons (AD=140%). But the CSI scores and γ parameter confirm the IR method as being at least superior to the random verification, thus emphasizing the need to use more than one statistic in a verification procedure.

Since Method 3 also overestimates the total rainfall (D=+40%), it is likely that the high magnitude of AD for this "VIS only" method (AD=108%) is adversely affected by this bias. In fact, multiplication of all satellite estimates by various factors F has revealed that AD is minimized at a common magnitude of 78% when F=0.7, 0.5 and 0.4 for Methods 1, 2, and 3 respectively. The first three methods, which differed only slightly in skill when examined in terms of CSI but which displayed appreciable differences in AD, again appear to be equivalent in skill when AD is minimized by an appropriate factor.

4. RELATIVE ACCURACY OF SATELLITE AND RAINGAUGE FIELDS

Interpolated rainfall fields from gauge densities ranging from 7/8 to 1/8 the full network shown in Fig. 1 have been simulated by a random omission of gauges. Verification statistics in terms of AD , CSI and γ are then derived by comparing the value of the interpolated rainfall field with the known but unused value at a gauge location. The results for AD in Fig. 5 are plotted as a function of the distance L_{NG} to the nearest gauge which has been used in the interpolation scheme. It is perhaps surprising to realize that even at the shortest distance interval 4 km $\leq L_{NG} <$10 km, the magnitude of AD exceeds 65%. While the scatter is not negligible, it is possible to equate the statistics already derived for the gauge-satellite point comparisons, Fig. 3 and Fig. 4,

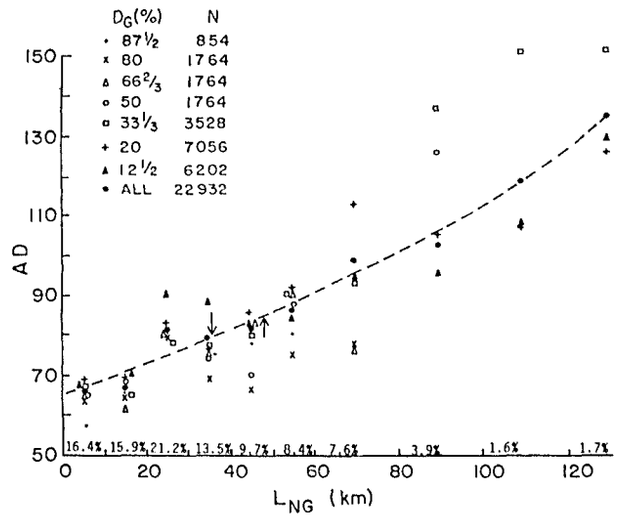

Fig. 5: Overall absolute difference AD of interpolated raingauge fields as a function of the distance L_{NG} to the nearest gauge. The statistics are further subdivided in terms of the relative gauge density D_G where D_G=100% is equivalent to a network of 1 gauge/1900 km^2. N is the number of comparisons for each D_G. The relative frequency of comparisons in each interval L_{NG} is indicated just above the x-axis.

with an equivalent accuracy of a rainfall field interpolated from a gauge network of a certain density. Thus, since AD for gauge-satellite comparisons of Method 1 is in the 80 to 85% range, we can state that the accuracy of a satellite rainfall estimate at a point is as good as that from an interpolated gauge field at a distance of 40 to 50 km from the nearest gauge. This distance, denoted by L^*, is indicated by arrows on Fig. 5. Similar tests with γ and CSI with thresholds from 0.5 to 8 mm have shown that L^* remains inside the 40 to 50 km range. Consequently, the satellite rainfall estimates over the grid areas of Fig. 1 for which there is no raingauge within a radius of 40 to 50 km are better than those obtained by interpolation from the existing gauges at farther distances.

Following the computation of the cumulative frequency distribution of L_{NG} for the network shown in Fig. 1, it has been found that only 16% of the area of interpolation is devoid of any gauges within 40 km. However, over the sparsely populated forested regions which are of practical concern for this research, the available gauge density is drastically less. The cumulative frequency distributions of L_{NG} have thus been derived for the reduced gauge densities which have been simulated. Assuming that the satellite accuracy is equivalent to that of an interpolated field at a distance L^* from the nearest gauge, Fig. 6 gives the percentage of

the area where the satellite accuracy exceeds that of a raingauge network of a given relative density D_G. For $L^*=40$ km and $D_G=33\%$, or 1 gauge/5700 km², the satellite rainfall information is more

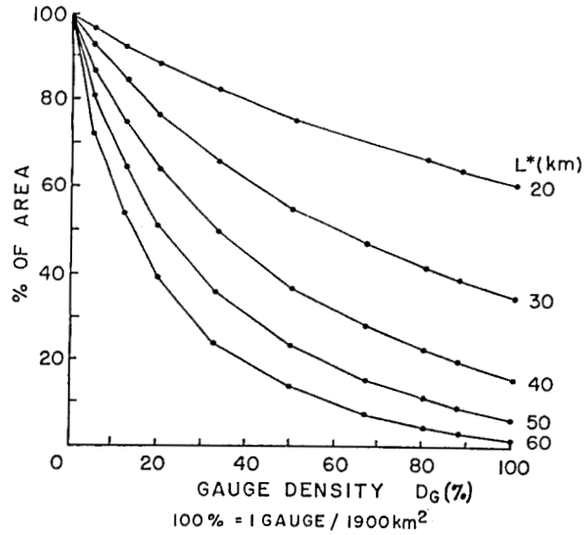

Fig. 6: Percentage of the area where the accuracy of satellite data of skill L^* exceeds that of raingauge network of a given relative density D_G.

accurate than that from interpolated gauge data over 50% of the area. This result implies that satellite rainfall estimates of the order of 4 to 10 hours during daylight are as good as those from a raingauge network of 1/3 the density shown in Fig. 1.

There are nearly 10^6 km² of forested area north and northwest of the boundary of gauge-interpolated fields shown in Fig. 1 for which the distribution of L_{NG} corresponds to a network of approximately $D_G=5\%$. Even with a pessimistic value of $L^*=50$ km, the satellite can provide improved daylight rainfall estimates over 80% of that territory, and thus be a valuable assistance to forest fire management.

5. CONCLUSIONS

The comparison of the satellite estimates for 14 summertime rainfall events is made with both the point gauge measurements and with interpolated gauge data. The overall absolute difference (AD) of 1739 point comparisons has been found to be of the order of 85% while the CSI, POD and FAR scores at the 2 mm level are of the order of 50, 70 and 35% respectively (Fig. 3).

A test on the relative skill of four satellite rainfall estimation techniques (Fig.4) has shown that methods that combine visible and IR data yield reduced error in terms of AD but the method based on visible data alone scored higher in terms of the CSI index at lower rainfalls ($R \leq 6$ mm). The skill of point IR data alone for mid-latitudes rainfall situations is inadequate on account of their overestimation of rainfall which causes AD to be higher than that for random comparisons.

By equating the satellite scores with those from interpolated fields at various gauge distances, (Fig. 5), it is concluded that the accuracy of satellite rainfall measurements is similar to that of an interpolated field at a distance of 40 to 50 km from the nearest gauge. This accuracy is equivalent to that of a network 1/3 the density of gauges shown on the enclosed area of Fig. 1.

Acknowledgements: This research is directly supported by a contract from the Canadian Forestry Service. We wish to thank Dr. J.B. Harrington of the Petawawa National Forestry Institute for his continuous advice and support of this project.

REFERENCES

Barret, E.C. and D.W. Martin, 1981: The use of satellite data in rainfall monitoring, Academic Press, 340 pp.

Cherna, E., A. Bellon, G.L. Austin, and A. Kilambi, 1985. An objective technique for the delineation and extrapolation of thunderstorms from GOES satellite data. J. of Geophysical Research, Vol. 90, No. D4, 6203-6210.

Donaldson, R.J., R.M. Dyer and M.J. Kraush 1975: An objective evaluation of techniques for predicting severe weather events. Preprints 9th Conf. Severe Local Storms, Norman, Amer. Met. Soc., 321-326.

Griffith, C.G., Woodley, W.L., Grube, P.G., Martin, D.W., Stout, J. and Sikdar, D.N. (1978). Rain estimation from geosynchronous satellite imagery - visible and infrared studies. Mon. Wea. Rev. 106, 1153-1171.

Lovejoy, S. and Austin, G.L.(1979). The delineation of rain areas from visible and IR satellite data for GATE and mid-latitudes. Atmosphere-Ocean 17, 77-92.

Negri, A.J., R.F. Adler and P.J. Wetzel, 1984: Rain estimation from satellites; an examination of the Griffith-Woodley Technique. J. Climate Appl. Meteor., 23, 102-116.

Stout, J.E., Martin, D.W. and Sikdar, D.N. (1979). Estimating GATE rainfall with geosynchronou satellite images. Mon. Wea. Rev. 107, 585-598.

Van Wagner, C., 1974: Structure of the Canadian forest fire weather index. Can. Forest. Serv., Petawawa Forest Exp. Sta., Publication No. 1333, 44 pp.

Wylie, D.P. and D. Laitsch, 1983: The impacts of different satellite data on rain estimation schemes. J. Climate Appl. Meteor., 22, 1270-1281.

9.5

ANNUAL AND INTERANNUAL VARIABILITY IN LARGE-SCALE CONVECTION OVER THE EASTERN PACIFIC AND TROPICAL SOUTH AMERICA

by

Phillip A. Arkin

Climate Analysis Center
NOAA/NWS/NMC
Washington, D.C. 20233

1. Introduction

Tropical convective precipitation, with the attendant release of latent heat, is one of the major forcing mechanisms of the general circulation of the atmosphere. Large-scale anomalies in tropical precipitation are closely associated with global-scale circulation anomalies (Rasmusson and Carpenter, 1982; Horel and Wallace, 1981). A careful monitoring of variations in tropical precipitation is of major importance in any attempt to diagnose the behavior of the global climate system. Knowledge of the actual precipitation averaged over large areas is of potentially great importance for both numerical weather prediction and simulations of the climate using general circulation models (Mintz, 1981).

The task of producing estimates of the areally-averaged rainfall for large regions is a challenging one. Rainfall may be measured at points--as, for example, by a raingauge--or by some sort of remote sensor. The remote sensors may be further subdivided into "direct," in which information on precipitation-sized droplets is measured, and "indirect," in which information on some by-product of the precipitation process, such as clouds, is measured. An example of a direct remote sensing technique is provided by weather radars. Complete global coverage with either radars or raingauges is, however, essentially impossible.

The obvious solution is to make use of some satellite-based remote sensing device. Direct remote sensing devices, those which measure some radiative property of hydrometeors themselves, may be mounted on orbiting spacecraft (Wilheit et al., 1977). However, the required technology has not yet reached a state in which such measurements are routinely made and precipitation estimates derived. Satellite-based indirect sensors, those which rely on measurements of some phenomenon (i.e., deep cold clouds) associated with rain, provide the only currently available means for obtaining estimates of large-scale convective precipitation over the greater portion of the earth and, in particular, over the tropical oceans on a regular long-term basis.

While a wide variety of such techniques has been developed since the advent of meteorological satellite observations, most are not capable of providing continuous estimates of rainfall averaged over large areas. An approach which seems to provide the economies needed to produce estimates on the desired scales, but which maintains the objectivity afforded by automated processing of digital data, is one which uses the relationship between areal coverage of cold cloud and rainfall found by Arkin (1979) and Richards and Arkin (1981). They showed that 50 to 75% of the variance in areally-averaged rainfall accumulations could be explained by a linear function of the mean fraction of the area covered by cloud having equivalent black body temperatures (EBBT) colder than thresholds ranging from 220K-250K. Largest values of explained variance were found for a threshold of 235K and for a spatial-averaging area of 2.5° latitude by 2.5° longitude (about 6×10^4 km^2). One of the surprising features of this work was the relative insensitivity of the relationship between fractional cloudiness and rainfall to changes in either the spatial- or temporal-averaging scale or in the threshold temperature.

These results, together with the results of Kilonsky and Ramage (1976), Griffith et al. (1978), Garcia (1981) and Negri et al. (1984) indicate that the extremely simple process of assigning an appropriate climatological rain rate to each unit area of raining cloud, apparently first proposed by Barrett (1970), exhibits a surprising degree of skill in defining temporally- and spatially-averaged rainfall on certain scales. In particular, the accuracies and resolutions required to diagnose important short period climate fluctuations (Rasmusson and Arkin, 1981) are obtainable by a threshold technique. This paper presents the 4-year mean annual cycle of monthly rainfall estimated from GOES IR data and compares the annual and interannual variability in estimated rainfall during the period to that obtained from station rainfall observations over the Americas.

2. Data

The data used in this study were derived from observations of upwelling radiation in the infrared spectral window by the U.S. GOES. A

temporal averaging scale of 1/2 month and a spatial scale of 2.5° were chosen. In order to adequately resolve the diurnal cycle, 8 images/day from each satellite (when available) at 3 hour intervals beginning at 0000 GMT are used. Since imagery from the western GOES satellite is offset by 15 minutes from the eastern, images from 15 minutes before each selected hour (i.e., 2345 GMT for 0000 GMT) are used. All pixels within the area 175°E to 25°W and 50°N to 50°S are sorted into boxes of size 2.5° latitude by 2.5° longitude. When both satellites are available, data west/east of 105°W are obtained from the western/eastern satellite. No overlapping data are used. During periods when only a single satellite is operating, its data are used as far west (or east) as possible. The basic data set consists of 16-class histograms of EBBT for half-months for each 2.5° x 2.5° box in the domain for each of 8 times of day.

In this paper, data covering the period December 1981 through November 1985 will be presented. It should be noted that although these data are temporally continuous over the majority of this region, there was no western GOES during the 6-month period December 1982-May 1983 and again from August 1984-November 1985. This caused a limitation in coverage during the earlier period to east of 130-140°W and during the latter to between 55°W and 150°W.

The rainfall estimates discussed in this paper are referred to as a GOES Precipitation Index (GPI). The GPI is calculated from the product of the mean fractional coverage of cloud colder than 235K in a 2.5° x 2.5° box, the length of the averaging period in hours, and a constant of 3 mm/hour. That is,

$$GPI = F_c * t * 3$$

where GPI is in mm, F_c is the fractional cloudiness (a dimensionless number between 0 and 1) and t is the length of the period (hours) for which F_c was the mean fractional cloudiness.

An attempt to use a relation derived in the eastern tropical Atlantic to estimate precipitation in other regions must be viewed with caution. The implicit hypothesis is that the convective precipitation process which generates the cold cloud is subject to only relatively small spatial and temporal variations. That is, convection which produces a certain amount of cold cloud for a certain production of rainfall in the eastern tropical Atlantic during summer will do approximately the same in other areas of the tropical oceans and in other seasons of the year. We also hypothesize that cloudiness and rainfall over continental regions will exhibit a similar relationship during convective regimes. While we do not have statistics to verify that such a universal application of the relationship derived during GATE is in fact justified, the results of Griffith et al. (1980) indicate that one type of indirect rainfall estimate derived for convective rainfall in Florida can be used across the tropical Atlantic and eastern tropical South America. Thus, the reader is asked to bear in mind two important caveats. First, the results presented are applicable only to precipitation produced by deep convection; and second, there will certainly prove to be some seasonal and regional inhomogeneities in the relation between areal extent of cold cloud and rainfall.

3. The Annual Cycle

The estimated 4-year mean monthly rainfall over the tropical oceans for DJF (Fig. 1) and JJA (Fig. 2), shows a number of interesting spatial features. In the Pacific, a band of rainfall greater than 100 mm is present during each season centered near 10°N. Another such band is found, somewhat further south, in the western Atlantic. These are the Inter-Tropical Convergence Zones (ITCZs). Another region of rainfall is centered between 10° and 15°S and the dateline, extending towards the southeast. This is the South Pacific Convergence Zone (SPCZ - Trenberth, 1976). Regions of relatively low rainfall are found both

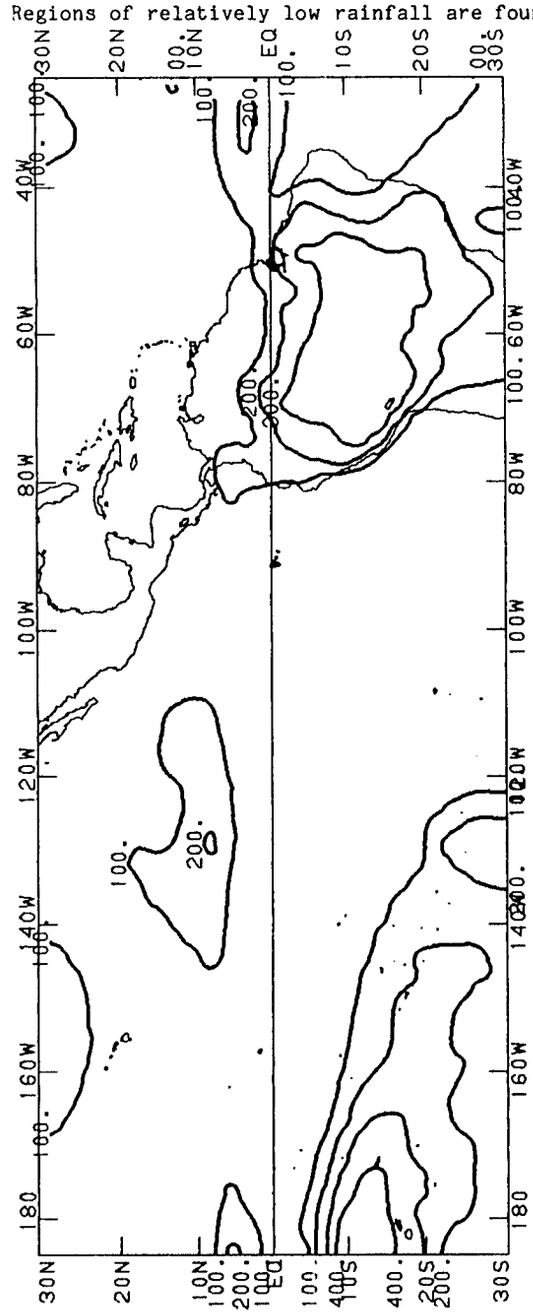

Figure 1. Four year monthly mean GOES Precipitation Index for DJF. Contour interval of 100 mm.

north and south of the ITCZs in each ocean. The Pacific ITCZ is strongest during JJA, when amounts >400mm are found over an area south of Central America. During this season, a relative minimum is found near 130°W, with values increasing to about 300mm further west. During the northern winter, an opposing pattern is seen, with a maximum found between 120-140°W and lower values to the east and west. Values near the date line and just north of the equator exhibit a small relative maximum. Values observed during DJF are considerably below those found during JJA. The SPCZ, on the other hand, exhibits peak values of >400mm near its northwestern extremity during DJF, with values about 100mm less during the other two seasons. The western end of the SPCZ is farthest north, near 10°S, during JJA, and near 15°S during DJF.

The Atlantic ITCZ exhibits a pronounced seasonal cycle in amplitude, with amounts ranging from >300mm/month during SON (not shown) to <200

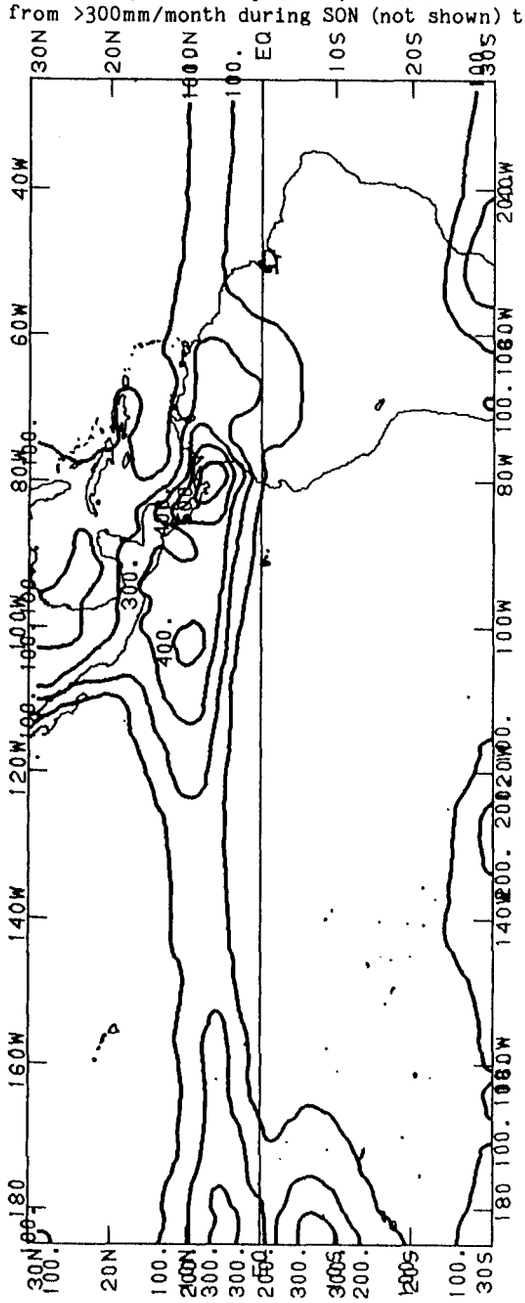

Figure 2. Four year monthly mean GOES Precipitation Index for JJA. Contour interval of 100 mm.

during MAM (not shown) and JJA. This feature is farthest north, centered near 5°N, during JJA and SON, and is centered near the equator during MAM. The dry zone in the Northern Atlantic is farthest west during DJF, while south of the equator JJA is the driest season. In the South Pacific, SON exhibits the greatest expanse of very dry conditions, while JJA and SON appear to be driest north of the equator.

The results shown in Fig. 2 are in rather good agreement with published estimates of the long-term mean rainfall over these regions. Dorman and Bourke (1979, 1981) determined the long-term mean rainfall in the Atlantic and Pacific Oceans from an adaptation of a method developed by Tucker (1961). Tucker used land station observations to assign a rainfall intensity to each observed weather type of the synoptic code. Dorman and Bourke (1978) determined that Tucker's coefficients were temperature dependent and developed empirical formulae relating the coefficients to the air temperature. Their maps of seasonal rainfall agree very well with ours. For example, the Atlantic ITCZ is shown to be approximately centered on the equator during MAM. Some of the longitudinal structure found in the Pacific ITCZ in Fig. 1 and 2 is not confirmed by Dorman and Bourke; and, in contrast to Jaeger (1976), both the Atlantic and Pacific ITCZs exhibit markedly greater amounts in some areas/seasons than found in our results. In this case, it is possible that some of the difference results from the apparently greater spatial resolution of their results, with the peak values being slightly smeared by the areal-averaging in the GPI.

4. Interannual Variability

In this section we present our findings on the ability of the GPI to reproduce interannual variations in observed rainfall. A serious obstacle to any such attempt is the scarcity of ground-based observations of rainfall. While there exist a great many rainfall observing stations in most continental regions, relatively few are widely available. We will discuss the interannual variability of GPI over tropical South America associated with the 1982-83 ENSO episode and with the breaking of the drought in the Northeast of Brazil during 1984 in comparison with station observations.

The ENSO episode of 1982-83 was the most extreme in at least the last 100 years (Rasmusson and Wallace, 1983). ENSO episodes are associated with variations in tropical precipitation in many parts of the globe (Rasmusson and Carpenter, 1983; Kousky et al., 1984).

The 1982-83 ENSO episode began during the northern summer of 1982 and began to strongly effect South America near the end of that year (Quiroz, 1983; Rasmusson and Wallace, 1983). The total GPI for the seasons DJF 1981-82 and MAM 1982 has been subtracted from the GPI for the same season during the following year to obtain an estimate of the interannual change in precipitation associated with the ENSO episode (Figs. 3 and 4). (In Figs. 3, 4 and 5, increase/decrease from 81-82 to 82-83 is

positive/negative and the contour interval is 100 mm with negative contours dashed. The interannual change at individual stations is plotted in large numerals.) A broad area of tropical South America east of the Andes and extending into the equatorial Atlantic exhibited strong decreases in GPI during DJF 1982-83 and MAM 1983 from the year before. The largest declines were centered near the mouth of the Amazon in both seasons. In both seasons, decreases of >200 mm were observed over areas of 10-15° of latitude and 30-40° of longitude.

Observations of rainfall at a number of stations in tropical Brazil during December 1982-May 1983 and the previous year (obtained from Monthly Climatic Data for the World) were differenced to obtain some idea of the accuracy of the GPI-estimated changes. Comparison of changes in seasonal totals at these stations with the corresponding changes in GPI (Figs. 3 and 4) indicates that the GPI has successfully captured the general distribution. The changes in GPI, however, are seen to be 1.5-2 times larger than the changes observed at individual stations.

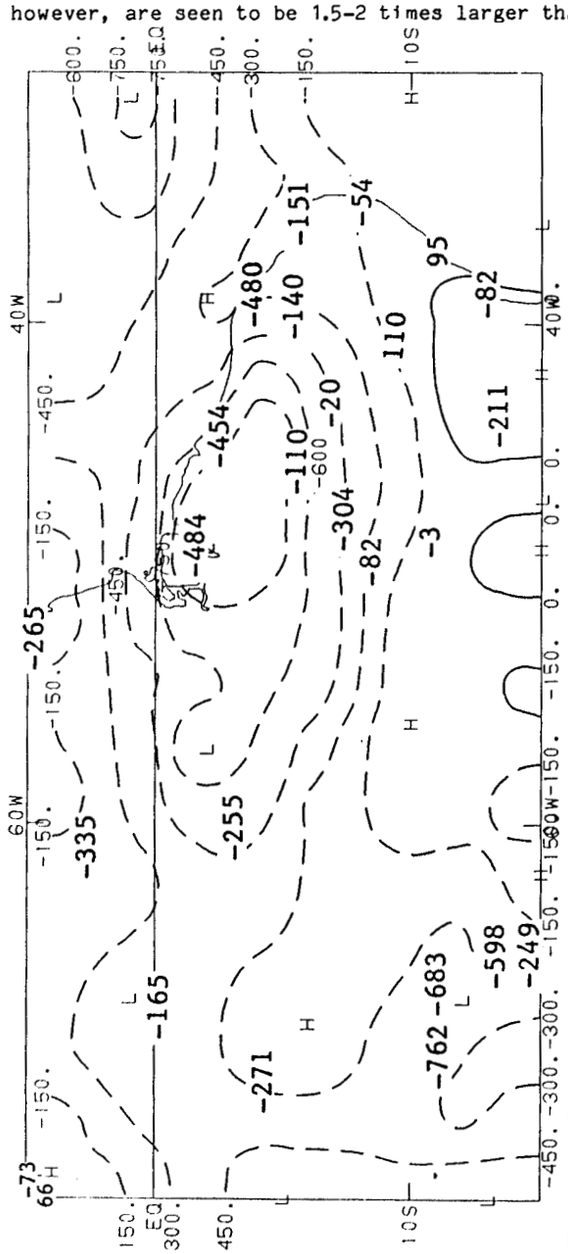

Figure 3. Difference between DJF 1981-82 and DJF 1982-83 GPI for tropical South America.

Despite the large decreases in GPI in much of equatorial South America during the 1982-83 ENSO episode, changes in the drought-prone Northeast of Brazil were quite small. It appears that the small changes in this region resulted from a continuation of a long-term drought rather than from the occurrence of near-normal rainfall. The difference between GPI during MAM 1984 and 1983 (Fig. 5) shows that strong increases were observed during 1984. These were associated with a return to normal or above normal precipitation (Moura and Kagano, 1985).

5. Summary and Conclusions

In this paper we have briefly reviewed an approach to estimation of large-scale convective precipitation using satellite data. A simple indirect technique, using the fraction of 2.5°x2.5° areas covered by pixels (picture elements) with EBBT < 235K in geostationary IR imagery, together with the linear relationship derived by Richards and Arkin (1981) for the GATE

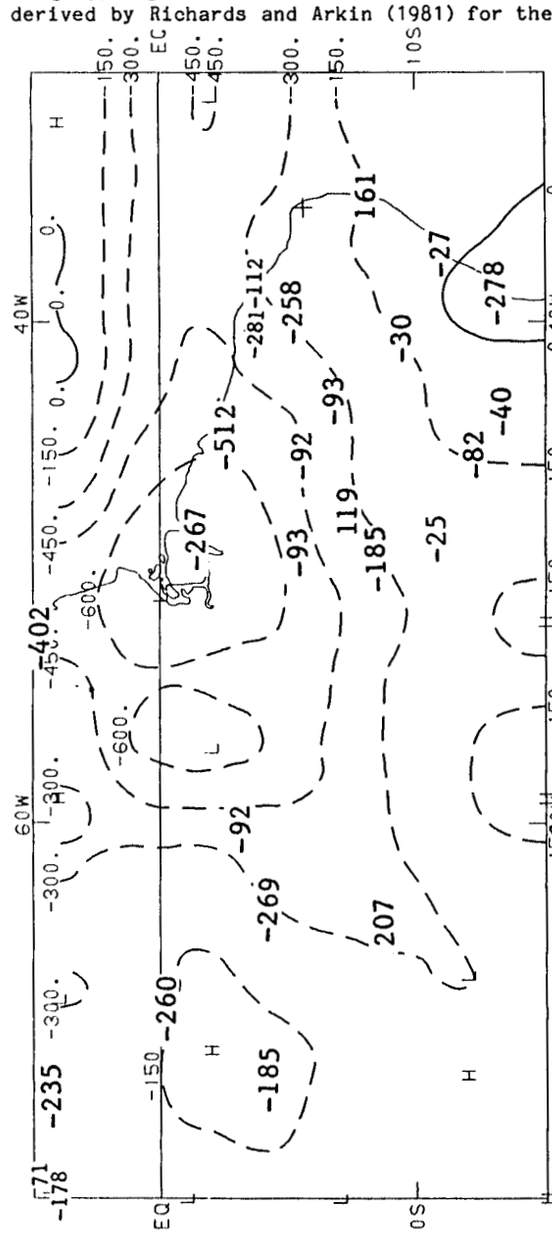

Figure 4. As in Fig. 3 except for MAM 1982 and MAM 1983.

A/B array, was applied to data from the U.S. geostationary satellites beginning in December 1981. The derived estimates (the GOES Precipitation Index - GPI) were used to describe the 4-year mean annual cycle in estimated rainfall. Year-to-year changes in GPI were then compared to changes in station observations of rainfall in tropical South America.

The spatial distribution and evolution of the GPI through the annual cycle appear quite realistic in comparison with published climatologies. GPI amounts were within the range of those published over the tropical oceans. Considering the difficulty in obtaining accurate estimates of areal-averaged oceanic precipitation from any source, it appears that the GPI might prove most valuable in the measurement of tropical oceanic rainfall. The GPI in tropical South America successfully represented the interannual variability found in observed convective rainfall, although the amplitude of GPI changes appeared to be somewhat higher than that of changes in observed rainfall.

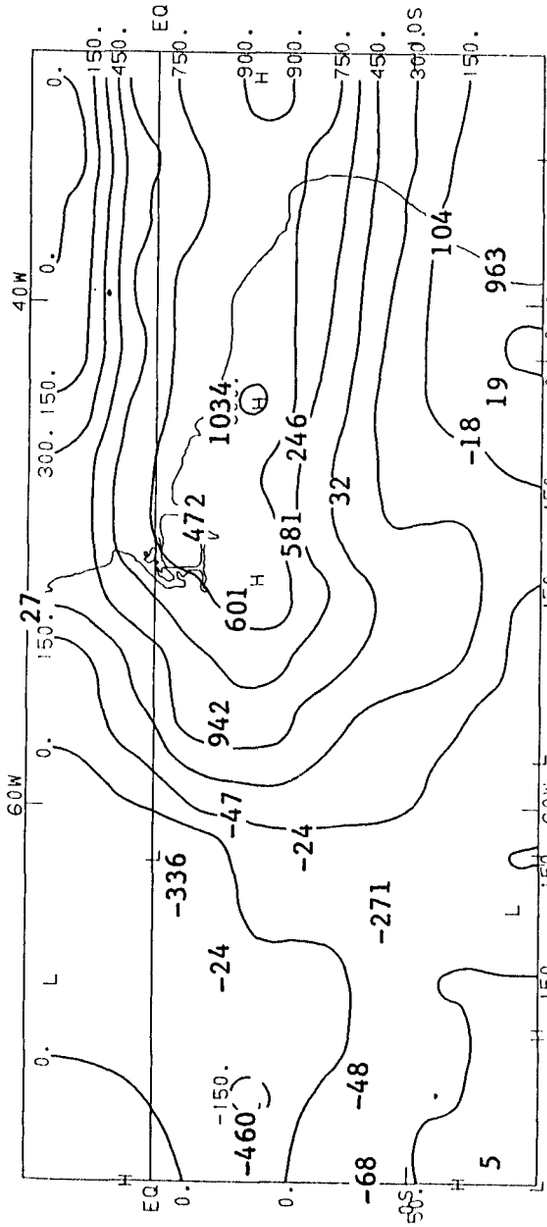

Figure 5. As in Fig. 3 except for MAM 1983 and MAM 1984.

Several conclusions may be drawn from these results:

1) The linear relationship between fractional coverage of cold cloud and rainfall obtained by Arkin (1979) and Richards and Arkin (1981) for the GATE area is at least approximately valid in other convective regions;

2) the GPI is successful at documenting the spatial and temporal variability in convective regimes with greater detail than is possible using station data alone;

3) the GPI probably provides a better estimate of tropical ocean rainfall for individual months and years than has ever been available from any source.

It is evident that two activities would, if pursued, have great potential for climate studies. Firstly, the statistical relationship between rainfall and coverage by cold cloud should be better documented in both space and time. The obvious method would be the conduction of a number of calibration studies in which detailed observations of the areally-averaged rainfall for a variety of areas and times of year would be compared to statistics of the cloud population as in Richards and Arkin (1981). Secondly, the spatial coverage of GPI-like estimates of convective rainfall could be expanded to cover the vast majority of the convective regions of the world by the acquisition of suitable statistics from all operating geostationary satellites. These estimates provide an initial solution to the problem of obtaining measurements of tropical oceanic rainfall for the Tropical Ocean/Global Atmosphere Program of the World Climate Research Program (WCRP, 1985).

REFERENCES

Arkin, P.A., 1979: The relationship between fractional coverage of high cloud and rainfall accumulations during GATE over the B-scale array. Mon. Wea. Rev., 107, 1382-1387.

Barrett, E.C. 1970: The estimation of monthly rainfall from satellite data. Mon. Wea. Rev., 98, 322-327.

Dorman, C.E., and R.H. Bourke, 1978: A temperature correction for Tucker's ocean rainfall estimates. Quart. J. Roy. Meteor. Soc., 104, 756-773.

_____, and _____, 1979: Precipitation over the Pacific Ocean, 30°S to 60°S. Mon. Wea. Rev., 107, 896-910.

_____, and _____, 1981: Precipitation over the Atlantic Ocean, 30°S to 70°N. Mon. Wea. Rev., 109, 554-563.

Garcia, O., 1981: A comparison of two satellite rainfall estimates for GATE. J. Appl. Meteor., 20, 430-438.

Griffith, C.G., W.L. Woodley, J.S. Griffin, and S.C. Stromatt, 1980: Satellite-Derived

Precipitation Atlas for GATE. NOAA Atlas Series, Environmental Research Laboratories, Boulder, CO 80303, 280 pp. [Superintendent of Documents, no. 0-315-309].

_____, _____, P.G. Grube, D.W. Martin, J. Stout, and D.N. Sikdar, 1978: Rain estimation from geosynchronous satellite imagery - visible and infrared studies. Mon. Wea. Rev., 106, 1153-1171.

Horel, J.D., and J.M. Wallace, 1981: Planetary-scale atmospheric phenomena associated with the Southern Oscillation. Mon. Wea. Rev., 109, 813-829.

Jaeger, L., 1976: Monatskarten des Niederschlags fur die ganze Erde. Berichte des Deutschen Wetterdienstes, Nr. 139 (Band 18). Offenbach A.M., 33 pp and plates.

Kilonsky, B.J., and C.S. Ramage, 1976: A technique for estimating tropical open-ocean rainfall from satellite observations. J. Appl. Meteor., 15, 972-975.

Kousky, V.E., M.T. Kagano, and I.F.A. Cavalcanti, 1984: A review of the Southern Oscillation: oceanic-atmospheric circulation changes and related rainfall anomalies. Tellus, 36A, 490-504.

Mintz, Y., 1981: A brief review of the present status of global precipitation measurements. Precipitation Measurements from Space - Workshop Report, NASA, Goddard Space Flight Center, Greenbelt, MD 20771, D1-D4.

Moura, A., and M.T. Kagano, 1985: Anomalous meteorological conditions over South America during the ENSO event 1982-83. Proc. of the First WMO Workshop on the Diagnosis and Prediction of Monthly and Seasonal Atmospheric Variations over the Globe, College Park, Maryland, July 29-August 2, 1985, (in press).

Negri, A.J., R.F. Adler, and P.J. Wetzel, 1984: Rainfall estimation from satellites: an examination of the Griffith-Woodley technique. J. Clim. and Appl. Meteor., 23, 102-116.

Quiroz, R.S., 1983: The climate of the "El Niño" winter of 1982-83 - A season of extraordinary climatic anomalies. Mon. Wea. Rev., 111, 1686-1706.

Rasmusson, E.M., and P.A. Arkin, 1981: Precipitation data for climate diagnostics. Precipitation Measurements from Space - Workshop Report, NASA, Goddard Space Flight Center, Greenbelt, MD 20771, D10-D18.

_____, and T.H. Carpenter, 1982: Variations in tropical sea surface temperature and surface wind fields associated with the Southern Oscillation/El Niño. Mon. Wea. Rev., 110, 534-584.

_____, and _____, 1983: The relationship between eastern equatorial Pacific sea surface temperatures and rainfall over India and Sri Lanka. Mon. Wea. Rev., 111, 517-528.

_____, and J.M. Wallace, 1983: Meteorological aspects of the El Niño/Southern Oscillation. Science, 222, 1195-1202.

Richards, F., and P. Arkin, 1981: On the relationship between satellite-observed cloud cover and precipitation. Mon. Wea. Rev., 109, 1081-1093.

Trenberth, K.E., 1976: Spatial and temporal variations of the Southern Oscillation. Quart. J. Roy. Meteor. Soc., 102, 639-653.

Tucker, G.G., 1961: Precipitation over the North Atlantic Ocean. Quart. J. Roy. Meteor. Soc., 87, 147-158.

WCRP, 1985: World Climate Research Programme: Implementation Plan, WCRP, Geneva, Switzerland (in press).

Wilheit, T.T., A.T. Chang, M.S.V. Rao, E.B. Rodgers, and J.S. Theon, 1977: A satellite technique for quantitatively mapping rainfall rates over the ocean. J. Appl. Meteor., 16, 551-560.

VALIDATION OF THE ESOC PRECIPITATION INDEX

Olli Turpeinen and Johannes Schmetz

European Space Operations Centre
Robert-Bosch-Str. 5
6100 Darmstadt, FRG

1. INTRODUCTION

The knowledge of the accumulation and distribution of precipitation is essential in a number of meteorological fields. Climatological and general circulation studies, agrometeorological applications and the validation of numerical weather prediction models need accurate information on precipitation. Unfortunately the coverage of the conventional network of rain stations has remained poor in many regions, the situation being especially deficient in the tropical ocean areas. Therefore it is obvious that fresh approaches to determine the precipitation have to be sought. Remote sensing seems to be a promising option. The geostationary satellites are particularly well suited for precipitation monitoring due to their excellent temporal and spatial coverage.

A number of scientists have already used data from geostationary satellites to estimate the precipitation (e.g. Arkin, 1979; Griffith et al., 1981; Stout et at., 1979). Many of their schemes are, however, unfeasible for use in deriving rainfall estimates over large areas of the globe due to the inclusion of the individual tracking of cloud entities throughout their lifetimes. The scheme has to be relatively simple if the coverage is near-global and the sampling is done frequently for a long period of time. The approach proposed by Arkin (1979) is considered appropriate for the global scale. He has shown that the fractional cloud cover colder than a certain temperature threshold is proportional to the accumulated precipitation. The scheme is proved to be reliable if it is integrated over an area larger than 150 x 150 km and over a time longer than 24 hours (Richards and Arkin, 1981).

There are, however, some limitations in the study by Arkin. First, the scheme has been tested only for the limited area of the GATE-experiment.

Secondly, the cloud top temperature is the only parameter considered, although it is obvious that two clouds with the same temperature can result in varying precipitation accumulations depending on the orography, wind shear and moisture conditions. The role of the humidity has been emphasised by Adler and Mack (1984). Therefore the upper tropospheric humidity (UTH), readily available from METEOSAT 6.3 µm - channel, is included in the ESOC precipitation index (EPI).

The purpose of this paper is two-fold :
(i) to test and validate EPI in four different geographical locations to find out whether it has a good correlation with the observed precipitation, independently of the area considered, and
(ii) to investigate the importance of the humidity in the determination of the accumulated precipitation. As a unique feature the upper tropospheric humidity (UTH) is included in EPI. So far no precipitation index has incorporated the humidity.

In the following chapter the satellite and ground truth data are described. The third section discusses the results and the analysis carried out.

2. DATA

Both satellite and ground truth data have been collected for the test period which ran from 03 October until 26 December, 1985. The data originated from four African countries : Ivory Coast, Kenya, Morocco and Tunisia. The location of each of them is displayed in Figure 1. Ivory Coast and Kenya lie in the equatorial region whereas Morocco and Tunisia are situated in the subtropical zone where convection is supplemented by occasional frontal passages.

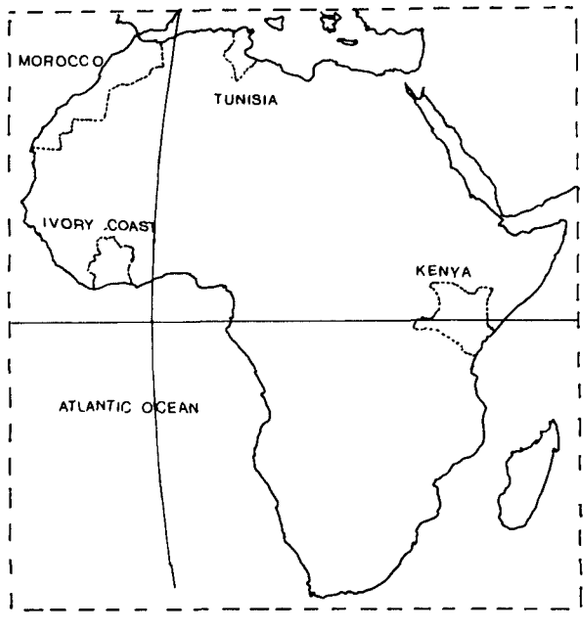

Fig. 1. The location of the four African countries considered.

2.1 Satellite Data

The EPI is stored for the whole test period over the territories of the four above-mentioned African Countries.

The EPI is determined as suggested by Arkin (1979). The fraction of pixels with the effective black-body temperature colder than 235 K in each METEOSAT segment (32 x 32 pixels) is counted every three hours. The results are summed over five days. The averaging interval (5 days), the area (1.5 x 1.5 degrees), and the threshold temperature (235 K) are selected based on the findings by Richards and Arkin (1981).

The original feature of the EPI is the incorporation of the UTH, which is determined on the basis of the radiance in the METEOSAT 6.3 µm-channel. The EPI in fact consists of three different indices which are classified according to the humidity values in the upper troposhere. The indices are calculated for the UTH-ranges of 75-100% (EPI-moist), 40-75% (EPI-normal) and 0-40% (EPI-dry), respectively. The Arkin-index is simply the sum of all three indices (EPI-all). The influence of the humidity is not exactly known but it is postulated that the drier the upper troposphere, the stronger the evaporation through entrainment and consequently the weaker the precipitation.

2.2 Ground Truth Data

Daily records from all regularly operating rain gauges from the four African countries were collected. The networks of the rain gauges are well-suited for this study due to a fairly even distribution of stations over the territories considered.

Digital radar data, which would have been very useful, was not available.

3. RESULTS

The test period consists of 17 five-day intervals. The variation of the precipitation as a function of time is shown in Fig. 2, where the EPI-all averaged over each of the four countries is displayed. The results from Ivory Coast and Kenya show the displacement of the ITCZ southwards towards the end of the year. The segments from Morocco and Tunisia report little precipitation in the beginning of the test period, but in the latter part higher values of the EPI-all are recorded, due to the passages of mid-latitude frontal systems.

The variation of the measured accumulated precipitation will be shown during the conference.

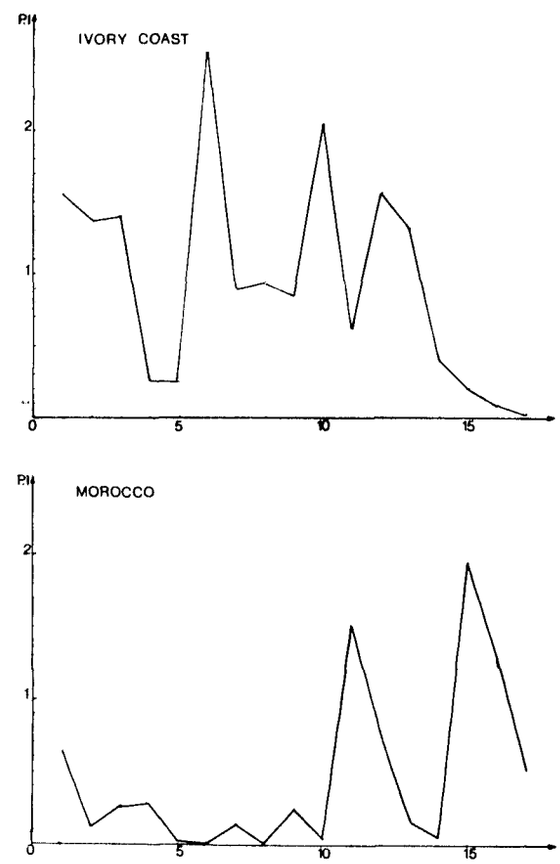

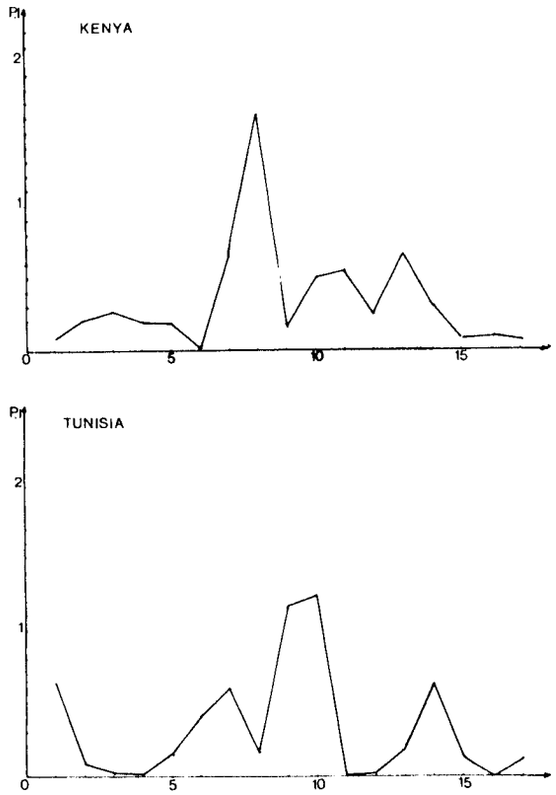

Fig. 2. The variation of the averaged precipitation index (EPI-all) as a function of time (in weeks).

The line of the best fit is calculated between the observed precipitation (P) and the three EPIs. In other words, the coefficients a, b and c in the following formula are optimised :

$$P = a \times EPI\text{-moist} + b \times EPI\text{-normal} + c \times EPI\text{-dry} \quad (1)$$

It is expected that $a > b > c$, since more precipitation is likely to fall in the moister atmospheres due to weaker evaporation.

To assess the role of the UTH, the multiple correlation coefficient between the measured precipitation and the three indices is determined. It will be compared with the correlation coefficient calculated between the measured precipitation and the EPI-all, where no humidity data are incorporated. The results will be discussed during the meeting.

4. ACKNOWLEDGEMENTS

We thank Prof. Achy from the Universite National Cote d'Ivoire, Dr. Alusa from Kenya Meteorological Department, Dr. Bensari from Direction de la Meteorologie Nationale Marocaine and Dr. Trabelsi from Institut National de la Meteorologie Tunisien for kindly providing us with the ground truth data. Appreciation is also expressed to Mr. Abidi and Mr. Belhouane for their excellent contributions.

5. REFERENCES

Arkin, P.A., 1979 : The relationship between fractional cloud coverage of high cloud and rainfall, accumulations during GATE over the B-scale array. Mon. Wea. Rev., 107, 1382-1387

Adler, R.F. and R.A. Mack, 1984 : Thunderstorm cloud height - rainfall rate relations for use with satellite rainfall estimation techniques. J. Clim. Appl. Met., 23, 280-296

Griffith, C.G., J.A. Augustine, and W.L. Woodley, 1981 : Satellite rain estimation in the U.S. high plains. J. Appl. Met., 20, 53-66

Richards, F., and P. Arkin, 1981 :On the relationship between satellite observed cloud cover and precipitation. Mon. Wea. Rev., 109, 1081-1093

Stout, J.E., D.W. Martin, and D.N. Sikdar, 1979 : Estimating GATE rainfall with geosynchronous satellite images. Mon. Wea. Rev., 107, 585-598

GLOBAL WIND MEASUREMENT FROM SPACE: DOPPLER LIDAR

D. E. Fitzjarrald

NASA
Marshall Space Flight Center, AL 35812

1. Introduction

The possibility of making direct wind measurements from space has intrigued atmospheric scientists since receipt of the first cloud pictures by the TIROS 1 satellite in 1960 (Vaughan, 1982). Indeed, tracking of clouds and other atmospheric features from satellite pictures has provided significant information about the dynamics of planetary atmospheres. These techniques have reached their apex in the Voyager flyby mission, which has probed the secrets of many planets, the latest being the puzzling atmosphere of Uranus (NASA JPL news report 1/26/86). Each measurement of planetary circulation is met with great interest by the media, who vie with one another to generate superlatives, and by scientists, who vie with one another to generate theories.

The earth's atmosphere has a rich and varied dynamics, and we are bound up with its vagaries for our very existence. In comparison with scientists analyzing pictures from some distant planet, those who want to understand our own atmosphere are cursed (or blessed) by familiarity. There are, in some regions, quite a lot of data concerning the motion of the atmosphere, and a long history of atmospheric research has generated sophisticated and complicated theories to explain the dynamics. Many conjectures need to be proved or disproved, but wind data are inadequate. To make a significant contribution in terrestrial atmospheric research, we need precise velocity measurements with high spatial and temporal resolution. After the first amazement and pleasure of views from space, we find that analyses of pictures, no matter how exhaustive, are no substitute for direct quantitative determination of wind profiles.

Since the first wind measurement by Doppler lidar (Huffaker, et al., 1970; see Bilbro, 1980, for a history of the technique), there have been several studies that investigated the possibilities of using this technique to obtain global wind fields. These include design studies for both the Space Shuttle (Martin, 1985) and a free-flying meteorological satellite (Gurk, 1985). There have also been, in the same time period, studies concerning the use and benefit of global wind profiles (Charney, et al., 1969; Phillips, 1983). The measurement technique has matured. Airborne and ground based Doppler lidar wind measurements show good results, (Bilbro, et al., 1984; Rothermel, et al., 1985; McCaul, et al., 1986), and hardware improvements continue to be made. The simulation and evaluation experiments have also matured (Atlas, et al., 1985; Dey, et al., 1985; Arnold, et al., 1985), and interim results indicate that measurements of global wind fields are extremely high on the list of priorities.

Two flight opportunities are being developed within NASA that would provide excellent platforms for a Doppler lidar wind profiler. The Manned Space Station (Reagan, 1984; Beggs, 1985) and its companion, the Earth Observing System, Eos (Butler, 1984) will both be ideal for terrestrial observations, and can provide the longterm, low-earth-orbit home needed for the line-of-sight, active measurement of the Doppler lidar. Both platforms will provide a synergism between the wind profile measurements and those of other earth-directed observations. In addition, resources shared between the lidar and other instruments will allow the task of wind measurement to be accomplished less expensively than would be possible with a dedicated, free-flying satellite.

Some scientific and engineering questions must be answered before a Doppler lidar system can be placed in space and used to determine global winds. The global distribution of atmospheric aerosols that contribute to backscatter at the CO_2 laser wavelengths of interest is crucial to an adequate feasibility assessment, so it has been the subject of considerable study (Hinkley, 1985). Recent work (Bowdle, 1985) indicates that the background aerosol concentration may be at the level that is just detectable from a reasonable satellite instrument, and that the amount of backscatter depends strongly on the wavelength of illumination. This means that the aerosol distribution must be better known than it is now. This effort is underway at the present time within NASA and will combine ground-based, airborne, and satellite observations. However, present data sources cannot give global aerosol backscatter data at the exact wavelength to be used in a space-based Doppler lidar. An important contribution would thus be to make a global backscatter measurement at the wavelength and sensitivity obtainable with a satellite instrument.

A laser of approximately the right power for a space-based lidar has been delivered to NOAA/ERL and is in use in their ground-based lidar system. Such an instrument has not been used in a spacecraft environment, however. Development and testing of flight hardware will certainly be necessary before a wind profiler can be deployed.

The actual quantity measured by a Doppler lidar is the velocity of the backscattering aerosols along the laser beam line of sight. In order to obtain a wind that is of use to meteorologists, the beam must be scanned so that a given volume of the atmosphere can be probed from more than one direction. This technique has been successful in obtaining wind fields in a horizontal plane from an aircraft (Bilbro, et al., 1984), but has not been attempted in any configuration approaching that of a spacecraft. Successful use of line of sight velocities to calculate wind speeds from orbit is another task that must be accomplished.

In this paper we present the results of a design study, the Shuttle Coherent Atmospheric Lidar Experiment (SCALE), designed to address the questions that must be solved before a global wind profiler can be designed and which can only be answered by a space flight experiment. Specifically, we

propose to deploy a Doppler lidar system on the Space Shuttle, scan the beam from orbit to obtain wind vectors, and measure the global distribution of aerosol backscatter. The experiment will demonstrate the operation of a space-based Doppler lidar and at the same time provide a unique data set to show the utility of measuring global winds.

2. Study limitations

The design philosophy is to keep the experiment simple, so that it remains a relatively cheap Spacelab operation and still provides the answers that are needed. For this reason we have chosen to use an existing and proven laser design with 2 J pulse energy, which is somewhat smaller than the 10 J that would be needed for a wind profiler. The lower Shuttle altitude, 200 km for the Shuttle vs. 500 km for the Space Station or Eos, means that the SCALE sensitivity will be better. We have chosen to use a telescope that is fixed in the Shuttle bay to eliminate the complexity and expense of scanning optics. Scanning the beam to make wind measurements will be done by movement of the entire Shuttle vehicle. The design study was carried out in all relevant areas far enough to determine that the system could be built using existing technology.

3. System sensitivity

Figure 1 shows the system sensitivity at various altitudes for three AFGL standard atmospheres using the nominal design altitude of 185 km, 2 J laser pulse energy, 1.25 m optics aperture, a signal to noise ratio of 5 db, and use of isotopic CO_2 so that the laser operates at 9.1 microns to avoid absorption by atmospheric CO_2. Operation at the isotopic line involves only modest cost and results in a significant increase in sensitivity.

4. Beam scanning, coverage, and ground truth

Figure 2 shows the ground projection every 10 sec (250 laser wind estimates) of the lidar line of sight in the scanning mode, ie. optics fixed in the Shuttle bay and the orbiter rotating at 2 deg/sec about its yaw axis. At the 25 Hz lidar pulse rate there will be sufficient line of sight estimates to calculate the wind in a 300 km swath along the flight track, as shown in figure 3, which gives the result of a computer simulation using a realistic simulated wind field and random errors. Wind estimates will be calculated for each 1 km of altitude along the beam during the scanning mode. At least 2 scans per orbit will be made to allow wind estimates to be compared with selected ground truth sources. At other times the line of sight velocities will be available for comparison.

Figures 4a and 4b show 24 hour repeating orbits for two possible SCALE missions. A number of ground target sites for backscatter and wind comparisons are shown on the figure. These sites include presently operating ground based lidars and other likely field comparison locations. A detailed Shuttle trajectory and lidar ground track is shown in figure 5 over the southern US showing the area for a detailed rawindsonde wind comparison in the MSFC area. The actual site for an intensive ground comparison will depend on the Shuttle trajectory that is obtained. Most of the Shuttle flights from Florida have an inclination of 28.5 deg, the same that will be used for the manned Space Station.

5. Laser transmitter, optics, and telescope

Figure 6 gives a summary of the SCALE laser study results. We conclude that it is feasible to use the existing laser design on the Shuttle, with some modifications. The pulse forming network will need to be redesigned, but the laser head itself will be suitable. The use of an already existing laser design is an important part of this design, since it assures that the performance of the system can be accurately anticipated, based on the operation of a ground based lidar. The 50 Hz pulse repetition of NOAA's windvan laser will be reduced to 25 Hz to conform with the power limitations of the Shuttle.

The system optics will be designed to withstand the launch loads by a combination of passive and active means, including an acoustic shroud and active alignment elements between major subgroups such as the interferometer, laser transmitter, and telescope. One of the interesting aspects of the telescope design is the need for lag angle compensation, which accounts for the change in angle of the scanning telescope during the time it takes a laser pulse to make the round trip to the earth. The preliminary optics design found that this can be readily accomplished within the telescope. The main mirror of the telescope will be constructed of a single piece of aluminum and will be diamond turned to the proper shape. Since we operate near 10 microns wavelength, the tolerances are not nearly as close as a telescope in the visible or uv regions, so the telescope is much cheaper.

6. Shuttle accommodations

A Spacelab pallet with support igloo was chosen to carry the SPACE instrument, as is shown in figure 7. The structure shown in figure 7 is schematic only and will consist of a spaceframe structure attached to the indicated pallet hard points. The results of the preliminary structures and laser analyses have been used to calculate a weights summary, which is given in figure 8. The power requirements are given in figure 9. Both the weight and power requirements are within the limits of a Spacelab pallet. The repetition rate of the laser can be chosen to match power available, with the design value being the 25 Hz that is used in figure 9. The system thermal schematic is shown in figure 10. The thermal load rejection capability of the Spacelab pallet is sufficient for the needs of the experiment. The command and data management system (CDMS) requirements are given in figure 11 and, as is the case for all the SCALE systems requirements, is well within the pallet capabilities.

Propellant usage for the beam scanning maneuver is given in figure 12, along with the total propellant consumed per day in figure 13. Total usage for a 5 day mission is within the Shuttle capabilities. The requirement may be relaxed by making no corrections during the 360 deg rotation, which would result in the axis of rotation pointing 10 deg off vertical at the end of the maneuver. This amount of deviation should be acceptable for the purpose of wind estimation. The scanning rate of 2 deg/sec is higher than has been used on the Shuttle to date, but according to simulations should cause no problem. This will be the subject of an short experiment on a future Shuttle flight.

7. Conclusions

The results of the study have confirmed that there are no engineering or technological reasons that the SCALE experiment cannot proceed. The scientific and engineering questions that will be answered and demonstrated by this experiment include nearly all of those that remain before a comprehensive Doppler lidar wind profiler can be designed, built, and placed in orbit. This experiment will be an economical and necessary step on the way toward global wind measurement on the Space Station or Earth Observing System.

8. References

Arnold, C., C. Dey, and W. Bostleman, 1985. Results of an Observing System Simulation Experiment Based on the Proposed Windsat Instrument, Proceedings of the Symposium and Workshop on Global Wind Measurements, NASA, July 29 - Aug. 1, 1985, Columbia, Maryland.

Atlas, R., E. Kalnay, W. Baker, J. Susskind, D. Reuter, M. Halem, 1985. Simulation Studies of the Impact of Future Observing Systems on Weather Prediction, Proceedings 7th Conference on Numerical Weather Prediction, Montreal, 17-20 June, 145-151.

Beggs, J. M., 1985. The Issue is Leadership, Aerospace America, v. 23, No. 9, 44-47.

Bowdle, D., 1985. Aerosol Sampling Strategies for a Global Aerosol Model, Proceedings of the Symposium and Workshop on Global Wind Measurements, NASA, July 29 - Aug. 1, 1985, Columbia, Maryland.

Bilbro, J., 1980. Atmosperhic Laser Doppler Velocimetry: An Overview, Optical Engineering, Vol.19, No. 4 533-542.

Bilbro, J., G. Fichtl, D. Fitzjarrald, M. Kraus, R. Lee, 1984. Airborne Doppler Lidar Wind Field Measurements, Bull. Am. Met. Soc., Bol. 65, No. 4, 348 359.

Butler, D., ed., 1984. The Earth Observing System, NASA TM 86129, August 1984.

Charney, J., M. Halem, R. Jastrow, 1969. Use of Incomplete Data to Infer the Present State of the Atmosphere, J. Atmos. Sce., 26, 1160-1163.

Dey, C., C. Arnold, W. Bostelman, 1985. Design of a Windsat Observing System Simulation Experiment, Proceedings of the Symposium and Workshop on Global Wind Measurements, NASA, July 29 - Aug. 1, 1985, Columbia, Maryland .

Gurk, H. M., 1985. Windsat Free-Flyer Using the Advanced TIROS-N Satellite, Proceedings of the Symposium and Workshop on Global Wind Measurements, NASA, July 29 - Aug. 1, 1985, Columbia, Maryland. See also RCA Corp., Feasibility Study of a Windsat Freeflyer, July 1983, Final Report NOAA contract NA82 RAC00141.

Hinkley, D., ed., 1985. Proceedings, Third NASA/NOAA Infrared Lidar Backscatter Workshop, NASA JPL, 1985, 245

Huffaker, M., A. Jelalian, J. Thomson, 1970. Laser Doppler System for the Detection of Aircraft Trailing Vortices, Proceedings IEEE, Vol 58 p. 322.

Martin, S., 1985. The Lockheed Windsat Study, Proceedings of the Symposium and Workshop on Global Wind Measurements, NASA, July 29 - Aug. 1, 1985, Columbia, Maryland. See also Lockheed Corp., Global Wind Measurement System, April 1981, Final report NOAA contract NA79 RAC00127.

McCaul, E. W., H. B. Bluestein, R. J. Doviak, 1986. Airborne Doppler Lidar Techniques for Observing Severe Thunderstorms, Submitted to Applied Optics.

Phillips, N. A., 1983. An Accuracy Goal for a Comprehensive Satellite Wind Measuring System, Mon. Wea. Rev., 111, 237-239.

Reagan, R., 1984. State of the Union Address to Congress, Congressional Record, Jan. 1984.

Rothermel, J., C. Kessinger, D. Davis, 1985. Dual-Doppler Lidar Measurement of Winds in the JAWS Experiment, J. Atmos. and Oceanic Tech., Vol. 2, No. 2, 138-147.

Vaughan, W. W., 1982. Meteorological Satellites: Some Early History. Proceedings of AIAA 20th Aerospace Sciences Meeting, Orlando FL, Jan. 11-14 1982. NASA CP 2227.

Acknowledgments

The laser study was prepared by S. Moody and the staff of Spectra Technology Corp. Wind field estimates were done by G. Emmitt and the staff of Simpson Weather Associates. Optics and telescope consultation design was done by D. Korsch of Korsch Optics Inc. The Spacelab accommodations study was done by the staff of the MSFC Preliminary Design Group under the direction of J. Mabry. System sensitivity calculations were done by J. Bilbro and the staff of the Electronic and Information Systems Lab of MSFC.

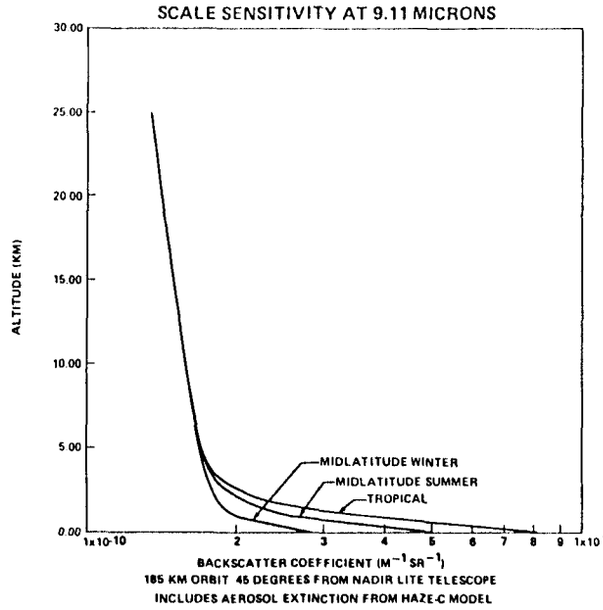

Figure 1 System Sensitivity 9.11 Microns

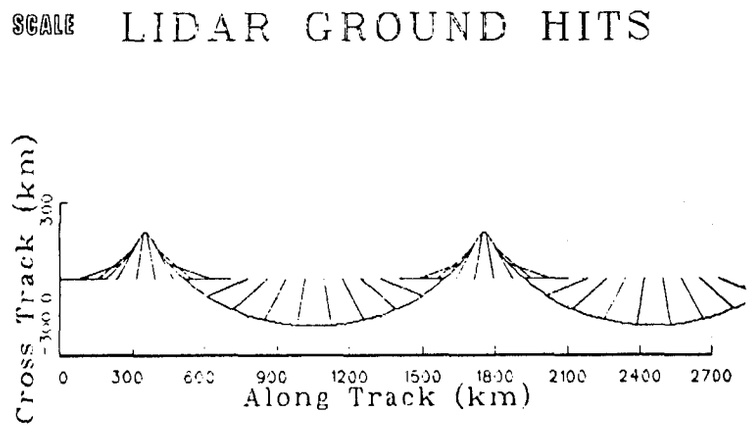

Figure 2 Ground Projection of Lidar Beam

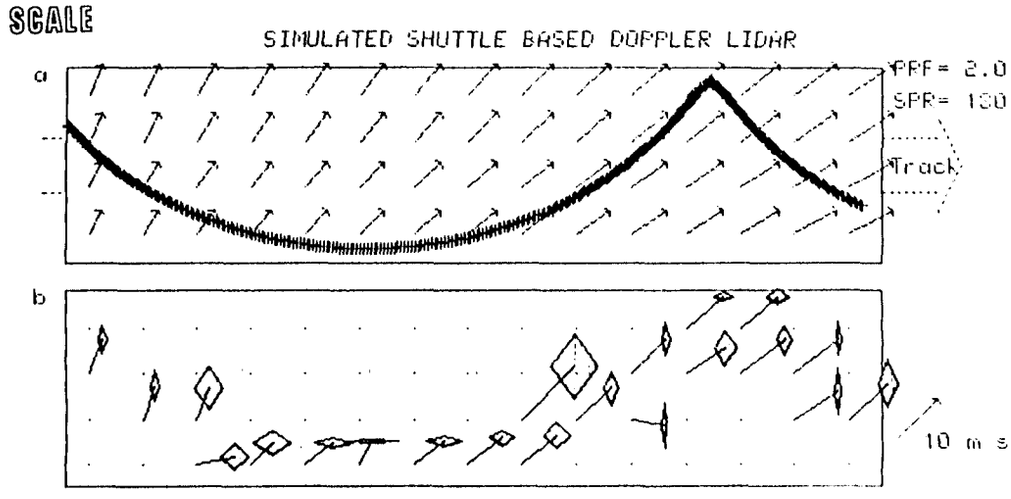

Figure 3 Computer Simulation of SCALE Measured Winds

SCALE

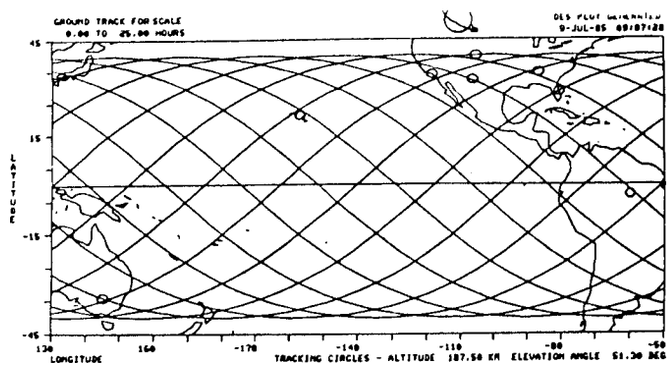

24 HOUR REPEATING ORBIT

INCLINATION 40 DEG

ALTITUDE 187.5 KM

TARGETS AVAILABLE (SHOWN BY - O)

	SITE	LATITUDE	LONGITUDE
✓	BOULDER, CO	40.0	-156.26
✓	HUNTSVILLE, AL	34.7	-86.6
✓	KSC, FL	28.5	-80.7
✓	MANAUS, BRAZIL	-3.06	-60.0
✓	MAUNA LOA, HA	21.2	-157.2
✓	MELBOURNE, AUSTRALIA	-34.2	145.0
	PASADENA, CA	34.1	-118.52
✓	WHITE SANDS, NM	32.4	-106.5

Figure 4a Shuttle Orbit 40 Deg Inclination

SCALE

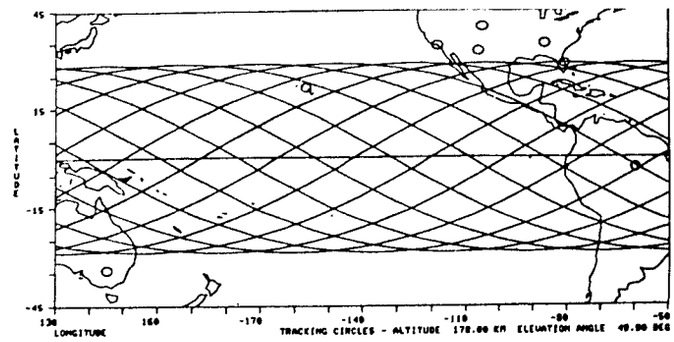

24 HOUR REPEATING ORBIT

INCLINATION 28.5 DEG

ALTITUDE 178 KM

TARGETS AVAILABLE (SHOWN BY - O)

	SITE	LATITUDE	LONGITUDE
	BOULDER, CO	40.0	-156.26
	HUNTSVILLE, AL	34.7	-86.6
✓	KSC, FL	28.5	-80.7
✓	MANAUS, BRAZIL	-3.06	-60.0
✓	MAUNA LOA, HA	21.2	-157.2
	MELBOURNE, AUSTRALIA	-34.2	145.0

Figure 4b SCALE Shuttle Orbit 40 Deg Inclination

SCALE

LIDAR GROUND HITS

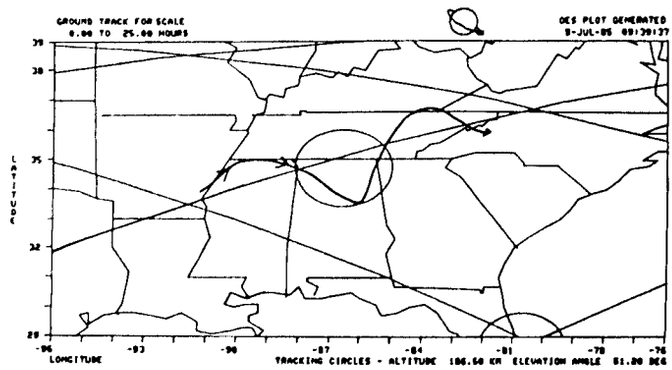

Figure 5 Laser Beam Ground Track During Scan

STI STUDY SHOWS SHUTTLE BASED "WINDVAN" CONVERSION FEASIBLE

- STUDY PREMISE – Take an existing design and see if it can be Shuttle qualified
- KEY RESULT – STI/NOAA "Windvan" CO2 lidar system can be Shuttle compatible
- WEIGHT, VOLUME, POWER REQUIREMENTS REASONABLE
- NO NEW TECHNOLOGY NEEDED
  - Repackaging and qualification engineering will be needed
- PRINCIPAL ENGINEERING/PACKAGING DESIGN MODIFICATIONS
  - Compact pulse poser
  - Solid state switch rather than thyratron
  - Launch harden certain components

Figure 6 Laser Study Results

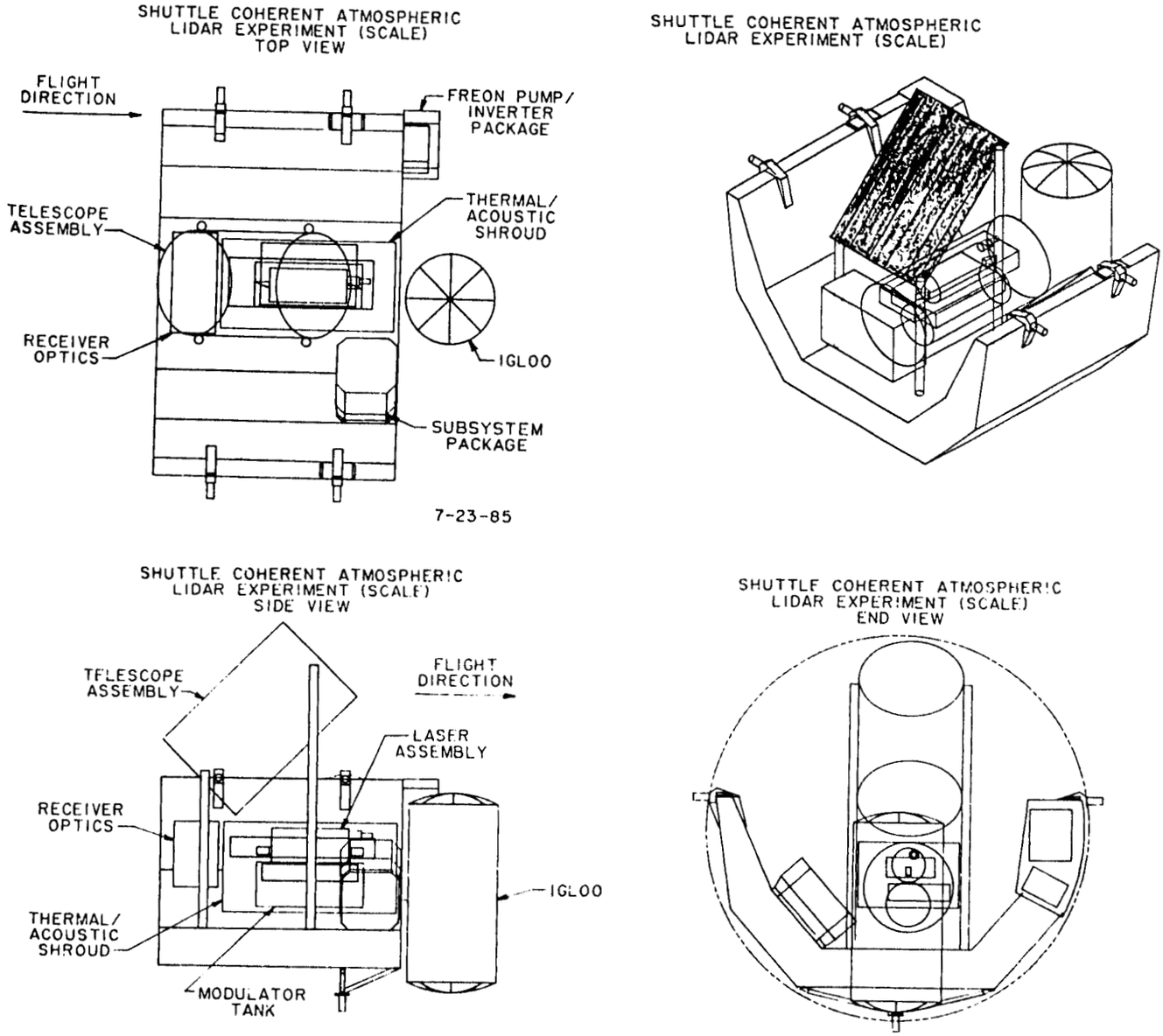

Figure 7 SCALE Apparatus on Spacelab Pallet

SCALE

SCALE

WEIGHT SUMMARY (KG)

SUBSYSTEM	WEIGHT
LASER (MECHANICAL)	225
LASER (ELECTRICAL)	455
THERMAL	48
C^3	30
OPTICS ASSEMBLY	30
STRUCTURAL SUBSYSTEM	150
ACOUSTIC SHELL AND LEAD FOAM	300
TABLE AND SPACE FRAME INCL. REC. OPTICS	100
SUBTOTAL LASER EQUIPMENT	1338
TELESCOPE	605
MTG STR	67
CONTINGENCY 10%	206
TOTAL EXPERIMENT WEIGHT	2216
MDE	
EXP. HX	14
COLD PLATES + SPRT FOR (3) + PLUMB.	52
TOTAL PALLET PAYLAOD	2282

NOTE: SPACELAB PALLET NOMINAL LOAD CARRYING CAPABILITY FOR PAYLOAD AND MISSION DEPENDENT EQUIPMENT (MDE), WITH AN IGLOO, IS 2880 KG.

Figure 8 Weight Summary

SCALE

SCALE ELECTRICAL POWER BUDGET

SCIENCE INSTRUMENTS	POWER REQUIRED (WATTS)
LASER (MECHANICAL)	75
LASER (ELECTRICAL) AT 25 Hz REPETITION RATE	1,300
THERMAL (ONE PUMP)	315
C^3	100
OPTICAL/STRUCTURAL	250
	2,040
SPACELAB (IGLOO AND PALLET)	
SUBSYSTEMS	
C&DM (W/HDR OPTION)	1,955
THERMAL	375
DISTRIBUTION AND CABLE LOSS (5%)	111
CONTINGENCY (15%)	333
TOTAL	4,814 WATTS

Figure 9 Power Budget

SCALE

THERMAL SYSTEM SCHEMATIC

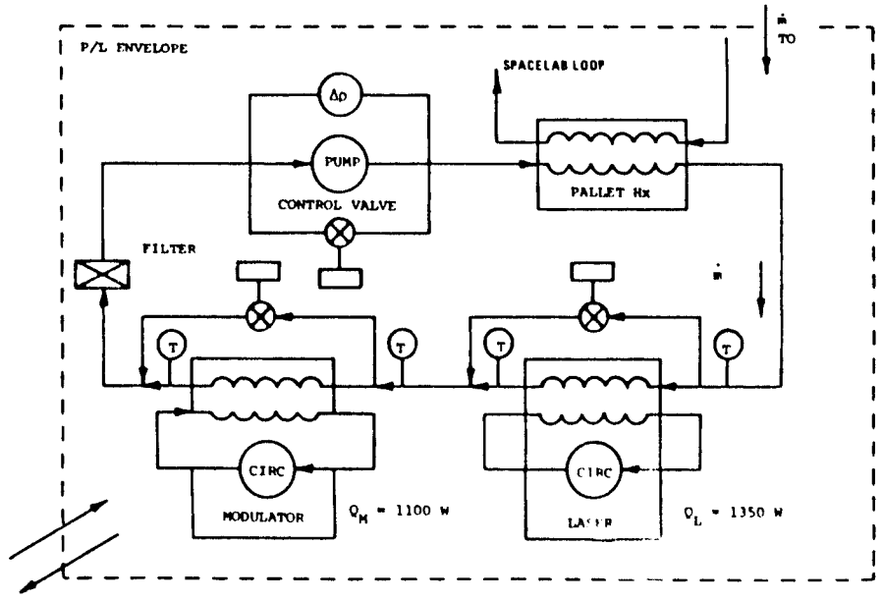

Figure 10 Thermal System

SCALE

SCALE

CDMS REQUIREMENTS

- HOUSEKEEPING
  - 120 KB/S DOWNLINK
  - REQUIRES SHUTTLE STATUS (POSITION, ATTITUDE, ETC.)
  - TEMPERATURE, PRESSURE, VOLTAGE, POWER, ETC. FROM EXPERIMENT
- SCIENCE DATA
  - RAW DATA
    - UP TO 3.5 MB/S DOWNLINK
  - PROCESSED DATA
    - 18 KB/S DOWNLINK
    - PROCESSED BY EXPERIMENT
    - DOPPLER MOMENTS AND CALCULATIONS
- VIDEO DATA
  - BORESIGHTED TV CAMERA
  - 4.5 MHZ CHANNEL
  - MAY RECORD DURING PEAK DATA DOWNLINK
- TOTAL DATA REQUIREMENT
  - 3.6 MB/S PLUS TV CHANNEL
  - DOWNLINK ALL DATA DURING NORMAL OPERATION
  - RECORD DATA WHILE IN MANEUVER
  - DOWNLINK RECORDED DATA WHILE OVER TARGETS OF NO INTEREST

Figure 11 Command and Data Management System

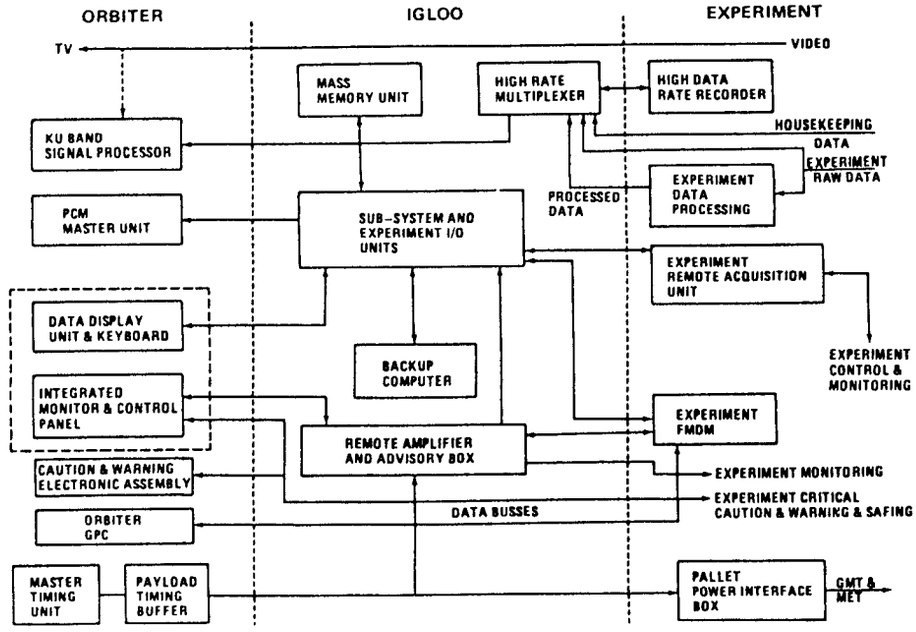

Figure 12 Command and Data Management Configuration

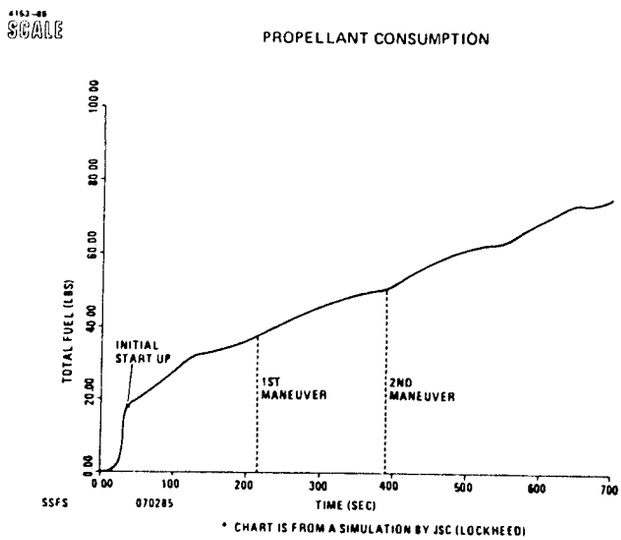

Figure 13 Propellant Consumption During Maneuver

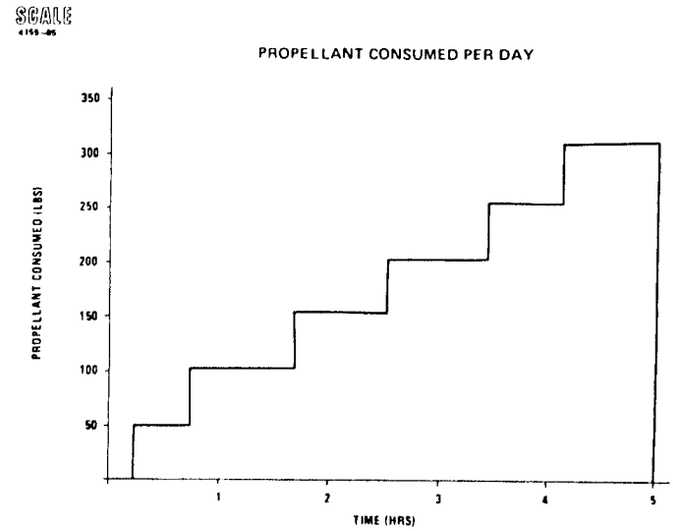

Figure 14 Propellant Consumption During Day

APPLICATIONS OF SPECIAL SENSOR MICROWAVE IMAGER (SSM/I) DATA

Captain Leslie A. Brenton and Major Clifford R. Matsumoto

Headquarters Air Weather Service
Scott Air Force Base, Illinois

1. INTRODUCTION

The Special Sensor Microwave Imager (SSM/I) is a joint Air Force and Navy project. Data will be processed in near real-time by the Air Force Global Weather Central (AFGWC) and Fleet Numerical Oceanography Center (FNOC). In addition, plans call for processing of data at Air Force and Navy direct readout sites.

This paper presents a brief description of the sensor, specifies the environmental parameters to be obtained from the data, and discusses the applications of the data by the Air Force and Navy.

2. SENSOR CHARACTERISTICS

The SSM/I is a seven-channel, four-frequency, linearly-polarized, passive microwave radiometer. The sensor measures dual-polarized, atmospheric and surface radiation at three frequencies (19.35, 37.0, and 85.5 GHz) and vertically-polarized radiation in the water vapor absorption band at 22.235 GHz. Footprint resolution is 12.5 km at 85.5 GHz and 25 km for other frequencies.

Scan width is 1394 km. This provides daily global coverage with some gaps equatorward of 50° latitude. About two-thirds of the earth's surface will have repeat coverage on successive days.

3. ENVIRONMENTAL PARAMETERS

From previous studies of microwave properties, the Scanning Multichannel Microwave Radiometer (SMMR) data, and simulation models, algorithms have been developed to determine 15 environmental parameters from the brightness temperatures with 25km resolution. These parameters are:

Surface wind speed: 3-29 $\pm$ 2 m/s

Liquid water content: 0-12.5 $\pm$ 0.1 kg/m^2

Cloud water content: 0-12.6 $\pm$ 0.1 kg/m^2

Water vapor content: 0-80 kg/m^2
polar latitudes: $\pm$ 1.0 kg/m^2
mid-latitudes: $\mp$ 2.0 kg/m^2
tropical latitudes: $\mp$ 3.0 kg/m^2

Precipitation rate: 0-61 $\pm$ 5 mm/hr

Cloud amount: 0-100 $\pm$ 20%

Surface moisture: 0-61 $\pm$ 3.8%

Land surface temperature: 180-340K
Over land: $\pm$ 2K (uncloudy)*
$\mp$ 3K (cloudy)
Over snow: $\mp$ 3K (uncloudy)*
$\mp$ 7K (cloudy)
* Cloud amount < 30% of water droplet clouds or any amount of cirrus.

Ice age: first-year, multi-year

Ice concentration: 0-100 $\pm$ 12%

Ice location: $\pm$ 12.5 km

Snow water content: 0-50 $\pm$ 3 cm
(indeterminate with cloud amount > 30%)

Snow edge location: $\pm$ 12.5 km

Atmospheric transmissivity: 0-100 $\pm$ 5%

Surface type: generic designations

Several algorithms exist for each parameter. They depend on climatic and surface type which are assigned using earth location. Eleven climatic types have been predetermined, and are based on latitude and season. Predetermined surface types are ocean, ice, possible ice, coast (50 km either side), and land. Further delineation is provided by the SSM/I data. Possible ice is designated ocean or ice depending on ice concentration. Land areas are delineated as:

Snow1 (over frozen ground).
Snow2 (over soil).
Glacial (very deep multi-year ice over land).
Frozen ground or wet snow (indistinguishable).
Arable soil (unfrozen soil with moisture).
Desert (very dry soil).
Heavy vegetation (vegetation masks surface).
Heavy precipitation (scattering by rain).
Flooded (lake, river, swamp, etc.).

Knowledge of the surface type is essential for accurate estimation of the environmental parameters since all parameters are indeterminate over some surfaces; for example, surface winds are indeterminate over land or in heavy precipitation. Table 1 lists the surface types over which each parameter can be determined. Parameters are not calculated for coastal or flooded areas because the mixture of land and water surfaces in the scenes is unknown.

The sensor measurements will be the only source of data for surface moisture, cloud water content and liquid water content. For most of the other environmental parameters provided, the SSM/I will be the only source of measurement over data-sparse areas. Additionally, the SSM/I will be the only all-weather source of ice data and the only extensive source of ocean surface wind speed.

Table 1: Parameters vs Surface Types. This table lists the surface types over which each parameter can be determined. Parameters are not calculated for surfaces identified as coast or flooded.

PARAMETER	SURFACE TYPE
Surface wind	Ocean
Ice Age, Edge, Concentration	Ice
Precipitation Rate	Ocean, frozen ground, arable soil, desert, heavy vegetation, heavy precipitation
Liquid Water Content	Ocean, frozen ground, arable soil, desert, heavy vegetation, heavy precipitation
Cloud Water Content	Ocean, frozen ground, ice, snow1, snow2, glacial, arable soil, desert, heavy vegetation
Atmospheric Water Vapor Content	Ocean
Surface Moisture	Snow2, arable soil, desert, heavy precipitation
Land Surface Temperature	Snow1, snow2, glacial, frozen ground, arable soil, desert, heavy vegetation
Snow Water Content, Edge	Snow1, snow2
Cloud Amount	Snow1, snow2, glacial, frozen ground, arable soil, desert, heavy precipitation
Transmissivity	All

4. APPLICATIONS

Numerous potential applications of SSM/I data have been identified by the Air Force and Navy. Some parameters will be input directly into models at the forecast centers. Most parameters will be available in mapped displays on the interactive systems at AFGWC, FNOC, and direct readout sites. Surface wind speed, land surface temperatures, and moisture parameters have application to the numerical analysis and forecast models at AFGWC and FNOC. Ice parameters will be sent to the Navy/NOAA Joint Ice Center to enhance their weekly summaries of ice data provided to AFGWC and FNOC.

Specialized models at AFGWC include the Real-Time Nephanalysis (RTNEPH), Agricultural Meteorology Model (AGROMET), and the snow analysis model. Parameters with applications to the RTNEPH are surface temperature, and moisture, ice, and snow parameters. Parameters applicable to AGROMET are surface moisture, surface temperature, ice and snow parameters, and precipitation rate. Ice and snow parameters will be input into the snow analysis model. SSM/I data will also be used by many special applications models.

Ocean surface winds are the key input to many of the oceanographic models run at FNOC. They include the Thermodynamic Ocean Prediction System (TOPS), Global Surface Current Model (GBLCURR), Global Spectral Ocean Wave Model (GSOWM), and the new RAYMODE Acoustic Model (which also uses output from TOPS). Output from GBLCURR is used in the Search and Rescue (SAR) model and GSOWM output is used for Optimum Track Ship Routing.

Through the use of interactive systems, SSM/I data may be combined with conventional data to provide a variety of diverse forecast support; i.e., electro-optical (E-O) systems, trafficability, and severe weather. A more complete list of potential applications appears in Table 2.

5. CONCLUDING REMARKS

The SSM/I is scheduled to fly on all future DMSP spacecraft beginning in mid-1987, and the Navy Remote Ocean Sensing System (N-ROSS) satellite. Once the SSM/I data become available, FNOC will start processing the data. Processing at AFGWC will begin when the computer upgrade is complete. FNOC will provide antenna temperatures, brightness temperatures, and environmental parameters (with earth location) to NESDIS for archival. Since the algorithms were developed from simulation, improvements to the algorithms are expected with the acquisition of actual data; consequently, there will be a year-long validation test. Data will be used operationally once they have been determined to be meteorologically consistent and reasonable.

Improved forecasts are expected with the acquisition and use of SSM/I data over data-sparse areas. Additionally, the SSM/I could provide corrections for water vapor to other

sensors, and improved moisture profiles when operated with a collocated Microwave Temperature and Water Vapor Sounder (SSM/TW). If SSM/I data can be combined with other data sources, such as infrared (IR), to produce parameters, further forecast improvements are likely.

6. REFERENCES:

Air Weather Service, 1985: Draft AWS DMSP Sensor Data Plan, Mission Sensor Microwave Imager (SSM/I) Annex and Mission Sensor Microwave Temperature and Water Vapor (SSM/TW) Sounder Annex, Headquarters Air Weather Service, Scott AFB, IL.

Clancy, R. M., 1986: Personal communication.

Heacock, E. L., 1985: ENVIROSAT-2000 Report, Comparison of the Defense Meteorological Satellite Program (DMSP) and the NOAA Polar-Orbiting Operational Environmental Satellite (POES) Program. US Dept of Commerce, NOAA, NESDIS, IV-23-32.

Hughes Aircraft Company, 1985: Special Sensor Microwave/Imager (SSM/I), Support and Services Technical Review. Contract No. F04701-84-C-0036, Denver Engineering Laboratory, Englewood, CO.

_____, 1985: Special Sensor Microwave/-Imager (SSM/I), Support and Services Technical Operating Report, Contract No. F04701-84-C-0036, Denver Engineering Laboratory, Englewood, CO, 93 pp.

Hollinger, M. P., and R. C. Lo, 1983, SSM/I Project Summary Report. NRL Memo Rpt 5055. Naval Research Laboratory, Washington DC, 106 pp.

Lo, R. C., 1983: A Comprehensive Description of the Mission Sensor Microwave Imager (SSM/I) Environmental Parameter Extraction Algorithm. NRL Memo Rpt 5199. Naval Research Laboratory, Washington DC, 48 pp.

Mitchell, J. L., et al, 1985: The REX and the US Navy GEOSAT. Naval Research Reviews. 37, 16-23.

Savage, R. C., 1986: Personal communication.

Table 2: Potential Applications of SSM/I Parameters (AF - Air Force only, N - Navy only).

PARAMETERS	APPLICATION
Surface Wind Speed	Tropical storm monitoring Numerical forecast models N - Ship routing Support of refueling operations Aircraft operations Wave generation and sea state Anti-submarine warfare Ocean rescue
Ice Parameters (thru Navy/NOAA Joint Ice Center)	AF - Cloud analysis & forecasting AGROMET Terrain data bases Electro-optical systems N - Ship Routing Iceberg avoidance Submarine operations Ocean rescue
Precipitation Rate	Tropical cyclone analysis & forecasting Communications attenuation Aircraft operations Electro-optical systems AF - AGROMET Flooding Support to Army trafficability & engineering concerns N - Ship routing Ocean noise models
Land Surface Temperature	AF - AGROMET Cloud analysis & forecasting Electro-optical systems
Cloud Water Content	Numerical forecast models Electro-optical systems Aircraft operations AF - Cloud analysis & forecasting
Liquid Water Content	Numerical forecast models Electro-optical systems AF - Cloud analysis & forecasting
Water Vapor Content	Numerical forecast models Electro-optical systems AF - Cloud analysis & forecasting N - Sea surface temperature estimates
Cloud Amount	Aircraft operations AF - Cloud analysis & forecasting
Surface Moisture	AF - AGROMET Trafficability Electro-optical systems N - Amphibious and riverine operations
Snow Parameters	Radar Systems AF - AGROMET Cloud analysis & forecasting Trafficability Electro-optical systems Terrain data bases
Transmissivity	Communications management Electro-optical systems

SPACE OPPORTUNITIES FOR TROPOSPHERIC CHEMISTRY RESEARCH

Joel S. Levine and James M. Hoell

NASA Langley Research Center
Hampton, Virginia 23665-5225

and

Robert J. McNeal

NASA Headquarters
Washington, DC 20546

1. INTRODUCTION

Tropospheric trace species affect the quality of the air that we breathe, impact the ecology of the biosphere, affect the photochemistry of ozone in the stratosphere, and control the climate of our planet. Tropospheric trace species are produced by a variety of processes, including industrial, technological, and combustion activities; microbiological metabolic processes; biomass burning, lightning; and various photochemical and chemical reactions in the troposphere. Sources of tropospheric trace species include urban areas, marshlands, grasslands, farmlands, forests, and the oceans. Over the last decade, it has become apparent that the troposphere is a complex chemical mixture of considerable photochemical/chemical activity. Tropospheric trace species have residence times that vary from a fraction of a second to many decades. The longer-lived trace species are distributed throughout the troposphere by atmospheric motions.

2. MEASUREMENT OF TROPOSPHERIC TRACE SPECIES FROM SPACE

Until very recently, the bulk of the research dealing with the distribution, photochemistry, and chemistry of trace species involved the middle and upper atmosphere. This is particularly true with respect to measurements of trace species from space. To date, measurements of tropospheric trace species have been obtained by only three spaceborne experiments: Measurements of tropospheric carbon monoxide were obtained by the MAPS (Measurement of Air Pollution from Satellites) experiment on the space shuttle (Reichle et al., 1982); measurements of ozone, water vapor, and aerosols were obtained down to cloudtops or as low as 2 km for clear skies by SAGE II (Stratospheric Aerosol and Gas Experiment) (Mauldin et al., 1985); and a number of tropospheric species were detected by the ATMOS (Atmospheric Trace Molecule Spectroscopy) experiment on a recent flight of the space shuttle.

The operational status of the space shuttle and the planned space station offer unique opportunities for obtaining measurements of tropospheric trace species from space. However, the scientific, engineering, and technological challenges of measuring tropospheric trace species from space are manyand include:

1. The presence of clouds and aerosols.
2. The presence of water vapor and carbon dioxide, which blanket much of the useful infrared spectrum.
3. The very small temperature difference between the surface and the troposphere.
4. The high pressure of the troposphere which blends spectral features, making isolation of a particular spectral signature very difficult.
5. The large abundance of certain species in the stratosphere, such as ozone and nitrogen dioxide, which conceal tropospheric abundance of these species from space.

To address these and other challenges affecting measurements of tropospheric trace species from space, a workshop on Space Opportunities for Tropospheric Chemistry Research was held at the NASA Goddard Institute for Space Studies in New York on September 9-13, 1985. The workshop was sponsored by the Tropospheric Chemistry Program, Earth Science and Applications Division, Office of Space Science and Applications (OSSA), NASA Headquarters. More than 40 experts from universities, industry, and Government participated in the workshop. The workshop participants considered both passive and

active remote sensing techniques, as well as possible tropospheric space missions.

3. KEY TROPOSPHERIC TRACE SPECIES

As a starting point, the workshop participants considered a list of key tropospheric trace gases for study from space discussed in a recent report of the National Academy of Sciences (1985). The Academy report categorized the key tropospheric species into either "first level" or "second level." Measurements of first-level gases from space may be achieved in a shorter timeframe than measurements of second-level gases. First level gases include water vapor (H_2O), ozone (O_3), carbon monoxide (CO), and methane (CH_4). Second level gases include nitrous oxide (N_2O), nitrogen dioxide (NO_2), ammonia (NH_3), sulfur dioxide (SO_2), chlorofluoromethanes, and hydrogen chloride (HCℓ).

Water vapor, ozone, carbon monoxide, and methane, the four first-level gases identified in the Academy report, impact both the climate of our planet (Ramanathan et al., 1985, and Dickinson and Cicerone, 1986) and the photochemistry/chemistry of the troposphere (Logan et al., 1971, and Graedel, 1985). All four gases are involved in the photochemical/chemical production and destruction of the hydroxyl radical (OH). The hydroxyl radical is the overwhelming chemical oxidizer and, hence, the pivotal chemically active gas in the troposphere. The hydroxyl radical controls the chemical destruction and the atmospheric lifetime of almost every tropospheric trace species. Unfortunately, in situ or remote sensing instrumentation for either ground-based or aircraft measurements of the hydroxyl radical in the "clean" remote troposphere have not yet been demonstrated. However, theoretical photochemical calculations involving all four first-level gases can lead to an understanding of the distribution and magnitude of the hydroxyl radical in the troposphere.

3.1 Water Vapor (Mixing ratio: 0.005 - 0.04)

Water vapor is the strongest absorber of infrared radiation in the atmosphere. The reaction of water vapor with excited oxygen atoms ($O(^1D)$) leads to the chemical production of the hydroxyl radical. The distribution of water vapor in the middle and upper troposphere is not known with great accuracy.

3.2 Ozone (Mixing ratio: 40 - 100 ppbv)

Ozone is both a radiatively and chemically active gas. Ozone absorbs solar ultraviolet radiation (in the stratosphere), and its photolysis in the troposphere leads to the production of excited oxygen atoms needed for the production of OH. Photochemical and chemical schemes initiated by a number of gases, including the oxides of nitrogen, methane, carbon monoxide, and nonmethane hydrocarbons, lead to the production of ozone in the troposphere.

3.3 Carbon Monoxide (Mixing ratio: 0.05 - 0.3 ppmv)

Carbon monoxide and methane control the chemical destruction of OH in the troposphere. Sources of carbon monoxide include the oxidation of methane and nonmethane hydrocarbons and fossil fuel burning. Direct tropospheric measurements since 1979 (Khalil and Rasmussen, 1984), as well as analyses of ground-based solar infrared spectra made in 1950-51 (Rinsland and Levine, 1985), indicate that tropospheric levels of carbon monoxide may be increasing about 2-6 percent per year.

3.4 Methane (Mixing ratio: 1.7 ppmv)

Methane absorbs infrared radiation and, hence, is a radiatively active gas. The methane oxidation chain initiated by the reaction of methane with the hydroxyl radical is a signficant source of carbon monoxide. Direct tropospheric measurements obtained since about 1977 (Rasmussen and Khalil, 1981; Seiler, 1982; Blake et al., 1982; and Khalil and Rasmussen, 1983), as well as analyses of ground-based solar infrared spectra made in 1951 (Rinsland et al., 1985), indicate that tropospheric levels of methane may be increasing about 1-2 percent per year. Theoretical photochemical calculations indicate that increasing levels of tropospheric carbon monoxide and methane over the last 35 years may have resulted in a 25 percent decrease in levels of the hydroxyl radical in the troposphere (Levine et al., 1985).

The workshop considered the passive and active remote sensing instrumentation and technology to obtain measurements of these gases and aerosols from space. Possible tropospheric missions were also considered. The results and recommendations of the workshop will be reviewed.

4. REFERENCES

Blake, L. E., E. W. Mayer, S. C. Tyler, Y. Makide, D. C. Montague, and F. S. Rowland, 1982: Global increase in atmospheric methane concentrations between 1978 and 1980, Geophys. Res. Lett., 9, 477-480.

Dickinson, R. E., and R. J. Cicerone, 1986: Future global warming from atmospheric trace gases, Nature, 319, 109-115.

Graedel, T. E., 1985: The photochemistry of the troposphere, The Photochemistry of Atmospheres: Earth, the Other Planets, and Comets, (J. S. Levine, editor), Academic Press, Inc., Orlando, 39-76.

Khalil, M. A. K., and R. A. Rasmussen, 1983: Sources, sinks, and seasonal cycles of atmospheric methane, J. Geophys. Res., 88, 5131-5144.

Khalil, M. A. K., and R. A. Rasmussen, 1984: Carbon monoxide in the Earth's atmosphere: Increasing trend, Science, 244, 54-56.

Levine, J. S., C. P. Rinsland, and G. M. Tennille, 1985: The photochemistry of methane and carbon monoxide in the troposphere in 1950 and 1985, Nature, 318, 254-257.

Logan, J. A., M. J. Prather, S. C. Wofsy, and M. B. McElroy, 1981: Tropospheric chemistry: A global perspective, J. Geophys. Res., 86, 7210-7254.

Mauldin, L. E., N. H. Zaun, M. P. McCormick, J. H. Guy, and W. R. Vaughn, 1985: Stratospheric Aerosol and Gas Experiment II Instrument: A functional description, Optical Engineering, 24, 307-312.

National Academy of Sciences, 1985: A strategy for Earth science from space in the 1980's, Part II: Solid Earth, oceans, and Biota, National Academy Press, 149 pages.

Ramanathan, V., R. J. Cicerone, H. H. Singh, and J. T. Kiehl, 1985: Trace gas trends and their potential role in climate change, J. Geophys. Res., 90, 5547-5566.

Rasmussen, R. A., and M. A. K. Khalil, 1981: Atmospheric methane: Trends and seasonal cycles, J. Geophys. Res., 86, 9826-9832.

Reichle, H. G., S. M. Beck, R. E. Haynes, W. D. Hesketh, J. A. Holland, W. D. Hypes, H. D. Orr, R. T. Sherill, H. A. Wallio, J. C. Casas, M. S. Saylor, and B. B. Gormsen, 1982: Carbon monoxide measurements in the troposphere, Science, 218, 1024-1026.

Rinsland, C. P., and J. S. Levine, 1985: Free tropospheric carbon monxide concentrations in 1950 and 1951 deduced from infrared total column amount measurements, Nature, 318, 250-254.

Rinsland, C. P., J. S. Levine, and T. Miles, 1985: Concentration of methane in the troposphere deduced from 1951 infrared solar spectra, Nature, 318, 245-249.

Seiler, W., 1982: The cycle of methane in the troposphere, paper presented at the 2nd Symposium on the Composition of the Non-Urban Troposphere, AMS-AGU-NASA, Williamsburg, VA, May 25-28, 1982.

10.6

INFRARED IMAGING AND SOUNDING FROM A GEOSTATIONARY BODY STABILIZED SPACECRAFT

Dominick J. Juarez
Edward W. Koenig

ITT Aerospace Optical Division
Fort Wayne, Indiana

INTRODUCTION

The next generation Geostationary Operational Environmental Satellite (GOES/IJK/LM) is to be a three axis, body stabilized spacecraft. Included as part of its instrument complement are improved Thermal Imaging and Sounding Instruments. These instruments have been improved over the combined Imager and Sounder on the present spin stabilized GOES in sensitivity, scan flexibility, and pointing accuracy.

Moreover, the new instruments are designed to be integral parts of the on-board stabilization and pointing determination system to maintain accurate (within 2 km) pointing of both instruments. Each instrument is capable of utilizing a visible detector array to sense fourth magnitude stars to assist in location and pointing accuracy determination.

The spacecraft layout (Figure 1) provides for the mounting of the instruments on the earth facing side of the spacecraft. The instruments are located in the Northeast and Northwest corners with their optical ports pointing to the Earth and their passive coolers pointing North. This righthand, lefthand mounting configuration allows the instruments to share a single passive cooler design with only optical input and electrical connection variations.

The instruments share a significant amount of design commonality. The sensor modules of the ITT Imager and Sounder are shown in Figure 2. Both instruments have 12 inch optical systems. Consequently, the scan mirrors are identical. The telescope configuration is near identical, their basic difference being in the prescription of their secondary mirrors. The scanner modules of both instruments also share the same design. The scanners have identical scan mirrors, driven by a DC torquer, controlled by an Inductosyn derived digital-controlled servo system. The Sensor Assembly thermal control and mechanical design also share commonality. The combination of louvers and electrical thermal control system is designed to limit diurnal temperature excursions of both sensor modules to $18^{\circ}C \pm 5^{\circ}C$. The electrical systems of both instruments also share near identical designs for power conversion, telemetry, and command circuitry.

Although the instruments share these common designs, they operate completely independent of each other. The instruments simultaneously perform their varied and unique task without compromise to either instrument's performance or data.

The instruments' designs incorporate many features to enhance reliability over previous GOES radiometric instruments: independent Sounder and Imager, redundancy, and no light bulbs. Design life is for over 5 years in orbit.

IMAGER DESCRIPTION

The GOES Imager is a multispectral imaging radiometer that has the following key features:

(1) Improved Sensitivity: The 3 axis body stabilized platform makes it possible for the new Imager to achieve a scan efficiency of approximately 80%. This results in a dwell time approximately 15 times greater than the previous GOES Imager. Consequently NEΔ T's that not only exceed the specifications, but are similar to those of the TIROS AVHRR, are possible. Other techniques such as cold filtering of the IR channels and optimization of detector cutoff wave lengths for each spectral band also contribute to the improvement in sensitivity expected.

(2) Greater Scan Flexibility: The digital scan positioning scanner can rapidly accommodate command to change the field scan. A normal full earth disc scan ($19^{\circ} \times 19^{\circ}$) is accomplished in 28.5 minutes. A priority interrupt could cause the scanner to interrupt this normal operational scenario and go directly to a discrete x, y position within the total scan field to perform a small area scan in a time-efficient manner and then resume its normal operational scenario from the point it left off. A 3000 x 3000 km area can be scanned in 3.1 minutes. A small area 633km x 633km can be scanned in just 20 seconds. This opens the possibility of interleaving frequent observation of mesoscale phemonona with minimum interference to full disc scan timing.

(3) Greater Pointing Accuracy: The present GOES Imager pointing determination is within 20 km on the earth. The GOES-Next Imager is expected to be within 2 km (0.25km design goal). A unique approach and combination of cooperative instrument and spacecraft systems/data make this possible.

Absolute pointing determination is enhanced by the Imager's ability to sense stars. If a separate star tracker were used, its pointing position would not be identical to that of the Imager due to S/C mounting misalignments and variations caused by S/C structural changes in orbit.

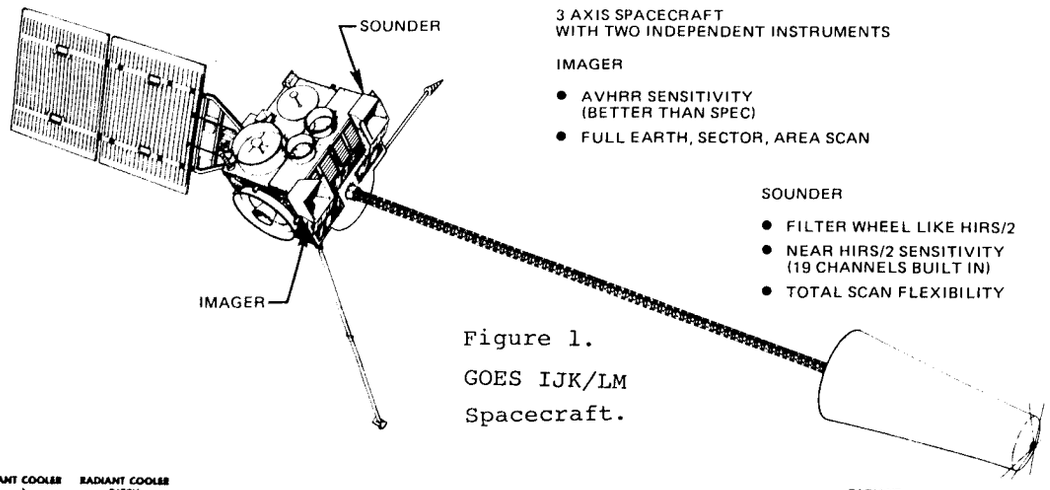

3 AXIS SPACECRAFT
WITH TWO INDEPENDENT INSTRUMENTS

IMAGER

- AVHRR SENSITIVITY (BETTER THAN SPEC)
- FULL EARTH, SECTOR, AREA SCAN

SOUNDER

- FILTER WHEEL LIKE HIRS/2
- NEAR HIRS/2 SENSITIVITY (19 CHANNELS BUILT IN)
- TOTAL SCAN FLEXIBILITY

Figure 1.
GOES IJK/LM
Spacecraft.

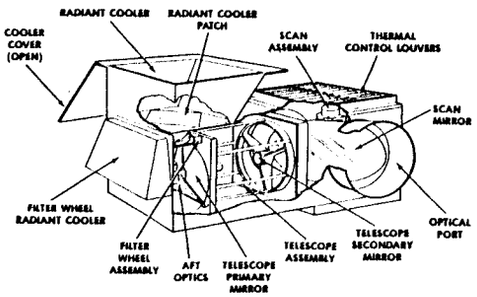

Sounder

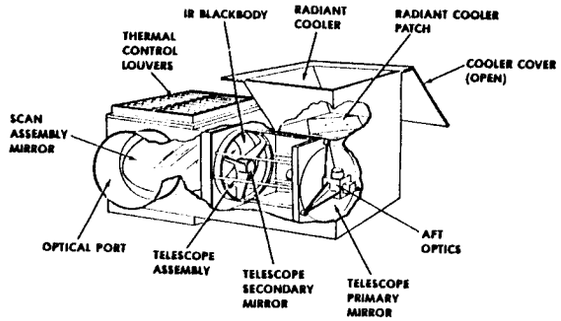

Figure 2.

Imager.

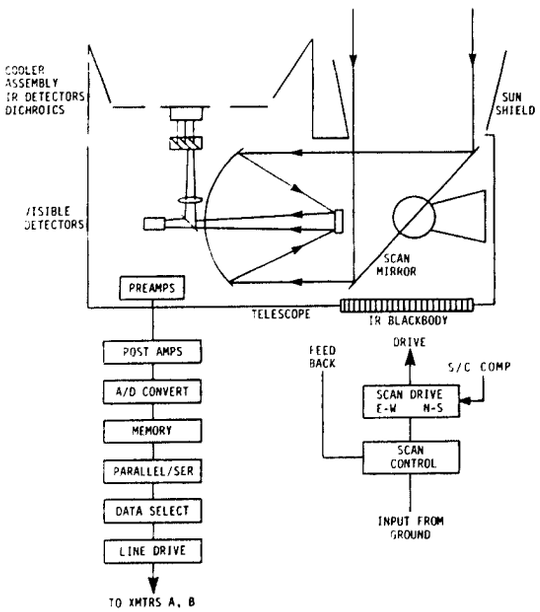

Figure 3. Imager Signal Flow.

Table 1. Imager Sensitivity.

CHANNEL	SPECTRUM (μm)	IGFOV (μr)	NEΔT OR S/N		AT SCENE TEMPERATURE
			SPEC	PLAN	
1	0.55 TO 0.75	28	$\geq$150:1	500:1	100% ALBEDO
2	3.80 TO 4.00	112	$<$1.4K	0.07K	300K
3	6.50 TO 7.00	224	$<$1.0K	0.20K	230K
4	10.20 TO 11.20	112	$<$0.35K	0.08K	300K
5	11.50 TO 12.50	112	$<$0.35K	0.10K	300K

Table 2. Imager Optical Performance.

REGISTRATION AND MODULATION TRANSFER FUNCTION (MTF)

	IFOV (μr)		ALIGNMENT (μr)		SYSTEM MTF (%) NYQUIST FREQ.	
CHANNEL	REQUIREMENT	PLAN	REQUIREMENT	PLAN	REQUIREMENT	PLAN*
1	25.2-28.0	26.6	14	12.3	32	41
2	100.8-112	106.4	14	12.3	22	40
3	168-224	196	14	12.3	22	41
4	84-112	98	14	12.3	22	33
5	84-112	98	14	12.3	22	31

* LISTED MTF ARE FOR DIFFRACTION-LIMITED OPTICS AND INCLUDE ELECTRONICS AND DETECTOR RESPONSES.

(4) Calibration: The Imager utilizes both a space look and an on-board 290 K blackbody to provide a two-point radiometric calibration approximately every 30 minutes. Space clamping to establish a DC reference is accomplished approximately every two minutes.
(5) IR Detector Cooling: A passive radiative cooler is used to cool all IR detectors to 105K.
(6) Signal Quantization: The detector analog electrical signals are amplified, filtered, and 10 bit digitized for all data channels.
(7) Data Rate: The Imager output data rate is 2.232 mega bits per second.

IMAGER SIGNAL FLOW

Figure 3 is a schematic representation of the Imager Sensor/Electronics. Input radiation from the earth scene is reflected from the scan mirror into a telescope. The aft optics split the radiation into five spectral channels. Four of these are infrared channels and one a visible channel. The detectors for the infrared channels are located within the passive radiative cooler. The visible detectors are not cooled and are located on the aft optics subassembly. The detectors convert the scene radiation to electrical signals which go to a pre-amplifier, post amplifier, filters, and to a 10 bit A to D converter. A sample and hold circuit samples all data channels simultaneously prior to digitization. The digitized data is then stored in registers and read serially to the S/C data transmission system.

DETAIL DESCRIPTION

The Imager sensor module is approximately 42.6" long, 18" wide, and 28" high. Its 5 spectral channels are listed in Table 1. The visible channel resolution of 28 microradians is equivalent to an area of one square kilometer at nadir. IR channels 2, 4, and 5 have ground resolutions of 4 square kilometers each and channel 3, the water vapor channel, is eight kilometers.

The detector configuration is shown in Figure 4. The IR detectors are completely redundant as are all of their respective electronics. The visible channel detectors consists of an eight element array located symmetrically about the optic axis. Each scan of the scene with the visible array sweep a swath of eight kilometers. Each IR channel has two detectors for normal operation and two for redundancy. Channel 3 has one active 8km detector and one redundant. All channels sweep a swath of 8 km as the mirror scans East to West or West to East.

The Imager Optical System divides the scene radiation into 5 spectral bands by means of dichroic beamsplitters and registers each spectral channel to each other to permit simultaneous viewing of the scene. Figure 5 schematically describes the Optical System. Windows serve to isolate the passive radiative cooler from the sensor module. The telescope is an F 12.25 Cassegrain with a focal length of 150 inches. The obsuration is 20% (linear) of the clear aperture and the extended field of view at the detectors 1.0 milliradian. Table 2 gives the requirements and planned optical performance for the GOES Imager.

The IR detectors are located on the patch of our radiant cooler shown schematically in Figure 6. The entire cooler is thermally isolated from the rest of the sensor module. A deployable cover protects the cooler prior to, during, and immediately after launch. After approximately two weeks in orbit, the spacecraft outgassing has decreased to a safe level to operate the cooler without contamination and the cover is deployed. When the IR detectors reach 105K the IR channels are operative.

The Imager Scan Subsystem Block diagram, Figure 7, depicts the utilization of an Inductosyn as the servo error generator. When given a digital address, Sin/Cos signals are impressed on the winding of the Inductosyn stators. Induced in the rotor of the inductosyn is a voltage caused by the phase/amplitude difference of the stator windings. This position error has motion compensation and known coherent errors added. It is used to drive a brushless DC motor through a given scan pattern at a fixed E/W rate and in steps N/S. The parameters of this system are shown in the Table 3.

SOUNDER

The Sounder is a nineteen-channel discrete-filter radiometer. Key features of the system design include: 1) high sensitivity for each channel sample permitting high quality soundings from each atmospheric column, 2) a small instantaneous geometric field of view to provide increased capability for clear column sounding, 3) multiple simultaneous samples and a high sampling rate which combine to provide rapid areal coverage and, 4) full aperture blackbody calibration, thermal control, space reference and 13-bit quantization.

The background of the GOES Sounder is that of the HIRS/2, providing distinct correlation of instrument operation and performance. A filter wheel rotating 10 times per second provides for data sampling at 10 steps per second. The filter complement is much like HIRS/2 in the selection of filters, bandwidth and noise equivalent radiance ($NE\Delta N$) requirements. The filter complement, selected by NOAA is intended to improve upon past instruments and the $NE\Delta N$ values are slightly higher than in HIRS as a trade-off for faster sounding coverage. Provision is made in the instrument for increased dwell-time which reduces the $NE\Delta N$ of each area sample at the expense of sounding rate.

SOUNDER CHARACTERISTICS

Characteristics of the GOES Sounder are given in Table 4. The detector and filter arrangement makes use of four spectral bands: longwave, midwave, shortwave and visible. Four detectors are simultaneously irradiated in each band, providing output from four nearly contiguous IGFOV. In this manner, the system can sample four 8km IGFOV each 0.1 seconds. A step of 10km (at nadir) provides for adjacent pixel separation, providing nearly independent atmospheric samples of each column.

The complement of filters and their general characteristics is given in Table 5. In this table we present a filter set which NOAA is reviewing at the time of writing (January). The final set and detailed system performance will be reported as the system is completed.

OPERATIONAL FEATURES

Scan control of the Sounder differs from that of either HIRS or VAS in that a fully-commandable set of coordinates may be directed to the satellite at any time. System design has included as much flexibility as possible to permit selective area and time, provide high location accuracy, and permit increased dwell for sensitivity improvement. The scan system is totally digitally controlled, permitting start and stop locations to be selected for both coordinates. Time selection is provided by a combination of location commands and an execute command. As shown in Figure 8, the scan is basically West-East in 10km steps, dropping 40km at the end of a line and returning East-West, continuing this pattern until the desired frame is completed. Provision is made for stopping at one location, repeating the selected frame, skip-stepping at 20km per step to increase the coverage rate, or increasing the time at each step location from 0.1 seconds to 0.2 seconds.

Location accuracy of the Sounder is aided by internal circuitry which maintains scan location and repeatability to very precise values. In addition, the perturbances of the spacecraft caused by either the Imager or Sounder mirror motion or by rotation or offset of the spacecraft are instantaneously detected and compensated in the scan control unit. This maintains the scanner line-of-sight at the true coordinate at all times. Location calibration of the Sounder is aided by a star sensing capability. Periodic checks of absolute location will confirm the instrument pointing accuracy and permit accurate monitoring of instrument and spacecraft pointing.

Table 4. Key Features of Sounder

Channels	Detector	IGFOV (spec max)	IGFOV (nomimal)
Longwave IR	HgCdTe	224 μrad	215 μrad dia.
Midwave IR	HgCdTe	224	215
Shortwave IR	InSb	224	215
Visible	Silicon	224	215

Detectors per channel	4 (sounding)
FOV Defining Element	Field stop
Telescope Aperture	31.1 cm dia.
Channel Separation	Dichroic
Channel Definition	Interference filters
Radiometric Calib	Space, 290K-IR BB
Freq of Space Clamp	3 minutes
Freq of IR Calib	30 minutes
IR Detector Temp	100K
Field Sampling	4 areas N-S, 10km centers
Scan Step Angle	280 μrad (10km nadir); 560 μrad optional
Step and Dwell Time	0.1 s; (0.2s and 0.4s optional)
Scan Capability	Full earth and space
Sounding Areas	10 km x 40 km to any
Optical Location	Star sensing
Signal Quantizing	13 bits all channels
Output Data Rate	32000 bits per second
System Power Average	74 watts
System Weight:	
Sensor Assembly	120 lb (54.5 kg)
Electronics Module	40 lb (18.2 kg)
Total	160 lb (72.7 kg)

DATA OUTPUT

The Sounder data is provided as a complete set for each 0.1 second sample. Radiometric data from the four IGFOV's, each sampling 19 channels, is sent to the ground in a serial data stream with 13 bit precision. Included with the radiometric data are housekeeping telemetry, reference blackbody temperatures, and location information. Periodic views of space and IR blackbody provide radiometric calibration. Electronic calibration signals provide for monitoring of amplifier and data system quality.

The initial down-link is not for the end user, but goes to the Control and Data Acquisition Station at Wallops Island. This data is checked and tagged with ground coordinates, then merged with the Imager data in a single data format for retransmission. The end user has the raw radiometric data, calibration information, and ground location information for his purposes.

The design of the Sounder is intended to provide the quality, accuracy, flexibility, and independence which will meet the needs of the sounding community for many years to come.

Table 5. SPECTRAL AND SENSITIVITY CHARACTERISTICS (VERSION II)

CHANNEL	CENTRAL WAVENUMBER (CM^{-1})	HALF PWR BW (CM^{-1})	1% ABS BW (CM^{-1})	0.1% ABS X MBW	MAX BR TEMP (K)	NEΔN SPECIFIED	NEΔN DESIRED
LW 1	680 ± 1.8	13 ± 3	40	4.5	255	0.66	0.25
2	696 ± 1.8	13 ± 3	40	4.5	260	0.58	0.25
3	711 ± 1.8	13 ± 2	40	4.5	270	0.54	0.25
4	733 ± 1.8	16 ± 2	40	4.5	290	0.45	0.25
4	736 ± 1.4	9 ± 1	40	4.5	290	0.80	0.25
5	748 ± 1.8	16 ± 3	40	4.5	300	0.44	0.20
6	790 ± 3	30 ± 4	60	4.5	315	0.25	0.15
7	832 ± 4	50 ± 7	120	4	330	0.16	0.06
MW 8	907 ± 5	50 ± 7	150	4.5	335	0.16	0.06
9	1030 ± 3	25 ± 3	70	4	310	0.33	0.12
10	1345 ± 6	55 ± 7	160	4	300	0.16	0.05
11	1425 ± 8	80 ± 9	240	4	285	0.12	0.04
12	1535 ± 6	60 ± 4	150	4	265	0.15	0.04
SW 13	2188 ± 4.4	23 ± 3	60	3.6	310	0.013	0.004
14	2210 ± 3	23 ± 2	60	3.6	295	0.013	0.004
15	2245 ± 4.4	23 ± 3	60	3.6	275	0.013	0.004
16	2420 ± 5	40 ± 5	100	3.6	330	0.0080	0.003
17	2513 ± 5	40 ± 5	100	3.6	335	0.0082	0.003
18	2671 ± 10	100 ± 10	300	3.6	335	0.0036	0.002
VIS 19	14367 ± 220	1000 ± 150	N/A	N/A	N/A	0.105A	0.045A

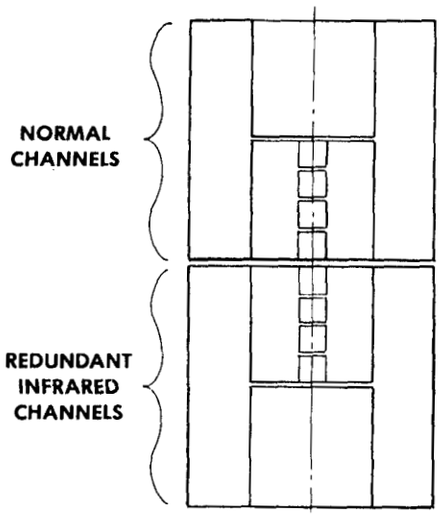

Figure 4. Imager Detector Pattern.

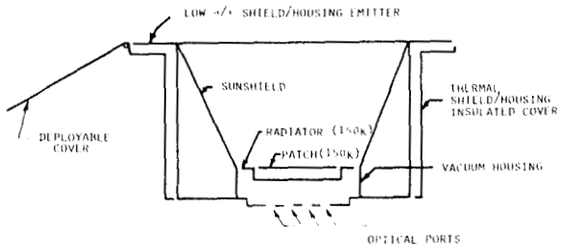

Figure 6. Cooler Parts.

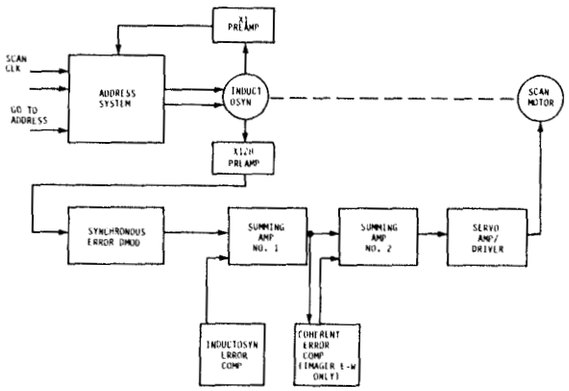

Figure 7. Scan Drive.

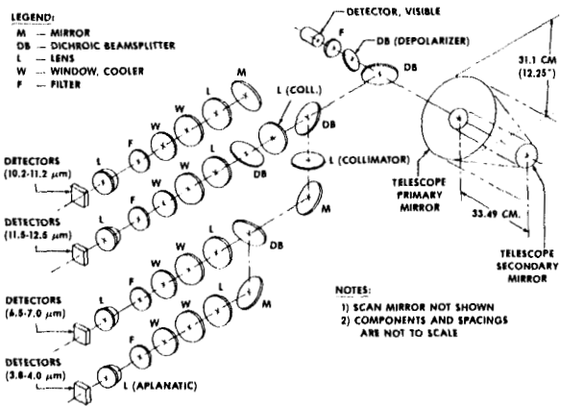

Figure 5. Imager Optics.

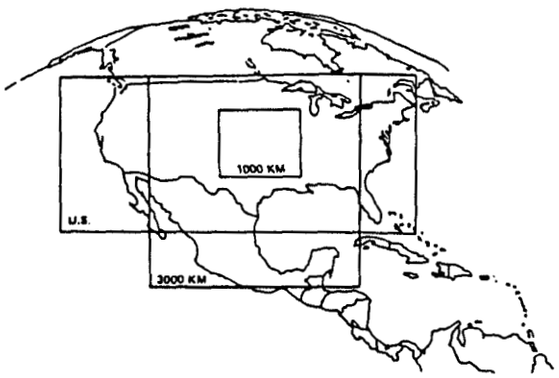

Figure 8. Sounder Scan Frames.

Table 3. Imager Scan Parameters

Parameters
Scan Velocity: 20°/sec (E-W)
Scan Length: 1 to 19° Typ
Frame Height: 1 line to 19° Typ
Turnaround Time 0.2 sec
Scan Step: 224 μ rad
Control Increment: 16 μ rad E-W
8 μ rad N-S
Scan Location Accuracy: 3-5 μ rad

Scan Commands
Start and End Location: X, Y
Frame Repeats: 0-63
Priority Frame, Star Sense

10.7 IDEAS FOR A FUTURE EARTH OBSERVING SYSTEM FROM GEOSYNCHRONOUS ORBIT

William E. Shenk[1], Verner E. Suomi[2], Fritz Von Bun[3], Forrest Hall[1], Wayne Esaias[1], Marvin Maxwell[1]

1. INTRODUCTION

Geosynchronous satellites have made very large contributions towards our knowledge and the prediction of mesoscale and other rapidly evolving meteorological phenomena. However, the observational guidelines published by the scientific community indicate the need for a much greater capability (e.g. The National Storm Program-Storm Central Phase-Preliminary Program Design, 1984; Federal Coordinator for Meteorological Services and Supporting Research, 1983; Envirosat-2000 Report, 1985; Uccellini, 1985).

The geosynchronous platform associated with the Space Station program is a strong possibility for a significant extension of the observation of meteorological phenomena beyond what's planned with the next generation operational geosynchronous satellite in the 1990's and should allow the development of new capabilities for earth survey and oceanography to complement the data from low orbiting satellites. The future Space Station program will make it possible to construct, test, and launch large systems into geosynchronous orbit. It may be possible to economically combine the needs of communications and earth observations into a single large geosynchronous platform.

2. GENERIC PROPERTIES OF SENSING FROM GEOSYNCHRONOUS ORBIT

There are generic properties of viewing from geosynchronous orbit that offer unique advantages for earth observation measurements. First, high temporal resolution can be achieved, which is limited only by instrument design. The high temporal resolution is commensurate with many small scale and rapidly changing phenomena. Any diurnal observation requirement is usually best satisfied with geosynchronous measurements as long as passive measurement techniques can be used. For earth survey and oceanographic surveillance the high temporal resolution is also extremely effective for sharply reducing the cloud interference and unfavorable atmospheric condition problems as well as allowing selectable viewing times and frequencies. The high temporal resolution means that time compositing can be used to minimum cloud/atmospheric effects when lower temporal resolution is needed than the measurement interval. The detection and monitoring of episodic events can be accomplished.

[1]Laboratory for Atmospheres
NASA/Goddard Space Flight Center
Greenbelt, MD 20771

[2]Space Science and Engineering Center
University of Wisconsin
Madison, WI 53706

[3]Office of Space Science and Applications
NASA Headquarters
Washington, DC 20546

Since the temporal resolution can be minutes or hours the anisotropic and/or thermal inertial characteristics of a surface or the atmosphere can be used as independent pieces of information. Measurement consistency checks can be made using data taken on successive views of the same area. High temporal resolution will allow near perfect time and space matching with data from other sources (e.g. low orbiting satellites, radar, radiosondes).

From geosynchronous orbit there is a consistent viewing geometry to any given earth location. Therefore the spatial resolution and the atmospheric slant path do not vary, so excellent interpretations can be made of spatial and temporal gradients. Thus, measurement differences are only caused by actual atmospheric or surface changes rather than being influenced by alterations in how the scene is viewed. The nearly stationary position of the satellite permits sensing dwell times that are only limited by scene coverage requirements for a given temporal resolution assuming a commensurate attitude control system. This is in contrast to sensors on low orbiting spacecraft which are moving at about 8 km/sec. The long sensing dwell times on the geosynchronous platform can be used to improve spatial resolutions to the diffraction limit, to obtain very high signal to noise data, and/or to make high spectral resolution measurements.

Since a large percentage of a hemisphere can be seen at one time from geosynchronous orbit sensors can be designed to provide nearly instantaneous coverage over large areas. One important result of this is that small scale, rapidly changing events (e.g. thunderstorms) can be surveyed quickly enough and their interactions with each other and the surrounding environment can be simultaneously determined.

Calibration difficulties are minimized since the same instrument is usually used for a particular measurement (e.g. cloud growth monitoring) throughout the sequence. On low orbiting satellites two similar sensors are often used for the same task (e.g. the profiling instruments on the NOAA spacecraft).

Stereography is possible if two geosynchronous platforms are located near each other such that there is an overlap in their coverage and the same high resolution imaging instruments are on each spacecraft. Cloud stereography from the GOES satellite has already been successfully demonstrated (Minzner, et al., 1978; Hasler, 1981) and the temperature independent cloud height information is more accurate and has higher spatial resolution than any known radiometric method.

Finally, the geosynchronous satellite can be its own data relay, i.e., it acts as its own communication spacecraft. Thus, the observations

Table 1

Geometric Effects on Observations

Zenith Angle Degrees	Distance from Nadir km	% of Hemisphere	Increase in IFOV along a Great Circle Arc Passing Through Nadir (%)
10	930	1	2
30	2,800	9	15
40	3,800	17	30
50	4,800	27	50
60	5,800	35	100

can be sent directly to any ground stations within the field of view of the satellite for analysis. Also, the data rates are often much lower than for comparable spatial resolution measurements from low orbit since the areas are selectable and often can be scanned at a slower rate. This is especially important for earth survey observations where a two order of magnitude reduction in data rate is very significant because it reduces complexity and cost (e.g., from 100 megabits/sec to 1 megabit/sec).

There are some limitations of the geosynchronous orbit. Complete coverage between 50°N and 50°S with reasonable viewing angles requires 6 geosynchronous satellites. However, the uses of the data at the start of the program are expected to be experimental. Thus, in general, only regional areas or less need to be covered, and therefore the lack of near global coverage is not a serious limitation. Large telescopes and/or antennas are needed since the distance is about 36,000 km to the earth's surface. The Space Station, with the ability to assemble, test, and then deploy to geosynchronous orbit, is important to the success of these large and, therefore, costly instruments. Finally, it is practical to utilize only passive sensing methods due to the great distance to the earth from geosynchronous altitude.

The constant location above the equator gives oblique, but constant, off zenith viewing angles. Table 1 shows how the off zenith viewing angle varies with the distance along the surface between the satellite nadir point and the point being observed, the percentage of a hemisphere that can be observed at that zenith angle or less, and the increase in the Instantaneous Field of View (IFOV) in the direction along a great cicle arc passing through nadir. The increase in the IFOV orthogonal to the arc is small as the zenith angle becomes larger.

3. METEOROLOGICAL UTILIZATION

Geosynchronous satellites are capable of obtaining data over large areas with high spatial, spectral and temporal resolution. Therefore, they are the best satellites for determining meteorological parameters that are associated with events that are small scale and/or change rapidly. These events include severe thunderstorms, other mesoscale convective systems, tropical and extratropical cyclones, frost and freeze situations, fog, and dust storms. Many of the measurements that are taken of these events can be used to detect and predict other localized phenomena, such as orographic effects and lake and sea breezes. The data can be used to initialize regional-scale and mesoscale models. The realism and sophistication of these models is progressing rapidly and by the late 1990's they will require the suggested observations. Some of the measurement requirements for synoptic- and hemisphere-scale meteorological systems and climate (e.g. winds, diurnal cloud changes) are met with geosynchronous satellite data.

Table 2 gives an example of a list of observation guidelines when severe thunderstorms are occurring (modified slightly from Shenk, et al., 1985). Table 2 shows that high horizontal and temporal resolutions are needed. Realistically only a geosynchronous orbit can satisfy the temporal requirements. This set of guidelines is one of the most difficult to satisfy since the significant portions of severe thunderstorms are small scale (~10 km) and evolve very rapidly (~min). When these needs are met many of the requirements for other mesoscale phenomena are also satisfied. There are tables similar to Table 1 for other mesoscale phenomena (GOES-Next Concept Study, 1981). When the observational guidelines are translated into instrument parameter specifications (e.g. spatial resolution, signal to noise, etc.) some of the horizontal and temporal resolution needs become even higher. A good example is the derivation of winds from cloud motion where a less than 1 km sensor horizontal resolution is needed to track small clouds to produce wind estimates on coarser (~20 km) grid scales.

During the 1990's the United States will have the next generation GOES operational satellites in orbit. The meteorological instrumentation will consist of a infrared sensor for measuring atmospheric temperature and moisture profiles and another sensor whose principal functions (besides providing routine images) will be to determine surface temperature, winds from cloud motions, high resolution lower troposphere moisture fields, cloud properties (amount. type, and height) and some precipitation information. In addition, during the 1990's, it is anticipated that some additional research sensors will be flown. These include microwave temperature and moisture profiling and imaging (principally for precipitation), ozone mapping, lightning mapping, and a next generation infrared temperature and moisture profiler to provide higher vertical resolution and accuracy. Thus, what we should consider for earth observation sensors for the Space Station geosynchronous platform should be those that are more advanced than both the operational and expected research instruments mentioned above. Naturally, if these research instruments have not been flown, they could be candidates for the Space Station geosynchronous platform.

Table 2

Severe Local Storm In-Progress
Observational Guidelines

Parameter	Resolution Horizontal (km)	Vertical (km)	Temporal (min)	Absolute Accuracy
Temperature:				
o Surface	5-15		10-30	±1-2°C**
o Profile, General	10-50	1-5*	30-120	±1-2°C**
o Profile, Thunderstorm and Immediate Vicinity	5-25	1-5*	1-10	±1-2°C**
Moisture:				
o Profile, General	10-50	1-5*	30-120	±5-15%RH
o Profile, Thunderstorm and Immediate Vicinity	5-25	1-5*	1-10	±5-15%RH
o Lower Tropospheric Moisture Gradient (e.g., Dry Line)	3-15		5-30	±10-25%RH
Surface Pressure:				
o General	10-50		30-120	0.5-1.0 mb**
o Thunderstorm and Immediate Vicinity	5-25		1-10	0.5-1.0 mb**
Winds:				
o Boundary Layer	5-20	0.2-1	5-30	±1-3m/sec
o Above Boundary Layer	10-50	1-5	15-60	±1-3m/sec
Precipitation:				
o Rate	3-50		3-30	±20-50%
o Type	1-10		1-10	Rain/Hail
o Yes/No	5-50		6-60	
Cloud Top Height	0.5-10	0.25	0.5-15	±250-500m

*Need 0.2 km vertical resolution for inversions
**Relative accuracy is one-half these values

While the expected developments in the GOES Program in the 1990's will result in a major increase in meteorological sensing capabilities there still will remain a number of substantial measuring deficiencies that can only be addressed by another enhancement level of instrumentation. The early generation microwave profiler, using a 4.4 m antenna, will provide temperature profile nadir resolutions in cloudy areas of about 35 km and moisture profile resolutions of approximately 20 km. However, resolutions of 5 km (see Table 2) are needed. Thus, much larger microwave antennas are required. An antenna of about 40 m is required to achieve a resolution of about 4 km if the 118 GHz region is used for temperature profiling. The 183 GHz region is needed for water vapor profiles and the resolution would be around 2 1/2 km. Precipitation mapping requires 1-3 km horizontal resolution to resolve individual convective cores. With high frequency microwave (i.e. 183 GHz) this resolution can be achieved with the 40 m antenna. With 2-3 km resolution, it should be feasible to track small precipitating convective cells over water underneath higher clouds to obtain winds. These could be especially valuable in storms (e.g., tropical cyclones). A 40 m antenna that is designed for high frequency microwave measurements will require assembly and extensive testing in low orbit before deployment to geosynchronous orbit.

Another capability that is needed for the detailed monitoring of strong convective areas (which is the most demanding type of cloud measurement) is high spatial and temporal resolution visible and infrared imaging. The time history of convective growth is related to convection intensity (Adler and Fenn, 1979) and to the subsequent precipitation volume produced by a cell. Infrared resolution of 1 km at 11 μm is required to accurately monitor the vertical rise rates of the cells (Adler, et al., 1983). Achievement of this resolution requires a ≥1 m optical diameter telescope that is diffraction limited. This telescope is also needed for solving another major deficiency area which is the resolutions needed for accurate cloud motion-wind determination (both day and night), to significantly improve surface temperature mapping, and much better general cloud property determination. The pacing horizontal resolutions are 200 m in the visible and 500-1000 m in the 11 μm infrared region that lead to the ≥1 m optical telescope.

The final major deficiency which can be addressed by the data from the platform is inadequate vertical temperature and moisture profile resolution. Even the next generation temperature profilers with $\frac{\Delta\lambda}{\lambda}$ = 0.1% spectral resolution are not expected to completely solve this problem. The best remote sensing instrument

for improving vertical resolution is lidar profiling (1-2 km vertical resoolution) but this is not yet practical from geosynchronous orbit. Therefore, the best approach is the next (and probably ultimate) step in passive profiling beyond the $\frac{\Delta\lambda}{\lambda}$ = 0.1% spectral resolution approach which is to resolve the wings of individual absorption lines with $\frac{\Delta\lambda}{\lambda}$ = 0.01% spectral resolution in the 4.3 μm CO_2 absorption region. Vertical resolutions of 2-3 km in the troposphere are possible (compared to 3-4 km with the $\frac{\Delta\lambda}{\lambda}$ = 0.1% spectral resolution and 5 km with current profilers). As Table 2 shows this will cover about half of the range of the requirement of 1-5 km. Another instrument that will contribute significantly to improving the accuracy of temperature profiling is total ozone mapping which can be used to accurately estimate tropopause height. Passive profile methods have lower accuracy in the tropopause region where there are sharp temperature changes. An independent estimate of the tropopause height from Nimbus 7 total ozone data has been shown to improve the profiles by about 1K in the upper troposphere and lower stratosphere. In addition the ozone data are extremely useful for estimating strong wind gradients associated with the jet stream (Shapiro, et al., 1982: Uccellini, et al., 1985) and in detecting and tracking volcanic eruptions (Krueger, 1983). The upper tropospheric mapping capability is being used in real time during this year's Genesis of Atlantic Lows Experiment (GALE).

Besides reducing the major deficiencies for some of the traditional meteorological parameters, there are some important special measurements that can be made. A sensor that could be used for lightning mapping, trace gas detection and mapping is a small instrument using area arrays of 2000 by 2000 detectors that could provide data with a ground resolution of 5 km. This would provide a field of view of 10,000 km on a side in the spectral region from 200 nm to 1000 nm. The telescope would have a focal length of 200 mm and an aperture of 5 cm. The spectral selection would be done using a filter wheel with filters appropriate to the observation needs.

As time and industrialization progress, the measurement of global pollution becomes more and more important. It is well known that the sky radiation is highly polarized at an angle near 90° from the sun. Aerosols and pollution depolarizes this radiation and thus these sources can be readily identified. In principle it should be possible to trace pollution plumes using this technique.

4. EARTH SURVEY UTILIZATION

The primary utilization of earth survey data from geosynchronous orbit would be for the monitoring of transient or episodic events that are not normally possible to monitor with the repeat cycle of a lower orbiting satellite over a given location. The geosynchronous orbit will also allow the sharp reduction of cloud and atmospheric effects, the use of anisotropic properties and thermal inertia of a scene as additional data sources, and the survey of stress related events whose detection requires flexible viewing times.

A number of important land related vegetation phenomena can be reliably observed only by sensors mounted onboard geosynchronous platforms. Thermal phenomena such as freeze damage and drought-induced canopy temperature elevation often occur for relatively brief periods during the day and can only be monitored by utilizing the finer scales of viewing frequency offered by geosynchronous platforms. This capability also permits monitoring of key vegetation related events which occur during relatively narrow phenological windows of two to three days. Events such as forest infestation by the Gypsy moth during the leaf extension state of deciduous trees, or the effect of high ambient temperatures on crop yields during wheat grain filling or corn pollination are two important examples.

Selectable viewing times permit the observation of drought induced wilting of vegetated canopies which, during the early stages of drought, occurs only during maximum daytime heating in the afternoon. For the remainer of the day, the canopy may appear totally normal. Episodic events such as flooding, fire, and wind driven soil erosion could only be observed given the flexible viewing schedule of the geosynchronous platform.

The continuity of viewing throughout each day also permits the best possible atmospheric conditions to be obtained for surface observations. This is extremely important since absolute radiometry needed for observing a host of vegetation phenomena is difficult if not impossible under many atmospheric conditions encountered with even daily coverage. For the tropics of course, more frequent coverage is needed to obtain minimally cloud free conditions. The geosynchronous platform also provides a unique station from which to acquire multiple sun angle illumination data needed to estimate many of the more intractable biophysical parameters such as biomass, leaf area, etc.

Snow and ice detection can further be improved by using a combination of very high visible resolution and imaging microwave data. The viewing angles are quite satisfactory for snow at midlatitudes and even suitable for detecting ice in lakes and coastal areas probably up to 70° of great circle arc from the subsatellite point. The liquid water content of snow is best measured using microwave. These observations used in conjunction with very high resolution visible imaging, have been quite successful in estimating snow water equivalent if the snow is not over 1 meter deep.

For these land survey observations the primary sensor will be an imaging radiometer with a clear aperture of one to two meters. This could share the same telescope that would be used for meteorology and oceanography. This diffraction limited observing system can provide the excellent signal to noise required for these advanced studies by adjusting the integration time to provide the required signal. The ground resolutions will be a function of wavelength and aperture size and are shown in Table 3 for the various spectral regions covered by the instrument. The nominal field of view for earth surveys will be 500 km wide and as long as desired.

Table 3

Spectral Regions (μm)	Instantaneous Field of View (m) 1 m Aperture	2 m Aperture
0.4 to 1.0	50 - 100	25 - 50
1.0 to 2.4	100 - 200	50 - 100
3.5 to 4.2	400	200
10.5 to 12.5	1000	500

Each of the spectral regions will be divided into a number of different spectral bands. The 40 m microwave antenna mentioned earlier would be suitable for the snow and ice investigations.

5. OCEANOGRAPHIC UTILIZATION

The oceanographic utilization of geosynchronous satellite data will focus on improvements in sea surface temperature measurement and ocean color sensing. The estimation of sea surface temperature can most likely be improved to $\leq$0.5K along with better coverage with the combination of the large high resolution imager mentioned earlier for earth survey and meteorological purposes and the 40 m microwave antenna providing low frequency microwave data.

This accuracy and better coverage could provide tropical oceanographers with a substantial improvement in their ability to monitor and follow events related to the El Nino and Southern Oscillation. One of the primary difficulties in the tropics is the removal of atmospheric and cloud effects, which are intimately tied with evolving ocean temperature fields. With a high resolution capability and a continuous sampling, many of these problems can be overcome.

There are several ocean color features that change with sufficient rapidity to substantially benefit from measurement from geosynchronous orbit. Ocean fronts and eddies, which are important as areas of enhanced fish concentration and for identifying strong current regions, can move a few miles in a day and are more reliably detected from ocean color rather than from thermal signatures. For example, loop currents in the Gulf Stream in the summer become difficult to thermally detect but are distinguishable from color features. They change location sufficiently in a day to require repeated monitoring. Nutrient concentrations near the ocean surface also can change rapidly, especially those associated with upwelling following the passage of a cyclone. Phytoplankton surface concentrations can vary by a factor of 4 over a few hours due to combinations of wind induced mixing and dilution, current motions, migration vertically in the water, and in response to nutrient increases. These processes present biases for once daily observations of phytoplankton abundance from polar platform ocean color sensors which could be accounted for and studied with repeated views from geoplatforms. Estuarine plumes can change dramatically in a few hours caused by tidal advection and changes in the winds. Knowledge of plume location and movement is important for ecology and where sedimentation will occur.

Another significant use of geosynchronous observations which is important not only to global energy balances but also to ocean heat fluxes and studies of marine photosynthesis is the derivation of surface incident radiation in the visible region. These analyses are presently being done with GOES observations for limited regions, and would represent an important continuation of observational capability.

There are constraints to using a geosynchronous orbit for ocean color observations. These arise from the generally very low albedo of the ocean, and therefore the need to account rigorously for atmospheric and surface reflection effects. The primary assumption made in deriving ocean leaving radiance values from satellite observations in the visible is that the ocean has zero reflectivity (is black) in the 700-1000 nm region, and that detected radiances in this interval are due to atmospheric scattering. This provides for a somewhat quantitative atmospheric correction. When the sun-sensor angles are high (resulting in extremely low values of ocean leaving radiance/atmospheric radiance), or when the angles and wind conditions are such that specular surface reflection of sunlight occurs, then both the atmospheric correction (marine aerosol optical depth) and information about water properties become meaningless. These conditions are minimized in polar orbiter instruments by selecting near-noon orbital crossing times and tilting the sensor away from the sun glitter. For a geosynchronous orbit, these effects will restrict the areas of meaningful observations to a variable fraction of the total field of view (on the order of 50%) depending on time of day and season. P. Koepke and H. Quenzel (1979) present a limited analysis of favorable viewing times for viewing aerosols from geosynchronous platforms which also suffices for the ocean color case.

The constraints would not jeopardize use of the observations to follow the short time scale phenomena in general, but would reduce the number of observations in certain regions on a given day. The long integration times enabled by "pointed" geosynchronous instruments is a decided benefit to maximizing the signal/noise ratio for the case of low surface incident light levels and the oceans in general, which requires higher sensitivity and/or quantization than for most land or atmospheric applications.

Ocean visible observations require 10-20 nm spectral resolution for a minimum of 8 channels in the 400-1000 nm region. The signal to noise ratios required are on the order of 300:1. Two or three channels in the thermal infrared are required for Sea Surface Temperature Observations, with calibration and signal to

noise equivalent to an accuracy of 0.1K at 300K. An observation interval of every 30 minutes with about 1 km spatial or near coastal studies, higher spatial resolution (0.2 km) would be useful since the spatial scales of features is smaller than in the open ocean, but many important questions can be addressed with continuous 1 km data which are presently beyond reach with existing capabilities. The same large aperture radiometer that will support the meteorological and land survey investigations can be used.

REFERENCES

Adler, R. F. and D. D. Fenn, 1979: Thunderstorm intensity as determined from satellite data, J. Appl. Meteor., 18, 502-517.

Adler, R. F., M. J. Markus, G. Szejwach, W. E. Shenk, and D. D. Fenn, 1983: Thunderstorm top structure observed by aircraft overflights with an infrared radiometer, J. Clim. & Appl. Meteor., 22, 579-593.

Envirosat-2000 Report (W. J. Hussey, ed.), 1985: NOAA satellite requirements forecast, National Oceanic and Atmospheric Administration, 113p. w/appendices.

Federal Coordinator for Meteorological Services and Supporting Research, 1983: Review of Federal research and data collection programs for improving tropical cyclone forecasting, FCM-R2-1982, 23p. w/appendices.

GOES-Next Concept Study, 1981: A Geostationary Operational Environmental Satellite (GOES)-Next concept study, Goddard Space Flight Center Tech Report 1906, 194p.

Hasler, A. F., 1981: Stereographic observations from geosynchronous satellites: An important new tool for the atmospheric sciences, Bull. Amer. Met. Soc., 22, 194-212.

Koepke, P. and H. Quenzel, 1979: Turbidity of the atmosphere determined from satellite: calculation of optimum viewing geometry, J. Geophys.Res., 84, 7847-7856.

Krueger, A. J., 1983: Sighting of the El Chichon sulfur dioxide clouds with the Nimbus 7 Total Ozone Mapping Spectrometer, Science, 220, 1377-1379.

Minzner, R. A., W. E. Shenk, R. D. Teagle and J. Steranka, 1978: Stereographic cloud heights from imagery of SMS/GOES satellites, Geophys. Res. Lett., 5, 21-24.

The National Storm Program, 1984: STORM-Central phase, preliminary program design, National Center for Atmospheric Research, 147p.

Shapiro, M. A., A. J. Krueger and P. J. Kennedy, 1982: Nowcasting the position and intensity of jet streams using a satellite-borne Total Ozone Mapping Spectrometer, in Nowcasting (K. A. Browning, ed.), Academic Press, 137-148.

Shenk, W. E., R. F. Adler, D. Chesters, J. Susskind and L. Uccellini, 1985: The rationale and suggested approaches for research geosynchronous satellite measurements for severe storms and mesoscale investigations, NASA Tech Memo 86185, Goddard Space Flight Center, Greenbelt, MD, 29p.

Uccellini, L. W., 1985: Observational requirements for the regional scale," Proceedings of the symposium and workshop on global wind measurements, July 29-August 1, 1985, NASA (in press).

Uccellini, L. W., D. Keyser, K. F. Brill and C. H. Wash, 1985: The Presidents' day cyclone of 18-19 February 1979: Influence of upstream trough amplification and associated tropopause folding on rapid cyclogenesis, Mon. Wea. Rev., 113, 962-988.

PASSIVE MICROWAVE RADIOMETER EXPERIMENT FOR GOES-NEXT

Thomas H. Vonder Haar

Colorado State University
Fort Collins, CO 80523

William E. Shenk

NASA/Goddard Space Flight Center
Greenbelt, MD 20771

Donald W. Graul

Ford Aerospace and Communications Corp.
Palo Alto, CA 94303

1. INTRODUCTION

NASA and NOAA have selected a new three-axis stabilized satellite as GOES-NEXT. It will be launched from the space shuttle and carry separate visible/infrared imaging and multi-channel infrared sounding instruments. This primary geostationary satellite for weather and climate purposes in the early 1990s is shown on the cover of this Preprint Volume. The instruments are improved versions of the AVHRR which has been successfully flown on a number of NOAA and INSAT satellites.

The Passive Microwave Radiometer (PMR) is a scientific experiment under consideration for flight on at least one of the new GOES spacecraft. It is shown in Figure 1 as the large 4.4 m primary reflector added to the basic GOES-NEXT (or GOES-I, J, K). Presently, a number of parallel scientific and engineering studies are required to refine the PMR experiment. Early results will be presented during the oral presentation at the conference.

2. SCIENTIFIC OBJECTIVES

PMR experiment objectives are to use a geostationary platform for the first time to obtain passive microwave imagery and soundings in a high time frequency mode to address several key scientific objectives. The scientific objectives, drawn from a concensus of U.S. scientists as defined in major national research programs and priorities, address present-day problems of atmospheric science at the mesoscale and in climate research.

New studies of developing mesoscale systems, isolated or intermeshed with larger scales of storms, will be possible by combining two aspects of the PMR:

a) high time frequency imaging ($\Delta t < 10$ minutes) over a 500 x 500 km sector and high time frequency temperature and moisture sounding ($\Delta t \sim 30$ minutes) over a 1000 x 1000 km sector, and

b) the ability to penetrate the extensive non-precipitating cloud masses which obscure important baroclinic development and intensification from observation by infrared sounding instruments.

Thus, the <u>first scientific objective</u> of PMR is to study the onset and early development stages of precipitating weather systems, including mesoscale convective systems (MCS's), extratropical storms and tropical storms.

Figure 2 is a schematic depiction of <u>severe storm</u> outbreak antecedent conditions. The clouds normally found within the warm sector of such a system severely limit the information on local thermodynamics and stability that can be obtained by present-day infrared sounders. Thus, scientists are limited to detailed diagnostic study of only those few such conditions that have been 'captured' by expensive ground networks launching serial rawinsondes. PMR will vastly enlarge our scientific data base on the four-dimensional structure of the atmosphere during severe storm antecedent conditions. Researchers using both conventional diagnostic and numerical model approaches will use the PMR results.

Another target for PMR-related research is the <u>Mesoscale Convective Complex</u> (MCC) which brings large amounts of precipitation to portions of the United States during the warmer seasons. Figure 3 is an infrared image showing the extensive middle and upper cloud cover from a MCC over the entire Mississippi Valley and

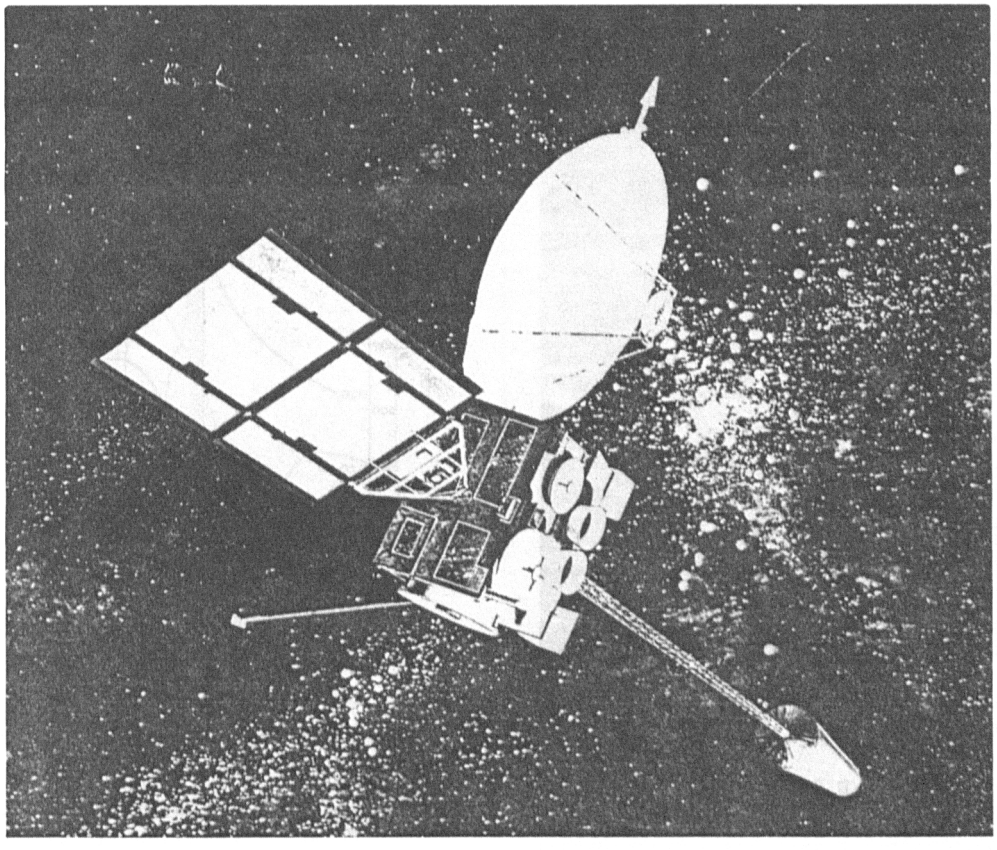

Fig. 1. Artist's conception of the PMR on a GOES satellite.

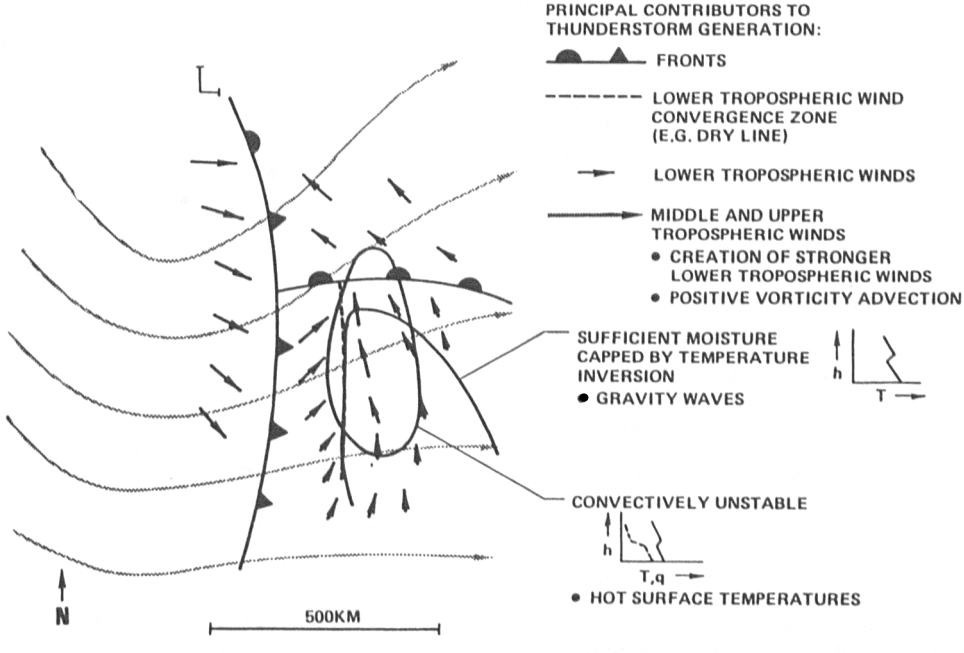

Fig. 2. Classic severe local storm outbreak antecedent conditions.

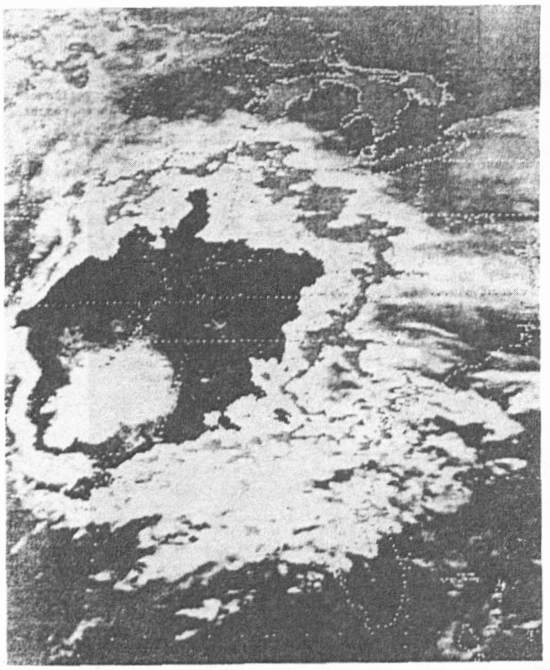

Fig. 3. Infrared GOES images of an MCC centered over Mississippi.

most of southeastern U.S. Figure 4 (from Maddox, 1981) shows a composite east-west cross section through an MCC with early scientific estimates of the associated temperature and moisture anomalies at the meso/synoptic scale. The PMR experiment will penetrate much of the cloud cover and allow measurement of these temperature and moisture anomalies. Previously, atmospheric scientists would rely only upon expensive research aircraft (in limited supply) to measure internal thermodynamic structures of MCC's.

As noted in the following section, the PMR imager will also be designed to measure the relative occurrence of precipitation. Thus, another scientific objective of PMR data is to complement ground-based radar and other measurements to allow a new, time-dependent view of the precipitation patterns in the MCC's, the extratropical storms and tropical storms.

The PMR experiment will address two special climate research objectives. Flying in a geostationary orbit in view of the United States, the PMR will be ideally located to study the variations of regional climate south and southwest of the U.S. Thus, it will greatly enhance our climate-related observations of the El Nino regions and the tropical convergence zones of the Western Hemisphere.

As a primary climate objective, PMR data will provide both a new precipitation index and much improved measurements of the largescale eddy flux of moisture between the tropics and midlatitudes in our region. There is mounting evidence that such tropical-midlatitude exchange processes are a key to skillful long range forecasts. The PMR experiment will measure and monitor these largescale eddy exchange

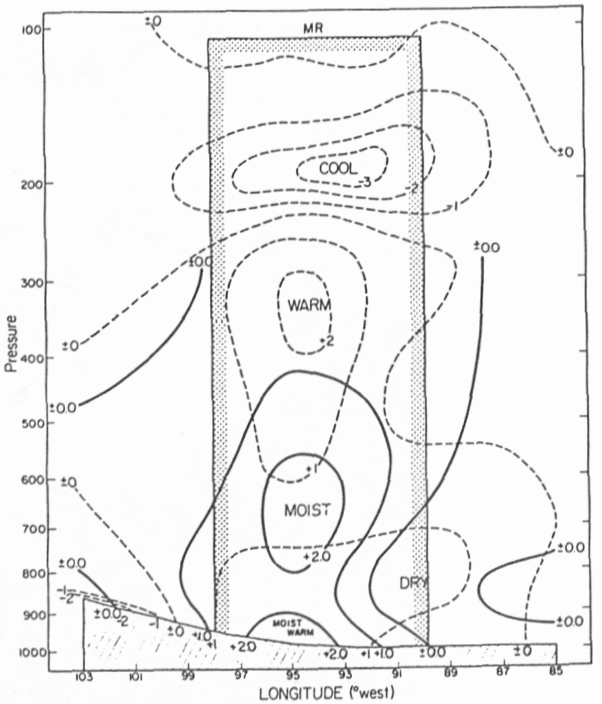

Fig. 4. Composite west to east cross section of midwestern MCCs

Temperature Anomalies (^{o}C) - Dashed Lines
Moisture Anomalies (g/kg) - Solid Lines

processes. Today, most of them are missed by our very inadequate rawinsonde network south and southwest of the U.S.

A second climate objective is to assist with international research on the variability of clouds. At present, our cloud detection methods applied to the cloud/radiation/climate feedback problem have only used infrared and visible measurements. Largescale cirrus clouds, especially at low latitudes, sometimes cover active precipitation regions, but sometimes they do not. The addition of PMR data for cloud climatology purposes will remove this ambiguity over the Western Hemisphere.

3. THE PMR INSTRUMENTATION

As a Passive Microwave Radiometer, PMR has options for channels across much of the spectrum shown in Figure 5. However, preliminary engineering/science tradeoffs have already begun to focus the likely channels to those in the millimeter wave regions (e.g. 30 GHZ to 300 GHZ). A firm boundary condition is imposed by the maximum size of a pre-structured antenna (primary reflector) which may be carried in the shuttle bay. Thus, the primary is 4.4 meters.

Several engineering options are under study regarding the configuration of the anteanna/receiver. In general, the GOES PMR consists of a receiver connected to a narrow beam, high gain antenna that may be pointed at any spot on earth, i.e. an 18° coverage cone. A

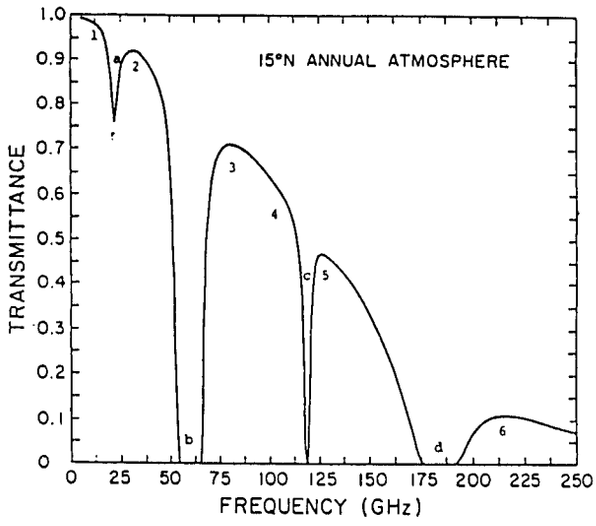

	WINDOWS f(GHz)	(cm)		ABSORPTION BANDS f(GHz)	(cm)	Gas
1	19.35	1.55	a	22.235	1.35	H_2O
2	37.0	.81	b	60.0	.5	O_2
3	89.5	.335	c	118.75	.25	O_2
4	100.0	.3	d	183.0	.164	H_2O
5	130.0	.23				
6	231.0	.13				

Fig. 5. Transmittance of the 15° N annual atmosphere

scan mechanism allows a matrix of 'spots' to be scanned to compose a scan frame or region as defined in Table 1. At an interval (e.g. 90 minutes) chosen to fit the GOES-NEXT spacecraft operation sequence, the primary reflector would be slewed (if desired) to another scan region.

The PMR or antenna electromagnetic specifications in the initial study are shown in Table 2. Five data channel frequencies are shown to allow sounding near H_2O and O_2 bands, as well as views in 'window' regions. Note that these specifications are under study and some (e.g. beam efficiency) may change in the final instrument design. Ground resolution, an important aspect of scientific data use, will range from about 35 km at the low to 15 km at the higher frequencies. Together with the time resolution (rescan time) shown in Table 1, this relatively high spatial resolution allows PMR to fully meet its science objectives.

4. IMPACT ON SPACECRAFT OPERATIONS

As a candidate experiment for GOES-NEXT, the PMR must meet its scientific objectives without interfering with normal operational use of GOES-NEXT. Preliminary studies show that while PMR makes good advantage of the 3-axis stabilization and concurrent visible and infrared measurements from GOES-NEXT, it will not perturb the normal operations. Indeed, it is planned to operate completely independent of the GOES imager and sounder. For example, the two other instruments could be focused upon storms over the U.S. while PMR viewed a growing hurricane in the tropics.

Table 1. Antenna Pointing Specifications

Scan frame	1000 x 1000 Km (and 500 x 500 Km)
Frame scan time	30 minutes (and 6 minutes)
Angular range	10° off earth center
Slew time	1 minute
Pointing error	0.01° absolute
Pointing error	0.003° line-to-line

Table 2. Antenna Electromagnetic Specifications

Frequencies	92, 118, 150, 183, 230 GHz
Polarization	Linear
Coverage	Highest gain pencil beam
Beam efficiency	85% minimum
Calibration	Cold and hot references
Diameter	4.40 meters
Weight	90 kilograms maximum
Surface tolerance	± 0.0017 inch rms
Beam width	0.03 degrees at 183 GHz

Extensive PMR/spacecraft interface studies will allow refinement of the PMR experiment plan and assure compatibility with the GOES-NEXT mission.

5. SUMMARY

We have described a new timely Passive Microwave Radiometer (PMR) experiment for GOES-NEXT. Hopefully, it will be in orbit in the early 1990's. The PMR, a multi-channel microwave radiometer, will allow new measurements of temperature and moisture structure and the presence of precipitation by penetrating much of the overlying cloud cover near significant weather systems. The PMR experiment has specific scientific objectives for mesoscale weather studies and for climate change.

Exciting new results from high frequency microwave radiometers flown on the NASA research aircraft (e.g. Wilheit, et al., 1982), from early satellites (e.g. Kidder, et al., 1978), and from today's operational sun-synchronous satellite (e.g. Purdom, et al., 1986) give strong evidence that the PMR experiment will be successful.

6. ACKNOWLEDGEMENTS

The authors thank the many scientists and engineers whose work has aided the conceptual design and preliminary definition of the GOES-PMR. We acknowledge support from our respective institutions in preparation of this paper. METSAT, Inc. provided additional staff support.

7. REFERENCES

Kidder, S. Q., W. M. Gray, and T. H. Vonder Haar, 1978: Estimating tropical cyclone central pressure and outer winds from satellite microwave data. Mon. Wea. Rev., 106, 1458-1464.

Maddox, R. A., 1981: The structure and life-cycle of midlatitude mesoscale convective complexes. Atmos. Sci. Paper No. 336 and Ph.D. Dissertation, Colorado State University, Fort Collins, CO, 311 p.

Purdom, J. F. W., D. W. Hillger, T. H. Vonder Haar, C. A. Johnson, D. A. Lubich, and P. Laybe, 1986: Development of mesoscale forecast products from satellite microwave sounding data. Preprints, Second Conf. Satellite Meteorology/Remote Sensing and Applications, May 12-16, 1986, Williamsburg, VA. Amer. Meteor. Soc.

Wilheit, T. T., A. T. C. Chang, J. L. King, E. B. Rodgers, R. A. Nieman, B. M. Krupp, A. S. Milman, J. S. Stratigos, and H. Siddalingaiah, 1982: Microwave radiometric observations near 19, 35, 92, and 183 GHz of precipitation in tropical storm Cora. J. Cli. Appl. Meteor., 21, 1137-1145.

ON THE ESTIMATION OF ANTECEDENT PRECIPITATION INDEX FROM REMOTE SENSING MEASUREMENTS

Alberto L. Flores

Departamento de Meteorología - Facultad de Ciencias Exactas y Naturales
Universidad de Buenos Aires
Buenos Aires, República Argentina

1. INTRODUCTION

The evaporation phenomenon in the natural surface environment is one of the main phases of the hydrological cycle. Water entering the evaporation phase comes from free water surfaces or from land surfaces totally or partially covered by vegetation. These components are still among the less understood aspects of the evaporation process, and it is still rather difficult to estimate quantitative values on a regional basis.

On land surfaces the soil moisture content of the upper layer is important in hydrology for partitioning rainfall into its runoff and infiltration components; while in meteorology, soil moisture determines the partitioning of net radiation into latent and sensible heat components. Thus, in order to get a reasonably good estimate of the evaporation, at least regionally, soil moisture should be known.

There are different methods for soil moisture determination (Schmugge et al, 1980). In this paper the remote sensing approach was used (Carlson et al., 1984; Flores and Carlson, 1985).

The soil moisture is closely related to ground temperature measurements from satellites, as was shown by Carlson et al. (1981) and Wetzel et al. (1984).

In assesing soil moisture amounts a parameter called Antecedent Precipitation Index has been used (Saxton and Lenz, 1967; Choudhury and Blanchard, 1983; Wetzel and Atlas, 1981).

In this paper a relationship between soil moisture availability and an Antecedent Precipitation Index is presented over a region located in Argentina, looking for an optimization of the precipitation estimation for short periods e. g., 10 - 30 days) with the ultimate goal: evaluation of evaporation in a near future.

2. THE METHOD

The soil moisture availability (M) is obtained from its relationship with the diurnal range of surface temperature. M is the one used by Manabe et al. (1969), defined by Budyko (1956) and its validity analized by Nappo (1975).

The steps of the method are:

a) simulation of diurnal temperature from a one dimensional boundary layer model,
b) repeat a) changing only one initialization variable of the model several times, being M precisely that variable (actually M and the thermal inertia; for further discussion see Carlson (1985)),
c) prepare a look-up table or a quadratic - regression equation of M on a pair of temperatures (T_1 , T_2) from the ones generated by the model. This pair should characterize the shape of the diurnal range of surface temperatures (see Polansky, 1982);
d) relate real (T_1 , T_2) values (e.g.: measured from satellite) with M through the solution obtained in c).

Up to this point M values were obtained but a ground truth value is required. This value is obtained from the Antecedent Precipitation Index (API) for the region:

$$API_i = API_{i-1} \; K + P_i$$

where API_i is the index value for the i-day, API_{i-1} the same for the i-1 day, K a recession coefficient and P_i the total i-day precipitation. Note that the i-day is a non-precipitating day. The next step is to intend a correlation between M and API. API should be representative of the previous rainfall if at least a period of two months is considered, but with some dependence on the recession coefficient value adopted (Saxton and Lenz, 1967).

In the way explained, a relationship between M and API for one day will be obtained. If two separate days are chosen, then a correlation and regression analysis could be performed for a several days period, as Flores and Carlson (1985) did for a region located in USA.

3. THE MODEL

The one dimensional planetary boundary layer model used is an updated version of the one used by Carlson et al. (1984) and Flores and Carlson (1985). A surface energy balance equation

is used at the ground-air interface, with fluxes of momentum, sensible and latent heat exchange through a surface transition layer, a turbulent surface layer and a convective mixing layer in the atmosphere. A diffusive heat flux was used in a substrate layer. The model is no stationary and vegetation is not parameterized.

The moisture availability appears in the heat flux equation,

$$L_e E_o = \frac{L_e (q_{os}(T_o) - q_a)}{R_a + R_{cv}} M$$

where the specific humiditiy difference refers to a saturated surface (subscrip zero) and the top of the surface layer (subscript a). R_a and R_{cv} refers respectively, to the eddy conduction resistance for moisture flux in the atmospheric surface layer and the resistance for the transition layer, which is envisioned to be a narrow region over which a combination of eddy, molecular and radiative fluxes coexist in some fashion (Carlson, 1985). L_e is the vaporization heat for water.

4. TARGET REGION AND DATA

The region was located over Argentina´s central part and runs east-west between 34°S and 39°S and its area covers approximately 800.000 square kilometers (Fig. 1), finally reduced to about 600.000 square kilometers due to the image processor procedures.

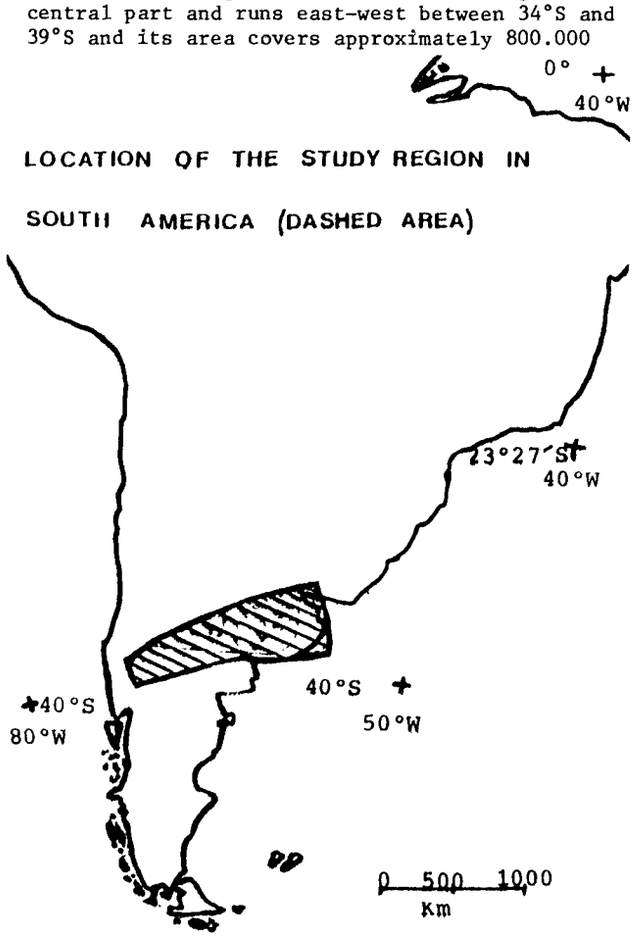

Figure 1

The analysis were performed for two days December 24, 1981 and January 18, 1982. The criteria for dates selection were: a) summer season and b) two cloud free days not separated more than a month or less than a week.

Infrared imagery from SMS/GOES east satellite was used to determine surface temperatures over the area. For each day two images were used: 12 GMT and 17 GMT. They were considered the best times to be used in order to get M field from thermal infrared (Polansky, 1982; Wetzel and Atlas, 1983). Four images partially overlapped were used to cover the area (depicted in Figs. 2 and 3). The infrared and visible images were supplied by the National Oceanic and Atmospheric Administration. The water vapor attenuation was corrected using a radiative transfer model provided by J. Price (see Carlson et al., 1984). All the image processing and modelling work was performed at The Pennsylvania State University on the Department of Meteorology´s computer facilities.

The model requires local initialization data. Four rawinsonde stations were used and daily synoptic charts. The substrate temperature was a climatological for the central part of the region.

The selection of the target area was based in the annual precipitation gradient from east to west. In the average it goes from 1000 mm (east) to 200 mm (west). The terrain is flat: from sea level in the east to less than 300 m in the west. Neither drought nor excess rainfall conditions existed in the region at that time. The area consists mainly of unirrigated rangeland and cropland.

The daily rainfall data were computed to obtain the API values; the beginning day was September 1, 1981. Seventy-one raingage stations were used, depicted as dots in Figs 2 and 3. The recession coefficient used for API was 0,92 chosen arbitrarily from literature (Saxton and Lenz, 1967; Choudhury et al., 1982) and kept constant for the region.

5. ANALYSIS AND RESULTS

M and API fields for the two dates were analized (not shown). The M and API fields difference between the days chosen (ΔM and ΔAPI) was analized (Figs. 2 and 3). Δ API values are in milimeters of precipitation. Visual inspection of the figures show a general agreement between them.

A correlation analysis was carried out using an overlapping 10 x 26 grid to obtain the pairs of values. The correlation coefficient (r) was 0,54. To improve this value a subregion with maximum M gradient was chosen. It was located in the central and upper central part of the area (Fig. 2). In this way, with only 54 values the r value was 0,81.

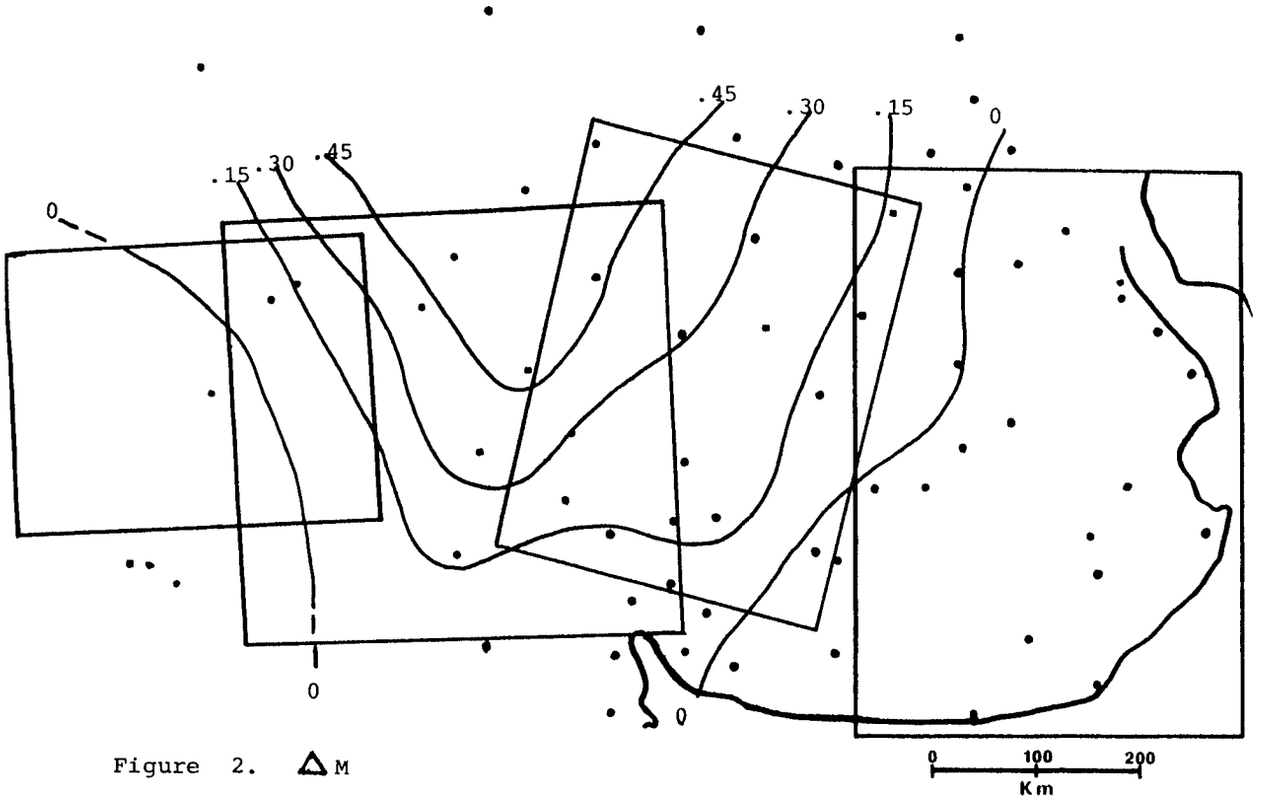

Figure 2. ΔM

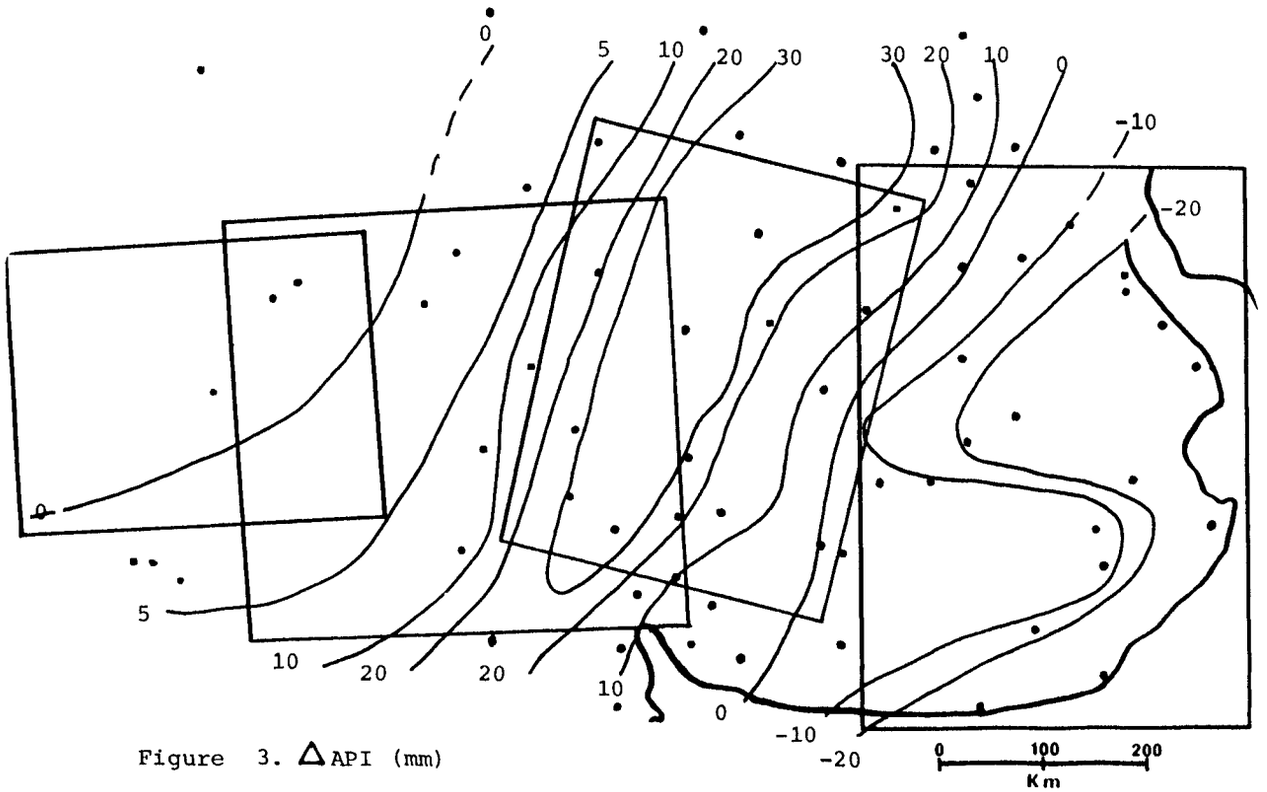

Figure 3. ΔAPI (mm)

A linear regression analysis was intended because no other relationship was suggested after a visual inspection on a ΔAPI vs ΔM dispersion diagram (not shown). M range for the sample was 0.45 while Δ API range was 80. The relationship was

$$\Delta \text{API(mm)} = -15 + 121 \Delta \text{M}$$

According to the t-ratios, the ordinate to origin and slope are significant (above 2.0) for the sample size (Davies, 1973). The correlation coefficient was also tested according to Fisher's "z" transformation (Brooks, 1953) and it is significant because it could be exceeded by a sample taken at random less than once in 100 samples. The -15 value indicates the rainfall needed for the region to keep ΔM zero for the period considered.

6. CONCLUSIONS

The analysis of a new source for soil moisture determination was applied for first time in South America. The approximations used could be improved. For example, the GOES pixels size (about 60-70 square kilometers) compared with the raingages network (about one per 9000 square kilometers) were far too small; a subregion with a higher density network should be used. The value of the recession coefficient should correspond to the different sections of the target area because there is an east-west change in soil and climate regime. For each image single radiosonde data were used to initialize the model and this could be improved too .

The model will be improved with the inclusion of vegetation, needed specially in the eastern half of the target area.

Within the time and space scale used, the possibilities of the method should be analyzed in depth because the results shown are significant in a region with sparse data.

7. REFERENCES

Brooks, C. E. and N. Carruthers, 1953: Handbook of Statistical Methods in Meteorology. H. M. S. Office, London.

Budyko, M. I., 1956: The heat balance of the earth's surface. Leningrad. Translation by U. S. Dept. of Commerce, Weather Bureau, 1958, Washington, D.C.

Carlson, T. N., 1985: Regional-scale estimates of surface moisture availability and thermal inertia using remote thermal measurements. Remote Sensing Rev., Vol. 1, 197-247.

-----, J. K. Dodd, S. G. Benjamin and J. N. Cooper, 1981: Remote estimation of surface energy balance, moisture availability and thermal inertia. J. Appl. Meteor., 20, 67-87.

-----, F. G. Rose and E. M. Perry, 1984: Regional-scale estimates of surface moisture availability from GOES infrared satellite measurements. Agron. Journal, 76, 972-979.

Choudhury, B. J. and B. J. Blanchard, 1983: Simulating soil water recession coefficients for agricultural watersheds. Water Resour. Bull. 19, No 2.

-----, ----- and C. M. Richardson, 1982: A simulation study of the recession coefficient for antecedent precipitation index. International Symp. on Hydrometeorology. American Water Resources Association, 69-71.

Davies, J. C., 1973: Statistics and data analysis in geology. John Wiley & Sons, New York.

Flores, A. L. and T. N. Carlson, 1985: Acerca de la estimacion de la disponibilidad de humedad en el suelo a partir de mediciones remotas. GEOACTA, Vol. 13.

Manabe, S., 1969: Climate and Ocean Circulation, I, The atmospheric circulation and the hydrology of the earth's surface. Mon. Wea. Rev., Vol. 97, 739-774.

Nappo, J. C., 1975: Parameterization of surface moisture and evaporation rate in a planetary boundary layer model. J. Appl. Meteor., Vol. 14, No 3.

Polansky, A. C., 1982: A method for diagnosing surface parameters using geostationary satellite imagery and boundary layer model. M. S. Thesis, Department of Meteorology, The Pennsylvania State University.

Saxton, K. E. and A. T. Lenz, 1967: Antecedent retention indices predict soil moisture. J. of the Hydraulics Div. Proceedings of the Amer. Society of Civil Engineers.

Schmugge, T. J. , T. J. Jackson and H. L. McKim: Survey of methods for soil moisture determination. Water Resour. Res., 16, 961-969.

Wetzel, P. J. and D. Atlas, 1981: Inference of precipitation through thermal infrared measurements of soil moisture. In D. Atlas and O. W. Thiele (ed.) Precipitation Measurements from Space Workshop Report. Goddard Laboratory for Atmospheric Sciences, Greenbelt, MD. Vol. 23.

----- and -----, 1983: Inference of soil moisture from geosynchronous satellite infrared observations. Proceedings of the AMS Conference on Agriculture and Forest Meteorology, Ft. Collins CO, April 1983, 178-181.

-----, ----- and R. Woodward, 1984: Determining soil moisture from geosynchronous satellite infrared data: A feasibility study. J. Clim. Appl. Meteor., 23, 375-391.

P4.38

ASSESSMENT OF MEASUREMENT ERROR DUE TO SAMPLING PERSPECTIVE IN THE SPACE-BASED DOPPLER LIDAR WIND PROFILER

S. H. Houston and G. D. Emmitt

Simpson Weather Associates, Inc.
Charlottesville, Virginia

1.0 INTRODUCTION

Simulation experiments for a space-based Doppler lidar wind profiler are being conducted to develop optimum wind vector computation algorithms. These algorithms must deal with measurement errors that are unique to this application of Doppler lidars. One error component arises from using a small number of independent radial wind observations distributed over large areas such that each observation has a different perspective on a wind field that may be characterized by large spatial and temporal variations. This error is largest along the satellite ground track and at the edges of the lidar scan domain.

In the assessment presented here idealized wind fields are used as inputs to the Doppler lidar wind profiling model. The radial wind estimates output by this model are passed through the Multi-Pair Algorithm (MPA) to yield a wind measurement for 300 x 300 km^2 areas (Emmitt, 1985). The derived divergence fields have been chosen to demonstrate the gradient patterns that are peculiar to the Doppler lidar sampling strategy and perspective.

2.0 RESULTS

The conical scan pattern used in our model of the Doppler lidar wind profiler is presented in Figure 1. Radial winds are computed for each lidar "shot" using an input wind field. Figure 2 shows an example of the wind vectors for a control wind field averaged over 300 x 300 km^2 boxes in the left half of the lidar scan domain. This control wind field is an idealized flow where $\partial u/\partial x = \partial v/\partial y = 10^{-6}$ sec^{-1} giving divergence values equal to 2.0 x 10^{-6} sec^{-1} for the field of wind vectors in Figure 2.

The MPA calculates wind vectors using each pair of radial wind estimates derived from the lidar wind profiler model in a scheme which incorporates the product of the spatial and angular separation weighting functions. The spatial separation weighting function gives higher weights to those pairs of radial wind estimates separated by the smallest distance, so the influence of gradients will be minimized. Since the optimum separation angle

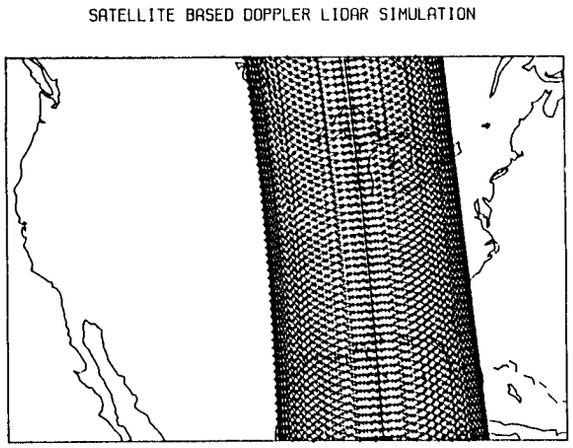

Fig. 1. Example of conical scan pattern for a polar orbiting space-based Doppler lidar wind profiler as it passes over the eastern U.S. The satellite height is 800 km, velocity is 7.5 km sec^{-1}, scan angle = 45°, PRF = 8 sec^{-1}, revolution rate = 10^{-1} sec^{-1}, and modulation amplitude = 0.33 (modulation amplitude is a function which controls the rate of rotation so that shot pair separation is optimized.)

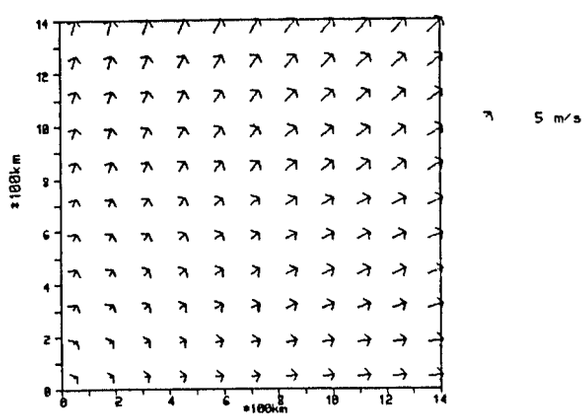

Fig. 2. Mean wind vectors on a 100 km grid where each vector is an estimate for a 300 x 300 km^2 box. The wind field used to produce these averaged winds has u_o = 1.0 m s^{-1}, v_o = 0.0 m s^{-1}, $\partial u/\partial x = \partial v/\partial y = 10^{-6}$ sec^{-1}.

between two radial wind estimates is 90°, the angular separation weighting function assigns lower weights as the angular separation values deviate further from 90°. Operating on the wind field in Figure 2 the Doppler lidar wind profiler model produces the vectors shown in Figure 3.

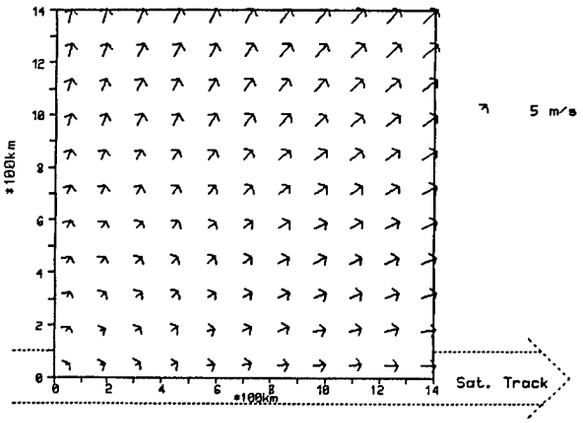

Fig. 3. Using the input wind field shown in Figure 2, the Doppler lidar profiler model produces estimates of the lidar winds for 300 x 300 km^2 areas. Note the satellite track location is along the lower edge of the larger 1400 x 1400 km^2 display domain.

In the vector format the MPA Doppler lidar wind estimates in Figure 3 appear to be in very good agreement with those shown in Figure 2. However, when divergence values are computed, the effects of sampling perspective become apparent (Figure 4). The error is greater than 25% for small areas near the satellite track and at the outer edges of the scan domain. The divergence values are very close to 2.0 x 10^{-6} sec^{-1} in the larger area of the domain between the inner and outer samples.

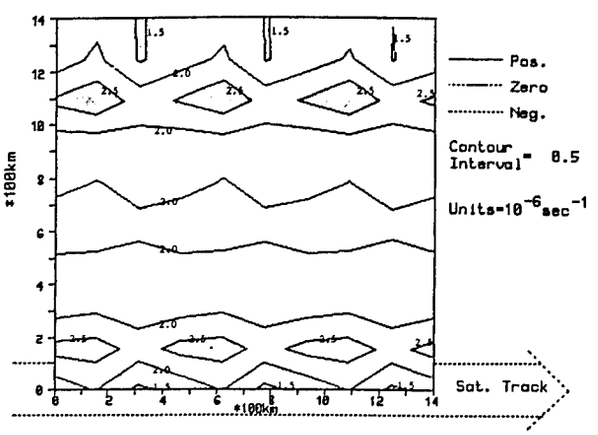

Fig. 4. Divergence field calculated for the Doppler lidar wind estimates in Figure 3. The contour interval is 0.5 x 10^{-6} sec^{-1}. The shaded areas indicate deviations of divergence from 2.0 x 10^{-6} (i.e. the input divergence for the wind in Figure 2) that are greater than 25%.

To further study the sampling perspective error, random fluctuations due to system noise and atmospheric turbulence having a Gaussian distribution are incorporated into the wind field. The resulting MPA Doppler lidar winds in Figure 5 again appear to be in very close agreement with the input winds of Figure 2. Figure 6 shows the divergence for the wind field with random fluctuations. There are some divergence errors greater than 50%, but these are again located in the outer regions of the scan domain. As before there are errors of greater than 25% close to the satellite track, but even with random noise added, the larger central region of the domain has a divergence value very close to 2.0 x 10^{-6} sec^{-1}.

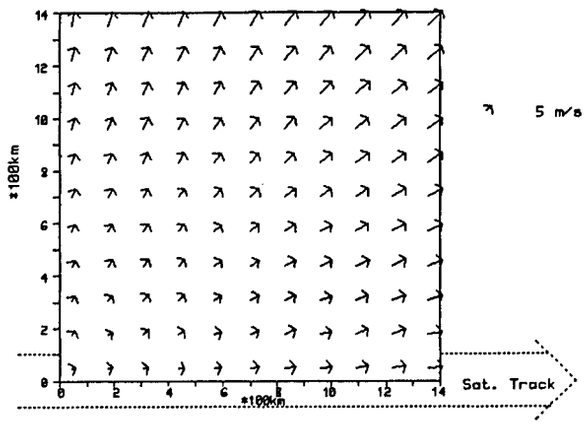

Fig. 5. MPA Doppler lidar wind profiler wind vectors with random fluctuations added to the input wind field for Figure 2. The random fluctuations are a Guassian distribution with $\sigma_u = \sigma_v = 0.15$ m s^{-1}, $\sigma_w = 0.05$ m s^{-1}, $\sigma_{system\ noise} = 0.35$ m s^{-1}.

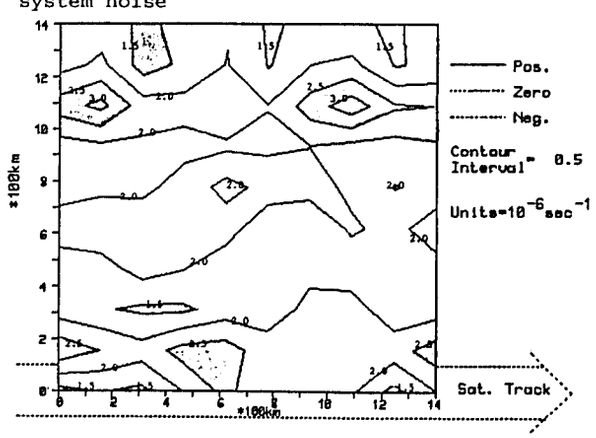

Fig. 6. Divergence field for simulated winds in Figure 5.

3.0 CONCLUSIONS

There is a sampling error in the simulated Doppler lidar wind profiler measurements due to angular and spatial separation between shots in a "shot pair." An algorithm has been developed to minimize the contribution of this error to the total measurement uncertainty. The multi-pair algorithm is a prototype and is continuously being reevaluated. Using model input winds such as those from the AVEVAS II

LAMPS model and the ECMWF "nature" run, a quantitative assessment of the sampling perspective error and its effects on predictive numerical models are currently underway.

4.0 ACKNOWLEDGEMENTS

This research is funded by NASA, Marshall Space Flight Center, under Contract #NAS8-35597 to Simpson Weather Associates, Inc.

5.0 REFERENCES

Emmitt, G. D., 1985. Doppler lidar sampling strategies and accuracies--regional scale. Proceedings of 1985 NASA Symposium and Workshop on Global Wind Measurements. 29 July-1 August, Columbia, MD.

CONSTRAINTS ON RESOLVING MESO-α AND MESO-β PHENOMENA USING A SPACE-BASED DOPPLER LIDAR WIND PROFILER

G. D. Emmitt and S. H. Houston

Simpson Weather Associates, Inc.
Charlottesville, Virginia 22902

1.0 INTRODUCTION

It has been proposed that a pulsed, coherent Doppler lidar system could be placed in a low earth orbit (~800 km) and scanned in a conical manner (Fig. 1) that would yield wind vectors in the cloud free regions around the globe. Initial feasibility studies concentrated on the use of a Doppler lidar to obtain spatial resolution of 300 km in the horizontal and 1 km in the vertical (Huffaker, 1978; NOAA, 1981; NASA, 1982). More recent and advanced studies have begun to address questions regarding the influence of coherent mesoscale atmospheric structures on the lidar wind computation algorithm (Emmitt, 1985). In this instance one is not trying to resolve the mesoscale fields but only assess their effects on the up-scale measurements.

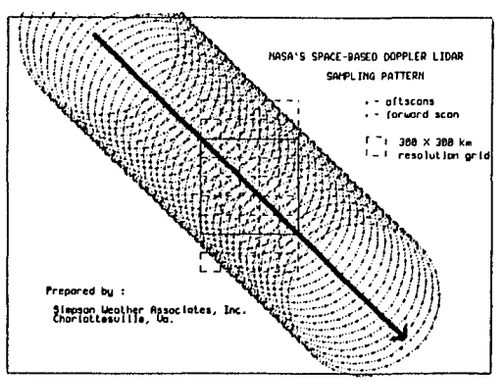

Fig. 1. Proposed conical scan pattern for a satellite based Doppler lidar. Dark arrow is the satellite ground track. In this case the orbit lidar parameters are:

Altitude	800 km
Satellite Orbital Speed	7.5 km s^{-1}
Scan Angle from Nadir	56°
Scan Period	20 seconds
Shot Frequency (PRF)	8 s^{-1}
Pulse Length	2 km

The authors developed lidar shot management and wind computation algorithms, which are used to probe the resolution limits and specify the nature of the constraints on resolving mesoscale (α and β) wind fields. These constraints are, in most instances, unique to the proposed Doppler lidar configuration and therefore lead to issues of tradeoffs and optimization. Several examples of simulated Doppler lidar performance in resolving wind gradient features are presented using currently proposed scan and signal processing parameters.

2.0 RESULTS

Simulation experiments have been conducted using a variety of input wind fields including mesoscale and GCM model outputs, objectively analyzed and gridded observational data and idealized control fields. To illustrate the nature of the Doppler lidar errors, only the latter type of input is used in the following presentation.

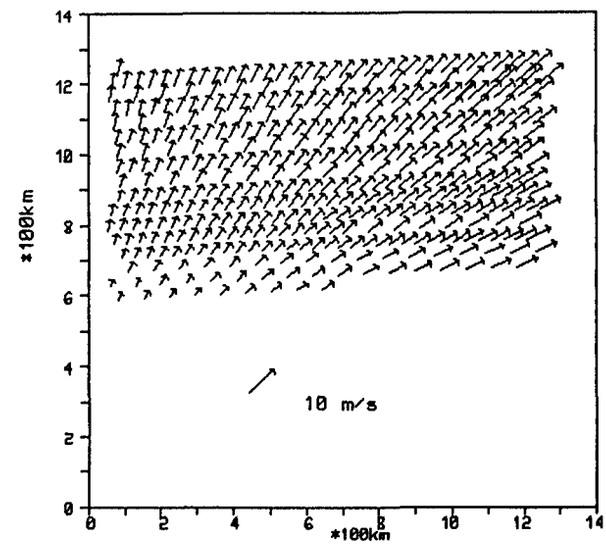

Fig. 2a. Input winds to Doppler lidar simulation model where u_o = 1.0 m s^{-1}; v_o = 0.0 m s^{-1}; du/dx = dv/dy = 4.0 x 10^{-6}; σ_u = σ_v = .15. The vectors displayed are only those at the location of shot pairs having a weighting function $\geq$.8 (1.0 being highest weight).

Each lidar shot produces a single measurement of the winds along a 2 km pulse. Lidar

shots are paired according to the multi-pair algorithm (MPA) to yield estimates of u and v with the assumption that the vertical component, w, of the wind is either very small when averaged along the 2 km pulse or is small when averaged over a specified horizontal domain. The angular and spatial separation between shots in a pair contribute to the measurement error. Since these separations are strictly a function of scan geometry we can weight or rank pairs by how close their angular separation is to 90° and their spatial separation is to 0.0 km. Having weighted each pair's estimation of the wind, we can choose to use only the best pairs to produce an estimation for a specified grid area.

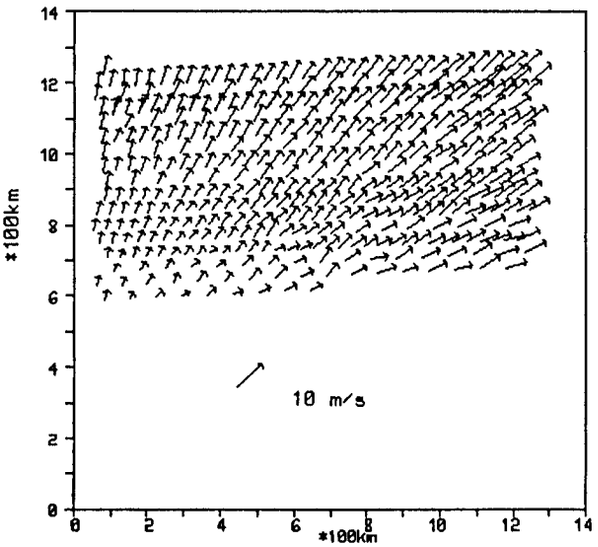

Fig. 2b. Output winds from Doppler lidar simulation model for input winds in 2a. Only those winds obtained from shot pairs having weighting functions $\geq$.8 are displayed.

In the simplest case a constant gradient in the u and v components is employed across the lidar scan domain (Figure 2a). The lidar scan parameters listed in the figure (2) caption are nominal and currently considered feasible. To simulate system noise and a background level of atmospheric turbulence at wavelengths less than 2 km, a random measurement error (RMS = .15 m s^{-1}) is used. In Figure 2b those pairs that have the better weights (.8 to 1) are shown with their wind estimates for the input field in Figure 2a. The constant gradient is resolved with very small errors (<2%). Although the lidar scan domain is from the ground track out to 1400-1500 km, only a fraction (~40%) of the domain contains pairs with angular separation sufficient enough to meet the .8 weighting threshold.

With a pulse repetition rate (prf) of 8, the shot density would be ~1 shot per 200 km^2 yielding an average spacing of 14 km. If each shot was a complete wind measurement, then the shortest wavelength feature that could be theoretically resolved would be 28 km. However, shots must be paired to obtain estimates of the u and v components and therefore the effective resolution is something other than 28 km. We have chosen to explore the limits of resolving smaller scale wind features, by inputting wind fields with divergent phenomena having wave lengths ranging from 200 to 50 km. Figures 3a, 3b, 4a, and 4b are examples of the input fields along with the simulated lidar wind fields. When the wavelength was reduced to 80 km there was little or no information obtained with the lidar. It is apparent that features with wavelengths less than 100 km might be seen as perturbations to the flow but any quantification of their magnitude would be unreliable.

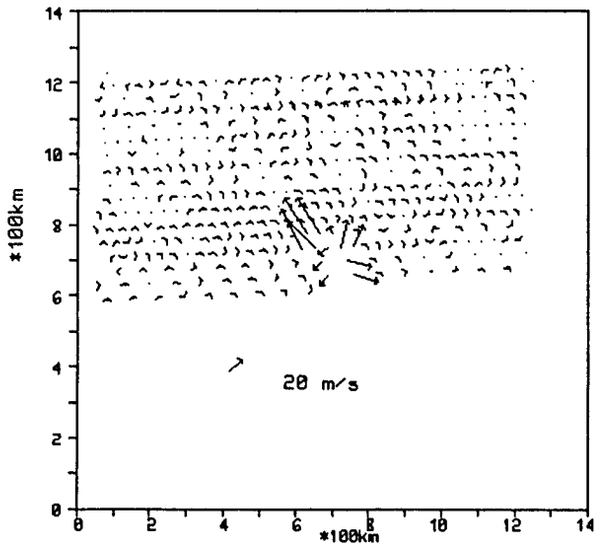

Fig. 3a. Input winds for a divergent feature (~5 x 10^{-4} s^{-1}) of wavelength 200 km embedded in a $u_o = v_o = du/dx = dv/dy = 0.0$ flow with a random component of $\sigma = .15$.

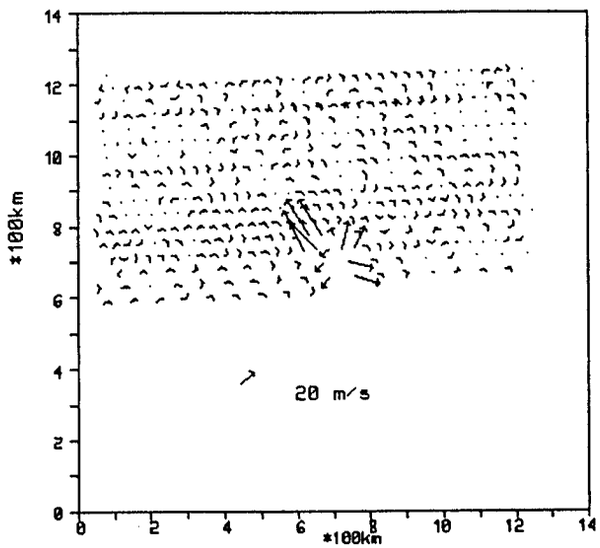

Fig. 3b. Output winds from Doppler lidar simulator model using inputs shown in 3a. As in Figure 2, only those pairs having weighting functions greater than .8 are displayed.

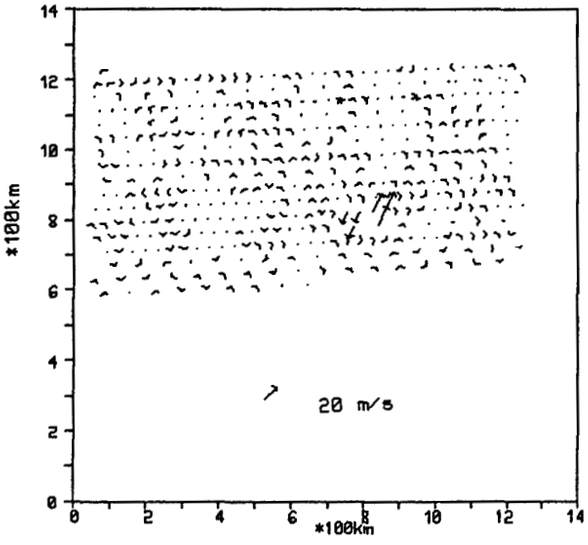

Fig. 4a. Input winds for a divergent feature (-5×10^{-4} s^{-1}) of wavelength 100 km embedded in a $u_o = v_o = du/dx = dv/dy = 0.0$ flow with a random component of = .15.

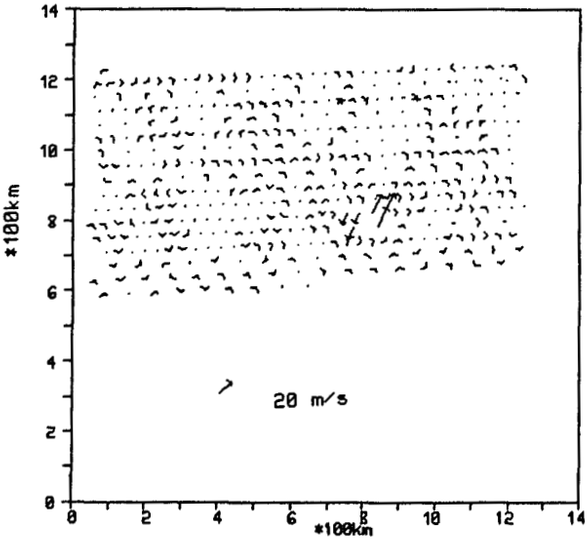

Fig. 4b. Output winds from Doppler lidar simulator model using inputs shown in 4a. As in Figure 2, only those pairs having weighting functions greater than .8 are displayed.

3.0 CONCLUSIONS

With the present constraints on lidar lifetime, scan rates and orbit altitudes, the limits of mesoscale wind feature resolution are close to wavelengths of 100 km, which is not surprising since the average distance between the higher quality shot pairs is ~50km--thus a Nyquist wavelength of 100 km.

4.0 ACKNOWLEDGEMENTS

This research has been funded by NASA under contract #NAS8-35597 to Simpson Weather Associates, Inc.

5.0 REFERENCES

Emmitt, G. D., 1985: Doppler lidar sampling strategies and accuracies--regional scale. Proceedings of 1985 NASA Symposium and Workshop on Global Wind Measurements. 29 July-1 August, Columbia, MD.

Global Wind Measuring Satellite System - Windsat, Final Report, NOAA Contract #NA79RAC00127. Prepared for U. S. Department of Commerce, NOAA, by Lockheed Missiles and Space Company, Inc., April 1981.

Huffaker, R. M., ed., 1978: Feasibility study of satellite-borne LIDAR global wind monitoring system. NOAA/ERL WPL-37, Sep.

NASA, 1982 (Frank Park, ed.): Feasibility Assessment: Satellite Doppler Lidar Wind Measuring System. NASA publication MSFC-MOSD-146.

ERBE DATA AND ITS VALIDATION

Bruce R. Barkstrom

Atmospheric Sciences Division
NASA Langley Research Center
Hampton, VA 23665

1. INTRODUCTION

The first satellite in the Earth Radiation Budget Experiment (ERBE) complement was launched on space shuttle Challenger on October 5, 1984. The second followed on the NOAA-9 satellite, launched on December 15, 1984. These two satellites, together with the third which is expected to be launched in mid-March 1986 on the NOAA-G vehicle, constitute the first multi-satellite mission designed to measure the three components of the Earth's radiation budget with state-of-the-art radiometric accuracy.

The instrument complement on these satellites consists of a pair of instrument packages: a scanning instrument and a nonscanner. The latter package contains four channels to view the Earth and one to monitor the solar "constant." Two of the Earth-viewing channels see from limb to limb; two see a footprint about 1000 km in diameter. One channel of each pair is sensitive to all wavelengths of reflected and emitted radiation. The other is sensitive only to reflected sunlight (over the wavelength range 0.2 μm to about 4 μm).

Each instrument package contains blackbody and shortwave calibration sources tied to the International Practical Temperature Scale (IPTS-68). The instruments also have the capability to observe the Sun, and, in the case of the scanner, space.

Coupled with this radiometric measurement and calibration capability is a complete ground data processing system. This system, developed with the full involvement of a science team with over 60 individuals, contains one of the most sophisticated radiation budget interpretation schemes yet applied to satellite data.

In addition to interpreting the instrument data, this system is responsible for Earth-locating the data, for choosing the appropriate angular and directional models to use in relating the satellite measurement to the instantaneous radiative power loss from the observed atmospheric column, and for averaging the data over time and space. It is also responsible for merging the streams of data from the three satellites and for producing appropriate products for the science team during the validation phase of the project, and later for the scientific community.

In this paper, we will discuss the philosophy and procedure by which the data will be validated.

2. VALIDATION PHILOSOPHY

As we have noted, the measurement of the Earth's radiation budget is a complex problem that may be broken down into three major components: radiation detection, instantaneous inversion to the top of the atmosphere, and averaging over time (Barkstrom, 1984; Barkstrom and Smith, 1986). In an abstract view, these three components may be regarded as transformations that take certain types of input data and convert them into other data streams. For example, a satellite radiation detector accepts incident radiation as its input, and is intended to output a stream of numerical telemetry information.

In order to produce a usable data product which successfully represents the "radiation budget," it is necessary to model the processes which have operated on the radiation leaving the top of the atmosphere. In other words, the ground data processing must contain the inverse transformations to the processes that have produced the raw data received on the ground.

The purpose of validation is to detect and, where possible, to correct errors in the form and content of these inverse transformations, as well as to estimate the residual uncertainty. On small and well understood problems, it is even possible to consider that validation of the measurement system consists of linearizing the data processing system about the nominal state and seeking a least squares solution for the perturbations to the nominal coefficients. However, for most satellite measurement systems, including those for measuring the Earth's radiation budget, such a scheme is impractical. In the Earth Radiation Budget Experiment (ERBE), for example, the inversion portion of the processing system contains angular-directional models which are functions of viewing and solar zenith angles, latitude, and geographic scene types. The sheer number of coefficients precludes any practical least squares revisions to these coefficients. Accordingly, a more practical procedure for validation must be found.

In the work that follows, various validation techniques that have been applied to ERBE will be discussed. One part of these techniques is the detection and diagnosis of errors or inconsistensies in the processing system. The second major part consists of corrections. In keeping track of these validation techniques it is helpful to subdivide them into instrument, inversion, and averag-

ing techniques, although they actually contribute to the validation of more than one part of the system.

3. INSTRUMENT VALIDATION

In dealing with radiometric data from satellite borne instruments, the first part of validation begins before launch with the design and ground calibration of the instruments. In the case of ERBE, for example, this portion of the measurement system included both the calibration of the detectors with radiation from a blackbody and an integrating sphere, as well as characterization of the spectral response of the instruments, characterization of the point spread function, and determination of the ties between the onboard calibration system and the ground calibration measurements.

In flight, the onboard calibration system becomes the first point at which the instrument detection of radiation can be checked (Cooper, et al., 1986). In the case of ERBE, observations of space have provided zero points, while internal calibration observations are checked the magnitude and stability of the gain of the detectors. Direct observations of the Sun provide an independent check of the instrumental gain (Lee, et al., 1986).

Beyond looks at onboard calibration sources, the next point of validation of the instrument data is the ability to cross-check instrument channels against one another. In the case of ERBE, this has involved taking scanner observations, determining what the scanner would have seen if it had been looking in the direction of a nonscanner channel, and adding up all of the scanner radiances that would have contributed to the nonscanner measurement. This provides data that can be directly compared with the nonscanner measurements. The results for ERBE have been extremely encouraging, producing agreement to better than 1%.

4. INVERSION VALIDATION

In validating the inversion portion of the processing, the tests available for diagnosing erroneous processing are much more indirect (Smith et al., 1986; Baldwin and Coakley, 1986). Partly, this arises because the inversion process itself involves estimating the energy loss for directions that are not observed when the satellite samples the emergent radiation field. Partly, it arises because inversion involves separating different types of surfaces, such as clear or cloudy areas, whose properties are not completely known and for which identification procedures are a matter of controversy.

Again, the validation process must begin before launch by assembling as trustworthy a set of angular models as can be found. These can be tested for reasonableness against theory, both by comparing with radiative transfer calculations and by using reciprocity relationships. For ERBE, this *a priori* information has come from the Nimbus-7 ERB observations, summarized by Taylor and Stowe (1984, 1986) as well as GOES.

To check on the models and the process by which the models are selected in the operational data processing software, ERBE has chosen to rely on validation by along-track scanning and by checks with correlative measurements and alternative scene identification methods.

In along-track scanning, a geographic region under the satellite track is sampled from as many different angles as possible. Since the scene is not likely to change appreciably over the 10 minutes or so that it is visible from the satellite, constancy of scene identification is a major criterion for successful validation of the satellite data interpretation. More detailed discussion of this validation technique will be provided by Smith et al. (1986).

5. AVERAGING VALIDATION

There are two sources of temporal variability in the reflected and emitted radiation from the Earth: solar zenith dependence of albedo and changes of scene type with time, notably caused by clouds. There are, accordingly, two parts to the validation of the averaging process.

The validation of the solar zenith angle dependence is primarily accomplished through the use of auxiliary information obtained as part of the inversion processing. Since the only observations that are available for constructing angular-directional models are radiances, these observations include the information needed to construct the diurnal variation in albedo with solar zenith angle. Both the Nimbus-7 ERB and GOES data have been used in constructing and validating ERBE albedo models.

The more difficult job of validating temporal averages is that of estimating the effect of variations that occurred when the satellites making the radiation budget measurements were not overhead. Over some portions of the globe, the interpolation between ERBE measurements can be checked through the use of geostationary satellite data, including GOES and Meteosat. Preliminary results of this validation process are discussed by Harrison et al. (1986), and Hunt et al. (1986).

6. CONCLUSION

Although the measurement of the radiation budget can be thought of very abstractly, it appears appropriate to the complexity of the problem to seek estimates of uncertainty that come directly from the observations themselves, rather than exhaustive theoretical analysis. Accordingly, in ERBE validation, emphasis has been given to various direct intercomparisons of one method of observing radiation against another. In the case of the instruments, the most direct intercomparisons are those looking at space, the Sun, and internal calibration sources. Next most directly, observations from one instrument channel can be compared with those from another. In the inversion and averaging portion of the processing system, validation becomes still more indirect, and depends much more heavily upon correlative information, such as alternative sampling of scenes and observations of limited regions of the Earth by geostationary satellites.

Acknowledgments. This work would have been impossible without the help of the ERBE Science Team. The full team is given in the article in the **Bulletin of the American Meteorological Society** (Barkstrom, 1984) or in Barkstrom and Smith (1986). The Principal Investigators are A. Berroir, R. Cess, C. Duncan, A. Gruber, E. Harrison, D. Hartmann, F. House, F. Huck, G. Hunt, R. Kandel, J. Kibler, M. King, A. Miller, A. Mecherikunnel, V. Ramanathan, E. Raschke, L. Smith, W. Smith, and T. Vonder Haar. In addition, presentation of ERBE results would have been impossible without the help of the ERBE Project Management, both at NASA Langley Research Center and at NASA Goddard Space Flight Center, as well as the ERBE Data Management Team, under the direction of J. F. Kibler.

REFERENCES

Baldwin, D. G. and J. A. Coakley, Jr., 1986: Validation of ERBE bidirectional models. *Proc. Sixth Conf. on Atmospheric Radiation*, Amer. Meteor. Soc., Williamsburg, VA, May 12-16, in press.

Barkstrom, B. R., 1984: The Earth Radiation Budget Experiment (ERBE). *Bull. Am. Meteor. Soc.*, **65**, 1170-1185.

Barkstrom, B. R. and G. L. Smith, 1986: The Earth Radiation Budget Experiment: An Overview. *Rev. Geophys.*, in press.

Cooper, J. E., B. R. Barkstrom, L. P. Kopia, M. R. Luther, N. Halyo, D. Chrisman, S. Choi, R. D. Cess, 1986: Initial flight performance of ERBE instruments. *Proc. Sixth Conf. on Atmospheric Radiation*, Amer. Meteor. Soc., Williamsburg, VA, May 12-16, in press.

Harrison, E. F., P. Minnis, and D. R. Brooks, 1986: First diurnal results from the Earth Radiation Budget Experiment. *Proc. Sixth Conf. on Atmospheric Radiation*, Amer. Meteor. Soc., Williamsburg, VA, May 12-16, in press.

Hunt, G. E., C. F. England, and Y. J. Zhu, 1986: Studies of the Earth's radiation budget using ERBE and Meteosat data. *Proc. Sixth Conf. on Atmospheric Radiation*, Amer. Meteor. Soc., Williamsburg, VA, May 12-16, in press.

Lee, R. B. III, B. R. Barkstrom, and M. R. Luther, 1986: Solar irradiance measurements using the Earth Radiation Budget Experiment solar monitors. *Proc. Sixth Conf. on Atmospheric Radiation*, Amer. Meteor. Soc., Williamsburg, VA, May 12-16, in press.

Smith, G. L., R. N. Green, B. A. Wielicki, J. T. Suttles, and L. M. Avis, 1986: ERBE data inversion. *Proc. Sixth Conf. on Atmospheric Radiation*, Amer. Meteor. Soc., Williamsburg, VA, May 12-16, in press.

Taylor, V. R. and L. L. Stowe, 1984: Reflectance characteristics of uniform Earth and cloud surfaces derived from Nimbus 7 ERB. *J. Geophys. Res.*, **89**, 4987-4996.

Taylor, V. R. and L. L. Stowe, 1986: Revised reflectance and emission models from Nimbus-7 ERB data. *Proc. Sixth Conf. on Atmospheric Radiation*, Amer. Meteor. Soc., Williamsburg, VA, May 12-16, in press.

J1.3

INITIAL FLIGHT PERFORMANCE OF ERBE INSTRUMENT

John E. Cooper, Bruce R. Barkstrom, Michael R. Luther, Leonard P. Kopia,
NASA Langley Research Center
Hampton, Virginia 23665-5225

Robert D. Cess,
State University of New York
Stoney Brook, New York

Nesim Haylo and Dan A. Chrisman
Information and Control Systems, Inc.
Hampton, Virginia 23666

Abstract of
Proposed Paper for Presentation at
Sixth Conference on Atmospheric Radiation
Williamsburg, Virginia
May 12-16, 1986

This paper presents the initial flight performance of the Earth Radiation Budget Experiment (ERBE) instruments onboard the Earth Radiation Budget Satellite (ERBS) launched on October 5, 1984, and the NOAA-9 satellite launched on December 12, 1984. Each satellite carries a nearly identical pair of ERBE instruments: a narrow field-of-view scanner and a wide field-of-view nonscanner. Instrument in-orbit operations, including internal and solar calibration sequences, are discussed along with an assessment of the instrument performance and stability obtained through periodic viewing of the Sun, space, and internal calibration sources.

SOLAR IRRADIANCE MEASUREMENTS USING THE EARTH RADIATION BUDGET EXPERIMENT SOLAR MONITORS

Robert B. Lee III, Bruce R. Barkstrom, and Michael R. Luther

NASA Langley Research Center
Hampton, Virginia 23665-5225

and

Robert D. Cess

State University of New York
Stony Brook, New York

1. INTRODUCTION

The Earth Radiation Budget Experiment (ERBE) solar monitors (SM) are the most recent pyrheliometers to be placed into orbit for the measurement of the solar irradiance. The monitors have been operating successfully from the National Aeronautics and Space Administration (NASA) Earth Radiation Budget Satellite (ERBS) and the National Oceanic and Atmospheric Administration NOAA-9 spacecraft platforms since October 25, 1984, and January 23, 1985, respectively. The measurements are designed primarily to provide inflight absolute calibration for the ERBE Earth-viewing radiometers which measure the Earth-reflected and Earth-emitted radiant exitances. The solar calibrations are performed typically every 2 weeks at times when the ERBS and NOAA-9 monitors and the Earth-viewing radiometers can observe the Sun almost simultaneously. Descriptions of the calibrations and radiometers have been given by Barkstrom (1984, 1985), and Luther (1986a, 1986b).

For the October 25, 1984, through June 26, 1985, period, the solar irradiance values (normalized to one astronomical unit) derived from the ERBS and NOAA-9 solar monitor measurements are presented and intercompared.

2. MEASUREMENT APPROACH

The solar monitor (Lee, 1985) is a shuttered absolute active cavity pyrheliometer, which is similar in design and operation with those of the Solar Maximum Mission Active Cavity Radiometer Irradiance Monitor (Willson, 1979). In the solar monitor measurement approach, the Sun is allowed to drift through the monitor's 13.6-degree field of view. When the Sun is in the field of view, the measurements consist of reference and observational cycles of 32-second durations. During the reference cycle and when the shutter is closed, the internal surface of the shutter is used to represent a near zero irradiance source. During the observational cycle and when the shutter is opened, irradiance from the Sun is allowed to enter the radiometer. Since the monitors have instrument time constants of approximately 3.3 seconds, it takes approximately 28 seconds for the output signal to reach 99.98 percent of its full-scale value. Consequently, the signals, corresponding to the last 4 seconds of each cycle, are used in the determination of the solar irradiance. During each cycle, 40 samples are obtained from the signal using a 13-bit analog to digital converter having a $\pm$ 0.5 count uncertainty. One digital count corresponds to approximately 0.6 W/m^2. During each orbit, at least two solar observational and three reference cycles are available when the Sun is within $\pm$ 3.0 degrees of the monitor's optical axis.

The data reduction approach for the shuttered solar irradiance measurements is based upon the electrical subsitution concept of calorimetry in which electrical energy generated internally by Joule heating is compared to external radiation which is absorbed by the pyheliometer, and their heating effects are assumed to be equivalent. In the measurement approach, the temperature of the primary detection cavity is maintained approximately 2 degrees Celsius above that of the reference cavity, using electrical heat dissipated in the primary cavity. When the shutter is closed and when the monitor is exposed to a near zero irradiance source, the electrical power dissipated in the cavity is used as the reference level. When the shutter is opened and when the solar radiation is allowed to enter, the solar radiation which is absorbed by the cavity causes the primary cavity temperature to rise. In order to maintain the constant temperature difference between the cavities, the amount of electrical power dissipated is reduced. The quasi-equilibrium level of the power is used to define the observational level. The difference in power is equivalent to the amount of solar power, absorbed by the primary cavity.

The data reduction model used to define the solar irradiance converts the power difference to the International System of Units, normalizes the irradiance to one astronomical unit, and corrects for the angular response of the monitor. In addition, it corrects for radiation losses from the primary cavity through the secondary aperture, and it corrects for variations in the primary aperture area and

electrical heater resistances as functions of temperature. The basic reduction model is decribed in detail by Kendall (1970), Willson (1979), Crommenlynck (1982), Brusa (1983), and Lee (1985). Lee (1985) has determined analytically that the monitor measurement precision and accuracy are less than ± 0.1 and ± 0.2 percent, respectively.

3. DISCUSSIONS

For the October 1984 through June 1985 period, the solar irradiance values derived from the ERBS and NOAA-9 solar monitors are presented as functions of time in Figure 1. The individual data points presented represent the average of at least two derived solar irradiance values, obtained during an orbit. For the December 3, 10, and 17, 1984, February 20, 1985, and April 3, 1985, ERBS orbits, there are 4, 10, 5, 6, and 4 solar irradiance values, respectively. The standard deviations in the individual values are typically ± 0.2 and ± 0.4 W/m^2 for the ERBS and NOAA-9 respectively. In Figure 1, the ERBS values are represented by the circles while the NOAA-9 values are denoted by the squares. It can be seen that 1365 W/m^2 is the typical value for the irradiance. For the January through June 1985 period, the means of the ERBS and NOAA-9 values were found to be 1364.7 ± 0.4 and 1365.1 ± 0.5 W/m^2, respectively. The fact that the mean values agree within 0.03 percent of each other provides considerable confidence in using the monitor measurement to calibrate absolutely the ERBE Earth-viewing radiometers.

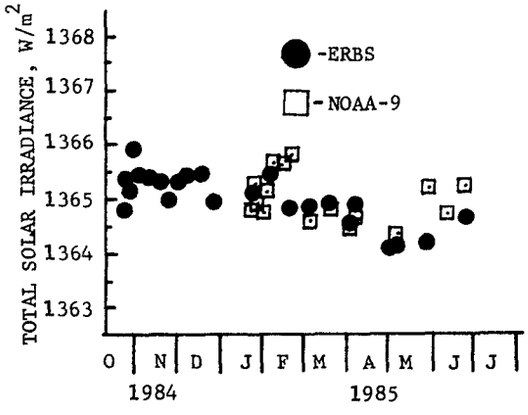

Figure 1. ERBS and NOAA-9 derived total optical solar irradiance values are presented for the October 25, 1984 through June 26, 1985 period.

In Figure 1, the most obvious features are the decreases in the ERBS and NOAA-9 solar irradiance values with time. The ERBS and NOAA-9 decreases were found to be approximately 0.07 and 0.04 percent, respectively. According to the results of Willson (1985), the efficiency of the primary cavities in absorbing the solar radiation could degrade approximately 0.02 percent during the first year in orbit and cause an equivalent decrease in the derived solar irradiance value. Frohlich (1985) also pointed out that the absorption efficiency could degrade 0.03 percent during the first year. Therefore, the remaining fractions of the observed ERBS and NOAA-9 decreases may be indicative of actual decreases in the solar irradiance. The results of Willson (1985) and Smith (1983) indicate that the solar irradiance periodically exhibits short term variations in which the irradiance may decrease for up to 6 months and then increase for an equivalent period of time. Therefore, at least 1 complete year of the ERBS and NOAA-9 values will have to be obtained and analyzed in order to define whether the observed decreases are long term (several years) or short term (less than a year) in nature.

Preliminary comparisons of the variations in the ERBS irradiance values with sunspot indices were conducted in order to correlate the variations with sunspot activity. Examination of the sunspot indices revealed extremely low variability, typically less than ± 0.1 percent. associated with solar minimum for solar cycle no. 23. The variations in the ERBS and NOAA-9 irradiance values were found to be of the order of the measurement precision. Therefore, positive correlations would be difficult to confirm. As solar maximum for solar cycle no. 23 is approached, it is expected that the variations in sunspot activity will be high enough to conduct meaningful correlation studies between variations in the solar irradiance and sunspot activity.

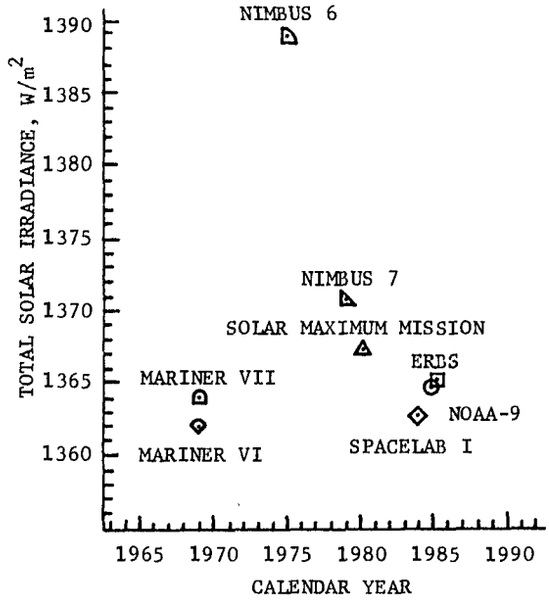

Figure 2. Comparisons are presented among the solar irradiance values derived from the Mariner VI and VII, Nimbus 6 Earth Radiation Budget (ERB) channel 3, Nimbus 7 ERB channel 10c, Solar Maximum Mission (SMM) Active Cavity Radiometer Irradiance Monitor, Spacelab I Belgium Royal Meteorological Institute, ERBS solar monitor, and NOAA-9 solar monitor spacecraft pyrheliometric experiments.

It should be noted that long-term irradiance decreases, occurring over several years, were observed by Willson (1985) and Smith (1983).

In Figure 2, the mean ERBS and NOAA-9 direct solar irradiance values, derived from the solar monitor measurements, are compared with those derived from the earlier NASA Mariner VI and VII (Plamondon, 1969), NOAA Nimbus 6 Earth Radiation Budget (ERB) channel 3 (Duncan, 1977), NOAA Nimbus 7 ERB channel 10c (Hickey, 1984), NASA Solar Maximum Mission Active Cavity Radiometer Irradiance Monitor (Willson 1984), NASA Spacelab I Belgium Royal Meteological Institute (Crommenlynck 1984) pyrheliometric spacecraft experiments. The Plamondon values were revised by Frohlich (1977) and the revised Mariner VI and VII values are presented in Figure 2. All of the spacecraft experiments used pyrheliometers of the self or semi-self calibrating cavity type with the exception of the Nimbus 6. It can be seen that the ERBS and NOAA-9 values agree within $\pm$ 0.3 percent of the values derived from the other self-calibrating pyrheliometers. This fact indicates that the monitors can provide reliable calibrations for the ERBE radiometers. In addition, the excellent agreement among the various spacecraft experiments suggests that simultaneous intercomparisons among the spacecraft experiments could be used to establish an absolute radiometric reference scale for space solar irradiance determinations, similar to the World Radiometric Reference scale which was established for ground-based, meteorological-based pyrheliometers. The December 10, 1984, NASA-sponsored intercomparison event among the Solar Maximum Mission, Nimbus 7, and ERBS experiments offers an excellent opportunity to establish the reference scale. The scheduled December 1986 NASA-sponsored intercomparisons offer an additional opportunity to confirm such a scale since the ERBS, NOAA-9, Solar Maximum Mission Active Cavity Radiometer Irradiance Monitor (ACRIM), Nimbus 7, Spacelab ACRIM, Spacelab Belgium Royal Meteorological Institute, and NOAA-G (ERBE spacecraft scheduled for a March 1986 launch) should be operational.

4. SUMMARY

For the October 1984 through June 1985 period, 1365 W/m^2 was derived as the typical solar irradiance value using the ERBS and NOAA-9 solar monitors. The ERBS and NOAA-9 derived solar irradiance values exhibited decreases between 0.07 and 0.04 percent. The observed decreases are believed to be caused by short-term decreases in the solar irradiance and not indicative of long-term (several years) decreases. The ERBS and NOAA-9 mean solar irradiance values were found to agree within $\pm$ 0.3 percent of the values derived from the earlier Mariner VI, Mariner VII, Nimbus 7, Solar Maximum Mission, and Spacelab I pyrheliometric experiments. The excellent agreement emphasizes the reliability of using the solar monitor measurements to calibrate absolutely the other ERBE radiometers. The solar monitor measurement precisions and accuracy are estimated to be less than $\pm$ 0.1 and $\pm$ 0.2 percent, respectively.

5. REFERENCES

Barkstrom, B. R., 1984: The Earth Radiation Budget Experiment (ERBE), Bulletin American Meteorological Society, Vol. 65, pp. 1170-1185.

Barkstrom, B. R., and Lee, R. B., 1985: Earth Radiation Budget Determinations Using Absolute Radiometry, Proceedings of an International Meeting/Advances in Absolute Radiometry (P. Foukal, Editor), Atmospheric and Environmental Research, Inc., Cambridge, MA., pp. 26-29.

Brusa, R. W., 1983: Solar Radiometry, Thesis Publication no. 5988, PMOD World Radiation Center, Davos, Switzerland.

Crommenlynck, D. A., 1982: Fundamentals of Absolute Pyrheliometry and Objective Characterization, NASA Conference Publication 2239, pp. 53-88.

Crommenlynck, D. A., 1984: Solar Irradiance Observations, Science, Vol. 225, pp. 180-181.

Duncan, C. H., Harrison, R. G., Hickey, J. R., Kendall, J. M., Thekaekara, M. P., and Willson, R. C., 1977: Rocket Calibration of the Nimbus 6 Solar Constant Measurements, Applied Optics, Vol. 16, No. 10, pp. 2690-2697.

Frohlich, C., 1977: Contemporay Measures of the Solar Constant, in The Solar Output and Its Variations (O. R. White, Editor), Associated University Press, Boulder, CO., pp. 93-109.

Frohlich, C., 1985: Radiometry at PMOD and the World Radiometric Reference, Proceedings of An International Meeting/Advances in Absolute Radiometry (P. Foukal, Editor), Atmospheric and Environmental Research, Inc., Cambridge, MA., pp. 1-5.

Hickey, J. R., Major, E. R., and Kyle, H. L., 1984; User's Guide for the Nimbus 7 ERB Solar Analysis Tape (ESAT), NASA Technical Memorandum 86143.

Kendall, J. M., and Berdahl, M., 1970: Two Blackbody Radiometers of High Accuracy, Applied Optics, Vol. 9, No. 5, pp. 1082-1091.

Lee, R. B., Luther, M. R., and Barkstrom, B. R., 1985: An Overview: Earth Radiation Budget Experiment (ERBE) Solar Monitor, J. of the National Technical Association, Vol. 59, No. 2, pp. 90-93.

Luther, M. R., Lee, R. B., Barkstrom, B. R., Cooper, J. E., Cess, R. D., and Duncan, C. H., 1986a; Solar Calibration Results from Two Earth Radiation Budget Experiment (ERBE) Instruments, Applied Optics, Vol. 25, No. 4, pp.

Luther, M. R., Cooper, J. E., and Taylor, G. R., 1986b: The Earth Radiation Budget Experiment Nonscanner Instrument, Geophysical Space Physics, Vol. 24, No. 2, pp.

Plamondon, J. A., 1969: The Mariner Mars 1969 Temperature Control Flux Monitor, JPL Space Programs Summary 37-58, Vol. III, pp. 162 (October 31, 1969).

Smith, E. A., Vonder Haar, T. H., Hickey, J. R., and Maschhoff, R., 1983: The Nature of Short Period Fluctuations in Solar Irradiance Received by the Earth, Climatic Change, 5, pp. 211-235.

Willson, R. C., 1979: Active Cavity Radiometer Type IV, Applied Optics, vol. 18, no. 2, pp. 179-188.

Willson, R. C., 1984: Measurements of Solar Total Irradiance and Its Variability, Space Science Reviews, Vol. 38, pp. 203-292.

Willson, R. C., 1985: Solar Irradiance Variability Monitoring by Active Cavity Radiometers, Proceedings of An International Meeting/ Advances in Absolute Radiometry (P. Foukal, Editor), Atmospheric and Environmental Research, Inc., Cambridge, MA, pp. 6-11.

ERBE DATA INVERSION

G. Louis Smith, Richard N. Green, Bruce A. Wielicki,
J. T. Suttles, and Lee M. Avis

Atmospheric Sciences Division
NASA Langley Research Center
Hampton, Virginia

1. INTRODUCTION

The Earth Radiation Budget Experiment (ERBE) is a system of three spacecraft with instrument packages for measuring the Earth's radiation balance to an accuracy which has been unattainable in previous experiments (Barkstrom, 1984; Barkstrom and Smith, 1986). This is possible through the use of multiple spacecraft which permits the determination of the diurnal cycle over the Earth, as well as extensive capabilities for in-flight calibration of the instruments. The instrumentation incudes a scanner, which is described by Kopia (1986), and a non-scanner package, which is described by Luther (1986).

The primary objective of the experiment is to determine the monthly averaged radiant exitances at the "top of the atmosphere" (TOA) over the Earth with a resolution of 250 km. In order to fulfill this objective, three fundamental steps must be performed to high accuracy. The first is to make high accuracy measurements, which is an instrument requirement. The second is to compute the instantaneous radiant exitances from these measurements; this step we call "inversion," as it is a problem in remote sensing. The final step is the computation of the daily and monthly averaged regional values from these instantaneous values. The procedures for this final step are described by Brooks et al. (1986).

In the present paper, the algorithms for the inversion of the measurements to TOA radiant exitances and the techniques which are used to validate the methods and results are briefly described. The inversion algorithms are discussed more fully in Smith et al. (1986).

2. SCANNING RADIOMETER ALGORITHMS

The inversion algorithms for the scanning radiometers evolved directly from the methods used by Raschke and Bandeen (1970) and Raschke et al. (1973). First, the radiances at the spacecraft are computed, taking into account the optical properties of the radiometers, after which the radiant exitances are computed, taking into account the directionality of the radiation field at TOA. Finally, the regional averages are computed on a 2.5°×2.5° grid.

The instrument ideally provides the broadband radiance measurement in each of three channels. The spectral responses of the various channels of the instrument, however, are not perfectly flat, but are rather complicated functions of wavelength, as shown in Figure 1. This effect is accounted for by essentially a regression method, whereby three channels (longwave, shortwave, and total) are used to estimate the broadband longwave and shortwave radiances taking into account the instrument spectral response. The equation is

$$\begin{bmatrix} L_{LW} \\ \\ L_{SW} \end{bmatrix} = C \begin{bmatrix} m_{TOT} \\ m_{LW} \\ m_{SW} \end{bmatrix} \tag{1}$$

where C is a matrix (in general 2×3) of regression coefficients for the given scene and is a function of viewing angles.

A scanning radiometer measures the upwelling radiance L from the scene to the instrument. This radiance varies with the direction, which is measured by the zenith angle a of the exiting ray and, for the reflected solar radiation, the azimuth angle ϕ of the ray relative to the Sun and the zenith angle θ_0 of the Sun at the scene. A bidirectional function $R(\theta_0,\theta,\phi)$ is defined to relate the radiance to the radiant exitance M at the top of the Earth-atmosphere system (TOA):

$$L(\theta_0,\theta,\phi) = \pi^{-1}R(\theta_0,\theta,\phi)M \tag{2}$$

This bidirectional function depends upon the scene; for example, whether the scene is cloud, land, etc. Bidirectional models have been developed, e.g., by Taylor and Stowe (1984) and Stuhlmann et al. (1985), and a typical model is shown in Figure 2 for cloud. In order to select the proper bidirectional model for the interpretation of the data, it is again necessary to identify the scene.

The scene identification procedure for ERBE first classifies the underlying surface by its geographic type (geotype): land, ocean, snow, desert or land-ocean mix (coastal regions).

The cloud cover is defined in terms of four classes: clear (less than 5% cloud cover), partly cloudy (between 5% and 50% cloud), mostly cloudy (between 50% and 95% cloud), and overcast (more than 95% cloudy).

The cloud class for a given measurement pair (shortwave and longwave radiances) is selected according to the measurement pair in a manner similar to a threshold method, but modified to account for the variance associated with each class, as illustrated in Figure 3. There is a distribution of measurement pairs within each class, as represented by the light lines. The shortwave-longwave plane is partitioned into regions according to which is the most probable scene identification for the measurement pair. The boundaries of these regions are indicated by the heavy solid lines in Figure 3. Thus, e.g., if a measurement pair falls within region I, given that the surface is ocean, it is identified as "clear ocean." The statistics required for this method are functions of solar and viewing zenith angles and the relative azimuth, and were compiled from Nimbus 7 ERB scanning radiometer data. For nighttime scene identification, the cloud class assignment is made according to only the longwave radiance in a manner analogous to the daytime case.

The data flow for analysis of scanning radiometer data is set up as shown in Figure 4. Using "global" spectral factors, approximate broadband shortwave and longwave radiances at the spacecraft are computed. The scene is then identified and the appropriate spectral factors are determined for the final calculation of the radiances. Also, a bidirectional model based on this scene type is used to estimate the radiant exitance for the pixel, i.e., the field of view of a single measurement, by use of equation (1). The instantaneous regional average is then computed by averaging all estimates of radiant exitance for pixels that fell in the region. A pixel is considered to be in the region if the pixel center falls within the region.

3. NONSCANNER ALGORITHMS

The WFOV radiometers receive radiation from the entire disc of the Earth atmosphere system, from limb to limb. One of these is a total radiometer and measures radiation of all wavelengths. The other measures the shortwave radiation, that is, the solar radiation reflected by the Earth. The WFOV measurement of longwave radiation from the Earth is thus the total radiation measurement minus the shortwave radiation measurement. The MFOV radiometers are similar to the WFOV radiometers except that they have field-of-view limiting apertures which restrict the area viewed by them to a circle on the Earth with a radius of 5° geocentric angle.

The measurement from a WFOV or MFOV radiometer at colatitude Θ_s and longitude Φ_s may be written as

$$m_\Lambda(\Theta_s,\Phi_s) = \iint_\Omega L(\Theta,\Phi,\theta,\phi) \cos\alpha \; S_\Lambda(\lambda) \; d\Omega \; d\lambda \qquad (3)$$

where Λ denotes the spectral channel (total or shortwave), Ω is the solid angle subtended at the radiometer, and S_Λ is the spectral response function of the radiometer. The Θ and Φ are the colatitude and longitude of the scene, and θ and ϕ are the zenith angle and azimuth angle relative to the Sun of the outgoing radiation. The integration over angle Ω is for $[0,2\pi]$ in azimuth and for $[0,\alpha_h]$ in nadir angle, where α_h is the nadir angle to the limb for the WFOV channels and is the nadir angle to the 5° geocentric angle circle on the Earth for the MFOV channels. The ERBE WFOV and MFOV data are analyzed using a shape factor technique and a numerical filter technique to produce two different output products.

The shape factor methods are based on the assumption that longwave radiant exitance or albedo is constant within the field of view, which permits that quantity to be moved across the integral sign, and the resulting integral expression, called a shape factor, can be evaluated. The radiant exitance or albedo can then be computed from the measurement and the shape factor. This method has been used, e.g., by Smith et al. (1977) for the analysis of WFOV measurements from the Nimbus 7 ERB.

The numerical filter is a one-dimensional resolution enhancement method conceived by House and Jafolla (1980) and further developed into the form used in the ERBE processing system by Green (1983). One is restricted to resolution enhancement only along track because there is no information from the WFOV or MFOV data in the cross-track direction. The estimate M of the radiant exitance is assumed to be given by a linear combination of the measurements m_k, according to

$$M_k = \sum_j \omega_j \, m_{k+j} \qquad (4)$$

The details of the inversion weights ω_j are described in Green (1983). For the analysis of reflected radiation, the same method is used except that the quantity being estimated is albedo rather than radiant exitance. For both the shortwave and longwave analyses, the bidirectional function R_Λ is computed for the scene type as identified by the scanning radiometer information. If scanner data are not available, then R_Λ is evaluated according to a global function which corresponds to a 50% cloud cover.

4. INVERSION VALIDATION TECHNIQUES

In this section, only a few of the validation techniques are described. In addition to these, methods are being employed and developed by other ERBE science team members.

In order to validate the ERBE results, the scanner results are first validated. Next, the nonscanner measurements are compared with those which would be expected from the scanner results. Finally, the radiant exitances at TOA computed from the nonscanning radiometers are intercompared with themselves and the scanner results.

For the scanner, the validation follows the steps of Figure 4. The computation of radiances from the measurements is checked by the three-

channel intercomparison method. The scene identification procedure is validated by use of data from the AVHRR aboard the NOAA 9 spacecraft. Finally, the bidirectional models are validated by occasionally operating the scanner in an along-track scan pattern, as opposed to the usual cross-track pattern.

The three-channel intercomparison makes use of the redundancy of the three channels to check their results. The shortwave and longwave radiances are first computed on the basis of all three channels, which gives the best estimates, and then on the basis of two channels at a time. The results are then differenced to give discrepancies. Color graphic displays of these discrepancies are very useful, as various types of problem areas have specific signatures. For a perfect operating system, the discrepancies are not expected to be zero, but should be unbiased and have a small variance.

In order to validate the scene identification algorithm, the spatial coherence method of Coakley and Bretherton (1982) is used over ocean, and a hybrid bispectral method developed by Minnis and Harrison (1984) is used over both ocean and land. Both of these methods use AVHRR data.

The alongtrack operation of the scanner provides multiple looks at the same scene from many angles, which gives a unique and valuable data set. If the directional and bidirectional models are correct, the resulting longwave and shortwave exitances will be the same for all angles. Thus, one may easily validate these models, and even generate them. Also, the limits of the ability of the scene identification algorithm to classify cloudiness off-nadir due to finite cloud effects can be checked.

The scanner results may be intercompared with the non-scanner measurements by using the scanner-derived longwave and shortwave radiant exitance field and the scene identification to evaluate the right-hand side of equation (1). This evaluation is done for areas representing both the WFOV and the MFOV radiometers to provide a check with the actual measurements. This computation for the WFOV radiometer at a point requires that the field at TOA be described from nadir to the limb. This in turn requires that data be used from the position 8 minutes prior to the checkpoint to 8 minutes after passage of the checkpoint.

The comparison at the spacecraft as described above is primarily a check on the instruments themselves. The intercomparison of the scanner WFOV and MFOV results at TOA is also of interest, mainly to demonstrate the level of agreement at various scales. If the measurement and analysis procedures are operating correctly, the fields at TOA should agree very closely at the largest scales, but one does not expect them to agree at the smaller scales, which only the scanner can resolve. Thus, the TOA intercomparison is on a scale-dependent basis.

5. CONCLUDING REMARKS

Algorithms have been described for the analysis of ERBE measurements to deduce radiant exitance of reflected solar radiation and Earth-emitted radiation at a reference level ("top of the atmosphere"). The analysis of the scanner accounts for the directionality and the spectrum of the radiation on the basis of the scene, which is inferred from the location and measurements. Wide and medium field-of-view measurements are analyzed by use of the shape factor method and also by use of a numerical filter technique for resolution enhancement along the orbit track. These techniques also use scene-dependent bidirectional models.

Techniques are also described by which the data and analysis methods are being validated. These techniques use intercomparisons of the various channels and ancillary data, e.g. from the AVHRR.

6. REFERENCES

Barkstrom, B. R., 1984: Earth Radiation Budget Experiment (ERBE), Bull. Amer. Met. Soc., 65, 1170-1185.

Barkstrom, B. R. and G. L. Smith, 1986: The Earth Radiation Budget Experiment (ERBE): Science and Implementation, Rev. Geophys. and Space Physics (in press).

Brooks, D. R., E. F. Harrison, P. Minnis, and R. S. Kandel, 1986: The Development of Algorithms for Understanding the Temporal and Spatial Variability of the Earth's Radiation Balance, Rev. Geophys. and Space Physics (in press).

Coakley, J. A., Jr. and F. P. Bretherton, 1982: Cloud Cover from High-Resolution Scanner Data: Detecting and Allowing for Partially Filled Fields of View, J. Geophs. Res., 87, C7, 4917-4932, June 20.

Green, R. N., 1983: Accuracy and Resolution of Earth Radiation Budget Estimates, J. Atmos. Sci., 40, 977-985.

House, F. B. and J. C. Jafolla, 1980: One Dimensional Technique for Enhancing Earth Radiation Budget Observations from Nimbus 7 Satellite. Proceedings, International Radiation Symposium, International Association of Meteorology and Atmospheric Physics, Fort Collins, Colorado.

Kopia, L. P., 1986: Earth Radiation Budget Experiment Scanner Instrument, Rev. Geophys. and Space Physics (in press).

Luther, M., 1986: The Earth Radiation Budget Experiment Non-Scanning Instrument, Rev. Geophys. and Space Physics (in press).

Minnis, P. and E. F. Harrison, 1984: Diurnal Variability of Regional Cloud and Clear-Sky Radiative Parameters Derived from GOES Data. Part I: Analysis Method, J. Clim. and Appl. Met., 23, 993-1011.

Raschke, E. and W.R. Bandeen, 1970: The Radiation Balance of the Planet Earth from Radiation Measurements of the Satellite Nimbus 2, J. Appl. Meteor., 9, 215-238.

Raschke, E., T. H. Vonder Haar, W. R. Bandeen, and M. Pasternak, 1973: The Annual Radiation Balance of the Earth-Atmosphere System During 1969-1970 from Nimbus 3 Measurements, J. Atmos. Sci., 30, 341-364.

Smith, G. L., R. N. Green, E. Raschke, L. M. Avis, B. A. Wielicki, and R. Davies, 1986: Inversion Methods for Satellite Studies of the Earth's Radiation Budget: Development of Algorithms for the ERBE Mission, Rev. Geophys. and Space Phys. (in press).

Smith, W. L., D. T. Hilleary, H. Jacobowitz, H. B. Howell, J. R. Hickey, and A. J. Drummond, 1977: Nimbus-6 Earth Radiation Budget Experiment, Appl. Opt., 16, 306-318.

Stuhlmann, R., P. Minnis, and G. L. Smith, 1985: Cloud Bidirectional Reflectance Functions: A Comparison of Experimental and Theoretical Results, Appl. Opt., 24, 396-401.

Taylor, V. R. and L. L. Stowe, 1984: Reflectance Characteristics of Uniform Earth and Cloud Surfaces Derived from Nimbus-7 ERB, J. Geophys. Res., 89, D4, 4987-4996.

7. ACKNOWLEDGMENTS

The authors gratefully acknowledge the contributions of many colleagues in the formulation of the algorithms which are described here. These include fellow members of ERBE Science Team: Prof. F. B. House of Drexel University, Prof. E. Raschke of the University of Cologne, and Dr. M. King and Dr. A. Mecherikunnel of the Goddard Space Flight Center, NASA. Co-investigators that have contributed to the inversion work include Drs. H. Jacobowitz, L. L. Stowe, and V. R. Taylor of NOAA; Dr. J. Coakley of NCAR; Prof. R. Davies of Purdue University; Dr. Shashi Gupta and J. Robbins of Kentron Corp.; and R. Arduini of Information and Control Systems Co.

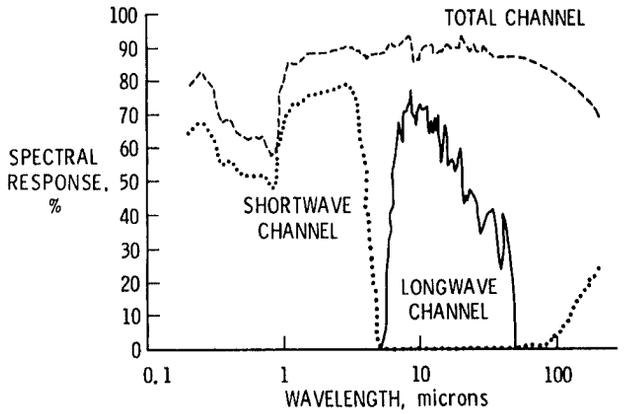

Fig. 1. Spectral responses of scanning radiometer channels.

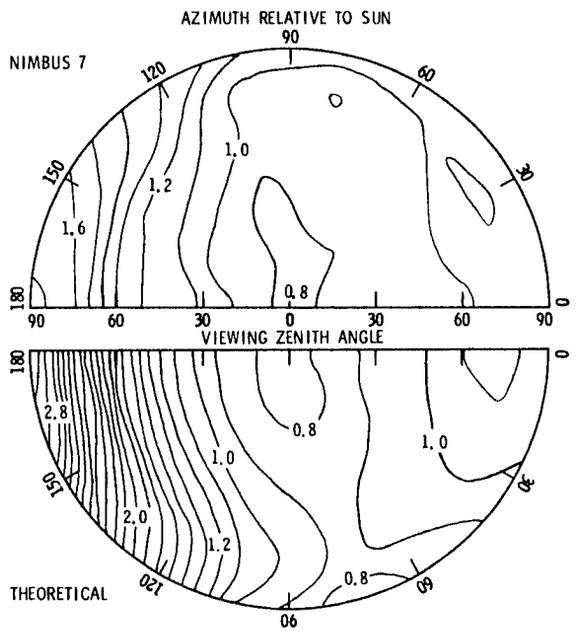

Fig. 2. Bidirectional functions based on Nimbus 7 ERB measurements and theory (from Stuhlmann et al., 1985).

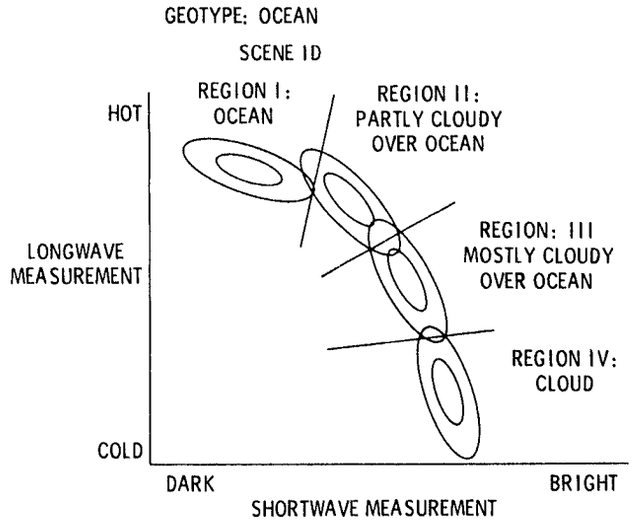

Fig. 3. Schematic of scene identification algorithm.

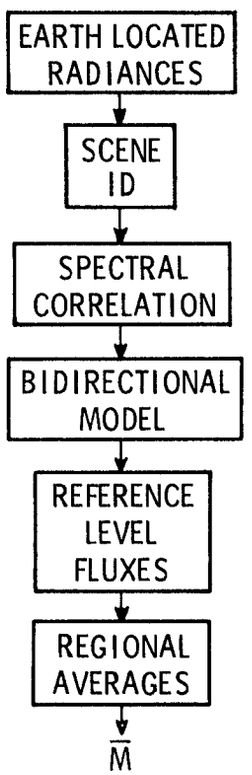

Fig. 4. Inversion processing steps.

J1.6

FIRST DIURNAL RESULTS FROM THE EARTH RADIATION BUDGET EXPERIMENT

Edwin F. Harrison, Patrick Minnis, and David R. Brooks

Atmospheric Sciences Division
NASA Langley Research Center
Hampton, Virginia 23665-5225

1. INTRODUCTION

The Earth Radiation Budget Experiment (ERBE) is currently flying aboard multiple satellites to provide improved temporal sampling for studying the diurnal variability of regional radiation over the world (Harrison et al., 1983 and Barkstrom, 1984). The first spacecraft of the ERBE mission, the Earth Radiation Budget Satellite (ERBS), was launched into a 57° inclined orbit during October 1984. This orbit has a nodal procession rate of about 5° per day relative to the Sun, so, with both day and night measurements, it covers 24 hours of local time in about 36 days at the Equator. The second satellite with ERBE instruments is the NOAA-9 spacecraft, which was launched in December 1984 into a Sun-synchronous orbit with equatorial crossing times of 0230 and 1430. The third ERBE satellite, NOAA-G, is scheduled for launch in March 1986. Its orbit will have equatorial crossing times of 0730 and 1930. This combination of satellites in different orbits will provide a significant improvement in the time and space sampling capability over previous single satellites designed for Earth radiation budget studies (e.g., Nimbus-7 ERB, see Jacobowitz et al., 1984). Each satellite of the ERBE mission has an instrument complement which includes a scanner (Kopia, 1986) with a 35-km spatial resolution, a medium-field-of-view nonscanner having a 1000-km resolution, and a wide-field-of-view nonscanner (Luther et al., 1986) that views the Earth from horizon to horizon. Both broadband shortwave (0.2- to 5.0-μm) and longwave (5.0- to 50.0-μm) radiation measurements are obtained from these instruments.

The purpose of this paper is to present some of the initial radiation results from the ERBS. Examples are given to demonstrate the diurnal variability of total and clear-sky regional radiative parameters. The ERBS results are also compared to inferred broadband measurements from the Geostationary Operational Environmental Satellite (GOES-6).

2. DATA ANALYSIS

November 1984 is the only month for which ERBS data have been completely processed and for which preliminary analysis has been completed at the time of this writing. This data set, however, is sufficient to illustrate the diurnal variability of Earth radiation parameters found over selected regions.

The analysis of the data involves several steps. First, each measurement is recorded in terms of instrument counts and then converted to broadband radiance by use of onboard calibration and spectral correction procedures (Smith et al., 1986). Secondly, each pair of longwave and shortwave radiances, or longwave radiance alone at night, is used in conjunction with the statistics of the radiances of Nimbus-7 ERB data (Taylor and Stowe, 1984) and a maximum likelihood estimate technique (Wielicki, private communication) to identify the scene of the ERBE measurements. The scenes are identified as either clear, partly cloudy, mostly cloudy, or overcast above the underlying geographical type (e.g., ocean, land, desert, or snow).

The instantaneous shortwave radiance at satellite altitude is then inverted to shortwave radiant exitance (SWRE) at the top of the atmosphere by applying an appropriate bidirectional model based on Nimbus-7 ERB data (Taylor and Stowe, 1984). The diurnal variation of albedo is then determined using the above SWRE value and applying directional models developed from Nimbus-7 ERB and GOES data (Brooks et al., 1986).

Instantaneous longwave radiant exitance (LWRE) is calculated from the longwave radiance and limb-darkening models (Taylor and Stowe, 1984). The hourly values of LWRE are generally determined from linear interpolation between satellite measurements; however, over land regions which have a significant diurnal variation in surface temperature (e.g., desert), a trigonometric model replaces the linear interpolation (Brooks and Minnis, 1984). Daily averages of the LWRE and SWRE or albedo are calculated from the hourly data, which consist of measurements or modeled values as described above. All of these results for each day are used in determining monthly-mean hourly and daily results for each 2.5° by 2.5° latitude-longitude region for the scanner and 5° and 10° regions for the medium- and wide-field-of-view nonscanners.

3. RESULTS

Figure 1 illustrates the variation of the monthly-mean hourly albedo and LWRE for November 1984 as determined from the ERBS scanner data taken over a southeastern Pacific Ocean region, located at 21.25°S and 136.25°W. The well-known dependence of albedo on solar zenith angle is evident in both the total and clear-sky results. A significant difference is exhibited between the total and clear-sky monthly-average hourly values. The integrated monthly mean albedo is 11% greater for the total than the clear-sky albedo due to

cloudiness. The monthly-average hourly cloud cover varies from about 42% near sunrise to about 60% at sunset based on analysis of GOES data over this region. Very little diurnal variability is observed in the LWRE (Fig. 1b). The total LWRE, however, is about 12% lower than the clear-sky longwave due to the middle- and high-altitude cloud cover.

The diurnal variability of albedo and LWRE over a high altitude desert in South America is shown in Figure 2. As a result of the monthly-average hourly cloud cover, which ranges from 20 to 40% over this region, the albedo for the total scene is approximately 8% greater than the clear-sky results. Both the clear-sky and total LWRE exhibit a strong diurnal cycle with a maximum value near mid-day and a minimum value at night.

4. VALIDATION

The key method selected for validation of the ERBE time and space averaging results involves the use of geostationary satellite (e.g., GOES) data. This high resolution, auxiliary data set provides hourly measurements of visible (0.5- to 0.7-μm) and infrared (10.5- to 12.5-μm) data with an 8-km spatial resolution. The GOES-6 (located near 107°W over the Equator) narrowband data are correlated to simultaneous ERBS data to obtain a quadratic spectral transfer function for estimating broadband radiances from narrowband data. For these correlations, the solar zenith angle, satellite viewing zenith and azimuth angles of ERBS and GOES are matched within a few degrees as in Minnis and Harrison (1984c). Preliminary correlations of GOES and ERBS data over the ocean are displayed in Figure 3 for shortwave radiation and in Figure 4 for longwave radiation. The multiple correlation coefficient between GOES and ERBS is 0.97 for both the longwave and shortwave results with an rms error of 4% for the longwave and 14% for the shortwave radiation. Although the inferred broadband radiance may not be as accurate as ERBS, GOES has the advantage of complete (hourly) local time sampling to help assess the ERBE's accuracy in accounting for the diurnal variability of the radiation quantities and cloud cover for areas within the GOES field of view.

Comparisons of total albedo and LWRE for the ERBS and GOES-6 are presented in Figures 5(a) and 5(b), respectively. Two sets of results are shown for the ERBS. The mean values of individual ERBS measurements, before directional modeling was applied, are compared with the monthly-average hourly values, which include the combination of ERBE measurements and directional modeling for albedo. When these combined results are compared to the GOES hourly data, good agreement is generally found. This demonstrates that ERBE's sampling and the data analysis algorithm account reasonably well for the diurnal variability of clouds, albedo, and LWRE. The ERBE albedo, however, is slightly higher than that of GOES in the afternoon when the cloud cover reaches a minimum as shown in Figure 5(c). These low-level clouds increase to a maximum amount at night. This diurnal cycle of cloudiness is typical for this region (Minnis and Harrison, 1984b). The cloud amounts in Figure 5(c) were derived from the high-resolution GOES data using the hybrid bispectral threshold technique of Minnis and Harrison (1984a).

The variability in the ERBE longwave mean hourly measurements is smoothed when linear interpolation was used to fill in the missing hours. The modeled ERBE results and GOES hourly data agree to within about 3%. This difference in LWRE may be due to differences in the spectral characteristics, limb-darkening models, and temporal sampling of ERBS and GOES. Because the clouds are near the ocean surface, very little diurnal variability is observed in the LWRE.

Another comparison of ERBS and GOES radiation parameters is illustrated in Figure 6 for a land region over western South America. Although considerable scatter is exhibited in the average hourly ERBE measurements, the results are again smoothed when the measurements are combined with models. Good agreement is generally obtained between modeled ERBE measurements and the GOES data for both albedo and longwave. The monthly-average hourly cloud cover (Fig. 6c) over this region is nearly constant except for a decrease at sunset.

5. CONCLUDING REMARKS

Preliminary radiation budget results have been presented for selected regions based on the November 1984 ERBS data. A brief description was given of the algorithms used in analyzing the ERBE measurements. Although these results are preliminary, significant differences were found between the total and clear-sky albedo as well as LWRE due to cloudiness. Various degrees of diurnal variability were observed in radiation parameters over the selected areas studied. The ERBE time-dependent results were validated by intercomparisons with GOES data. Future ERBE results will include measurements from two and, eventually, three satellites to further improve the temporal and spatial sampling capability for detailed diurnal studies of regional broadband radiation budgets over the entire Earth.

6. ACKNOWLEDGMENTS

The authors would like to express their appreciation to the following members of the ERBE Science Team for their contributions to the development of the ERBE time and space averaging algorithms: B. Barkstrom, R. Green and B. Wielicki of NASA Langley Research Center; G. Campbell and T. Vonder Haar of Colorado State University; J. Coakley and V. Ramanathan of NCAR; C. England and G. Hunt of Imperial College; D. Hartmann of the University of Washington; L. Stowe, R. Taylor, A. Gruber and A. Miller of NOAA; R. Kandel of Dynamique de CNRS Ecole Polytechnique; and W. Smith and L. Herman of the University of Wisconsin. In addition, we would like to especially thank Joyce Satran of System

Development Corporation for her contribution to the development and testing of the ERBE time and space averaging software and G. Gibson, D. Young and P. Spence of PRC Kentron for their contributions to the analysis and graphical presentation of the ERBE and GOES data.

7. REFERENCES

Barkstrom, B. R., 1984: The Earth radiation budget experiment (ERBE), Bull. Amer. Meteor. Soc., 65, 1170-1185.

Brooks, D. R. and P. Minnis, 1984: Comparison of longwave diurnal models applied to simulations of the Earth radiation budget experiment. J. Climate and Appl. Meteor., 23, 156-160.

Brooks, D. R., E. F. Harrison, P. Minnis, J. T. Suttles, and R. S. Kandel, 1986: Development of algorithms for understanding the temporal and spatial variability of the Earth's radiation balance. Reviews of Geophys., (in press).

Harrison, E. F., P. Minnis, and G. G. Gibson, 1983: Orbital and cloud cover sampling analyses for multisatellite Earth radiation budget experiments. J. Spacecraft and Rockets, 20, 491-495.

Jacobowitz, H., R. T. Tighe, and The Nimbus 7 ERB Experiment Team, 1984: The Earth radiation budget derived from the Nimbus 7 ERB experiment. J. Geophys. Res., 89, 4997-5010.

Kopia, L. P., 1986: The Earth radiation budget experiment scanner instrument. Reviews of Geophys., (in press).

Luther, M. R., J. E. Cooper, and G. R. Taylor, 1986: The Earth radiation budget experiment nonscanner instrument. Reviews of Geophys. (in press).

Minnis, P. and E. F. Harrison, 1984a: Diurnal variability of regional cloud and clear-sky radiative parameters derived from GOES data. Part I: Analysis method. J. Climate Appl. Meteor., 23, 993-1011.

_____ and _____, 1984b: Diurnal variability of regional cloud and clear-sky radiative parameters derived from GOES data. Part II: November 1978 cloud distributions. J. Climate Appl. Meteor., 23, 1012-1031.

_____ and _____, 1984c: Diurnal variability of regional cloud and clear-sky radiative parameters derived from GOES data. Part III: November 1978 radiative parameters. J. Climate Appl. Meteor., 23, 1032-1051.

Smith, G. L., R. N. Green, E. Raschke, L. M. Avis, B. A. Wielicki, and R. Davies, 1986: Inversion methods for satellite studies of the Earth's radiation budget. Reviews of Geophys. (in press).

Taylor, G. R. and L. L. Stowe, 1984: Reflectance characteristics of uniform Earth and cloud surfaces derived from Nimbus-7 ERB. J. Geophys. Res., 89, 4987-4996.

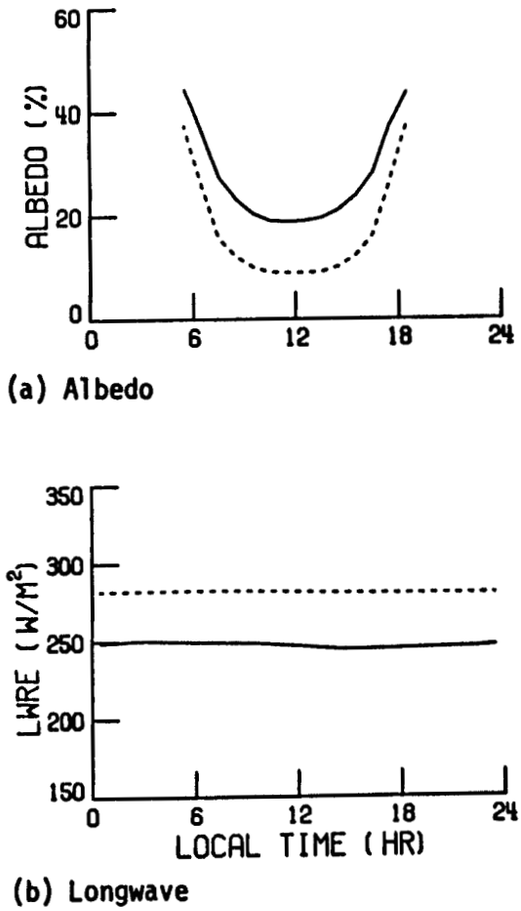

Figure 1. Radiative parameters for November 1984 from ERBS for a 2.5° x 2.5° ocean region at latitude = 21.25°S, longitude = 136.25°W. Dashed lines show clear-sky results and solid lines indicate data for the total scene.

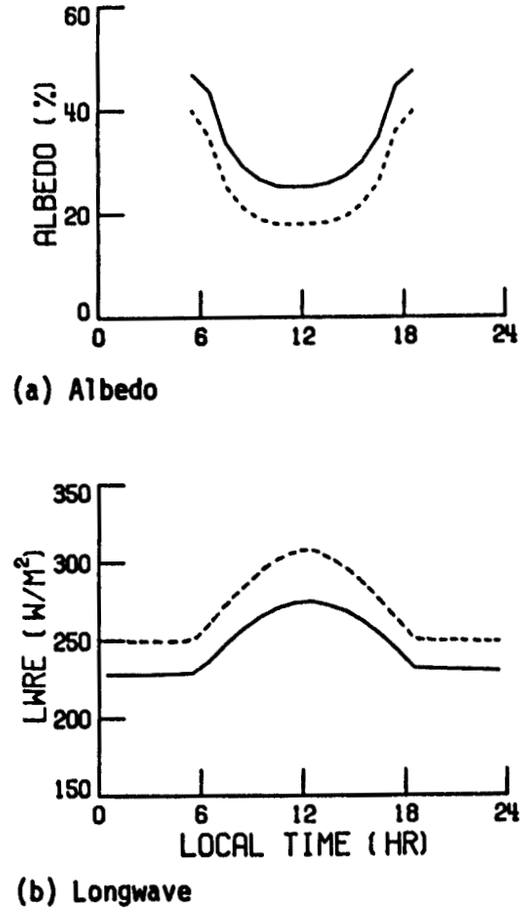

Figure 2. Same as figure 1 except for a land (desert) region at latitude = 21.25°S, longitude = 66.25°W.

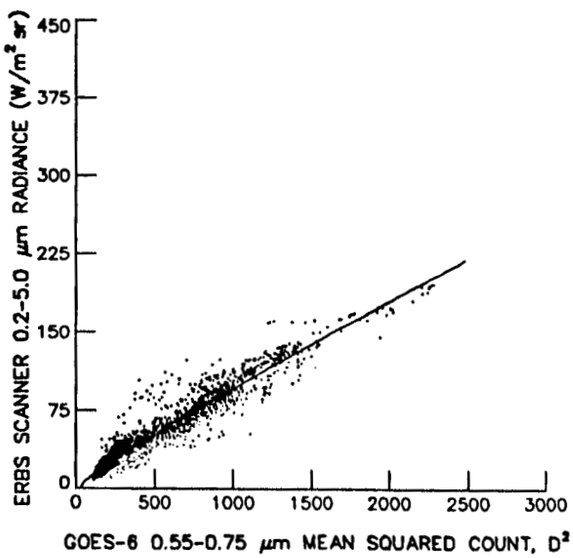

Figure 3. Correlation of GOES visible data with ERBS shortwave radiances over ocean for November 1984.

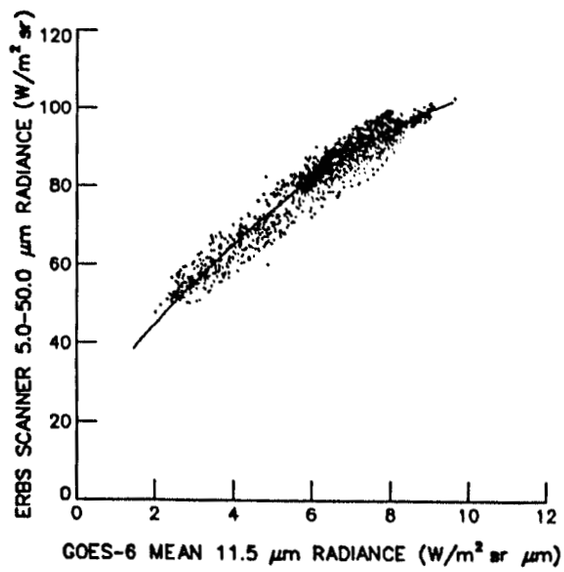

Figure 4. Correlation of GOES infrared and ERBS longwave radiances over ocean for November 1984.

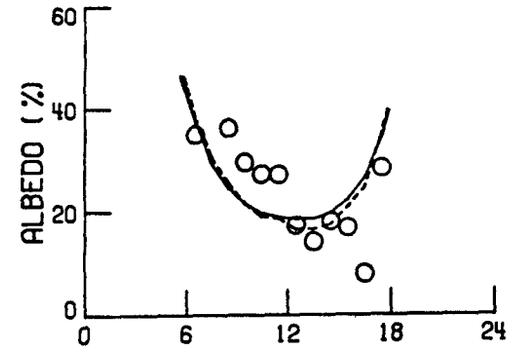

(a) Albedo

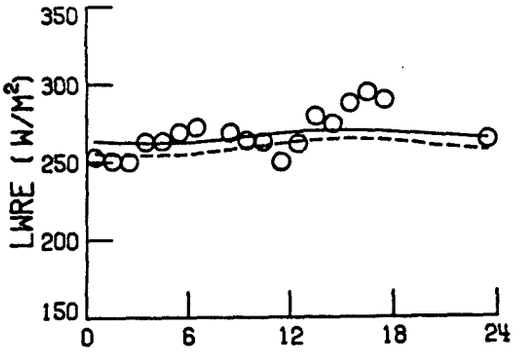

(b) Longwave

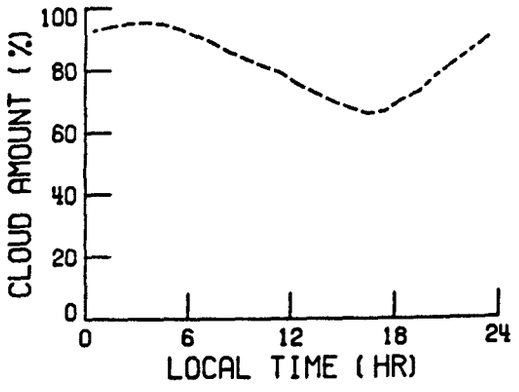

(c) Cloud cover

Figure 5. Radiative parameters and cloud amount for a 2.5° x 2.5° ocean region at latitude = 21.25°S, longitude = 81.25°W for November 1984. Solid lines indicate ERBS monthly-hourly data, dashed lines are GOES results, and circles show ERBS measurements before modeling.

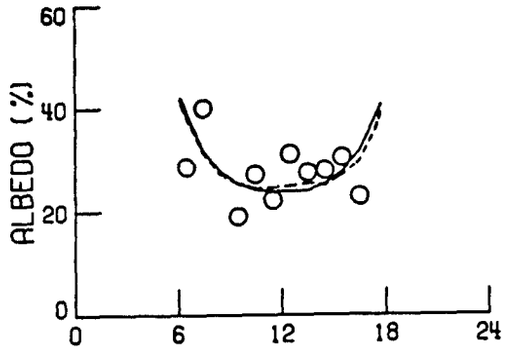

(a) Albedo

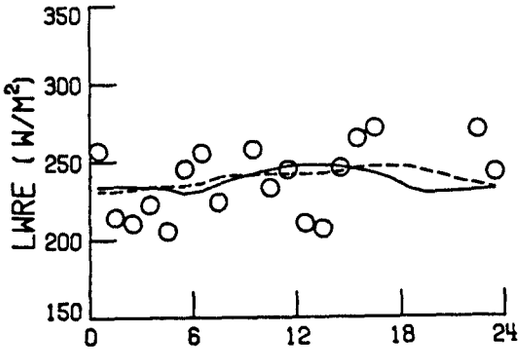

(b) Longwave

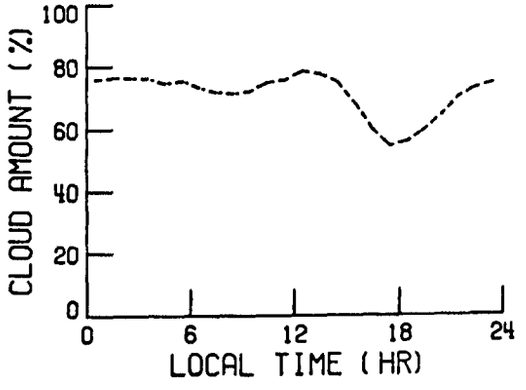

(c) Cloud cover

Figure 6. Same as figure 5 except for a land region at latitude = 21.25°S, longitude = 61.25°W.

REVISED REFLECTANCE AND EMISSION MODELS FROM NIMBUS-7 ERB DATA

V. Ray Taylor and Larry L. Stowe

NOAA/NESDIS
Washington, D. C. 20233

1. INTRODUCTION

At the Fifth Conference on Atmospheric Radiation(CAR5), Nimbus-7 ERB reflectance and emission models were described by Taylor et al. (1983a and b). These models were to be used in processing data from the Earth Radiation Budget Experiment(ERBE). At the time of CAR5, it was noted that the quality of the models might be improved by more accurately identifiying cloudiness associated with the Nimbus-7 ERB data.

Substantial improvements in the Nimbus-7 cloud detection algorithm have made it possible to rework the models and to increase the accuracy of their application in the processing of ERBE data. This paper will describe differences between the earlier models and the latest available version (hereafter, 'old' and 'new', respectively). For detailed information about Nimbus 7 ERB data, corollary data bases, and data processing methods, please see the CAR5 references as well as an earlier description of such models (Taylor and Stowe, 1984). A description of the new Nimbus-7 cloud detection algorithm and some initial results may be found in Stowe, et al.(1985).

Nimbus-7 cloud detection previously relied upon infra-red measurements from the THIR instrument and departures of equivalent black-body temperature from climatology. The inference of current surface temperatures from climatology and the lack of visible wave-length information both led to errors in cloud detection. This was especially true for low clouds in the tropics where the surface and cloud temperatures are often indistinguishable. The lack of reliable surface temperature information over land also precluded the development of accurate nighttime emission models. In the improved cloud detection scheme, a surface temperature analysis is utilized which comes from 3-hourly Air Force 3-D Nephanalysis data. In addition, reflectance data from an ultra-violet channel of the Nimbus-7 TOMS instrument is used in conjunction with THIR for cloudiness determination. Unfortunately, TOMS data were not available for the first 65 days of the old ERB data set. The new data set is then reduced to 205 days (from 270), and covers a period from April 1, 1978 to June 22, 1980.

Each reflectance or emission bidirectional model is comprised of parameters computed for specific ranges (bins) of illumination and viewing conditions and for a given surface type. These parameters include mean radiances (vis., IR), standard deviations (vis., IR), correlation coefficients and anisotropic factors (AFs). AF for each bin is defined as the ratio of the mean bin radiance to the equivalent isotropic radiance of the upwelling hemisphere. The AF is calculated by integrating the mean radiances of all bins over the upwelling hemisphere to obtain the outgoing flux, dividing the flux by pi (giving equivalent isotropic radiance), and dividing the result into each mean bin radiance. The outgoing flux is retained as a parameter of each model. For visible data, the ratio of this flux to the incoming solar flux is the albedo. For each surface type, the relationship between albedo and solar zenith angle constitutes a directional reflectance model.

In the ERBE application, a flux estimate is made by dividing an observed radiance by the appropriate AF and multiplying by pi. The other model parameters are used in making the scene type determination.

The new models for ERBE have been developed for 10 surface types. Four of these (ocean, non-desert land, desert and snow/ice) are for nominally clear (<5% cloud) conditions. The remaining six surface types are for 'partly cloudy' (5-50% clouds), 'mostly cloudy' (50-95% clouds) and 'overcast' (>95% clouds), each over underlying surfaces of uniform (>95%) land (including deserts) or water. We have not yet developed revised models for other mixed (coastal) or cloud level (low, middle, high) surfaces, though these will be investigated in the near future. In the current ERBE application, coastal situations are dealt with by averaging ocean and land models for corresponding cloud conditions.

2. REFLECTANCE MODELS

To evaluate the changes from the old to new reflectance models, we have examined contour plots of anisotropic factor as well as tabular listings of these and the other model parameters. No contour plots are shown here since these patterns remained largely unchanged. Examples may be found in Taylor and Stowe (1984). The directional reflectance models have been plotted and these will be used to illustrate the changes between the old and the new data.

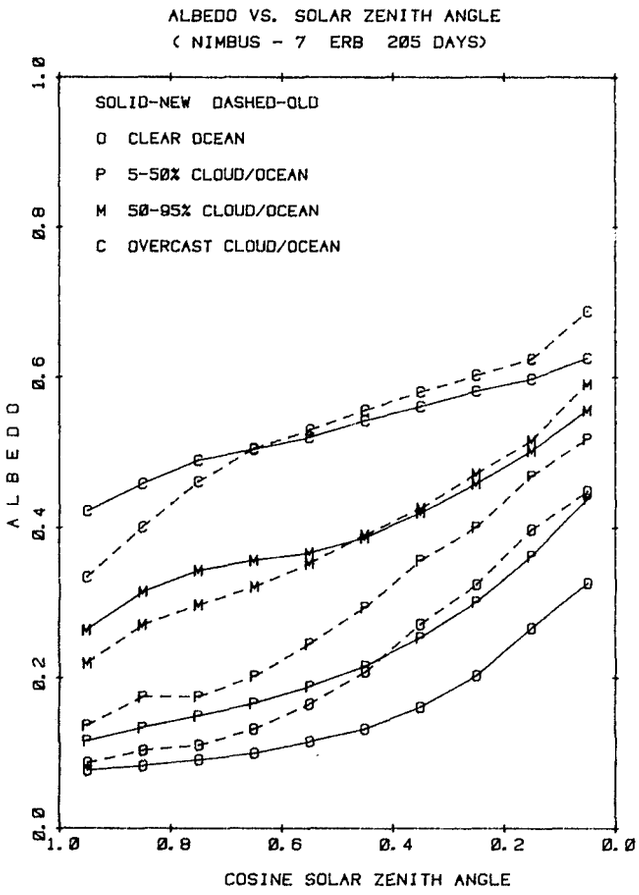

Fig. 1 Directional reflectance models for ocean and cloud over ocean.

Fig. 1 shows a comparison of visible directional models for the four cloudiness conditions associated with underlying uniform ocean surfaces. The greatest changes occur for clear and partly cloudy sky conditions. Because the albedos and standard deviations of bin radiances for clear ocean are very much smaller in the new data, it is obvious that contaminating cloudiness in the old model has been largely removed. The new directional reflectance model for clear ocean is also in good agreement with a corresponding model derived from GOES data by Minnis and Harrison (1984).

Changes in the partly cloudy curve very much parallel the changes for clear ocean, showing that these observations have also undergone considerable redistribution. For small solar zenith angles the overcast curve has become more linear and the mostly cloudy curve less linear. The new versions of these two curves are more parallel than the old curves. Because of the correlation between solar zenith angle and latitude in the ERB data, smaller solar zenith angles correspond to tropical regions. It is in the tropics where the old cloud algorithm was recognized to be most faulty in systematically underestimating the amount of low clouds.

In the processing of ERBE data, a single albedo vs. solar zenith angle function is used in the identification of ERBE data with a particular surface type and later also to convert an instantaneous flux into a daily average. Directional reflectance models must be optimized for both applications.

Fig. 2 shows a similar set of albedo curves for varying amounts of cloud over land. For the clear condition, only non-desert land is included, with desert being considered seperatly. Desert is included with all other land types where any significant amount (½5%) of cloud is present. Land is comprised of surfaces whose reflectance varies widely as a result of changing vegetation and topography. To the extent that the mixture of land types varies with latitude, the albedo curve will also vary. This effect would be most noticable for clear conditions and would lessen as the land becomes more obscured by cloudiness.

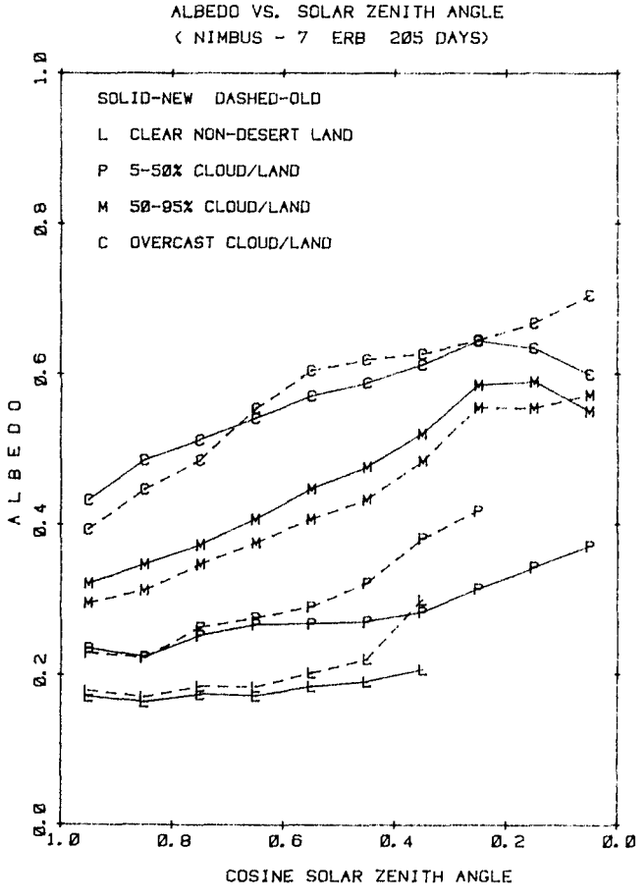

Fig. 2 Directional reflectance models for non-desert land and cloud over land.

The new albedo curves for clear land and partly cloudy over land are uniformly and slightly darker than the old curves for solar zenith angles less than approx. 65 deg. For larger solar zenith angles, corresponding to polar regions, populations become small and the computed albedo becomes more uncertain. The mostly cloudy/land curve for the new data almost exactly parallels the old curve and has a uniformaly higher albedo, except for the final point at near grazing sun angles (84-90 deg.). We are uncertain why both mostly cloudy and overcast curves indicate a decreasing albedo in the last two solar zenith angle intervals. The shape of the old curve for mostly cloudy does show an indication of the downturn. The old overcast curve also includes cloud over snow (the new does not). The old curve might have showed the downturn if snow were excluded from it, but such an operation

cannot now be easily done. We have constructed curves from the new data where overcast over snow is not excluded and find that the downturn disappears. A possible explanation for the low-sun darkening may involve intensified cloud shadow effects at grazing sun angles. Such effects might be missing over oceans in polar regions at least, since these overcasts might not be as cumuliform as over land.

Albedo curves for the remaining surfaces, snow/ice and deserts, are shown in fig. 3 for the old and new data. For deserts, the uniform darkening is probably largely due to the use of TOMS data in the cloud detection algorithm. In the ultra-violet, deserts and other land types appear about as dark as oceans and are highly contrasted with clouds. This means that scattered cloudiness over the typically warm surface of the deserts could have been mis-identified as clear in the old data and more easily detected by the new algorithm.

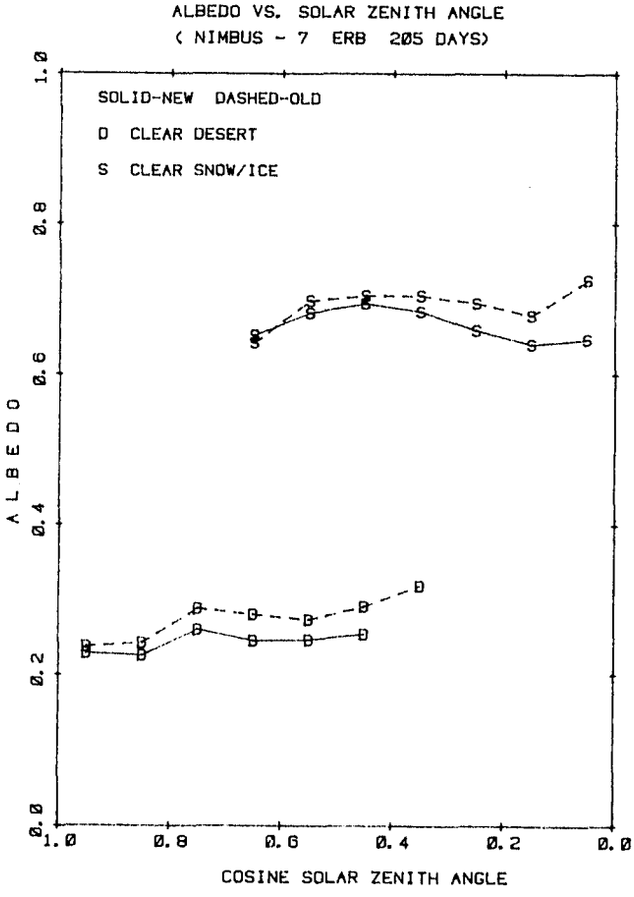

Fig. 3 Directional reflectance models for desert and snow surfaces.

TOMS data is not used to detect cloudiness over snow, since the reflectance of these two surfaces is similar in the u/v. Also, the surface temperature analysis is also not used for Antarctica and leaves the treatment of data in that region virtually unchanged. Two antarctic summers were represented in the old data set while only one is in the improved data. Since icecap snow is generally more reflective than snow in other regions, its diminished amount causes the average albedo to be slightly lower.

3. EMISSION MODELS

Emission models for ERBE using the old cloud detection algorithm were developed for daytime only. Especially over land, cloud amounts could not be estimated with sufficient accuracy to develop reliable nighttime emission models. The use of near-current surface temperature analyses in the new algorithm has alleviated this restriction and nighttime models for all 10 ERBE surfaces have been created.

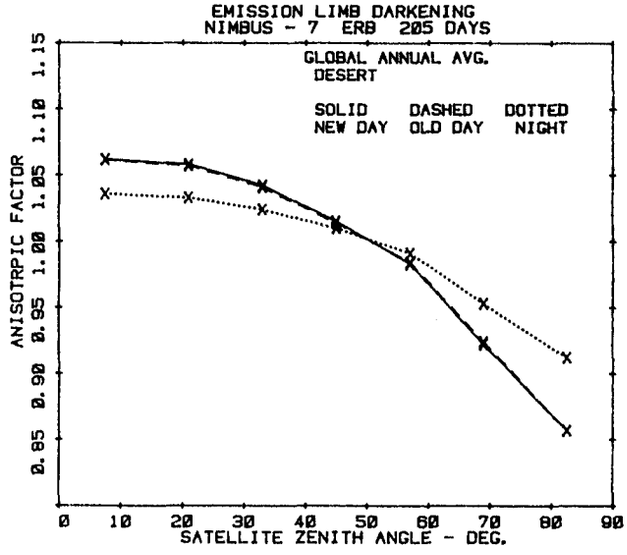

Fig. 4 Anisotropic emission functions for clear desert.

Daytime and nighttime emission models are constructed for each surface type by calculating the anisotropic factor as a function of satellite zenith (viewing) angle only, within each of the four seasons and ten equal intervals of latitude. The emission is assumed to be azimuth independent. Not all of the 800 possible combinations are sufficiently populated to calculate reliable models and some are missing altogether. For example, no data at all exists for snow/ice models in the tropics or for deserts at polar latitudes. For those models which are well populated, a preliminary examination shows very few significant changes between the old and new data (daytime only).

To efficiently show overall changes between old and new daytime emission models and the difference between these and the nighttime models, AFs and emitted radiances were averaged over the seasons and latitude zones. Fig. 4 shows global annual averages of desert anisotropic emission factor for old daytime, new daytime, and nighttime. This particular surface type is selected as an example since it shows a large amount of limb-darkening in the daytime as well as a large difference between the daytime and nighttime. Of such global annual averages, only clear non-desert land shows values almost as large for both limb-darkening and day/night difference. All of the other surface types show much smaller values for both quantities. Individual models for particular seasons and latitude zones may be quite different from the global annual average, though these are few in number. For example, partly cloudy land areas in the tropics at a given season, do show even

larger limb-darkening amounts than deserts. In this instance, though, the change from daytime to nighttime is not be as great.

By comparing the set of curves in fig. 4 with the upper set of curves in fig. 5, the relationship may be seen between anisotropic factors and bin averages of emitted radiance. The former are derived from the latter by dividing the radiance average of each bin by the emitted flux (proportional to the area under the curve) and multiplying by pi. Also shown in fig. 5 are the radiance curves for snow/ice. These are the least limb-darkened of the surface types considered. The emission values for overcast cloud are generally similar to snow, but cloud shows more limb-darkening, probably because of foreshortening effects associated with vertical temperature structure. That is, when viewing vertically developed clouds at progressively larger viewing angles, higher and colder surfaces obscure lower and warmer ones seen from more vertical views. This can have much the same effect as limb-darkening due to atmospheric absorption.

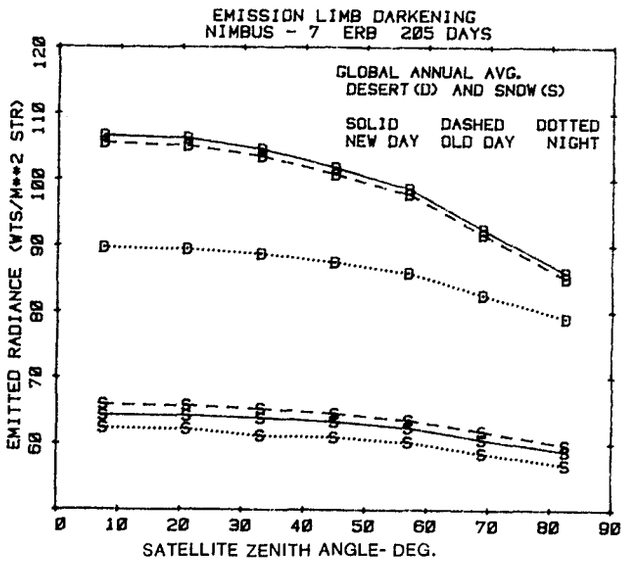

Fig. 5 Emitted radiance averages for desert and snow surfaces.

In figs. 4 and 5 it may be seen that emission changes from the old to the new data sets are quite small. This seems to be generally true for global annual averages of the other surfaces as well. Significant changes from daytime to nighttime are seen mostly for clear land and desert and these changes are progressively smaller as more cloud obscures the underlying surface.

4. CONCLUSIONS AND FUTURE STUDIES

The Nimbus-7 cloud detection algorithm has been improved in 2 ways. First, surface temperatures are now based upon 3-hourly current analyses rather than being estimated from climatology. Secondly, it is now possible to detect clouds using ultra-violet data from the TOMS instrument in addition to the infra-red measurements of the THIR instrument. The most noticeable effect of these changes is the more accurate detection of low clouds and the ability to accurately estimate cloud amount at night.

Generally, the bi-directional patterns of anisotropic reflectance factor did not change significantly in the new models. For clear ocean, however, while the patterns remained relatively unchanged, the bin standard deviations of visible radiance were very much lower. Significant changes in the directional reflectance models were noted for clear ocean, partly cloudy over ocean, overcast over ocean in the tropics, and both mostly cloudy and overcast over land in polar regions.

Changes between old and new daytime emission models are generally quite small. Also, changes between new daytime and nighttime emission models are small for most surfaces. Desert and non-desert land do vary significantly from day to night, as does, to a lesser extent, partly cloudy over land.

In the application of anisotropic emission functions, it has been assumed that the first and last values of each function extend to satellite zenith angles of 0 and 90 deg., respectively. It is known that some bias in the flux estimate could be introduced by this assumption since the data are not evenly distributed across these bins. In the near future, other analysis schemes involving curve fitting and higher resolution zenith angle bins will be tried.

We will develop reflectance and emission models for different cloud levels and types and are especially interested in the detection of cirrus and the study of its radiative properties. The directional reflectance models which were shown here may also evolve as we seek to properly interpret latitude effects inherent in the Nimbus-7 ERB data set. One of our recent studies, in progress, indicates that the directional models for clouds are composites of relationships that change with latitude according to a changing mixture of cloud types.

5. REFERENCES

1. Minnis, P. and E. F. Harrison, 1984: Diurnal Variability of Regional Cloud and Clear Sky Radiative Parameters Derived from GOES Data. Part III: November 1978 Radiative Parameters, Journal of Climate and Applied Meteorology, Vol. 23, No. 7, pp. 1032-1051.

2. Stowe, L. L., P. P. Pellegrino, P. H. Hwang, P. K. Bhartia, T. F. Eck, C. G. Wellemeyer, S. M. Read and C. S. Long, 1985: Validation of Nimbus-7 Cloud Products, Proc. Intn'l Rad. Symp., A. Deepak Pub., 228-231.

3. Taylor, V. R., L. L. Stowe and J. M. Vilardo, 1983: Nimbus-7 ERB Reflectance Models for ERBE Processing, AMS Fifth Conference on Atmospheric Radiation, Baltimore Maryland.

4. Taylor, V. R., J. M. Vilardo, L. L. Stowe and S. K. Vemury, 1983: Nimbus-7 ERB Emission Models for ERBE processing, Fifth Conference on Atmospheric Radiation, Baltimore Maryland.

5. Taylor, V. R. and L. L. Stowe, 1984: Reflectance Characteristics of Uniform Earth and Cloud Surfaces Derived from Nimbus-7 ERB, Journal of Geophysical Research, Vol. 89, No. D4.

ERBE BIDIRECTIONAL MODEL CONSISTENCY CHECK

D.G. Baldwin, and J.A. Coakley, Jr.

National Center for Atmospheric Research *
Boulder, Colorado 80307

1. INTRODUCTION

ERBE relies on scene identification and directional models to convert radiances observed with the ERBE scanner to radiant exitances. Errors in both scene identification and directional models thus contribute directly to errors in the estimated exitances. Here we attempt to isolate potential errors in the directional models.

2. BIDIRECTIONAL MODELS

ERBE derives its directional models and its scene identification procedures from the results of the NIMBUS-7 ERB experiment. The ERB scanner has a spatial resolution (90 km)^2 that differs from those of the ERBE scanner (30 km)^2. The radiometric calibrations of the two instruments may also differ. Because the dependence of reflected radiances on emitted radiances is a nonlinear function of scene type, we would expect that both the procedures for scene identification and the directional models used by ERBE to be affected by differences in the spatial resolutions of the two instruments, if not by the possible differences in their radiometric calibrations. To determine how such differences might affect ERBE results, we use the ERBS scanner to derive pseudo-directional models and compare these models with the ERB derived counterparts. Should the two models agree, errors caused by differences in calibration and spatial resolution could safely be judged as insignificant.

To derive the directional models from the ERBS scanner data, we make the assumption common to all previous developments of directional models– namely that on average, the radiant exitance associated with a particular scene is independent of the viewing geometry, the geographic location and the time of observation. This assumption allows us to derive pseudo-directional models directly from the ERBS unfiltered radiances. The pseudo-directional model for bin i, ρ_i, is given by

$$\rho_{li} = \frac{< m_l >_i}{2/\pi \sum_i \mu_i < m_l >_i \Delta\mu_i \Delta\phi_i} = \frac{< R_l >_i}{2/\pi \sum_i \mu_i < R_l >_i \Delta\mu_i \Delta\phi_i} \qquad (1)$$

where script m_{li} is the ERBS unfiltered radiance for model l and bin i; R_{li} is the bidirectional reflectivity for model l and bin i; μ_i is the cosine of the solar zenith angle, ϕ_i is the azimuth angle, and the product $\Delta\mu_i\Delta\phi_i$ represents the bin area. The averaged quantities in (1) are over all pixels in bin i. The sum in the denominator of (1) is over all bins containing at least some minimum number of observations. We call the model "pseudo" because the ERBS orbit fails to capture data for some of the angular bins.

3. IMPACT OF ERRORS

To assess the implication of these differences for the ERBE derived radiant excitances, we compute differences in the excitances typical of 2.5° latitude longitude boxes. We also intend to develop models with ERBE scanner data at degraded resolution in order to study the influence of spatial resolution on scene identification and the directionality of the observed radiances.

ACKNOWLEDGEMENTS

This work was supported by NASA-ERBE grant L9477B.

* The National Center for Atmospheric Research is sponsored by the National Science Foundation.

LIMB-DARKENING FUNCTIONS FOR THE EARTH-ATMOSPSHERE SYSTEM OVER DESERT SCENES

David R. Brooks

Atmospheric Sciences Division
NASA Langley Research Center
Hampton, Virginia

1. INTRODUCTION

The radiant energy balance of the Earth's deserts is currently of particular interest because such areas have not yet been studied extensively from satellites that have been subjected to rigorous radiometric calibration. Data from the Earth Radiation Budget Experiment (ERBE) have been used to examine the behavior of longwave (LW) radiance as a function of viewing zenith angle for three major desert regions: the Sahara, the Saudi Arabian Peninsula, and Australia. This study has led to a better understanding of the limb-darkening function for desert scenes and has also shed some light on the problems of automated scene identification algorithms as applied to large sets of satellite data.

The Earth Radiation Budget Experiment has provided a number of opportunities for studying the behavior of desert-atmosphere systems. Most of the major surface features of the Earth are visible from the 57° orbit of the Earth Radiation Budget Satellite (ERBS). In addition to its usual crosstrack scanning mode, the ERBE scanner instrument has also been operated in an alongtrack mode. This mode is ideal for examining the limb-darkening phenomenon because any point along the satellite groundtrack may be viewed from a complete range of viewing zenith angles at essentially constant solar zenith angle. Preliminary processing in the alongtrack mode has been done for January 19, 23, and 27, 1985. The November 1984 crosstrack data are also available for studying the limb-darkening problem. In this case, the crosstrack data for a particular region and day have been averaged at each scan position of the scanner instrument and associated with the mean viewing zenith angle at each scan position.

2. THE LIMB-DARKENING PHENOMENON

The variation of LW radiance with viewing zenith angle is a result of absorption along the increasing atmospheric path length between the instrument and the point being viewed on the surface. Nearly all surfaces (including cloud "surfaces" over most parts of the Earth) are limb-darkened, i.e., they appear colder when viewed from a large zenith angle. For a plane-parallel atmosphere, the path is proportional to the secant of the viewing zenith angle. For a spherical Earth-atmosphere system, the Earth's curvature prevents the path length from approaching infinity as viewing zenith angle approaches 90°. The LW radiance may be represented by an equation of form

$$L(\theta) = L_0 P^x \qquad (1)$$

where P is the ratio of atmospheric path length at viewing zenith angle θ to overhead atmospheric path length and L_0 is the radiance measured at a viewing zenith angle of 0°. This formulation applies to an optically thin atmosphere--loosely speaking, one for which the atmosphere never totally obscures the underlying surface--and, with regard to the distinctions made in the early paper by Schwarzschild (1906), implies that the Earth's atmosphere is in adiabatic rather than radiative equilibrium. This simple one-parameter formulation has been shown to agree well with detailed radiative transfer calculations applied to satellite data (Gupta, 1983; Gupta et al., 1985).

It is often the case that ERBE LW radiances are poorly represented by a single-parameter path length formulation applied to a full range of viewing zenith angles. A modified function of form

$$L(\theta) = L_0 p^x - a[p(\theta) - p(\theta = 60^o)],\ \theta > 60° \qquad (2)$$

has been used to represent the ERBE data for viewing zenith angles greater than 60°. The "extra" term in equation (2) must account for a variety of contributors to the observed limb darkening at large viewing angles. These include the increasing opacity of the atmosphere and possible saturation of the atmopsheric transmittance, the point spread function of the ERBE scanner instrument, the contamination of the ERBE field-of-view with space-viewing pixels as the optical axis of the scanner approaches the horizon, and the increasing size and decreasing homogeneity of the scene in the ground footprint as viewed from the fixed-field-of-view instrument. The last of these effects may result in cloud contamination of the clear scene and may lead to increased ambiguity in the scene identification process.

The geometric and electronic effects of the ERBE scanner are accounted for in the operational processing software. The correction for space contamination of the field of view at large viewing zenith angles is

insignificant for the operational ERBE processing, as the LW radiances are not inverted to LW radiant exitance for viewing zenith angles large enough to be affected by space-view contamination. However, it is relevant for specific studies of limb darkening, and has been included in the present analysis.

3. CLEAR SCENE IDENTIFICATION FOR DESERT SCENES

Data from the ERBE have the apparent advantage of having been identified as to the underlying geography and separated into four cloud categories: clear, partly cloudy, mostly cloudly, and overcast. The scene identification algorithms are statistical in nature and can be expected to perform erratically over highly variable surfaces where there is an insufficient data base of meteorological or climatological information to support a threshold-driven scene identification approach. In addition, the "clear" category accepts a cloud contamination of up to about 10%. Two specific problems with identification of clear desert surfaces are first, the difficulty of assigning fixed infrared thresholds for surfaces with large diurnal variability and, second, the added complexity of the cloud identification problem when the underlying surface is very bright.

Significant cloud cover may regularly be found over the African and Australian deserts during November. It is generally true that for many desert conditions, the ERBE scene identification is a function of viewing zenith angle. Specifically, desert scenes observed from large viewing zenith angles are often more likely to be identified as partly or mostly cloudy than scenes observed from overhead. This does not cause difficulties in the overall ERBE evaluation of the radiating properties of the scene, but it will in applications that seek to evaluate, for example, limb darkening for specific clear scene types. Stated another way, examination of the ERBE data supports the view that the scene identification process becomes ambiguous largely because the increasing atmospheric opacity at larger viewing zenith angles tends to minimize the difference in LW radiance among the various scene types.

The ERBE scene identification performance for three selected desert scenes during the January 1985 alongtrack scanner operation is illustrated in Table 1. In each case, the scene identifications have been grouped according to viewing zenith angle, in 10° bins. The total number of measurements in each bin is given for the "all" classification. For each scene classification, the fraction of the total measurements falling in that classification is given. If the scene classification is independent of viewing zenith angle, the fraction for each scene type should be constant for each viewing zenith angle bin.

Each set of data represents a single ERBS flyover of a desert region. These regions encompass most of the western half of Australia, the Sahara, and the Saudi Arabian Peninsula. In all cases, coastal areas are avoided to prevent contamination of the scene with ocean views. As each flyover takes only a few minutes, the solar zenith angle is nearly constant during the flyover. On the "inbound" leg of the flyover, the measurements are made at essentially constant relative azimuth; on the "outbound" leg, the relative azimuth is shifted by 180°. The specific conditions illustrated in Table 1 are individual cases and not necessarily representative of the overall behavior of the regions.

The data used to generate Table 1 are illustrated graphically in Figures 1-3. For each scene type, the dependence of LW radiation on viewing zenith angle may be seen. A characteristic feature of the ERBE LW data is the increasing ambiguity among clear and cloudy scene classifications as viewing zenith angle increases whenever the algorithms detect a mixture of clear-cloudy conditions, especially during the day. This effect is notable in the Australian data. Note also in the Australian data the large azimuthal asymmetry in the overcast scene; this is thought to be caused by a combination of ambiguity about the scene when viewed from opposite directions relative to the Sun and a real difference in the appearance of cloudy scenes under these opposite conditions. The nighttime Sahara data do not exhibit any azimuthal asymmetry, but the scene ambiguity for viewing zenith angles greater than 60° is still evident. In the Saudi scene, viewed on the same day and also at night, the ERBE scene identification algorithms detected only clear surfaces. In this case, the limb-darkening curve is remarkably smooth. These results are consistent with an analysis of cloud identification from satellites using GOES data (Minnis, 1986); this study concluded that overestimation of cloud fraction (especially for high clouds and total cloud cover) is relatively insignificant for viewing zenith angles less than about 50°, but increases rapidly when the viewing zenith angle exceeds about 60°, and that this problem is most severe for total and high cloud cover.

4. PARAMETERIZATION OF LIMB-DARKENING FUNCTIONS

Limb darkening for clear desert scenes has been parameterized according to equations (1) and (2). The results for the data of Figures 1-3 are shown in Table 2. The difference in the levels of limb darkening between the Sahara-Saudi, and Australian deserts, as expressed by the parameter x, reflects the fact that the Australian scene is observed during daytime in the Southern Hemisphere's late spring season. Therefore, the surface temperature and water vapor profiles, the two dominant factors in limb darkening, may differ greatly from their Northern Hemisphere counterparts.

In principle, the day-to-day variability of of limb darkening due to fluctuations in surface temperature and atmospheric composition can be examined with the aid of daily data from the November 1984 ERBE crosstrack scanner. The limb-darkening phenomenon has been parameterized for all the Sahara and Saudi Arabian Peninsula data for November 6-30. The data have been separated into daytime and nighttime measurements, and a summary of the limb-darkening parameters are presented in Table 3. Although it is true that desert scenes are more limb-darkened at night than they are during the

day, as expected, the wide variation in the parameters reflects the fact that each daily set of daytime or nighttime data taken in the crosstrack scanning mode is a composite of measurements taken in different places at different times.

5. CONCLUSIONS

These preliminary ERBE results have been used for testing and validation of the operational software and data products. It should be stressed that there is presently no evidence that the current operational ERBE limb-darkening models will produce significant error in estimates of LW radiant exitance over long temporal or large spatial scales. However, it is clear that a better understanding of the ERBE LW measurements, with some parameterization along the lines suggested above, is required to interpret and characterize the radiative behavior of individual scenes as a function of specific viewing and solar conditions. Toward this end, the ERBE data need to be decoupled as much as possible from their intimate association with a particular set of scene identification algorithms, geographical distributions, and instrument constraints. Because of the nearly ideal conditions under which the alongtrack scan mode obtains measurements of LW radiance, these data merge as the best hope for fruitful investigation of the limb-darkening phenomenon. It has been demonstrated that a simple path length parameterization of ERBE radiances can be used to characterize and differentiate among surface types when this parameterization is restricted to viewing angles no greater than 60°.

6. REFERENCES

Gupta, S. K., 1983: A radiative transfer model for surface radiation budget studies. J. Quant. Spectrosc. Radiat. Transfer, 29, 5, 419-427.

Gupta, S. K.; S. N. Tiwari, C. S. Vemuru, and J. T. Suttles, 1985: Infrared limb-darkening effects for the Earth-atmopshere system. AIAA Journal, 23, 3, 405-409.

Minnis, P., 1986: Viewing zenith angle dependence of cloudiness from satellites. J. Geophs. Res., submitted, 1986.

Schwarzschild, K., 1906: On the equilibrium of the sun's atmosphere, as published in the Nachrichten von der Königlichen Gesellschaft der Wissenschaften zu Göttingen. Math.-phys. Klasse, 195, p. 41, and reprinted in Selected Papers on the Transfer of Radiation, ed. D. H. Menzel, Dover Publications, N.Y., 1966.

Table 1.

Desert scene identification as a function of viewing zenith angle from selected ERBE measurements

Scene	Date	Scene type	Viewing zenith angle, deg 0-10	10-20	20-30	30-40	40-50	50-60	60-70	70-80
Australia	19 Jan.	all	402	403	401	404	405	389	316	204
(θ_0 = 57°, pm)		clear desert	.42	.42	.40	.37	.38	.35	.28	.04
		partly cloudy	.21	.21	.24	.26	.21	.29	.37	.59
		mostly cloudy	.15	.17	.18	.19	.23	.24	.23	.37
		overcast	.20	.19	.17	.18	.19	.12	.11	.00
Sahara	19 Jan.	all	759	809	805	792	773	767	620	405
(θ_0 = 122°, am)		clear desert	.73	.73	.72	.70	.76	.72	.71	.71
		partly cloudy	.14	.14	.16	.16	.11	.14	.13	.09
		mostly cloudy	.11	.10	.09	.10	.10	.08	.10	.14
		overcast	.02	.03	.03	.03	.03	.05	.06	.05
Saudi	19 Jan.	all	257	258	256	256	257	257	198	133
(θ_0 = 108°, pm)		clear desert	1.00	1.00	1.00	1.00	1.00	.99	.98	.96

Table 2

Limb-darkening parameters for selected desert scenes from the January 19, 1985, ERBE along-track data set

Region	θ_0, deg	x	$a(\theta_0>60°)$
Australia	57 (pm)	-0.2116	3.184
Sahara	122 (am)	-0.0998	1.854
Saudi	108 (pm)	-0.0974	1.241

Table 3

Summary of limb-darkening parameters for November 6-30, 1984, ERBE crosstrack LW measurements in the Sahara and Saudi Arabian Peninsula

$\bar{x}$	s_x	$\bar{a}$	s_a
Daytime			
-0.1360	0.0285	1.2645	1.8673
Nighttime			
-0.1080	0.0287	1.0104	1.4603

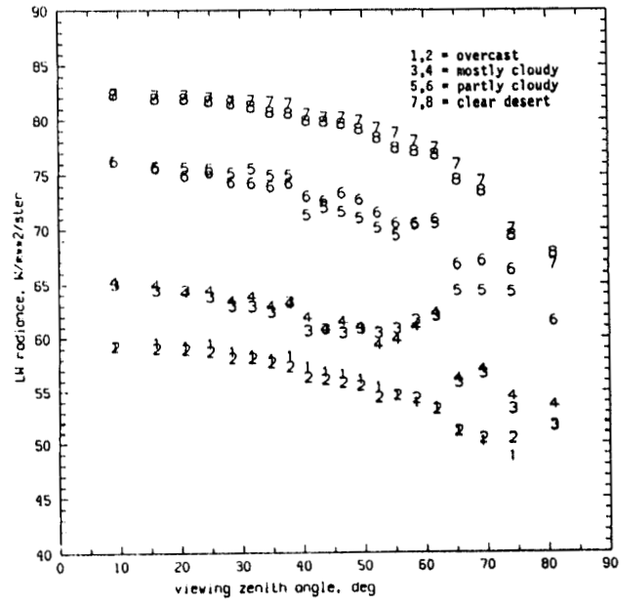

Figure 2. LW radiance vs. viewing zenith angle over the Sahara.

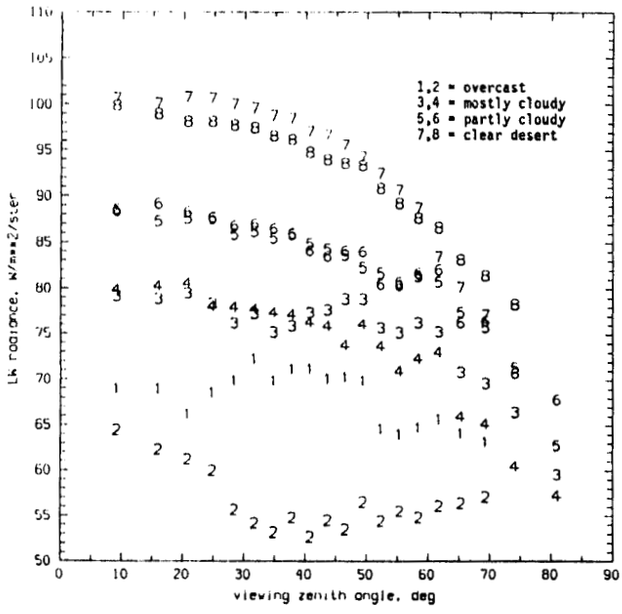

Figure 1. LW radiance vs. viewing zenith angle over Australia.

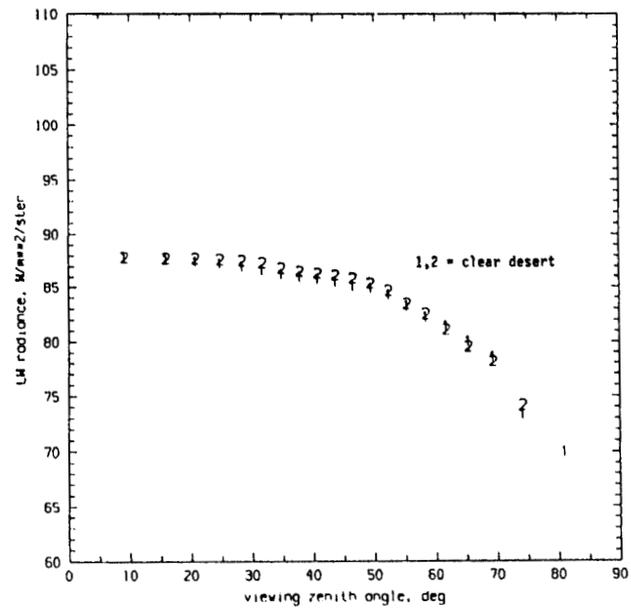

Figure 3. LW radiance vs. viewing zenith angle over the Saudi Arabian Peninsula.

AN APPROACH FOR VERIFYING CLEAR-SKY RADIATION MODELS WITH ERBS SCANNER MEASUREMENTS

V. Ramanathan and P. Downey

National Center for Atmospheric Research *
Boulder, Colorado 80307

1. INTRODUCTION

One of the unique features of the earth radiation budget experiment (ERBE) is that, for the first time in the history of the earth radiation budget (ERB) measurement program, it will provide on a routine basis, estimates of clear-sky top-of-the atmosphere longwave and solar radiation fluxes. This additional feature will enable ERBE to address two key issues that are of fundamental importance to climate. The first issue concerns verification of clear-sky radiation treatment in climate models and the second issue concerns the estimation of cloud-radiative forcing from ERB measurements (e.g., see Ramanathan, 1985).

In this study, we explore the possibility of using ERBE clear-sky longwave radiances for validating radiation models. This is accomplished by attempting a detailed intercomparison of measured and computed radiances. The purpose of this paper is more to outline the novel and rigorous approach adopted for the validation than to cite the results. Nevertheless, we will cite results to illustrate the validity of our approach. However, the results should be considered preliminary since ERBE algorithms that convert the radiometer "signature" to radiances and fluxes are currently undergoing a detailed validation process. Indeed, studies such as the present one are part of the comprehensive validation program that is being undertaken by the ERBE project.

2. THE DATA SELECTION PROCEDURE

The clear-sky fluxes are obtained from the scanning radiometers on board the Earth Radiation Budget Satellite (ERBS). The scanner has three channels: (i) the total channel which measures both the reflected solar and emitted longwave radiation, (ii) the shortwave channel which employs an optical filter to capture only the reflected solar radiaiton; (iii) the longwave channel with a filter to filter most of the radiation shortwave of 4 μm. The ERBE algorithm retrieves clear-sky longwave values by analyzing the scanner radiances for maximum values, i.e., by employing a threshold approach. These estimates are the basic data set used in the present study. This data set covers the region from 60°N to 60°S for the period Nov. 6, 1984 to Nov. 30, 1984. To this data set, we employ the following selection procedure to minimize ambiguities in interpreting the data set:

(a) The study is limited to night time conditions. The nighttime restriction enables us to use the total channel for estimates of longwave fluxes. We also do not include desert regions.

(b) We adopt radiances rather than fluxes. Furthermore, we adopt only the filtered radiances. Although we restrict our study to the total channel which doesn't have a filter, the radiance incidence on the total channel is filtered slightly because of the telescope mirror.

(c) In order to minimize cloud-contaminated regions, we adopt only those regions for which the spatial standard deviation, σ, of the radiance is less than 1%. The σ for any scanner pixel is computed from radiances of five pixels including the pixel of interest and the four surrounding pixels. This constraint follows from the work of Coakley and Bretherton (1979) which demonstrated that clear-sky oceanic regions are characterized by very small variances in the longwave fluxes.

3. THE RADIATION MODEL AND INPUT DATA FOR THE MODEL

The model includes the effects of H_2O, CO_2, O_3, CH_4 and N_2O. For H_2O, the model computes radiances in 5 cm^{-1} intervals by employing the Malkmus expression for transmittances for line absorption. The model also includes a continuum transmission to account for the effects of farwing absorption that are ignored in the 5 cm^{-1} model. The farwing transmission was derived to yield agreement with line-by-line calculations. In addition, the model includes the e-type continuum. The model fluxes for the top of the atmosphere agree with line-by-line calculations within 1% for a variety of atmospheric profiles ranging from subarctic winter to tropical conditions (Tables 1a and 1b show an example of the comparison for mid-latitude summer conditions).

* The National Center for Atmospheric Research is sponsored by the National Science Foundation.

Table 1a: Model intercomparison (H_2O lines only)

Profile: Mid-latitude Summer
Spectral domain: 0–2200 cm^{-1}
Units: W m^{-2}

Model	Upflux (0 mb)
Present	336.3
Line–by–line (Arking)*	334.4
Line–by–line (Fels)*	333.96

* These results were kindly provided by Drs. Arking and Fels and have also been cited in ICRCCM (1984).

Table 1b: Model intercomparison (H_2O, CO_2, O_3, CH_4 and N_2O)

Profile: Mid-latitude Summer
Spectral domain: 0–3000 cm^{-1}
Units: W m^{-2}

Model	Upflux (0 mb)
Present	287
Line–by–line (Arking)*	285.78

The model input paramaters are specified as follows: The temperature and humidity are specified from radiosonde measurements appropriate for the time and location of ERBE observation. Zonal average November climatological distribution is adopted for ozone. The surface is assumed to be a black emitter. The computed spectral radiances are multiplied by the instrument spectral response function to obtain the filtered radiances.

4. SELECTION OF DATA FOR THE COMPARISON

The following criteria are employed to select the data obtained for the comparison study.

(i) The radiosonde station location should lie within 30 km of the ERBE clear-sky region.

(ii) The time at which ERBE clear-sky data is taken should fall within 1 hour of the radiosonde data.

(iii) The radiosonde data should extend at least up to 50 mb.

(iv) Once the above conditions are met, we adopt only those pixels for which ERBE reports clear-sky conditions for the four surrounding pixels.

(v) Relative humidity error criterion: The rms error in radiosonde measurements of relative humidity is about 5% for temperatures greater than 273°K and about 10% for temperatures less than 273°K. Hence, the error in absolute humidity becomes large for very dry regions. In view of the above, we include only those soundings for which the rms error divided by the actual relative humidity is less than 50%.

5. RESULTS

There are about 2000 radiosonde soundings per day such that for the 25 days in November considered in this study, there are a total of roughly 50000 soundings. However, only 49 soundings satisfy all of the constraints imposed in this study (see Sections 2 and 4 for details).

First, it should be noted that the present radiation model overestimates the outgoing radiance by 1 to 1.5% since it ignores the following radiation processes: 9-10 μm bands of CO_2; 14 μm bands of O_3; H_2O absorption shortwave of 4.5 μm; CO_2 absorption in the vicinity of 4 μm; trace gases such as CFCs, NH_3, HNO_3 and others (see Ramanathan et al., 1985 for a complete list); and background tropospheric aerosols. Although individually these processes have a small effect, their collective effect is of the order of 1 to 1.5%. Hence, if the input data to the model, the radiation model and the ERBE radiances were free of errors, the computed radiances should be larger than the observed ones by about 1 to 1.5%.

The frequency distributions of the percent difference are shown in Figs. 1a and 1b. For Fig. 1a, the surface is assumed to be black. Fig. 1b is a sensitivity calculation, in which the surface emissivity is assumed to be non–black in the 8-12μm region and is 0.95 for ocean and 0.9 for land. However, we ignore reflection of radiation by the surface. Before interpreting the results in Fig. 1, we examined the validity of the results by considering the sensitivity of the results to a variety of parameters including: viewing zenith angle; spatial variance of radiance; maximum and minimum dew point depression; and local time of observation (to name a few). Remarkably enough, the difference between computed

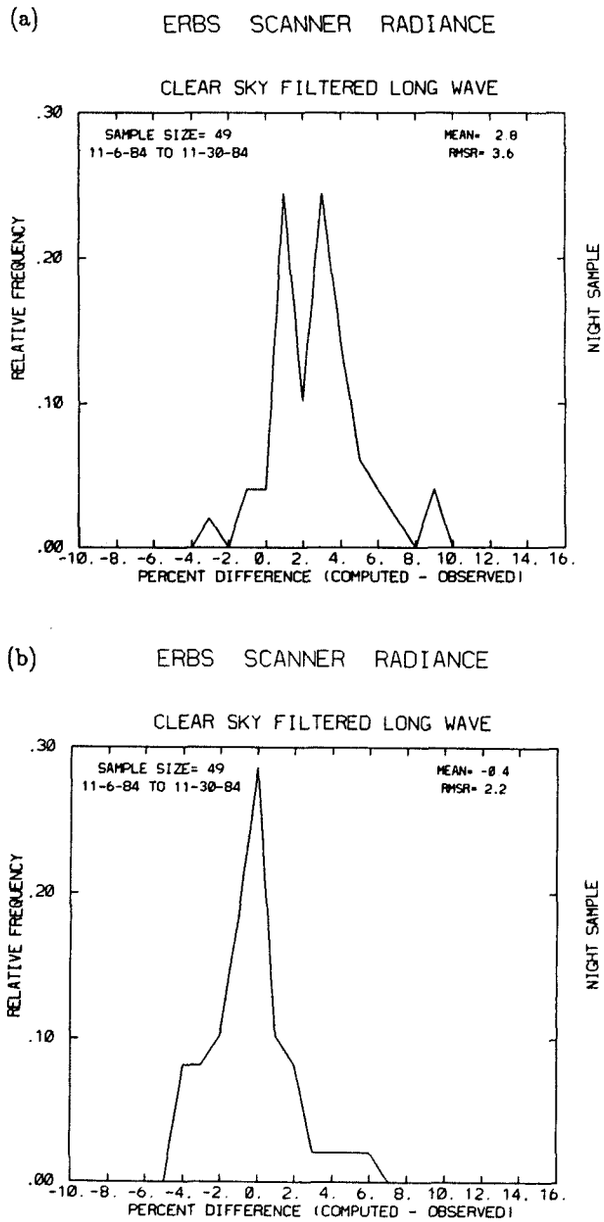

Figure 1. Frequency distribution of percent difference between computed and observed night time filtered radiances. The relative frequency, *i.e.*, no. of samples for each 1% difference divided by the total number is plotted. (a) surface emissivity is 1. (b) non-black emissivity in the 8-12 μm region. Since the reflection of radiation is ignored, this case overestimates the non-black effects by about 50%.

and observed was nearly independent of these parameters. For example, Figures 2 and 3 respectively show percent difference in radiance as a function of viewing zenith angle and of the normalized spatial standard deviation of the radiance. The near insensitivity to viewing zenith angle also leads to the encouraging conclusion that the scanner radiance does not suffer from viewing angle dependent error. The insensitivity to the percent variance suggests that the data we have chosen are effectively free from cloud contamination. Now comparing Figs. 1a and 1b, it is seen that the surface emissivity makes a substantial impact on the mean error. This difference clearly suggests that additional work is required in specifying emissivity in models. The overall picture that emerges from Fig. 1 is that the present approach of selecting regions for validation of models holds significant promise.

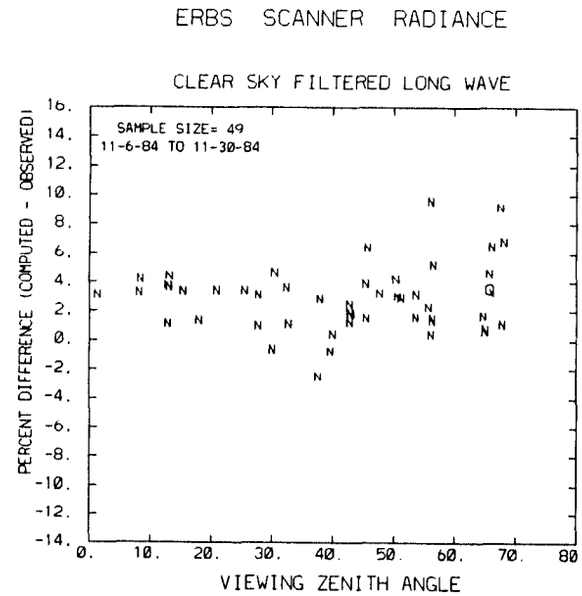

Figure 2. Percent difference between computed and observed night time filtered radiances plotted as a function of viewing zenith angle.

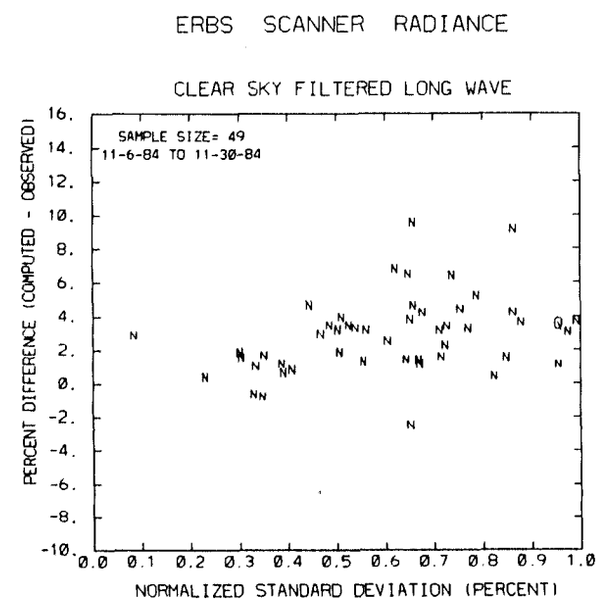

Figure 3. Percent difference in night time filtered radiance as a function of normalized standard deviations, N. $N = (\sigma/R) \times 100$. R is the mean of 5 pixel radiances, *i.e.*, the pixel of interest and the four surrounding pixels and σ is the standard deviation of the radiances.

6. SUMMARY

In summary, the validation study thus far has revealed the following encouraging features. The consistency between computed and observed radiances and the insensitivity of the difference (between computed and observed) to several satellite and meteorological parameters clearly raise the exciting possibility of using scanner radiances for radiation model validation and for retrieving cloud-radiative forcing. However, a sample size of 49 is still not sufficient to arrive at firm conclusions but this problem can easily be solved by employing data for additional months. The next step is then to examine if the rms difference in Fig. 1 can be explained based on known uncertainties in input data and in scanner radiances. If the rms difference can be explained by these factors, then the sort of results shown in Fig. 1 can be used to validate clear-sky radiation theory.

ACKNOWLEDGEMENTS

This project was partially funded by NASA ERBE grant L9477B. We acknowledge valuable discussions with Prof. R.D. Cess and Dr. B.R. Barkstrom. We are indebted to Dr. A. Arking and Dr. S.B. Fels for providing computer output of their line-by-line calculations.

REFERENCES

Barkstrom, B.R., 1984: The earth radiation budget experiment. *Bulletin of the American Meterol. Soc.*, **65**, 1170–1185.

Coakley, J.A., and F.P. Bretherton, 1982: Cloud cover from high resolution scanner data: Detecting and allowing for partially filled fields of view. *J. Geophys. Res.* **87**, 4917–4932.

ICRCCM (1984): The intercomparison of radiation codes in climate models (ICRCCM). *World Climate Programme Report* **95**. Eds: F.M. Luther and Y. Fouguart. December, 1984.

Ramanathan, V., 1985: Scientific use of surface radiation budget data for climate studies. 30 pp. In the *World Climate Research Programme Report* of the Workshop on Surface Radiation Budget for Climate Applications. Eds: J.T. Sottles and G. Ohning. Report available in draft form.

Ramanathan, V., R.J. Cicerone, H.B. Singh, and J.T. Kiehl, 1985: Trace gas trends and their potential role in climate change. *J. Geophys. Res.* **90**, 5547–5566.

COMPARISON OF ERBE INFERRED AND MODEL COMPUTED CLEAR-SKY ALBEDOS

B.P. Briegleb and V. Ramanathan

National Center for Atmospheric Research *
Boulder, Colorado 80307

1. INTRODUCTION

Clear-sky planetary albedo is an important climate variable that not only determines the amount of solar radiation absorbed under cloudless conditions, but also determines the degree to which clouds modulate the absorbed solar radiation. It is important therfore to validate the climate modeling practice of specifying bulk values of reflectivity for regions of several hundred km^2 or greater.

Briegleb et.al. (1986; hereafter referred to as BMRH), compared regional clear-sky albedos inferred from GOES observations with model computations. That study was confined to most of North and South America and their adjacent ocean regions for November. Albedos over oceans agreed to within $\pm.01$, while albedos over land agreed to within $\pm.02$, both within the computed and observed uncertainties.

In this paper, the computed clear-sky planetary albedos from BMRH are compared with preliminary clear-sky albedos inferred from ERBS observations taken during November 1984. As a first step, we confine our attention exclusively to ocean surfaces.

Our objectives in undertaking this study are twofold: First, a detailed comparison of the preliminary ERBE results with computed clear-sky albedos will contribute to the process of validation of the algorithms used by ERBE to infer clear-sky albedos; next, once the ERBE data are validated by the above and other independent validation procedures, the ERBE data could then be used to verify the treatment of clear-sky albedos in climate models.

2. OBSERVED CLEAR-SKY ALBEDOS

The observations used in this study are the preliminary November 1984 ERBS S-9 scanner data. As part of the standard ERBE scientific products, the monthly mean clear-sky albedo is estimated. However, these albedos derive from a scene identification algorithm that allows for up to 5% cloud cover contamination, which may bias the comparison with computed clear-sky albedos.

In order to minimize the effects of clouds, we retrieve a second estimate of the clear-sky albedo from the November 1984 S-9 scanner observations. For each 2.5° x 2.5° ERBE ocean region, we isolate the observations from the entire month whose ERBE scene identification results in at least 80% clear sky identifications for all pixels falling within that region. The albedos for these observations are corrected from their local time values to local noon using the ERBE directional model for the ocean scene type. From this set of clear-sky local noon albedos, we isolate the minimum albedo from the entire month. About 80% of all possible ERBE 2.5° x 2.5° ocean regions between $\pm 60°$ latitude returned minimum albedos; the remaining regions were not sampled because of persistent cloud cover during November 1984.

Although this second estimate of the clear-sky albedo helps to minimize the effects of cloud, it still relies on the ERBE clear-sky scene identification. One way to determine the uncertainty due to cloud cover contamination is to use the estimated spatial standard deviation of clear-sky albedo provided in the ERBE S-9 data. This quantity represents the spatial variability of the clear-sky pixels for the retrieved minimum albedo. These values are typically $\pm.02$.

3. COMPUTATION OF CLEAR-SKY ALBEDOS

The radiative transfer model of BMRH is used in this comparison study. The model albedos are computed on a 1° x 1° resolution; the albedos within each ERBE 2.5° x 2.5° region are obtained by linearlly averaging the 1° x 1° results.

Basically, the BMRH model is a plane-parallel delta-Eddington radiative transfer model that accounts for O_3,O_2,CO_2, and H_2O gaseous absorption and background aerosol absorption. The model also accounts for molecular and aerosol scattering. The ocean surface albedo model accounts for both direct and diffuse incident radiation.

The uncertainties in the model computations are due to the use of zonal mean climatological O_3 and H_2O amounts for November, the use of a climatological ocean aerosol model, and the use of an ocean surface albedo model appropriate for low surface-wind speeds and typical hydrosol amounts. As reported in BMRH, these uncertainties yield typical albedo uncertainties of $\pm.01$.

4. RESULTS

Figure 1 shows a histogram of computed minus inferred local noon clear-sky albedos. All 2.5° x 2.5° ERBE regions satisfying the retrieval criterion of section 2 are included (about 3800) in this figure. The mean difference is $+.001$, with a standard deviation of .017.

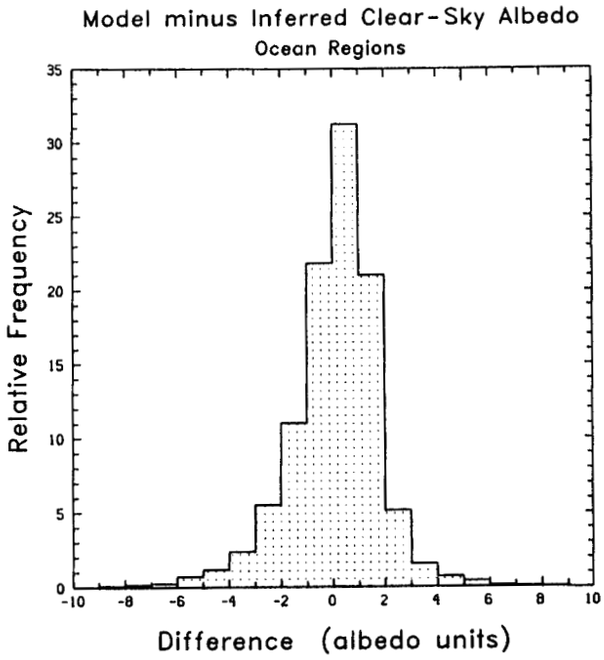

Figure 1. Histogram of computed minus inferred local noon clear-sky albedos over ocean; November 1984 Preliminary ERBS S-9 data.

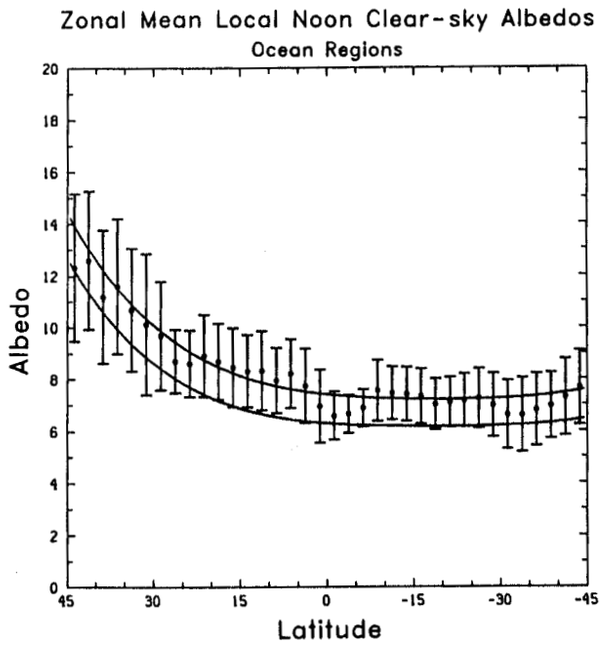

Figure 2. Zonal mean local noon clear-sky albedos over ocean. Solid lines are computed with (upper) and without marine aerosol; dots are inferred albedos from November 1984 Preliminary ERBS S-9 data; error bars show standard deviation about the zonal mean.

Figure 2 shows the zenith angle dependence of the computed and inferred local noon clear-sky albedos. The solid lines show the aerosol-free computations (lower curve) and the computations with background marine aerosol. The zonal mean minimum local noon clear-sky albedos inferred from the ERBE observations are also shown, along with ± standard deviation about the zonal mean.

There appears to be no significant differences between the computed and observed albedos in these figures. We consider these favorable comparisons to be a positive step towards validating the ERBE algorithms for inferring clear-sky albedo over ocean.

5. ACKNOWLEDGEMENTS

Part of this work was supported by NASA-ERBE grant L9477B.

6. REFERENCES

Briegleb, B. P.,P. Minnis, V. Ramanathan, E. Harrison, 1986: Comparison of Regional Clear-Sky Albedos Inferred from Satellite Observations and Model Computations, J. Clim. Appl. Met., 25,214-226.

INTERCOMPARISON OF PRELIMINARY EARTH RADIATION BUDGET SATELLITE (ERBS) FLUX ESTIMATES AND GEOSTATIONARY SATELLITE MULTI-SPECTRAL "VAS" RADIANCE MEASUREMENTS

Leroy D. Herman[1] and William L. Smith[2]

[1] National Oceanic and Atmospheric Administration
Systems Design and Applications Branch

[2] Cooperative Institute for Meteorological Satellite Studies
Space Science and Engineering Center
Madison, Wisconsin

1. INTRODUCTION

The Earth Radiation Budget Satellite (ERBS) provides radiation observations from the earth and its atmosphere. The observations are for two broad spectral bands, a long-wave band of 5-200 microns and a short-wave band of .2-5 microns. These data are recorded on board by both a scanner and two non-scanner instruments. The scanner, whose observations are one set of data used in this study, have a resolution of approximately 36 by 48 kilometers.

The other set of data used for this study is obtained from the VISSR Atmospheric Sounder (VAS) on board GOES-6. Observations from the VAS are obtained in 12 spectral channels with a resolution of either 14 or 8 kilometers. The oversampled 14 km Multi-Spectral Image (MSI) data from VAS is used in this study to obtain temporal coincidence with the ERBS coverage. Theoretical studies (Smith and Woolf, 1982) indicate that a strong relationship exists between the multi-spectral radiance observations obtained in this mode and the outgoing long-wave radiation flux. Channel 7 (12.7μ) is particularly sensitive to low level moisture whereas channel 8 (11.2μ), the infrared window, possesses high sensitivity to surface temperature and cloudiness.

Knowledge of the relationship between the VAS and ERBS instruments will be very useful for climate studies. One application of this information is to the study of the diurnal cycle of cloudiness and radiation. With hourly observations from VAS, more complete information becomes available in the western hemisphere for studying the diurnal cycle and for estimating daily averages from the satellite ERBE system.

This paper develops a preliminary relationship between the outgoing long-wave radiation flux as detected by ERBS and the spectral radiances observed by the VAS MSI channels which are most strongly correlated to the earth-atmosphere outgoing long-wave radiation flux.

2. LONG-WAVE INTERCOMPARISON

2.1 Data Selection

The first revised, but preliminary ERBS tape released by NASA-Langley which possesses data for the same time that a VAS data set was available is for February 7, 1985. In order to compare and form relationships between the data from the two satellites the observations from each must be nearly simultaneous. Since the area of VAS coverage is fixed, comprising North and South America and the surrounding oceanic region, ERBS passes over this region provide the only opportunity for comparison. A nearly ideal ERBS orbit is available on this date, passing over the VAS subpoint at the equator near 108°W. This orbit covers a region with a diversity of cloud types beginning near 40°N in the eastern U.S. extending into the Gulf of Mexico to the Yucatan peninsula. This pass crosses the jet stream and includes a region where cirrus is widespread (see Figure 1).

Ordinarily, cloud motion is greatest in the jet stream. As a test of the comparison method this region of coverage was chosen since it is the most difficult weather type to be encountered. The technique applied involved computer selection of points for comparison. The goal was to select a region starting at 40°N on the ERBS tape and choose points that gave good coverage, minimized redundancy, and retained good resolution, recognizing that the resolution for all satellites is best near their subpoint track and is worse near the horizon. Since there is considerable ERBS scanner observation redundancy at the satellite subpoint the solution was to require a minimum distance of 30 kilometers between the points selected along a scan line. Each ERBE scan line contains 62 elements; to avoid the low resolution regions near the horizon, the first and last 11 elements along each line were excluded. Of the remaining 40 elements redundancy elimination near the middle of each scan line reduced the average number of data points selected from each scan line to 26. Observations were selected from 100 scan lines giving a total of 2583 picture points. An outline of the ERBS long-wave top of the atmosphere region is shown in Figure 2.

After the data point locations were chosen from the ERBS tape, the closest locations to the preliminary points were found in the VAS/MSI data. The oversampled VAS data have a spatial resolution approximately five times better than the ERBS so an average of 25 VAS observations

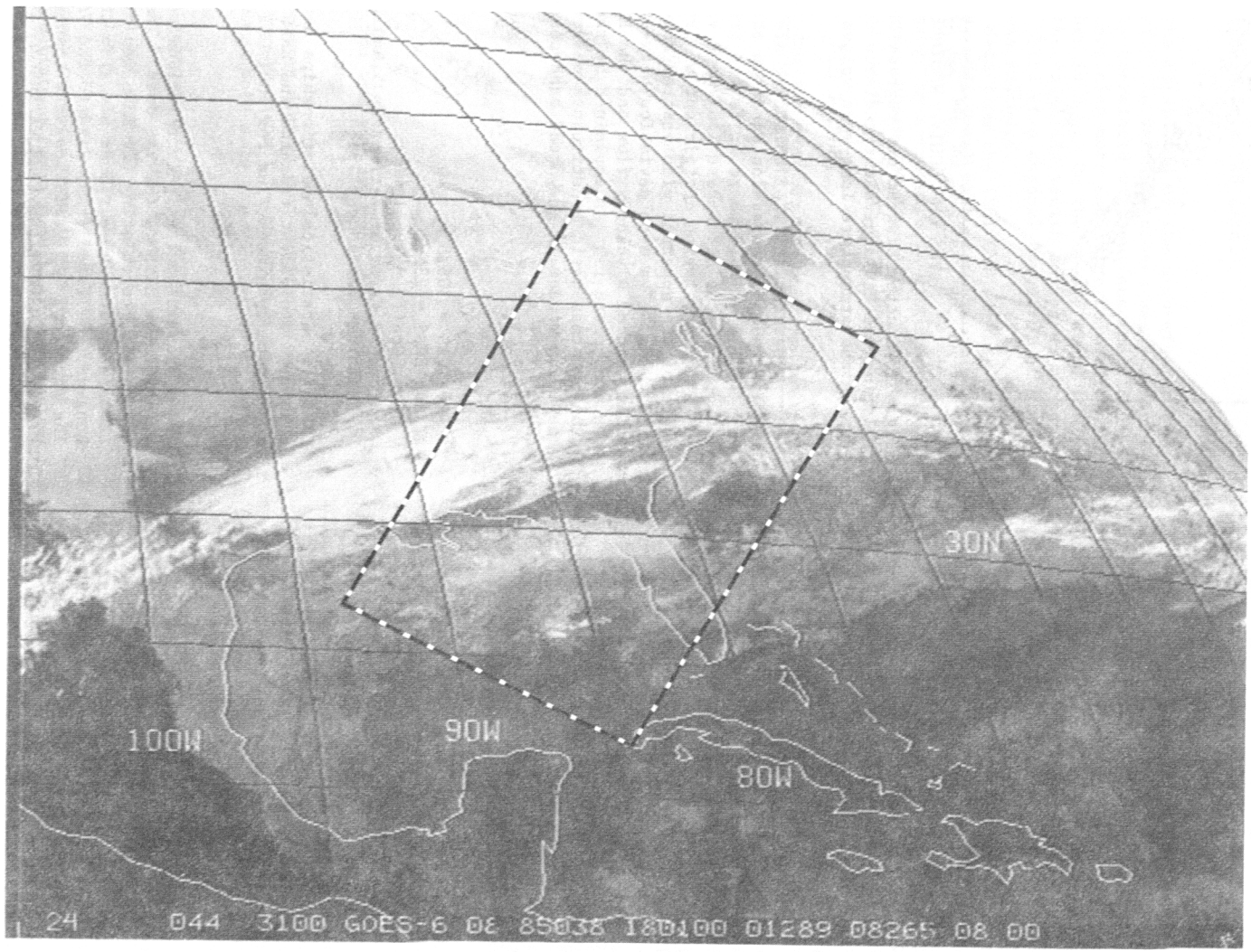

Fig. 1. VAS infrared picture for 1801 GMT February 7, 1985 showing region matched by ERBS orbit.

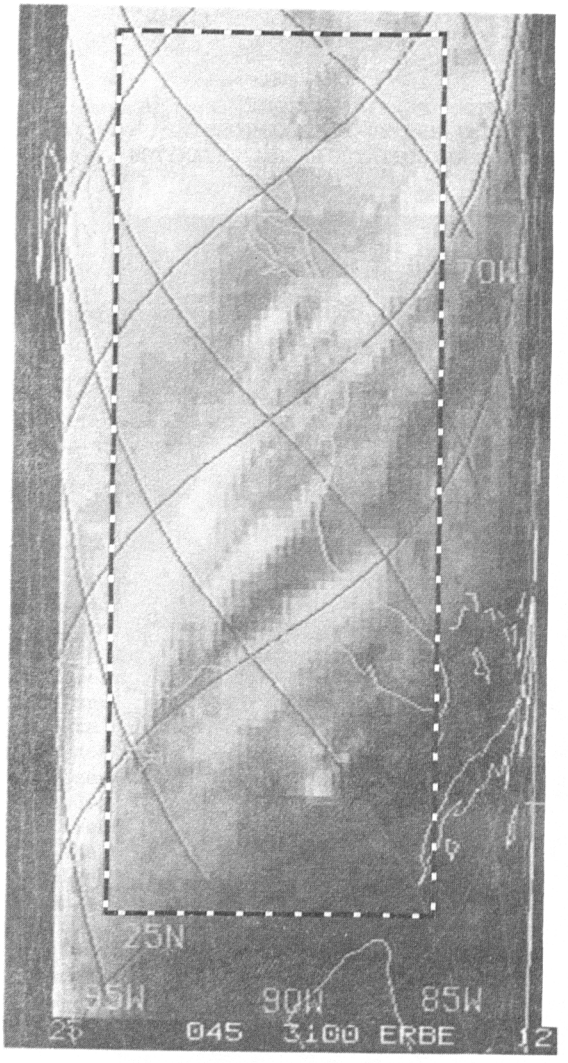

Fig. 2. ERBS top of the atmosphere flux for near 1800 GMT February 7, 1985 showing region matched with VAS picture.

overlapping the ERBS observation was computed. In order to insure comparisons of uniform scene fields of view, a limit on the range between the maximum and the minimum VAS brightness temperatures of 5°C in the channel 8 data was chosen. After applying this criteria, 697 samples remained.

2.2 Regression Relationships

The quality of fit of a simple linear relationship (not shown) between the VAS channel 8 brightness temperatures and ERBS top of the atmosphere long-wave values indicated that a higher order regression relationship was needed. Also, it is better to correlate quantities converted to the same physical units. As a result, equivalent blackbody fluxes were computed from the VAS brightness temperatures using the Stephan Boltzman law: $R_{v8} = \sigma T^4$ where σ is the Stephan Boltzman constant, T is the VAS brightness temperature, and R_{v8} is the equivalent VAS blackbody flux. The regression line obtained from this relation and the scatter of the data about this line are shown in Figure 3.

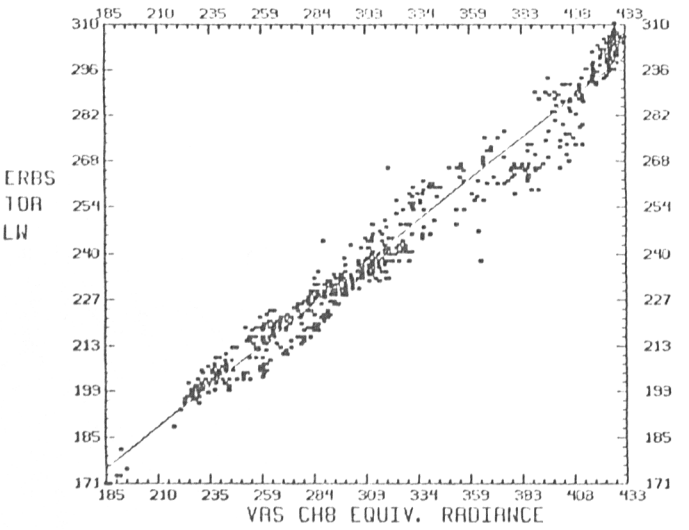

Fig. 3. Scatter diagram and regression line relating the VAS equivalent radiance to the ERBS top of the atmosphere long-wave values.

The statistics of this case are shown in Table 1 and the regression equation obtained was: $R_E = .507\ R_v - 80.7$ where R_E is the predicted ERBS top of the atmosphere long wave value. Note the high correlation coefficient of .9841, in spite of the apparent wide scatter about the line. The large mean deviation between the VAS 11 μm channel blackbody flux and the ERBS top of the atmosphere flux is explained by the absorption by atmospheric constituents observed outside the 11 μm window in the broad band observed by ERBS.

Num = 697
Avg VAS = 306.5
Avg ERBS = 235.2
Cor. Coeff. = .9841
Standard Error of Estimate = 5.940
Explained Variance = .9684

Table 1. Statistical relationships between VAS channel 8 equivalent radiance and ERBS top of the atmosphere long wave flux for 1801 GMT February 7, 1985.

Several multiple correlations were produced relating the ERBS to the VAS data. These were run separately, correlating the ERBS top of the atmosphere long-wave values and also the ERBS long-wave filtered (raw) data to the VAS data. The source of VAS variables were channels 7 and 8, and the secant function of the VAS satellite zenith angle of observation.

As shown in Table 2, one of the best results obtained was for the multiple correlation of R_E, the ERBS top of the atmosphere long-wave with: R_{v7}, the equivalent blackbody flux radiance for VAS channel 7; R_{v8}, the equivalent blackbody flux for VAS channel 8; sec Θ, secant of the satellite zenith angle of the VAS observation.

	Step 1	Step 2	Step 3
Variable	σT_{v7}^4	sec Θ	σT_8^4
Cor. Coeff.	.9874	.9881	.9882
Standard Error of Estimate	5.295	5.142	5.128
Explained Variance	.9749	.9763	.9765

Table 2. Step-wise multiple regression statistics for predicting ERBS top of the atmosphere long-wave values from VAS data.

On the first step of the step-wise multiple regression the variable chosen was R_{v7} since it is highly correlated with surface and cloud radiation, and also more sensitive to water vapor emission than is R_{v8}. On the second step, the secant of the satellite zenith angle was chosen, and on the third step channel 8 equivalent black-body flux was included.

The data from the 1801 GMT sample was augmented by additional data from the next ERBS pass at 1930 GMT. The additional data was obtained using the same criteria discussed above. Two areas were chosen for diversity of scene, centered near 10°W 120°W and 40°N 100°W.

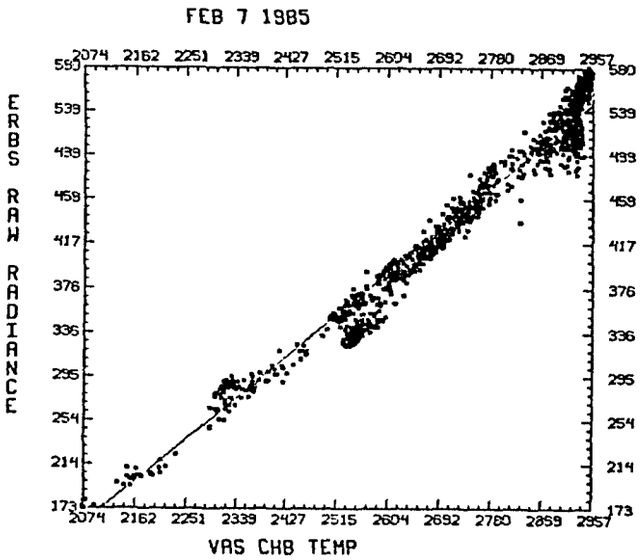

Fig. 4. Scatter diagram and regression line relating the VAS channel 8 temperature to the ERBS raw radiance. Both axis are multiplied by 10.

The scatter of the data is shown in Figure 4. The wide scatter at the warm end where temperatures are greater than 290°K appear to be due to the inability of the channel 8 window to detect the variation of low level moisture commonly found over the ocean surface. Table 3 shows the statistics for the multiple regression on this sample. The final relation found was:

$$R_E = 1.052\sigma T_{v7}^4 - .3995\sigma T_{v8}^4 - 1.195 \sec \Theta + 44.36$$

	Step 1	Step 2	Step 3
Variable	σT_{v7}^4	σT_{v8}^4	sec Θ
Cor. Coeff.	.9847	.9858	.9859
Standard Error of Estimate	6.735	6.478	6.468
Explained Variance	.9696	.9719	.9720

Table 3. Expanded sample step-wise multiple regression statistics for predicting ERBS top of the atmosphere long wave values from VAS data.

3. FURTHER WORK

The relationship found here for uniform fields will be checked against an independent data set to validate its usefulness. Even if it appears to stand up to such a test, it must be remembered that the preliminary ERBS data it comes from has not itself been fully validated, especially the TOA modeling. Hence revisions may be necessary, though in all probability any changes would be expected to be small. Application of the relationship to determine the diurnal cycle and the specification of daily average fluxes from the ERBS for various regimes will be presented at the meeting.

4. ACKNOWLEDGEMENTS

Thanks to Harold Woolf for assistance with VAS algorithms. Funding for this research has been provided by the NASA, ERBE project through Grant NASA-16507.

J1.17

COMPARISON OF NIMBUS 7 AND ERBE RADIATION BUDGET MEASUREMENTS

G.G. Campbell and T.H. Vonder Haar

CIRA Colorado State University
Ft. Collins, Colorado

D.L. Hartmann, R. Kandel, G.E. Hunt, and A. Mecherinkunnel
ERBE Science Team Members

F. House, A. Ingersoll, H.L. Kyle, R. Maschhoff, and L.L. Stowe
Nimbus 7 Experiment Team Members

1. Introduction

A new era of Earth Radiation Budget observations began in November, 1984 with the Earth Radiation Budget Experiment (ERBE) (Barkstrom, 1984). These observations overlap with series of observations begun in November, 1978 from the Nimbus 7 spacecraft (Jacobowitz et al,1984, Kyle et al,1984). The radiation budget is the basic boundary condition determining the Earth's climate. We can improve our understanding of the earth's climate by studying the fluctuations in the average weather which provide natural climate experiments providing that we have an accurate mean climatology for comparison. Our purpose in this study is to compare these two data sets to determine if they can be combined into a long term climatology of measurements which can be used to measure fluctuations or trends in the climate.

2. Data

At this time we are limited to observations from November 1984 because the final analysis scheme is still under final testing for the ERBE. There are three instruments in the ERBE system, a Wide Field of View (WFOV) intergrating sensor, a Medium Field of View sensor (MFOV), and a scanning instrument with a field of view less than 100km. Some processing errors have been detected in the preliminary ERBE data set for the WFOV and MFOV products (ERBE Science Team, 1985). We have then confined our ERBE study to the scanner whose data has been analysed onto a 2.5 degree latitude, longitude grid. The instrument is flying on a drifting satellite with inclination of 60 degrees, so an approximate diurnal average measurement is obtained in one month. For both data sets we limited our study to the monthly mean products because these are the measurements with the highest accuracy available from each system. Figure 1 shows the November mean Emitted Exitance and figure 2 shows the Albedo from ERBE.

The WFOV sensor system on Nimbus 7 has been operating since November, 1978. It provides measurements from a sun synchronous orbit crossing the equator near noon and midnight. The original data has resolution of about 1500 km so at first sight the observations are a smoothed out version of the ERBE scanner measurements.

3. Similarities

There are large differences between the two sets of measurements. Figure 3 shows a scatter plot of corresponding locations from each. Only the region from 50 North to 50 South has been considered since the ERBE space craft has an orbit inclination of 60 degrees. Several least squares regressions are possible between the two data sets. First one can do a total least square fit which allows random error in each coordinate. Alternately one can do a linear regression of x on y or y on x. Thus three lines are plotted on the scatter plot. In the figures the slope is designated by A and the intercept by B. For numerical comparisons we will assign the ERBE data as a standard so we will select the slope and intercept which will change the Nimbus 7 to best match the ERBE. This is designated as DY in the scatter plots. The slope of 1.42 and intercept of -110 W/m2 exemplify the difference. These big differences are the result of the smoothing produced by the WFOV measurement system.

A deconvolution procedure was applied to the data (Campbell and Vonder Haar, 1980) which in essence enhances the highs and lows producing figures 4 and 5. The deconvolution truncates the data at spherical harmonic order 15. To have a fair comparison we have also truncated the ERBE data fields to spherical harmonic 15. Now a correlation between two systems shows very good correspondence, figures 6 and 7. The fact that the slope of the correlation of the emitted exitance is 1.01 ($\pm$.01) shows the two data sets to be calibrated to the same radiometric scale. The slope of the fit line for the albedo of .90 ($\pm$.02) seems to show a big difference.

A superposition of the zonal averages (fig 8,9) shows the emitted exitance to be nearly identical in the northern hemisphere and around the equator. But south of 20 South a systematic deviation appears. We will argue below that this difference is produced by different diurnal sampling. The albedoes from the two systems do not match as well, with some significant differences just north of the equator. Separation of the zonal average into land and ocean components shows most of the difference occurs over the land.

It is not possible to construct global averages directly from the ERBE data because of the satellite orbit cuts off the data around 60 North and 60 South. Table 1 shows the area averages for the region from 50 North to 50 South. The full area averages are virtually identical, but there is some residual difference between the land and ocean areas in the albedo.

Table 1 Regional averages for 50 North to 50 South

	Emitted Exitance (W/m2)			Albedo		
	All	Ocean	Land	All	Ocean	Land
N7 Raw	245.2	246.4	242.5	.266	.253	.299
N7 Decon	245.7	246.9	242.8	.264	.249	.304
ERBE Raw	246.5	248.7	241.6	.268	.257	.297
ERBE SPH	246.5	248.4	242.2	.268	.259	.291

4. Differences

Subtracting the two fields (fig. 10 and 11) show some significant deviations especially over the land. From an examination the first four years of Nimbus 7 data, regional fluctuations of 5 to 10 W/m2 occur in the monthly averages in the emitted exitance. This provides an objective matching requirement, the differences between systems should be less than the differences in monthly means from year to year. To detect changes in radiation budget, the ERBE and Nimbus 7 for the same month should match up to better than 5 W/m2. The differences seen in figure 11 are around 5 W/m2 with bigger differences over the land, often more than 10 W/m2.

The differences in albedo are confined to the continental areas. A fluctuation level between .025 and .05 is seen in the Nimbus 7 albedo data and the system differences are often bigger. This land ocean difference produces the slope of the line shown in figure 7. The difference between Nimbus 7 and ERBE appears then to be a mismatch in one or both measurement and analysis systems.

5. Discussion

To try to explain the differences, we have looked at the diurnal variations measured by the ERBE system. The measurement of the emitted exitance diurnal variation in ERBE is made from interpolations of the measurements at two to four different hours on each day of observation (Brooks et al.,1984). An average of noon and midnight (plus or minus one hour) from ERBE differs by more than 5 W/m2 from the 24 hour average in some land regions. This implies that the simple average of noon + midnight as done in Nimbus 7 is not accurate. Before attempting to derive a diurnal correction for Nimbus 7, more monthly comparisons will be needed.

The diurnal average albedo construction is much more complex in ERBE. Both a directional and bidirectional reflection model are used in reducing the measured radiances for ERBE. In the Nimbus 7 the albedo is calculated from the flux at satellite altitude devided by the maximum diffuse reflected flux and then a small directional correction is multiplied in. Both of these schemes are subject to model approximations. Since the biggest differences are over land, where one would expect bigger diurnal changes, the difference probably is caused by the different sampling of the diurnal changes. Nimbus 7 measures at only one local time of the day, where as ERBE samples at band of local times which changes from month to month. Estimating a diurnal correction to a full daylight average for either system is tougher than for the emitted exitance because less than half as many measurements are obtained from ERBE (half the measurements are made at night).

To summarize: the albedoes are the same over very large scale but significant differences appear over the land. The emitted exitances are closer to matching than the albedo. Adjustments to the emitted exitance are possible for the diurnal sampling bias probably present in Nimbus 7.

6. Conclusion

The archive data of Nimbus 7 is totally different than the ERBE monthly mean product from the scanner. After deconvolution of the Nimbus 7 the two data sets are very similar. The emitted exitance values are close enough together to be combined into a common climate time series if adjustments are made for diurnal sampling. More experience will be needed, especially with the two satellite situation in ERBE before an accurate diurnal correction for Nimbus can be established. One should remember that the purpose for including a drifting satellite in the ERBE was in fact to measure this diurnal variation. Thus finally the combined emitted exitances can be used to monitor year to year fluctuations in the climate to the 5 W/m2 level.

The albedo differences are probably due to diurnal variations either from geometrical reflection effects or true diurnal changes. Whether accurate diurnal corrections are possible remains for futher analysis. The systematic differences in albedo are larger than climate fluctuations, so combining the two data sets is not possible with this ERBE data processing and the deconvoluted Nimbus 7. This also precludes using the net radiation for combined Nimbus 7, ERBE year to year studies without extensive corrections.

We expect to examine other overlaping months before the oral presentation of these results, so our quantitative conclusions are subject to change. Several papers will be presented at this meeting on internal ERBE comparisons and with other satellite measurements. These will combine to determine the final accuracy of the ERBE results.

7. Acknowledgements

Both the Nimbus 7 Experiment Team and the ERBE Science Team made valuable contributions to the preparation of these two data sets. Special thanks goes to B. Barkstrom for critical comments. P. Ardanuy, B. Groveman, D. Randel and K. Dean also contributed. This research was supported by NASA contracts NAS1-16465 to Colorado State University and NAG-1-449 to the Research Institute of Colorado.

8. References

Barkstrom, B., 1984, The Earth Radiation Budget Experiment (ERBE), Bull. Amer. Meteor. Soc. 65, 11, pp. 1170-1184.

Brooks, D.R., E. Harrison, P. Minnis, J.T. Suttles, and R.S. Kandel, 1986, Developement of Algorithms for Understanding the Temporal and Spatial Variability of the Earth's Radiation Balance, Rev. of Geophys., in press.

Campbell G.G. and T.H. Vonder Haar, 1980, Climatology of Radiation Budget Measurements from Satellites, Atmos. Sci. Pap. 322, Colorado State Univ., Ft. Collins, CO.

Jacobowitz, H., R.J. Tighe, and the NIMBUS 7 ERB Experiment Tean, The Earth radiation budget derived from the Nimbus 7 ERB experiment, J. Geophys. Res., 89 , pp. 4997-5010.

Kyle, H.L., F.B. House, P.E. Ardanuy, H. Jacobowitz, R.H. Maschhoff and J.R. Hickey, New in-flight calibration adjustment of the Nimbus 6 and 7 earth radiation budget wide field of view radiometers, J. Geophys. Res., 89 , pp. 5057-5076.

ERBE Science Team, 1985, Minutes of the ERBE Science Team Meeting, December 1985, Unpublished, Available from NASA.

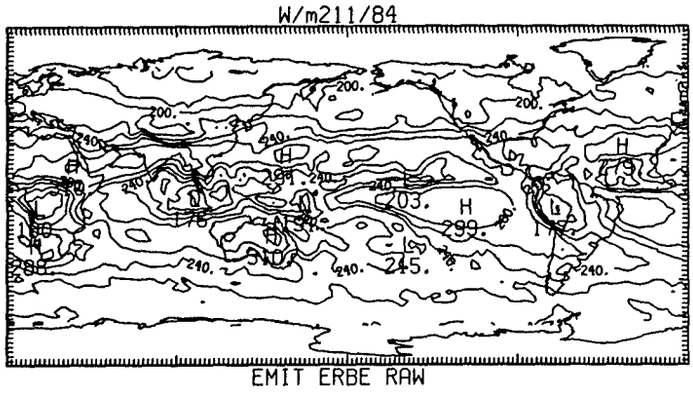

Figure 1. ERBE November, 1984 monthly mean emitted exitance from the scanner.

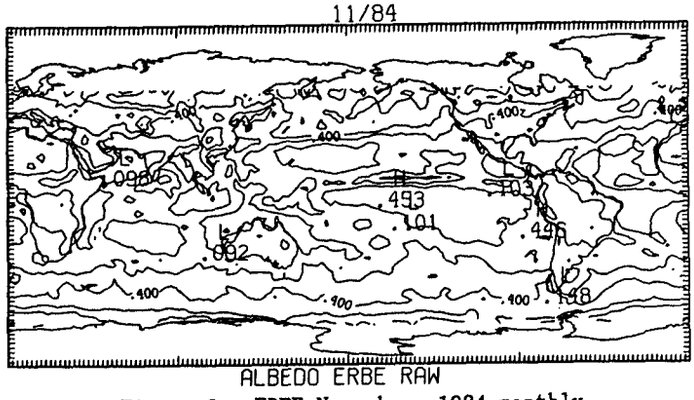

Figure 2. ERBE November, 1984 monthly mean albedo.

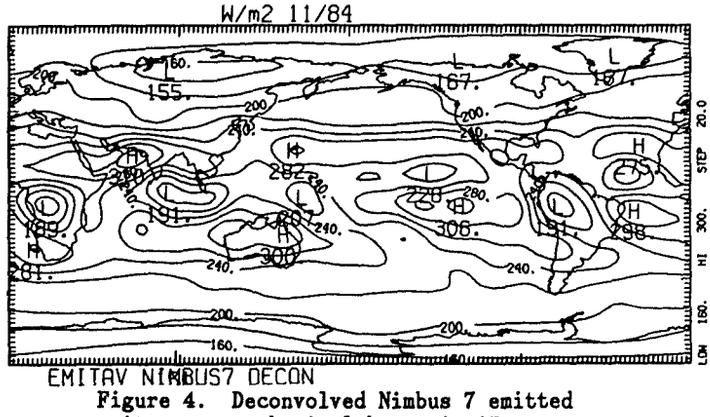

Figure 4. Deconvolved Nimbus 7 emitted exitance to spherical harmonic 15.

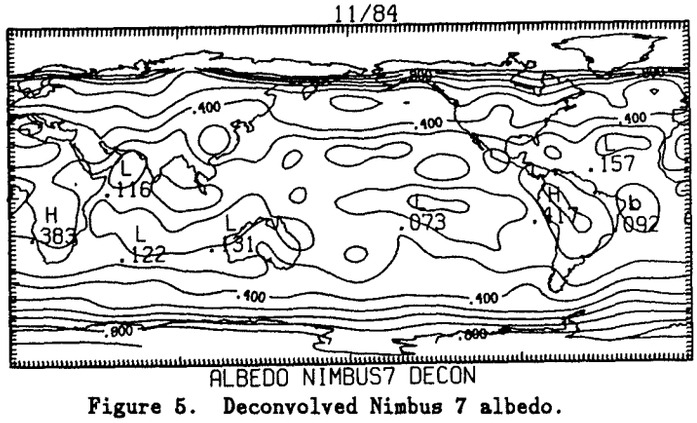

Figure 5. Deconvolved Nimbus 7 albedo.

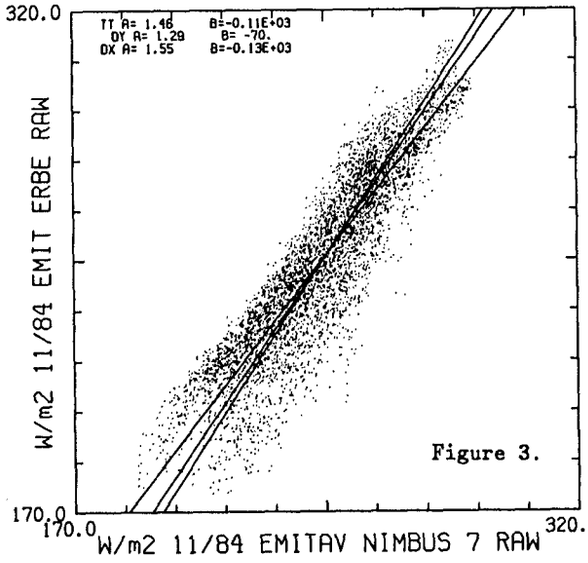

Figure 3.

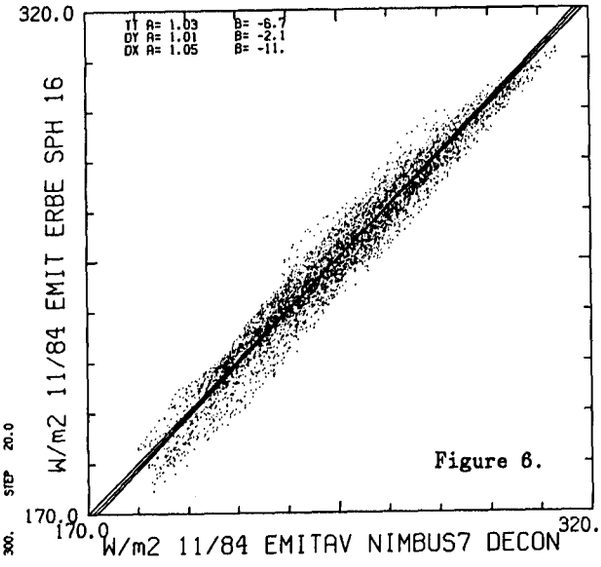

Figure 6.

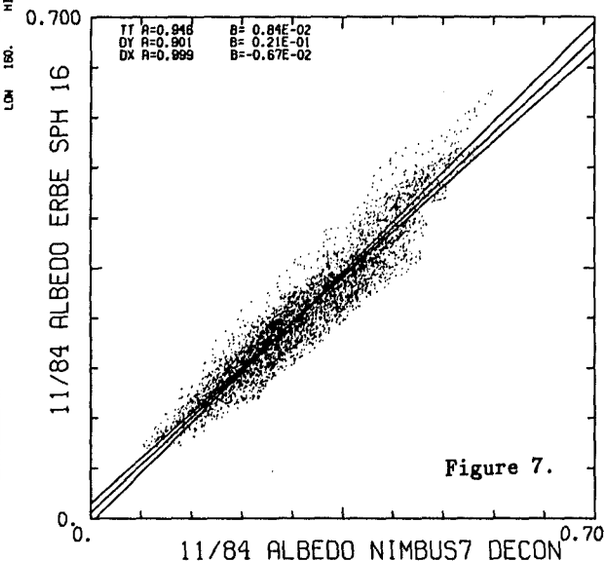

Figure 7.

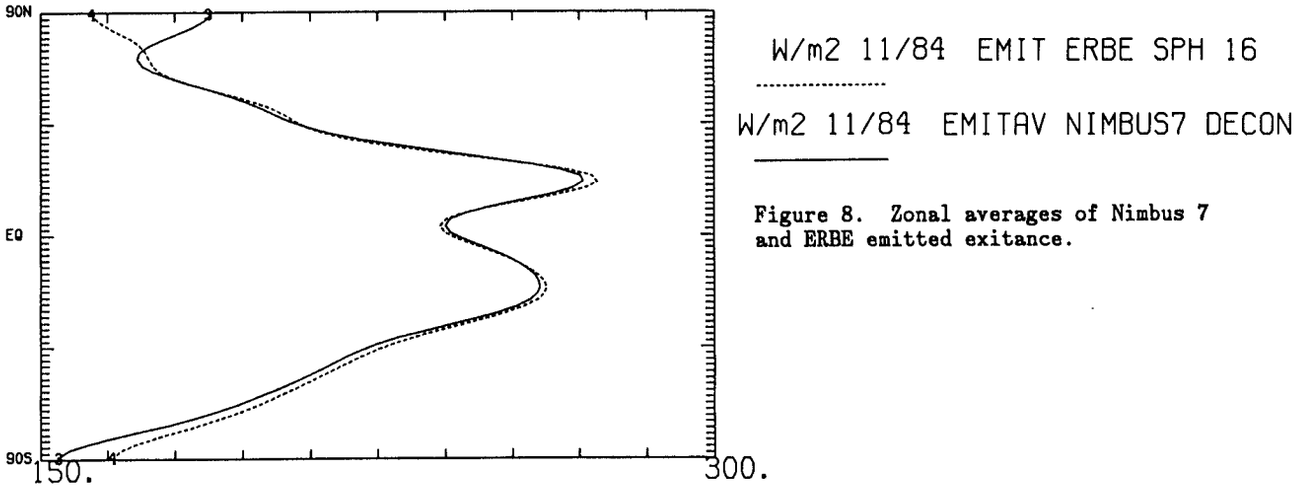

Figure 8. Zonal averages of Nimbus 7 and ERBE emitted exitance.

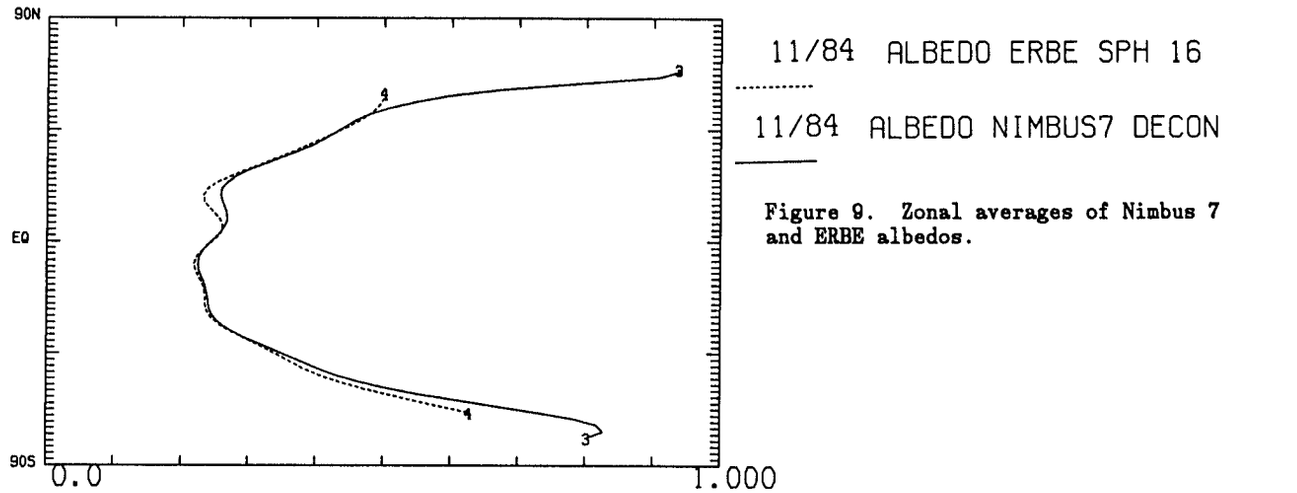

Figure 9. Zonal averages of Nimbus 7 and ERBE albedos.

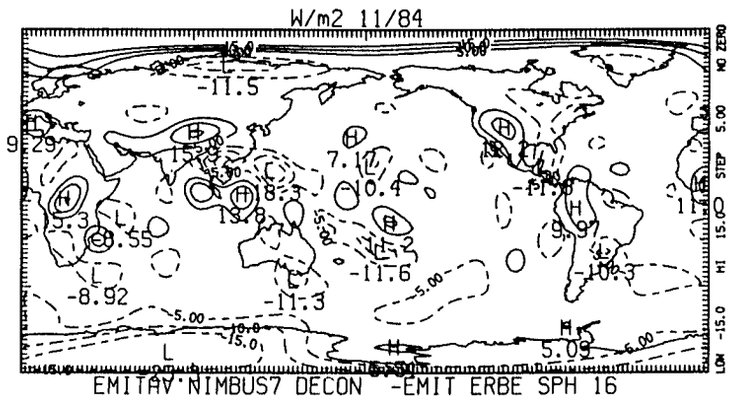

Figure 10. Nimbus 7 minus ERBE emitted exitance. Dashed lines indicate negative areas. Notice that many land areas are positive (Nimbus 7 higher than ERBE).

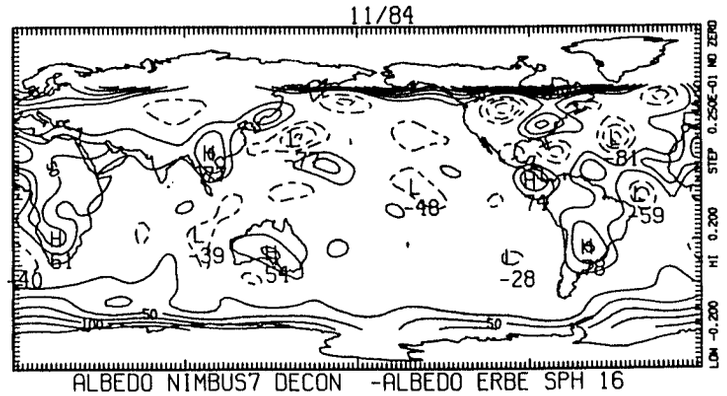

Figure 11. Nimbus 7 minus ERBE albedo. Notice that Nimbus 7 is generally higher than ERBE in the land areas.

J2.1

SATELLITE AND AIRCRAFT MEASUREMENTS OF STRATOSPHERIC AEROSOL PARTICLES

M. P. McCormick

Atmospheric Sciences Division
NASA Langley Research Center
Hampton, VA 23665

1. INTRODUCTION

Over the past 2 decades, lidars have been used to study the stratospheric aerosol. The earliest measurements found enhanced levels near 20 km which were later attributed to volcanic eruptions, the first being due to the March 1963 eruption of Agung. Other volcanic perturbations were later recognized by lidar such as those due to the eruptions of Fuego (October 1974), Agustine (January 1976), Mount St. Helens (May 1980), Alaid (April 1981), one of unknown origin (January 1982), and then El Chichon (April 1982). Other eruptions probably perturbed the stratosphere during this period, but have gone unnoticed due to the limited number and latitudinal distribution of lidars in the world and the limited number of other sensors capable of making stratospheric aerosol measurements. Lidars do offer, however, a very useful tool for studying the occurrence and temporal variation of volcanic perturbations, thus providing important data for studying the impact and effects of volcanic eruptions, and using aerosols as tracers, atmospheric motions.

The first satellite sensor developed for the long-term measurement of stratospheric aerosols was SAM II, launched in October 1978. It remains operational today and has produced, for the first time, an aerosol climatology in the Arctic and Antarctic regions. SAM II was followed into Earth orbit by SAGE I in February 1979 and obtained about 3 years of measurements over latitudes from 79°N to 79°S. SAGE II was launched from shuttle in October 1984 into an orbit similar to SAGE I, and remains operational today. SAGE I also made measurements of ozone and nitrogen dioxide, while SAGE II, in addition to these, makes water vapor measurements.

This SAM-SAGE series of satellite sensors utilizes the technique of solar occultation; that is, they conduct their measurements during each spacecraft sunrise and sunset, recording the effects of the attenuation of aerosols and gases in the Earth's atmospheric limb between satellite and Sun. Because of the high signal-to-noise provided by the strong solar source and the fact that the instrument is self calibrating before (sunset) or after (sunrise) each measurement event, profiles with high accuracy and vertical resolution are obtainable. A description of these instruments can be found in McCormick et al. (1979) and Mauldin et al. (1985), and the mathematical techniques used for the production of its species' profiles are given in Chu and McCormick (1979) and Chu (1986).

During the period 1979 through 1982, many volcanic eruptions perturbed the stratospheric aerosol as indicated above. SAGE I and SAM II have provided a valuable global data set on these perturbations (Kent and McCormick, 1984), and SAM II and SAGE II continue to observe the effects of the largest of these, El Chichon. The NASA Langley Research Center lidars, both airborne and groundbased, have also provided a valuable regional and single-point data set (McCormick, 1982; McCormick et al., 1978). This was enhanced by the fact that the 1982 eruption of El Chichon occurred between the SAGE I and SAGE II operational measurements and, therefore, the Langley airborne lidar was especially valuable in providing data over a 2-year series of campaigns covering 90°N to 56°S (McCormick et al., 1984), which complemented greatly the SAM II polar measurements and various groundbased and other measurements.

This paper will describe data obtained from these lidar and satellite measurements, especially those pertaining to the impact of the eruptions of El Chichon.

2. RESULTS

El Chichon is located in southern Mexico (17.3°N, 93.2°W) and erupted with four major eruptions between March 28 and April 4, 1982, with the largest occurring on April 4. The clouds of stratospheric material from these eruptions spread westward, circling the globe in 3 weeks (Matson and Robock, 1984) and were detected by lidar at Mauna Loa on April 9 with record-setting scattering ratios at an altitude of 26-km (DeLuisi et al., 1983). Subsequent lidar (McCormick et al., 1984) and in situ balloon measurements (Hofmann and Rosen, 1983) showed material extending up to about 30-km altitude with two layers separated by a region of minimum concentration at 21-km. The upper layer contained the most mass and optical depth (McCormick and Swissler, 1983; Spinhirne, 1983) and a very different size distribution (Hofmann and Rosen, 1984). Perturbing effects of the El Chichon cloud became apparent on several satellite sensors producing artifacts in their data sets (Bandeen and Fraser, 1982). These signals, however, provided a useful means for mapping the movement of the El Chichon cloud (Krueger, 1983; Barth et al., 1983; Strong, 1984).

Figure 1 shows the lidar integrated backscatter at NASA Langley (37°N, 76°W) from 1974 through the middle of 1985. The integral is calculated from the tropopause to 30 km which always

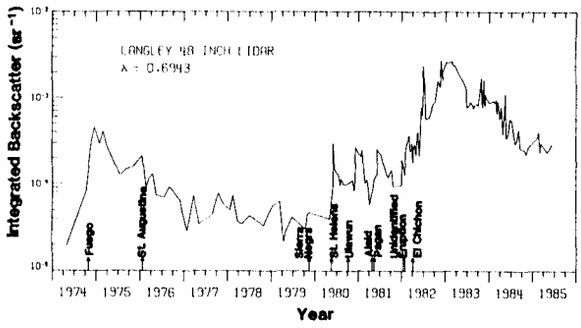

Fig. 1. Integrated backscatter from the tropopause through 30-km for the NASA Langley ruby lidar at 37°N, 76°W.

includes the stratospheric layer at this latitude. The time of eruption for volcanoes known to have placed material into the stratosphere are annotated on the abscissa. Note the record begins with the increase and subsequent decay caused by the October 1974 eruption of Fuego in Guatamala (McCormick et al., 1978) and continues to 1979 with only the high latitude eruption of St. Augustine reported (Remsberg et al., 1976). The period 1978-1979 was thought to be one in which little or no volcanic enhancement exists. This was soon changed, however, by the eruptions of Mount St. Helens, Ulawun, Alaid, Pagan, an unidentified eruption, and then the largest since Agung, and possibly the largest in the Northern Hemisphere in the last 70 years, El Chichon. As can be seen in Figure 1, integrated backscatter increased by an order of magnitude over the highest values measured after the Mount St. Helens eruption. This record is for 37°N and, as such, is very dependent upon the location of the particular eruption. Alaid, for example, is at a high northern latitude, and its effects were barely perceptible at 37°N. The Mount St. Helens (46°N) cloud, however, moved past 37°N soon after its eruption as can be observed in Figure 1. Also, note the large increase in July 1982. This was due to the transport of a small piece of the upper layer produced by El Chichon. The bulk of the upper layer was constrained to approximately 10°S to 30°N for about the first 6 months after El Chichon's eruption. The lower altitude layer produced from El Chichon, however, did move much more rapidly toward the poles. The first indication at Langley of the El Chichon perturbation was the detection of its lower cloud on April 29, 1982. The lower material reached the north polar region as soon as late April 1982.

Figure 2 gives backscatter profiles at Langley from July 1982 to November 1983, showing the original upper layer and the subsequent decrease in peak scattering and altitude and smoothing of the layer. Figure 3 presents integrated backscatter from five airborne lidar campaigns. Note that peak values of 9 x 10^{-2} were recorded in July 1982 at low latitudes, approximately an order of magnitude greater than the highest values later observed at Langley (37°N). The May 1983 plot clearly shows the global distribution (assuming this aircraft "slice" through latitudes over limited longitudes is typical of the globe) with peak values at about 50°N, a lesser peak over the latitude of the volcano, and smaller yet amounts in the Southern Hemisphere.

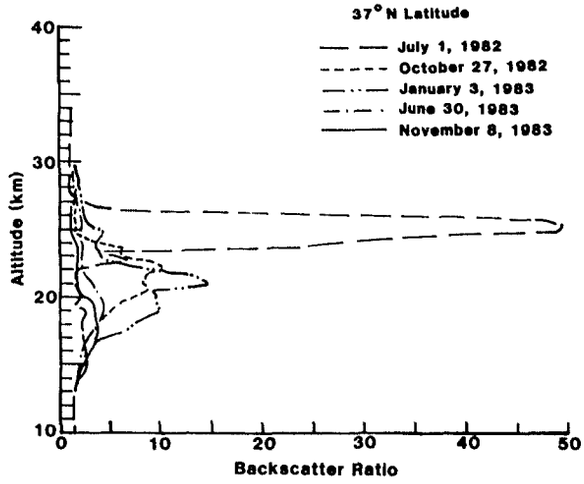

Fig. 2. Backscatter ratio profiles at λ = 0.6943 μm taken at the NASA Langley Research Center.

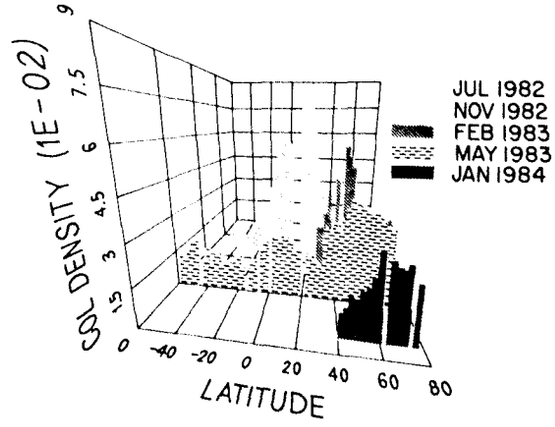

Fig. 3. Column density calculated from stratospheric integrated backscatter for five airborne lidar missions during 1982-1984.

Figure 4 is a compilation of lidar data taken from reports in the Smithsonian's Scientific Event Alert Network Bulletins. Plotted is the value of peak backscatter ratio minus 1 (aerosol backscatter ratio) at λ = 0.6943 μm from various Northern Hemisphere stations. The λ = 1.06 μm values reported from Fukuoka have been converted to λ = 0.6943 μm as given by McCormick and Swissler (1984). The peak backscatter for

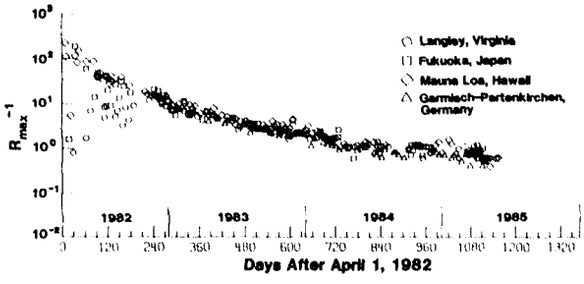

Fig. 4. Peak aerosol backscatter ratios at λ = 0.6943 μm for various Northern Hemisphere lidar stations.

approximately the first 9 months to a year after the eruption was from the upper layer (>20 km) as shown in Figure 2. Figure 4 shows clearly the effect of station latitude. Immediately after the eruption, the lowest latitude lidar station detected the highest values. As the upper cloud moved northward past 30°N in about late October, the higher latitude stations detected the upper layer and all stations subsequently recorded the same value of peak backscatter. Evidently, the cloud became much more homogeneous at the peak altitude. In general, the lower latitude stations with higher tropopauses will record the highest altitudes for the peak. Presently (January 1986), the aerosol peak value recorded at Langley is about 0.4 at 18 to 19 km.

SAM II 1 μm optical depths peaked in January 1983 at values of about 5×10^{-2} in the Arctic and about one-half that value in the Antarctic. Optical depth values peaked at 20°N during the October-November 1982 airborne lidar campaign at about 0.15 for $\lambda = 0.44$ μm (Spinhirne, 1983). Higher values obviously occurred in the fresh volcanic cloud as it initially circled the Earth. Stratospheric temperatures were also affected. Labitzke et al. (1983) have shown that the 30-mb temperatures between 10°N and 30°N during July-October 1982 were significantly warmer than in the same months in the previous 18 years. Peak temperature deviations coincided with maximum aerosol enhancement both in altitude and latitude. These findings are consistent with 1-dimensional radiative-convective models which predict that aerosols from a major eruption like El Chichon should cause a warming in the stratosphere and cooling near the Earth's surface (Hansen et al., 1978). Robock (1984) calculated that the aerosols produced by El Chichon should cool the surface by 1.0 to 1.4C at high northern latitudes in the spring and fall of 1984 and 1985, and that the Northern Hemisphere annual average should decrease by 0.4 to 0.5C in 1984 and 1985.

Table 1 gives a listing of the eruptions described above and an estimate of the total global injection produced by them. Clearly, El Chichon produced the largest impact since Agung, about 24 times greater.

Name	Date	Location	Global Mass Loading (10^{12}g)	Source
Agung	Mar. 1963	(8.4°S, 115.5°E)	16	Deirmendjian (1973)
			30	Cadle, et al. (1976, 1977)
Fuego	Oct. 1974	(14.5°N, 90.9°W)	6	Cadle, et al. (1976, 1977)
			3	Lazrus, et al. (1979)
"Background - 1979"			0.57	Kent and McCormick (1984)
Sierra Negra	Nov. 1979	(0.8°S, 91.2°W)	0.16	Kent and McCormick (1984)
Mt. St. Helens	May 1980	(46.2°N, 122.2°W)	0.55	Kent and McCormick (1984)
Ulawun	Oct. 1980	(5°S, 151.3°E)	0.18	Kent and McCormick (1984)
Alaid Pagan	Apr. 1981 May 1981	(50.8°N, 155.5°E) (18.1°N, 145.8°E)	0.5	Kent and McCormick (1984)
Unidentified Source	Jan. 1982	(Tropical Source)	0.85	Mroz, et al. (1983)
El Chichon	Apr. 1982	(17.3°N, 93.2°W)	12	McCormick (1983)

A decay of the global aerosol mass produced by the eruption of El Chichon has occurred since early 1983. Using the lidar and SAM II data sets, McCormick and Swissler (1986) have estimated the 1/e decay rate for the Northern Hemisphere and a time interval of a year or more, to be 10-11 months. This period, and the period from the eruption to maximum stratospheric effect (3-6 months), are similar to those found for earlier eruptions.

SUMMARY

The 1982 eruptions of El Chichon produced the largest perturbation to the stratospheric aerosol since Agung, and possibly the greatest perturbation in the Northern Hemisphere in the last 70 years. The stratospheric impact of this eruption and its effects were one of the best studied, if not the best studied, in history. This was due of course to the technology available in remote and in situ sensing from satellite and other platforms and the large number of researchers interested in its study. The studies surrounding the 1980 eruption of Mount St. Helens and the validation of SAM II, SAGE I, and SAGE II probably helped also, due to the widespread cooperation among scientists organized for these efforts.

These efforts have shown that the stratospheric cloud produced from the eruption of El Chichon reached an altitude of at least 30-km, with early peak at 26-km. The cloud circled the globe in about 3-weeks and meridional transport of the lower less massive material was observed at mid- and high northern latitudes by lidar within a few weeks of the eruption. Movement of the upper cloud was slower, with a zonal belt of the more massive aerosol existing between about 10°S and 30°N for about 6 months after the eruption. By the end of 1982, this cloud was well dispersed globally. A maximum stratospheric loading of 1.2×10^{13}g (12 megatonnes) was observed about 3-6 months after the eruption. Stratospheric aerosol optical depths in the visible were as high as 0.15 to 0.2 during this peak period as measured by sunphotometers on aircraft platforms. The impact to the Arctic and Antarctic regions peaked in January 1983 with weekly averaged stratospheric optical depths at $\lambda = 1$ μm of about 0.05 to 0.1 in the Arctic and about one-half to one-third that in the Antarctic. Average 1/e decay times for the aerosol optical depth or mass loading was determined from SAM II and lidar to be 10-11 months.

These aerosols impacted the stratospheric temperatures significantly and are predicted to cool the surface by 1.0 to 1.4C at high northern latitudes in the spring and fall of 1984 and 1985 and the Northern Hemisphere annual average by 0.4 to 0.5C in 1984 and 1985. These results have an important implication on the detection of CO_2 induced climate change. In addition, these aerosols offer new surfaces for heterogeneous chemistry important for the study of ozone depletion. Finally, the stratospheric aerosol was shown to have a deleterious effect on various spacecraft remote sensors.

REFERENCES

Bandeen, W. R. and R. S. Fraser, 1982: Radiative effects of the El Chichon volcanic eruption: Preliminary results concerning remote sensing, NASA Technical Memorandum 84959.

Barth, C. A., R. W. Sanders, R. J. Thomas, B. M. Jakosky and R. A. West, 1983: Formation of the El Chichon aerosol cloud, Geophys. Res. Lett., 10, 993-996.

Cadle, R. D., C. S. Kiang, and J. F. Louis, 1976: The global scale dispersion of the eruption clouds from major volcanic eruptions, J.

Chu, W. P., 1986: Inversion of SAGE II measurements, Proceedings of AMS Sixth Conference on Atmospheric Radiation, Williamsburg, Virginia, May 13-16.

Deirmendjian, D., 1973: On volcanic and other particulate turbidity anomalies, Advan. Geophys., 16, 267-296.

DeLuisi, J. J., E. G. Dutton, K. L. Coulson, T. E DeFoor, and G. B. Mendonca, 1983: On some radiative features of the El Chichon volcanic stratospheric dust cloud and a cloud of unknown origin observed at Mauna Loa, J. Geophys. Res., 88, 6769-6772.

Hansen, J. E., W. Wang, and A. A. Lacis, 1978: Mount Agung eruption provides test of a global climatic perturbation, Science, 199, 1065-1068.

Hofmann, D. J. and J. M. Rosen, 1983: Sulfuric acid droplet formation and growth in the stratosphere after the 1982 eruption, of El Chichon, Science, 22, 325-327.

Hofmann, D. J. and J. M. Rosen, 1984: Measurement of the sulfuric acid weight percent in the stratospheric aerosol from the El Chichon eruption, Geof. Int., 23-3, 309-320.

Kent, G. S. and M. P. McCormick, 1984: SAGE and SAM II measurements of global stratospheric aerosol optical depth and mass loading, J. Geophys. Res., 89, 5303-5313.

Krueger, A. J., 1983: Sighting of El Chichon sulfur dioxide clouds with the Nimbus 7 Total Ozone Mapping Spectrometer, Science, 23.

Labitzke, K., B. Naujokot and M. P. McCormick, 1983: Temperature effects on the stratosphere of the April 4, 1982 eruption of El Chichon, Mexico, Geophys. Res. Lett., 10, 24-26.

Lazrus, A. L., R. D. Cadle, B. W. Gandrud, J. P. Greenberg, B. J. Huebert, and W. I. Rose, Jr., 1979: Surphur and halogen chemistry of the stratosphere and of volcanic eruption plumes, J. Geophys. Res., 84, 7869-7875.

Matson, M. and A. Robock, 1984: Satellite detection of the 1982 El Chichon eruptions and stratospheric dust cloud, Geof. Int., 23-2, 117-127.

Mauldin, L. E., N. H. Zaun, M. P. McCormick, J. H. Guy and W. R. Vaughan, 1985: Stratospheric Aerosol and Gas Experiment II instrument: A functional description, Opt. Eng., 24, 307-321.

McCormick, M. P., T. J. Swissler, W. P. Chu, and W. H. Fuller, Jr., 1978: Post-volcanic stratospheric aerosol decay as measured by lidar, J. Atmos. Sci., 35, no. 7.

McCormick, M. P., P. Hamill, T. J. Pepin, W. P. Chu, T. J. Swissler, and L. R. McMaster, 1979: Satellite studies of the stratospheric aerosol, Bull. Amer. Met. Soc., 60, no. 9, 1038-1046.

McCormick, M. P., 1982: Lidar measurements of Mount St. Helens effluents, Opt. Eng., 21, 340-342.

McCormick, M. P. and T. J. Swissler, 1983: Stratospheric aerosol mass and latitudinal distribution of the El Chichon eruption cloud for October, 1982, Geophys. Res.

McCormick, M. P. and T. J. Swissler, 1984: Scientific Event Alert Network, vol. 9, no. 10.

McCormick, M. P., T. J. Swissler, W. H. Fuller, W. H. Hunt and M. T. Osborn, 1984: Airborne and ground-based lidar measurements of the El Chichon stratospheric aerosol from 90°N to 56°S, Geof. Int., 23-2, 187-221.

McCormick, M. P. and T. J. Swissler, 1986: Temporal variation and decay of the El Chichon stratospheric aerosol. (Submitted to J. Geophys. Res.).

Mroz, E. J., A. S. Mason and W. A. Sedlicek, 1983: Stratospheric sulfate from El Chichon and the mystery volcano, Geophys. Res. Lett., 10, 873-876.

Remsberg, E. E., E. V. Browell, and G. B. Northam, 1976: Lidar measurement of stratospheric dust from St. Augustine Volcano, Bull. Amer. Met. Soc., 57, no. 9, 1151-1153.

Robock, A., 1984: Climate model simulations of the effects of the El Chichon eruption, Geof. Int., 23-3, 403-414.

Spinhirne, J. D., 1983: El Chichon eruption cloud: Latitudinal variation of the spectral optical thickness for October 1982, Geophys. Res. Lett., 10, 881-884.

Strong, A. E., 1984: Monitoring El Chichon aerosol distribution using NOAA-7 satellite AVHRR sea surface temperature observation, Geof. Int., 23-2, 129-142.

STRATOSPHERIC AEROSOL AND GAS EXPERIMENT (SAGE II)

Leonard R. McMaster

Atmospheric Sciences Division
NASA Langley Research Center
Hampton, VA 23665

1. INTRODUCTION

SAGE II, launched from shuttle aboard the Earth Radiation Budget Satellite (ERBS) in October 1984, is the fourth in a series of satellite-borne stratospheric aerosol monitoring instruments flown by NASA. The solar occultation technique was employed in each case because of the relatively large signal available and its inherent self-calibration. As depicted in Figure 1, the attenuation of solar radiation through the

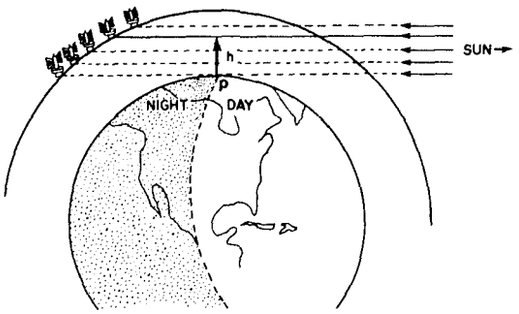

Fig 1. Solar occultation measurement geometry

Earth's atmosphere is measured by the instrument during satellite sunrise and sunset periods from the top of the atmosphere down to where the solar radiation is blocked by the Earth's horizon or cloud tops. Note that since the unattenuated solar radiation is measured prior to each sunset and following each sunrise, the measured signal can be normalized to exoatmospheric values, eliminating the requirement for precise solar intensity measurements to determine atmospheric transmission. These solar attenuation profiles are thus obtained at various spectral wavelengths corresponding to constituent extinction in the atmosphere and later mathematically inverted to aerosol extinction and gaseous constituent concentration profiles. The solar occultation viewing geometry from Earth orbit also allows these constituent profiles to be mapped globally for studying the temporal and spatial variability of the stratosphere.

The Stratospheric Aerosol Measurement I (SAM I), the first instrument to use this technique from space, was flown on the Apollo-Soyuz Test Project in July 1975 (Pepin, 1977). It employed a single spectral channel at 1 μm for aerosols and only collected four profiles to test the technique and instrument design from a space platform. The SAM II instrument, also employing a single spectral channel at 1 μm for aerosols, was launched on the Nimbus 7 spacecraft in October 1978 (McCormick, 1979). SAM II, which collects data only in the polar regions because of the Nimbus 7 high noon sun-synchronous orbit, is still collecting data today after 7 years of successful operation. The Stratospheric Aerosol and Gas Experiment I (SAGE I) was launched February 1979 aboard the Application Explorer Mission 2 (AEM2) spacecraft (McCormick, 1979). SAGE I had four spectral channels at 1.0, 0.6, 0.45, and 0.385 μm for measuring the atmospheric extinction of aerosols, ozone, and nitrogen dioxide, and was in an orbit that allowed collection of data from 79°S to 79°N latitude. The SAGE I instrument collected data for 3 years until the AEM-2 spacecraft power subsystem failed. The most recent of these experiments, SAGE II, employs a seven spectral channel radiometer for measuring aerosols, ozone, nitrogen dioxide, and water vapor.

2. ERBS/SAGE II MISSION

The SAGE II experiment is part of the Earth Radiation Budget Satellite (ERBS) designed to monitor the Earth's incoming and outgoing radiation as part of NASA's climate program. The specific objectives of SAGE II are to (1) map vertical profiles of stratospheric aerosols, ozone, nitrogen dioxide, and water vapor with a 1-km vertical resolution, and determine high altitude cloud coverage globally from 80°S to 80°N; (2) study the seasonal and global variations in these clouds and in stratospheric constituents in order to understand their effect on Earth radiation budget and climate; (3) utilize stratospheric aerosols and gases as atmospheric tracers to study circulation, sources and sinks of these species, and transient phenomena such as volcanic eruptions; and (4) investigate atmospheric chemistry involving these gaseous species and study the optical and physical properties of aerosols.

The seven spectral channels employed by SAGE II were thus selected to measure the atmospheric extinction due to aerosols, ozone, nitrogen dioxide, and water vapor. The relative contribution of constituent extinction to the total extinction observed in each channel is shown in Figure 2. The ozone absorption channel is shown at 600 nm, the peak of the Chappuis band. The 452- and 448-nm channels have relatively narrow bandwidths and are located on and off a nitrogen dioxide absorption feature to allow a differential absorption measurement of nitrogen dioxide. The water vapor absorption channel is shown at 940 nm in the ρ-band. The other three channels

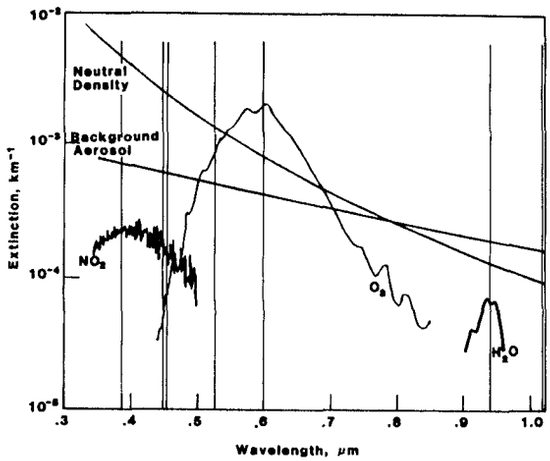

Fig. 2 Variation in atmospheric extinction due to aerosols, NO_2, O_3, H_2O and Rayleigh scattering at 18 km from 0.3 to 1.02 μm.

were selected to measure neutral density and aerosol extinction with minimum ozone, nitrogen dioxide, and water vapor interference.

ERBS/SAGE II was launched by shuttle and then boosted into a 57° inclination, 610-km circular orbit by an onboard propulsion system. This orbit provides 30 solar occultation measurements each day, 15 sunrise events, each separated by approximately 24° longitude at approximately the same latitude, plus 15 sunset events in a similar manner. Globally, these measurements will cover 80°S to 80°N latitude throughout a year's operation as shown in Figure 3. The ERBS mission requires a minimum of 1 year of operation, but the current estimates of remaining expendable fuel would suggest a lifetime of more than 10 years.

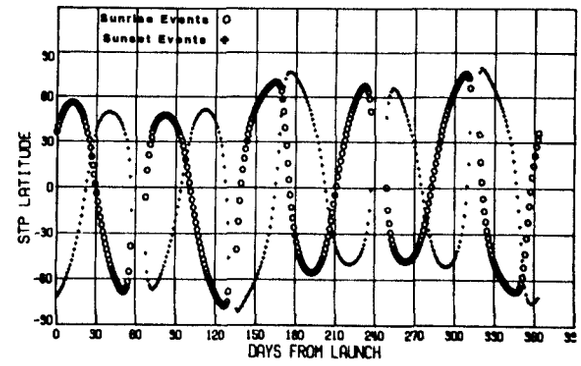

Fig. 3. Latitude of solar occultation measurements sub-tangent point (STP) versus time for satellite observations from 57° inclination, 610 km circular orbit.

3. SAGE II INSTRUMENT DESCRIPTION

The SAGE II instrument is a seven-channel radiometer consisting of an elevation scan mirror, telescope, and grating spectrometer as shown in Figure 4. The telescope is a spherical Cassegrian with a 5.1-cm aperture and an f-number of 30, which forms a diffraction-limited image of the Sun at the field stop. An external scan mirror reflects the solar radiation into the telescope, scanning the solar image across the field stop, which also serves as the entrance slit to the spectrometer. The field stop defines the instrument instantaneous field-of-view and is rectangular in shape, 0.5 arc minutes in elevation by 2.5 arc minutes in azimuth. At the ERBS/SAGE II orbit altitude, this corresponds to approximately 0.5 km by 2.5 km on the Earth's horizon.

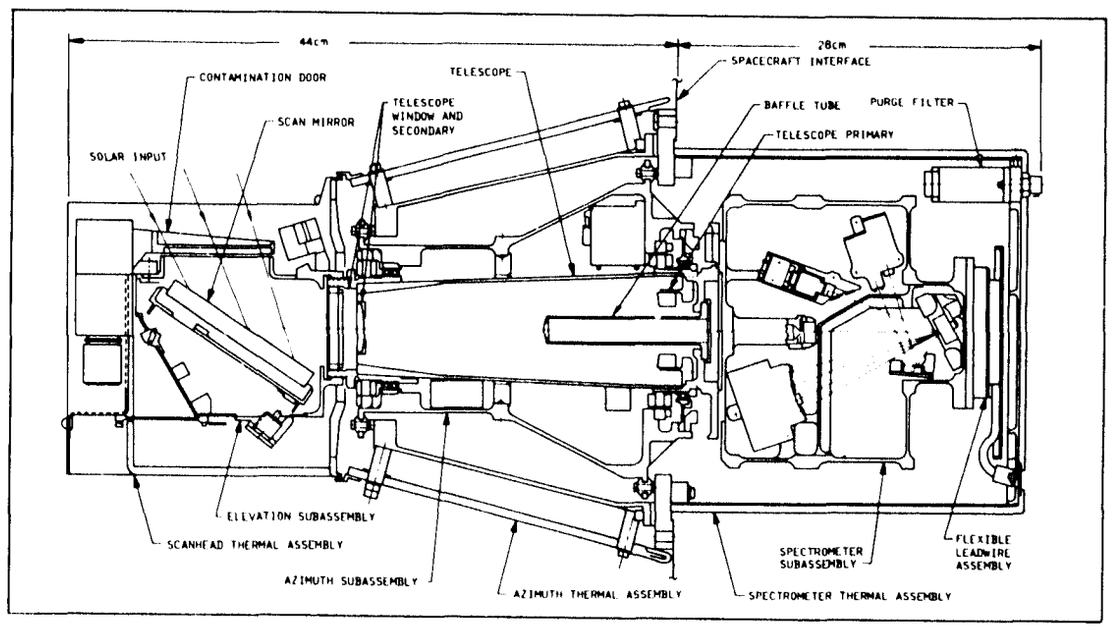

Fig. 4 SAGE II instrument assembly.

The spectrometer utilizes a holographic grating to disperse the solar radiation into the seven radiometric channels with the properties shown in Table I. Channels 1, 3, 4, 6, and 7 use the first order reflection with the spectral bandwidth, except for channel 6, defined by the exit slit on the Rowland Circle. Channel 6 employs an interference filter to achieve its relatively narrow bandwidth. Channels 2 and 5 use zero order reflection with interference filters to define their bandwidth, because they could not be physically accommodated on the Rowland Circle.

Silicon photo diodes are used to collect the dispersed solar radiation in each of the seven channels. The solar radiance data from the seven channels are digitized with a 12-bit analog-to-digital converter, yielding a dynamic range of more than 3000 for each channel. An active thermal control is utilized in the spectrometer to reduce the temperature sensitivity, resulting in a noise level of less than 1 count in 4096 counts for the detection system.

Table I

SAGE II spectrometer characteristics

Channel Number	Primary Constituent Detected	Center Wavelength (nm)	Bandwidth (nm)
1	Aerosol	1019.7	19.6
2	H_2O	935.5	20.0
3	O_3	599.9	14.5
4	Aerosol	525.0	14.8
5	NO_2, Aerosol	452.4	1.9
6	NO_2	447.5	3.2
7	Neutral Density, Aerosol	384.6	19.8

4. SAGE II INSTRUMENT OPERATION

Prior to each spacecraft sunrise or sunset event, the SAGE II instrument is turned on and rotated to the predicted azimuth angle of the event. The timing of these commands and the predicted azimuth angles are stored in an onboard memory system which is periodically updated from the ground. Once at the predicted angle, pointing control of the instrument is transferred to a pair of Sun sensors, and when the Sun comes into their field-of-view, the instrument is pointed at the Sun within ±1 arc minute of the radiometric center. At that time, the elevation mirror is scanned rapidly over its 10° field-of-view to acquire the Sun in elevation. The scan mirror then slows down to a 15 arc minutes per sec rate, back and forth across the solar disk as the Sun sets or rises with respect to the Earth's horizon.

The radiometric data are sampled at a rate of 64 Hz. Coupled with the 15 arc minute per sec mirror scan rate, approximately four samples are collected in each km. In processing the data, these radiance data are averaged to obtain the 1-km vertical resolution constituent profiles. The science data, along with various engineering data, are stored in an onboard tape recorder during each sunrise or sunset event and periodically telemetered to the ground.

5. SAGE II DATA VALIDATION

Validation of the SAGE II data will consist of determining the instrument radiometric measurement precision and the comparison of derived products with correlative observations. Through prelaunch testing and post launch engineering data evaluation, the precision of the radiometric data has been determined to be better than ±0.1% (Mauldin, 1985).

During the first year of operation, three major field campaigns were conducted to collect correlative aerosol, ozone, nitrogen dioxide, and water vapor data, including groundbased and airborne aerosol lidar observation, balloon and airborne in situ particle counters, rocket and balloon-borne ozone measurement, and balloon-borne, nitrogen dioxide, and water vapor measurements. A preliminary comparison of these data with SAGE II derived profiles indicate excellent agreement. Correlative observations collected by numerous European and other international scientists will be compared with the SAGE II data in the future.

6. SUMMARY

The SAGE II seven-channel radiometer was launched in October 1984 and has successfully operated for over a year collecting aerosol, ozone, nitrogen dioxide, and water vapor profiles from 80°S to 80°N latitude. The in-orbit performance to date has been excellent. Science data are currently being evaluated through extensive comparisons with correlative measurements. Preliminary results of this effort indicate excellent data quality and achievement of all instrument objectives.

REFERENCES

Mauldin, L. E., M. P. McCormick, L. R. McMaster, and W. R. Vaughan, 1985: The Stratospheric Aerosol and Gas Experiment II (SAGE II) design and in-orbit performance, SPIE 2nd International Technical Symposium on Optical and Electro-Optical Applied Science and Engineering, Cannes, France, Paper No. 589018, November.

McCormick, M. P., Patrick Hamill, T. J. Pepin, W. P. Chu, T. J. Swissler, and L. R. McMaster, 1979: Satellite studies of stratospheric aerosols, Bull. Amer. Meteor. Soc., 60, 1038-1046.

Pepin, T. J., M. P. McCormick, W. P. Chu, F. Simon, T. J. Swissler, R. R. Adams, K. H. Crumbly, and W. H. Fuller, Jr., 1977: Stratospheric aerosol measurements, NASA SP-421, 127-136.

J2.3

INVERSION OF SAGE II MEASUREMENTS

W. P. Chu

Atmospheric Sciences Division
NASA Langley Research Center
Hampton, VA 23665

1. INTRODUCTION

This paper summarizes the procedures for retrieving atmospheric constituent vertical profiles from solar radiance measurements obtained from the satellite instrument SAGE II. The SAGE II instrument is the latest of the series of occultation instruments specifically designed for the remote sensing of stratospheric aerosols and gases. Previous instruments in the series consisted of SAM, SAM II, and SAGE. They are all Sun pointing, multi-wavelength radiometers operating in the solar occultation mode for measuring selected atmospheric species showing extinction characteristics in the visible to near IR spectral wavelength region. A detailed description of their operation has been given by McCormick et al. (1979).

The general characteristic of the SAGE II instrument has been discussed by Mauldin et al. (1985). Briefly, the instrument vertically scans the solar image during both spacecraft sunrise and sunset events. Solar radiance is measured, limited by the instrument's vertical field-of-view of 0.5 arc-minute at seven spectral wavelength bands located at 0.385, 0.448, 0.453, 0.525, 0.60, 0.94, and 1.02 micrometers. The spectral bandwidth for five of the channels is about 150 Angstrom. The two exceptions are located at 0.448 and 0.453 micrometers and are used for differential measurement of NO_2 absorption. Their spectral bandwidths are about 20 Angstrom. The 0.94-micrometer channel is used for measurement of water vapor. The 0.6-micrometer channel is located at the peak of the ozone Chappuis band, and is most sensitive to ozone absorption. Measurements at the other wavelength channels are used to retrieve the aerosol extinction versus wavelength characteristics from 0.385 to 1.02 micrometers.

For routine data processing, the SAGE II seven-channel solar radiance data are converted to atmospheric slant path transmission value before the inversion can be performed. The procedure for reducing the solar scan data into transmission profile has been discussed by Chu and McCormick (1979). All the solar scan radiance data are merged together to generate seven slant path transmissions versus tangent altitude profiles. The scan data are then averaged into 1-kilometer vertical increments to provide the mean slant path transmission value at each km altitude. The standard deviation calculated from the averaging process is used to generate the estimated uncertainty for the slant path transmission values.

2. METHODOLOGY

2.1 General Approach

The procedures for inverting the SAGE II data follows the general approach used in the inversion of the SAGE data which was discussed by Chu and McCormick (1979). Since the SAGE II data consist of 7-wavelength measurements compared to 4-wavelength measurements located at 1.0, 0.6, 0.45, and 0.385 micrometers for SAGE, the SAGE inversion scheme had to be modified for SAGE II data processing, thus providing characterization of the aerosol extinction versus wavelength behavior. A two-step retrieval scheme has been developed for the SAGE II inversion which can be applied to the 7-wavelength slant path transmission data. The first step in the inversion process is to separate the contribution to the slant path transmission measurements from each species at the 7-wavelength bands for each altitude level. Then the vertical profile for each species can be inverted from the individual slant path transmission versus altitude profile.

2.2 Ozone and Aerosol Retrieval

The SAGE II measured slant path transmission profile when converted to the optical depth profile at the five wavelength channels located at 1.02, 0.6, 0.525, 0.453, and 0.385 micrometer can be written as follows:

$$\delta_{\lambda i} = \delta_{\lambda i}(\text{aerosol}) + \delta_{\lambda i}(\text{ozone}) + \delta_{\lambda i}(\text{Ray}) + \delta_{\lambda i}(NO_2) \qquad (1)$$

where $\delta_{\lambda i}$ is the optical depth measurement at wavelength λ and altitude level i. It consists of contributions from aerosol, ozone, NO_2, and molecular scattering (Rayleigh scattering). The Rayleigh component is removed based on calculations using the given temperature vertical profile data from the National Weather Service of NOAA. The NO_2 component is removed from the differential absorption measurement between the 0.448 and the 0.453 micrometer data as discussed in the next section. Marquardt's nonlinear algorithm (Marquardt, 1963) is used to separate the ozone and aerosol contributions in equation 1. The aerosol slant path optical depth versus wavelength behavior is assumed to be described by a nonlinear quadratic polynomial in the variable λ.

The results obtained from the Marquardt algorithm applied to each altitude level are the slant path optical depth profiles for ozone at 0.6 micrometers aerosol optical depth profiles at 1.02, 0.525, 0.453, and 0.385 micrometers. These five slant path optical depth profiles can be written in the following form:

$$\delta_i = \sum P_{ij} \beta_j \qquad (2)$$

where P_{ij} is the optical path length in the j level for tangent height in the i level, and the β_i is the vertical extinction profile for the individual species. The above equation is then inverted with Twomey's modification of Chahine's nonlinear algorithm (Twomey et al., 1977). A slight modification of this algorithm incorporates some smoothing of the retrieved profiles by averaging the inverted result during each iterative cycle. The above mentioned smoothing is only applied to the profile at high altitude where the concentration of the species is small and decreasing very rapidly. Iteration is stopped when the residue between the actual measurement and the calculated measurement approaches the estimated uncertainty of the measurement.

2.3 NO_2 Retrieval

The NO_2 signature is mainly manifested in the differential measurement between 0.453 and 0.448 micrometer data. By ratioing the slant path transmission of these two-channel data, the differential transmission profile is obtained which contains, in addition to the NO_2 signature, contributions from Rayleigh scattering, some ozone absorption, and some aerosol scattering. In processing the NO_2 data, a first order estimate of the NO_2 optical depth profile is obtained after the removal of the Rayleigh component. This first order estimate for NO_2 is used for the correction in the aerosol and ozone retrieval. After the ozone and aerosol optical depth profiles are obtained from the previous procedure, they are used to remove their contributions from the differential transmission data. The NO_2 vertical profile is then inverted using equation (2) for the NO_2 slant path optical depth profile. The inversion scheme used here is identical to the one used in the ozone and aerosol inversion.

2.4 Water Vapor Retrieval

By ratioing the 0.94 to the 1.02 micrometer transmission profiles, a differential transmission profile containing predominately the water vapor absorption signature is obtained with some residual signature from ozone absorption, aerosol, and Rayleigh scattering. The interfering signatures can be removed from the water vapor data using the results from the ozone and aerosol retrievals. The water vapor transmission profile is inverted using the original Chahine's nonlinear algorithms (Chahine, 1970). The transmission profiles for water vapor are calculated using an emissivity growth approximation. The data base used for the emissivity growth approximation is calculated using the Fourier transform method (Gordley and Russell, 1981). The accuracy of the Fourier transform method for calculating the water vapor absorption signature has been compared with the FASTCODE calculation and was found to be in good agreement. The emissivity growth approximation technique has been found to be accurate and fast for calculating the water vapor transmission profile appropriated for the SAGE II measurements under different water vapor concentration, temperatures, and pressure levels.

2.5 Estimation of Uncertainty for Inverted Data

The uncertainty associated with the inverted profile from the SAGE II measurements is calculated based on the estimated measurement errors from the various noise sources. The error sources for the SAGE II measurements consist of random noise in the radiance measurement, pointing uncertainty, altitude determination error, and the uncertainty in the calculated Rayleigh component from the given temperature profile (Chu and McCormick, 1979). The estimated measurement errors are obtained from the root-mean-square of the various error source terms. For the inverted SAGE II 6-wavelength profiles (aerosol, ozone, and NO_2 profiles), the estimated errors are calculated similar to the method described by Russell et al. (1981) whereby the measurement error array is multiplied by an error sensitivity matrix to give the uncertainty associated with the inverted results. The error sensitivity matrix for these cases is the inverse of the path length matrix as described by equation (2). However, for the water vapor profile retrieval, the error sensitivity matrix has to be calculated from the emissivity growth approximation technique.

3. CONCLUSION

This paper summarizes the procedures used by NASA Langley Research Center personnel to process the SAGE II measurements for producing vertical profiles of aerosol extinction at four wavelengths, and ozone, NO_2, and water vapor concentrations. These procedures are more complicated compared to the earlier SAGE inversion approach, but they still satisfy the requirements of accuracy and efficiency for processing the SAGE II data. Comparison of the SAGE II retrieved profiles to correlative measurements has been performed, and the results will be discussed in another paper by Swissler (1986) during this conference.

4. REFERENCES

Chahine, M. T., 1970: Inverse problems in radiative transfer: Determination of atmospheric parameters, J. Atmos. Sci., 2, 960-966.

Chu, W. P. and M. P. McCormick, 1979: Inversion of stratospheric aerosol and gaseous constituents from spacecraft solar extinction data in the 0.38 - 1.0 μm wavelength region, Appl. Opt., 1, 1404-1413.

Gordley, L. L. and J. M. Russell, 1981: Rapid inversion of LIMS radiance data using an emissivity growth approximation, Appl. Opt., 2, 807-813.

Marquardt, D. W., 1963: An algorithm for least-squares estimation of nonlinear parameters, J. Soc. Ind. Math., 1, 431-441.

Mauldin, L. E., N. H. Zuan, M. P. McCormick, J. H. Guy, and W. R. Vaughan, 1985: Stratospheric Aerosol and Gas Experiment II instrument: A functional description, Opt. Eng., 2, 307-312.

McCormick, M. P., P. Hamill, T. J. Pepin, W. P. Chu, T. J. Swissler, and L. R. McMaster, 1979: Satellite studies of the stratospheric aerosol, Bull. Amer. Meteor. Soc., 6, 1038-1046.

Russell, P. B., M. P. McCormick, T. J. Swissler, W. P. Chu, J. M. Livingston, W. H. Fuller, J. M. Rosen, D. J. Hofmann, L. R. McMaster, D. C. Wood, and T. J. Pepin, 1981: Satellite and correlative measurements of the stratospheric aerosol II: Comparison of measurements made by SAM II, dustsondes and an airborne lidar, J. Atmos. Sci., 3 , 1295-1312.

Twomey, S., B. Herman, and R. Rabinoff, 1977: An extension to the Chahine method of inverting the radiative transfer equation, J. Atmos. Sci., 34, 1085-1096.

GLOBAL DISTRIBUTION OF SAGE II DATA PRODUCTS

D. Rind, G. Russell, J. Lerner

Goddard Space Flight Center
Institute for Space Studies
New York, NY 10025

1. INTRODUCTION

The SAGE II instrument is currently producing assessments of the atmospheric concentrations of O_3, H_2O, NO_2, and aerosol optical thicknesses at four wavelengths (385μ, 453μ, 525μ, and 1020μ). One advantage of this satellite-retrieved data set is that it is possible to determine global distributions, and relate the results to source distributions, atmospheric dynamical patterns or chemical variations. The retrieval method produces vertical distributions above specific locations which depend upon the relation of the orbit to sunrise/sunset. During one month this results in up to 900 records distributed unevenly over the globe. To produce global maps requires first positioning of the data geographically, and then interpolating between data points. Care must be taken to ensure that the interpolation does not introduce imaginary patterns.

2. TECHNIQUE

The coarse resolution version of the GISS general circulation model divides the earth into approximately 800 grid boxes (with a resolution of 8° latitude by 10° longitude). It is thus commensurate with the number of data points produced by the SAGE II instrument in one month. In order to produce maps of the global distributions of the SAGE II data, we thus adopted the following procedure. Each data point was interpolated to the standard pressure levels from 300mb to 0.2mb, and entered into the appropriate general circulation model grid box. If more than one value was recorded during the month for that grid box, the values were averaged. With all the data points so positioned, we then interpolated between grid boxes to fill in missing data, with the interpolation extending up to two grid boxes east-west or north-south. Interpolations of this distance did not seem to distort the basic patterns, and they are consistent with the practice of averaging data within each grid box. It should be noted that due to the spacing of the data retrieval, and the retrieval process itself, very small-scale horizontal structure is probably not obtainable.

3. RESULTS

Global distributions have been generated for the following pressure levels (in mb): 300, 250, 200, 150, 100, 70, 50, 30, 10, 5, 2, 1, 0.4 and 0.2 The following quantities have been plotted: O_3, H_2O, NO_2, and aerosol optical thicknesses at the four frequencies. Relevant data products produced by NMC and included on the data tapes such as temperature and height have also been plotted. In addition, NMC provides an estimate of the tropopause pressure. Maps of the distribution of this value have been generated, and used to distinguish the stratospheric concentrations of the data. Thus additional plots include the stratospheric column integral of O_3, H_2O, NO_2, and aerosol optical thicknesses.

The data to be discussed here is for April, 1985. During this month data was retrieved at sunset in the Northern Hemisphere, and sunrise in the Southern Hemisphere. Monthly maps of the global distributions are thus not only averaged over time, they include a diurnal bias between hemispheres. This is of special importance for NO_2 due to its photochemistry, but may affect all species in the upper troposphere as convective penetration can vary diurnally.

Coldest temperatures for this month from 150-30mb were found in the tropics, from 300-200mb at high latitudes, and above 10mb at high southern latitudes. Warmest temperatures below 200mb occurred in the tropics, from 150-30mb at high northern latitudes, and from 10-5mb again in the tropics. Warm air was found over the North Pacific from 10-5mb, while at higher altitudes warmest temperatures occurred over the North Atlantic. Upper tropospheric troughs over eastern Canada, eastern Asia and the North Pacific extended to 150mb; above, the best defined troughs existed over the western and eastern North Atlantic, disappearing by 30mb. Polar lows exist throughout, becoming very weak in the lower stratosphere, while above 30mb the Southern Hemisphere polar low predominates, with the Northern Hemisphere polar low shifting into the eastern Hemisphere. These fields are representative of early spring in the Northern Hemisphere, with remnants of the warm North Pacific high and cold North Atlantic trough still visible, while the Southern Hemisphere is moving towards its winter appearance. The tropopause is highest over the tropics (around 100mb) and lowest at high northern latitudes (300mb), again typical for this time. The meteorological data from which these results were derived correspond only to those observations taken at the locations and times at which SAGE retrievals were performed.

Ozone concentrations from 200-10mb are greatest in the polar region, especially in the Aleutian area, with somewhat lower values in the

North Atlantic trough. Minimum values occur at low latitudes. Gradients largely disappear by 30mb, and from 10-5mb there is a tropical maximum with minimum values at high latitudes over the North Atlantic. From 2-1mb peak values occur at high sourthern latitudes, with little variation elsewhere. The tropical minima at the higher pressures are often in the troposphere, at the same time as the high latitude maxima are in the stratosphere. The maxima follow the warm ridge and avoid the trough in the lower stratosphere. At higher levels the tropical maxima is presumably a photochemical effect, while in the upper stratosphere the high southern latitude maxima occurs at the end of local summer. Peak gradients of 8ppmv occur at 10mb between the equatorial peaks and the North Atlantic polar minimum.

NO_2 distributions are complicated by the sunrise/sunset effect. At levels up through 70mb there are large concentrations in specific equatorial regions, possibly associated with penetrating convection. From 100-50mb minimum values occur in the Northern Hemisphere (sunset), differences about 1ppb. At 30mb there is a general equatorial minimum. From 10-5mb, the low and subtropical latitudes of the Northern Hemisphere are now 3ppb greater than those in the Southern Hemisphere. At 2mb the hemisphere ratio again reverses, with the Southern Hemisphere now 1ppb greater.

Water vapor values also show an equatorial peak up through 70mb in specific regions. Outside of these areas, low latitude values are still much larger than those at high latitudes (by some 55ppm at 150mb, but remember this is still the troposphere at low latitudes). By 70mb there is a general tropical minima of 1-3ppmv outside of the regions of possible convective penetration. From 50mb-1mb the Southern Hemisphere values are generally larger than those in the Northern Hemisphere by 1-2ppm. At 5mb-2mb there is a slight peak (about 1-2ppm) at high southern latitudes, while by 1mb the Southern Hemisphere again shows values in general about 2ppm larger than in the Northern Hemisphere.

In the equatorial upper troposphere there are occasional very large optical thicknesses in all the aerosol channels over the Amazon, tropical Africa, Indian Ocean and western Pacific -- in somewhat similar locations to the peaks seen in the N_2O and H_2O distributions, and their location suggests penetrative convection. The peaks extend up through the 70mb level; optical thicknesses are a factor of 10 or more larger than the tropical minima.
From 50-30mb Southern Hemisphere values are slightly larger than those in the Northern Hemisphere, with minimum values occuring at the highest latitudes, especially in the Northern Hemisphere.

The stratospheric column amounts depend on the definition of the tropopause. Ozone values are in general agreement with expectation - large values (0.46cm) at Northern Hemisphere high latitudes, with peaks correlated with the location of tropospheric troughs, and small values (0.24cm) occurring in the tropics. NO_2 values are large in the tropical peak regions (.0013cm), with even larger values at high latitudes of both hemispheres. Minimum values occur at other tropical locations, with values of .00015. Water vapor has a tropical peak value of 23cm over the Amazon; otherwise tropical minima are 0-2cm, with 4-8cm at high latitudes. It remains a question as to whether the large NO_2 values are actually in the stratosphere, as well as the water vapor above the Amazon.

4. CONCLUSIONS

Maps of the global distributions of the SAGE II data products can help in visualizing the processes occurring. Difficulties arise in deciphering the sunrise/sunset differences, as well as in determining the exact location of the tropopause. Are large tropospheric values being convected into the stratosphere? Analysis of subsequent months, and correlative experiments may help resolve these issues.

DISPERSION CHARACTERISTICS OF VOLCANICALLY INJECTED AEROSOL AS SEEN BY SAGE I, SAM II, AND SAGE II

Geoffrey S. Kent

Science and Technology Corporation
Hampton, Virginia

1. INTRODUCTION

Data obtained from three satellite experiments and by the NASA/LRC airborne lidar system has been used to study the dispersion of aerosol injected into the stratosphere by several volcanic eruptions occurring since 1979. The satellite experiments are the Stratospheric Aerosol and Gas Experiment I (SAGE I), Stratospheric Aerosol and Gas Experiment II (SAGE II) and Stratospheric Aerosol Measurements II (SAM II), all of which measure stratospheric aerosol extinction at a wavelength of 1 μm (McCormick et al., 1978, Mauldin et al., 1983). The latitudinal coverage and periods of operation of these satellites are shown in Table 1(a). Table 1(b) gives the latitudes and times of eruption of those volcanoes known to have injected material into the stratosphere. Of particular significance is the gap between the final SAGE I measurements and the first SAGE II measurements (October, 1984) during which the eruption of El Chichon occurred.

The common satellite data product is a vertical profile of aerosol extinction at a wavelength of 1 μm for the location of each satellite measurement. By use of a suitable conversion factor, this may be used to derive an approximate value for the mass of aerosol present. The extinction may also be used to derive the extinction ratio, defined as the ratio of 1 μm aerosol extinction to the local 1 μm molecular extinction. This is analogous to the aerosol backscattering ratio commonly derived from lidar measurements. It is an approximately conserved quantity under transport and, for that reason, particularly useful for the study of atmospheric movements.

Table 1(a)

Satellite occultation experiments

Satellite	Latitude Coverage	Period of Operation
SAGE I	74°S - 74°N	Feb 1979-Nov 1981
SAGE II	75°S - 75°N	Oct 1984-Present
SAM II	80°S-64°S;64°N-80°N	Oct 1978-Present

Table 1(b)

Volcanic eruptions, 1979-1985, significantly affecting the stratosphere

Date	Volcano	Location
Nov 13, 1979	Sierra Negra	0.8°S, 91.2°W
May 18, 1980	St. Helens	46.2°N, 122.2°W
Oct 7, 1980	Ulawun	5.0°S, 151.3°E
Apr 27, 1981	Alaid	50.8°N, 155.5°E
May 15, 1981	Pagan	18.1°N, 145.8°E
Dec 1981 - Jan 1982	Unknown	Low Latitude
Mar 28 - Apr 4, 1982	El Chichon	17.3°N, 93.2°W

2. STRATOSPHERIC AEROSOL DISPERSION FOLLOWING THE 1979-1981 VOLCANIC ERUPTIONS

Of the five significant eruptions occurring between 1979 and 1981, three occurred in low latitudes and two in high northern latitudes. The maximum altitude reached by any material from these eruptions was 23-24 km. Subsequent stratospheric effects were monitored by SAGE I and SAM II. Detailed dispersion patterns for the stratospheric aerosol varied but the following general characteristics were noted.

1. The majority of the material from the high latitude eruptions remained within the same hemisphere.

2. The material from low latitude eruptions dispersed into both hemispheres, transport being seasonably controlled and greatest into the winter hemisphere.

3. Subject to (1) and (2) above, the aerosol tended to become concentrated into three latitudinal zones (a) 20°S - 20°N; (b) <40°S and (c) >40°N, with minimum concentrations between latitudes 30° and 40°.

3. AEROSOL DISPERSION FOLLOWING THE ERUPTIONS OF EL CHICHON

The eruptions of El Chichon in March and April, 1984 differed from the earlier eruptions, not only in the much greater magnitude of the stratospheric effects but also in the altitude to which material was injected, which was at least 30 km. At the time of this eruption, SAGE I had ceased operation and SAGE II was not yet operating. The movement of the stratospheric cloud was monitored by the NASA/LRC airborne lidar system (McCormick, et al., 1984) as well as by other experiments. These showed the dispersion to be altitude dependent. During the first few months following the eruption, material below about 21 km spread rapidly northward while material above this altitude was still mainly confined to the latitude band south of 25°N. This upper material began spreading northward in significant quantities in June-July 1982 and continued throughout the northern summer and fall. Dispersion into the southern hemisphere was less extensively monitored but SAM II observations showed that volcanic aerosol had reached the Antarctic region by December, 1982.

4. SAGE II OBSERVATIONS OF THE EL CHICHON AEROSOL

SAGE II observations commenced in October 1984. By this time, the El Chichon aerosol cloud was well dispersed globally, it was concentrated into three principal latitude zones as described in Section 2 for earlier eruptions, with approximately equal mass loading in each zone. In contrast to the mass loading, maximum aerosol extinction ratios (and, hence, aerosol mixing ratios) still occurred within the low latitude zone. The existence of this reservoir of higher aerosol mixing ratio both in the SAGE II data and also in the earlier SAGE I data (pre-volcanic) has enabled a study to be made of a regular seasonal movement of material from low to high latitudes.

In late 1984 and early 1985, a typical high northern latitude extinction ratio profile had a peak value of about 10-15 at an altitude of 15-18 km. In November and December 1984, an appreciable number of profiles were found showing an extra high altitude layer with a layer maximum at an altitude of 25 km or greater. Examples of "normal" and "anomalous" profiles are shown in Fig. 1. Examination of SAGE I data, both before and after any volcanic eruptions, showed a similar phenomenon. Moreover, the occurrence of these "anomalous" layers is seasonal in both hemispheres, maximum numbers being found in winter with very low or zero occurrence in mid-summer. Both local production and microphysical change are unlikely mechanisms for the creation of these "anomalous" high altitude layers. The only place, where matching extinction ratios are to be found at similar altitudes, is within the low latitude zone. The inference from the data is that we are observing seasonal movement of material, at altitudes in the region of 25 kms, from low latitudes into the winter hemisphere. This result is consistent with recent work by Leovy et al. (1985), where poleward transport of ozone in the middle stratosphere into the winter hemisphere is shown to be associated with planetary scale stratospheric waves.

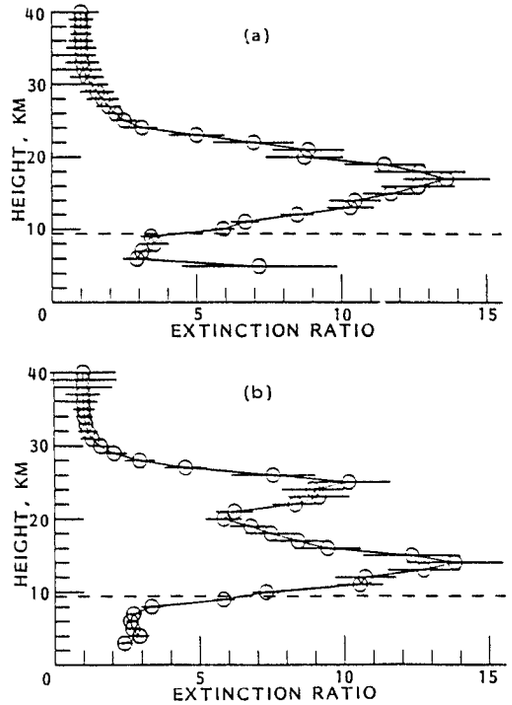

Fig. 1. SAGE II extinction ratio profiles obtained on 16 November 1984.

(a) Normal profile, 48.5°N, 69.6°W
(b) Anomalous profile, 48.0°N, 148.7°E

5. ACKNOWLEDGMENTS

This work was carried out under NASA contract NAS1-17959.

6. REFERENCES

Leovy, C. B., C-R. Sun, M. H. Hitchman, E. E. Remsberg, J. M. Russell, III, L. L. Gordley, J. C. Gille, and L. V. Lyjak, 1985: Transport of ozone in the middle stratosphere: evidence for planetary wave breaking, J. Atmos. Sci., 42, 230-244.

Mauldin, III, L. E., N. H. Zaun, M. P. McCormick, Jr., J. H. Guy, and W. R. Vaughan, 1985: Stratospheric Aerosol and Gas Experiment II instrument: a functional description, Opt. Engr., 24, 307-312.

McCormick, M. P., P. Hamill, T. J. Pepin, W. P. Chu, T. J. Swissler, and L. R. McMaster, 1979: Satellite studies of the stratospheric aerosol, Bull. Amer. Meteor. Soc., 60, 1038-1046.

McCormick, M. P., T. J. Swissler, W. H. Fuller, W. H. Hunt, and M. T. Osborn, 1984: Airborne and ground-based lidar measurements of the El Chichon stratospheric aerosol from 90°N to 56°S, Geof. Int, 23-2, 187-221.

J2.6

MEASUREMENTS OF LOWER STRATOSPHERIC/UPPER TROPOSPHERIC WATER VAPOR BY THE SAGE II INSTRUMENT

J. C. Larsen

SASC Technologies, Inc.
17 Research Drive
Hampton, VA 23666

L. R. McMaster, M. P. McCormick, W. P. Chu

Atmospheric Sciences Division
NASA Langley Research Center
Hampton, VA 23665

1. INTRODUCTION

The Stratospheric Aerosol and Gas Experiment II (SAGE II) is a seven channel spectrometer which infers the vertical distribution of stratospheric aerosols, ozone, nitrogen dioxide and water vapor from the extinction of solar radiation measured during spacecraft sunrise/sunset. SAGE II was deployed by the space shuttle on October 5, 1984 as part of the ERB satellite package and scientific data acquisition commenced October 24. A detailed description of the instrument package, measurement technique and retrieval algorithm may be found in companion papers in these proceedings by McMaster (1986) and Chu (1986). To date, over a years worth of water vapor data has been obtained with global coverage ranging from 80° S to 80° N at altitudes from 45 km down to the cloud tops or 2 km in cloud free regions. This unique data set will be used to establish a global water vapor climatology and improve our understanding of aerosol formation mechanisms and tropospheric/stratospheric exchange processes. Since SAGE II is the first experiment to remotely sense upper tropospheric water vapor from space we will present preliminary data from the lower stratospheric/upper tropospheric altitude regions. Due to the preliminary nature of the data we will be concerned more with validating the data set than with presenting and discussing temporal or spatial variations of the water vapor concentrations. We will present zonal means for the month of April 1985 and compare them to the tropospheric water vapor given in Oort (1983) below 300 mb and the LIMS water vapor as described in Russell et al. (1984) above 100 mb. We know of no global long-term data set which covers the intermediate 100 mb to 300 mb region.

2. COMPARISON TO HISTORICAL WATER VAPOR MEASUREMENTS

In this section we will present selected monthly zonal means for April 1985 and compare them to two well known water vapor compilations, the LIMS measurements as described by Russell et al. (1984) and the Global Atmospheric Circulation Statistics, 1958-1973 (GACS) developed by Oort (1983). The two data sets are fundamentally different in several ways. The LIMS experiment used the technique of thermal infrared limb scanning to remotely sense water vapor from space with near global coverage (64°S to 84°N) from October 24, 1978 to May 28, 1979. In contrast, the GACS water vapor climatology is developed from several different data sets composed primarily of rawinsonde observations. Southern hemisphere climatology is based on the 1963 to 1973 time period while the northern hemisphere includes an additional 5 year period, from 1958 to 1963. Longitudinal coverage obtained with the LIMS experiment is very uniform in both hemispheres, while most GACS rawinsonde data are taken over land at fixed locations which determines the longitudinal coverage. The GACS data have altitude coverage from 1000 mb to 300 mb while the LIMS experiment covers 100 mb to 1 mb. In spite of the differences in measurement techniques, sampling biases and time frames among the experiments, comparing SAGE II to these water vapor distributions can provide helpful insights as to the quality of the data.

To remove data contaminated by clouds and noisy transmission data each SAGE II profile was screened by using information from the retrieved water vapor mixing ratio and the slant path transmissions for the 1.02 μm aerosol and 0.94 μm water vapor channels. Figure 1 illustrates typical measured slant path transmission for the 1.02 μm and 0.94 μm channels. The differential water vapor slant path transmission is also shown. The differential transmission must be

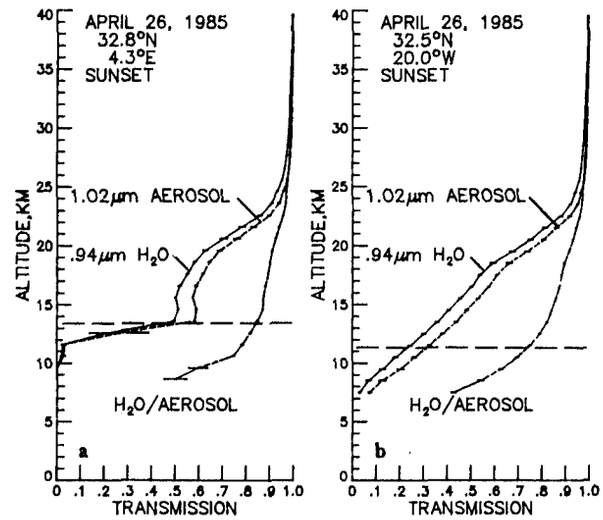

Figure 1. Measured slant path transmissions vs. altitude for cloudy (a) and cloud free (b) conditions. Error bars are the estimated standard deviation uncertainty. Horizontal dashed line indicates the tropopause height.

further corrected for Rayleigh scattering, aerosol and ozone signature before the water vapor retrieval can be performed. The error bars indicate the estimated standard deviation of the slant path transmission which is based on the scan averaging error. The meteorological cloud at 12.5 km in Figure 1a can be identified very easily by looking at the rapid drop in transmission when the cloud is first encountered. Water vapor data at and below the cloud level are deleted from further consideration. The SAGE II data set is initially biased toward cloud free conditions since the retrieval process is terminated when thick clouds are observed. Removing the cloud contaminated data reinforces this trend. Water vapor data that are inferred from noisy transmission data are deleted at and below any level where the error bars of the 1.02 μm and 0.94 μm channels overlap or when the absolute level of the slant path transmissions drop below the noise levels. These two checks prevent the water vapor from being used when the differential slant path transmission has been calculated from indeterminate or very low signal levels. The final screen applied to the data looks for a water vapor mixing ratio several times greater than the saturation mixing ratio of water. This situation occasionally happens if the differential slant path transmissions are not corrected for the interferring signatures properly. This screening process has been applied to the April zonal means presented in this paper.

At the start of April, SAGE II sunset and sunrise events were located at 62° N and 46° N, respectively. By the fifth of April the sunset events had moved to 76° N while the sunrise events moved to the equator. On April 23 sunrise events were located at 55° S and moved north to 46° S by the end of the month. The locations of the sunset events slowly moved south reaching 12° N at the end of the month. Thus, the northern high latitudes were sampled early in the month while the southern high latitudes were sampled toward the end of the month. Because of this a monthly zonal mean for a particular latitude band may be more representative of a specific time period such as the second week of the month, for example, than for a full month. Table 1 shows the total possible number of events for April at selected middle and high latitudes after being grouped into 10° latitude bins centered on the latitude shown. Also shown are the number of suitable events remaining after the data screening process is applied at 10 km and 5 km.

TABLE 1

SAGE II Global Coverage for Selected 10° Latitude Bins in April 1985

Center Latitude	Total Events	Remaining Events at 10 km	Remaining Events at 5 km	Tropopause km
60° N	83	69	6	9.0
40° N	56	17	0	11.1
30° N	48	13	1	13.6
30° S	30	21	15	15.5
40° S	44	22	10	13.4
60° S	42	19	4	10.0

Figures 2, 3 and 4 present the preliminary SAGE II zonal means for April 1985 for 30°, 40° and 60° N and S, respectively. The preliminary SAGE II data are compared to the LIMS and GACS data in these figures. The SAGE II zonal means were calculated with 10° latitude bins while the LIMS data used 4° bins and the GACS data was averaged in 5° bins. The SAGE II measurement error bars show the zonally averaged standard deviation of the estimated measurement error. The estimated error in turn is derived from the random error in the differential transmission, uncertainties in correcting the interference signatures and uncertainties inherent to the water vapor retrieval itself. Thus, the estimated error includes both random and bias components. The variation of the mean values shows less variation than that expected from the

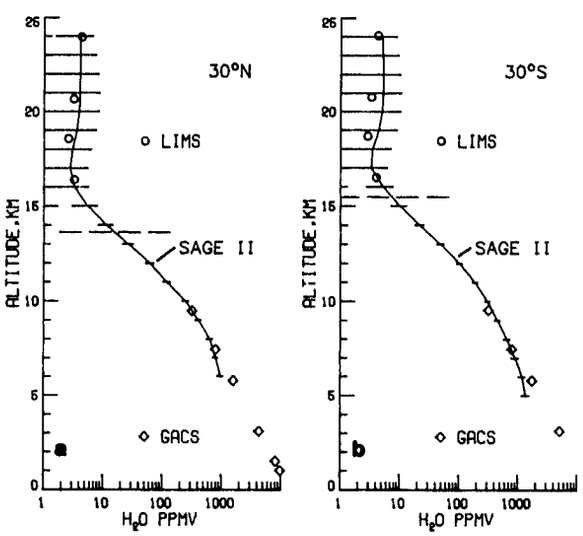

Figure 2. Comparison of the SAGE II preliminary data, LIMS and Global Atmospheric Circulation Statistics monthly zonal means for April at 30° N (a) and 30° S (b). Horizontal dashed line indicates the average tropopause height.

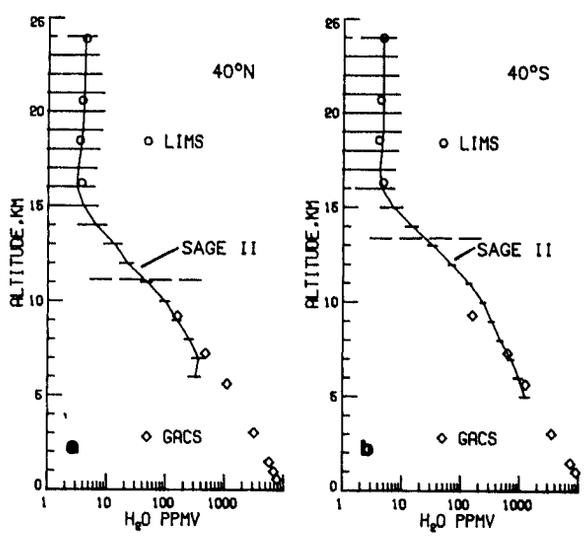

Figure 3. Comparison of the SAGE II preliminary data, LIMS and Global Atmospheric Circulation Statistics monthly zonal means for April at 40° N (a) and 40° S (b). Horizontal dashed line indicates the average tropopause height.

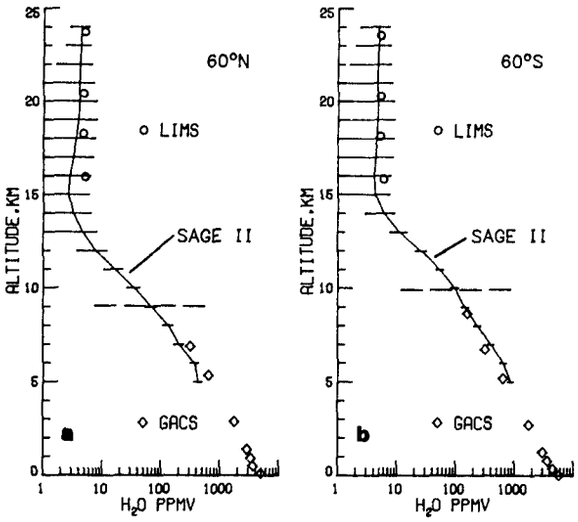

Figure 4. Comparison of the SAGE II preliminary data, LIMS and Global Atmospheric Circulation Statistics monthly zonal means for April at 60° N (a) and 60° S (b). Horizontal dashed line indicates the average tropopause height.

estimated error. The number of events in each zonal mean as a function of altitude is qualitatively described by Table 1 and must be taken into consideration along with the diverse origins of the three data sets when comparing them. Overall, the agreement is quite good. SAGE II and LIMS zonal averages agree to better than 1.5 ppmv everywhere with a few exceptions. The major exception is at 30° S where SAGE II is greater than LIMS by 2.0 ppmv. Possibly this is due to be a problem with modeling the aerosol signal in the water vapor channel. SAGE II water vapor zonal means in equatorial regions (not shown) where the aerosol layer at 20 km is very distinct show similar perturbations. Work is currently underway on ways to improve the aerosol correction in the water vapor channel. Agreement with the GACS data is also quite good as can be seen in Figures 2, 3 and 4. A relative accuracy of 10.% for the GACS water vapor is given by Oort (1983) at low altitudes and from the GACS annual and seasonal variability statistics we estimate an annual variability of approximately 10% for April at the altitudes where the SAGE II and GACS data overlap. When these two factors are considered the SAGE II and GACS data agree except for a single point at 40° S.

3. DISCUSSION

Because of the many differences (measurement techniques, sampling biases and observation periods) between SAGE II and the comparison data sets we do not expect to fully resolve the remaining measurement discrepancies. It is quite possible that some of the remaining discrepancies represent a natural change in the water vapor distribution. However, a comparison such as this one is an obvious first step in the data validation process. Our next effort is to compare the SAGE II water vapor data with nearly simultaneous water vapor sonde data obtained by the Naval Research Laboratory of NOAA in Boulder, Colorado and to the current NMC upper air radiosonde data.

Although the SAGE II water vapor data are preliminary at this time, the agreement between it and other global data sets for the month of April is quite good. In addition, the SAGE II data shows a smooth transition from the LIMS data at 100 mb to the GACS data at 300 mb. The comparison has allowed us to identify several areas which need additional work. We have shown that SAGE II has the capability to provide measurements of water vapor in the lower stratosphere/upper troposphere which will improve our knowledge of the global water vapor climatology.

4. ACKNOWLEDGMENTS

The authors would like to thank C. Trepte of SASC Technologies, Inc. for many helpful discussions.

REFERENCES

Chu, W. P., 1986: Inversion of SAGE II Measurements. Proceedings of the Sixth Conference on Atmospheric Radiation, Williamsburg, Va., May 13-16, 1986.

McMaster, L. R., 1986: Stratospheric Aerosol and Gas Experiment (SAGE II). Proceedings of the Sixth Conference on Atmospheric Radiation, Williamsburg, Va., May 13-16, 1986.

Oort, A. H., 1983: Global Atmospheric Circulation Statistics, 1958-1973: NOAA Professional Paper 14, U. S. Government Printing Office: 1983-404-474.

Russell, J. M., J. C. Gille, E. E. Remsberg, L. L. Gordley, P. L. Bailey, H. Fischer, A. Girard, S. R. Drayson, W. F. J. Evans, and J. E. Harries, 1984: Validation of water vapor results measured by the Limb Infrared Monitor of the Stratosphere experiment on Nimbus 7, J. Geophys. Res., 89, 5115-5124.

J2.7

VARIATION IN THE POLAR STRATOSPHERIC AEROSOL DURING THE SOUTHERN WINTER OF 1984

C. R. Trepte

SASC Technologies, Inc.
17 Research Drive
Hampton, VA 23666

1. INTRODUCTION

In a recent study by Kent et al. (1985) it was shown that a systematic change in the stratospheric aerosol distribution occurred at high northern latitudes during the 1979-1980 winter season. It was observed that the aerosol layer descended in altitude within the polar vortex and a strong gradient in aerosol extinction was established across the polar night jet stream above about 14 km. Further observation showed that the redistribution of aerosol optical properties inside the vortex persisted until the breakup of the vortex in spring. Analysis of 2 other winter seasons for the northern hemisphere showed a similar distribution in late winter (Wang and McCormick, 1985).

It is natural to examine the behavior of the stratospheric aerosols in the Southern Hemisphere under similar conditions. The austral winter season of 1984 is selected because of the availability of aerosol data from 2 satellite experiments. A major distinction is apparent, however, in the character of aerosol properties between the two studies; the former (Kent et al., 1985) was conducted using aerosols observed under near background conditions while this study examines aerosol still highly influenced by the eruption of El Chichon in 1982.

2. SAM II AND SAGE II OBSERVATIONS

Since October 1978, near continuous observations of the polar stratospheric aerosol distribution have been made by the Stratospheric Aerosol Measurement (SAM) II instrument. The basic inferred product is aerosol extinction at a wavelength of 1 μm and a vertical resolution of 1 km (McCormick et al., 1979 and Chu and McCormick, 1979). In this paper an alternative form, extinction ratio is used because in the absence of aerosol formation or loss processes and microphysical changes it behaves as a conservative tracer. SAM II measurements are made between latitudes of about 64° and 80° with the most extreme latitudes sampled at the equinoxes and the lowest latitudes sampled at the solstices. In a 24 hour period, approximately 14 observations are made in each polar region. During a winter season in the southern hemisphere, most sample opportunities lie within the polar vortex unlike the situation in the arctic region where the vortex changes shape and orientation with respect to the pole frequently. This allows the SAM II sensor to make measurements outside the vortex.

It is now possible to extend the latitudinal coverage of aerosol optical properties beyond polar latitudes with the recent launch of the Stratospheric Aerosol and Gas Experiment (SAGE) II. Unfortunately because of the orbital characteristics of the Earth Radiation Budget Satellite (ERBS) spacecraft, mid and high latitudes are sampled by SAGE II for only limited periods separated by intervals of several weeks to a month or more (McMaster, 1986). Compounded with the late launch data of ERBS with respect to this austral winter and the periodic coverage of the instrument, the usefulness of the SAGE II data for this analysis is limited to the period prior to the break up of the vortex in late November 1984. Nevertheless, aerosol profiles observed outside the vortex provide a comparison for profiles observed by SAM II at higher latitudes.

Figure 1 shows 3 SAM II 1. μm aerosol extinction ratio profiles taken at different periods of the 1984 winter season. In each plot, the horizontal lines represent error bars and the dashed line denotes the reported height of the local tropopause. The first plot (Figure 1a) shows a typical extinction ratio profile prior to the formation of the vortex in early April. The profile taken on March 12, 1984 has extinction ratio values ranging from the peak at about 13 km of approximately 14 to values near 1.2 above 24 km. In sharp contrast, the profile observed nearly 8 months later (Figure 1b) has a shape distinctly different from the previous one. Extinction ratio values are significantly lower at the peak and fall quickly to values between 1.2 and 2.0 above 16 km. Profiles like this one are characteristic of other profiles observed for a period of a month or more earlier. At the beginning of summer, the last profile shown in this sequence (Figure 1c) shows the reappearance of higher extinction ratio values above 16 km. This observed behavior is consistent with a similar pattern found by Kent et al. (1985).

As noted earlier, the shape of an extinction ratio profile during winter strongly depends upon its location relative to the polar night jet stream. The 50 mb synoptic situation for November 24, 1984 is displayed in Figure 2. The triangles denote the locations of SAM II measurements for this date with the solid filled triangle indicating the position of the profile illustrated in Fig. 1b. It is apparent that this profile lies on the cyclonic side of the jet stream axis or inside the vortex near its center.

Shown also on the figure are the measurement locations for the SAGE II instrument indicated by circles for the same day. Here the SAGE II profiles all lie outside the vortex. The solid circle indicates the location of a single SAGE II extinction ratio profile displayed in Figure 3. This profile is representative of conditions prevailing at the sampled latitude and does not represent an anomalous case. Large differences in extinction ratio values are evident between the SAGE II and SAM II (Figure 1b) observations, particularly above about 16 km. A strong gradient in aerosol concentration must

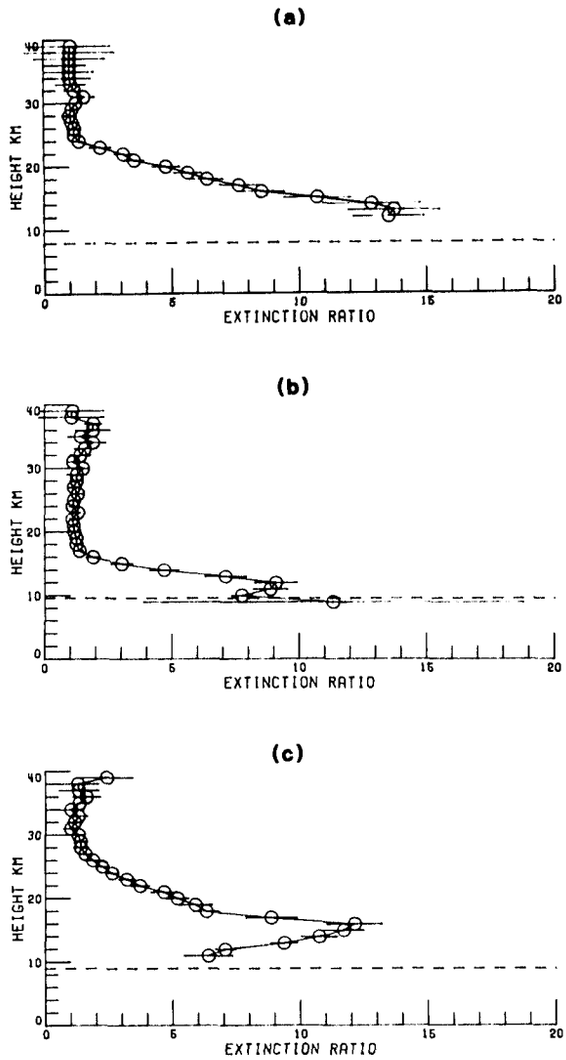

Fig. 1. SAM II extinction ratio profiles observed in the southern hemisphere. Error bars are represented by horizontal lines and the tropopause altitude is denoted by the dashed line. The profiles were obtained for (a) on March 12, 1984 at 77.6° S and 117.3° E, (b) on November 24, 1984 at 67.8° S and 4.4° E, and (c) on December 20, 1984 at 64.6° S and 15.6° E.

exist between these two observations and it is likely, as shown later, that the greatest variation occurs in the vicinity of the jet stream core. Also of interest is the strong enhancement at the peak and its slight upward displacement from the profiles seen in Figure 1a and Figure 1c. This feature may be due in part to a latitudinal dependence, especially the vertical differences. The magnitude of the peak, however, is still under investigation at this time.

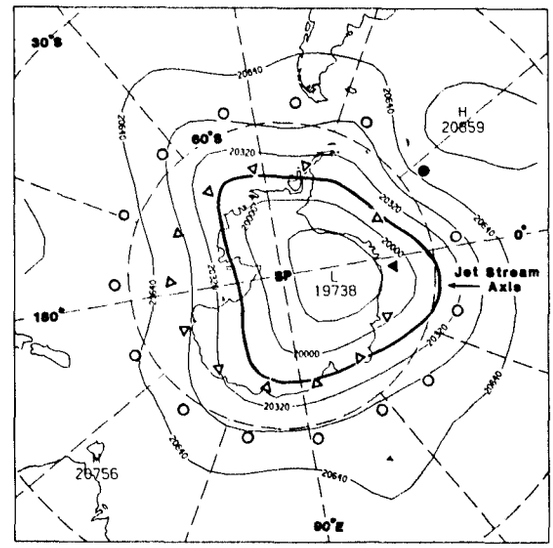

Fig. 2. Location of SAM II measurements are shown by triangles and SAGE II measurements are indicated by circles on the 50 mb meteorological analysis map for November 24, 1984. Geopotential altitudes are shown in meters. The solid triangle denotes the location of the SAM II profile shown in Fig. 1b and the solid circle indicates the location of the SAGE II profile shown in Fig. 3.

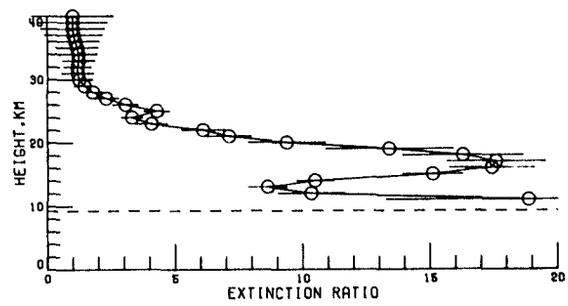

Fig. 3. SAGE II extinction ratio profile obtained on November 24, 1984 at 55.9° S and 28.9° W.

3. VARIATION OF EXTINCTION RATIO DURING THE WINTER SEASON

To examine the behavior of aerosol concentration over the complete winter season (March to December), each extinction ratio value observed at an altitude of 19 km is presented in Figure 4. This altitude is chosen because of its close proximity to the 50 mb pressure surface where the determination of a profile's location relative to the jet stream could be made. The data have also been screened to remove events with error bars greater than 50 percent and the inclusion of clouds. In addition, an attempt was made to account for particle growth or evaporation due to changing temperature conditions. This microphysical change occurs because aerosols

seek to maintain their equilibrium with ambient water vapor. Using a simple model, the extinction ratio is adjusted to a reference temperature of 223 K which is typical of summer conditions at 19 km. This adjusted version of extinction ratio is presented in Figure 4 because it is a more conserved quantity and a better indicator of transport processes.

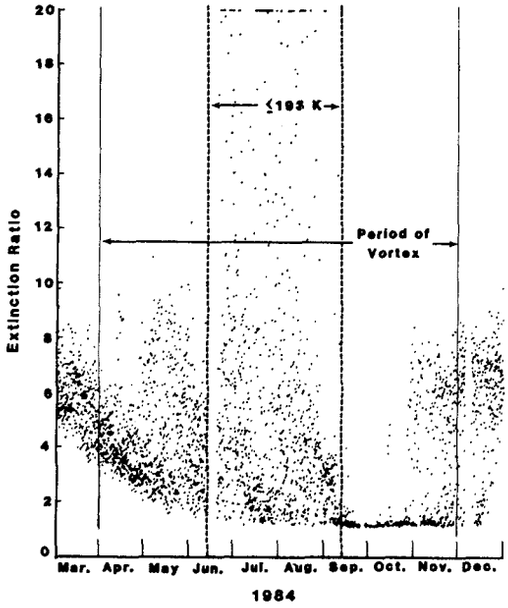

Fig. 4. SAM II temperature-adjusted extinction ratio values observed at 19 km from March to December 1984. The region contained within the thin vertical lines indicates the approximate period the vortex was present on 50 mb maps. The area shown between the dashed vertical lines shows the approximate period temperatures $\leq$ 193 K.

Examination of Figure 4 shows four distinct periods with different aerosol properties. The first period shows a steady loss of aerosols as extinction ratio values decline from between 6 to 9 in early March to values between 2 to 6 at the end of April. Next, in early May there is a rise in the value of some data points which culminates in the period of June thru the first of September. Maximum values shown are peaked at 20 but are in fact larger, their true values being disregarded for illustrative purposes. As indicated in the figure, this period of higher values corresponds closely to the period in which some 50 mb temperatures were $\leq$ 193 K. At temperatures near 193 K and below rapid growth in particle size occurs (Yue and Deepak, 1981 and Steele et al., 1983) and the simple extinction adjustment described above is incapable of handling them. These anomalously high extinction ratio events are referred to as Polar Stratospheric Clouds (PSCs) and have been observed in the SAM II data set for other years (McCormick et al., 1982).

During this same 4 month period, some of the adjusted extinction ratio values also continue to decrease in magnitude. By June values as low as 1.6 are observed with lower values found in July and August. These same low values are seen until mid December. As would be expected from theory, the enhanced values disappear when the 50 mb temperatures are greater than 193 K in mid September. It is during this period that the region sampled showed only a very low concentration of aerosols until mid and late October. This feature agrees well with the annual periods of low optical depth reported by McCormick et al., (1981).

Towards the end of October, there are sporadic events where the extinction ratio data increases up to values of about 8. The number of these events becomes more frequent in November and becomes the rule by the end of December when there is no evidence of the winter vortex in the daily synoptic maps. Further inspection of the 50 mb maps shows that these relatively higher extinction ratio events tended to lie outside the vortex, as illustrated by the SAGE II profile in Figure 3, or near the axis of the jet stream.

4. SUMMARY

The aerosol distribution observed by SAM II and SAGE II for the austral winter of 1984 shows that within the vortex, a lowering of the extinction ratio occurs above at least 19 km. Measurements outside the vortex or near the axis of the jet stream show profiles with higher aerosol concentrations. It is inferred that a strong gradient in aerosol is established across the jet stream. The data also show that Polar Stratospheric Clouds are present for a period of about 3 months at 19 km and that a region of low aerosol concentration remains undisturbed for 4 or more weeks. As the southern polar vortex weakens and changes shape, air with more aerosol is observed. It is likely that this is due to both the shrinking nature of the vortex and the gradual mixing of air along the peripheral of the vortex. These features are in good agreement with results presented by Kent et al. (1985) for a northern winter season.

The lowering of the aerosol concentration appears to be related to an overall descent of the aerosol layer within the vortex. Kent et al. attribute this to a general subsidence of air. In the case presented here, however, particle sedimentation must account for a portion of the downward movement of the layer since PSC's are more prevalent and occur for a longer period.

Acknowledgments. The author would like to thank W. P. Chu and G. S. Kent for their helpful discussions and advice. This research was supported by the National Aeronautics and Space Administration.

REFERENCES

Chu, W. P., and M. P. McCormick, 1979: Inversion of stratospheric aerosol and gaseous constituents from spacecraft solar extinction data in the 0.38-1.0 μm wavelength region. Appl. Opt., 18, 1404-1423.

Kent, G. S., C. R. Trepte, U. O. Farrukh, and M. P. McCormick, 1985: Variation in the stratospheric aerosol associated with the north polar vortex as measured by the SAM II satellite sensor, J. Atmos. Sci., 42, 1536-1551.

McCormick, M. P., P. Hamill, T. J. Pepin, W. P. Chu, T. J. Swissler, and L. R. McMaster, 1979: Satellite studies of the stratospheric aerosol. Bull. Amer. Meteor. Soc., 60, 1038-1046.

_____, and collaborators, 1981: High-latitude stratospheric aerosols measured by the SAM II satellite system in 1978 and 1979. Science, 214, 328-331.

_____, H. M. Steele, P. Hamill, W. P. Chu and T. J. Swissler, 1982: Polar stratospheric cloud sightings by SAM II. J. Atmos. Sci., 39, 1387-1397.

McMaster, L. R., 1986: Stratospheric aerosol and gas experiment (SAGE II). Companion paper in these preceedings.

Steele, H. M., P. Hamill, M. p. McCormick, and T. J. Swissler, 1984: The formation of polar stratospheric clouds. J. Atmos. Sci., 40, 2055-2067.

Wang, P-H. and M. P. McCormick, 1985: Variations in stratospheric aerosol optical depth during northern warmings. J. Geophys. Res., 90, 10597-10606.

Yue, G. K., and A. Deepak, 1981: Modeling of growth and evaporation effects on the extinction of 1.0 μm solar radiation traversing stratospheric sulfuric acid aerosols. Appl. Opt., 20, 3669-3675.

A STUDY OF THE STRATOSPHERIC AEROSOL SIZE DISTRIBUTION UTILIZING PRELIMINARY DATA FROM SAGE II AND CORRELATIVE MEASUREMENTS

Pi-Huan Wang

Science and Technology Corporation
Hampton, Virginia 23666

M. P. McCormick

Atmospheric Sciences Division NASA-Langley Research Center
Hampton, Virginia 23665

T. J. Swissler

SASC Technologies, Incorporated
Hampton, Virginia 23666

G. K. Yue

Atmospheric Sciences Division NASA-Langley Research Center
Hampton, Virginia 23665

1. INTRODUCTION

In order to obtain global scale information on stratospheric aerosols in a nearly continuous mode, NASA has developed three satellite instruments in the last 10 years, namely, the Stratospheric Aerosol Measurement II (SAM II), and the Stratospheric Aerosol and Gas Experiment I and II (SAGE I, SAGE II). SAM II is a one-channel radiometer specially designed to measure aerosol extinction at 1 μm wavelength in the earth's polar regions. SAGE I is a four-channel instrument with aerosol information contained in the extinction measurements centered at two wavelengths, i.e., 1. μm and .45 μm. The SAGE II instrument is a seven-channel radiometer which measures aerosol extinction at four different wavelengths, 1.02, 0.525, 0.45, and 0.385 μm. The other channels in the SAGE I and SAGE II instruments are used for measuring stratospheric gases. They both measure stratospheric ozone and nitrogen dioxide, and SAGE II also measures stratospheric water vapor. The water vapor information is important since the size of the aerosol particles is directly affected by the ambient water vapor concentration (Steele and Hamill, 1981). The detailed aspects of the SAM II and SAGE I measurements have been reported by McCormick et al. (1979) and McCormick (1982), and a description of the SAGE II instrument has been given by Mauldin et al., (1984).

It is clear that the aerosol physical and chemical properties are important information for understanding the radiative characteristics and the governing processes in determining the distribution of this stratospheric layer (Turco et al., 1979; Lenoble and Brogniez, 1985). The objective of this study is to investigate these properties including aerosol size distribution and composition utilizing SAGE II multi-wavelength aerosol extinction and water vapor measurements. The emphasis is also made toward understanding the aerosol size information contained in the SAGE II aerosol extinction measurements. The inference of the aerosol size distribution from satellite instruments is desirable due to the fact that they provide global coverage observations. As mentioned earlier SAM II is a one-channel instrument, no information of aerosol size distribution can be extracted from the extinction measurements. With the two-channel extinction measured at 1.0 and 0.45 μm from the SAGE I instrument, a simple model size distribution can be obtained (Yue and Deepak, 1983). Since the SAGE II instrument is equipped with four aerosol channels and also one additional channel for measuring water vapor, the SAGE II observations are expected to make substantial improvements in determining the physical and chemical properties of stratospheric aerosols. Since, in many cases, correlative ground truth measurements, including aerosol size distribution, as well as lidar backscattering are conducted for data validation purposes, the derivation of aerosol size distribution based on SAGE II observations, including water vapor and aerosol extinctions, provide an alternative means for data comparison.

2. APPROACH AND DATA DESCRIPTION

In deriving the chemical composition, it is assumed that the stratospheric aerosols are sulfuric acid/water droplets. There is ample evidence in supporting this assumption (e.g., Rosen, 1971; Russell et al., 1981; Oberbeck et al., 1983; etc.). With this assumption, the equilibrium acid weight percentage and refractive index at SAGE II aerosol wavelengths for observed temperature and humidity can be calculated (Steel and Hamill, 1981; Yue and Deepak, 1981). Recently, this method of

determining the refractive index has also been employed in development of model refractive index for stratospheric aerosols (Russell and Hamill, 1984).

To infer the aerosol size distribution based on SAGE II multi-wavelength aerosol extinction measurements, a modified Levenberg-Marquardt algorithm (Morer et al., 1980) is adopted for determining the optimal solution of the model size distribution parameters in the least squares sense. Both lognormal and modified gamma models are included in this analysis. Furthermore, the analysis has also been extended by introducing the correlative lidar backscatter measurements at 0.532 and 0.6943 μm in retrieving a bi-mode aerosol size distribution. Results of the derived size distributions can be compared with correlative size measurements. In the single mode cases the derived size distributions are used to calculate the backscatter coefficients at lidar wavelengths, which can be used to compare with correlative lidar measurements.

The data set used in this study includes the preliminary profiles of SAGE II water vapor and multi-wavelength aerosol extinctions obtained at Laramie, Wyoming, on November 30, 1984, and the correlative measurements of the University of Wyoming dustsonde and the NASA LaRC airborne lidar. The dustsonde used in this ground truth mission is a six-channel optical particle counter. It measures the number of particles having a radius larger than r microns (N_r; r = 0.01, 0.15, 0.25, 0.95, 1.2, and 1.8 μm) (Hofmann and Rosen, 1982). The NASA LaRC airborne lidar system consists of a ruby laser (λ = 0.6943 μm), and a Nd:YAG laser (λ = 1.06 μm). The latter can be operated in a frequency-doubled manner and provide a vertical profile of backscatter at 0.532 μm.

3. RESULTS AND DISCUSSION

3.1 Aerosol Composition

Figure 1 shows the water vapor pressure

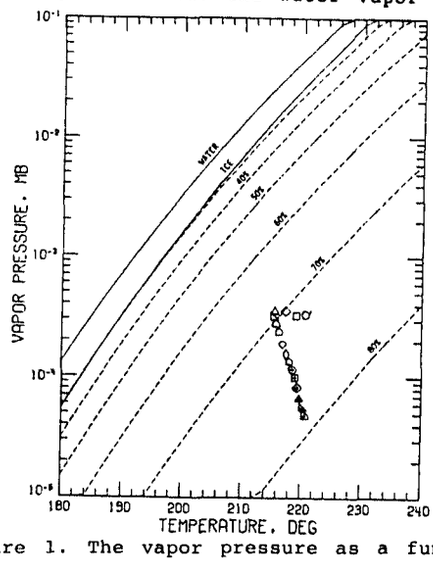

Figure 1. The vapor pressure as a function of temperature over water, ice and six different H_2SO_4 weight percentage of sulpheric-water solutions. The 16 symbols are the SAGE II water vapor observations (see text).

as a function of temperature over water, ice, and six different H_2SO_4 weight percentages of sulphuric acid-water solutions (dashed lines). The 16 symbols in Fig. 1 represent the distribution of SAGE II measurements on November 30, 1984 on this vapor pressure versus temperature space. These 16 symbols, which begin with O and end with ⊕, correspond to the measured results of SAGE II instrument at altitudes from 15 km up to 30 km, respectively, with a 1km increment. As shown in Figure 1, this set of SAGE II Laramie measurements suggest an approximate composition of 73% H_2SO_4 and 27% H_2O by weight for the stratospheric aerosol droplets. This composition information of H_2SO_4 of the aerosol droplets at a particular level between 15 and 30 km is then used to infer the refractive indexes at SAGE II aerosol wavelengths. The derived refractive indexes are incorporated into the retrieval study of aerosol size distribution at the corresponding altitude level.

3.2 Aerosol Size Distribution

In the single mode analyses, the SAGE II 4-channel aerosol extinction measurements are used to derive the 3 parameters which appear in the lognormal representation, and 4 in modified gamma. To obtain the bi-mode distribution, the correlative lidar backscatter observations at ruby and green wavelengths are utilized, together with the 4-channel SAGE II aerosol extinctions in determining the six parameters appearing in the bi-lognormal expression. The

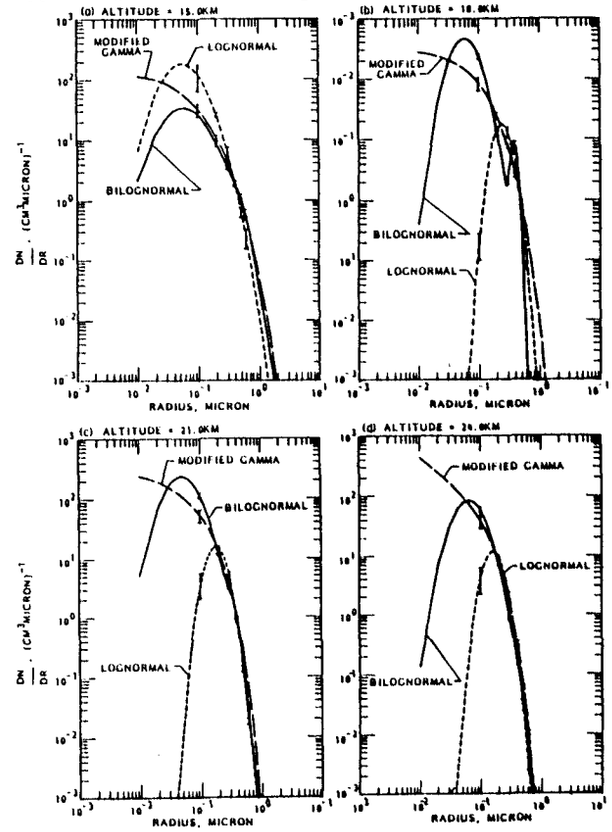

Figure 2. Stratospheric aerosol size distributions derived from SAGE II aerosol extinctions at; (a) 15 km, (b) 18 km, (c) 21 km, and (d) 24 km.

retrieved aerosol size distributions at altitudes 15, 18, 21, and 24 km are displayed in Figs. 2a to d. The distinct features of these retrieved size distributions are the relatively close agreement of the distribution in size range between approximately 0.2 and 0.7 μm among the three different models adopted in this study. In the case of bi-lognormal model analysis, the retrieved results indicate a second mode of the size distribution near 0.38 μm. This second mode appears to be occurring in a layer centered at an altitude of 19 km. It is interesting to note that the results of the two single mode analyses appear to distribute themselves in a smoothed fashion around the bi-modal distribution near the size range where the second mode occurred.

We have calculated the backscatter corresponding to ruby and green lidar wavelengths using the retrieved two single mode aerosol size distributions. The computed results are compared with lidar observations. Figs. 3a and b show the results of comparison for green and ruby backscatter, respectively. In general, there is a reasonable agreement between the observations and the derived results based on retrieved size distributions, especially below about 23 km at both wavelengths. However, differences are noticeable at the altitude of 24 km. In addition, the retrieved aerosol size distribution on 30 November 1984 leads to ruby backscatter which is greater than the observations above 25 km (Fig. 3a).

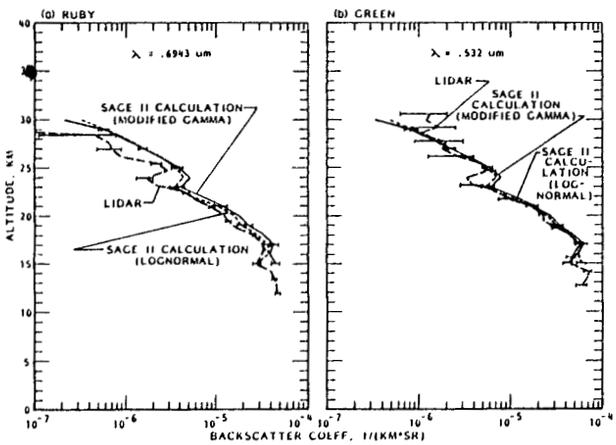

Figure 3. Comparison of the backscatter coefficients between Lidar observations and the calculations based on retrieved aerosol size distributions from SAGE II aerosol extinctions.

To compare with the correlative dustsonde observations, the retrieved analytic size models are used to obtain the integrated size number $N_{.15}$ and $N_{.25}$. It is found that the retrieved aerosol size distributions yield values of $N_{.15}$ which are higher than those of dustsonde measurements for all the three analytic models. On the other hand, substantial improvement is found in the results of $N_{.25}$ calculated using bi-lognormal representation. Some improvement of the results of a modified gamma model over the lognormal distribution is also noticeable for this particular case.

3.3 Aerosol Size Information of SAGE II Multiwavelength Aerosol Extinctions

To examine the information content of the SAGE II multiwavelength aerosol extinction observation with respect to the particle size distribution, the variations of the normalized extinction efficiency factor (Q) at SAGE II aerosol wavelengths as a function of aerosol radius are calculated and displayed in Fig. 4. This normalized efficiency factor indicates the relative weight of the aerosol size to the contribution of the observed extinction. Thus, the radius, at which the efficiency factor shows a maximum, corresponds to the aerosol size with the maximum information embedded in the observed extinction at the particular wavelength. With this understanding, one can see that the maximum aerosol size information of the SAGE II aerosol extinction data set is within the radius range of approximately 0.25 μm to 0.80 μm. Another source of information about the limits of the retrievable radius range is the so-called ratio criterion (Heintzenberg et al., 1981). According to this criterion, there is no information about aerosol size distribution that can be extracted from optical measurements at any two wavelengths in a radius range within which the ratio of the

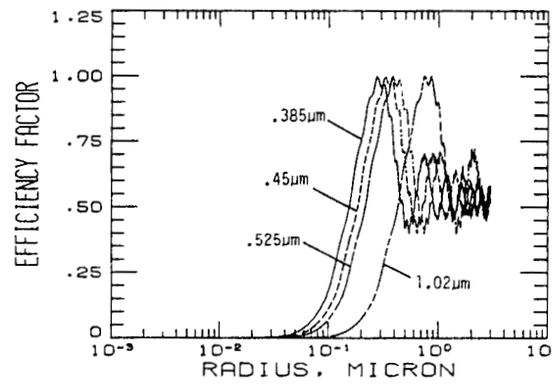

Figure 4. Efficiency factors at SAGE II aerosol wavelengths for background atmospheric aerosols.

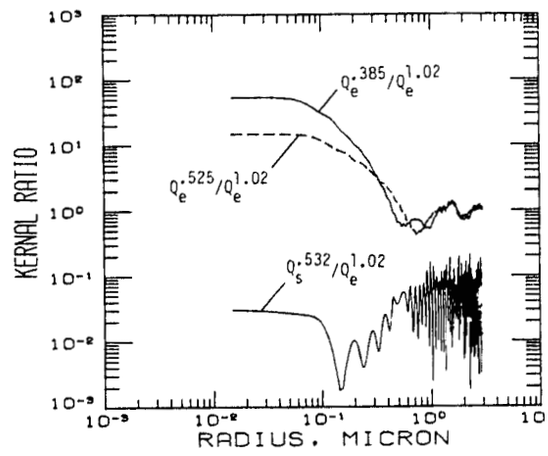

Figure 5. Ratios of efficient factors at different wavelengths for background stratospheric aerosols.

two corresponding efficiency factors is a constant. Applying this criterion, we have calculated the ratio of $Q_e^{.525}/Q_e^{1.02}$ and $Q_e^{.385}/Q_e^{1.02}$ (Fig. 5). Figure 5 shows also the ratio of $Q_s^{.532}/Q_e^{1.02}$. As one can see from Fig. 5, the non-invertible radius range extends below the radius of 0.1 μm and also beyoned about 1.0 μm. However, as one would expect, the information content near these limits becomes relatively poor as revealed by the distributions of the efficiency factor in Fig. 4.

4. Summary

In this paper, we have presented the initial analysis of stratospheric aerosol composition and size distributions based on preliminary data sets of SAGE II and correlative ground observations on 30 November 1984 at Laramie, Wyoming. A modified Levenberg-Marquardt algorithm is adopted for determining the optimal solution of model size distribution parameters in the least squares sense. In addition, the information content of the SAGE II aerosol extinctions with respect to the aerosol size distribution is also discussed.

5. Acknowledgment

The authors wish to thank Drs. W. P. Chu, J. Lenoble, G. W. Grams, P. B. Russell, J. M. Livingston and A. Deepak for helpful comments and discussions. The authors are also grateful to Drs. J. M. Rosen and D. J. Hofmann for providing them the Dustsonde results, and to W. H. Fuller and M. T. Osborn for preparing the Lidar profiles. P.-H. Wang is supported by NASA Contract NAS1-17959. T. J. Swissler is supported by NASA Contract NAS1-17022.

6. References

Heintzenberg, J., H. Muller, H. Quenzel, and E. Thomalla, 1981: Information content of optical data with respect to aerosol properties: numerical studies with a randomized minimization-search-technique inversion algorithm. Appl. Opt., 20, 1308-1315.

Hofmann, D. J., and J. M. Rosen, Balloon-borne observations of stratospheric aerosol and condensation nuclei during the year following the Mt. St. Helens eruption, J. Geophys. Res., 87, 11,039,1982.

Lenoble, J., and C. Brogniez, 1985: Information on stratospheric aerosol characteristics contained in the SAGE satellite multiwavelength extinction measurements, Appl. Opt., 24, 1054-1063.

Mauldin, E., 1984: Stratospheric Aerosol and Gas Experiment II instrument: a functional description, Opt. Engr., 24, 307-312.

McCormick, M. P., P. Hamill, T. J. Pepin, W. P. Chu, T. J. Swissler and L. R. McMaster, 1979: Satellite studies of the stratospheric aerosol. Bull. Amer. Meteor. Soc., 60, 1038-1046.

McCormick, M. P., 1982: Aerosol measured from earth orbiting spacecraft, Adv. Space Rev., 2, 73-86.

More, J. J., B. S. Garbow, and K. E. Hillstrom, 1980: User guide for MINPACK-1. Report ANL-80-74, Argonne National Laboratory, Argonne, JL. (NTIS).

Oberbeck, V. R., E. F. Danielsen, K. G. Snetsinger, and G. V. Ferry, 1983: Effect of the eruption of El Chichon on stratospheric aerosol size and composition. Geophys. Res. Lett., 10, 1021-1024.

Rosen, J. M., The boiling point of stratospheric aerosols, J. Appl. Meteorol., 10, 1044,1971.

Russell, P. B., T. J. Swissler, M. P. McCormick, W. P. Chu, J. M. Livingston, and T. J. Pepin, 1981: Satellite and correlative measurements of the stratospheric aerosol, I: an optical model for data conversions, J. Atmos. Sci., 38, 1279-1294.

Russell, P. B., and P. Hamill, 1984: Spatial Variation of Stratospheric Aerosol acidity and model refractive index: Implications of recent results. J. Atmos. Sci., 41, 1781-1790.

Steele, H. M., and P. Hamill, 1981: Effects of temperature and humidity on the growth and optical properties of sulphuric acid-water droplets in the stratosphere, J. Aerosol Sci., 12, 517-528.

Turco, R. P., P. Hamill, O. B. Toon, R. C. Whitten, and C. S. Kiang, A one-dimensional model describing aerosol formation and evolution in the stratosphere: I. Physical processes and mathematical analogs, J. Atmos. Sci., 36, 669-771, 1979.

Yue, G. K., and A. Deepak, 1983: Retrieval of stratospheric aerosol size distribution from atmospheric extinction of solar radiation at two wavelengths, Appl. Opt., 22, 1639-1645.

Yue, G. K., and A. Deepak, 1981: Modeling of growth and evaporation effects on the extinction of 1.0 μm solar radiation traversing stratospheric sulfuric acid aerosols. Appl. Opt., 20, 3669-3675.

RETRIEVAL OF AEROSOL SIZE DISTRIBUTION MOMENTS FROM MULTIWAVELENGTH PARTICULATE EXTINCTION DATA

John M. Livingston
SRI International, Menlo Park, CA 94025

Philip B. Russell
NASA Ames Research Center, Moffett Field, CA 94035

1. INTRODUCTION

An analytic technique for deriving aerosol size distribution moments from multiwavelength remote sensing measurements was proposed by Twomey and Howell (1967) and Twomey (1974). Their method, called the eigenvalue method because it is based on eigenanalyses of the kernel covariance matrix, approximates an appropriate moment weighting function $w(r)$, where $w(r) = r, r^2, r^3$, etc., by a linear combination of the corresponding kernel functions $k(\lambda,r)$. The same linear combination of the measurements can then be used to infer the particular moment. That is, for particulate extinction measurements $E_p(\lambda)$ taken at wavelengths $\lambda_i, \lambda_{i+1},\ldots,\lambda_N$, if

$$w(r) \approx \sum_{i=1}^{N} a_i k(\lambda_i,r),$$

where the $k(\lambda_i,r)$ are the Mie extinction cross sections, then

$$\int w(r)n(r)dr \approx \sum_{i=1}^{N} a_i \int k(\lambda_i,r)n(r)dr = \sum_{i=1}^{N} a_i E_p(\lambda_i),$$

where $n(r)$ is the differential particle size distribution. Since many aerosol properties of interest, such as particle-layer mass, area, and effective particle size, are either moments or combinations of moments of the aerosol size distribution, this technique, in principle, can be used to derive these quantities.

A computer routine has been developed that incorporates this methodology to invert multiwavelength particulate extinction measurements taken by the satellite-borne SAGE II sunphotometer. In this paper, the routine is applied first to synthetic particulate extinction measurements that were calculated at SAGE II wavelengths from Mie theory using both model analytical stratospheric aerosol size distributions and a series of pre- and post-El Chichon stratospheric aerosol size distributions measured by a wire impactor. Inferred moments and moment uncertainties are presented. The routine is then applied to actual measurements taken by SAGE II during the April 1985 Brazil correlative experiment, and inferred moments are compared with corresponding moments derived from application of an extinction-to-moment conversion ratio method to the same data set.

2. DESCRIPTION OF RETRIEVAL ROUTINE

Our particular adaptation of the Twomey and Howell eigenvalue methodology is an iterative procedure that uses an analytical function, which we call a compression size distribution, to approximate the true particle size distribution. The compression size distribution is a rapidly varying function of particle radius -- in particular, a lognormal, modified gamma, or power law function -- that is used to weight both the extinction kernels and the moment weighting functions before an eigenanalysis of the kernel covariance matrix is performed. It is analogous to the size distribution weighting function that has been used by Herman et al. (1971) and King et al. (1978) in constrained linear inversion problems.

The first iteration (zeroth order) compression size distribution is determined by an interpolation and table-lookup method (Box and Lo, 1976) that relates the coefficients of a least-squares fit (on a log-log scale) of particulate extinction versus wavelength to specific parameters of the compression function, where the parameters have been derived by Mie scattering calculations that assume a particular set of refractive indices. The compression distribution is then normalized by requiring its calculated 1.0-μm extinction to equal the true 1.0-μm value (with or without the addition of random extinction errors). Before each subsequent iteration, the routine tries to optimize agreement between the approximated and true "compressed" moment weighting functions by using inferred values of the particle effective radius and effective variance (combinations of size distribution moments) to adjust related parameters of the compression function.

3. RETRIEVALS FOR SYNTHETIC MEASUREMENTS

The eigenvalue technique has been applied to synthetic particulate extinction measurements calculated from a standard set of analytical stratospheric aerosol size distributions (Russell et al., 1981) and an assumed set of wavelength-dependent refractive indices corresponding to an aerosol composition of 75% sulfuric acid and 25% water. Figure 1 presents results from a three-wavelength (λ = 0.385, 0.453, 1.02 μm) retrieval that uses a lognormal compression size distribution and assumes no particulate extinction uncertainties. The deviation of each inferred moment

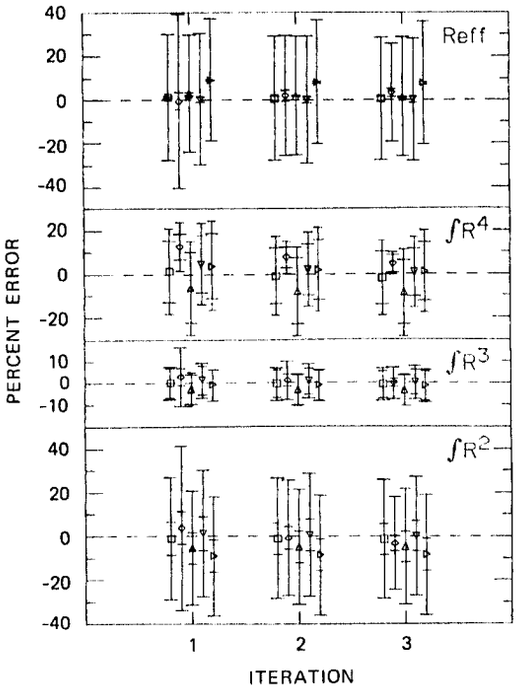

Figure 1 Retrieval errors and moment uncertainty estimates for moments derived by application of eigenvalue method to synthetic particulate extinction measurements calculated at wavelengths 0.385, 0.453, and 1.02 μm from five model stratospheric aerosol size distributions.

from its respective true value is expressed as percent error, and is shown for three iterations of the inversion routine. Results are presented for five model size distributions: lognormal (nonvolcanic) - □, modified gamma-1 (haze H) - ◊, zold-1 (nonvolcanic) - Δ, zold-2 (postvolcanic soluble) - ∇, and modified gamma-3 (AFGL volcanic) - ▷. Each size distribution had a dustsonde channel ratio $N_{0.15}/N_{0.25} = 3$, where N_r is the number of particles with radius ≥ r. In general, retrieved moments agree well with the model values, although estimates of both the bias (error bars with narrow ticks) associated with the orthogonal approximation to the true moment weighting function and the unbiased moment uncertainty (error bars with wide ticks) tend to overestimate the errors.

Simulated particulate extinction measurements have also been calculated at SAGE II wavelengths by using a set of 14 separate stratospheric aerosol size distributions measured by the NASA Ames Wire Impactor (AWI) at altitudes near 20 km before and after the eruption of El Chichon in April 1982 -- in particular, from October 1981 through December 1983. Moments have been inferred by inverting these simulated extinction measurements, with and without the addition of random errors, in two- and three-wavelength retrievals.

Little difficulty was encountered in retrieving model size distribution moments for either two- or three-wavelength inversions with no random extinction errors. Furthermore, the inclusion of such errors was successfully handled for a two-wavelength inversion. However, when a three-wavelength retrieval with random extinction uncertainties was attempted, the occurrence of negative moment expansion coefficients, a(λ), typically resulted in non-physical moment inferences and/or unacceptably large moment uncertainties due to amplification of the relative extinction uncertainties.

This led to development of a wavelength combination technique that combines information at adjacent wavelengths when measurement uncertainties become excessively large. In short, extinction kernels at the two shortest wavelengths are weighted by the inverse square of their respective uncertainties and then summed to yield a new "combined wavelength" kernel. (In order to yield the proper units, this new kernel includes a weighting factor, the "combined" uncertainty, which is derived by taking the sum of the squares of the inverse uncertainties.) This same procedure is then applied to the extinction measurements at these two wavelengths to produce a "combined" extinction measurement.

Figure 2 presents composite results from a three-wavelength retrieval that utilizes this wavelength combination technique to invert synthetic particulate extinction measurements (with associated random errors indicated by error bars) that were calculated at wavelengths 0.385, 0.453 and 1.02 μm from the AWI-measured size distributions. Retrieved moments (labeled TWOHOW) are shown after three iterations of the routine;

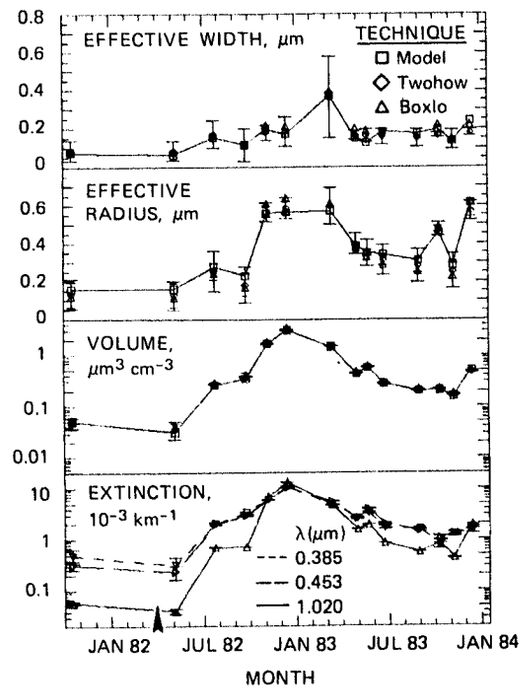

Figure 2 Synthetic particulate extinction measurements (with random uncertainties) calculated from a series of pre- and post-El Chichon (arrow) Ames Wire Impactor-measured stratospheric aerosol size distributions; moments and moment uncertainties inferred by application of Twomey and Howell (1967) eigenvalue retrieval technique and Box and Lo (1976) fit method to the synthetic measurements.

error bars display the bias estimate (narrow ticks) and the total uncertainty (wide ticks) in the inferred moment. The latter uncertainty includes both uncertainties in the synthetic extinction measurements and uncertainties in the derived moment expansion coefficients. Also shown for comparison are corresponding moments (labeled BOXLO) that were calculated directly from the adjusted compression size distribution. Clearly, the moment retrievals successfully monitored both volume and particle size changes that occurred during the one-and-one-half years following the eruption of El Chichon. This is significant because these size distributions exhibited a wide range of aerosol concentrations and particulate extinction coefficients, and thus they provide a particularly stringent performance test for the inversion routine.

The rms differences between model and TWOHOW-inferred moments are presented separately in Figure 3 for the nonvolcanic (October 1981 and May 1982 only) and volcanic (post-May 1982) AWI-measured size distributions. Results prior to the eruption are not as good as those following the eruption because of large relative errors in the particulate extinction values at wavelengths 0.385 μm and 0.453 μm caused by the small particle-to-gas extinction ratios at these two wavelengths during nonvolcanic conditions. In general, results derived using the TWOHOW technique are about one-and-one-half times as accurate as those calculated from the BOXLO method, with the exception of the nonvolcanic effective width.

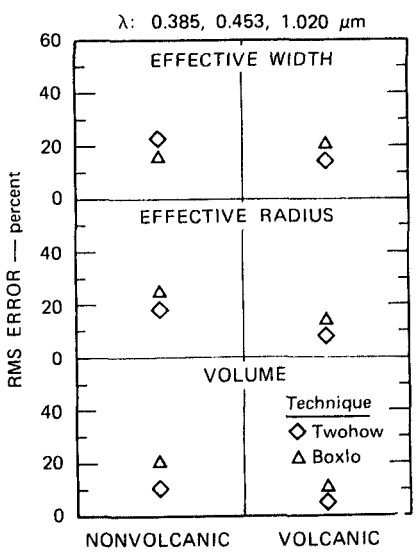

Figure 3 Root-mean-square differences between true and inferred moments shown in Figure 2 for pre- and post-El Chichon wire impactor-measured stratospheric aerosol size distributions.

4. RETRIEVAL FOR A SAGE II MEASUREMENT: COMPARISON WITH CONVERSION RATIO RESULTS

The eigenvalue moment retrieval routine has also been used to derive inferences of the third moment (volume) of the stratospheric aerosol size distribution from selected particulate extinction measurements made by SAGE II during the April 1985 Brazil correlative measurement experiment. For comparison, separate inferences have been obtained through application of a conversion ratio technique to the same measurements.

The conversion ratio method utilizes vertical profiles of observed wavelength particulate extinction ratios $[E_p(\lambda)/E_p(1.02\ \mu m)]$ for $\lambda = 0.385$, 0.453, 0.525 μm to select mean conversion ratio quantities (such as volume-to-extinction ratio and particle effective radius) that have been generated from Mie scattering calculations at the SAGE II wavelengths for an appropriate set of refractive indices and model stratospheric aerosol size distributions. The resultant vertical profiles of conversion ratios are then combined with the measured 1.02 μm particulate extinction profile to yield profiles of inferred moments of the actual stratospheric aerosol size distribution. Application of the conversion ratio method to the April 6 Brazil SAGE II sunrise

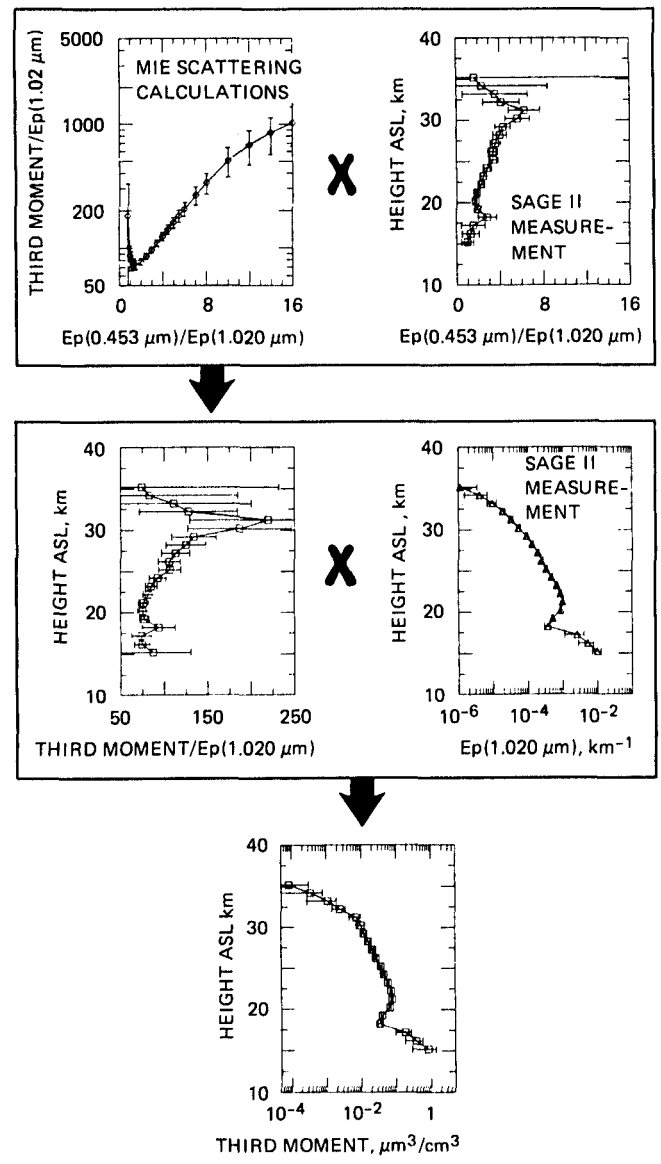

Figure 4 Derivation of third moment by application of conversion ratio method to SAGE II particulate extinction measurements at wavelengths 0.453 and 1.02 μm for Brazil sunrise event of April 6, 1985.

event using data at 0.453 and 1.02 μm is displayed in Figure 4. Corresponding moments have also been derived by separate applications of the conversion ratio method to the measured profiles of $E_p(0.385\ \mu m)/E_p(1.02\ \mu m)$ and $E_p(0.453\ \mu m)/E_p(1.02\ \mu m)$, and values generally agree to within about fifteen percent.

Figure 5 presents third moment inferences derived from application of both the eigenvalue method and the conversion ratio method to the April 6 SAGE II measurements at altitudes 20.2 km, 25.2 km and 30.2 km. Inferred moments and moment uncertainties are shown for three iterations of the eigenvalue moment retrieval routine. Three-wavelength inversions were performed separately using the measurements at wavelengths 0.385, 0.453 and 1.02 μm, and at 0.453, 0.525 and 1.02 μm, with the measurements at the two shortest wavelengths combined in each case. The range of moment values derived by the conversion ratio method at each altitude is presented. Conversion ratio uncertainties are not shown, but ranged from 6% to 15% at 20.2 km, 9% to 16% at 25.2 km, and 21% to 65% at 30.2 km, with the largest uncertainties associated with moments derived from the $E_p(0.525\ \mu m)/E_p(1.02\ \mu m)$ ratios. The increase in conversion ratio moment uncertainties with altitude is the result of propagation of larger measurement uncertainties at the greater altitudes. At each height, inferred moments using the two separate methods of retrieval agree with each other within their respective uncertainties.

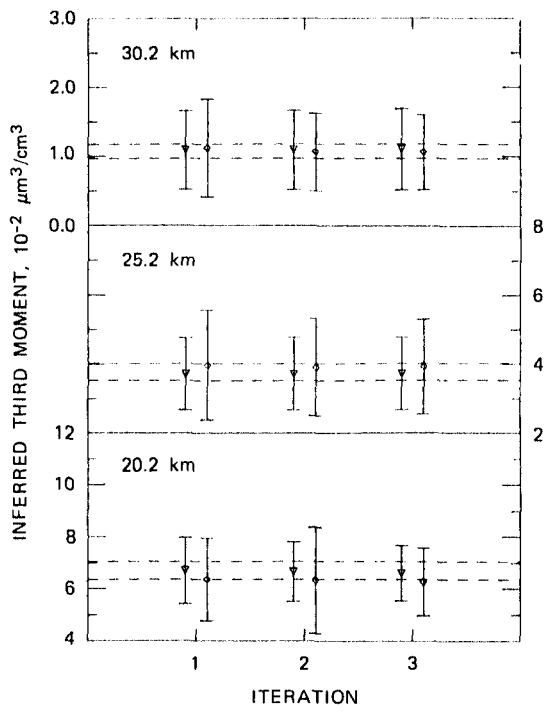

Figure 5 Moment inferences and uncertainties for eigenvalue retrievals using April 6, 1985 Brazil SAGE II particulate extinction measurements at wavelengths 0.385, 0.453, and 1.02 μm (▽), and 0.453, 0.525, and 1.02 μm (◇); corresponding range of moment inferences (dashed lines) derived by application of conversion ratio technique to same data.

A four-wavelength retrieval (λ=0.385, 0.453, 0.525, 1.02 μm) using the eigenvalue routine was also performed on this same set of SAGE II measurements. At each altitude, the third moment inferred after the first iteration was slightly larger than, but well within the respective uncertainty limits of, the corresponding moment inferred from the three-wavelength retrieval. Unfortunately, moments retrieved from the four-wavelength inversion increased with successive iterations at 20.2 km and, to a lesser degree, also at 25.2 km. The source of this troublesome instability has not been diagnosed. However, the 30.2 km result was stable.

5. SUMMARY

A routine has been developed that incorporates the eigenvalue methodology of Twomey and Howell (1967) to derive moments of the stratospheric aerosol size distribution from multiwavelength particulate extinction measurements. This routine has been applied to synthetic extinction measurements calculated from analytical stratospheric aerosol size distributions and from stratospheric aerosol size distributions measured by a wire impactor before and after the eruption of El Chichon. In general, retrieved moments have been found to agree well with the moments of the input size distributions. Additionally, the routine has been used to infer the third moment (volume) from selected measurements taken by the SAGE II sensor during a single April 1985 sunrise event. These moment inferences agree within the measurement and retrieval uncertainties with corresponding moments inferred using a conversion ratio technique.

6. ACKNOWLEDGEMENT

This research was supported by the National Aeronautics and Space Administration under Contract NAS1-16393.

7. REFERENCES

Box, M. A. and S. Lo, 1976: Approximate determination of aerosol size distributions. J. Appl. Meteor., 15, 1068-1076.

Herman, B. M., S. R. Browning and J. R. Reagan, 1971: Determination of aerosol size distributions from lidar measurements. J. Atmos. Sci., 28, 763-771.

King, M. D., D. M. Byrne, B. M. Herman and J. R. Reagan, 1978: Aerosol size distributions obtained by inversion of spectral optical depth measurements. J. Atmos. Sci., 35, 2153-2167.

Russell, P. B., T. J. Swissler, M. P. McCormick, W. P. Chu, J. M. Livingston and T. J. Pepin, 1981: Satellite and correlative measurements of the stratospheric aerosol. I: An optical model for data conversions. J. Atmos. Sci., 38, 1279-1294.

Twomey, S. and H. B. Howell, 1967: Some aspects of the optical estimation of microstructure in fog and cloud. Appl. Opt., 6, 2125-2131.

Twomey, S., 1974: Information content in remote sensing. Appl. Opt., 13, 942-945.

PROCEEDINGS OF THE FIRST SINO-AMERICAN WORKSHOP ON

MOUNTAIN METEOROLOGY

EDITORS

Elmar R. Reiter, Zhu Baozhen and Qian Yongfu

Beijing, China

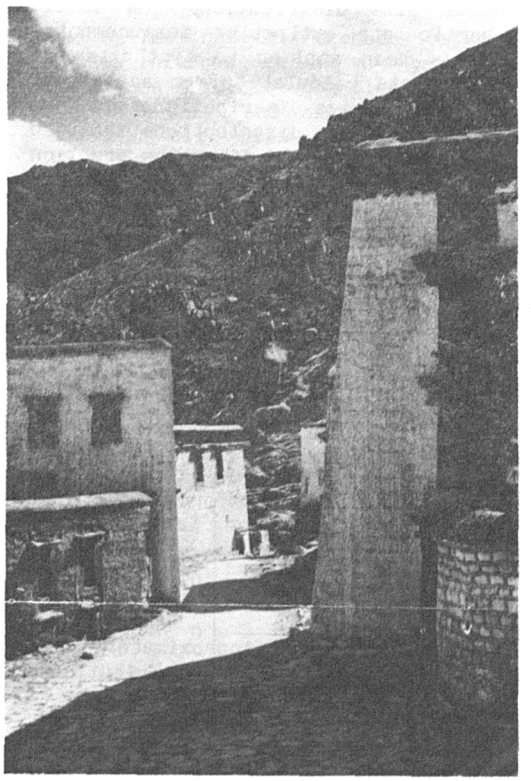

山地气象学

Proceedings of the First Sino-American Workshop on Mountain Meteorology sponsored by the Chinese Academy of Sciences and the U.S. National Academy of Sciences, held during May 18-23, 1982 in Beijing, China, have been published by the Science Press (Beijing, China).

The book includes both theoretical and applied aspects of the physical and dynamical processes involved in mountain meteorology. A perusal of this volume with its analysis of recent research and development and the latest observational techniques will provide the reader with a focus for future exploration, study, and major efforts.

Mountains of various scales on earth exert an important effect on regional weather and climate, and can also have significant and far-reaching effects on weather events and the general circulation on a global basis.

The weather and climate in China is greatly affected by the Tibetan Plateau just as the weather and climate in the United States is greatly affected by the Rocky Mountains. Thirty-two papers represent three important subjects, namely: (1) the dynamic and thermal effects of the Tibetan Plateau and Rocky Mountains on the general circulation in the Northern Hemisphere, (especially the effects on occurrence and development of the Asian summer monsoon); and on the numerical models with large scale topography included; (2) the effects of the varied-scale topography on the occurrence and development of heavy rainfalls and local severe storms; the effects of the Rocky Mountains on genesis and outbreak of local severe storms and tornadoes; and the effects of the Andes and the Alps on the genesis, development and movement of extratropical cyclones; and (3) the mountain-valley circulation and their effects on some meteorological fields.

The book will be of special interest to meteorologists, theoreticians, research workers, meteorology students/teachers, and weather forecasters. Also, those scientists working in the fields of hydrology, hydrometeorology, and geography will find it pertinent.

Session Topics:

**Planetary and Large-Scale Effects of Mountains on General Circulation and Climate: Observational Aspects*

**Planetary and Large-Scale Effects of Mountains on General Circulation and Climate: Theoretical Aspects*

**Planetary and Large-Scale Effects of Mountains on General Circulation and Climate: Numerical Modelling*

**Mesoscale Effects of Mountains on Heavy Rainfall and Severe Local Storms: Observational Aspects*

**Mountain-Valley Circulations and Their Effects on Meteorological Fields*

699 Pages—Hardcover
Published—1984
Price—$42.50
(Plus $2.00 postage & handling)

Send order and remittance to:

AMERICAN METEOROLOGICAL SOCIETY
45 Beacon St., Boston, MA 02108

SELECTED LIST OF WMO PUBLICATIONS

The American Meteorological Society (AMS), as part of its objectives to disseminate knowledge in the atmospheric and related oceanic and hydrologic sciences, has been distributing WMO publications to residents of Canada and the United States during this past year. The AMS would like to take this opportunity to thank you for the encouraging response to this new endeavor. We look forward to your continued support during the coming months. Announcements of new and currently available publications will be made in forthcoming issues of The Bulletin.

All prices listed below are quoted in U.S. Dollars. (Availability and prices are subject to change without notice.) Orders and inquiries from residents of U.S.A. and Canada should be directed to: American Meterological Society, Attn: WMO Publication Center, 45 Beacon Street, Boston, MA 02108, U.S.A. Remittance must accompany all orders; only after receipt of payment will the order be processed. Add $3.00 per book for postage and handling. Payment from Canadian clients must be made by a draft on a U.S. Bank or by International Money Order. Checks or money orders should be made payable to the AMS in U.S. dollars. Residents of all other countries should direct orders and inquiries to: World Meteorological Organization, Publications Sales Unit, P.O. Box No. 5, CH-1211 Geneva 20, Switzerland.

WMO Bulletin - Quarterly Subscription

Number of Years	Surface Mail	Airmail
1	$ 48.00	$ 66.00
2	78.00	107.00
3	109.00	150.00

WMO 5 - Composition of the WMO - Quarterly Subscription

Number of Years	Surface Mail	Airmail
1	$ 60.00	$ 77.00
2	110.00	145.00
3	150.00	200.00
Single issue	17.00	20.00

WMO No.		*$ Unit Price*
Atlases		
Climatic Atlas of Europe. Volume I: Maps of Mean Temperature and Precipitation		$150.00
Climatic Atlas of South America. Volume I: Maps of Mean Temperature and Precipitation		175.00
Climatic Atlas of North and Central America. Volume I: Maps of Mean Temperature and Precipitation		150.00
Climatic Atlas of Asia. Volume I: Maps of Mean Temperature and Precipitation		180.00
International Cloud Atlas, Abridged Edition, 1956		36.00
International Cloud Album for Observers in Aircraft, 1956		9.00
Basic Documents		
15 - Basic Documents No. 1 - (Excluding Technical Regulations), 2nd Edition, 1984		$30.00
60 - Basic Documents No. 3 - Agreements and Working Arrangements with other International Organizations, 1983		18.00
Technical Regulations		
49 - Technical Regulations - Basic Documents No. 2 (loose leaf; requires one cover)		
Vol. I General, 2nd Edition, 1984		$25.00
Vol. II Meteorological Services for International Air Navigation, 1976		OOP**
Vol.III Hydrology, 1979		12.00
Cover		8.00
555 - Technical Regulations - Hydrology and International Hydrological Codes, 1980		20.00
558 - Manual on Marine Meteorological Services, 1981		20.00
Weather Reporting: Stations, Data Processing and Transmissions		
9 - Weather Reporting		
Vol. A Observing Stations: Basic Volume:		$115.00
Subscription to Supplement Service (Bi-Annual):	surface mail	134.00
	airmail	140.00
Vol. B Data Processing: Basic Volume:		60.00
Subscription to Supplement Service (Bi-Annual):	surface mail	30.00
	airmail	37.00
Vol. C Transmissions: Basic Volume:		125.00
Subscription to Supplement Service (Bi-Monthly):	surface mail	132.00
	airmail	160.00
Vol. D Information for Shipping: Basic Volume:		150.00
Subscription to Supplement Service (Bi-Monthly):	surface mail	96.00
	airmail	120.00
Covers for Basic Volumes:		
Vol. A and B (each require 1 cover)		16.00
Vol. C (requires 4 covers)		16.00
Vol. D (requires 3 covers)		8.00

***Currently out of stock and unavailable from AMS or WMO*

American Meteorological Society, 45 Beacon St., Boston, Mass. 02108

WMO No.		$ Unit Price

Operational Manuals

306 - *Manual on Codes*		
Vol. I International Codes, 1984 Edition	(w/out cover)	$80.00
	(w/cover)	90.00
Vol. II Regional Codes and National Coding Practices, 1982 Edition	(w/out cover)	40.00
	(w/cover)	50.00
485 - *Manual on the Global Data-Processing System* (Vol. I and II one binder)		32.00
Vol. I Global Aspects, 1977		
Vol. II Regional Aspects, 1980		
491 - *International Operations Handbook for Measurement of Background Atmospheric Pollution*, 1978		30.00
544 - *Manual on the Global Observing System* (Vol. I and II one binder), 1981		20.00

Guides

8 - *Guide to Meteorological Instruments and Observing Practices*, 5th Edition, 1983	$38.00
100 - *Guide to Climatological Practices*, 2nd Edition, 1983	35.00
114 - *Guide to Qualifications and Training of Meteorological Personnel Employed in the Provision of Meteorological Services for International Air Navigation*, 1974	12.00
134 - *Guide to Agricultural Meteorological Practices*, 2nd Edition, 1981	25.00
168 - *Guide to Hydrological Practices* -	
Vol. I Data Acquisition and Processing, 1981	33.00
Vol. II Analysis, Forecasting and other Applications, 1983	40.00
305 - *Guide on the Global Data-Processing System*, 1982	21.00
471 - *Guide to Marine Meteorological Services*, 2nd Edition, 1982	26.00
488 - *Guide on the Global Observing System*, 1977	42.00
623 - *Guide to the IGOSS Data-Processing and Services System*, 1983	5.00
636 - *Guide on the Automation of Data-Processing Centers*, 1985	20.00

Training Manuals

240 - *Compendium of Training Facilities for Meteorology and Operational Hydrology*, 6th Edition, 1982	$50.00
258 - *Guidelines for Education and Training of Personnel in Meteorology and Operational Hydrology*, 3rd Edition, 1984	25.00
266 - *Compendium of Lecture Notes for Training Class IV Meteorological Personnel*	
Vol. I Earth Science, 1970	20.00
Vol. II Meteorology, 2nd Edition, 1984	33.00
364 - *Compendium of Meteorology for use by Class I and II Meteorological Personnel*	
Vol. I Part 1 Dynamic Meteorology, 1973	35.00
Part 2 Physical Meteorology, 1973	25.00
Part 3 Synoptic Meteorology, 1978	32.00
Vol. II Part 1 General Hydrology, 1977	10.00
Part 2 Aeronautical Meteorology, 1978	14.00
Part 3 Marine Meteorology, 1979	11.00
Part 4 Tropical Meteorology, 1979	30.00
Part 5 Hydrometeorology, 1985	13.00
Part 6 Air Chemistry and Air Pollution Meteorology, 1985	20.00
432 - *Proceedings of the WMO/IAMAP Symposium on Education and Training in Meteorology and Meteorological Aspects of Environmental Problems (Caracas, February 1975)*; 1975	50.00
489 - *Compendium of Training Facilities in Environmental Problems Related to Meteorology and Operational Hydrology*, 1977	22.00
492 - *Lectures on Forecasting of Tropical Weather, Including Tropical Cyclones, with Particular Relevance to Africa. Proceedings of WMO Seminar, Dakar November 1976*; 1977	42.00
493 - *Proceedings of the Meeting on Education and Training in Meteorological Aspects of Atmospheric Pollution and Related Environmental Problems. Research Triangle Park, U.S.A., January-February 1977*; 1977	40.00
593 - *Lecture Notes for Training Class IV Agricultural Meteorological Personnel*, 1982	14.00
634 - *Guidelines for Comprehensive Data-Processing in Operational Hydrology and Land Water Management*	*
622 - *Compendium of Lecture Notes on Meteorological Instruments for Class II and Class IV Personnel*, 1985	*

Operational Hydrology Reports

337 - *Automatic Collection and Transmission of Hydrological Observations*, O.H.R. 2; 1973	$15.00
341 - *Benefit and Cost Analysis of Hydrological Forecasts. A State-of-the-Art Report*, O.H.R. 3; 1973	12.00
419 - *Meteorological and Hydrological Data Required in Planning and Development of Water Resources*, O.H.R. 5; 1975	10.00
425 - *Hydrological Forecasting Practices*, O.H.R. 6; 1975	21.00

* *In preparation*

American Meteorological Society, 45 Beacon St., Boston, Mass. 02108

WMO No.	$ Unit Price

Operational Hydrology Reports (cont'd)

433 - *Hydrological Network Design and Information Transfer. Proceedings of the International Seminar, Newcastle upon Tyne, U.K., August 1974*, O.H.R. 8; 1976	30.00
461 - *Casebook of Examples of Organization and Operation of Hydrological Services*, O.H.R. 9; 1977	$22.00
476 - *Hydrological Application of Atmospheric Vapour Flux Analyses*, O.H.R. 11; 1977	10.00
513 - *Applications of Remote Sensing to Hydrology*, O.H.R. 12; 1979	10.00
519 - *Manual on Stream Gauging* (2 Vol. set in one binder), O.H.R. 13; 1980	52.00
559 - *Hydrological Data Transmission*, O.H.R. 14; 1981	5.00
560 - *Selection of Distribution Types for Extremes of Precipitation*, O.H.R. 15; 1981	6.00
561 - *Measurement of River Sediments*, O.H.R. 16; 1981	7.00
576 - *Case Studies of National Hydrological Data Banks (Planning, Development and Organization)*, O.H.R. 17; 1981	10.00
577 - *Flash Flood Forecasting*, O.H.R. 18; 1981	6.00
580 - *Concepts and Techniques in Hydrological Network Design*, O.H.R. 19; 1982	6.00
587 - *Long-Range Water-Supply Forecasting*, O.H.R. 20; 1982	6.00
589 - *Methods of Correction for Systematic Error in Point Precipitation Measurement for Operational Use*, O.H.R. 21; 1982	10.00
635 - *Casebook on Operational Assessment of Areal Evaporation*, O.H.R. 22; 1985	17.00

Reports on Marine Science Affairs

499 - *Meteorological Aspects of the Contributions Presented at the Joint Oceanographic Assembly (Edinburgh, September 1976)*, M.S.A. 12; 1978	$10.00
500 - *Present Techniques of Tropical Storm Surge Prediction*, M.S.A. 13; 1978	20.00
548 - *Satellite Data Requirements for Marine Meteorological Services*, M.S.A. 14; 1980	17.00
595 - *The Preparation and Use of Weather Maps by Mariners* (update of T.N. 72), M.S.A. 15; 1982	11.00

Special Environmental Reports

372 - *A Brief Survey of Meteorology as Related to the Biosphere*, S.E.R. 4; 1973	$12.00
403 - *Drought (Lectures from 25th WMO Executive Committee)*, S.E.R. 5; 1975	18.00
440 - *Determination of the Atmospheric Contribution of Petroleum Hydrocarbons to the Ocean*, S.E.R. 6; 1976	16.00
448 - *Weather, Climate and Human Settlements*, S.E.R. 7; 1976	12.00
455 - *The Quantitative Evaluation of the Risk of Disaster from Tropical Cyclones*, S.E.R. 8; 1976	50.00
459 - *An Evaluation of Climate and Water Resources for Development of Agriculture in the Sudano-Sahelian Zone of West Africa*, S.E.R. 9; 1976	40.00
460 - *Report and Proceedings of the WMO Air Pollution Measure Techniques Conference (APOMET), Gothenburg, October 1976*, S.E.R. 10; 1977	35.00
496 - *Systems of Evaluating and Predictng the Effects of Weather and Climate on Wildland Fires*, S.E.R. 11; 1978	10.00
504 - *Implementation Plan for the Determination of the Atmospheric Contribution of Petroleum Hydrocarbons to the Oceans*, S.E.R. 12; 1979	10.00
517 - *Meteorology and the Human Environment - Lectures Presented at the 29th Session of the WMO Executive Committee*, S.E.R. 13; 1979	6.00
563 - *Proceedings of the Symposium on the Development of Multi-Media Monitoring of Environmental Pollution (Riga 1978)*, S.E.R. 15; 1980	45.00
647 - *Papers Presented at the WMO Technical Conference on Observation and Measurements of Atmospheric Contaminants (TECOMAC)*, S.E.R. 16; 1985	53.00

Technical Notes

391 - *Meteorology and the Colorado Potato Beetle*, T.N. 137; 1975	$15.00
392 - *Drought and Agriculture*, T.N. 138; 1975	30.00
394 - *Upper-Air Sounding Studies* (Vols. I and II), T.N. 140; 1975	25.00
400 - *Utilization of Aircraft Meteorological Reports* (Rev. of T.N. 80), T.N. 141; 1975	10.00
423 - *Rice and Weather*, T.N. 144; 1975	12.00
424 - *Economic Benefits of Climatological Services*, T.N. 145; 1975	15.00
426 - *Cost and Structure of Meteorological Services with Special Reference to the Problem of Developing Countries*, T.N. 146; 1975	18.00
431 - *Review of the Present Knowledge of Plant Injury by Air Pollution*, T.N. 147; 1976	12.00
436 - *Controlled Climate and Plant Research*, T.N. 148; 1976	12.00
438 - *Urban Climatology and its Relevance to Urban Design*, T.N. 149; 1976	15.00
441 - *Application of Building Climatology to Problems of Housing and Building for Human Settlements*, T.N. 150; 1976	16.00
458 - *Crop-Weather Models and Their Use in Yield Assessments*, T.N. 151; 1977	18.00
467 - *Radiation Regime of Inclined Surfaces*, T.N. 152; 1977	18.00
478 - *The Scientific Planning and Organization of Precipitation Enhancement Experiments, with Particular Attention to Agricultural Needs*, T.N. 154; 1977	10.00

WMO No.	$ Unit Price

Technical Notes (cont'd)

482 - *Forecasting Techniques of Clear Air Turbulence Including that Associated with Mountain Waves*, T.N. 155; 1977	10.00
487 - *Techniques of Frost Prediction and Methods of Frost and Cold Protection*, T.N. 157; 1978	35.00
495 - *Handbook of Meteorological Forecasting for Soaring Flight*, T.N. 158; 1978	$18.00
497 - *Weather and Parasitic Animal Disease*, T.N. 159; 1978	30.00
498 - *Soya Bean and Weather*, T.N. 160; 1978	20.00
507 - *The Application of Atmospheric Electricity Concepts and Methods to other Parts of Meteorology*, T.N. 162; 1978	20.00
526 - *The Economic Value of Agrometeorological Information and Advice*, T.N. 164; 1980	10.00
530 - *The Planetary Boundary Layer*, T.N. 165; 1980	20.00
532 - *Meteorological Factors Affectng the Epidemiology of the Cotton Leaf Worm and Pink Bollworm*, T.N. 167; 1980	10.00
536 - *The Role of Agrometeorology in Agricultural Development and Investment Projects*, T.N. 168; 1980	10.00
550 - *Meteorological and Hydrological Aspects of Siting and Operation of Nuclear Power Plants*, T.N. 170	
Vol. I Meteorological Aspects, 1985	•
Vol. II Hydrological Aspects, 1981	25.00
554 - *Fog and Reduced Visability Due to Fog at Aerodromes*, T.N. 171; 1985	•
557 - *Meteorological Aspects of the Utilization of Solar Radiation as an Energy Source + Annex: World Maps of Relative Global Radiation*, T.N. 172; 1981	45.00
566 - *The Effect of Meteorological Factors on Crop Yields and Methods of Forecasting the Yield*, T.N. 174; 1982	7.00
575 - *Meteorological Aspects of the Utilization of Wind as an Energy Source*, T.N. 175; 1981	36.00
583 - *Tropospheric Chemistry and Air Pollution*, T.N. 176; 1982	14.00
581 - *Review of Atmospheric Diffusion Models for Regulatory Applications*, T.N. 177; 1982	7.00
591 - *Meteorological Aspects of Certain Processes Affectng Soil Degradation - Especially Erosion*, T.N. 178; 1983	51.00
597 - *A Study of Agroclimatology of the Humid Tropics of South-East Asia*, T.N. 179; 1982	40.00
620 - *Weather-Based Mathematical Models for Estimating Development and Ripening of Crops*, T.N. 180; 1983	12.00
625 - *Use of Radar in Meteorology*, T.N. 181; 1985	*
629 - *Analysis of Data from International Experiments on Lucerne*, T.N. 182; 1985	*
630 - *Severe Convective Weather in Relation to Inflight Phase*, T.N. 183; 1985	*
633 - *Land-Use and Agro-System Management Under Severe Climatic Conditions*, T.N. 184; 1985	*
641 - *Meteorological Observations using NAVAID Methods*, T.N. 185; 1985	*
494 - *The Role of Satellites in WMO Programmes in the 1980's*, W.W.W. 36; 1977	$41.00
528 - *World Weather Watch - WMO Tropical Cyclone Project - Sub Project No. 6 - Operational Techniques for Forecasting Tropical Cyclone Intensity and Movement*, 1979	40.00
535 - *World Weather Watch - The Plan and Implementation Programme 1980-1983*; 1979	25.00
553 - *Conversion of Grid-Point Data into Meteorological Maps with a Mini-Computer System*, W.W.W. 37; 1980	5.00
617 - *World Weather Watch - The Plan and Implementation Programme (1984-1987)*; 1983	15.00

World Weather Watch Status Reports

601 - *World Weather Watch - 11th Status Report on Implementation*, 1982	$25.00
639 - *World Weather Watch - 12th Status Report on Implementation*, 1984	25.00

General Reference Publications

2 - *Meteorological Services of the World*, 1985	$50.00
47 - *International List of Selected, Supplementary and Auxilliary Ships*, 1985	37.00
174 - *Catalogue of Meteorological Data for Research*	
Part I Published Synoptic and Climatological Data, 1965	30.00
Part II Meteorological stations with Observational Series Extending over 80 years or more, 1970	20.00
Part III Meteorological Data Recorded on Media Usable by Automatic Data-Processing Machines, 1972	50.00
Part IV Sources of Additional Data Needed for Research on Climatic Change, 1979	17.00
259 - *WMO Sea-Ice Nomenclature*, 1970 (Vol. I and II one binder)	50.00
Vol. I Terminology and Codes	
Vol. II Illustrated Glossary	

Publications of General Interest

385 - *International Glossary of Hydrology*, 1974	$40.00
420 - *Proceedings of a WMO Technical Conference on Automated Meteorological Systems (TECAMS), Washington, D.C., February 1975*; 1975	58.00

• *In preparation*

American Meteorological Society, 45 Beacon St., Boston, Mass. 02108

WMO No.		$ Unit Price

Publications of General Interest (cont'd)

463	- *Weather and Water*, 1977	5.00
469	- *International Global Data-Processing System Plan to Support the 1st GARP Global Experiment (WWW)*, 1977	18.00
477	- *Solar Energy. Proceedings of the WMO/UNESCO Symposium, Geneva, August-September 1976*; 1977	$50.00
481	- *Proceedings of the Symposium on the Agrometeorology of the Maize (Corn) Crop, July 1976*; 1977	55.00
510	- *Papers Presented at the WMO Symposium on Boundary Layer Physics Applied to Specific Problems of Air Pollution (Norrkoping, June 1978)*; 1978	35.00
523	- *The Atmospheric Boundary Layer*, 1979	20.00
537	- *Proceedings of the World Climate Conference - A Conference of Experts on Climate and Mankind, Geneva, February 1979*; 1979	40.00
542	- *Climatic Changes and Their Effects on the Biosphere*, 1980	30.00
543	- *Man and Climatic Variability*, 1980	3.00
570	- *Automatic Weather Stations for Tropical Cyclone Areas*, 1981	15.00
573	- *Typhoon Operational Experiment - A General Description (TOPEX Report No. 3)*, 1981	7.00
574	- *Sea-Ice Information Services in the World*, 1981	15.00
578	- *Proceedings of the Technical Conference on Climate - Asia and West Pacific (Guangzhou, China, 15-20 December 1980)*; 1981	28.00
582	- *Integrated Global Ocean Services Systems - General Plan and Implementation Programme 1982-1985*, 1982	6.00
585	- *Satellites in Meteorology, Oceanography and Hydrology*, 1982	5.00
596	- *Proceedings of the Technical Conference on Climate - Africa (Arusha, 25-30 January 1982)*; 1982	35.00
608	- *Twentieth Anniversary of the World Weather Watch - Opportunities and Outlook for Improved World Weather Watch*, 1983	11.00
616	- *First WMO Long-Term Plan Part I: Overall Policy and Strategy (1984-1993)*; 1983	11.00
624	- *Meteorology Aids Food Production*, 1985	4.00
627	- *The Next Decade Meteorology and Operational Hydrology in the Service of Mankind - A Policy for Advancement*, 1985	5.00
632	- *Proceedings of the Climate Conference for Latin America and the Carribean 1983*; 1984	37.00
637	- *Meteorology and Public Safety*, 1985	4.00
643	- *Meteorology and Society*, 1985	9.00

Commission, Congress, Executive and Annual Reports

508	- *Resolutions of Congress and Executive Committee*, 1985	$35.00
547	- *8th World Meteorological Congress - Proceedings*, 1980	30.00
568	- *Scientific Lectures Presented at the 8th World Meteorological Congress, Geneva 1979*; 1981	11.00
590	- *Commission for Instruments and Methods of Observation - Abridged Final Report of the 8th Session (1981)*; 1982	20.00
598	- *Commission for Atmospheric Sciences - Abridged Final Report of the 8th Session*, 1982	25.00
599	- *WMO Executive Committee 34th Session - Abridged Report with Resolutions*, 1982	25.00
602	- *Commission for Aeronautical Meteorology - Abridged Final Report of the 7th Session*, 1982	25.00
603	- *Long-Range Transport of Sulphur in the Atmosphere and Acid Rain - Lectures Presented at the 33rd Session of the WMO Executive Committee*, 1983	8.00
606	- *Consolidated Report on the Voluntary Co-operation Programme Including Projects Approved for Circulation in 1982-1983*; 1983	15.00
609	- *Annual Report of the World Meteorological Organization, 1982-83*; 1983	25.00
611	- *Commission for Basic Systems - Abridged Final Report of the 8th Session*, 1983	25.00
614	- *Scientific Lectures Presented at the 9th World Meteorological Congress, Geneva 1983*; 1985	10.00
615	- *Ninth World Meteorological Congress - Abridged Report with Resolutions*, 1983	30.00
619	- *WMO Executive Council 35th Session - Abridged Final Report with Resolutions*, 1983	25.00
628	- *Annual Report of the World Meteorological Organization (1983)*; 1984	25.00
638	- *Commission for Hydrology (CHY) - Abridged Final Report of the 7th Session*, 1985	25.00
640	- *Commission for Marine Meteorology (CMM) - Abridged Final Report of the 9th Session*, 1985	25.00
644	- *Annual Report of the World Meteorological Organization (1984)*; 1985	25.00
648	- *WMO Executive Committee 36th Session - Abridged Final Report with Resolutions*, 1984	25.00
649	- *Scientific Lectures Presented at the 36th Session of the WMO Executive Committee*, 1984	*
651	- *Commission for Instrument and Methods of Observation - Abridge Final Report of the 9th Session (1982)*	*

Reports of Sessions of Regional Associations

594	- *Regional Association III (South America) - Abridged Final Report of 8th Session*, 1982	$20.00
604	- *Regional Association V (South-West Pacific) - Abridged Final Report of the 8th Session (1982)*; 1983	25.00

* *In preparation*

American Meteorological Society, 45 Beacon St., Boston, Mass. 02108

WMO No.		$ Unit Price

Reports of Sessions of Regional Associations (cont'd)

	; 1983	25.00
605 - *Regional Association VI (Europe) - Abridged Final Report of the 8th Session (1982)*	1983	25.00
607 - *Regional Association I (Africa) - Abridged Final Report of the 8th Session (1982)*	1985	25.00
642 - *Regional Association II (Asia) - Abridged Final Report of the 8th Session (1982)*		

Garp Special Reports

Report of the Seminar on Progress in Diagnostic Studies of the Global Atmospheric Circulation as a Result of the Global Weather Experiment (August 1984), No. 42; 1985	$27.00
Report of the Seminar on Progress in Numerical Modelling and the Understanding of Predictability as a Result of the Global Weather Experiment (October 1984), No. 43, 1985	27.00
Report of the Seminar on Progress in Tropical Meteorology as a Result of the Global Weather Experiment (October 1984), No. 44; 1985	40.00

ALPHABETICAL LIST OF OUT OF PRINT PUBLICATIONS

The AMS has a limited supply of the following WMO publications. These titles are considered out of print and are only available from the AMS. Orders for these publications will be processed on a "first come first serve" basis. Unprocessed orders will be returned promptly.

208 - *A Note on Climatological Normals*, T.N. 84; 1967	$ 5.00
355 - *Airflow Over Mountains Research*, 1973	27.00
378 - *An Introduction to Agrotopoclimatology*, T.N. 133; 1974	25.00
413 - *Applications of Satellite Data to Aeronautical Meteorology*, 1975	32.00
249 - *Artificial Modification of Clouds and Precipitation* , T.N. 105; 1969	8.00
*** - *Beaufort Scale of Wind Force (Technical & Operational Aspects)*, M.S.A. 3; 1970	5.00
612 - *Commission for Agricultural Meteorology - Abridged Final Report 8th Session*; 1983	25.00
600 - *Commission for Climatology & Application of Meteorology - Abridged Report 8th Session*; 1983	25.00
282 - *Commission for Hydrological & Meteorological Services - Abridged Final Report*, 1970	8.00
584 - *Commission for Marine Meteorology - Abridged Final Report of 8th Session*; 1981	5.00
512 - *Compatability of Upper Air Data*, T.N. 163; 1978	20.00
434 - *Compendium of Lecture Notes in Marine Meteorology for Class III and Class IV Personnel*, 1976	25.00
240 - *Compendium of Training Facilities for Meteorology & Operational Hydrology* 5th Edition , 1980	40.00
588 - *Consolidated Report on the Voluntary Co-Operation Program Including Projects Approved in 1981*; 1982	15.00
359 - *Environmental Factors in Operations to Combat Oil Spills*, M.S.A. 9; 1973	5.00
233 - *Estimation of Maximum Floods*, T.N. 98; 1969	45.00
565 - *First Planning Meeting for TOPEX, Report No. 1*; 1980	10.00
*** - *Global Ocean Research Report*, M.S.A. 1; 1970	5.00
159 - *High Level Forecasting for Turbine Engined Aircraft Operations Over Africa & Middle East*, T.N. 64; 1964	24.00
257 - *How to Become a Meteorologist*, 1970	2.75
475 - *Information on the Application of Meteorological Satellite Data in Routine Operations and Research*, 1977	34.00
429 - *Intercomparison of Conceptual Models Used in Operational Hydrological Forecasting*, O.H.R. 7; 1975	22.00
491 - *International Operations Handbook for Measurement of Background Atmospheric Pollution*, 1978	30.00
551 - *Lecture Notes for Training Class II and Class III Agricultural Meteorological Personnel*, 1980	18.00
332 - *Manual For Estimation of Probable Maximum Precipitation*, O.H.R. 1; 1973	20.00
197 - *Manual on Meteorological Observing in Transport Aircraft*, 1st Edition, 1966	4.00
225 - *Measurement of Peak Discharge by Indirect Methods*, T.N. 90; 1968	10.00
251 - *Meteorological Aspects of Air Pollution*, 1970	12.00
243 - *Meteorology and Grain Storage*, T.N. 101; 1969	10.00
138 - *Meteorology and the Migration of Desert Locusts*, T.N. 54; 1963	25.00
226 - *Methods In Use For The Reduction of Atmospheric Pressure*, T.N. 91; 1981	10.00
427 - *Modern Developments in Hydrometry, Vol. II - Papers Submitted by Authors and Discussion of Introductory Reports and Papers* (Vol. I out of print and out of stock), 1976	16.00
388 - *Mulching Effects on Plant Climate and Yield*, T.N. 136; 1975	20.00
549 - *Papers Presented at the WMO Tech. Conference on Regional and Global Observation of Atmospheric Pollution Relative to Climate*, S.E.R. 14; 1980	31.00
133 - *Protection Against Frost Damage*, T.N. 51; 1963	11.00

****Order By Title*

American Meteorological Society, 45 Beacon St., Boston, Mass. 02108

WMO No.		$ Unit Price
Out of Print Publications (cont'd)		
524	- *Regional Association IV (North & Central America) - Hurricane Operational Plan*; 1979	23.00
586	- *Regional Association IV (North & Central America) - Abridged Final Report 8th Session*; 1982	25.00
383	- *Review of Urban Climatology 1968-1973*, T.N. 134; 1974	25.00
539	- *Review of Urban Climatology 1973-1976*, T.N. 169; 1979	10.00
283	- *Satellite and Computer Applications to Synoptic Meteorology*, 1971	15.00
312	- *Selected Papers on Meteorology as Related To the Human Environment*, S.E.R. 2; 1971	30.00
199	- *Some Methods of Climatological Analysis*, T.N. 81; 1966	9.00
178	- *Statistical Analysis and Prognosis in Meteorology*, T.N. 71; 1966	41.00
231	- *The Measurement of Atmospheric Radioactivity*, T.N. 94; 1968	30.00
618	- *Tropical Cyclone Operational Plan for the South West Indian Ocean*, 1983	18.00
450	- *WMO Symposium on the Interpretation of Broadscale NWP Products for Local Forecasting Purposes, Warsaw, 11-16 October 1976*; 1976	30.00
399	- *WMO/IAMAP Scientific Conference on Weather Modification, Tashkent, 1-7 October 1973*; 1974	50.00
162	- *WMO/IUGG Symposium on Research & Development Aspects of Long-range Forecasting*, T.N. 66; 1965	40.00
562	- *Weather and Airborne Organisms*, T.N. 173; 1980	12.00
113	- *Weather and Food* (Freedom from Hunger Campaign, Basic Study No. 1), 1962	2.00
533	- *World Meteorological Congress - Abridged Report with Resolutions, 8th Session*; 1979	45.00

Announcing the tenth edition. . .

Curricula in the Atmospheric, Oceanic, and Related Sciences: 1984

This new and expanded version of the Society-sponsored series of biennial reports on academic curricula surveying U.S. and Canadian colleges and universities offering degrees or majors in the atmospheric sciences, physical or dynamical oceanography, and hydrology is cosponsored by the University Corporation for Atmospheric Research.

The report includes information for 99 schools on academic and key research personnel, types of degrees granted, undergraduate and/or graduate courses and credits, types of financial support, research programs and their principal investigators, numbers of degrees granted, and descriptions of special facilities. A summary consolidation of key data is included.

The educational and reference information contained in this volume is an indispensable resource to prospective students, to those involved in career planning and counseling, and to the entire atmospheric, oceanographic, and hydrologic community.

Colleges and Universities in the United States and Canada

ISBN 0-933876-59-9

Over 350 pages—price $12.00

(add $2.00 postage/handling)

Send orders and remittance to:

American Meteorological Society
45 Beacon Street, Boston, MA 02108

A FIELD GUIDE TO THE ATMOSPHERE

VINCENT J. SCHAEFER / JOHN A. DAY

THE PETERSON FIELD GUIDE SERIES

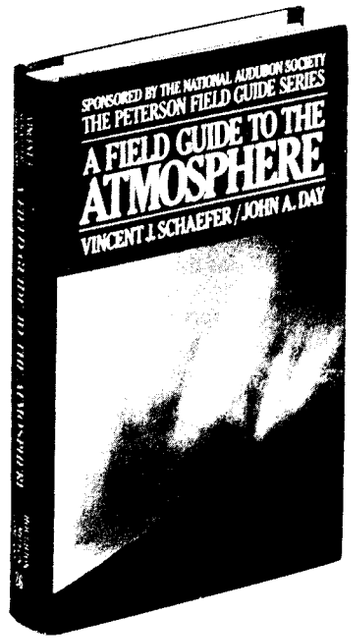

A unique guide to the skin of air that surrounds the earth and to the phenomena that can be observed there — air pollution and tropical storms, cumulus clouds and contrails, mist and graupel.

This book tells how to judge the condition of the atmosphere — and forecast the weather — by watching the shapes of clouds, the color of the sky, and the visibility of landmarks. It tells how to photograph clouds from an airplane, how to make clouds in a freezer, and how to catch a snowflake's image in a bit of plastic.

Chapters on unusual clouds, severe storms, color in the atmosphere, particles in the atmosphere, precipitation, weather modification, and simple experiments that can be performed in any home make this *Field Guide* a brilliant introduction to meteorology.

March 1981
Nonfiction/Nature
384 pp. 4½ x 7¼
32 color photographs,
337 b/w photographs
53 line drawings
ISBN 24080-8

$13.95 add $1.00 postage

Send order and remittance to:

American Meteorological Society
45 Beacon St., Boston, Mass. 02108

AMERICAN METEOROLOGICAL SOCIETY

SINCE 1919

serving an international membership in the atmospheric and related hydrospheric sciences

PROFESSIONAL SERVICES

ACTIVITIES

EDUCATION

MEMBERSHIP

YOU AND AMS

YOU AND AMS

MEMBERSHIP IN THE AMS MEANS THAT . . . .

YOU can keep abreast of the latest techniques and developments in the atmospheric sciences and related fields in industry, government, education and private meteorology.

YOU can participate in and attend local chapter meetings, national conferences and specialized symposia thus contributing and gaining in knowledge and stature.

YOU can receive the various quality journals and publications of the AMS at a reduced rate.

YOU can receive job opportunity listings.

YOU can obtain guidance material and expert counsel.

YOU can associate with fellow meteorologists and other distinguished scientists and develop lasting professional and personal friends.

YOU can continue your technical education and keep pace with scientific advancement.

YOU can provide leadership for students, the scientific community, the public and AMS.

YOU can support and contribute to the major programs that lead to scientific progress and educational development of the world.

WHETHER YOUNG OR EXPERIENCED . . . . .

AMS NEEDS YOU

Write for an application:

American Meteorological Society
45 Beacon Street
Boston, MA 02108